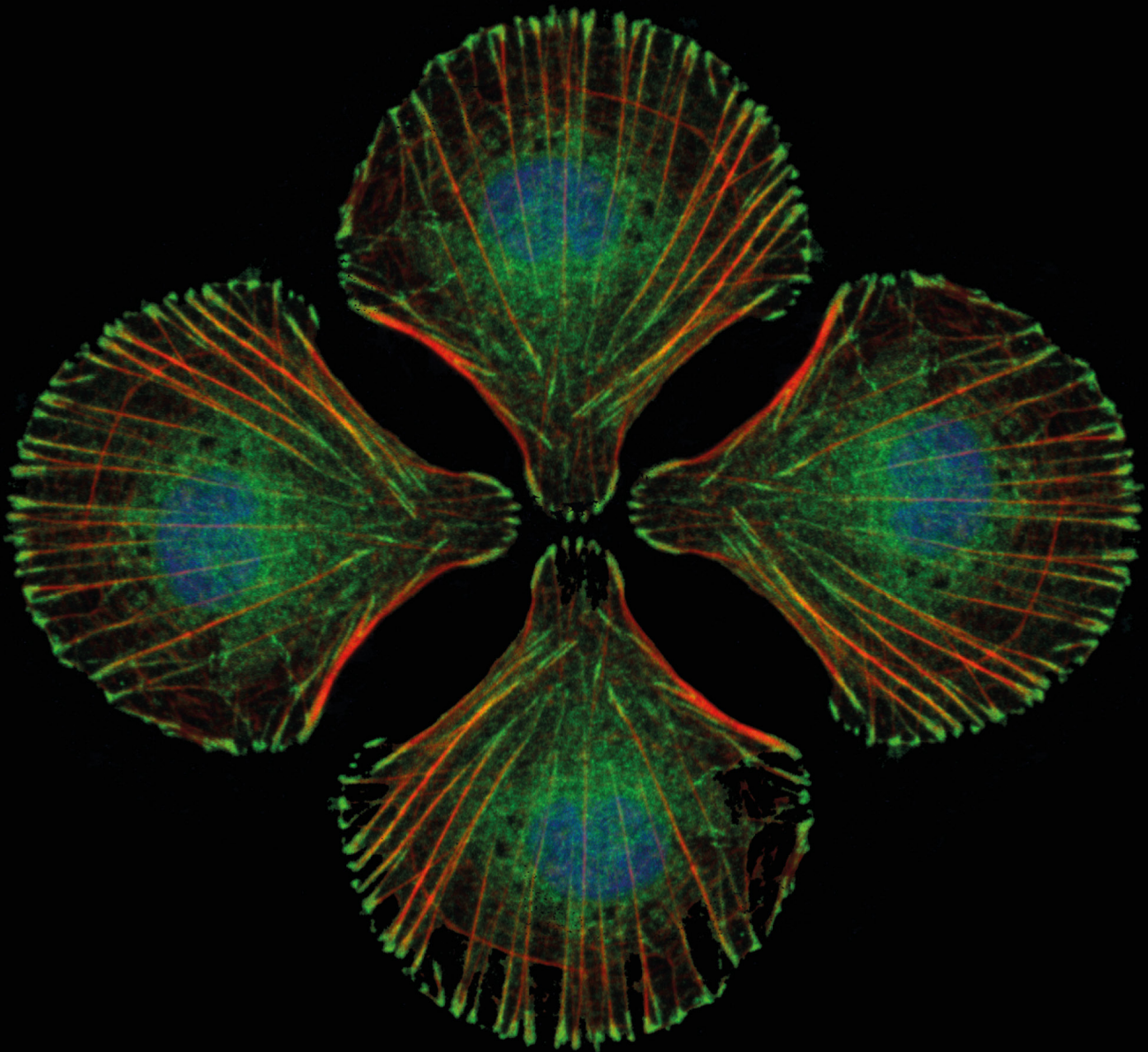


# PHYSICO-CHEMICAL CONTROL OF CELL FUNCTION

EDITED BY: Cesare Gargioli, Giancarlo Forte and Alberto Rainer  
PUBLISHED IN: Frontiers in Physiology





# frontiers

## Frontiers Copyright Statement

© Copyright 2007-2019 Frontiers Media SA. All rights reserved.

All content included on this site, such as text, graphics, logos, button icons, images, video/audio clips, downloads, data compilations and software, is the property of or is licensed to Frontiers Media SA ("Frontiers") or its licensees and/or subcontractors. The copyright in the text of individual articles is the property of their respective authors, subject to a license granted to Frontiers.

The compilation of articles constituting this e-book, wherever published, as well as the compilation of all other content on this site, is the exclusive property of Frontiers. For the conditions for downloading and copying of e-books from Frontiers' website, please see the Terms for Website Use. If purchasing Frontiers e-books from other websites or sources, the conditions of the website concerned apply.

Images and graphics not forming part of user-contributed materials may not be downloaded or copied without permission.

Individual articles may be downloaded and reproduced in accordance with the principles of the CC-BY licence subject to any copyright or other notices. They may not be re-sold as an e-book.

As author or other contributor you grant a CC-BY licence to others to reproduce your articles, including any graphics and third-party materials supplied by you, in accordance with the Conditions for Website Use and subject to any copyright notices which you include in connection with your articles and materials.

All copyright, and all rights therein, are protected by national and international copyright laws.

The above represents a summary only. For the full conditions see the Conditions for Authors and the Conditions for Website Use.

ISSN 1664-8714

ISBN 978-2-88945-998-8

DOI 10.3389/978-2-88945-998-8

## About Frontiers

Frontiers is more than just an open-access publisher of scholarly articles: it is a pioneering approach to the world of academia, radically improving the way scholarly research is managed. The grand vision of Frontiers is a world where all people have an equal opportunity to seek, share and generate knowledge. Frontiers provides immediate and permanent online open access to all its publications, but this alone is not enough to realize our grand goals.

## Frontiers Journal Series

The Frontiers Journal Series is a multi-tier and interdisciplinary set of open-access, online journals, promising a paradigm shift from the current review, selection and dissemination processes in academic publishing. All Frontiers journals are driven by researchers for researchers; therefore, they constitute a service to the scholarly community. At the same time, the Frontiers Journal Series operates on a revolutionary invention, the tiered publishing system, initially addressing specific communities of scholars, and gradually climbing up to broader public understanding, thus serving the interests of the lay society, too.

## Dedication to Quality

Each Frontiers article is a landmark of the highest quality, thanks to genuinely collaborative interactions between authors and review editors, who include some of the world's best academicians. Research must be certified by peers before entering a stream of knowledge that may eventually reach the public - and shape society; therefore, Frontiers only applies the most rigorous and unbiased reviews.

Frontiers revolutionizes research publishing by freely delivering the most outstanding research, evaluated with no bias from both the academic and social point of view. By applying the most advanced information technologies, Frontiers is catapulting scholarly publishing into a new generation.

## What are Frontiers Research Topics?

Frontiers Research Topics are very popular trademarks of the Frontiers Journals Series: they are collections of at least ten articles, all centered on a particular subject. With their unique mix of varied contributions from Original Research to Review Articles, Frontiers Research Topics unify the most influential researchers, the latest key findings and historical advances in a hot research area! Find out more on how to host your own Frontiers Research Topic or contribute to one as an author by contacting the Frontiers Editorial Office: [researchtopics@frontiersin.org](mailto:researchtopics@frontiersin.org)

# PHYSICO-CHEMICAL CONTROL OF CELL FUNCTION

Topic Editors:

**Cesare Gargioli**, University of Rome Tor Vergata, Italy

**Giancarlo Forte**, International Clinical Research Center (FNUSA-ICRC), Czechia

**Alberto Rainer**, Università Campus Bio-Medico di Roma, Italy

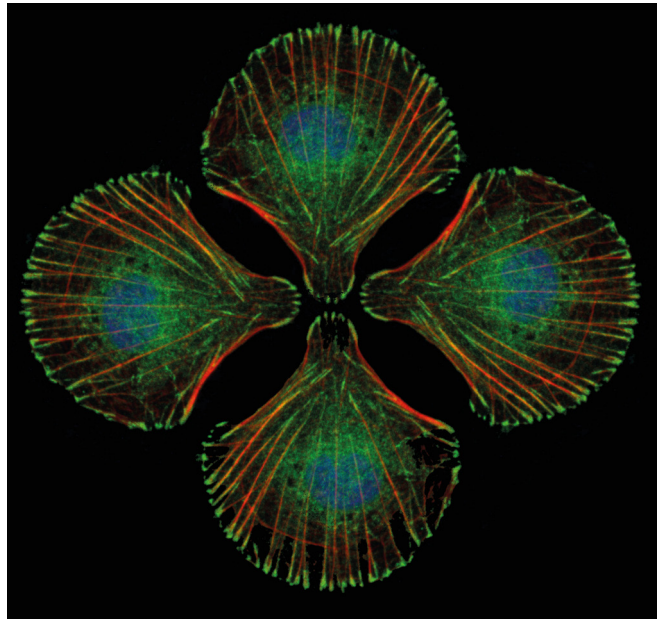


Image credit: Giancarlo Forte

Extracellular Matrix (ECM) has been considered for a long time merely a scaffold sustaining cell and tissue function. Despite this simplistic view shared by many, nowadays ECM and their mechanic-physical and chemical characteristic acquired a progressive larger role actively regulating cell life: survival, proliferation, gene expression and differentiation. The interplay between cells and the ECM is continuously controlled at the cell level in a dynamic way. While cells synthesize the raw components of the ECM, this in turn impacts on cell function by providing chemical, topographical and mechanical hints. Such stimuli have been proven to control several aspects of cell function, including survival, proliferation, differentiation and migration. The molecular pathways activated by cells in response to the physical cues arising from the ECM are being disclosed and thus the possibility to control cell function through materials design is becoming more realistic.

Current in vitro protocols, relying in 2D cell culture system, entail reductionist approaches to the complexity of cell-ECM interaction and result in cells rapidly losing their distinctive functions in culture.

Understanding and replicating the 3D microenvironmental cues affecting cell function appears as a mandatory requirement for the development of next-generation biomaterials, as well as for the establishment of more physiologically relevant and predictive in vitro models of diseases. Such an effort will require a multidisciplinary approach at the convergence of biophysics, biology, nanotechnology, and bioengineering.

**Citation:** Gargioli, C., Forte, G., Rainer, A., eds. (2019). Physico-Chemical Control of Cell Function. Lausanne: Frontiers Media. doi: 10.3389/978-2-88945-998-8

# Table of Contents

- 06 Editorial: Physico-Chemical Control of Cell Function**  
Alberto Rainer, Giancarlo Forte and Cesare Gargioli
- 09 The Effect of Scaffold Modulus on the Morphology and Remodeling of Fetal Mesenchymal Stem Cells**  
Abdul Jalil Rufaihah, Suganya Cheyyatraivendran, Muhammad Danial Mohd Mazlan, Kenrich Lim, Mark Seow Khoon Chong, Citra Nurfarah Zaini Mattar, Jerry Kok Yen Chan, Theodoros Kofidis and Dror Seliktar
- 29 Biomechanical Characterization at the Cell Scale: Present and Prospects**  
Francesco Basoli, Sara Maria Giannitelli, Manuele Gori, Pamela Mozetic, Alessandra Bonfanti, Marcella Trombetta and Alberto Rainer
- 50 Small Force, Big Impact: Next Generation Organ-on-a-Chip Systems Incorporating Biomechanical Cues**  
Ece Ergir, Barbara Bachmann, Heinz Redl, Giancarlo Forte and Peter Ertl
- 58 Integration of in vitro and in silico Models Using Bayesian Optimization With an Application to Stochastic Modeling of Mesenchymal 3D Cell Migration**  
Francisco Merino-Casallo, Maria J. Gomez-Benito, Yago Juste-Lanas, Ruben Martinez-Cantin and Jose M. Garcia-Aznar
- 75 The Importance of Biophysical and Biochemical Stimuli in Dynamic Skeletal Muscle Models**  
Babette Maleiner, Janine Tomasch, Philipp Heher, Oliver Spadiut, Dominik Rünzler and Christiane Fuchs
- 99 Engineering of Human Skeletal Muscle With an Autologous Deposited Extracellular Matrix**  
Lieven Thorrez, Katherine DiSano, Janet Shansky and Herman Vandenburg
- 110 Extracellular Collagen VI has Prosurvival and Autophagy Instructive Properties in Mouse Fibroblasts**  
Silvia Castagnaro, Martina Chrisam, Matilde Cescon, Paola Braghetta, Paolo Grumati and Paolo Bonaldo
- 124 Advanced and Rationalized Atomic Force Microscopy Analysis Unveils Specific Properties of Controlled Cell Mechanics**  
Guido Caluori, Jan Pribyl, Martin Pesl, Jorge Oliver-De La Cruz, Giorgia Nardone, Petr Skladal and Giancarlo Forte
- 135 Drug Repurposing for Duchenne Muscular Dystrophy: The Monoamine Oxidase B Inhibitor Saffinamide Ameliorates the Pathological Phenotype in mdx Mice and in Myogenic Cultures From DMD Patients**  
Libero Vitiello, Manuela Marabita, Elisa Sorato, Leonardo Nogara, Giada Forestan, Vincent Mouly, Leonardo Salviati, Manuel Acosta, Bert Blaauw and Marcella Canton
- 147 Tuning RGD Motif and Hyaluronan Density to Study Integrin Binding**  
Cornelia Zapp, Burcu B. Minsky and Heike Boehm

- 155** *Generation and Neuronal Differentiation of hiPSCs From Patients With Myotonic Dystrophy Type 2*  
Paola Spitalieri, Rosa V. Talarico, Michela Murdocca, Luana Fontana, Marzia Marcaurelio, Elena Campione, Roberto Massa, Giovanni Meola, Annalucia Serafino, Giuseppe Novelli, Federica Sangiuolo and Annalisa Botta
- 169** *Dysfunction of Sister Chromatids Separation Promotes Progression of Hepatocellular Carcinoma According to Analysis of Gene Expression Profiling*  
Baozhen Sun, Guibo Lin, Degang Ji, Shuo Li, Guonan Chi and Xingyi Jin
- 180** *Toward Morphologically Relevant Extracellular Matrix in Vitro Models: 3D Fiber Reinforced Hydrogels*  
Ashok Williams, James F. Nowak, Rachel Dass, Johnson Samuel and K. L. Mills
- 190** *Metabolic Changes Associated With Muscle Expression of SOD1<sup>G93A</sup>*  
Gabriella Dobrowolny, Elisa Lepore, Martina Martini, Laura Barberi, Abigail Nunn, Bianca Maria Scicchitano and Antonio Musarò
- 199** *Cellular Mechanotransduction: From Tension to Function*  
Fabiana Martino, Ana R. Perestrelo, Vladimír Vinarský, Stefania Pagliari and Giancarlo Forte
- 220** *Every Breath you Take: Non-invasive Real-Time Oxygen Biosensing in Two- and Three-Dimensional Microfluidic Cell Models*  
Helene Zirath, Mario Rothbauer, Sarah Spitz, Barbara Bachmann, Christian Jordan, Bernhard Müller, Josef Ehgartner, Eleni Priglinger, Severin Mühleder, Heinz Redl, Wolfgang Holnthoner, Michael Harasek, Torsten Mayr and Peter Ertl
- 232** *AFM Monitoring the Influence of Selected Cryoprotectants on Regeneration of Cryopreserved Cells Mechanical Properties*  
Martin Golan, Sarka Jelinkova, Irena Kratochvílová, Petr Skládal, Martin Pešl, Vladimír Rotrekl and Jan Pribyl
- 242** *Vesicle-Mediated Control of Cell Function: The Role of Extracellular Matrix and Microenvironment*  
Gorjana Rackov, Noemi Garcia-Romero, Susana Esteban-Rubio, Josefa Carrión-Navarro, Cristobal Belda-Iniesta and Angel Ayuso-Sacido
- 254** *Vascular Morphogenesis in the Context of Inflammation: Self-Organization in a Fibrin-Based 3D Culture System*  
Beate M. Rüger, Tanja Buchacher, Alexander Giurea, Bernd Kubista, Michael B. Fischer and Johannes M. Breuss



# Editorial: Physico-Chemical Control of Cell Function

Alberto Rainer<sup>1</sup>, Giancarlo Forte<sup>2</sup> and Cesare Gargioli<sup>3\*</sup>

<sup>1</sup> Department of Engineering, Università Campus Bio-Medico di Roma, Rome, Italy, <sup>2</sup> Center for Translational Medicine, International Clinical Research Center, St Anne's University Hospital, Brno, Czechia, <sup>3</sup> Department of Biology, Tor Vergata University, Rome, Italy

**Keywords:** ECM, extra cellular matrix, physico-chemical parameter, cell biology, scaffold matrix, mechanical and topographical cues

## Editorial on the Research Topic

### Physico-Chemical Control of Cell Function

The mechanical properties of the extracellular matrix (ECM) are fundamental in controlling cell behavior. Evidence has been given that ECM mechanics and nanotopography are at least as important as the biochemical cues for cells to decide about their survival, proliferation, migration, and fate (Engler et al., 2006).

The interplay between cells and the ECM is continuously controlled at the cell level in a dynamic way and is tightly controlled by negative and positive feedback loops.

Cells synthesize the raw components of the ECM and remodel it; in turn, ECM impacts on cell function by providing chemical, topographical and mechanical hints (Calvo et al., 2013). This consideration calls for an increasing attention toward the investigation of new and performing biomimetic scaffold matrices mirroring ECM mechano-physical and chemical properties (Fuoco et al., 2016).

Here we propose a collection of original articles, reviews and technical reports having the aim to provide readers with a comprehensive overview on: (1) the role and nature of mechanical cues arising from ECM in determining cell function; (2) the molecular mechanisms underlining cell response to ECM mechanics and nanotopography; (3) the current experimental tools used to mimic ECM dynamics as well as to observe and interpret cell mechanosensing. Also, we offer few significant contributions regarding the generation on new *in vitro* and *in silico* models of cell-matrix interaction.

In a comprehensive review, Martino et al. revise the current knowledge on intracellular mechanosensing pathways using a concentric approach starting from the site of cell-ECM physical interaction, the focal adhesion, and going down to the nucleus, where specific genetic programs are activated in response to mechanical stimuli. The response to mechanical challenge has been recently shown to entail the reinforcement of cell-matrix interaction and the development of cell force (Nardone et al., 2017).

In this context, the use of atomic force microscopy (AFM) allows for nanoscale mapping of cell mechanical properties and topography in living cells, thus allowing for subcellular and live monitoring of cellular processes, like cytoskeleton rearrangement and cell shaping.

Caluori et al. question the benefits and limitations of currently used mechanical models for post-processing and interpretation of AFM data in order to quantify the impact of such models on the final evaluation of cellular elasticity.

The versatility of AFM platform allowed Golan et al. to propose nanoindentation as a strategy to monitor and characterize frozen cell recovery by measuring changes in their elastic properties.

## OPEN ACCESS

### Edited and reviewed by:

Geoffrey A. Head,  
Baker Heart and Diabetes Institute,  
Australia

### \*Correspondence:

Cesare Gargioli  
cesare.gargioli@uniroma2.it

### Specialty section:

This article was submitted to  
Integrative Physiology,  
a section of the journal  
Frontiers in Physiology

**Received:** 13 February 2019

**Accepted:** 14 March 2019

**Published:** 03 April 2019

### Citation:

Rainer A, Forte G and Gargioli C  
(2019) Editorial: Physico-Chemical  
Control of Cell Function.  
Front. Physiol. 10:355.  
doi: 10.3389/fphys.2019.00355

Mechanobiology-on-a-chip is regarded as the future avenue to set up *in vitro* physiological and pathological models of *in vivo* conditions. In this Topic, Ergir et al. critically revise the recent advances in lab-on-a-chip platforms in the context of mechanobiology models and elaborate on the next-generation physiological and pathological organ-on-a-chip models.

Additionally, Basoli et al. introduce and critically discuss the recent advances in optical, magnetic, and acoustic tweezers to investigate the mechanobiology of living cells. Together with active and sensing substrates produced by manipulating biomaterials chemistry or by microfabrication techniques, strategies based on such technologies appear to expand the potential of classical AFM approaches.

Among the tools used to study cell-ECM interaction, artificial, and natural scaffolds play an important part. A major issue in 3D scaffold preparation is the diffusion of nutrients and oxygen to the core of the construct. This limitation poses serious concerns when parenchymatic substitutes are planned.

To overcome this problem, Zirath et al. developed microfluidic devices containing embedded sensor arrays and able to monitor local oxygen levels. The devices are proposed to investigate oxygen consumption rates of hydrogel-based cell cultures, the establishment of oxygen gradients within cell culture chambers and the influence of microfluidic material, surface coatings, cell densities, and medium flow rate on the respiratory activities of selected cell types.

In a classical mechanobiology study, Rufaihah et al. elaborate on the effects of scaffold stiffness on fetal mesenchymal stem cells by using semi-synthetic hydrogels made of PEG-Fibrinogen. On the same line, Williams et al. propose an original study in which fiber-reinforced composite hydrogels were fabricated by far field electrospinning with the aid of guiding electrodes and gravity-assisted, droplet-based system to deposit the hydrogel component. The authors show that the fibrous component is able to slightly increase scaffold elastic modulus, thus controlling cell morphology.

In this context, the original paper by Rüger et al. addresses the suitability of 3D explant culture in fibrin hydrogels as a disease-related platform to integrate complex cell-cell and cell-ECM interactions with associated paracrine signaling patterns.

One of the most represented components in ECM is collagen, the molecule responsible for the scaffolding properties of the matrix and whose derangement has been associated to a number of severe pathological conditions.

By investigating the *in vitro* behavior of fibroblasts obtained from a Col6a1<sup>-/-</sup> mouse, the group of Castagnaro et al. emphasizes the critical effects of collagen VI on cell autophagy regulation and survival, thus offering a model for pathologies based on its depletion.

The body district being more affected by collagen VI depletion is muscle. We host in the Topic three papers related to muscle biology: the group coordinated by Maleiner et al. provides a clear and comprehensive review of skeletal muscle development, while emphasizing the need for novel, more representative models of muscle diseases *in vitro*.

Additionally, the original paper by the group of Thorrez et al. describes an original protocol based on fibrin and collagen I scaffolding materials to control the visco-elastic properties of adult skeletal muscle progenitor-derived bioartificial muscles. The fine-tuning of the components provided clues to find a compromise between cell differentiation and the angiogenesis required to support this process.

The milieu cells are exposed to also includes surrounding cells and the products they release to exert paracrine effects.

Extracellular vesicles (EVs), a broad category including exosomes, microvesicles, and apoptotic bodies, have been lately subject to intense investigation as mediators of cell-to-cell paracrine communication at short and long distances.

Rackov et al.'s group revises the recent discoveries that EVs can transport and release enzymes involved in ECM remodeling, thus actively contributing to cell function and tumor spreading.

Tumor microenvironment is characterized by increased hyaluronan and altered integrin binding, this condition being credited of favoring metastatization. While Zapp et al. report on a new method to prepare self-assembled monolayers on gold surfaces, co-presenting the cell adhesive RGD motif and small hyaluronan molecules, to investigate integrin binding, Sun et al.'s group adopted a fully *in silico* bioinformatics approach to identify the enriched and dysregulated pathways in 362 hepatocellular carcinoma tissues, which, as expected, include ECM-responsive elements.

Vitiello et al. propose an original study in which the repurposing of safinamide, a monoamine oxidase inhibitor already in the clinical pipeline for neurological diseases, is used to treat dystrophic patients. They demonstrate the efficacy of the drug *in vitro* by testing the compounds on myogenic culture derived from *mdx* dystrophic mice and Duchenne Muscular Dystrophy (DMD) patients.

While this paper takes advantage of DMD patient-derived myoblasts, Spitalieri et al. describe the generation of the first two induced pluripotent stem cell lines coming from patients diagnosed with myotonic dystrophy type 2 and successfully managed to push them to neuronal differentiation, thus producing a new, valuable patient-specific *in vitro* disease model. This disease model complements the study by the group of Dobrowolny et al., investigating the role of mutations in superoxide dismutase 1 contribution to amyotrophic lateral sclerosis phenotype.

Finally, underlining the need for new *in silico* predictive tools, the paper proposed by Merino-Casallo et al. adopts a Bayesian optimization to predict the behavior of cells in a 3D environment by mimicking the existence of controlled mechano-chemical constraints.

In conclusion, this topic collects a number of interesting studies dealing with the manifold aspects of cell-matrix interplay, showing knotty lapels regarding the intimate interaction tying ECM and cells. This interaction is yet to be fully untangled.



## AUTHOR CONTRIBUTIONS

All authors listed have made a substantial, direct and intellectual contribution to the work, and approved it for publication.

## REFERENCES

- Calvo, F., Ege, N., Grande-Garcia, A., Hooper, S., Jenkins, R. P., Chaudhry, S. I., et al. (2013). Mechanotransduction and YAP-dependent matrix remodelling is required for the generation and maintenance of cancer-associated fibroblasts. *Nat. Cell Biol.* 15, 637–646. doi: 10.1038/ncb2756
- Engler, A. J., Sen, S., Sweeney, H. L., and Discher, D. E. (2006). Matrix elasticity directs stem cell lineage specification. *Cell* 126, 677–689. doi: 10.1016/j.cell.2006.06.044
- Fuoco, C., Cannata, S., and Gargioli, C. (2016). Could a functional artificial skeletal muscle be useful in muscle wasting? *Curr. Opin. Clin. Nutr. Metab. Care* 19, 182–187. doi: 10.1097/MCO.00000000000000271

## FUNDING

GF was supported by the European Regional Development Fund-Project MAGNET (Number CZ.02.1.01/0.0/0.0/15\_003/0000492).

Nardone, G., Oliver-De La Cruz, J., Vrbsky, J., Martini, C., Pribyl, J., Skládál, P., et al. (2017). YAP regulates cell mechanics by controlling focal adhesion assembly. *Nat. Commun.* 8:15321. doi: 10.1038/ncomms15321

**Conflict of Interest Statement:** The authors declare that the research was conducted in the absence of any commercial or financial relationships that could be construed as a potential conflict of interest.

Copyright © 2019 Rainer, Forte and Gargioli. This is an open-access article distributed under the terms of the Creative Commons Attribution License (CC BY). The use, distribution or reproduction in other forums is permitted, provided the original author(s) and the copyright owner(s) are credited and that the original publication in this journal is cited, in accordance with accepted academic practice. No use, distribution or reproduction is permitted which does not comply with these terms.



# The Effect of Scaffold Modulus on the Morphology and Remodeling of Fetal Mesenchymal Stem Cells

Abdul Jalil Rufaihah<sup>1†</sup>, Suganya Cheyyatraivendran<sup>1†</sup>, Muhammad Danial Mohd Mazlan<sup>1</sup>, Kenrich Lim<sup>1</sup>, Mark Seow Khoon Chong<sup>2</sup>, Citra Nurfarah Zaini Mattar<sup>3</sup>, Jerry Kok Yen Chan<sup>3</sup>, Theodoros Kofidis<sup>1,4\*</sup> and Dror Seliktar<sup>5,6\*</sup>

<sup>1</sup> Department of Surgery, Yong Loo Lin School of Medicine, National University of Singapore, Singapore, Singapore, <sup>2</sup> Division of Bioengineering, School of Chemical and Biomedical Engineering, Nanyang Technological University, Singapore, Singapore, <sup>3</sup> Department of Obstetrics and Gynaecology, National University of Singapore, Singapore, Singapore, <sup>4</sup> Department of Cardiac, Thoracic and Vascular Surgery, National University Heart Centre Singapore, National University Health System, Singapore, Singapore, <sup>5</sup> Nanoscience and Nanotechnology Initiative, National University of Singapore, Singapore, Singapore, <sup>6</sup> Faculty of Biomedical Engineering, Technion – Israel Institute of Technology, Haifa, Israel

## OPEN ACCESS

### Edited by:

Cesare Gargioli,  
Università degli Studi di Roma Tor  
Vergata, Italy

### Reviewed by:

Paola Braghetta,  
Università degli Studi di Padova, Italy  
Lieven Thorrez,  
KU Leuven Kulak, Belgium

### \*Correspondence:

Theodoros Kofidis  
kofidis\_theodoros@nuhs.edu.sg  
Dror Seliktar  
dror@bm.technion.ac.il

<sup>†</sup>First authors

### Specialty section:

This article was submitted to  
Integrative Physiology,  
a section of the journal  
Frontiers in Physiology

**Received:** 16 March 2018

**Accepted:** 17 October 2018

**Published:** 21 December 2018

### Citation:

Rufaihah AJ,  
Cheyyatraivendran S, Mazlan MDM,  
Lim K, Chong MSK, Mattar CNZ,  
Chan JKY, Kofidis T and Seliktar D  
(2018) The Effect of Scaffold Modulus  
on the Morphology and Remodeling  
of Fetal Mesenchymal Stem Cells.  
*Front. Physiol.* 9:1555.  
doi: 10.3389/fphys.2018.01555

Hydrogel materials have been successfully used as matrices to explore the role of biophysical and biochemical stimuli in directing stem cell behavior. Here, we present our findings on the role of modulus in guiding bone marrow fetal mesenchymal stem cell (BMfMSC) fate determination using semi-synthetic hydrogels made from PEG-fibrinogen (PF). The BMfMSCs were cultivated in the PF for up to 2 weeks to study the influence of matrix modulus (i.e., cross-linking density of the PF) on BMfMSC survival, morphology and integrin expression. Both two-dimensional (2D) and three-dimensional (3D) culture conditions were employed to examine the BMfMSCs as single cells or as cell spheroids. The hydrogel modulus affected the rate of BMfMSC metabolic activity, the integrin expression levels and the cell morphology, both as single cells and as spheroids. The cell seeding density was also found to be an important parameter of the system in that high densities were favorable in facilitating more cell-to-cell contacts that favored higher metabolic activity. Our findings provide important insight about design of a hydrogel scaffold that can be used to optimize the biological response of BMfMSCs for various tissue engineering applications.

**Keywords:** hydrogel, scaffold, tissue engineering, matrix stiffness, biomaterials, PEGylated fibrinogen

## INTRODUCTION

Mesenchymal stem cells (MSCs) are multipotent stromal cells which differentiate into multiple connective tissue lineages (osteoblasts, chondrocytes, and adipocytes) under permissive stimulation both *in vitro* and *in vivo* (Krebsbach et al., 1999; Zhang et al., 2010). Adult MSCs are readily isolated from the bone marrow and are able to retain their multipotent differentiation capacity while expanding through multiple passages (Zhang et al., 2010). Recent studies have shown that adult MSCs can be differentiated into specific cells under defined growth conditions or biophysical stimulation (Caplan, 2015). For example, adult MSCs can differentiate into endothelial-like cells after treatment with vascular endothelial growth factor (VEGF) (Oswald et al., 2004). This ability further substantiates their potential to be applied for therapeutic purposes such as in tissue repair

and regeneration, where a specific cell lineage is required (Miao et al., 2006). In previous studies, the application of adult MSCs in bone injuries such as calvarial or femoral defects accelerated and improved healing in small and large animal models (mouse, rat, and ovine) (Petite et al., 2000; Cowan et al., 2004; Meinel et al., 2006). However, the main drawbacks of using adult MSCs for tissue repair are the additional trauma associated with the cell harvest, the likelihood that harvesting will yield substantially fewer cells than required for the therapy, and the inevitable need to substantially expand the harvested MSC populations (Redondo et al., 2017). Other limitations of adult MSCs include the inherent heterogeneity of the cell source as well as the age and medical condition of the donor (Redondo et al., 2017). Heterogeneous cell populations require enrichment of the multipotent cells. MSCs of older or chronically sick donors are hard to obtain from the bone marrow and are subjected to age-related decreases in potency (O'Donoghue and Chan, 2006; Zhang et al., 2010). Alternative sources of multipotent cells are sought in order to overcome these limitations. One such potential source is fetal tissue cells, or fetal MSCs (fMSCs) (Campagnoli et al., 2001), which have greater self-renewal and differentiation capacity, longer telomeres, greater telomerase activity, and express additional human telomerase reverse transcriptase. fMSCs are also more readily expandable *in vitro*, and senesce later on during their *in vitro* culture when compared to adult MSCs (O'Donoghue and Chan, 2006).

Hydrogels can provide temporary physical support (i.e., scaffolding) for stem cells to attach, grow and differentiate (Seliktar, 2012). Additionally, transplantation of cells (i.e., cell therapy) into damaged or diseased tissues without a physical support has been shown to be much less effective (Fuoco et al., 2012). Previous studies demonstrated that direct injection of cardiomyocytes delivered in PEG-fibrinogen (PF) hydrogels to the damaged heart following myocardial infarction (MI) increased the viability of the transplanted cells and minimized the infarct size as well as increased angiogenesis in the damaged tissue – when compared to injection of cardiomyocytes without a hydrogel scaffold (Shapira-Schweitzer et al., 2009). Hydrogels can also provide a biomimetic niche to enhance stem cell attachment, proliferation, and differentiation (Nguyen and West, 2002; Naito et al., 2013; Redondo et al., 2017). A major hindrance in the clinical application of stem cells is this ability to guide cell differentiation to specific lineages (O'Donoghue and Chan, 2006). Indeed, as fetal stem cells are multipotent, they could potentially differentiate along an undesired pathway (Chan et al., 2007), whereas the therapeutic effects are contingent upon efficient differentiation along the desired lineage (Chan et al., 2006; Kennea et al., 2009).

Numerous hydrogels have been developed with the objective of guiding stem cell differentiation and enhancing the efficacy of stem cell therapy (Naito et al., 2013; Narayanan et al., 2014; Anjum et al., 2016; Hogrebe and Gooch, 2016; Moshayedi et al., 2016). These hydrogels are often categorized based on the origin of their polymeric constituents: synthetic or biological (Seliktar, 2005). Synthetic hydrogels can be synthesized with precise shape, mechanics, and degradation properties; each of these being tailored to the needs of a particular biomedical application.

Synthetic hydrogels made from poly (ethylene glycol) (PEG), for example, have been used in tissue engineering, most notably for cartilage applications (Fan and Wang, 2015; Neumann et al., 2016; Wang et al., 2017). These materials have also been used for the expansion of stem cells in bioreactors (Dias et al., 2017). The drawbacks of using synthetic materials such as PEG include lack of cell adhesion motifs on the polymer, which can lead to poor cell survival. Biological hydrogels offer natural biofunctional motifs on the polymer backbone that can enhance stem cell survival by promoting cell adhesion, proliferation, differentiation, and enzymatic activity. A variety of protein-based hydrogels made from collagen, fibrin or silk fibroin have been used for tissue engineering of bone, cartilage and other applications. However, the use of biological materials could give rise to certain problems in tissue engineering, including limited control over mechanical properties, unregulated biodegradation, possible disease transmission and poor reproducibility (Campagnoli et al., 2001).

Semi-synthetic materials have been proposed to overcome limitation of the synthetic and biological hydrogels (Almany and Seliktar, 2005; Dikovskiy et al., 2006; Berkovitch and Seliktar, 2017). The semi-synthetic hydrogels consist of both biological and synthetic polymer constituents, often incorporating bioactive molecules into malleable cross-linked synthetic polymer networks (Lutolf and Hubbell, 2005). One group of semi-synthetic hydrogels in particular – those that mimic the extracellular matrix (ECM) – are becoming more common in cell-based therapy and tissue engineering applications. These hydrogels are designed to possess specific functions that regulate cell fate based on known interactions between cells and natural ECM molecules. We have developed a class of ECM-mimetic semi-synthetic hydrogels using combinations of natural denatured fibrinogen and synthetic hydrophilic polymers (Gonen-Wadman et al., 2007, 2011; Shachaf et al., 2010). These materials can be formed into hydrogels by mild photochemistry in the presence of cells, thus enabling three-dimensional (3D) culture of the encapsulated cells. The cells interact with the materials by virtue of both biological motifs on the fibrinogen and biophysical cues emanating from the structural properties of the matrix. In this system, the structural properties are controlled by the synthetic polymer constituent; higher concentrations of synthetic polymer increase the cross-linking density and thereby alter the matrix modulus.

In this study, we investigated how different degrees of matrix cross-linking in a PF hydrogel influences the behavior of bone marrow fetal mesenchymal stem cells (BMfMSCs) in both two-dimensional (2D) and 3D culture environments. Specifically, we sought to understand how the modulus affects cell morphology, cell metabolism and cell interactions with the matrix. We made materials containing different amounts of PEG-diacrylate (PEG-DA) and similar amounts of fibrinogen; the higher PEG-DA concentrations resulted in stiffer, more crosslinked PF hydrogels. BMfMSCs were cultured on top of, or within the PF hydrogels, and important parameters of these cells were assessed at various time-points. The results provided evidence as to the modulus-dependent behavior of BMfMSCs both in 2D and 3D culture conditions.

## MATERIALS AND METHODS

### Synthesis of PEG-Diacrylate and PEG-Fibrinogen

The covalent conjugation of bovine fibrinogen (Bovogen Biologicals Pty Ltd., Australia) to the modified PEG-diacrylate (PEG-DA) was followed according to the published protocols (Elbert and Hubbell, 2001; Dikovsky et al., 2006). Briefly, a 7 mg ml<sup>-1</sup> solution of fibrinogen in 10 mM phosphate-buffered saline (PBS) with 8M urea was prepared with 0.45 mg ml<sup>-1</sup> tris (2-carboxyethyl) phosphine hydrochloride (TCEP-HCl) (Sigma, United States). The solution pH was adjusted to 8.0 by addition of NaOH. PEG-DA was prepared from Poly (ethylene glycol)-diol (linear PEG-OH, 10 kDa) using the acryloyl chloride method described elsewhere (Elbert et al., 2001). The PEG-DA was dissolved in 10 mM PBS and 8M Urea to give a concentration of 280 mg ml<sup>-1</sup>, and added to the fibrinogen/TCEP-HCl solution at a volumetric ratio of 6:1 (fibrinogen/TCEP-HCl:PEG-DA). A Michael-type addition reaction between the PEG-DA and the fibrinogen cysteines was used to PEGylate the fibrinogen with diacrylate-functionalized PEG, as described elsewhere (Halstenberg et al., 2002; Rizzi et al., 2006). This PEGylation reaction was done for 3 h in the dark inside a mixture vessel with a thermostatic jacket (Lenz Laborglas, Germany) at a temperature of 22.5°C. Immediately afterward, an equal volume of PBS-8M urea was added to the reaction solution for dilution, and then the reaction product was precipitated with the addition of acetone (Aik Moh Paints and Chemicals Pte Ltd., Singapore), at a volumetric ratio of 4:1 (volume of acetone to volume of diluted reaction solution). The PEGylated fibrinogen reaction product that precipitated from the liquid phase was collected by centrifuging the liquid for 5 min at 20 RCF (relative centrifugal force). The supernatant liquid was removed and discarded. The collected precipitate was dissolved in PBS-8M Urea at a 1.8:1 volumetric ratio of PBS-8M Urea to precipitate volume. A tangential flow filtration method was used to purify and concentrate the modified fibrinogen reaction product against 10 mM PBS (ratio of 80:1 v/w PBS to precipitant) down to a concentration of 8–12 mg ml<sup>-1</sup> using a Centrimate cassette (50 kDa MW cutoff, Pall Corporation, Port Washington, NY, United States). The purified solution was passed through a high shear fluid processor (Microfluidics M110-P, United States) and sterile filtered using a 0.2 micron VacuCap 90 filter (Pall Corporation, United States). The fibrinogen concentration of the sterile PEGylated fibrinogen solution was characterized after filtration using a NanoDrop<sup>TM</sup> 2000 Spectrophotometer (Thermo Fisher, Waltham, MA, United States).

### Preparation of PF Hydrogel and Characterization

Hydrogels were prepared from a PF hydrogel precursor solution, which is comprised of sterile PEGylated fibrinogen solution (8 mg ml<sup>-1</sup>), 0.1% (w/v) sterile Irgacure<sup>®</sup>2959 photoinitiator (Ciba, Switzerland), and varying amounts of sterile PEG-DA cross-linker for controlling the hydrogel stiffness. Cells were introduced to this PF hydrogel precursor solution, and gelation

was facilitated by a light-activated free-radical polymerization reaction, according to published protocols (Schmidt et al., 2006). Briefly, 0.1% (w/v) Irgacure<sup>®</sup>2959 photoinitiator was added to the PEGylated fibrinogen from a photoinitiator stock solution of 10% Irgacure<sup>®</sup>2959 in deionized water containing 70% (v/v) ethanol. PEG-DA was added to this solution at different concentrations to increase the hydrogel crosslinking, from a 15% (w/v) stock solution of PEG-DA in PBS, as detailed elsewhere (Singh et al., 2013). Five different stiffness levels of the hydrogels were chosen using additional PEG-DA percentages (w/v) added to the PEGylated fibrinogen solution as follows: 0% PEG-DA (PF, native hydrogel without additional PEG-DA; Composition A), 0.5% PEG-DA (Composition B), 1% PEG-DA (Composition C), 1.5% PEG-DA (Composition D), and 2% PEG-DA (Composition E). The final concentration of fibrinogen in the solution was 8 mg ml<sup>-1</sup> for all compositions; this was achieved by diluting the sterile PEGylated fibrinogen solution with PBS beforehand.

### Rheological Characterization

Rheological characterization was done using AR-G2 rheometer (TA Instrument, United States) as described elsewhere (Gonen-Wadmany et al., 2011; Mironi-Harpaz et al., 2012). A PF hydrogel precursor solution of 200 µl was loaded onto a 20 mm diameter parallel-plate geometry. The PF solution was equilibrated for 1 min before being exposed to 365 nm UV light with the intensity of 5 mW cm<sup>-1</sup> from an Omnicure Series 2000 light source (Excelitas Technologies Corp., Waltham, MA, United States). Shear modulus data from dynamic time-sweeps were collected during the photopolymerization of the PF solution upon activation with the UV light source. At the end of the crosslinking process, the shear loss modulus (G'') and shear storage modulus (G')

### Bone Marrow Fetal Mesenchymal Stem Cells

#### Samples and Ethics

Fetal tissue collection for this research was approved by the Domain Specific Review Board of the National University Hospital, Singapore (DSRB/2006/00154) in compliance with international guidelines regarding the use of fetal tissue for research. Informed written consent was obtained from pregnant women for the usage of fetal tissue for research purposes. Fetal gestational age was determined by ultrasonic crown-rump or femur length measurement. Fetal long bones (femur and humerus) were collected for the isolation of BMfMSC after the pregnancy was medically terminated. Samples were collected from pregnancies at 18–22 weeks gestation.

#### Isolation of Bone Marrow Fetal Mesenchymal Stem Cells

BMfMSC were isolated according to published protocols (Chan et al., 2006, 2007). Briefly, the long bones (femur and humerus) were dissected out and muscle tissues were carefully removed; the bones were wiped with 70% ethanol to prevent myoblast contamination. The two distal ends of the long bone were sliced open and cell suspension were obtained by using a syringe needle flushing of phosphate buffer made from 1M monobasic (18.4 ml)

and 1M dibasic (31.6 ml) potassium phosphate in 1 l volume of double distilled H<sub>2</sub>O; The solution was injected at one end of the opening and collected at the other end under a 70  $\mu$ m cell strainer (Biomed Diagnostics, United States). The cell suspension solution was then introduced with Ficoll-Paque (GE Healthcare, United Kingdom), which would separate the mononuclear cells from the red blood cells and plasma. After centrifugation, the upper layer was aspirated and the mononuclear cell layer was obtained at the interphase. The cells collected at the interphase were washed with PBS and centrifuged again, before suspending them with growth medium. The cell suspension was plated on a cell culture flask (Nunc, United States) and incubated in a 37°C incubator with 5% CO<sub>2</sub>. Spindle-shaped adherent cells were recovered from the primary cultures after 4–7 days and non-adherent cells were removed during medium changes every 2–3 days.

### Cell Culture and Formation of Spheroids

BMfMSC were cultured in a flask coated with 0.2% of gelatin, filled with Dulbecco' Modified Eagle Medium (DMEM), supplemented with 10% fetal bovine serum (FBS), which would be referred to as growth medium hereafter, in a 37°C incubator with 5% CO<sub>2</sub>. The spheroids were made by using AggreWell™800 (STEMCELL Technologies, Vancouver, BC, Canada) according to the standard protocol by the company.

### Bone Marrow Fetal Mesenchymal Stem Cell Characterization

#### Immunophenotype

The BMfMSCs undergo both immunocytochemistry and flow cytometry screening to test for the cluster of differentiation (CD) marker. CD73, CD90, CD105, CD34, and CD45 were the markers tested. All the primary antibodies were purchased from Miltenyi Biotec, Bergisch Gladbach, Germany and corresponding fluorophore-conjugated secondary antibodies were from Life Technologies (now Thermo Fisher Scientific, United States). For flow cytometry: BMfMSCs were thawed in a 37°C water bath and diluted with growth medium before centrifugation at 400  $\times$  g for 5 min. The cell pellet was collected and suspended with 1 ml of FACS buffer (Sigma-Aldrich, United States) which consist of 1% bovine serum in 2 mM EDTA PBS and aliquoted to 100  $\mu$ l each in 2 ml eppendorf tubes. In each 2 ml eppendorf tube, 10  $\mu$ l of antibody (CD marker) was added and incubated in the dark. After 30 min, the cell suspension was centrifuged at 400  $\times$  g for 5 min to obtain the cell pellet. The cell pellet was washed with PBS and underwent centrifugation twice. The cell pellet was suspended with FACS buffer before being analyzed through the machine. For immunocytochemistry: Monolayer cultured BMfMSCs were fixed with 4% formalin and permeabilized with acetone and methanol at a ratio of 1:1 at –20°C. After the fixation and permeabilization step, the BMfMSC were blocked with 1% bovine serum albumin in 2 mM EDTA PBS at room temperature. The samples were washed with PBS three times and the primary antibody diluted with PBS (1:10 dilution) was added for 1.5 h and incubated at 4°C. The primary antibody was removed and the cells were washed with PBS. The secondary antibody was

diluted with PBS (1:100 dilutions) and added for incubation (30 min). The cells were then washed with PBS and imaged with an Olympus FV-100 (Olympus, United States) using imaging software and a 20 $\times$ /0.45 and 40 $\times$ /0.45 objective lens.

### Multipotent Differentiation

For bone differentiation: BMfMSCs were seeded at  $2 \times 10^4$  cell cm<sup>-2</sup> in a culture plate with growth medium. After overnight culture, the growth medium was changed to a bone differentiation medium [growth medium supplemented with 10<sup>-8</sup> M dexamethasone, 0.2 mM ascorbic acid, 10 mM b-glycerol phosphate (all Sigma-Aldrich, United States)] and the medium was changed every 3 days for duration of 2 weeks. Cell changes in shape and the production of calcium salts and phosphates were detected through Alizarin Red (Sigma-Aldrich, United States) and Von Kossa (Sigma-Aldrich, United States) staining, respectively. For adipogenic differentiation: BMfMSCs were seeded at  $2 \times 10^4$  cells cm<sup>-2</sup> with growth medium. After overnight culture, the growth medium was changed to fat differentiation induction medium [growth medium supplemented with 5 mg ml<sup>-1</sup> Insulin, 10<sup>-4</sup> M Dexamethasone, 6  $\times$  10<sup>-3</sup>M Indomethacin (all Sigma-Aldrich, United States)] and incubated for 3 days. After 3 days, the fat differentiation induction medium was changed to a growth medium and incubated for an additional 3 days. This step was done three times. Lipids vacuoles were visible after 14–21 days and were verified by oil red O (Sigma-Aldrich, United States) staining. For chondrogenic differentiation: BMfMSCs were suspended in chondrogenic differentiation medium [growth medium supplemented with 10 ng ml<sup>-1</sup> TGF-B3, 100 nM dexamethasone, 50 ug ml<sup>-1</sup> ascorbic acid, 100 ug ml<sup>-1</sup> sodium pyruvate, 40 ug ml<sup>-1</sup> proline and 1x ITS (all Sigma-Aldrich, United States)] at room temperature after being centrifuged twice at 150  $\times$  g for 5 min. After the third centrifugation of the cells, they were kept in the incubator. Medium was changed every 2–3 days for 25 days. Cell pellets were harvested and fixed before being embedded with formalin and paraffin to undergo sectioning (4  $\mu$ m thick slices). The samples were deparaffinized and rehydrated before alcian blue staining (Sigma-Aldrich, United States).

### Cell Morphology and Remodeling

For 2D: Both BMfMSCs (7,000 cells) and BMfMSC-spheroids (4,000 cells per spheroid) were seeded on top of polymerized PF hydrogel in a single well of a 15-well  $\mu$ -Slide Angiogenesis plate (Ibidi GmbH, Germany) before medium was added. For 3D: The precursor PF solution (50  $\mu$ l, 8 mg ml<sup>-1</sup>) was mixed with BMfMSCs (15,000 cells) or BMfMSC-spheroids and polymerized for 3 min under a UV lamp (365 nm, 4–5 mW cm<sup>-2</sup>) before medium was added. At each time point, at least six hydrogel samples of the BMfMSCs and BMfMSC-spheroids – six spheroids in each sample for both the 2D and 3D – were fixed with 4% paraformaldehyde and permeabilized with 0.1% Triton-X. The cells were stained with Alexa Fluor® 488 Phalloidin (Life Technologies, now Thermo Fisher Scientific, United States) to visualize the arrangement of the actin filaments and counter-stained with Hoechst 33342

(Life Technologies, now Thermo Fisher Scientific, United States) for imaging the nucleus. Images were taken using a Zeiss LSM 700 Laser Scanning Microscope (Carl Zeiss AG, Oberkochen, Germany). Lamellipodia were visually quantified as the thin cytoplasmic sheets that extended at the front of the cells; whereas filopodia were visually quantified as the finger-like projections at the edges of the cells. Quantifications were performed on at least four micrographs for each sample of each treatment and composition.

## Cell Metabolism

Cell metabolism was measured by using an alamarBlue® Assay. Resazurin X100 (Sigma-Aldrich, St. Louis, MO, United States) was dissolved with PBS to give a stock concentration of 10 mg ml<sup>-1</sup>. To obtain the working solution, the dissolved stock solution was further diluted with PBS to give a concentration of 1 mg ml<sup>-1</sup>. After polymerization of the gel, medium and alamarBlue were added to the samples with a ratio of 10:1. At each time point period, the solution was extracted and a fresh batch of medium and alamarBlue were added in. The extracted samples were measured using a NanoDrop™ 2000 Spectrophotometer (Thermo Fisher, Waltham, MA, United States) at two specific wavelengths (570 nm and 600 nm) and the percentage of reduction of alamarBlue was calculated. At least six samples for each composition were assessed for analysis.

## Gene Expression

For both 2D and 3D BMfMSCs and BMfMSC-spheroids, RNA was extracted using ReliaPrep™ RNA Cell Miniprep System (Promega, Madison, WI, United States). The PF hydrogels were degraded with collagenase from *Clostridium histolyticum* (Sigma-Aldrich, St. Louis, MO, United States) at the concentration of 0.001 g/ml for 6 h for 2D and 24 h for 3D. After the isolation of the RNA, cDNA was synthesized using QuantiTect® Reverse Transcription Kit (QIAGEN, Hilden, Germany) and stored at -20°C. Real Time PCR was performed in triplicates using Taqman Universal PCR Master Mix [Applied Biosystems (now Thermo Fisher Scientific), Foster City, CA, United States]) and Bio-Rad CFX96 Thermal Cycler machine as per manufacturer's instructions to check on the expression of integrin complexes on both 2D and 3D environments. The qPCR protocol was as follows: 10 min heat activation at 95°C. After which, 40 cycles were repeated for the following: 15 s of 95°C and 1 min of 60°C. Primers that were used were purchased from Life Technologies, now Thermo Fisher Scientific, United States. The assay IDs for the primers used are as follows: α5 Integrin, Hs01547673\_m1; β1 Integrin, Hs00559595\_m1; β3 Integrin, Hs01001469\_m1; β3 Integrin ID: Hs01001469\_m1; β5 Integrin, Hs00174435\_m1. The housekeeping gene 18S was used as a reference (Hs99999901\_s1). These primers were reported for use with qPCR in prior studies (Bergmann et al., 2011; Frittoli et al., 2014; Plessl et al., 2015; Raman et al., 2016). All gene expression data was normalization with respect to the expression levels of the composition A group, for each of the respective treatments. The formulae used to normalize the data was the same as reported by

Livak and Schmittgen (2001) and Schmittgen and Livak (2008), as follows:

$$\Delta Ct = Ct(A) - Ct_{ref}(A) \text{ (reference gene is 18S)}$$

$$\Delta\Delta Ct = (\Delta Ct \text{ of experiment}) - (\Delta Ct \text{ of control})$$

Fold change = 2<sup>-(ΔΔCt)</sup> = this delta delta Ct is the simple formula being used to calculate relative fold gene expression of samples when doing qPCR. At least six samples for each composition were assessed for analysis.

## Statistical Analysis

The quantification analysis of the tube length was done by using WimTube software analysis and all the graphs were plotted using Microsoft Excel. Data was presented as group mean ± standard deviations (SD) which was done using Microsoft Excel software. Comparisons between groups and different time points were done using a one-way analysis of variance (one-way ANOVA) with SPSS Software (V.16). Bonferroni or Games Howell *post hoc* tests were used based on Levene's Test analysis output. Significance was established at  $p < 0.05$ .

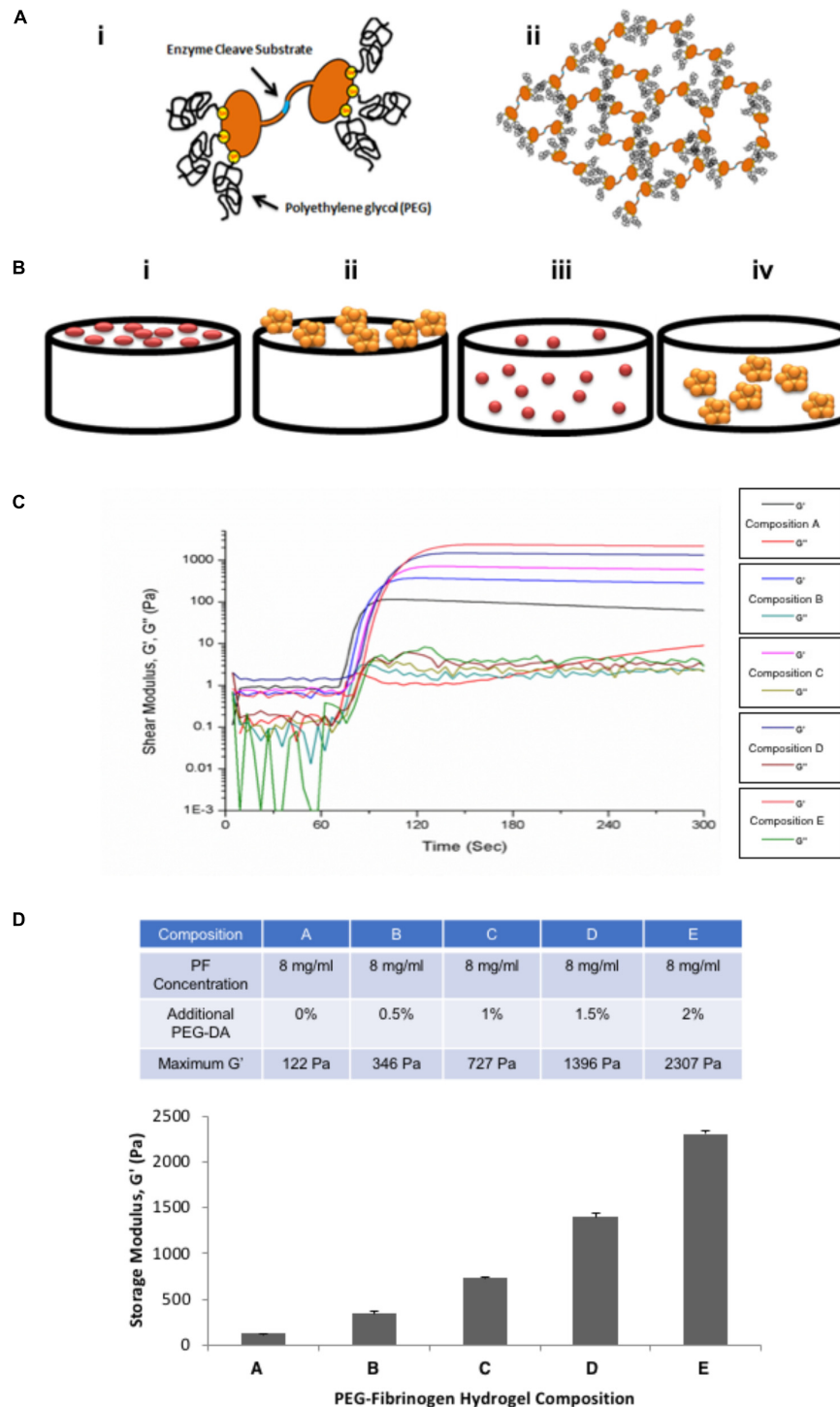
## RESULTS

### Characteristics and Mechanical Properties of PF Hydrogels

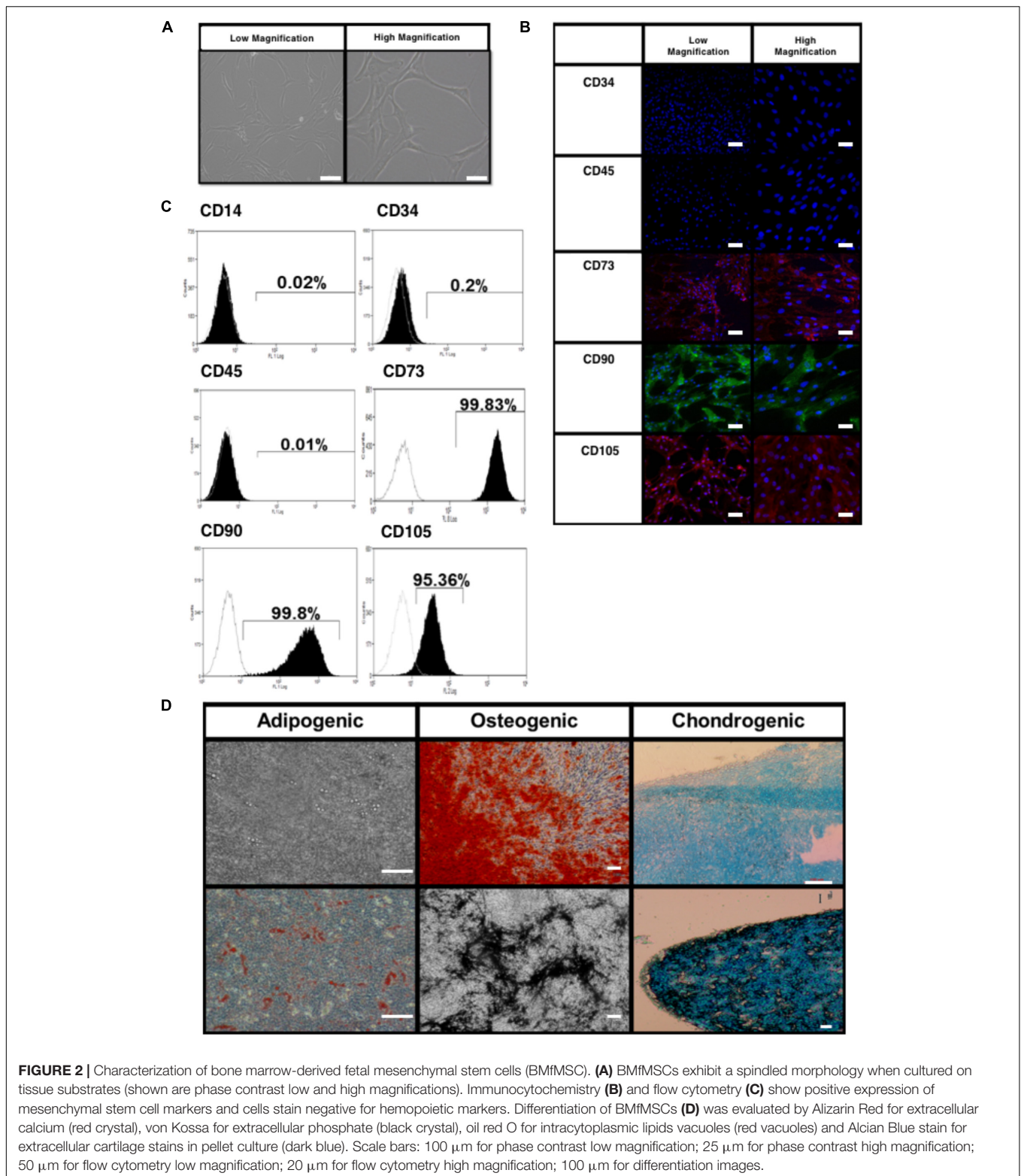
Schematic illustrations of the PF hydrogel preparation as well as the experimental design for single cell BMfMSCs and BMfMSC-spheroids seeded on the surface of the PF hydrogels or encapsulated inside the PF hydrogel are shown in **Figures 1A,B**. The protein concentration in the PF solution was measured to be 10.26 mg ml<sup>-1</sup> using a NanoDrop spectrophotometer at a wavelength of 280 nm (Rufaihah et al., 2013). During the preparation of the PF hydrogel precursor solution, PBS was added to dilute the fibrinogen concentration to 8 mg ml<sup>-1</sup> and PEG-DA was added to increase the crosslinking and the material's maximum shear storage modulus. The mechanical properties with and without the addition of PEG-DA were rheologically analyzed and the crosslinking kinetics are shown in **Figure 1C**. The maximum values of the shear storage modulus,  $G'$  (Pa), which represented the complete cross-linked state of the PF hydrogel, were significantly affected by the increased concentrations of additional PEG-DA as shown in **Figure 1D** ( $p < 0.05$ ).

### Characterization of BMfMSCs

The BMfMSCs exhibited a spindle shaped morphology when cultured on plastic substrates as seen by phase contrast microscopy (**Figure 2A**). Immunophenotype of the BMfMSCs were assessed by immunocytochemistry and flow cytometry. Immunostaining was negative for hemopoietic markers (CD34, CD45) and positive for mesenchymal markers (CD105, CD73) and adhesion molecules (CD90) (**Figure 2B**). Flow cytometry



**FIGURE 1 | (A)** Schematic illustration of PEG-fibrinogen (PF) hydrogel assembly. (i) Denatured fibrinogen fragments covalently attach to PEG in order to form a hydrogel precursor with protease cleavage sites (blue) and multiple thiol groups (yellow) which conjugate with functionalized PEG-diacrylate (PEG-DA). (ii) Assembly of PF hydrogels by light-activated radical-polymerization with additional PEG-DA resulting in a cross-linked hydrogel network. **(B)** Schematic illustration of experimental design: (i) BMfMSCs as single cells seeded on the surface of the hydrogel (2D); (ii) BMfMSC-spheroids on the surface of the hydrogel (2D); (iii) BMfMSCs as single cells cultured within the hydrogel (3D). There were six spheroids in each hydrogel for 2D and 3D cultures; (iv) BMfMSC-spheroids cultured within the hydrogel (3D). **(C)** Shear rheometry data from dynamic time-sweep tests performed during the photo-polymerization of the PF hydrogel precursor with photoinitiator upon activation with a long-wave ultra-violet (UV) light source after 60 s; the graph shows the shear storage modulus ( $G'$ , Pa) and shear loss modulus ( $G''$ , Pa) of various PF hydrogel compositions. **(D)** Graphical representation showing average values of the plateau shear storage modulus of various PF hydrogel as a function of percent additional PEG-DA cross-linker (table shows the average of the maximum storage modulus values of the different hydrogel compositions tested).



data also confirmed the presence of both mesenchymal and adhesion markers CD105 (95.25%), CD73 (99.57%), CD 90 (99.28%) and the absence of hemopoietic markers CD34 (2.81%) and CD45 (5.62%) (**Figure 2C**).

The BMfMSCs readily differentiated into adipogenic, osteogenic and chondrogenic lineages under their respective inductive culture conditions. For adipogenesis, BMfMSCs were cultured in adipogenic inductive medium for 21 days.



The presence of intracytoplasmic lipid vacuoles was confirmed by oil red O staining (**Figure 2D**). For osteogenesis, BMfMSCs were cultured in osteogenic inductive medium for 14 days and stained with von Kossa and Alizarin Red staining to detect the secretion of extracellular calcium and phosphate crystals, respectively (**Figure 2D**). For chondrogenic differentiation, BMfMSC pellets were cultured in chondrogenic inductive medium for 25 days and stained with Alcian Blue Stain to detect the ECM of proteoglycans (**Figure 2D**).

## Cell Metabolism

The alamarBlue was used as a reagent for evaluating cellular health; it assess whether cells have enough energy to proliferate. The metabolism of BMfMSC-spheroids (**Figure 3**) and BMfMSC single cell cultures (**Figure 4**), seeded on the surface of the PF hydrogel (i.e., 2D culture) or encapsulated in the PF hydrogel (i.e., 3D culture) showed different metabolic rates for each respective culture condition at the different time points. For example, there was a significant decrease in metabolic activity in the BMfMSC-spheroids from day 2 to day 6 in 2D culture [**Figures 3A(i), B(i)**]. In 3D culture of BMfMSC-spheroids, there was a significant reduction in metabolic activity of encapsulated cells in composition A and composition C hydrogels from day 3 to day 9, whereas in composition D and composition E hydrogels, there was a significant increase in metabolic activity from day 3 to day 9 (**Figure 3B**).

In 2D BMfMSC single cell culture, there was a significant increase in metabolic activity from day 2 to day 6 on composition B and composition C hydrogels (**Figure 4A**). The metabolic activity of BMfMSC single cell cultures in the 3D PF hydrogel constructs decreased significantly from day 3 to day 9 (**Figure 4B**), following a similar trend to that of the BMfMSC-spheroids in 2D culture (**Figure 3A**).

## Cell Morphology and Remodeling

The BMfMSCs as single cells seeded on the surface of PF hydrogels of differing degrees of stiffness displayed both lamellipodia and filopodia starting at day 4 onward (**Figure 5A** and **Table 1**). Hydrogels having low levels of PEG-DA crosslinker (compositions A, B, and C) showed more filopodia at day 6, whereas on compositions D and E, the cells showed more lamellipodia. The BMfMSC-spheroids seeded on the surface of PF hydrogels also showed lamellipodia and filopodia from day 4 onward and showed extensive protrusions at day 6 (**Figure 5B**). The composition A and composition E hydrogels contained cells with more lamellipodia at day 6, whereas composition B and composition D hydrogels contained cells with more filopodia; the composition C hydrogel contained cells that showed similar levels of lamellipodia and filopodia.

The BMfMSCs that were encapsulated in PF hydrogels showed lamellipodia and filopodia from day 3 onward (**Figure 6A** and **Table 2**). In composition A, composition D and composition E hydrogels, only lamellipodia were observed at day 6, whereas in composition B and composition C hydrogels, a mixture of lamellipodia and filopodia were observed at day 6. The composition D and composition E hydrogels contained cells with extensive protrusions of lamellipodia at day 9 and day 12.

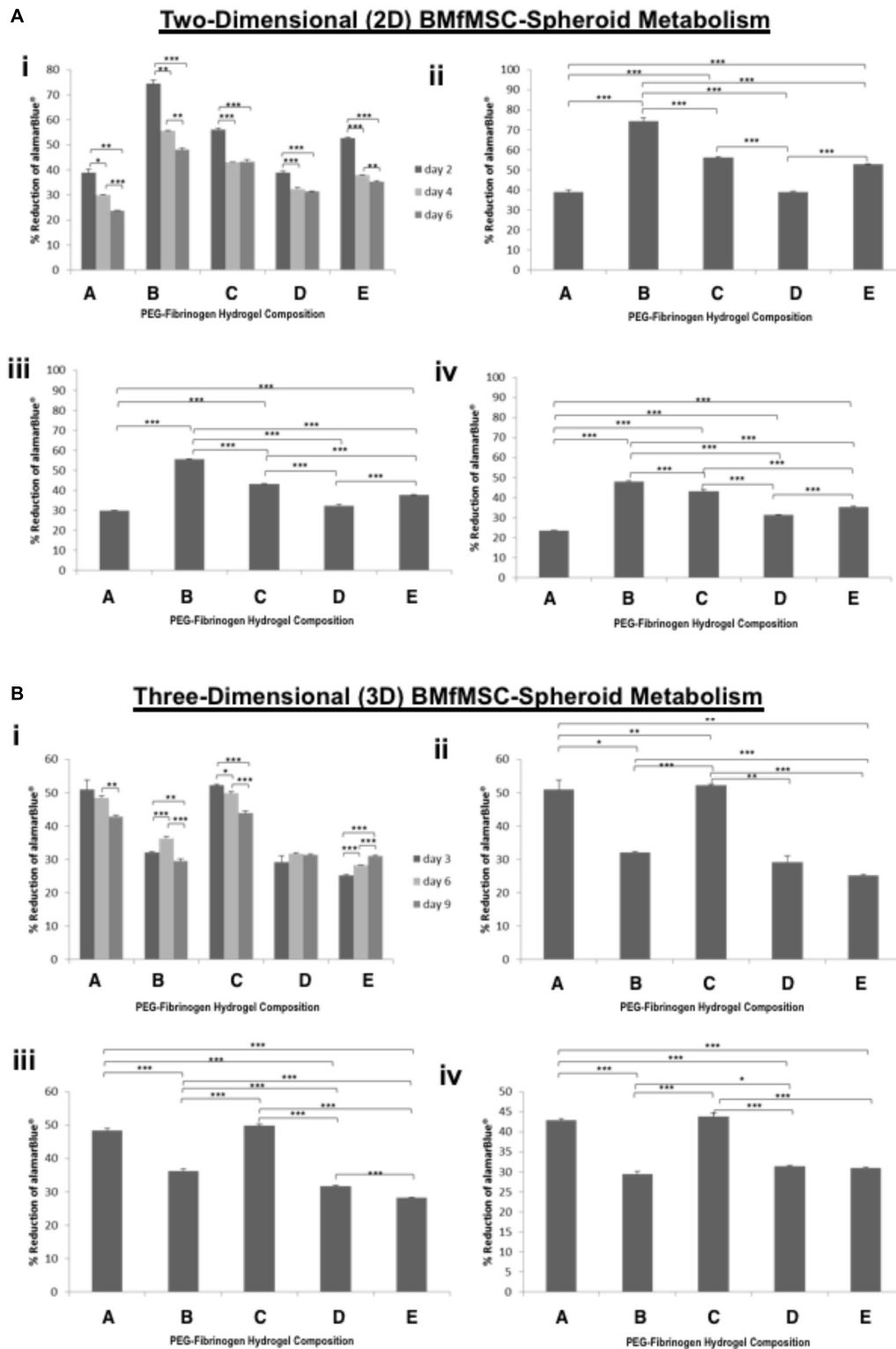
The composition D hydrogels contained cells with moderate levels of filopodia and composition E hydrogel contained cells with slight protrusions of the same at day 14. The BMfMSC-spheroids encapsulated in PF hydrogel showed lamellipodia and filopodia from day 6 onward (**Figure 6B**). The composition A, composition C and composition E hydrogels contained cells presenting similar protrusions of lamellipodia and filopodia at day 9 and the other two hydrogel groups contained cells showing pronounced filopodia protrusions. At day 12, the composition A contained cells with extensive lamellipodia protrusions, the composition B and composition E hydrogels contained cells with equal protrusions of both, whereas the composition C and composition D contained cells with more filopodia protrusions. At day 14, more lamellipodia were observed in cells on the composition A and composition D hydrogels, whereas more filopodia were observed on the composition B composition C and composition E hydrogels.

The quantitative analysis of total cell tube length using WimTube software showed highly variable results for both single cell cultures of BMfMSCs and BMfMSC-spheroids with hydrogels of varying stiffness in 2D and 3D (**Figure 7**). The BMfMSC-spheroids in the composition B hydrogel group exhibited significantly more total tube length than the other four hydrogel groups for both 2D and 3D experiments (**Figure 7A**). For the single cell BMfMSCs in the composition A hydrogel group, the total tube length measured was significantly higher than the other four hydrogels in both 2D and 3D studies (**Figure 7B**). At least four micrographs for each sample ( $n = 1$ ) were quantified for this assessment; a minimum of six samples were used for the data analysis of each composition.

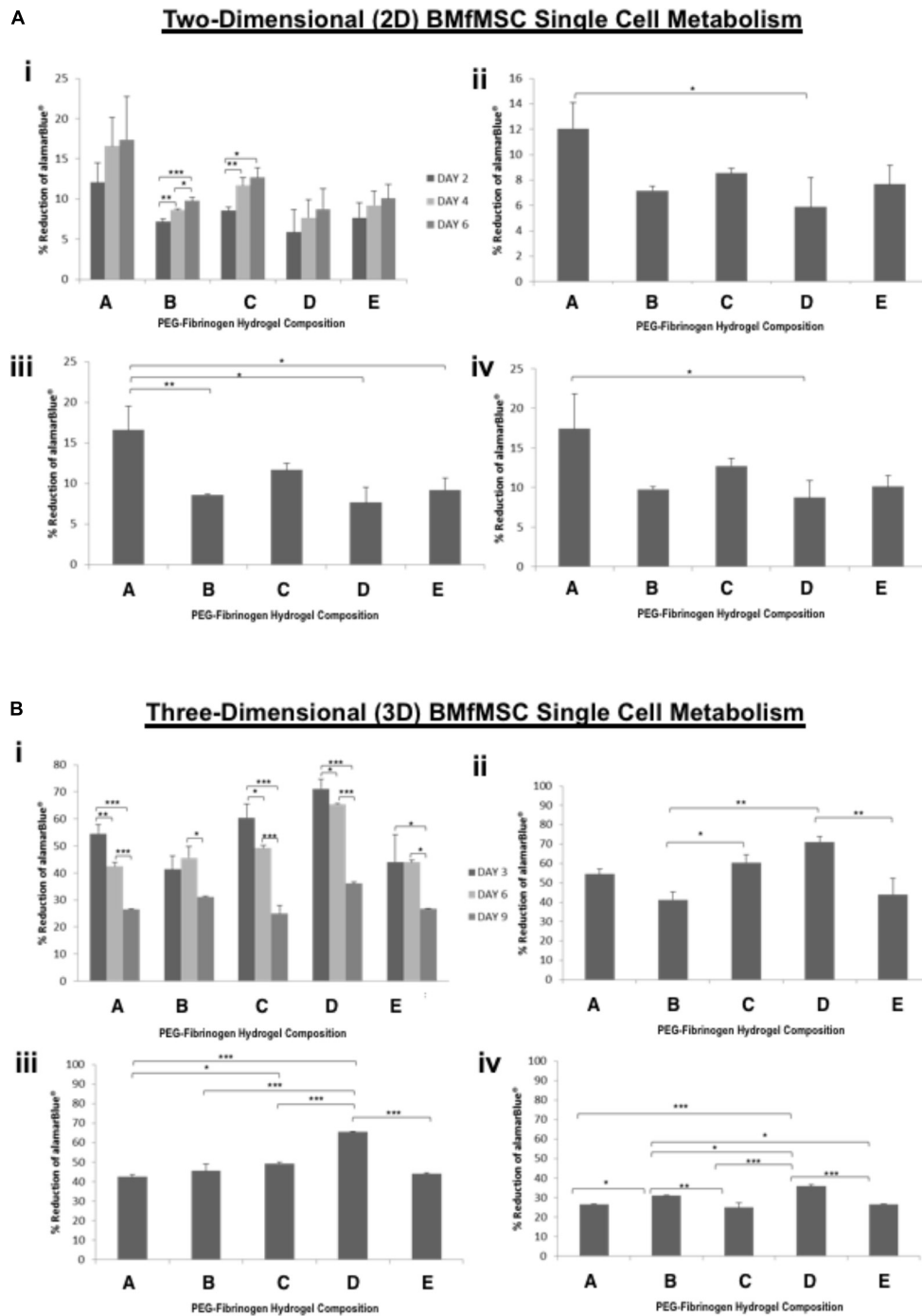
## Gene Expression

Quantitative reverse transcription PCR (qRT-PCR) results showed different expression of integrin subunits such as  $\alpha_5$ ,  $\beta_1$ ,  $\beta_3$  and  $\beta_5$  integrin subunits for BMfMSC single cells and BMfMSC-spheroids in different hydrogel groups both in 2D and 3D experiments (**Table 3**). In the single cell 2D experiments, BMfMSCs on composition D hydrogel expressed an increase in  $\alpha_5$ ,  $\beta_1$  and  $\beta_5$  integrin subunits by 13.5-fold, 16.5-fold, and 3.9-fold, respectively, as compared to the expression levels of BMfMSCs seeded on composition A hydrogel at day 2. The expression levels of that group were drastically reduced by day 4 and too low to be detected at day 6. In the BMfMSC-spheroid 2D experiments, the composition B and composition D hydrogel showed a 12.8-fold and 2.7-fold increase in expression of  $\alpha_5$  integrin subunit compared to the expression on composition A hydrogels. Although the expression of  $\beta_3$  integrin subunit was analyzed, their levels were undetected in both the 2D single cell and the spheroid experiments. A minimum of six samples were used for the analysis of each composition and treatment.

In the 3D single cell experiments, BMfMSCs in composition B hydrogels showed a 14.4-fold increase in expression of  $\beta_1$  integrin subunit compared to those in composition A hydrogels at day 3 but the same treatment showed 1.3-fold more expression of  $\beta_1$  integrin subunit compared to that of the composition A hydrogel at day 14. The BMfMSCs on the composition E hydrogels showed



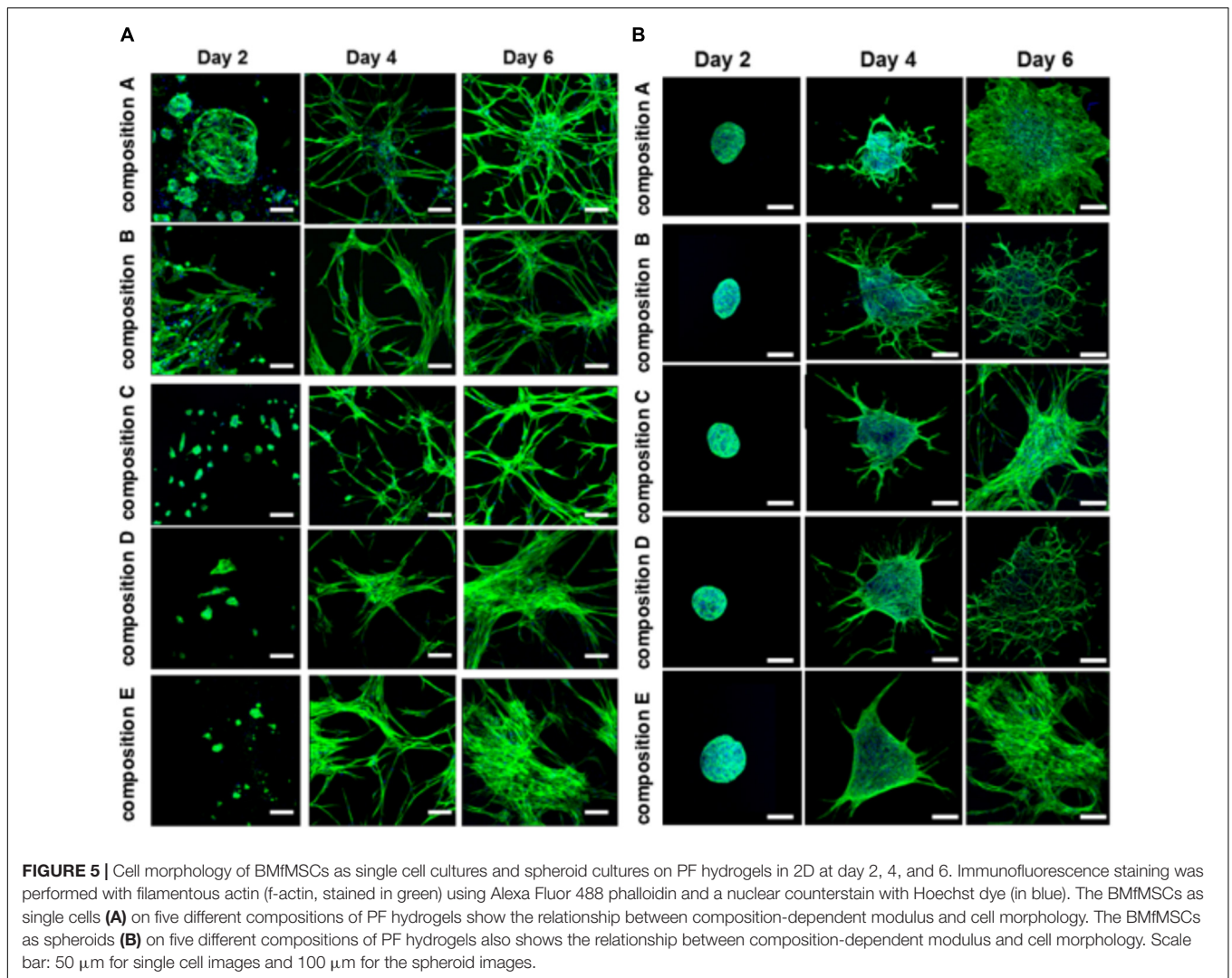
**FIGURE 3 |** Proliferation of BMfMSC-spheroid cultures in 2D and 3D is affected by PF hydrogel modulus. **(A)** The percent reduction in alamarBlue staining is directly proportional to the cell metabolism of BMfMSC-spheroids seeded on top of the five different compositions of PF hydrogels. The alamarBlue summary for all time-point (i) is broken down for statistical analysis on day 2 (ii), day 4 (iii), and day 6 (iv). **(B)** The percent reduction in alamarBlue for the BMfMSC-spheroids encapsulated in five different compositions of PF hydrogels is summarized for all time-point (i) and broken down for statistical analysis on day 3 (ii), day 6 (iii), and day 9 (iv). Data is expressed as the mean plus/minus standard deviations. Statistical significance between days or compositions was presented by: \* $p < 0.05$ ; \*\* $p < 0.01$  and \*\*\* $p < 0.001$  ( $n \geq 6$ ).



**FIGURE 4 |** AlamarBlue for BMfMSCs as single cell cultures in 2D and 3D is affected by PF hydrogel modulus. **(A)** The percent reduction in alamarBlue staining is directly proportional to the cell metabolism of BMfMSCs as single cells seeded on top of the five different compositions of PF hydrogels. The proliferation summary for all time-point (i) is broken down for statistical analysis on day 2 (ii), day 4 (iii), and day 6 (iv). **(B)** The percent reduction in alamarBlue for the BMfMSCs as single cells encapsulated in five different compositions of PF hydrogels is summarized for all time-point (i) and broken down for statistical analysis on day 3 (ii), day 6 (iii), and day 9 (iv). Data is expressed as the mean plus/minus standard deviations. Statistical significance between days or compositions was presented by: \* $p < 0.05$ ; \*\* $p < 0.01$  and \*\*\* $p < 0.001$  ( $n \geq 6$ ).

20.3-fold, 3.8-fold, 10.9-fold increase in expression of  $\beta_1$ ,  $\beta_3$ , and  $\beta_5$  integrin subunits, respectively, compared to those in composition A hydrogel at day 14.

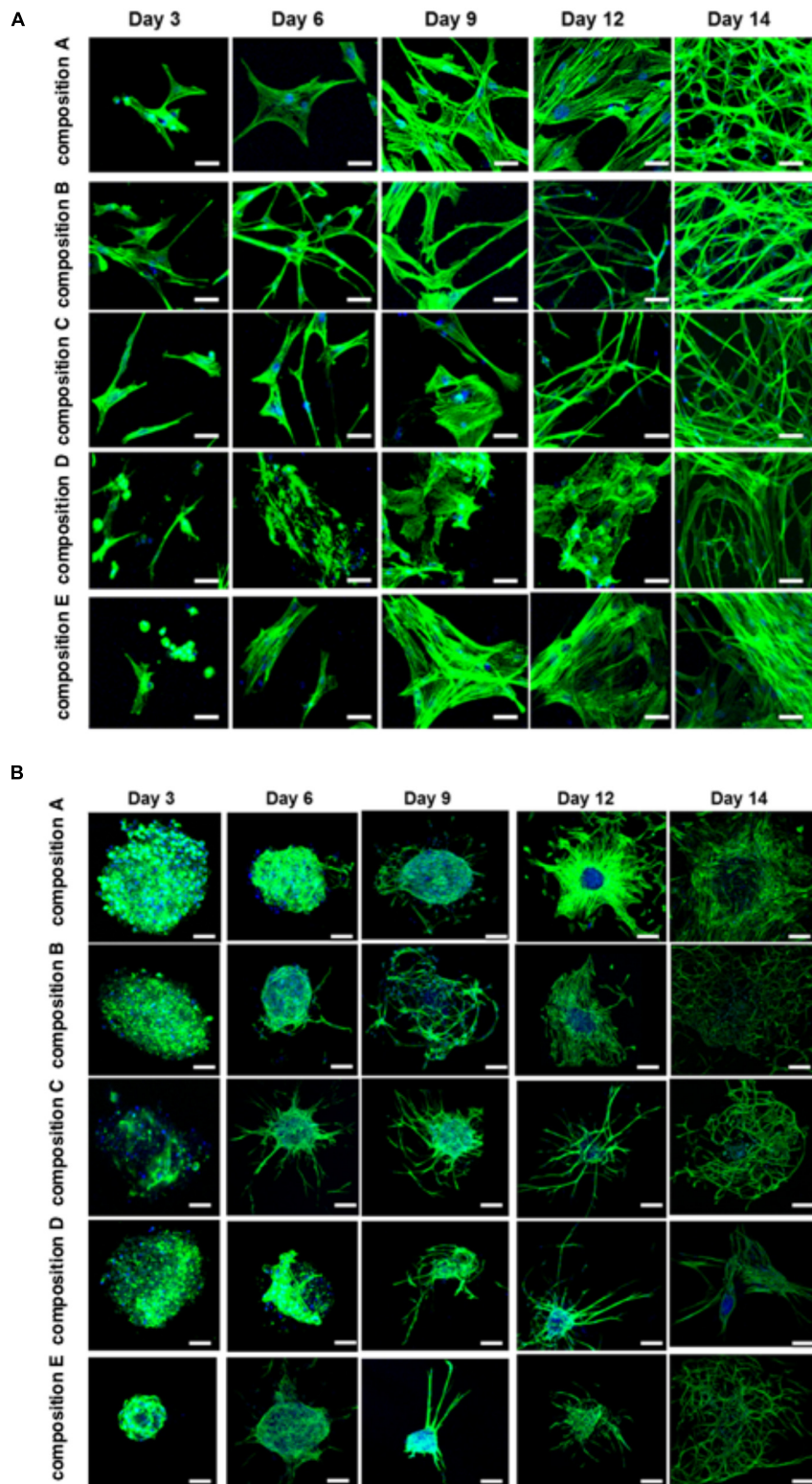
The BMfMSC-spheroids encapsulated in composition E hydrogel showed a 15-fold and 16.3-fold increase in expression of  $\alpha_5$  integrin subunit at day 3 and day 6, respectively, compared



**FIGURE 5 |** Cell morphology of BMfMSCs as single cell cultures and spheroid cultures on PF hydrogels in 2D at day 2, 4, and 6. Immunofluorescence staining was performed with filamentous actin (f-actin, stained in green) using Alexa Fluor 488 phalloidin and a nuclear counterstain with Hoechst dye (in blue). The BMfMSCs as single cells **(A)** on five different compositions of PF hydrogels show the relationship between composition-dependent modulus and cell morphology. The BMfMSCs as spheroids **(B)** on five different compositions of PF hydrogels also shows the relationship between composition-dependent modulus and cell morphology. Scale bar: 50  $\mu\text{m}$  for single cell images and 100  $\mu\text{m}$  for the spheroid images.

**TABLE 1 |** Levels of lamellipodia and filopodia in BMfMSCs as single cells and as spheroids in 2D, as assessed from immunofluorescence staining ( $n \geq 6$ ).

Time point	Composition	2D BMfMSCs as single cells		2D BMfMSC-spheroids	
		Lamellipodia	Filopodia	Lamellipodia	Filopodia
Day 2	A	–	–	–	–
	B	–	–	–	–
	C	–	–	–	–
	D	–	–	–	–
	E	–	–	–	–
Day 4	AB	++	++++	++	+++
	C	+	++	+	+
	D	++	+	++	+
	E	++	+	++	+
Day 6	A	++	+++	+++	–
	B	++	+++	–	+++
	C	++	+++	++	++
	D	+++	+	–	+++
	E	+++	+	+++	+



**FIGURE 6 |** Cell morphology of BMfMSCs as single cell cultures and spheroid cultures in PF hydrogels in 3D at day 3, 6, 9, 12, and 14. Immunofluorescence staining was performed with filamentous actin (f-actin, stained in green) using Alexa Fluor 488 phalloidin and a nuclear counterstain with Hoechst dye (in blue). The BMfMSCs as single cells (**A**) on five different compositions of PF hydrogels show the relationship between composition-dependent modulus and cell morphology. The BMfMSCs as spheroids (**B**) on five different compositions of PF hydrogels also shows the relationship between composition-dependent modulus and cell morphology. Scale bar: 20  $\mu\text{m}$  for the single cell images and 100  $\mu\text{m}$  for the spheroid images.

**TABLE 2** | Levels of lamellipodia and filopodia in BMfMSCs as single cells and as spheroids in 3D, as assessed from immunofluorescence staining ( $n \geq 6$ ).

Time point	Composition	3D BMfMSC as single cells		3D BMfMSC-spheroids	
		Lamellipodia	Filopodia	Lamellipodia	Filopodia
Day 3	A	+	–	–	–
	B	+	+	–	–
	C	+	+	–	–
	D	+	+	–	–
	E	+	–	–	–
Day 6	A	+	–	+	+
	B	+	+	+	+
	C	+	+	+	++
	D	+	–	+	--
	E	+	–	+	++
Day 9	A	+	+	+	+
	B	+	+	+	++
	C	+	+	++	++
	D	+++	–	+	++
	E	+++	–	+	+
Day 12	A	+	+	+++	+
	B	–	++	+	+
	C	–	++	–	++
	D	+++	–	+	++
	E	+++	–	++	++
Day 14	A	+	+++	+++	+
	B	+	+++	–	+++
	C	+	+++	+	+++
	D	+	++	++	+
	E	+++	+	+	+++

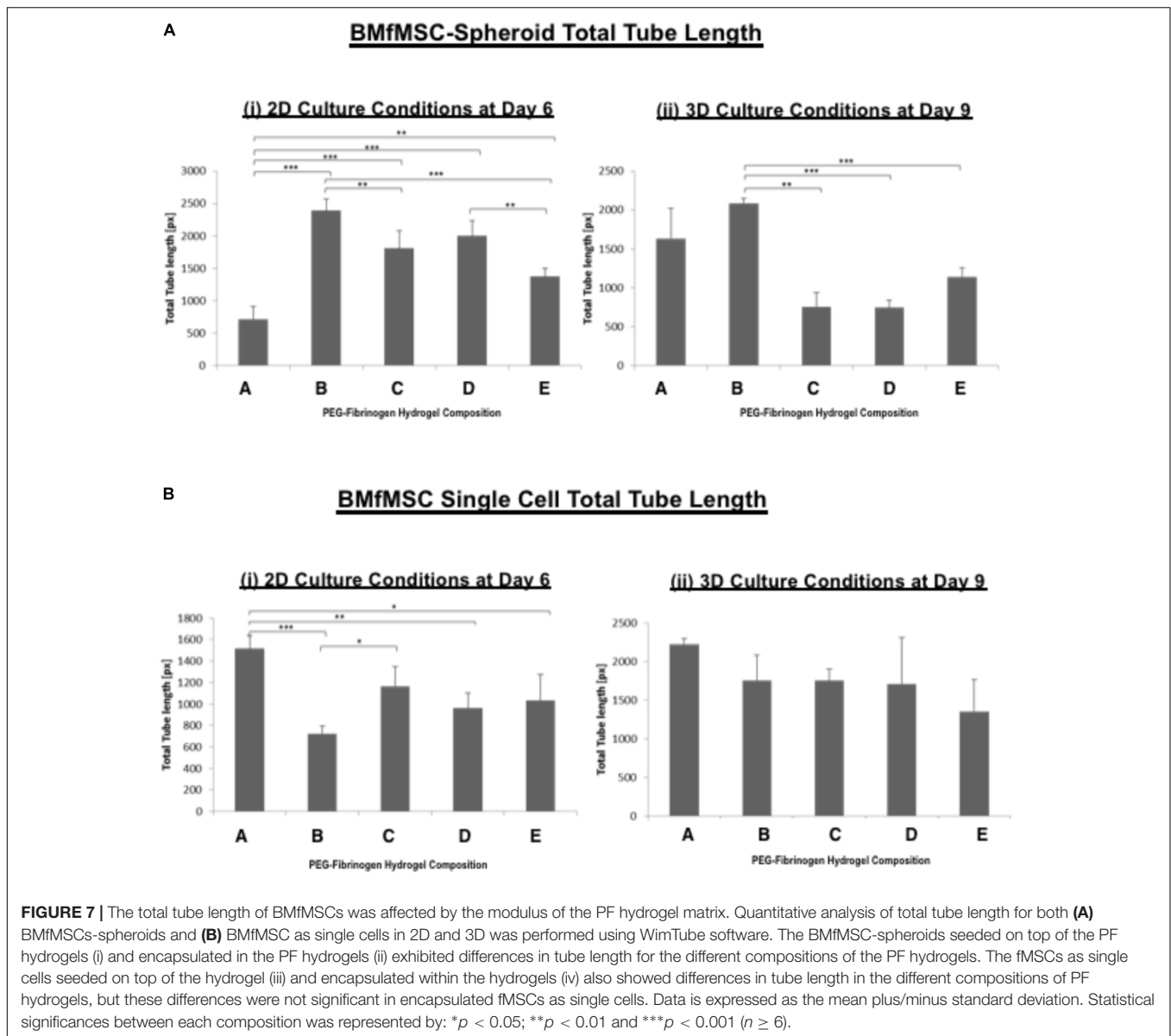
to those in composition A hydrogels. BMfMSC-spheroids encapsulated in composition E hydrogels showed an 8.1-fold, 12.6-fold, and 20.7-fold increase in expression of  $\beta_1$ ,  $\beta_3$ , and  $\beta_5$  integrin subunits, respectively, compared to those in composition A hydrogel at day 3. At day 6, composition E hydrogels showed a 4-fold, 11-fold, and 19.3-fold increase in expression of  $\beta_1$ ,  $\beta_3$ , and  $\beta_5$  integrin subunits, respectively, compared to those in composition A hydrogel. The expression of  $\beta_1$ ,  $\beta_3$ , and  $\beta_5$  integrin subunits were too low to be detected at the later time points of the experiments (from day 9 to day 12).

## DISCUSSION

Mesenchymal stem cells have been clinically tested for treating several disorders, including bone ailments, cardiovascular diseases, nervous system disorders, and autoimmune diseases (Parekkadan and Milwid, 2010; Hollweck et al., 2012). Although the reports from these clinical studies have had mixed results, there are some indications where MSCs have had a beneficial impact. For example, human patients receiving MSC transplants following MI have shown significant improvements in cardiac output parameters at early time-points (Chen et al., 2004). Ischemic cardiomyopathy patients receiving MSC grafts indicated increased functional capacity, better quality-of-life

and improved ventricular remodeling (Hare et al., 2012). Two MSC-treated osteoarthritis patients demonstrated significant increase in total reduction in their visual analog scale (VAS) scores at 12 weeks post-treatment (Pak, 2011). Four early-stage systemic lupus erythematosus patients treated with allogeneic MSCs showed stable disease remission for 12–18 months (Sun et al., 2009). Six out of 10 spinal cord injured patients treated with MSCs measured improvement in motor function scores of the upper extremities and three of them reported improvement in their daily living activities (Park et al., 2012). MRI data for these patients also showed beneficial electrophysiological changes at 30 months follow-up post-intervention.

Human fMSCs may be a good source of stem cells for tissue repair in certain indications (O'Donoghue and Chan, 2006). In bone tissue engineering applications, fMSCs exhibited greater proliferation capacity, robust osteogenic potential and lower immunogenicity, as compared to adult MSCs (Zhang et al., 2010, 2012). Clinical experience using allogeneic HLA-mismatched fMSC transplantation resulted in engraftment and differentiation into bone in a human female fetus with multiple intrauterine fractures, even though the recipient was immunocompetent (Le Blanc et al., 2005). After 10 months of transplantation, 7.4% of Y positive cells in the whole genome and 0.3% of XY positive cells in slides were identified in bone biopsy specimens and the bone histology revealed normal bone trabeculae. After 2



years, the child's psychomotor development and growth were normal.

Pre-clinical experience with fMSCs in other indications have also demonstrated efficacy in treating tissue disorders. Airey et al. (2004) injected human fMSCs intraperitoneally into sheep fetuses and demonstrated successful engraftment of these cells into the hearts of fetal lambs *in utero*. They reported no differences in engraftment of hMSCs from adult bone marrow, fetal brain, and fetal liver. Chan et al. (2007) transplanted fMSCs into dystrophic mice at E14-E16 gestation and observed widespread, long-term engraftment with indication of myogenic differentiation of MSCs into skeletal and myocardial muscle as well as other cell types, including hepatocytes. The same group used fMSCs to demonstrate enhancement of phenotype in a mouse model of Type III Osteogenesis Imperfecta (OI) and found that donor cells were localized to bone and expressed osteoblast

lineage genes and produced the extracellular bone structural protein osteopontin (Guillot et al., 2008).

The benefits of fMSC therapy notwithstanding, there are still several limitations that hinder efficacy, most notably cell survival and localized integration of the cell graft in the harsh environment of the diseased or injured tissue (Burdick et al., 2016). Hydrogels have been proposed as a carrier to deliver grafted cells while temporarily protecting them and localizing their therapeutic effects (Seliktar, 2012). However, the modulus of the hydrogels has to be carefully considered because it can affect stem cell renewal, structure, function and commitment to differentiation into target cells (Kersch et al., 2016). Lv et al. (2015) elucidated the mechanism by which stem cells differentiate and grow in response to a substrate stiffness that mimics the physiological condition of the cells based on the observations that a hydrogel substrate with a

**TABLE 3 |** Gene expression analysis showing the expression of  $\alpha_5$ ,  $\beta_1$ ,  $\beta_3$ , and  $\beta_5$  integrin subunits for 2D BMfMSCs as single cells in 2D (i); for BMfMSC-spheroids in 2D (ii); for 3D BMfMSCs as single cell in 3D (iii); and for BMfMSC-spheroids in 3D (iv).

**(i) 2D BMfMSC single cell gene expression (n ≥ 6).**

Time point	Composition	Fold change relative to composition A		
		$\beta_1$	$\beta_5$	$\alpha_5$
Day 2	A	1	1	1
	B	0.62	0.68	1.30
	C	0.59	1.86	2.52
	D	16.46	3.87	13.5
	E	3.22	11.9	–
Day 4	A	1	1	1
	B	0.18	0.16	–
	C	0.20	0.15	0.50
	D	0.47	0.37	0.42
	E	–	4.64	–
Day 6	A	–	1	–
	B	–	0.27	–
	C	–	0.44	–
	D	–	1.50	–
	E	–	2.61	–

**(ii) 2D BMfMSC-Spheroid Gene Expression (n ≥ 6).**

Time point	Composition	Fold change relative to composition A		
		$\beta_1$	$\beta_5$	$\alpha_5$
Day 2	A	1	1	1
	B	3.31	2.3	–
	C	6.29	7	–
	D	–	33.6	–
	E	3.22	4.8	1.33
Day 4	A	1	1	–
	B	1.33	1.26	–
	C	–	4.93	–
	D	3.48	5.22	–
	E	5.64	6.68	–
Day 6	A	1	1	1
	B	1.198	1	12.75
	C	1.1	0.72	–
	D	–	4.58	2.65
	E	–	4.88	–

**(iii) 3D BMfMSC-single cell gene expression (n ≥ 6).**

Time point	Composition	Fold change relative to composition A		
		$\beta_1$	$\beta_3$	$\beta_5$
Day 3	A	1	1	1
	B	14.4	–	29.06
	C	0.76	0.71	–
	D	–	–	24.11
	E	–	–	17

(Continued)

**TABLE 3 |** Continued

Time point	Composition	Fold change relative to composition A		
		$\beta_1$	$\beta_3$	$\beta_5$
Day 6	A	1	–	1
	B	0.13	–	2.15
	C	–	–	0.06
	D	–	–	3.24
	E	–	–	–
Day 9	A	1	1	1
	B	1.15	1.59	2.12
	C	2.77	0.79	1.4
	D	11.98	–	12.51
	E	–	–	–
Day 12	A	1	1	1
	B	0.85	–	3.19
	C	1.37	–	1.55
	D	1.44	–	–
	E	–	–	–
Day 14	A	1	1	1
	B	1.3	0.24	0.64
	C	1.07	0.28	0.79
	D	2.55	2.46	2.36
	E	20.25	3.8	10.87

**(iv) 3D BMfMSC-spheroid gene expression (n ≥ 6).**

Time point	Composition	Fold change relative to composition A			
		$\beta_1$	$\beta_3$	$\beta_5$	$\alpha_5$
Day 3	A	1	1	1	1
	B	1.15	0.97	3.48	2.75
	C	0.65	0.76	1.05	1.15
	D	0.62	1.13	0.14	0.66
	E	8.08	12.61	20.651	14.97
Day 6	A	1	1	1	1
	B	1.05	0.79	3.14	3.2
	C	0.46	0.69	1.13	1.28
	D	0.48	1.01	0.34	0.89
	E	4.04	10.98	19.30	16.25
Day 9	A	–	–	–	1
	B	–	–	–	–
	C	–	–	–	0.99
	D	–	–	–	1.34
	E	–	–	–	0.52
Day 12	A	–	–	–	–
	B	–	–	–	–
	C	–	–	–	–
	D	–	–	–	–
	E	–	–	–	–
Day 14	A	–	–	–	1
	B	–	–	–	0.28
	C	–	–	–	0.17
	D	–	–	–	1.75
	E	–	–	–	5.06



Young's modulus ( $E$ ) that matches the stiffness of the native tissue ECM directs the stem cell differentiation toward that corresponding tissue lineage. Hydrogel substrates mimicking ECM properties of pancreas ( $E = 1.2$  kPa), brain ( $E = 0.1$  to  $1$  kPa), muscle ( $E = 8$  to  $17$  kPa), bone tissue ( $E = 25$  to  $40$  kPa), and cartilage ( $E = 3$  kPa) direct MSCs to differentiate into beta cells, neurocytes, myoblasts, osteoblasts and chondrocytes, respectively. Several other studies reported similar findings when investigating how stem cell behavior corresponded to matrix stiffness, analyzing gene expression changes and intracellular signaling cascades emanating from mechanical cues from the culture substrate (Engler et al., 2006; Narayanan et al., 2014; Wang et al., 2014).

We studied the behavior of BMfMSCs (as single cells) or BMfMSC-spheroids under the influence of five different stiffness levels of PF hydrogels having storage shear modulus ranging from  $G' = 120$  Pa to  $2,300$  Pa. These values correspond to Young's modulus values of  $E = 360$  Pa to  $6,900$  Pa. Our results indicate that the modulus of the PF hydrogels, altered by varying the relative amount of PEG-DA crosslinker, affected gene expression. The response of the cells culminated as different cell morphologies and metabolic activities in both 2D and 3D environments. In a 2D environment, for example, there was a significant increase in metabolic activity of single cell BMfMSCs in contrast to the BMfMSC-spheroids, where there was a significant decrease in the metabolic activity from day 2 to day 6. We also found that there was a minimum seeding density required for the BMfMSC single cell experiments to enable these outcomes (7,000 cells per well).

In the 3D environment, the results were more confounding. Single BMfMSCs encapsulated in PF hydrogels showed a significant decrease in metabolic activity from day 3 to day 9, yet BMfMSC-spheroids encapsulated in certain PF hydrogels behaved differently. For example, in composition A and composition C hydrogels, there was a significant decrease in metabolic activity from day 3 to day 9, whereas in composition D and composition E hydrogels, there was an increase in metabolic activity for the same time points. Interestingly, the composition B hydrogels provided a similar 3D culture platform for the growth of both single cells and spheroids; exhibiting the same metabolic activity pattern from day 3 to day 6. (i.e., the metabolic activity increased from day 3 to 6 and then showed a drastic decrease by day 9). Our results thus suggest that in addition to the modulus of the hydrogel and cell seeding density, the culture condition of single cells versus spheroids also influences the metabolism of the cells.

The different modulus of the PF hydrogels influenced morphological changes in the BMfMSCs, reflecting the dependency of morphogenesis on matrix modulus. For example, in 2D experiments, as the stiffness of the hydrogel increased, more protrusions of actin rich structures at the cell surface (i.e., lamellipodia) were observed for single cell cultures whereas more filopodia were observed for BMfMSC-spheroids at later time points of the study. Filopodia are actin filament bundles that protrude from lamellipodia to form spikes which can sense the ECM and direct cell migration. They serve as a type of mechanical sensor for migrating cells to identify suitable adhesion sites on neighboring cells (Xue et al., 2010). These

protrusions also contribute to other cellular processes including wound healing, chemotaxis, adhesion, and neuronal growth cone formation (Mattila and Lappalainen, 2008). Filopodia can turn into lamellipodia in order to coordinate cell motility in response to surface topography (Collart et al., 2014). In this 2D study, BMfMSC-spheroids on composition B and composition D hydrogels form better cellular interconnections by exhibiting more filopodia at day 6. In contrast, the single cell BMfMSC cultures showed more filopodia at composition A, composition B and composition C, suggesting strong cellular interconnections as early as day 4. Another interesting finding was that when cell density was increased to 12,000 BMfMSCs per well in the single cell cultures, more lamellipodia were observed at the earlier time points in lower stiffness PF hydrogels (data not shown).

In 3D experiments, single cell BMfMSC cultures showed unique structural changes and exhibited only lamellipodia within the lowest (composition A) and highest stiffness hydrogels (composition D and composition E), whereas BMfMSCs encapsulated in composition B and composition C hydrogels exhibited both lamellipodia and filopodia at day 6. The encapsulation of BMfMSCs in moderate stiffness hydrogels could most likely sense their neighboring cells rapidly and form strong cellular interconnections. The BMfMSC-spheroids encapsulated in the PF hydrogels exhibited extensive lamellipodia and filopodia by day 9 in culture. At day 12, more filopodia were observed with an increase in stiffness of the hydrogels. The different levels of filopodia exhibited by the cells was identified across different time points. However, we found that certain modulus values of the PF hydrogel support higher degree of filopodia formation. Previous studies have elucidated that filopodia in MSCs may be involved in wound healing and tissue regeneration (Ryu et al., 2013; Mobasserri et al., 2017). Thus, by altering the stiffness of the hydrogel, BMfMSCs could be tuned to express more filopodia, thereby making them more amenable for specific tissue repair applications. Previous studies have also suggested the importance of filopodia activity for other functions (da Costa et al., 2012; Eke et al., 2017), including for the commencement of MSC differentiation into an osteoblastic lineage (Cassidy et al., 2014).

Several studies suggest that ECM guides cell adhesion, migration and encourages differentiation by activating certain integrin subunits (Dalby et al., 2014; Kshitiz Afzal et al., 2015). Hamidouche et al. (2009) demonstrated that activation of  $\alpha_5$ -integrin expression could direct MSCs toward osteoblastic differentiation. Schwab et al. (2013) showed that increased expression of  $\alpha_5$  and  $\alpha_V$  integrin subunits have positive effects on osteoblastic differentiation of MSCs. They also showed that the  $\alpha_5$  integrin subunit has a positive role in guiding MSCs toward osteoblastic differentiation while  $\beta_3$  integrin subunit suppresses such differentiation. In our 2D single cell experiments, composition C and composition D hydrogels showed greatest expression of  $\alpha_5$  integrin subunit compared to the composition A at the initial time point. However, the expression level decreased drastically and diminished at the later time points. In 2D spheroid experiments, composition B hydrogels showed a 12.7-fold increase in  $\alpha_5$

integrin subunit compared to the composition A hydrogels at the later time points of the study, although the expression level was initially low. Considering the data from Schwab et al. (2013) and our observations on  $\alpha_5$ -integrin expression, with the complete absence of  $\beta_3$  integrin subunit in the 2D experiments, we speculate that these PF hydrogel formulations together with BMfMSCs could potentially be used for osteoblastic differentiation.

In our 3D single cell experiments, composition D and composition E hydrogels showed more than two to three times the expression levels of  $\beta_3$  integrin subunit compared to the composition A hydrogel at day 14. The 3D spheroid experiments showed that the composition E hydrogels have higher expression levels of  $\beta_3$  integrin subunit compared to composition E hydrogels at day 3 and day 4. Previous research determined that a medium stiffness substrate that promotes  $\beta_3$  integrin subunit expression can also mediate MSCs toward a myogenic differentiation pathway (Yu et al., 2013). Du et al. (2011) suggested that a soft matrix enhances  $\beta_1$  integrin subunit internalization, which in turn promoted endocytosis factors and resulted in the expression of neuronal genes in stem cells. Previous studies have stated that reduced  $\beta_1$  integrin activation could lead to keratinocyte differentiation (Lv et al., 2015). We found increased expression of  $\beta_1$  integrin subunit when BMfMSCs were encapsulated as single cells in the higher stiffness composition E hydrogels, but observed the absence of  $\beta_1$  integrin subunit expression when BMfMSCs were seeded as single cells in composition E hydrogels. Taken together, we speculate that the right combination of BMfMSC culture conditions (i.e., single cells or spheroids) and optimal modulus of the PF hydrogel could be designed to promote upregulation or suppression of  $\beta_1$  integrin subunit expression for lineage-specific differentiation to muscle, nerve or other tissue types.

In previous experiments using pericyte-derived stem cells and muscle-derived satellite cells as single cell cultures within optimized PF hydrogels, we did maximize differentiation to muscle lineages by fine tuning of the hydrogel modulus to approximately  $G' = 200$  Pa (Fuoco et al., 2012, 2014, 2015; Costantini et al., 2017). We speculate that the mid-stiffness PF hydrogels together with single cell BMfMSCs in 3D culture may likewise have optimal properties to support myogenic differentiation and related applications, although further studies would be required to verify this hypothesis.

## Limitations

We analyzed the metabolism and morphogenesis of BMfMSCs in or on hydrogels of varying stiffness based on correlations found in previous studies and our gene expression analysis. However, we did not evaluate the specific lineage determination of the cells. Future experiments must be performed to identify specifically how the different stiffness environments affect the lineage of the BMfMSCs as well as their proliferation and self-renewal. Further studies are also needed to optimize specific differentiation environments and media compositions,

and to study the functional assays of transplanted cells to determine the ideal hydrogel for each specific clinical application. For example, BMfMSCs in the appropriate stiffness hydrogel could be cultured in myogenic differentiation medium for a particular time frame and could be tested for myogenic gene expression, as part of a complete strategy to enhance tissue regeneration following muscle injury. Further studies, including transplantation of hydrogels with differentiated cells into a myocardial repair model to examine their role and efficacy in improving the diseased state are also required to substantiate our hypotheses.

## CONCLUSION

Based on the results, different degrees of PF hydrogel stiffness influenced the distribution of F-actin filaments, metabolic activity of BMfMSCs, tube length and also the expression levels of several integrin subunits. The stiffness of the PF hydrogel could be altered by varying amounts of PEG-DA crosslinker in the hydrogel composition. We also found that cell seeding density is an important factor which promotes sufficient cell-to-cell contact, and that such interactions must take place before remodeling could occur in or on the PF hydrogels. Our findings provide valuable information for scaffold design for a wide range of applications and also suggest methods with which to optimize cell culture in responsive hydrogel scaffolds.

## AUTHOR CONTRIBUTIONS

AR and SC designed the experiments, conducted the research, analyzed the data, supervised the research, and prepared the manuscript. MM and KL designed and performed the experiments, analyzed the data, and prepared the manuscript. MC, CM, JC, TK, and DS designed the experiments, analyzed the data, supervised the research, and prepared the manuscript.

## FUNDING

The authors would like to acknowledge funding support from National Research Foundation (NRF)-Technion-NUS Grant for Regenerative Medicine Initiative in Cardiac Restoration Therapy. The authors would also like to acknowledge funding support from the Israel Science Foundation, grant no. 1245/14.

## ACKNOWLEDGMENTS

The authors would like to thank Dedy Sandikin from Department of Obstetrics and Gynaecology, NUS for assisting with the isolation of the BMfMSC and characterization of the stem cells.

## REFERENCES

- Airey, J. A., Almeida-Porada, G., Colletti, E. J., Porada, C. D., Chamberlain, J., Movsesian, M., et al. (2004). Human mesenchymal stem cells form Purkinje fibers in fetal sheep heart. *Circulation* 109, 1401–1407. doi: 10.1161/01.CIR.0000124222.16321.26
- Almany, L., and Seliktar, D. (2005). Biosynthetic hydrogel scaffolds made from fibrinogen and polyethylene glycol for 3D cell cultures. *Biomaterials* 26, 2467–2477. doi: 10.1016/j.biomaterials.2004.06.047
- Anjum, F., Lienemann, P. S., Metzger, S., Biernaskie, J., Kallos, M. S., and Ehrbar, M. (2016). Enzyme responsive GAG-based natural-synthetic hybrid hydrogel for tunable growth factor delivery and stem cell differentiation. *Biomaterials* 87, 104–117. doi: 10.1016/j.biomaterials.2016.01.050
- Bergmann, O., Zdunek, S., Alkask, K., Druid, H., Bernard, S., and Frisen, J. (2011). Identification of cardiomyocyte nuclei and assessment of ploidy for the analysis of cell turnover. *Exp. Cell Res.* 317, 188–194. doi: 10.1016/j.yexcr.2010.08.017
- Berkovitch, Y., and Seliktar, D. (2017). Semi-synthetic hydrogel composition and stiffness regulate neuronal morphogenesis. *Int. J. Pharm.* 523, 545–555. doi: 10.1016/j.ijpharm.2016.11.032
- Burdick, J. A., Mauck, R. L., and Gerecht, S. (2016). To serve and protect: hydrogels to improve stem cell-based therapies. *Cell Stem Cell* 18, 13–15. doi: 10.1016/j.stem.2015.12.004
- Campagnoli, C., Roberts, I. A., Kumar, S., Bennett, P. R., and Bellantuono, I. (2001). Identification of mesenchymal stem/progenitor cells in human first-trimester fetal blood, liver, and bone marrow. *Blood* 98, 2396–2402. doi: 10.1182/blood.V98.8.2396
- Caplan, A. I. (2015). Adult mesenchymal stem cells: when, where, and how. *Stem Cells Int.* 2015:628767. doi: 10.1155/2015/628767
- Cassidy, J. W., Roberts, J. N., Smith, C. A., Robertson, M., White, K., Biggs, M. J., et al. (2014). Osteogenic lineage restriction by osteoprogenitors cultured on nanometric grooved surfaces: the role of focal adhesion maturation. *Acta Biomater.* 10, 651–660. doi: 10.1016/j.actbio.2013.11.008
- Chan, J., O'Donoghue, K., Gavina, M., Torrente, Y., Kennea, N., Mehmet, H., et al. (2006). Galectin-1 induces skeletal muscle differentiation in human fetal mesenchymal stem cells and increases muscle regeneration. *Stem Cells* 24, 1879–1891. doi: 10.1634/stemcells.2005-0564
- Chan, J., Waddington, S. N., O'Donoghue, K., Kurata, H., Guillot, P. V., Gotherstrom, C., et al. (2007). Widespread distribution and muscle differentiation of human fetal mesenchymal stem cells after intrauterine transplantation in dystrophic mdx mouse. *Stem Cells* 25, 875–884. doi: 10.1634/stemcells.2006-0694
- Chen, S. L., Fang, W. W., Ye, F., Liu, Y. H., Qian, J., Shan, S. J., et al. (2004). Effect on left ventricular function of intracoronary transplantation of autologous bone marrow mesenchymal stem cell in patients with acute myocardial infarction. *Am. J. Cardiol.* 94, 92–95. doi: 10.1016/j.amjcard.2004.03.034
- Collart, P., Dutilleul, Y., Panayotov, I., Secret, E., Cunin, F., Gergely, C., et al. (2014). Initial stem cell adhesion on porous silicon surface: molecular architecture of actin cytoskeleton and filopodial growth. *Nanoscale Res. Lett.* 9:564. doi: 10.1186/1556-276X-9-564
- Costantini, M., Testa, S., Mozetic, P., Barbetta, A., Fuoco, C., Fornetti, E., et al. (2017). Microfluidic-enhanced 3D bioprinting of aligned myoblast-laden hydrogels leads to functionally organized myofibers in vitro and in vivo. *Biomaterials* 131, 98–110. doi: 10.1016/j.biomaterials.2017.03.026
- Cowan, C. M., Shi, Y. Y., Aalami, O. O., Chou, Y. F., Mari, C., Thomas, R., et al. (2004). Adipose-derived adult stromal cells heal critical-size mouse calvarial defects. *Nat. Biotechnol.* 22, 560–567. doi: 10.1038/nbt958
- da Costa, D. S., Pires, R. A., Frias, A. M., Reis, R. L., and Pashkuleva, I. (2012). Sulfonic groups induce formation of filopodia in mesenchymal stem cells. *J. Mater. Chem.* 22, 7172–7178. doi: 10.1039/c2jm15762d
- Dalby, M. J., Gadegaard, N., and Oreffo, R. O. (2014). Harnessing nanotopography and integrin-matrix interactions to influence stem cell fate. *Nat. Mater.* 13, 558–569. doi: 10.1038/nmat3980
- Dias, A. D., Elicson, J. M., and Murphy, W. L. (2017). Microcarriers with synthetic hydrogel surfaces for stem cell expansion. *Adv. Healthc. Mater.* 6:1700072. doi: 10.1002/adhm.201700072
- Dikovskiy, D., Bianco-Peled, H., and Seliktar, D. (2006). The effect of structural alterations of PEG-fibrinogen hydrogel scaffolds on 3-D cellular morphology and cellular migration. *Biomaterials* 27, 1496–1506. doi: 10.1016/j.biomaterials.2005.09.038
- Du, J., Chen, X., Liang, X., Zhang, G., Xu, J., He, L., et al. (2011). Integrin activation and internalization on soft ECM as a mechanism of induction of stem cell differentiation by ECM elasticity. *Proc. Natl. Acad. Sci. U.S.A.* 108, 9466–9471. doi: 10.1073/pnas.1106467108
- Eke, G., Mangir, N., Hasirci, N., MacNeil, S., and Hasirci, V. (2017). Development of a UV crosslinked biodegradable hydrogel containing adipose derived stem cells to promote vascularization for skin wounds and tissue engineering. *Biomaterials* 129, 188–198. doi: 10.1016/j.biomaterials.2017.03.021
- Elbert, D. L., and Hubbell, J. A. (2001). Conjugate addition reactions combined with free-radical cross-linking for the design of materials for tissue engineering. *Biomacromolecules* 2, 430–441. doi: 10.1021/bm0056299
- Elbert, D. L., Pratt, A. B., Lutolf, M. P., Halstenberg, S., and Hubbell, J. A. (2001). Protein delivery from materials formed by self-selective conjugate addition reactions. *J. Control. Release* 76, 11–25. doi: 10.1016/S0168-3659(01)00398-4
- Engler, A. J., Sen, S., Sweeney, H. L., and Discher, D. E. (2006). Matrix elasticity directs stem cell lineage specification. *Cell* 126, 677–689. doi: 10.1016/j.cell.2006.06.044
- Fan, C. J., and Wang, D. A. (2015). A biodegradable PEG-based micro-cavitary hydrogel as scaffold for cartilage tissue engineering. *Eur. Polym. J.* 72, 651–660. doi: 10.1016/j.eurpolymj.2015.02.038
- Frittoli, E., Palamidessi, A., Marighetti, P., Confalonieri, S., Bianchi, F., Malinverno, C., et al. (2014). A RAB5/RAB4 recycling circuitry induces a proteolytic invasive program and promotes tumor dissemination. *J. Cell Biol.* 206, 307–328. doi: 10.1083/jcb.201403127
- Fuoco, C., Rizzi, R., Biondo, A., Longa, E., Mascaro, A., Shapira-Schweitzer, K., et al. (2015). In vivo generation of a mature and functional artificial skeletal muscle. *EMBO Mol. Med.* 7, 411–422. doi: 10.15252/emmm.201404062
- Fuoco, C., Salvatori, M. L., Biondo, A., Shapira-Schweitzer, K., Santoleri, S., Antonini, S., et al. (2012). Injectable polyethylene glycol-fibrinogen hydrogel adjuvant improves survival and differentiation of transplanted mesoangioblasts in acute and chronic skeletal-muscle degeneration. *Skelet Muscle* 2:24. doi: 10.1186/2044-5040-2-24
- Fuoco, C., Sangalli, E., Vono, R., Testa, S., Sacchetti, B., Latronico, M. V., et al. (2014). 3D hydrogel environment rejuvenates aged pericytes for skeletal muscle tissue engineering. *Front. Physiol.* 5:203. doi: 10.3389/fphys.2014.00203
- Gonen-Wadman, M., Goldshmid, R., and Seliktar, D. (2011). Biological and mechanical implications of PEGylating proteins into hydrogel biomaterials. *Biomaterials* 32, 6025–6033. doi: 10.1016/j.biomaterials.2011.04.055
- Gonen-Wadman, M., Oss-Ronen, L., and Seliktar, D. (2007). Protein-polymer conjugates for forming photopolymerizable biomimetic hydrogels for tissue engineering. *Biomaterials* 28, 3876–3886. doi: 10.1016/j.biomaterials.2007.05.005
- Guillot, P. V., Abass, O., Bassett, J. H., Shefelbine, S. J., Bou-Gharios, G., Chan, J., et al. (2008). Intrauterine transplantation of human fetal mesenchymal stem cells from first-trimester blood repairs bone and reduces fractures in osteogenesis imperfecta mice. *Blood* 111, 1717–1725. doi: 10.1182/blood-2007-08-105809
- Halstenberg, S., Panitch, A., Rizzi, S., Hall, H., and Hubbell, J. A. (2002). Biologically engineered protein-graft-poly(ethylene glycol) hydrogels: a cell adhesive and plasmin-degradable biosynthetic material for tissue repair. *Biomacromolecules* 3, 710–723. doi: 10.1021/bm015629o
- Hamidouche, Z., Fromiguet, O., Ringe, J., Haupl, T., Vaudin, P., Pages, J. C., et al. (2009). Priming integrin alpha5 promotes human mesenchymal stromal cell osteoblast differentiation and osteogenesis. *Proc. Natl. Acad. Sci. U.S.A.* 106, 18587–18591. doi: 10.1073/pnas.0812334106
- Hare, J. M., Fishman, J. E., Gerstenblith, G., DiFede, D. L., Velazquez, D. L., Zambrano, J. P., et al. (2012). Comparison of allogeneic vs autologous bone marrow-derived mesenchymal stem cells delivered by transendocardial injection in patients with ischemic cardiomyopathy: the POSEIDON randomized trial. *JAMA* 308, 2369–2379. doi: 10.1001/jama.2012.25321
- Hogrebe, N. J., and Gooch, K. J. (2016). Direct influence of culture dimensionality on human mesenchymal stem cell differentiation at various matrix stiffnesses using a fibrous self-assembling peptide hydrogel. *J. Biomed. Mater. Res. A* 104, 2356–2368. doi: 10.1002/jbm.a.35755

- Hollweck, T., Hagl, C., and Eissner, G. (2012). Mesenchymal stem cells from umbilical cord tissue as potential therapeutics for cardiomyodegenerative diseases - a review. *Int. J. Mol. Cell. Med.* 1, 119–132.
- Kennea, N. L., Waddington, S. N., Chan, J., O'Donoghue, K., Yeung, D., Taylor, D. L., et al. (2009). Differentiation of human fetal mesenchymal stem cells into cells with an oligodendrocyte phenotype. *Cell Cycle* 8, 1069–1079. doi: 10.4161/cc.8.7.8121
- Kerscher, P., Turnbull, I. C., Hodge, A. J., Kim, J., Seliktar, D., Easley, C. J., et al. (2016). Direct hydrogel encapsulation of pluripotent stem cells enables ontomimetic differentiation and growth of engineered human heart tissues. *Biomaterials* 83, 383–395. doi: 10.1016/j.biomaterials.2015.12.011
- Krebsbach, P. H., Kuznetsov, S. A., Bianco, P., and Robey, P. G. (1999). Bone marrow stromal cells: characterization and clinical application. *Crit. Rev. Oral Biol. Med.* 10, 165–181. doi: 10.1177/10454411990100020401
- Kshitz Afzal, J., Kim, S. Y., and Kim, D. H. (2015). A nanopography approach for studying the structure-function relationships of cells and tissues. *Cell Adh. Migr.* 9, 300–307. doi: 10.4161/cam.29359
- Le Blanc, K., Gotherstrom, C., Ringden, O., Hassan, M., McMahon, R., Horwitz, E., et al. (2005). Fetal mesenchymal stem-cell engraftment in bone after in utero transplantation in a patient with severe osteogenesis imperfecta. *Transplantation* 79, 1607–1614. doi: 10.1097/01.TP.0000159029.48678.93
- Livak, K. J., and Schmittgen, T. D. (2001). Analysis of relative gene expression data using real-time quantitative PCR and the  $2^{-\Delta \Delta C_T}$  method. *Methods* 25, 402–408. doi: 10.1006/meth.2001.1262
- Lutolf, M. P., and Hubbell, J. A. (2005). Synthetic biomaterials as instructive extracellular microenvironments for morphogenesis in tissue engineering. *Nat. Biotechnol.* 23, 47–55. doi: 10.1038/nbt1055
- Lv, H., Li, L., Sun, M., Zhang, Y., Chen, L., Rong, Y., et al. (2015). Mechanism of regulation of stem cell differentiation by matrix stiffness. *Stem Cell Res. Ther.* 6:103. doi: 10.1186/s13287-015-0083-4
- Mattila, P. K., and Lappalainen, P. (2008). Filopodia: molecular architecture and cellular functions. *Nat. Rev. Mol. Cell Biol.* 9, 446–454. doi: 10.1038/nrm2406
- Meinel, L., Betz, O., Fajardo, R., Hofmann, S., Nazarian, A., Cory, E., et al. (2006). Silk based biomaterials to heal critical sized femur defects. *Bone* 39, 922–931. doi: 10.1016/j.bone.2006.04.019
- Miao, Z. N., Jin, J., Chen, L., Zhu, J. Z., Huang, W., Zhao, J. D., et al. (2006). Isolation of mesenchymal stem cells from human placenta: comparison with human bone marrow mesenchymal stem cells. *Cell Biol. Int.* 30, 681–687. doi: 10.1016/j.cellbi.2006.03.009
- Mironi-Harpaz, I., Wang, D. Y., Venkatraman, S., and Seliktar, D. (2012). Photopolymerization of cell-encapsulating hydrogels: crosslinking efficiency versus cytotoxicity. *Acta Biomater.* 8, 1838–1848. doi: 10.1016/j.actbio.2011.12.034
- Mobasser, R., Tian, L., Soleimani, M., Ramakrishna, S., and Naderi-Manesh, H. (2017). Bio-active molecules modified surfaces enhanced mesenchymal stem cell adhesion and proliferation. *Biochem. Biophys. Res. Commun.* 483, 312–317. doi: 10.1016/j.bbrc.2016.12.146
- Moshayedi, P., Nih, L. R., Lorente, I. L., Berg, A. R., Cinkornpumin, J., Lowry, W. E., et al. (2016). Systematic optimization of an engineered hydrogel allows for selective control of human neural stem cell survival and differentiation after transplantation in the stroke brain. *Biomaterials* 105, 145–155. doi: 10.1016/j.biomaterials.2016.07.028
- Naito, H., Yoshimura, M., Mizuno, T., Takasawa, S., Tojo, T., and Taniguchi, S. (2013). The advantages of three-dimensional culture in a collagen hydrogel for stem cell differentiation. *J. Biomed. Mater. Res. A* 101, 2838–2845. doi: 10.1002/jbm.a.34578
- Narayanan, K., Lim, V. Y., Shen, J., Tan, Z. W., Rajendran, D., Luo, S. C., et al. (2014). Extracellular matrix-mediated differentiation of human embryonic stem cells: differentiation to insulin-secreting beta cells. *Tissue Eng. A* 20, 424–433. doi: 10.1089/ten.TEA.2013.0257
- Neumann, A. J., Quinn, T., and Bryant, S. J. (2016). Nondestructive evaluation of a new hydrolytically degradable and photo-clickable PEG hydrogel for cartilage tissue engineering. *Acta Biomater.* 39, 1–11. doi: 10.1016/j.actbio.2016.05.015
- Nguyen, K. T., and West, J. L. (2002). Photopolymerizable hydrogels for tissue engineering applications. *Biomaterials* 23, 4307–4314. doi: 10.1016/S0142-9612(02)00175-8
- O'Donoghue, K., and Chan, J. (2006). Human fetal mesenchymal stem cells. *Curr. Stem Cell Res. Ther.* 1, 371–386. doi: 10.2174/157488806778226768
- Oswald, J., Boxberger, S., Jorgensen, B., Feldmann, S., Ehninger, G., Bornhauser, M., et al. (2004). Mesenchymal stem cells can be differentiated into endothelial cells in vitro. *Stem Cells* 22, 377–384. doi: 10.1634/stemcells.22-3-377
- Pak, J. (2011). Regeneration of human bones in hip osteonecrosis and human cartilage in knee osteoarthritis with autologous adipose-tissue-derived stem cells: a case series. *J. Med. Case Rep.* 5:296. doi: 10.1186/1752-1947-5-296
- Parekkadan, B., and Milwid, J. M. (2010). Mesenchymal stem cells as therapeutics. *Annu. Rev. Biomed. Eng.* 12, 87–117. doi: 10.1146/annurev-bioeng-070909-105309
- Park, J. H., Kim, D. Y., Sung, I. Y., Choi, G. H., Jeon, M. H., Kim, K. K., et al. (2012). Long-term results of spinal cord injury therapy using mesenchymal stem cells derived from bone marrow in humans. *Neurosurgery* 70, 1238–1247; discussion 1247. doi: 10.1227/NEU.0b013e31824387f9
- Petite, H., Viateau, V., Bensaid, W., Meunier, A., de Pollak, C., Bourguignon, M., et al. (2000). Tissue-engineered bone regeneration. *Nat. Biotechnol.* 18, 959–963. doi: 10.1038/79449
- Plessl, K., Haider, S., Fiala, C., Pollheimer, J., and Knofler, M. (2015). Expression pattern and function of Notch2 in different subtypes of first trimester cytotrophoblast. *Placenta* 36, 365–371. doi: 10.1016/j.placenta.2015.01.009
- Raman, K., Aeschbacher, S., Bossard, M., Hochgruber, T., Zimmermann, A. J., Kaufmann, B. A., et al. (2016). Whole blood gene expression differentiates between atrial fibrillation and sinus rhythm after cardioversion. *PLoS One* 11:e0157550. doi: 10.1371/journal.pone.0157550
- Redondo, P. A., Pavlou, M., Loizidou, M., and Cheema, U. (2017). Elements of the niche for adult stem cell expansion. *J. Tissue Eng.* 8:2041731417725464. doi: 10.1177/2041731417725464
- Rizzi, S. C., Ehrbar, M., Halstenberg, S., Raeber, G. P., Schmoekel, H. G., Hagenmuller, H., et al. (2006). Recombinant protein-co-PEG networks as cell-adhesive and proteolytically degradable hydrogel matrixes. Part II: biofunctional characteristics. *Biomacromolecules* 7, 3019–3029. doi: 10.1021/bm060504a
- Rufaihah, A. J., Vaibavi, S. R., Plotkin, M., Shen, J., Nithya, V., Wang, J., et al. (2013). Enhanced infarct stabilization and neovascularization mediated by VEGF-loaded PEGylated fibrinogen hydrogel in a rodent myocardial infarction model. *Biomaterials* 34, 8195–8202. doi: 10.1016/j.biomaterials.2013.07.031
- Ryu, Y. J., Cho, T. J., Lee, D. S., Choi, J. Y., and Cho, J. (2013). Phenotypic characterization and in vivo localization of human adipose-derived mesenchymal stem cells. *Mol. Cells* 35, 557–564. doi: 10.1007/s10059-013-0112-z
- Schmidt, O., Mizrahi, J., Elisseff, J., and Seliktar, D. (2006). Immobilized fibrinogen in PEG hydrogels does not improve chondrocyte-mediated matrix deposition in response to mechanical stimulation. *Biotechnol. Bioeng.* 95, 1061–1069. doi: 10.1002/bit.21072
- Schmittgen, T. D., and Livak, K. J. (2008). Analyzing real-time PCR data by the comparative C(T) method. *Nat. Protoc.* 3, 1101–1108. doi: 10.1038/nprot.2008.73
- Schwab, E. H., Halbig, M., Glenske, K., Wagner, A. S., Wenisch, S., and Cavalcanti, E. (2013). A.,-Adam, distinct effects of RGD-glycoproteins on Integrin-mediated adhesion and osteogenic differentiation of human mesenchymal stem cells. *Int. J. Med. Sci.* 10, 1846–1859. doi: 10.7150/ijms.6908
- Seliktar, D. (2005). Extracellular stimulation in tissue engineering. *Ann. N. Y. Acad. Sci.* 1047, 386–394. doi: 10.1196/annals.1341.034
- Seliktar, D. (2012). Designing cell-compatible hydrogels for biomedical applications. *Science* 336, 1124–1128. doi: 10.1126/science.1214804
- Shachaf, Y., Gonen-Wadmany, M., and Seliktar, D. (2010). The biocompatibility of Pluronic (R) F127 fibrinogen-based hydrogels. *Biomaterials* 31, 2836–2847. doi: 10.1016/j.biomaterials.2009.12.050
- Shapira-Schwartz, K., Habib, M., Gepstein, L., and Seliktar, D. (2009). A photopolymerizable hydrogel for 3-D culture of human embryonic stem cell-derived cardiomyocytes and rat neonatal cardiac cells. *J. Mol. Cell. Cardiol.* 46, 213–224. doi: 10.1016/j.yjmcc.2008.10.018
- Singh, R. K., Seliktar, D., and Putnam, A. J. (2013). Capillary morphogenesis in PEG-collagen hydrogels. *Biomaterials* 34, 9331–9340. doi: 10.1016/j.biomaterials.2013.08.016
- Sun, L., Akiyama, K., Zhang, H., Yamaza, T., Hou, Y., Zhao, S., et al. (2009). Mesenchymal stem cell transplantation reverses multiorgan dysfunction in

- systemic lupus erythematosus mice and humans. *Stem Cells* 27, 1421–1432. doi: 10.1002/stem.68
- Wang, J. Q., Zhang, F. J., Tsang, W. P., Wan, C., and Wu, C. (2017). Fabrication of injectable high strength hydrogel based on 4-arm star PEG for cartilage tissue engineering. *Biomaterials* 120, 11–21. doi: 10.1016/j.biomaterials.2016.12.015
- Wang, T., Lai, J. H., Han, L. H., Tong, X., and Yang, F. (2014). Chondrogenic differentiation of adipose-derived stromal cells in combinatorial hydrogels containing cartilage matrix proteins with decoupled mechanical stiffness. *Tissue Eng. A* 20, 2131–2139. doi: 10.1089/ten.tea.2013.0531
- Xue, F., Janzen, D. M., and Knecht, D. A. (2010). Contribution of filopodia to cell migration: a mechanical link between protrusion and contraction. *Int. J. Cell. Biol.* 2010:507821. doi: 10.1155/2010/507821
- Yu, H., Lui, Y. S., Xiong, S., Leong, W. S., Wen, F., Nurkafhianto, H., et al. (2013). Insights into the role of focal adhesion modulation in myogenic differentiation of human mesenchymal stem cells. *Stem Cells Dev.* 22, 136–147. doi: 10.1089/scd.2012.0160
- Zhang, Z.-Y., Teoh, S.-H., Hui, J. H. P., Fisk, N. M., Choolani, M., and Chan, J. K. Y. (2012). The potential of human fetal mesenchymal stem cells for off-the-shelf bone tissue engineering application. *Biomaterials* 33, 2656–2672. doi: 10.1016/j.biomaterials.2011.12.025
- Zhang, Z. Y., Teoh, S. H., Teo, E. Y., Khoon Chong, M. S., Shin, C. W., Tien, F. T., et al. (2010). A comparison of bioreactors for culture of fetal mesenchymal stem cells for bone tissue engineering. *Biomaterials* 31, 8684–8695. doi: 10.1016/j.biomaterials.2010.07.097

**Conflict of Interest Statement:** The authors declare that the research was conducted in the absence of any commercial or financial relationships that could be construed as a potential conflict of interest.

The handling Editor declared a past co-authorship with one of the authors DS.

Copyright © 2018 Rufaihah, Cheyyatraivendran, Mazlan, Lim, Chong, Mattar, Chan, Kofidis and Seliktar. This is an open-access article distributed under the terms of the Creative Commons Attribution License (CC BY). The use, distribution or reproduction in other forums is permitted, provided the original author(s) and the copyright owner(s) are credited and that the original publication in this journal is cited, in accordance with accepted academic practice. No use, distribution or reproduction is permitted which does not comply with these terms.



# Biomechanical Characterization at the Cell Scale: Present and Prospects

Francesco Basoli<sup>1</sup>, Sara Maria Giannitelli<sup>1</sup>, Manuele Gori<sup>1</sup>, Pamela Mozetic<sup>2</sup>,  
Alessandra Bonfanti<sup>3</sup>, Marcella Trombetta<sup>1</sup> and Alberto Rainer<sup>1,4\*</sup>

<sup>1</sup> Department of Engineering, Università Campus Bio-Medico di Roma, Rome, Italy, <sup>2</sup> Center for Translational Medicine, International Clinical Research Center, St. Anne's University Hospital, Brno, Czechia, <sup>3</sup> Department of Engineering, University of Cambridge, Cambridge, United Kingdom, <sup>4</sup> Institute for Photonics and Nanotechnologies, National Research Council, Rome, Italy

## OPEN ACCESS

### Edited by:

Pamela Davern,  
Baker Heart and Diabetes Institute,  
Australia

### Reviewed by:

Paola Campagnolo,  
University of Surrey, United Kingdom  
Huseyin Cagatay Yalcin,  
Qatar University, Qatar

### \*Correspondence:

Alberto Rainer  
a.rainer@unicampus.it

### Specialty section:

This article was submitted to  
Integrative Physiology,  
a section of the journal  
Frontiers in Physiology

Received: 01 April 2018

Accepted: 24 September 2018

Published: 15 November 2018

### Citation:

Basoli F, Giannitelli SM, Gori M,  
Mozetic P, Bonfanti A, Trombetta M  
and Rainer A (2018) Biomechanical  
Characterization at the Cell Scale:  
Present and Prospects.  
Front. Physiol. 9:1449.  
doi: 10.3389/fphys.2018.01449

The rapidly growing field of mechanobiology demands for robust and reproducible characterization of cell mechanical properties. Recent achievements in understanding the mechanical regulation of cell fate largely rely on technological platforms capable of probing the mechanical response of living cells and their physico-chemical interaction with the microenvironment. Besides the established family of atomic force microscopy (AFM) based methods, other approaches include optical, magnetic, and acoustic tweezers, as well as sensing substrates that take advantage of biomaterials chemistry and microfabrication techniques. In this review, we introduce the available methods with an emphasis on the most recent advances, and we discuss the challenges associated with their implementation.

**Keywords:** cell mechanics, cell-generated forces, AFM, tweezing methods, MEMS, traction force microscopy, mechanotransduction, mechanobiology

## INTRODUCTION

Cells are complex biological units that can sense the physico-chemical cues and stimuli from their surrounding environment, and actively respond to them by triggering biomechanical reactions that include cell growth, proliferation, differentiation, motility and even apoptosis (Galbraith and Sheetz, 1998; Huang and Ingber, 1999). Forces generated by cells regulate several biological activities such as cell adhesion, signaling, biochemical routes and metabolic functions, and can be pivotal mechanisms in orchestrating and coordinating the morphogenetic pathways that control tissue and organ development and homeostasis (Mammoto and Ingber, 2010; Maugeri-Saccà and De Maria, 2018; Miroshnikova et al., 2018). In the last decade, several studies focused on the generation, transmission and regulation of signaling pathways and molecular mechanisms within single cells and tissue environments (Geiger and Bershadsky, 2001; Chen et al., 2004; Maloney et al., 2010; Nardone et al., 2017). Advances in cell mechanics have fuelled the development of tools for the mechanical characterization of biological entities at the cellular and subcellular scale (Norman et al., 2008; Zheng and Zhang, 2011). The study of how mechanical properties influence cell behavior in relation to their surrounding microenvironment both in healthy conditions and in disease requires a profound knowledge of extracellular and/or intracellular forces, stiffness values and mechanical stresses from micro- to nano-scales (Butcher et al., 2009; Alcaraz et al., 2018). This knowledge would allow researchers to better understand both the evolution of intracellular architectures

and how cells interact with the external environment. This will lead to the investigation of the biomechanical regulation of cell fate in the framework of development, physiology and disease, at the physico-chemical level (Park et al., 2010; Hoffman et al., 2011; Moulding et al., 2012; Sun Y. et al., 2012).

Cells are viscoelastic, and as such they have both an elastic and a time-dependent, viscous behavior. A viscoelastic material typically possesses characteristics such as stress-relaxation, creep, strain-rate sensitivity and hysteresis (Pal, 2014). Stress relaxation occurs when a material is subjected to a fixed strain, and the stress developed by the material is decreasing with time. Creep, on the contrary, is the behavior of a material subjected to constant stress and experiencing a time-dependent elongation. Strain rate sensitivity means that the stress-strain response of a material depends upon the speed at which strain is applied (strain rate). Lastly, hysteresis describes the fact that loading and unloading curves for a viscoelastic material do not follow the same path. The areal difference between the two curves represents the loss of energy due to internal friction in the material.

Recent advances in the development of novel techniques and tools for cell mechanics characterization, and the design of *ad hoc* technological platforms have introduced the possibility to accurately trap and manipulate single cells at the microscale level (Finer et al., 1994; Park et al., 2005; Roth et al., 2013; Guo et al., 2016; and reviewed in Rajagopalan and Saif, 2011; Zheng and Zhang, 2011; Polacheck et al., 2013), for application in many interdisciplinary areas of research, such as biophysics, biomedicine, tissue engineering, and materials science.

Here, we will summarize the latest advances in the research area of cell biomechanics, and we will focus on the modern technological approaches and mechanical testing systems developed in the last decade by combining theoretical, experimental, and numerical models, for pursuing a realistic description of cell mechanical behavior. First, we will introduce the established techniques and available tools, highlighting the differences between active and passive stimulation methods. We will provide a brief description of atomic force microscopy (AFM) and AFM-derived methods, and then we will explore thoroughly the tweezing methods, including optical, magnetic and acoustic tweezers. Also, we will outline the role of microengineered platforms, such as Micro-Electro-Mechanical Systems, micro/nanopillars, microfluidic devices, and hydrogel stretching methods (highlighting the underlying technology and mathematical modeling) for cellular force measurements. Finally, we will critically discuss the future outlooks of such technological tools and the challenges that still need to be addressed to understand the structural and mechanical complexity of living tissues.

## CLASSIFICATION

Measuring forces at the cell–extracellular matrix (ECM) interface is a critical aspect for fully understanding cell–ECM interactions and how the ECM regulates cellular function. This has boosted the development of technological platforms achieving force measurements at the cellular and subcellular scale.

It is possible to divide these technologies in two broad categories: (i) active stimulation methods, which measure cell response to mechanical force application, and (ii) passive stimulation methods, which can only sense mechanical forces generated by cells without applying any external force.

Mechanical cell responses to external inputs have largely been studied using active single-cell manipulation approaches, such as:


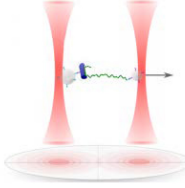
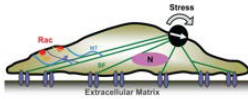
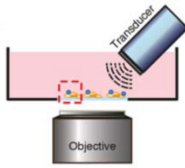
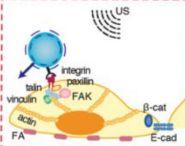
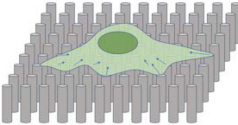
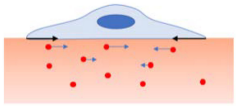
- Atomic force microscopy (AFM) (Lam et al., 2011): AFM relies on microcantilevers to induce a deformation in the cell. From the deflection of the cantilever, it is possible to measure local mechanical properties and to generate maps across the cell surface.
- Tweezing methods, which encompass three main techniques.
  - Optical tweezers (OTs) (Galbraith et al., 2002): OTs rely on a laser beam to create a potential well for trapping small objects within a defined region. Optical tweezers can be used to micromanipulate cells as well as intracellular components (i.e., organelles) and quantitatively measure the binding force of a single cell to diverse types of ECM substrates (Guck et al., 2001; Wang et al., 2005), or to evaluate physical interactions between subcellular structures (Sparkes et al., 2018)
  - Magnetic tweezers (MTs) (Hu et al., 2004): these devices rely on the use of magnetic microbeads. Magnetic fields are produced either by movable permanent magnets or by electromagnets (Ziemann et al., 1994).
  - Acoustic tweezers (ATs) (Guo et al., 2015): ATs can manipulate biological samples using sound waves with low intensity power and low impact on cell viability, and without the need for any invasive contact, tagging, or biochemical labeling.

In the passive methods, the main goal is the evaluation of cell-generated forces using flexible substrates:

- Microengineered platforms: these are microfabricated platforms, including both silicon-based devices (micro-electro-mechanical systems, MEMS) produced through integrated circuit manufacturing processes, as well as elastomeric (i.e., polydimethylsiloxane, PDMS) devices produced through replica molding (Tan et al., 2003; Kim et al., 2009).
- Traction Force Microscopy (TFM): TFM exploits elastic substrates with known mechanical properties and fluorescence/confocal microscopy. In its original version, cells were cultured on flexible silicone sheets with different compliance. During cell action, silicone patterns wrinkled and this could be visualized under a light microscope (Harris et al., 1980). An evolution of this method implies the use of flexible sheets with embedded beads. Positions of the beads are tracked during the experiments and cell-generated forces are derived from the analysis of bead displacement field (Lee et al., 1994).

A summary of the available techniques with a brief description of their advantages and disadvantages, their range of detection, and a simple sketch is reported in **Table 1**.

**TABLE 1** | Summary of the most relevant techniques for cell mechanical characterization.

Mode	Technique	Sketch	Typ. force range	Strengths/limitations	References
ACTIVE	AFM	 <p>Adapted from: Liu et al. (2012)</p>	5 pN ÷ 10 nN	<ul style="list-style-type: none"> <li>✓ Wide force range –well established technique</li> <li>× Direct contact with the specimen otherwise tip must be labeled</li> </ul>	Lam et al., 2011
	TWEEZING OPTICAL	 <p>Adapted from: Håti et al. (2015)</p>	0.1 ÷ 100 pN	<ul style="list-style-type: none"> <li>✓ High sensitivity</li> <li>✓ Wide force range</li> <li>× Heating issues</li> </ul>	Guck et al., 2001; Galbraith et al., 2002; Wang et al., 2005
	MAGNETIC	 <p>Adapted from Poh et al. (2009)</p>	0.01 ÷ 100 pN	<ul style="list-style-type: none"> <li>✓ High sensitivity</li> <li>✓ Wide force range</li> <li>× Custom equipment – little standardization</li> </ul>	Wang et al., 1993; Ziemann et al., 1994; Hu et al., 2004
	ACOUSTIC	  <p>Adapted from: Topal et al. (2018)</p>	0.1 ÷ 30 nN	<ul style="list-style-type: none"> <li>✓ Highly cytocompatible</li> <li>× Fewer force and stress application modalities</li> </ul>	Ding et al., 2013; Guo et al., 2015; Li et al., 2015
PASSIVE	MICRO-ENGINEERED PLATFORMS		10 <sup>-12</sup> ÷ 10 <sup>-3</sup> N	<ul style="list-style-type: none"> <li>✓ Different designs translate into extremely wide force range</li> <li>✓ Stability, scalability of manufacturing process</li> <li>✓ Sophisticated microfabrication procedures/facilities</li> </ul>	Yang and Saif, 2005; Polacheck and Chen, 2016
	TRACTION FORCE MICROSCOPY		2 ÷ 120 nN	<ul style="list-style-type: none"> <li>✓ Widespread (needs standard lab equipment)</li> <li>✓ Easily coupled with microscopy equipment (i.e., fluorescence/confocal)</li> <li>✓ 2D/3D measurements</li> <li>× Computationally demanding</li> <li>× Non-linear behavior of ECM-mimicking hydrogels</li> </ul>	Polacheck and Chen, 2016

For each technique, the force range and a brief description of the main strengths and limitations are reported.



## ATOMIC FORCE MICROSCOPY (AFM)

Among the available techniques for measuring the mechanical properties of biological tissues, AFM has been extensively used over the years thanks to its capability to cover, with nanometer resolution, the pathophysiological range of stiffness values of tissue samples, while probing local cell-ECM mechanical interactions (Dufrêne and Pelling, 2013).

AFM is a very powerful technique that allows cell biologists to probe the morphology of living cells, mechanical and adhesive properties of single biomolecules, as well as to quantify and to spatially map cell mechanics and physical properties. AFM can operate under a wide variety of physiological conditions: biological samples can be imaged in fluid environments, and live-monitored in real-time. Moreover, AFM can be combined with many optical microscopy techniques (e.g., correlated fluorescence-AFM studies) (Kodera et al., 2010; El-Kirat-Chatel and Dufrêne, 2012; Martínez-Martin et al., 2012) to simultaneously visualize single cells to extract additional information. An in-depth description of AFM functioning principles is not in the scope of the present review. For a more detailed description of the AFM, the reader may refer to Dufrêne and Pelling (2013) and Kasas et al. (2018).

Designed to study surface morphology, AFM has been used for many years as a tool for high-resolution imaging of surfaces. AFM uses a very sharp silicon micro-fabricated tip fixed at the end of a cantilever beam to scan the surface. After positioning the tip a few nm from the scanned surface, this is subjected to a short-range interaction with the sample during which the cantilever deflects. Deformations are recorded measuring the angular deflection of a laser beam aligned to the cantilever end on a multi-segment photodiode. Thus, while the tip raster scans the sample in the X-Y directions with very precise piezoelectric scanners, a detailed image of the 3-D topography of the sample is generated (Kasas et al., 2018).

Besides imaging, AFM force spectroscopy has been also used to apply mechanical forces to biological systems over scales ranging from cells to single molecules to study their mechanical response (Zemła et al., 2018) and measure their mechanical and adhesive properties.

An early approach to measure nano-mechanical properties of biological samples consisted in the analysis of specimen height profile when subjected to multiple scans at different force levels through the AFM tips, estimating the elastic modulus by the force-deformation relationship (Kis et al., 2002).

Further development involved the use of the tip-cantilever system as an active scanning probe. In the “pushing experiments” the AFM tip is indented against the sample while recording its response through a force/distance curve, or force/indentation curve, which represents the deformation of the cantilever given a prescribed force or the required force to push the tip to a definite depth into the sample (Zemła et al., 2018).

The recorded curve can be used to calculate the sample stiffness by algorithms that take into account several parameters, such as the geometry of the tip and the depth of indentation

(Harris and Charras, 2011; Dufrêne and Pelling, 2013). Alcaraz et al. (2018) presented a very exhaustive methodology to select the right tip geometry (from the four-sided pyramidal or the spherical commercial tips to the cylindrical tips made by milling a commercial pyramidal tip by mean of a focused ion beam) considering the topology of the sample to be studied and the goal of the study.

Several studies focused on the computational modeling of the force-versus-indentation curve, where different contact models between cell and tip have been proposed in order to properly account for different geometries: Hertz model (Hertz, 1896), which describes the elastic deformation of two spheres, Sneddon model (Sneddon, 1965) which describes the elastic deformation of conical or paraboloidal tips on a flat sample, JKR model, which also considers adhesive forces, Tatara (1989) model, case of a spherical sample compressed between two parallel plates, Multiscale Decomposition Analysis (Digiuni et al., 2015), which quantifies the non-linear mechanical response of the cantilever above cell wall indentation, and the Multi-Regime (Bonilla et al., 2015), which considers cells as a multi-spring system. Lately, to overcome a common drawback to these methods (i.e., sample, tip and substrate are assumed to be homogenous bodies with well-defined geometries, a rough approximation of real conditions), the use of finite element modeling (FEM) is emerging as a possible solution in order to better consider the local effects of the tip-sample interactions (Kasas et al., 2017) on the recorded measurements.

A remarkable example of the importance of adopting the right computational model in AFM data analysis is reported by Mercadé-Prieto et al. (2013). They showed that the stiffness values measured by AFM indentation on *Saccharomyces cerevisiae* cell wall were two orders of magnitude lower than those obtained by micromanipulation studies. The authors ascribed such discrepancies to the use of mathematical models that are inappropriate to fit the experimental data. In fact, the classical Hertz-Sneddon model, based on the assumption that the whole cell is a homogeneous material, does not hold for tissues with a complex hierarchical structure. The problem was solved by implementing a new FEM-based model, which considered the yeast cell wall as made of a soft external layer and a stiffer inner layer.

Another relevant AFM application is represented by the so called “pulling experiments”. In this case, the tip of the AFM is used to pull the cell instead of applying a compressive force on it. This technique allows to localize cell surface molecules and to study their elasticity and adhesion (Hinterdorfer and Dufrêne, 2006; Puchner and Gaub, 2009).

The AFM tip often needs to be functionalized with specific moieties or biomolecules that specifically interact with the surface of the cell. Once the probe is brought in contact with the cell surface and a molecular interaction occurs between the tip and the probed molecule (contact time), the cantilever position is perturbed. The tip will firstly bend downwards while being retained by the interacting molecules. Ultimately, the retracting force possessed by the cantilever beam will lead to the detachment of the modified AFM tip from the investigated surface. Therefore, it is possible to measure the force applied on the cantilever beam by the interacting molecules and to draw a

retraction curve that contains characteristic “rupture events” that represent the required force to break a single molecule interaction. Moreover, by imposing different stretching speeds, it is possible to evaluate the potential energy parameters of the molecular interactions, leading to an estimation of the binding strength of a given receptor (Karácsony and Akhremitchev, 2011; Dufrêne and Pelling, 2013).

An interesting approach, exploiting AFM in a passive mode, is represented by the work of Liu et al. (2012), who developed a technique to study the contractile force of cardiomyocytes. They first brought the AFM cantilever to gently touch the living, beating cells, then locked the z-piezo and let the contraction forces of the cell deflect the cantilever. This method allowed to quantitatively measure several parameters, including elastic modulus, contractile force, beat rate and beat duration.

The understanding of how nanomechanical forces induce signaling, and how this is transmitted through the cellular architecture was achieved by the combination of AFM and optical techniques.

AFM mechanical measurements made while scanning the cells with different optical microscopy procedures (Lehenkari et al., 2000; Haupt et al., 2006), such as fluorescence microscopy or laser scanning confocal microscopy, led to many important observations on the origins of mechano-sensitivity and the processes of mechano-transduction in living cells. Several groups have independently demonstrated how cells are extremely sensitive to small local forces by using fluorescent fusion proteins coupled with live cell dyes. For example, the local indentation of living cells with an AFM tip with forces in the order of  $10^{-9}$  N, influences their behavior making them generate an inner response by signaling and structural events (e.g., calcium release, membrane blebbing, cytoskeletal deformation, and organelle rearrangement) (Charras and Horton, 2002; Silberberg et al., 2008; Veraitch et al., 2011; Guolla et al., 2012). AFM records force-distance curves by plotting the force acting on the probe as a function of the probe-sample separation distance. Nanomechanical and nanoadhesive properties of the living material can be extracted from the experimental data by using the available physical models (Formosa-Dague et al., 2018).

Many studies have been conducted using AFM as a probe for the understanding of cell behavior under external mechanical stress. Those studies showed the wide range (from as low as 0.02 kPa up to 400 kPa) of the elastic modulus of living cells, as it has been extensively reviewed and accurately tabulated by Kuznetsova et al. (2007).

In the standard indentation method, cells need to be firmly attached to the substrate. This may raise problems for non-adherent cells in suspension. Many methods have been presented to overcome this issue, and have already been described in the literature (Kuznetsova et al., 2007). However, effects on the cell elastic modulus caused by the immobilization (Dulińska et al., 2006) (e.g., poly-L-lysine solution for native erythrocytes attachment to glass surface, Dulińska et al., 2006) should be expected and they should be taken into account during the estimation of the elastic modulus to avoid under or over estimation (Rosenbluth et al., 2006). Moreover, since cells are

not homogenous, heterogeneous mechanical properties can be expected at different positions within the cell. For example, Mathur et al. (2000) reported high variation in the elastic modulus for human umbilical vein endothelial cells (HUVEC) measured over the nucleus, in its proximity, or near the edge of the cell body, with the nuclear area being stiffer than the rest of the cell body. Similarly, variability of local mechanical properties was reported for many other cell types, including bovine pulmonary artery endothelial cells (Costa and Yin, 1999), cardiomyocytes (Shroff et al., 1995), etc. Cell thickness is also a factor to be taken into account, as it can affect the measurement of the elastic modulus (Mahaffy et al., 2004).

Even though the interpretation of AFM data is not straightforward, this technique has the advantage to be coupled with microscopic observation, for the convenient analysis of the mechanisms of cell function through a deeper knowledge of the cell behavior under stress (Kuznetsova et al., 2007). For example, Pesen and Hoh (2005) perturbed the assembly of cytoskeleton components using drugs. By combining AFM analysis with confocal fluorescence microscopy (CFM), they were able to study the subcellular organization of different cytoskeletal components, clearly showing that the elastic response of cells is mostly due to the network of actin filaments. With the combined AFM-CFM approach, they also characterized the local micromechanical architecture of the cell cortex in bovine pulmonary artery endothelial cells.

More recently, Fallqvist et al. (2016) used a drug that disrupts the cellular actin network (Latrunculin B) to study how the actin cytoskeleton influences the mechanical properties of fibroblasts. They confirmed that the disruption of the actin network reduced cellular stiffness, while increasing the relaxation rate of the cytoplasm. They hypothesized that the actin network is responsible for both the viscous properties of the cell and its stiffness. Similar experiments, based on the disruption of the cytoskeleton using different molecules (e.g., cytochalasin D and nocodazole for actin microfilaments and microtubules, respectively) in order to evaluate their connection with cell mechanical properties, were extended to primary chondrocytes, endothelial cells, fibroblasts, hepatocellular carcinoma cells, and fibrosarcoma cells (Grady et al., 2016).

AFM allowed scientists to take another step forward in the understanding of the relationship between mechanical properties and cell behavior during the mechanisms of cell differentiation and aging. Reorganization of cytoskeleton and modifications in mechanical properties seem to be correlated with the cell cycle stages (Collinsworth et al., 2002; Zhang et al., 2004). AFM studies conducted on HUVEC (Sato et al., 2004) and human epithelial cells (Berdyeva et al., 2005) correlate cell elasticity and culture period. The obtained values of stress over time show an increase in *in vitro* cell rigidity during aging. Lieber et al. (2004) also used AFM nanoindentation on isolated cardiomyocytes from young and old male hybrid rats (Fischer 344 Brown Norway F1), discovering a correlation between the increase in their apparent elastic modulus and aging.

Understanding the effects of diseases on cell mechanical properties also represents a major application of AFM. The

direct link between structure and functions is the reason for the increasing number of studies that aim to correlate the change of the mechanical properties with pathological conditions involving numerous diseases and biological structures. These aspects have extensively been reviewed (Morton and Baker, 2014; Gautier et al., 2015; Dinu et al., 2016; Rianna and Radmacher, 2016) and will be summarized next. A notable example of the AFM application in this context comes from the work of Sun N. et al. (2012). As a model for investigating dilated cardiomyopathy (DCM), the authors generated cardiomyocytes (CMs) derived from induced pluripotent stem cells (iPSCs) from patients with a familial point mutation in the gene encoding cardiac troponin T. They measured the contractile force of such iPSC-CMs through AFM using a silicon nitride cantilever tip with a cellular indentation of around 100–200 nm, and applying a 100 pN contraction force to cells. This technique allowed them to detect much weaker single-cell contraction forces in the DCM iPSC-CMs compared to control iPSC-CMs from healthy individuals of the same family cohort.

Another remarkable example of using AFM to perform force mapping measurements between normal and defective cells was recently given by Nardone et al. (2017). In this work, the authors studied the interplay between the activity of the Hippo pathway effector Yes-Associated Protein (YAP) and formation of focal adhesions (FAs, sub-cellular protein complexes that act as linkages between integrin-ECM connection and the cytoskeleton) in physiological and simil-pathological conditions. They compared genetically modified YAP-deficient adipose tissue-derived mesenchymal stem cells (AD-MSCs) grown onto different substrates with normal AD-MSCs via force mapping AFM measurements, thus providing novel insights into the mechanism of YAP mechanosensing activity in regulating the assembly of FAs.

Considering their important role in numerous physiological and pathological processes (atherosclerosis, blood pressure regulation, etc.), mechanical alterations of endothelial cells due to pathological events have been extensively studied (Szymonski et al., 2015). For example, AFM indentation measurements on *ex vivo* specimens of abdominal and common iliac aorta from cholesterol-fed rabbits were performed with the aim to assess the mechanical properties of endothelial cells as a function of the biological site and of disease progression (Hayashi and Higaki, 2017). Further, it was demonstrated that cholesterol greatly increased both stiffness and viscosity of human umbilical cord vein endothelial cells (Yan et al., 2017)

Dulińska et al. (2006) investigated the changes in the elastic modulus of erythrocytes from patients with different types of anemias, concluding that the elastic properties of pathological erythrocytes are two to three times higher than normal cells. Besides anemia, erythrocytes were shown to modify their mechanical properties also in other pathologies (e.g., Parkinson's disease, Alzheimer disease, etc.), as summarized in previous reviews (Mukherjee et al., 2015).

In recent years, the discovery that the mechanical properties of single cells are closely related to cancer development has significantly increased the number of publications in this area. Many of these studies are based on the possibility of using

AFM as an early cancer detection instrument, by exploiting the nano-mechanical modifications induced by cancer (Kasas et al., 2018). AFM has been used in many studies on different cancer typologies (e.g., bladder, Abidine et al., 2015; cervix, Zhao et al., 2015; oral mucosa, Park et al., 2016; bone, Wang et al., 2016; prostate, Efremov et al., 2015; lung, Han et al., 2016; brain, Ciasca et al., 2016). All these studies agree that it is possible to distinguish cancer cells from their healthy counterparts by analyzing their mechanical properties and correlating them with other relevant cell features, such as morphology, migration potential and invasiveness (Lekka, 2016). We report here a few examples of the ongoing research on one of the most common type of cancer in woman, that is breast cancer.

Plodinec et al. (2012) demonstrated the strong link between cancer progression and a substantial softening of tumor epithelial cells compared with normal mammary tissue using AFM high-resolution stiffness mapping. They suggested a direct connection between metastatic potential of cancer cells and cell softening in the primary tumor. Ansardamavandi et al. (2016) used AFM to analyze *ex vivo* bioptical specimens of breast tissue, showing a general stiffness modification in cellular and non-cellular regions associated to cancer development. In particular, they reported softening of the cellular regions of cancerous tissues compared to their healthy counterparts, while the fibrous regions slightly stiffened. Another study by Coceano et al. (2016), based on the comparison of the elastic modulus of different human breast cancer cell lines, showed that cell aggressiveness (and hence infiltration potential) correlated with a reduction in cell stiffness. This research showed that AFM indentation technique is potentially able to probe human breast biopsies at the tissue level, representing a possible marker for cancer diagnosis in future.

As a last remark of this section, it has to be pointed out that AFM analysis is generally restricted to the outer surface of cell membranes and it is not able to directly investigate intracellular structures, as the cantilever cannot scan the inside of a cell membrane. To overcome this limitation, Usukura et al. (2012, 2016) have applied an “unroofing” methodology, consisting in the breakage of the cellular membrane and the removal of cytoplasmic-soluble component, to allow the AFM probe directly access cytoskeleton and organelles.

## TWEEZING METHODS

Mechanical forces generated by cells, along with those developed by the surrounding environment and externally applied to cells, are involved in the regulation of the physiological functions of bio-molecules. Besides leading the required actions for tissue development and homeostasis (i.e., stretching, bending, repositioning, and alignment), these forces also enable and regulate cell functions such as activation of signaling pathways, transcription, cellular differentiation and proliferation (Polacheck and Chen, 2016). Such forces, acting at the molecular level, range from a few piconewtons to several nanonewtons. To investigate those mechanical properties of biomolecules and their interactions, many different devices and methodologies have

been developed. Among them, tweezers have undergone a significant development in the last three decades, allowing the manipulation of individual molecules within cells with extraordinary precision. These powerful single-molecule tools include: (i) optical tweezers for high precision measurements of forces through optical micromanipulation, down to the single-molecule level (Hénon et al., 1999); (ii) magnetic tweezers for the simultaneous manipulation and recording in real time of forces using tethered magnetic beads; (iii) acoustic tweezers for manipulating cells in three dimensions using sound waves.

## Optical Tweezers (OTs)

Laser trapping, better known as OTs, and invented by Ashkin et al. (1986), became one of the most widely used single molecule tools in biology. In fact, OTs are especially suited to manipulate mesoscopic systems, which are characterized by forces ranging from femtoNewtons to nanoNewtons, length scales ranging from tens of nanometers to hundreds of micrometers, and time scales ranging upward from one microsecond (Grier, 2003; Fazal and Block, 2011). These ranges cover those experienced by biological molecules in their native environment (i.e., many of the inter- and intracellular processes). The working mechanism of OTs is based on focusing a laser beam, introduced through a high numerical aperture objective, onto a dielectric micro-particle, in such a way that the interaction with the laser light stably traps the particle close to the beam focus. Usually polystyrene or silica microspheres are bounded to molecules of interest and, upon being trapped by the OTs, used as handles for the manipulation of cells. Forces arising from the radiation pressure of a highly focused light beam are responsible for the dielectric particles entrapment (Ashkin et al., 1987), where the dominant component of the force is along the gradient of the electric field and pushes the dielectric particles toward the center of the focused beam. In a small region around the center, the trap behaves like a linear Hooke's spring. The value of the trap elastic constant is determined by calibration techniques, normally by thermal fluctuations of the position of the trapped particle (Lisica and Grill, 2017). Therefore, once a particle has been trapped, it is enough to change the position of the focus to move it, using the laser beam in the same way of a pair of tweezers. Thus, one of the main advantages of OTs over other techniques, such as MTs (described below), is represented by the possibility to modify the trap position in all three dimensions at high frequencies by moving the laser beam. For example, this is required to probe multiple conformational states of microscopic particles, such as proteins.

Many OT configurations and geometries exist to fulfill the diverse biological applications that have been studied in the last three decades. They can be divided in two large groups: static configurations (i.e., single bead, two-bead, three-bead), and dynamic configurations (i.e., force-clamp, position-clamp, Dynamic Force Spectroscopy). The reader will find a deeper and more detailed description of such OT configurations and geometries in the reviews and articles that have been written on this subject (Capitanio and Pavone, 2013).

In the study of mechanical properties, the use of microbeads as handles (or grips) to probe force is necessary to overcome the fact that most cells, due to their size, shape and adherent properties, are not conducive to direct optical tweezing. While some cell types – e.g., red blood cells (RBCs), yeast cells and spermatozoa – are easily tweezed (Dholakia and Reece, 2006), the majority cannot, demanding for alternative models (Zhang and Liu, 2008). For example, thermal and hydrodynamic effects on the biomechanical properties of biological cell membrane in physiological flow were studied by OTs using unilamellar vesicles (Foo et al., 2003, 2004), which are widely accepted as a model for studies over cell mechanical properties (Ichikawa and Yoshikawa, 2001).

Concerning RBCs, since it was shown that their mechanical properties change following structural or molecular alterations induced by different kind of diseases (e.g., gastrointestinal tumor and malaria) (Suresh et al., 2005), studies of their biomechanical properties have been performed by OTs using silica beads bound to the membrane, in either single-trap (Lim et al., 2004) or dual-trap (Hénon et al., 1999) configuration. Among the technical improvements for RBC studies, it is worth reporting the following two techniques: (i) a three-laser trap setup that has been used to initially stretch RBCs in different directions and then, by simultaneously removing the three OTs, to study the recovery and the cell relaxation time (i.e., time taken by a deformed cell to go back to the undeformed state), which differentiates the cell age (Bronkhorst et al., 1995); (ii) the use of a focused evanescent wave illumination technique, which goes under the name of single beam near-field laser trapping, which allows stretching, rotating and folding RBCs (Gu et al., 2007).

A significant advancement in analysis throughput using optical trapping has been reported by Guck et al. (2005) who used two counter-propagating divergent beams to stably trap and deform cells flowing in a microfluidic channel, thereby achieving flow-cytometric measurement of single cell viscoelasticity.

OTs have also been used to study cell membranes and subcellular organelles (Wei et al., 2008; Yalcin et al., 2009). In this case, it is typical to use micron-sized beads anchored to the subcellular structure of interest. OTs have been used to stretch chondrocytes to measure the bead/membrane tether formation force, uncovering that the process of chondrocyte adhesion is directly related to the culture time (Huang et al., 2003). The different tether length of fibroblasts and human mesenchymal stem cells (hMSCs) was also measured, demonstrating that membrane mechanics dramatically affects MSC differentiation (Titushkin and Cho, 2006). Among the other applications of OTs, it is worth reporting their use in different human cell studies, such as: holographic OT techniques to investigate hyaluronan-mediated adhesion processes of chondrocytes (Curtis and Spatz, 2004) and OTs experiments for elucidating the short-term binding of fibroblasts to fibronectin-coated glass (Thoumine et al., 2000), the mechanics of cellular adhesion to artificial artery polymer templates (Knöner et al., 2006), and the interaction forces between human bone cells and implant surfaces (Andersson et al., 2007).

Besides allowing a dynamic analysis of the mechanical properties of cells (Huang et al., 2003), OTs can be also used in the

study of tissues (López-Quesada et al., 2014) without alterations to the embryonic development. When using lasers on biological samples, there is always a big concern regarding photodamage. Considering that biological samples are almost transparent to the near-infrared wavelengths that are normally employed to trap particles by laser traps (Neuman et al., 1999), this problem is minimized. Thus, this compatibility with cellular specimens allows the use of OTs in living cells (Monachino et al., 2017). In this field, it is worth to highlight the papers by Nan et al. (2008) and Sims and Xie (2009), in which OTs were developed and used for sub-millisecond tracking of organelles cargoed by the molecular motors kinesins and dyneins. Hendricks et al. (2012) applied OTs to study bi-directional transport of phagocytosed latex beads (LBCs) along microtubules of living mammalian macrophages, suggesting that bidirectional transport of LBCs is driven by opposing teams of stably bound motors that operate near force balance. Thus, OTs offer a wide set of methodologies that make them suitable for trapping and potentially measuring fluid forces also *in vivo*. A breakthrough in that direction was made by Zhong et al. (2013) who trapped RBCs using OTs in the capillary vessels of mouse ears. Clearly, this approach shows limitations when the events of interest are located deep in tissues. Other examples of studies in tissues are given by the recent work of Bambardekar et al. (2015), who accurately measured the tension forces between adjacent cells of a *Drosophila* embryo by deforming cell junctions with oscillating OTs, and by Johansen et al. (2016), who demonstrated the potential of optical tweezing in a living zebrafish (ZF) embryo exploiting its relative optical transparency. One of the major obstacles for all the *in vivo* studies is the calibration of the optical trap, since the heterogeneity of both cell size and refractive index limits the use of OTs in realistic *in vivo* contexts. Recently, the feasibility of *in situ* calibration of the optical trap stiffness ( $k$ ) and the position detection sensitivity ( $1/\beta$ ) has been demonstrated *in vivo* in the yolk sac of living ZF. Moreover, the study provided measures of the viscoelastic properties of ZF embryo yolk over an order of magnitude of stress-strain amplitude (Staunton et al., 2017). Harlepp et al. (2017) demonstrated the possibility to use OTs for measuring flow profiles and drag forces imposed to trapped RBCs of living ZF embryos.

## Magnetic Tweezers (MTs)

MTs arose as one of the most widely used and powerful tools for the analysis of molecular forces and for the micromanipulation of cells, mainly thanks to their capability of applying torque (Oberstrass et al., 2012). The possibility to be integrated with a range of powerful light microscopy imaging modes, as well as their high force, spatial, and temporal sensitivity (Gosse and Croquette, 2002; Kilinc and Lee, 2014) have greatly widened MTs applications.

The development of MTs is relatively recent and allows the application and measurement of forces ranging from pico- to nanoNewtons using magnetic micro-beads, under a generated magnetic field gradient. Therefore, MTs are mainly used in biological applications for: single molecule force measurements (SMFM) or extra-cellular and intra-cellular (magnetic beads

are located outside and inside the cell, respectively) micromanipulation. Moreover, similarly to other biophysical methods, MTs have a very low interference with the specimen, which is very important in research involving mechanotransduction (De Vlaminck and Dekker, 2012; Oddershede, 2012; Monachino et al., 2017).

A typical MTs setup is composed by a tracking system, which is usually made of an optical microscope and various magnetic elements that can be made either by permanent magnets or electromagnets (Xin et al., 2017).

All the components are normally chosen and assembled for the specific force to be applied to the system. It is possible to control the magnetic force by changing the size and shape of the magnet, by changing its magnetization orientation, or by varying the distance between the magnets and the magnetic beads. MTs allow the application of stretching/pulling forces, which are perpendicular to the biological sample substrate, or twisting forces parallel to the biological sample substrate (Shang and Lee, 2007; Kilinc et al., 2012; Tabdili et al., 2012). These operations are even easier by using electromagnets, i.e., generating the field by electrical current passing through a coil. Likewise, it is possible to precisely control the magnetic field and to easily switch its magnitude and direction and the number of poles.

Most magnetic particles used as force transducer in MTs studies are superparamagnetic (SPM) or weakly ferromagnetic. SPM particles are mainly used for their relatively high susceptibility and zero residual magnetization (O'Mahony et al., 2013), while ferromagnetic nanoparticles, thanks to their high saturation magnetization, are normally chosen where there is a weak external magnetic field and the particle size is limited.

Despite a great share of research on MTs concentrates on the development of electromagnets and system design, yet the experiments are typically based on commercial magnetic beads; thus, the possibility to widen their properties and characteristics by achieving different shapes, sizes and element compositions is pivotal for enhancing MTs performances (Zhang and Wang, 2012; Tavecchi et al., 2013). Nowadays, many companies sell iron oxide SPM beads with diameters ranging from 0.1 to 100  $\mu\text{m}$  and with a wide selection of chemically modified or biologically functionalized surfaces. As an example, nanorods, thanks to the possibility of combining multiple metallic elements (Zhang et al., 2011; Lin et al., 2012) or alloys (Zhang and Wang, 2012) into a single structure, have been successfully used to enhance properties for target applications (e.g., in torque measurements the need to have small particles with high torque sensitivity and small stretching force) or to introduce multiple functionalities, such as magneto-optically active materials (Zhang et al., 2011).

In the near future, novel MTs probes made of magnetic beads with enhanced properties, such as programmable shape changes (Tavecchi et al., 2013) or collapsing under the exposure to weak magnetic fields (Fuhrer et al., 2013), could further widen the application fields of this technique.

MTs were subject to many updates and enhancements through the years, and some of the early limitations (i.e., the extreme difficulty to measure torques in the range of 10 pN·nm, typical of DNA, the impossibility to decouple twisting torque from stretching force, and the necessity to apply an external torque

in order to study the natural torque of a molecule), were overcome by alternative approaches that have been widely described in many reviews (Kilinc and Lee, 2014). For example, approaches like “soft MTs” (Mosconi et al., 2011), “rotor bead tracking” (Oberstrass et al., 2012), “freely orbiting MTs” (Lipfert et al., 2011) and “magnetic torque tweezers” (Lipfert et al., 2010) were developed to decouple torque from stretching force. Moreover, the raise of a series of instruments called “electromagnetic torque tweezers” sensible to stretching forces from 10 fN to 10 pN and with torsional stiffness ranging from zero to 1000 pN·nm/rad (Janssen et al., 2012), creates a category of instruments with broad ranges of force and torque. Other approaches also make the most of the simple and flexible MTs design by combining it with other force probing techniques (e.g., OTs, TFM, and many others), building a huge variety of instrumental setups tailored to different applications. For a more detailed insight on the technical aspects of MTs we suggest to refer to Kilinc and Lee (2014) and Tanase et al. (2007).

MTs equipment is easy to assemble and cheap. However, MTs are not widely commercialized and research laboratories possess their own highly customized tools, thus they are not standardized. This aspect is of particular importance considering that the use of electromagnets may affect the behavior of biomolecules by hysteresis of the magnetic field and heat generation around the sample (Rocha, 2015).

In the near future, the integration with other biophysical measurements, the development and fabrication of new classes of multi-functional magnetic particles with enhanced magnetic properties, or different programmable geometries, could expand the potential uses of MTs pushing forward the current boundaries of the methodology.

MTs have been used for analyzing local viscoelastic properties of the cytoplasm (Bausch et al., 1999), for testing different membrane structures with distinct characteristics as in the case of intracellular organelles, for probing the molecular basis of cell mechanics (including the linkage mechanisms of transmembrane integrins to different component of the cytoskeleton), and for studying the chromatin structure, function, and the detailed nuclear architecture.

MTs have been used in several studies to explore how cells respond to mechanical forces. Wang et al. (1993) applied a twisting force to integrins on the surface of endothelial cells, using arginine-glycine-aspartic acid (RGD) peptide-coated magnetic beads, observing the actin cytoskeleton dependent stiffening response. Glogauer et al. (1995, 1997) placed permanent magnets over cell cultures in order to vertically pull collagen-coated magnetic beads attached to the cell surface. Using this method, they were able to perform both single cell analysis, for example measuring a modification of the intracellular calcium content in response to force, and bulk biochemical measurements on large populations of cells, that allowed them to show an increase of protein tyrosine phosphorylation in response to force. Zhao et al. (2007) used this approach to show the activation of RhoA by imposing a tension on integrins via collagen coated magnetic beads. Matthews (2006) used MTs to determine the effects of applying tension on magnetic beads coated with integrin ligands

and showed the involvement of RhoA signaling pathways in the cellular response. Marjoram et al. (2016) evaluated single cell response to force pulses. They analyzed the effects of tension on VE-cadherin on endothelial cells, reporting an increase in RhoA activation and a decrease in Rac1 activation, a change in the phosphorylation levels of protein tyrosine, and a stiffening response to trains of short force pulses. Saphirstein et al. (2013) used MTs to investigate the mechanobiology of aortic tissue. Their results show that the focal adhesions of the vascular smooth muscle cells (VSMC), and particularly the FAK/Src complex, act as a regulator of aortic stiffness. Considering that the increase in aortic stiffness is linked to cardiovascular disease, the obtained results make FAs as a potential novel therapeutic target.

MTs have frequently been coupled with other techniques to gather more accurate information. Optical Magnetic Twisting Cytometry (OMTC), a technique of applying twisting torques to cells in culture, has been used by different groups (Fabry et al., 2001; Puig-de-Morales et al., 2004; Trepap et al., 2007) to study how different force regimes (i.e., modifying frequency or amplitude) applied to cells resulted in cellular reinforcement (stiffening) or fluidization (softening). Na and Wang (2008) combined FRET with MTs to study rapid mechanochemical signaling in live cells, and they demonstrated that pre-stressed cytoskeleton promoted rapid activation of Src protein upon force. With a similar setup, Poh et al. (2009) showed that a local stress in the physiological magnitude range, applied through integrins on human airway smooth muscle cells, can directly and rapidly activate Rac GTPase, independently of Src activity. MTs have also been used in combination with microengineered platforms (Lin et al., 2012). The induced cellular contractile response to force and torque applied through nanowires bound to (or internalized by) bovine pulmonary artery smooth muscle cells (SMCs) was measured with arrays of elastic micropillars force sensors. The authors reported that the contractile response was connected to the actuation frequency, but was not dependent on the applied force or torque magnitude. Moreover, they observed a global enhancement of cell traction forces following the application of a localized torque. Recently, Bidan et al. (2018) applied a combination of MTs and TFM on deformable substrates enabling local and dynamic mechanical stimulation of cells plated on a continuous surface. Substrates consisted of a layer of soft elastomer embedding spatially arranged magnetic micropillars, that could be locally actuated by means of a MTs setup. The induced localized deformation of the substrate could be quantified by tracking fluorescent microbeads that were also embedded under the elastomer surface.

## Acoustic Tweezers (ATs)

In 1991, an article from Wu (1991) showed the possibility to stably trap a 270  $\mu\text{m}$  latex particle or a cluster of frog eggs in a potential well generated by two collimated focused ultrasonic beams propagating along opposite directions in water. This technique, originally termed “acoustical tweezers”, is nowadays better known as ATs.

ATs are based on the concept that a stable potential well can be created by radiation pressure at the physical focal point of a focused ultrasonic beam (Wu and Du, 1990). This technique foresees the use of piezoelectric transducers positioned so that their beams focal points can be held a few millimeters apart, creating the potential well. Moving the transducers or tuning their frequency results in the displacement of the potential well and in the trapped objects to be moved alongside.

Manipulating biological specimens by acoustic waves, ATs present many advantages (Friend and Yeo, 2011; Ding et al., 2013) compared to similar techniques (i.e., optical and MTs). First of all, the emitted mechanical vibrations have such a low intensity (power intensity ca. 10 million times lower than OTs) that they have a minimal impact on cell viability and function, not altering cell characteristics. Moreover, particles or cells can be suspended into their preferred medium (i.e., culture medium or ECM) and moved in a contactless way, avoiding contamination. Also, there is no need for the manipulated cell to undergo surface modifications or labeling, so that cells maintain their shape, size, refractive index, charge and other native properties. Finally, the ATs platform can be made of a single, integrated micro-device, avoiding any moving parts and/or complicated setup procedures, which make the system very easy to use (Guo et al., 2016). In this regard, the implementation of surface acoustic wave (SAW) transducers (Ahmed et al., 2016) for on-chip manipulation of cells has been reported (Voiculescu and Nordin, 2012; Ding et al., 2014; Nguyen et al., 2017).

In summary, acoustic devices, not suffering from some of the drawbacks affecting other methods (i.e., no need of optical purified sample, possibility to manipulate large particles or cells, lower damage to biological samples) (Hwang et al., 2014; Huang et al., 2015; Li et al., 2015), have been demonstrated to successfully perform many microscale functions such as separation, alignment, patterning, enrichment and transportation of cells and microparticles (Friend and Yeo, 2011; Ding et al., 2013; Bourquin et al., 2014; Gesellchen et al., 2014; Guo et al., 2015; Li et al., 2015), and are considered to be a very attractive non-invasive approach for the manipulation of cells and particles for biomedical and biophysical applications (Lam et al., 2016).

An evolution of ATs with a high significance for the study of cell mechanobiology has been introduced by Fan et al. (2013). The authors used RGD-coated, ultrasound-excitable lipid microbubbles, that were bound to the membrane of living cells and targeted by ATs for their mechanical actuation. This technique, which goes under the name of acoustic tweezing cytometry (ATC), produces a rapid acoustic radiation force on the microbubbles that provokes the contractility of the intracellular cytoskeleton. Hence, ATC provides an effective method to apply mechanical stress to cells with no reported negative effects on cell physiology (Liu, 2016). As an example, Heureaux et al. (2014) engineered retinal pigment epithelial cells for the expression of bacterial mechanosensitive channel of large conductance (MscL), and challenged the cytoskeleton with localized stress by integrin-bound microbubbles, demonstrating the possibility to gate the MscL by a mechanical actuation

that targets the integrin-focal adhesion-cytoskeleton connection. As a further improvement, Chen et al. (2015) developed an ATC methodology exploiting the acoustic interaction force between two cell-bound microbubbles, that is resulting from the scattering of the incident primary ultrasound field. The generated secondary acoustic radiation force (sARF) has the same magnitude for each of the microbubbles and is attractive, independently of the orientation of the primary ultrasound pulses. For this reason, two-bubble ATC (TB-ATC) technique provides advantages in the experimental setup and in the measurement of subcellular biomechanical properties. Using TB-ATC, the same research group demonstrated that ATC stimulation promotes cytoskeletal contractility and enhances osteogenesis of human mesenchymal stromal cells via YAP activation (Xue et al., 2017).

## TRACTION FORCE MICROSCOPY (TFM)

Among passive approaches, TFM was one of the first and most broadly used techniques for measuring cell forces, providing maps of stresses at the cell surface. Ideally, every cell adherent to a soft substrate exerts a contractile force able to deform it to a measurable extent. Over the years, several TFM methods exploiting flexible 2D synthetic substrates of known mechanical properties have been reported. One of the first experiments introduced by Harris et al. (1980) used soft silicone rubber as cell substrate and provided maps of traction forces by measuring the size of the out-of-plane wrinkles generated by cell contraction. Although the force direction and magnitude are derived from wrinkles inspection by phase contrast microscopy, this approach is highly qualitative and the reported deformation cannot be compared across systems.

Therefore, researchers started to use fluorescence beads to monitor the deformation of thin hydrogel films, thereby gathering quantitative information. In standard TFM, micro/nanoscale fluorescent beads are embedded into the substrate or attached on the surface and used as fiduciary markers to be optically tracked in space and time. A common TFM experiment consists in imaging the bead positions in a stressed state (cell-loaded image) when cells seeded on the substrate start to contract. After releasing cell tractions by detaching the cell (i.e., by trypsinization), a new image is captured to determine the position of the beads in the unstressed state (unloaded or reference image). A displacement map of the deformed substrate – a map showing how each pixel deviates from its reference position due to the force exerted by the cell – is then derived from the two images either by single particle tracking or by digital image correlation (Franck et al., 2011).

To avoid the use of a reference image, recent advancements have involved the controlled dispensing of fluorescent markers (e.g., using the electrohydrodynamic NanoDrip printing technique) with regular spacing on the gel surface (Bergert et al., 2016). Alternatively, instead of using fluorescent beads distributed throughout the substrate, a modified version of TFM has been implemented by Balaban et al. (2001) who adapted

soft lithography to embed patterns of fluorescent photoresist markers right under the substrate surface. Once the computational framework and imaging system are set up, measurements can be systematically performed and traction maps derived from the displacements through a variety of computational methods (Butler et al., 2002; Munoz, 2016). Since the beads are much smaller in size than a cell, TFM has allowed scientists to map forces with subcellular resolution enabling the characterization of the force dynamics involved in numerous biological and pathological processes, including cell adhesion, migration, differentiation, and metastatic potential (Engler et al., 2006; Indra et al., 2011; Jannat et al., 2011; Koch et al., 2012).

Polyacrylamide (PA) or silicon-based gels are typically used as substrates for TFM (Roca-Cusachs et al., 2017). Both types of gels exhibit a linear elastic behavior under deformations produced by cell traction, and their Young's modulus (i.e., linear elastic modulus) can be varied over a range of several orders of magnitude. Furthermore, unlike native ECM, their mechanical properties do not change significantly during a single measurement since they are not degraded by biochemical factors released by the cells, including cell proteases. Although this is advantageous for cellular traction measurements, evidences from the literature revealed a significant effect of cell-mediated degradation of ECM matrices on cellular traction profiles (Khetan et al., 2013).

Thus, TFM has been rapidly extended from the computation of the 2D force field imparted by an individual cell on a 2D flat substrate to the quantification of forces in more realistic environments with a dramatic increment of computational time. The first step toward this goal has been the extension of TFM measurements to multicellular clusters (Trepap et al., 2009) and 2D substrates of arbitrary stiffness profiles (Sunyer et al., 2016). Furthermore, although the 2D TFM can approximate many experimental conditions, cells usually exert 3D forces on the adhering substrates and the normal traction component is often comparable to the in-plane one (Bastounis et al., 2014). Thus, to obtain a more accurate characterization of 3D traction field of cells cultured on a 2D substrate (often referred to as 2.5D tractions), TFM methods have been further modified and implemented to track bead displacements in 3D with confocal microscopy.

Another issue, even more tricky, is represented by the analysis of 3D force field exerted by cells encapsulated in 3D ECMs. In all the methods presented so far, cells are seeded on 2D substrates, while cells *in vivo* are embedded in 3D matrices, and their phenotype and shape is strikingly affected by the surrounding cell environment. However, greater use of 3D TFM is hindered not only by the limits in acquiring sub-micrometer scale features in 3D (Hall et al., 2013), but also by the more heterogeneous and mechanically complex properties of natively-derived fibrous components of the ECM compared to the synthetic materials used for 2D measurements (Hall et al., 2013). Unlike the 2D/2.5D cases, in which the properties of the substrate can be tightly engineered by researchers, the 3D

ECM undergoes continuous remodeling that involves deposition, reorganization and degradation, precluding a straightforward interpretation of the deformation/force fields. Just to give an example, it is impossible to clearly discriminate if a large deformation in the proximity of a cell is induced by high cell traction or by a change in mechanical properties related to ECM remodeling. Moreover, natural ECMs are composed of fibers with highly non-linear behavior and randomly distributed in the same microscopic volume element. Although these 3D traction approaches have still limited applicability compared to 2D TFM, they have already evidenced a different cell mechanical behavior between 3D and 2D environments, as demonstrated for forces applied by MDA-MB-231 breast carcinoma cells in 3D polymers that appear to be independent of concentration and stiffness of the surrounding matrix (Steinwachs et al., 2016).

Collagen type I hydrogel is a common ECM-mimicking material for 3D cell culture. Particle tracking techniques have successfully led to the quantification of pericellular collagen deformations during tumor cell invasion and migration through a 3D collagen matrix (Bloom et al., 2008; Koch et al., 2012). However, the non-linear force-displacement response of this hydrogel prevents quantification of traction forces from the deformations using classical mechanics approaches. Other studies report quantitative finite-element based methods to measure cell-generated forces in physiologically-mimicking 3D biopolymeric matrices with highly non-linear mechanical response such as collagen and fibrin gels (Steinwachs et al., 2016). Alternatively, to avoid the issues associated with non-linearity, 3D traction fields have been computed by Legant et al. (2010) using synthetic, matrix metalloprotease (MMP)-cleavable polyethylene glycol (PEG) gels. These synthetic hydrogels exhibit linearly elastic behavior in the range of deformations produced by single cells, and the possibility to track beads in this material has successfully led to the measurement of cellular tractions in 3D. Although a significant improvement has been made, this method still assumes that the material only undergoes elastic deformation (Palacio et al., 2013) and a lot of work still needs to be done to fully incorporate non-linear and poroelastic models of hydrogel substrates into routine algorithms improving data quality at large deformations.

Since traction forces play a fundamental role in many biological processes including embryogenesis, angiogenesis, inflammation, wound healing and metastasis, the application of TFM has allowed better understanding of cellular and molecular mechanisms of these processes (Wang and Li, 2010; Li and Wang, 2011; Malandrino et al., 2018).

One of the basic TFM biological applications is the measurement of traction forces imparted by single cells on a 2D substrate. For example, a maximum displacement of around 1.2  $\mu\text{m}$ , corresponding to a traction stress of about 250 Pa, has been found by Yang et al. (2006) for human patellar tendon fibroblasts seeded on a type I collagen-coated PA substrate. More interestingly, as traction forces vary depending on cell type, TFM measurements can be useful in detecting cell phenotypic changes. On this basis, TFM has been successfully applied to



detect differentiated cells and to distinguish between fibroblasts and myofibroblasts obtained from the differentiation of rabbit corneal stromal cells in conditioned media (Chen et al., 2007). Going beyond the measurement of traction forces applied by single cells, TFM has also found applications to explore the behavior of cellular aggregates (Li et al., 2009), with particular regard to the mechanisms behind collective cell migration (Treat et al., 2009).

In addition, taking advantage of microfluidics and micro-technologies, a recent trend is represented by the integration of TFM with miniaturized mechanically actuated systems to investigate cellular forces under dynamic conditions mimicking physiological stimuli, e.g., shear flow (Shiu et al., 2004), mechanical stretch (Gavara et al., 2008), and chemokine gradients (Del Alamo et al., 2007).

In this way, TFM has been applied to observe spatiotemporal patterns of forces in settings that are more representative of physiological and pathological *in vivo* conditions (Cho et al., 2016). As a major outcome, this technique could have a pivotal role in the development of *in vitro* cell culture models of several diseases, especially if associated with changes in cell contractility (e.g., hypertension, muscle dystrophy, etc.), to ease diagnostic screening and therapeutic treatments. A leading example is represented by the *in vitro* model developed by Li et al. (2008) who investigated the contractility of micropatterned C2C12 skeletal muscle cells using TFM with the aim to obtain a fast screening platform for therapy of Duchenne muscular dystrophy.

While effective in a variety of biological applications, further advancements in TFM are needed to improve spatial resolution, enable real time assays, and measure forces within 3D matrices in a high-throughput manner (Colin-York and Fritzsche, 2018).

## MICROENGINEERED PLATFORMS

As an alternative to TFM, microfabricated platforms have been investigated to measure cellular tractions in controlled mechanical environments. A variety of approaches has been described in the literature, but a classification into two major classes can be performed (Rajagopalan and Saif, 2011); hard silicon-based devices and soft polymer/gel devices.

The first category includes silicon devices fabricated through integrated circuit manufacturing processes, the so-called Micro-Electro-Mechanical Systems (MEMS). In this case, cells are contacted with compliant silicon elements that deform in response to cellular forces altering their electrical response, as extensively reviewed by Polacheck and Chen (2016). The design flexibility of MEMS translates into the possibility of force measurements along multiple axes, coupled to unprecedented measurable force range ( $10^{-12} \div 10^{-3}$  N; Sun and Nelson, 2007). Notable examples of MEMS devices for cell biomechanical characterization are represented by the work of Matsudaira et al. (2017) who developed a silicon piezoresistive cantilever platform for measuring the beating contraction force of iPS-derived cardiomyocytes, and that of Takahashi et al., 2016 who designed a MEMS force plate to measure single cell horizontal and vertical

traction forces. Although the majority of these devices are passive, approaches to single-cell mechanical actuation using MEMS have to be acknowledged (Scuor et al., 2006; Antonioli et al., 2014), also integrating force sensing capabilities besides actuation ones (Fior et al., 2011; Zhang and Dong, 2012).

The second category of microengineered platforms encompasses soft polymer and gel microsystems obtained through soft-lithography techniques. On the one hand, these polymer-based devices require the use of image analysis to quantify cell-induced displacements due to the difficulties in the integration of electronic components into such devices. On the other hand, the higher biocompatibility and optical transparency of these systems, together with the possibility to easily tune surface chemistry and mechanical properties to better mimic mechanical *in vivo* environment, have made them increasingly popular for mechanobiology studies (Rajagopalan and Saif, 2011).

Among polymer-based substrates, microfabricated (vertically arranged) micropillar arrays have been applied to the measurement of forces exerted by single adhesion sites of a cell in constructs with as few as 100–600 cells (Polacheck and Chen, 2016). These structures are obtained by soft lithography, consisting in replica molding of a patterned silicon master using commercial silicone elastomer (PDMS). After microcontact printing of ECM proteins over the micropillar tips, cells can adhere and spread, exerting contractile forces that deflect the underlying pillars as simple cantilever beams. If the deflection is sufficiently small compared with the height of the posts, the displacement of the cantilever beam tip and the force are proportional. Thus, traction forces can be directly calculated from optically measured micropillar deflections, provided that the constant of the spring is known. An exhaustive description of how to fabricate the silicon masters and elastomeric replicas, as well as cell culture procedures, immunofluorescence imaging and traction force evaluation on these substrates can be found in previous works (Yang et al., 2011; Gupta et al., 2015).

PDMS micro/nanopillars have been successfully applied to investigate forces exerted by different cells, including fibroblasts, endothelial cells, stem cells, etc., at both cellular and subcellular levels (Nelson et al., 2005; Fu et al., 2010; Ghassemi et al., 2012). In particular, these systems have gained great interest as tool for measuring forces in cells that cannot be isolated or easily expanded, such as cardiomyocytes and human iPSCs, leading to high-throughput, low volume screening platforms for cardiac studies (Boudou et al., 2012; Serrao et al., 2012; Hinson et al., 2015).

As for TFM, micropillar arrays have also been integrated with miniaturized actuating systems to detect cell–ECM interactions under dynamic conditions mimicking physiological ones (Shao and Fu, 2014). For instance, coupling micropillar arrays to microfluidic channels allowed measurement of cell contractile forces under laminar shear flow (Lam et al., 2012a) or during chemotaxis-regulated cell migration (Ricart et al., 2011). Mechanical actuation of micropillar arrays was also pursued as a tool to study the response of cells to external mechanical stimuli, exploiting either vacuum-driven mechanical stretching (Lam et al., 2012b; Mann et al., 2012) or magnetic actuation

of micropillars embedding magnetic nanowires (Sniadecki et al., 2007).

Compared to TFM measurements, the use of micro/nanopillar sensing elements has a few advantages. First, a reference image is not required since displacements can be calculated from undeformed pillar positions. Second, cellular forces are derived from the deformation of single polymeric structures, leading to a simpler and less computationally expensive calculation. Finally, heterogeneous mechanical environments can be obtained by simply altering micropillar geometries that influence substrate stiffness.

Stiffness can be varied over a wide range of values through the modulation of pillar structural parameters, such as height and diameter. Tan et al. (2003) constructed circular posts with 3  $\mu\text{m}$  diameter, 11  $\mu\text{m}$  height and 6  $\mu\text{m}$  spacing, corresponding to a stiffness of 32  $\text{nN}\cdot\mu\text{m}^{-1}$  per post using standard photolithography and PDMS replica molding. Access to improved microfabrication processes such as high-resolution lithography and deep reactive-ion etching (DRIE) has led to the reduction of pillar diameter to the sub-micrometer level, and to the increase of micropillar aspect ratio (du Roure et al., 2005; Yang et al., 2007; Kim et al., 2009). Using a combination of nanosphere lithography and plasma etching, Shiu et al. (2018) have recently further scaled down micropillar geometries, obtaining epoxy-based photoresist structures that were 250 nm in diameter and 1.5  $\mu\text{m}$  in height, with a spacing of 800 nm and a stiffness of 79  $\text{nN}\cdot\mu\text{m}^{-1}$ .

It is worth mentioning that the discrete adhesive surface that cells sense on micropillars might affect the recruitment of integrins and adhesion proteins. This may in turn influence the morphology of cell-ECM adhesions, thereby creating a bias in the measurements. In this regard, the use of sub-micrometer pillars with reduced center-to-center distance (Yang et al., 2007; Fu et al., 2010; Ghassemi et al., 2012) might provide a closer resemblance to continuous tissue culture substrates as demonstrated by the increasing number of papers reporting comparable behaviors for several cell types (e.g., fibroblasts, endothelial cells, smooth muscle cells, MSCs, and embryonic stem cells) when cultured on PDMS micro/nano-pillar arrays and on continuous substrates (Yang et al., 2007, 2011). It also has to be acknowledged that micropillar technology restricts the achievable stiffness range compared to continuum substrates used in TFM (Miroshnikova et al., 2018), not achieving the fabrication of ultra-compliant arrays equivalent to the softest PA gels. Moreover, although the elastomeric replicas can be manufactured in a standard laboratory, the production of the original master requires sophisticated microfabrication facilities and equipment that are not common in research laboratories. Additionally, calculating an effective stiffness of micropillar substrates to be compared with physiological parameters is not an easy task, even if some approaches have been proposed (Ghibaudo et al., 2008). The simplest and most common approach is to approximate the polymeric material as linear elastic, and to express the spring constant of the micropillar from the classical beam theory<sup>1</sup>. However, such a theory

is only valid in the linear regime of small deformations (Li et al., 2007). Xiang and LaVan (2007) have integrated shear strain and large deflection theory and demonstrated that, for deflection-to-length ratios less than 20%, the difference between using the small or the large deflection model was less than 10%. Furthermore, other issues related to the non-negligible effect of the elastic deformation of the pillar substrate (Zhao et al., 2005) and to the effect of materials viscoelasticity under dynamic analysis with different loading time/frequency (Lin et al., 2008) should be taken into account. A detailed survey of the advantages and disadvantages of the different analytical and computational models is out of the scope of this review and has been exhaustively described elsewhere (Zheng and Zhang, 2011).

## CONCLUSION AND FUTURE OUTLOOK

Cellular mechanics is of primary importance in many pathophysiological processes. Mechanical forces elicit several biological processes in a cell, not only changing the ability of a cell to respond to exogenous signals and stimuli, but also dramatically influencing the way in which differentiation decisions are made during development.

The classical methods of fluorescence microscopy and spectroscopy can be used to detect the position, distribution and dynamics in real-time of single molecules, but they are not able to provide detailed information on the mechanical features, on the functional state of biomolecules or on the interactions between biological systems on a molecular scale. In the last decades, remarkable advancements have been made in devising novel and effective techniques for identifying and handling single molecules for the structural and functional study of biomolecules in physiological conditions. These techniques can be divided into active and passive, and they allow studying *in vitro* the mechanical properties of cells by generating or detecting forces down to the pN range.

In this review, various methods applied to the field of mechanobiology have been described. Attention was focused on active measurement methods (i.e., atomic force microscopy, optical/magnetic/acoustic tweezing) and on passive ones (TFM, MEMS, and microfabricated substrates). This review highlights the improvements brought to the single techniques to better characterize biological entities. Among these advancements, we emphasize the importance of investigating the biological response in conditions similar to the physiological environment and for longer time without inducing cell damage, along with the study of cellular responses to a given biomechanical stimulus in 3D conditions, thus recreating the tissue microenvironment, in order to obtain a response closer to reality. The proper measurement of physico-mechanical entities, on a cellular and subcellular scale, in a physiological or pathological condition is indeed extremely challenging due to the complexity of recapitulating an *in vivo* context that contributes to the generation and propagation of cellular forces. Discriminating the contribution of each component in the complex *in vivo* microenvironment of a living tissue is not completely feasible yet. Except for the most recent

<sup>1</sup>Under small deflection assumptions, pillar elastic constant can be expressed as  $k = 3\pi ED^4/64H^3$ , where E, D and H are the elastic modulus of PDMS, the diameter and the height of the pillar, respectively.

advances in the use of high-resolution OTs (that suffer from limitations in analyzing events located deep in tissues) and MTs combined with single molecule confocal microscopy and FRET technology to measure fluid forces *in vivo* and to track mechanotransduction in living cells, a single cell must be isolated from its surrounding environment and cultured on a suitable substrate in order to allow researchers to perform measurements and analyze its mechanical behavior, which is a much more simplified context compared to native tissues. Furthermore, there are many physico-chemical conditions (e.g., temperature, surface energy) and mechano-structural factors (e.g., strain stiffening, pressure, cell geometry) that may have significant effects on measurement accuracy. However, these conditions cannot be easily recreated *in vitro*. Therefore, to date, such aspects represent a significant limitation to the correct prediction of cell mechanical behaviors.

Among the different methodologies taken into consideration in mechanobiology studies, AFM represents a well-established and widely used technique, which can give a topographic image of cells and biomolecules, enabling a deeper investigation into the dynamic properties of the analyzed sample, for instance in terms of molecular interactions required for the adhesion of a single cell to a substrate. Furthermore, technical improvements to the setup have allowed AFM measurements to be performed in culture conditions and in combination with fluorescence microscopy. However, the technique has limitations in terms of measurement speed and costs of the instrument itself.

Unlike AFM, tweezing technologies allow users to study both cellular stiffness and intracellular mechanisms (such as endocytosis) using specific molecules or marked particles. Tweezing techniques still suffer from some limitations: in particular, OTs can damage cells after prolonged exposure to high powered lasers. This problem has been partially overcome by implementing MTs and ATs.

On the other hand, MEMS technology affords the possibility to fabricate extremely complex electromechanical systems and platforms either in 2D or 3D fashion, at the micrometer scale. By using a wide range of materials having different chemical or physical features, MEMS devices can integrate miniaturized mechanical and electro-mechanical elements that can be exploited for diverse purposes.

Thanks to major steps forward in the development of microfabrication and microfluidics, cell biomechanics and mechanotransduction mechanisms can be studied in dynamic conditions, simulating pathophysiological stimuli, in a 3D-like microenvironment. These fast-growing technologies have been advancing our understanding on how various cell types and tissues sense and respond to mechanical stimuli, opening the way toward new strategies for investigating dynamic and complex biological phenomena, such as embryonic development and migratory response of tumor cells. A correct quantification and understanding of cell mechanical behavior may indeed provide an essential foundation for studying and envisaging the development of several diseases.

In addition, TFM methods have been combined with 3D systems, with the support of confocal microscopy, for observing

tractions on cell surface, and for mapping 3D stress and strain fields of single cells encapsulated in elastic and viscoelastic materials. The future of this technology may be represented by its application to synthetic and natural fibrous gels for monitoring traction fields of isolated cells embedded in either synthetic or naturally derived fibrous materials, such as collagen, with the ambitious aim of recapitulating a physiologically relevant environment in terms of biophysical and biochemical parameters.

In conclusion, countless techniques have been developed for the study of mechanobiology and the understanding of the role of mechanical stimuli on cellular response. Altogether, the coupling of biological, physico-chemical, and engineering knowledge has allowed scientists to develop technological platforms that hold great promise for a comprehensive study of cell mechanobiology.

As a future perspective, we expect technological progresses to drive the advancement of the above described methods, resulting in an extended range of applicable and measurable forces, and an improved spatio-temporal resolution. The next generation of tools to measure cellular forces is expected to create complex cell microenvironments through the use of combinatorial guidance cues in a single experiment, so that single cells can experience a dynamically changing set of mechanical and biochemical conditions more representative of *in vivo* settings. In this regard, we will probably assist to a tighter convergence of the technologies, as expected for high-speed AFM and OTs (Ando, 2018) in order to combine nanoscale resolution imaging with manipulation capabilities at the molecular level. The attention of researchers in the field of mechanobiology will reliably be drawn to the measurement of cell and tissue mechanical properties *in vivo*. In this scenario, MEMS devices have the potential to detain a leading role in light of their extremely wide force range and design flexibility.

The challenge remains in translating the accumulating evidence of mechanical regulation of cell functions in physiology and disease into next-generation diagnoses and treatments.

## AUTHOR CONTRIBUTIONS

FB, SG, MG, PM, AB, MT, and AR wrote and revised the manuscript.

## ACKNOWLEDGMENTS

PM acknowledges funding from the European Social Fund and the European Regional Development Fund (CZ.02.1.01/0.0/0.0/15\_003/0000492 “Unveiling the molecular determinants of aging to design new therapeutics – MAGNET”). AR acknowledges the financial support from Università Campus Bio-Medico di Roma: Internal Grant Program (0015-2014 “GUT2.0”) and Technology Transfer Grant (009-2017 “ITHACa”) in the framework of INTESE project (co-funded by Regione Lazio, grant # FILAS-RU-2014-1193).

## REFERENCES

- Abidine, Y., Laurent, V. M., Michel, R., Duperray, A., and Verdier, C. (2015). Local mechanical properties of bladder cancer cells measured by AFM as a signature of metastatic potential. *Eur. Phys. J. Plus* 130:202. doi: 10.1140/epjp/i2015-15202-6
- Ahmed, D., Ozcelik, A., Bojanala, N., Nama, N., Upadhyay, A., Chen, Y., et al. (2016). Rotational manipulation of single cells and organisms using acoustic waves. *Nat. Commun.* 7:11085. doi: 10.1038/ncomms11085
- Alcaraz, J., Otero, J., Jorba, I., and Navajas, D. (2018). Bidirectional mechanobiology between cells and their local extracellular matrix probed by atomic force microscopy. *Semin. Cell Dev. Biol.* 73, 71–81. doi: 10.1016/j.semcdb.2017.07.020
- Andersson, M., Madgavkar, A., Stjern Dahl, M., Wu, Y., Tan, W., Duran, R., et al. (2007). Using optical tweezers for measuring the interaction forces between human bone cells and implant surfaces: system design and force calibration. *Rev. Sci. Instrum.* 78:074302. doi: 10.1063/1.2752606
- Ando, T. (2018). High-speed atomic force microscopy and its future prospects. *Biophys. Rev.* 10, 285–292. doi: 10.1007/s12551-017-0356-5
- Ansardamavandi, A., Tafazzoli-Shadpour, M., Omidvar, R., and Jahanzad, I. (2016). Quantification of effects of cancer on elastic properties of breast tissue by atomic force microscopy. *J. Mech. Behav. Biomed. Mater.* 60, 234–242. doi: 10.1016/j.jmbbm.2015.12.028
- Antonilli, F., Maggiolino, S., Scuor, N., Gallina, P., and Sbaizero, O. (2014). A novel MEMS device for the multidirectional mechanical stimulation of single cells: preliminary results. *Mech. Mach. Theory* 78, 131–140. doi: 10.1016/j.mechmachtheory.2014.03.009
- Ashkin, A., Dziedzic, J. M., Bjorkholm, J. E., and Chu, S. (1986). Observation of a single-beam gradient force optical trap for dielectric particles. *Opt. Lett.* 11:288. doi: 10.1364/OL.11.000288
- Ashkin, A., Dziedzic, J. M., and Yamane, T. (1987). Optical trapping and manipulation of single cells using infrared laser beams. *Nature* 330, 769–771. doi: 10.1038/330769a0
- Balaban, N. Q., Schwarz, U. S., Riveline, D., Goichberg, P., Tzur, G., Sabanay, I., et al. (2001). Force and focal adhesion assembly: a close relationship studied using elastic micropatterned substrates. *Nat. Cell Biol.* 3, 466–472. doi: 10.1038/35074532
- Bambardekar, K., Clément, R., Blanc, O., Chardès, C., and Lenne, P.-F. (2015). Direct laser manipulation reveals the mechanics of cell contacts in vivo. *Proc. Natl. Acad. Sci. U.S.A.* 112, 1416–1421. doi: 10.1073/pnas.1418732112
- Bastounis, E., Meili, R., Álvarez-González, B., Francois, J., del Álamo, J. C., et al. (2014). Both contractile axial and lateral traction force dynamics drive amoeboid cell motility. *J. Cell Biol.* 204, 1045–1061. doi: 10.1083/JCB.201307106
- Bausch, A. R., Möller, W., and Sackmann, E. (1999). Measurement of local viscoelasticity and forces in living cells by magnetic tweezers. *Biophys. J.* 76, 573–579. doi: 10.1016/S0006-3495(99)77225-5
- Berdyeva, T. K., Woodworth, C. D., and Sokolov, I. (2005). Human epithelial cells increase their rigidity with ageing in vitro: direct measurements. *Phys. Med. Biol.* 50, 81–92. doi: 10.1088/0031-9155/50/1/007
- Bergert, M., Lendenmann, T., Zündel, M., Ehret, A. E., Panozzo, D., Richner, P., et al. (2016). Confocal reference free traction force microscopy. *Nat. Commun.* 7:12814. doi: 10.1038/ncomms12814
- Bidan, C. M., Fratzl, M., Coullomb, A., Moreau, P., Lombard, A. H., Wang, I., et al. (2018). Magneto-active substrates for local mechanical stimulation of living cells. *Sci. Rep.* 8:1464. doi: 10.1038/s41598-018-19804-1
- Bloom, R. J., George, J. P., Celedon, A., Sun, S. X., and Wirtz, D. (2008). Mapping local matrix remodeling induced by a migrating tumor cell using three-dimensional multiple-particle tracking. *Biophys. J.* 95, 4077–4088. doi: 10.1529/biophysj.108.132738
- Bonilla, M. R., Stokes, J. R., Gidley, M. J., and Yakubov, G. E. (2015). Interpreting atomic force microscopy nanoindentation of hierarchical biological materials using multi-regime analysis. *Soft Matter* 11, 1281–1292. doi: 10.1039/c4sm02440k
- Boudou, T., Legant, W. R., Mu, A., Borochin, M. A., Thavandiran, N., Radisic, M., et al. (2012). A microfabricated platform to measure and manipulate the mechanics of engineered cardiac microtissues. *Tissue Eng. Part A* 18, 910–919. doi: 10.1089/ten.tea.2011.0341
- Bourquin, Y., Syed, A., Reboud, J., Ranford-Cartwright, L. C., Barrett, M. P., and Cooper, J. M. (2014). Rare-cell enrichment by a rapid, label-free, ultrasonic isopycnic technique for medical diagnostics. *Angew. Chemie Int. Ed.* 53, 5587–5590. doi: 10.1002/anie.201310401
- Bronkhorst, P. J., Streekstra, G. J., Grimbergen, J., Nijhof, E. J., Sixma, J. J., and Brakenhoff, G. J. (1995). A new method to study shape recovery of red blood cells using multiple optical trapping. *Biophys. J.* 69, 1666–1673. doi: 10.1016/S0006-3495(95)80084-6
- Butcher, D. T., Alliston, T., and Weaver, V. M. (2009). A tense situation: forcing tumour progression. *Nat. Rev. Cancer* 9, 108–122. doi: 10.1038/nrc2544
- Butler, J. P., Tolić-Nørrelykke, I. M., Fabry, B., and Fredberg, J. J. (2002). Traction fields, moments, and strain energy that cells exert on their surroundings. *Am. J. Physiol. Physiol.* 282, C595–C605. doi: 10.1152/ajpcell.00270.2001
- Capitanio, M., and Pavone, F. S. (2013). Interrogating biology with force: single molecule high-resolution measurements with optical tweezers. *Biophys. J.* 105, 1293–1303. doi: 10.1016/j.bpj.2013.08.007
- Charras, G. T., and Horton, M. A. (2002). Single cell mechanotransduction and its modulation analyzed by atomic force microscope indentation. *Biophys. J.* 82, 2970–2981. doi: 10.1016/S0006-3495(02)75638-5
- Chen, C. S., Tan, J., and Tien, J. (2004). Mechanotransduction at cell-matrix and cell-cell contacts. *Annu. Rev. Biomed. Eng.* 6, 275–302. doi: 10.1146/annurev.bioeng.6.040803.140040
- Chen, D., Sun, Y., Gudur, M. S. R., Hsiao, Y.-S., Wu, Z., Fu, J., et al. (2015). Two-bubble acoustic tweezing cytometry for biomechanical probing and stimulation of cells. *Biophys. J.* 108, 32–42. doi: 10.1016/j.bpj.2014.11.050
- Chen, J., Li, H., SundarRaj, N., and Wang, J. H.-C. (2007). Alpha-smooth muscle actin expression enhances cell traction force. *Cell Motil. Cytoskeleton* 64, 248–257. doi: 10.1002/cm.20178
- Cho, Y., Park, E. Y., Ko, E., Park, J.-S., and Shin, J. H. (2016). Recent advances in biological uses of traction force microscopy. *Int. J. Precis. Eng. Manuf.* 17, 1401–1412. doi: 10.1007/s12541-016-0166-x
- Ciasca, G., Sassun, T. E., Minelli, E., Antonelli, M., Papi, M., Santoro, A., et al. (2016). Nano-mechanical signature of brain tumours. *Nanoscale* 8, 19629–19643. doi: 10.1039/c6nr06840e
- Coccano, G., Yousafzai, M. S., Ma, W., Ndoye, F., Venturelli, L., Hussain, I., et al. (2016). Investigation into local cell mechanics by atomic force microscopy mapping and optical tweezer vertical indentation. *Nanotechnology* 27:065102. doi: 10.1088/0957-4484/27/6/065102
- Colin-York, H., and Fritzsche, M. (2018). The future of traction force microscopy. *Curr. Opin. Biomed. Eng.* 5, 1–5. doi: 10.1016/j.COBE.2017.10.002
- Collinsworth, A. M., Zhang, S., Kraus, W. E., and Trusek, G. A. (2002). Apparent elastic modulus and hysteresis of skeletal muscle cells throughout differentiation. *Am. J. Physiol. Physiol.* 283, C1219–C1227. doi: 10.1152/ajpcell.00502.2001
- Costa, K. D., and Yin, F. C. (1999). Analysis of indentation: implications for measuring mechanical properties with atomic force microscopy. *J. Biomech. Eng.* 121, 462–471. doi: 10.1115/1.2835074
- Curtis, J. E., and Spatz, J. P. (2004). “Getting a grip: hyaluronan-mediated cellular adhesion,” in *Proceedings of the International Society for Optics and Photonics*, eds K. Dholakia and G. C. Spalding (Washington, DC: SPIE), 455–466. doi: 10.1117/12.560049
- De Vlaminck, I., and Dekker, C. (2012). Recent advances in magnetic tweezers. *Annu. Rev. Biophys.* 41, 453–472. doi: 10.1146/annurev-biophys-122311-100544
- Del Álamo, J. C., Meili, R., Alonso-Latorre, B., Rodríguez-Rodríguez, J., Aliseda, A., Firtel, R. A., et al. (2007). Spatio-temporal analysis of eukaryotic cell motility by improved force cytometry. *Proc. Natl. Acad. Sci. U.S.A.* 104, 13343–13348. doi: 10.1073/pnas.0705815104
- Dholakia, K., and Reece, P. (2006). Optical micromanipulation takes hold. *Nano Today* 1, 18–27. doi: 10.1016/S1748-0132(06)70019-6
- Digiuni, S., Berne-Dedieu, A., Martínez-Torres, C., Szecsi, J., Bendahmane, M., Arneodo, A., et al. (2015). Single cell wall nonlinear mechanics revealed by a multiscale analysis of AFM force-indentation curves. *Biophys. J.* 108, 2235–2248. doi: 10.1016/j.bpj.2015.02.024
- Ding, X., Li, P., Lin, S.-C. S., Stratton, Z. S., Nama, N., Guo, F., et al. (2013). Surface acoustic wave microfluidics. *Lab Chip* 13, 3626–3649. doi: 10.1039/c3lc50361e

- Ding, X., Peng, Z., Lin, S.-C. S., Geri, M., Li, S., Li, P., et al. (2014). Cell separation using tilted-angle standing surface acoustic waves. *Proc. Natl. Acad. Sci. U.S.A.* 111, 12992–12997. doi: 10.1073/pnas.1413325111
- Dinu, C. Z., Dong, C., and Hu, X. (2016). Current status and perspectives in atomic force microscopy-based identification of cellular transformation. *Int. J. Nanomedicine* 11, 2107–2018. doi: 10.2147/IJN.S103501
- du Roure, O., Saez, A., Buguin, A., Austin, R. H., Chavrier, P., Silberzan, P., et al. (2005). Force mapping in epithelial cell migration. *Proc. Natl. Acad. Sci. U.S.A.* 102, 2390–2395. doi: 10.1073/pnas.0408482102
- Dufrène, Y. F., and Pelling, A. E. (2013). Force nanoscopy of cell mechanics and cell adhesion. *Nanoscale* 5:4094. doi: 10.1039/c3nr00340j
- Dulińska, I., Targosz, M., Strojny, W., Lekka, M., Czuba, P., Balwiercz, W., et al. (2006). Stiffness of normal and pathological erythrocytes studied by means of atomic force microscopy. *J. Biochem. Biophys. Methods* 66, 1–11. doi: 10.1016/j.jbbm.2005.11.003
- Efremov, Y. M., Dokrunova, A. A., Efremenko, A. V., Kirpichnikov, M. P., Shaitan, K. V., and Sokolova, O. S. (2015). Distinct impact of targeted actin cytoskeleton reorganization on mechanical properties of normal and malignant cells. *Biochim. Biophys. Acta Mol. Cell Res.* 1853, 3117–3125. doi: 10.1016/j.bbamcr.2015.05.008
- El-Kirat-Chatel, S., and Dufrène, Y. F. (2012). Nanoscale imaging of the Candida–macrophage interaction using correlated fluorescence-atomic force microscopy. *ACS Nano* 6, 10792–10799. doi: 10.1021/nn304116f
- Engler, A. J., Sen, S., Sweeney, H. L., and Discher, D. E. (2006). Matrix elasticity directs stem cell lineage specification. *Cell* 126, 677–689. doi: 10.1016/j.cell.2006.06.044
- Fabry, B., Maksym, G. N., Butler, J. P., Glogauer, M., Navajas, D., and Fredberg, J. J. (2001). Scaling the micro rheology of living cells. *Phys. Rev. Lett.* 87:148102. doi: 10.1103/PhysRevLett.87.148102
- Fallqvist, B., Fielden, M. L., Pettersson, T., Nordgren, N., Kroon, M., and Gad, A. K. B. (2016). Experimental and computational assessment of F-actin influence in regulating cellular stiffness and relaxation behaviour of fibroblasts. *J. Mech. Behav. Biomed. Mater.* 59, 168–184. doi: 10.1016/j.jmbm.2015.11.039
- Fan, Z., Sun, Y., Di, C., Tay, D., Chen, W., Deng, C. X., et al. (2013). Acoustic tweezing cytometry for live-cell subcellular modulation of intracellular cytoskeleton contractility. *Sci. Rep.* 3:2176. doi: 10.1038/srep02176
- Fazal, F. M., and Block, S. M. (2011). Optical tweezers study life under tension. *Nat. Photonics* 5, 318–321. doi: 10.1038/nphoton.2011.100
- Finer, J. T., Simmons, R. M., and Spudich, J. A. (1994). Single myosin molecule mechanics: piconewton forces and nanometre steps. *Nature* 368, 113–119. doi: 10.1038/368113a0
- Fior, R., Maggolino, S., Codan, B., Lazzarino, M., and Sbaizero, O. (2011). “A study on the cellular structure during stress solicitation induced by BioMEMS” in *Proceedings of the Annual International Conference of the IEEE Engineering in Medicine and Biology Society*, (Boston, MA: IEEE), 2455–2458. doi: 10.1109/IEMBS.2011.6090682
- Foo, J.-J., Liu, K.-K., and Chan, V. (2003). Thermal effect on a viscously deformed liposome in a laser trap. *Ann. Biomed. Eng.* 31, 354–362. doi: 10.1114/1.1555626
- Foo, J. J., Liu, K. K., and Chan, V. (2004). Viscous drag of deformed vesicles in optical trap: Experiments and simulations. *AICHE J.* 50, 249–254. doi: 10.1002/aic.10023
- Formosa-Dague, C., Duval, R. E., and Dague, E. (2018). Cell biology of microbes and pharmacology of antimicrobial drugs explored by atomic force microscopy. *Semin. Cell Dev. Biol.* 73, 165–176. doi: 10.1016/j.semcdb.2017.06.022
- Franck, C., Maskarinec, S. A., Tirrell, D. A., and Ravichandran, G. (2011). Three-dimensional traction force microscopy: a new tool for quantifying cell-matrix interactions. *PLoS One* 6:e17833. doi: 10.1371/journal.pone.0017833
- Friend, J., and Yeo, L. Y. (2011). Microscale acoustofluidics: microfluidics driven via acoustics and ultrasonics. *Rev. Mod. Phys.* 83, 647–704. doi: 10.1103/RevModPhys.83.647
- Fu, J., Wang, Y.-K., Yang, M. T., Desai, R. A., Yu, X., Liu, Z., et al. (2010). Mechanical regulation of cell function with geometrically modulated elastomeric substrates. *Nat. Methods* 7, 733–736. doi: 10.1038/nmeth.1487
- Fuhrer, R., Schumacher, C. M., Zeltner, M., and Stark, W. J. (2013). Soft iron/silicon composite tubes for magnetic peristaltic pumping: frequency-dependent pressure and volume flow. *Adv. Funct. Mater.* 23, 3845–3849. doi: 10.1002/adfm.201203572
- Galbraith, C. G., and Sheetz, M. P. (1998). Forces on adhesive contacts affect cell function. *Curr. Opin. Cell Biol.* 10, 566–571. doi: 10.1016/S0955-0674(98)80030-6
- Galbraith, C. G., Yamada, K. M., and Sheetz, M. P. (2002). The relationship between force and focal complex development. *J. Cell Biol.* 159, 695–705. doi: 10.1083/jcb.200204153
- Gautier, H. O. B., Thompson, A. J., Achouri, S., Koser, D. E., Holtzmann, K., Moendarbary, E., et al. (2015). Atomic force microscopy-based force measurements on animal cells and tissues. *Methods Cell Biol.* 125, 211–235. doi: 10.1016/BS.MCB.2014.10.005
- Gavara, N., Roca-Cusachs, P., Sunyer, R., Farré, R., and Navajas, D. (2008). Mapping cell-matrix stresses during stretch reveals inelastic reorganization of the cytoskeleton. *Biophys. J.* 95, 464–471. doi: 10.1529/biophysj.107.124180
- Geiger, B., and Bershadsky, A. (2001). Assembly and mechanosensory function of focal contacts. *Curr. Opin. Cell Biol.* 13, 584–592. doi: 10.1016/S0955-0674(00)00255-6
- Gesellchen, F., Bernassau, A. L., Déjardin, T., Cumming, D. R. S., and Riehle, M. O. (2014). Cell patterning with a heptagon acoustic tweezer – application in neurite guidance. *Lab Chip* 14, 2266–2275. doi: 10.1039/C4LC00436A
- Ghassemi, S., Meacci, G., Liu, S., Gondarenko, A. A., Mathur, A., Roca-Cusachs, P., et al. (2012). Cells test substrate rigidity by local contractions on submicrometer pillars. *Proc. Natl. Acad. Sci. U.S.A.* 109, 5328–5333. doi: 10.1073/pnas.1119886109
- Ghibaudo, M., Saez, A., Trichet, L., Xayaphoummine, A., Browaeys, J., Silberzan, P., et al. (2008). Traction forces and rigidity sensing regulate cell functions. *Soft Matter* 4, 1836–1843. doi: 10.1039/b804103b
- Glogauer, M., Arora, P., Yao, G., Sokholov, I., Ferrier, J., and McCulloch, C. A. (1997). Calcium ions and tyrosine phosphorylation interact coordinately with actin to regulate cytoprotective responses to stretching. *J. Cell Sci.* 110 (Pt 1), 11–21.
- Glogauer, M., Ferrier, J., and McCulloch, C. A. (1995). Magnetic fields applied to collagen-coated ferric oxide beads induce stretch-activated Ca<sup>2+</sup> + flux in fibroblasts. *Am. J. Physiol.* 269(5 Pt 1), C1093–C1104. doi: 10.1152/ajpcell.1995.269.5.C1093
- Gosse, C., and Croquette, V. (2002). Magnetic tweezers: micromanipulation and force measurement at the molecular level. *Biophys. J.* 82, 3314–3329. doi: 10.1016/S0006-3495(02)75672-5
- Grady, M. E., Composto, R. J., and Eckmann, D. M. (2016). Cell elasticity with altered cytoskeletal architectures across multiple cell types. *J. Mech. Behav. Biomed. Mater.* 61, 197–207. doi: 10.1016/j.jmbm.2016.01.022
- Grier, D. G. (2003). A revolution in optical manipulation. *Nature* 424, 810–816. doi: 10.1038/nature01935
- Gu, M., Kuriakose, S., and Gan, X. (2007). A single beam near-field laser trap for optical stretching, folding and rotation of erythrocytes. *Opt. Express* 15:1369. doi: 10.1364/OE.15.001369
- Guck, J., Ananthakrishnan, R., Mahmood, H., Moon, T. J., Cunningham, C. C., and Käs, J. (2001). The optical stretcher: a novel laser tool to micromanipulate cells. *Biophys. J.* 81, 767–784. doi: 10.1016/S0006-3495(01)75740-2
- Guck, J., Schinkinger, S., Lincoln, B., Wottawah, F., Ebert, S., Romeyke, M., et al. (2005). Optical deformability as an inherent cell marker for testing malignant transformation and metastatic competence. *Biophys. J.* 88, 3689–3698. doi: 10.1529/biophysj.104.045476
- Guo, F., Li, P., French, J. B., Mao, Z., Zhao, H., Li, S., et al. (2015). Controlling cell-cell interactions using surface acoustic waves. *Proc. Natl. Acad. Sci. U.S.A.* 112, 43–48. doi: 10.1073/pnas.1422068112
- Guo, F., Mao, Z., Chen, Y., Xie, Z., Lata, J. P., Li, P., et al. (2016). Three-dimensional manipulation of single cells using surface acoustic waves. *Proc. Natl. Acad. Sci. U.S.A.* 113, 1522–1527. doi: 10.1073/pnas.1524813113
- Guolla, L., Bertrand, M., Haase, K., and Pelling, A. E. (2012). Force transduction and strain dynamics in actin stress fibres in response to nanonewton forces. *J. Cell Sci.* 125, 603–613. doi: 10.1242/jcs.088302
- Gupta, M., Kocgozlu, L., Sarangi, B. R., Margadant, F., Ashraf, M., and Ladoux, B. (2015). Micropillar substrates: a tool for studying cell mechanobiology. *Biophys. Methods Cell Biol.* 125, 289–308. doi: 10.1016/bs.mcb.2014.10.009
- Hall, M., Long, R., Feng, X., Huang, Y., Hui, C. Y., and Wu, M. (2013). Toward single cell traction microscopy within 3D collagen matrices. *Exp. Cell Res.* 319, 2396–2408. doi: 10.1016/j.yexcr.2013.06.009

- Han, Y., Wang, J., Wang, K., and Dong, S. (2016). Fabrication of atomic force microscope spherical tips and its application in determining the mechanical property of cancer cells. *Micro Nano Lett.* 11, 881–884. doi: 10.1049/mnl.2016.0319
- Harlepp, S., Thalmann, F., Follain, G., and Goetz, J. G. (2017). Hemodynamic forces can be accurately measured in vivo with optical tweezers. *Mol. Biol. Cell* 28, 3252–3260. doi: 10.1091/mbc.E17-06-0382
- Harris, A. K., Wild, P., and Stopak, D. (1980). Silicone rubber substrata: a new wrinkle in the study of cell locomotion. *Science* 208, 177–179. doi: 10.1126/science.6987736
- Harris, A. R., and Charras, G. T. (2011). Experimental validation of atomic force microscopy-based cell elasticity measurements. *Nanotechnology* 22:345102. doi: 10.1088/0957-4484/22/34/345102
- Häti, A. G., Aachmann, F. L., Stokke, B. T., Skjåk-Bræk, G., and Sletmoen, M. (2015). Energy landscape of alginate-epimerase interactions assessed by optical tweezers and atomic force microscopy. *PLoS One* 10:e0141237. doi: 10.1371/journal.pone.0141237
- Haupt, B. J., Pelling, A. E., and Horton, M. A. (2006). Integrated confocal and scanning probe microscopy for biomedical research. *ScientificWorldJournal* 6, 1609–1618. doi: 10.1100/tsw.2006.269
- Hayashi, K., and Higaki, M. (2017). Stiffness of intact endothelial cells from fresh aortic bifurcations of atherosclerotic rabbits-atomic force microscopic study. *J. Cell. Physiol.* 232, 7–13. doi: 10.1002/jcp.25379
- Hendricks, A. G., Holzbaier, E. L. F., and Goldman, Y. E. (2012). Force measurements on cargoes in living cells reveal collective dynamics of microtubule motors. *Proc. Natl. Acad. Sci. U.S.A.* 109, 18447–18452. doi: 10.1073/pnas.1215462109
- Hénon, S., Lenormand, G., Richert, A., and Gallet, F. (1999). A new determination of the shear modulus of the human erythrocyte membrane using optical tweezers. *Biophys. J.* 76, 1145–1151. doi: 10.1016/S0006-3495(99)77279-6
- Hertz, H. (1896). Ueber die Berührung fester elastischer Körper. *J. für die reine und Angew. Math.* 92, 156–171.
- Heureaux, J., Chen, D., Murray, V. L., Deng, C. X., and Liu, A. P. (2014). Activation of a bacterial mechanosensitive channel in mammalian cells by cytoskeletal stress. *Cell. Mol. Bioeng.* 7, 307–319. doi: 10.1007/s12195-014-0337-8
- Hinson, J. T., Chopra, A., Nafisi, N., Polacheck, W. J., Benson, C. C., Swist, S., et al. (2015). HEART DISEASE. Titin mutations in iPSC cells define sarcomere insufficiency as a cause of dilated cardiomyopathy. *Science* 349, 982–986. doi: 10.1126/science.aaa5458
- Hinterdorfer, P., and Dufrière, Y. F. (2006). Detection and localization of single molecular recognition events using atomic force microscopy. *Nat. Methods* 3, 347–355. doi: 10.1038/nmeth871
- Hoffman, B. D., Grashoff, C., and Schwartz, M. A. (2011). Dynamic molecular processes mediate cellular mechanotransduction. *Nature* 475, 316–323. doi: 10.1038/nature10316
- Hu, S., Eberhard, L., Chen, J., Love, J. C., Butler, J. P., Fredberg, J. J., et al. (2004). Mechanical anisotropy of adherent cells probed by a three-dimensional magnetic twisting device. *Am. J. Physiol.* 287, C1184–C1191. doi: 10.1152/ajpcell.00224.2004
- Huang, P.-H., Chan, C. Y., Li, P., Nama, N., Xie, Y., Wei, C.-H., et al. (2015). A spatiotemporally controllable chemical gradient generator via acoustically oscillating sharp-edge structures. *Lab Chip* 15, 4166–4176. doi: 10.1039/c5lc00868a
- Huang, S., and Ingber, D. E. (1999). The structural and mechanical complexity of cell-growth control. *Nat. Cell Biol.* 1, E131–E138. doi: 10.1038/13043
- Huang, W., Anvari, B., Torres, J. H., Lebaron, R. G., and Athanasiou, K. A. (2003). Temporal effects of cell adhesion on mechanical characteristics of the single chondrocyte. *J. Orthop. Res.* 21, 88–95. doi: 10.1016/S0736-0266(02)00130-4
- Hwang, J. Y., Lim, H. G., Yoon, C. W., Lam, K. H., Yoon, S., Lee, C., et al. (2014). Non-contact high-frequency ultrasound microbeam stimulation for studying mechanotransduction in human umbilical vein endothelial cells. *Ultrasound Med. Biol.* 40, 2172–2182. doi: 10.1016/j.ultrasmedbio.2014.03.018
- Ichikawa, M., and Yoshikawa, K. (2001). Optical transport of a single cell-sized liposome. *Appl. Phys. Lett.* 79, 4598–4600. doi: 10.1063/1.1430026
- Indra, I., Undyala, V., Kadow, C., Thirumurthi, U., Dembo, M., and Beningo, K. A. (2011). An in vitro correlation of mechanical forces and metastatic capacity. *Phys. Biol.* 8:015015. doi: 10.1088/1478-3975/8/1/015015
- Jannat, R. A., Dembo, M., and Hammer, D. A. (2011). Traction forces of neutrophils migrating on compliant substrates. *Biophys. J.* 101, 575–584. doi: 10.1016/j.bpj.2011.05.040
- Janssen, X. J. A., Lipfert, J., Jäger, T., Daudey, R., Beekman, J., and Dekker, N. H. (2012). Electromagnetic torque tweezers: a versatile approach for measurement of single-molecule twist and torque. *Nano Lett.* 12, 3634–3639. doi: 10.1021/nl301330h
- Johansen, P. L., Fenaroli, F., Evensen, L., Griffiths, G., and Koster, G. (2016). Optical micromanipulation of nanoparticles and cells inside living zebrafish. *Nat. Commun.* 7:10974. doi: 10.1038/ncomms10974
- Karácsony, O., and Akhremitchev, B. B. (2011). On the detection of single bond ruptures in dynamic force spectroscopy by AFM. *Langmuir* 27, 11287–11291. doi: 10.1021/la202530j
- Kasas, S., Gmur, T., and Dietler, G. (2017). “Finite-element analysis of microbiological structures,” in *The World of Nano-Biomechanics*, ed. A. Ikai (Amsterdam: Elsevier), 199–218. doi: 10.1016/B978-0-444-63686-7.00011-0
- Kasas, S., Stupar, P., and Dietler, G. (2018). AFM contribution to unveil pro- and eukaryotic cell mechanical properties. *Semin. Cell Dev. Biol.* 73, 177–187. doi: 10.1016/j.semcdb.2017.08.032
- Khetan, S., Guvendiren, M., Legant, W. R., Cohen, D. M., Chen, C. S., and Burdick, J. A. (2013). Degradation-mediated cellular traction directs stem cell fate in covalently crosslinked three-dimensional hydrogels. *Nat. Mater.* 12, 458–465. doi: 10.1038/nmat3586
- Kilinc, D., Blasiak, A., O’Mahony, J. J., Suter, D. M., and Lee, G. U. (2012). Magnetic tweezers-based force clamp reveals mechanically distinct apCAM domain interactions. *Biophys. J.* 103, 1120–1129. doi: 10.1016/j.bpj.2012.08.025
- Kilinc, D., and Lee, G. U. (2014). Advances in magnetic tweezers for single molecule and cell biophysics. *Integr. Biol.* 6, 27–34. doi: 10.1039/c3ib40185e
- Kim, D.-H., Wong, P. K., Park, J., Levchenko, A., and Sun, Y. (2009). Microengineered platforms for cell mechanobiology. *Annu. Rev. Biomed. Eng.* 11, 203–233. doi: 10.1146/annurev-bioeng-061008-124915
- Kis, A., Kasas, S., Babić, B., Kulik, A. J., Benoît, W., Briggs, G. A. D., et al. (2002). Nanomechanics of microtubules. *Phys. Rev. Lett.* 89:248101. doi: 10.1103/PhysRevLett.89.248101
- Knöner, G., Rolfé, B. E., Campbell, J. H., Parkin, S. J., Heckenberg, N. R., and Rubinsztein-Dunlop, H. (2006). Mechanics of cellular adhesion to artificial artery templates. *Biophys. J.* 91, 3085–3096. doi: 10.1529/biophysj.105.076125
- Koch, T. M., Münster, S., Bonakdar, N., Butler, J. P., and Fabry, B. (2012). 3D traction forces in cancer cell invasion. *PLoS One* 7:e33476. doi: 10.1371/journal.pone.0033476
- Kodera, N., Yamamoto, D., Ishikawa, R., and Ando, T. (2010). Video imaging of walking myosin V by high-speed atomic force microscopy. *Nature* 468, 72–76. doi: 10.1038/nature09450
- Kuznetsova, T. G., Starodubtseva, M. N., Yegorenkov, N. I., Chizhik, S. A., and Zhdanov, R. I. (2007). Atomic force microscopy probing of cell elasticity. *Micron* 38, 824–833. doi: 10.1016/j.MICRON.2007.06.011
- Lam, K. H., Li, Y., Li, Y., Lim, H. G., Zhou, Q., and Shung, K. K. (2016). Multifunctional single beam acoustic tweezer for non-invasive cell/organism manipulation and tissue imaging. *Sci. Rep.* 6:37554. doi: 10.1038/srep37554
- Lam, R. H. W., Sun, Y., Chen, W., and Fu, J. (2012a). Elastomeric microposts integrated into microfluidics for flow-mediated endothelial mechanotransduction analysis. *Lab Chip* 12, 1865–1873. doi: 10.1039/c2lc21146g
- Lam, R. H. W., Weng, S., Lu, W., and Fu, J. (2012b). Live-cell subcellular measurement of cell stiffness using a microengineered stretchable micropost array membrane. *Integr. Biol.* 4, 1289–1298. doi: 10.1039/c2ib20134h
- Lam, W. A., Chaudhuri, O., Crow, A., Webster, K. D., Li, T.-D., Kita, A., et al. (2011). Mechanics and contraction dynamics of single platelets and implications for clot stiffening. *Nat. Mater.* 10, 61–66. doi: 10.1038/nmat2903
- Lee, J., Leonard, M., Oliver, T., Ishihara, A., and Jacobson, K. (1994). Traction forces generated by locomoting keratocytes. *J. Cell Biol.* 127, 1957–1964. doi: 10.1083/jcb.127.6.1957
- Legant, W. R., Miller, J. S., Blakely, B. L., Cohen, D. M., Genin, G. M., and Chen, C. S. (2010). Measurement of mechanical tractions exerted by cells in three-dimensional matrices. *Nat. Methods* 7, 969–971. doi: 10.1038/nmeth.1531
- Lehenkari, P. P., Charras, G. T., Nykänen, A., and Horton, M. A. (2000). Adapting atomic force microscopy for cell biology. *Ultramicroscopy* 82, 289–295. doi: 10.1016/S0304-3991(99)00138-2

- Lekka, M. (2016). Discrimination between normal and cancerous cells using AFM. *Bionanoscience* 6, 65–80. doi: 10.1007/s12668-016-0191-3
- Li, B., Li, F., Puskar, K. M., and Wang, J. H.-C. (2009). Spatial patterning of cell proliferation and differentiation depends on mechanical stress magnitude. *J. Biomech.* 42, 1622–1627. doi: 10.1016/j.jbiomech.2009.04.033
- Li, B., Lin, M., Tang, Y., Wang, B., and Wang, J. H.-C. (2008). A novel functional assessment of the differentiation of micropatterned muscle cells. *J. Biomech.* 41, 3349–3353. doi: 10.1016/j.jbiomech.2008.09.025
- Li, B., and Wang, J. H.-C. (2011). Fibroblasts and myofibroblasts in wound healing: Force generation and measurement. *J. Tissue Viability* 20, 108–120. doi: 10.1016/j.jtvt.2009.11.004
- Li, B., Xie, L., Starr, Z. C., Yang, Z., Lin, J.-S., and Wang, J. H.-C. (2007). Development of micropost force sensor array with culture experiments for determination of cell traction forces. *Cell Motil. Cytoskeleton* 64, 509–518. doi: 10.1002/cm.20200
- Li, P., Mao, Z., Peng, Z., Zhou, L., Chen, Y., Huang, P.-H., et al. (2015). Acoustic separation of circulating tumor cells. *Proc. Natl. Acad. Sci. U.S.A.* 112, 4970–4975. doi: 10.1073/pnas.1504484112
- Lieber, S. C., Aubry, N., Pain, J., Diaz, G., Kim, S. J., and Vatner, S. F. (2004). Aging increases stiffness of cardiac myocytes measured by atomic force microscopy nanoindentation. *Am. J. Physiol. Heart Circ. Physiol.* 287, H645–H651. doi: 10.1152/ajpheart.00564.2003
- Lim, C. T., Dao, M., Suresh, S., Sow, C. H., and Chew, K. T. (2004). Large deformation of living cells using laser traps. *Acta Mater.* 52, 1837–1845. doi: 10.1016/j.actamat.2003.12.028
- Lin, I.-K., Liao, Y.-M., Liu, Y., Ou, K.-S., Chen, K.-S., and Zhang, X. (2008). Viscoelastic mechanical behavior of soft microcantilever-based force sensors. *Appl. Phys. Lett.* 93, 251907. doi: 10.1063/1.3056114
- Lin, Y.-C., Kramer, C. M., Chen, C. S., and Reich, D. H. (2012). Probing cellular traction forces with magnetic nanowires and microfabricated force sensor arrays. *Nanotechnology* 23:075101. doi: 10.1088/0957-4484/23/7/075101
- Lipfert, J., Kerssemakers, J. W. J., Jäger, T., and Dekker, N. H. (2010). Magnetic torque tweezers: measuring torsional stiffness in DNA and RecA-DNA filaments. *Nat. Methods* 7, 977–980. doi: 10.1038/nmeth.1520
- Lipfert, J., Wiggins, M., Kerssemakers, J. W. J., Pedaci, F., and Dekker, N. H. (2011). Freely orbiting magnetic tweezers to directly monitor changes in the twist of nucleic acids. *Nat. Commun.* 2:439. doi: 10.1038/ncomms1450
- Lisica, A., and Grill, S. W. (2017). Optical tweezers studies of transcription by eukaryotic RNA polymerases. *Biomol. Concepts* 8, 1–11. doi: 10.1515/bmc-2016-0028
- Liu, A. P. (2016). Biophysical tools for cellular and subcellular mechanical actuation of cell signaling. *Biophys. J.* 111, 1112–1118. doi: 10.1016/j.bpj.2016.02.043
- Liu, J., Sun, N., Bruce, M. A., Wu, J. C., and Butte, M. J. (2012). Atomic force mechanobiology of pluripotent stem cell-derived cardiomyocytes. *PLoS One* 7:e37559. doi: 10.1371/journal.pone.0037559
- López-Quesada, C., Fontaine, A.-S., Farré, A., Joseph, M., Selva, J., Egea, G., et al. (2014). Artificially-induced organelles are optimal targets for optical trapping experiments in living cells. *Biomed. Opt. Express* 5:1993. doi: 10.1364/BOE.5.001993
- Mahaffy, R. E., Park, S., Gerde, E., Käs, J., and Shih, C. K. (2004). Quantitative analysis of the viscoelastic properties of thin regions of fibroblasts using atomic force microscopy. *Biophys. J.* 86, 1777–1793. doi: 10.1016/S0006-3495(04)74245-9
- Malandrino, A., Kamm, R. D., and Moendarbary, E. (2018). In vitro modeling of mechanics in cancer metastasis. *ACS Biomater. Sci. Eng.* 4, 294–301. doi: 10.1021/acsbomaterials.7b00041
- Maloney, J. M., Nikova, D., Lautenschläger, F., Clarke, E., Langer, R., Guck, J., et al. (2010). Mesenchymal stem cell mechanics from the attached to the suspended state. *Biophys. J.* 99, 2479–2487. doi: 10.1016/j.bpj.2010.08.052
- Mammoto, T., and Ingber, D. E. (2010). Mechanical control of tissue and organ development. *Development* 137, 1407–1420. doi: 10.1242/dev.024166
- Mann, J. M., Lam, R. H. W., Weng, S., Sun, Y., and Fu, J. (2012). A silicone-based stretchable micropost array membrane for monitoring live-cell subcellular cytoskeletal response. *Lab Chip* 12, 731–740. doi: 10.1039/C2LC20896B
- Marjoram, R. J., Guilluy, C., and Burridge, K. (2016). Using magnets and magnetic beads to dissect signaling pathways activated by mechanical tension applied to cells. *Methods* 94, 19–26. doi: 10.1016/j.jymeth.2015.09.025
- Martinez-Martin, D., Carrasco, C., Hernando-Perez, M., de Pablo, P. J., Gomez-Herrero, J., Perez, R., et al. (2012). Resolving structure and mechanical properties at the nanoscale of viruses with frequency modulation atomic force microscopy. *PLoS One* 7:e30204. doi: 10.1371/journal.pone.0030204
- Mathur, A. B., Truskey, G. A., and Reichert, W. M. (2000). Atomic force and total internal reflection fluorescence microscopy for the study of force transmission in endothelial cells. *Biophys. J.* 78, 1725–1735. doi: 10.1016/S0006-3495(00)76724-5
- Matsudaira, K., Nguyen, T.-V., Shoji, K. H., Tsukagoshi, T., Takahata, T., and Shimoyama, I. (2017). MEMS piezoresistive cantilever for the direct measurement of cardiomyocyte contractile force. *J. Micromech. Microeng.* 27:105005. doi: 10.1088/1361-6439/aa8350
- Mathews, B. D. (2006). Cellular adaptation to mechanical stress: role of integrins, Rho, cytoskeletal tension and mechanosensitive ion channels. *J. Cell Sci.* 119, 508–518. doi: 10.1242/jcs.02760
- Maugeri-Sacca, M., and De Maria, R. (2018). The Hippo pathway in normal development and cancer. *Pharmacol. Ther.* doi: 10.1016/J.PHARMTHERA.2017.12.011
- Mercadé-Prieto, R., Thomas, C. R., and Zhang, Z. (2013). Mechanical double layer model for *Saccharomyces Cerevisiae* cell wall. *Eur. Biophys. J.* 42, 613–620. doi: 10.1007/s00249-013-0909-x
- Miroshnikova, Y. A., Le, H. Q., Schneider, D., Thalheim, T., Rübbsam, M., Bremicker, N., et al. (2018). Adhesion forces and cortical tension couple cell proliferation and differentiation to drive epidermal stratification. *Nat. Cell Biol.* 20, 69–80. doi: 10.1038/s41556-017-0005-z
- Monachino, E., Spenkelnik, L. M., and van Oijen, A. M. (2017). Watching cellular machinery in action, one molecule at a time. *J. Cell Biol.* 216, 41–51. doi: 10.1083/jcb.201610025
- Morton, K. C., and Baker, L. A. (2014). Atomic force microscopy-based bioanalysis for the study of disease. *Anal. Methods* 6, 4932–4955. doi: 10.1039/C4AY00485J
- Mosconi, F., Allemand, J. F., and Croquette, V. (2011). Soft magnetic tweezers: a proof of principle. *Rev. Sci. Instrum.* 82:034302. doi: 10.1063/1.3531959
- Moulding, D. A., Moendarbary, E., Valon, L., Record, J., Charras, G. T., and Thrasher, A. J. (2012). Excess F-actin mechanically impedes mitosis leading to cytokinesis failure in X-linked neutropenia by exceeding Aurora B kinase error correction capacity. *Blood* 120, 3803–3811. doi: 10.1182/blood-2012-03-419663
- Mukherjee, R., Saha, M., Routray, A., and Chakraborty, C. (2015). Nanoscale surface characterization of human erythrocytes by atomic force microscopy: a critical review. *IEEE Trans. Nanobioscience* 14, 625–633. doi: 10.1109/TNB.2015.2424674
- Munoz, J. J. (2016). Non-regularised inverse finite element analysis for 3D traction force microscopy. *Int. J. Numer. Anal. Model.* 13, 763–781.
- Na, S., and Wang, N. (2008). Application of fluorescence resonance energy transfer and magnetic twisting cytometry to quantify mechanochemical signaling activities in a living cell. *Sci. Signal.* 1:pl1. doi: 10.1126/scisignal.134pl1
- Nan, X., Sims, P. A., and Xie, X. S. (2008). Organelle tracking in a living cell with microsecond time resolution and nanometer spatial precision. *ChemPhysChem* 9, 707–712. doi: 10.1002/cphc.200700839
- Nardone, G., Oliver-De, La Cruz, J., Vrbsky, J., Martini, C., Pribyl, J., et al. (2017). YAP regulates cell mechanics by controlling focal adhesion assembly. *Nat. Commun.* 8:15321. doi: 10.1038/ncomms15321
- Nelson, C. M., Jean, R. P., Tan, J. L., Liu, W. F., Sniadecki, N. J., Spector, A. A., et al. (2005). Emergent patterns of growth controlled by multicellular form and mechanics. *Proc. Natl. Acad. Sci. U.S.A.* 102, 11594–11599. doi: 10.1073/pnas.0502575102
- Neuman, K. C., Chadd, E. H., Liou, G. F., Bergman, K., and Block, S. M. (1999). Characterization of photodamage to *Escherichia coli* in optical traps. *Biophys. J.* 77, 2856–2863. doi: 10.1016/S0006-3495(99)77117-1
- Nguyen, V., Kaulen, C., Simon, U., and Schnakenberg, U. (2017). Single interdigital transducer approach for gravimetric SAW sensor applications in liquid environments. *Sensors* 17:2931. doi: 10.3390/s17122931
- Norman, J. J., Mukundan, V., Bernstein, D., and Pruitt, B. L. (2008). Microsystems for biomechanical measurements. *Pediatr. Res.* 63, 576–583. doi: 10.1203/PDR.0b013e31816b2ec4
- Oberstrass, F. C., Fernandes, L. E., and Bryant, Z. (2012). Torque measurements reveal sequence-specific cooperative transitions in supercoiled DNA. *Proc. Natl. Acad. Sci. U.S.A.* 109, 6106–6111. doi: 10.1073/pnas.1113532109

- Oddershede, L. B. (2012). Force probing of individual molecules inside the living cell is now a reality. *Nat. Chem. Biol.* 8, 879–886. doi: 10.1038/nchembio.1082
- O'Mahony, J. J., Platt, M., Kilinc, D., and Lee, G. (2013). Synthesis of superparamagnetic particles with tunable morphologies: the role of nanoparticle-nanoparticle interactions. *Langmuir* 29, 2546–2553. doi: 10.1021/la3047565
- Pal, S. (ed.). (2014). "Mechanical properties of biological materials," in *Design of Artificial Human Joints & Organs* (Boston, MA: Springer), 23–40. doi: 10.1007/978-1-4614-6255-2\_2
- Palacio, J., Jorge-Peñas, A., Muñoz-Barrutia, A., Ortiz-de-Solorzano, C., de Juan-Pardo, E., and García-Aznar, J. M. (2013). Numerical estimation of 3D mechanical forces exerted by cells on non-linear materials. *J. Biomech.* 46, 50–55. doi: 10.1016/j.jbiomech.2012.10.009
- Park, J., Ryu, J., Choi, S. K., Seo, E., Cha, J. M., Ryu, S., et al. (2005). Real-time measurement of the contractile forces of self-organized cardiomyocytes on hybrid biopolymer microcantilevers. *Anal. Chem.* 77, 6571–6580. doi: 10.1021/ac0507800
- Park, S., Jang, W.-J., and Jeong, C.-H. (2016). Nano-biomechanical validation of epithelial-mesenchymal transition in oral squamous cell carcinomas. *Biol. Pharm. Bull.* 39, 1488–1495. doi: 10.1248/bpb.b16-00266
- Park, Y., Best, C. A., Badizadegan, K., Dasari, R. R., Feld, M. S., Kuriabova, T., et al. (2010). Measurement of red blood cell mechanics during morphological changes. *Proc. Natl. Acad. Sci. U.S.A.* 107, 6731–6736. doi: 10.1073/pnas.0909533107
- Pesen, D., and Hoh, J. H. (2005). Micromechanical architecture of the endothelial cell cortex. *Biophys. J.* 88, 670–679. doi: 10.1529/BIOPHYSJ.104.049965
- Plodinec, M., Loparic, M., Monnier, C. A., Obermann, E. C., Zanetti-Dallenbach, R., Oertle, P., et al. (2012). The nanomechanical signature of breast cancer. *Nat. Nanotechnol.* 7, 757–765. doi: 10.1038/nnano.2012.167
- Poh, Y.-C., Na, S., Chowdhury, F., Ouyang, M., Wang, Y., and Wang, N. (2009). Rapid activation of Rac GTPase in living cells by force is independent of Src. *PLoS One* 4:e7886. doi: 10.1371/journal.pone.0007886
- Polacheck, W. J., and Chen, C. S. (2016). Measuring cell-generated forces: a guide to the available tools. *Nat. Methods* 13, 415–423. doi: 10.1038/nmeth.3834
- Polacheck, W. J., Li, R., Uzel, S. G. M., and Kamm, R. D. (2013). Microfluidic platforms for mechanobiology. *Lab Chip* 13, 2252–2267. doi: 10.1039/c3lc41393d
- Puchner, E. M., and Gaub, H. E. (2009). Force and function: probing proteins with AFM-based force spectroscopy. *Curr. Opin. Struct. Biol.* 19, 605–614. doi: 10.1016/j.SBI.2009.09.005
- Puig-de-Morales, M., Millet, E., Fabry, B., Navajas, D., Wang, N., Butler, J. P., et al. (2004). Cytoskeletal mechanics in adherent human airway smooth muscle cells: probe specificity and scaling of protein-protein dynamics. *Am. J. Physiol. Physiol.* 287, C643–C654. doi: 10.1152/ajpcell.00070.2004
- Rajagopalan, J., and Saif, M. T. A. (2011). MEMS sensors and microsystems for cell mechanobiology. *J. Micromech. Microeng.* 21:054002. doi: 10.1088/0960-1317/21/5/054002
- Rianna, C., and Radmacher, M. (2016). "Cell mechanics as a marker for diseases: Biomedical applications of AFM," in *Proceedings of the AIP Conference Proceedings* (Melville, NY: AIP Publishing LLC), 020057. doi: 10.1063/1.4960276
- Ricart, B. G., Yang, M. T., Hunter, C. A., Chen, C. S., and Hammer, D. A. (2011). Measuring traction forces of motile dendritic cells on micropost arrays. *Biophys. J.* 101, 2620–2628. doi: 10.1016/j.bpj.2011.09.022
- Roca-Cusachs, P., Conte, V., and Treppe, X. (2017). Quantifying forces in cell biology. *Nat. Cell Biol.* 19, 742–751. doi: 10.1038/ncb3564
- Rocha, M. S. (2015). Extracting physical chemistry from mechanics: a new approach to investigate DNA interactions with drugs and proteins in single molecule experiments. *Integr. Biol.* 7, 967–986. doi: 10.1039/C5IB00127G
- Rosenbluth, M. J., Lam, W. A., and Fletcher, D. A. (2006). Force microscopy of nonadherent cells: a comparison of leukemia cell deformability. *Biophys. J.* 90, 2994–3003. doi: 10.1529/biophysj.105.067496
- Roth, K. B., Eggleton, C. D., Neeves, K. B., and Marr, D. W. M. (2013). Measuring cell mechanics by optical alignment compression cytometry. *Lab Chip* 13, 1571–1577. doi: 10.1039/c3lc41253a
- Saphirstein, R. J., Gao, Y. Z., Jensen, M. H., Gallant, C. M., Vetterkind, S., Moore, J. R., et al. (2013). The focal adhesion: a regulated component of aortic stiffness. *PLoS One* 8:e62461. doi: 10.1371/journal.pone.0062461
- Sato, H., Kataoka, N., Kajiyama, F., Katano, M., Takigawa, T., and Masuda, T. (2004). Kinetic study on the elastic change of vascular endothelial cells on collagen matrices by atomic force microscopy. *Colloids Surf. B Biointerfaces* 34, 141–146. doi: 10.1016/j.colsurfb.2003.12.013
- Scuor, N., Gallina, P., Panchawagh, H. V., Mahajan, R. L., Sbaizero, O., and Sergo, V. (2006). Design of a novel MEMS platform for the biaxial stimulation of living cells. *Biomed. Microdevices* 8, 239–246. doi: 10.1007/s10544-006-8268-3
- Serrao, G. W., Turnbull, I. C., Ancukiewicz, D., Kim, D. E., Kao, E., Cashman, T. J., et al. (2012). Myocyte-depleted engineered cardiac tissues support therapeutic potential of mesenchymal stem cells. *Tissue Eng. Part A* 18, 1322–1333. doi: 10.1089/ten.TEA.2011.0278
- Shang, H., and Lee, G. U. (2007). Magnetic tweezers measurement of the bond lifetime-force behavior of the IgG-protein a specific molecular interaction. *J. Am. Chem. Soc.* 129, 6640–6646. doi: 10.1021/JA071215C
- Shao, Y., and Fu, J. (2014). Integrated micro/nanoengineered functional biomaterials for cell mechanics and mechanobiology: a materials perspective. *Adv. Mater.* 26, 1494–1533. doi: 10.1002/adma.201304431
- Shiu, J. Y., Aires, L., Lin, Z., and Vogel, V. (2018). Nanopillar force measurements reveal actin-cap-mediated YAP mechanotransduction. *Nat. Cell Biol.* 20, 262–271. doi: 10.1038/s41556-017-0030-y
- Shiu, Y.-T., Li, S., Marganski, W. A., Usami, S., Schwartz, M. A., Wang, Y.-L., et al. (2004). Rho mediates the shear-enhancement of endothelial cell migration and traction force generation. *Biophys. J.* 86, 2558–2565. doi: 10.1016/S0006-3495(04)74311-8
- Shroff, S. G., Saner, D. R., and Lal, R. (1995). Dynamic micromechanical properties of cultured rat atrial myocytes measured by atomic force microscopy. *Am. J. Physiol. Physiol.* 269, C286–C292. doi: 10.1152/ajpcell.1995.269.1.C286
- Silberberg, Y. R., Pelling, A. E., Yakubov, G. E., Crum, W. R., Hawkes, D. J., and Horton, M. A. (2008). Mitochondrial displacements in response to nanomechanical forces. *J. Mol. Recognit.* 21, 30–36. doi: 10.1002/jmr.868
- Sims, P. A., and Xie, X. S. (2009). Probing dynein and kinesin stepping with mechanical manipulation in a living cell. *Chemphyschem* 10, 1511–1516. doi: 10.1002/cphc.200900113
- Sneddon, I. N. (1965). The relation between load and penetration in the axisymmetric boussinesq problem for a punch of arbitrary profile. *Int. J. Eng. Sci.* 3, 47–57. doi: 10.1016/0020-7225(65)90019-4
- Sniadecki, N. J., Anguelouch, A., Yang, M. T., Lamb, C. M., Liu, Z., Kirschner, S. B., et al. (2007). Magnetic microposts as an approach to apply forces to living cells. *Proc. Natl. Acad. Sci. U.S.A.* 104, 14553–14558. doi: 10.1073/pnas.0611613104
- Sparkes, I., White, R. R., Coles, B., Botchway, S. W., and Ward, A. (2018). "Using optical tweezers combined with total internal reflection microscopy to study interactions between the ER and Golgi in plant cells," in *The Plant Endoplasmic Reticulum: Methods and Protocols*, eds C. Hawes and V. Kriechbaumer (New York, NY: Springer), 167–178. doi: 10.1007/978-1-4939-7389-7\_13
- Staunton, J. R., Blehm, B., Devine, A., and Tanner, K. (2017). In situ calibration of position detection in an optical trap for active microrheology in viscous materials. *Opt. Express* 25, 1746–1761. doi: 10.1364/OE.25.001746
- Steinwachs, J., Metzner, C., Skodzek, K., Lang, N., Thieversen, I., Mark, C., et al. (2016). Three-dimensional force microscopy of cells in biopolymer networks. *Nat. Methods* 13, 171–176. doi: 10.1038/nmeth.3685
- Sun, N., Yazawa, M., Liu, J., Han, L., Sanchez-Freire, V., Abilez, O. J., et al. (2012). Patient-specific induced pluripotent stem cells as a model for familial dilated cardiomyopathy. *Sci. Transl. Med.* 4:130ra47. doi: 10.1126/scitranslmed.3003552
- Sun, Y., and Nelson, B. J. (2007). MEMS capacitive force sensors for cellular and flight biomechanics. *Biomed. Mater.* 2, S16–S22. doi: 10.1088/1748-6041/2/1/S03
- Sun, Y., Villa-Diaz, L. G., Lam, R. H. W., Chen, W., Krebsbach, P. H., and Fu, J. (2012). Mechanics regulates fate decisions of human embryonic stem cells. *PLoS One* 7:e37178. doi: 10.1371/journal.pone.0037178
- Sunyer, R., Conte, V., Escibano, J., Elosegui-Artola, A., Labernadie, A., Valon, L., et al. (2016). Collective cell durotaxis emerges from long-range intercellular force transmission. *Science* 353, 1157–1161. doi: 10.1126/science.aaf7119
- Suresh, S., Spatz, J., Mills, J. P., Micoulet, A., Dao, M., Lim, C. T., et al. (2005). Connections between single-cell biomechanics and human disease states:



- gastrointestinal cancer and malaria. *Acta Biomater.* 1, 15–30. doi: 10.1016/j.actbio.2004.09.001
- Szymonski, M., Targosz-Korecka, M., and Malek-Zietek, K. E. (2015). Nano-mechanical model of endothelial dysfunction for AFM-based diagnostics at the cellular level. *Pharmacol. Rep.* 67, 728–735. doi: 10.1016/j.pharep.2015.05.003
- Tabdili, H., Langer, M., Shi, Q., Poh, Y.-C., Wang, N., and Leckband, D. (2012). Cadherin-dependent mechanotransduction depends on ligand identity but not affinity. *J. Cell Sci.* 125, 4362–4371. doi: 10.1242/jcs.105775
- Takahashi, H., Jung, U. G., Kan, T., Tsukagoshi, T., Matsumoto, K., and Shimoyama, I. (2016). Rigid two-axis MEMS force plate for measuring cellular traction force. *J. Micromech. Microeng.* 26:105006. doi: 10.1088/0960-1317/26/10/105006
- Tan, J. L., Tien, J., Pirone, D. M., Gray, D. S., Bhadriraju, K., and Chen, C. S. (2003). Cells lying on a bed of microneedles: an approach to isolate mechanical force. *Proc. Natl. Acad. Sci. U.S.A.* 100, 1484–1489. doi: 10.1073/pnas.0235407100
- Tanase, M., Biais, N., and Sheetz, M. (2007). Magnetic tweezers in cell biology. *Methods Cell Biol.* 83, 473–493. doi: 10.1016/S0091-679X(07)83020-2
- Tatara, Y. (1989). Extensive theory of force-approach relations of elastic spheres in compression and in impact. *J. Eng. Mater. Technol.* 111:163. doi: 10.1115/1.3226449
- Tavacoli, J. W., Bauër, P., Fermigier, M., Bartolo, D., Heuvingh, J., and du Roure, O. (2013). The fabrication and directed self-assembly of micron-sized superparamagnetic non-spherical particles. *Soft Matter* 9:9103. doi: 10.1039/c3sm51589c
- Thoumine, O., Kocian, P., Kottelat, A., and Meister, J. J. (2000). Short-term binding of fibroblasts to fibronectin: optical tweezers experiments and probabilistic analysis. *Eur. Biophys. J.* 29, 398–408. doi: 10.1007/s002490000087
- Titushkin, I., and Cho, M. (2006). Distinct membrane mechanical properties of human mesenchymal stem cells determined using laser optical tweezers. *Biophys. J.* 90, 2582–2591. doi: 10.1529/biophysj.105.073775
- Topal, T., Hong, X., Xue, X., Fan, Z., Kanetkar, N., Nguyen, J. T., et al. (2018). Acoustic tweezing cytometry induces rapid initiation of human embryonic stem cell differentiation. *Sci. Rep.* 8:12977. doi: 10.1038/s41598-018-30939-z
- Trepat, X., Deng, L., An, S. S., Navajas, D., Tschumperlin, D. J., Gerthoffer, W. T., et al. (2007). Universal physical responses to stretch in the living cell. *Nature* 447, 592–595. doi: 10.1038/nature05824
- Trepat, X., Wasserman, M. R., Angelini, T. E., Millet, E., Weitz, D. A., Butler, J. P., et al. (2009). Physical forces during collective cell migration. *Nat. Phys.* 5, 426–430. doi: 10.1038/nphys1269
- Usukura, E., Narita, A., Yagi, A., Ito, S., and Usukura, J. (2016). An unroofing method to observe the cytoskeleton directly at molecular resolution using atomic force microscopy. *Sci. Rep.* 6:27472. doi: 10.1038/srep27472
- Usukura, J., Yoshimura, A., Minakata, S., Youn, D., Ahn, J., and Cho, S.-J. (2012). Use of the unroofing technique for atomic force microscopic imaging of the intra-cellular cytoskeleton under aqueous conditions. *J. Electron Microsc.* 61, 321–326. doi: 10.1093/jmicro/dfs055
- Veraitch, F., Hernandez, D., Mason, C., Pelling, A. E., and Veraitch, F. S. (2011). Precisely delivered nanomechanical forces induce blebbing in undifferentiated mouse embryonic stem cells. *Cell Health Cytoskelet.* 3, 23–34. doi: 10.2147/CHC.S13863
- Voiculescu, I., and Nordin, A. N. (2012). Acoustic wave based MEMS devices for biosensing applications. *Biosens. Bioelectron.* 33, 1–9. doi: 10.1016/j.bios.2011.12.041
- Wang, J. H.-C., and Li, B. (2010). “The principles and biological applications of cell traction force microscopy,” in *Microscopy: Science, Technology, Applications and Education*, eds A. Méndez-Vilas, and J. Díaz (Badajoz: Formatex Research Center), 449–458.
- Wang, N., Butler, J. P., and Ingber, D. E. (1993). Mechanotransduction across the cell surface and through the cytoskeleton. *Science* 260, 1124–1127. doi: 10.1126/science.7684161
- Wang, X., Yang, Y., Hu, X., Kawazoe, N., Yang, Y., and Chen, G. (2016). Morphological and mechanical properties of osteosarcoma microenvironment cells explored by atomic force microscopy. *Anal. Sci.* 32, 1177–1182. doi: 10.2116/analsci.32.1177
- Wang, Y., Botvinick, E. L., Zhao, Y., Berns, M. W., Usami, S., Tsien, R. Y., et al. (2005). Visualizing the mechanical activation of Src. *Nature* 434, 1040–1045. doi: 10.1038/nature03469
- Wei, M.-T., Zaorski, A., Yalcin, H. C., Wang, J., Hallow, M., Ghadiali, S. N., et al. (2008). A comparative study of living cell micromechanical properties by oscillatory optical tweezers. *Opt. Express* 16, 8594–8603. doi: 10.1364/OE.16.008594
- Wu, J., and Du, G. (1990). Acoustic radiation force on a small compressible sphere in a focused beam. *J. Acoust. Soc. Am.* 87, 997–1003. doi: 10.1121/1.399435
- Wu, J. R. (1991). Acoustical tweezers. *J. Acoust. Soc. Am.* 89, 2140–2143. doi: 10.1121/1.400907
- Xiang, Y., and LaVan, D. A. (2007). Analysis of soft cantilevers as force transducers. *Appl. Phys. Lett.* 90:133901. doi: 10.1063/1.2716376
- Xin, Q., Li, P., He, Y., Shi, C., Qiao, Y., Bian, X., et al. (2017). Magnetic tweezers for the mechanical research of DNA at the single molecule level. *Anal. Methods* 9, 5720–5730. doi: 10.1039/C7AY01495C
- Xue, X., Hong, X., Li, Z., Deng, C. X., and Fu, J. (2017). Acoustic tweezing cytometry enhances osteogenesis of human mesenchymal stem cells through cytoskeletal contractility and YAP activation. *Biomaterials* 134, 22–30. doi: 10.1016/j.biomaterials.2017.04.039
- Yalcin, H. C., Hallow, K. M., Wang, J., Wei, M. T., Ou-Yang, H. D., and Ghadiali, S. N. (2009). Influence of cytoskeletal structure and mechanics on epithelial cell injury during cyclic airway reopening. *Am. J. Physiol. Lung Cell. Mol. Physiol.* 297, L881–L891. doi: 10.1152/ajplung.90562.2008
- Yan, B., Ren, J., Liu, Y., Huang, H., Zheng, X., and Zou, Q. (2017). Study of cholesterol depletion effect on nanomechanical properties of human umbilical vein endothelial cell via rapid broadband atomic force microscopy. *J. Biomech. Eng.* 139:034501. doi: 10.1115/1.4035260
- Yang, M. T., Fu, J., Wang, Y.-K., Desai, R. A., and Chen, C. S. (2011). Assaying stem cell mechanobiology on microfabricated elastomeric substrates with geometrically modulated rigidity. *Nat. Protoc.* 6, 187–213. doi: 10.1038/nprot.2010.189
- Yang, S., and Saif, T. (2005). Micromachined force sensors for the study of cell mechanics. *Rev. Sci. Instrum.* 76:044301. doi: 10.1063/1.1863792
- Yang, M. T., Sniadecki, N. J., and Chen, C. S. (2007). Geometric considerations of micro- to nanoscale elastomeric post arrays to study cellular traction forces. *Adv. Mater.* 19, 3119–3123. doi: 10.1002/adma.200701956
- Yang, Z., Lin, J.-S., Chen, J., and Wang, J. H.-C. (2006). Determining substrate displacement and cell traction fields—a new approach. *J. Theor. Biol.* 242, 607–616. doi: 10.1016/j.jtbi.2006.05.005
- Zemla, J., Danilkiewicz, J., Orzechowska, B., Pabijan, J., Seweryn, S., and Lekka, M. (2018). Atomic force microscopy as a tool for assessing the cellular elasticity and adhesiveness to identify cancer cells and tissues. *Semin. Cell Dev. Biol.* 73, 115–124. doi: 10.1016/j.semcdb.2017.06.029
- Zhang, H., and Liu, K.-K. (2008). Optical tweezers for single cells. *J. R. Soc. Interface* 5, 671–690. doi: 10.1098/rsif.2008.0052
- Zhang, J. S., Kraus, W. E., and Truskey, G. A. (2004). Stretch-induced nitric oxide modulates mechanical properties of skeletal muscle cells. *Am. J. Physiol. Physiol.* 287, C292–C299. doi: 10.1152/ajpcell.00018.2004
- Zhang, L., and Dong, J. (2012). Design, fabrication, and testing of a SOI-MEMS-based active microprobe for potential cellular force sensing applications. *Adv. Mech. Eng.* 4: 785798. doi: 10.1155/2012/785798
- Zhang, Y., DaSilva, M., Ashall, B., Doyle, G., Zerulla, D., Sands, T. D., et al. (2011). Magnetic manipulation and optical imaging of an active plasmonic single-particle Fe–Au nanorod. *Langmuir* 27, 15292–15298. doi: 10.1021/la203863p
- Zhang, Y., and Wang, Q. (2012). Magnetic-plasmonic dual modulated FePt–Au ternary heterostructured nanorods as a promising nano-bioprobes. *Adv. Mater.* 24, 2485–2490. doi: 10.1002/adma.201103991
- Zhao, X., Zhong, Y., Ye, T., Wang, D., and Mao, B. (2015). Discrimination between cervical cancer cells and normal cervical cells based on longitudinal elasticity using atomic force microscopy. *Nanoscale Res. Lett.* 10:482. doi: 10.1186/s11671-015-1174-y
- Zhao, X.-H., Laschinger, C., Arora, P., Szasz, K., Kapus, A., and McCulloch, C. A. (2007). Force activates smooth muscle actin promoter activity through

- the Rho signaling pathway. *J. Cell Sci.* 120, 1801–1809. doi: 10.1242/jcs.001586
- Zhao, Y., Lim, C. C., Sawyer, D. B., Liao, R., and Zhang, X. (2005). Cellular force measurements using single-spaced polymeric microstructures: isolating cells from base substrate. *J. Micromech. Microeng.* 15, 1649–1656. doi: 10.1088/0960-1317/15/9/006
- Zheng, X. R., and Zhang, X. (2011). Microsystems for cellular force measurement: a review. *J. Micromech. Microeng.* 21:054003. doi: 10.1088/0960-1317/21/5/054003
- Zhong, M.-C., Wei, X.-B., Zhou, J.-H., Wang, Z.-Q., and Li, Y.-M. (2013). Trapping red blood cells in living animals using optical tweezers. *Nat. Commun.* 4:1768. doi: 10.1038/ncomms2786
- Ziemann, F., Rädler, J., and Sackmann, E. (1994). Local measurements of viscoelastic moduli of entangled actin networks using an oscillating magnetic bead micro-rheometer. *Biophys. J.* 66, 2210–2216. doi: 10.1016/S0006-3495(94)81017-3
- Conflict of Interest Statement:** The authors declare that the research was conducted in the absence of any commercial or financial relationships that could be construed as a potential conflict of interest.

Copyright © 2018 Basoli, Giannitelli, Gori, Mozetic, Bonfanti, Trombetta and Rainer. This is an open-access article distributed under the terms of the Creative Commons Attribution License (CC BY). The use, distribution or reproduction in other forums is permitted, provided the original author(s) and the copyright owner(s) are credited and that the original publication in this journal is cited, in accordance with accepted academic practice. No use, distribution or reproduction is permitted which does not comply with these terms.



# Small Force, Big Impact: Next Generation Organ-on-a-Chip Systems Incorporating Biomechanical Cues

Ece Ergir<sup>1,2†</sup>, Barbara Bachmann<sup>2,3,4,5†</sup>, Heinz Redl<sup>3,4,5</sup>, Giancarlo Forte<sup>1,6,7\*</sup> and Peter Ertl<sup>2,4,5\*</sup>

<sup>1</sup> Center for Translational Medicine, International Clinical Research Center, St. Anne's University Hospital, Brno, Czechia,

<sup>2</sup> Faculty of Technical Chemistry, Institute of Applied Synthetic Chemistry and Institute of Chemical Technologies

and Analytics, Vienna University of Technology, Vienna, Austria, <sup>3</sup> AUVA Research Centre, Ludwig Boltzmann Institute

for Experimental and Clinical Traumatology, Vienna, Austria, <sup>4</sup> Austrian Cluster for Tissue Regeneration, Vienna, Austria,

<sup>5</sup> Kompetenzzentrum für MechanoBiologie (INTERREG V-A Austria – Czech Republic Programme, ATCZ133), Vienna,

Austria, <sup>6</sup> Competence Center for Mechanobiology (INTERREG V-A Austria – Czech Republic Programme, ATCZ133), Brno,

Czechia, <sup>7</sup> Department of Biomaterials Science, Institute of Dentistry, University of Turku, Turku, Finland

## OPEN ACCESS

### Edited by:

Leonardo Alexandre

Peyré-Tartaruga,

Universidade Federal do Rio Grande do Sul (UFRGS), Brazil

### Reviewed by:

Khashayar Khoshmanesh,

RMIT University, Australia

Irena Levitan,

University of Illinois at Chicago,

United States

T. Alexander Quinn,

Dalhousie University, Canada

### \*Correspondence:

Giancarlo Forte

giancarlo.forte@fnusa.cz

Peter Ertl

peter.ertl@tuwien.ac.at

<sup>†</sup>These authors have contributed equally to this work

### Specialty section:

This article was submitted to

Integrative Physiology,

a section of the journal

Frontiers in Physiology

Received: 01 April 2018

Accepted: 18 September 2018

Published: 09 October 2018

### Citation:

Ergir E, Bachmann B, Redl H,

Forte G and Ertl P (2018) Small Force,

Big Impact: Next Generation

Organ-on-a-Chip Systems

Incorporating Biomechanical Cues.

Front. Physiol. 9:1417.

doi: 10.3389/fphys.2018.01417

Mechanobiology-on-a-chip is a growing field focusing on how mechanical inputs modulate physico-chemical output in microphysiological systems. It is well known that biomechanical cues trigger a variety of molecular events and adjustment of mechanical forces is therefore essential for mimicking *in vivo* physiologies in organ-on-a-chip technology. Biomechanical inputs in organ-on-a-chip systems can range from variations in extracellular matrix type and stiffness and applied shear stresses to active stretch/strain or compression forces using integrated flexible membranes. The main advantages of these organ-on-a-chip systems are therefore (a) the control over spatiotemporal organization of *in vivo*-like tissue architectures, (b) the ability to precisely control the amount, duration and intensity of the biomechanical stimuli, and (c) the capability of monitoring in real time the effects of applied mechanical forces on cell, tissue and organ functions. Consequently, over the last decade a variety of microfluidic devices have been introduced to recreate physiological microenvironments that also account for the influence of physical forces on biological functions. In this review we present recent advances in mechanobiological lab-on-a-chip systems and report on lessons learned from these current mechanobiological models. Additionally, future developments needed to engineer next-generation physiological and pathological organ-on-a-chip models are discussed.

**Keywords:** microfluidics, mechanobiology, organ-on-a-chip, lab-on-a-chip, *in vitro* organ models, mechanical cell actuation

## INTRODUCTION

Conventional mammalian cell culture systems are predominantly based on two-dimensional (2D) monolayer cultures to study cellular mechanisms in pharmaceutical research, toxicology and biomedicine. Even though 2D cell culture models are routinely used, they fail to recapitulate the spatiotemporal dynamics that cells encounter *in vivo*. The discrepancy between *in vitro*

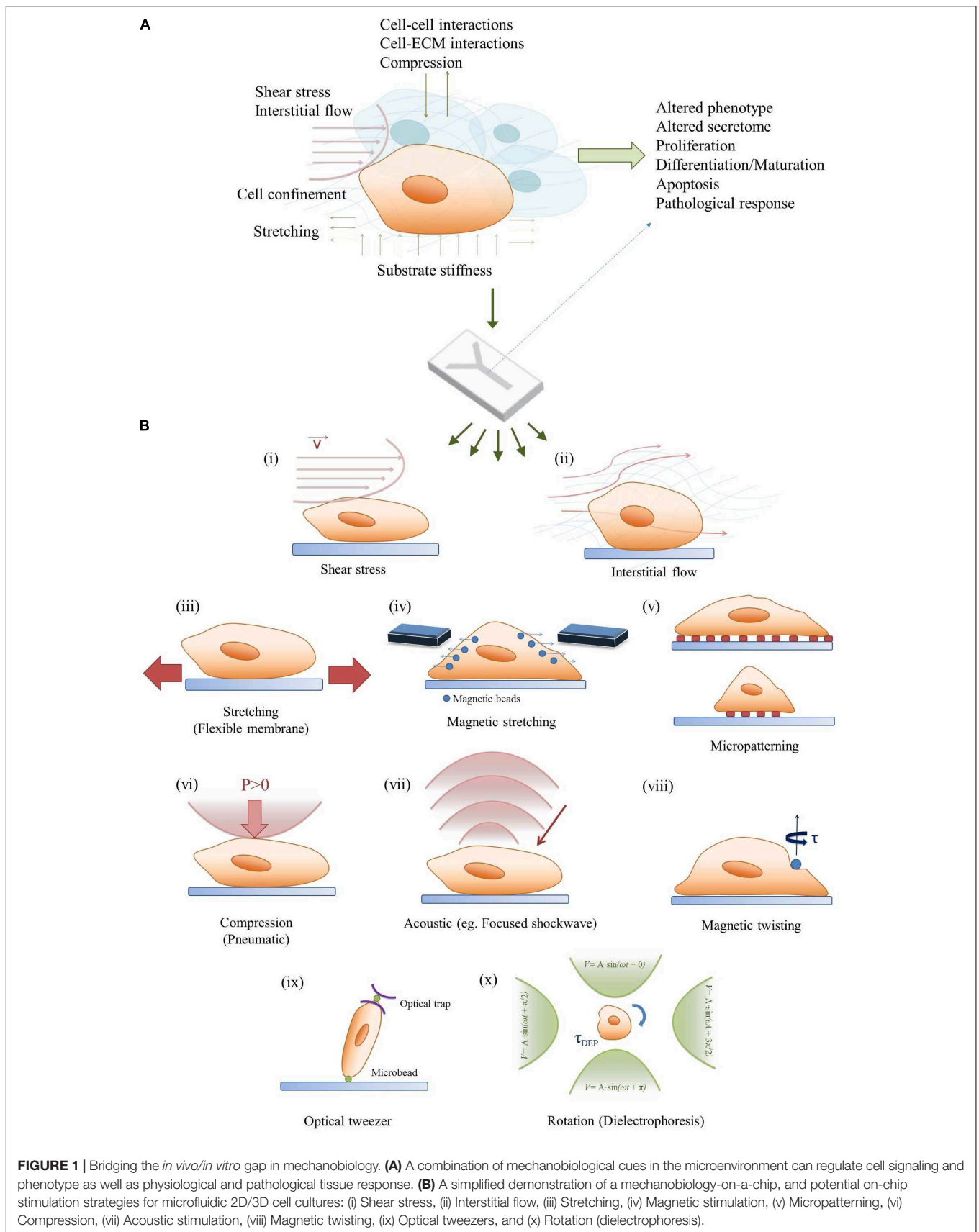
monolayers and native tissue structures leads in many cases to altered phenotype, cell morphology and behavior, thus rendering results from 2D cell-based assays questionable (Baker and Chen, 2012). To overcome the drawbacks associated with 2D monocultures, recent cell cultivation setups aim to re-engineer the physiological cellular microenvironment of native tissues. This can be accomplished by moving toward three-dimensional (3D) culture systems through cultivating cells in hydrogels, scaffolds or aggregates (Chen et al., 2002; Drury and Mooney, 2003; Griffith and Swartz, 2006; Fennema et al., 2013). The implementation of 3D cell culture systems by itself allows for indirect mechanical stimulation by controlling the rigidity and stiffness of the extracellular matrix, which has shown to modulate cellular responses (Engler et al., 2006; Kumar, 2014). Additionally, 3D-tissue models can be further subjected to dynamic mechanical stimuli including fluid flow, stretch/strain and compression. The application of indirect and/or direct mechanical stimuli in tissue cultures has become a rapidly growing research field that is commonly known as mechanobiology (Eyckmans et al., 2011). It is important to highlight that almost every tissue of a human body is subjected to either constant or temporary mechanical stimuli. This means that the application of mechanobiological forces represents a vital step toward the establishment of physiological microenvironments *in vitro* (Wang and Thampatty, 2006; Jansen et al., 2015). To date a variety of mechanobiological forces, shown in **Figure 1A**, have been employed in 2D and 3D *in vitro* cultures including (a) matrix stiffness that mimic the respective Young's moduli of native tissue, (b) fluid flow in vascular systems and interstitial tissue, (c) stretch/strain mechanisms in the lung, heart and gastrointestinal tract as well as (d) compression in the musculoskeletal system (Lovett et al., 2009; Riehl et al., 2012; Shachar et al., 2012; Ahearne, 2014). These mechanobiological systems demonstrated improved cell-to-cell and cell-to-matrix interactions resulting in significant progress in recapitulating physiological microenvironments *in vitro*. Although these tissue models led to substantial advances in understanding mechanobiology on a macroscale, common tissue engineering-based approaches require sizeable amounts of cells as well as reagents but lack precise control over location and amount of the stimulus. A commonly accepted solution in fostering our understanding of biomechanical effects is taking the tissue to the microscale. This can be accomplished by mimicking cellular microenvironments in microfluidic devices, which not only offer a decrease in cell numbers and consumables but also allow precise control over spatio-temporal stiffness and growth factor gradients as well as mechanical stimulus type, amount and location (Huh et al., 2011; Bhatia and Ingber, 2014; Rothbauer et al., 2015; van Duinen et al., 2015). In other words, microdevices can be used to investigate contractility, cell confinement and micropatterning, all of which are crucial in gaining deeper insights into mechanobiological phenomena. Moreover, microfluidic chips are compatible with high resolution microscopy for cell observation and also allow the integration of actuators and sensors, which provides the opportunity to trigger and monitor cellular behavior *in situ*. Overall this review focuses on emerging physiologically relevant

micro-tissue models in mechanobiology-on-a-chip setups in both culture environments since 2012, shortly summarized in **Table 1**.

## MICROFLUIDIC MECHANOBIOLOGY IN MONOLAYERS AND BARRIER MODELS

### Shear Stress

Microfluidic devices with their laminar flow regimes have widely been used to expose cells to fluid flow induced shear stress. This has led to substantial improvements in understanding the mechanobiological effect of shear stress variations on endothelial cells in vascular models but also in osteocyte, cardiomyocyte and epithelial cell biology. In particular, fluid flow plays a major role in vascular biology as the endothelial cell lining layer inside blood vessels is constantly exposed to pulsatile blood flow (Baratchi et al., 2017). Subjecting endothelial cells to physiological unidirectional or disturbed shear stress patterns has been shown to significantly alter cell morphology and phenotype. For example, it has been shown that shear stress influences nanoparticle uptake of endothelial cells where higher flow rates led to reduced uptake. Using an *in vitro* as well as *in silico* approach, Charwat et al. (2018) found that clathrin-mediated uptake of nanoparticles is drastically reduced when exceeding shear forces of 1.8 dyn/cm<sup>2</sup>, implying an important role of shear stress when investigating *in vitro* nanoparticle uptake. Another study, published by Griep et al. (2013), successfully recreated the smallest unit of the blood brain barrier using immortalized brain endothelial cells to study barrier integrity in the presence of physiological shear force. While unidirectional shear stress plays an important role in assessing healthy vessel physiology, microfluidic devices can also be utilized to create bi- and multidirectional flow patterns for mimicking endothelial pathology. Such disturbed flow patterns allow for flow type-dependent gene expression profiling of endothelial cells (Zheng et al., 2017) as well as observation of leucocyte – endothelial cell interactions (Venugopal Menon et al., 2018) and the role of glucose uptake in endothelial dysfunction (Patibandla et al., 2014) for modeling inflammation and hyperglycemia in atherosclerosis. The effect of shear stress on endothelial cells and microfluidic technologies have recently been extensively reviewed elsewhere (Smith and Gerecht, 2014; Haase and Kamm, 2017; Kim et al., 2017). Furthermore, microfluidic devices have also been used outside of endothelial research to record phenotypic transformations of aortic valve interstitial cells during applied shear stress and to monitor morphological changes of osteocytes during application of flow. Additionally, Middleton et al. (2017a) showed that in the presence of shear stress, cell to cell interactions of osteocytes co-cultured with osteoclast are enhanced, leading to the improved mechanical response of bone cells. A more detailed review on monitoring cell-cell interaction using microfluidic devices was recently published by Rothbauer et al. (2017). Altogether, microfluidic devices are an important tool to study shear stress, but while the effects on endothelial cells have been studied extensively, other cell types



**FIGURE 1 |** Bridging the *in vivo/in vitro* gap in mechanobiology. **(A)** A combination of mechanobiological cues in the microenvironment can regulate cell signaling and phenotype as well as physiological and pathological tissue response. **(B)** A simplified demonstration of a mechanobiology-on-a-chip, and potential on-chip stimulation strategies for microfluidic 2D/3D cell cultures: (i) Shear stress, (ii) Interstitial flow, (iii) Stretching, (iv) Magnetic stimulation, (v) Micropatterning, (vi) Compression, (vii) Acoustic stimulation, (viii) Magnetic twisting, (ix) Optical tweezers, and (x) Rotation (dielectrophoresis).

**TABLE 1** | Summary on recent reports on mechanobiological approaches for cell manipulation in microfluidic devices.

Biomechanical stimulus	Organ culture	Cell type	Environment	Reference
Interstitial flow	Vasculature	Primary	3D	Hsu et al., 2013; Jeon et al., 2014; Kim S. et al., 2016
Interstitial flow	Brain	Primary	3D	Park et al., 2015; Wang et al., 2018
Interstitial flow	Liver	Primary	3D	Lee et al., 2013
Substrate stiffness	–	Cell line	2D	Garcia et al., 2015
Electromechanical	–	Primary	2D	Pavesi et al., 2015
Shear stress	Vasculature	Primary	2D	Charwat et al., 2018
Shear stress	–	Cell line	2D	Soffe et al., 2017
Shear stress	Blood brain barrier	Cell line	2D	Griep et al., 2013
Shear stress	Aortic valve	Primary	2D	Wang et al., 2017
Shear stress	Blood brain barrier	Primary	2D/3D	Brown et al., 2015
Shear stress	Blood brain barrier	Cell line	2D/3D	Sellgren et al., 2015
Shear stress	Extravasation	Primary	3D	Jeon et al., 2015
Shear stress	Vasculature	Primary	3D	Kim et al., 2013
Shear stress	Bone	Cell line	2D	Middleton et al., 2017a,b
Shear stress	Bone	Primary	3D	Altmann et al., 2014
Shear stress	Vasculature	Primary	2D	Zheng et al., 2017
Shear stress	Vasculature	Primary	2D	Venugopal Menon et al., 2018
Shear stress	Vasculature	Primary	2D	Patibandla et al., 2014
Stretching	Lung	Primary and cell line	2D	Huh et al., 2010, 2012; Benam et al., 2016; Hassell et al., 2017; Jain et al., 2018
Stretching	Gut	Primary and cell line	2D	Kim H.J. et al., 2016; Villenave et al., 2017
Stretching	Heart	Primary	2D	Ugolini et al., 2016, 2017
Stretching	Muscle	Primary and cell line	2D	Michielin et al., 2015
Stretching	Vasculature	Primary	2D	Zhou and Niklason, 2012
Stretching	–	Primary	3D	Liu et al., 2016
Stretching	Heart	Primary	3D	Marsano et al., 2016; Occhetta et al., 2018
Stretching	–	Cell line	3D	Li et al., 2016
Stretching	–	–	2D/3D	Gizzi et al., 2017
Stretching	Artery	Primary	2D	van Engeland et al., 2018
Compression	Bone	Primary	2D	Park et al., 2012
Compression	Vasculature	Primary	2D	Sticker et al., 2017

The dashes (–) identify studies with devices without a defined target organ, tissue or cell culture.

and different co-culture models would certainly benefit from further research.

## Stretching

In contrast to shear-dependent mechanobiological effects, microfluidic devices have recently come into focus for their ability to engineer miniaturized functional barrier units. Different from the aforementioned models where cells are grown in monolayer in microchannels, these systems aim to recreate the smallest possible unit of an organ by mimicking the barrier between two monolayers. An overview of such a microfluidic device including the respective cell actuation can be found in **Figure 1B**. The cells are cultivated back-to-back on cyclically stretched flexible membranes emulating organotypic movements. With the most famous example still being the Lung-on-a-Chip published by Huh et al. (2010), a number of similar systems have since been used to investigate a variety of different barrier models. For example, using the same microdevice containing a flexible membrane that is stretched by applying vacuum to two air channels on either side of the cultivation chamber, different pathological scenarios have been

recapitulated, including pulmonary edema (Huh et al., 2012), small-airway inflammation (Benam et al., 2016), orthotopic lung cancer extravasation, growth and therapy (Hassell et al., 2017) and intravascular thrombosis assessment (Jain et al., 2018). A similar device has also been used to mimic bacterial overgrowth, inflammatory bowel disease (Kim H.J. et al., 2016) and virus infection (Villenave et al., 2017) in a gut-on-a-chip system and to study the effect of cyclic strain on proliferation and adaptive responses of cardiac fibroblasts (Ugolini et al., 2016, 2017) and to study endothelial cell and smooth muscle cell signaling under hemodynamic loading (van Engeland et al., 2018). A different design approach to exert stretch/strain forces in microfluidic cell cultures employ pressurized air to deflect a membrane on which cells are cultured. Cyclic mechanical actuation of a myoblast cell line and primary myoblasts using such a device is demonstrated in a muscular dystrophy model (Michielin et al., 2015) and to recreate the cyclic strain of blood vessels (Zhou and Niklason, 2012). While most examples in the literature focus on uniaxial stretching, a computationally informed, vacuum-actuated multi-axial microfluidic chip device has recently been developed that allows programmable actuation

along different directions (Gizzi et al., 2017), further advancing the opportunities for mechanobiological on-chip investigations from the broadly used uniaxial strain barrier model devices.

## Compression and Other Novel Methods

A relatively new approach for mechanobiological stimulation in microfluidic devices is cellular compression. Even though this has been shown to stimulate the osteogenic differentiation of stem cells (Park et al., 2012) and used to investigate wound healing (Sticker et al., 2017), further studies need to be conducted to improve our understanding of compression-based biomechanical stimuli. Other methods to incorporate mechanobiological signals in microchips exploit the fact that microfluidics is ideally suited to create and monitor spatiotemporal gradients. For example, Soffe et al. (2017) showed that human embryonic kidney cells respond to shear stress gradients using trapezoid microchannel geometries, while García et al. (2015) investigated the effects of substrate stiffness gradients on cell behavior (Soffe et al., 2017). A sophisticated approach is reported by Pavesi et al. (2015): cells were subjected to multiple mechanical stimuli by adding the possibility of simultaneous electrical stimulation. The dual-stimulation strategy led to morphological and phenotypical cellular changes as well as altered cytoskeletal fiber orientation in mesenchymal stem cells. Nonetheless, while all the mentioned studies report an increase in physiological behavior of the cultured cells upon the exposure to mechanobiological cues, recreating of physiological microenvironment in a two-dimensional cultivation setup remains challenging.

## MICROFLUIDIC MECHANOBIOLOGY IN THE THIRD DIMENSION

Even though the above described microfluidic 2D models seem suitable for recreating lining layers and barrier models, they still do not resemble physiological tissue architecture since most cells reside in a three-dimensional tissue matrix in their native environment. Hence, the third dimension remains an important issue that needs to be considered when aiming to re-engineer organ models *in vitro*. It is important to note that the physiological tissue microenvironment is composed of a variety of complex physical properties ranging from cell-cell interactions to the extracellular matrix composition and biomechanical stimuli such as dynamic stretching and compression. This biological complexity, to date, poses a significant challenge, since only a limited number of studies incorporating 3D mechanobiology on microfluidic chips have been reported.

### Interstitial Flow

Additional to utilizing microfluidic devices in endothelial biology for investigating the effect of shear stress on monolayers, microchips are routinely used to determine the effects of interstitial flow on 3D vasculo- and angiogenesis. One approach involves the combination of vasculature with fluid flow where endothelial cells are co-cultured with supporting mural cells in hydrogels to generate blood vessels via vasculogenesis or

angiogenesis. Hsu et al. (2013) developed a microfluidic device that is based on a resistive circuit concept to create an array of vascularized microtissue chambers. Interstitial fluid flow in the physiological range of 0.5 to 10  $\mu\text{m/s}$  showed enhanced vessel-like structure formation corroborating similar studies from Jeon et al. (2014) for blood angiogenesis and from Kim S. et al. (2016) for lymphangiogenesis (Hsu et al., 2013). A more detailed review of recent advances in on-chip vascularization was recently published by Haase and Kamm (2017). However, microfluidics not only provides the perfect tool for exploring the importance of interstitial flow in endothelial cell biology but also for bone and brain organ-on-a-chip devices. In a recent study by Altmann et al. (2014), the morphogenesis of 3D cultured human primary alveolar bone osteoblasts under static and microfluidic growth conditions was compared. The cells were allowed to form aggregates in 300  $\mu\text{m}$  cavities with fibronectin coating in poly (methyl methacrylate)-based chips and exposed to perfusion of 15, 30, and 60  $\mu\text{l/min}$  flow rates. It was found that fluid flow lead to more distinct morphogenesis and more bone-specific gene expression and extracellular matrix formation after 7 days of culture. Additionally, Park et al. (2015) reported the design of a microfluidic chip-based 3D neurospheroid culture consisting in concave microwell arrays in which interstitial flow was generated by an osmotic micropump system. The results of the study showed that when neurospheroids are cultured under flow conditions, larger and more complex neural networks were formed compared to static culture. In a more recent 3D brain model, human induced pluripotent stem cell derived organoids were integrated into a microdevice using three-dimensional Matrigel. The on-chip cultured organoids showed improved neural differentiation and cortical organization under perfusion culture as well as enhanced expression of cortical layer markers, thus demonstrating the importance of 3D culture and mechanical fluid flow in enhancing brain organogenesis (Wang et al., 2018). Furthermore, Brown et al. (2015) created a complex physiologically relevant blood-brain-barrier model based on a back-to-back culture of endothelial cells that mimic blood vasculature with a co-culture of astrocytes, pericytes and hydrogel-embedded neurons that showed improved tight-junction formation under fluid flow conditions. These examples show that interstitial flow plays a crucial role for recreating physiological microenvironments and call for further research including a variety of other organ models.

### Stretching and Compression in 3D

Other than the sophisticated stretch/strain devices for monolayer barrier models, compression and stretching of 3D microfluidic organ models is still in its infancy. One of the first applications involve a 3D cell construct that is exposed to cyclic mechanical strain to develop a beating heart-on-a-chip (Marsano et al., 2016). In this study, human induced pluripotent stem cell-derived cardiomyocytes were embedded in a fibrin gel prior to injection into the microdevices, and subsequently exposed to mechanical stimulation using a deformable PDMS (Polydimethylsiloxane) membrane (10% uniaxial strain, 1 Hz frequency). Interestingly, the mechanically stimulated constructs showed similar gene

expression levels of cardiac markers when compared to non-actuated controls. However, the mechanical stimulus resulted in decreased expression of MYH6 (a marker for less developed phenotype), thus indicating superior cardiac maturity compared to static conditions. Furthermore, elongated cardiac-like morphology was observed in the mechanically stimulated constructs. Recently, the same group employed a similar concept to propose a model of cardiac fibrosis by applying cyclic mechanical stretch to cardiac fibroblasts embedded in a 3D fibrin hydrogel. By exploiting this strategy, the authors claim to be able to mimic some of the key steps of cardiac fibrosis onset in a timely fashion: early fibroblast proliferation, their phenotype switch into myofibroblasts, extracellular matrix deposition and its final stiffening (Occhetta et al., 2018). An alternative microfluidic device containing deformable membranes was developed to investigate differentiation associated matrix production using a real-time stiffness sensor. The authors showed that mesenchymal stromal cells embedded in hydrogels and subjected to dynamic mechanical stimulation undergo myofibroblast differentiation and synthesize collagen, leading to gel stiffening (Liu et al., 2016). In another study, 3D responses of cells were quantified in the presence of extreme strain within 3D hydrogel matrices. Here, micro-magnetically actuated synthetic tissue cultures were developed and consisted of a polyethylene glycol dimethacrylate hydrogel layer containing iron microspheres, and a stiffness tunable gelatin methacryloyl hydrogel containing a population of fibroblasts. Using this magnetic field focusing device, strain-dependent proliferation, spreading, polarization, differentiation, and matrix adhesion was studied (Li et al., 2016). Although the system can be used to readily adjust mechanical strain within 3D hydrogel cell cultures, some limitations remain concerning extracellular matrix porosity and non-fibrous matrices not being representative of the cell environment in a real tissue. **Table 1** lists currently available technologies according to applied stimuli, organ culture and cell type using microfluidic 2D as well as 3D cell culture systems.

## CONCLUDING REMARKS AND FURTHER PERSPECTIVES

The combination of microfabrication-based technologies with complex biology has enabled the development of advanced *in vitro* models capable of culturing and analyzing cell and tissue constructs under physiologically relevant conditions (Ertl, 2015; Rothbauer et al., 2015, 2017). While microfluidic models for 2D mechanical stimulation involving stretch and strain has been widely investigated, the application of physiologically relevant axial strain in 3D cell culture systems is still

## REFERENCES

- Ahearne, M. (2014). Introduction to cell-hydrogel mechanosensing. *Interface Focus* 4:20130038. doi: 10.1098/rsfs.2013.0038
- Altmann, B., Löchner, A., Swain, M., Kohal, R. J., Giselbrecht, S., Gottwald, E., et al. (2014). Differences in morphogenesis of 3D cultured primary human osteoblasts under static and microfluidic growth conditions. *Biomaterials* 35, 3208–3219. doi: 10.1016/j.biomaterials.2013.12.088
- Baker, B. M., and Chen, C. S. (2012). Deconstructing the third dimension – how 3D culture microenvironments alter cellular cues. *J. Cell Sci.* 125, 3015–3024. doi: 10.1242/jcs.079509
- in its infancy. To date only few microdevices have been developed that are capable of recreating mechanobiological relevant three-dimensional cellular microenvironments. Current mechanobiology-on-a-chip advances are hindered by both technological shortcomings and the limited reliability of current *in vitro* 3D cell culture systems. One possible solution to improve fabrication speed, precision, material selection, and (bio)compatibility could be stereolithography, which already enables (a) additive manufacturing of microchannels down to 300  $\mu\text{m}$  and (b) the integration of pneumatic valves for automated cell handling and manipulation of complex biological structures on chip. Next generation microfluidic devices will need to contain computer-controlled valves and micropumps for fluid-mechanical stimulation of cells (Rogers et al., 2015; Chen et al., 2016) and integrated actuators to reliably regulate and modify mechanical forces on tissue constructs. Furthermore, future microfluidic devices will need to address current limitations in microdevice operation to minimize the need for bulky off-chip equipment such as pumps, heaters, microscope, gas-supply, and connectors. While the incorporation of micropumps and -valves or alternative approaches for on-chip fluid handling have already been demonstrated in state-of-the-art devices (Sung et al., 2010; Kim et al., 2012; Hasenberg et al., 2015), integrated sensing solutions that replace off-chip detection methods are still scarce. The integration of micro- and nanosensors will ultimately enable the investigation of dynamic cellular responses to any imaginable physical, chemical and biological stimuli, thus providing detailed information on tissue behavior down to the molecular level. In conclusion, given the complexity of *in vivo* biological architectures of tissues and organs, next generation mechanobiology-on-a-chip systems will need to significantly increase the similarity of *in vitro* 3D biologically inspired constructs using highly integrated, fully automated and miniaturized cell analysis systems.

## AUTHOR CONTRIBUTIONS

EE and BB conceived the general structure of the review, revised the existing literature, and drafted the manuscript. HR, GF, and PE revised the text and contributed to the final manuscript.

## FUNDING

This work was funded by the European Union's INTERREG V-A AT-CZ program (ATCZ133), the European Social Fund and European Regional Development Fund–Project MAGNET (No. CZ.02.1.01/0.0/0.0/15\_003/0000492).



- Baratchi, S., Khoshmanesh, K., Woodman, O. L., Potocnik, S., Peter, K., and McIntyre, P. (2017). Molecular sensors of blood flow in endothelial cells. *Trends Mol. Med.* 23, 850–868. doi: 10.1016/j.molmed.2017.07.007
- Benam, K. H., Villenave, R., Lucchesi, C., Varone, A., Hubeau, C., Lee, H.-H., et al. (2016). SL Small airway-on-a-chip enables analysis of human lung inflammation and drug responses *in vitro*. *Nat. Methods* 13, 151–157. doi: 10.1038/nmeth.3697
- Bhatia, S. N., and Ingber, D. E. (2014). Microfluidic organs-on-chips. *Nat. Biotechnol.* 32, 760–772. doi: 10.1038/nbt.2989
- Brown, J. A., Pensabene, V., Markov, D. A., Allwardt, V., Diana Neely, M., Shi, M., et al. (2015). Recreating blood-brain barrier physiology and structure on chip: a novel neurovascular microfluidic bioreactor. *Biomicrofluidics* 9:054124. doi: 10.1063/1.4934713
- Charwat, V., Olmos Calvo, I., Rothbauer, M., Kratz, S. R. A., Jungreuthmayer, C., Zanghellini, J., et al. (2018). Combinatorial In Vitro and in silico approach to describe shear-force dependent uptake of nanoparticles in microfluidic vascular models. *Anal. Chem.* 90, 3651–3655. doi: 10.1021/acs.analchem.7b04788
- Chen, C., Mehl, B. T., Munshi, A. S., Townsend, A. D., Spence, D. M., and Martin, R. S. (2016). 3D-printed microfluidic devices: fabrication, advantages and limitations—a mini review. *Anal. Methods* 8, 6005–6012. doi: 10.1039/C6AY01671E
- Chen, G., Ushida, T., and Tateishi, T. (2002). Scaffold design for tissue engineering. *Macromol. Biosci.* 2, 67–77.
- Drury, J. L., and Mooney, D. J. (2003). Hydrogels for tissue engineering: scaffold design variables and applications. *Biomaterials* 24, 4337–4351. doi: 10.1016/S0142-9612(03)00340-5
- Engler, A. J., Sen, S., Sweeney, H. L., and Discher, D. E. (2006). Matrix elasticity directs stem cell lineage specification. *Cell* 126, 677–689. doi: 10.1016/j.cell.2006.06.044
- Ertl, P. (2015). Recent advances of biologically inspired 3D microfluidic hydrogel cell culture systems. *Cell Biol. Cell Metab.* 2:005. doi: 10.24966/CBCM-1943/100005
- Eyckmans, J., Boudou, T., Yu, X., and Chen, C. S. (2011). A hitchhiker's guide to mechanobiology. *Dev. Cell* 21, 35–47. doi: 10.1016/j.devcel.2011.06.015
- Fennema, E., Rivron, N., Rouwkema, J., van Blitterswijk, C., and de Boer, J. (2013). Spheroid culture as a tool for creating 3D complex tissues. *Trends Biotechnol.* 31, 108–115. doi: 10.1016/j.tibtech.2012.12.003
- García, S., Sunyer, R., Olivares, A., Noailly, J., Atencia, J., and Trepast, X. (2015). Generation of stable orthogonal gradients of chemical concentration and substrate stiffness in a microfluidic device. *Lab Chip* 15:12. doi: 10.1039/C5LC00140D
- Gizzi, A., Giannitelli, S. M., Trombetta, M., Cherubini, C., Filippi, S., De Ninno, A., et al. (2017). Computationally informed design of a multi-axial actuated microfluidic chip device. *Sci. Rep.* 7:5489. doi: 10.1038/s41598-017-05237-9
- Griep, L. M., Wolbers, F., De Wagenaar, B., Ter Braak, P. M., Weksler, B. B., Romero, I. A., et al. (2013). BBB on CHIP: microfluidic platform to mechanically and biochemically modulate blood-brain barrier function. *Biomed. Microdev.* 15, 145–150. doi: 10.1007/s10544-012-9699-7
- Griffith, L. G., and Swartz, M. A. (2006). Capturing complex 3D tissue physiology in vitro. *Nat. Rev. Mol. Cell Biol.* 7, 211–224. doi: 10.1038/nrm1858
- Haase, K., and Kamm, R. D. (2017). Advances in on-chip vascularization. *Regen. Med.* 12, 285–302. doi: 10.2217/rme-2016-0152
- Hasenberg, T., Mühleder, S., Dotzler, A., Bauer, S., Labuda, K., Holnthoner, W., et al. (2015). Emulating human microcapillaries in a multi-organ-chip platform. *J. Biotechnol.* 216, 1–10. doi: 10.1016/j.jbiotec.2015.09.038
- Hassell, B. A., Goyal, G., Lee, E., Sontheimer-Phelps, A., Levy, O., Chen, C. S., et al. (2017). Human organ chip models recapitulate orthotopic lung cancer growth, therapeutic responses, and tumor dormancy in Vitro. *Cell Rep.* 21, 508–516. doi: 10.1016/j.celrep.2017.09.043
- Hsu, Y.-H., Moya, M. L., Hughes, C. C. W., George, S. C., and Lee, A. P. (2013). A microfluidic platform for generating large-scale nearly identical human microphysiological vascularized tissue arrays. *Lab Chip* 13, 2990–2998. doi: 10.1039/c3lc50424g
- Huh, D., Hamilton, G. A., and Ingber, D. E. (2011). From 3D cell culture to organs-on-chips. *Trends Cell Biol.* 21, 745–754. doi: 10.1016/j.tcb.2011.09.005
- Huh, D., Leslie, D. C., Matthews, B. D., Fraser, J. P., Jurek, S., Hamilton, G. A., et al. (2012). A human disease model of drug toxicity-induced pulmonary edema in a lung-on-a-chip microdevice. *Sci. Transl. Med.* 4:159ra147. doi: 10.1126/scitranslmed.3004249
- Huh, D., Matthews, B. D., Mammoto, A., Montoya-Zavala, M., Hsin, H. Y., and Ingber, D. E. (2010). Reconstituting organ-level lung functions on a chip. *Science* 328, 1662–1668. doi: 10.1126/science.1188302
- Jain, A., Barrile, R., van der Meer, A. D., Mammoto, A., Mammoto, T., De Ceunynck, K., et al. (2018). Primary human lung alveolus-on-a-chip model of intravascular thrombosis for assessment of therapeutics. *Clin. Pharmacol. Ther.* 103, 332–340. doi: 10.1002/cpt.742
- Jansen, K. A., Donato, D. M., Balcioglu, H. E., Schmidt, T., Danen, E. H. J., and Koenderink, G. H. (2015). A guide to mechanobiology: where biology and physics meet. *Biochim. Biophys. Acta Mol. Cell Res.* 1853, 3043–3052. doi: 10.1016/j.bbamcr.2015.05.007
- Jeon, J. S., Bersini, S., Gilardi, M., Dubini, G., Charest, J. L., Moretti, M., et al. (2015). Human 3D vascularized organotypic microfluidic assays to study breast cancer cell extravasation. *Proc. Natl. Acad. Sci. U.S.A.* 112, 214–219. doi: 10.1073/pnas.1417115112
- Jeon, J. S., Bersini, S., Whisler, J. A., Chen, M. B., Dubini, G., Charest, J. L., et al. (2014). Generation of 3D functional microvascular networks with mural cell-differentiated human mesenchymal stem cells in microfluidic vasculogenesis systems. *Integr. Biol.* 6, 555–563. doi: 10.1039/c3ib40267c
- Kim, H. J., Li, H., Collins, J. J., and Ingber, D. E. (2016). Contributions of microbiome and mechanical deformation to intestinal bacterial overgrowth and inflammation in a human gut-on-a-chip. *Proc. Natl. Acad. Sci. U.S.A.* 113, E7–E15. doi: 10.1073/pnas.1522193112
- Kim, S., Chung, M., and Jeon, N. L. (2016). Three-dimensional biomimetic model to reconstitute sprouting lymphangiogenesis in vitro. *Biomaterials* 78, 115–128. doi: 10.1016/j.biomaterials.2015.11.019
- Kim, J., Kang, M., Jensen, E. C., and Mathies, R. A. (2012). Lifting gate polydimethylsiloxane microvalves and pumps for microfluidic control. *Anal. Chem.* 84, 2067–2071. doi: 10.1021/ac202934x
- Kim, S., Kim, W., Lim, S., and Jeon, J. (2017). Vasculature-On-A-Chip for In vitro disease models. *Bioengineering* 4:E8. doi: 10.3390/bioengineering4010008
- Kim, S., Lee, H., Chung, M., and Jeon, N. L. (2013). Engineering of functional, perfusable 3D microvascular networks on a chip. *Lab Chip* 13:1489. doi: 10.1039/c3lc41320a
- Kumar, S. (2014). Cellular mechanotransduction: stiffness does matter. *Nat. Mater.* 13, 918–920. doi: 10.1038/nmat4094
- Lee, S.-A., No, D. Y., Kang, E., Ju, J., Kim, D.-S., and Lee, S.-H. (2013). Spheroid-based three-dimensional liver-on-a-chip to investigate hepatocyte-hepatic stellate cell interactions and flow effects. *Lab Chip* 13:3529. doi: 10.1039/c3lc50197c
- Li, Y., Huang, G., Li, M., Wang, L., Elson, E. L., Jian Lu, T., et al. (2016). An approach to quantifying 3D responses of cells to extreme strain. *Sci. Rep.* 6:19550. doi: 10.1038/srep19550
- Liu, H., Simmons, C. A., and Sun, Y. (2016). A microfabricated platform with on-chip strain sensing and hydrogel arrays for 3D mechanical stimulation of cells. *Proc. IEEE Int. Conf. Micro Electro Mech. Syst.* 4, 267–270. doi: 10.1109/MEMSYS.2016.7421611
- Lovett, M., Lee, K., Edwards, A., and Kaplan, D. L. (2009). Vascularization strategies for tissue engineering. *Tissue Eng. Part B Rev.* 15, 353–370. doi: 10.1089/ten.teb.2009.0085
- Marsano, A., Conficconi, C., Lemme, M., Occhetta, P., Gaudiello, E., Votta, E., et al. (2016). Beating heart on a chip: a novel microfluidic platform to generate functional 3D cardiac microtissues. *Lab Chip* 16, 599–610. doi: 10.1039/C5LC01356A
- Michielin, F., Serena, E., Pavan, P., and Elvassore, N. (2015). Microfluidic-assisted cyclic mechanical stimulation affects cellular membrane integrity in a human muscular dystrophy in vitro model. *RSC Adv.* 5, 98429–98439. doi: 10.1039/C5RA16957G
- Middleton, K., Al-Dujaili, S., Mei, X., Günther, A., and You, L. (2017a). Microfluidic co-culture platform for investigating osteocyte-osteoclast signalling during fluid shear stress mechanostimulation. *J. Biomech.* 59, 35–42. doi: 10.1016/j.jbiomech.2017.05.012
- Middleton, K., Kondiboyina, A., Borrett, M., Cui, Y., Mei, X., and You, L. (2017b). Microfluidics approach to investigate the role of dynamic similitude in osteocyte mechanobiology. *J. Orthop. Res.* 36, 663–671. doi: 10.1002/jor.23773

- Occhetta, P., Isu, G., Lemme, M., Conficconi, C., Oertle, P., Rätz, C., et al. (2018). A three-dimensional in vitro dynamic micro-tissue model of cardiac scar formation. *Integr. Biol.* 10, 174–183. doi: 10.1039/C7IB00199A
- Park, J., Lee, B. K., Jeong, G. S., Hyun, J. K., Lee, C. J., and Lee, S.-H. (2015). Three-dimensional brain-on-a-chip with an interstitial level of flow and its application as an in vitro model of Alzheimer's disease. *Lab Chip* 15, 141–150. doi: 10.1039/C4LC00962B
- Park, S.-H., Sim, W. Y., Min, B.-H., Yang, S. S., Khademhosseini, A., and Kaplan, D. L. (2012). Chip-based comparison of the osteogenesis of human bone marrow- and adipose tissue-derived mesenchymal stem cells under mechanical stimulation. *PLoS One* 7:e46689. doi: 10.1371/journal.pone.0046689
- Patibandla, P. K., Rogers, A. J., Giridharan, G. A., Pallero, M. A., Murphy-Ullrich, J. E., and Sethu, P. (2014). Hyperglycemic arterial disturbed flow niche as an in vitro model of atherosclerosis. *Anal. Chem.* 86, 10948–10954. doi: 10.1021/ac503294p
- Pavesi, A., Adriani, G., Rasponi, M., Zervantonakis, I. K., Fiore, G. B., and Kamm, R. D. (2015). Controlled electromechanical cell stimulation on-a-chip. *Sci. Rep.* 5:11800. doi: 10.1038/srep11800
- Riehl, B. D., Park, J.-H., Kwon, I. K., and Lim, J. Y. (2012). Mechanical stretching for tissue engineering: two-dimensional and three-dimensional constructs. *Tissue Eng. Part B Rev.* 18, 288–300. doi: 10.1089/ten.teb.2011.0465
- Rogers, C. I., Qaderi, K., Woolley, A. T., and Nordin, G. P. (2015). 3D printed microfluidic devices with integrated valves. *Biomicrofluidics* 9:16501. doi: 10.1063/1.4905840
- Rothbauer, M., Wartmann, D., Charwat, V., and Ertl, P. (2015). Recent advances and future applications of microfluidic live-cell microarrays. *Biotechnol. Adv.* 33(Pt 1), 948–961. doi: 10.1016/j.biotechadv.2015.06.006
- Rothbauer, M., Zirath, H., and Ertl, P. (2017). Recent advances in microfluidic technologies for cell-to-cell interaction studies. *Lab Chip* 10:1. doi: 10.1039/C7LC00815E
- Sellgren, K. L., Hawkins, B. T., and Grego, S. (2015). An optically transparent membrane supports shear stress studies in a three-dimensional microfluidic neurovascular unit model. An optically transparent membrane supports shear stress studies in a three-dimensional microfluidic neurovascular unit model. *Biomicrofluidics* 9:061102. doi: 10.1063/1.4935594
- Shachar, M., Benishti, N., and Cohen, S. (2012). Effects of mechanical stimulation induced by compression and medium perfusion on cardiac tissue engineering. *Biotechnol. Prog.* 28, 1551–1559. doi: 10.1002/btpr.1633
- Smith, Q., and Gerecht, S. (2014). Going with the flow: microfluidic platforms in vascular tissue engineering. *Curr. Opin. Chem. Eng.* 3, 42–50. doi: 10.1016/j.coche.2013.11.001
- Soffe, R., Baratchi, S., Nasabi, M., Tang, S. Y., Boes, A., McIntyre, P., et al. (2017). Lateral trapezoid microfluidic platform for investigating mechanotransduction of cells to spatial shear stress gradients. *Sensors Actuat. B Chem.* 251, 963–975. doi: 10.1016/j.snb.2017.05.145
- Sticker, D., Lechner, S., Jungreuthmayer, C., Zanghellini, J., and Ertl, P. (2017). Microfluidic migration and wound healing assay based on mechanically induced injuries of defined and highly reproducible areas. *Anal. Chem.* 89, 2326–2333. doi: 10.1021/acs.analchem.6b03886
- Sung, J. H., Kam, C., and Shuler, M. L. (2010). A microfluidic device for a pharmacokinetic-pharmacodynamic (PK-PD) model on a chip. *Lab Chip* 10, 446–455. doi: 10.1039/B917763A
- Ugolini, G. S., Pavesi, A., Rasponi, M., Fiore, G. B., Kamm, R., and Soncini, M. (2017). Human cardiac fibroblasts adaptive responses to controlled combined mechanical strain and oxygen changes in vitro. *eLife* 6:e22847. doi: 10.7554/eLife.22847
- Ugolini, G. S., Rasponi, M., Pavesi, A., Santoro, R., Kamm, R., Fiore, G. B., et al. (2016). On-chip assessment of human primary cardiac fibroblasts proliferative responses to uniaxial cyclic mechanical strain. *Biotechnol. Bioeng.* 113, 859–869. doi: 10.1002/bit.25847
- van Duinen, V., Trietsch, S. J., Joore, J., Vulto, P., and Hankemeier, T. (2015). Microfluidic 3D cell culture: from tools to tissue models. *Curr. Opin. Biotechnol.* 35, 118–126. doi: 10.1016/j.copbio.2015.05.002
- van Engeland, N. C. A., Pollet, A. M. A. O., den Toonder, J. M. J., Bouten, C. V. C., Stassen, O. M. J. A., and Sahlgren, C. M. (2018). A biomimetic microfluidic model to study signalling between endothelial and vascular smooth muscle cells under hemodynamic conditions. *Lab Chip* 18, 1607–1620. doi: 10.1039/c8lc00286j
- Venugopal Menon, N., Tay, H. M., Pang, K. T., Dalan, R., Wong, S. C., Wang, X., et al. (2018). A tunable microfluidic 3D stenosis model to study leukocyte-endothelial interactions in atherosclerosis. *APL Bioeng.* 2:16103. doi: 10.1063/1.4993762
- Villeneuve, R., Wales, S. Q., Hamkins-Indik, T., Papafragkou, E., Weaver, J. C., Ferrante, T. C., et al. (2017). Human gut-on-a-chip supports polarized infection of coxsackie B1 virus in vitro. *PLoS One* 12:e0169412. doi: 10.1371/journal.pone.0169412
- Wang, J. H.-C., and Thampatty, B. P. (2006). An introductory review of cell mechanobiology. *Biomech. Model. Mechanobiol.* 5, 1–16. doi: 10.1007/s10237-005-0012-z
- Wang, X., Lee, J., Ali, M., Kim, J., and Lacerda, C. M. R. (2017). Phenotype transformation of aortic valve interstitial cells due to applied shear stresses within a microfluidic chip. *Ann. Biomed. Eng.* 45, 2269–2280. doi: 10.1007/s10439-017-1871-z
- Wang, Y., Wang, L., Guo, Y., Zhu, Y., and Qin, J. (2018). Engineering stem cell-derived 3D brain organoids in a perfusable organ-on-a-chip system. *RSC Adv.* 8, 1677–1685. doi: 10.1039/C7RA11714K
- Zheng, C., Zhang, X., Li, C., Pang, Y., and Huang, Y. (2017). Microfluidic device for studying controllable hydrodynamic flow induced cellular responses. *Anal. Chem.* 89, 3710–3715. doi: 10.1021/acs.analchem.7b00013
- Zhou, J., and Niklason, L. E. (2012). Microfluidic artificial “vessels” for dynamic mechanical stimulation of mesenchymal stem cells. *Integr. Biol.* 4, 1487–1497. doi: 10.1039/c2ib00171c

**Conflict of Interest Statement:** The authors declare that the research was conducted in the absence of any commercial or financial relationships that could be construed as a potential conflict of interest.

Copyright © 2018 Ergir, Bachmann, Redl, Forte and Ertl. This is an open-access article distributed under the terms of the Creative Commons Attribution License (CC BY). The use, distribution or reproduction in other forums is permitted, provided the original author(s) and the copyright owner(s) are credited and that the original publication in this journal is cited, in accordance with accepted academic practice. No use, distribution or reproduction is permitted which does not comply with these terms.



# Integration of *in vitro* and *in silico* Models Using Bayesian Optimization With an Application to Stochastic Modeling of Mesenchymal 3D Cell Migration

Francisco Merino-Casallo<sup>1</sup>, Maria J. Gomez-Benito<sup>1</sup>, Yago Juste-Lanas<sup>1</sup>, Ruben Martinez-Cantin<sup>2,3</sup> and Jose M. Garcia-Aznar<sup>1\*</sup>

## OPEN ACCESS

### Edited by:

Alberto Rainer,  
Università Campus Bio-Medico, Italy

### Reviewed by:

Alessandra Bonfanti,  
University of Cambridge,  
United Kingdom  
Alessandro Loppini,  
Università Campus Bio-Medico, Italy

### \*Correspondence:

Jose M. Garcia-Aznar  
jmgaraz@unizar.es

### Specialty section:

This article was submitted to  
Integrative Physiology,  
a section of the journal  
Frontiers in Physiology

**Received:** 01 March 2018

**Accepted:** 17 August 2018

**Published:** 11 September 2018

### Citation:

Merino-Casallo F, Gomez-Benito MJ, Juste-Lanas Y, Martinez-Cantin R and Garcia-Aznar JM (2018) Integration of *in vitro* and *in silico* Models Using Bayesian Optimization With an Application to Stochastic Modeling of Mesenchymal 3D Cell Migration. *Front. Physiol.* 9:1246. doi: 10.3389/fphys.2018.01246

<sup>1</sup> Multiscale in Mechanical and Biological Engineering, Department of Mechanical Engineering, Aragón Institute of Engineering Research, Universidad de Zaragoza, Zaragoza, Spain, <sup>2</sup> Centro Universitario de la Defensa, Zaragoza, Spain, <sup>3</sup> SigOpt, Inc., San Francisco, CA, United States

Cellular migration plays a crucial role in many aspects of life and development. In this paper, we propose a computational model of 3D migration that is solved by means of the tau-leaping algorithm and whose parameters have been calibrated using Bayesian optimization. Our main focus is two-fold: to optimize the numerical performance of the mechano-chemical model as well as to automate the calibration process of *in silico* models using Bayesian optimization. The presented mechano-chemical model allows us to simulate the stochastic behavior of our chemically reacting system in combination with mechanical constraints due to the surrounding collagen-based matrix. This numerical model has been used to simulate fibroblast migration. Moreover, we have performed *in vitro* analysis of migrating fibroblasts embedded in 3D collagen-based fibrous matrices (2 mg/ml). These *in vitro* experiments have been performed with the main objective of calibrating our model. Nine model parameters have been calibrated testing 300 different parametrizations using a completely automatic approach. Two competing evaluation metrics based on the Bhattacharyya coefficient have been defined in order to fit the model parameters. These metrics evaluate how accurately the *in silico* model is replicating *in vitro* measurements regarding the two main variables quantified in the experimental data (number of protrusions and the length of the longest protrusion). The selection of an optimal parametrization is based on the balance between the defined evaluation metrics. Results show how the calibrated model is able to predict the main features observed in the *in vitro* experiments.

**Keywords:** 3D mesenchymal migration, fibroblast, chemotaxis, platelet derived growth factor, phosphoinositide 3-kinase, tau-leaping algorithm, Bayesian optimization, *in-vitro in-silico* integration

## INTRODUCTION

Cell migration is a fundamental event in a wide variety of physiological processes, spanning from embryogenesis (Knecht and Bronner-Fraser, 2002; Martin and Parkhurst, 2004), angiogenesis (Lamallice et al., 2007; Spill et al., 2015), osteogenesis (Reina-Romo et al., 2012), inflammatory response (Luster et al., 2005), immune response (Bogle and Dunbar, 2010), and wound healing (Shaw and Martin, 2009; Valero et al., 2014a), to develop diseases such as cancer and metastasis formation (Franz et al., 2002; Condeelis et al., 2005; Condeelis and Pollard, 2006).

Cell migration can present different characteristics according to the dimensionality in which it is produced. Thus, cell migration on 2D surfaces has been widely studied and is typically characterized by a balance between counteracting traction and adhesion forces (Sunyer et al., 2016; Escribano et al., 2018). However, cells generally migrate in a 3D extracellular matrix (ECM) adopting different migration strategies regulated by several factors such as the cell type and the properties of the ECM. In these 3D environments, the mechanisms governing cell migration are far less understood due to both the technical challenges and the complexity of migratory behaviors (Zhu and Mogilner, 2016).

Based on the cell type and the cellular microenvironment (Te Boekhorst et al., 2016; Talkenberger et al., 2017)—in particular ECM parameters such as density, porosity and stiffness—, individual cells migrate using two distinct mechanisms (Friedl and Wolf, 2010; Swaney et al., 2010; Bear and Haugh, 2014). When cells are unable to adhere to the ECM, they modify their shape and squeeze through the ECM pores by using the amoeboid migration, which is very efficient—rapid cell locomotion (cell speed  $\sim 10 \mu\text{m}/\text{min}$ )—and it is observed in cells such as neutrophils and T cells (immune system) (Beauchemin et al., 2007; Lämmermann et al., 2008; Swaney et al., 2010). In contrast, whenever cells adhesion to the ECM is high, they degrade the ECM to pass through by using the mesenchymal migration mode, which is very inefficient—cell displacement is very slow (cell speed  $< 1 \mu\text{m}/\text{min}$ )—and it is observed in cells such as fibroblast (wound healing) and osteoblasts (bone formation) (Friedl and Wolf, 2010). This mesenchymal migration mode is investigated in this paper.

*In vitro* experiments have become increasingly sophisticated in order to reproduce as accurate as possible the natural biological surroundings of organisms from *in vivo* studies. As *in vitro* studies have increased their sophistication, their requirements have also grown in complexity. Due to the complexity and the expensive lab work of *in vitro* experiments, *in silico* studies have a complementary role in understanding mesenchymal cell migration. Computer-based mathematical models allow performing a vast number of controlled and reproducible experiments with much lower associated costs. In fact, these computational models can be classified according to several factors such as the numerical approach of the biological processes: continuous (Vermolen and Javierre, 2012; Valero et al., 2014b; Serrano-Alcalde et al., 2017), discrete (Meineke et al., 2001; Bentley et al., 2009; Scianna et al., 2012; Scianna and Preziosi, 2014; Van Liedekerke et al., 2015), or hybrid (Alber et al.,

2007; Bauer et al., 2009; Daub and Merks, 2013; Milde et al., 2014; González-Valverde and García-Aznar, 2018). In addition, they can also be classified according to the type of movement that cells develop as individual (Schlüter et al., 2012; Trichet et al., 2012; Ribeiro et al., 2017; Moure and Gomez, 2018), if cells migrate independently, or collective, forming an interconnected meshwork or cluster (Bazmara et al., 2015; González-Valverde et al., 2016; Norton and Popel, 2016; Camley and Rappel, 2017; Escribano et al., 2018). Computational models can also be classified as mechanical (Zaman et al., 2005; Borau et al., 2011), biochemical (Hatakeyama et al., 2003; Provenzano et al., 2008), or mechano-chemical (Kim et al., 2015, 2018; Moure and Gomez, 2017; Ribeiro et al., 2017).

More recently, different authors (Sun and Zaman, 2017; Kim et al., 2018; Mark et al., 2018) have focused their works in the combination of *in vitro* experiments and *in silico* modeling in order to elucidate the influence of specific factors on individual and collective cell migration. The combination of both methodologies opens new opportunities for research, because models allow the simulation of *in vitro* conditions in order to directly obtain additional information not available from experiments, but that can be indirectly evaluated *in-vitro*. For example, recently, Sunyer et al. (2016) analyzed collective cell durotaxis, combining experiments with numerical models in order to understand that the difference of stiffness sensed by cells at both edges of the cell monolayer promotes the directional migration.

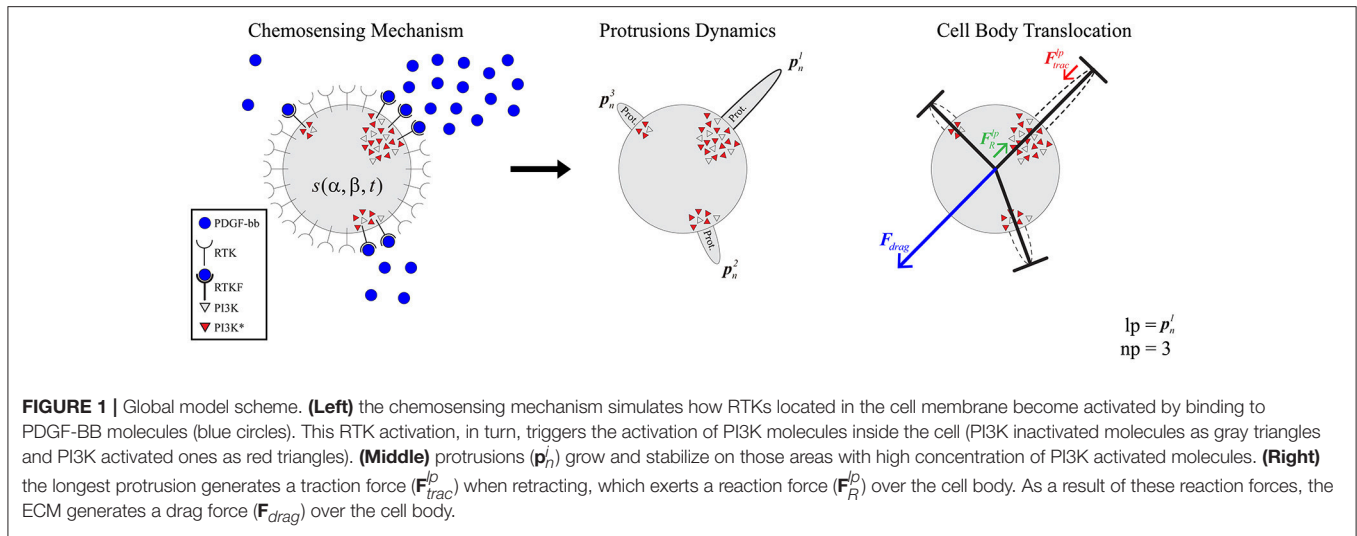
In this work, we propose to establish a new strategy based on the Bayesian optimization (BO) technique, which combines numerical simulations relied on a mathematical model and *in vitro* experiments in order to calibrate the model's parameters. In particular, a mechano-chemical model of individual mesenchymal 3D migration is presented, with a focus on accelerating the numerical simulations that determine the 3D migration trajectories. This strategy allows the full integration of numerical models and experimental measurements in order to improve knowledge of how cells regulate this mesenchymal 3D migration.

## MATERIALS AND METHODS

This section is organized in order to describe how experimental measurements and numerical simulations can be integrated in a consistent way. To facilitate their explanation, first, we briefly describe the mathematical model of cell migration (Ribeiro et al., 2017) and its numerical implementation. Next, we show the results from *in-vitro* experiments and their quantification. Then, we present how both results can be combined by means of Bayesian optimization in order to calibrate the numerical model with the experimental results. Finally, we test the potential of our calibrated numerical model under different chemoattractant concentrations and gradients.

### Model Description

The selected model to simulate 3D cell migration is based on a previous one (Ribeiro et al., 2017) (**Figure 1**). Here, we describe the main aspects of this model in order to understand



how the full calibration of this model is developed. This model assumes that cell migration can be described by three clearly differentiated stages. During the first stage the cellular chemosensing mechanism allows cells to probe the chemical cues located on their surroundings through different membrane receptors (Roca-Cusachs et al., 2013; Moreno-Arotzena et al., 2015). In particular, the focus is on how fibroblasts detect molecules of the chemo-attractant factor Platelet-derived Growth Factor (PDGF from now on) through a specific cell surface receptor, the tyrosine kinases one (also known as RTK) (Cao et al., 2004; Poukkula et al., 2011). The second stage simulates how the activation of these receptors triggers intracellular processes that regulate the onset of dendritic protrusions in different directions throughout the ECM (Weiger et al., 2010; Liou et al., 2014). In fact, these protrusions can protrude (pushing the matrix) and contract (pulling the matrix). Lastly, the third stage models how the dynamics of these protrusions regulate cell migration in 3D (Campellone and Welch, 2010; Starke et al., 2013; Moreno-Arotzena et al., 2014) by establishing a relation between the contractile force generated by each protrusion and the cell body translocation.

Next, these three main stages of the process of cell migration are described in greater detail. But first, the model of 3D cell behavior is defined.

### Modeling Cell Behavior

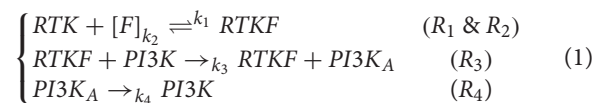
The 3D structure of the cell is geometrically modeled as a set of one-dimensional bars representing dendritic protrusions (Ribeiro et al., 2017). Those bars are located in a three-dimensional environment and diverge from a central connecting point that represents the cell body. This central connecting point—which can be associated to the cell nucleus or the cell centrosome—exists solely for modeling purposes as the point where all the bars are connected (Figure 1 right).

### Modeling the Chemosensing Mechanism

This first stage models how the chemically reacting system that allows the cell to sense the chemo-attractant factor (located in the surrounding ECM) evolves through time (Figure 1 left).

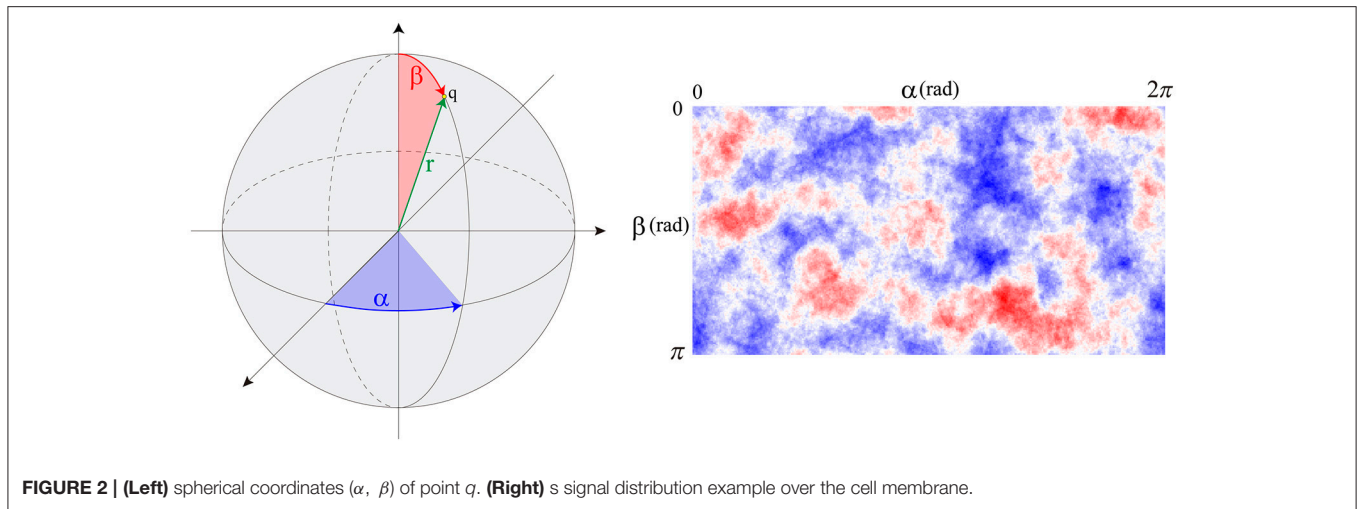
It is assumed that the only signal pathway guiding protrusion dynamics is the one including just a chemo-attractant factor located in the ECM, RTKs in the cell membrane and PI3K molecules inside the cellular body. The PDGF has been chosen as the chemical factor to interact with the cell due to its pivotal role in regenerative processes (Chen et al., 2007; Friedlaender et al., 2013; Elangovan et al., 2014; Shah et al., 2014). However, the model could be extrapolated to other growth factors.

In order to replicate the cellular chemosensing mechanism, our model simulates the interaction between different species through time. From a temporal perspective, the simplified mathematical model that mimics this chemosensing mechanism is based on a set of reactions (Equation 1) (Hatakeyama et al., 2003; Hawkins et al., 2006) and defined by a set of differential equations (Equation S1 of the Supplementary Material).



From a spatial perspective, it is assumed that membrane receptors such as RTKs are homogeneously distributed over the cell surface. However, the activation density of such membrane receptors depends on the distribution of chemoattractant molecules ( $F$ ). In particular, there are more activated RTK receptors (RTKF) on those areas of the cell surface surrounded by a higher concentration  $[F]$ . In contrast, on those areas of the cell surface surrounded by a lower concentration  $[F]$ , there are less activated receptors. Thus, cells are able to sense the spatial distribution of  $F$ .

Two sources of stochasticity in cell migration are associated to the chemosensing mechanism: the evolution of the chemically reacting system (defined by Equation 1 for the proposed model) and the activation of RTKs based on the concentration of chemoattractant molecules surrounding the cell. Therefore, the chemical reactions defined by Equation (1) are assumed to be stochastic processes described by a Poisson distribution (Ueda and Shibata, 2007). This premise makes possible to consider receptor activation over a domain with varying concentration



**FIGURE 2 | (Left)** spherical coordinates  $(\alpha, \beta)$  of point  $q$ . **(Right)**  $s$  signal distribution example over the cell membrane.

**TABLE 1 |** Equations associated with the chemosensing mechanism.

Spatial persistence of PI3K <sub>A</sub> (2D convolution over the cell surface)	$s_t(\alpha, \beta) = \int_{-\infty}^{+\infty} \int_{-\infty}^{+\infty} d_{PI3K_A}(u, v) \cdot g(\alpha - u, \beta - v) dudv$	(Equation 2)
Tempo-Spatial variation of PI3K <sub>A</sub>	$s = s(\alpha, \beta, t_k) = \sum_{t=t_0}^{t_k} s_t(\alpha, \beta)$	(Equation 3)

$s_t(\alpha, \beta)$ : amount of activated PI3K (PI3K<sub>A</sub>) across the cell membrane surface at a time  $t$ .  
 $d_{PI3K_A}(\alpha, \beta)$ : distribution of PI3K<sub>A</sub> molecules across the membrane.  
 $g(\alpha, \beta)$ : a convolution window roughly the size of a protrusion.  
 $t_0, t_k$ : time period through which  $s_t(\alpha, \beta)$  is sampled at 1 Hz and evaluated at 5-min intervals.  
 $s(\alpha, \beta, t_k)$ : the cumulative signal of PI3K<sub>A</sub> ( $s$  from now on) at time  $t_k$ .

of factor  $F$  to be a multivariate non-homogeneous Poisson's distribution. Therefore, it is possible to model this activation of RTKs by means of the Inverse Method described by Saltzman et al. (2012).

By computing an approximate solution of this problem, it is possible to evaluate at any given time ( $t_k$ ) the variation of PI3K<sub>A</sub> in any specific location of the cell surface. In order to estimate this spatio-temporal variation we defined the variable  $s(\alpha, \beta, t_k)$  which stores the spatial persistence of PI3K<sub>A</sub> activation across time ( $t_k$ ), in a space location of the cell surface defined by coordinates  $(\alpha, \beta)$  (Figure 2)—since we are dealing with a 3D model of a cell, we represent the cell membrane as a flat surface defined by the polar coordinates  $\alpha$  and  $\beta$ . Therefore, the signal  $s = s(\alpha, \beta, t_k)$  is evaluated at a fixed time  $t_k$  by means of the convolution function, taking into account the temporal evolution of the chemical signal in this surface location and its surroundings—roughly an area the size of a protrusion section. The model equations guiding the chemosensing mechanism are summarized in Table 1.

We assume that cell's consumption of chemoattractants is negligible. Thus, the chemoattractant chemical profile does not change with time.

### Modeling Protrusion Dynamics

Once the tempo-spatial variation of activated PI3K (PI3K<sub>A</sub>,  $s$ ) is estimated, it is possible to determine protrusions location

by means of a set of thresholds ( $s_{birth}$ ,  $s_{exp}$ , and  $s_{ret}$ ) that act as a signal filter. In particular,  $s_{birth}$  represents the minimal amount of signal  $s$  that cells need to develop new protrusions, as suggested by many authors (Ueda and Shibata, 2007; Weiger et al., 2010; Jilkine and Edelstein-Keshet, 2011; Chen et al., 2017); those points inside the cellular body where  $s$  is higher than  $s_{birth}$  are considered locations where novel protrusions sprout. Furthermore, any pre-existing protrusion becomes reinforced if, in its location,  $s$  is higher than  $s_{exp}$ . However, if there is not enough signal  $s$  for the protrusion to remain active, it becomes unstable; in those points where  $s$  is lower than  $s_{ret}$  pre-existing protrusions retract and disappear (Table 2). Besides, in order to simplify the search of signal  $s$  peaks where protrusions centroids are localized, an internal model parameter ( $s_{binary}$ ) is used to transform  $s$  into a binary signal. This means that only during the protrusions localization, any surface point where  $s$  is lower than  $s_{binary}$  becomes 0 whereas every surface point with  $s$  greater or equal to  $s_{binary}$  becomes 1.

In addition, it is assumed that this signal variation  $\delta s$  also regulates, in conjunction with the ECM mechanical properties, the protrusive stretch characteristics due to the cytoskeleton activity.

Therefore, protrusions generate forces against the ECM. Consequently, the mechanical properties of the ECM act as a regulator for the extension or retraction of protrusions, as suggested by Liou et al. (2014) (Figure 3). This behavior is

**TABLE 2** | Equations associated with the protrusions dynamics.

Protrusion $i$	$\mathbf{p}_n^i = \ \mathbf{p}_n^i\  \mathbf{e}_i$	(Equation 4)
Free <i>exp./ret.</i> (ECM does not restrict protrusions deformation)	$\varepsilon_k^f = \begin{cases} \frac{1}{\ \mathbf{p}^i\ } \frac{\alpha_{exp} \delta_s}{(\beta_{exp} + \delta_s)}, & \delta_s \geq 0 \text{ (expansion)} \\ \frac{1}{\ \mathbf{p}^i\ } \frac{\alpha_{ret} \delta_s}{(\beta_{ret} + \delta_s)}, & \delta_s < 0 \text{ (retraction)} \end{cases}$	(Equation 5)
Free <i>exp./ret.</i> Cauchy's strain tensor	$\tilde{\varepsilon}_k^f = \varepsilon_k^f \mathbf{e}_i \otimes \mathbf{e}_i$	(Equation 6)
Constrained <i>exp./ret.</i> by the ECM	$\tilde{\varepsilon}_k^c = \mathbf{S} [(\mathbf{C}_I - \mathbf{C}_M) \mathbf{S} + \mathbf{C}_M]^{-1} \mathbf{C}_I \tilde{\varepsilon}_k^f$ (Eshelby's theory)	(Equation 7)
Constrained <i>exp./ret.</i> (ECM does restrict protrusions deformation)	$\varepsilon_k^{EXP} = \begin{cases} \varepsilon_{exp}^c, & (\ \mathbf{p}_n^i\  = 0) \text{ and } (s_{birth} < s) \\ 0, & (\ \mathbf{p}_n^i\  = 0) \text{ and } (s_{birth} \geq s) \\ \varepsilon_{exp}^c, & (\ \mathbf{p}_n^i\  > 0) \text{ and } (s_{exp} < s) \\ 0, & (\ \mathbf{p}_n^i\  > 0) \text{ and } (s_{exp} \geq s) \end{cases}$ $\varepsilon_k^{RET} = \begin{cases} \varepsilon_{ret}^c, & s_{ret} \leq s \\ -1, & s_{ret} > s \end{cases}$	(Equation 8)
	Where $\varepsilon_k^c$ comes from the inverse of Equation 6 after computing the constrained <i>exp./ret.</i> of Equation 7.	
Protrusion length	$\mathbf{p}_{n+1}^i = (1 + \varepsilon_k^{EXP} + \varepsilon_k^{RET}) \ \mathbf{p}_n^i\  \mathbf{e}_i$	(Equation 9)

$\mathbf{p}_n^i$ : protrusion  $i$  at time interval  $n$ .

$\|\mathbf{p}_n^i\|$ : length of protrusion  $i$  at time interval  $n$ .

$\mathbf{e}_i$ : unit vector of the protrusion longitudinal axis.

$k$ : *exp* (expansion), *ret* (retraction).

$\varepsilon_k^f$ : free expansion/retraction stretch rate field (see **Figure 3**).

$\alpha_{exp}$ ,  $\beta_{exp}$ ,  $\alpha_{ret}$ ,  $\beta_{ret}$ : parameters that regulate protrusion expansion/retraction.

$\delta_s$ : increment in signal  $s$  between two time instants.

$\mathbf{S}$ : ellipsoid shape tensor.

$\mathbf{C}_I$ : elasticity tensor of the protrusion.

$\mathbf{C}_M$ : elasticity tensor of the surrounding ECM.

$\tilde{\varepsilon}_k^c$ : Cauchy's strain tensor of protrusion free expansion or retraction (see **Figure 3**).

$\varepsilon_k^c$ : constrained expansion/retraction stretch rate field.

$\varepsilon_k^{EXP}$ : longitudinal stretch rate due to the dendritic expansion.

Both  $\tilde{\varepsilon}_k^c$  and  $\tilde{\varepsilon}_k^f$  are in Voigt notation and represent the second-order stretch tensors  $\varepsilon_k^c$  and  $\varepsilon_k^f$  respectively. For this approach, it is considered a linear elastic behavior for the ECM.

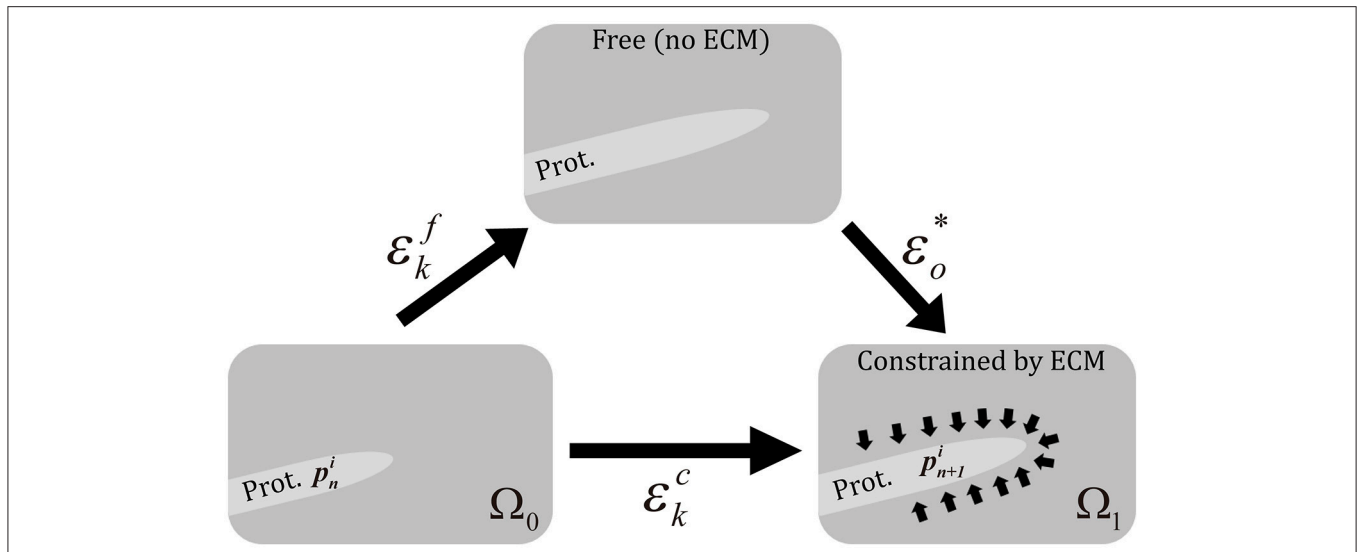
simulated by considering protrusions analogous to an elastic inclusion (ellipsoid) embedded in the ECM, applying Eshelby's analytical solution of ellipsoidal elastic inclusions in an elastic infinite body (Eshelby, 1957). We consider that during this second stage protrusions grow inside a collagen-based fibrous matrix and they adhere to ECM fibers. Thus, we consider the ECM behaves as a linear elastic material that constrains the growth of protrusions. In fact, during this growth, protrusions push to the ECM deforming it and the elastic properties of the ECM regulate this deformation. In this case we quantify the growth of the protrusion and the deformation of the ECM by means of the Eshelby's theory, assuming the protrusion as an inclusion that is embedded in the ECM. Moreover, in all the cases we assume infinitesimal deformation.

Equations guiding protrusions dynamics are summarized in **Table 2**.

### Modeling Cell Body Translocation

Finally, based on the experimental observations of how protrusions determine cell body translocation (Moreno-Arotzena et al., 2015; Del Amo et al., 2017; Movilla et al., 2018),

it is assumed that the longest protrusion determines cell motion directly. The longest protrusion presents a larger adhesion surface and, consequently, adhesion proteins have higher probability to connect with the ECM. Every cell protrusion, except the leading one, becomes non-adherent and, as a result, they are all dragged by the cell during cell motion. The retraction of the leading protrusion generates a reaction force ( $\mathbf{F}_R^p$ ) supported by the cell body. Thus, by focusing just on the reaction force generated by the longest protrusion ( $\mathbf{F}_R^p$ ), it is possible to estimate the exerted drag force ( $\mathbf{F}_{drag}$ ) by the ECM on the cell body (**Figure 1** right). As a result, both cell speed and position can be estimated at any given time  $t$  following the definition proposed by Borau et al. (2011), which takes into account the ECM viscosity. During the third stage we model the cell body translocation and, as the position of the cell center is modified, we assume the cell body is on the fluid component of the ECM. Thus, we consider that the cell is moving through a fluid. As a result, and in order to compute the drag force exerted by the ECM on the cell body, we take into account the viscosity of the ECM. The equations guiding cell body translocation are summarized in **Table 3**.



**FIGURE 3 |** Scheme of the three different configurations in protrusion dynamics.  $\epsilon_k^f$  represents the free expansion/retraction (ECM does not restrict protrusions deformation) Cauchy's strain tensor.  $\epsilon_0^*$  is the compatibility Cauchy's strain tensor.  $\epsilon_k^c$  represents the total deformation Cauchy's strain tensor. We assume infinitesimal deformation.

**TABLE 3 |** Equations associated with the body translocation.

Force equilibrium equation	$F_{drag} + F_R^p = 0$	(Equation 10)
Drag force exerted by the ECM on the cell body	$F_{drag} = -6\pi r\eta\mathbf{v}$	(Equation 11)
Contractile force generated by each protrusion	$F_{trac}^i = -\alpha_{adhesion} \cdot \mathbf{p}^i = -F_R^i$	(Equation 12)
Final force equilibrium equation	$-6\pi r\eta\mathbf{v} + \alpha_{adhesion} \cdot \mathbf{p}^p = 0$	(Equation 13)

$F_{drag}$ : drag force exerted by the ECM on the cell body.  
 $F_R^p$ : reaction force supported by the cell body due to the retraction force of the longest protrusion ( $p$ ).  
 $r$ : cell radius.  
 $\eta$ : ECM viscosity.  
 $\mathbf{v}$ : cell speed.  
 $F_{trac}^i$ : contractile force of protrusion  $i$ .  
 $\alpha_{adhesion}$ : constant that defines adhesion.  
 $\mathbf{p}^i$ : vector representing the protrusion  $i$ .  
 $\mathbf{p}^p$ : vector representing the longest protrusion.  
Traction forces  $F_{trac}^i$  are assumed identical in magnitude to their corresponding reaction forces  $F_R^i$ .

We assume that there is a mechanical balance between the traction force of the adherent protrusion ( $F_{trac}^p$ ), the longest one, and its corresponding reaction force ( $F_R^p$ ) supported by the cell body due to  $F_{trac}^p$  (Figure 1 right). Equation (12) defines a relationship between the contractile force magnitude ( $F_{trac}^p$ ), due to actomyosin activity, and the protrusion length.

### Numerical Implementation

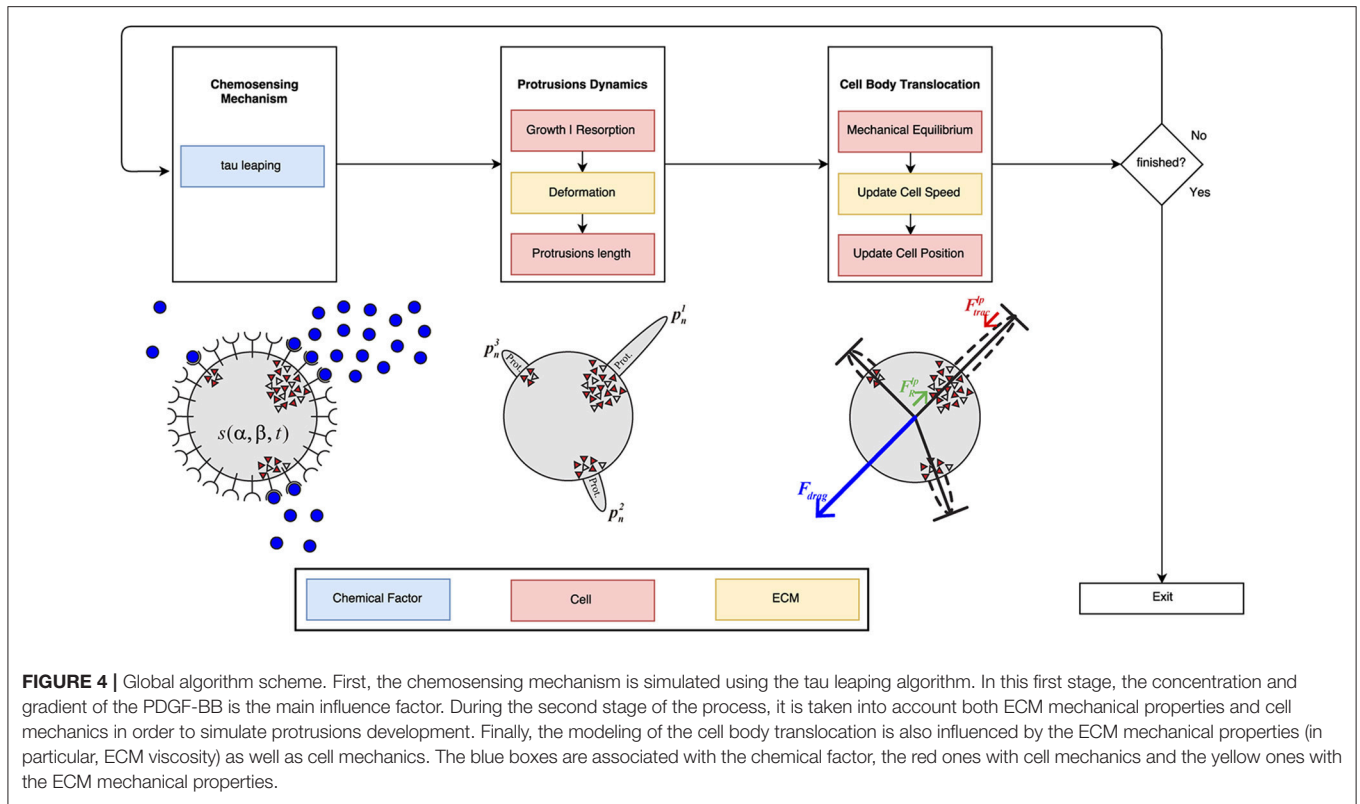
Our computational model has been designed using a scheme based on the three fundamental mechanisms: chemosensing mechanism, protrusions dynamics, and the cell body translocation (Figure 4). These three stages have been implemented in Python using powerful packages and libraries for scientific computing such as Numpy (van der Walt et al., 2011) and SciPy (Jones et al., 2001) to maximize the model's performance.

The stochastic time evolution of the given set of reactions ( $R_1$ ,  $R_2$ ,  $R_3$ , and  $R_4$ ) had been numerically simulated by using, originally, the Stochastic Simulation Algorithm (SSA; also known as the Gillespie Algorithm) (Gillespie, 1976, 1977) in the first version of this work (Ribeiro et al., 2017). However, the SSA is considered too slow for our purposes and a faster alternative is proposed, the tau-leaping algorithm (Gillespie, 2001; Cao et al., 2006). The SSA computes an exact solution of the time evolution of a chemically reacting system. In contrast, the tau-leaping algorithm estimates a good enough<sup>1</sup> approximation (Lok, 2004; Cazzaniga et al., 2006) by leaping over many reactions at once using Poisson random numbers.

The tau-leaping method tries to accelerate stochastic simulations by approximating the frequency of each reaction being fired in the next specified time interval  $[t, t + \tau]$ . By comparison, the SSA focuses only on one reaction per time interval which may be prohibitively small (Anderson et al., 2011).

<sup>1</sup>The "good-enough" expression used here to describe the accuracy of the tau-leaping algorithm comes from previous works such as Lok (2004) where he states that "One acceleration strategy is to abandon absolute mathematical precision in favor of a good-enough approximation. Gillespie has also been a pioneer in this effort. One of his strategies is called 'tau-leaping.'" This statement is considered valid as long as the leap condition is satisfied, i.e., as long as the probability of each reaction taking place does not change significantly over the time leap.





As long as the value of  $\tau$  is small enough so the leap condition<sup>2</sup> is satisfied, it is possible to compute a good approximation of the evolution of a given chemically reacting system.

It is worth to mention that neither the SSA nor the tau-leaping algorithm use a fixed time step to simulate the evolution of biologically reacting systems like the one presented in this work. Instead, they compute a new value  $\tau$  in each iteration based on the current state of the system and a random variable.

The initial amounts of each reactant as well as the reaction rates ( $k_1, k_2, k_3$ , and  $k_4$ ) used are included in **Table 4**.

Based on the spatial distribution of PI3K<sub>A</sub> molecules as well as their concentration on those locations, protrusion growth is then set. Protrusion final length is computed by applying Eshelby's solution of ellipsoidal elastic inclusions in an infinite elastic body. Mechanical equations are analytically solved using a computational algorithm. An elastic modulus of 104 Pa is assumed for the ECM based on previous experimental works of gels with a concentration of 2 mg/ml collagen type I (Movilla et al., 2018; Valero et al., 2018).

Lastly, the mechanical equilibrium associated to protrusion-generated forces is solved. Then, taking into account that the longest protrusion is the one leading cell migration, it is

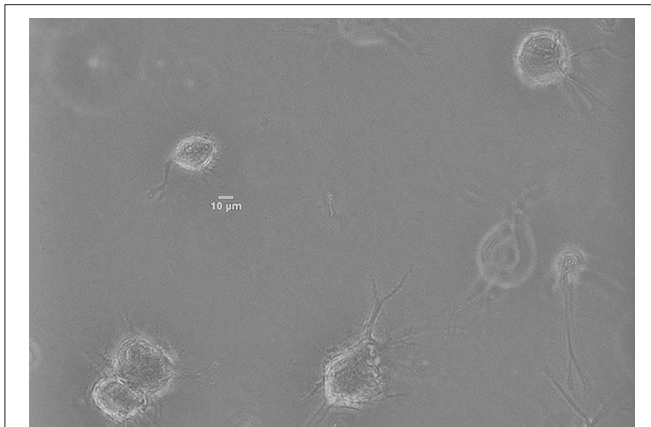
**TABLE 4 |** Initial amounts of each reactant as well as the reaction rates obtained from literature.

Reactant	Initial amount	Equation	References
RTK	4275	(1)	Paralkar et al., 1992
RTKF	0	(1)	Estimated
PI3K	$75 \times 10^3$	(1)	Hatakeyama et al., 2003
PI3K <sub>A</sub>	0	(1)	Estimated
$k_1$	$735 \text{ nM}^{-1} \cdot \text{s}^{-1}$	(1)	Heinecke et al., 2009
$k_2$	$0.01 \text{ s}^{-1}$	(1)	Heinecke et al., 2009
$k_3$	$0.0004 \text{ s}^{-1}$	(1)	Hatakeyama et al., 2003
$k_4$	$1 \text{ s}^{-1}$	(1)	Hatakeyama et al., 2003

computed both cell speed and position in the following time increment.

We decouple the simulation of the chemosensing mechanism from the other two stages of the model (protrusions dynamics and cell body translocation) because we are considering two different time scales in our model. In fact, the chemical and mechanical events occur at different time scales. In order to accurately simulate the proposed chemically reacting system we are using the iterative tau leaping algorithm with a variable associated time step  $\tau$  in the range [0.5, 1.5] seconds. However, to model protrusion dynamics and the cell body translocation we are using a time step  $dt$  of 5 min. Actually, it is because variations in the signal  $s$  (Equation 2) between two consecutive time steps

<sup>2</sup>The leap condition is an accuracy-assuring restriction which states that during the time interval  $[t, t + \tau]$  the probability of each reaction channel  $R_j$  being fired should remain approximately constant even though all reaction channels may be fired several times.



**FIGURE 5 |** Norman Human Dermal Fibroblast (NHDF) cultured in 3D collagen-based fibrous matrix (2 mg/ml collagen). Image was captured with a Nikon D-Eclipse Microscope with a Plan Fluor 200x magnification (20x Objective) and phase contrast.

$t$  and  $t + \tau$  are really small whereas protrusions require more noticeable variations of the chemical signal in order to change their current state. As a result, it is required to keep track of the cumulative variation  $\delta s$ .

## Development and Quantification of *in vitro* Experiments

Once we have numerically implemented the proposed model, we have to calibrate its parameters in order to optimize the performance of this computational model. We calibrate the model here presented by comparing the results of its simulations with experimental data. In particular, we focus on two different features to fit the model's parameters: the length of the longest protrusion and the number of protrusions of the migrating cell. As a result, we have performed *in vitro* studies to get accurate experimental measurements of the length of the longest protrusion and the number of protrusions.

*In vitro* experiments have been performed by culturing Normal Human Dermal Fibroblasts (NHDF)—human skin primary cells—within 2 mg/ml collagen gels at a concentration of  $2.5 \times 10^5$  cells/ml, and temperature and atmosphere conditions have been maintained at 37°C and 5% CO<sub>2</sub>. Immediately after the seeding, cells' evolution has been monitored with multidimensional microscopy for 4 h (from 0 to 4 h), every 5 min and 5 μm of Z axis, with 200x magnification (20x objective) and phase contrast (Figure 5). We have chosen a 2 mg/ml collagen concentration because it already implies a matrix pore size (< 1 μm) (Fraleay et al., 2010). Individual cell protrusions have been quantified by in-house Matlab algorithms (Moreno-Arotzena et al., 2015). For each image stack, best Z has been chosen in order to maximize accuracy and minimize the complexity of the manual analysis of both the cell body and its protrusions. Single cell analysis of four different samples has been performed for the given collagen concentration (2 mg/ml).

FGM<sup>TM</sup>-2 (Fibroblast Growth Medium-2) has been used to support the growth of primary human fibroblasts. It contains a

supplementation of GA-1000, recombinant human insulin 0.5%, HFGF-B GF, and 2% of Fetal Bovine Serum. Thus, these *in vitro* experiments only include a very low and fixed concentration of growth factors included in the culture medium; they do not include any chemoattractant gradient.

## Model Calibration Using Bayesian Optimization

During the last couple of decades, as the available computational power has greatly increased, so has the complexity of *in silico* models and the number of parameters included in those models. As a result, the complexity of the calibration process has also increased. However, it is still often the case that this calibration process is performed using a very manual approach. Each parameter must be tuned manually despite the search space being usually too vast to be effectively navigated. Besides, there may be interactions or dependencies between some parameters. This process can be very tedious, especially when dealing with *in silico* simulations that require several hours of execution time.

This calibration process can be mapped to a non-linear optimization problem where the objective is to find the simulation parameters that best fits the *in vitro* experiments. In this way, we are able to automate the process. However, most non-linear optimization solvers require a large number of iterations, gradient information of the fitting function or they are sensible to local optima. In our case, the large number of iterations could make the problem intractable as the evaluation of the fitting function associated to our *in silico* model is very costly because it requires several simulations of our stochastic model.

More formally, we are looking for the set of optimal experiment parameters  $x$  that satisfy:

$$x^* = \arg \max_{x \in \chi} f(x), \quad (14)$$

where  $f$  is the fitting function between the *in vitro* and the *in silico* models and  $X$  is the parameter search space as defined in Table 5.

Bayesian optimization, also called Efficient Global Optimization (EGO) (Jones et al., 1998) is a general purpose black-box optimization methodology that it is characterized for requiring a very small number of iterations before reaching global optimization. Thus, it is especially suitable for experimental design and calibration of expensive processes (Shahriari et al., 2016). Bayesian optimization uses a probabilistic surrogate model of the target function combined with optimal decision theory to drive the search toward the global optimum in less iterations than popular non-linear optimization alternatives like PSO (Kennedy and Eberhart, 1995), CMA-ES (Hansen et al., 2003) or L-BFGS (Nocedal, 1980). In the case of Bayesian optimization, the surrogate model uses machine learning to capture previous iterations acting as a memory of the full optimization process. Meanwhile, the decision component carefully selects the next query at each iteration.

In the case of simulation calibration, there are many variables that can be used for fitting, some of them might be even

competing. Then, we can redefine the problem as one of multi-objective, multicriteria optimization or Pareto optimization:

$$x^* = \arg \max_{x \in \mathcal{X}} (f_1(x), f_2(x), \dots, f_n(x)), \quad (15)$$

In this case, the objective is not only to find a single optimal value for the simulator parameters, but to find the whole set of Pareto optimal points, that is, those points that dominate the rest of the points. Although this is a completely different problem, the seminal work of Knowles (2006) extended the Bayesian optimization methodology to the multi-objective setup.

There are several pieces of software that implements Bayesian optimization, like BayesOpt (Martinez-Cantin, 2014). A full review can be found in Shahriari et al. (2016). However, many of them do not support multi-objective optimization and those that do support multiple criteria are very limited in terms of other features. In this work, we have used SigOpt<sup>3</sup> (Martinez-Cantin et al., 2018) for its support for parallelization and multi-objective optimization. Besides, it provides other features like the parameter importance, which will be discussed in the Results section.

For our experiments, we have decided to fit two competing metrics: the length of the longest protrusion ( $lp$ ) as well as the number of protrusions ( $np$ ) (Figure 1). The fitting of the *in silico* values with respect to the *in vitro* measurements is computed using the Bhattacharyya coefficient (also known as  $BC$ ), which has been widely used to compare the similarity or discriminate of two continuous or discrete distributions (Comaniciu et al., 2000). In fact, for discrimination it corresponds to the upper bound of the Bayesian error when performing Bayesian hypothesis testing with symmetric cost functions and uninformative priors (Nielsen, 2014). Note that, Bayesian hypothesis testing already includes a penalization for model complexity and priors result in a regularization effect, being less sensitive to overfitting than classical hypothesis testing (Kass and Raftery, 1995).

In particular, histograms of both *in vitro* and *in silico* experiments are used as discrete distributions to compute those metrics (Equation 16).

$$BC = \sum_{i=1}^n \sqrt{\text{hist}_{in vitro}^i \cdot \text{hist}_{in silico}^i} \quad (16)$$

$\text{hist}^i$  represents the value of the  $i$ -th histogram bin defined as the probability of occurrences of values in the range  $(x_{i-1}, x_i]$ .

The selection of metrics affects model calibration, so we have carefully selected the metrics with a greater influence on cell migration to the best of our knowledge. Moreover, these metrics are based on experimental measurements that we are able to accurately quantify. However, there are other measurements based on cell motion, such as the instant cell speeds, that are so low that we are not able to quantify them with the required accuracy. For those metrics it is only possible to perform a qualitative analysis. Although our proposed metrics are based on just two quantities measured in the experimental data: the length

of the longest protrusion and the number of protrusions, we consider that both variables are fundamental in the regulation of the final 3D cell motion. In particular, experimental observations (Moreno-Arotzena et al., 2015; Del Amo et al., 2017; Movilla et al., 2018) suggest that the length of the longest protrusion has great influence over the cell speed whereas the number of protrusions has a great impact on the cell trajectory (whether it is random or directional).

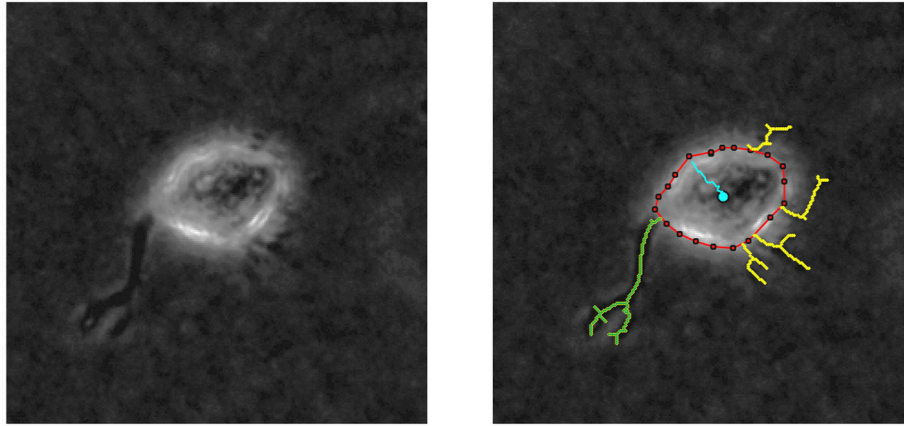
Optimizing the BC function can be considered as a form of Bayesian learning in the sense that we are trying to fit a model that best represents the distribution of the data, and therefore maximizing the posterior. Similarly, optimizing the BC can be seen as a form of Bayesian hypothesis testing where we are rejecting all the models with higher Bayesian error.

Furthermore, Bayesian optimization is a black-box method, meaning that it does not require specific knowledge about the metric, and that metrics can be easily interchanged. Thus, the same methodology can be applied to any other feature or any other similarity metric, such as KL-divergence or any other loss function. Besides, we can include metrics not directly related to the data such as cost, time, etc. These metrics can be competing, meaning that one metric cannot be improved without another metric suffering. As a result, the solutions distributed in the Pareto set might be distributed in a complex way. Thus, sample efficient search like Bayesian optimization is of paramount importance. Besides, the resulting Pareto front allows the expert user to balance the competing metrics a posteriori, choosing the most convenient parametrization in different circumstances.

## Model Validation Using Different Chemoattractant Concentrations and Gradients

After calibrating the numerical model, we have to validate it, testing their predictive ability to simulate different cell responses under different chemical gradients. This validation process allows us to prove that the proposed model does not only accurately replicate the results used to calibrate it, but also new ones, so that there has been no overfitting during the calibration process. In the preceding calibration process, we have used quantitative results related to both the length of the longest protrusion and the number of protrusions of migrating NHDF from *in vitro* experiments without any chemoattractant gradient. However, the validation process of this computational model is based on qualitative observations of migrating cells surrounded by a chemoattractant factor diffusing throughout the ECM (Song et al., 2006; Bosgraaf and Van Haastert, 2009). We have simulated six different extracellular environments. Three of these extracellular environments include different PDGF gradients ( $10^{-1}$ ,  $10^0$ ,  $10^1 \mu M/mm$ ) but a fixed PDGF concentration at the initial cell's position ( $0.8 \mu M$ ). The other three extracellular environments include a fixed PDGF gradient ( $10^0 \mu M/mm$ ) but different PDGF concentrations at the initial cell's position (0.08, 0.8, and  $8.0 \mu M$ ). Twenty simulations have been executed for each extracellular environment, using the same seeds used during the calibrating process. The comparison between *in vitro* and

<sup>3</sup><https://sigopt.com/>



**FIGURE 6 | (Left)** Phase contrast example of a NHDF cell cultivated in a 2 mg/ml collagen gel, with 200x magnification (20x objective) acquired using multidimensional microscopy. **(Right)** Protrusion analysis performed by in-house Matlab algorithms; red line delimits cell body, yellow lines represent the protrusions, and blue line shows cell body displacement. In this case, the longest protrusion is the green one and the number of protrusions is 5.

*in silico* results is based on qualitative observations of the velocity component in the direction of the chemotactic gradient ( $v_x$ ).

We assume a fixed growth factor profile without any induced modifications of the spatial gradient due to the growth factor diffusion throughout the ECM. Thus, the chemoattractant chemical profile is assumed to be temporally stable as the inlets and outlets of our system keep a fixed growth factor profile during our 4-h simulation.

## RESULTS

By means of *in vitro* experiments in fibroblasts, it is possible to quantify both the length of every protrusion, as well as the number of protrusions generated at every checkpoint  $t$  ( $t = 0, 5, 10, \dots, 240$  min). **Figure 6** shows an example of the images generated by multidimensional microscopy and the posterior protrusions analysis performed using in-house Matlab algorithms. However, our model focuses on the length of only the longest protrusion at each temporal checkpoint  $t$ , ignoring the length of the other protrusions, as explained in Section Modeling Cell Body Translocation. Therefore, during the calibration process the comparison between *in vitro* and *in silico* experiments is performed by means of the  $BC$  using these two features (length of the longest protrusion and the number of protrusions generated by migrating cells).

During calibration, for every iteration in the optimization loop, 20 simulations replicating the *in vitro* scenario of a 2 mg/ml collagen ECM have been executed—in order to capture the stochastic nature of our model. Those 20 simulations used 20 different seeds in order to initialize the global random number generator of our model. Once the 20 simulations have been completed, their associated histograms are computed by means of a computer-based algorithm. These histograms (e.g., **Figure 7** bottom) are compared with the *in vitro* histograms (**Figure 7** top) using the proposed evaluation metrics  $BC_{lp}$  and  $BC_{np}$  (defined in

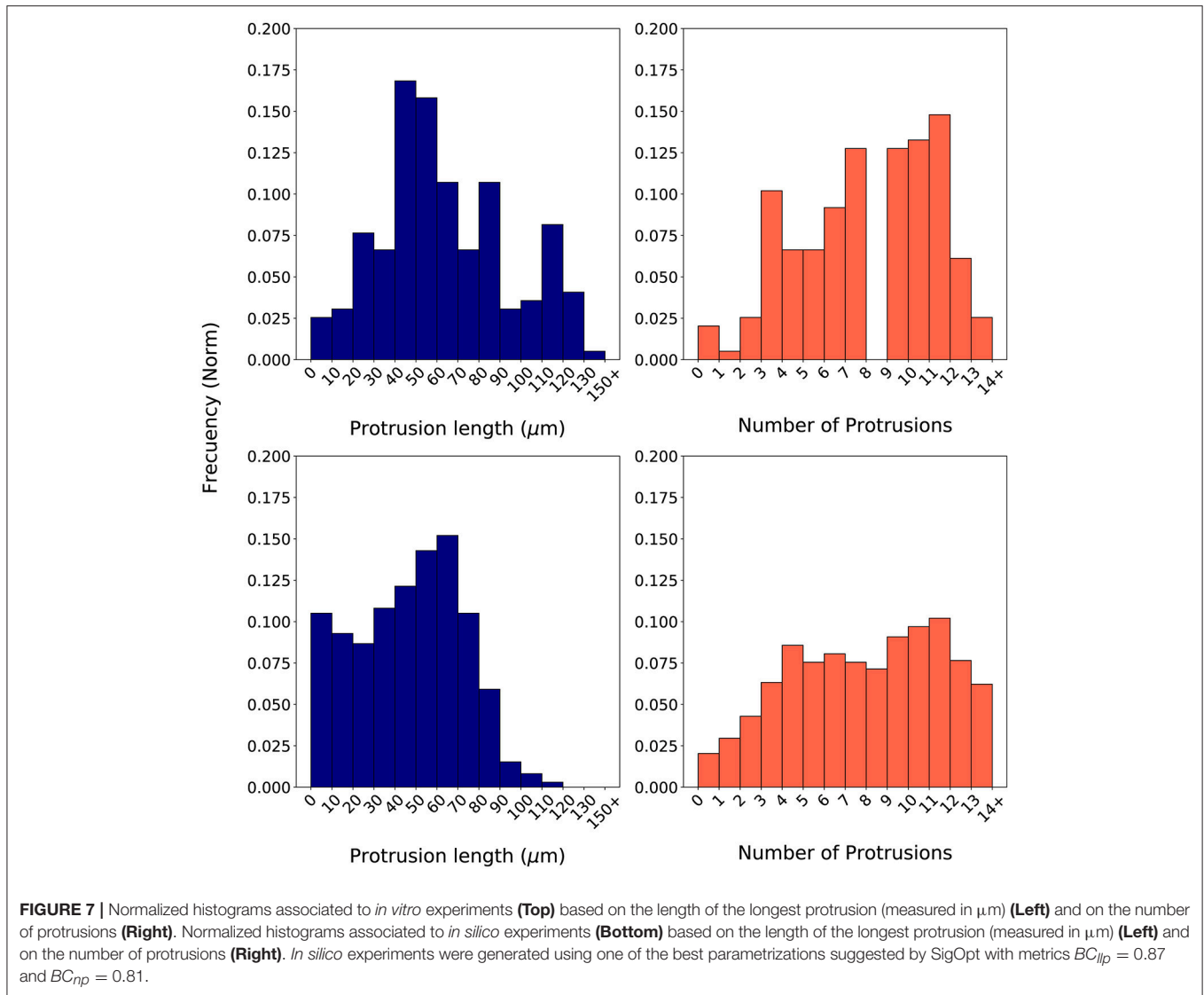
Equations 18, 19 respectively and based on Equation 16).

$$BC_{lp} = \frac{\sum_{i=1}^N BC_{lp}^i}{N}, \quad N = 20, \quad (18)$$

$$BC_{np} = \frac{\sum_{i=1}^N BC_{np}^i}{N}, \quad N = 20, \quad (19)$$

In order to compute the two metrics using the  $BC$ , it is required to generate the associated histograms for both the longest protrusion length and the total number of protrusions. Histograms associated to *in vitro* experiments using a cellular microenvironment based on 2 mg/ml collagen gels show how the protrusion length ranges from over  $0 \mu\text{m}$  to almost  $140 \mu\text{m}$ . However, most of the longest protrusions have a length in the interval  $40\text{--}60 \mu\text{m}$  (**Figure 7** top left). Regarding the number of protrusions, there is a high dispersion, ranging from 1 to 14 protrusions in each individual fibroblast during migration (**Figure 7** top right). **Figure 7** (bottom) shows an example of a couple of histograms associated to the *in silico* experiments. In this case, we have generated *in silico* histograms using the best parametrization suggested by SigOpt with metrics  $BC_{lp} = 0.87$  and  $BC_{np} = 0.81$  (**Figure 7** bottom). These histograms show how, although the length of the longest protrusions is between 0 and more than  $150 \mu\text{m}$ , there is a peak in the interval  $60\text{--}80 \mu\text{m}$  (**Figure 7** bottom left). Regarding the number of protrusions, there are usually about 9 to 12 in each fibroblast during migration (**Figure 7** bottom right). When comparing measurements of the length of the longest protrusion, the mean values are  $63.71$  (*in vitro*) vs.  $65.98$  (*in silico*), whereas the standard deviations are  $31.20$  (*in vitro*) vs.  $26.82$  (*in silico*). For the measurements of the number of protrusions, the mean values are  $7.57$  (*in vitro*) vs.  $7.38$  (*in silico*), whereas the standard deviations are  $3.27$  (*in vitro*) vs.  $4.00$  (*in silico*).

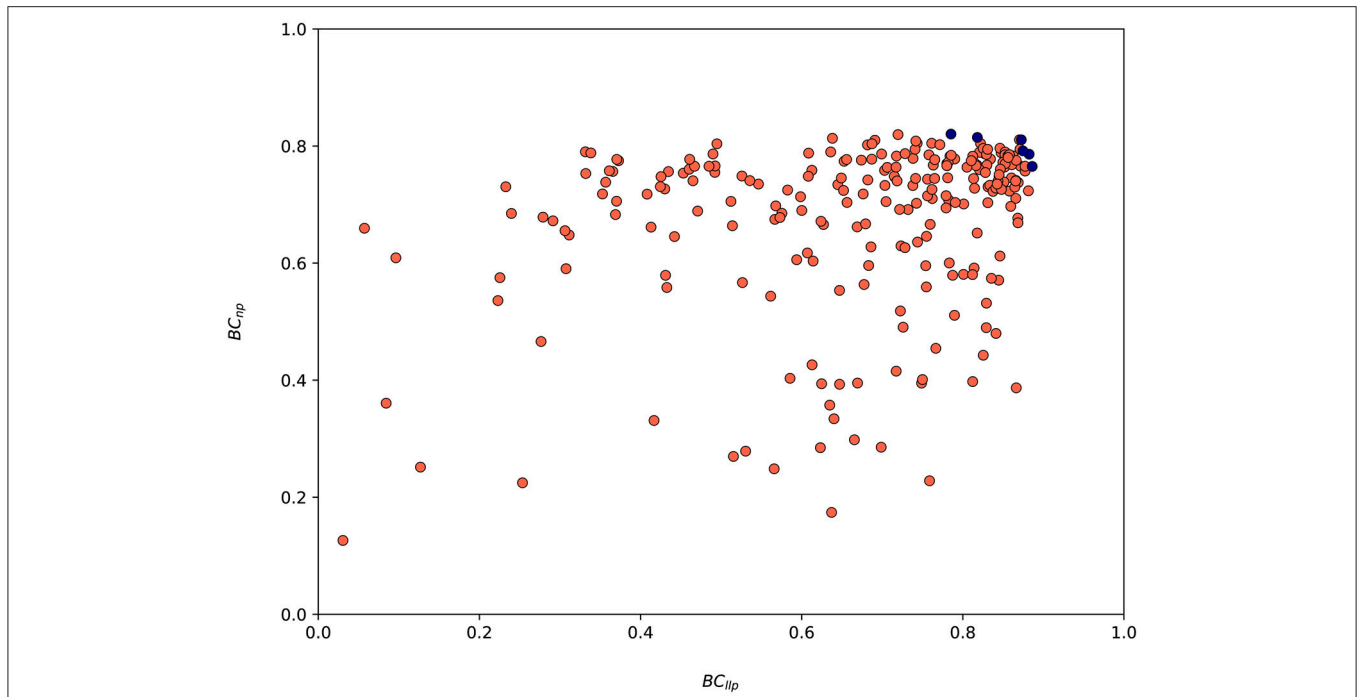
The values of both metrics  $BC_{lp}$  and  $BC_{np}$  for every suggested parametrization by SigOpt are shown in **Figure 8**. SigOpt is able to find parametrizations with higher values of the  $BC_{lp}$  (even



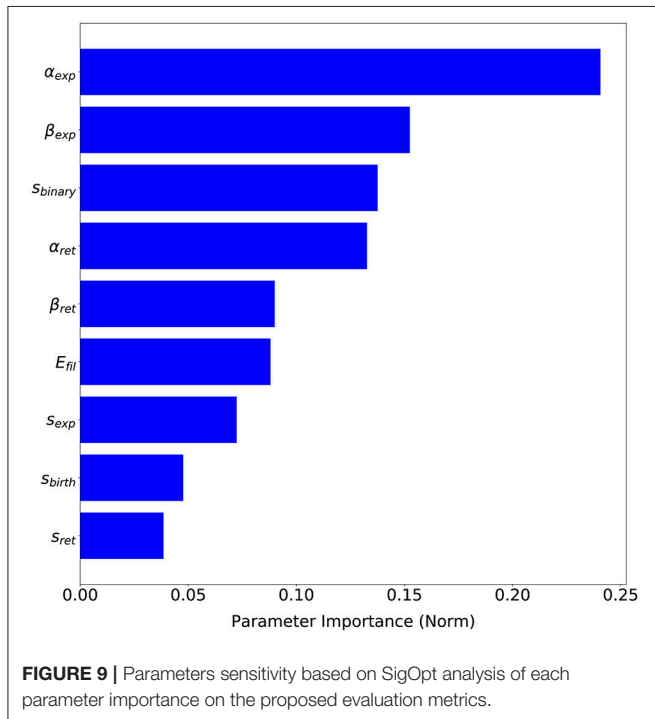
higher than 0.9) than the  $BC_{np}$  (always lower than 0.8). Besides, the majority of the parametrizations suggested by SigOpt are higher than 0.7 for both metrics (35.67%), with slightly better results for the metric related with the length of the longest protrusion (Figure 8).

A total of nine parameters of the model have been calibrated (Table 5). The range of values for each parameter has also been established in order to define the search space (Table 5). Note that in this case, the search space includes both continuous regions in the real space and discrete values for integer parameters. Thus becoming a mixed-integer programming problem, much harder to be optimized than just real spaces (non-linear optimization) or integer spaces (combinatorial optimization). For some parameters we have established a range based on the values used in Ribeiro et al. (2017), whereas for others such as  $E_{protrusion}$  we have determined a range based on values found in literature. In addition, for the parameters related to  $s$  signal ( $s_{birth}$ ,  $s_{exp}$ ,  $s_{ret}$ , and  $s_{binary}$ ), we have analyzed the values of

$s$  at different time steps. These ranges should be biologically relevant. For example, the range of the parameter  $E_{protrusion}$  (protrusions elastic modulus) includes the value given in Mofrad and Kamm (2006) and Li et al. (2014). We have also automatically discarded any parametrization with  $s_{ret} \geq s_{birth}$  or  $s_{ret} \geq s_{exp}$  or  $s_{exp} \geq s_{birth}$  because from a biological perspective they are invalid (the minimal amount of signal required for the onset of new protrusions,  $s_{birth}$ , and for the reinforcement of pre-existing protrusions,  $s_{exp}$ , cannot be lower than the minimal amount of chemotactic signal  $s$  required to remain active and not disappear,  $s_{ret}$ ; the minimal amount of signal required for the onset of new protrusions,  $s_{birth}$ , cannot be lower than the minimal amount for the reinforcement of pre-existing protrusions either). The parametrization selected as the optimal one after 300 iterations of the calibration process using SigOpt is summarized in Table 2. For example, the best value for the elastic modulus is  $10^7 Pa$ . The best parametrization, with metrics  $BC_{llp} = 0.87$  and  $BC_{np} = 0.81$ , have been selected due to the balance between both metrics.



**FIGURE 8 |** Values associated to both metrics ( $BC_{ip}$  and  $BC_{np}$ ) for the 300 model parametrizations suggested by SigOpt during the calibration process. Red circles are associated to every parametrization tested whereas the blue ones represent Pareto optimal points (parametrizations where one metric cannot be improved without another metric suffering) and form an approximate Pareto frontier.



**FIGURE 9 |** Parameters sensitivity based on SigOpt analysis of each parameter importance on the proposed evaluation metrics.

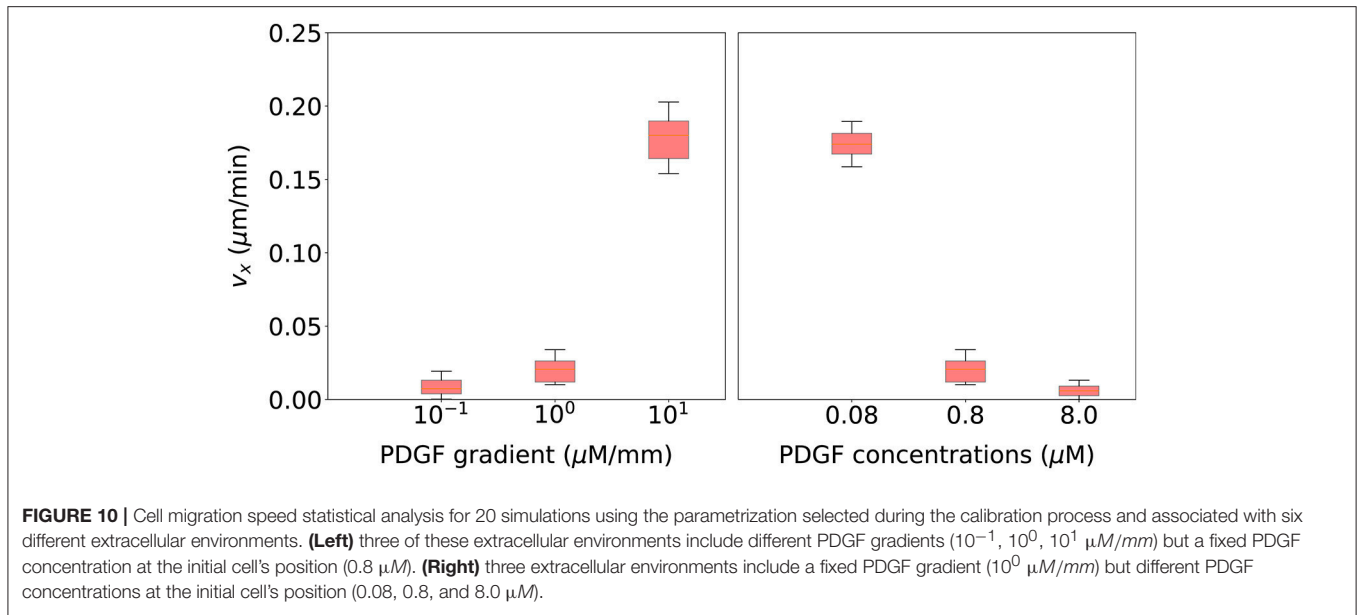
The advantage of having a probabilistic surrogate model of the metrics is that we can perform other types of data analysis during the optimization process. SigOpt also offers

**TABLE 5 |** Model parameters calibrated using Bayesian optimization with SigOpt.

Parameter	Calibrated value	Equation	Range
$E_{protrusion}$	$10^7 Pa$	(7)	$10^j, j \in \{4, 5, \dots, 10\}$
$S_{birth}$	85	(9)	$\mathbb{Z} \in [0, 100]$
$S_{exp}$	76	(9)	$\mathbb{Z} \in [0, 100]$
$S_{ret}$	0	(9)	$\mathbb{Z} \in [0, 100]$
$\alpha_{exp}$	0.14 mm	(7)	$\mathbb{R} \in [0.01, 0.2]$
$\beta_{exp}$	100	(7)	$\mathbb{R} \in [0.1, 100]$
$\alpha_{ret}$	0.05 mm	(7)	$\mathbb{R} \in [0.01, 0.2]$
$\beta_{ret}$	54.86	(7)	$\mathbb{R} \in [0.1, 100]$
$S_{binary}$	62500		$12500 + 2000 \cdot j, j \in \{0, 1, \dots, 100\}$

The calibrated values are associated to the parametrization considered the best one (with computed metrics  $BC_{ip} = 0.87$  and  $BC_{np} = 0.81$ ). The given ranges have been established at the beginning of the calibration process and leave them unchanged.

an importance analysis of each parameter on the metrics (see **Figure 9**), i.e., how influential each parameter is on the metrics, that is, how much the metric values change with variations of each parameter. This analysis gives us valuable insights on our model performance. Although every parameter has some influence over the metrics output,  $\alpha_{exp}$ , a parameter which computes the free expansion/retraction stretch rate field (during the protrusion dynamics stage) is the most important parameter (24.06%). The parameters  $\beta_{exp}$ , also used to compute the free expansion/retraction stretch rate field, and



*s<sub>binary</sub>*, used to simplify the search of signal *s* peaks where protrusions centroids are localized, are the second and third most influential parameters on the metrics (15.25 and 13.76%, respectively). Lastly, *s<sub>birth</sub>* and *s<sub>exp</sub>* are the ones with the least importance on our evaluation metrics (4.76 and 3.86%, respectively).

Finally, we validate this computational model using qualitative observations based on cell motion of migrating cells surrounded by different chemoattractant gradients. **Figure 10** (left) shows that as the PDGF gradient grows, cell's velocity in the direction of the chemotactic gradient increases too. Thus, cells are following a more directional trajectory which agrees with experimental observations from Bosgraaf and Van Haastert (2009). On the other hand, **Figure 10** (right) shows that as the PDGF concentration surrounding the cell increases, cell's velocity in the direction of the chemotactic gradient decreases. In this case, cells are following a more random trajectory. This fall in the effective speed of the cell is thought to be associated with receptor saturation (Song et al., 2006).

## DISCUSSION

Understanding the process of cell migration is a really difficult endeavor since it is a biological process coordinated by multiple factors. Temperature (Higazi et al., 1996), adhesion sites in the ECM (Cukierman et al., 2001), ECM mechanical properties and architecture (Wolf et al., 2013) as well as the gradient of chemical factors (Devreotes and Janetopoulos, 2003), modulate cell migration, by regulating the signaling pathways and intracellular cytoskeleton and adhesion organization (Paul et al., 2016).

According to our experimental observations (Moreno-Arotzena et al., 2015; Del Amo et al., 2017; Movilla et al., 2018) cells tend to present two different behaviors: they increase the number of stable protrusions, in which case each protrusion is

shorter; or they decrease the number of stable protrusions, in which case at least some of them are longer. In the first case, protrusions compete and there is not any preferential movement. In the second case, normally cells present a defined movement in the direction of the longest protrusion.

Several assumptions are made regarding the mechanical model of the ECM. First, we consider the ECM as an isotropic material. Nevertheless, the ECM is anisotropic due to the different fiber directions (Valero et al., 2018). Second, the mechanical properties of the ECM are assumed homogeneous, thus we do not consider the heterogeneity associated to the distribution of the fibers. Third, ECM remodeling is not considered in this model. However, this is an acceptable approximation for preliminary studies of cell motility in collagen gels, which allows us to use the Eshelby's theory.

Due to the complexity of cell migration, computational models have been widely used to improve its understanding (Rangarajan and Zaman, 2008; Mak et al., 2016; Chen et al., 2017). Cell migration include several stochastic processes such as the evolution of chemically reacting systems. The Stochastic Simulation Algorithm (SSA) (Gillespie, 1976, 1977) has been widely used to numerically simulate the stochastic behavior of biochemical reactions. However, the SSA is considered too slow for many practical applications (Gillespie, 2001, 2007). This effect occurs clearly in our case: even though the SSA offers an exact solution, simulations take too long to finish (an average of 10.77 h of execution time for each simulations of 4 h of cell migration). The tau leaping algorithm has been considered a good fit for our purposes: it gives us a "good-enough" approximation (see footnote 1) of the temporal evolution of our biochemical system and allows us to optimize the numerical performance of our mechanochemical model (an average of 1.28 h of execution time for each simulation of 4 h of cell migration). Thus, reducing the computational cost to almost an order of magnitude.

Although in most computational works (Bauer et al., 2009; Bentley et al., 2009; Vermolen and Javierre, 2012; Daub and Merks, 2013; Talkenberger et al., 2017; Escribano et al., 2018; González-Valverde and García-Aznar, 2018; Kim et al., 2018; Moure and Gomez, 2018) authors perform strong efforts to validate models comparing experimental results with numerical ones, there is a lack of full integration of both kind of results. However, this paper presents a relevant step forward in this direction, showing a novel methodology that integrates both modeling strategies (*in vitro* and *in silico*) by means of the application of Bayesian optimization during the calibration process.

The complexity of the calibration process of any model grows rapidly with the number of parameters. Another factor that greatly increases the complexity of the calibration process is the stochastic nature of some biological models such as the one presented in this paper. Stochastic models require the execution of several simulations for each model parametrization in order to capture the results variation associated to the stochastic randomness. Moreover, if the execution of each simulation takes more than a couple of minutes, a manual approach for this calibration process becomes highly prone to inefficiencies.

When choosing the values for each model parameter using such a manual approach, it is usually the case that researchers turn to literature as their starting point. Then, they perform some manual tuning so simulations results fit approximately the experimental data. Generally, researchers start by modifying just a couple of parameters using some values considered biologically relevant. Then, they analyze how those parameters influence the model output based on the different values tested. They iterate over this process by picking a couple of the remaining parameters in every iteration—ideally, the selected parameters in each iteration are related to each other. This manual approach is really tedious since the modification of some parameters can potentially require the recalibration of some already calibrated parameters. If the model includes a large number of parameters, researchers could start this tuning process by performing a sensitivity analysis (Saltelli, 2002; Bauer et al., 2009; Bentley et al., 2009; Borau et al., 2012; Vermolen and Javierre, 2012; Daub and Merks, 2013; Escribano et al., 2015, 2018; Talkenberger et al., 2017) in order to focus on those parameters with a higher importance on the model output. Due to computational and time restrictions, this manual step does not generally include more than a couple of iterations, even though it is becoming more and more common to have access to a High-Throughput Computing (HTC) environment—which can reduce the required times to run those simulations by parallelizing them.

This paper proposes the application of the Bayesian optimization technique to reduce these inefficiencies. Bayesian optimization, which has been applied to solve a wide range of problems such as machine learning applications (Snoek et al., 2012), robot planning (Martinez-Cantin et al., 2009), simulation design (Brochu et al., 2010), biochemistry (Czarnecki et al., 2015), and dynamical modeling of biological systems (Ulmasov et al., 2016), offers an automated approach for this calibration process. Furthermore, the Bayesian optimization

technique is able to minimize the number of parametrizations to test on the computational model and find a good enough fit to *in vitro* observations. In our case, from the 300 different parametrizations tested during the calibration process, only 6 parametrizations (2%) have the two metrics considered ( $BC_{llp}$  and  $BC_{np}$ ) below 0.5. On the other hand, SigOpt suggests 107 parametrizations (35.67%) with both metrics above 0.7.

Clearly, the methodology here presented—based on the application of Bayesian optimization to compare the results of *in vitro* and *in silico* experiments—has allowed to identify the key parameters that regulates individual 3D fibroblast migration embedded in a collagen-based matrix. In particular, this novel methodology has been applied during the development of a stochastic model that simulates a chemically reacting system based on the biochemical interaction between the PDGF and a specific type of cell surface receptors, the RTKs. This interaction, in turn, triggers a metabolic cascade of internal signaling that activates a cellular chemosensing mechanism. Moreover, the model's calibration has been proven to be a valid and not an overfitted one during the final validation process. In order to validate the selected parametrization, we have simulated cell migration with a diffused chemoattractant factor throughout the ECM and qualitatively compare observations based on cell's velocity in the direction of the chemotactic gradient with results from previous experimental works (Song et al., 2006; Bosgraaf and Van Haastert, 2009). Our results are in agreement with those from *in vitro* experiments, cells follow a more directional motion as the chemoattractant gradient increases. However, when the chemoattractant concentration surrounding the cell reaches a saturation point cells start to lose the ability to sense the chemical cues.

In conclusion, the tau leaping algorithm allows to optimize the performance of stochastic models based on biochemical kinetics by greatly reducing the execution time of its simulations. In addition, by means of Bayesian optimization it is possible to perform model parameters calibration in a very efficient and completely automatic way. As a result, this novel methodology will improve the development of *in silico* models for a better understanding of cell migration.

## AUTHOR CONTRIBUTIONS

FM-C, MG-B, and JG-A designed research; FM-C, MG-B, YJ-L, and JG-A performed research; YJ-L performed *in vitro* experiments, FM-C, MG-B, RM-C, and JG-A analyzed data; FM-C, MG-B, YJ-L, RM-C, and JG-A wrote the paper; FM-C, MG-B, and RM-C defined Bayesian optimization setup and FM-C built a code for the model and performed all simulations.

## FUNDING

FM-C was supported by Spanish Ministry of Economy and Competitiveness (Grant no: BES-2016-076291). MG-B, YJ-L, and JG-A were supported by the European Research Council (Grant no: ERC2012-StG306571) and the Spanish Ministry of Economy



and Competitiveness (Grant no: DPI2015-64221-C2-1-R). RM-C was supported by the Spanish Ministry of Economy and Competitiveness (Grant no: DPI2015-65962-R).

## ACKNOWLEDGMENTS

The authors would like to acknowledge Frederico O. Ribeiro assistance during the model's development and SigOpt Inc. for

their assistance and support with their Bayesian optimization framework.

## SUPPLEMENTARY MATERIAL

The Supplementary Material for this article can be found online at: <https://www.frontiersin.org/articles/10.3389/fphys.2018.01246/full#supplementary-material>

## REFERENCES

- Alber, M., Chen, N., Lushnikov, P. M., and Newman, S. A. (2007). continuous macroscopic limit of a discrete stochastic model for interaction of living cells. *Phys. Rev. Lett.* 99:168102. doi: 10.1103/PhysRevLett.99.168102
- Anderson, D. F., Ganguly, A., and Kurtz, T. G. (2011). Error analysis of tau-leap simulation methods. *Ann. Appl. Probab.* 21, 2226–2262. doi: 10.1214/10-AAP756
- Bauer, A. L., Jackson, T. L., and Jiang, Y. (2009). Topography of extracellular matrix mediates vascular morphogenesis and migration speeds in angiogenesis. *PLoS Comput. Biol.* 5:e1000445. doi: 10.1371/journal.pcbi.1000445
- Bazmara, H., Soltani, M., Sefidgar, M., Bazargan, M., Mousavi Naenian, M., and Rahmim, A. (2015). The vital role of blood flow-induced proliferation and migration in capillary network formation in a multiscale model of angiogenesis. *PLoS ONE* 10:e0128878. doi: 10.1371/journal.pone.0128878
- Bear, J. E., and Haugh, J. M. (2014). Directed migration of mesenchymal cells: where signaling and the cytoskeleton meet. *Curr. Opin. Cell Biol.* 30, 74–82. doi: 10.1016/j.CEB.2014.06.005
- Beauchemin, C., Dixit, N. M., and Perelson, A. S. (2007). Characterizing T cell movement within lymph nodes in the absence of antigen. *J. Immunol.* 178, 5505–5512. doi: 10.4049/JIMMUNOL.178.9.5505
- Bentley, K., Mariggi, G., Gerhardt, H., and Bates, P. A. (2009). Tipping the balance: robustness of tip cell selection, migration and fusion in angiogenesis. *PLoS Comput. Biol.* 5:e1000549. doi: 10.1371/journal.pcbi.1000549
- Bogle, G., and Dunbar, P. R. (2010). T cell responses in lymph nodes. *Wiley Interdiscip. Rev. Syst. Biol. Med.* 2, 107–116. doi: 10.1002/wsbm.47
- Borau, C., Kamm, R. D., and García-Aznar, J. M. (2011). Mechano-sensing and cell migration: a 3D model approach. *Phys. Biol. Phys. Biol. Phys. Biol.* 8, 66008–66013. doi: 10.1088/1478-3975/8/6/066008
- Borau, C., Kim, T., Bidone, T., García-Aznar, J. M., and Kamm, R. D. (2012). Dynamic mechanisms of cell rigidity sensing: insights from a computational model of actomyosin networks. *PLoS ONE* 7:e49174. doi: 10.1371/journal.pone.0049174
- Bosgraaf, L., and Van Haastert, P. J. M. (2009). Navigation of chemotactic cells by parallel signaling to pseudopod persistence and orientation. *PLoS ONE* 4:e6842. doi: 10.1371/journal.pone.0006842
- Brochu, E., Brochu, T., and de Freitas, N. (2010). “A Bayesian interactive optimization approach to procedural animation design,” in *Proc. 2010 ACM SIGGRAPH/Eurographics Symp. Comput. Animat.* (Madrid), 103–112.
- Camley, B. A., and Rappel, W.-J. (2017). Physical models of collective cell motility: from cell to tissue. *J. Phys. D Appl. Phys.* 50:113002. doi: 10.1088/1361-6463/aa56fe
- Campellone, K. G., and Welch, M. D. (2010). A nucleator arms race: cellular control of actin assembly. *Nat. Rev. Mol. Cell Biol.* 11, 237–251. doi: 10.1038/nrm2867
- Cao, R., Björndahl, M. A., Religa, P., Clasper, S., Garvin, S., Galter, D., et al. (2004). PDGF-BB induces intratumoral lymphangiogenesis and promotes lymphatic metastasis. *Cancer Cell* 6, 333–345. doi: 10.1016/j.CCR.2004.08.034
- Cao, Y., Gillespie, D. T., and Petzold, L. R. (2006). Efficient step size selection for the tau-leaping simulation method. *J. Chem. Phys.* 124:044109. doi: 10.1063/1.2159468
- Cazzaniga, P., Pescini, D., Besozzi, D., and Mauri, G. (2006). *Tau Leaping Stochastic Simulation Method in P Systems*. Berlin; Heidelberg: Springer Berlin Heidelberg.
- Chen, J., Weihs, D., and Vermolen, F. J. (2017). A model for cell migration in non-isotropic fibrin networks with an application to pancreatic tumor islets. *Biomech. Model. Mechanobiol.* 17, 367–386. doi: 10.1007/s10237-017-0966-7
- Chen, R. R., Silva, E. A., Yuen, W. W., and Mooney, D. J. (2007). Spatio-temporal VEGF and PDGF delivery patterns blood vessel formation and maturation. *Pharm. Res.* 24, 258–264. doi: 10.1007/s11095-006-9173-4
- Comaniciu, D., Ramesh, V., and Meer, P. (2000). “Real-time tracking of non-rigid objects using mean shift,” in *Proceedings IEEE Conference on Computer Vision and Pattern Recognition, CVPR 2000 (Cat. No. PR00662)* (Hilton Head Island, SC: IEEE Comput. Soc), 142–149.
- Condeelis, J., and Pollard, J. W. (2006). Macrophages: obligate partners for tumor cell migration, invasion, and metastasis. *Cell* 124, 263–266. doi: 10.1016/j.CELL.2006.01.007
- Condeelis, J., Singer, R. H., and Segall, J. E. (2005). THE GREAT ESCAPE: when cancer cells hijack the genes for chemotaxis and motility. *Annu. Rev. Cell Dev. Biol.* 21, 695–718. doi: 10.1146/annurev.cellbio.21.122303.120306
- Cukierman, E., Pankov, R., Stevens, D. R., and Yamada, K. M. (2001). Taking cell-matrix adhesions to the third dimension. *Science* 294, 1708–1712. doi: 10.1126/science.1064829
- Czarnecki, W. M., Podlowska, S., and Bojarski, A. J. (2015). Robust optimization of SVM hyperparameters in the classification of bioactive compounds. *J. Cheminform.* 7:38. doi: 10.1186/s13321-015-0088-0
- Daub, J. T., and Merks, R. M. H. (2013). A cell-based model of extracellular-matrix-guided endothelial cell migration during angiogenesis. *Bull. Math. Biol.* 75, 1377–1399. doi: 10.1007/s11538-013-9826-5
- Del Amo, C., Borau, C., Movilla, N., Asín, J., and García-Aznar, J. M. (2017). Quantifying 3D chemotaxis in microfluidic-based chips with step gradients of collagen hydrogel concentrations. *Integr. Biol.* 9, 339–349. doi: 10.1039/C7IB00022G
- Devreotes, P., and Janetopoulos, C. (2003). Eukaryotic chemotaxis: distinctions between directional sensing and polarization. *J. Biol. Chem.* 278, 20445–20448. doi: 10.1074/jbc.R300010200
- Elangovan, S., D’Mello, S. R., Hong, L., Ross, R. D., Allamargot, C., Dawson, D. V., et al. (2014). The enhancement of bone regeneration by gene activated matrix encoding for platelet derived growth factor. *Biomaterials* 35, 737–747. doi: 10.1016/j.BIOMATERIALS.2013.10.021
- Escribano, J., Sánchez, M. T., and García-Aznar, J. M. (2015). Modeling the formation of cell-matrix adhesions on a single 3D matrix fiber. *J. Theor. Biol.* 384, 84–94. doi: 10.1016/j.JTBI.2015.07.015
- Escribano, J., Sunyer, R., Sánchez, M. T., Trepát, X., Roca-Cusachs, P., and García-Aznar, J. M. (2018). A hybrid computational model for collective cell durotaxis. *Biomech. Model. Mechanobiol.* 17, 1037–1052. doi: 10.1007/s10237-018-1010-2
- Eshelby, J. D. (1957). The determination of the elastic field of an ellipsoidal inclusion, and related problems. *Proc. R. Soc. A Math. Phys. Eng. Sci.* 241, 376–396. doi: 10.1098/rspa.1957.0133
- Fraleigh, S., Feng, Y., Krishnamurthy, R., Kim, D. H., Celedon, A., Longmore, G. D. D., et al. (2010). A distinctive role for focal adhesion proteins in three-dimensional cell motility. *Nat. Cell Biol.* 12, 598–604. doi: 10.1038/ncb2062
- Franz, C. M., Jones, G. E., and Ridley, A. J. (2002). Cell migration in development and disease. *Dev. Cell* 2, 153–158. doi: 10.1016/S1534-5807(02)00120-X
- Friedl, P., and Wolf, K. (2010). Plasticity of cell migration: a multiscale tuning model. *J. Cell Biol.* 188, 11–19. doi: 10.1083/jcb.200909003
- Friedlaender, G. E., Lin, S., Solchaga, L. A., Snel, L. B., and Lynch, S. E. (2013). The role of recombinant human platelet-derived growth factor-BB (rhPDGF-BB) in orthopaedic bone repair and regeneration. *Curr. Pharm. Des.* 19, 3384–3390. doi: 10.2174/1381612811319190005
- Gillespie, D. T. (1976). A general method for numerically simulating the stochastic time evolution of coupled chemical reactions. *J. Comput. Phys.* 22, 403–434. doi: 10.1016/0021-9991(76)90041-3

- Gillespie, D. T. (1977). Exact stochastic simulation of coupled chemical reactions. *J. Phys. Chem.* 81, 2340–2361. doi: 10.1021/j100540a008
- Gillespie, D. T. (2001). Approximate accelerated stochastic simulation of chemically reacting systems. *J. Chem. Phys.* 115, 1716–1733. doi: 10.1063/1.1378322
- Gillespie, D. T. (2007). Stochastic simulation of chemical kinetics. *Annu. Rev. Phys. Chem.* 58, 35–55. doi: 10.1146/annurev.physchem.58.032806.104637
- González-Valverde, I., and García-Aznar, J. M. (2018). Mechanical modeling of collective cell migration: an agent-based and continuum material approach. *Comput. Methods Appl. Mech. Eng.* 337, 246–262. doi: 10.1016/j.cma.2018.03.036
- González-Valverde, I., Semino, C., and García-Aznar, J. M. (2016). Phenomenological modelling and simulation of cell clusters in 3D cultures. *Comput. Biol. Med.* 77, 249–260. doi: 10.1016/j.compbiomed.2016.08.019
- Hansen, N., Müller, S. D., and Koumoutsakos, P. (2003). Reducing the time complexity of the derandomized evolution strategy with Covariance Matrix Adaptation (CMA-ES). *Evol. Comput.* 11, 1–18. doi: 10.1162/106365603321828970
- Hatakeyama, M., Kimura, S., Naka, T., Kawasaki, T., Yumoto, N., Ichikawa, M., et al. (2003). A computational model on the modulation of mitogen-activated protein kinase (MAPK) and Akt pathways in heregulin-induced ErbB signalling. *Biochem. J.* 373, 451–463. doi: 10.1042/BJ20021824
- Hawkins, P. T., Anderson, K. E., Davidson, K., and Stephens, L. R. (2006). Signalling through Class I PI3Ks in mammalian cells. *Biochem. Soc. Trans.* 34, 647–662. doi: 10.1042/BST0340647
- Heinecke, K., Seher, A., Schmitz, W., Mueller, T. D., Sebald, W., and Nickel, J. (2009). Receptor oligomerization and beyond: a case study in bone morphogenetic proteins. *BMC Biol.* 7:59. doi: 10.1186/1741-7007-7-59
- Higazi, A. A., Kniss, D., Manuppello, J., Barnathan, E. S., and Cines, D. B. (1996). Thermotaxis of human trophoblastic cells. *Placenta* 17, 683–687. doi: 10.1016/S0143-4004(96)80019-1
- Jilkine, A., and Edelstein-Keshet, L. (2011). A Comparison of mathematical models for polarization of single eukaryotic cells in response to guided cues. *PLoS Comput. Biol.* 7:e1001121. doi: 10.1371/journal.pcbi.1001121
- Jones, D. R., Schonlau, M., and Welch, W. J. (1998). Efficient global optimization of expensive black-box functions. *J. Glob. Optim.* 13, 455–492. doi: 10.1023/A:1008306431147
- Jones, E., Oliphant, T., and Peterson, P. (2001). *{SciPy}: Open Source Scientific Tools for {Python}*. Available online at: <https://www.scipy.org/citing.html>
- Kass, R. E., and Raftery, A. E. (1995). Bayes factors. *J. Am. Stat. Assoc.* 90:773. doi: 10.2307/2291091
- Kennedy, J., and Eberhart, R. (1995). “Particle swarm optimization,” in *Proceedings of IEEE International Conference on Neural Networks (ICNN)* (Nagoya: IEEE), 1942–1948.
- Kim, M. C., Silberberg, Y. R., Abeyaratne, R., Kamm, R. D., and Asada, H. H. (2018). Computational modeling of three-dimensional ECM-rigidity sensing to guide directed cell migration. *Proc. Natl. Acad. Sci. U.S.A.* 115, E390–E399. doi: 10.1073/pnas.1717230115
- Kim, M. C., Whisler, J., Silberberg, Y. R., Kamm, R. D., and Asada, H. H. (2015). Cell invasion dynamics into a three dimensional extracellular matrix fibre network. *PLOS Comput. Biol.* 11:e1004535. doi: 10.1371/journal.pcbi.1004535
- Knecht, A. K., and Bronner-Fraser, M. (2002). Induction of the neural crest: a multigene process. *Nat. Rev. Genet.* 3, 453–461. doi: 10.1038/nrg819
- Knowles, J. (2006). ParEGO: a hybrid algorithm with on-line landscape approximation for expensive multiobjective optimization problems. *IEEE Trans. Evol. Comput.* 10, 50–66. doi: 10.1109/TEVC.2005.851274
- Lamallice, L., Le Boeuf, F., and Huot, J. (2007). Endothelial cell migration during angiogenesis. *Circ. Res.* 100, 782–794. doi: 10.1161/01.RES.0000259593.07661.1e
- Lämmermann, T., Bader, B. L., Monkley, S. J., Worbs, T., Wedlich-Söldner, R., Hirsch, K., et al. (2008). Rapid leukocyte migration by integrin-independent flowing and squeezing. *Nature* 453, 51–55. doi: 10.1038/nature06887
- Li, T., Gu, Y. T., Oloyede, A., and Yarlagadda, P. K. (2014). Molecular investigation of the mechanical properties of single actin filaments based on vibration analyses. *Comput. Methods Biomech. Biomed. Eng.* 17, 616–622. doi: 10.1080/10255842.2012.706279
- Liou, Y. R., Torng, W., Kao, Y. C., Sung, K. B., Lee, C. H., and Kuo, P. L. (2014). Substrate stiffness regulates filopodial activities in lung cancer cells. *PLoS ONE* 9:e89767. doi: 10.1371/journal.pone.0089767
- Lok, L. (2004). The need for speed in stochastic simulation. *Nat. Biotechnol.* 22, 964–965. doi: 10.1038/nbt0804-964
- Luster, A. D., Alon, R., and von Andrian, U. H. (2005). Immune cell migration in inflammation: present and future therapeutic targets. *Nat. Immunol.* 6, 1182–1190. doi: 10.1038/ni1275
- Mak, M., Spill, F., Kamm, R. D., and Zaman, M. H. (2016). Single-cell migration in complex microenvironments: mechanics and signaling dynamics. *J. Biomech. Eng.* 138:021004. doi: 10.1115/1.4032188
- Mark, C., Metzner, C., Lautscham, L., Strissel, P. L., Strick, R., and Fabry, B. (2018). Bayesian model selection for complex dynamic systems. *Nat. Commun.* 9:1803. doi: 10.1038/s41467-018-04241-5
- Martin, P., and Parkhurst, S. M. (2004). Parallels between tissue repair and embryo morphogenesis. *Development* 131, 3021–3034. doi: 10.1242/dev.01253
- Martinez-Cantin, R. (2014). BayesOpt: a bayesian optimization library for nonlinear optimization, experimental design and bandits. *J. Mach. Learn. Res.* 15, 3915–3919. Available online at: <http://www.jmlr.org/papers/v15/martinezcantin14a.html>
- Martinez-Cantin, R., de Freitas, N., Brochu, E., Castellanos, J., and Doucet, A. (2009). A Bayesian exploration-exploitation approach for optimal online sensing and planning with a visually guided mobile robot. *Auton. Robots* 27, 93–103. doi: 10.1007/s10514-009-9130-2
- Martinez-Cantin, R., Tee, K., and McCourt, M. (2018). “Practical Bayesian optimization in the presence of outliers,” in *International Conference on Artificial Intelligence and Statistics (AISTATS)* (Lanzarote).
- Meineke, F. A., Potten, C. S., and Loeffler, M. (2001). Cell migration and organization in the intestinal crypt using a lattice-free model. *Cell Prolif.* 34, 253–266. doi: 10.1046/j.0960-7722.2001.00216.x
- Milde, F., Tauriello, G., Haberkern, H., and Koumoutsakos, P. (2014). SEM++: a particle model of cellular growth, signaling and migration. *Comput. Particle Mech.* 1, 211–227. doi: 10.1007/s40571-014-0017-4
- Mofrad, M., and Kamm, R. (eds.). (2006). *Cytoskeletal Mechanics: Models and Measurements in Cell Mechanics (Cambridge Texts in Biomedical Engineering)*. Cambridge: Cambridge University Press.
- Moreno-Arotzena, O., Borau, C., Movilla, N., Vicente-Manzanares, M., and García-Aznar, J. M. (2015). Fibroblast migration in 3D is controlled by haptotaxis in a non-muscle myosin II-dependent manner. *Ann. Biomed. Eng.* 43, 3025–3039. doi: 10.1007/s10439-015-1343-2
- Moreno-Arotzena, O., Mendoza, G., Córdor, M., Rübreg, T., and García-Aznar, J. M. (2014). Inducing chemotactic and haptotactic cues in microfluidic devices for three-dimensional *in vitro* assays. *Biomicrofluidics* 8:064122. doi: 10.1063/1.4903948
- Moure, A., and Gomez, H. (2017). Phase-field model of cellular migration: three-dimensional simulations in fibrous networks. *Comput. Methods Appl. Mech. Eng.* 320, 162–197. doi: 10.1016/j.cma.2017.03.025
- Moure, A., and Gomez, H. (2018). Three-dimensional simulation of obstacle-mediated chemotaxis. *Biomech. Model. Mechanobiol.* doi: 10.1007/s10237-018-1023-x. [Epub ahead of print].
- Movilla, N., Borau, C., Valero, C., and García-Aznar, J. M. (2018). Degradation of extracellular matrix regulates osteoblast migration: a microfluidic-based study. *Bone* 107, 10–17. doi: 10.1016/j.bone.2017.10.025
- Nielsen, F. (2014). Generalized Bhattacharyya and Chernoff upper bounds on Bayes error using quasi-arithmetic means. *Pattern Recognit. Lett.* 42, 25–34. doi: 10.1016/j.patrec.2014.01.002
- Nocedal, J. (1980). Updating quasi-Newton matrices with limited storage. *Math. Comput.* 35, 773–773. doi: 10.1090/S0025-5718-1980-0572855-7
- Norton, K. A., and Popel, A. S. (2016). Effects of endothelial cell proliferation and migration rates in a computational model of sprouting angiogenesis. *Sci. Rep.* 6:36992. doi: 10.1038/srep36992
- Paralkar, V. M., Weeks, B. S., Yu, Y. M., Kleinman, H. K., and Reddi, A. H. (1992). Recombinant human bone morphogenetic protein 2B stimulates PC12 cell differentiation: potentiation and binding to type IV collagen. *J. Cell Biol.* 119, 1721–1728. doi: 10.1083/JCB.119.6.1721
- Paul, C. D., Hung, W. C., Wirtz, D., and Konstantopoulos, K. (2016). Engineered models of confined cell migration. *Annu. Rev. Biomed. Eng.* 18, 159–180. doi: 10.1146/annurev-bioeng-071114-040654
- Poukkula, M., Cliffe, A., Changede, R., and Rørth, P. (2011). Cell behaviors regulated by guidance cues in collective migration of border cells. *J. Cell Biol.* 192, 513–524. doi: 10.1083/jcb.201010003

- Provenzano, P. P., Inman, D. R., Eliceiri, K. W., Trier, S. M., and Keely, P. J. (2008). Contact guidance mediated three-dimensional cell migration is regulated by Rho/ROCK-dependent matrix reorganization. *Biophys. J.* 95, 5374–5384. doi: 10.1529/BIOPHYSJ.108.133116
- Rangarajan, R., and Zaman, M. H. (2008). Modeling cell migration in 3D. *Cell Adh. Migr.* 2, 106–109. doi: 10.4161/cam.2.2.6211
- Reina-Romo, E., Gómez-Benito, M. J., Dominguez, J., and García-Aznar, J. M. (2012). A lattice-based approach to model distraction osteogenesis. *J. Biomech.* 45, 2736–2742. doi: 10.1016/j.jbiomech.2012.09.004
- Ribeiro, F. O., Gómez-Benito, M. J., Folgado, J., Fernandes, P. R., and García-Aznar, J. M. (2017). Computational model of mesenchymal migration in 3D under chemotaxis. *Comput. Methods Biomech. Biomed. Eng.* 20, 59–74. doi: 10.1080/10255842.2016.1198784
- Roca-Cusachs, P., Sunyer, R., and Trepas, X. (2013). Mechanical guidance of cell migration: lessons from chemotaxis. *Curr. Opin. Cell Biol.* 25, 543–549. doi: 10.1016/j.CEB.2013.04.010
- Saltelli, A. (2002). Sensitivity analysis for importance assessment. *Risk Anal.* 22, 579–590. doi: 10.1111/0272-4332.00040
- Saltzman, E. A., Drew, J. H., Leemis, L. M., and Henderson, S. G. (2012). Simulating multivariate nonhomogeneous poisson processes using projections. *ACM Trans. Model. Comput. Simul.* 22, 1–13. doi: 10.1145/2331140.2331143
- Schlüter, D. K., Ramis-Conde, I., and Chaplain, M. A. (2012). Computational modeling of single-cell migration: the leading role of extracellular matrix fibers. *Biophys. J.* 103, 1141–1151. doi: 10.1016/j.BPJ.2012.07.048
- Scianna, M., and Preziosi, L. (2014). A cellular Potts model for the MMP-dependent and -independent cancer cell migration in matrix microtracks of different dimensions. *Comput. Mech.* 53, 485–497. doi: 10.1007/s00466-013-0944-6
- Scianna, M., Preziosi, L., and Wolf, K. (2012). A Cellular Potts model simulating cell migration on and in matrix environments. *Math. Biosci. Eng.* 10, 235–261. doi: 10.3934/mbe.2013.10.235
- Serrano-Alcalde, F., García-Aznar, J. M., and Gómez-Benito, M. J. (2017). The role of nuclear mechanics in cell deformation under creeping flows. *J. Theor. Biol.* 432, 25–32. doi: 10.1016/j.JTBI.2017.07.028
- Shah, P., Keppler, L., and Rutkowski, J. (2014). A review of platelet derived growth factor playing pivotal role in bone regeneration. *J. Oral Implantol.* 40, 330–340. doi: 10.1563/AAID-JOI-D-11-00173
- Shahriari, B., Swersky, K., Wang, Z., Adams, R. P., and de Freitas, N. (2016). Taking the human out of the loop: a review of bayesian optimization. *Proc. IEEE* 104, 148–175. doi: 10.1109/JPROC.2015.2494218
- Shaw, T. J., and Martin, P. (2009). Wound repair at a glance. *J. Cell Sci.* 122, 3209–3213. doi: 10.1242/jcs.031187
- Snoek, J., Larochelle, H., and Adams, R. P. (2012). “Practical Bayesian optimization of machine learning algorithms,” in *Conference on Neural Information Processing Systems (NIPS)* (Lake Tahoe, NV).
- Song, L., Nadkarni, S. M., Bödeker, H. U., Beta, C., Bae, A., Franck, C., et al. (2006). Dictyostelium discoideum chemotaxis: threshold for directed motion. *Eur. J. Cell Biol.* 85, 981–989. doi: 10.1016/j.EJCB.2006.01.012
- Spill, F., Guerrero, P., Alarcon, T., Maini, P. K., and Byrne, H. M. (2015). Mesoscopic and continuum modelling of angiogenesis. *J. Math. Biol.* 70, 485–532. doi: 10.1007/s00285-014-0771-1
- Starke, J., Maaser, K., Wehrle-Haller, B., and Friedl, P. (2013). Mechanotransduction of mesenchymal melanoma cell invasion into 3D collagen lattices: filopod-mediated extension-relaxation cycles and force anisotropy. *Exp. Cell Res.* 319, 2424–2433. doi: 10.1016/J.YEXCR.2013.04.003
- Sun, M., and Zaman, M. H. (2017). Modeling, signaling and cytoskeleton dynamics: integrated modeling-experimental frameworks in cell migration. *Wiley Interdiscip. Rev. Syst. Biol. Med.* 9:e1365. doi: 10.1002/wsbm.1365
- Sunyer, R., Conte, V., Escribano, J., Elosegui-Artola, A., Labernadie, A., Valon, L., et al. (2016). Collective cell durotaxis emerges from long-range intercellular force transmission. *Science* 353, 1157–1161. doi: 10.1126/science.aaf7119
- Swaney, K. F., Huang, C. H., and Devreotes, P. N. (2010). Eukaryotic chemotaxis: a network of signaling pathways controls motility, directional sensing, and polarity. *Annu. Rev. Biophys.* 39, 265–289. doi: 10.1146/annurev.biophys.093008.131228
- Talkenberger, K., Cavalcanti-Adam, E. A., Voss-Böhme, A., and Deutsch, A. (2017). Amoeboid-mesenchymal migration plasticity promotes invasion only in complex heterogeneous microenvironments. *Sci. Rep.* 7:9237. doi: 10.1038/s41598-017-09300-3
- Te Boekhorst, V., Preziosi, L., and Friedl, P. (2016). Plasticity of cell migration *in vivo* and *in silico*. *Annu. Rev. Cell Dev. Biol.* 32, 491–526. doi: 10.1146/annurev-cellbio-111315-125201
- Trichet, L., Le Digabel, J., Hawkins, R. J., Vedula, S. R., Gupta, M., Ribault, C., et al. (2012). Evidence of a large-scale mechanosensing mechanism for cellular adaptation to substrate stiffness. *Proc. Natl. Acad. Sci. U.S.A.* 109, 6933–6938. doi: 10.1073/pnas.1117810109
- Ueda, M., and Shibata, T. (2007). Stochastic signal processing and transduction in chemotactic response of eukaryotic cells. *Biophys. J.* 93, 11–20. doi: 10.1529/BIOPHYSJ.106.100263
- Ulmasov, D., Baroukh, C., Chachuat, B., Deisenroth, M. P., and Misener, R. (2016). Bayesian optimization with dimension scheduling: application to biological systems. *Comput. Aided Chem. Eng.* 38, 1051–1056. doi: 10.1016/B978-0-444-63428-3.50180-6
- Valero, C., Amaveda, H., Mora, M., and García-Aznar, J. M. (2018). Combined experimental and computational characterization of crosslinked collagen-based hydrogels. *PLoS ONE* 13:e0195820. doi: 10.1371/journal.pone.0195820
- Valero, C., Javierre, E., García-Aznar, J. M., and Gómez-Benito, M. J. (2014a). A cell-regulatory mechanism involving feedback between contraction and tissue formation guides wound healing progression. *PLoS ONE* 9:e92774. doi: 10.1371/journal.pone.0092774
- Valero, C., Javierre, E., García-Aznar, J. M., and Gómez-Benito, M. J. (2014b). Nonlinear finite element simulations of injuries with free boundaries: application to surgical wounds. *Int. J. Numer. Methods Biomed. Eng.* 30, 616–633. doi: 10.1002/cnm.2621
- van der Walt, S., Colbert, S. C., and Varoquaux, G. (2011). The NumPy array: a structure for efficient numerical computation. *Comput. Sci. Eng.* 13, 22–30. doi: 10.1109/MCSE.2011.37
- Van Liedekerke, P., Palm, M. M., Jagiella, N., and Drasdo, D. (2015). Simulating tissue mechanics with agent-based models: concepts, perspectives and some novel results. *Comput. Particle Mech.* 2, 401–444. doi: 10.1007/s40571-015-0082-3
- Vermolen, F. J., and Javierre, E. (2012). A finite-element model for healing of cutaneous wounds combining contraction, angiogenesis and closure. *J. Math. Biol.* 65, 967–996. doi: 10.1007/s00285-011-0487-4
- Weiger, M. C., Ahmed, S., Welf, E. S., and Haugh, J. M. (2010). Directional persistence of cell migration coincides with stability of asymmetric intracellular signaling. *Biophys. J.* 98, 67–75. doi: 10.1016/J.BPJ.2009.09.051
- Wolf, K., Te Lindert, M., Krause, M., Alexander, S., Te Riet, J., Willis, A. L., et al. (2013). Physical limits of cell migration: control by ECM space and nuclear deformation and tuning by proteolysis and traction force. *J. Cell Biol.* 201, 1069–1084. doi: 10.1083/jcb.201210152
- Zaman, M. H., Kamm, R. D., Matsudaira, P., and Lauffenburger, D. A. (2005). Computational model for cell migration in three-dimensional matrices. *Biophys. J.* 89, 1389–1397. doi: 10.1529/BIOPHYSJ.105.060723
- Zhu, J., and Mogilner, A. (2016). Comparison of cell migration mechanical strategies in three-dimensional matrices: a computational study. *Interface Focus* 6:20160040. doi: 10.1098/rsfs.2016.0040

**Conflict of Interest Statement:** RM-C was employed by company SigOpt, Inc.

The remaining authors declare that the research was conducted in the absence of any commercial or financial relationships that could be construed as a potential conflict of interest.

The reviewer AL and handling editor declared their shared affiliation at the time of the review.

Copyright © 2018 Merino-Casallo, Gomez-Benito, Juste-Lanas, Martinez-Cantin and Garcia-Aznar. This is an open-access article distributed under the terms of the Creative Commons Attribution License (CC BY). The use, distribution or reproduction in other forums is permitted, provided the original author(s) and the copyright owner(s) are credited and that the original publication in this journal is cited, in accordance with accepted academic practice. No use, distribution or reproduction is permitted which does not comply with these terms.



# The Importance of Biophysical and Biochemical Stimuli in Dynamic Skeletal Muscle Models

**Babette Maleiner<sup>1,2</sup>, Janine Tomasch<sup>1,2</sup>, Philipp Heher<sup>2,3,4</sup>, Oliver Spadiut<sup>5</sup>, Dominik Rünzler<sup>1,2</sup> and Christiane Fuchs<sup>1,2\*</sup>**

## OPEN ACCESS

### Edited by:

Alberto Rainer,  
Università Campus Bio-Medico, Italy

### Reviewed by:

Cesare Gargioli,  
Università degli Studi di Roma Tor  
Vergata, Italy  
Sara Maria Giannitelli,  
Università Campus Bio-Medico, Italy  
Carmen Escobedo-Lucea,  
University of Helsinki, Finland

### \*Correspondence:

Christiane Fuchs  
cfuchs1@mgh.harvard.edu

### †Present Address:

Christiane Fuchs,  
Wellman Center for Photomedicine,  
Massachusetts General Hospital,  
Boston, MA, United States

### Specialty section:

This article was submitted to  
Integrative Physiology,  
a section of the journal  
Frontiers in Physiology

**Received:** 18 December 2017

**Accepted:** 30 July 2018

**Published:** 22 August 2018

### Citation:

Maleiner B, Tomasch J, Heher P,  
Spadiut O, Rünzler D and Fuchs C  
(2018) The Importance of Biophysical  
and Biochemical Stimuli in Dynamic  
Skeletal Muscle Models.  
*Front. Physiol.* 9:1130.  
doi: 10.3389/fphys.2018.01130

<sup>1</sup> Department of Biochemical Engineering, University of Applied Sciences Technikum Wien, Vienna, Austria, <sup>2</sup> The Austrian Cluster for Tissue Regeneration, Vienna, Austria, <sup>3</sup> Ludwig Boltzmann Institute for Experimental and Clinical Traumatology/AUVA Research Center, Vienna, Austria, <sup>4</sup> Trauma Care Consult GmbH, Vienna, Austria, <sup>5</sup> Institute of Chemical Engineering, Vienna University of Technology, Vienna, Austria

Classical approaches to engineer skeletal muscle tissue based on current regenerative and surgical procedures still do not meet the desired outcome for patient applications. Besides the evident need to create functional skeletal muscle tissue for the repair of volumetric muscle defects, there is also growing demand for platforms to study muscle-related diseases, such as muscular dystrophies or sarcopenia. Currently, numerous studies exist that have employed a variety of biomaterials, cell types and strategies for maturation of skeletal muscle tissue in 2D and 3D environments. However, researchers are just at the beginning of understanding the impact of different culture settings and their biochemical (growth factors and chemical changes) and biophysical cues (mechanical properties) on myogenesis. With this review we intend to emphasize the need for new *in vitro* skeletal muscle (disease) models to better recapitulate important structural and functional aspects of muscle development. We highlight the importance of choosing appropriate system components, e.g., cell and biomaterial type, structural and mechanical matrix properties or culture format, and how understanding their interplay will enable researchers to create optimized platforms to investigate myogenesis in healthy and diseased tissue. Thus, we aim to deliver guidelines for experimental designs to allow estimation of the potential influence of the selected skeletal muscle tissue engineering setup on the myogenic outcome prior to their implementation. Moreover, we offer a workflow to facilitate identifying and selecting different analytical tools to demonstrate the successful creation of functional skeletal muscle tissue. Ultimately, a refinement of existing strategies will lead to further progression in understanding important aspects of muscle diseases, muscle aging and muscle regeneration to improve quality of life of patients and enable the establishment of new treatment options.

**Keywords:** skeletal muscle tissue engineering, stimulation strategies, bioreactors, myokines, skeletal muscle disease models, biomaterials, myogenesis

## INTRODUCTION

The field of regenerative medicine and tissue engineering (TE) is still one of the fastest growing research areas in biomedical science. Previous TE efforts mostly focused on tissues and organs that are associated with diseases occurring at high frequencies in 1<sup>st</sup> world countries, such as the heart and the musculoskeletal apparatus with a strong emphasis on bone, cartilage, and ligaments. Muscle tissue, which for long has been relatively neglected, has gained more attention in the TE community recently. The view on muscle evolved from being the tissue mainly responsible for locomotion, thermogenesis and postural support to an endocrine organ able to secrete cytokines (termed myokines) that exert beneficial effects on surrounding tissues (Pedersen, 2011).

Tissue-specific stem cells, termed satellite cells (Beauchamp et al., 2000; Zammit et al., 2004; Yin et al., 2013; Han et al., 2016) are responsible for maintaining the regenerative capacity of skeletal muscle. Upon injury, satellite cells can re-enter the cell cycle, proliferate and either fuse to existing myofibers or generate myofibers *de novo*. Since their discovery in 1961 (Katz, 1961; Mauro, 1961), extensive research has been conducted on the regulatory mechanisms guiding satellite cell activity and their role in healthy and diseased muscle (Seale and Rudnicki, 2000; Zammit et al., 2004, 2006; Yin et al., 2013).

### Pathologic Muscle States and Muscle Loss

Skeletal muscle TE (SMTE) aims at the functional restoration of either lost, atrophic or impaired muscle tissue. Of late, the field has particularly emphasized using cellular and acellular therapeutic approaches for pathological muscle states such as muscular dystrophies, sarcopenia, or traumatic volumetric muscle loss. In the young, regeneration generally occurs efficiently as skeletal muscle can cope with slight injuries due to its high regenerative potential. However, regeneration is inefficient when trauma causes extensive damage or when the muscle is affected by a chronic pathology. This is especially severe in the elderly, where the regenerative capacity of muscle is diminished due to a decrease in the muscle stem cell pool. This leads to progressive replacement of muscle with scar and fat tissue, causing substantial deteriorations in muscle function and motility and thus quality of life. In addition, the loss of muscle associated with aging (sarcopenia) affects a growing number of patients as the global increase in life expectancy leads to population aging. Thus there is an unmet clinical need for approaches to restore or maintain muscle function, especially in the older population which is highly affected by muscle wasting and atrophy (Chargé and Rudnicki, 2004; Ryall et al., 2008; Carosio et al., 2011; Blau et al., 2015). In contrast to sarcopenia, genetic muscle diseases, such as muscular dystrophies (MDs), result in progressive muscle weakening and breakdown starting already in childhood or middle age. MDs are a group of more than 30 rare hereditary diseases caused by mutations leading to either a dysfunction in, or lack of proteins essential for muscle stability (Theadom et al., 2014; Smith et al., 2016). MDs greatly vary in the type of muscle affected (some forms of MD may affect cardiac muscle), extent of muscle weakness, the age of onset,

the rate of progression and the pattern of inheritance (Theadom et al., 2014).

Duchenne muscular dystrophy (DMD) is the most common MD affecting approximately 1 in 5,000 males (Goyenville et al., 2011; Mah et al., 2014; Romitti et al., 2015; Stark, 2015; Yiu and Kornberg, 2015). DMD is caused by the absence of functional dystrophin, either through deletion, point mutations, insertions or duplication. Dystrophin is a structural protein, which acts as a linker between the cytoskeleton (via the dystroglycan complex) and the surrounding extracellular matrix (ECM). Dystrophin stabilizes muscle cells under mechanical load and is essential for the maintenance of the intracellular structural organization of muscle cytoskeletal proteins in the contractile apparatus (Ervasti and Sonnemann, 2008; Constantin, 2014; Gawlik et al., 2014). Thus, lack of dystrophin predisposes muscle fibers to fragility in response to mechanical forces, leading to continuous cycles of muscle de- and regeneration (Serrano et al., 2011). Recent evidence additionally suggests that dystrophin is directly involved in regulating satellite cell behavior and that satellite cells from dystrophin knock out animals show lower proliferation rates as well as functional impairment (Sacco et al., 2010; Dumont et al., 2015b; Almada and Wagers, 2016; Dumont and Rudnicki, 2016). As a result, the muscle stem cell (satellite cell) pool is prematurely exhausted, a phenomenon somewhat analogous with aging (Webster and Blau, 1990), which eventually leads to muscle weakness, loss of motility and, in the worst case, premature death (Emery, 1993). Other MD types include Becker MD, a less severe variant of DMD, Emery-Dreifuss MD, facioscapulohumeral MD, congenital MD, limb-girdle MD or myotonic MD (Theadom et al., 2014).

To date, there is no cure for MDs. Although symptomatic treatments such as physical or drug therapies are used to delay disease progression, the prognosis for people with chronic muscle pathologies is poor. This creates a considerable world-wide socioeconomic burden for health systems, patients and caregivers alike. Sarcopenia accounts for roughly \$18.5 billion per year in direct healthcare costs in the U.S. (Janssen et al., 2004; Beaudart et al., 2014). A cross-sectional study in 2014 reported the mean annual direct costs per DMD patient to range from 23,920\$ to 54,270\$ in Europe and the U.S., which is 7 to 16 times higher than the mean annual per capita health expenditures in these countries (Landfeldt et al., 2014). A more recent study focusing on European DMD patients and their caregivers provided similar figures but identified direct non-healthcare costs as the main part of total annual costs (Cavazza et al., 2016).

In the past, research on regenerative therapies for diseased skeletal muscle mostly focused on methods to deliver healthy myogenic cells or to restore the endogenous myogenic potential of satellite cells (Dumont et al., 2015a). Although satellite cell transplantation holds great therapeutic potential for MDs, the vast number of cells needed for treatment and their phenotypic changes after prolonged *in vitro* culture limit this approach. In addition to the restoration of the stem cell pool and host myofiber repair, healthy myogenic donor cells can also act as vectors to (re)establish expression of normal (wild-type) alleles in the muscle fibers they fuse to (Partridge et al., 1989). However, the pathomechanisms leading to MD phenotypes, muscle wasting,

and atrophy are still not fully understood. In addition, the fact that some MD animal models do not faithfully recapitulate the respective disease creates another burden for translation of novel therapies into clinics. Therefore, tissue engineered *in vitro* muscle (disease) model systems can serve as an alternate pre-clinical approach to gain further insight into the molecular causes and potential treatments of chronic pathological muscle states.

## Skeletal Muscle TE

Current clinical strategies to restore muscle function are limited to symptomatic treatments and, consequently, healthcare costs are progressively rising; e.g., healthcare costs of direct and indirect traumatic injury in the year 2000 was greater than \$400 billion in the US (Corso et al., 2006). SMTE constitutes a promising tool to lower this immense socioeconomic burden, as it enables the creation of new muscle to replace lost tissue without the need of donor tissue. Furthermore, SMTE can be used to study muscle development, and the impact of biomaterials and mechanical cues on myogenesis and muscular disorders in *in vitro* (disease) models (Juhas et al., 2015). Conducting traditional studies on muscle biology in 3D settings, which more closely mimic the physiological microenvironment of the whole organ (Bursac et al., 2015), is the new state of the art in this rapidly growing field (Figure 1). However, so far, TE only successfully entered clinics when it comes to skin, bone or cartilage replacement and regeneration (Horch et al., 2000; Chang et al., 2003; Kojima et al., 2003; Kopp et al., 2004; Oakes, 2004; Vangness et al., 2004).

Current clinical approaches to compensate for lost skeletal muscle tissue are to transfer skeletal muscle tissue from other sites of the body to the area of injury (free functional muscle transfer). However, this causes donor site morbidity and an extra surgical procedure resulting in additional stress for the patient (Qazi et al., 2015). The gold standard is the use of freestanding flaps which include functional vessels as tissue grafts. Although free functional muscle transfer is still considered the best option for restoring function in otherwise non-reconstructable muscles, a return to pre-injury levels of muscle strength and functionality does not usually occur. Thus, many research groups are now focusing on *in vitro* SMTE, providing new remarkable data for this field, some of which will be discussed in more detail in the subsequent sections (Engler et al., 2004; Huang et al., 2004; Matsumoto et al., 2007; Lam et al., 2009; van der Schaft et al., 2013; Kurth et al., 2015; Bersini et al., 2016). To date, the majority of *in vitro* SMTE strategies aim at creating functional skeletal muscle tissue in the lab to offer new therapeutic possibilities for patients suffering from volumetric muscle loss, sarcopenia or genetic muscle disorders (Law et al., 1993; Guettier-Sigrist et al., 1998). Given the current clinical treatment limitations and the rising prevalence of pathological muscle states (especially sarcopenia), these patients would greatly benefit from further research on alternative therapeutic approaches.

Another approach is *in vivo* SMTE which involves introducing cells with myogenic potential (Bach et al., 2004), either as bolus injections or in combination with a scaffold biomaterial, into the site of injury to form and regenerate new muscle tissue (McCullen et al., 2011). However, this strategy is limited by the

vast amount of cells needed (Bach et al., 2004). Alternatively, the cell-free approach of *in situ* SMTE has been introduced (Jana et al., 2013; Wang et al., 2014), where instructive biomaterials are grafted into a muscle defect to trigger the endogenous regenerative potential and regenerate the diseased tissue via release of bioactive signaling molecules from the biomaterial implanted into the patient (Qazi et al., 2015). *Ex vivo* SMTE demonstrates an alternative strategy to *in vivo* approaches, where autologous cells are expanded in cell culture beforehand and eventually reintroduced into the defect site for regeneration (Barrilleaux et al., 2006; Stern et al., 2009).

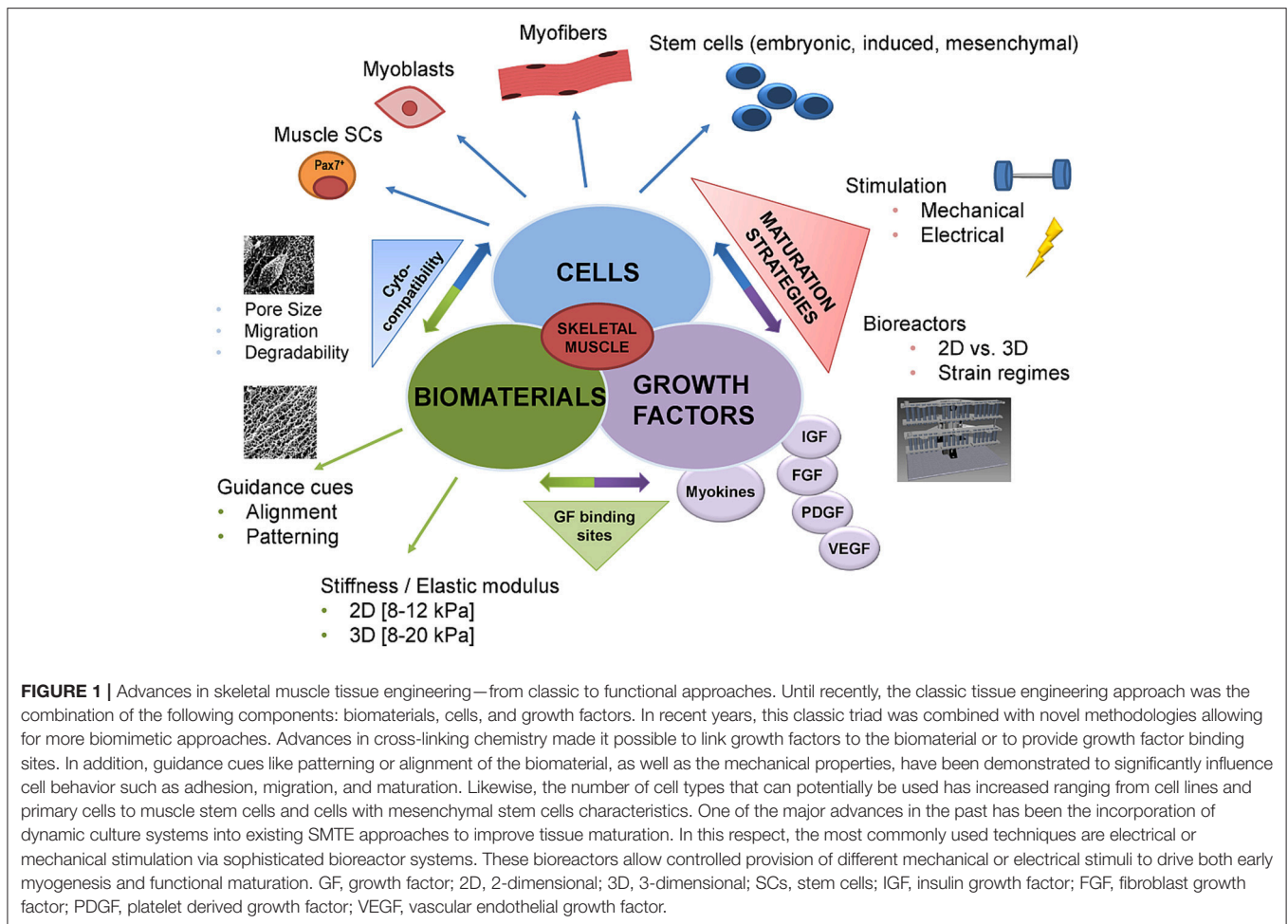
With this review we would like to highlight the state of the art in SMTE, trigger ideas for refinements and provide the scientific community with putative strategies and criteria to increase the performance and maturity of tissue engineered muscle. Additionally, we give an outlook on future challenges and general considerations for SMTE applications in healthy and diseased muscle.

## Factors Influencing the Myogenic Outcome (*in vitro* and *in vivo*)

*In vitro* SMTE relies on efficient maturation strategies to generate functional 3D skeletal muscle constructs, which firstly requires biomaterials as scaffolds. These scaffold matrices should offer adequate physicochemical properties as well as bioactive cues like incorporated growth factors to enhance myogenic differentiation or cell adhesion motives to improve cellular attachment. Additionally, potent myogenic cells that are able to differentiate into mature myotubes under appropriate environmental conditions are a prerequisite (Bursac et al., 2015). Finally, effective stimulation strategies in the form of mechanical, electrical or electromechanical stimulation are needed to trigger cell alignment, fusion, and differentiation (Figure 2). After densely packed arrays of aligned myotubes are generated, the ultimate goal is to implement methods to (pre)vascularize and innervate such muscle constructs before they can serve as functional transplants.

## Biomaterials in SMTE

Natural biomaterials are biocompatible and biodegradable, and thus constitute favorable biomaterials for SMTE. They possess tunable mechanical and structural properties such as porosity, topographical cues, and the option of functionalization with growth factors and/or cell adhesion motives. Furthermore, natural hydrogel materials can be molded into different shapes, which is advantageous for repairing volumetric muscle defects that usually have irregular shapes. However, natural biomaterials harbor potential immunogenicity and sometimes lack of mechanical strength (ASM International, 2003; Qazi et al., 2015). The most commonly used natural biomaterials in SMTE are **collagen** (Vandenburgh et al., 1988; Shansky et al., 1997; Okano and Matsuda, 1998a,b; Powell et al., 2002; Cheema et al., 2003; Kroehne et al., 2008; Bian and Bursac, 2009; Rhim et al., 2010; Hinds et al., 2011; Ma et al., 2011; Smith et al., 2012), **fibrin** (Huang et al., 2004; Beier et al., 2006; Borschel et al., 2006; Matsumoto et al., 2007; Bian and Bursac, 2009, 2012; Lam et al., 2009; Hinds et al., 2011; Page et al., 2011; Liu et al., 2012, 2013;

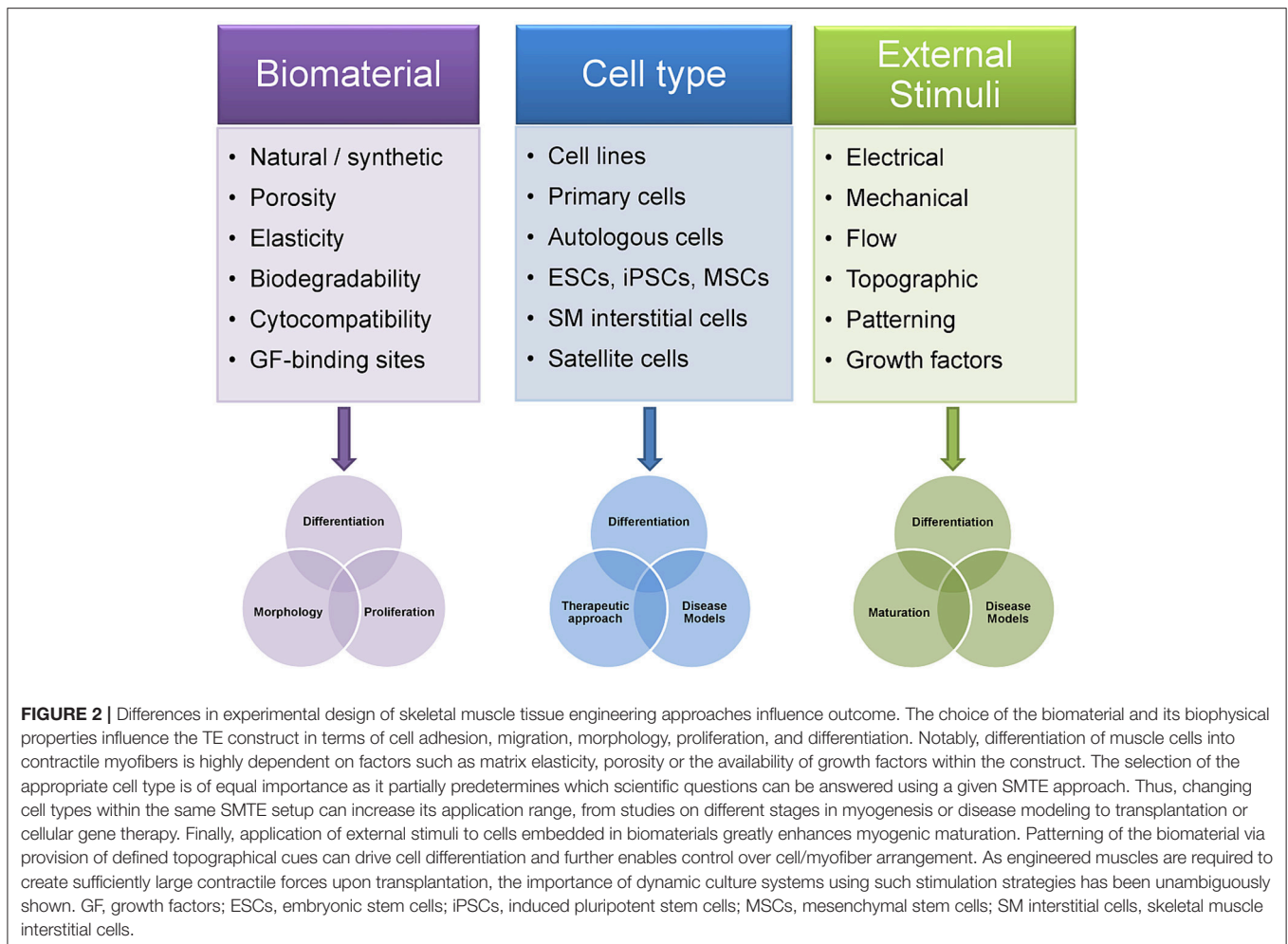


Heher et al., 2015), **alginate** (Shapiro and Cohen, 1997; Hill et al., 2006a,b; Borselli et al., 2010, 2011; Liu et al., 2012; Wang et al., 2014), **Matrigel<sup>®</sup>** (Grefte et al., 2012; Juhas and Bursac, 2014), **hyaluronic acid (HA)** (Wang et al., 2009; Rossi et al., 2011; Monge et al., 2012), **gelatin** (Hosseini et al., 2012; Yang et al., 2014), **silk fibroin** (Mandal and Kundu, 2009), **chitosan** (Jana et al., 2013), and **decellularized tissues** (Borschel et al., 2004; Conconi et al., 2005; De Coppi et al., 2006; Mase et al., 2010; Merritt et al., 2010; Machingal et al., 2011; Perniconi et al., 2011; DeQuach et al., 2012; Wolf et al., 2012; Corona et al., 2014; Sicari et al., 2014). Common synthetic biomaterials are manufactured from biodegradable polyesters of **polyglycolic acid**, **polyethylene glycol (PEG)**, **polycaprolactone**, **poly(lactic-co-glycolic acid)**, and **poly-L-lactic acid** (Huang et al., 2006a; Choi et al., 2008; Jun et al., 2009; Aviss et al., 2010; Kim et al., 2010a,b; Ku et al., 2012; Chen et al., 2013; Yang et al., 2014). These synthetic biomaterials are versatile in use as they are degradable (over weeks to years, depending on the formulation and degree of cross-linking), allow for precise control over their physicochemical properties (e.g., degradation rate, stiffness/elasticity or the presence of topographical or biochemical cues) and usually are considerably cheaper than natural biomaterials. Additionally, they can be used in the form of hydrogels (Grizzi et al., 1995). However,

they do not always support cell attachment and adhesion, can potentially cause inflammatory responses (after degradation or through prolonged persistence at the injury site *in vivo*) and lack biomimicry of the native ECM (Kim et al., 2010b). Therefore, they are often combined or coated with natural biomaterials to present biological recognition cues e.g. integrin-binding motives like Arg-Gly-Asp to increase cell attachment (Qazi et al., 2015). An overview of commonly used biomaterials for SMTE and their advantages and disadvantages is given in **Table 1**.

### Hydrogels

Hydrogels are particularly popular in SMTE due to their tunability regarding structure, shape and mechanical stability as well as their amenability to incorporate contact guidance and biochemical cues. Additionally, hydrogels can be functionalized with growth factors or other bioactive molecules to enhance regeneration (Hill et al., 2006a; Ostrovidov et al., 2014; Qazi et al., 2015). 3D hydrogels promote a spatially uniform cell distribution after encapsulation, enabling the generation of dense tissue constructs through high initial cell seeding densities and hydrogel compaction by the cells over time. The high amount of cell-cell contacts promotes and enhances myogenic fusion and increases



myofiber length and thickness (Heher et al., 2015). Furthermore, 3D environments mimic the physiological conditions of the tissue more closely than 2D cultures. The use of hydrogel-based biomaterials is a promising strategy to introduce therapeutic myogenic precursor cells into a defect for subsequent formation of new muscle tissue *in vivo* (Han et al., 2016). Notably, hydrogels can be injected in a minimally invasive manner to support or fill void spaces after muscle trauma or disease (Qazi et al., 2015).

Collagen is the most abundant protein in the human body and the main constituent of natural ECM, which is why it has been used in a multitude of TE applications (Lee et al., 2001). However, if muscle satellite cells (MuSCs) are used, laminin has to be added to match the specific integrin complex formed by  $\alpha 7$  and  $\beta 1$  isoforms (Blanco-Bose et al., 2001). In a pioneering study, Vandenberg et al used collagen gels to incorporate and differentiate avian myoblasts into contractile myotubes with structural characteristics similar to neonatal myofibers (Vandenberg et al., 1988). Since then, many other groups have used myogenic precursor cells combined with collagen hydrogels (Cheema et al., 2003; Rhim et al., 2007; Ma et al., 2011; Smith et al., 2012). Okano et al. highlighted that C2C12 myoblasts combined with 3D collagen gels led to differentiation into

multinucleated aligned myotubes, successful capillary infiltration *in vivo*, and remodeling after implantation (Okano and Matsuda, 1998b).

Another natural biomaterial for hydrogel production is alginate, a polysaccharide found in seaweed, rendering it a feasible and cheap hydrogel source (Boontheekul et al., 2005; Andrejcsk et al., 2013). An advantage of alginate hydrogels is the possibility to modify them, for example by introducing cell adhesive ligands or adjusting stiffness and degradability (Shapiro and Cohen, 1997; Hill et al., 2006a,b; Borselli et al., 2010; Liu et al., 2012). Alginate hydrogels are used in many medical applications, including wound healing management or the delivery of bioactive molecules due to their low toxicity and good biocompatibility (Lee and Mooney, 2012).

The ECM component HA is also used for the fabrication of hydrogels by photo cross-linking via UV light treatment (Han et al., 2016) or by chemical cross-linking (Luo et al., 2000; Collinsworth et al., 2002; Zhang et al., 2016). HA enhances myoblast proliferation and differentiation. However, degradation by hyaluronidases *in vivo* is difficult to control, which may lead to apoptosis of the introduced cells due to loss of attachment to the material (Han et al., 2016).



**TABLE 1** | Commonly used biomaterials and their useful properties for SMTE.

<b>Biomaterial</b>	<b>Natural/ Synthetic</b>	<b>Advantages</b>	<b>Disadvantages</b>	<b>Types of scaffolds</b>	<b>Authors</b>
Fibrin	Natural	Biocompatible, biodegradable, combination of materials possible, functionalization with growth factors, cell encapsulation, injectable, cell adhesive cues, tunable porosity, can enhance myoblast differentiation	Potential immunogenicity, limitation in fabrication due to denaturation, lack of mechanical strength	Hydrogels (application as 3D scaffolds), 2D patterned surfaces, coatings	ASM International, 2003; Huang et al., 2004; Borschel et al., 2006; Matsumoto et al., 2007; Bian and Bursac, 2009, 2012; Lam et al., 2009; Liu et al., 2013; Heher et al., 2015; Qazi et al., 2015
Collagen	Natural	Biocompatible, biodegradable, combination of materials possible, interconnectivity, macroporous structure, topographical cues, cell adhesive cues, tunable porosity, can enhance myoblast differentiation, injectable	Potential immunogenicity, limitation in fabrication due to denaturation, lack of mechanical strength	Hydrogels (application as 3D scaffolds), 2D patterned surfaces, coatings	Vandenburgh et al., 1988; Shansky et al., 1997; Okano and Matsuda, 1998a,b; Powell et al., 2002; ASM International, 2003; Cheema et al., 2003; Kroehne et al., 2008; Bian and Bursac, 2009; Rhim et al., 2010; Hinds et al., 2011; Ma et al., 2011; Smith et al., 2012; Qazi et al., 2015; Han et al., 2016
Gelatin	Natural	Biocompatible, biodegradable, combination of materials possible, topographical cues, can enhance myoblast differentiation	Potential immunogenicity, limitation in fabrication due to denaturation, lack of mechanical strength	Coatings	ASM International, 2003; Hosseini et al., 2012; Yang et al., 2014; Qazi et al., 2015
Alginate	Natural	Biocompatible, biodegradable, high surface area, interconnectivity, functionalization with growth factors, cell encapsulation, injectable, cell adhesive cues, tunable porosity, macroporous structure, minimally invasive	Potential immunogenicity, limitation in fabrication due to denaturation, lack of mechanical strength, need for adhesive cues (RGD)	Hydrogels (application as 3D scaffolds)	ASM International, 2003; Hill et al., 2006a,b; Borselli et al., 2011; Liu et al., 2012; Wang et al., 2014; Qazi et al., 2015; Han et al., 2016
Chitin/ chitosan	Natural	Biocompatible, biodegradable, topographical cues, varying mechanical properties, tunable porosity	Potential immunogenicity, limitation in fabrication due to denaturation, lack of mechanical strength	Grooved scaffolds, application as 3D scaffolds	ASM International, 2003; Jana et al., 2013; Qazi et al., 2015
Decellularized tissues/ECM	Natural	Tunable structural integrity, native structural and biochemical cues, matches host tissue, mechanical properties, bioactive	Potential immunogenicity, processing relies on chemical/biological agents which break down natural ECM structure, acquisition of material more complicated - especially for human tissue	Hydrogels (application as 3D scaffolds), full thickness <i>in vitro</i>	ASM International, 2003; Borschel et al., 2004; Conconi et al., 2005; De Coppi et al., 2006; Masse et al., 2010; Merritt et al., 2010; Machingal et al., 2011; Perniconi et al., 2011; DeQuach et al., 2012; Wolf et al., 2012; Corona et al., 2014; Sicart et al., 2014; Qazi et al., 2015
Hyaluronic acid	Natural	Biocompatible, biodegradable, tunability, injectable, cell encapsulation, minimally invasive	Potential immunogenicity, limitation in fabrication due to denaturation	Hydrogels (application as 3D scaffolds)	ASM International, 2003; Rossi et al., 2011; Wang et al., 2014; Qazi et al., 2015; Han et al., 2016
PEG	Synthetic	Biocompatible, high tunability, injectable, cell encapsulation, minimally invasive	Recellularization is slow, poor support in remodeling, lack of adhesive sites for cell attachment	Hydrogels (application as 3D scaffolds)	Kim et al., 2010b; Bao Ha et al., 2013; Qazi et al., 2015; Han et al., 2016
PLLA	Synthetic	Biocompatible, combination of materials possible, offer topographical cues, tunability (e.g., groove width and depth), electrically conductive, can enhance myoblast differentiation	Recellularization is slow, poor support in remodeling, lack of adhesive sites for cell attachment	2D patterned surfaces, electrospun fibers with tunable ridge width, alignment and variable composition of polymer material	Gunatillake et al., 2003; Huang et al., 2006a; Bao Ha et al., 2013; Qazi et al., 2015

*(Continued)*

TABLE 1 | Continued

Biomaterial	Natural/ Synthetic	Advantages	Disadvantages	Types of scaffolds	Authors
PLGA	Synthetic	Biocompatible, biodegradable, combination of materials possible, offer topographical cues, tunability (e.g., groove width and depth), electrically conductive, can enhance myoblast differentiation	Recellularization is slow, poor support in remodeling, lack of adhesive sites for cell attachment	2D patterned surfaces, electrospun fibers with tunable ridge width, alignment and variable composition of polymer material	Gunatillake et al., 2003; Aviss et al., 2010; Bao Ha et al., 2013; Yang et al., 2014; Qazi et al., 2015
PCL	Synthetic	Biocompatible, biodegradable, combination of materials possible, offer topographical cues, tunability (e.g., groove width and depth), electrically conductive, can enhance myoblast differentiation, can be used in drug delivery systems	Recellularization is slow, poor support in remodeling, lack of adhesive sites for cell attachment	2D patterned surfaces electrospun fibers with tunable ridge width, alignment and variable composition of polymer material	Gunatillake et al., 2003; Choi et al., 2008; Kim et al., 2010b; Ku et al., 2012; Bao Ha et al., 2013; Chen et al., 2013; Qazi et al., 2015

Fibrin is a favored biomaterial to produce hydrogels. It is the end-product of the blood clotting cascade, formed when fibrinogen is cleaved by thrombin (Helgerson et al., 2004). As fibrin is a natural component of the human body like collagen and HA, it provides attractive features, including biocompatibility, biodegradability and non-toxicity. Encapsulating myogenic cells in fibrin hydrogels provides cues to trigger growth and differentiation into myotubes and eventually to myofibers (Juhas et al., 2015). Further advantageous features include tunability of its structural network, modifiable polymerization (Han et al., 2016) and the potential for incorporating growth factors (Ahmed et al., 2008). Some studies claim fibrin to be superior to other biomaterials (e.g., collagen I) due to the strong integrin binding (integrin  $\alpha 7$  and  $\alpha 5$ ) of myotubes to fibrin (Morishima-Kawashima et al., 1995; Papers and Mayer, 2003). This effect is more pronounced in fibrin, as myotubes do not have the collagen I specific integrin  $\alpha 2$  receptor. Therefore, a fibrin environment is more conducive to distributing contractile forces from myocytes (Juhas et al., 2015). The major drawback of fibrin is finding an appropriate material density that balances the required material integrity to mimic natural stiffness and sufficient porosity for nutrient transport and cell migration (Helgerson et al., 2004; Brown and Barker, 2014). Fibrin hydrogels have been used successfully in numerous SMTE approaches using different stimuli to enhance differentiation (Huang et al., 2004; Borschel et al., 2006; Matsumoto et al., 2007; Lam et al., 2009; Liu et al., 2013; Heher et al., 2015).

Injectable hydrogels derived from decellularized muscle ECM may offer a more flexible approach than whole decellularized muscles (DeQuach et al., 2012). Although muscle ECM breakdown and subsequent processing into hydrogels destroys all existing architectural cues of the ECM (such as the vascular bed), the hydrogel formulation's composition in terms of proteins, growth factors and cytokines is preserved and can still instruct endogenous regenerative processes. Importantly, hydrogels can be produced from xenogeneic ECM sources, such as porcine dermis, submucosa or urinary bladder (Wolf et al., 2012; Badylak et al., 2016), circumventing the need for autologous muscle ECM which would be inapplicable in clinics due to donor site morbidity.

Synthetic hydrogels based on PEG are cytocompatible and offer tremendous variability for chemical manipulation. For SMTE applications, PEG can be tailored to mimic the natural stiffness of skeletal muscle tissue (Juhas et al., 2015) and seems to be a promising biomaterial for myogenic differentiation (Han et al., 2016). Laminin-coated PEG hydrogels, as an example of combined synthetic and natural materials, favored MuSC proliferation and differentiation *in vitro* (Han et al., 2016). PEG combined with fibrinogen constitutes a promising scaffold to embed skeletal muscle-derived pericytes (Fuoco et al., 2014) or mesoangioblasts (Fuoco et al., 2012, 2015) and favors differentiation of cells and regeneration of muscle tissue. Moreover, PEG-based hydrogels can be functionalized with different growth factors to directly promote muscle regeneration *in situ*, recruit endogenous stem cells to the site of injury, or enhance differentiation of muscle progenitor cells on/in the gel (Hammers et al., 2012; Rybalko et al., 2015).

## Cells for Muscle Tissue Engineering

Another essential factor influencing the myogenic outcome is choosing appropriate cells when generating functional muscle tissue constructs. The pool of cell types scientists can choose from has grown enormously in recent years and a variety of cell populations that are able to differentiate along the myogenic lineage have been identified (Fishman et al., 2013). In addition, new techniques, such as the generation of patient-specific induced pluripotent stem cells (iPSCs) or gene editing via the CRISPR/Cas9 technology have opened new therapeutic possibilities, especially for the treatment of MDs.

The two main groups of cells potentially being used for SMTE are either freshly isolated and expanded primary cells or immortalized cell lines. The main application of immortalized cells is the establishment of model systems, whereas primary cells are used in clinical applications and for implant studies. Myoblasts, satellite cells and stem cells from various sources are employed in different therapeutic approaches to improve muscle regeneration and function (Bach et al., 2004). The most prominent type of primary myogenic cells are MuSCs, which demonstrate a high proliferative capacity, have the ability to self-renew and differentiate into myotubes (Zammit et al., 2004; Qazi et al., 2015). Autologous MuSCs cultured with homologous acellular muscular matrices enhances their engraftment, and subsequently those matrices can be used as transplants to compensate for tissue loss (Marzaro et al., 2002). A drawback is that they have poor survival and engraftment rates after injection into damaged tissue (Mouly et al., 2005). MuSCs can be isolated either via enzymatic digestion of muscle tissue or via cellular outgrowth by plating single muscle fibers onto protein-coated dishes, which serve as a niche for satellite cells (Zammit et al., 2006; Juhas et al., 2015). However, a drawback of satellite cells is that once activated and differentiated into myotubes they cannot be brought back to a self-renewing state. Thus, the pool of cells able to proliferate and build new myotubes is eventually exhausted (Shadrin et al., 2016).

Over the years, other tissue resident cells have been discovered, namely interstitial skeletal muscle progenitor cells, which constitute a heterogeneous cell pool and seem to derive from the interstitium near the blood vessels (Shadrin et al., 2016). They offer a great regenerative potential and have already been used in studies of rodent and human SMTE. Pw1 interstitial cells, a fraction of interstitial skeletal muscle progenitor cells (Relaix et al., 1996), originate upstream of MuSCs in the muscle precursor lineage and can induce the formation of MuSCs. Therefore, their presence is a key factor in the satellite cell niche (Malecova and Puri, 2012). In the murine model, Pw1 interstitial cells enhanced muscle regeneration by releasing paracrine growth factors. Other subsets of skeletal muscle interstitial cells that play important roles in inducing muscle differentiation are fibroadipogenic progenitors, pericytes, and mesoangioblasts. All three cell populations are promising for SMTE approaches, since they are capable of ameliorating myogenic regeneration, offer high proliferative rates, and can be genetically modified (Minasi et al., 2002; Dellavalle et al., 2007; Tonlorenzi et al., 2007; Crisan et al., 2008; Joe et al., 2010; Birbrair et al., 2013; Ostrovidov

et al., 2015). These characteristics also increase their relevance for potential MD treatments (Sampaolesi et al., 2003, 2006; Tedesco and Cossu, 2012; Meregalli et al., 2013). Furthermore, these cells are suitable for regenerative medicine approaches due to their good survival rates and their ability to fuse to preexisting myofibers, thereby promoting muscle regeneration *in vivo* (De Angelis et al., 1999; Minasi et al., 2002; Dellavalle et al., 2007; Tonlorenzi et al., 2007; Joe et al., 2010; Tedesco and Cossu, 2012).

Another cell type with great potential for regenerative medicine is mesenchymal stem cells (MSCs). MSCs are multipotent cells capable of migrating to the site of injury to promote tissue repair (Ferrari et al., 1998; Dezawa et al., 2005) and reducing inflammation (Sassoli et al., 2012). MSCs are able to differentiate into the myogenic lineage (Dezawa et al., 2005). Furthermore, they enhance muscle fiber formation and regeneration *in vivo* (Ferrari et al., 1998; De Bari et al., 2003; Koponen et al., 2007; Lee et al., 2011; Sassoli et al., 2012). This might be due to their support of functional satellite cells when implanted in murine muscle tissue (De Bari et al., 2003) and through recovery of expressed mechano growth factor, which is crucial for skeletal muscle maintenance and repair (Goldspink, 1999). This positive effect on muscle regeneration has been validated in *in vivo* disease models, where autologous MSCs were transplanted into crush trauma injuries in rats (von Roth et al., 2012; Qazi et al., 2015). MSCs' therapeutic effects may also stem from their ability to secrete soluble paracrine factors (Gnecchi et al., 2008; Sassoli et al., 2012) including Interleukin (IL)-6, IL-10, stromal cell-derived factor (Gnecchi et al., 2005; Kortessidis et al., 2005; Zhang et al., 2007; Yin et al., 2011), vascular endothelial growth factor, fibroblast growth factor (FGF), IL-1, matrix metalloproteinases (MMPs), platelet derived growth factor, transforming growth factor  $\beta$ , angiopoietin (Kinnaird et al., 2004), hepatocyte growth factor, and adrenomedullin (Ohnishi et al., 2007; Wynn, 2008; Tang et al., 2010). Via secretion of these factors, MSCs assert substantial anti-inflammatory effects by modulating the immune response (Le Blanc and Mougiakakos, 2012). However, a study by Ferrari et al reported that bone-marrow transplantation did not ameliorate the dystrophic phenotype in *mdx* mice, a widely used mouse model for DMD (Ferrari et al., 2001). One suggested reason for the low regenerative potential of MSCs in this setting was that a vast number of cell types is present in the bone-marrow, which resulted in relatively low numbers of MSCs actually being transplanted in the course of a bone-marrow transplantation (reviewed by Forcales, 2015). Alternative cells used for SMTE are L6 rat myoblasts, neonatal muscle-derived progenitor cells and xenogeneic cells derived from adult muscles from other species (van der Schaft et al., 2013).

Human or murine embryonic stem cells represent another regularly used source for obtaining skeletal myoblasts. It is possible to obtain CD73<sup>+</sup> multipotent mesenchymal precursors, which can be differentiated into myoblasts by co-culturing them with C2C12 cells (Barberi et al., 2005). Since their generation by Yamanaka and Takahashi (2006), iPSCs have been widely implemented in different research areas. This technique makes it possible to reprogram cells directly from patients for autologous

cell therapy of MDs (Meregalli et al., 2014; Quattrocelli et al., 2015). Since iPSCs can be derived from healthy or diseased patients, they offer great potential in TE for disease modeling and drug testing (Wobma and Vunjak-Novakovic, 2016). Such autologous patient-derived cells are non-immunogenic and, in addition, genetic defects can be corrected during *ex vivo* culture using tools such as CRISPR/Cas9. Interestingly, iPSCs generated from mesoangioblasts were shown to fuse to existing muscle with higher efficiency than iPSCs generated from fibroblasts (Quattrocelli et al., 2015). An important proof-of-concept study was performed by Tedesco et al., who used genetically corrected iPSCs derived from myoblasts or fibroblasts of limb-girdle MD patients, differentiated them into mesoangioblasts and grafted them into affected muscles in a humanized limb-girdle MD mouse model (Tedesco et al., 2012). This not only ameliorated the dystrophic phenotype and restored the depleted satellite cell pool, but importantly also demonstrated that treatment with patient-specific iPSC-derived cells can be utilized for stem cell therapy in MDs. However, it has to be noted that there are still limitations regarding both the use of embryonic stem cells, which raise ethical concerns (An and Li, 2014), and iPSCs, which entail the risk of genetic recombination and tumor formation. To date, iPSC-based regenerative stem cell therapies have not entered clinics due to these safety considerations (Lee et al., 2009; Cittadella Vigodarzere and Mantero, 2014).

Finally, one of the most widely used cell line in SMTE are C2C12 murine myoblasts, established in 1977 from MuSCs derived from a C3H mouse (Yaffe and Saxel, 1977). Many researchers start their initial experiments with these cells, as they are easy to cultivate, proliferate rapidly, and differentiate well upon serum deprivation. Thus, they represent an ideal tool to evaluate new biomaterials or bioreactor systems for the generation of skeletal muscle tissue. However, due to the immortalization of the cells, translation into clinical use is not feasible. Human cell lines, however, may still serve as attractive cells for *in vitro* studies. A recent transcriptomics analysis revealed that immortalization of C25 human myoblasts neither interferes with their myogenic potential, nor with any other aspect of cell physiology—apart from the elicited protection against senescence (Thorley et al., 2016). Biomimetic *in vitro* skeletal muscle disease models employing patient-derived human myoblast lines may therefore provide a higher predictive capability than rodent *in vivo* models.

## Stimulation Strategies for Enhancing Maturation of 3D Bioengineered Muscle Constructs

Besides choosing the appropriate biomaterial and cell type, another key element that needs to be addressed is suitable stimulation strategies (either mechanical-, electrical-, or electromechanical-stimulation), which are indispensable for enhanced muscle maturation *in vitro*. Cells are highly responsive to their microenvironment such as the surrounding ECM, mechanical forces, and biochemical signals. Furthermore, the mechanical properties of biomaterials, such as the material

stiffness or the presence of distinct microarchitectural features, can influence cellular behavior tremendously (Engler et al., 2006, 2007; Cittadella Vigodarzere and Mantero, 2014). The stiffness/elasticity of a material is usually assessed by measuring the Young's modulus (elastic modulus) which is determined by a material's composition and capability for deformation.

One strategy to mimic the natural environment is the application of biochemical and/or biophysical stimulation to engineered constructs. Exercise can be simulated by the application of mechanical stimuli, such as cyclic and/or static strain. Exercise leads to the activation of satellite cells and subsequent fusion to already existing myofibers *in vitro* (Tatsumi et al., 2001) through triggering the release of hepatocyte growth factor and nitric oxide (NO) radicals, which in turn activate the satellite cells. NO is produced by nitric oxide synthases which are up-regulated by exercised or injured muscle tissue *in vitro* and *in vivo* (Tatsumi, 2010).

Regarding myogenesis, passive (e.g., bone elongation during development) as well as active (e.g., exercising during sport) mechanical stretching is essential for the development of skeletal muscle from embryonic to adult tissue (Goldspink et al., 1992; Heher et al., 2015). An appropriate stimulation protocol can exert a positive effect on gene regulation, protein expression and thus proliferation and differentiation of cells (Goldspink et al., 1992; Powell et al., 2002; Goldspink, 2003). Furthermore, exercise training improves fusion and alignment of myofibers (Vandenburgh and Karlisch, 1989; Corona et al., 2012; Heher et al., 2015), and enhances the generation of mature myofibers (Goldspink, 2003). Morphologically, mature skeletal muscle tissue is characterized by widespread sarcomeric patterning, which is indispensable for contraction. Moreover, mechanical stimulation causes an increase in the cross-striations of the tissue and a switch of myosin heavy chain isoforms from embryonic to adult (Juhas et al., 2015).

One of the first studies implementing mechanical stimulation was conducted by Goldberg et al. in which hypertrophy was induced by overloading of synergistic muscle within just 24 h (Goldberg, 1967; Armstrong et al., 1979). Further sophisticated mechanical stimulation protocols were conducted using bioreactors with mechanical stimuli to create dynamic 2D or 3D culture systems. These studies are listed in more detail in **Table 2** (Vandenburgh and Karlisch, 1989; Okano and Matsuda, 1998b; Powell et al., 2002; Auluck et al., 2005; Cheema et al., 2005; Matsumoto et al., 2007; Liao et al., 2008; Moon et al., 2008; Candiani et al., 2010; Machingal et al., 2011; Corona et al., 2012; Smith et al., 2012; Heher et al., 2015; Qazi et al., 2015).

Muscle tissue can also be stimulated with electrical stimulation, which positively affects myogenic gene regulation as well as protein expression (Goldspink et al., 1992; Powell et al., 2002; Goldspink, 2003). Motor neurons are responsible for innervating muscle fibers and the signal inducing contraction of the muscle tissue is distributed via branched axons (Purves et al., 2001). Electrical stimulation aims to recapitulate the processes of innervation by fast and slow motor neurons, which are responsible for the switch of muscle fiber types (Wehrle et al., 1994; Khodabakus et al., 2015). Electrical stimulation of mouse myoblasts improves myogenic differentiation (Park

**TABLE 2 |** Summary of bioreactor systems with corresponding mechanical stimulation protocols.

Cells	Biomaterial	Set-up	2D/3D culture	Stress regime, frequency [Hz]	Strain [%]	Time span of stimulation	Outcome	Authors
<b>MECHANICAL STIMULATION</b>								
Embryonic avian pectoralis muscle cells	Collagen constructs	Mechanical cell stimulator device (computerized)	3D	Cyclic ramp stretch at a rate of 0.35 mm/h	Up to 300%	3 days	Increase of proliferation, fusion and myotube length	Vandenburgh and Karlisch, 1989
C2C12 myoblasts	Collagen hydrogel	Stimulation of rod-shaped tissue via custom-designed stress chamber	3D	Cyclic, 60Hz	5%	7 days	Dense, oriented myotubes	Okano and Matsuda, 1998b
Myoblasts	Porous collagen scaffold	Stimulation via bio-Stretch system	3D	Continuous or cyclic uniaxial rapid ramp stretch (RRS) or cyclical ramp strain (CRS)	7.5 and 15%	6h	MMP-2 expression, and hence extracellular matrix remodeling, is up-regulated in response to strain	Auluck et al., 2005
Human skeletal muscle cells	Collagen/Matrigel® Mix	Stimulation of hBAMs by custom-made mechanical cell stimulator	3D	5-pulse at 5 Hz bursts for 2 min afterwards 28 min resting phase	5% on day 8–10, 10% on day 10–12, 15% on day 12–16	8 days	Enhance myofiber diameter and area diminished tissue stiffness	Powell et al., 2002
Myoblasts	Fibrin	Use of custom-made device	3D	Tensile strain	25 or 50%	7 days	Fiber alignment along direction of strain	Matsumoto et al., 2007
Primary muscle precursor cells	Collagen based acellular ECM scaffolds	Computerized bioreactor system	3D	Cyclic stretch	10%	5–21 days	Generation of fast twitch and tetanic force after implantation	Moon et al., 2008
Adult rat Muscle progenitor cells (MPCs)	BAM scaffolds from acellular bladder ECM	Stimulation via computer-controlled bioreactor system	3D	Cyclic stretch 3x per min, for the first 5 mins every hour	10%	7 days	After implanting improved host recovery	Machingal et al., 2011; Corona et al., 2012
Rat primary cells	Collagen	Sliding chamber model	2D	Isometric tension	n/a	21 days	3D constructs made of aligned myotubes	Smith et al., 2012
C2C12 myoblasts	Collagen constructs	Mechanical loads applied by tensioning culture force monitor bioreactor	3D	Repetitive cyclic stretch Ramp stretch	1% 10%	up to 12 h	IGF-1 $\alpha$ > upregulated by single ramp stretch, reduced by repetitive cyclic stretch MGF > upregulated by single ramp stretch and cyclic stimulation	Cheema et al., 2005
C2C12 myoblasts	Aligned electrospun polyurethane (PU) fibers	Tubular custom-made setup, computer program controlled	2D/3D	Repetitive cyclic stretch, 1 Hz for 1 h every 6h	5 or 10% with or without pre-strain of 5% static	2–14 days	Alignment, contractile proteins	Liao et al., 2008
C2C12 myoblasts	Biodegradable microfibrillar scaffold [DegraPol(R)]	Stimulation of constructs via custom made bioreactor	3D	2 days ramp stretch (3.3%), afterwards cyclic stretch (5 pulse, 0.5 Hz, 3.4% burst stretches	6.7%	7–10 days	Enhanced MHC expression	Candiani et al., 2010
C2C12 myoblasts	Fibrin hydrogels	Stimulation of constructs via MagneTissue bioreactor	3D	Static strain	10%	9 days	Increased gene expression, myotube diameter and length	Heher et al., 2015

et al., 2008) and enhances their contractile properties compared to unstimulated controls (Salmons et al., 2005; Fujita et al., 2007). In monolayer myogenic cultures, twitches happen spontaneously after the formation of myotubes, but electrical stimulation is needed for a controlled and sustained contraction. Chronic periods of electrical stimulation are relevant for the formation of mature phenotypes in muscle tissue constructs as well as to improve their contractile properties (Kasper et al., 2017). Many groups have applied sophisticated electrical stimulation protocols to muscle cells *in vitro* (Stern-Straeter et al., 2005; Huang et al., 2006b; Fujita et al., 2007; Donnelly et al., 2010; Langelan et al., 2011; Khodabukus and Baar, 2012) (Table 3).

To the best of our knowledge, so far there is only one published study combining both electro- and mechanical stimulation for engineering mature muscle constructs (Liao et al., 2008) (Table 3). In literature, there is only one bioreactor system reported, which combines the application of electrical and mechanical stimulation of 3D constructs. It is a commercially available system from EBERS Medical Technology, Spain, and allows for media perfusion under sterile conditions (Kasper et al., 2017). An overview of bioreactor systems used in SMTE with their used electrical stimulation protocols and the observed outcome is given in Table 3.

## Myokines Released by Exercised Muscle Tissue and Their Effect on Various Tissue Types

Myokines are another factor influencing muscle as well as other tissues and therefore might offer an interesting therapeutic option to treat patients in future. They are released by muscle tissue in response to exercise training. It is known that regular exercise has beneficial effects on overall health status. Accumulating epidemiologic evidence suggests that physical activity plays an independent role in preventing frequent chronic diseases like osteoporosis, diabetes, Alzheimer's, osteoarthritis or degenerative muscle conditions, and that the beneficial effects of exercise training are partially due to secreted myokines (Dunstan, 2011; Pedersen, 2011; Egan and Zierath, 2013).

Skeletal muscle has been recognized as an endocrine organ due to its ability to produce, store and secrete hormones and myokines. In particular, myokines are able to affect and regulate inflammatory and metabolic processes in muscle and in many other tissues in an endocrine or paracrine manner (Pedersen and Febbraio, 2008; Pedersen, 2009; Girgis et al., 2014; Tagliaferri et al., 2015). To date, there are 69 putative myokines, which are released via exercise training (Catoire et al., 2014).

So far, the most prominently investigated myokines are IL-6 (Pedersen, 2009), IL-7 (Haugen et al., 2010), IL-8 (Nielsen and Pedersen, 2007), IL-15 (Quinn et al., 2008), leukemia inhibitory factor (Broholm et al., 2011), FGF-21 (Izumiya et al., 2008; Hojman et al., 2009), insulin-like 6 (Zeng et al., 2010), follistatin-like 1 (Ouchi et al., 2008), musculin (Nishizawa et al., 2004), irisin (Boström et al., 2012), myonectin (Seldin et al., 2012), secreted protein acidic rich in cysteine (SPARC) (Songsorn et al., 2016), and Meteorin-like 1 (Rao et al., 2014).

IL-6 is a pleiotropic myokine and acts on muscle tissue by influencing satellite cell activation and differentiation, which is usually triggered by stress due to injury or mechanical stimulation (Muñoz-Cánoves et al., 2013). It is the first myokine to be released after acute exercise (Agarwal, 2017). Besides primarily acting on muscle, other organs such as adipose tissue, the liver and the brain are responsive to secreted IL-6 (Pedersen et al., 2001). Secondly, it negatively regulates pro-inflammatory cytokines (Pedersen and Febbraio, 2008; Benatti and Pedersen, 2014) such as tumor necrosis factor alpha and elevates levels of anti-inflammatory cytokines e.g., IL-10 and IL-1 receptor antagonist released from leukocytes (Pedersen et al., 2001). On the other hand, IL-6 is also considered a pro-inflammatory cytokine. Therefore, further investigations are needed to identify the exact role of IL-6 in muscle and other influenced tissues (Abeywardena et al., 2009).

Leukemia inhibitory factor belongs to the IL-6 superfamily (Rose-John et al., 2006) and is secreted by hypertrophic muscle (Spangenburg and Booth, 2006; Serrano et al., 2008; Guerci et al., 2012). It is also released upon resistance training in human muscle and in electrically stimulated cultured human myoblasts (Broholm et al., 2011). Studies in rodents demonstrated that production of IL-6 and leukemia inhibitory factor help to regenerate muscle tissue after injury by activating satellite cells (Barnard et al., 1994; Kurek et al., 1996, 1997; Zhang et al., 2013).

Irisin is a hormone-like myokine secreted during exercise (Boström et al., 2012). It plays an important role in bone-muscle cross talk, and supposedly influences both tissues (Colaïanni et al., 2017). This might explain why diseases like osteoporosis and sarcopenia are linked to each other (Reginster et al., 2015). Studies suggest that myokines like IL-6, IL-8, and IL-15 indirectly influence bone via acting on other tissues, while irisin affects bone tissue directly by increasing the differentiation of osteoblasts *in vitro* as well as enhancing cortical bone mass *in vivo* (Colaïanni et al., 2014, 2015, 2017; Colaïanni and Grano, 2015). Irisin also reduces body weight when administered to obese patients (Colaïanni et al., 2017). Another study showed that irisin uptake reduces body weight due to increased adipocyte and glucose metabolism and even elevated oxygen intake levels in an animal model (Boström et al., 2012). Irisin has the potential to transform white adipose tissue into brown adipose tissue, which is metabolically very active. This is supposed to ameliorate obesity and is called browning (Bartelt and Heeren, 2013). Furthermore, Colaïanni et al. conducted a study in which they analyzed conditioned media from muscle cells of mice performing exercise training. They found that Irisin levels in the media caused a stronger differentiation of bone marrow stromal cells into osteoblasts (Colaïanni et al., 2014).

Another myokine, Meteorin-like 1, also induces adipose tissue browning (Rao et al., 2014). The myokines IL-8 and Fstl-1 both induce angiogenesis (Nielsen and Pedersen, 2007), the latter by inducing endothelial cell-mediated neovascularization in ischemic tissue (Ouchi et al., 2008).

IL-15 as well as IL-15 receptor alpha are involved in anabolic/catabolic regulation of skeletal muscle tissue (Quinn et al., 1995; Quinn, 2002; Furmanczyk and Quinn, 2003; Riechman et al., 2004; Busquets et al., 2005; Pistilli et al.,

**TABLE 3 |** Summary of bioreactor systems with corresponding electrical and electro-mechanical stimulation protocols.

Cells	Biomaterial	Set-up	2D/3D culture	Stress regime, frequency (Hz), (V), pulse width, strain (%)	Time span of stimulation	Outcome	Authors
<b>ELECTRICAL STIMULATION</b>							
Primary rat myoblasts	Fibrin	Biphasic stimulation of culture slide chamber via platinum electrodes	3D	6.8 mA (4 ms duration), bursts at 250 ms > intervals every 4 s	Up to 8 days	No evidence of differentiation and fusion	Stern-Straeter et al., 2005
Rat primary cells (fast muscle)	Fibrin	Stimulation of myoid constructs via custom build force transducer	3D	5 pulses at 20 Hz/4 s at 5 V, 1.5 ms	After culturing of 14 days	Increase in contractility and an enhancement of 15% in TPT and 14% in 1/2 RT	Huang et al., 2006b
90% C2C12, 10% 3T3	Fibrin	Stimulation of myoid constructs via custom-made stimulation bioreactor	3D	4 pulses, periods at 1.25, 2.5 and 5 V/mm, 0.1 ms in a 400 ms train, recovery of 3.6 s	7 days	2.5 V/mm seemed to be the optimum as it demonstrated a stronger force production and excitability	Donnelly et al., 2010
90% C2C12, 10% 3T3	Fibrin	Stimulation of constructs via custom-made electrical stimulator	2D/3D	0.7, 1, 1.4 V/mm, 0.25 to 1, 4, 9, and 16 ms pulse width	24 h	Electrical field higher than 0.7–2.5 V/mm + pulse width of 1–4 ms > showed enhanced force productions, stronger force dynamics	Khodabukus and Baar, 2012
C2C12	n/a	Electrical pulse stimulation of coverslips	2D	40 V/60 mm, 1 Hz	8 days after differentiation for 1, 2, or 6 h	Development of contractile activity by application of 2 h stimulation at 1 Hz, decrease of contractility when applying electrical stimulus for more than 4 h	Fujita et al., 2007
C2C12, muscle progenitor cells (MPCs)	Collagen type I	Bipolar field stimulation of mBAMs via C-Pace Culture Pacer	2D/3D	4 V/cm, 6 ms pulses at 2 Hz	48 h started on day 0, 1, 2, or 3	More mature cross-striations in MPC mBAMs than C2C12 and fast to slow MHC isoform switch in MPC mBAMs	Langelan et al., 2011
<b>ELECTROMECHANICAL STIMULATION</b>							
Cells	Biomaterial	Set-up	2D/3D Culture	Stress regime, pulse width, frequency (Hz), Strain (%)	Time span of stimulation	Outcome	Authors
C2C12 myoblasts	Electro spun polyurethane (PU)	Tubular custom-made set up, computer program controlled	2D/3D	Cyclic stretch, 4 V/mm, 1 Hz, 5%	1 h mechanical strain, resting time 5 h + 7 days of electrical stimuli	Enhanced myotube formation, increase in alpha actinin + MHC	Liao et al., 2008

2007). IL-15 enhances the expression of myosin heavy chain in differentiating myocytes (Quinn et al., 1995) and myotubes (Quinn, 2002; Furmanczyk and Quinn, 2003). One session of resistance exercise is sufficient to increase IL-15 levels in trained and untrained humans (Riechman et al., 2004). Furthermore, Quinn et al found high levels of IL-15 to reduce fat mass and therefore lower adiposity in mice (Quinn et al., 2008).

In 2012, Seldin et al. identified another myokine called myonectin. Higher levels of myonectin were secreted into the media by differentiated C2C12 compared to non-differentiated cells. Furthermore, exercise elevated the expression of myonectin in muscle and it is putatively involved in the cross talk between muscle and other tissues like liver and adipose tissue (Seldin et al., 2012).

Another exercise-induced myokine, musculin, is activated by calcium signaling via the AKT pathway (Subbotina et al., 2015). Its function is to enhance mitochondrial biogenesis, which improves physical perseverance (Nishizawa et al., 2004; Subbotina et al., 2015).

SPARC is a myokine found in humans and mice and secreted during muscle contraction (Songsorn et al., 2016). Catoire et al. first identified SPARC to be released upon exercise training through secretome analysis (Catoire et al., 2014). SPARC affects many crucial mechanisms in the cell such as regulation of cell shape, differentiation and adhesion (Murphy-Ullrich and Sage, 2014). SPARC additionally affects insulin secretion in humans (Harries et al., 2013) and erythropoiesis in mice (Luo et al., 2012). Interestingly, the duration of the exercise seems to be more important than the intensity of the exercise for its secretion (Songsorn et al., 2016).

## Disease Models

To this day there are no effective cures for muscular dystrophies, hence there is an urgent need for models mimicking them. Novel biomimetic disease modeling platforms could offer a way to understand and study underlying mechanisms of such diseases and furthermore to test potential treatment options. Muscular dystrophy disease models have been used to study the underlying mechanisms, course of the disease over time, as well as therapeutic agents. Some of these will be discussed in the next sections. Animal models are the cornerstone of research on elucidating the mechanisms underlying dystrophies and on developing new treatment strategies. To date, there are around 50 *in vivo* animal models for studying muscular dystrophies in various species ranging from invertebrates (e.g., *Caenorhabditis elegans*), non-mammalian vertebrates, especially zebrafish (Guyon et al., 2007), to mammals (e.g., mice, rats, dogs, and pigs) (McGreevy et al., 2015). The most commonly utilized mammalian DMD models are the mdx mouse model, the mdx utrophin double mutant mouse model (mdx:utrn<sup>-/-</sup>) and the canine x-linked MD model (cxmd) (Banks and Chamberlain, 2008). A frequently used model system is the mdx mouse that carries a mutation in the dystrophin gene, resulting in a DMD phenotype. However, there are significant differences in the course of the disease in human DMD patients and mdx mice regarding characteristics, such as lifespan, severity, timeline, body weight, impact on

other physiological functions and many more (Partridge, 2010). Canine DMD models offer a way to overcome these obstacles, as they present fewer differences to the human DMD pathology regarding the aforementioned characteristics. Furthermore, dystrophic dogs are more suitable for studies using gene therapy approaches than mice, since the former presents a closer simulation of the human immune response toward introduction of vectors for gene repair and replacement (McGreevy et al., 2015). Thus, development of new strategies to introduce vectors evading the immune system is facilitated (Duan, 2015).

## *In vitro* Skeletal Muscle Disease Models

Despite the immense amount of knowledge gained on the pathophysiology of skeletal muscle diseases, animal models entail certain disadvantages and ethical considerations. They cannot recapitulate the exact manifestation of the disease in regard of physiological, biochemical and clinical conditions as they appear in the human body. This has prompted research trying to find appropriate time and cost effective alternatives (Banks and Chamberlain, 2008; Benam et al., 2015). Furthermore, results gained from *in vivo* drug testing setups frequently fail when translated to the clinics, due to major differences in underlying molecular mechanisms between different species. *In vitro* human disease models are a potential way to overcome these limitations. They can more closely mimic human pathological conditions concerning tissue and organ specific cell types (Benam et al., 2015) through the possibility of using patient-derived cells, which reflects the patient's individual skeletal muscle physiology and the disease progression in the dystrophic state (Smith et al., 2016). Moreover, it is possible to change single parameters within these systems and study the resulting effects, which constitutes another advantage of *in vitro* disease modeling (Bersini et al., 2016).

In general, miniaturizing disease models has gained attraction in the past years, as it allows reduction in cell number and reagents (and, thus, overall costs), while maintaining the quality of results. Additionally, the assessment of results and provision of external stimuli can be carried out in a precise and controlled manner. Thus, research on microfluidic devices for disease modeling has emerged in recent years (Bersini et al., 2016). One microfluidic system by Ferreira et al used a different approach in modeling dystrophy. Instead of using cells with a diseased phenotype, they established a device that mimicked the cellular environment of dystrophies. This was done by using different ECM compositions and applying a concentration gradient of basic FGF (bFGF), which is known to be released upon muscle injury. Thereby, it was possible to assess the influence of bFGF and different substrates on myoblast recruitment in normal or DMD simulating environments (Ferreira et al., 2015).

Another miniaturized 2D *in vitro* disease model was published by Serena et al, who created myotubes derived from primary myoblasts from healthy donors as well as patients suffering from DMD cultured on polyacrylamide hydrogels. This was achieved through adequate substrate design, including appropriate mechanical properties (i.e., a Young's modulus of 15 kPa). Furthermore, micro-patterning the substrate in parallel lanes to enhance myotube alignment and coatings with the



adhesion molecules laminin, fibronectin and Matrigel<sup>®</sup> were utilized as well. Thereby, it was possible to generate myotubes positive for myosin heavy chain II and  $\alpha$ -actinin that developed a highly ordered sarcomeric patterning. Furthermore, myotubes generated from healthy donors exhibited dystrophin expression. This is a key aspect for assessing the functionality of DMD therapies, as they often aim at restoring dystrophin expression (Serena et al., 2010). The basic principle of this test system was recently used to study the potential of mesoangioblasts in DMD treatment as they ameliorated dystrophin distribution in DMD myoblasts (Serena et al., 2016).

The course of dystrophies varies widely from one patient to another, as the mutations causing the disease are very heterogeneous, ranging from severe forms completely lacking dystrophin to a partially functioning truncated form of the protein. This variance cannot be considered in animal or standard *in vitro* models. Creating iPSCs from patient-derived cells offers a solution to this problem, since it allows direct comparison of the pathological phenotype of the patient and the cultured cells. This makes drug screening results and the evaluation of specific genetic aberrations more reliable. Therefore, they present a promising tool for modeling a variety of diseases. Also, recent advances in the field of iPSC research have boosted the efficiency of reprogramming. Myogenic progenitor-derived iPSCs showed good engraftment after transplantation, were able to regenerate myofibers and could repopulate the stem cell niche (Darabi et al., 2012; Meregalli et al., 2014; Kodaka et al., 2017). Nevertheless, this approach also bears certain disadvantages such as the lengthy processes involved in generating iPSCs and inducing differentiation into iPSC-derived myogenic progenitors, or the need to integrate so-called reprogramming factors, which could have unknown implications on the phenotype of the disease (Smith et al., 2016). Tanaka et al. were able to create myotubes from human iPSCs derived from Miyoshi Myopathy patients through inducible MyoD1 expression. These myotubes exhibited hallmarks of the disease, such as the role of Dysferlin during this disease. A lack of Dysferlin expression led to inefficient membrane repair, which could be overcome by an induced overexpression of Dysferlin, rescuing dystrophic myotubes and leading to a healthy phenotype. These results suggest that this model has the potential to shed light on the pathology of the disease, and may be applicable to other types of dystrophies (Tanaka et al., 2013). Another study using human iPSCs from DMD and Becker MD patients was published by Abujarour et al. Human iPSCs were subjected to MyoD1 overexpression, inducing myogenic commitment and finally yielding myotubes. To investigate whether this model has the potential to be used for drug testing, dystrophic myotubes were subjected to IGF-1 and Wnt7a treatment, factors that elicit skeletal muscle hypertrophy. A treatment with these two factors resulted in significant increase in fiber diameter, suggesting usability of this model for drug testing (Abujarour et al., 2014). Nevertheless, to date these models have not been used to test drugs or other therapies for DMD.

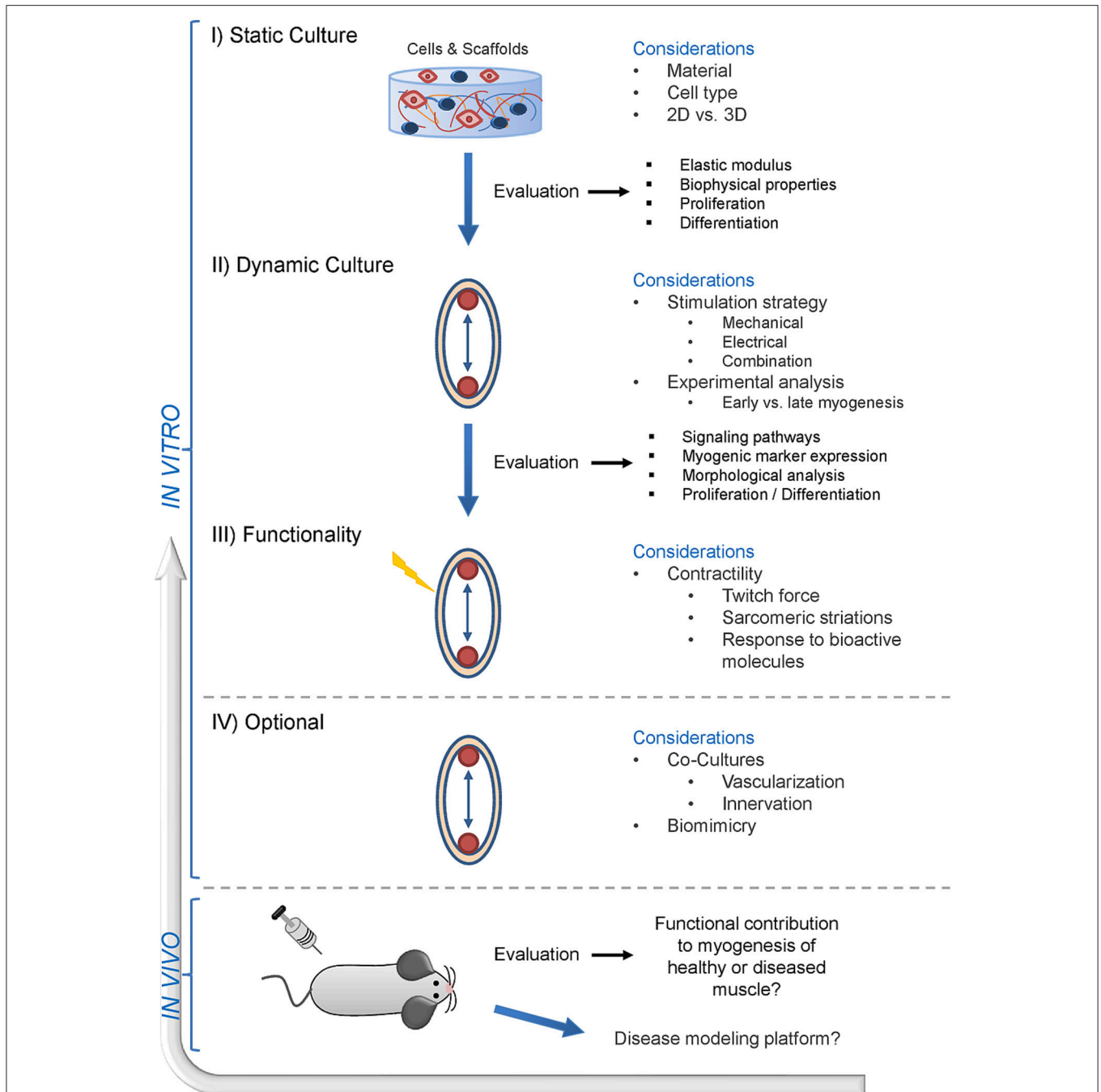
However, it is not possible to accurately mimic the complex organization of tissues *in vivo* using 2D disease models.

Thus, drug-screening results gained from these systems cannot directly be translated for the use in clinical studies. To overcome the limitations of 2D cell-based systems, more recent research has focused on the development of 3D systems that more adequately reflect the *in vivo* situation (Nam et al., 2015), where cells can interact with the matrix they are embedded in and form 3D structures (Bersini et al., 2016). A 3D drug testing platform was established by Madden and colleagues using human primary myoblasts grown in so-called myobundles generated by incorporation in fibrinogen and Matrigel<sup>®</sup> frames using polydimethylsiloxane molds. The bundles differentiated into chemically and electrically responsive muscle-like constructs capable of contraction. To prove their suitability for drug screening, the myobundles were treated with three different drugs, namely statins that induce muscle weakness, chloroquine that induces autophagy and clenbuterol which increases hypertrophy in low doses but leads to apoptosis and necrosis at higher concentrations. Overall, treatment with these compounds resulted in the expected outcomes. Therefore, this model appears suitable for drug testing. However, its usability as a disease model to study the pathophysiology of dystrophies remains to be established, as it has only been examined with cells derived from healthy donors (Madden et al., 2015). Thus, there is only one actual *in vitro* skeletal muscle disease model reported in 3D so far. This model used dystrophic myoblasts from *mdx* mice that were incorporated in natural hydrogels (collagen type I or fibrin) that were cast around posts. The resultant myotubes were electrically stimulated and contractile force generation was measured. In addition, 31 compounds that have the potential to serve as DMD drugs were screened by measuring changes in force generation upon treatment. Since this system works semi-automatically and in a 96-well culture format it is considered a potential high-throughput system for testing novel drugs for MD treatment. The major drawback of this model, however, is that it used murine cells. Thus, the results do not account for possible differences in drug response between humans and mice. Furthermore, the phenotype of the engineered constructs appeared to be closer to neonatal than adult according to the myosin heavy chain profiles (Vandenburgh et al., 2008).

In summary, there is still a great need for further research in the field of 3D skeletal muscle disease modeling. The creation of mature and functional *in vitro* muscle constructs could help enhance our fundamental understanding of the skeletal muscle physiology. Hence, the next step would be to create appropriate and translatable disease model systems to bring *in vitro* research one step closer to the *in homine* situation.

## FUTURE PERSPECTIVES OF SKELETAL MUSCLE TISSUE ENGINEERING

When it comes to SMTE approaches, the fact that 2D culture systems behave fundamentally different from 3D systems has often been overlooked. Hence, results from 2D experiments may not be directly compared or even translated to 3D settings. Identifying applicable treatment options will require



**FIGURE 3 |** Envisioned future of skeletal muscle tissue engineering—a suggested workflow. This schematic presents a skeletal muscle tissue engineering workflow including stage-specific experimental considerations. Initially, the compatibility of biomaterials with potent myogenic cells has to be evaluated. This first step also involves the decision whether the cells will be cultured and grown in a 2D (monolayer on a pliant matrix) or 3D (encapsulation into a pliant matrix) environment. This still represents a static cell culture, where only the first steps in the SMTE approach are addressed. Evaluation of the biophysical matrix properties, biocompatibility and effects of the biomaterial on cell proliferation/differentiation can be evaluated via this process. The second step involves dynamic culture of the evaluated biomaterial and cells, where the main consideration is which stimulation strategy will be implemented into the culture system—ranging from mechanical to electrical stimulation or a combination of both. The third step addresses the functional analysis of the engineered muscle construct via twitch force measurements. At this point, contractile muscle constructs can furthermore be tested for their response to drugs with known effects, which is a prerequisite for later application of engineered muscle tissue in drug screening studies. An ideal setup would involve co-cultures to engineer muscle tissue with built-in vascular and neuronal structures to further enhance muscle maturity and contractility. After successful *in vitro* evaluation, the final step is the translation into animal models to test for the contribution of the engineered muscle to myogenesis and regeneration in healthy and/or diseased muscle. Ultimately, the knowledge gained from *in vivo* experiments can also be transferred back to *in vitro* setups for the generation of disease models.

engineering of functional 3D muscle tissue constructs. In this respect, several questions need to be addressed: (I) When does one look at gene expression levels or signaling pathways involved in muscle development or differentiation? (II) What are representative time points for the evidence of mature and functional muscle tissue? (III) Which analytical tools and methods can be applied for the morphological and functional assessment of skeletal muscle tissue constructs? (IV) How can a given biomaterial recapitulate the physiological environment supporting the myogenic potential of the cells?

Therefore, there is urgent need for standardized dynamic 3D model systems to enable comparability of results. Additionally, careful deliberation of the choice of biomaterial, cell type and the external stimuli, prior to the start of the actual experimental SMTE approach, may help to improve the outcome and save valuable time (Figure 2). The field of SMTE would greatly benefit from a workflow of criteria, factors, and analytical methods, which could be utilized by researchers globally. Here we provide a putative example of such a workflow that displays different experimental and developmental stages in *in vitro* SMTE culture systems, and produces results that are translatable to *in vivo* settings (Figure 3). It suggests analytical tools for endpoint analysis and evaluation of requirements for achieving SMTE constructs with desirable properties (e.g., determination of elastic modulus, activation of involved signaling pathways and expression of myogenic markers and functional characteristics). Optimization of dynamic culture conditions comprises a thorough cell biological analysis including investigation of signaling pathways involved in myogenesis, muscle hypertrophy and proliferation, myogenic gene expression profiling, morphological analysis through immunofluorescence staining for contractile proteins, calculation of the fusion index and the quantification of sarcomeric striations—the latter indicating a certain degree of muscle maturity. Finally, environmental culture conditions should be fine-tuned, e.g., applying external stimuli including appropriate training. Such stimuli are commonly applied via bioreactor systems, which contribute to the desired outcome of engineering 3D skeletal muscle constructs by recapitulating physiological or pathophysiological muscle states. A unified SMTE approach following certain design criteria would render results between groups more comparable, possibly accelerating and streamlining new therapeutic discoveries and advancements in the field of SMTE.

## CONCLUSION

Numerous sophisticated SMTE strategies exist, ranging from basic 2D to complex dynamic 3D setups, and researchers have a plethora of biomaterials and cell types to choose from. Nevertheless, to date the clear majority of SMTE approaches have failed to achieve broad clinical utility due to several reasons: (I) Systemic elucidation of suitable cell types and biomaterials as well as stimulation protocols (to induce muscle maturation) are still ongoing. (II) The pathomechanisms of a variety of MDs are still poorly understood which limits the clinical

success of cell therapeutic approaches. Hence, model systems for developmental/mechanistic and pathophysiological studies (disease models) are urgently needed to perform drug screenings for potential new treatment options. Currently, the focus is on finding reliable physiological models to further understand and study the pathophysiological processes in MDs. (III) Although acellular approaches bypass the general risks associated with (stem) cell therapy, many seemingly promising biomaterials have ultimately failed to meet the physical and native requirements to drive muscle regeneration.

ESC- and iPSC-derived myogenic precursors are increasingly used for drug screening purposes in disease models, while immortalized cell lines are used for initial testing of novel biomaterials and/or bioreactor systems. In an optimal scenario, autologous primary muscle (stem) cells directly derived from the patient would be used for personalized therapeutic approaches or disease models that involve the use of either undifferentiated or preconditioned cells. Although the current pool of applicable cells permits many different methodologies, each cell type has its limitations. However, advances in cell biology will establish adequate culture conditions in the future which will ideally diminish the phenotypic changes of cell types suitable for SMTE during *ex vivo* culture. Biomaterial systems that can serve as artificial satellite cell niches have already improved the efficiency of cell grafting in *in vivo* studies, and a more thorough evaluation of the satellite cell niche composition and microarchitecture will further improve current cell-based therapies. Finally, strategies for *in vitro* pre-vascularization and innervation will likely enhance the functional contribution of engineered muscle transplants to repair muscle *in vivo*. In addition, co-culture systems will allow studies on the interface between the different cell types in the muscle construct. Furthermore, myokines might offer novel therapeutic opportunities in the future, due to their positive effects on muscle as well as on other tissues. In *in vitro* culture systems, they might also be useful as supplements which can act as supportive factors for myogenesis, thereby improving the myogenic outcome of engineered muscle tissue constructs.

Therefore, elevating SMTE to the next level will require a thorough re-evaluation of biomaterial and cell sources as well as fine-tuning of stimulation techniques. Additionally, taking the above-mentioned criteria into account and implementing them into current research strategies will yield novel skeletal muscle (disease) model systems helping to improve therapeutic approaches to finally translate them into clinical setups.

## AUTHOR CONTRIBUTIONS

CF: PI of the project, preparation of the manuscript, design of the figures; BM: preparation of the manuscript and tables; JT: contributed to cell part and disease model part of manuscript, revising the manuscript; PH: preparation of the manuscript and help in figure design, revising the manuscript; OS: PhD supervisor of BM, corrections of the manuscript and input on figures and tables; DR: finances the project, head of department of biochemical engineering, corrections of the manuscript and input on figures and tables.

## FUNDING

This work was supported by the Signal Tissue (MA23#18-08) and the FFG COIN Disease Tissue (FFG #845443) Project.

## REFERENCES

- Abeywardena, M. Y., Leifert, W. R., Warnes, K. E., Varghese, J. N., and Head, R. J. (2009). Cardiovascular biology of interleukin-6. *Curr. Pharmaceut. Des.* 15, 1809–1821. doi: 10.2174/138161209788186290
- Abujarour, R., Bennett, M., Valamehr, B., Lee, T. T., Robinson, M., Robbins, D., et al. (2014). Myogenic differentiation of muscular dystrophy-specific induced pluripotent stem cells for use in drug discovery. *STEM CELLS Transl. Med.* 3, 149–160. doi: 10.5966/sctm.2013-0095
- Agarwal, M. (2017). Cardiovascular response and serum interleukin-6 level in concentric vs. eccentric exercise. *J. Clin. Diagn. Res.* 11, 4–8. doi: 10.7860/JCDR/2017/25281.9703
- Ahmed, T. A., Dare, E. V., and Hincke, M. (2008). Fibrin: a versatile scaffold for tissue engineering applications. *Tissue Engineering B Rev.* 14, 199–215. doi: 10.1089/ten.teb.2007.0435
- Almada, A. E., and Wagers, A. J. (2016). Molecular circuitry of stem cell fate in skeletal muscle regeneration, ageing and disease. *Nat. Rev. Mol. Cell Biol.* 17, 267–279. doi: 10.1038/nrm.2016.7
- An, Y., and Li, D. (2014). Engineering skeletal muscle tissue in bioreactor systems. *Chin. Med. J.* 127, 4130–4139.
- Andrejcsk, J. W., Cui, J., Chang, W. G., Devalliere, J., Pober, J. S., and Saltzman, W. M. (2013). Paracrine exchanges of molecular signals between alginate-encapsulated pericytes and freely suspended endothelial cells within a 3D protein gel. *Biomaterials* 34, 8899–8908. doi: 10.1016/j.biomaterials.2013.08.008
- Armstrong, R. B., Marum, P., Tullson, P., and Saubert, C. W. (1979). Acute hypertrophic response of skeletal muscle to removal of synergists. *J. Appl. Physiol.* 46, 835–842. doi: 10.1152/jappl.1979.46.4.835
- ASM International (2003). *Overview of Biomaterials and Their Use in Medical Devices*. ASM International.
- Auluck, A., Mudera, V., Hunt, N. P., and Lewis, M. P. (2005). A three-dimensional *in vitro* model system to study the adaptation of craniofacial skeletal muscle following mechanostimulation. *Eur. J. Oral Sci.* 113, 218–224. doi: 10.1111/j.1600-0722.2005.00215.x
- Aviss, K. J., Gough, J. E., and Downes, S. (2010). Aligned electrospun polymer fibres for skeletal muscle regeneration. *Eur. Cells Mater.* 19, 193–204. doi: 10.22203/eCM.v019a19
- Bach, A. D., Beier, J. P., Stern-Staeter, J., and Horch, R. E. (2004). Skeletal muscle tissue engineering. *J. Cell. Mol. Med.* 8, 413–422. doi: 10.1111/j.1582-4934.2004.tb00466.x
- Badylak, S. F., Dziki, J. L., Sicari, B. M., Ambrosio, F., and Boninger, M. L. (2016). Mechanisms by which acellular biologic scaffolds promote functional skeletal muscle restoration. *Biomaterials* 103, 128–136. doi: 10.1016/j.biomaterials.2016.06.047
- Banks, G. B., and Chamberlain, J. S. (2008). “Chapter 9: The value of mammalian models for duchenne muscular dystrophy in developing therapeutic strategies,” in *Current Topics in Developmental Biology*, eds R. S. Krauss. Elsevier Inc. doi: 10.1016/S0070-2153(08)00609-1
- Bao Ha, T., Le, M. T., Nguyen, D., and Minh, D. (eds.). (2013). “Naturally derived biomaterials: preparation and application,” in *Regenerative Medicine and Tissue Engineering*. doi: 10.5772/55668
- Barberi, T., Willis, L. M., Soccì, N. D., and Studer, L. (2005). Derivation of multipotent mesenchymal precursors from human embryonic stem cells. *PLoS Med.* 2:e161. doi: 10.1371/journal.pmed.0020161
- Barnard, W., Bower, J., Brown, M. A., Murphy, M., and Austin, L. (1994). Leukemia inhibitory factor (LIF) infusion stimulates skeletal muscle regeneration after injury: injured muscle expresses lif mRNA. *J. Neurol. Sci.* 123, 108–113. doi: 10.1016/0022-510X(94)90211-9
- Barrilleaux, B., Phinney, D. G., Prockop, D. J., and O'Connor, K. C. (2006). Review: *ex vivo* engineering of living tissues with adult stem cells. *Tiss. Eng.* 12, 3007–3019. doi: 10.1089/ten.2006.12.3007
- Bartelt, A., and Heeren, J. (2013). Adipose tissue browning and metabolic health. *Nat. Rev. Endocrinol.* 10, 24–36. doi: 10.1038/nrendo.2013.204
- Beauchamp, J. R., Heslop, L., Yu, D. S., Tajbakhsh, S., Kelly, R. G., Wernig, A., et al. (2000). Expression of CD34 and Myf5 defines the majority of quiescent adult skeletal muscle satellite cells. *J. Cell Biol.* 151, 1221–1233. doi: 10.1083/jcb.151.6.1221
- Beaudart, C., Rizzoli, R., Bruyère, O., Reginster, J.-Y., and Biver, E. (2014). Sarcopenia: burden and challenges for public health. *Arch. Public Health* 72:45. doi: 10.1186/2049-3258-72-45
- Beier, J. P., Stern-Staeter, J., Foerster, V. T., Kneser, U., Stark, G. B., and Bach, A. D. (2006). Tissue engineering of injectable muscle: three-dimensional myoblast-fibrin injection in the syngeneic rat animal model. *Plastic Reconstr. Surg.* 118, 1113–1121. doi: 10.1097/01.prs.0000221007.97115.1d
- Benam, K. H., Dauth, S., Hassell, B., Herland, A., Jain, A., Jang, K.-J., et al. (2015). Engineered *in vitro* Disease Models. *Annu. Rev. Pathol.* 10, 195–262. doi: 10.1146/annurev-pathol-012414-040418
- Benatti, F. B., and Pedersen, B. K. (2014). Exercise as an anti-inflammatory therapy for rheumatic diseases—myokine regulation. *Nat. Rev. Rheumatol.* 11, 86–97. doi: 10.1038/nrrheum.2014.193
- Bersini, S., Arrigoni, C., Lopa, S., Bongio, M., Martin, I., and Moretti, M. (2016). Engineered miniaturized models of musculoskeletal diseases. *Drug Discovery Today* 21, 1429–1436. doi: 10.1016/j.drudis.2016.04.015
- Bian, W., and Bursac, N. (2009). Engineered skeletal muscle tissue networks with controllable architecture. *Biomaterials* 30, 1401–1412. doi: 10.1016/j.biomaterials.2008.11.015
- Bian, W., and Bursac, N. (2012). Soluble miniagrin enhances contractile function of engineered skeletal muscle. *FASEB J.* 26, 955–965. doi: 10.1096/fj.11-187575
- Birbrair, A., Zhang, T., Wang, Z.-M., Messi, M. L., Enikolopov, G. N., Mintz, A., et al. (2013). Role of pericytes in skeletal muscle regeneration and fat accumulation. *Stem Cells Dev.* 22, 2298–2314. doi: 10.1089/scd.2012.0647
- Blanco-Bose, W. E., Yao, C.-C., Kramer, R. H., and Blau, H. M. (2001). Purification of mouse primary myoblasts based on  $\alpha 7$  integrin expression. *Exp. Cell Res.* 265, 212–220. doi: 10.1006/excr.2001.5191
- Blau, H. M., Cosgrove, B. D., and Ho, A. T. (2015). The central role of muscle stem cells in regenerative failure with aging. *Nat. Med.* 21, 854–862. doi: 10.1038/nm.3918
- Boontheekul, T., Kong, H.-J., and Mooney, D. J. (2005). Controlling alginate gel degradation utilizing partial oxidation and bimodal molecular weight distribution. *Biomaterials* 26, 2455–2465. doi: 10.1016/j.biomaterials.2004.06.044
- Borschel, G. H., Dennis, R. G., and Kuzon, W. M. (2004). Contractile skeletal muscle tissue-engineered on an acellular scaffold. *Plastic Reconstr. Surg.* 113, 595–602. doi: 10.1097/01.PRS.0000101064.62289.2F
- Borschel, G. H., Dow, D. E., Dennis, R. G., and Brown, D. L. (2006). Tissue-engineered axially vascularized contractile skeletal muscle. *Plastic Reconstr. Surg.* 117, 2235–2242. doi: 10.1097/01.prs.0000224295.54073.49
- Borselli, C., Cezar, C. A., Shvartsman, D., Vandenburgh, H. H., and Mooney, D. J. (2011). The role of multifunctional delivery scaffold in the ability of cultured myoblasts to promote muscle regeneration. *Biomaterials* 32, 8905–8914. doi: 10.1016/j.biomaterials.2011.08.019
- Borselli, C., Storrie, H., Benesch-Lee, F., Shvartsman, D., Cezar, C., Lichtman, J. W., et al. (2010). Functional muscle regeneration with combined delivery of angiogenesis and myogenesis factors. *Proc. Natl. Acad. Sci. U.S.A.* 107, 3287–3292. doi: 10.1073/pnas.0903875106

## ACKNOWLEDGMENTS

We would like to acknowledge DI Dr. Andreas Teuschl, DI Dr. Karl H. Schneider, Carina Hromada, and Prof. Dr. Heinz Redl for their valuable input.

- Boström, P., Wu, J., Jedrychowski, M. P., Korde, A., Ye, L., Lo, J. C., et al. (2012). A PGC1 alpha dependent myokine that drives brown fat like development of white fat and thermogenesis. *Nature* 481, 463–468. doi: 10.1038/nature10777
- Broholm, C., Laye, M. J., Brandt, C., Vadalasetty, R., Pilegaard, H., Pedersen, B. K., et al. (2011). LIF is a contraction-induced myokine stimulating human myocyte proliferation. *J. Appl. Physiol.* 111, 251–259. doi: 10.1152/jappphysiol.01399.2010
- Brown, A. C., and Barker, T. H. (2014). Fibrin-based biomaterials: Modulation of macroscopic properties through rational design at the molecular level. *Acta Biomater.* 10, 1502–1514. doi: 10.1016/j.actbio.2013.09.008
- Bursac, N., Juhas, M., and Rando, T. A. (2015). Synergizing engineering and biology to treat and model skeletal muscle injury and disease. *Annu. Rev. Biomed. Eng.* 17, 217–242. doi: 10.1146/annurev-bioeng-071114-040640
- Busquets, S., Figueras, M. T., Meijnsing, S., Carbó, N., Quinn, L. S., Almendro, V., et al. (2005). Interleukin-15 decreases proteolysis in skeletal muscle: a direct effect. *Int. J. Mol. Med.* 16, 471–476. doi: 10.3892/ijmm.16.3.471
- Candiani, G., Riboldi, S. A., Sadr, N., Lorenzoni, S., Neuenschwander, P., Montevecchi, F. M., et al. (2010). Cyclic mechanical stimulation favors myosin heavy chain accumulation in engineered skeletal muscle constructs. *J. Appl. Biomater. Biomech.* 8, 68–75.
- Carosio, S., Berardinelli, M. G., Aucello, M., and Musarò, A. (2011). Impact of ageing on muscle cell regeneration. *Ageing Res. Rev.* 10, 35–42. doi: 10.1016/j.arr.2009.08.001
- Catoire, M., Mensink, M., Kalkhoven, E., Schrauwen, P., and Kersten, S. (2014). Identification of human exercise-induced myokines using secretome analysis. *Physiol. Gen.* 46, 256–267. doi: 10.1152/physiolgenomics.00174.2013
- Cavazza, M., Kodra, Y., Armeni, P., De Santis, M., López-Bastida, J., Linertová, R., et al. (2016). Social/economic costs and health-related quality of life in patients with Duchenne muscular dystrophy in Europe. *Eur. J. Health Econ.* 17, 19–29. doi: 10.1007/s10198-016-0782-5
- Chang, S. C., Tobias, G., Roy, A. K., Vacanti, C. A., and Bonassar, L. J. (2003). Tissue engineering of autologous cartilage for craniofacial reconstruction by injection molding. *Plastic Reconstr. Surg.* 112, 793–799. doi: 10.1097/01.PRS.0000069711.31021.94
- Chargé, S. B., and Rudnicki, M. A. (2004). Cellular and molecular regulation of muscle regeneration. *Physiol. Rev.* 84, 209–238. doi: 10.1152/physrev.00019.2003
- Cheema, U., Brown, R., Mudera, V., Yang, S. Y., McGrouther, G., and Goldspink, G. (2005). Mechanical signals and IGF-I gene splicing *in vitro* in relation to development of skeletal muscle. *J. Cell. Physiol.* 202, 67–75. doi: 10.1002/jcp.20107
- Cheema, U., Yang, S.-Y., Mudera, V., Goldspink, G. G., and Brown, R. A. (2003). 3-D *in vitro* model of early skeletal muscle development. *Cell Motility Cytoskeleton* 54, 226–236. doi: 10.1002/cm.10095
- Chen, M.-C., Sun, Y.-C., and Chen, Y.-H. (2013). Electrically conductive nanofibers with highly oriented structures and their potential application in skeletal muscle tissue engineering. *Acta Biomaterialia* 9, 5562–5572. doi: 10.1016/j.actbio.2012.10.024
- Choi, J. S., Lee, S. J., Christ, G. J., Atala, A., and Yoo, J. J. (2008). The influence of electrospun aligned poly( $\epsilon$ -caprolactone)/collagen nanofiber meshes on the formation of self-aligned skeletal muscle myotubes. *Biomaterials* 29, 2899–2906. doi: 10.1016/j.biomaterials.2008.03.031
- Cittadella Vigodarzere, G., and Mantero, S. (2014). Skeletal muscle tissue engineering: strategies for volumetric constructs. *Front. Physiol.* 5:362. doi: 10.3389/fphys.2014.00362
- Colaiani, G., Cinti, S., Colucci, S., and Grano, M. (2017). Irisin and musculoskeletal health. *Ann. N. Y. Acad. Sci.* 1402, 5–9. doi: 10.1111/nyas.13345
- Colaiani, G., Cuscito, C., Mongelli, T., Oranger, A., Mori, G., Brunetti, G., et al. (2014). Irisin enhances osteoblast differentiation *in vitro*. *Int. J. Endocrinol.* 2014:902186. doi: 10.1155/2014/902186
- Colaiani, G., Cuscito, C., Mongelli, T., Pignataro, P., Buccoliero, C., Liu, P., et al. (2015). The myokine irisin increases cortical bone mass. *Proc. Natl. Acad. Sci. U.S.A.* 112, 12157–12162. doi: 10.1073/pnas.1516622112
- Colaiani, G., and Grano, M. (2015). Role of Irisin on the bone – muscle functional unit. *BoneKEY Rep.* 4, 1–4. doi: 10.1038/bonekey.2015.134
- Collinsworth, A. M., Zhang, S., Kraus, W. E., and Truskey, G. A. (2002). Apparent elastic modulus and hysteresis of skeletal muscle cells throughout differentiation. *AJP Cell Physiol.* 283, C1219–C1227. doi: 10.1152/ajpcell.00502.2001
- Conconi, M. T., De Coppi, P., Bellini, S., Zara, G., Sabatti, M., Marzaro, M., et al. (2005). Homologous muscle acellular matrix seeded with autologous myoblasts as a tissue-engineering approach to abdominal wall-defect repair. *Biomaterials* 26, 2567–2574. doi: 10.1016/j.biomaterials.2004.07.035
- Constantin, B. (2014). Dystrophin complex functions as a scaffold for signalling proteins. *Biochim. Biophys. Acta* 1838, 635–642. doi: 10.1016/j.bbamem.2013.08.023
- Corona, B. T., Machingal, M. A., Criswell, T., Vadhavkar, M., Dannahower, A. C., Bergman, C., et al. (2012). Further development of a tissue engineered muscle repair construct *in vitro* for enhanced functional recovery following implantation *in vivo* in a murine model of volumetric muscle loss injury. *Tissue Eng.* 18, 1213–1228. doi: 10.1089/ten.tea.2011.0614
- Corona, B. T., Ward, C. L., Baker, H. B., Walters, T. J., and Christ, G. J. (2014). Implantation of *in vitro* tissue engineered muscle repair constructs and bladder acellular matrices partially restore *in vivo* skeletal muscle function in a rat model of volumetric muscle loss injury. *Tissue Eng.* 20, 705–715. doi: 10.1089/ten.TEA.2012.0761
- Corso, P., Finkelstein, E., Miller, T., Fiebelkorn, I., and Zaloshnja, E. (2006). Incidence and lifetime costs of injuries in the United States. *Inj. Prev.* 12, 212–218. doi: 10.1136/ip.2005.010983
- Crisan, M., Yap, S., Casteilla, L., Chen, C.-W., Corselli, M., Park, T. S., et al. (2008). A perivascular origin for mesenchymal stem cells in multiple human organs. *Cell Stem Cell* 3, 301–313. doi: 10.1016/j.stem.2008.07.003
- Darabi, R., Arpke, R. W., Irion, S., Dimos, J. T., Grskovic, M., Kyba, M., et al. (2012). Human ES- and iPS-derived myogenic progenitors restore DYSTROPHIN and improve contractility upon transplantation in dystrophic mice. *Cell Stem Cell* 10, 610–619. doi: 10.1016/j.stem.2012.02.015
- De Angelis, L., Berghella, L., Coletta, M., Lattanzi, L., Zanchi, M., Cusella-De Angelis, M. G., et al. (1999). Skeletal myogenic progenitors originating from embryonic dorsal aorta coexpress endothelial and myogenic markers and contribute to postnatal muscle growth and regeneration. *J. Cell Biol.* 147, 869–878. doi: 10.1083/jcb.147.4.869
- De Bari, C., Dell’Accio, F., Vandennebee, F., Vermeesch, J. R., Raymackers, J.-M., and Luyten, F. P. (2003). Skeletal muscle repair by adult human mesenchymal stem cells from synovial membrane. *J. Cell Biol.* 160, 909–918. doi: 10.1083/jcb.200212064
- De Coppi, P., Bellini, S., Conconi, M. T., Sabatti, M., and Simonato, E., Gamba, P. G., et al. (2006). Myoblast–acellular skeletal muscle matrix constructs guarantee a long-term repair of experimental full-thickness abdominal wall defects. *Tissue Eng.* 12, 1929–1936. doi: 10.1089/ten.2006.12.1929
- Dellavalle, A., Sampaolesi, M., Tonlorenzi, R., Tagliafico, E., Sacchetti, B., Perani L., et al. (2007). Pericytes of human skeletal muscle are myogenic precursors distinct from satellite cells. *Nat. Cell Biol.* 9, 255–267. doi: 10.1038/ncb1542
- DeQuach, J. A., Lin, J. E., Cam, C., Hu, D., Salvatore, M. A., Sheikh, F., et al. (2012). Injectable skeletal muscle matrix hydrogel promotes neovascularization and muscle cell infiltration in a hindlimb ischemia model. *Eur. Cells Mater.* 23, 400–412; discussion 412. doi: 10.22203/eCM.v023a31
- Dezawa, M., Ishikawa, H., Itokazu, Y., Yoshihara, T., Hoshino, M., Takeda, S., et al. (2005). Bone marrow stromal cells generate muscle cells and repair muscle degeneration. *Science* 309, 314–317. doi: 10.1126/science.1110364
- Donnelly, K., Ph, D., Khodabukus, A., Philp, A., Deldicque, L., Dennis, R. G., Baar, K., et al. (2010). A novel bioreactor for stimulating skeletal muscle *in vitro*. *Tissue Eng. Part C Methods* 16, 711–718. doi: 10.1089/ten.TEC.2009.0125
- Duan, D. (2015). Duchenne muscular dystrophy gene therapy in the canine model. *Hum. Gene Ther. Clin. Dev.* 26, 57–69. doi: 10.1089/humc.2015.006
- Dumont, N. A., Bentzinger, C. F., Sincennes, M.-C., and Rudnicki, M. A. (2015a). Satellite cells and skeletal muscle regeneration. *Compr. Physiol.* 5, 1027–1059. doi: 10.1002/cphy.c140068
- Dumont, N. A., and Rudnicki, M. A. (2016). Targeting muscle stem cell intrinsic defects to treat Duchenne muscular dystrophy. *NPJ Regen. Med.* 1:16006. doi: 10.1038/npjregenmed.2016.6

- Dumont, N. A., Wang, Y. X., von Maltzahn, J., Pasut, A., Bentzinger, C. F., Brun, C. E., et al. (2015b). Dystrophin expression in muscle stem cells regulates their polarity and asymmetric division. *Nat. Med.* 21, 1455–1463. doi: 10.1038/nm.3990
- Dunstan, D. (2011). Diabetes: exercise and T2DM—move muscles more often! *Nat. Rev. Endocrinol.* 7, 189–190. doi: 10.1038/nrendo.2011.35
- Egan, B., and Zierath, J. R. (2013). Exercise metabolism and the molecular regulation of skeletal muscle adaptation. *Cell Metab.* 17, 162–184. doi: 10.1016/j.cmet.2012.12.012
- Emery, A. E. (1993). Duchenne muscular dystrophy-Meryon's disease. *Neuromuscul. Disord.* 3, 263–266.
- Engler, A. J., Griffin, M. A., Sen, S., Bönnemann, C. G., Sweeney, H. L., and Discher, D. E. (2004). Myotubes differentiate optimally on substrates with tissue-like stiffness: pathological implications for soft or stiff microenvironments. *J. Cell Biol.* 166, 877–887. doi: 10.1083/jcb.200405004
- Engler, A. J., Sen, S., Sweeney, H. L., and Discher, D. E. (2006). Matrix elasticity directs stem cell lineage specification. *Cell* 126, 677–689. doi: 10.1016/j.cell.2006.06.044
- Engler, A. J., Sweeney, H. L., Discher, D. E., and Schwarzbauer, J. E. (2007). Extracellular matrix elasticity directs stem cell differentiation. *J. Musculoskeletal Neuronal Interact.* 7:335.
- Ervasti, J. M., and Sonnemann, K. J. (2008). Biology of the striated muscle dystrophin-glycoprotein complex. *Int. Rev. Cytol.* 265, 191–225. doi: 10.1016/S0074-7696(07)65005-0
- Ferrari, G., Cusella-De Angelis, G., Coletta, M., Paolucci, E., Stornaiuolo, A., Cossu, G., et al. (1998). Muscle regeneration by bone marrow-derived myogenic progenitors. *Science* 279, 1528–1530. doi: 10.1126/science.279.5356.1528
- Ferrari, G., Stornaiuolo, A., and Mavilio, F. (2001). Bone-marrow transplantation: failure to correct murine muscular dystrophy. *Nature* 411, 1014–1015. doi: 10.1038/35082631
- Ferreira, M. M., Dewi, R. E., and Heilshorn, S. C. (2015). Microfluidic analysis of extracellular matrix-bFGF crosstalk on primary human myoblast chemoproliferation, chemokinesis, and chemotaxis. *Int. Biol.* 7, 569–579. doi: 10.1039/C5IB00060B
- Fishman, J. M., Tyraskis, A., Maghsoudlou, P., Urbani, L., Totonelli, G., Birchall, M. A., et al. (2013). Skeletal muscle tissue engineering: which cell to use? *Tissue Eng. Part B Rev.* 19, 503–515. doi: 10.1089/ten.teb.2013.0120
- Forcales, S.-V. (2015). Potential of adipose-derived stem cells in muscular regenerative therapies. *Front. Aging Neurosci.* 7:123. doi: 10.3389/fnagi.2015.00123
- Fujita, H., Nedachi, T., and Kanzaki, M. (2007). Accelerated de novo sarcomere assembly by electric pulse stimulation in C2C12 myotubes. *Exp. Cell Res.* 313, 1853–1865. doi: 10.1016/j.yexcr.2007.03.002
- Fuoco, C., Rizzi, R., Biondo, A., Longa, E., Mascaro, A., Shapira-Schweitzer, K., et al. (2015). *In vivo* generation of a mature and functional artificial skeletal muscle. *EMBO Mol. Med.* 7, 411–422. doi: 10.15252/emmm.201404062
- Fuoco, C., Salvatori, M. L., Biondo, A., Shapira-Schweitzer, K., Santoleri, S., Antonini, S., et al. (2012). Injectable polyethylene glycol-fibrinogen hydrogel adjuvant improves survival and differentiation of transplanted mesoangioblasts in acute and chronic skeletal-muscle degeneration. *Skel. Muscle* 2:24. doi: 10.1186/2044-5040-2-24
- Fuoco, C., Sangalli, E., Vono, R., Testa, S., Sacchetti, B., Latronico, M. V., et al. (2014). 3D hydrogel environment rejuvenates aged pericytes for skeletal muscle tissue engineering. *Front. Physiol.* 5:203. doi: 10.3389/fphys.2014.00203
- Furmanczyk, P. S., and Quinn, L. S. (2003). Interleukin-15 increases myosin accretion in human skeletal myogenic cultures. *Cell Biol. Int.* 27, 845–851. doi: 10.1016/S1065-6995(03)00172-0
- Gawlik, K. I., Holmberg, J., and Durbeej, M. (2014). Loss of dystrophin and  $\beta$ -sarcoglycan significantly exacerbates the phenotype of laminin  $\alpha$ 2 chain-deficient animals. *Am. J. Pathol.* 184, 740–752. doi: 10.1016/j.ajpath.2013.11.017
- Girgis, C. M., Mokbel, N., and DiGirolamo, D. J. (2014). Therapies for musculoskeletal disease: can we treat two birds with one stone? *Curr. Osteoporosis Rep.* 12, 142–153. doi: 10.1007/s11914-014-0204-5
- Gnecchi, M., He, H., Liang, O. D., Melo, L. G., Morello, F., Mu, H., et al. (2005). Paracrine action accounts for marked protection of ischemic heart by Akt-modified mesenchymal stem cells. *Nat. Med.* 11, 367–368. doi: 10.1038/nm0405-367
- Gnecchi, M., Zhang, Z., Ni, A., and Dzau, V. J. (2008). Paracrine mechanisms in adult stem cell signaling and therapy. *Circ. Res.* 103, 1204–1219. doi: 10.1161/CIRCRESAHA.108.176826
- Goldberg, A. (1967). Work-induced growth of skeletal muscle in normal and hypophysectomized rats. *Am. J. Physiol.* 213, 1193–1198.
- Goldspink, G. (1999). Changes in muscle mass and phenotype and the expression of autocrine and systemic growth factors by muscle in response to stretch and overload. *J. Anat.* 194 (Pt 3), 323–334. doi: 10.1046/j.1469-7580.1999.19430323.x
- Goldspink, G. (2003). Gene expression in muscle in response to exercise. *J. Muscle Res. Cell Motility* 24, 121–126. doi: 10.1023/A:1026041228041
- Goldspink, G., Scutt, A., Loughna, P. T., Wells, D. J., Jaenicke, T., and Gerlach, G. F. (1992). Gene expression in skeletal muscle in response to stretch and force generation. *Am. J. Physiol.* 262, R356–R363. doi: 10.1152/ajpregu.1992.262.3.R356
- Goyenvalle, A., Seto, J. T., Davies, K. E., and Chamberlain, J. (2011). Therapeutic approaches to muscular dystrophy. *Hum. Mol. Genet.* 20, R69–R78. doi: 10.1093/hmg/ddr105
- Grefte, S., Vullingsh, S., Kuijpers-Jagtman, A. M., Torensma, R., and Von den Hoff, J. W. (2012). Matrigel, but not collagen I, maintains the differentiation capacity of muscle derived cells *in vitro*. *Biomed. Materials* 7:55004. doi: 10.1088/1748-6041/7/5/055004
- Grizzi, I., Garreau, H., Li, S., and Vert, M. (1995). Hydrolytic degradation of devices based on poly(DL-lactic acid) size-dependence. *Biomaterials* 16, 305–311. doi: 10.1016/0142-9612(95)93258-F
- Guerci, A., Lahoute, C., Hébrard, S., Collard, L., Graindorge, D., Favier, M., et al. (2012). Srf-dependent paracrine signals produced by myofibers control satellite cell-mediated skeletal muscle hypertrophy. *Cell Metab.* 15, 25–37. doi: 10.1016/j.cmet.2011.12.001
- Guettier-Sigrist, S., Coupin, G., Braun, S., Warter, J.-M., and Poindron, P. (1998). Muscle could be the therapeutic target in SMA treatment. *J. Neurosci. Res.* 53, 663–669. doi: 10.1002/(SICI)1097-4547(19980915)53:6<663::AID-JNR4>3.0.CO;2-3
- Gunatillake, P. A., Adhikari, R., and Gadegaard, N. (2003). Biodegradable synthetic polymers for tissue engineering. *Eur. Cells Materials* 5, 1–16. doi: 10.22203/eCem.v005a01
- Guyon, J. R., Steffen, L. S., Howell, M. H., Pusack, T. J., Lawrence, C., and Kunkel, L. M. (2007). Modeling human muscle disease in zebrafish. *Biochim. Biophys. Acta* 1772, 205–215. doi: 10.1016/j.bbadis.2006.07.003
- Hammers, D. W., Sarathy, A., Pham, C. B., Drinnan, C. T., Farrar, R. P., and Suggs, L. J. (2012). Controlled release of IGF-I from a biodegradable matrix improves functional recovery of skeletal muscle from ischemia/reperfusion. *Biotechnol. Bioeng.* 109, 1051–1059. doi: 10.1002/bit.24382
- Han, W. M., Jang, Y. C., and García, A. J. (2016). Engineered matrices for skeletal muscle satellite cell engraftment and function. *Matrix Biol.* 60–61, 96–109. doi: 10.1016/j.matbio.2016.06.001
- Harries, L. W., McCulloch, L. J., Holley, J. E., Rawling, T. J., Welters, H. J., and Kos, K. (2013). A role for SPARC in the moderation of human insulin secretion. *PLoS ONE* 8:68253. doi: 10.1371/journal.pone.0068253
- Haugen, F., Norheim, F., Lian, H., Wensaas, A. J., Dueland, S., Berg, O., et al. (2010). IL-7 is expressed and secreted by human skeletal muscle cells. *Am. J. Physiol. Cell Physiol.* 298, C807–C816. doi: 10.1152/ajpcell.00094.2009
- Heher, P., Maleiner, B., Prüller, J., Teuschl, A. H., Kollmitzer, J., Monforte, X., et al. (2015). A novel bioreactor for the generation of highly aligned 3D skeletal muscle-like constructs through orientation of fibrin via application of static strain. *Acta Biomaterialia* 24, 251–265. doi: 10.1016/j.actbio.2015.06.033
- Helgersson S. L., Seelich T., DiOrion, J., Tawil, J. B., Bittner, K., and Spaethe, R. (2004). *Fibrin, Encyclopedia of Biomaterials and Biomedical Engineering*. (New York, NY: Marcel Dekker), 603–610.
- Hill, E., Boontheekul, T., and Mooney, D. J. (2006a). Designing scaffolds to enhance transplanted myoblast survival and migration. *Tissue Eng.* 12, 1295–1304. doi: 10.1089/ten.2006.12.1295
- Hill, E., Boontheekul, T., and Mooney, D. J. (2006b). Regulating activation of transplanted cells controls tissue regeneration. *Proc. Natl. Acad. Sci. U.S.A.* 103, 2494–2499. doi: 10.1073/pnas.0506004103

- Hinds, S., Bian, W., Dennis, R. G., and Bursac, N. (2011). The role of extracellular matrix composition in structure and function of bioengineered skeletal muscle. *Biomaterials* 32, 3575–3583. doi: 10.1016/j.biomaterials.2011.01.062
- Hojman, P., Pedersen, M., Nielsen, A. R., Krogh-Madsen, R., Yfanti, C., Akerstrom, T., et al. (2009). Fibroblast growth factor-21 is induced in human skeletal muscles by hyperinsulinemia. *Diabetes* 58, 2797–2801. doi: 10.2337/db09-0713
- Horch, R. E., Debus, M., Wagner, G., and Stark, G. B. (2000). Cultured human keratinocytes on type I collagen membranes to reconstitute the epidermis. *Tissue Eng.* 6, 53–67. doi: 10.1089/107632700320892
- Hosseini, V., Ahadian, S., Ostrovidov, S., Camci-Unal, G., Chen, S., Kaji, H., et al. (2012). Engineered contractile skeletal muscle tissue on a microgrooved methacrylated gelatin substrate. *Tissue Eng. Part A* 18, 2453–2465. doi: 10.1089/ten.tea.2012.0181
- Huang, N. F., Patel, S., Thakar, R. G., Wu, J., Hsiao, B. S., Chu, B., et al. (2006a). Myotube assembly on nanofibrous and micropatterned polymers. *Nano Lett.* 6, 537–542. doi: 10.1021/nl060060o
- Huang, Y.-C., Dennis, R. G., and Baar, K. (2006b). Cultured slow vs. fast skeletal muscle cells differ in physiology and responsiveness to stimulation. *AJP Cell Physiol.* 291, C11–C17. doi: 10.1152/ajpcell.00366.2005
- Huang, Y.-C., Dennis, R. G., Larkin, L., Baar, K. (2004). Rapid formation of functional muscle *in vitro* using fibrin gels. *J. Appl. Physiol.* 98, 706–713. doi: 10.1152/jappphysiol.00273.2004
- Izumiya, Y., Bina, H. A., Ouchi, N., Akasaki, Y., Kharitonov, A., and Walsh, K. (2008). FGF21 is an Akt-regulated myokine. *FEBS Lett.* 582, 3805–3810. doi: 10.1016/j.febslet.2008.10.021
- Jana, S., Cooper, A., and Zhang, M. (2013). Chitosan scaffolds with unidirectional microtubular pores for large skeletal myotube generation. *Adv. Healthcare Mater.* 2, 557–561. doi: 10.1002/adhm.201200177
- Janssen, I., Shepard, D. S., Katzmarzyk, P. T., and Roubenoff, R. (2004). The healthcare costs of sarcopenia in the United States. *J. Am. Geriatrics Soc.* 52, 80–85. doi: 10.1111/j.1532-5415.2004.52014.x
- Joe, A. W., Yi, L., Natarajan, A., Le Grand, F., So, L., Wang, J., et al. (2010). Muscle injury activates resident fibro/adipogenic progenitors that facilitate myogenesis. *Nat. Cell Biol.* 12, 153–163. doi: 10.1038/ncb2015
- Juhas, M., and Bursac, N. (2014). Roles of adherent myogenic cells and dynamic culture in engineered muscle function and maintenance of satellite cells. *Biomaterials* 35, 9438–9446. doi: 10.1016/j.biomaterials.2014.07.035
- Juhas, M., Ye, J., and Bursac, N. (2015). Design, evaluation, and application of engineered skeletal muscle. *Methods* 99, 81–90. doi: 10.1016/j.ymeth.2015.10.002
- Jun, I., Jeong, S., and Shin, H. (2009). The stimulation of myoblast differentiation by electrically conductive sub-micron fibers. *Biomaterials* 30, 2038–2047. doi: 10.1016/j.biomaterials.2008.12.063
- Kasper, A. M., Turner, D. C., Martin, N. R. W., and Sharples, A. P. (2017). Mimicking exercise in three-dimensional bioengineered skeletal muscle to investigate cellular and molecular mechanisms of physiological adaptation. *J. Cell. Physiol.* 233, 1985–1998. doi: 10.1002/jcp.25840
- Katz, B. (1961). The termination of the afferent nerve fibre in the muscle spindle of the frog. *Biol. Sci.* 243, 222–240. doi: 10.1098/rstb.1961.0001
- Khodabukus, A., and Baar, K. (2012). Defined electrical stimulation emphasizing excitability for the development and testing of engineered skeletal muscle. *Tissue Eng. Part C Methods* 18, 349–357. doi: 10.1089/ten.tec.2011.0364
- Khodabukus, A., Baehr, L. M., Bodine, S. C., and Baar, K. (2015). Role of contraction duration in inducing fast-to-slow contractile and metabolic protein and functional changes in engineered muscle. *J. Cell. Physiol.* 230, 2489–2497. doi: 10.1002/jcp.24985
- Kim, M. H., Hong, H. N., Hong, J. P., Park, C. J., Kwon, S. W., Kim, S. H., et al. (2010a). The effect of VEGF on the myogenic differentiation of adipose tissue derived stem cells within thermosensitive hydrogel matrices. *Biomaterials* 31, 1213–1218. doi: 10.1016/j.biomaterials.2009.10.057
- Kim, M. S., Jun, I., Shin, Y. M., Jang, W., Kim, S. I., and Shin, H. (2010b). The development of genipin-crosslinked poly(caprolactone) (PCL)/gelatin nanofibers for tissue engineering applications. *Macromol. Biosci.* 10, 91–100. doi: 10.1002/mabi.200900168
- Kinnaird, T., Stabile, E., Burnett, M. S., Lee, C. W., Barr, S., Fuchs, S., et al. (2004). Marrow-derived stromal cells express genes encoding a broad spectrum of arteriogenic cytokines and promote *in vitro* and *in vivo* arteriogenesis through paracrine mechanisms. *Circulation Res.* 94, 678–685. doi: 10.1161/01.RES.0000118601.37875.AC
- Kodaka, Y., Rabu, G., and Asakura, A. (2017). Skeletal muscle cell induction from pluripotent stem cells. *Stem Cells Int.* 2017, 1–16. doi: 10.1155/2017/1376151
- Kojima, K., Bonassar, L. J., Ignatz, R. A., Syed, K., Cortiella, J., and Vacanti, C. A. (2003). Comparison of tracheal and nasal chondrocytes for tissue engineering of the trachea. *Ann. Thoracic Surg.* 76, 1884–1888. doi: 10.1016/S0003-4975(03)01193-7
- Koponen, J. K., Kekkarainen, T., Heinonen, S. E., Laitinen, A., Nystedt, J., Laine, J., et al. (2007). Umbilical cord blood-derived progenitor cells enhance muscle regeneration in mouse hindlimb ischemia model. *Mol. Ther.* 15, 2172–2177. doi: 10.1038/sj.mt.6300302
- Kopp, J., Jeschke, M. G., Bach, A. D., Kneser, U., and Horch, R. E. (2004). Applied tissue engineering in the closure of severe burns and chronic wounds using cultured human autologous keratinocytes in a natural fibrin matrix. *Cell Tiss. Banking* 5, 81–87. doi: 10.1023/B:CATB.0000034082.29214.3d
- Kortesidis, A., Zannettino, A., Isenmann, S., Shi, S., Lapidot, T., and Gronthos, S. (2005). Stromal-derived factor-1 promotes the growth, survival, and development of human bone marrow stromal stem cells. *Blood* 105, 3793–3801. doi: 10.1182/blood-2004-11-4349
- Kroehne, V., Heschel, I., Schügner, F., Lasrich, D., Bartsch, J. W., and Jockusch, H. (2008). Use of a novel collagen matrix with oriented pore structure for muscle cell differentiation in cell culture and in grafts. *J. Cell. Mol. Med.* 12, 1640–1648. doi: 10.1111/j.1582-4934.2008.00238.x
- Ku, S. H., Lee, S. H., and Park, C. B. (2012). Synergic effects of nanofiber alignment and electroactivity on myoblast differentiation. *Biomaterials* 33, 6098–6104. doi: 10.1016/j.biomaterials.2012.05.018
- Kurek, J. B., Bower, J. J., Romanella, M., Koentgen, F., Murphy, M., and Austin, L. (1997). The role of leukemia inhibitory factor in skeletal muscle regeneration. *Muscle Nerve* 20, 815–822. doi: 10.1002/(SICI)1097-4598(199707)20:7<andgt;815::AID-MUS5andgt;3.0.CO;2-A
- Kurek, J. B., Nouri, S., Kannourakis, G., Murphy, M., and Austin, L. (1996). Leukemia inhibitory factor and interleukin-6 are produced by diseased and regenerating skeletal muscle. *Muscle Nerve* 19, 1291–1301. doi: 10.1002/(SICI)1097-4598(199610)19:10andlt;1291::AID-MUS6andgt;3.0.CO;2-9
- Kurth, F., Franco-Obregón, A., Casarosa, M., Küster, S. K., Wuertz-Kozak, K., and Dittrich, P. S. (2015). Transient receptor potential vanilloid 2-mediated shear-stress responses in C2C12 myoblasts are regulated by serum and extracellular matrix. *FASEB J.* 29, 4726–4737. doi: 10.1096/fj.15-275396
- Lam, M. T., Huang, Y. C., Birla, R. K., and Takayama, S. (2009). Microfeature guided skeletal muscle tissue engineering for highly organized 3-dimensional free-standing constructs. *Biomaterials* 30, 1150–1155. doi: 10.1016/j.biomaterials.2008.11.014
- Landfeldt, E., Lindgren, P., Bell, C. F., Schmitt, C., Guglieri, M., Straub, V., et al. (2014). The burden of Duchenne muscular dystrophy: an international, cross-sectional study. *Neurology* 83, 529–536. doi: 10.1212/WNL.0000000000000669
- Langelaan, M. L., Boonen, K. J., Rosaria-Chak, K. Y., van der Schaft, D. W., Post, M. J., and Baaijens, F. P. (2011). Advanced maturation by electrical stimulation: Differences in response between C2C12 and primary muscle progenitor cells. *J. Tissue Eng. Regenerat. Med.* 5, 529–539. doi: 10.1002/term.345
- Law, P. K., Goodwin, T. G., Fang, Q., Deering, M. B., Duggirala, V., Larkin, C., et al. (1993). Cell transplantation as an experimental treatment for Duchenne muscular dystrophy. *Cell Transplant.* 2, 485–505. doi: 10.1177/096368979300200607
- Le Blanc, K., and Mougiakakos, D. (2012). Multipotent mesenchymal stromal cells and the innate immune system. *Nat. Rev. Immunol.* 12, 383–396. doi: 10.1038/nri3209
- Lee, C. H., Singla, A., and Lee, Y. (2001). Biomedical applications of collagen. *Int. J. Pharmaceut.* 221, 1–22. doi: 10.1016/S0378-5173(01)00691-3
- Lee, H., Park, J., Forget, B. G., and Gaines, P. (2009). Induced pluripotent stem cells in regenerative medicine: an argument for continued research on human embryonic stem cells. *Regen. Med.* 4, 759–769. doi: 10.2217/rme.09.46

- Lee, J. W., Fang, X., Krasnodembskaya, A., Howard, J. P., and Matthay, M. A. (2011). Concise review: mesenchymal stem cells for acute lung injury: role of paracrine soluble factors. *Stem Cells* 29, 913–919. doi: 10.1002/stem.643
- Lee, K. Y., and Mooney, D. J. (2012). Alginate: properties and biomedical applications. *Prog. Polymer Sci.* 37, 106–126. doi: 10.1016/j.progpolymsci.2011.06.003
- Liao, I.-C., Liu, J. B., Bursac, N., and Leong, K. W. (2008). Effect of electromechanical stimulation on the maturation of myotubes on aligned electrospun fibers. *Cell. Mol. Bioeng.* 1, 133–145. doi: 10.1007/s12195-008-0021-y
- Liu, J., Xu, H. H., Zhou, H., Weir, M. D., Chen, Q., and Trotman, C. A. (2013). Human umbilical cord stem cell encapsulation in novel macroporous and injectable fibrin for muscle tissue engineering. *Acta Biomaterialia* 9, 4688–4697. doi: 10.1016/j.actbio.2012.08.009
- Liu, J., Zhou, H., Weir, M. D., Xu, H. H., Chen, Q., and Trotman, C. A. (2012). Fast-degradable microbeads encapsulating human umbilical cord stem cells in alginate for muscle tissue engineering. *Tissue Eng. Part A* 18, 2303–2314. doi: 10.1089/ten.tea.2011.0658
- Luo, Y., Kirker, K. R., and Prestwich, G. D. (2000). Cross-linked hyaluronic acid hydrogel films: new biomaterials for drug delivery. *J. Controlled Release* 69, 169–184. doi: 10.1016/S0168-3659(00)00300-X
- Luo, Z., Luo, P., Yu, Y., Zhao, Q., Zhao, X., and Cheng, L. (2012). SPARC promotes the development of erythroid progenitors. *Exp. Hematol.* 40, 828–836. doi: 10.1016/j.exphem.2012.06.002
- Ma, J., Holden, K., Zhu, J., Pan, H., and Li, Y. (2011). The application of three-dimensional collagen-scaffolds seeded with myoblasts to repair skeletal muscle defects. *J. Biomed. Biotechnol.* 2011:812135. doi: 10.1155/2011/812135
- Machingal, M. A., Corona, B. T., Walters, T. J., Kesireddy, V., Koval, C. N., Dannahower, A., et al. (2011). A tissue-engineered muscle repair construct for functional restoration of an irrecoverable muscle injury in a murine model. *Tissue Eng. Part A* 17, 2291–2303. doi: 10.1089/ten.tea.2010.0682
- Madden, L., Juhas, M., Kraus, W. E., Truskey, G. A., and Bursac, N. (2015). Bioengineered human myobundles mimic clinical responses of skeletal muscle to drugs. *eLife* 4:e04885. doi: 10.7554/eLife.04885
- Mah, J. K., Korngut, L., Dykeman, J., Day, L., Pringsheim, T., and Jette, N. (2014). A systematic review and meta-analysis on the epidemiology of Duchenne and Becker muscular dystrophy. *Neuromuscul. Disord.* 24, 482–491. doi: 10.1016/j.nmd.2014.03.008
- Malecova, B., and Puri, P. L. (2012). “Mix of Mics”- phenotypic and biological heterogeneity of “multipotent” muscle interstitial cells (MICs). *J. Stem Cell Res. Ther.* (Suppl 11):004.
- Mandal, B. B., and Kundu, S. C. (2009). Cell proliferation and migration in silk fibroin 3D scaffolds. *Biomaterials* 30, 2956–2965. doi: 10.1016/j.biomaterials.2009.02.006
- Marzaro, M., Conconi, M. T., Perin, L., Giuliani, S., Gamba, P., De Coppi, P., et al. (2002). Autologous Satellite Cell Seeding Improves *in vivo* Biocompatibility of Homologous Muscle Acellular Matrix Implants. [Accessed April 6, 2017]. Available online at: <http://www.ingentaconnect.com/content/sp/ijmm/2002/00000010/00000002/art00009>
- Mase, V. J., Hsu, J. R., Wolf, S. E., Wenke, J. C., Baer, D. G., Owens, J., et al. (2010). Clinical application of an acellular biologic scaffold for surgical repair of a large, traumatic quadriceps femoris muscle defect. *Orthopedics* 33:511. doi: 10.3928/01477447-20100526-24
- Matsumoto, T., Sasaki, J., Alsborg, E., Egusa, H., Yatani, H., and Sohmura, T. (2007). Three-dimensional cell and tissue patterning in a strained fibrin gel system. *PLoS ONE* 2:1211. doi: 10.1371/journal.pone.0001211
- Mauro, A. (1961). Satellite cell of skeletal muscle fibers. *J. Biophys. Biochem. Cytol.* 9, 493–495. doi: 10.1083/jcb.9.2.493
- McCullen, S. D., Chow, A. G., and Stevens, M. M. (2011). *In vivo* tissue engineering of musculoskeletal tissues. *Curr. Opin. Biotechnol.* 22, 715–720. doi: 10.1016/j.copbio.2011.05.001
- McGreevy, J. W., Hakim, C. H., McIntosh, M. A., and Duan, D. (2015). Animal models of Duchenne muscular dystrophy: from basic mechanisms to gene therapy. *Dis. Model. Mech.* 8, 195–213. doi: 10.1242/dmm.018424
- Meregalli, M., Farini, A., Belicchi, M., Parolini, D., Cassinelli, L., Razini, P., et al. (2013). Perspectives of stem cell therapy in Duchenne muscular dystrophy. *FEBS J.* 280, 4251–4262. doi: 10.1111/febs.12083
- Meregalli, M., Farini, A., Sitzia, C., and Torrente, Y. (2014). Advancements in stem cells treatment of skeletal muscle wasting. *Front. Physiol.* 5:48. doi: 10.3389/fphys.2014.00048
- Merritt, E. K., Cannon, M. V., Hammers, D. W., Le, L. N., Gokhale, R., Sarathy, A., et al. (2010). Repair of traumatic skeletal muscle injury with bone-marrow-derived mesenchymal stem cells seeded on extracellular matrix. *Tissue Eng. Part A* 16, 2871–2881. doi: 10.1089/ten.tea.2009.0826
- Minasi, M. G., Riminucci, M., De Angelis, L., Borello, U., Berarducci, B., Innocenzi, A., et al. (2002). The meso-angioblast: a multipotent, self-renewing cell that originates from the dorsal aorta and differentiates into most mesodermal tissues. *Development* 129, 2773–2783.
- Monge, C., Ren, K., Berton, K., Guillot, R., Peyrade, D., and Picart, C. (2012). Engineering muscle tissues on microstructured polyelectrolyte multilayer films. *Tissue Eng. Part A* 18, 1664–1676. doi: 10.1089/ten.tea.2012.0079
- Moon, D. G., Christ, G., Stitzel, J. D., Atala, A., and Yoo, J. J. (2008). Cyclic mechanical preconditioning improves engineered muscle contraction. *Tissue Eng. Part A* 14, 473–482. doi: 10.1089/ten.tea.2007.0104
- Morishima-Kawashima, M., Hasegawa, M., Takio, K., Suzuki, M., Yoshida, H., Titani, K., et al. (1995). Proline-directed and non-proline-directed phosphorylation of PHF-tau. *J. Biol. Chem.* 270, 823–829. doi: 10.1074/jbc.270.2.823
- Mouly, V., Aamiri, A., Périé, S., Mamchaoui, K., Barani, A., Bigot, A., et al. (2005). Myoblast transfer therapy: is there any light at the end of the tunnel? *Acta Myologica* 24, 128–133.
- Muñoz-Cánoves, P., Scheele, C., Pedersen, B. K., and Serrano, A. L. (2013). Interleukin-6 myokine signaling in skeletal muscle: a double-edged sword? *FEBS J.* 280, 4131–4148. doi: 10.1111/febs.12338
- Murphy-Ullrich, J. E., and Sage, E. H. (2014). Revisiting the matricellular concept. *Matrix Biol.* 37, 1–14. doi: 10.1016/j.matbio.2014.07.005
- Nam, K.-H., Smith, A. S., Lone, S., Kwon, S., and Kim, D.-H. (2015). Biomimetic 3D tissue models for advanced high-throughput drug screening. *J. Lab. Autom.* 20, 201–215. doi: 10.1177/2211068214557813
- Nielsen, A. R., and Pedersen, B. K. (2007). The biological roles of exercise-induced cytokines: IL-6, IL-8, and IL-15. *Appl. Physiol. Nutr. Metab.* 32, 833–839. doi: 10.1139/H07-054
- Nishizawa, H., Matsuda, M., Yamada, Y., Kawai, K., Suzuki, E., Makishima, M., et al. (2004). Musclin, a novel skeletal muscle-derived secretory factor. *J. Biol. Chem.* 279, 19391–19395. doi: 10.1074/jbc.C400066200
- Oakes, B. W. (2004). Orthopaedic tissue engineering: from laboratory to the clinic. *Med. J. Aust.* 180(5 Suppl.), S35–S38.
- Ohnishi, S., Sumiyoshi, H., Kitamura, S., and Nagaya, N. (2007). Mesenchymal stem cells attenuate cardiac fibroblast proliferation and collagen synthesis through paracrine actions. *FEBS Lett.* 581, 3961–3966. doi: 10.1016/j.febslet.2007.07.028
- Okano, T., and Matsuda, T. (1998a). Muscular tissue engineering: capillary-incorporated hybrid muscular tissues *in vivo* tissue culture. *Cell Transplant.* 7, 435–442.
- Okano, T., and Matsuda, T. (1998b). Tissue engineered skeletal muscle: preparation of highly dense, highly oriented hybrid muscular tissues. *Cell Transplant.* 7, 71–82.
- Ostrovidov, S., Hosseini, V., Ahadian, S., Fujie, T., Parthiban, S. P., Ramalingam, M., et al. (2014). Skeletal muscle tissue engineering: methods to form skeletal myotubes and their applications. *Tissue Eng. B* 20. doi: 10.1089/ten.teb.2013.0534
- Ostrovidov, S., Shi, X., Sadeghian, R. B., Salehi, S., Fujie, T., Bae, H., et al. (2015). Stem cell differentiation toward the myogenic lineage for muscle tissue regeneration: a focus on muscular dystrophy. *Stem Cell Rev. Rep.* 11, 866–884. doi: 10.1007/s12015-015-9618-4
- Ouchi, N., Oshima, Y., Ohashi, K., Higuchi, A., Ikegami, C., Izumiya, Y., et al. (2008). Follistatin-like 1, a secreted muscle protein, promotes endothelial cell function and revascularization in ischemic tissue through a nitric-oxide synthase-dependent mechanism. *J. Biol. Chem.* 283, 32802–32811. doi: 10.1074/jbc.M803440200
- Page, R. L., Malcuit, C., Vilner, L., Vojtic, I., Shaw, S., Hedblom, E., et al. (2011). Restoration of skeletal muscle defects with adult human cells delivered on fibrin microthreads. *Tissue Eng. Part A* 17, 2629–2640. doi: 10.1089/ten.tea.2011.0024
- Papers, J. B. C., and Mayer, U. (2003). Integrins: redundant or important players in skeletal muscle. *J. Biol. Chem.* 278, 14587–14590. doi: 10.1074/jbc.R200022200



- Park, H., Bhalla, R., Saigal, R., Radisic, M., Watson, N., Langer, R., et al. (2008). Effects of electrical stimulation in C2C12 muscle constructs. *J. Tiss. Eng. Regenerat. Med.* 2, 279–287. doi: 10.1002/term.93
- Partridge, T. (2010). The potential of exon skipping for treatment for duchenne muscular dystrophy. *J. Child Neurol.* 25, 1165–1170. doi: 10.1177/0883073810371130
- Partridge, T. A., Morgan, J. E., Coulton, G. R., Hoffman, E. P., and Kunkel, L. M. (1989). Conversion of mdx myofibres from dystrophin-negative to -positive by injection of normal myoblasts. *Nature* 337, 176–179. doi: 10.1038/337176a0
- Pedersen, B. K. (2009). Edward F. Adolph distinguished lecture: muscle as an endocrine organ: IL-6 and other myokines. *J. Appl. Physiol.* 107, 1006–1014. doi: 10.1152/jappphysiol.00734.2009
- Pedersen, B. K. (2011). Muscles and their myokines. *J. Exp. Biol.* 214, 337–346. doi: 10.1242/jeb.048074
- Pedersen, B. K., and Febbraio, M. A. (2008). Muscle as an endocrine organ.pdf. *Physiol. Rev.* 88, 1379–1406. doi: 10.1152/physrev.90100.2007
- Pedersen, B. K., Steensberg, A., and Schjerling, P. (2001). Muscle-derived interleukin-6: Possible biological effects. *J. Physiol.* 536, 329–337. doi: 10.1111/j.1469-7793.2001.0329c.xd
- Perniconi, B., Costa, A., Aulino, P., Teodori, L., Adamo, S., and Coletti, D. (2011). The pro-myogenic environment provided by whole organ scale acellular scaffolds from skeletal muscle. *Biomaterials* 32, 7870–7882. doi: 10.1016/j.biomaterials.2011.07.016
- Pistilli, E. E., Siu, P. M., and Alway, S. E. (2007). Interleukin-15 responses to aging and unloading-induced skeletal muscle atrophy. *Am. J. Physiol. Cell Physiol.* 292, C1298–C1304. doi: 10.1152/ajpcell.00496.2006
- Powell, C. A., Smiley, B. L., Mills, J., and Vandeburgh, H. H. (2002). Mechanical stimulation improves tissue-engineered human skeletal muscle. *AJP Cell Physiol.* 283, C1557–C1565. doi: 10.1152/ajpcell.00595.2001
- Purves, D., Augustine, G. J., Fitzpatrick, D., Katz, L. C., LaMantia, A. S., McNamara, J. O., et al. (eds.). (2001). *Neuroscience*, 2nd Edn. Sunderland, MA: Sinauer Associates.
- Qazi, T. H., Mooney, D. J., Pumberger, M., Geissler, S., and Duda, G. N. (2015). Biomaterials based strategies for skeletal muscle tissue engineering: existing technologies and future trends. *Biomaterials* 53, 502–521. doi: 10.1016/j.biomaterials.2015.02.110
- Quattrocchi, M., Swinnen, M., Giacomazzi, G., Camps, J., Barthélemy, I., Ceccarelli, G., et al. (2015). Mesodermal iPSC – derived progenitor cells functionally regenerate cardiac and skeletal muscle. *J. Clin. Invest.* 125, 4463–4482. doi: 10.1172/JCI82735
- Quinn, L. (2002). Overexpression of interleukin-15 induces skeletal muscle hypertrophy *in vitro*: implications for treatment of muscle wasting disorders. *Exp. Cell Res.* 280, 55–63. doi: 10.1006/excr.2002.5624
- Quinn, L. S., Anderson, B. G., Strait-Bodey, L., Stroud, A. M., and Argilés, J. M. (2008). Oversecretion of interleukin-15 from skeletal muscle reduces adiposity. *AJP Endocrinol. Metab.* 296, E191–E202. doi: 10.1152/ajpendo.90506.2008
- Quinn, L. S., Haugk, K. L., and Grabstein, K. H. (1995). Interleukin-15: a novel anabolic cytokine for skeletal muscle. *Endocrinology* 136, 3669–3672. doi: 10.1210/endo.136.8.7628408
- Rao, R. R., Long, J. Z., White, J. P., Svensson, K. J., Lou, J., Lokurkar, I., et al. (2014). Meteorin-like is a hormone that regulates immune-adipose interactions to increase beige fat thermogenesis. *Cell* 157, 1279–1291. doi: 10.1016/j.cell.2014.03.065
- Reginster, J.-Y., Beaudart, C., Buckinx, F., and Bruyère, O. (2015). Osteoporosis and sarcopenia: two diseases or one?. *Curr. Opin. Clin. Nutr. Metab. Care* 19, 31–36. doi: 10.1097/MCO.0000000000000230
- Relaix, F., Weng, X., Marazzi, G., Yang, E., Copeland, N., Jenkins, N., et al. (1996). Pw1, a novel zinc finger gene implicated in the myogenic and neuronal lineages. *Dev. Biol.* 177, 383–396. doi: 10.1006/dbio.1996.0172
- Rhim, C., Cheng, C. S., Kraus, W. E., and Truskey, G. A. (2010). Effect of microRNA modulation on bioartificial muscle function. *Tiss. Eng.* 16, 3589–3597. doi: 10.1089/ten.tea.2009.0601
- Rhim, C., Lowell, D. A., Reedy, M. C., Slentz, D. H., Zhang, S. J., Kraus, W. E., et al. (2007). Morphology and ultrastructure of differentiating three-dimensional mammalian skeletal muscle in a collagen gel. *Musc. Nerve* 36, 71–80. doi: 10.1002/mus.20788
- Riechman, S. E., Balasekaran, G., Roth, S. M., and Ferrell, R. E. (2004). Association of interleukin-15 protein and interleukin-15 receptor genetic variation with resistance exercise training responses. *J. Appl. Physiol.* 97, 2214–2219. doi: 10.1152/jappphysiol.00491.2004
- Romitti, P. A., Zhu, Y., Puzhankara, S., James, K. A., Nabukera, S. K., Zamba, G. K. D., et al. (2015). Prevalence of Duchenne and Becker muscular dystrophies in the United States. *Pediatrics* 135, 513–521. doi: 10.1542/peds.2014-2044
- Rose-John, S., Scheller, J., Elson, G., and Jones, S. A. (2006). Interleukin-6 biology is coordinated by membrane-bound and soluble receptors: role in inflammation and cancer. *J. Leukocyte Biol.* 80, 227–236. doi: 10.1189/jlb.1105674
- Rossi, C. A., Flaibani, M., Blaauw, B., Pozzobon, M., Figallo, E., Reggiani, C., et al. (2011). *In vivo* tissue engineering of functional skeletal muscle by freshly isolated satellite cells embedded in a photopolymerizable hydrogel. *FASEB J.* 25, 2296–2304. doi: 10.1096/fj.10-174755
- Ryall, J. G., Schertzer, J. D., and Lynch, G. S. (2008). Cellular and molecular mechanisms underlying age-related skeletal muscle wasting and weakness. *Biogerontology* 9, 213–228. doi: 10.1007/s10522-008-9131-0
- Rybalko, V. Y., Pham, C. B., Hsieh, P.-L., Hammers, D. W., Merscham-Banda, M., Suggs, L. J., et al. (2015). Controlled delivery of SDF-1 $\alpha$  and IGF-1: CXCR4(+) cell recruitment and functional skeletal muscle recovery. *Biomater. Sci.* 3, 1475–1486. doi: 10.1039/C5BM00233H
- Sacco, A., Mourkioti, F., Tran, R., Choi, J., Llewellyn, M., Kraft, P., et al. (2010). Short telomeres and stem cell exhaustion model duchenne muscular dystrophy in mdx/mTR Mice. *Cell* 143, 1059–1071. doi: 10.1016/j.cell.2010.11.039
- Salmons, S., Ashley, Z., Sutherland, H., Russold, M. F., Li, F., and Jarvis, J. C. (2005). Functional electrical stimulation of denervated muscles: basic issues. *Artificial Organs* 29, 199–202. doi: 10.1111/j.1525-1594.2005.29034.x
- Sampaolesi, M., Blot, S., D'Antona, G., Granger, N., Tonlorenzi, R., Innocenzi, A., et al. (2006). Mesoangioblast stem cells ameliorate muscle function in dystrophic dogs. *Nature* 444, 574–579. doi: 10.1038/nature05282
- Sampaolesi, M., Torrente, Y., Innocenzi, A., Tonlorenzi, R., D'Antona, G., Pellegrino, M. A., et al. (2003). Cell therapy of  $\alpha$ -sarcoglycan null dystrophic mice through intra-arterial delivery of mesoangioblasts. *Science* 301, 487–492. doi: 10.1126/science.1082254
- Sassoli, C., Zecchi-Orlandini, S., and Formigli, L. (2012). Trophic actions of bone marrow-derived mesenchymal stromal cells for muscle repair/regeneration. *Cells* 1, 832–850. doi: 10.3390/cells1040832
- Seale, P., and Rudnicki, M. A. (2000). A new look at the origin, function, and “stem-cell” status of muscle satellite cells. *Dev. Biol.* 218, 115–124. doi: 10.1006/dbio.1999.9565
- Seldin, M. M., Peterson, J. M., Byerly, M. S., Wei, Z., and Wong, G. W. (2012). Myonectin (CTRP15), a novel myokine that links skeletal muscle to systemic lipid homeostasis. *J. Biol. Chem.* 287, 11968–11980. doi: 10.1074/jbc.M111.336834
- Serena, E., Zatti, S., Reghelin, E., Pasut, A., Cimetta, E., and Elvassore, N. (2010). Soft substrates drive optimal differentiation of human healthy and dystrophic myotubes. *Integr. Biol.* 2, 193–201. doi: 10.1039/b921401a
- Serena, E., Zatti, S., Zoso, A., Lo Verso, F., Tedesco, F. S., Cossu, G., et al. (2016). Skeletal muscle differentiation on a chip shows human donor mesoangioblasts' efficiency in restoring dystrophin in a Duchenne muscular dystrophy model. *Stem Cells Transl. Med.* 5, 1676–1683. doi: 10.5966/sctm.2015-0053
- Serrano, A. L., Baeza-Raja, B., Perdiguero, E., Jardí, M., and Muñoz-Cánoves, P. (2008). Interleukin-6 is an essential regulator of satellite cell-mediated skeletal muscle hypertrophy. *Cell Metab.* 7, 33–44. doi: 10.1016/j.cmet.2007.11.011
- Serrano, A. L., Mann, C. J., Vidal, B., Ardite, E., Perdiguero, E., and Muñoz-Cánoves, P. (2011). Cellular and molecular mechanisms regulating fibrosis in skeletal muscle repair and disease. *Curr. Top Dev. Biol.* 2096, 167–201. doi: 10.1016/B978-0-12-385940-2.00007-3
- Shadrin, I. Y., Khodabukus, A., and Bursac, N. (2016). Striated muscle function, regeneration, and repair. *Cell. Mol. Life Sci.* 73, 4175–4202. doi: 10.1007/s00018-016-2285-z
- Shansky, J., Chromiak, J., Del Tatto, M., and Vandeburgh, H. (1997). A simplified method for tissue engineering skeletal muscle organoids *in vitro*. *In Vitro Cell. Devel. Biol. Animal* 33, 659–661. doi: 10.1007/s11626-997-0118-y
- Shapiro, L., and Cohen, S. (1997). Novel alginate sponges for cell culture and transplantation. *Biomaterials* 18, 583–590. doi: 10.1016/S0142-9612(96)00181-0

- Sicari, B. M., Rubin, J. P., Dearth, C. L., Wolf, M. T., Ambrosio, F., Boninger, M., et al. (2014). An acellular biologic scaffold promotes skeletal muscle formation in mice and humans with volumetric muscle loss. *Sci. Transl. Med.* 6, 234ra58–234ra58. doi: 10.1126/scitranslmed.3008085
- Smith, A. S., Passey, S., Greensmith, L., Mudera, V., and Lewis, M. P. (2012). Characterization and optimization of a simple, repeatable system for the long term *in vitro* culture of aligned myotubes in 3D. *J. Cell. Biochem.* 113, 1044–1053. doi: 10.1002/jcb.23437
- Smith, A. S. T., Davis, J., Lee, G., Mack, D. L., and Kim, D. H. (2016). Muscular dystrophy in a dish: engineered human skeletal muscle mimetics for disease modeling and drug discovery. *Drug Discovery Today* 21, 1387–1398. doi: 10.1016/j.drudis.2016.04.013
- Songsorn, P., Ruffino, J., and Vollaard, N. B. (2016). No effect of acute and chronic supramaximal exercise on circulating levels of the myokine SPARC. *Eur. J. Sport Sci.* 17, 447–452. doi: 10.1080/17461391.2016.1266392
- Spangenburg, E. E., and Booth, F. W. (2006). Leukemia inhibitory factor restores the hypertrophic response to increased loading in the LIF(–/–) mouse. *Cytokine* 34, 125–130. doi: 10.1016/j.cyto.2006.05.001
- Stark, A. E. (2015). Determinants of the incidence of Duchenne muscular dystrophy. *Ann. Transl. Med.* 3:287. doi: 10.3978/j.issn.2305-5839.2015.10.45
- Stern, M. M., Myers, R. L., Hammam, N., Stern, K. A., Eberli, D., Kritchevsky, S. B., et al. (2009). The influence of extracellular matrix derived from skeletal muscle tissue on the proliferation and differentiation of myogenic progenitor cells *ex vivo*. *Biomaterials* 30, 2393–2399. doi: 10.1016/j.biomaterials.2008.12.069
- Stern-Straeter, J., Bacha, A. D., Stangenberg, L., Foerster, V. T., Horsch, R. E., Stark, G. B., et al. (2005). Impact of electrical stimulation on three-dimensional myoblast cultures - a real-time RT-PCR study. *J. Cell. Mol. Med.* 9, 883–892. doi: 10.1111/j.1582-4934.2005.tb00386.x
- Subbotina, E., Sierra, A., Zhu, Z., Gao, Z., Koganti, S. R., Reyes, S., et al. (2015). Musclin is an activity-stimulated myokine that enhances physical endurance. *Proc. Natl. Acad. Sci. U.S.A.* 112, 16042–16047. doi: 10.1073/pnas.1514250112
- Tagliaferri, C., Wittrant, Y., Davicco, M. J., Walrand, S., and Coxam, V. (2015). Muscle and bone, two interconnected tissues. *Ageing Res. Rev.* 21, 55–70. doi: 10.1016/j.arr.2015.03.002
- Tanaka, A., Woltjen, K., Miyake, K., Hotta, A., Ikeya, M., Yamamoto, T., et al. (2013). Efficient and reproducible myogenic differentiation from human ips cells: prospects for modeling miyoshi myopathy *in vitro*. *PLoS ONE* 8. doi: 10.1371/annotation/63972dc9-3a31-43d0-ad52-bc46fd948c03
- Tang, J., Wang, J., Guo, L., Kong, X., Yang, J., Zheng, F., et al. (2010). Mesenchymal stem cells modified with stromal cell-derived factor 1 $\alpha$  improve cardiac remodeling via paracrine activation of hepatocyte growth factor in a rat model of myocardial infarction. *Mol. Cells* 29, 9–19. doi: 10.1007/s10059-010-0001-7
- Tatsumi, R. (2010). Mechano-biology of skeletal muscle hypertrophy and regeneration: possible mechanism of stretch-induced activation of resident myogenic stem cells. *Animal Sci. J.* 81, 11–20. doi: 10.1111/j.1740-0929.2009.00712.x
- Tatsumi, R., Sheehan, S. M., Iwasaki, H., Hattori, A., and Allen, R. E. (2001). Mechanical stretch induces activation of skeletal muscle satellite cells *in vitro*. *Exp. Cell Res.* 267, 107–114. doi: 10.1006/excr.2001.5252
- Tedesco, F. S., and Cossu, G. (2012). Stem cell therapies for muscle disorders. *Curr. Opin. Neurol.* 25, 597–603. doi: 10.1097/WCO.0b013e32835f7288
- Tedesco, F. S., Gerli, M. F., Perani, L., Benedetti, S., Ungaro, F., Cassano, M., et al. (2012). Transplantation of genetically corrected human ipsc-derived progenitors in mice with limb-girdle muscular dystrophy. *Sci. Transl. Med.* 4, 140ra89–140ra89. doi: 10.1126/scitranslmed.3003541
- Theadom, A., Rodrigues, M., Roxburgh, R., Balalla, S., Higgins, C., Bhattacharjee, R., et al. (2014). Prevalence of muscular dystrophies: a systematic literature review. *Neuroepidemiology* 43, 259–268. doi: 10.1159/000369343
- Thorley, M., Duguez, S., Mazza, E. M. C., Valsoni, S., Bigot, A., Mamchaoui, K., et al. (2016). Skeletal muscle characteristics are preserved in hTERT/cdk4 human myogenic cell lines. *Skeletal Muscle* 6:43. doi: 10.1186/s13395-016-0115-5
- Tonlorenzi, R., Dellavalle, A., Schnapp, E., Cossu, G., and Sampaolesi, M. (2007). "Isolation and characterization of Mesoangioblasts from Mouse, Dog, and Human tissues," in *Current Protocols in Stem Cell Biology* (Hoboken, NJ: John Wiley and Sons, Inc.), Unit 2B.1.
- van der Schaft, D. W., van Spreuwel, A. C., Boonen, K. J., Langelan, M. L., Bouten, C. V., and Baaijens, F. P. (2013). Engineering skeletal muscle tissues from murine myoblast progenitor cells and application of electrical stimulation. *J. Vis. Exp.* 73:e4267. doi: 10.3791/4267
- Vandenburgh, H., Shansky, J., Benesch-Lee, F., Barbata, V., Reid, J., Thorrez, L., et al. (2008). Drug-screening platform based on the contractility of tissue-engineered muscle. *Muscle Nerve* 37, 438–447. doi: 10.1002/mus.20931
- Vandenburgh, H. H., and Karlisch, P. (1989). Longitudinal growth of skeletal myotubes *in vitro* in a new horizontal mechanical cell stimulator. *In Vitro Cell. Dev. Biol. J. Tissue Cult. Assoc.* 25, 607–616.
- Vandenburgh, H. H., Karlisch, P., and Farr, L. (1988). Maintenance of highly contractile tissue-cultured avian skeletal myotubes in collagen gel. *In Vitro Cell. Dev. Biol.* 24, 166–174.
- Vangness, C. T., Kurzweil, P. R., and Lieberman, J. R. (2004). Restoring articular cartilage in the knee. *Am. J. Orthopedics* 33, 29–34.
- von Roth, P., Duda, G. N., Radojewski, P., Preininger, B., Strohschein, K., Röhner, E., et al. (2012). Intra-arterial msc transplantation restores functional capacity after skeletal muscle trauma. *The Open Orthopaedics J.* 6, 352–356. doi: 10.2174/1874325001206010352
- Wang, L., Cao, L., Shansky, J., Wang, Z., Mooney, D., and Vandenburgh, H. (2014). Minimally invasive approach to the repair of injured skeletal muscle with a shape-memory scaffold. *Mol. Ther.* 22, 1441–1449. doi: 10.1038/mt.2014.78
- Wang, W., Fan, M., Zhang, L., Liu, S. H., Sun, L., and Wang, C. Y. (2009). Compatibility of hyaluronic acid hydrogel and skeletal muscle myoblasts. *Biomed. Materials* 4:25011. doi: 10.1088/1748-6041/4/2/025011
- Webster, C., and Blau, H. M. (1990). Accelerated age-related decline in replicative life-span of Duchenne muscular dystrophy myoblasts: Implications for cell and gene therapy. *Somatic Cell Mol. Genet.* 16, 557–565. doi: 10.1007/BF01233096
- Wehrle, U., Düsterhöft, S., and Pette, D. (1994). Effects of chronic electrical stimulation on myosin heavy chain expression in satellite cell cultures derived from rat muscles of different fiber-type composition. *Differentiation* 58, 37–46. doi: 10.1046/j.1432-0436.1994.5810037.x
- Wobma, H., and Vunjak-Novakovic, G. (2016). Tissue engineering and regenerative medicine 2015: a year in review. *Tissue Eng.* 20, 1–16. doi: 10.1089/ten.TEB.2015.0535
- Wolf, M. T., Daly, K. A., Reing, J. E., and Badylak, S. F. (2012). Biologic scaffold composed of skeletal muscle extracellular matrix. *Biomaterials* 33, 2916–2925. doi: 10.1016/j.biomaterials.2011.12.055
- Wynn, T. (2008). Cellular and molecular mechanisms of fibrosis. *J. Pathol.* 214, 199–210. doi: 10.1002/path.2277
- Yaffe, D., and Saxel, O. (1977). Serial passaging and differentiation of myogenic cells isolated from dystrophic mouse muscle. *Nature* 270, 725–727. doi: 10.1038/270725a0
- Yamanaka, S., and Takahashi, K. (2006). Induction of pluripotent stem cells from mouse embryonic and adult fibroblast cultures by defined factors. *Cell* 126, 663–676. doi: 10.1016/j.cell.2006.07.024
- Yang, H. S., Ieronimakis, N., Tsui, J. H., Kim, H. N., Suh, K.-Y., Reyes, M., et al. (2014). Nanopatterned muscle cell patches for enhanced myogenesis and dystrophin expression in a mouse model of muscular dystrophy. *Biomaterials* 35, 1478–1486. doi: 10.1016/j.biomaterials.2013.10.067
- Yin, H., Price, F., and Rudnicki, M. A. (2013). Satellite cells and the muscle stem cell niche. *Physiol. Rev.* 93, 23–67. doi: 10.1152/physrev.00043.2011
- Yin, Q., Jin, P., Liu, X., Wei, H., Lin, X., Chi, C., et al. (2011). SDF-1 $\alpha$  inhibits hypoxia and serum deprivation-induced apoptosis in mesenchymal stem cells through PI3K/Akt and ERK1/2 signaling pathways. *Mol. Biol. Rep.* 38, 9–16. doi: 10.1007/s11033-010-0071-9
- Yiu, E. M., and Kornberg, A. J. (2015). Duchenne muscular dystrophy. *J. Paediatr. Child Health* 51, 759–764. doi: 10.1111/jpc.12868
- Zammit, P. S., Golding, J. P., Nagata, Y., Hudon, V., Partridge, T. A., and Beauchamp, J. R. (2004). Muscle satellite cells adopt divergent fates: a mechanism for self-renewal? *J. Cell Biol.* 166, 347–357. doi: 10.1083/jcb.200312007
- Zammit, P. S., Partridge, T. A., and Yablonka-Reuveni, Z. (2006). The skeletal muscle satellite cell: the stem cell that came in from the cold. *J. Histochem. Cytochem.* 54, 1177–1191. doi: 10.1369/jhc.6R6995.2006

- Zeng, L., Akasaki, Y., Sato, K., Ouchi, N., Izumiya, Y., and Walsh, K. (2010). Insulin-like 6 is induced by muscle injury and functions as a regenerative factor. *J. Biol. Chem.* 285, 36060–36069. doi: 10.1074/jbc.M110.160879
- Zhang, C., Li, Y., Wu, Y., Wang, L., Wang, X., and Du, J. (2013). Interleukin-6/signal transducer and activator of transcription 3 (STAT3) pathway is essential for macrophage infiltration and myoblast proliferation during muscle regeneration. *J. Biol. Chem.* 288, 1489–1499. doi: 10.1074/jbc.M112.419788
- Zhang, M., Mal, N., Kiedrowski, M., Chacko, M., Askari, A. T., Popovic, Z. B., et al. (2007). SDF-1 expression by mesenchymal stem cells results in trophic support of cardiac myocytes after myocardial infarction. *FASEB J.* 21, 3197–3207. doi: 10.1096/fj.06-6558com
- Zhang, Y., Heher, P., Hilborn, J., Redl, H., and Ossipov, D. A. (2016). Hyaluronic acid-fibrin interpenetrating double network hydrogel prepared *in situ* by orthogonal disulfide cross-linking reaction for biomedical applications. *Acta Biomaterialia* 38, 23–32. doi: 10.1016/j.actbio.2016.04.041

**Conflict of Interest Statement:** The authors declare that the research was conducted in the absence of any commercial or financial relationships that could be construed as a potential conflict of interest.

The reviewer SG and handling Editor declared their shared affiliation.

Copyright © 2018 Maleiner, Tomasch, Heher, Spadiut, Rünzler and Fuchs. This is an open-access article distributed under the terms of the Creative Commons Attribution License (CC BY). The use, distribution or reproduction in other forums is permitted, provided the original author(s) and the copyright owner(s) are credited and that the original publication in this journal is cited, in accordance with accepted academic practice. No use, distribution or reproduction is permitted which does not comply with these terms.



# Engineering of Human Skeletal Muscle With an Autologous Deposited Extracellular Matrix

Lieven Thorrez<sup>1\*</sup>, Katherine DiSano<sup>2</sup>, Janet Shansky<sup>3</sup> and Herman Vandenburg<sup>3</sup>

<sup>1</sup> Tissue Engineering Laboratory, Department of Development and Regeneration, KU Leuven Kulak, Kortrijk, Belgium,

<sup>2</sup> School of Medicine, Case Western Reserve University, Cleveland, OH, United States, <sup>3</sup> Department of Pathology, The Miriam Hospital, Brown University, Providence, RI, United States

Adult skeletal muscle progenitor cells can be embedded in an extracellular matrix (ECM) and tissue-engineered to form bio-artificial muscles (BAMs), composed of aligned post-mitotic myofibers. The ECM proteins which have been used most commonly are collagen type I and fibrin. Fibrin allows for *in vitro* vasculogenesis, however, high concentrations of fibrinolysis inhibitors are needed to inhibit degradation of the ECM and subsequent loss of BAM tissue structure. For *in vivo* implantation, fibrinolysis inhibition may prove difficult or even harmful to the host. Therefore, we adapted *in vitro* culture conditions to enhance the deposition of *de novo* synthesized collagen type I gradually replacing the degrading fibrin ECM. The *in vitro* viscoelastic properties of the fibrin BAMs and deposition of collagen were characterized. BAMs engineered with the addition of proline, hydroxyproline, and ascorbic acid in the tissue culture medium had a twofold increase in Young's Modulus, a 2.5-fold decrease in maximum strain, and a 1.6-fold increase in collagen deposition. Lowering the fibrin content of the BAMs also increased Young's Modulus, decreased maximum strain, and increased collagen deposition. Tissue engineering of BAMs with autologous ECM may allow for prolonged *in vivo* survival.

**Keywords:** tissue engineering, skeletal muscle, collagen, fibrin, extracellular matrix, viscoelastic properties

## INTRODUCTION

Adult skeletal muscle progenitor cells can be engineered *ex vivo* into contractile tissues containing post-mitotic myofibers (Vandenburg and Kaufman, 1979). To obtain 3D tissues, proliferating human myogenic cells are embedded in ECM hydrogels and then differentiated to form organized myofibers. Myofiber alignment occurs due to the uniaxial passive forces generated in the gel when it contracts away from its casting mold containing two attachment sites. The resulting engineered muscle bundles are termed as bio-artificial muscles (BAMs). BAMs were demonstrated to provide insights in drug screening (Vandenburg et al., 2008, 2009; Vandenburg, 2010) and disease modeling (Chromiak and Vandenburg, 1992; Vandenburg et al., 2009; Lee and Vandenburg, 2013). Ultimately, BAMs may provide a replacement for damaged or atrophied muscle tissue

**Abbreviations:** AFM, atomic force microscopy; BAM, bio-artificial muscle; bFGF, basic fibroblast growth factor; DAB, 3,3'-diaminobenzidine; EBM-2, endothelial cell basal medium-2; ECM, extracellular matrix; FBS, fetal bovine serum; HGF, hepatocyte growth factor; HUVEC, human umbilical vein endothelial cell; PLG, poly-lactide-co-glycolide; SEM, standard error of the mean; SkGM, skeletal muscle growth medium; VEGF, vascular endothelial growth factor.

## OPEN ACCESS

### Edited by:

Cesare Gargioli,  
Università degli Studi di Roma Tor  
Vergata, Italy

### Reviewed by:

Valentina Di Felice,  
Università degli Studi di Palermo, Italy  
Bert Blaauw,  
Università degli Studi di Padova, Italy

### \*Correspondence:

Lieven Thorrez  
lieven.thorrez@kuleuven.be

### Specialty section:

This article was submitted to  
Integrative Physiology,  
a section of the journal  
Frontiers in Physiology

**Received:** 13 April 2018

**Accepted:** 18 July 2018

**Published:** 20 August 2018

### Citation:

Thorrez L, DiSano K, Shansky J and  
Vandenburg H (2018) Engineering  
of Human Skeletal Muscle With an  
Autologous Deposited Extracellular  
Matrix. *Front. Physiol.* 9:1076.  
doi: 10.3389/fphys.2018.01076

(Powell C.A. et al., 2002). In addition, the progenitor cells can be genetically engineered to secrete therapeutic proteins such as growth hormone, VEGF, and blood clotting factor IX. When these cells are then used to create BAMs which are implanted, they can serve as an *in vivo* protein delivery system (Vandenburgh et al., 1991, 1996, 1998; Lu et al., 2001, 2002; Shansky et al., 2006a; Thorrez et al., 2006). BAMs with post-mitotic muscle fibers have a better safety profile than injecting individual proliferating and migrating cells in the host because of reversibility of implants in case of an adverse event (Vandenburgh et al., 1998; Lu et al., 2001, 2002; Thorrez et al., 2006). *Ex vivo* differentiated myofibers exhibit improved cell survival kinetics when compared to implanted myoblasts, with a gradual loss of viability over 30–60 days after implantation (Vandenburgh et al., 1996; Thorrez et al., 2006). The latter may be partially due to poor myofiber tension maintenance *in vivo* (Thorrez et al., 2006). Seeding cells on a biodegradable scaffold is an approach which may provide temporary mechanical strength to the tissue and help maintain myofiber tension. However, with scaffolds, myofiber alignment remains a critical issue and scaffold degradation products may affect myofiber survival (Thorrez et al., 2008). Successful transplantation of skeletal muscle cells (either myoblasts or myofibers) for structural repair or *ex vivo* gene therapy applications thus requires further optimization for long term cell survival.

In most of the work we published up to date, type I collagen has been used to form the hydrogel, motivated by the fact that it is the most prominent ECM protein in adult skeletal muscle (Vandenburgh, 1988). Initially, rat tail collagen I was used (Vandenburgh et al., 1988), but with the aim of developing a clinical product, clinically approved collagen type I (Zyderm) was used (Thorrez et al., 2006). We found however, that Zyderm strongly inhibits vascularization of the BAMs *in vivo* (Thorrez et al., 2006). Vascularization of the BAMs is desirable to allow for an efficient delivery of nutrients to the myofibers and offloading of the therapeutic protein. Even secretion of high levels of VEGF from Zyderm BAMs is unable to overcome this anti-angiogenic effect (Thorrez et al., 2006). Therefore, an alternative clinically approved ECM protein was needed to allow vascularization of BAMs.

Fibrin is commercially available (e.g., Tisseel) and is used widespread in clinical applications as a tissue glue. It is also used as an ECM in many other bioengineering applications due to its structural and mechanical properties (Helgerson et al., 2004). The structural properties of the fibrin gel can be varied by manipulating a number of parameters, such as the fibrinogen and thrombin concentration, additional crosslinking, and ion concentration (Helgerson et al., 2004). Fibrin extracellular matrices are subject to degradation *in vitro* and *in vivo* via fibrinolysis. This can be inhibited *in vitro* by adding the enzymatic inhibitors aprotinin and/or tranexamic acid to the culture medium. Although this prevents fibrin degradation *in vitro*, once fibrin is used *in vivo*, it is subject again to fibrinolysis. In previous studies, when fibrin was used as an ECM for tissue engineering, the fibrin was reabsorbed within 2 weeks (Beier et al., 2006).

In this paper, we present an adapted *in vitro* engineering procedure to improve viscoelastic properties of BAMs and circumvent BAM degradation due to proteolysis of fibrin. Deposition of autologous collagen by (myo)fibroblasts present in the BAMs may be induced by adding supplements to the culture media *in vitro*. Functional collagen contains a large amount of amino acids that have been post-translationally modified, specifically proline to hydroxyproline. The conversion of proline to hydroxyproline is catalyzed by the enzyme prolyl 4-hydroxylase which requires ascorbic acid (vitamin C) for its enzymatic function (Nelson and Cox, 2005). Proline and hydroxyproline constitute roughly 30% of the amino acids in collagen, stabilize the helix and increase the amount of hydrogen bonds (Nelson and Cox, 2005). Experiments were performed in which the effect of proline, hydroxyproline, and ascorbic acid as media supplements were evaluated to determine effects on autologous collagen deposition in fibrin BAMs and changes related to viscoelastic characteristics. We investigate the effects of this medium supplementation together with other parameters including fibrin density, fibrin crosslinking, and cell density.

## MATERIALS AND METHODS

### Muscle Progenitor Cell Isolation and Culture

Primary human skeletal muscle cells were isolated by needle biopsy of the vastus lateralis from healthy adult volunteers (Powell et al., 1999; Powell C.A. et al., 2002; Shansky et al., 2006b) and cells were 70% myogenic on average as determined by desmin staining (Powell C.A. et al., 2002). Biopsy and isolation protocols have been previously described in detail (Powell et al., 1999; Powell C.A. et al., 2002; Powell C. et al., 2002; Shansky et al., 2006b) and were approved by the Institution Clinical Review Board of the Miriam Hospital. Human skeletal myoblasts were cultured in human SkGM, SkGM/15 [SkGM Bullet Kit (Cambrex Bio Science, Walkersville, MD, United States) + 15% (v/v) FBS]. Cells were cultured in a 37°C, 5% CO<sub>2</sub> incubator and media was changed every other day.

### Engineering of Fibrin BAMs

BAMs 20 mm in length were engineered in an elliptical, shallow-welled silicone mold affixed to the bottom of a standard six-well tissue culture plate. Two stainless steel pins (1 mm diameter) were placed into the mold 20 mm apart and served as an attachment site. Custom-made transfer devices (for transfer to the viscoelastic testing device) made of stainless steel cylinder (inner diameter 0.038 in) bent in a U-shape were inserted over the pins. Two million skeletal myoblasts were used for each BAM. Cells were mixed with fibrin ECM [0.25–4 mg/ml fibrinogen + 0.5–2 U/ml thrombin (Tisseel, Baxter)] in a total volume of 500 µl. In some experiments FXIII (0.4 U/ml) was added. Cell-ECM mixes were incubated at 37°C and 5% CO<sub>2</sub> for 2 h followed by addition of 8–10 ml SKGM/15 containing 1,000 U/ml aprotinin (Trasylo<sup>TM</sup>). Where indicated, the following media supplements were added: 40 mg/L L-proline (Sigma), 10 mg/l trans-4-hydroxy-L-proline (Sigma), and 0.1 mM

L-ascorbic acid 2-phosphate (Sigma). The solidified cell-ECM was detached from the silicone mold using a sterile fine dentistry tool (FST). This enabled the cells to contract around the pins and form unidirectional, aligned myofibers.

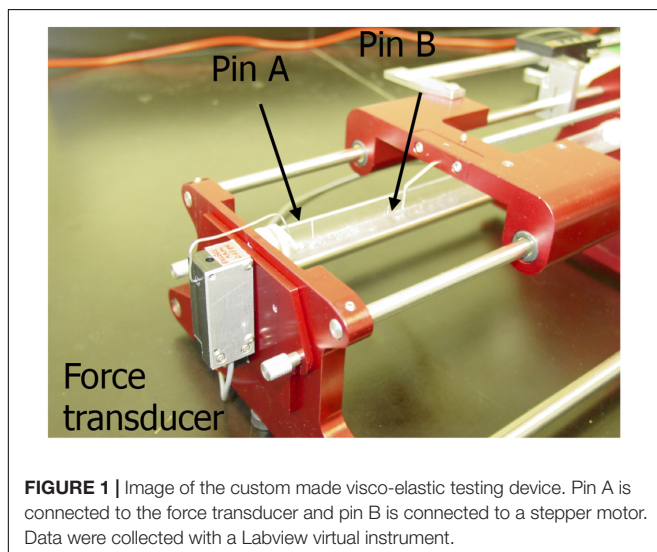
After 2 days, myoblast fusion into post-mitotic myofibers was induced by incubation in differentiation medium [high glucose DMEM (Gibco), 50  $\mu$ g/ml bovine serum albumin (Cambrex), 50  $\mu$ g/ml gentamicin (Sigma), 10 ng/ml epidermal growth factor (Cambrex), and 10  $\mu$ g/ml insulin (Cambrex)] with 1,000 U/ml aprotinin and with or without supplements. For some BAMs, aprotinin was stopped at day 5. Medium was changed every 2–3 days and BAMs were kept at 37°C, 5% CO<sub>2</sub>. BAMs were maintained in culture for 7–14 days before viscoelastic testing.

### Collagen (Zyderm) Control BAMs

Collagen BAMs were engineered in a manner previously described (Powell et al., 1999; Powell C. et al., 2002; Powell C.A. et al., 2002; Shansky et al., 2006b; Thorrez et al., 2006; Decroix et al., 2015). Briefly, 2 million human myoblasts were mixed in 1 ml of a 1 mg/ml collagen type I ECM (Zyderm™, Inamed) and treated similar to the fibrin BAMs. Manual detachment from the mold was not needed since the collagen ECM does not adhere to the silicone mold as much as the fibrin ECM.

### Viscoelastic Testing of BAMs

Before testing, BAMs were imaged and center diameter was measured using ScopePhoto software. The viscoelastic testing of the BAMs was performed using a custom-made device (Figure 1), consisting of a force transducer and a stepper motor connected to two different pins. Hardware was controlled by a virtual instrument designed in Labview software (National Instrument). The two pins are set within a fluid cylinder filled with PBS at 36–37°C. BAMs were stretched at 0.9 cm/min until 2,500  $\mu$ N.



Recorded data were imported into Microsoft Excel. Stress was calculated by dividing force by cross sectional area. A stress–strain curve was created, and the slope of the linear region of the curve was recorded as Young's Modulus.

### Force Generation

BAMs were electrically stimulated via two platinum electrodes 4 mm apart on either side of the BAM. The voltage and stimulus were controlled using a custom designed LabVIEW program. Maximum isometric tetanic force was obtained by applying an electrical stimulus of 40 V at 40 Hz with 4 ms-wide pulses.

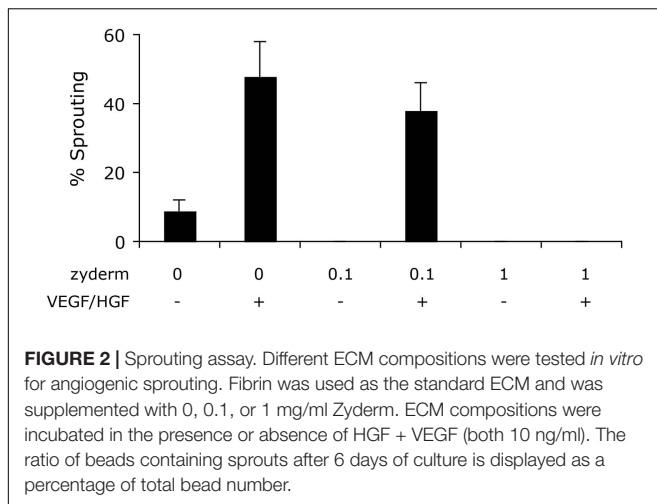
### Sprouting Assay

Sprouting assay was performed as described by Matsumoto et al. (2007). Briefly, dextran beads (Cytodex3, GE Healthcare, Piscataway, NJ, United States) were coated with HUVECs and resuspended at 800 beads/ml in fibrinogen solution (3 mg/ml) containing aprotinin (5 mg/ml). The resulting solution was mixed with a thrombin solution (2 U/mL) in a 5:4 ratio. Where indicated, either 0.1 or 1 mg/ml Zyderm was added to the fibrin. A total of 450  $\mu$ L of this solution was then poured into each well of a 24-well plate and the plates placed in an incubator for 20 min. EBM-2 (Cambrex), which contains 2% FBS, was used as the medium for cell culture and where indicated, 10 ng/mL HGF (rhHGF, Chemicon) and 10 ng/mL VEGF were added. The ratio of beads containing sprouts, as a function of total bead number, was calculated after 6 days of culture using microscopic examination of the cultures.

### Histology

BAMs were fixed in 4% formaldehyde for 1 h and rinsed 3  $\times$  5 min in PBS.

For tropomyosin staining, samples were permeabilized with methanol, incubated with mouse anti-tropomyosin antibody (Sigma #T9283) 1:100, followed by a secondary biotinylated anti-mouse IgG and then a preformed avidin and biotinylated horse radish peroxidase complex (Vector Laboratories, Burlingame, CA, United States). Development was by addition of DAB to produce a brown precipitate. Fixed BAMs were sent out for cross-sectional sectioning and hematoxylin and eosin staining (Mass Histology Service, Worcester, MA, United States). Slides were deparaffinized and then gradually rehydrated from 100% ethanol to H<sub>2</sub>O and stained for collagen using Accustain Trichrome Stains (Masson) (Sigma-Aldrich). The Trichrome protocol was adapted as follows. Slides were soaked overnight in Bouin's solution (Sigma), stained in hematoxylin (Sigma), and then rinsed in running tap water. The slides were then placed in Biebrich scarlet acid fuchsin (Sigma), followed by 12 min in a working phosphotungstic/phosphomolybdic acid solution (Sigma), and then 6 min in an aniline blue Solution (Sigma). Sections were rinsed in double distilled water in between every staining step. The slides were then destained for 1 min using a 1% acetic acid solution (Sigma), dehydrated with ethanol, and mounted in Polymount (Polysciences Inc.).



## Quantification of Deposited Collagen

A total of 12–15 non-overlapping images of each BAM were taken on a Zeiss Axiovert 25 microscope with a 40× objective using Scopephoto. The percentage of collagen (blue area) was quantified for each image with Metamorph Offline ver 6.3 and was recorded in Microsoft Excel.

## Statistics

Statistical analysis was performed using InStat (Graphpad) software. Non-parametric ANOVA tests (Kruskal–Wallis) with Dunn's post tests were used. All data are presented as mean ± SEM and significance levels are indicated with \* $P < 0.05$ , \*\* $P < 0.01$ , and \*\*\* $P < 0.001$ .

## RESULTS

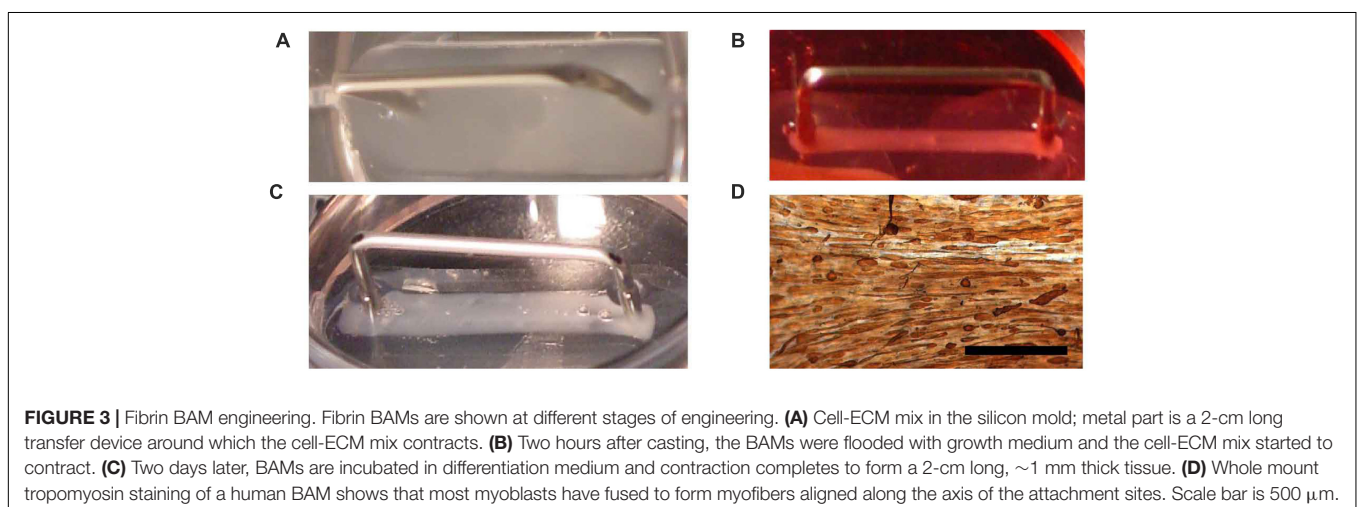
### Sprouting Assay

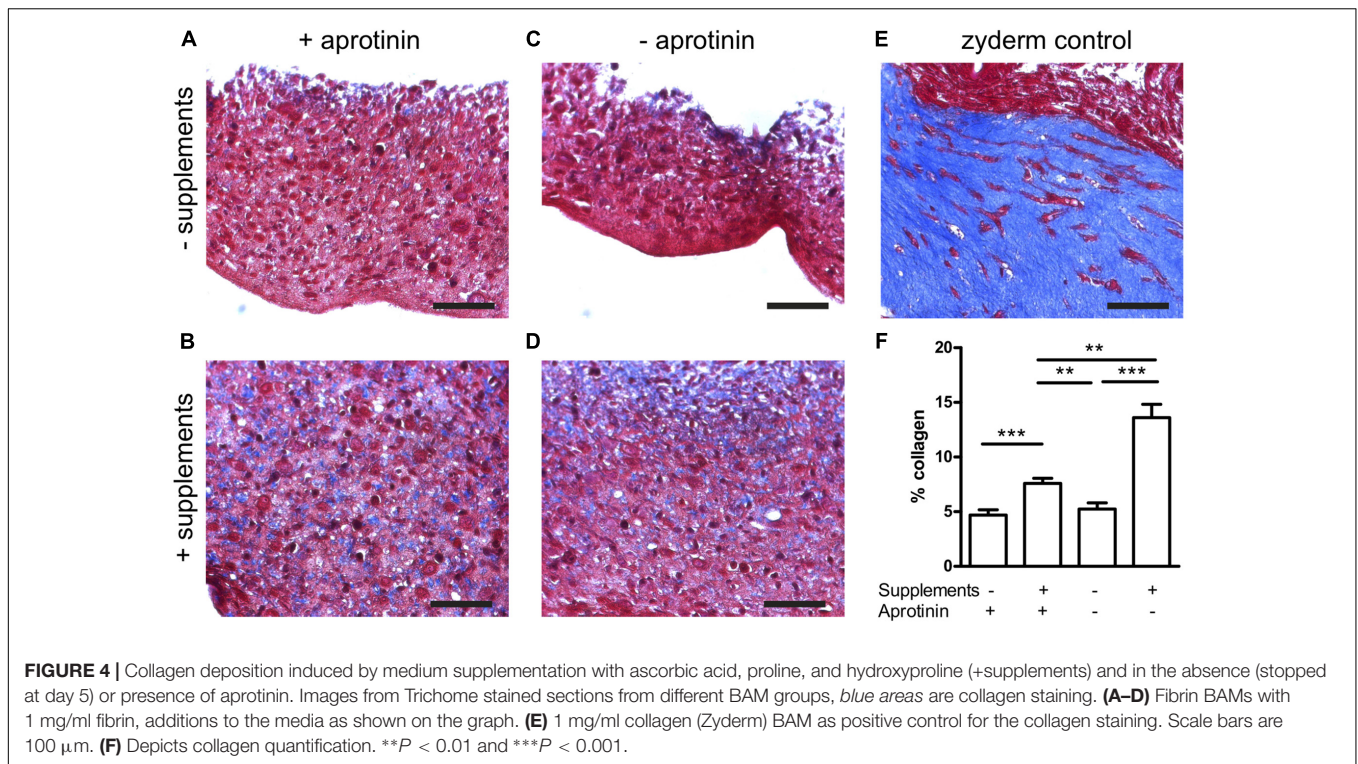
To compare different ECM compositions for angiogenic potential, we performed a bead sprouting assay. Standard ECM

composition was fibrin, supplemented with no, 0.1 or 1 mg/ml collagen I (Zyderm<sup>TM</sup>). All ECM compositions were tested in the presence or absence of the angiogenic growth factors HGF and VEGF (10 ng/ml each). After 6 days of culture, sprouting beads were quantified relative to total beads (**Figure 2**). In the absence of Zyderm,  $9 \pm 3\%$  sprouting beads were present, which increased to  $48 \pm 10\%$  in the presence of growth factors. However, when Zyderm was added, no sprouting was observed without growth factors. Even in the presence of growth factors, 1 mg/ml Zyderm completely abolished sprouting. These data prompted us to search for engineering methods where the Zyderm collagen I could be omitted.

### Stimulation of Collagen Deposition

As a substitution for the collagen I, fibrin was used as the ECM. Several conditions for engineering of fibrin BAMs were investigated. Since fibrin is degraded by fibrinolysis, we added aprotinin to the medium to inhibit fibrinolysis. Since fibrinolysis also occurs *in vivo*, we investigated a way to avoid construct degradation by fibrinolysis. Omission of aprotinin at day 5 of the engineering procedure allowed for gradual fibrinolysis during the remaining culture time. In a first series of experiments, we aimed at the enhancement of autologous collagen deposition to counteract the detrimental effect of fibrinolysis on tissue integrity and strength. To enhance autologous collagen deposition, culture medium was supplemented with ascorbic acid (0.1 mM), proline (40 mg/l), and hydroxyproline (10 mg/l). Similar to our previous work with collagen-based BAMs (Thorrez et al., 2006), BAMs contained 2 million human myoblasts. Different steps of the engineering process are depicted in **Figure 3**. Within minutes after combining the fibrinogen, thrombin and cells, the ECM gelled (**Figure 3A**). When media was added, the cell-ECM mix was manually detached from the silicon mold, allowing the cells to contract and attach solely to the pins (**Figure 3B**). Switching to differentiation medium at day 2 induced cell fusion and further contraction of the BAM (**Figure 3C**). The BAMs were maintained *in vitro* for 7–14 days before they underwent further characterization. Tropomyosin staining indicated that

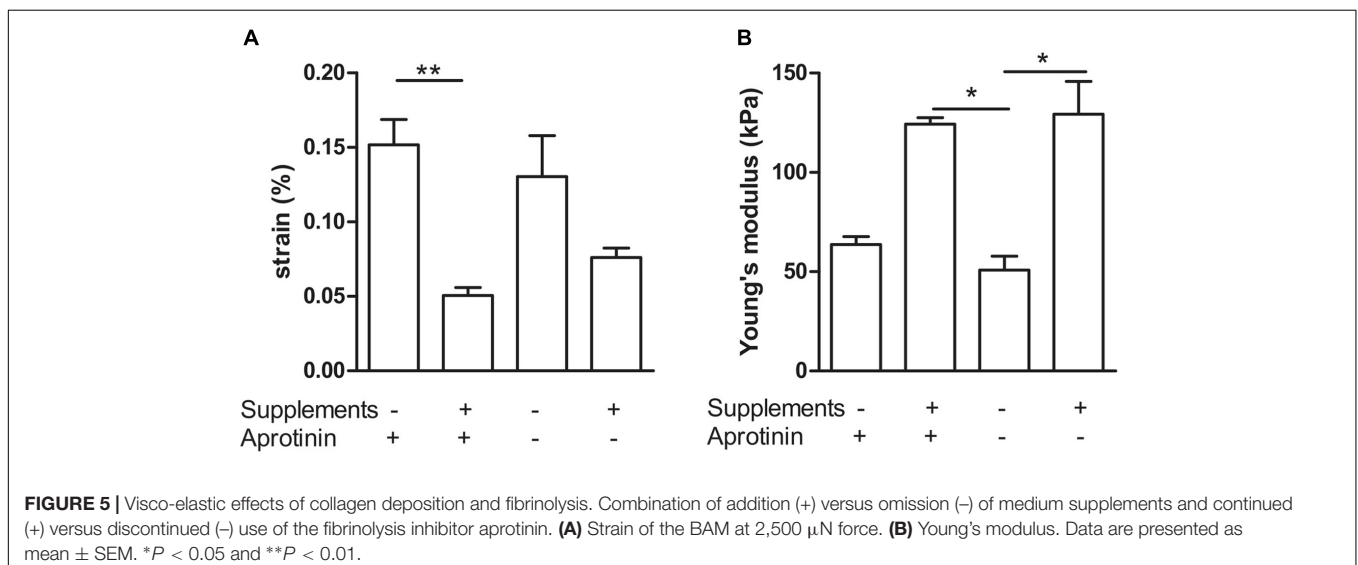




myoblasts had fused to form myofibers aligned in one direction (Figure 3D).

Collagen deposited by the cells in the fibrin BAMs was visualized on histological sections with Masson’s Trichrome stain as a blue color (Figure 4). Collagen BAM sections were used as a positive control. In the standard condition without supplements and in the presence of aprotinin, 4.7 ± 0.5% collagen was deposited (Figures 4A,F). However, when supplements were added, this significantly (*P* < 0.001) increased 1.6 fold to 7.6 ± 0.5% (Figures 4B,F). When aprotinin was stopped without

the supplements, the BAM integrity was severely affected by day 14 as the fibrin had started degrading and only 5.2 ± 0.6% collagen had been deposited (Figures 4C,F). When supplements had been given, then even in the absence of aprotinin (and thus in fibrinolytic conditions) degradation of the BAM structure was not visible and 13.6 ± 1.2% collagen had been deposited (Figures 4D,F). This was not only significantly (*P* < 0.001) than when not giving supplements, but also higher (*P* < 0.01) than the BAMs given supplements when aprotinin was also present. Both changes together, adding supplements and omitting





aprotinin, resulted in a 2.9-fold increase of collagen content. In the absence of supplements, there was no significant difference in collagen deposition whether or not aprotinin was stopped on day 5.

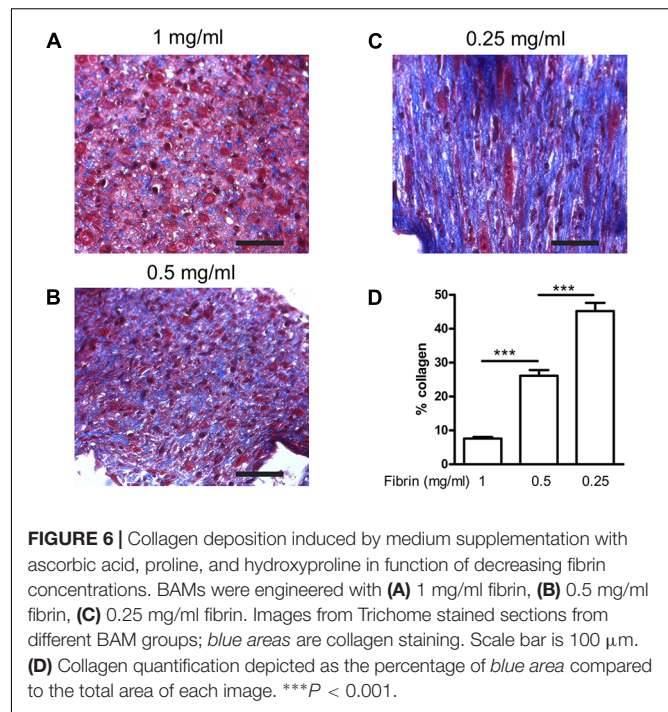
To further quantify the effects of medium supplementation and induction of fibrinolysis, we determined visco-elastic parameters. With a custom made visco-elastic testing device (**Figure 1**), we mechanically stretched the BAMs and recorded stress–strain curves. Based on these curves, we measured the strain of the BAM when 2,500  $\mu\text{N}$  force was applied and calculated Young's modulus ( $n = 4\text{--}7$  for each group). A low percentage (% of original length) of strain indicates that the BAM resists the applied force better. The stress–strain profiles display a non-linear toe region followed by a linear region (data not shown). The slope of this linear region of the forward curve corresponds to Young's Modulus. We compared the effects of supplement addition and continued versus discontinued use of aprotinin. Results are shown in **Figure 5**. When supplements were added, the strain significantly ( $P < 0.01$ ) decreased threefold from  $15.2 \pm 1.7\%$  to  $5.1 \pm 0.5\%$  in the presence of aprotinin (**Figure 5A**). Omitting the aprotinin did not significantly affect the strain. Young's modulus increased twofold, from  $63.7 \pm 4$  kPa to  $124.3 \pm 3.2$  kPa when supplements were added in the presence of aprotinin. When aprotinin was stopped, Young's modulus significantly increased from  $50.9 \pm 7.0$  kPa in the absence of supplements to  $129.3 \pm 16.6$  kPa in the presence of supplements ( $P < 0.05$ ). Independently of supplement presence (either present or absent), the omission of aprotinin did not affect Young's modulus.

### Decrease of Fibrin Content

Next, we determined how much the initial fibrin content affects the collagen deposition, by reducing it to 0.5 and 0.25 mg/ml, in the presence of supplements. The collagen content further significantly ( $P < 0.001$ ) increased to  $26.1 \pm 1.7\%$  and  $45.2 \pm 2.4\%$ , respectively (**Figure 6**). Decreasing fibrin content did not significantly affect the strain when force was applied (**Figure 7A**). Also Young's modulus did not significantly change when decreasing to 0.5 mg/ml fibrin, but significantly increased ( $P < 0.001$ ) from  $124.3 \pm 3.2$  kPa to  $199.8 \pm 10.5$  kPa when fibrin content was further decreased to 0.25 mg/ml (**Figure 7B**). This increase in Young's modulus with decreasing fibrin content was due to the smaller cross-sectional area of the BAM. The cross-sectional area decreased from  $0.51 \pm 0.17$  mm<sup>2</sup> (1 mg/ml) to  $0.28 \pm 0.05$  mm<sup>2</sup> (0.25 mg/ml).

### Effects of Cell Number and Fibrin Cross-Linking

To determine if we could further improve the mechanical strength of the BAMs, we examined two strategies: An increase in cell number and the cross-linking of fibrin. Fibrin can be crosslinked with factor XIII (FXIII), which is a transglutaminase. Effects of these modifications, measured at 7 days post casting are shown in **Figure 8**. The effect of FXIII addition was a significant ( $P < 0.05$ ) decrease in Young's modulus from  $64.9 \pm 17.6$  kPa to  $13.7 \pm 4.2$  kPa when using 2 million cells. Increasing the cell



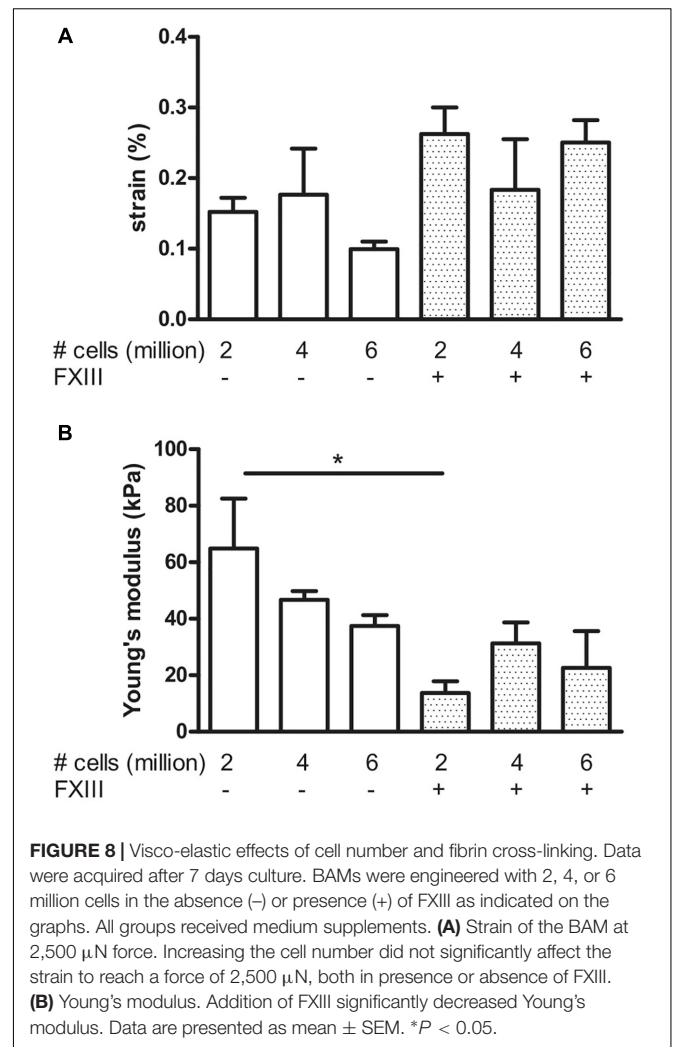
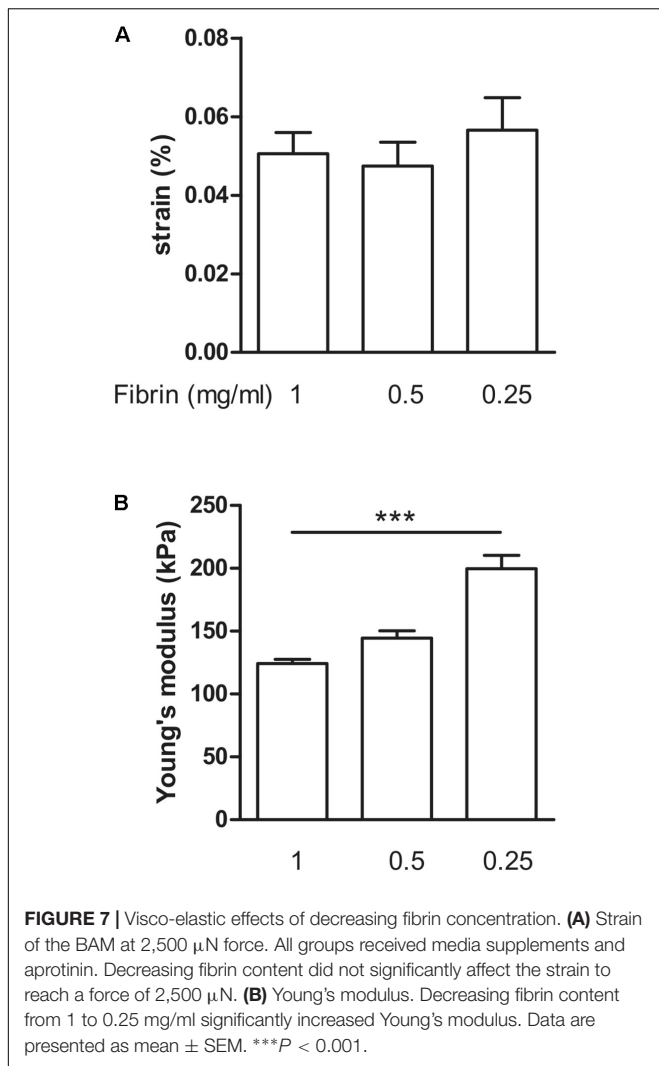
number to 4 or 6 million cells did not significantly change the strain nor Young's modulus, independent of FXIII addition.

### Contractile Properties of BAMs

To assess muscle functionality, we determined contractile force generated by electrical stimulation. The stimulation parameters to generate maximal tetanic force had been determined previously for this system (Lee and Vandenburg, 2013). Field stimulation was performed with two platinum electrodes 4 mm apart on either side of the BAM. Maximum isometric tetanic force was obtained by applying an electrical stimulus of 40 V at 40 Hz with 4 ms wide pulses. Absolute force exerted by the BAM was normalized for cross-sectional area. As a reference, we used BAMs engineered with Zyderm. These BAMs were able to generate  $829 \pm 49$   $\mu\text{N}/\text{mm}^2$  force at 14 days post casting (**Figure 9**). The BAMs engineered with 1 mg/ml fibrin in the presence of media supplements did not differ significantly ( $985 \pm 58$   $\mu\text{N}/\text{mm}^2$ ) (**Figure 9**). Force was lower when culture time decreased to 7 days ( $630 \pm 90$   $\mu\text{N}/\text{mm}^2$ ). When FXIII had been added, this force was even lower:  $189 \pm 64$   $\mu\text{N}/\text{mm}^2$ . A similar absolute force was generated at 14 days by BAMs engineered with a lower fibrin content, however, due to the decreased cross-sectional area, the normalized force increased to  $1,608 \pm 107$   $\mu\text{N}/\text{mm}^2$  for 0.5 mg/ml fibrin and  $2,215 \pm 123$   $\mu\text{N}/\text{mm}^2$  for 0.25 mg/ml fibrin (**Figure 9**).

### DISCUSSION

Bio-artificial muscle composed of aligned human skeletal myofibers, have been successfully engineered *in vitro* and have potential applications in regenerative medicine and gene therapy.

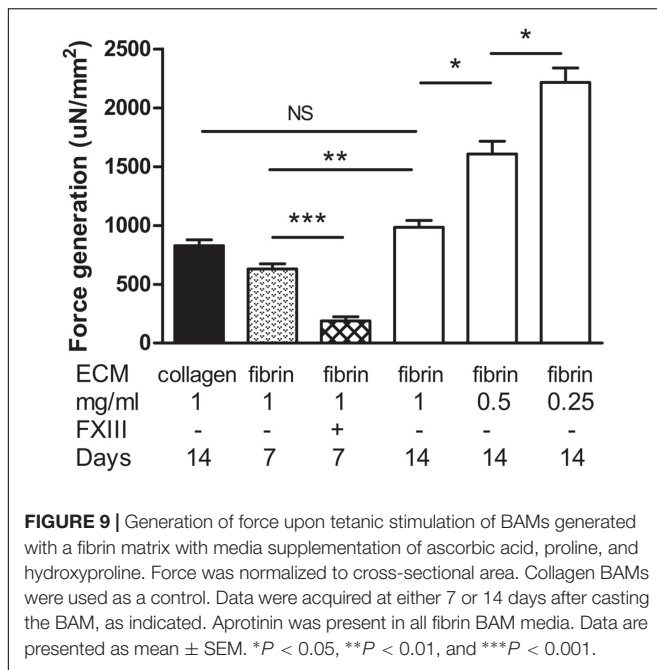


BAMs in most of our previous work have been engineered scaffold-free in a hydrogel since using a synthetic PLG scaffold negatively affected myofiber alignment and degradation products were observed *in vivo* (Thorrez et al., 2008). However, when a clinically approved collagen type I (Zyderm) ECM was used for *in vivo* implantation, these BAMs did not get vascularized, leading to an impaired cell survival (Thorrez et al., 2006). This was not entirely surprising, since Zyderm is clinically used as a bulking agent for reconstructive surgery so the collagen I is processed to minimize host interaction. Therefore, we investigated the use of an alternative ECM composition for BAM engineering. Fibrin (Tisseel) is FDA-approved and widely used in the clinic as a tissue glue. Studies have shown that Tisseel fibrin can be vascularized *in vivo* (Cesarman-Maus and Hajjar, 2005).

Here, we demonstrate *in vitro* that fibrin as an ECM allows for angiogenic sprouting, but addition of collagen I (Zyderm) completely abolishes this effect (Figure 2). These results are in agreement with the *in vivo* anti-angiogenic nature of Zyderm as observed previously (Thorrez et al., 2006). Addition of HGF and VEGF was previously shown to greatly increase sprout formation

(Matsumoto et al., 2007). With the fibrin ECM we indeed observed this effect, but even in the presence of these factors the anti-angiogenic effect of Zyderm at a relevant concentration (1 mg/ml) could not be overcome.

However, when applied as a tissue glue, Tisseel is reabsorbed during the wound healing process in 10–14 days (Spotnitz, 2014) and when mixed with myoblasts and injected intramuscularly, the fibrin matrix was completely dissolved after 2 weeks (Beier et al., 2006). Therefore, either fibrinolysis *in vivo* needs to be inhibited or autologous ECM deposition from the BAM needs to be stimulated to (partially) replace the degraded fibrin. We investigated the latter option by stimulating collagen deposition. Ascorbic acid has already been known for a long time to stimulate collagen deposition (Schwarz et al., 1981). It has been used to stimulate collagen deposition from human tenocytes for tendon tissue engineering (Hakimi et al., 2014), from vascular interstitial cells for heart valve tissue engineering (Wu et al., 2017) and from fibroblasts for vascular graft tissue engineering (Patel et al., 2018). The use of ascorbic acid-releasing scaffolds has also been suggested for use in pelvic floor repair (Mangir et al., 2016). The triple helical



structure of collagen arises from the abundance of three amino acids: Glycine, proline, and hydroxyproline. Proline and hydroxyproline residues permit the sharp twisting of the collagen helix and play key roles in collagen stability (Jenkins et al., 2003). So, in addition to ascorbic acid, we also supplemented the media with hydroxyproline and proline. The primary human skeletal muscle myogenic cell isolates used in this study contained about 30% fibroblasts. It is known that fibroblasts secrete collagen and other important ECM components (Schwartz et al., 1979).

Fibrin BAMs were successfully engineered *in vitro*. **Figures 3A–C** displays the contraction of the cell-ECM mix during *in vitro* culture. After 4 days in differentiation medium, myofibers expressing tropomyosin (**Figure 3D**) had formed that aligned along the axis of the attachment sites. The fibrin BAMs were cultured in the absence or presence of the media supplements for 14 days, and we determined collagen content after 14 days *in vitro*. Addition of proline, hydroxyproline, and ascorbic acid significantly enhanced *de novo* collagen deposition in the BAMs from 4.7 to 7.6%.

Fibrin degradation can be controlled by modulating the fibrinolysis. Aprotinin is required in media during the first days in culture after the BAM engineering to prevent fibrinolysis. Allowing fibrinolysis by stopping aprotinin addition at day 5 to simulate what happens after *in vivo* implantation of the BAMs had no significant effect on the BAMs when no media supplements were present. In the presence of supplements, no significant effect was observed on Young's modulus or strain at 2,500  $\mu$ N, but when fibrinolysis was allowed to take place a significantly greater amount of the ECM was composed of collagen.

The supplement effect was present both in the presence or absence of fibrinolysis. However, by stopping aprotinin

addition and thus allowing for fibrinolysis, we observed a further increase in collagen production to 13.6% (**Figure 4**). This is consistent with a previous report showing that vascular smooth muscle cells cultured in fibrin increased their collagen deposition due to decreasing concentrations of the fibrinolysis inhibitor  $\epsilon$ -aminocaproic acid (Ahmann et al., 2010).

BAM mechanical strength was evaluated by visco-elastic testing. BAMs to which the media supplements proline, hydroxyproline, and ascorbic acid were added displayed a significantly higher Young's modulus than BAMs which lacked these media supplements. This effect was demonstrated both in the presence and the absence (stopped at day 5) of aprotinin. Addition of proline, hydroxyproline, and ascorbic acid increased the stiffness of the BAMs, allowing to resist 2,500  $\mu$ N force at lower strain. Therefore, the addition of proline, hydroxyproline, and ascorbic acid enhances the amount of collagen *de novo* deposited by the cells in the fibrin BAMs and renders them more resistant to strain by externally applied force.

Collagen deposition and visco-elastic properties of the BAMs changed with varying fibrinogen content. When a lower concentration of fibrinogen was used for engineering the BAMs, more collagen was deposited, up to 45.2%. Moreover, a higher Young's modulus was measured, and BAMs were able to still respond to 2,500  $\mu$ N of force with a low strain.

Bonds formed by transglutaminase exhibit a higher resistance to proteolysis. Therefore, we used FXIII, a transglutaminase which cross-links fibrin in the BAM engineering process. FXIII resulted in a slight increase of strain at 2,500  $\mu$ N applied force and a lower Young's modulus. Also, we varied the number of cells per BAM. The cell number did not significantly change the visco-elastic parameters of the BAM.

The elastic moduli of native murine muscle have been measured by others with the use of AFM (Engler et al., 2004). Results varied from a Young's modulus of an extensor digitorum longus muscle of  $12 \pm 4$  kPa (Engler et al., 2004) to  $61 \pm 5$  kPa for single fibers of the flexor digitorum brevis muscle (Defranchi et al., 2005). AFM measurements on monolayer murine myoblasts yielded a Young's modulus of  $11.5 \pm 1.3$  kPa for undifferentiated myoblasts, increasing to  $45.3 \pm 4.0$  kPa after 8 days of differentiation (Collinsworth et al., 2002). This increase is consistent with our data; we observed a Young's modulus in the range of 40–60 kPa 7 days after casting (**Figure 8**), increasing to a range of 50–200 kPa measured at 14 days after casting (**Figures 5, 7**). However, AFM measurement of the elastic modulus differs from our measurement method. First, AFM is based on measurements with a small cantilever, which registers local forces on a cellular scale rather than a whole-tissue scale, whereas our method measured forces generated by the entire tissue. Second, the AFM cantilever registers forces perpendicular (transversal) to the alignment of the myofibers, whereas tensile testing measures forces in the longitudinal direction, similar to the direction in which a muscle exerts its function. Therefore, we believe that tensile testing provides information which is physiologically more relevant than AFM measurements. Tensile testing of tissue engineered skeletal muscle has been reported to

yield a Young's modulus in the range of 12–31 kPa (Heher et al., 2015). However, in the latter study, a murine cell line was used, fibrin densities were much higher (10–40 mg/ml) and the fusion index (15–30%) was lower than what we obtain with human cells (70%) (Gholobova et al., 2015).

Important for muscle physiology is the amount of force that can be generated by the myofibers upon electrical stimulation. Fibrin (1 mg/ml) BAMs, cultured in the presence of media supplements, were able to generate  $985 \pm 58 \mu\text{N}/\text{mm}^2$  force at 14 days after casting. This was similar to collagen BAMs ( $829 \pm 49 \mu\text{N}/\text{mm}^2$ ). However, the fibrin BAMs at 14 days had a larger cross-sectional area, so the absolute force generation of the BAMs was higher. When decreasing the fibrin content, this absolute force remained similar, but due to decreased cross-sectional area, the normalized force increased, up to  $2,215 \pm 123 \mu\text{N}/\text{mm}^2$  for 0.25 mg/ml fibrin. Cross-linking of fibrin with FXIII significantly impeded force generation ( $189 \pm 64 \mu\text{N}/\text{mm}^2$ ). The forces we report here are in the same range as what we and others previously reported (Huang et al., 2005; Brady et al., 2008; Vandenburgh et al., 2008; Fuoco et al., 2015; Madden et al., 2015; Martin et al., 2017; Kasper et al., 2018). Forces exerted by excised tibialis anterior muscle were around 1–2 mN (Cook et al., 2016), thus the forces we obtain are only slightly lower. A longer culture time *in vitro* may further enhance contractile properties (Lee and Vandenburgh, 2013).

Other methods to increase collagen deposition may be utilized in parallel to or instead of stimulation by ascorbic acid. For example, addition of fibrin degradation products (Ahmann et al., 2010) and electrical stimulation (Rahimi et al., 2014) have been shown to enhance collagen deposition. Furthermore, ascorbic acid has a toxic effect at higher concentration, but magnesium ascorbyl phosphate, a stable derivative of ascorbic acid, was shown to be usable at higher concentrations with human tenocytes (Hakimi et al., 2014).

A limitation of the current study is that BAMs were cultured under static conditions. Mechanical conditioning of BAMs has been reported to maintain a constant elastic modulus over 8 days of stretching, whereas control BAMs become stiffer (Powell C.A. et al., 2002). Another future challenge is to study the effect of the collagen deposition *in vivo*. Importantly, it remains to be seen if the deposited collagen does allow angiogenesis in the BAM. The lack of angiogenesis in the BAM which we observed previously (Thorrez et al., 2006) may also be partly due to the lack of tension of the myofibers after implantation. This tension may be needed for proper myofiber morphology and vascularization. New ways of implanting BAMs under tension need to be developed.

## REFERENCES

- Ahmann, K. A., Weinbaum, J. S., Johnson, S. L., and Tranquillo, R. T. (2010). Fibrin degradation enhances vascular smooth muscle cell proliferation and matrix deposition in fibrin-based tissue constructs fabricated *in vitro*. *Tissue Eng. Part A* 16, 3261–3270. doi: 10.1089/ten.TEA.2009.0708
- Beier, J. P., Stern-Straeter, J., Foerster, V. T., Kneser, U., Stark, G. B., and Bach, A. D. (2006). Tissue engineering of injectable muscle: three-dimensional myoblast-fibrin injection in the syngeneic rat animal model. *Plast. Reconstr. Surg.* 118, 1113–1121. doi: 10.1097/01.prs.0000221007.97115.1d
- Brady, M. A., Lewis, M. P., and Muder, V. (2008). Synergy between myogenic and non-myogenic cells in a 3D tissue-engineered craniofacial skeletal muscle construct. *J. Tissue Eng. Regen. Med.* 2, 408–417. doi: 10.1002/term.112
- Cesarman-Maus, G., and Hajjar, K. A. (2005). Molecular mechanisms of fibrinolysis. *Br. J. Haematol.* 129, 307–321. doi: 10.1111/j.1365-2141.2005.05444.x
- Chromiak, J. A., and Vandenburgh, H. H. (1992). Glucocorticoid-induced skeletal muscle atrophy *in vitro* is attenuated by mechanical stimulation. *Am. J. Physiol.* 262, C1471–C1477. doi: 10.1152/ajpcell.1992.262.6.C1471
- Collinsworth, A. M., Zhang, S., Kraus, W. E., and Truskey, G. A. (2002). Apparent elastic modulus and hysteresis of skeletal muscle cells throughout
- Alternatively, inclusion of certain growth factors may facilitate the vascularization process (Thorrez et al., 2006). Neurotrophic (Iwakawa et al., 2001) and angiogenic (Wong et al., 2003) factors can be incorporated in fibrin by simply suspending the factor in the hydrogel. Most likely a combination of these growth factors will be needed; indeed inclusion of VEGF<sub>165</sub> with bFGF or VEGF<sub>121</sub> was shown to induce more mature blood vessels than the individual growth factors (Wong et al., 2003). Bioactive peptides can also be enzymatically linked to the fibrin matrix (Schense et al., 2000).

## CONCLUSION

In conclusion, contracted, differentiated BAMs can be successfully engineered in a fibrin ECM. The addition of proline, hydroxyproline, and ascorbic acid to the media, together with decreasing the fibrinogen content, increases the visco-elastic properties of the BAMs as well as the amount of *de novo* collagen ECM deposited. This physico-chemical modulation of the ECM may be beneficial for future *in vivo* applications by maintaining BAM consistency and survival while allowing angiogenesis.

## AUTHOR CONTRIBUTIONS

LT and HV contributed conception and designed the experiments. LT, JS, and KD performed the experiments and statistical analysis. LT and KD wrote the first draft of the manuscript. HV and LT acquired funding for the work. LT, HV, JS, and KD wrote sections of the manuscript.

## FUNDING

This research was funded through a fellowship from the Belgian American Educational Foundation (LT), AFM-Telethon trampoline grant 19802 and the Research Foundation-Flanders (FWO) grant 1529817N.

## ACKNOWLEDGMENTS

We would like to thank Jim Staruk for assistance with the Trichrome stain, Geoff Williams for assistance with imaging and quantification and Dr. Melanie Gerard for critical reading.

- differentiation. *Am. J. Physiol. Cell Physiol.* 283, C1219–C1227. doi: 10.1152/ajpcell.00502.2001
- Cook, C. A., Huri, P. Y., Ginn, B. P., Gilbert-Honick, J., Somers, S. M., Temple, J. P., et al. (2016). Characterization of a novel bioreactor system for 3D cellular mechanobiology studies. *Biotechnol. Bioeng.* 113, 1825–1837. doi: 10.1002/bit.25946
- Decroix, L., Van Muylder, V., Desender, L., Sampaolesi, M., and Thorrez, L. (2015). Tissue clearing for confocal imaging of native and bio-artificial skeletal muscle. *Biotech. Histochem.* 90, 424–431. doi: 10.3109/10520295.2015.1019564
- Defranchi, E., Bonaccorso, E., Tedesco, M., Canato, M., Pavan, E., Raiteri, R., et al. (2005). Imaging and elasticity measurements of the sarcolemma of fully differentiated skeletal muscle fibres. *Microsc. Res. Tech.* 67, 27–35. doi: 10.1002/jemt.20177
- Engler, A. J., Griffin, M. A., Sen, S., Bönnemann, C. G., Sweeney, H. L., and Discher, D. E. (2004). Myotubes differentiate optimally on substrates with tissue-like stiffness: pathological implications for soft or stiff microenvironments. *J. Cell Biol.* 166, 877–887. doi: 10.1083/jcb.200405004
- Fuoco, C., Rizzi, R., Biondo, A., Longa, E., Mascaro, A., Shapira-Schweitzer, K., et al. (2015). In vivo generation of a mature and functional artificial skeletal muscle. *EMBO Mol. Med.* 7, 411–422. doi: 10.15252/emmm.201404062
- Gholobova, D., Decroix, L., Van Muylder, V., Desender, L., Gerard, M., Carpentier, G., et al. (2015). Endothelial network formation within human tissue-engineered skeletal muscle. *Tissue Eng. Part A* 21, 2548–2558. doi: 10.1089/ten.TEA.2015.0093
- Hakimi, O., Poulson, R., Thakkar, D., Yapp, C., and Carr, A. (2014). Ascorbic acid is essential for significant collagen deposition by human tenocytes in vitro. *Oxid. Antioxid. Med. Sci.* 3, 119–127. doi: 10.5455/oams.030514.or.063
- Heher, P., Maleiner, B., Prüller, J., Teuschl, A. H., Kollmitzer, J., Monforte, X., et al. (2015). A novel bioreactor for the generation of highly aligned 3D skeletal muscle-like constructs through orientation of fibrin via application of static strain. *Acta Biomater.* 24, 251–265. doi: 10.1016/j.actbio.2015.06.033
- Helgerson, S., Seelich, T., DiOrto, J., Tawil, B., Bittner, L., and Spaethe, R. (2004). "Fibrin," in *Encyclopedia of Biomaterials and Biomedical Engineering*, eds G. Wnek and G. Bowlin (New York, NY: Marcel Dekker, Inc.), 603–610.
- Huang, Y.-C., Dennis, R. G., Larkin, L., and Baar, K. (2005). Rapid formation of functional muscle in vitro using fibrin gels. *J. Appl. Physiol.* 98, 706–713. doi: 10.1152/jappphysiol.00273.2004
- Iwakawa, M., Mizoi, K., Tessier, A., and Itoh, Y. (2001). Intraspinal implants of fibrin glue containing glial cell line-derived neurotrophic factor promote dorsal root regeneration into spinal cord. *Neurorehabil. Neural Repair* 15, 173–182. doi: 10.1177/154596830101500304
- Jenkins, C. L., Bretscher, L. E., Guzei, I. A., and Raines, R. T. (2003). Effect of 3-hydroxyproline residues on collagen stability. *J. Am. Chem. Soc.* 125, 6422–6427. doi: 10.1021/ja034015j
- Kasper, A. M., Turner, D. C., Martin, N. R. W., and Sharples, A. P. (2018). Mimicking exercise in three-dimensional bioengineered skeletal muscle to investigate cellular and molecular mechanisms of physiological adaptation. *J. Cell Physiol.* 233, 1985–1998. doi: 10.1002/jcp.25840
- Lee, P. H. U., and Vandenburgh, H. H. (2013). Skeletal muscle atrophy in bioengineered skeletal muscle: a new model system. *Tissue Eng. Part A* 19, 2147–2155. doi: 10.1089/ten.TEA.2012.0597
- Lu, Y., Shansky, J., Del Tatto, M., Ferland, P., McGuire, S., Marszalkowski, J., et al. (2002). Therapeutic potential of implanted tissue-engineered bioartificial muscles delivering recombinant proteins to the sheep heart. *Ann. N. Y. Acad. Sci.* 961, 78–82. doi: 10.1111/j.1749-6632.2002.tb03055.x
- Lu, Y., Shansky, J., Del Tatto, M., Ferland, P., Wang, X., and Vandenburgh, H. (2001). Recombinant vascular endothelial growth factor secreted from tissue-engineered bioartificial muscles promotes localized angiogenesis. *Circulation* 104, 594–599. doi: 10.1161/hc3101.092215
- Madden, L., Juhas, M., Kraus, W. E., Truskey, G. A., and Bursac, N. (2015). Bioengineered human myobundles mimic clinical responses of skeletal muscle to drugs. *eLife* 4:e04885. doi: 10.7554/eLife.04885
- Mangir, N., Bullock, A. J., Roman, S., Osman, N., Chapple, C., and MacNeil, S. (2016). Production of ascorbic acid releasing biomaterials for pelvic floor repair. *Acta Biomater.* 29, 188–197. doi: 10.1016/j.actbio.2015.10.019
- Martin, N. R. W., Turner, M. C., Farrington, R., Player, D. J., and Lewis, M. P. (2017). Leucine elicits myotube hypertrophy and enhances maximal contractile force in tissue engineered skeletal muscle in vitro. *J. Cell. Physiol.* 232, 2788–2797. doi: 10.1002/jcp.25960
- Matsumoto, T., Yung, Y. C., Fischbach, C., Kong, H. J., Nakaoka, R., and Mooney, D. J. (2007). Mechanical strain regulates endothelial cell patterning in vitro. *Tissue Eng.* 13, 207–217. doi: 10.1089/ten.2006.0058
- Nelson, D., and Cox, M. (2005). *Lehninger Principles of Biochemistry*, 4th Edn. New York, NY: W.H. Freeman and Co.
- Patel, B., Xu, Z., Pinnock, C. B., Kabbani, L. S., and Lam, M. T. (2018). Self-assembled collagen-fibrin hydrogel reinforces tissue engineered adventitia vessels seeded with human fibroblasts. *Sci. Rep.* 8:3294. doi: 10.1038/s41598-018-21681-7
- Powell, C., Shansky, J., Tatto, M., Del Forman, D. E., Hennessey, J., Sullivan, K., et al. (1999). Tissue-engineered human bioartificial muscles expressing a foreign recombinant protein for gene therapy. *Hum. Gene Ther.* 10, 565–577. doi: 10.1089/10430349950018643
- Powell, C. A., Smiley, B. L., Mills, J., and Vandenburgh, H. H. (2002). Mechanical stimulation improves tissue-engineered human skeletal muscle. *Am. J. Physiol. Cell Physiol.* 283, C1557–C1565. doi: 10.1152/ajpcell.00595.2001
- Powell, C., Shansky, J., Del Tatto, M., and Vandenburgh, H. H. (2002). Bioartificial muscles in gene therapy. *Methods Mol. Med.* 69, 219–231.
- Rahimi, N., Swennen, G., Verbruggen, S., Scibiorek, M., Molin, D. G., and Post, M. J. (2014). Short stimulation of electro-responsive PAA/fibrin hydrogel induces collagen production. *Tissue Eng. Part C Methods* 20, 703–713. doi: 10.1089/ten.TEC.2013.0596
- Schense, J. C., Bloch, J., Aebischer, P., and Hubbell, J. A. (2000). Enzymatic incorporation of bioactive peptides into fibrin matrices enhances neurite extension. *Nat. Biotechnol.* 18, 415–419. doi: 10.1038/74473
- Schwartz, C. E., Hellerqvist, C. G., and Cunningham, L. W. (1979). Attaching human fibroblasts secrete a type I procollagen rich in 3-hydroxyproline. *Biochem. Biophys. Res. Commun.* 90, 240–246. doi: 10.1016/0006-291X(79)91616-4
- Schwarz, R. I., Mandell, R. B., and Bissell, M. J. (1981). Ascorbate induction of collagen synthesis as a means for elucidating a mechanism of quantitative control of tissue-specific function. *Mol. Cell. Biol.* 1, 843–853. doi: 10.1128/MCB.1.9.843
- Shansky, J., Creswick, B., Lee, P., Wang, X., and Vandenburgh, H. (2006a). Paracrine release of insulin-like growth factor 1 from a bioengineered tissue stimulates skeletal muscle growth in vitro. *Tissue Eng.* 12, 1833–1841.
- Shansky, J., Ferland, P., McGuire, S., Powell, C., Del Tatto, M., Nackman, M., et al. (2006b). "Tissue engineering human skeletal muscle for clinical applications," in *Culture of Cells for Tissue Engineering*, eds R. Freshney and G. Vunjak-Novakovic (Hoboken, NJ: Wiley-Interscience), 239–258.
- Thorrez, L., Shansky, J., Wang, L., Fast, L., VandenDriessche, T., Chuah, M., et al. (2008). Growth, differentiation, transplantation and survival of human skeletal myofibers on biodegradable scaffolds. *Biomaterials* 29, 75–84. doi: 10.1016/j.biomaterials.2007.09.014
- Thorrez, L., Vandenburgh, H., Callewaert, N., Mertens, N., Shansky, J., Wang, L., et al. (2006). Angiogenesis enhances factor IX delivery and persistence from retrievable human bioengineered muscle implants. *Mol. Ther.* 14, 442–451. doi: 10.1016/j.ymthe.2006.03.019
- Spotnitz, W. D. (2014). Fibrin sealant: the only approved hemostat, sealant, and adhesive—a laboratory and clinical perspective. *ISRN Surg.* 2014:203943. doi: 10.1155/2014/203943
- Vandenburgh, H. (2010). High-content drug screening with engineered musculoskeletal tissues. *Tissue Eng. Part B Rev.* 16, 55–64. doi: 10.1089/ten.TEB.2009.0445
- Vandenburgh, H., Del Tatto, M., Shansky, J., Goldstein, L., Russell, K., Genes, N., et al. (1998). Attenuation of skeletal muscle wasting with recombinant human growth hormone secreted from a tissue-engineered bioartificial muscle. *Hum. Gene Ther.* 9, 2555–2564. doi: 10.1089/hum.1998.9.17-2555
- Vandenburgh, H., Del Tatto, M., Shansky, J., Lemaire, J., Chang, A., Payumo, F., et al. (1996). Tissue-engineered skeletal muscle organoids for reversible gene therapy. *Hum. Gene Ther.* 7, 2195–2200. doi: 10.1089/hum.1996.7.17-2195
- Vandenburgh, H., and Kaufman, S. (1979). In vitro model for stretch-induced hypertrophy of skeletal muscle. *Science* 203, 265–268. doi: 10.1126/science.569901

- Vandenburgh, H., Shansky, J., Benesch-Lee, F., Barbata, V., Reid, J., Thorrez, L., et al. (2008). Drug-screening platform based on the contractility of tissue-engineered muscle. *Muscle Nerve* 37, 438–447. doi: 10.1002/mus.20931
- Vandenburgh, H., Shansky, J., Benesch-Lee, F., Skelly, K., Spinazzola, J. M., Saponjian, Y., et al. (2009). Automated drug screening with contractile muscle tissue engineered from dystrophic myoblasts. *FASEB J.* 23, 3325–3334. doi: 10.1096/fj.09-134411
- Vandenburgh, H. H. (1988). A computerized mechanical cell stimulator for tissue culture: effects on skeletal muscle organogenesis. *Vitro Cell. Dev. Biol.* 24, 609–619. doi: 10.1007/BF02623597
- Vandenburgh, H. H., Hatfaludy, S., Karlisch, P., and Shansky, J. (1991). Mechanically induced alterations in cultured skeletal muscle growth. *J. Biomech.* 24, 91–99. doi: 10.1016/0021-9290(91)90380-6
- Vandenburgh, H. H., Karlisch, P., and Farr, L. (1988). Maintenance of highly contractile tissue-cultured avian skeletal myotubes in collagen gel. *Vitro Cell. Dev. Biol.* 24, 166–174. doi: 10.1007/BF02623542
- Wong, C., Inman, E., Spaethe, R., and Helgerson, S. (2003). New technologies and diagnostic tools fibrin-based biomaterials to deliver human growth factors. *Thromb. Haemost.* 89, 573–582. doi: 10.1055/s-0037-1613389
- Wu, Y., Puperi, D. S., Grande-Allen, K. J., and West, J. L. (2017). Ascorbic acid promotes extracellular matrix deposition while preserving valve interstitial cell quiescence within 3D hydrogel scaffolds. *J. Tissue Eng. Regen. Med.* 11, 1963–1973. doi: 10.1002/term.2093

**Conflict of Interest Statement:** The authors declare that the research was conducted in the absence of any commercial or financial relationships that could be construed as a potential conflict of interest.

Copyright © 2018 Thorrez, DiSano, Shansky and Vandenburgh. This is an open-access article distributed under the terms of the Creative Commons Attribution License (CC BY). The use, distribution or reproduction in other forums is permitted, provided the original author(s) and the copyright owner(s) are credited and that the original publication in this journal is cited, in accordance with accepted academic practice. No use, distribution or reproduction is permitted which does not comply with these terms.



# Extracellular Collagen VI Has Prosurvival and Autophagy Instructive Properties in Mouse Fibroblasts

Silvia Castagnaro<sup>1</sup>, Martina Chrisam<sup>1</sup>, Matilde Cescon<sup>1</sup>, Paola Braghetta<sup>1</sup>, Paolo Grumati<sup>1,2</sup> and Paolo Bonaldo<sup>1,3\*</sup>

<sup>1</sup> Department of Molecular Medicine, University of Padova, Padova, Italy, <sup>2</sup> Institute of Biochemistry II, Goethe University, Frankfurt, Germany, <sup>3</sup> CRIBI Biotechnology Center, University of Padova, Padova, Italy

## OPEN ACCESS

### Edited by:

Cesare Gargioli,  
Università degli Studi di Roma  
"Tor Vergata", Italy

### Reviewed by:

Marco Segatto,  
Università degli Studi di Milano, Italy  
Theodora Pavidou,  
IAKENTRO, Greece

### \*Correspondence:

Paolo Bonaldo  
bonaldo@bio.unipd.it

### Specialty section:

This article was submitted to  
Integrative Physiology,  
a section of the journal  
Frontiers in Physiology

**Received:** 30 April 2018

**Accepted:** 30 July 2018

**Published:** 17 August 2018

### Citation:

Castagnaro S, Chrisam M, Cescon M, Braghetta P, Grumati P and Bonaldo P (2018) Extracellular Collagen VI Has Prosurvival and Autophagy Instructive Properties in Mouse Fibroblasts. *Front. Physiol.* 9:1129. doi: 10.3389/fphys.2018.01129

Collagen VI (ColVI) is an abundant and distinctive extracellular matrix protein secreted by fibroblasts in different tissues. Human diseases linked to mutations on ColVI genes are primarily affecting skeletal muscle due to non-cell autonomous myofiber defects. To date, it is not known whether and how fibroblast homeostasis is affected by ColVI deficiency, a critical missing information as this may strengthen the use of patients' fibroblasts for preclinical purposes. Here, we established primary and immortalized fibroblast cultures from ColVI null (*Col6a1*<sup>-/-</sup>) mice, the animal model of ColVI-related diseases. We found that, under nutrient-stringent condition, lack of ColVI affects fibroblast survival, leading to increased apoptosis. Moreover, *Col6a1*<sup>-/-</sup> fibroblasts display defects in the autophagy/lysosome machinery, with impaired clearance of autophagosomes and failure of Parkin-dependent mitophagy. *Col6a1*<sup>-/-</sup> fibroblasts also show an increased activation of the Akt/mTOR pathway, compatible with the autophagy impairment, and adhesion onto purified ColVI elicits a major effect on the autophagic flux. Our findings reveal that ColVI ablation in fibroblasts impacts on autophagy regulation and cell survival, thus pointing at the new concept that this cell type may contribute to the pathological features of ColVI-related diseases.

**Keywords:** collagen VI, autophagy, mitophagy, apoptosis, fibroblasts, lysosomes

## INTRODUCTION

The ECM microenvironment plays a crucial role for tissue homeostasis and ensures proper functionality through physical interactions and structural support. Several ECM components are involved in key cellular pathways other than the mere cell-matrix adhesion, such as activation and presentation of soluble factors, preservation of the stem cell niche, and signal transduction into cells (Hynes, 2009; Gattazzo et al., 2014). Recent studies also revealed that some ECM proteins are

**Abbreviations:** 3-MA, 3-methyladenine; AMPK, AMP-activated protein kinase; BM, Bethlem myopathy; CCCP, carbonyl cyanide m-chlorophenylhydrazone; ColVI, collagen VI; CQ, chloroquine; ECM, extracellular matrix; Erk1/2, extracellular signal-regulated kinases 1 and 2; LAMP-2, lysosomal-associated membrane protein 2; MAP1LC3B/LC3, microtubule-associated protein 1 light chain 3B; MEF, mouse embryonic fibroblasts; mTOR, mammalian target of rapamycin; PI, propidium iodide; Raptor, regulatory-associated protein of TOR; rpS6, ribosomal protein S6; SQSTM1/p62, sequestosome 1; TFEB, transcription factor EB; UCMD, Ullrich congenital muscular dystrophy; Ulk1, Unc-51 like autophagy activating kinase 1.

able to modulate macroautophagy (Neill et al., 2014). Macroautophagy (hereafter referred to as autophagy) is the degradative cellular pathway that involves the formation of double-membrane vesicles (autophagosomes) engulfing long-lived proteins, damaged organelles and pathogens, and delivering them to lysosomes for degradation and recycling (Boya et al., 2013). Extra- and intracellular nutrient and growth factor availability regulates autophagy by means of a complex machinery of interactors that enable a balanced adaptive response (Feng et al., 2014). Indeed, both defective and excessive activation of autophagy are detrimental for cell homeostasis and result in human degenerative pathologies (Levine and Kroemer, 2008; Schneider and Cuervo, 2014). The roles of the ECM on autophagy regulation are increasingly evident, although still under dissection (Neill et al., 2014; Buraschi et al., 2017).

Collagen VI is a major ECM protein forming a distinct microfibrillar network with a broad distribution in several embryonic and adult tissues (Cescon et al., 2015). It is composed of three major genetically distinct chains,  $\alpha 1(\text{VI})$ ,  $\alpha 2(\text{VI})$  and  $\alpha 3(\text{VI})$ , which associate intracellularly to form a triple helical monomer, followed by assembly into disulfide-bonded dimers and tetramers (Colombatti et al., 1995). After secretion in the extracellular space, tetramers associate in a non-covalent fashion forming beaded microfilaments, which are deposited in the ECM and interact with a number of other ECM and cell surface molecules (Kuo et al., 1997; Cescon et al., 2015). Mutations of ColVI genes in humans cause a range of diseases with variable onset and progression and primarily affecting skeletal muscles, including UCMD, BM and myosclerosis myopathy (Merlini et al., 2008b; Bönnemann, 2011; Bushby et al., 2014). A common and characteristic feature of these diseases is the involvement of joints, skin and connective tissue defects. The most characterized model of ColVI-related diseases is the ColVI null (*Col6a1*<sup>-/-</sup>) mouse, which displays an early onset myopathic phenotype with spontaneous apoptosis and accumulation of dysfunctional mitochondria within myofibers, due to defective regulation of autophagy (Irwin et al., 2003; Grumati et al., 2010). Similar defects were found in muscle biopsies of UCMD and BM patients (Angelin et al., 2007; Merlini et al., 2008a; Grumati et al., 2010), and following the demonstration that reactivation of autophagy by different means is beneficial in recovering the structural and functional defects of *Col6a1*<sup>-/-</sup> mice, a pilot clinical trial in UCMD and BM patients by 1-year low-protein diet was successful in reactivating autophagy (Castagnaro et al., 2016). Although ColVI deficiency has a major impact on muscle fibers, the main producers of this protein in skeletal muscle, as in other tissues, are interstitial fibroblasts (Braghetta et al., 2008; Zou et al., 2008). Fibroblast cultures from patients' skin biopsies are extensively used to assess the effects of different mutations of ColVI genes in the synthesis, assembly, secretion and ECM deposition of the protein (Zhang et al., 2002; Pan et al., 2003; Jimenez-Mallebrera et al., 2006; Merlini et al., 2008a). Retention of mutated ColVI was observed in patients' fibroblasts rather than in myofibers, suggesting that fibroblasts themselves may significantly contribute to the pathogenesis of ColVI diseases (Zou et al., 2008). However, no study until now investigated

whether and how lack of ColVI impacts on the homeostasis and survival of fibroblasts.

In this work, we show that autophagy regulation is impaired in fibroblasts lacking ColVI. We generated immortalized fibroblasts from wild-type (WT) and *Col6a1*<sup>-/-</sup> animals, and found that ColVI ablation triggers spontaneous apoptosis and defects in the autophagy-lysosome machinery of fibroblasts, together with a deregulation in the activity of the TFEB and of the mTOR signaling pathway. Moreover, we provide evidence that fibroblast adhesion onto purified native ColVI has instructive roles in promoting cell survival and autophagy, thus revealing a direct regulation of autophagy by extracellular ColVI.

## MATERIALS AND METHODS

### Cell Culture and Transfection

Primary murine embryonic fibroblasts (MEF) were prepared by dissociation of E13.5 embryos generated from WT and *Col6a1*<sup>-/-</sup> mice in the C57BL/6N background (Irwin et al., 2003; Grumati et al., 2010). Animal procedures were approved by the Ethics Committee of the University of Padova, in accordance to EU Directive for animal experiments, and authorized by the Italian Ministry of Health. MEF were cultured in Dulbecco's modified Eagle's medium (DMEM; Gibco) supplemented with 10% fetal bovine serum (FBS; Life Technologies), 0.2 M L-glutamine and 1:100 penicillin-streptomycin (Life Technologies). Early passage MEF were immortalized using a pMSE plasmid encoding for SV40 large T-antigen (SV40LT, kindly provided by Dr. M. Sandri, University of Padova) by microporation (Neon<sup>®</sup> Transfection System, MPT100, Life Technologies). MEF lines stably expressing GFP-LC3 were obtained from E12 embryos generated from GFP-LC3 mice (Mizushima et al., 2004) (provided by Riken BRC; GFP-LC3#53 strain, RBRC00806) and GFP-LC3::*Col6a1*<sup>-/-</sup> mice (Chrisam et al., 2015). For all the experiments, MEF were cultured in DMEM supplemented with 10% FBS (complete medium) and maintained in a humidified incubator containing 5% CO<sub>2</sub> at 37°C, and periodically tested for contamination with LookOut<sup>®</sup> Mycoplasma PCR Detection Kit (Sigma-Aldrich). For ColVI expression studies, cells were cultured 3–7 days in complete medium supplemented with 0.25 mM ascorbic acid. When indicated, cells were plated on plastic dishes coated with 5  $\mu\text{g}/\text{cm}^2$  purified murine native ColVI (Irwin et al., 2003) or with collagen I (C8919, Sigma-Aldrich), and cultured for 3 days. For transfection experiments,  $0.8 \times 10^5$  cells were plated on 12 mm glass coverslips, grown to 80% confluence and transfected with pMitoRed (kindly provided by Dr. L. Scorrano, University of Padova), mCherry-Parkin (Addgene plasmid 23956), YFP-Parkin (Addgene plasmid 23955; Narendra et al., 2008) or GFP-TFEB (kindly provided by Dr. M. Sandri, University of Padova) plasmids using Lipofectamine<sup>™</sup> LTX (Life Technologies), according to manufacturer's guidelines. After 4 h, transfected cells were washed in complete DMEM without antibiotics and cultured 18–20 h before fixation with 4% paraformaldehyde in phosphate-buffered saline (PBS). When indicated, the following additional treatments were used on subconfluent cells (about 80% confluence): 3 or 6 h serum



withdrawal; 50  $\mu\text{M}$  CQ (Sigma-Aldrich); 250–500  $\mu\text{M}$  3-MA (Sigma-Aldrich); 20  $\mu\text{M}$  CCCP (Sigma-Aldrich). Finally, cells were harvested and processed for flow cytometry analyses or fixed for 10 min with ice-cold acetone/methanol (1:1) at  $-20^{\circ}\text{C}$ .

## Immunofluorescence on Cells

Fixed cells were washed three times in PBS, treated for 30 min with 10% goat serum (Sigma-Aldrich) and incubated for 2 h at room temperature or overnight at  $4^{\circ}\text{C}$  with the following primary antibodies: rabbit anti-ColVI (AS72, kindly supplied by Dr. A. Colombatti, CRO Aviano), mouse anti-fibronectin (kindly supplied by Dr. A. Colombatti), rabbit anti- $\alpha 1(\text{VI})$  (Santa Cruz Biotechnology), guinea pig anti- $\alpha 3(\text{VI})$  (kindly supplied by Dr. R. Wagener, University of Cologne), rat anti-LAMP-2 (Abcam), rabbit anti-LC3 (Cell Signaling Technologies), rabbit anti-Tom20 (Santa Cruz Biotechnology). After three washing in PBS, slides were incubated for 1 h with the following secondary antibodies: anti-mouse Cy2, anti-rabbit Cy2, anti-rabbit Cy3, anti-rat Cy3 (all Jackson ImmunoResearch); IRIS anti-rabbit Cy5.5 (Cyanine Technologies). Nuclei were stained with Hoechst 33258 (Sigma-Aldrich). Slides were mounted in 80% glycerol-PBS and analyzed with a Leica SP5 confocal microscope. Colocalization was quantified in merged images, after thresholding of individual frames, using the JACoP plugin of the ImageJ software. The percentage of cells with enlarged lysosomes was calculated by manual counting of the cells with at least two enlarged LAMP-2-positive lysosomes on total cell number per field, using thirty randomly chosen image fields. The percentage of cells with tubular or fragmented mitochondria was estimated by manual analysis of mitochondrial morphology in at least thirty randomly chosen fields. Mean data are representative of at least five independent biological samples.

## TUNEL Assay

Terminal deoxynucleotidyl transferase dUTP-mediated nick-end labeling (TUNEL) analysis was performed on acetone/methanol fixed MEF using the Dead End Fluorometric *In situ* Apoptosis Detection System (Promega). Cells, grown on slides and fixed in acetone/methanol, were washed and incubated for 10 min with the equilibration buffer. Then the slides were incubated with a buffer containing fluorescent nucleotides, terminal deoxynucleotidyl transferase (TdT), and Hoechst 33258 (Sigma-Aldrich) for 1 h at  $37^{\circ}\text{C}$ . The reaction was blocked with SSC solution (300 mM NaCl, 30 mM sodium citrate). After being washed three times in PBS, slides were mounted using 80% glycerol. Hoechst was used to counterstain all nuclei and TUNEL-positive nuclei were determined by counting randomly selected fields using a Zeiss Axioplan microscope.

## Flow Cytometry

Wild-type and *Col6a1*<sup>-/-</sup> MEF were plated (200,000 cells/well) in 12-well plates by adhesion onto either plastic, purified ColVI or collagen I, and cultured for 24 h. Cells were washed in PBS, and incubated for 3 or 6 h in complete medium or in serum-free medium. When indicated, 1  $\mu\text{M}$  staurosporine or 250–500  $\mu\text{M}$  3-MA (Sigma-Aldrich) were added to the serum-free medium. Apoptosis was determined using the Annexin V

(AnV)-FITC Apoptosis detection kit (eBioscience). Cells were harvested, washed with PBS and incubated in 195  $\mu\text{l}$  binding buffer containing 5  $\mu\text{l}$  AnV-FITC for 15 min at room temperature in the dark, according to the manufacturer's protocol. Cells were finally incubated with 1  $\mu\text{g}/\mu\text{l}$  PI and samples were immediately analyzed on a FACSCanto flow cytometer equipped with FACS Diva software (BD Biosciences), using FL-1 and FL-2 settings. Forward scatter and side scatter (morphology parameters) were performed to discriminate live cells (AnV-negative and PI-negative), early apoptotic cells (AnV-positive and PI-negative), late apoptotic cells (AnV-positive and PI-positive), and AnV-negative and PI-positive cells (mainly necrotic). For each sample 10,000 events were collected from five independent biological replicates. Results were analyzed using Flowing Software v2.5.0 (Turku Centre for Biotechnology, University of Turku).

## Quantitative Real-Time PCR (qRT-PCR)

500,000 MEF of each genotype were plated in 6-well plates, in triplicate, and cultured for 2 days (autophagy studies) or 4 days (ColVI expression). For the analysis of ColVI genes, cells were cultured until post-confluence in DMEM containing 10% FBS, in the presence or absence of 0.25 mM ascorbic acid. For the analysis of autophagy genes, cells were washed in PBS, then cultured for 3 h in medium with or without FBS. RNA extraction was performed by adding 1 ml/well TRIzol Reagent (Life Technologies) directly on cultured cells and following the manufacturer's protocol. RNA was quantified using a Nanodrop ND-1000 instrument (Nanodrop Technologies) and 1  $\mu\text{g}$  total RNA was retrotranscribed using the SuperScript III First-Strand Synthesis System for RT-PCR (Life Technologies), following manufacturer's instructions. Resulting cDNAs were used to perform quantitative real time PCR using Rotor-Gene SYBR Green PCR Kit mastermix (Qiagen) with the RotorGeneQ instrument from Qiagen. Primer sequences are provided in **Supplementary Table S1**.

## Western Blotting

Mouse embryonic fibroblasts ( $0.5 \times 10^6$  cells/ml) were cultured in 6-well plates for 2 days. When indicated, multiwell plates were coated with 5  $\mu\text{g}/\text{cm}^2$  native ColVI or collagen I as described above. Cells were washed once in PBS and harvested with a cell lifter in lysis buffer (50 mM Tris-HCl, pH 7.5, 150 mM NaCl, 20 mM EDTA, 0.5% NP40), and supplemented with phosphatase inhibitors (Cocktail II P5726, Sigma-Aldrich) and proteases inhibitors (Complete EDTA-free, Roche). Cell lysates were then sonicated twice for 15 s using a Bioruptor (Diagenode) and the cleared cell lysates were quantified with the BCA Protein Assay kit (Pierce). SDS-PAGE of protein lysates (20 or 30  $\mu\text{g}$ ) was performed under reducing condition, using 3–8%, 4–12%, 10%, or 12% polyacrylamide Novex NuPAGE Bis-Tris gels (Life Technologies) and electrotransferred onto PVDF membrane (Merck Millipore). Membranes were blocked for 1 h in 5% milk in Tris-buffered saline, 0.1% Tween 20 (Sigma-Aldrich) and incubated 1 h at room temperature or overnight at  $4^{\circ}\text{C}$  with the primary antibodies diluted 1:1000 in TBST with 5% BSA. For a complete list of the antibodies, see **Supplementary Table S2**. Membranes were then washed three times and incubated for

1 h at room temperature with horseradish peroxidase-conjugated secondary antibodies (Amersham BioSciences) diluted 1:1000 in TBST and 5% milk. Detection was performed by SuperSignal West Pico or Dura Chemiluminescent Substrate and CL-X Posure Film (Thermo Scientific), using  $\beta$ -actin as a loading control. When needed, membranes were stripped using a stripping buffer (25 mM glycine, 1% SDS, pH 2.0) and re-probed. Western blots were performed in at least three independent experiments. Densitometric measurements were obtained with the ImageJ software, by normalizing the signal of each band to the corresponding  $\beta$ -actin band or to the non-phosphorylated form of protein. When indicated, each band was normalized to the first lane (arbitrarily set as 1) of the relative gel.

## Statistical Analysis

All results are expressed as means  $\pm$  SEM. Statistical analyses were performed by one way ANOVA with *post hoc* Bonferroni-correction where appropriate, as indicated in figure legends, or by Student's *t*-test for unpaired data. GraphPad Prism software was used, and  $P < 0.05$  was considered statistically significant.

## RESULTS

### Immortalized Mouse Fibroblasts Secrete ColVI and Organize an ECM

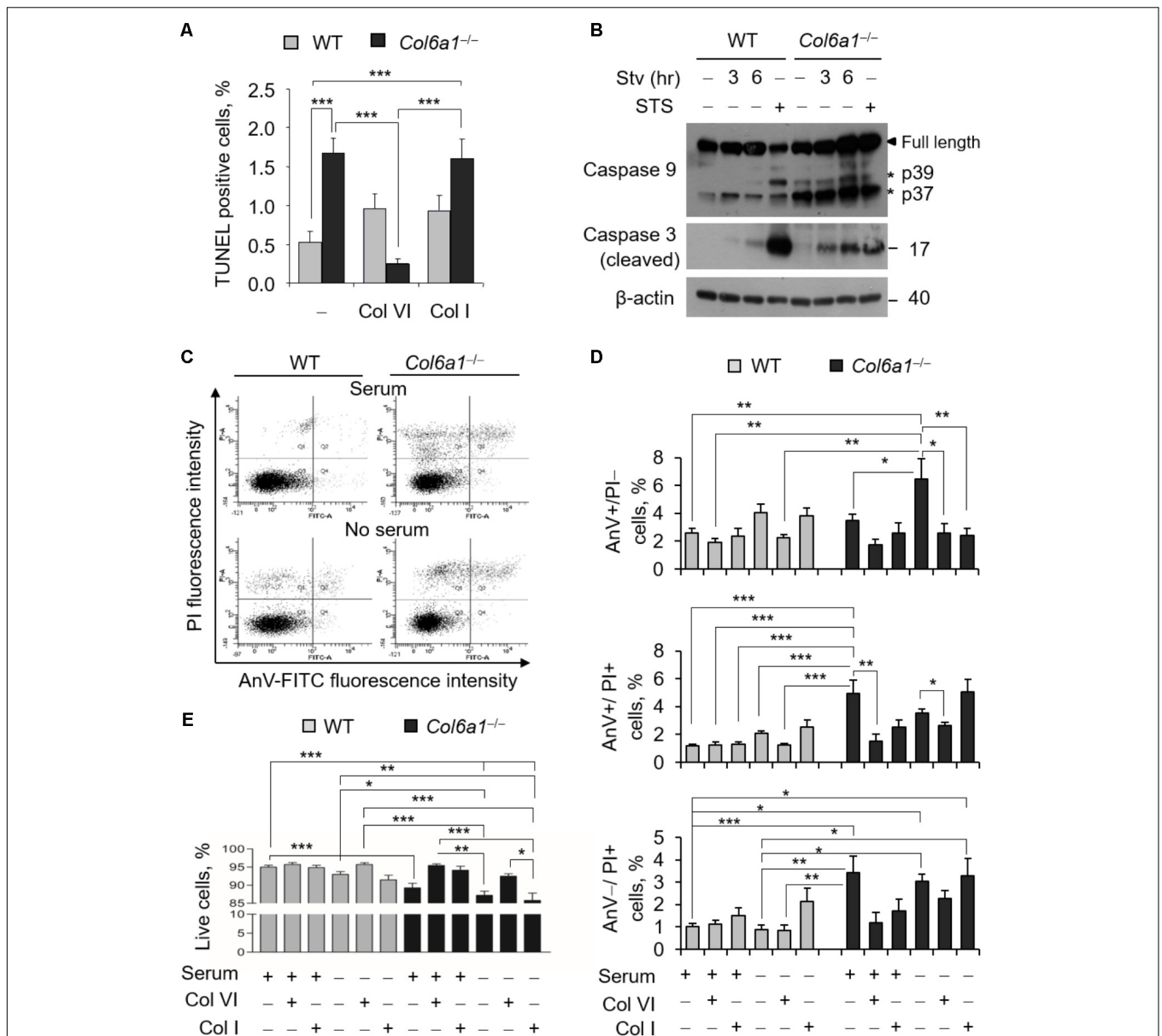
We established stable fibroblast cultures from WT and *Col6a1*<sup>-/-</sup> mice, and analyzed by different approaches the production of ColVI and other ECM proteins. Immunofluorescence showed the presence of organized ColVI filaments in the extracellular space of WT fibroblasts, whereas labeling was negative in *Col6a1*<sup>-/-</sup> cultures as expected (Supplementary Figure S1A). Fibronectin was detected in the ECM of both WT and *Col6a1*<sup>-/-</sup> fibroblasts, and as previously reported (Tillet et al., 1994) its labeling was strictly interconnected to ColVI staining (Supplementary Figures S1A,B). Western blotting confirmed the presence of ColVI chains in cell extracts and culture media of WT fibroblasts, and ascorbic acid promoted secretion of the protein in WT cultures (Supplementary Figure S1C). In the absence of  $\alpha 1$ (VI) chain, the intracellular protein levels of the other two chains were strongly decreased and ColVI secretion was abolished in *Col6a1*<sup>-/-</sup> fibroblasts (Supplementary Figure S1C). qRT-PCR analysis showed that WT fibroblasts express high levels of *Col6a1*, *Col6a2* and *Col6a3* transcripts (Supplementary Figure S1D). In *Col6a1*<sup>-/-</sup> fibroblasts, *Col6a1* transcripts were undetectable as expected, whereas *Col6a3* transcript levels were markedly decreased and *Col6a2* mRNA levels were similar to WT fibroblasts (Supplementary Figure S1D). Given the presence of low but discrete amounts of intracellular  $\alpha 2$ (VI) and  $\alpha 3$ (VI) polypeptides in *Col6a1*<sup>-/-</sup> fibroblasts, we assessed whether the non-secreted ColVI chains were degraded through the autophagic pathway. This analysis did not reveal any colocalization of intracellular  $\alpha 3$ (VI) with autophagosome dots, suggesting that the unassembled ColVI chains are not degraded via the autophagy-lysosome pathway (Supplementary Figures S1E,F).

### ColVI Ablation Triggers Fibroblast Apoptosis via Caspase Activation

To evaluate the incidence of apoptosis in WT and *Col6a1*<sup>-/-</sup> fibroblasts, we first performed TUNEL analysis. Apoptotic nuclei were markedly increased in ColVI null fibroblasts (Figure 1A). Notably, apoptosis was significantly decreased in *Col6a1*<sup>-/-</sup> fibroblasts following adhesion onto purified ColVI for 2 days, whereas adhesion on collagen type I, used as a control ECM substrate, did not display the same effect (Figure 1A). Western blotting showed increased levels of cleaved caspases 3 and 9 in *Col6a1*<sup>-/-</sup> fibroblasts compared to WT ones, both in standard conditions and following serum starvation for 3 or 6 h (Figure 1B and Supplementary Figure S2). We further assessed cell death by flow cytometry, following cell labeling with AnV and PI. PI staining allows to discriminate between early apoptotic/healthy cells, having an intact membrane, and late stage apoptotic/necrotic cells, in which compromised membranes allow the incorporation of the dye. Flow cytometry confirmed that apoptosis incidence was increased in *Col6a1*<sup>-/-</sup> fibroblasts with respect to WT ones, particularly after serum depletion (Figures 1C,D). Indeed, the percentage of AnV-positive/PI-negative (early apoptotic) cells was increased in *Col6a1*<sup>-/-</sup> fibroblasts after serum depletion, and adhesion onto ColVI decreased the number of early apoptotic cells in these cultures (Figure 1D, upper panel). The percentage of AnV-positive/PI-positive (late apoptotic) cells was higher in *Col6a1*<sup>-/-</sup> fibroblasts than in WT cells, and adhesion onto ColVI rescued late apoptotic events both in standard conditions and following serum withdrawal (Figure 1D, middle panel). In addition, the percentage of AnV-negative/PI-positive cells was also significantly increased in *Col6a1*<sup>-/-</sup> cultures, both in complete medium and after serum starvation (Figure 1D, lower panel). Collectively, when evaluating live cells, *Col6a1*<sup>-/-</sup> fibroblasts were less viable when compared to WT fibroblasts, both under standard conditions and after serum depletion for 3 h (Figure 1E) or 6 h (data not shown). Interestingly, 2-day culture onto purified ColVI decreased the incidence of apoptosis in *Col6a1*<sup>-/-</sup> cultures both under standard conditions and after serum withdrawal, thus improving the survival of *Col6a1*<sup>-/-</sup> fibroblasts in both conditions (Figure 1E). By contrast, when grown onto a control coating made of collagen I, *Col6a1*<sup>-/-</sup> fibroblasts did not rescue cell viability after serum withdrawal (Figures 1D,E).

### The Autophagic Flux Is Impaired in *Col6a1*<sup>-/-</sup> Fibroblasts

To examine whether autophagy was affected in *Col6a1*<sup>-/-</sup> fibroblasts, we first investigated autophagosome formation, by evaluating the conversion of cytosolic MAP1LC3B (LC3-I) to its lipidated form (LC3-II), as well as autophagy-dependent protein degradation, by monitoring protein level of the specific cargo receptor Sqstm1/p62 protein, both in complete medium and after 3 h serum withdrawal. Western blotting showed that the LC3-II/LC3-I ratio was decreased in *Col6a1*<sup>-/-</sup> fibroblasts after serum withdrawal (Figures 2A,B). In addition, p62 protein levels were decreased in *Col6a1*<sup>-/-</sup> fibroblasts with respect to

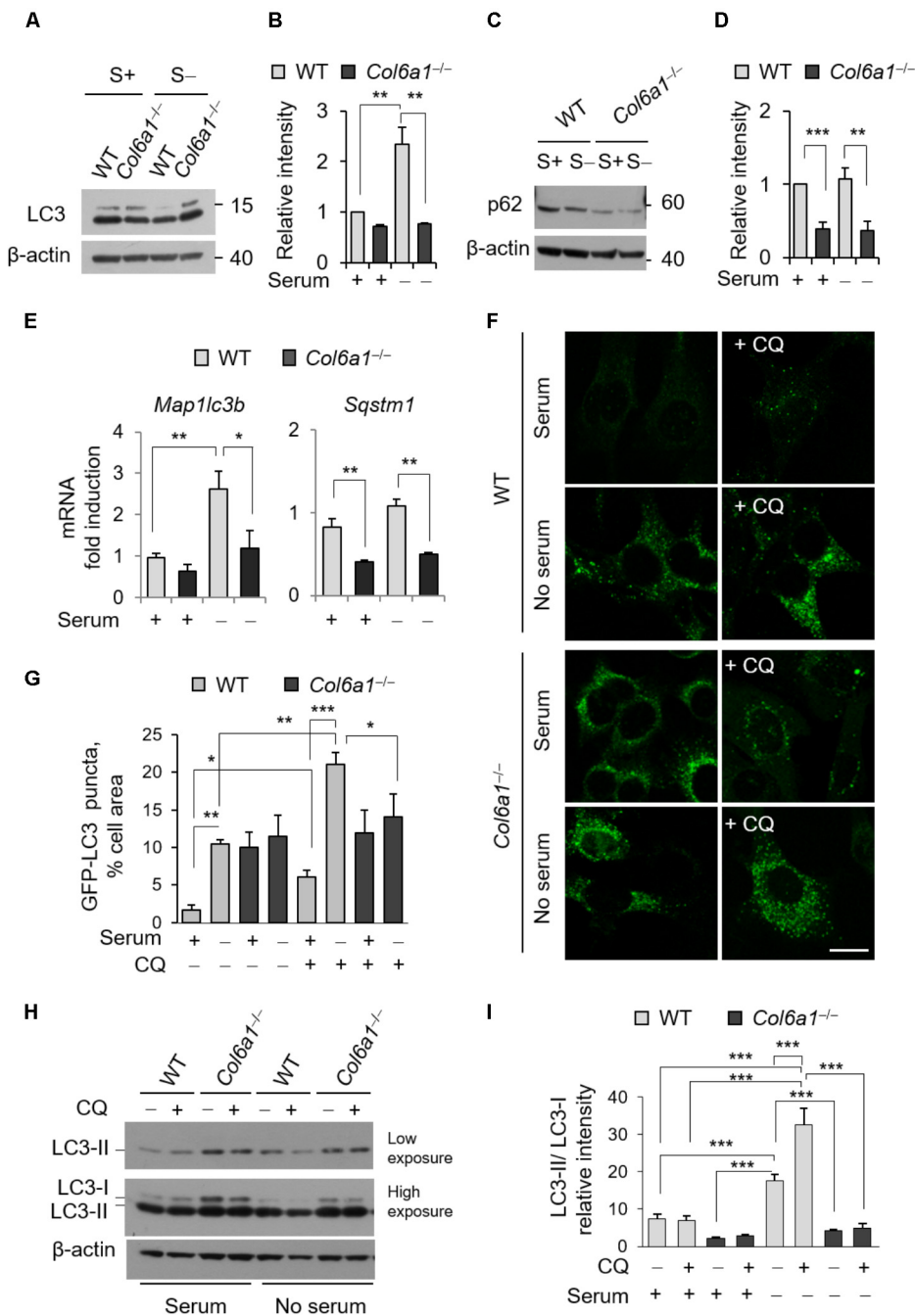


**FIGURE 1 |** Apoptosis is increased in *Col6a1*<sup>-/-</sup> fibroblasts and adhesion onto ColVI rescues the phenotype. **(A)** Quantification of TUNEL-positive nuclei in WT and *Col6a1*<sup>-/-</sup> fibroblasts cultured for 2 days on plastic wells (-), or on wells coated with purified ColVI (Col VI) or collagen I (Col I) proteins. **(B)** Western blot analysis of total cell extracts from WT and *Col6a1*<sup>-/-</sup> fibroblasts cultured in complete DMEM with 10% serum, or following serum starvation for 3 and 6 h. Where indicated, cells were treated with 1 μM staurosporine for positive control of caspase activation. **(C-E)** Flow cytometry analysis for AnV and PI in WT and *Col6a1*<sup>-/-</sup> fibroblasts cultured for 2 days on plastic, ColVI (Col VI), or collagen I (Col I), and serum depleted for the final 3 h where indicated. Data indicate the average for 10,000 cells collected in at least five independent biological samples. **(C)** Representative dot plots of flow cytometry analysis for AnV and PI. **(D)** Histograms of the quantification of cellular events obtained by flow cytometry, as shown in C. Percentages of AnV-positive/PI-negative (early apoptotic cells, top panel), AnV-positive/PI-positive (late apoptotic cells, middle panel), and AnV-negative/PI-positive cells (bottom panel) are shown. **(E)** Quantification of the percentage of live cells (AnV- and PI-negative cells) in the different conditions. Data represents the mean of at least five independent experiments, and were analyzed by ANOVA test with Bonferroni correction. \**P* < 0.05; \*\**P* < 0.01; \*\*\**P* < 0.001. AnV, annexin V; PI, propidium iodide; STS, staurosporine; Stv, serum starvation.

WT, both under basal conditions and after serum withdrawal (**Figures 2C,D**). Gene expression analysis by qRT-PCR showed that the transcriptional activation of LC3 was defective in ColVI deficient fibroblasts, as we did not detect any significant increase of *Map1lc3b* mRNA levels in *Col6a1*<sup>-/-</sup> cultures after serum starvation, at difference from WT ones (**Figure 2E**). *Sqstm1*

transcript levels were down-regulated in *Col6a1*<sup>-/-</sup> fibroblasts, in agreement with the decrease of p62 protein levels and independently of serum starvation (**Figure 2E**).

We also monitored autophagosome formation by detection of GFP-positive puncta in fibroblasts derived from *Col6a1*<sup>+/+</sup>::GFP-LC3 and *Col6a1*<sup>-/-</sup>::GFP-LC3 reporter mice



**FIGURE 2 |** The autophagic flux is impaired in *Col6a1*<sup>-/-</sup> fibroblasts. **(A–D)** Western blot analysis of LC3 and p62 in total cell extracts from WT and *Col6a1*<sup>-/-</sup> fibroblasts in complete medium (S+) or following serum withdrawal for 3 h (S-). **(B, D)** Show respectively the LC3-II/LC3-I ratio **(B)** and the p62/β-actin ratio **(D)**, as determined by densitometric quantification of the western blots as in **(A, C)**. Values for WT fibroblasts in complete medium were arbitrarily set to 1. Data represents the mean of at least three independent experiments. **(E)** qRT-PCR analysis of *Map1lc3b* and *Sqstm1* mRNA levels. Data represents the mean of at least three independent experiments. **(F)** Fluorescence microscopy detection of LC3-positive puncta in WT and *Col6a1*<sup>-/-</sup> fibroblasts derived from *Col6a1*<sup>+/+</sup>::GFP-LC3 and *Col6a1*<sup>-/-</sup>::GFP-LC3 mice, respectively, and maintained in complete medium or subjected to serum starvation for 3 h. LC3 puncta (autophagosomes) accumulate in *Col6a1*<sup>-/-</sup> fibroblasts both in complete medium and serum starved conditions. Scale bar, 25 μm. **(G)** Quantification of GFP-LC3 puncta per cell area, as shown in **(F)**. **(H)** Western blot analysis of total cell extracts from WT and *Col6a1*<sup>-/-</sup> fibroblasts in complete medium (S+) or following serum withdrawal for 3 h (S-). The autophagic flux, as determined by the analysis of LC3 lipidation in the absence or presence of 50 μM CQ treatment, is shown. **(I)** Densitometric quantification of the relative intensity of LC3-II/LC3-I ratio of three independent western blot experiments, as in **(H)**. Data were analyzed by ANOVA test with Bonferroni correction. \**P* < 0.05; \*\**P* < 0.01; \*\*\**P* < 0.001.

(**Figure 2F**). *Col6a1*<sup>+/+</sup>::GFP-LC3 fibroblasts displayed few GFP-positive puncta in complete medium, while 3 hr serum starvation elicited a sixfold increase of GFP-positive puncta (**Figure 2G**). To investigate the dynamics of the autophagic flux we used CQ, an inhibitor of lysosome acidification. Treatment of *Col6a1*<sup>+/+</sup>::GFP-LC3 fibroblasts with 50  $\mu$ M CQ led to a marked accumulation of autophagosomes both in basal conditions and upon serum starvation, showing an increase in the autophagy flux upon serum withdrawal as expected (**Figures 2F,G**). In contrast, *Col6a1*<sup>-/-</sup>::GFP-LC3 fibroblasts displayed massive accumulation of GFP-positive puncta already in complete medium condition, without any substantial variation in the number of fluorescent puncta after serum starvation or following CQ treatment (**Figures 2F,G**). Consistently, western blotting showed that 3 h serum starvation elicited a marked increase of the LC3-II/LC3-I ratio in WT fibroblasts both in the absence and in the presence of CQ (two- and four-fold increase, respectively), indicating increased autophagy induction (**Figures 2H,I**). In particular, LC3-II/LC3-I ratio of WT fibroblasts was increased when CQ was added to serum starved cultures, pointing at the extensive formation of autophagosomes in response to starvation. Differently, *Col6a1*<sup>-/-</sup> fibroblasts did not display any significant increase of the LC3-II/LC3-I ratio after serum starvation (which was significantly decreased with respect to WT cells) and no further increase after CQ treatment (**Figures 2H,I**).

The presence of accumulated autophagosomes in *Col6a1*<sup>-/-</sup> fibroblasts, together with the increased spontaneous apoptosis (**Figure 1**), prompted the possibility that an autophagy-dependent cell death may occur in ColVI deficient fibroblasts. To test this hypothesis, we investigated the incidence of AnV- and PI-positive cells in the absence or presence of the autophagy inhibitor 3-MA. Treatment with 3-MA for 3 h led to a dose-dependent increase of cell death both in WT and *Col6a1*<sup>-/-</sup> fibroblasts (**Supplementary Figure S3**), thus excluding the possibility of a substantial influence of autophagy-dependent cell death in ColVI deficient fibroblasts.

## ColVI Ablation Affects Lysosomes and Impairs Autophagosome-Lysosome Fusion

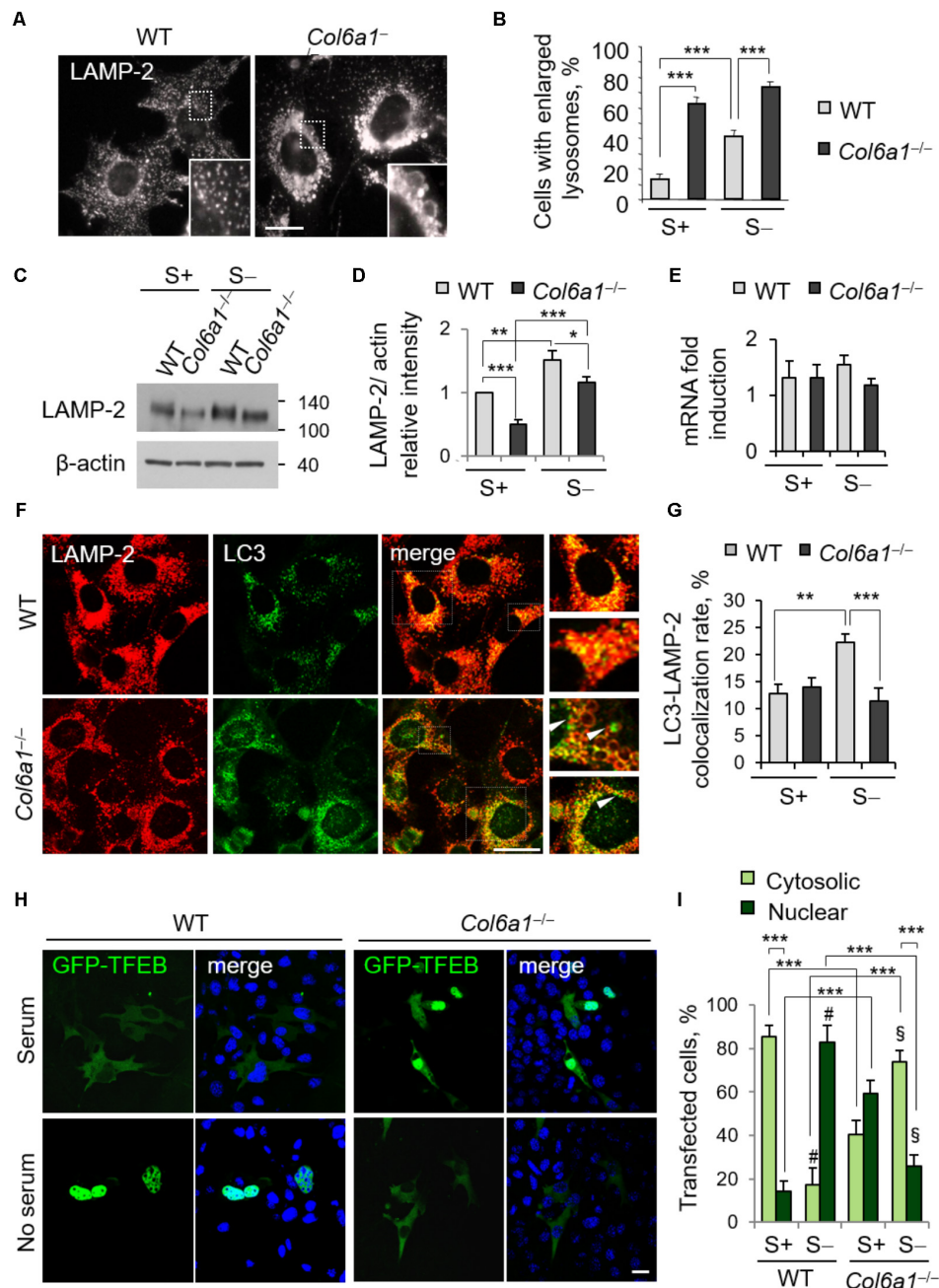
The finding that lack of ColVI causes autophagosome accumulation pointed at an impairment of the autophagy-lysosome machinery in *Col6a1*<sup>-/-</sup> fibroblasts, with a defective “off-rate” of the autophagic flux. Thus, we analyzed lysosomes and their fusion with autophagosomes. Immunostaining with the lysosomal marker LAMP-2 revealed high amounts of enlarged lysosomes in *Col6a1*<sup>-/-</sup> fibroblasts, whereas in WT cultures lysosomes appeared as smaller punctuate structures (**Figure 3A**). Enlarged lysosomes were only detectable in WT fibroblasts after serum depletion (albeit to a lesser extent when compared to *Col6a1*<sup>-/-</sup> cells) or following CQ treatment (**Figure 3B** and **Supplementary Figure S4**). Moreover, the increased number of enlarged lysosomes in *Col6a1*<sup>-/-</sup> fibroblasts appeared to be independent on serum starvation (**Figure 3B**). Interestingly, when compared to WT, *Col6a1*<sup>-/-</sup> fibroblasts also displayed a decrease in LAMP-2 protein levels (**Figures 3C,D**), which

was not paralleled by a decrease of *Lamp2* mRNA levels (**Figure 3E**). We further analyzed the final stages of fusion between autophagosomes and lysosomes, by performing co-immunostaining for LC3 and LAMP-2 (**Figure 3F** and **Supplementary Figure S5**). In WT cultures, co-localization of autophagosomes with lysosomes (fusion events) was almost doubled upon serum depletion-induced autophagy, whereas in *Col6a1*<sup>-/-</sup> cultures the co-localization of LAMP-2 and LC3 was not affected by serum depletion (**Figure 3G**), indicating defective autophagosome-lysosome fusion. Analysis of *Col6a1*<sup>+/+</sup>::GFP-LC3 and *Col6a1*<sup>-/-</sup>::GFP-LC3 fibroblasts provided similar results (**Supplementary Figure S6**).

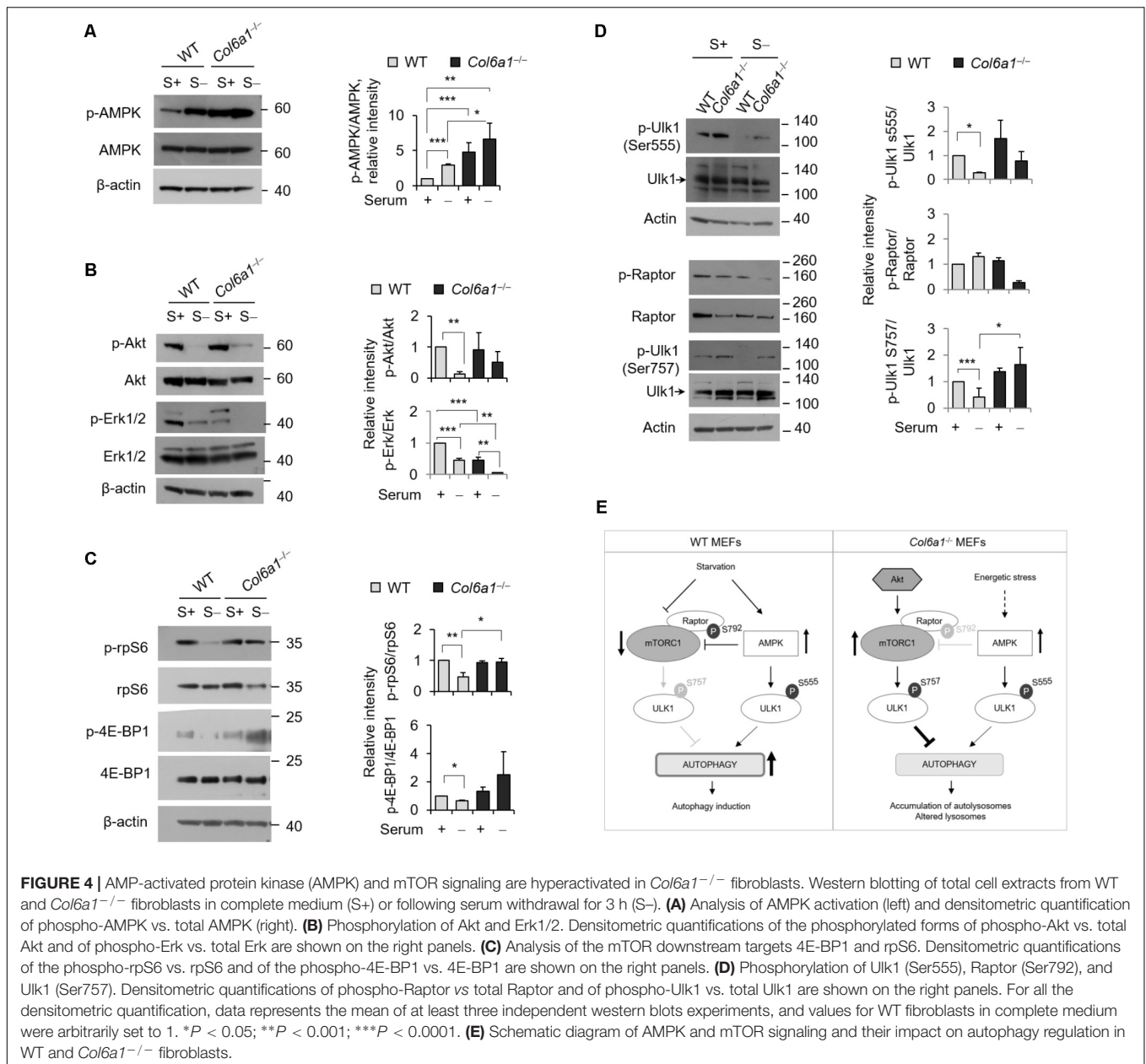
A proper cross-talk between autophagosomes and lysosomes is fundamental to ensure an efficient completion of the autophagy process. The accumulation of autophagosomes and the lysosomal abnormalities prompted us to investigate whether the cellular clearance via lysosomes was affected in *Col6a1*<sup>-/-</sup> fibroblasts. One of the master regulators of lysosomal function and autophagy is the TFEB. The extracellular signal-regulated kinase 2 (Erk2) and mTOR coordinate TFEB retention in the cytosol, thus regulating its activity. Under nutrient depletion, TFEB rapidly shuttles to the nucleus and activates its translational program (Settembre et al., 2011; Russell et al., 2014). Hence, we investigated TFEB cellular localization following transfection with a GFP-TFEB construct. As expected, in WT fibroblasts serum depletion induced TFEB translocation from the cytosol to the nucleus, and indeed the majority of cells showed GFP-TFEB in the nucleus after 3 h serum depletion (from 14% in complete medium, to 82% in serum starvation; **Figures 3H,I**). Conversely, in *Col6a1*<sup>-/-</sup> fibroblasts the nutrient availability-dependent cellular localization of GFP-TFEB was strongly affected. Indeed, in complete medium, 59% of *Col6a1*<sup>-/-</sup> cells displayed GFP-TFEB already in the nucleus, whereas after 3 h serum depletion nuclear translocation of GFP-TFEB was markedly reduced, being present in 26% of cells (**Figures 3H,I**).

## *Col6a1*<sup>-/-</sup> Fibroblasts Display Altered Activity of Autophagy Regulatory Signals and of the mTOR Pathway

We analyzed the activation of AMPK and found that the levels of phosphorylated AMPK were increased in *Col6a1*<sup>-/-</sup> cultures, with respect to WT ones (**Figure 4A**). Analysis of the activation status of Akt and of Erk1/2, two kinases acting on autophagy, showed that Akt phosphorylation was slightly enhanced in *Col6a1*<sup>-/-</sup> cultures after serum starvation, whereas both Erk1/2 kinases were much less phosphorylated in *Col6a1*<sup>-/-</sup> cultures compared to WT ones, both in basal conditions and after serum starvation (**Figure 4B**). Furthermore, the mTOR axis was persistently activated in *Col6a1*<sup>-/-</sup> fibroblasts after serum deprivation, as revealed by phosphorylation of 4E-BP1 and of the S6 ribosomal protein (rpS6), two major downstream targets of mTORC1 (**Figure 4C**). To assess the coordinated activity of AMPK and of Akt/mTOR axis in these cultures, we analyzed the phosphorylation status of Ulk1 at two different sites (Ser555 and Ser757), which are known to be essential for the coordination of AMPK and mTOR concurrent activity (Russell et al., 2014),



**FIGURE 3** | Collagen VI ablation leads to defects in autolysosome formation and TFEB translocation. **(A)** Immunofluorescence for LAMP-2, showing normal lysosomes in WT fibroblasts and enlarged lysosomes in *Col6a1*<sup>-/-</sup> fibroblasts. The insets show a magnification of the respective boxed areas. Scale bar, 25 μm. **(B)** Quantification of cells containing at least two enlarged lysosomes. Data represent the mean percentages ± SEM of cells with enlarged lysosomes, as determined from thirty images per condition. **(C)** Western blot analysis of LAMP-2 in WT and *Col6a1*<sup>-/-</sup> fibroblasts, in complete medium (S+) or following serum withdrawal for 3 h (S-). **(D)** Densitometric quantification of the relative LAMP-2/β-actin ratio of three independent western blot experiments, as in **(C)**. The value for WT fibroblasts in complete medium was arbitrarily set to 1. **(E)** qRT-PCR analysis of *Lamp2* mRNA levels. **(F)** Co-immunostaining for LAMP-2 and LC3 in WT and *Col6a1*<sup>-/-</sup> fibroblasts, following 3 h serum withdrawal. The right panels show a higher magnification of the boxed area of the respective merged image. *Col6a1*<sup>-/-</sup> fibroblasts display impaired autophagosome (green puncta) fusion with lysosomes (red) (arrowheads). Scale bar, 25 μm. **(G)** Co-localization rate of LC3 and LAMP-2 staining in complete medium (S+) or following serum withdrawal for 3 h (S-). Mean percentages ± SEM were calculated for at least fifteen images per condition. **(H)** Representative fluorescence microscopy images of WT and *Col6a1*<sup>-/-</sup> fibroblasts in complete medium and after 3 h serum withdrawal, following transfection with a GFP-TFEB expression construct (green). Nuclei were stained with Hoechst (blue). Scale bar, 25 μm. **(I)** Quantification of transfected WT and *Col6a1*<sup>-/-</sup> fibroblasts showing either cytosolic or nuclear GFP-TFEB, as shown in **(G)**. Data represents the mean of at least three independent experiments, and were analyzed by ANOVA test with Bonferroni correction. \**P* < 0.05; \*\**P* < 0.001; \*\*\**P* < 0.0001; #*P* < 0.001 for the comparison between WT complete medium and WT no serum; § *P* < 0.001 for the comparison between *Col6a1*<sup>-/-</sup> complete medium and *Col6a1*<sup>-/-</sup> no serum. S+, complete medium; S-, 3 h serum withdrawal.



and the AMPK-dependent phosphorylation of the Raptor at Ser792 (Gwinn et al., 2008). Analysis of the AMPK-mediated phosphorylation of Ulk1 at Ser555 (Egan et al., 2011; Kim et al., 2011) showed that this phosphorylation decreased in WT fibroblasts, but not in *Col6a1*<sup>-/-</sup> fibroblasts, after serum withdrawal (Figure 4D). In addition, Raptor phosphorylation appeared to be decreased in ColVI null cells after serum depletion, with respect to WT (Figure 4D), in agreement with a decreased AMPK-mediated inhibition of mTOR activity. Consistently, mTOR dependent phosphorylation of Ulk1 at Ser757, able to prevent Ulk1 and AMPK interaction and linked to autophagy inhibition (Kim et al., 2011), showed a persistent phosphorylation in *Col6a1*<sup>-/-</sup> fibroblasts after serum deprivation (Figure 4D). A schematic representation of these

findings and their impact on autophagy regulation in WT and *Col6a1*<sup>-/-</sup> fibroblasts is shown in Figure 4E.

## Autophagy Is Modulated by Adhesion Onto ColVI

To evaluate whether addition of ColVI could impinge on autophagy, we cultured WT and *Col6a1*<sup>-/-</sup> fibroblasts onto purified ColVI and subjected them to serum starvation as described above. Culture onto native ColVI elicited an effect on LC3 lipidation in both WT and *Col6a1*<sup>-/-</sup> fibroblasts (Figure 5). Indeed, starvation-induced lipidation of LC3 was increased when *Col6a1*<sup>-/-</sup> fibroblasts were cultured onto ColVI (Figures 5A,B). Analysis of the LC3-II/-I ratio showed that basal autophagy in

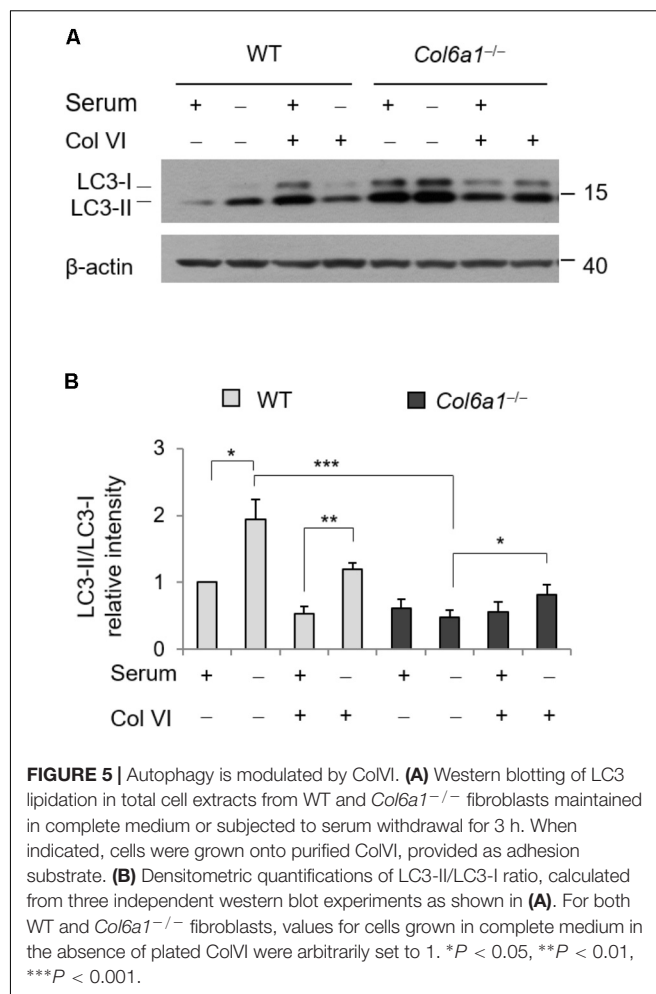
complete medium was decreased in WT fibroblasts adhering on ColVI, but starvation-induced stimulation of autophagy was maintained (Figures 5A,B).

### *Col6a1*<sup>-/-</sup> Fibroblasts Display Fragmented Mitochondria and Mitophagy Defects

In agreement with previous finding in cell cultures derived from muscle biopsies of UCMD and BM patients (Sabatelli et al., 2012), *Col6a1*<sup>-/-</sup> fibroblasts displayed a higher percentage of fragmented mitochondria than WT fibroblasts (Figure 6). We labeled mitochondria with different probes, using MitoTracker, pMitoRed and Mito-YFP plasmids, and we consistently found that fragmented mitochondria were more than twofold increased in *Col6a1*<sup>-/-</sup> fibroblasts when compared to WT fibroblasts (Figures 6A,B). We then analyzed the efficiency of mitochondria removal via mitophagy, a selective form of autophagy (Youle and Narendra, 2011), by performing co-immunolocalization analysis of mitochondria and autophagosomes/autolysosomes after serum withdrawal. Toward this aim, we used fibroblasts derived from *Col6a1*<sup>+/+</sup>::GFP-LC3 and *Col6a1*<sup>-/-</sup>::GFP-LC3 mice and stained mitochondria and lysosomes with the Tom20 and LAMP-2 markers, respectively. This analysis confirmed defective mitochondria elongation and decreased autophagosome-lysosome fusion in *Col6a1*<sup>-/-</sup> fibroblasts (Supplementary Figure S6). Interestingly, *Col6a1*<sup>-/-</sup> fibroblasts displayed increased co-localization of mitochondria with autophagosomes/lysosomes when compared to WT fibroblasts (Supplementary Figure S6B). To assess whether mitochondrial clearance by autophagy was functional in *Col6a1*<sup>-/-</sup> fibroblasts, we transfected cells with YFP-Parkin (Narendra et al., 2008) and pMitoRed constructs (Figure 6C). Notably, YFP-Parkin was more frequently translocated to mitochondria in *Col6a1*<sup>-/-</sup> fibroblasts (more than 10-fold increase with respect to WT fibroblasts) already in basal conditions (Figure 6D). We evaluated mitochondria removal by monitoring Tom20 immunostaining after 24 hr treatment with CCCP, used as mitochondrial uncoupler, and found that the mitochondrial pool was markedly decreased in WT fibroblasts, but not in *Col6a1*<sup>-/-</sup> fibroblasts, after CCCP-induced damage (Figure 6E).

## DISCUSSION

ColVI exerts a broad range of physiological functions in different tissues, being particularly abundant in skeletal muscle, peripheral nerves and connective tissues (Cescon et al., 2015). Although in skeletal muscle ColVI is produced by fibroblasts, and not by myofibers (Braghetta et al., 2008; Zou et al., 2008), muscles represent the most affected tissue in human pathologies caused by mutations of *COL6* genes, such as BM and UCMD (Bönnemann, 2011; Bushby et al., 2014). Therefore, at difference from other muscular dystrophies and inherited muscle disorders, ColVI-related myopathies represent a unique class of non-cell-autonomous disease of skeletal muscles, since the mutated protein downstream the primary genetic defect is not produced by the myofibers themselves, but by fibroblasts

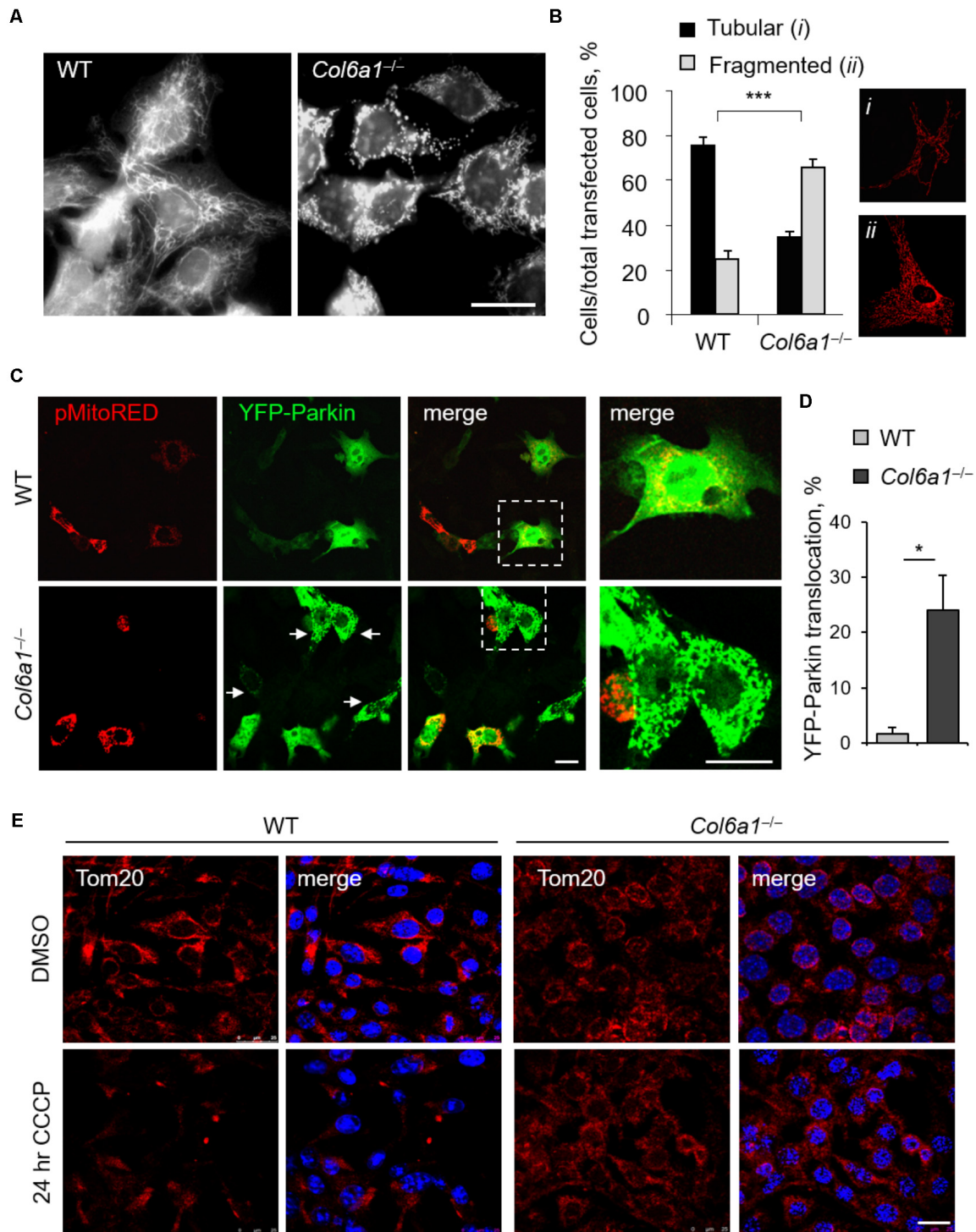


**FIGURE 5 |** Autophagy is modulated by ColVI. **(A)** Western blotting of LC3 lipidation in total cell extracts from WT and *Col6a1*<sup>-/-</sup> fibroblasts maintained in complete medium or subjected to serum withdrawal for 3 h. When indicated, cells were grown onto purified ColVI, provided as adhesion substrate. **(B)** Densitometric quantifications of LC3-II/LC3-I ratio, calculated from three independent western blot experiments as shown in **(A)**. For both WT and *Col6a1*<sup>-/-</sup> fibroblasts, values for cells grown in complete medium in the absence of plated ColVI were arbitrarily set to 1. \* $P < 0.05$ , \*\* $P < 0.01$ , \*\*\* $P < 0.001$ .

(Zou et al., 2008). Although previous studies revealed that ColVI deficiency in the ECM has a major impact in the survival and homeostasis of muscle fibers (Cescon et al., 2015), the cellular and molecular consequences of ColVI deficiency in fibroblasts themselves are still unknown. In the present study, we investigated the consequences of ColVI ablation in fibroblasts, using immortalized fibroblasts derived from WT and ColVI null mice.

We previously demonstrated that lack of ColVI leads to a failure of the autophagic machinery in skeletal muscles, impinging on myofiber homeostasis and turnover of damaged organelles, and finally causing myofiber death (Irwin et al., 2003; Grumati et al., 2010). Our present data reveal that ColVI ablation also impinges on fibroblast homeostasis, thus suggesting that the muscle damage which arises in *Col6a1*<sup>-/-</sup> mice may be sustained and exacerbated by fibroblast intrinsic defects and pointing at fibroblasts as active players in the pathogenesis of ColVI-related diseases. Our findings indicate that fibroblasts lacking ColVI are not able to fulfill their autophagic needs, in particular under stress-inducing conditions. Indeed, *Col6a1*<sup>-/-</sup> fibroblasts display increased LC3 protein levels that do not correlate with autophagy induction, as revealed by the analysis of LC3 protein





**FIGURE 6 |** Mitochondrial network is more fragmented and Parkin-dependent mitophagy is impaired in *Col6a1*<sup>-/-</sup> fibroblasts. **(A)** Representative micrograph of MitoTracker-labeled mitochondria of WT and *Col6a1*<sup>-/-</sup> fibroblasts. Scale bar, 25  $\mu$ m. **(B)** Quantification of cells showing tubular (i) or fragmented (ii) mitochondrial network in WT and *Col6a1*<sup>-/-</sup> fibroblasts, following transfection with mitochondrial fluorescent plasmids (pMitoRed, as in the representative panels i and ii). Data represents the mean of at least five independent biological replicates.  $***P < 0.001$ . **(C)** Representative micrographs of WT and *Col6a1*<sup>-/-</sup> fibroblasts transfected with YFP-Parkin and pMitoRed plasmids. Arrows point at mitochondria-translocated YFP-Parkin. The right panels show a higher magnification of the boxed area of the respective merged image. Scale bar, 25  $\mu$ m. **(D)** Quantification of cells with mitochondria-located YFP-Parkin in WT and *Col6a1*<sup>-/-</sup> fibroblasts, as in **(C)**. Data represents the mean of at least three independent biological replicates.  $*P < 0.05$ . **(E)** Immunostaining for the mitochondrial marker Tom20 (red) in WT and *Col6a1*<sup>-/-</sup> fibroblasts following 24 h treatment with 20  $\mu$ M CCCP (or DMSO as a control). Nuclei were stained with Hoechst (blue). Scale bar, 25  $\mu$ m.

levels and gene expression. In parallel, *Col6a1*<sup>-/-</sup> fibroblasts massively accumulate LC3-positive autophagosomes in basal condition, independently of serum starvation or CQ treatment. These findings indicate that *Col6a1*<sup>-/-</sup> fibroblasts are not able to degrade autophagosomes and their content, accumulating them inside the cells. In addition, both protein and transcript levels for p62 are decreased in *Col6a1*<sup>-/-</sup> fibroblasts. Literature studies showed that decreased p62 mRNA translation can be linked to reduced phosphorylation of Erk1/2 (Lee et al., 2010; Kim et al., 2014) and/or aberrant activation of TFEF translational program (Settembre et al., 2011), as indeed displayed by *Col6a1*<sup>-/-</sup> fibroblasts in our study, which show a marked disbalance of the cytosolic and nuclear pools of TFEF, not only after serum withdrawal but also in complete medium. Altogether, these findings strongly support the concept of an impairment of the autophagy-lysosome machinery in ColVI-deficient fibroblasts.

It is well established that proper activation of autophagy is essential for the turnover of aged and dysfunctional cellular organelles, such as mitochondria (Komatsu et al., 2007; Youle and Narendra, 2011; Schneider and Cuervo, 2014). Mitochondria are the main energy producers of the cell, and they are organized in a very dynamic network regulated by fusion and fission processes, which ensure the maintenance of healthy organelles and act in concert with cell decision programs or remodeling (Youle and Narendra, 2011; Pernas and Scorrano, 2016). We investigated the mitochondrial network morphology and found that *Col6a1*<sup>-/-</sup> fibroblasts display enhanced mitochondrial fragmentation when compared to WT fibroblasts, a feature often linked to mitochondria dysfunction (Jheng et al., 2012; Toyama et al., 2016). Interestingly, it was recently shown that activation of AMPK is sufficient to promote fragmentation of the mitochondrial network, even in the absence of mitochondrial stress (Toyama et al., 2016). Notably, the mitochondrial fragmentation displayed by *Col6a1*<sup>-/-</sup> fibroblasts resembles the alterations found in primary cell cultures derived from BM and UCMD muscle biopsies (Sabatelli et al., 2012). The enhanced mitochondrial fission in *Col6a1*<sup>-/-</sup> fibroblasts is also associated with mitochondrial translocation of Parkin, a protein that is actively recruited to the outer mitochondrial membrane of damaged mitochondria (Narendra et al., 2008). Despite the high rate of Parkin translocation in *Col6a1*<sup>-/-</sup> fibroblasts, mitochondria turnover does not occur properly in these cells, as confirmed by their response to mitochondria-depolarizing treatments, likely due to the inability of *Col6a1*<sup>-/-</sup> fibroblasts to correctly activate and complete the autophagic process.

To throw light into the defects displayed in *Col6a1*<sup>-/-</sup> fibroblast, we analyzed the interplay between AMPK, Akt and mTORC1 signaling, which is essential for the autophagic response to nutrients (Russell et al., 2014). AMPK is an energy sensor of the cell, becoming active under metabolic stress (Russell et al., 2014). The markedly increased AMPK phosphorylation we found in *Col6a1*<sup>-/-</sup> fibroblasts points at a strong energy impairment in these cells, both in basal and under starvation conditions. AMPK is involved in autophagy activation, via Ulk1 phosphorylation and mTORC1 inhibition (Kim et al., 2011; Shang and Wang, 2011; Russell et al., 2014). Indeed, AMPK controls the recruitment of 14-3-3 proteins to mTORC1

complex and its inactivation by phosphorylation of the subunit Raptor at its Ser792 residue (Gwinn et al., 2008). In *Col6a1*<sup>-/-</sup> fibroblasts, we found that AMPK-dependent phosphorylation of Ulk1 at its specific target residue Ser555 is acting toward autophagy activation when nutrients are depleted. In addition, these cells show a trend toward increased phosphorylation of Raptor. Despite AMPK pathway activation, upon serum starvation *Col6a1*<sup>-/-</sup> fibroblasts display increased activity of Akt, a serine threonine kinase which negatively regulates autophagy induction in mammalian cells, by acting on mTORC1 signaling (Manning and Cantley, 2007). In agreement with this, we found increased mTORC1 activation in *Col6a1*<sup>-/-</sup> fibroblasts concurrent with autophagy induction by starvation, as revealed by enhanced phosphorylation of the mTORC1 downstream targets rpS6 and 4E-BP1. The increased mTORC1 activity further elicits an increase in the inhibitory Ser757 phosphorylation of Ulk1, which is critical in antagonizing the interaction between Ulk1 and AMPK and inhibiting autophagy induction (Egan et al., 2011; Kim et al., 2011). Thus, although AMPK over-activation is expected to enhance autophagy induction in *Col6a1*<sup>-/-</sup> fibroblasts, the process is strongly counteracted by active mTORC1, leading to autophagosome accumulation and an impairment of the autophagic flux in *Col6a1*<sup>-/-</sup> fibroblasts (Castagnaro, 2015).

The accumulation of autophagic vesicles we observed in ColVI-deficient fibroblasts may also rely on impaired lysosomal degradation (Huynh et al., 2007). The presence of lysosomal defects in *Col6a1*<sup>-/-</sup> fibroblasts under basal condition, as revealed by the presence of enlarged lysosomes together with lower LAMP-2 levels, could be sufficient to impair autophagosome-lysosome fusion. Indeed, LAMP-1 and LAMP-2 are required for proper autolysosome formation and hence for the removal of autophagosomes (Huynh et al., 2007). In addition, it is known that during autophagy the lysosomal function itself is regulated by the fusion of autophagosomes with lysosomes and relies upon mTORC1 suppression (Zhou et al., 2013). Thus, the alteration of lysosomal morphology in *Col6a1*<sup>-/-</sup> fibroblasts is consistent with the sustained mTORC1 activity and the decreased autolysosome formation. Taken together, these results point at a failure of autophagy completion in *Col6a1*<sup>-/-</sup> fibroblasts, sustained both by defective lysosomal function and by mTORC1 deregulation. In this context, it is worthy to underline that also the regulation of TFEF, a master regulator of lysosomal biogenesis, activated in the presence of lysosomal stress (Settembre et al., 2011), is markedly altered in the absence of ColVI.

Although deeper investigations are needed to better clarify the effects of fibroblast adhesion onto ColVI, our findings suggest that ColVI *per se* owns prosurvival effects and autophagy-instructive properties, similarly to what was already seen for other ECM proteins (Tuloup-Minguez et al., 2011; Neill et al., 2014). Our work opens the possibility for future studies aimed at dissecting the molecular signals involved in this regulation and in the transduction of autophagy regulatory effects from the extracellular milieu within the cells. Indeed, several ECM proteins, including decorin, laminin-2, krigle V, endostatin, and endorepellin, are emerging as primary regulators of autophagy

(Neill et al., 2014, 2017). Among collagens, collagen types I and IV were found to elicit autophagy modulation in HeLa cells when provided as adhesion substrates, but a detailed mechanistic understanding of these effects is still lacking (Tuloup-Minguez et al., 2011). In addition, ECM modulation of autophagy often takes place in a nutrient availability-independent manner, suggesting an intrinsic ability to supervise and constrain extracellular factors that trigger this catabolic response, in order to harmonize cell responses (Neill et al., 2014).

Future work is needed to understand in detail the intricate and multifaceted aspects of ColVI biology and functions in skeletal muscles and in other tissues. On the other hand, the present study provides further insights into the dynamic nature of the ECM, in particular of one of the major constituents of muscle ECM. ColVI produced by fibroblasts in the muscle-associated connective tissue may allow the fine-tuning of skeletal muscle response to different types of stress, as underlined by the fact that ColVI deficiency causes muscle pathology in mice and humans. In addition, the findings of the present study provide novel clues for the pathomolecular defects of ColVI-related diseases and for the identification of new targets for therapy. Indeed, it is well known that fibroblasts and connective tissue actively cooperate with myofibers and other cell types to maintain the physiological properties and activities of skeletal muscle (Murphy et al., 2011). Finally, considering the increasing need for non-invasive strategies in clinical studies of ColVI-related myopathies (Castagnaro et al., 2016), these findings pave the way for the prospective use of fibroblasts in clinical studies aimed at monitoring the response to therapeutic treatments in ColVI-related disorders.

## AUTHOR CONTRIBUTIONS

SC designed and performed the experiments, analyzed, provided interpretation to the data, and wrote the manuscript. MCh

## REFERENCES

- Angelin, A., Tiepolo, T., Sabatelli, P., Grumati, P., Bergamin, N., Golfieri, C., et al. (2007). Mitochondrial dysfunction in the pathogenesis of Ullrich congenital muscular dystrophy and prospective therapy with cyclosporins. *Proc. Natl. Acad. Sci. U.S.A.* 104, 991–996. doi: 10.1073/pnas.0610270104
- Bönnemann, C. G. (2011). The collagen VI-related myopathies: muscle meets its matrix. *Nat. Rev. Neurol.* 7, 379–390. doi: 10.1038/nrneurol.2011.81
- Boya, P., Reggiori, F., and Codogno, P. (2013). Emerging regulation and functions of autophagy. *Nat. Cell Biol.* 15, 713–720. doi: 10.1038/ncb2788
- Braghetta, P., Ferrari, A., Fabbro, C., Bizzotto, D., Volpin, D., Bonaldo, P., et al. (2008). An enhancer required for transcription of the Col6a1 gene in muscle connective tissue is induced by signals released from muscle cells. *Exp. Cell Res.* 314, 3508–3518. doi: 10.1016/j.yexcr.2008.08.006
- Buraschi, S., Neill, T., and Iozzo, R. V. (2017). Decorin is a devouring proteoglycan: remodeling of intracellular catabolism via autophagy and mitophagy. *Matrix Biol.* doi: 10.1016/j.matbio.2017.10.005 [Epub ahead of print].
- Bushby, K. M. D., Collins, J., and Hicks, D. (2014). Collagen type VI myopathies. *Adv. Exp. Med. Biol.* 802, 185–199. doi: 10.1007/978-94-007-7893-1-12
- Castagnaro, S. (2015). *Extracellular Collagen Type VI has Prosurvival and Autophagy Instructive Properties in Mouse Embryonic Fibroblasts*. Ph.D. thesis, University of Padova, Padua.

performed quantitative RT-PCR and contributed to manuscript writing and revision. MCE assisted with mitochondrial measurements. PBr contributed to manuscript writing. PG conceived and designed the experiments. PBo coordinated the study, and contributed to manuscript writing and revision.

## FUNDING

This work was supported by the Italian Ministry of Education, University and Research (Grants RBAP11Z3YA\_003 and 2015FBNB5Y), Telethon Foundation (Grant GGP14202), and Cariparo Foundation (Starting Grants 2015) and the University of Padova.

## ACKNOWLEDGMENTS

We acknowledge Noboru Mizushima for providing us with GFP-LC3 reporter mice. Results and comments of this work previously appeared on the Ph.D. thesis of SC, deposited in the web archive of the University of Padova. We also thank Alfonso Colombatti and Raimund Wagener for the antibodies against collagen VI and fibronectin; Marco Sandri for pMSE-SV40LT and GFP-TFEB plasmids; Luca Scorrano for pMitoRed plasmid; Richard J. Youle for Parkin expression plasmid.

## SUPPLEMENTARY MATERIAL

The Supplementary Material for this article can be found online at: <https://www.frontiersin.org/articles/10.3389/fphys.2018.01129/full#supplementary-material>

- Castagnaro, S., Pellegrini, C., Pellegrini, M., Chrisam, M., Sabatelli, P., Toni, S., et al. (2016). Autophagy activation in COL6 myopathic patients by a low-protein-diet pilot trial. *Autophagy* 12, 2484–2495. doi: 10.1080/15548627.2016.1231279
- Cescon, M., Gattazzo, F., Chen, P., and Bonaldo, P. (2015). Collagen VI at a glance. *J. Cell Sci.* 128, 3525–3531. doi: 10.1242/jcs.169748
- Chrisam, M., Pirozzi, M., Castagnaro, S., Blaauw, B., Polishchuck, R., Cecconi, F., et al. (2015). Reactivation of autophagy by spermidine ameliorates the myopathic defects of collagen VI-null mice. *Autophagy* 11, 2142–2152. doi: 10.1080/15548627.2015.1108508
- Colombatti, A., Mucignat, M. T., and Bonaldo, P. (1995). Secretion and matrix assembly of recombinant type VI collagen. *J. Biol. Chem.* 270, 13105–13111. doi: 10.1074/jbc.270.22.13105
- Egan, D. F., Shackelford, D. B., Mihaylova, M. M., Gelino, S., Kohnz, R. A., Mair, W., et al. (2011). Phosphorylation of ULK1 (hATG1) by AMP-activated protein kinase connects energy sensing to mitophagy. *Science* 331, 456–461. doi: 10.1126/science.1196371
- Feng, Y., He, D., Yao, Z., and Klionsky, D. J. (2014). The machinery of macroautophagy. *Cell Res.* 24, 24–41. doi: 10.1038/cr.2013.168
- Gattazzo, F., Urciuolo, A., and Bonaldo, P. (2014). Extracellular matrix: a dynamic microenvironment for stem cell niche. *Biochim. Biophys. Acta* 1840, 2506–2519. doi: 10.1016/j.bbagen.2014.01.010

- Grumati, P., Coletto, L., Sabatelli, P., Cescon, M., Angelin, A., Bertaggia, E., et al. (2010). Autophagy is defective in collagen VI muscular dystrophies, and its reactivation rescues myofiber degeneration. *Nat. Med.* 16, 1313–1320. doi: 10.1038/nm.2247
- Gwinn, D. M., Shackelford, D. B., Egan, D. F., Mihaylova, M. M., Mery, A., Vasquez, D. S., et al. (2008). AMPK phosphorylation of raptor mediates a metabolic checkpoint. *Mol. Cell* 30, 214–226. doi: 10.1016/j.molcel.2008.03.003
- Huynh, K. K., Eskelinen, E. L., Scott, C. C., Malevanets, A., Saftig, P., and Grinstein, S. (2007). LAMP proteins are required for fusion of lysosomes with phagosomes. *EMBO J.* 26, 313–324. doi: 10.1038/sj.emboj.7601511
- Hynes, R. O. (2009). The extracellular matrix: not just pretty fibrils. *Science* 326, 1216–1219. doi: 10.1126/science.1176009
- Irwin, W. A., Bergamin, N., Sabatelli, P., Reggiani, C., Megighian, A., Merlini, L., et al. (2003). Mitochondrial dysfunction and apoptosis in myopathic mice with collagen VI deficiency. *Nat. Genet.* 35, 367–371. doi: 10.1038/ng1270
- Jheng, H. F., Tsai, P. J., Guo, S. M., Kuo, L. H., Chang, C. S., Su, I. J., et al. (2012). Mitochondrial fission contributes to mitochondrial dysfunction and insulin resistance in skeletal muscle. *Mol. Cell. Biol.* 32, 309–319. doi: 10.1128/MCB.05603-11
- Jimenez-Mallebrera, C., Maioli, M. A., Kim, J., Brown, S. C., Feng, L., Lampe, A. K., et al. (2006). A comparative analysis of collagen VI production in muscle, skin and fibroblasts from 14 Ullrich congenital muscular dystrophy patients with dominant and recessive COL6A mutations. *Neuromuscul. Disord.* 16, 571–582. doi: 10.1016/j.nmd.2006.07.015
- Kim, J., Kundu, M., Viollet, B., and Guan, K. L. (2011). AMPK and mTOR regulate autophagy through direct phosphorylation of Ulk1. *Nat. Cell Biol.* 13, 132–141. doi: 10.1038/ncb2152
- Kim, J. H., Hong, S. K., Wu, P. K., Richards, A. L., Jackson, W. T., and Park, J. I. (2014). Raf/MEK/ERK can regulate cellular levels of LC3B and SQSTM1/p62 at expression levels. *Exp. Cell Res.* 327, 340–352. doi: 10.1016/j.yexcr.2014.08.001
- Komatsu, M., Waguri, S., Koike, M., Sou, Y. S., Ueno, T., Hara, T., et al. (2007). Homeostatic levels of p62 control cytoplasmic inclusion body formation in autophagy-deficient mice. *Cell* 131, 1149–1163. doi: 10.1016/j.cell.2007.10.035
- Kuo, H. J., Maslen, C. L., Keene, D. R., and Glanville, R. W. (1997). Type VI collagen anchors endothelial basement membranes by interacting with type IV collagen. *J. Biol. Chem.* 272, 26522–26529. doi: 10.1074/jbc.272.42.26522
- Lee, S. J., Pfluger, P. T., Kim, J. Y., Nogueiras, R., Duran, A., Pagès, G., et al. (2010). A functional role for the p62-ERK1 axis in the control of energy homeostasis and adipogenesis. *EMBO Rep.* 11, 226–232. doi: 10.1038/embor.2010.7
- Levine, B., and Kroemer, G. (2008). Autophagy in the pathogenesis of disease. *Cell* 132, 27–42. doi: 10.1016/j.cell.2007.12.018
- Manning, B. D., and Cantley, L. C. (2007). AKT/PKB signaling: navigating downstream. *Cell* 129, 1261–1274. doi: 10.1016/j.cell.2007.06.009
- Merlini, L., Angelin, A., Tiepolo, T., Braghetta, P., Sabatelli, P., Zamparelli, A., et al. (2008a). Cyclosporin A corrects mitochondrial dysfunction and muscle apoptosis in patients with collagen VI myopathies. *Proc. Natl. Acad. Sci. U.S.A.* 105, 5225–5229. doi: 10.1073/pnas.0800962105
- Merlini, L., Martoni, E., Grumati, P., Sabatelli, P., Squarzone, S., Urciuolo, A., et al. (2008b). Autosomal recessive myosclerosis myopathy is a collagen VI disorder. *Neurology* 71, 1245–1253. doi: 10.1212/01.wnl.0000327611.01687.5e
- Mizushima, N., Yamamoto, A., Matsui, M., Yoshimori, T., and Ohsumi, Y. (2004). In vivo analysis of autophagy in response to nutrient starvation using transgenic mice expressing a fluorescent autophagosome marker. *Mol. Biol. Cell* 15, 1101–1111. doi: 10.1091/mbc.E03-09-0704
- Murphy, M. M., Lawson, J. A., Mathew, S. J., Hutcheson, D. A., and Kardon, G. (2011). Satellite cells, connective tissue fibroblasts and their interactions are crucial for muscle regeneration. *Development* 138, 3625–3637. doi: 10.1242/dev.064162
- Narendra, D., Tanaka, A., Suen, D. F., and Youle, R. J. (2008). Parkin is recruited selectively to impaired mitochondria and promotes their autophagy. *J. Cell Biol.* 183, 795–803. doi: 10.1083/jcb.200809125
- Neill, T., Schaefer, L., and Iozzo, R. V. (2014). Instructive roles of extracellular matrix on autophagy. *Am. J. Pathol.* 184, 2146–2153. doi: 10.1016/j.ajpath.2014.05.010
- Neill, T., Sharpe, C., Owens, R. T., and Iozzo, R. V. (2017). Decorin-evoked paternally expressed gene 3 (PEG3) is an upstream regulator of the transcription factor EB (TFEB) in endothelial cell autophagy. *J. Biol. Chem.* 292, 16211–16220. doi: 10.1074/jbc.M116.769950
- Pan, T. C., Zhang, R. Z., Sudano, D. G., Marie, S. K., Bönnemann, C. G., and Chu, M. L. (2003). New molecular mechanism for Ullrich congenital muscular dystrophy: a heterozygous in-frame deletion in the COL6A1 gene causes a severe phenotype. *Am. J. Hum. Genet.* 73, 355–369. doi: 10.1086/377107
- Pernas, L., and Scorrano, L. (2016). Mito-morphosis: mitochondrial fusion, fission, and cristae remodeling as key mediators of cellular function. *Annu. Rev. Physiol.* 78, 505–531. doi: 10.1146/annurev-physiol-021115-105011
- Russell, R. C., Yuan, H. X., and Guan, K. L. (2014). Autophagy regulation by nutrient signaling. *Cell Res.* 24, 42–57. doi: 10.1038/cr.2013.166
- Sabatelli, P., Palma, E., Angelin, A., Squarzone, S., Urciuolo, A., Pellegrini, C., et al. (2012). Critical evaluation of the use of cell cultures for inclusion in clinical trials of patients affected by collagen VI myopathies. *J. Cell. Physiol.* 227, 2927–2935. doi: 10.1002/jcp.23039
- Schneider, J. L., and Cuervo, A. M. (2014). Autophagy and human disease: emerging themes. *Curr. Opin. Genet. Dev.* 26, 16–23. doi: 10.1016/j.gde.2014.04.003
- Settembre, C., Di Malta, C., Polito, V. A., Garcia Arencibia, M., Vetrini, F., Erdin, S., et al. (2011). TFEB links autophagy to lysosomal biogenesis. *Science* 332, 1429–1433. doi: 10.1126/science.1204592
- Shang, L., and Wang, X. (2011). AMPK and mTOR coordinate the regulation of Ulk1 and mammalian autophagy initiation. *Autophagy* 7, 924–926. doi: 10.4161/auto.7.8.15860
- Tillet, E., Wiedemann, H., Golbik, R., Pan, T. C., Zhang, R. Z., Mann, K., et al. (1994). Recombinant expression and structural and binding properties of alpha 1(VI) and alpha 2(VI) chains of human collagen type VI. *Eur. J. Biochem.* 221, 177–185. doi: 10.1111/j.1432-1033.1994.tb18727.x
- Toyama, E. Q., Herzig, S., Courchet, J., Lewis, T. L. Jr, Losón, O. C., Hellberg, K., et al. (2016). AMP-activated protein kinase mediates mitochondrial fission in response to energy stress. *Science* 351, 275–281. doi: 10.1126/science.aab4138
- Tuloup-Minguez, V., Greffard, A., Codogno, P., and Botti, J. (2011). Regulation of autophagy by extracellular matrix glycoproteins in HeLa cells. *Autophagy* 7, 27–39. doi: 10.4161/auto.7.1.13851
- Youle, R. J., and Narendra, D. P. (2011). Mechanisms of mitophagy. *Nat. Rev. Mol. Cell Biol.* 12, 9–14. doi: 10.1038/nrm3028
- Zhang, R. Z., Sabatelli, P., Pan, T. C., Squarzone, S., Mattioli, E., Bertini, E., et al. (2002). Effects on collagen VI mRNA stability and microfibrillar assembly of three COL6A2 mutations in two families with Ullrich congenital muscular dystrophy. *J. Biol. Chem.* 277, 43557–43564. doi: 10.1074/jbc.M207696200
- Zhou, J., Tan, S. H., Nicolas, V., Bauvy, C., Yang, N. D., Zhang, J., et al. (2013). Activation of lysosomal function in the course of autophagy via mTORC1 suppression and autophagosome-lysosome fusion. *Cell Res.* 23, 508–523. doi: 10.1038/cr.2013.11
- Zou, Y., Zhang, R. Z., Sabatelli, P., Chu, M. L., and Bönnemann, C. G. (2008). Muscle interstitial fibroblasts are the main source of collagen VI synthesis in skeletal muscle: implications for congenital muscular dystrophy types Ullrich and Bethlem. *J. Neuropathol. Exp. Neurol.* 67, 144–154. doi: 10.1097/nen.0b013e3181634fef

**Conflict of Interest Statement:** The authors declare that the research was conducted in the absence of any commercial or financial relationships that could be construed as a potential conflict of interest.

Copyright © 2018 Castagnaro, Chrisam, Cescon, Braghetta, Grumati and Bonaldo. This is an open-access article distributed under the terms of the Creative Commons Attribution License (CC BY). The use, distribution or reproduction in other forums is permitted, provided the original author(s) and the copyright owner(s) are credited and that the original publication in this journal is cited, in accordance with accepted academic practice. No use, distribution or reproduction is permitted which does not comply with these terms.



# Advanced and Rationalized Atomic Force Microscopy Analysis Unveils Specific Properties of Controlled Cell Mechanics

Guido Caluori<sup>1,2</sup>, Jan Pribyl<sup>2\*</sup>, Martin Pesl<sup>1,3,4</sup>, Jorge Oliver-De La Cruz<sup>5</sup>, Giorgia Nardone<sup>5</sup>, Petr Skladal<sup>2</sup> and Giancarlo Forte<sup>5,6</sup>

<sup>1</sup> International Clinical Research Center of the St. Anne's University Hospital Brno (FNUSA-ICRC), Interventional Cardiac Electrophysiology, Brno, Czechia, <sup>2</sup> Central European Institute of Technology of Masaryk University, Nanobiotechnology, Brno, Czechia, <sup>3</sup> Department of Biology, Faculty of Medicine, Masaryk University, Brno, Czechia, <sup>4</sup> First Department of Internal Medicine/Cardioangiology, St. Anne's Hospital, Masaryk University, Brno, Czechia, <sup>5</sup> International Clinical Research Center of the St. Anne's University Hospital Brno (FNUSA-ICRC), Center for Translational Medicine, Brno, Czechia, <sup>6</sup> Department of Biomaterials Science, Institute of Dentistry, University of Turku, Turku, Finland

## OPEN ACCESS

### Edited by:

Angelica Merlot,  
University of New South Wales,  
Australia

### Reviewed by:

Axel Hollmann,  
Consejo Nacional de Investigaciones  
Científicas y Técnicas (CONICET),  
Argentina  
Gurvinder Singh,  
University of Sydney, Australia  
Christine Kranz,  
Universität Ulm, Germany

### \*Correspondence:

Jan Pribyl  
pribyl@nanobio.cz

### Specialty section:

This article was submitted to  
Integrative Physiology,  
a section of the journal  
Frontiers in Physiology

**Received:** 31 March 2018

**Accepted:** 25 July 2018

**Published:** 17 August 2018

### Citation:

Caluori G, Pribyl J, Pesl M, Oliver-De La Cruz J, Nardone G, Skladal P and Forte G (2018) Advanced and Rationalized Atomic Force Microscopy Analysis Unveils Specific Properties of Controlled Cell Mechanics. *Front. Physiol.* 9:1121. doi: 10.3389/fphys.2018.01121

The cell biomechanical properties play a key role in the determination of the changes during the essential cellular functions, such as contraction, growth, and migration. Recent advances in nano-technologies have enabled the development of new experimental and modeling approaches to study cell biomechanics, with a level of insights and reliability that were not possible in the past. The use of atomic force microscopy (AFM) for force spectroscopy allows nanoscale mapping of the cell topography and mechanical properties under, nearly physiological conditions. A proper evaluation process of such data is an essential factor to obtain accurate values of the cell elastic properties (primarily Young's modulus). Several numerical models were published in the literature, describing the depth sensing indentation as interaction process between the elastic surface and indenting probe. However, many studies are still relying on the nowadays outdated Hertzian model from the nineteenth century, or its modification by Sneddon. The lack of comparison between the Hertz/Sneddon model with their modern modifications blocks the development of advanced analysis software and further progress of AFM promising technology into biological sciences. In this work, we applied a rationalized use of mechanical models for advanced postprocessing and interpretation of AFM data. We investigated the effect of the mechanical model choice on the final evaluation of cellular elasticity. We then selected samples subjected to different physicochemical modulators, to show how a critical use of AFM data handling can provide more information than simple elastic modulus estimation. Our contribution is intended as a methodological discussion of the limitations and benefits of AFM-based advanced mechanical analysis, to refine the quantification of cellular elastic properties and its correlation to undergoing cellular processes *in vitro*.

**Keywords:** atomic force microscopy, cell biomechanics, BEEC, force mapping, mechanical modeling, stiffness tomography, Hippo pathway, mechanotransduction

## INTRODUCTION

The determination of the biomechanical properties of cells and their surrounding extracellular matrix (ECM) unveils fundamental insights to understand the development and the features of healthy and pathological conditions (Yim and Sheetz, 2012). Cellular mechanics is a dynamic process originating from the disposition and interaction of the cytoskeletal proteins (mainly actin microtubules and intermediate filaments) (Ahmed et al., 2015; Huber et al., 2015), and by its coupling to the cell nucleus (Li et al., 2014). The appropriate organization and composition of the cytoskeleton allows cells to proceed in their cell cycle (Nakaseko and Yanagida, 2001; Heng and Koh, 2010) and to adapt to environmental changes [e.g., drugs (Li et al., 2015), ECM composition (Klaas et al., 2016), applied forces and substrate stiffness Discher et al., 2005] via mechano-transduction pathways (Huang et al., 2004). A common regulation mechanism resides in the formation of focal adhesions between the actin-integrin transmembrane complex and target ECM binding sites (Huang et al., 2004). Focal adhesion formation induces the upregulation of different biomolecular cascades, including the Hippo pathway through YAP and TAZ transcription factors (Benham-Pyle et al., 2015). The alteration of cytoskeletal homeostasis is common in many pathological processes. For instance, in cancer metastasizing, actin fibers are remodeled so that stiffness can drop sensibly, thus providing sufficient motility to invade neighboring tissues (Cross et al., 2007). Skeletal and cardiac muscle myotubules alteration can lead to impaired excitation-contraction coupling in dystrophinopathies (Kerr et al., 2015). Endothelial cells can respond to altered fluid dynamics and increased shear-stress with hypertrophy and tissue stiffening (Lu and Kassab, 2011).

It has become clear that, to fully understand biomechanical features, a multiscale approach is indispensable (Bausch and Kroy, 2006). A characterization of the biomechanical molecules is a paramount step, for which immunocytochemistry and live staining microscopy are powerful approaches to visualize cytoskeletal spatiotemporal organization. Nevertheless, techniques based on molecular approaches still struggle to establish methods for quantitative evaluation (Alhoussein et al., 2016). At the cellular level, most of the molecular complexity can be ignored to rely on established continuum-based mechanical models (Huang et al., 2004). In this way, it is possible to describe biomechanical features in terms of stresses (forces) and strains (displacement) (Moeendarbary and Harris, 2014), linking them through concentrated parameters such as elastic (or Young's) modulus, and loss modulus (Guz et al., 2014). Force-displacement relationships can be measured through passive methods (e.g., particle tracking techniques) (Wirtz, 2009), or active ones, such as optical tweezers (Ayala et al., 2016), magnetic beads (Marjoram et al., 2016), polymeric micropillars (Hanson et al., 2015), or depth sensing instrumentation (Oyen, 2015). Among the latter typology, atomic force microscopy (AFM) applies precisely controlled forces through a nanosized indenter placed on a cantilever, whose position is defined by a piezoelectric actuator. The sweeping vertical motion of the AFM tip allows the recording of force-distance curves (FDC) (Butt

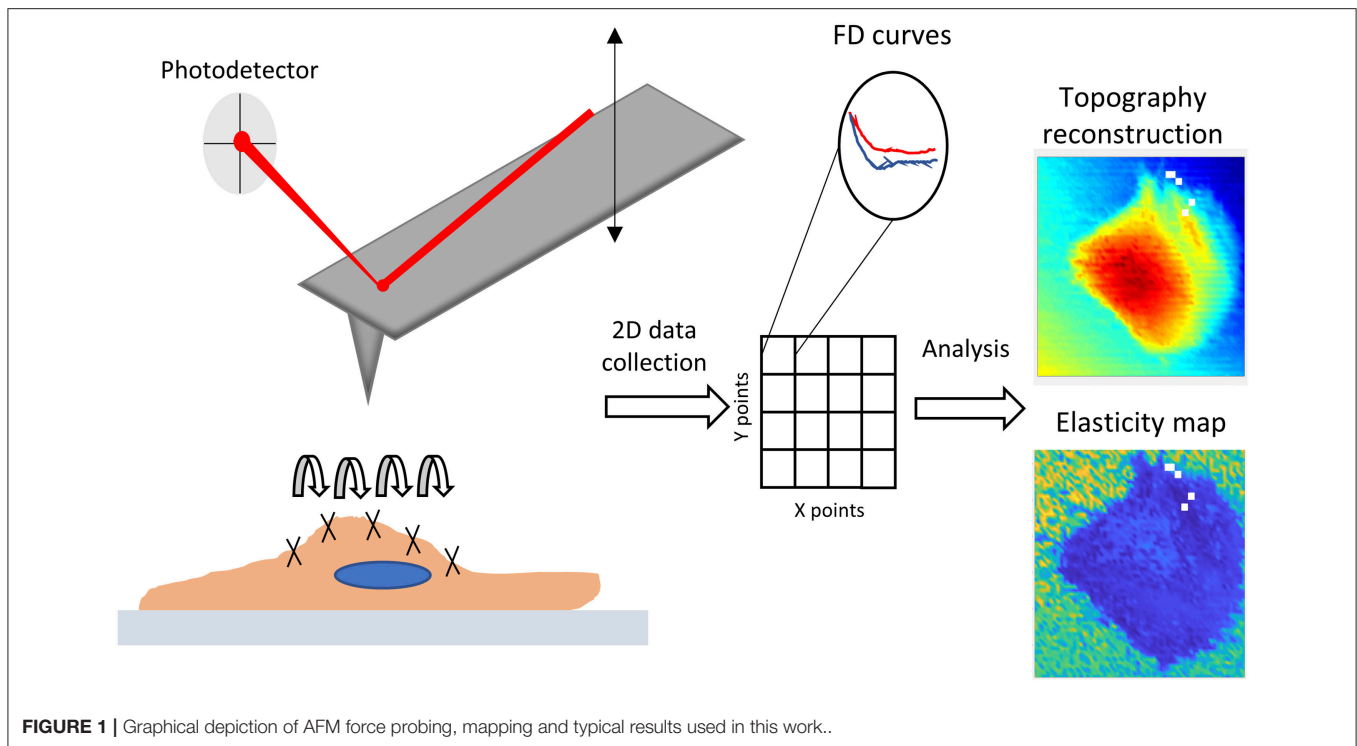
et al., 2005), which contain information on cellular stiffness, and, through model-based interpretation, on the related viscoelastic parameters. FDCs can be performed pointwise on a 2D grid, creating a so-called force-volume map. The typical process and results of probing mechanical properties with AFM force mapping are shown in **Figure 1**. The attractiveness of AFM for biological samples is well-known, and it resides in the non-destructive nature of the technique, the minimal preparation necessary to analyze biological samples in liquids, and the nanometric resolution of both applied force and measured indentations (Müller and Dufrêne, 2008). The technique is easily integrated with optical microscopy (Geisse, 2009; Cascione et al., 2017), and scalable from cell population to subcellular domains. So far, AFM has been applied extensively in the field of biomechanical studies (Engler et al., 2007; Pesl et al., 2016; Li et al., 2017; Alcaraz et al., 2018; Borin et al., 2018; Zemła et al., 2018). Despite its potential, the heterogeneous methodology and simplistic models applied to data interpretation can lead to biased results. These facts call for a better understanding and a rationalized use of the methods, ideally aiming to a procedural standardization among AFM users (Schillers et al., 2017). For these reasons, in this work we show how the rationalized use of different AFM methodologies alone, with standardized data acquisition, can increment the information content for the understanding of environmental changes or gene-editing effects on cellular biomechanics.

## MATERIALS AND METHODS

### Cell Culture

All the cells analyzed in this work were prepared as previously described by Nardone et al. (2017). Briefly, ASC52telo, hTERT immortalized adipose-derived mesenchymal stem cells (AD-MSC, ATCC SCRC-4000) were purchased from American Type Culture Collection (ATCC, Manassas, USA). CAL51 cancer cell lines were a gift of Dr L. Krejčí (Department of Biology, Masaryk University, Brno, Czech Republic). The cells were cultured in high glucose DMEM medium (DMEM high Glucose 4.5  $\text{g l}^{-1}$ , Lonza, Basel, Switzerland) supplemented with 10% fetal bovine serum, 2 mM L-glutamine and 100 U  $\text{ml}^{-1}$  penicillin/streptomycin. For the mechanical trials following down-regulation of the Hippo pathway, responsible for promoting proliferation and survival of breast cancer cells (Shi et al., 2015), YAP-deficient CAL51 lines (CAL51-C3) were produced by CRISPR/Cas9 technology. Guiding RNA was designed to hit exon 1 of *YAP1* gene, which is common to all nine *YAP1* splicing variants.

Cells for AFM experiments were seeded on fibronectin (FN)-coated 34 mm polystyrene (PS) Petri dishes (TPP, Trasadingen, Switzerland), FN-coated glass coverslips, and poly-L-lysine-coated (PLL) PS dishes. All the samples were let to attach for 2 days before medium change and force-mapping. The cells were kept in a 5%  $\text{CO}_2$ , 37°C incubator prior to experiments. Single 2 ml vials filled with medium were kept open in incubator to provide physiological pH at the start of every mapping.



**FIGURE 1** | Graphical depiction of AFM force probing, mapping and typical results used in this work..

## Atomic Force Microscopy

Force-volume maps were recorded using a JPK NanoWizard 3 (JPK, Berlin, Germany) AFM system, embedded in an inverted light microscope Olympus IX-81. Scanning range of the AFM head was 100–100–15  $\mu\text{m}$ , in X-Y-Z axis, respectively. Non-coated silicon nitride AFM cantilevers Hydra 2R-100N (AppNano, California, USA) were used for all the experiments. This cantilever model presents a pyramidal silicon tip (half angle to edge  $18^\circ$ ) and has nominal spring constant  $0.01 \text{ N m}^{-1}$ . The system was calibrated before each experiment with the following procedure. The cantilever chip was mounted on the scanner head and exposed to sterilizing UVC light for 30 min. Then, the scanner head was placed on top of a clean Petri dish filled with 2 ml double-distilled water. The dish was encased in a Petri dish heater (JPK, temperature set at  $37^\circ\text{C}$ ), and equipped with a fluid exchange needle system. The cantilever was immersed in liquid, the laser spot was aligned at its free extremity, and the system was let to stabilize for 15 min. The laser photodetector was centered, and the cantilever tip was approached to the Petri dish surface. A single FDC (15  $\mu\text{m}$  vertical sweep, 3 s extension time, z-closed loop enabled) was performed to estimate the system deflection sensitivity. Then, the cantilever was withdrawn at least 1 mm away from the surface, to allow the estimation of the spring constant by the thermal noise method (Butt and Jaschke, 1995). The relative error of the calibration method was estimated at 6.72%, comparable with other error sources like the point of contact detection (6.21% as measured on rigid calibrating surface).

After calibration, the water-filled Petri dish was substituted with one containing the sample. No thermal drift was observed in time, due to reduced reflective coating of the cantilever. Microscope objective with 10x magnification was used to find appropriate cell-covered regions. Force maps were performed over an area of  $100 \times 100 \mu\text{m}$  following a square  $64 \times 64$  grid. For all the experiments, the maximal setpoint relative to the baseline was 1 nN, the indentation speed was  $30 \mu\text{m s}^{-1}$ , and the sampling frequency was 2 kHz. The average mapping time was 45 min, and after each force map, the dish medium was exchanged with fresh medium from incubator. We scanned single cells for AD-MSK or multicellular colonies for CAL51 (both C3 or wild type, WT).

## Biomechanical Data Interpretation

The obtained force maps were processed in a Matlab R2017b graphic user interface (Mathworks, Natick, Massachusetts, USA), using state-of-the-art algorithms and mechanical models. Specifically, the approaching part of each set of FDC was detrended to set the non-contact portion of the curve to zero. Subsequently, the point of contact between the sample and the cantilever tip was assessed by trial point followed by power law fitting. The trial point was obtained by detection of a force bigger than four times the standard deviation of the first 25% of the curve. The final contact point was obtained by intersecting a linear fitting in the non-contact region with a quadratic fitting in the contact region (Cogollo et al., 2011). The quadratic fit has the form:

$$P = \alpha(h - h_c)^m \quad (1)$$

Where  $P$  is the force,  $h$  is the position of the vertical piezoelectric crystal,  $h_c$  is the piezo position at the contact point,  $\alpha$  is a constant containing properties of the indenter geometry and the sample elastic modulus, and  $m = 2$  for conical and pyramidal indenters (Merle et al., 2014). Once the point of contact is found, load-indentation curves are calculated by subtracting the cantilever deflection from the displacement (Cogollo et al., 2011), with the formula:

$$\delta = h^* - d \quad (2)$$

Where  $\delta$  is the sample indentation,  $h^*$  is the position of the vertical piezoelectric actuator after contact and  $d$  the deflection of the cantilever. The experimental points of the calculated load-indentation curves were fitted by a smoothed spline, and values of elastic modulus were finally extracted at different indentation levels using three different mechanical models. Maximal indentation admitted was 500 nm. The evaluation of the Young's modulus at multiple indentation levels allowed us to construct stiffness tomography maps (Roduit et al., 2009). Indentation speed was kept constant; thus, we could ignore the viscous component of the cell biomechanics during comparisons. The implemented models will be briefly explained.

### Sneddon and Bilodeau Model

The Sneddon's model follows the classical Hertzian theory for indentation of an infinite, purely elastic half-space with a uniformly defined conical indenter (Poon et al., 2008) or body of revolution (Sneddon, 1965). For pyramidal indenters, a more realistic model for AFM probing tips, a corrected solution was introduced by Bilodeau (1992). The elastic modulus is obtained by the following equation:

$$E = \frac{P(1 - \nu^2)}{0.7453 \tan \theta \delta^2} \quad (3)$$

where  $\nu$  is the Poisson's ratio (0.5 for incompressible materials) and  $\theta$  is the half angle of the pyramidal indenter.

### Oliver and Pharr Model

The method of Oliver and Pharr is a modification of the Sneddon's theory which accounts for the changing load-indentation slope, due to the indentation-dependent contact area of an axisymmetric indenter (VanLandingham et al., 2001; Poon et al., 2008). No hysteresis between non-contact region of the curves or plastic deformation was observable during multiple indentations. The modulus is calculated by:

$$E = \frac{S(1 - \nu^2)\sqrt{\pi}}{2\sqrt{A}} \quad (4)$$

where  $A = \delta^2 \pi (\tan \theta)^2$  is the projected area of the pyramidal indenter, and  $S$  is the derivative of  $P$  over  $\delta$ .

### Bottom Effect Cone Correction Model

The bottom effect cone correction (BECC) model is a modification of Sneddon's model which amends the assumptions

of infinite half-space, by considering the sample height (Gavara and Chadwick, 2012). The elastic modulus is calculated by:

$$E = \frac{3\pi P}{8 \tan \theta} \left\{ 1 + 1.7795 \frac{2 \tan \theta}{\pi} \frac{\delta}{H} + 16(1.7795^2) \tan \theta^2 \frac{\delta^2}{H^2} \right\}^{-1} \quad (5)$$

where the  $H$  is the local height of the sample. It is worth mentioning that if we exclude the term on the right side between brackets, we obtain the Sneddon's elastic modulus. In the presented experiments,  $H$  is extracted after calculating a flattened topographical map, in order to avoid biases due to the sample tilt.

A graphical description of the analysis algorithm is shown in **Supplementary Materials**.

## Statistical Methods

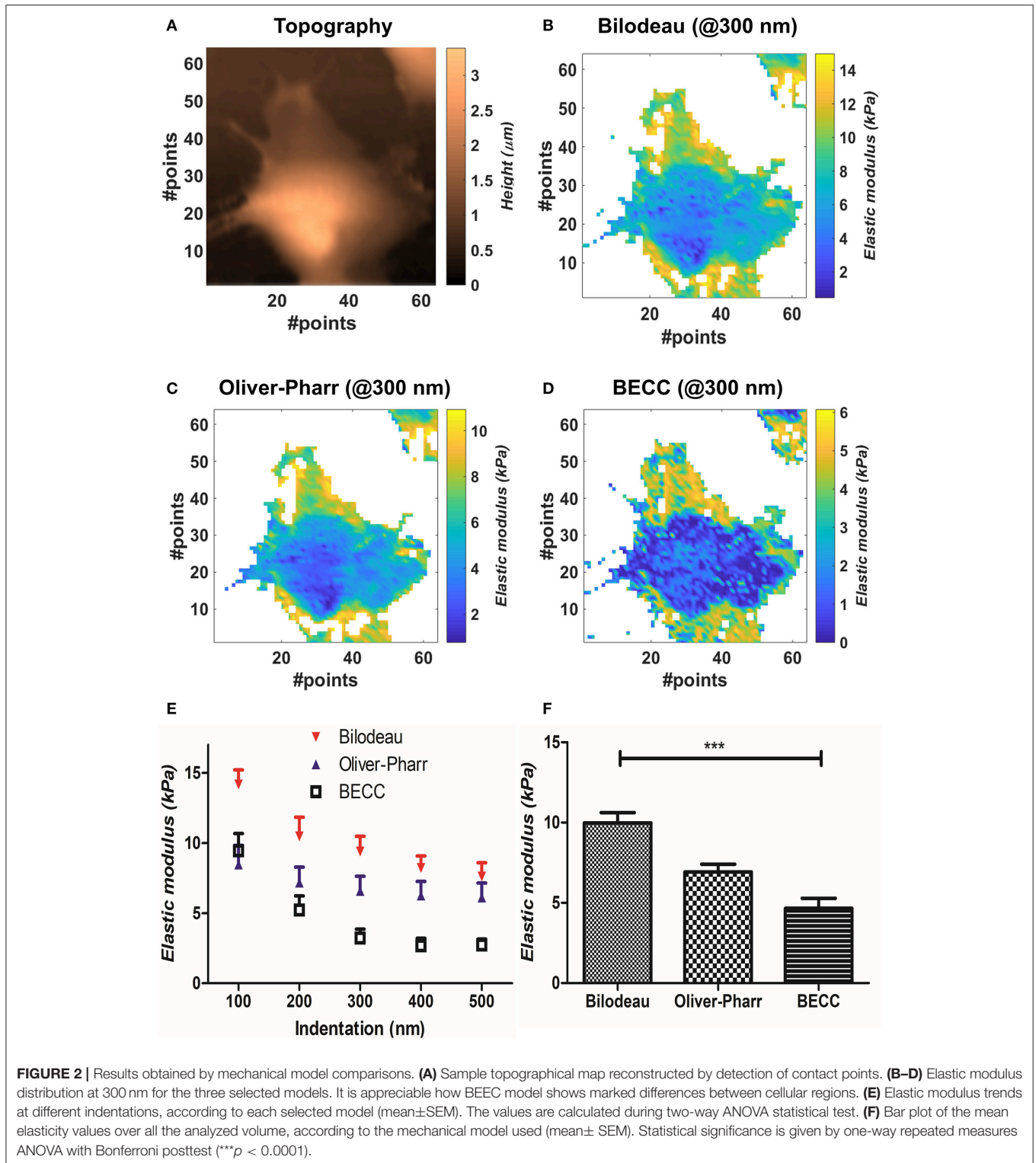
Statistical analysis was performed in Prism 5.0 (GraphPad Software, La Jolla, CA-USA) or Matlab. All the datasets were firstly evaluated for normality distribution by Kolmogorov-Smirnov test, and, once passed, were presented as mean  $\pm$  SEM. For the model comparison, repeated-measures one/two-way analysis of variance (ANOVA) with Bonferroni posttest were used. For the evaluation of the substrate effect, Welch's ANOVA test followed by Games-Howell test was performed, due to the datasets being non-homoscedastic. For the evaluation of YAP genetic knockout effect, two-way ANOVA with Bonferroni posttest and Student's  $t$ -test with Welch's correction were used. Statistical significance was accepted with  $p$ -values smaller than 0.05. Sample sizes were based on previously published experiments, in which statistical differences were identified.

## RESULTS

### Effect of the Model Selection

We compared the selected mechanical models on well-spread cellular samples of AD-MSCs (i.e., where the substrate was clearly identifiable), cultivated on a standard fibronectin-coated Petri dish. Starting from the obtained map of contact points (**Figure 2A**), the appropriate model was used to estimate the Young's modulus over the whole force map, at five different indentation levels (100–200–300–400–500 nm). We performed two-way repeated measures ANOVA, with matching on the indentation levels, to assess whether using different models on the same samples will lead to statistically different results (**Figure 2E**). Across the measured samples ( $N = 5$ ), the model choice accounted for largely significant difference ( $p < 0.0001$ ). The test returned also a significant justification for matching ( $p < 0.0001$ ), together with an accountable difference due to the different indentation levels ( $p = 0.0027$ ). Bonferroni's posttest showed at which indentations the models start to diverge: Bilodeau's and Oliver-Pharr's models differ before 400 nm; BECC and Oliver-Pharr's show this tendency after 300 nm; BECC and Bilodeau's models differ significantly at each fixed indentation. For more details on the significance levels, the reader is addressed to **Supplementary Materials**. We then performed repeated measures one-way ANOVA using all the values calculated across the cell volumes, categorizing them only by the model used.





The test returned significant difference between the datasets and significant justification for matching ( $p < 0.001$ , **Figure 2F**).

We then compared the results obtainable by the selected mechanical models. Globally, the Bilodeau's model led to the

highest overestimation of the elastic modulus ( $9.9 \pm 2.6$  kPa), when compared to the values obtained by Oliver-Pharr's ( $6.92 \pm 0.96$  kPa) and BECC ( $4.7 \pm 2.9$  kPa). The BECC model showed the highest coefficient of variation across the samples

and the indented volume (61.5%), followed by Bilodeau's model (26.0%) and Oliver-Pharr's (13.9%). When considered at the same indentation level, Bilodeau's and Oliver-Pharr's showed smooth distribution of the elastic modulus over the cell body, whereas BECC showed marked and detailed differences between softer and harder regions (Figures 2B–D). We observed how all the BECC and Oliver-Pharr's models stabilized at 300 nm of indentation (slope of the mean elastic modulus 0.34 and 0.54  $\text{Panm}^{-1}$ , respectively), whilst the Bilodeau's model is still affected by depth-dependent trend (1.17  $\text{Panm}^{-1}$ ). The comparative model trends are shown in Figure 2E.

## Effect of the Substrate

We evaluated the effect of substrate stiffness on the elastic modulus at 300 nm for AD-MSC single cells force maps. We used the BECC model to exploit its higher discrimination capabilities and stability, given the fact that the sample substrate was clearly identifiable across the force map. Figures 3A,B show representative results of selected points belonging either to the probed cell or to the culture substrate. Cells plated on FN-coated Petri dish (polystyrene, PS, according to Figures 3C,D), FN-coated glass (Glass) and PLL-coated Petri dish (PLL) were analyzed in this section (Figure 3C,  $N = 5$ , for each group). We performed Welch's ANOVA due to the significantly different variance among groups assessed by Bartlett's test ( $p = 0.0007$ ). Strong difference between the groups was observed ( $p < 0.0001$ ) and multiple comparisons were evaluated with the Games-Howell test. The latter returned a statistical difference among all the comparisons ( $p = 0.0126$  PS vs. glass;  $p = 0.0058$  glass vs. PLL;  $p = 0.0052$  PS vs. PLL). The same tests were performed for the substrate stiffness, measured at 10 nm (Figure 3D). Significant difference across the groups was confirmed ( $p < 0.0001$ ) and the multiple comparisons showed no statistical difference between the PS and PLL group, albeit significant difference between glass and the other two groups ( $p = 0.455$  PS vs. PLL;  $p = 0.0062$  PS vs. glass;  $p = 0.0058$  glass vs. PLL).

We therefore proceeded to compare the elastic modulus values calculated for the different cell groups. The PLL group showed the lowest Young's modulus ( $0.5151 \pm 0.24$  kPa), followed by PS samples ( $6.323 \pm 1.273$  kPa) and glass ones ( $13.4 \pm 3.050$  kPa). The increased stiffness between glass and PS samples was correlated with the increased stiffness of the substrate ( $9.545 \pm 2.1$  and  $1.59 \pm 0.16$  MPa respectively), whereas the measured PLL stiffness was similar to the PS one ( $1.88 \pm 0.47$  MPa).

## Effect of Genetic Manipulation

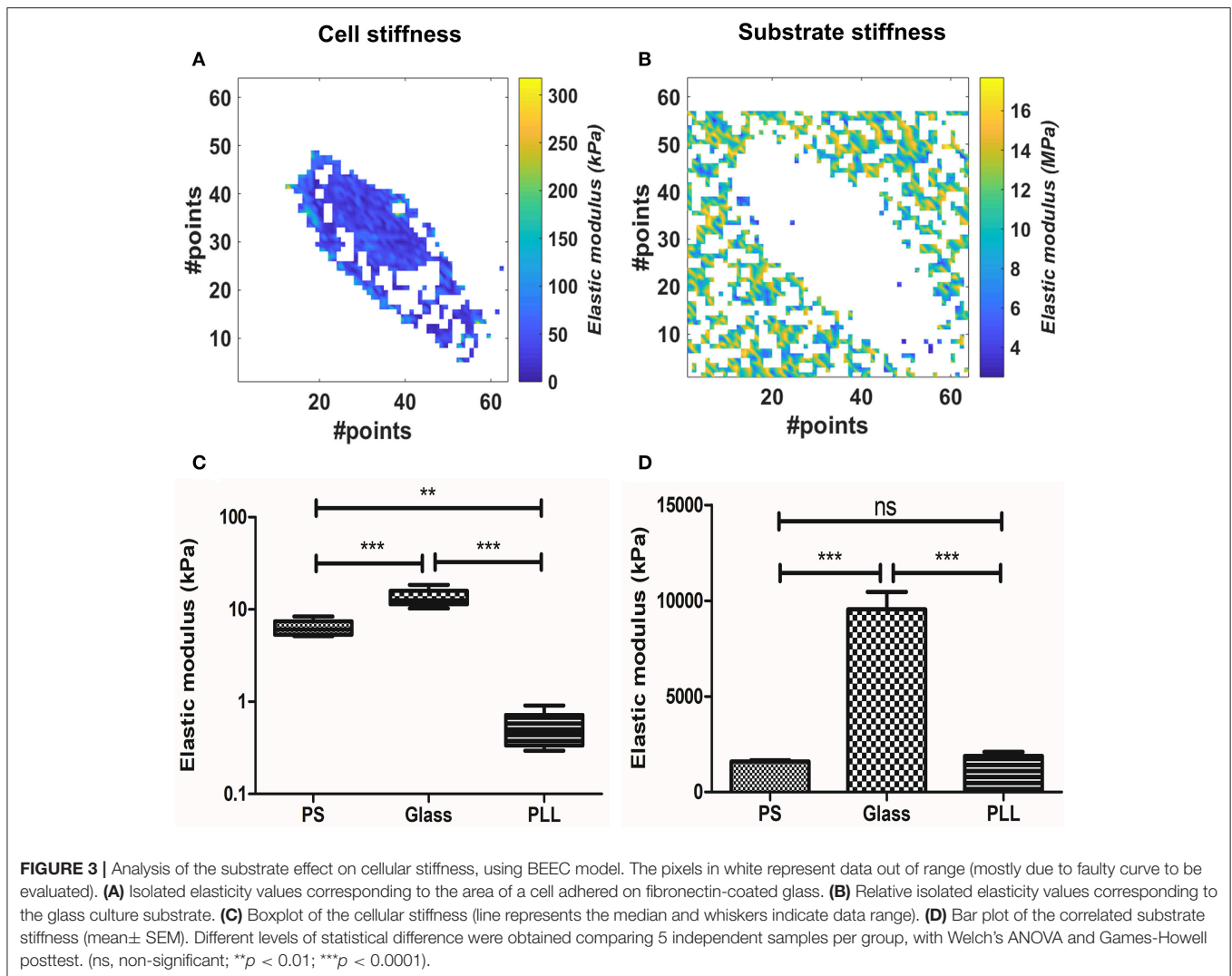
We measured YAP-deficient cell line CAL51-C3 in comparison with healthy control (CAL51-WT). The cellular samples typically grew in colonies, and this made impossible to identify univocally the position of the substrate. Therefore, Oliver-Pharr's model, which presented the higher stability after the BECC one, was used to calculate the samples elastic modulus, at 300 nm indentation. We compared separately the contribution of harder parts (referred further as nuclear bodies) and softer parts (perinuclear regions). The names were chosen after correlation with topographical images. CAL51-WT samples showed multiple cells per map, organized in a monolayer fashion

(Figures 4A,B); conversely, CAL51-C3 aggregated and showed a pronounced spheroidal shape, with hardly distinguishable single cells (Figures 4C,D). Two-way ANOVA was used to estimate if the YAP-deficiency or the subcellular region significantly affected the stiffness results. Both genetic modification and considered region played significant role in the determination of the Young's modulus ( $p < 0.0001$ ). Bonferroni posttest showed a significant difference between the stiffness of the nuclear regions between the two groups ( $p < 0.001$ ), whereas no statistical difference could be found for the perinuclear regions. We observed an apparently different contribution of the nuclear bodies to the sample stiffness, between the two cellular groups. Thus, we calculated the fraction occupied by the nuclear region in the whole cell area. The obtained values were compared using Student's *t*-test with Welch's correction for uneven variances. The group means resulted significantly different ( $p = 0.0003$ ).

According to these outcomes, we compared the values calculated for the Young modulus and the nuclear area fraction. CAL51-C3 presented a significantly decreased nuclear stiffness ( $1.36 \pm 0.57$  kPa,  $N = 5$ ) compared to CAL51-WT ( $3.04 \pm 0.83$  kPa,  $N = 5$ ), whilst no difference was observable between the perinuclear regions ( $0.39 \pm 0.13$  kPa, WT, vs.  $0.23225 \pm 0.02018$  kPa, C3). These results are shown in Figure 4E. The area occupied by the nuclear region was in percentage higher in the WT samples ( $74.6 \pm 2.485\%$ ) compared to the C3 ones ( $24.1 \pm 9.6\%$ ). These results are summed up in Figure 4F.

## DISCUSSION

The first question of this methodological work focused on influence of the selected biomechanical model on the evaluation of cellular stiffness. We have observed how the choice among three linearly elastic mechanical models greatly affects the calculated stiffness values, at different indentation levels. As first result, we saw how the Bilodeau's modification of Sneddon's theory leads to the highest estimation of the cell stiffness. This can be explained by the breaking of the assumption of infinitely thick sample, or small indentations (Dimitriadis et al., 2002; Radmacher, 2007) over an adhered cell sample. This effect is accounted in the BECC model (Gavara and Chadwick, 2012), by explicit introduction of the sample height in the calculations, and partially mitigated by including the indentation-dependent area of contact in the Oliver-Pharr's one (VanLandingham et al., 2001). Whilst one could limit the analysis to small indentations, levels above 300 nm have shown generally increased stiffness throughout all the models used. This is most probably due to the measurement noise in proximity of the contact point. The interpretation of the FDCs requires a precise, however indirect (Benítez et al., 2013), identification of the point of contact between indenter and samples (Melzak et al., 2010), as small errors can lead to one order of magnitude changes in the calculated elastic modulus (Crick and Yin, 2007). Furthermore, force-indentation relationship is dependent on the junction between the sample and the substrate, to such a way that an adhered sample requires higher force to be indented (Chadwick, 2002). The firm or loose adhesion is a paramount issue in AFM

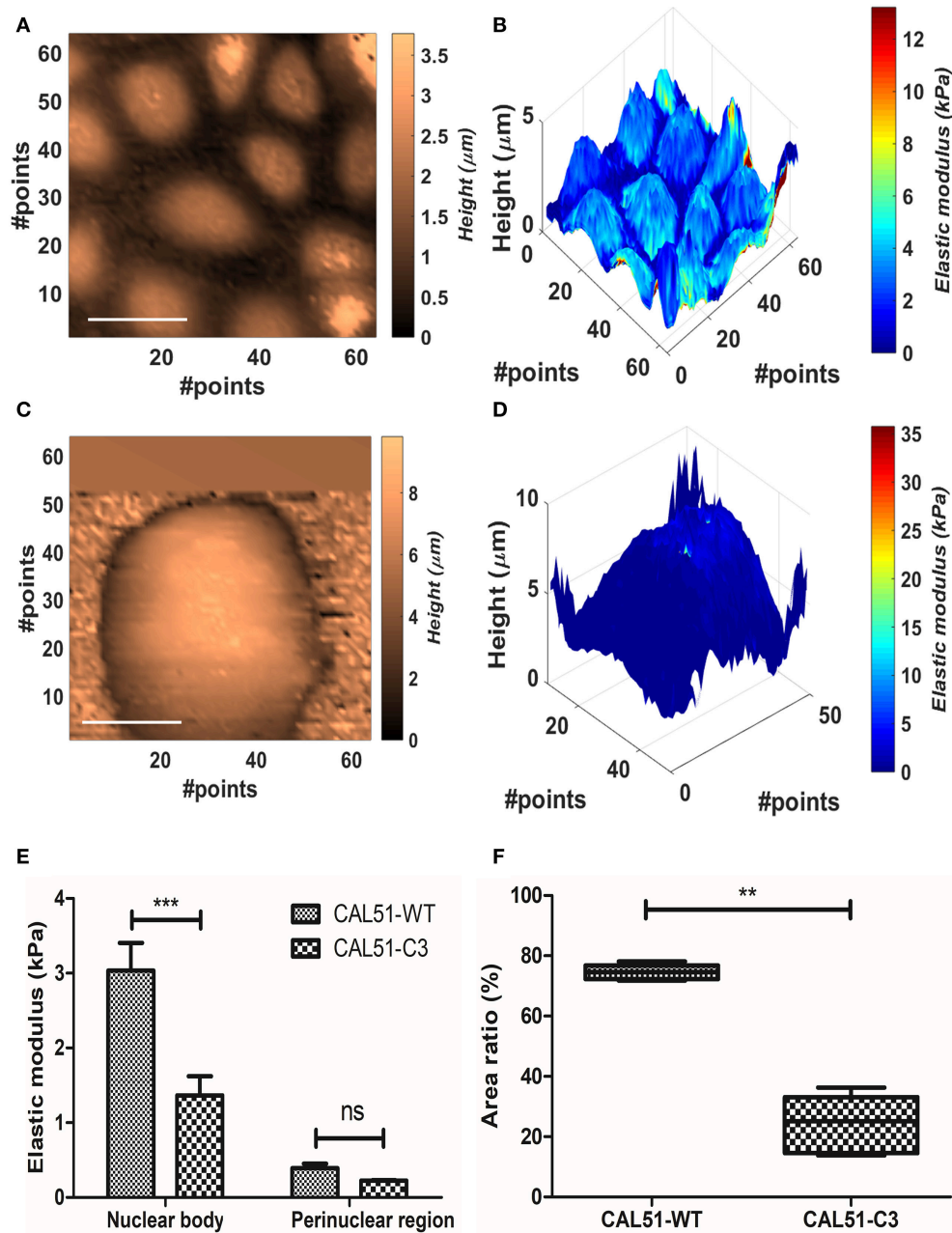


measures, as it was shown in previously reported studies that the simple application of the Hertzian model can lead to artificially low Young's modulus (Dokukin et al., 2013). These issues pose difficulty in limiting uniformly the indentation level on spatially anisotropic materials such as cells. Such anisotropic properties were confirmed by the significant effect of the indentation level selected for the stiffness tomography, and the observed surface heterogeneity of the elasticity maps. For all these considerations, the BECC model seems to be the elective choice, thanks to its observed level of discrimination between hard and soft areas, and higher stability rate at increasing depths. Nevertheless, this model is not applicable when the substrate (i.e., an area with clear contact point and linear repulsive regime) is not clearly identifiable. This is the case of biological samples which typically grow in large colonies or monolayers, such as stem cells or uniform cell lines. In this case, the Oliver-Pharr's method provides the second-best characteristics, according to stability rate. It is worth mentioning that all the considerations discussed so far are relevant for models in which the cell-probe interface

is well-defined, such as the one presented. Other more complex models, such as the pericellular brush model for spherical indenters, could help to separate the effect of plasma membrane protein layer from the cellular bulk (Sokolov et al., 2013), limiting at least the uncertainty in the detection of the point of contact.

We then applied the two optimal models to case-specific scenarios, in which cell biomechanics is controlled by the surrounding environment or by gene editing.

Surprisingly, we could not find a previous reported application of BECC model over a whole cell. The effect of the substrate stiffness was assessed using BECC model to interpret the force maps measured on AD-MSC cells grown in FN-coated PS/glass surfaces, or PLL-coated PS surface. The implemented statistical tests showed significant differences between all these three groups. Furthermore, the increasing stiffness between the samples grown on glass compared to the ones grown on PS is correlated with the stiffness of the substrate. This is most probably due to the well-known proportional dependency of



**FIGURE 4 |** Analysis of the YAP mutation effect on cell mechanics. **(A,B)** Contact point and stiffness tomography maps showing topographical and biomechanical distribution of CAL51-WT cells. Scalebar is 30  $\mu\text{m}$ . **(C,D)** Contact point and stiffness tomography maps of CAL51-C3 colonies. The cells pass from monolayer distribution to spheroidal aggregation due to lack of focal adhesions. Scalebar is 30  $\mu\text{m}$ . **(E)** Bar plot showing elastic modulus differences between two identified regions with different levels of elasticity nuclear and perinuclear, (mean  $\pm$  SEM). Statistical difference was obtained with two-way ANOVA with Bonferroni posttest (ns, non-significant;  $***p < 0.001$ ). **(F)** Boxplot showing the difference in area fraction covered by the nuclear body (line represents the median and whiskers indicate data range). The significant reduction in the mutated samples can reflect the nuclear shape change due to cytoskeletal instability. Statistical difference is obtained using Student's *t*-test with Welch's correction ( $**p < 0.001$ ).

diverse cell types' cytoskeletal synthesis and contractility on the substrate rigidity (Solon et al., 2007). AD-MSC have been shown to respond to substrate stiffness alteration, but to the best knowledge of the authors this is the first direct characterization of this effect on AD-MSC with AFM force mapping (Keremidarska-Markova et al., 2017), but to the best knowledge of the authors this is the first direct characterization of this effect on AD-MSC

with AFM force mapping. On the contrary, the observed plummeting of the cell stiffness on PLL-coated surfaces did not correlate with the substrate rigidity. This absence of correlation is most probably due to the biochemical alteration of the cellular mechanics, since PLL is able to abrogate focal adhesions formation regardless the substrate stiffness (Nardone et al., 2017). A lack of focal adhesion is directly correlated to inhibited cell

contractility (Balaban et al., 2001), which is measured by AFM in stiffness decrease.

The targeted knockout of the *YAP1* gene in CAL51 cell line altered sensibly the cell colonies morphology and biomechanics. We firstly observed how the mutated line presented low attachment, and spheroidal shape of the cell colonies, alternatively spreading in monolayer for WT. We then noticed two distinct distribution peaks among the elasticity values. By selecting these two distribution regions and correlating them with topographical images, we inferred observing harder oval nuclear regions (Dvir et al., 2015) and softer perinuclear regions. We did not refer to the latter as cytoplasmic areas since the cell-cell edge was not detectable by force mapping. Statistical analysis showed that stiffness decrease was significant only in the nuclear areas, whereas no significant difference was found across the perinuclear regions of the two groups. This phenomenon can be explained by the absence of focal adhesions assembly, due to the downregulation of the Hippo mechano-transduction pathway by *YAP1* knockout (Nardone et al., 2017). This pathway is fundamental in the regulation of cytoskeleton (actin, myosin II) stability, and consequently the nuclear stiffening in response to mechanical forces. These biomechanical evidences can additionally be correlated with the surface fraction occupied by the stiffer nuclear region, significantly lower for the mutated line. The decrease of area fraction can be explained with the shape change of the nucleus, elongated by cytoskeletal fibers in spread cells and rounded in non-adhering samples. This 3D change, while preserving the total volume, will be sensed by the AFM as decrease in cross-sectional area.

## CONCLUSIONS

We have demonstrated how rationalized methodologies concerning AFM measurements and data interpretation can unveil deeper insights than simple biomechanics. To do so, we have applied classical and refined biomechanical models to biophysically and biochemically-controlled samples. We have discussed how the selected mechanical model significantly affects the final results, and this dependency must be considered. The choice of the mechanical model is ultimately conditioned by the sample geometry and substrate properties. The use of advanced AFM methods, such as stiffness tomography, can reveal important 3D heterogeneities of the cellular samples. Simultaneous use of AFM interpretation techniques on hard and soft samples allows scientists to discriminate between physical and biochemical effects on cell elasticity. The combination of reconstructed topography and elasticity maps can reveal selective mutation-induced cellular changes. We hope this methodological work will help the scientific

## REFERENCES

- Ahmed, W. W., Fodor, É., and Betz, T. (2015). Active cell mechanics: measurement and theory. *Biochim. Biophys. Acta* 1853, 3083–3094. doi: 10.1016/j.bbamcr.2015.05.022
- Alcaraz, J., Otero, J., Jorba, I., and Navajas, D. (2018). Bidirectional mechanobiology between cells and their local extracellular matrix probed by atomic force microscopy. *Semin. Cell Dev. Biol.* 73, 71–81. doi: 10.1016/j.semcdb.2017.07.020

community in understanding the potential of advanced AFM applications, and the underlying complexity of its interpretation techniques, for the quantitative advanced analysis of biological samples.

## AUTHOR CONTRIBUTIONS

GC designed and programmed the software routine utilized in this study. He also performed data analysis and wrote the results and discussion part of the work. JP conducted the atomic force microscopy experiments and supervised the writing of the manuscript with MP. PS supported AFM experiments and contributed to manuscript preparation. JO and GN designed and produced the cellular samples described. GF supervised and approved the cellular experiments and contributed to the AFM financing.

## FUNDING

CIISB research infrastructure project LM2015043 funded by MEYS CR is gratefully acknowledged for the financial support of the measurements at the CF Nanobiotechnology. Supported by the projects projects no. LQ1601 (CEITEC 2020) and no. LQ1605 from the National Program of Sustainability II (MEYS CR) and by the project FNUSA-ICRC no. CZ.1.05/1.1.00/02.0123 (OP VaVpI). This work was funded by the European Social Fund and European Regional Development Fund-Project MAGNET (No.CZ.02.1.01/0.0/0.0/15\_003/0000492).

## DATA AVAILABILITY STATEMENT

All results obtained this study are included in the manuscript and the supplementary files. The datasets and the raw data can be made available to any qualified researcher under reasonable request.

## ACKNOWLEDGMENTS

The authors would like to thank the JPK support for sharing the force maps file structure and Dr. David Necas at CEITEC VUT, Brno, for the assistance in the first stages of the software programming.

## SUPPLEMENTARY MATERIAL

The Supplementary Material for this article can be found online at: <https://www.frontiersin.org/articles/10.3389/fphys.2018.01121/full#supplementary-material>

- Alhoussein, G., Shanti, A., Farhat, I. A., Timraz, S. B., Alwahab, N. S., Pearson, Y. E., et al. (2016). A spatiotemporal characterization method for the dynamic cytoskeleton. *Cytoskeleton* 73, 221–232. doi: 10.1002/cm.21297
- Ayala, Y. A., Pontes, B., Ether, D. S., Pires, L. B., Araujo, G. R., Frases, S., et al. (2016). Rheological properties of cells measured by optical tweezers. *BMC Biophys.* 9:5. doi: 10.1186/s13628-016-0031-4
- Balaban, N. Q., Schwarz, U. S., Riveline, D., Goichberg, P., Tzur, G., Sabanay, I., et al. (2001). Force and focal adhesion assembly: a close relationship

- studied using elastic micropatterned substrates. *Nat. Cell Biol.* 3, 466–472. doi: 10.1038/35074532
- Bausch, A. R., and Kroy, K. (2006). A bottom-up approach to cell mechanics. *Nat. Phys.* 2, 231–238. doi: 10.1038/nphys260
- Benham-Pyle, B. W., Pruitt, B. L., and Nelson, W. J. (2015). Mechanical strain induces E-cadherin-dependent Yap1 and  $\beta$ -catenin activation to drive cell cycle entry. *Science* 348, 1024–1027. doi: 10.1126/science.aaa4559
- Benítez, R., Moreno-flores, S., Bolos, V. J., and Toca-Herrera, J. L. (2013). A new automatic contact point detection algorithm for AFM force curves: automatic contact point detection for AFM curves. *Microsc. Res. Tech.* 76, 870–876. doi: 10.1002/jemt.22241
- Bilodeau, G. G. (1992). Regular pyramid punch problem. *J. Appl. Mech.* 59, 519–523.
- Borin, D., Pecorari, I., Pena, B., and Sbaizero, O. (2018). Novel insights into cardiomyocytes provided by atomic force microscopy. *Semin. Cell Dev. Biol.* 73, 4–12. doi: 10.1016/j.semcdb.2017.07.003
- Butt, H. J., Cappella, B., and Kappel, M. (2005). Force measurements with the atomic force microscope: Technique, interpretation and applications. *Surf. Sci. Rep.* 59, 1–152. doi: 10.1016/j.surfrep.2005.08.003
- Butt, H. J., and Jaschke, M. (1995). Calculation of thermal noise in atomic force microscopy. *Nanotechnology* 6:1. doi: 10.1088/0957-4484/6/1/001
- Cascione, M., de Matteis, V., Rinaldi, R., and Leporatti, S. (2017). Atomic force microscopy combined with optical microscopy for cells investigation. *Microsc. Res. Tech.* 80, 109–123. doi: 10.1002/jemt.22696
- Chadwick, R. (2002). Axisymmetric indentation of a thin incompressible elastic layer. *SIAM J. Appl. Math.* 62, 1520–1530. doi: 10.1137/S0036139901388222
- Cogollo, J. F. S., Tedesco, M., Martinoia, S., and Raiteri, R. (2011). A new integrated system combining atomic force microscopy and micro-electrode array for measuring the mechanical properties of living cardiac myocytes. *Biomed. Microdev.* 13, 613–621. doi: 10.1007/s10544-011-9531-9
- Crick, S. L., and Yin, F. C.P. (2007). Assessing micromechanical properties of cells with atomic force microscopy: importance of the contact point. *Biomech. Model. Mechanobiol.* 6, 199–210. doi: 10.1007/s10237-006-0046-x
- Cross, S. E., Jin, Y. S., Rao, J., and Gimzewski, J. K. (2007). Nanomechanical analysis of cells from cancer patients. *Nat. Nanotechnol.* 2, 780–783. doi: 10.1038/nnano.2007.388
- Dimitriadis, E. K., Horkay, F., Maresca, J., Kachar, B., and Chadwick, R. S. (2002). Determination of elastic moduli of thin layers of soft material using the atomic force microscope. *Biophys. J.* 82, 2798–2810. doi: 10.1016/S0006-3495(02)75620-8
- Discher, D. E., Janmey, P., and Wang, Y. (2005). Tissue cells feel and respond to the stiffness of their substrate. *Science* 310, 1139–1143. doi: 10.1126/science.1116995
- Dokukin, M. E., Guz, N. V., and Sokolov, I. (2013). Quantitative study of the elastic modulus of loosely attached cells in afm indentation experiments. *Biophys. J.* 104, 2123–2131. doi: 10.1016/j.bpj.2013.04.019
- Dvir, L., Nissim, R., Alvarez-Elizondo, M. B., and Weihs, D. (2015). Quantitative measures to reveal coordinated cytoskeleton-nucleus reorganization during *in vitro* invasion of cancer cells. *New J. Phys.* 17:043010. doi: 10.1088/1367-2630/17/4/043010
- Engler, A. J., Rehfeldt, F., Sen, S., and Discher, D. E. (2007). Microtissue elasticity: measurements by atomic force microscopy and its influence on cell differentiation. *Methods Cell Biol.* 83, 521–545. doi: 10.1016/S0091-679X(07)83022-6
- Gavara, N., and Chadwick, R. S. (2012). Determination of the elastic moduli of thin samples and adherent cells using conical atomic force microscope tips. *Nat. Nanotechnol.* 7, 733–736. doi: 10.1038/nnano.2012.163
- Geisse, N. A. (2009). AFM and combined optical techniques. *Mater. Today* 12, 40–45. doi: 10.1016/S1369-7021(09)70201-9
- Guz, N., Dokukin, M., Kalaparthy, V., and Sokolov, I. (2014). If cell mechanics can be described by elastic modulus: study of different models and probes used in indentation experiments. *Biophys. J.* 107, 564–575. doi: 10.1016/j.bpj.2014.06.033
- Hanson, L., Zhao, W., Lou, H.-Y., Lin, Z. C., Lee, S. W., Chowdary, P., et al. (2015). Vertical nanopillars for *in situ* probing of nuclear mechanics in adherent cells. *Nat. Nanotechnol.* 10, 554–562. doi: 10.1038/nnano.2015.88
- Heng, Y. W., and Koh, C. G. (2010). Actin cytoskeleton dynamics and the cell division cycle. *Int. J. Biochem. Cell Biol.* 42, 1622–1633. doi: 10.1016/j.biocel.2010.04.007
- Huang, H., Kamm, R. D., and Lee, R. T. (2004). Cell mechanics and mechanotransduction: pathways, probes, and physiology. *Am. J. Physiol. Cell Physiol.* 287, C1–C11. doi: 10.1152/ajpcell.00559.2003
- Huber, F., Boire, A., López, M. P., and Koenderink, G. H. (2015). Cytoskeletal crosstalk: when three different personalities team up. *Curr. Opin. Cell Biol.* 32, 39–47. doi: 10.1016/j.ccb.2014.10.005
- Keremidarska-Markova, M., Hristova, K., Vladkova, T., and Krasteva, N. (2017). Adipose-derived mesenchymal stem cell behaviour on pdms substrates with different hardness. *Comptes rendus de l'Académie bulgare des Sciences* 70, 663–670.
- Kerr, J. P., Robison, P., Shi, G., et al. (2015). Detyrosinated microtubules modulate mechanotransduction in heart and skeletal muscle. *Nat. Comm.* 6:8526. doi: 10.1038/ncomms9526
- Klaas, M., Kangur, T., Viil, J., Mäemets-Allas, K., Minajeva A., Vadi, K. et al. (2016). The alterations in the extracellular matrix composition guide the repair of damaged liver tissue. *Sci. Rep.* 6:27398. doi: 10.1038/srep27398
- Li, M., Dang, D., Liu, L., Xi, N., and Wang, Y. (2017). Atomic Force Microscopy in characterizing cell mechanics for biomedical applications: a review. *IEEE Trans. Nanobiosci.* 16, 523–540. doi: 10.1109/TNB.2017.2714462
- Li, M., Liu, L., Xi, N., and Wang, Y. (2015). Nanoscale monitoring of drug actions on cell membrane using atomic force microscopy. *Acta Pharmacol. Sin.* 36, 769–782. doi: 10.1038/aps.2015.28
- Li, Q., Kumar, A., Makhija, E., and Shivashankar, G. V. (2014). The regulation of dynamic mechanical coupling between actin cytoskeleton and nucleus by matrix geometry. *Biomaterials* 35, 961–969. doi: 10.1016/j.biomaterials.2013.10.037
- Lu, D., and Kassab, G. S. (2011). Role of shear stress and stretch in vascular mechanobiology. *J. R. Soc. Interface* 8, 1379–1385. doi: 10.1098/rsif.2011.0177
- Marjoram, R. J., Guilluy, C., and Burridge, K. (2016). Using magnets and magnetic beads to dissect signaling pathways activated by mechanical tension applied to cells. *Methods* 94, 19–26. doi: 10.1016/j.jymeth.2015.09.025
- Melzak, K. A., Moreno-Flores, S., Yu, K., Kizhakkedathu, J., and Toca-Herrera, J. L. (2010). Rationalized approach to the determination of contact point in force-distance curves: application to polymer brushes in salt solutions and in water. *Microsc. Res. Tech.* 73, 959–964. doi: 10.1002/jemt.20851
- Merle, B., Maier, V., and Durst, K. (2014). Experimental and theoretical confirmation of the scaling exponent 2 in pyramidal load displacement data for depth sensing indentation. *Scanning* 36, 526–529. doi: 10.1002/sca.21151
- Moendarbary, E., and Harris, A. R. (2014). Cell mechanics: principles, practices, and prospects. *WIREs Syst. Biol. Med.* 6, 371–388. doi: 10.1002/wsbm.1275
- Müller, D. J., and Dufrene, Y. F. (2008). Atomic force microscopy as a multifunctional molecular toolbox in nanobiotechnology. *Nat. Nanotechnol.* 3, 261–269. doi: 10.1038/nnano.2008.100
- Nakaseko, Y., and Yanagida, M. (2001). Cell biology: cytoskeleton in the cell cycle. *Nature* 412, 291–292. doi: 10.1038/35085684
- Nardone, G., Oliver-De La Cruz, J., Vrbsky, J., Martini, C., Pribyl, J., Skládal, P., et al. (2017). YAP regulates cell mechanics by controlling focal adhesion assembly. *Nat. Commun.* 8:15321. doi: 10.1038/ncomms15321
- Oyen, M. L. (2015). Nanoindentation of hydrated materials and tissues. *Curr. Opin. Solid State Mater. Sci.* 19, 317–323. doi: 10.1016/j.cossms.2015.03.001
- Pesl, M., Pribyl, J., Acimovic, I., Vilotic, A., Jelinkova, S., Salykin, A., et al. (2016). Atomic force microscopy combined with human pluripotent stem cell derived cardiomyocytes for biomechanical sensing. *Biosens. Bioelectron.* 85, 751–757. doi: 10.1016/j.bios.2016.05.073
- Poon, B., Rittel, D., and Ravichandran, G. (2008). An analysis of nanoindentation in linearly elastic solids. *Int. J. Solids Struct.* 45, 6018–6033. doi: 10.1016/j.ijsolstr.2008.07.021
- Radmacher, M. (2007). Studying the mechanics of cellular processes by atomic force microscopy. *Methods Cell Biol.* 83, 347–372. doi: 10.1016/S0091-679X(07)83015-9
- Roduit, C., Sekatski, S., Dietler, G., Catsicas, S., Lafont, F., and Kasas, S. (2009). Stiffness tomography by atomic force microscopy. *Biophys. J.* 97, 674–677. doi: 10.1016/j.bpj.2009.05.010
- Schillers, H., Rianna, C., Schäpe, J., Luque, T., Doschke, H., Wälte, M. et al. (2017). Standardized nanomechanical atomic force microscopy procedure (snap) for measuring soft and biological samples. *Sci. Rep.* 7:5117. doi: 10.1038/s41598-017-05383-0

- Shi, P., Feng, J., and Chen, C. (2015). Hippo pathway in mammary gland development and breast cancer. *Acta Biochim. Biophys. Sin.* 47, 53–59. doi: 10.1093/abbs/gmu114
- Sneddon, I. N. (1965). The relation between load and penetration in the axisymmetric boussinesq problem for a punch of arbitrary profile. *Int. J. Eng. Sci.* 3, 47–57. doi: 10.1016/0020-7225(65)90019-4
- Sokolov, I., Dokukin, M. E., and Guz, N. V. (2013). Method for quantitative measurements of the elastic modulus of biological cells in AFM indentation experiments. *Methods* 60, 202–213. doi: 10.1016/j.ymeth.2013.03.037
- Solon, J., Levental, I., Sengupta, K., Georges, P. C., and Janmey, P. A. (2007). Fibroblast adaptation and stiffness matching to soft elastic substrates. *Biophys. J.* 93, 4453–4461. doi: 10.1529/biophysj.106.101386
- VanLandingham, M. R., Villarrubia, J. S., Guthrie, W. F., and Meyers, G. F. (2001). Nanoindentation of polymers: an overview. *Macromol. Symp.* 167, 15–44. doi: 10.1002/1521-3900(200103)167:1<AID-MASY15>3.0.CO;2-T
- Wirtz, D. (2009). Particle-tracking microrheology of living cells: principles and applications. *Annu. Rev. Biophys.* 38, 301–326. doi: 10.1146/annurev.biophys.050708.133724
- Yim, E. K., and Sheetz, M. P. (2012). Force-dependent cell signaling in stem cell differentiation. *Stem Cell Res. Ther.* 3:41. doi: 10.1186/scrt132
- Zemła, J., Danilkiewicz, J., Orzechowska, B., Pabijan, J., Seweryn, S., and Lekka, M. (2018). Atomic force microscopy as a tool for assessing the cellular elasticity and adhesiveness to identify cancer cells and tissues. *Semin. Cell Dev. Biol.* 73, 115–124. doi: 10.1016/j.semcdb.2017.06.029

**Conflict of Interest Statement:** The authors declare that the research was conducted in the absence of any commercial or financial relationships that could be construed as a potential conflict of interest.

Copyright © 2018 Caluori, Pribyl, Pesl, Oliver-De La Cruz, Nardone, Skladal and Forte. This is an open-access article distributed under the terms of the Creative Commons Attribution License (CC BY). The use, distribution or reproduction in other forums is permitted, provided the original author(s) and the copyright owner(s) are credited and that the original publication in this journal is cited, in accordance with accepted academic practice. No use, distribution or reproduction is permitted which does not comply with these terms.



# Drug Repurposing for Duchenne Muscular Dystrophy: The Monoamine Oxidase B Inhibitor Safinamide Ameliorates the Pathological Phenotype in *mdx* Mice and in Myogenic Cultures From DMD Patients

Libero Vitiello<sup>1,2</sup>, Manuela Marabita<sup>3</sup>, Elisa Sorato<sup>4</sup>, Leonardo Nogara<sup>3</sup>, Giada Forestan<sup>4</sup>, Vincent Mouly<sup>5</sup>, Leonardo Salviati<sup>6</sup>, Manuel Acosta<sup>6</sup>, Bert Blaauw<sup>2,3,4</sup> and Marcella Canton<sup>3,4,6\*</sup>

<sup>1</sup> Department of Biology, University of Padova, Padova, Italy, <sup>2</sup> Interuniversity Institute of Myology, Padova, Italy, <sup>3</sup> Venetian Institute of Molecular Medicine (VIMM), Padova, Italy, <sup>4</sup> Department of Biomedical Sciences, University of Padova, Padova, Italy, <sup>5</sup> UMRS 974 UPMC-INSERM, Center for Research in Myology, Paris, France, <sup>6</sup> Fondazione Istituto di Ricerca Pediatrica Città della Speranza – IRP, Padova, Italy

## OPEN ACCESS

### Edited by:

Cesare Gargioli,  
Università degli Studi di Roma Tor  
Vergata, Italy

### Reviewed by:

Milica Marinkovic,  
Università degli Studi di Roma Tor  
Vergata, Italy  
Luca Madaro,  
Fondazione Santa Lucia (IRCCS), Italy

### \*Correspondence:

Marcella Canton  
marcella.canton@unipd.it

### Specialty section:

This article was submitted to  
Integrative Physiology,  
a section of the journal  
Frontiers in Physiology

**Received:** 13 April 2018

**Accepted:** 23 July 2018

**Published:** 14 August 2018

### Citation:

Vitiello L, Marabita M, Sorato E,  
Nogara L, Forestan G, Mouly V,  
Salviati L, Acosta M, Blaauw B and  
Canton M (2018) Drug Repurposing  
for Duchenne Muscular Dystrophy:  
The Monoamine Oxidase B Inhibitor  
Safinamide Ameliorates  
the Pathological Phenotype in *mdx*  
Mice and in Myogenic Cultures From  
DMD Patients. *Front. Physiol.* 9:1087.  
doi: 10.3389/fphys.2018.01087

Oxidative stress and mitochondrial dysfunction play a crucial role in the pathophysiology of muscular dystrophies. We previously reported that the mitochondrial enzyme monoamine oxidase (MAO) is a relevant source of reactive oxygen species (ROS) not only in murine models of muscular dystrophy, in which it directly contributes to contractile impairment, but also in muscle cells from collagen VI-deficient patients. Here, we now assessed the efficacy of a novel MAO-B inhibitor, safinamide, using *in vivo* and *in vitro* models of Duchenne muscular dystrophy (DMD). Specifically, we found that administration of safinamide in 3-month-old *mdx* mice reduced myofiber damage and oxidative stress and improved muscle functionality. *In vitro* studies with myogenic cultures from *mdx* mice and DMD patients showed that even cultured dystrophic myoblasts were more susceptible to oxidative stress than matching cells from healthy donors. Indeed, upon exposure to the MAO substrate tyramine or to hydrogen peroxide, DMD muscle cells displayed a rise in ROS levels and a consequent mitochondrial depolarization. Remarkably, both phenotypes normalized when cultures were treated with safinamide. Given that safinamide is already in clinical use for neurological disorders, our findings could pave the way toward a promising translation into clinical trials for DMD patients as a classic case of drug repurposing.

**Keywords:** muscular dystrophy, mitochondrial ROS, monoamine oxidase, oxidative stress, safinamide, DMD, *mdx*

## INTRODUCTION

Duchenne muscular dystrophy (DMD) is the one of the most common and severe forms of inherited muscular dystrophies. Despite improvements in palliative and support care, it is still invariably lethal because of cardiac-respiratory failure (Davies and Nowak, 2006; Shin et al., 2013), usually between the second and third decade of life. The only clinically available therapies rely on



steroid anti-inflammatory molecules, although a number of other drugs are presently in clinical trials (Rosenberg et al., 2015; Guiraud and Davies, 2017). Two genetic-based drugs have recently been approved for clinical use (Fairclough et al., 2013), but they are aimed at patients bearing defined mutations and their efficacy is still marginal.

Even though the genetic bases of most inherited muscular dystrophies have been characterized, the underlying pathogenic mechanisms remain somewhat elusive. Mitochondrial dysfunction has been shown to play a key role (Irwin et al., 2003; Angelin et al., 2007; Merlini et al., 2008; Millay et al., 2008; Palma et al., 2009; Menazza et al., 2010; Sorato et al., 2014; Chartier et al., 2015), although in the case of DMD, the mechanisms connecting lack of dystrophin, a sub-sarcolemmal protein, to mitochondrial alterations are unclear. A likely candidate is oxidative stress, as highlighted by several studies (Disatnik et al., 1998; Rando, 2002; Tidball and Wehling-Henricks, 2007; Williams and Allen, 2007; Whitehead et al., 2008; Lawler, 2011; Canton et al., 2014). In this regard, we previously demonstrated that monoamine oxidase (MAO), a mitochondrial enzyme widely studied in the central nervous system, is an essential source of reactive oxygen species (ROS) in dystrophic muscles (Menazza et al., 2010). The two isoforms of MAO, A and B, located in the outer mitochondrial membrane, catalyze the oxidative deamination of biogenic amines generating aldehydes, ammonia, and H<sub>2</sub>O<sub>2</sub>, which are removed by enzymatic scavengers in physiological conditions (Youdim et al., 2006). We have already reported that MAO expression and activity increase in muscles from two murine models of muscular dystrophies, *mdx* for DMD and *Col6a1*<sup>-/-</sup> mice for collagen VI-related myopathies (Menazza et al., 2010). This results in excessive levels of H<sub>2</sub>O<sub>2</sub>, which in turn alters the redox homeostasis and causes myofibrillar protein oxidation, hampering contractile function. Importantly, treatment with pargyline, an inhibitor of both MAO isoforms, reduced oxidation of tropomyosin and led to improvements in the phenotype of dystrophic mice (Menazza et al., 2010). The involvement of MAO in muscular dystrophy has also been seen in *in vitro* myoblasts cultures obtained from patients with collagen VI myopathies (Sorato et al., 2014). Specifically, in these cells, pargyline treatment reduced ROS accumulation and mitochondrial dysfunction, while normalizing the occurrence of apoptosis. These findings proved that MAO-dependent ROS accumulation is directly linked to mitochondrial dysfunction and suggested that it is upstream of the opening of the permeability transition pore (Sorato et al., 2014).

In our previous researches, pargyline was chosen as a “proof-of-principle” molecule in assessing MAO role in muscular dystrophy, thanks to its strong and irreversible inhibitory effect. However, its use in patients is hampered by significant side effects and its clinical use has been discontinued in favor of different, well-tolerated MAO inhibitors that are now commonly used in clinics for neurological disorders (Youdim et al., 2006). Among these, inhibitors specific for MAO-B, which are mainly used for treatment of Parkinson disease, have the advantage of not causing the severe side effects seen with drugs inhibiting MAO-A. In the present study, we investigate for the first time the specific role of MAO-B in cultured muscle cells from DMD

patients and in skeletal muscles of *mdx* mice, by using the novel pharmacological MAO-B inhibitor safinamide. Our data demonstrate that accumulation of ROS related to MAO-B activity not only plays a crucial role in the loss of cell viability and contractile impairment of dystrophic skeletal muscles but also in the mitochondrial dysfunction occurring in DMD myogenic cultures, thereby pointing at safinamide as a promising candidate for DMD therapy.

## MATERIALS AND METHODS

### Chemicals

Safinamide was kindly provided by Zambon SpA (batch 14A03C0483) and dissolved in water or phosphate-buffered saline (PBS). Unless otherwise stated, all chemicals used were purchased from Sigma-Aldrich.

### Mice and Safinamide *in vivo* Treatments

Wild-type C57BL/10ScSnJ and *mdx* mice (C57BL/10ScSn-*Dmd*<sup>mdx/J</sup>) were obtained from Charles River and Jackson Laboratories, respectively, and were bred and maintained in the animal facility of the Venetian Institute for Molecular Medicine (VIMM). Safinamide (20 or 40 mg/kg/day), prednisolone (2 mg/kg/day), or vehicle (PBS) were administered by daily intra peritoneal injection for 7 or 30 days in 3-month-old *mdx* and C57BL/10ScSn male mice. The doses of safinamide were chosen based on preliminary data obtained by ZambonGroup. At the end of the treatment, animals were first analyzed for force measurements and then sacrificed for muscle harvesting. Collected samples were then stored in liquid nitrogen until use. All *in vivo* experiments were approved by the Institutional Animal Care and Use Committee of the University of Padova.

### Muscle Functional Assessment

Muscle function *in vivo* was assessed for the *gastrocnemius* muscle, as described previously (Blaauw et al., 2008). Briefly, mice were anesthetized, and electrodes were placed on either side of the sciatic nerve, while the common peroneal nerve was cut. Muscle torque production was measured using a lever system (Aurora Scientific 305B). A lever arm of 2.1 mm was used for all groups, as no major differences in body weight between various groups was observed. Eccentric contractions were performed by moving the foot backward at a velocity of 40 mm/s while the *gastrocnemius* was stimulated with a frequency sufficient to induce full tetanic fusion (100 Hz). Contractions were repeated once every 20 s to avoid inducing fatigue.

### Analyses of Oxidation State in Skeletal Muscles

#### Dihydroethidium Staining

Dihydroethidium (DHE) is oxidized by ROS, forming ethidium bromide, which emits red fluorescence when intercalates with DNA (Benov et al., 1998). *Gastrocnemius* cryosections (10 μm thick) were incubated with 5 μM DHE (Sigma) for 30 min at 37°C in degassed PBS, washed twice in PBS, mounted and

visualized using an inverted microscope Leica DMI6000B, as previously described (Menazza et al., 2010). Data were acquired and analyzed using Metamorph software (Universal Imaging).

### Tropomyosin Oxidation

Assessment of tropomyosin oxidation was carried out by western blot analyses. Protein extracts were prepared homogenizing tissue samples in ice-cold PBS, pH 7.2 containing a protease inhibitor mix, subjected to PAGE, and then transferred onto nitrocellulose, as detailed in (Canton et al., 2006). Immunoblotting were then stained with an anti-tropomyosin antibody (anti-Tm, CH1 clone, Sigma-Aldrich). In anti-Tm immunoblots, the presence of high-molecular-mass bands was attributed to the oxidation-driven formation of disulphide cross-bridges (DCB), by comparing electrophoreses carried out in the absence or in the presence of  $\beta$ -mercaptoethanol, as previously described (Canton et al., 2006). Quantitation of Tm oxidation was performed by densitometric analysis of the bands obtained under non-reducing conditions, using the ImageJ software<sup>1</sup>. DCB density was normalized to the actin density in Red Ponceau, to account for differences in sample loading. Data were expressed as percentage of DCB relative to vehicle-treated *mdx* mice.

### Pathological Markers

Cross-sections (7  $\mu$ m thick) were prepared and processed for hematoxylin and eosin (H&E) staining. For the morphometric analysis of myofiber CSAs, we counted between 5000 and 6000 *gastrocnemius* fibers per mouse, by means of ImageJ software. Images were acquired from least three non-sequential sections from each muscle. The same images were also analyzed to assess the percentage of centrally nucleated fibers.

Membrane permeability of skeletal fibers, used as a marker of necrosis, was visualized by immunohistochemical staining with IgG (Blaauw et al., 2008). Cryosections (10  $\mu$ m thick) were incubated with anti-mouse fluorescein isothiocyanate-conjugated IgG, washed twice with PBS, mounted, and visualized with an Olympus IMT-2 inverted microscope as previously described (Menazza et al., 2010) using excitation/emission cubes of 488/525 + 25 nm bandpass.

### Creatine Kinase Assay

Serum creatine kinase (CK) was performed using a dedicated assay kit (BioAssay Systems, Hayward, CA, United States), following manufacturer's instructions. Blood was collected by cardiac puncture from animals anesthetized with pentobarbital. Immediately after bleeding, animals were killed by cervical dislocation. Sera were separated by centrifugation at 300  $\times$  g for 5 min and were stored at  $-80^{\circ}\text{C}$  until use.

### Myogenic Cell Cultures

Murine myoblasts were isolated from the diaphragm of 2- to 3-month-old *mdx* mice with a standard enzymatic (Collagenase I) digestion/serial pre-plating technique.

Primary DMD and control myoblasts were kindly provided by the "Telethon Bio-Bank" ("Besta" Neurology Institute, Milan,

Italy) and by the Neuroscience Department of the University of Padova. Primary myoblasts (both murine and human) were expanded in gelatin-coated dishes with proliferation medium: F12 medium (Invitrogen), 20% fetal bovine serum (FBS, Invitrogen), 5 ng/mL FGFb (Immunotools), penicillin-streptomycin mix (Invitrogen). Myoblast differentiation in myotubes was induced by switching confluent cultures to differentiate medium: high-glucose DMEM, 2% horse serum (Invitrogen), 10 mg/mL insulin (from bovine pancreas, Sigma-Aldrich), penicillin-streptomycin mix (Invitrogen). Immortalized human myoblasts, kindly provided by the Institut de Myologie (Pitié-Salpêtrière Hospital, Paris, France), had been obtained as described in Mamchaoui et al. (2011) by double transduction with hTERT and cdk4. Cells were expanded in proliferation medium: M199-DMEM mix (1:4 ratio), 20% FBS, Fétuin 25  $\mu$ g/ml (Invitrogen), hEGF 5 ng/ml (Immunotools), Insulin 5  $\mu$ g/ml (Sigma-Aldrich), Dexamethasone 0.2  $\mu$ g/ml (Sigma-Aldrich), 20% FBS, penicillin-streptomycin mix (Invitrogen). For differentiation, confluent cultures were exposed to a serum-free medium comprising DMEM (Invitrogen), insulin 10  $\mu$ g/ml (Sigma-Aldrich), and penicillin-streptomycin mix (Invitrogen) for 5–7 days.

### ROS Detection

Reactive oxygen species were detected using the fluorescent probe MitoTracker Red CM-H2XRos (MTR, Molecular Probes, Eugene, OR, United States). Myoblasts were seeded onto 24-mm diameter gelatine-coated glass coverslips placed in six-well plates, and then kept for 2 days in the appropriate growth medium. For myotubes, upon reaching confluence cells were switched to the appropriate differentiation medium and kept in culture for 6–8 days. For the experiments, cells were rinsed once and then incubated with either MAO inhibitor pargyline (100  $\mu$ M, determined from previous experiments) or 1  $\mu$ M safinamide for 20 min in serum-free media, followed by the addition of  $\text{H}_2\text{O}_2$  (100  $\mu$ M) or tyramine (100  $\mu$ M) for 45 min. Working concentration of safinamide was determined in preliminary experiments using a 0.5–4  $\mu$ M concentration range, which indicated 1  $\mu$ M as the lowest dose with highest response (data not shown). Finally, myoblasts were loaded with MTR (20 nM) for 15 min. All the steps were carried out at  $37^{\circ}\text{C}$  with 5%  $\text{CO}_2$ . Myoblasts were then washed twice, and the chambered coverslips were transferred to a Leica DMI6000B microscope, equipped with a digital camera. Mitochondrial fluorescence was measured in 10–15 random fields per chamber, and data were averaged per field. For each group, four to six chambers were analyzed. Experiments with the various compounds were always performed in parallel with their respective untreated controls. Fluorescence emission was monitored by using 560  $\pm$  20 nm excitation and 645  $\pm$  37 nm emission filter setting. Data were acquired and analyzed using Metafluor software (Universal Imaging).

### Mitochondrial Membrane Potential and Complex I Activity

Mitochondrial membrane potential was measured based upon the accumulation of tetramethylrhodamine methyl ester (TMRM,

<sup>1</sup><https://imagej.net/ImageJ1>

Molecular Probes) as previously described (Sorato et al., 2014). Myotubes from DMD patients and healthy donors were obtained as described above and treated with H<sub>2</sub>O<sub>2</sub> (100  $\mu$ M) for 30 min in the absence or presence of safinamide pre-treatment (1  $\mu$ M, added 20 min before hydrogen peroxide). Medium was then replaced with serum-free media supplemented with 25 nM TMRM for 30 min, and cellular fluorescence images were acquired with a Leica DMI6000B microscope. Data were acquired and analyzed using Metafluor software (Universal Imaging). For detection of fluorescence, 540  $\pm$  20 nm excitation and 590 nm long-pass emission filter settings were used. Clusters of several mitochondria were identified as regions of interest (ROI), and fields not containing cells were taken as the background. To exclude artifacts due to the different loading capacity of the various cells, which could be erroneously interpreted as  $\Delta\Psi$ m differences, sequential digital images were acquired before and after the addition of carbonyl cyanide-*p*-trifluoromethoxy-phenylhydrazone (FCCP, 4  $\mu$ M), a protonophore that fully depolarizes mitochondria.  $\Delta\Psi$ m was estimated as the difference in TMRM fluorescence intensity before and after FCCP of ROI from at least 30 cells. Experiments with the different agents as described above were always performed in comparison with untreated cells. Fluorescence values from the latter were considered as 100%. Complex I activity was measured in myotube lysates using the specifically designed spectrophotometric assay described in Spinazzi et al. (2012).

## Data Analysis and Statistical Procedures

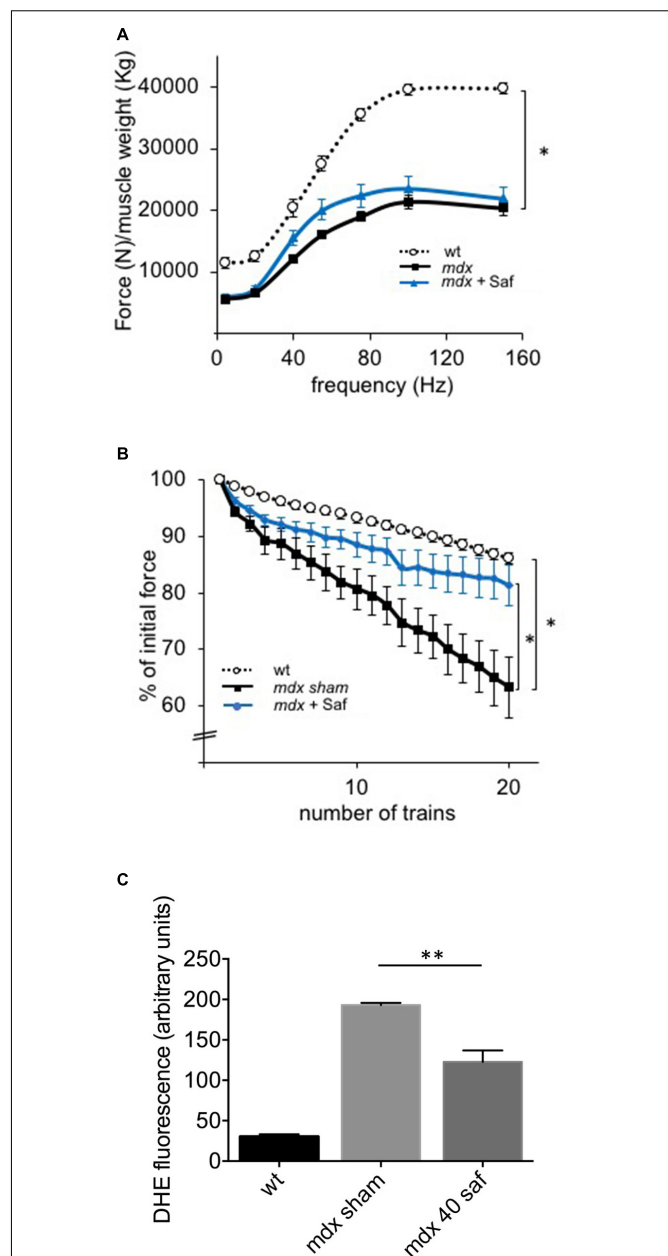
Data are expressed as the mean  $\pm$  SEM. Analyses were carried out using ANOVA ordinary one-way test followed by Tukey's multiple comparison test using the Prism software; values with  $p < 0.05$  were considered significant.

## RESULTS

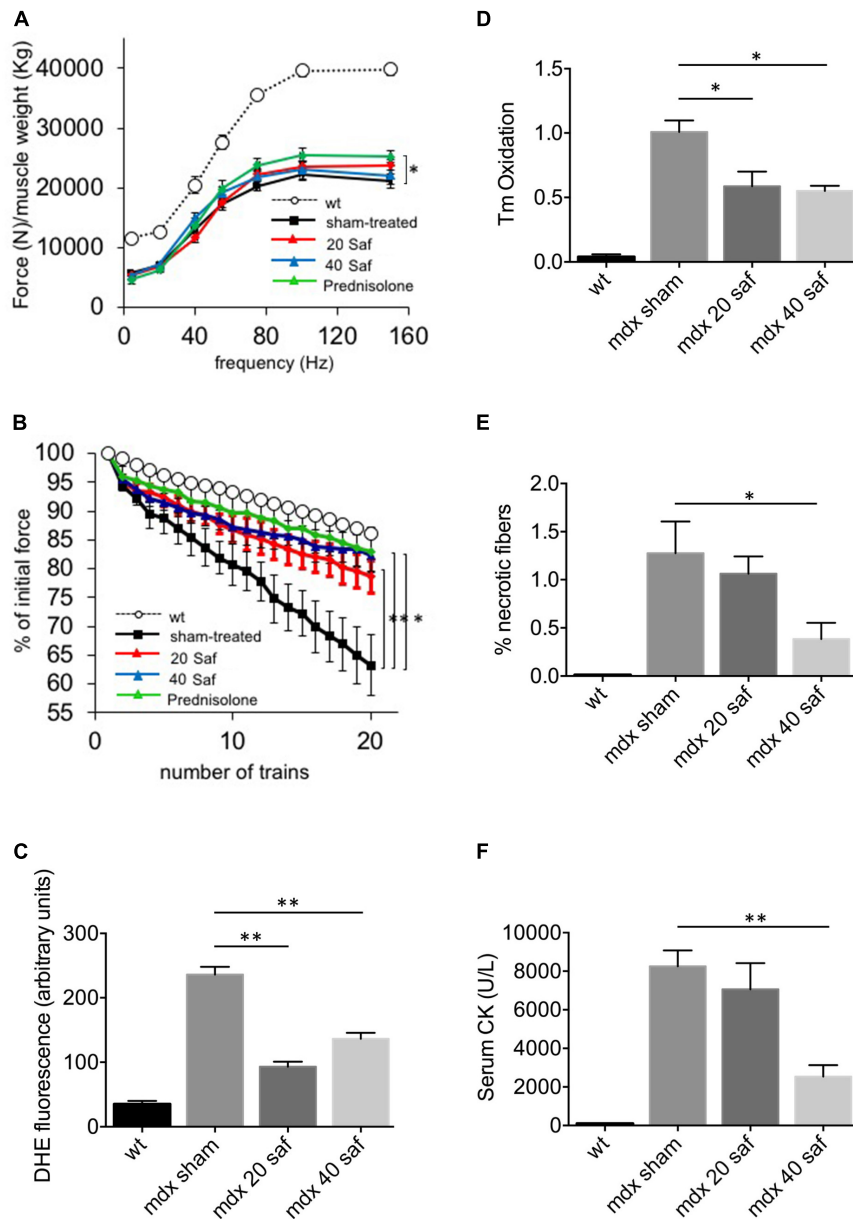
### Treatment of mdx Mice With Safinamide Ameliorates Muscle Pathology

In the first round of *in vivo* experiments, adult *mdx* mice (3-month-old) were subjected to daily intraperitoneal delivery of safinamide (40 mg/kg/day) for 1 week. At the end of the treatment, mice were subjected to a set of *in vivo* force measurements after electrical stimulation of the sciatic nerve as described in the M&M section, after which they were sacrificed to harvest specific muscles for further analyses. Even though safinamide did not lead to significant improvements in normalized force (Figure 1A), treated animals showed a strong and significant reduction in force drop upon eccentric contractions, a typical hallmark of dystrophic muscles (Figure 1B). Upon harvesting, *gastrocnemius* muscles were then sectioned and subjected to DHE staining to quantify intracellular ROS. Our findings indicated a significant reduction in the extent of oxidative stress between treated and control mice (Figure 1C).

A second cohort of *mdx* mice was then treated for a longer period, 1 month, and with two different doses of safinamide (20 and 40 mg/kg/day), with the same administration protocol. Once again, muscle function was then assessed *in vivo* in terms



**FIGURE 1** | One-week treatment with safinamide rescued functional alterations and oxidative stress in *mdx* mice. Three-month-old *mdx* mice were treated for 7 days with intra-peritoneal injections of either safinamide (40 mg/kg/day) or vehicle alone ( $n = 8$  for each condition). Eight syngeneic, wild-type animals were used as reference. **(A)** *In vivo* force–frequency curves of GC muscles from sham- or safinamide-treated *mdx* mice showed the expected drop in normalized force compared to wild type, but no significant improvement with safinamide. **(B)** *In vivo* recordings during eccentric contractions showed a reduced force drop (measured as percent of initial force after 20 eccentric contraction *in vivo*) in safinamide-treated compared to sham-treated animals. **(C)** Quantification of DHE fluorescence in *gastrocnemius* muscle cryosections from mice treated with vehicle alone (sham) or with safinamide showed reduced ROS accumulation after safinamide treatment. **(C)** Value from wild-type animals was statistically different from those found in both *mdx* counterparts; significance bars were omitted for the sake of chart readability. Data are expressed as mean  $\pm$  SEM; \* $p < 0.05$  and \*\* $p < 0.01$ .



**FIGURE 2** | One-month treatment with safinamide rescued functional alterations, oxidative stress, and fiber degeneration in *mdx* mice. Three-month mice were treated for 30 days with intra-peritoneal injections of either safinamide (20 or 40 mg/kg/day), prednisolone, or vehicle alone ( $n = 6$  for each condition). Eight syngeneic, wild-type animals were used as reference. **(A)** Force–frequency curves of gastrocnemius muscles from vehicle-treated or safinamide-treated mice showed no significant improvement of normalized force in safinamide-treated animals. **(B)** *In vivo* recordings during eccentric contractions showed a reduced force drop (measured as percent of initial force after 20 eccentric contraction *in vivo*) in safinamide-treated compared to sham-treated animals. **(C)** Quantification of DHE fluorescence in gastrocnemius muscle cryosections from sham- and safinamide-treated mice. **(D)** Oxidation of tropomyosin in gastrocnemius muscles from sham- and safinamide-treated mice. Y axis reports the amounts of oxidized tropomyosin normalized to that present in sham-treated animals. **(E)** Quantification of the necrotic fibers by means of immunohistochemical staining for IgG in gastrocnemius muscle from sham- and safinamide-treated mice. Y axis reports the amounts of oxidized tropomyosin normalized to that present in sham-treated animals. **(F)** Quantification of the levels of creatine kinase (CK) in the blood of sham- and safinamide-treated mice. **(A,C–F)** values from wild-type animals were always statistically different from those found in all *mdx* counterparts; significance bars were omitted for the sake of chart readability. Data are expressed as mean  $\pm$  SEM; \* $p < 0.05$  and \*\* $p < 0.01$ .

of resistance to eccentric contractions and of normalized force production. Both safinamide regimens induced a significant improvement in the resistance against eccentric contractions (Figure 2A), while no significant improvement in normalized

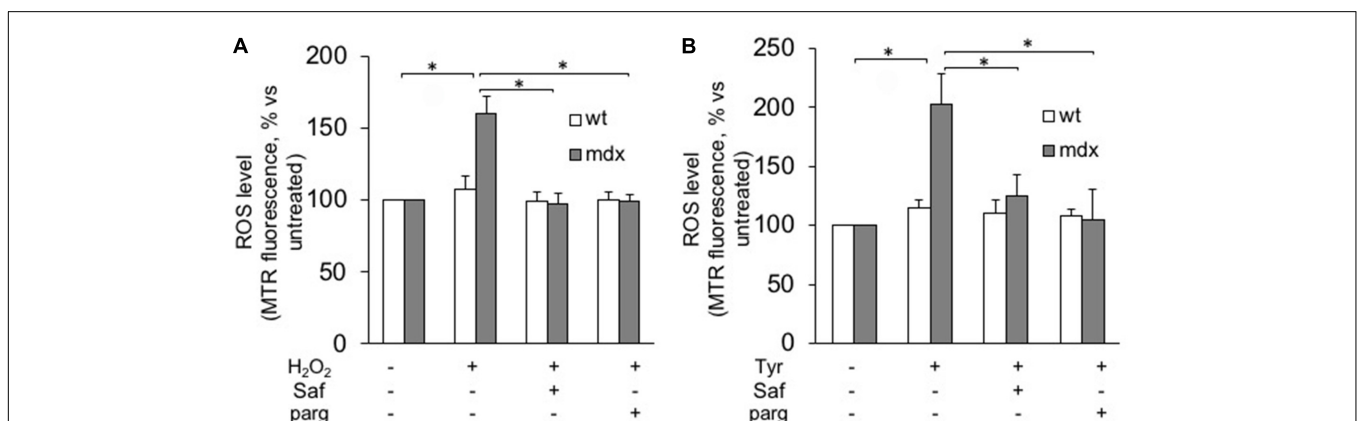
force could be found in safinamide-treated *mdx* mice compared to controls (Figure 2B). In parallel, a set of *mdx* mice was treated for the same length of time with the glucocorticoid prednisolone (i.p., 2 mg/kg/day), the standard treatment for DMD patients

which is also effective in mice (Keeling et al., 2007 and references therein). Interestingly, the functional improvement found in these mice was comparable to that found with safinamide in the eccentric contraction tests, while the effect on normalized force reached statistical significance only in prednisolone-treated mice (Figures 2A,B). DHE staining on *gastrocnemius* sections were in agreement with the results of the short-term experiments, as they confirmed that both safinamide regimens significantly reduced intracellular ROS (Figure 2C and Supplementary Figure S1). In addition, in these animals, we measured the levels of tropomyosin oxidation, in order to verify whether MAO-B-dependent ROS accumulation could cause oxidative modifications of myofibrillar proteins. The rationale of this choice relied on our previous observation that, among myofibrillar proteins, tropomyosin is particularly susceptible to oxidative stress (Canton et al., 2006; Menazza et al., 2010). We observed a marked reduction in oxidation of tropomyosin with both safinamide treatments (Figure 2D and Supplementary Figure S1). To investigate whether other pathological features found in dystrophic muscles had been affected by the 1-month treatment, we then quantified the number of necrotic fibers present in the *gastrocnemius* muscles of treated and control mice by immunofluorescence, using an anti-murine IgG antibody to label fibers containing serum immunoglobulin in their sarcoplasm. In this case, safinamide at 40 mg/kg led to a significant reduction in the percentage of necrotic fibers (Figure 2E and Supplementary Figure S2). Since necrosis of muscle fibers leads to a steep increase in circulating CK, making it a hallmark of Duchenne dystrophy in humans and in mice, we also compared serum CK levels between treated and untreated animals. Figure 2F shows how the treatment with 40 mg/kg safinamide led to an almost fourfold reduction of CK activity in serum. Finally, we also performed standard histological evaluations of the sections (by means of H&E staining), analyzing the percentage of centrally nucleated fibers and the distribution of fiber diameters, both indicators of the regenerative status of a striated muscle. No

differences were found between treated and control animals in either case (Supplementary Figure S2).

## Safinamide Reduces Oxidative Stress and Mitochondrial Dysfunction in Murine Dystrophic Myoblasts

Next, we isolated myoblasts from *mdx* and *wild-type* mice and proceeded to evaluate their susceptibility to oxidative stress. To this aim, we used a protocol that we and others had already exploited to mimic the oxidative stress occurring in several disease states (Disatnik et al., 1998; Sorato et al., 2014), in which proliferating myoblasts are exposed to hydrogen peroxide (100  $\mu$ M) for 1 h in the presence or in the absence of MAO inhibitors. The rationale of such treatment is that both muscles from *mdx* mice and DMD patients are constantly exposed to high levels of ROS produced by the infiltrated phagocytic cells (Chen and Nunez, 2010). Among them, hydrogen peroxide is more stable and diffuses through membranes. In our experiments, we tested safinamide at a 1- $\mu$ M concentration, as well as pargyline, a strong, first-generation inhibitor of both MAO-A and MAO-B, at 100  $\mu$ M. After the challenge with hydrogen peroxide, ROS levels were assessed by exposing muscle cells to a redox sensitive fluorescent probe (Mitotracker, CM-H<sub>2</sub>XRos) and measuring the corresponding fluorescence emission (Sorato et al., 2014). Our data show that this protocol greatly increased ROS levels in *mdx* but not in *wild-type* myoblasts and, importantly, such accumulation was suppressed by treatment with safinamide and pargyline (Figure 3A and Supplementary Figure S3). The effect elicited by MAO-B inhibition appears superimposable to that induced by inhibiting both MAO isoforms. It should be noticed that no obvious morphological signs of cell death were detected in any condition with either *mdx* or *wild-type* cells (data not shown), a somewhat expected observation given the combination of relatively low hydrogen peroxide concentration and short time of exposure.



**FIGURE 3 |** MAO-B inhibition reduces ROS accumulation in response to oxidative stress in myoblasts from *mdx* mice. Myoblasts from *mdx* and *wild-type* (wt) mice were incubated for 1 h with (A) H<sub>2</sub>O<sub>2</sub> (100  $\mu$ M) or (B) tyramine (Tyr, 100  $\mu$ M) in the absence or in the presence of 1  $\mu$ M safinamide or 100  $\mu$ M pargyline (parg). ROS levels were assessed by Mitotracker Red CM-H<sub>2</sub>XRos (MTR, 25 nM). Data expressed as the MTR fluorescence after 1 h from the addition of H<sub>2</sub>O<sub>2</sub> (or Tyr) were normalized to the values obtained in the absence of stimuli for each sample. Data are the mean  $\pm$  SEM of three experiments, each using cells originating from different preps. \* $p$  < 0.05 and \*\* $p$  < 0.01.

Next, we assessed the role of MAO and its activity in an alternative way, by incubating our murine myoblasts with tyramine, a typical MAO substrate whose oxidative deamination generates hydrogen peroxide as a by-product. Once again, higher levels of ROS were detected in *mdx* myoblasts as compared with *wild-type* cells, and they were blunted by safinamide treatment (Figure 3B). Finally, it should be noticed that in the absence of the above-described stressors no significant differences in ROS levels were observed between *mdx* and *wild-type* myoblasts (not shown).

## Safinamide Reduces Oxidative Stress and Mitochondrial Dysfunction in Human Dmd Myoblasts and Myotubes

The efficacy of safinamide in reducing ROS formation was then tested in myoblasts and myotubes obtained from cultured human myoblasts. Specifically, we used primary cultures derived from muscle biopsies (one healthy donor and two DMD patients), as well as immortalized myoblasts (Mamchaoui et al., 2011) (two healthy donors and two DMD patients, see Table 1 for details). The rationale of using both primary and immortalized cells derived from the fact that we wished to rule out the possible effect of two potentially relevant drawbacks commonly found in the former, namely a relatively low myogenicity and the unavoidable presence in the cultures of varying amounts of non-myogenic cells (Mamchaoui et al., 2011).

Similarly to what had been done with murine cells, human myogenic cultures were challenged with hydrogen peroxide in the presence or in the absence of MAO inhibitors. In this

case, though, the experiments were performed not only on cultured myoblasts but also on differentiated myotubes. For the former, Figure 4A shows how ROS levels increased upon exposure to hydrogen peroxide in primary DMD myoblasts and, importantly, that once again they were brought back to the levels found in non-dystrophic cells by the treatment with safinamide. Importantly, the hydrogen peroxide challenge did not affect myoblasts from healthy donors, in accordance with our present data in murine cells and with our previous data in human cells (Sorato et al., 2014). The same type of experiment was then performed on myotubes differentiated from the same cell preparations. Similarly to myoblasts, upon exposure to hydrogen peroxide DMD myotubes were found to be more susceptible to oxidative stress than myotubes from healthy donors and the rise in ROS levels was prevented by safinamide (Figure 4B).

Next, we investigated whether these findings held true in cultures comprising only myoblasts, thanks to the use of the above-mentioned immortalized cell lines. Upon hydrogen peroxide stimulation, both myoblasts (Figure 5A and Supplementary Figure S4) and myotubes (Figure 5B and Supplementary Figure S4) from immortalized DMD cells displayed increased ROS levels, which were reduced to levels comparable to those found in controls by the inhibition of MAO-B. As in primary cultures, hydrogen peroxide challenge had no effect on the ROS levels found in cells derived from healthy donors. These finding not only confirmed the increased susceptibility of DMD cells to oxidative stress but also indicated that the biological mechanism(s) leading to such phenomenon were indeed intrinsic to the myogenic cells and did not depend on the interaction with the non-myogenic fraction of primary cultures.

Finally, we also assessed the effect of safinamide on mitochondrial membrane potential, by means of the fluorescent probe TMRM, after inducing oxidative stress with hydrogen peroxide. Similarly to what was seen with ROS levels, the presence of hydrogen peroxide had a marked effect in DMD myotubes – namely, a reduction in mitochondrial membrane potential – but not in control cells. Once again, treatment with safinamide prevented such drop (Figure 6). We hypothesized

TABLE 1 | Patients' description.

	Age at time of biopsy	Type of mutation
DMD 1 (primary cells)	24 months	Del ex 44
DMD 2 (primary cells)	24 months	Del ex 8–17
DMD 3 (immortalized cells)	20 months	Del ex 48–50
DMD 4 (immortalized cells)	20 months	Del ex 45–52

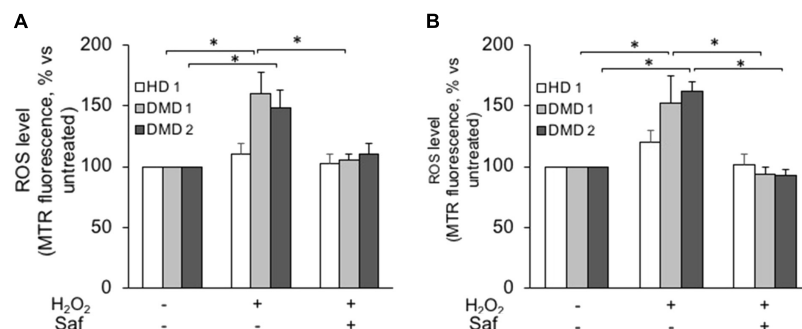
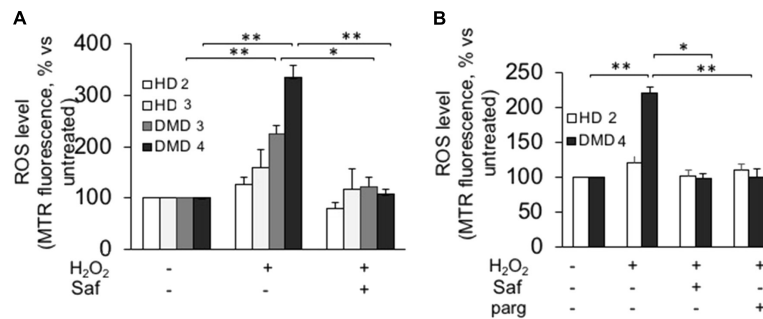


FIGURE 4 | MAO-B inhibition decreases ROS accumulation in response to oxidative stress in primary cultured myoblasts and myotubes from DMD patients. Primary myoblasts (A) or myotubes (B) from one healthy donor (HD 1) and DMD patients (DMD 1 and DMD 2) were loaded with Mitotracker Red CM-H<sub>2</sub>XRos (MTR, 25 nM). Oxidative stress was induced by H<sub>2</sub>O<sub>2</sub> addition (100 μM) with or without 1 μM safinamide, as a 20-min pre-treatment. Data expressed as the MTR fluorescence after 1 h from H<sub>2</sub>O<sub>2</sub> were normalized to the values obtained in the absence of stimuli for each sample. Data are the mean ± SEM of three experiments per cell prep. \**p* < 0.05.



**FIGURE 5 |** MAO-B inhibition reduces ROS accumulation in response to H<sub>2</sub>O<sub>2</sub> in immortalized cell lines from DMD patients. Immortalized myoblasts (**A**) and myotubes (**B**) obtained from healthy donors (HD 2 and HD 3) and DMD patients (DMD 3 and DMD 4) were loaded with Mitotracker Red CM-H<sub>2</sub>XRos as described in **Figure 4**. Oxidative stress was induced by H<sub>2</sub>O<sub>2</sub> addition (100  $\mu$ M) in the absence or presence of 1  $\mu$ M safinamide or 100  $\mu$ M pargyline, as a 20 min pre-treatment. Data expressed as the MTR fluorescence after 1 h from H<sub>2</sub>O<sub>2</sub> were normalized to the values obtained in the absence of stimuli for each sample. Data are the mean  $\pm$  SEM of three experiments per cell prep. \* $p < 0.05$  and \*\* $p < 0.01$ .

that the increased levels of ROS in DMD myotubes could affect mitochondrial membrane potential by decreasing the activity of the respiratory chain. For this reason, we evaluated the activity of Complex I in myotubes from a healthy donor and a DMD patient used for membrane potential determination, but found no differences between the two (data not shown).

## DISCUSSION

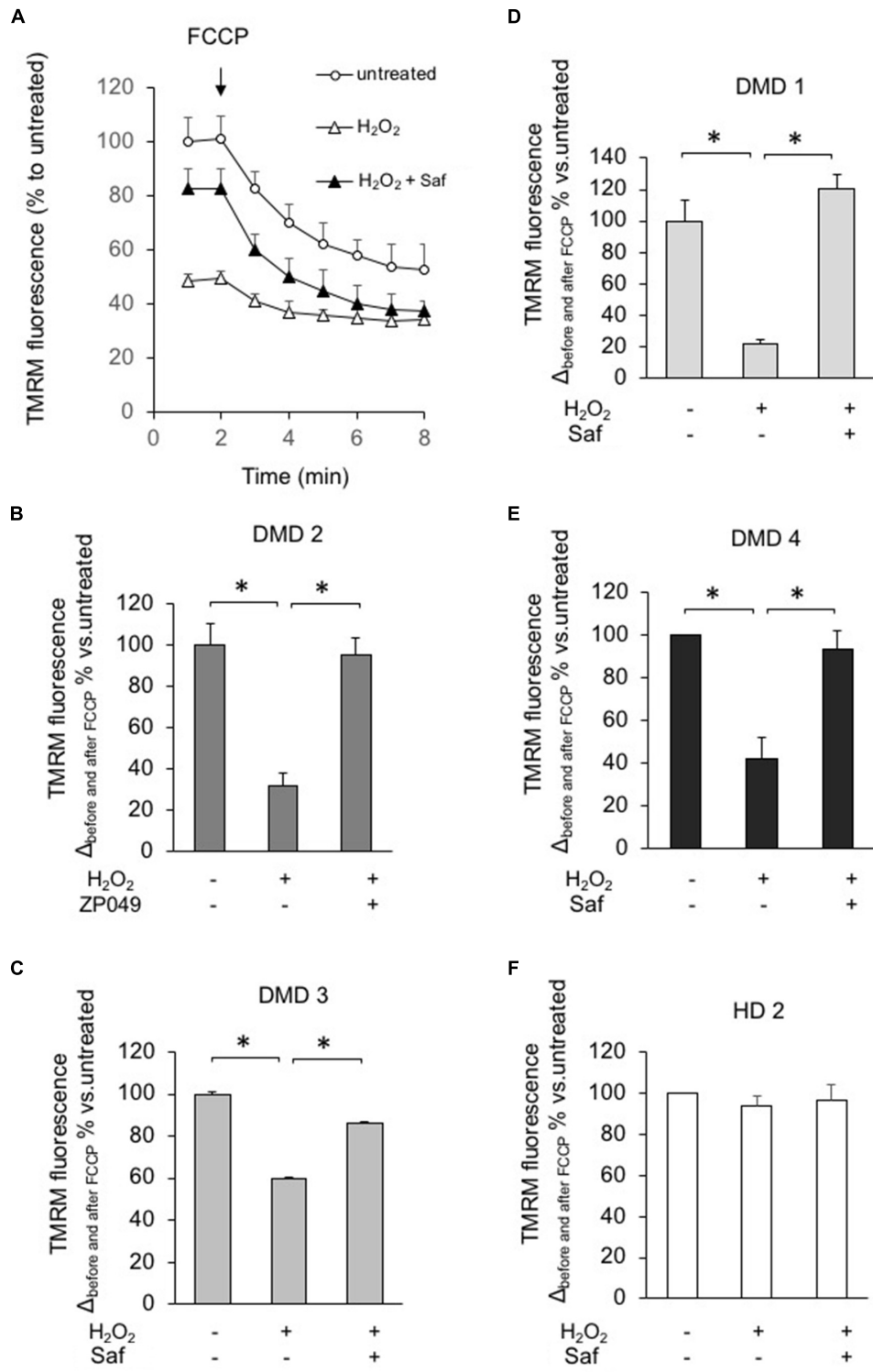
Many biological and medical issues related to muscular dystrophies are far from being conclusively addressed, thus hampering the development of adequate interventions. The identification and exploitation of novel pharmacological agents is, therefore, urgently needed to improve clinical management of Duchenne patients. The data, we present here, investigate the mitochondrial enzyme MAO-B as a promising target toward such goal. In particular, building on our previous findings, the present study provides two novel aspects: (i) in the context of DMD, MAO-B plays a key role in determining oxidative stress, and (ii) a novel inhibitor for this isoform significantly improves functional impairment occurring in *mdx* mice and can protect myotubes of DMD patients from mitochondrial dysfunction.

The first part of our study has been carried out *in vivo*, analyzing both force production and histo-pathological features. For the former, we investigated two parameters: force loss upon eccentric contractions and normalized force. The rationale of this choice is that one of the main aspects of DMD, as well as other muscular dystrophies, is the susceptibility of skeletal muscles to activity-induced muscle damage (Blaauw et al., 2010; Rader et al., 2016). While the exact molecular mechanism(s) behind the increased sensitivity to eccentric contractions is not known, multiple reports have shown that reducing oxidative stress can be beneficial (Whitehead et al., 2008). Furthermore, a central role of mitochondria in activity-dependent increases in pathological oxidative stress has also been reported in a different kind of myopathy, i.e., central core disease (Durham et al., 2008). Our data indicate that in *mdx* mice the MAO-B-dependent increase in mitochondrial

ROS production plays an important role in decreasing force production during repeated eccentric contractions. Interestingly, the positive effect of inhibiting MAO-B could be seen even after a short (1 week) treatment, suggesting a mechanism that does not involve extensive tissue remodeling. While specific experiments will be needed to clarify this point, it is tempting to hypothesize that the molecular mechanism(s) involved in the positive effect of safinamide on rescuing activity-induced force loss are related to an increase in calcium levels within the mitochondria due to the opening of stretch-dependent calcium channels (Yeung et al., 2005). As for the normalized force production, treated animals consistently yield higher values than controls, but the differences never reached statistical significance, hence suggesting that ROS levels are not a main player in the mechanism(s) leading to the decreased isometric force in *mdx* muscles, or longer treatment periods are required to induce significant changes.

Analysis of muscle sections in treated animals confirmed that safinamide did decrease ROS levels in the fibers of treated animals as well as the oxidative status of a key component of the contractile apparatus (tropomyosin), hence providing new insights on the molecular mechanism(s) linking dystrophin deficiency to protein oxidation. Under the histopathological point of view, our data also showed that MAO-B inhibition provided a significant protection from fiber degeneration, as demonstrated by the decrease in CK serum levels and by the lower count of necrotic fibers. These findings suggest that the end mechanism(s) leading to fiber death are linked, at least in part, to the excessive production of ROS. On the other hand, our analyses of fiber size and percentage of central nuclei did not show any effect of safinamide, thereby suggesting that, at least in our experimental setting, changes in the levels of intracellular ROS do not affect the processes of muscle regeneration. In order to confirm such hypothesis, though, specific experiments with animals treated with safinamide at a younger age (i.e., before or during the occurrence of the initial massive degeneration/regeneration bout) will be needed.

In view of a possible drug repurposing, it is also important to stress how the functional benefits obtained with safinamide were



**FIGURE 6 |** MAO-B inhibition reduces mitochondrial dysfunction in response to H<sub>2</sub>O<sub>2</sub> in myotubes from DMD patients. DMD or HD myotubes (from primary and immortalized cells) were exposed to H<sub>2</sub>O<sub>2</sub> (100  $\mu$ M) in the absence or presence of 1  $\mu$ M safinamide, as a 20 min pre-treatment and then loaded with TMRM (25 nM) to monitor the mitochondrial membrane potential  $\Delta\Psi_m$ . **(A)** Representative kinetics of TMRM fluorescence intensity in one experiment with primary myotubes from patient DMD2. Single data points are the average of at least 15 individual myotubes. When indicated, FCCP (4  $\mu$ M) was added to collapse  $\Delta\Psi_m$ . In the absence of safinamide, H<sub>2</sub>O<sub>2</sub> treatment caused a drastic drop in the initial membrane potential, which led to a small difference in  $\Delta\Psi_m$  before and after FCCP. **(B–F)** Charts representing the variation in TMRM fluorescence intensities obtained in each condition before and after FCCP; one chart per cell type. Values in Y axis are expressed as percentage, considering the value in untreated cells as 100%. Each cell type was analyzed in two independent experiments. \**p* < 0.05.



quite similar to those seen in our animals upon treatment with prednisolone, one of the glucocorticoids that at present represent the only standard therapy for Duchenne patients. Such finding is even more relevant in view of the fact that while glucocorticoids are usually effective in delaying loss of ambulation (McDonald et al., 2018), their chronic use present severe side-effects (e.g., severe bone demineralization) that in many cases can actually force discontinuation. On the other hand, the new generation of MAO-B inhibitors to which safinamide belongs exerts far fewer unwanted side-effects, not only compared to glucocorticoids but also to the older, non-specific MAO inhibitors. MAO-B molecular structure has been identified at high resolution (Binda et al., 2002, 2004), thus allowing the design of highly specific inhibitors that have the advantage to avoid the risk of hypertensive crises that is associated to inhibition of the MAO-A isoform. Indeed, MAO-B specific inhibitors are currently used in treatment of several neurological disorders (Youdim et al., 2006).

The involvement of mitochondria in DMD pathogenesis has been reported both in patients and in animal models, for instance in terms of deficit of electron transport respiratory chain components and of enzymes of the tricarboxylic acid cycle (Timpani et al., 2015). As a downstream consequence, the ATP levels in these muscles were found to be severely reduced causing altered ionic homeostasis and oxidative stress (Rodriguez and Tarnopolsky, 2003; Ramadasan-Nair et al., 2014). Our *in vitro* experiments with murine and human myoblast cultures clearly indicated that cells derived from dystrophic muscles have a higher susceptibility to oxidative stress compared to non-dystrophic counterparts. To the best of our knowledge, this is the first study that explores the source of excess ROS in myogenic cultures isolated from DMD patients, establishing a causal relationship between MAO-B-dependent increased ROS levels and mitochondrial dysfunction.

A remarkable aspect of our findings is that in dystrophic cells higher sensitivity to oxidative stress appears to be independent from dystrophin expression, given that in *in vitro* cultures the dystrophin gene is expressed in myotubes but not in myoblasts. This finding is in agreement with previous studies showing that the impaired metabolism observed in *mdx* myoblasts was independent of dystrophin-deficiency (Onopiuk et al., 2009). In this regard, it should be noticed that recent evidences have demonstrated the expression of dystrophin in activated satellite cells, where it plays an important role in establishing their capability for asymmetric division (Dumont et al., 2015). The authors also confirmed the absence of dystrophin in proliferating myoblasts and while they did not investigate the exact timing and mechanism of disappearance, they showed that already at 72 h after activation of satellite cells dystrophin could be seen only in a small proportion of them. For these reasons, our evidences indicate that myoblasts derived from a dystrophic muscle maintain a series of metabolic alterations even after prolonged *in vitro* cultures; the presence of specific epigenetic markings originated *in vivo* in the context of dystrophic muscle seems to be a likely explanation, although specific experiments will be needed to confirm this hypothesis. In this regard, it is interesting to notice that Disatnik et al. (1998) reported no increased sensitivity to oxidative stress in myoblasts cultures

prepared from newborn *mdx* mice, a developmental stage in which there is no overt dystrophic phenotype. The use of both primary and immortalized cells allowed us to demonstrate that the molecular mechanisms leading to the peak of oxidative stress present in DMD cells take place specifically within myoblasts. By the same token, the fact that in our assays immortalized cells showed the same phenotype found in primary cultures further confirms that the former are a reliable alternative to the latter, while presenting clear advantages in terms of long-term availability and reproducibility.

At present, our findings do not provide indications about the mechanisms linking MAO-mediated oxidative stress to mitochondrial depolarization. As a preliminary attempt, we verified whether the accumulation of ROS in DMD myotubes affected the activity of NADH dehydrogenase, the complex of the respiratory chain that is more susceptible to oxidative stress, but found no differences between healthy donor and DMD cells. Further studies will be aimed at characterizing the molecular targets of MAOB-dependent ROS increased levels.

Overall, these results provide clear evidence of safinamide efficacy in reducing oxidative stress in dystrophic skeletal muscle. Importantly, though, safinamide treatment should not be considered just another case of antioxidant therapy, as it does not act as a general ROS scavenger. Such an approach could actually be cause of some concerns, considering that small amounts of ROS are required for intracellular signaling. On the contrary, safinamide act by specifically preventing the formation of a subset of mitochondrial ROS that becomes disproportionate in pathological conditions because of MAO over activation.

## AUTHOR CONTRIBUTIONS

BB and MC contributed conception and design of the study. LV, MM, ES, LN, GF, MA, BB, and MC performed the experiments and the subsequent data analyses. VM provided the immortalized cells and contributed to the drafting of the manuscript. MA and LS contributed conception of specific experiments. LV, MC, and BB wrote the manuscript.

## FUNDING

This work was supported by Zambon SpA, Italy to MC.

## ACKNOWLEDGMENTS

We gratefully acknowledge Carolina Soccol for assistance with the experiments; Elsa Melloni (Zambon SpA), Gloria Padoani (Zambon SpA), Claudia Forni (Zambon SpA), Silvia Vailati (Zambon SpA), and Luca Bello for helpful discussion.

## SUPPLEMENTARY MATERIAL

The Supplementary Material for this article can be found online at: <https://www.frontiersin.org/articles/10.3389/fphys.2018.01087/full#supplementary-material>

## REFERENCES

- Angelin, A., Tiepolo, T., Sabatelli, P., Grumati, P., Bergamin, N., Golfieri, C., et al. (2007). Mitochondrial dysfunction in the pathogenesis of Ullrich congenital muscular dystrophy and prospective therapy with cyclosporins. *Proc. Natl. Acad. Sci. U.S.A.* 104, 991–996. doi: 10.1073/pnas.0610270104
- Benov, L., Szejnberg, L., and Fridovich, I. (1998). Critical evaluation of the use of hydroethidine as a measure of superoxide anion radical. *Free Radic. Biol. Med.* 25, 826–831. doi: 10.1016/S0891-5849(98)00163-4
- Binda, C., Hubalek, F., Li, M., Edmondson, D. E., and Mattevi, A. (2004). Crystal structure of human monoamine oxidase B, a drug target enzyme monotonically inserted into the mitochondrial outer membrane. *FEBS Lett.* 564, 225–228. doi: 10.1016/S0014-5793(04)00209-1
- Binda, C., Newton-Vinson, P., Hubalek, F., Edmondson, D. E., and Mattevi, A. (2002). Structure of human monoamine oxidase B, a drug target for the treatment of neurological disorders. *Nat. Struct. Biol.* 9, 22–26. doi: 10.1038/nsb732
- Blaauw, B., Agatea, L., Toniolo, L., Canato, M., Quarta, M., Dyar, K. A., et al. (2010). Eccentric contractions lead to myofibrillar dysfunction in muscular dystrophy. *J. Appl. Physiol.* 108, 105–111. doi: 10.1152/jappphysiol.00803.2009
- Blaauw, B., Mammucari, C., Toniolo, L., Agatea, L., Abraham, R., Sandri, M., et al. (2008). Akt activation prevents the force drop induced by eccentric contractions in dystrophin-deficient skeletal muscle. *Hum. Mol. Genet.* 17, 3686–3696. doi: 10.1093/hmg/ddn264
- Canton, M., Menazza, S., and Di Lisa, F. (2014). Oxidative stress in muscular dystrophy: from generic evidence to specific sources and targets. *J. Muscle Res. Cell Motil.* 35, 23–36. doi: 10.1007/s10974-014-9380-2
- Canton, M., Skyschally, A., Menabò, R., Boengler, K., Gres, P., Schulz, R., et al. (2006). Oxidative modification of tropomyosin and myocardial dysfunction following coronary microembolization. *Eur. Heart J.* 27, 875–881. doi: 10.1093/eurheartj/ehi751
- Chartier, A., Klein, P., Pierson, S., Barbezier, N., Gidaro, T., Casas, F., et al. (2015). Mitochondrial dysfunction reveals the role of mRNA poly(A) tail regulation in oculopharyngeal muscular dystrophy pathogenesis. *PLoS Genet.* 11:e1005092. doi: 10.1371/journal.pgen.1005092
- Chen, G. Y., and Nunez, G. (2010). Sterile inflammation: sensing and reacting to damage. *Nat. Rev. Immunol.* 10, 826–837. doi: 10.1038/nri2873
- Davies, K. E., and Nowak, K. J. (2006). Molecular mechanisms of muscular dystrophies: old and new players. *Nat. Rev. Mol. Cell Biol.* 7, 762–773. doi: 10.1038/nrm2024
- Disatnik, M. H., Dhawan, J., Yu, Y., Beal, M. F., Whirl, M. M., Franco, A. A., et al. (1998). Evidence of oxidative stress in mdx mouse muscle: studies of the pre-necrotic state. *J. Neurol. Sci.* 161, 77–84. doi: 10.1016/S0022-510X(98)00258-5
- Dumont, N. A., Wang, Y. X., von Maltzahn, J., Pasut, A., Bentzinger, C. F., Brun, C. E., et al. (2015). Dystrophin expression in muscle stem cells regulates their polarity and asymmetric division. *Nat. Med.* 21, 1455–1463. doi: 10.1038/nm.3990
- Durham, W. J., Aracena-Parks, P., Long, C., Rossi, A. E., Goonasekera, S. A., Boncompagni, S., et al. (2008). RyR1 S-nitrosylation underlies environmental heat stroke and sudden death in Y522S RyR1 knockin mice. *Cell* 133, 53–65. doi: 10.1016/j.cell.2008.02.042
- Fairclough, R. J., Wood, M. J., and Davies, K. E. (2013). Therapy for Duchenne muscular dystrophy: renewed optimism from genetic approaches. *Nat. Rev. Genet.* 14, 373–378. doi: 10.1038/nrg3460
- Guiraud, S., and Davies, K. E. (2017). Pharmacological advances for treatment in Duchenne muscular dystrophy. *Curr. Opin. Pharmacol.* 34, 36–48. doi: 10.1016/j.coph.2017.04.002
- Irwin, W. A., Bergamin, N., Sabatelli, P., Reggiani, C., Megighian, A., Merlini, L., et al. (2003). Mitochondrial dysfunction and apoptosis in myopathic mice with collagen VI deficiency. *Nat. Genet.* 35, 367–371. doi: 10.1038/ng1270
- Keeling, R. M., Golumbek, P. T., Streif, E. M., and Connolly, A. M. (2007). Weekly oral prednisolone improves survival and strength in male mdx mice. *Muscle Nerve* 35, 43–48. doi: 10.1002/mus.20646
- Lawler, J. M. (2011). Exacerbation of pathology by oxidative stress in respiratory and locomotor muscles with Duchenne muscular dystrophy. *J. Physiol.* 589, 2161–2170. doi: 10.1113/jphysiol.2011.207456
- Mamchaoui, K., Trollet, C., Bigot, A., Negroni, E., Chaouch, S., Wolff, A., et al. (2011). Immortalized pathological human myoblasts: towards a universal tool for the study of neuromuscular disorders. *Skelet. Muscle* 1:34. doi: 10.1186/2044-5040-1-34
- McDonald, C. M., Henricson, E. K., Abresch, R. T., Duong, T., Joyce, N. C., Hu, F., et al. (2018). Long-term effects of glucocorticoids on function, quality of life, and survival in patients with Duchenne muscular dystrophy: a prospective cohort study. *Lancet* 391, 451–461. doi: 10.1016/S0140-6736(17)32160-8
- Menazza, S., Blaauw, B., Tiepolo, T., Toniolo, L., Braghetta, P., Spolaore, B., et al. (2010). Oxidative stress by monoamine oxidases is causally involved in myofiber damage in muscular dystrophy. *Hum. Mol. Genet.* 19, 4207–4215. doi: 10.1093/hmg/ddq339
- Merlini, L., Angelin, A., Tiepolo, T., Braghetta, P., Sabatelli, P., Zamparelli, A., et al. (2008). Cyclosporin A corrects mitochondrial dysfunction and muscle apoptosis in patients with collagen VI myopathies. *Proc. Natl. Acad. Sci. U.S.A.* 105, 5225–5229. doi: 10.1073/pnas.0800962105
- Millay, D. P., Sargent, M. A., Osinska, H., Baines, C. P., Barton, E. R., Vuagniaux, G., et al. (2008). Genetic and pharmacologic inhibition of mitochondrial-dependent necrosis attenuates muscular dystrophy. *Nat. Med.* 14, 442–447. doi: 10.1038/nm1736
- Onopiuk, M., Brutkowski, W., Wierzbička, K., Wojciechowska, S., Szczepanowska, J., Fronk, J., et al. (2009). Mutation in dystrophin-encoding gene affects energy metabolism in mouse myoblasts. *Biochem. Biophys. Res. Commun.* 386, 463–466. doi: 10.1016/j.bbrc.2009.06.053
- Palma, E., Tiepolo, T., Angelin, A., Sabatelli, P., Maraldi, N. M., Basso, E., et al. (2009). Genetic ablation of cyclophilin D rescues mitochondrial defects and prevents muscle apoptosis in collagen VI myopathic mice. *Hum. Mol. Genet.* 18, 2024–2031. doi: 10.1093/hmg/ddp126
- Rader, E. P., Turk, R., Willer, T., Beltran, D., Inamori, K., Peterson, T. A., et al. (2016). Role of dystroglycan in limiting contraction-induced injury to the sarcomeric cytoskeleton of mature skeletal muscle. *Proc. Natl. Acad. Sci. U.S.A.* 113, 10992–10997. doi: 10.1073/pnas.1605265113
- Ramadasan-Nair, R., Gayathri, N., Mishra, S., Sunitha, B., Mythri, R. B., Nalini, A., et al. (2014). Mitochondrial alterations and oxidative stress in an acute transient mouse model of muscle degeneration: implications for muscular dystrophy and related muscle pathologies. *J. Biol. Chem.* 289, 485–509. doi: 10.1074/jbc.M113.493270
- Rando, T. A. (2002). Oxidative stress and the pathogenesis of muscular dystrophies. *Am. J. Phys. Med. Rehabil.* 81, S175–S186. doi: 10.1097/00002060-200211001-00018
- Rodriguez, M. C., and Tarnopolsky, M. A. (2003). Patients with dystrophinopathy show evidence of increased oxidative stress. *Free Radic. Biol. Med.* 34, 1217–1220. doi: 10.1016/S0891-5849(03)00141-2
- Rosenberg, A. S., Puig, M., Nagaraju, K., Hoffman, E. P., Villalta, S. A., Rao, V. A., et al. (2015). Immune-mediated pathology in Duchenne muscular dystrophy. *Sci. Transl. Med.* 7:299rv294. doi: 10.1126/scitranslmed.aaa7322
- Shin, J., Tajrishi, M. M., Ogura, Y., and Kumar, A. (2013). Wasting mechanisms in muscular dystrophy. *Int. J. Biochem. Cell Biol.* 45, 2266–2279. doi: 10.1016/j.biocel.2013.05.001
- Sorato, E., Menazza, S., Zulian, A., Sabatelli, P., Gualandi, F., Merlini, L., et al. (2014). Monoamine oxidase inhibition prevents mitochondrial dysfunction and apoptosis in myoblasts from patients with collagen VI myopathies. *Free Radic. Biol. Med.* 75, 40–47. doi: 10.1016/j.freeradbiomed.2014.07.006
- Spinazzi, M., Casarin, A., Pertegato, V., Salviati, L., and Angelini, C. (2012). Assessment of mitochondrial respiratory chain enzymatic activities on tissues and cultured cells. *Nat. Protoc.* 7, 1235–1246. doi: 10.1038/nprot.2012.058
- Tidball, J. G., and Wehling-Henricks, M. (2007). The role of free radicals in the pathophysiology of muscular dystrophy. *J. Appl. Physiol.* 102, 1677–1686. doi: 10.1152/jappphysiol.01145.2006
- Timpani, C. A., Hayes, A., and Rybalka, E. (2015). Revisiting the dystrophin-ATP connection: how half a century of research still implicates mitochondrial dysfunction in Duchenne Muscular Dystrophy aetiology. *Med. Hypotheses* 85, 1021–1033. doi: 10.1016/j.mehy.2015.08.015

- Whitehead, N. P., Pham, C., Gervasio, O. L., and Allen, D. G. (2008). N-Acetylcysteine ameliorates skeletal muscle pathophysiology in mdx mice. *J. Physiol.* 586, 2003–2014. doi: 10.1113/jphysiol.2007.148338
- Williams, I. A., and Allen, D. G. (2007). The role of reactive oxygen species in the hearts of dystrophin-deficient mdx mice. *Am. J. Physiol. Heart Circ. Physiol.* 293, H1969–H1977. doi: 10.1152/ajpheart.00489.2007
- Yeung, E. W., Whitehead, N. P., Suchyna, T. M., Gottlieb, P. A., Sachs, F., and Allen, D. G. (2005). Effects of stretch-activated channel blockers on  $[Ca^{2+}]_i$  and muscle damage in the mdx mouse. *J. Physiol.* 562, 367–380. doi: 10.1113/jphysiol.2004.075275
- Youdim, M. B., Edmondson, D., and Tipton, K. F. (2006). The therapeutic potential of monoamine oxidase inhibitors. *Nat. Rev. Neurosci.* 7, 295–309. doi: 10.1038/nrn1883

**Conflict of Interest Statement:** MC was co-holder (with three other colleagues who did not participate to the present study) of a patent covering the use of a specific class of MAO-B inhibitors for the therapy of muscular dystrophies. As

of April 2018, such patent, which does not cover the molecule presented in the present study, has been sold by the University of Padova to a private company.

The remaining authors declare that the research was conducted in the absence of any commercial or financial relationships that could be construed as a potential conflict of interest.

The reviewer MM and handling Editor declared their shared affiliation at the time of the review.

Copyright © 2018 Vitiello, Marabita, Sorato, Nogara, Forestan, Mouly, Salviati, Acosta, Blaauw and Canton. This is an open-access article distributed under the terms of the Creative Commons Attribution License (CC BY). The use, distribution or reproduction in other forums is permitted, provided the original author(s) and the copyright owner(s) are credited and that the original publication in this journal is cited, in accordance with accepted academic practice. No use, distribution or reproduction is permitted which does not comply with these terms.



# Tuning RGD Motif and Hyaluronan Density to Study Integrin Binding

Cornelia Zapp<sup>1,2</sup>, Burcu B. Minsky<sup>1†</sup> and Heike Boehm<sup>1,2\*</sup>

<sup>1</sup> Department of Cellular Biophysics, Max Planck Institute for Medical Research, Heidelberg, Germany, <sup>2</sup> Physical Chemistry, Heidelberg University, Heidelberg, Germany

## OPEN ACCESS

### Edited by:

Alberto Rainer,  
Università Campus Bio-Medico, Italy

### Reviewed by:

Francesca Cavaliere,  
University of Melbourne, Australia  
Filippo Rossi,  
Politecnico di Milano, Italy

### \*Correspondence:

Heike Boehm  
heike.boehm@mpimf-  
heidelberg.mpg.de

### † Present address:

Burcu B. Minsky,  
Department of Biological Sciences,  
Smith College, Northampton, MA,  
United States

### Specialty section:

This article was submitted to  
Integrative Physiology,  
a section of the journal  
Frontiers in Physiology

**Received:** 22 February 2018

**Accepted:** 10 July 2018

**Published:** 07 August 2018

### Citation:

Zapp C, Minsky BB and Boehm H  
(2018) Tuning RGD Motif  
and Hyaluronan Density to Study  
Integrin Binding.  
*Front. Physiol.* 9:1022.  
doi: 10.3389/fphys.2018.01022

Well-controlled surfaces with immobilized substrates enable novel approaches to investigate specific aspects of biological processes related to cell adhesion or motility. A subset of integrins, cellular transmembrane glycoproteins, recognize the evolutionarily conserved tripeptide sequence RGD, and anchor cells to their surrounding proteins as well as mediate bidirectional signaling. In this study, the main question was how co-presentation of hyaluronan (HA), an essential component of the extracellular matrix (ECM), and the RGD motif affect integrin binding. We report a method to prepare self-assembled monolayers on gold surfaces, co-presenting the cell adhesive RGD motif and small HA molecules, to investigate integrin containing proteoliposome binding. This technique enables an independent adjustment of the RGD motif and HA density while maintaining a passivating background: Layer formation and subsequent interactions with  $\alpha_{IIb}\beta_3$  integrins, which are reconstituted in liposomes, was monitored by label-free quartz crystal microbalance with dissipation monitoring (QCM-D). Exceeding a critical RGD motif density of 40% results in enhanced binding of proteoliposomes. Co-presentation studies with varying HA and constant RGD motif density demonstrate that marginal amounts of HA are sufficient to prevent integrin binding. These findings are of specific importance in relation to cancer cell microenvironments, which show highly enriched HA in the surrounding ECM to reduce adhesion properties.

**Keywords:** QCM-D, hyaluronan, integrins, cell adhesion, proteoliposomes

## INTRODUCTION

Nature has generated well-adapted processes and materials through natural selection. Thus, nature in its remarkable diversity provides an extraordinary collection of strategies. These can be exploited as a source of inspiration and adopted for biological applications. As such, the interdisciplinary field of biomimetics research encompasses many specialty areas in biology, materials science, and nanotechnology. The fundamental idea is to generate synthetic systems to mimic biological concepts or to accomplish biological tasks. One approach to utilize this synthetic biological concept is the “bottom-up” approach, in which a minimal number of synthetic or biological molecules are combined to realize a desired function (Tu and Tirrell, 2004; Benner and Sismour, 2005; Purnick and Weiss, 2009). Molecular biomaterials can be fabricated in a “bottom-up” approach, in which molecules adopt a defined arrangement and consequently produce novel macromolecular assemblies. Molecular assembly can be applied to modulate surface properties of a material’s interface, where chemical, physical, and biological processes

are maintained. Surfaces are of foremost importance in biological systems, since surface-cell interactions modulate how cells attach to the material. Specifically modified surfaces may serve as a research platform to study specific aspects of cell interaction.

The extracellular matrix (ECM) is a complex dynamic meshwork consisting of diverse macromolecules, which are secreted by the embedded cells within the tissue and provide biochemical and structural support. Cells sense chemical, topographic and mechanical features via specific cellular receptors and mediate the assembling of adhesion complexes to transfer information via signaling pathways (Geiger and Yamada, 2011; Jansen et al., 2017). Thus, cell adhesion to the surrounding matrix and neighboring cells plays a key role in many cellular processes including survival, differentiation and proliferation (Berrier and Yamada, 2007). Integrins are the most abundant and fundamental matrix receptors on animal cells (Mecham, 2011). These transmembrane heterodimeric glycoproteins fulfill two main functions: (1) attachment of cells to the ECM and (2) inducing bidirectional signal transduction between the ECM and cells (Streuli, 2016; Gauthier and Roca-Cusachs, 2018). A prevalently surface-displayed and evolutionarily conserved RGD motif consists of the three amino acids arginine, glycine, and aspartate. The RGD motif is present in various proteins of the ECM, for instance fibronectin, vitronectin, and fibrinogen (Mecham, 2011). A subset of integrins specifically recognize RGD repeats to anchor cells to the ECM and mediate bidirectional signaling. Therefore, studying cell adhesion demands precise control of RGD immobilization on the artificial surfaces to focus mainly on the surface properties required for cellular interactions via integrins and prevent non-specific protein attachment.

The non-sulfated glycosaminoglycan hyaluronan (HA) is a major non-proteinaceous component of the ECM and is formed of repeating disaccharide units of glucuronic acid and *N*-acetyl glucosamine. HA provides structural support, maintains tissue hydration, and serves as a lubricant in certain tissues (Dicker et al., 2014). HA interacts with a large number of HA-binding proteins (hyaladherins), matrix components and cells. Its temporal and spatial distribution as well as size plays critical roles in numerous biological processes, e.g., wound healing, inflammation and tumor progression (Dicker et al., 2014). Although HA is an essential component of extracellular structures and is reported to contribute to diverse cellular functions, little is known about its role in cellular adhesion processes. It has been reported, that HA can have both adhesive and anti-adhesive properties as well as promote cell detachment (Evanko et al., 2007; Cao et al., 2009). Moreover, showing that inhibition of CD44 on hematopoietic progenitor cells prevents rolling and adhesion to an HA-coated surface (Hanke et al., 2014) or that HA mediates also early, long-ranging adhesive interactions between cells and the surrounding surface, which precede integrin-mediated adhesion and formation of focal adhesions (Zimmerman et al., 2002; Zaidel-Bar et al., 2004) demonstrates the importance of HA specific interactions. In order to understand the role of HA in the dynamic process of cell adhesion, we aim to establish a synthetic model with reduced complexity, giving us the opportunity to focus on the repulsive forces of HA.

Numerous studies have applied the chemical functionalization of surfaces with desired properties to study the effect on cell structures, metabolism, viability or proliferation among others (Yao et al., 2013; Jeon et al., 2014; Ventre and Netti, 2016). One approach for the chemical functionalization of surfaces is the formation of self-assembled monolayers (SAMs) on gold surfaces through thiol residues (Love et al., 2005). Thereby precise control over the properties of the designed biological interfaces can be exerted by the molecular structure and the surrounding environment.

Alkanethiols terminated with oligo(ethylene glycol) moieties (OEG-alkanethiols) form SAMs on gold surfaces, which are resistant to unspecific protein adsorption. These surfaces have been exploited in several studies including cell adhesion or stem cell differentiation (Tidwell et al., 1997; Arima and Iwata, 2015; Hao et al., 2016; Almeida and Shukla, 2017).

The well-defined surfaces employed in this study were prepared according to the protocol published by Minsky et al. (2016), in which a controlled immobilization strategy in a two-layer system, simultaneously prevents unspecific protein binding and enables adjusting of the immobilization density on a surface. For this purpose SAMs are formed spontaneously on gold surfaces by co-adsorption of two functionalized oligo(ethylene glycol)-alkanethiols and unfunctionalized OEG-alkanethiols. By tuning the ratio of the two components, the density of the surface-displayed motif can be defined while a passivating background is maintained.

Work in our lab has focused on designing a bioinspired and well-controlled artificial integrin adhesion model system, in which surfaces, including the RGD binding motif and/or HA on an otherwise passivating background layer represent ECM mimetic, and reconstituted transmembrane integrins within lipid vesicles represents cell mimetic. Integrins form non-covalently associated heterodimeric complexes of an  $\alpha$ - and a  $\beta$ -subunit, each having a large extracellular domain, a membrane spanning region and a short cytoplasmic domain (Hynes, 2002; Barczyk et al., 2010). In order to resemble the natural arrangement, isolated  $\alpha_{IIb}\beta_3$  integrins were reconstituted into liposomes, built up of amphiphilic molecules forming phospholipid bilayers and surrounding an aqueous unit (Akbarzadeh et al., 2013).

Within this study large unilamellar liposomes and liposomes with reconstituted  $\alpha_{IIb}\beta_3$  integrin (hereinafter referred to as proteoliposomes) were prepared by detergent removal (Erb et al., 1997). The aim of this study is to address the question of how co-presentation of HA and the RGD motif in varying densities impacts the attachment of integrins.

## MATERIALS AND METHODS

### Chemicals

Purified L- $\alpha$ -phosphatidylcholine (eggPC) and L- $\alpha$ -phosphatidyl-DL-glycerol (eggPG) were purchased from Avanti Lipids Polar Inc. (Alabaster, AL, United States). Biobeads SM-2 (20–50 mesh size) were obtained from Bio-Rad Laboratories Inc. (Hercules, CA, United States). Triton X-100, sodium cyanoborohydride, and propargylamine

were purchased from Sigma-Aldrich (Steinheim, Germany). Hyaluronic acid sodium salt ( $M_r = 10$  kDa, sHA) was procured from LifeCore Biomedial (Chaska, MN, United States). HS-(CH)<sub>11</sub>-EG<sub>3</sub>-OH (EG<sub>3</sub>OH) and HS-(CH)<sub>11</sub>-EG<sub>6</sub>-N<sub>3</sub> (EG<sub>6</sub>N<sub>3</sub>) were obtained from Prochimia (Sopot, Poland). Alkylated RGD peptide (sequence: GRGDSP) was purchased from Peptide Specialty Laboratories GmbH (Heidelberg, Germany). Dialysis tube (MWCO: 3,500 Da) was purchased from VWR (Radnor, PA, United States). Integrin  $\alpha_{IIb}\beta_3$  was extracted from outdated human blood platelets obtained by the Red Cross Germany, according to the protocol from Müller et al. with modifications (Müller et al., 1993; Hu et al., 2000).

### Proteoliposome Preparation by Detergent Removal

The protein was reconstituted into proteoliposomes according to the general procedure developed by Erb et al. (1997). Typically, an equimolar lipid mixture of eggPC/eggPG (0.43  $\mu$ mol each) was vacuum-dried and resuspended in 1 mL buffer B (20 mM TRIS, 50 mM NaCl, 1 mM CaCl<sub>2</sub>, and 0.1% Triton X-100 at pH 7.4). For the preparation of proteoliposomes, the lipids were solubilized in 827  $\mu$ L buffer B and 174  $\mu$ L integrin  $\alpha_{IIb}\beta_3$  (0.23 mg/mL) was added to a final protein:lipid ratio of 1:5,000. Afterwards, the mixture was incubated at 37°C for 2 h under shaking. The detergent Triton X-100 was removed with 50 mg Bio-Beads SM-2 under stirring for 3.5 h. After removing the Bio-Beads SM-2, the detergent removal step was repeated. The obtained solution was stored at 4°C for a total maximum of 24 h. Before usage the resulting vesicles were processed by extrusion with a nominal 100 nm pore membrane (Whatman, Maidstone, United Kingdom) 11 times using a mini-extruder apparatus (Avanti Polar Lipids Inc., Alabaster, AL, United States). DLS measurements show an average size of  $137.7 \pm 41.9$  nm for pure liposomes and  $162.1 \pm 41.7$  nm for proteoliposomes. Vesicles were generally prepared at a nominal lipid concentration of  $\sim 0.675$  mg/mL, and then diluted 1:20 in 20 $\times$  activation buffer (1 $\times$  activation buffer: 50 mM NaCl, 20 mM TRIS, 1 mM CaCl<sub>2</sub>, 1 mM MgCl<sub>2</sub>, and 1 mM MnCl<sub>2</sub>, pH 7.4) before the experiment.

### Sample Preparation for Formation of a Functionalized Self-Assembled Monolayer

Click reaction was performed using TRIS buffer (100 mM, pH 8.5), ascorbic acid (100 mM), EG<sub>6</sub>N<sub>3</sub> (150  $\mu$ M) and alkylated RGD peptide sequence (480  $\mu$ M) in the presence of 1 mM CuSO<sub>4</sub>. After 1.5 h at RT the reaction was stopped by adding EDTA (1 mM) to chelate copper. Mixtures with different ratios were prepared by diluting EG<sub>6</sub>RGD with EG<sub>3</sub>OH and adjusted to a total thiol concentration of 100  $\mu$ M in passivation buffer. Surfaces were prepared by immobilization of this OEG mixture on the gold surface of the quartz crystal microbalance with dissipation monitoring (QCM-D) sensor, followed by a final washing step in passivation buffer.

### Quartz Crystal Microbalance With Dissipation Monitoring Measurements

For QCM-D experiments a fully automated Q-sense Omega Auto instrument (Biolin Scientific AB, Västra Frölunda, Sweden) with gold-coated quartz crystal electrodes (QSX301, Q-sense, AT-cut, 4.95 MHz, Biolin Scientific AB, Västra Frölunda, Sweden) was used. The system was operated in flow mode with a flow rate of 20  $\mu$ L/min at 24°C. Frequency and dissipation data were collected from six overtones ( $n = 3, 5, 7, 9, 11, 13$ ). Prior to use the electrodes were cleaned in a 5:1:1 solution of water, 30% hydrogen peroxide and 25% ammonia at 75°C for 10 min and activated in an UV/Ozone cleaner (ProCleaner, Bioforce Nanosciences, Ames, IA, United States) for 10 min. The Omega Auto includes a fully automated sample handling of four sensors in parallel and each sequence of an experiment was performed in duplicates. Changes in dissipation and normalized frequency,  $\Delta f = \Delta f/n$ , of the seventh overtone ( $n = 7$ ) are presented in the graphs. Frequency and dissipation changes were calculated by averaging over the last 5 min of the buffer wash before adding the samples and the final buffer wash. Buffers used as baselines were passivation buffer (50 mM NaCl, 20 mM TRIS, 1 mM CaCl<sub>2</sub>, and 1 mM MgCl<sub>2</sub>, pH 7.4), activation buffer (passivation buffer with 1 mM MnCl<sub>2</sub>, pH 7.4), and TRIS buffer (100 mM, pH 8.5).

### Synthesis of End-Alkylated Hyaluronan

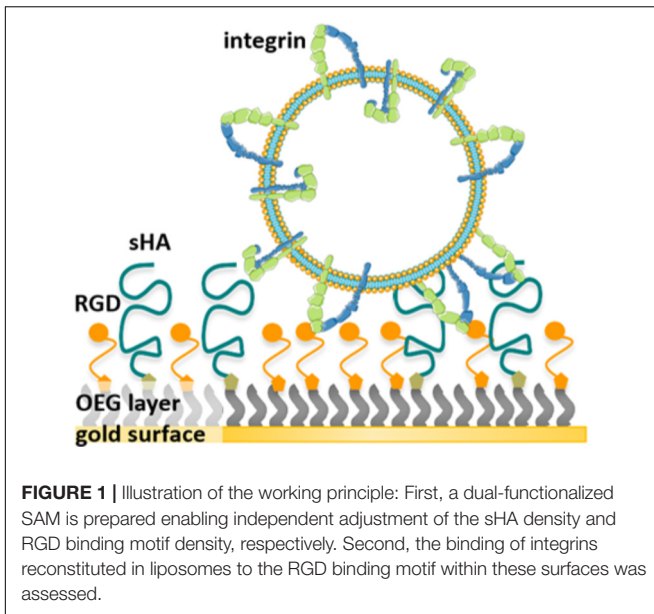
Functionalization at the reducing *N*-acetylglucosamine unit of sHA was performed according to the protocol established by Lee et al. (2008). In short, 100 mg sHA and propargylamine (523 mM) were dissolved in borate buffer (20 mL, 100 mM, pH 8.5) containing sodium chloride (400 mM) for 2 h at RT. After adding sodium cyanoborohydride (200 mM) the solution was stirred for 5 d at 40°C. The mixture was dialyzed once against water, containing sodium chloride and hydrochloric acid, followed by water containing hydrochloric acid for 2 d. Prior to storage at  $-20^\circ\text{C}$  the end-alkylated sHA was lyophilized.

### Preparation of a Dual-Functionalized Self-Assembled Monolayer

For preparing the dual functionalized surfaces, a constant ratio of EG<sub>6</sub>RGD (40%) was mixed with EG<sub>3</sub>OH and EG<sub>6</sub>N<sub>3</sub> (0–100% EG<sub>6</sub>N<sub>3</sub>). After immobilization of this OEG mixture on the gold surface of the QCM-D sensor, end-alkylated HA (1.875 mg/mL) was conjugated to the EG<sub>6</sub>N<sub>3</sub> in the presence of ascorbic acid (100 mM) and CuSO<sub>4</sub> (1 mM) in TRIS buffer (100 mM, pH 8.5). Finally, the surface was washed with TRIS buffer to remove unbound molecules.

## RESULTS AND DISCUSSION

Within this study dual-functionalized surfaces were prepared by co-presenting the RGD motif and HA in varying densities on a passivating background. The average contour length of the short HA (sHA < 10 kDa) is around 24 nm and its radius of gyration is around 5.3 nm (Takahashi et al., 1999; Buhler and Boué, 2004). A mixture of OEGs, containing OEG-alkanethiol

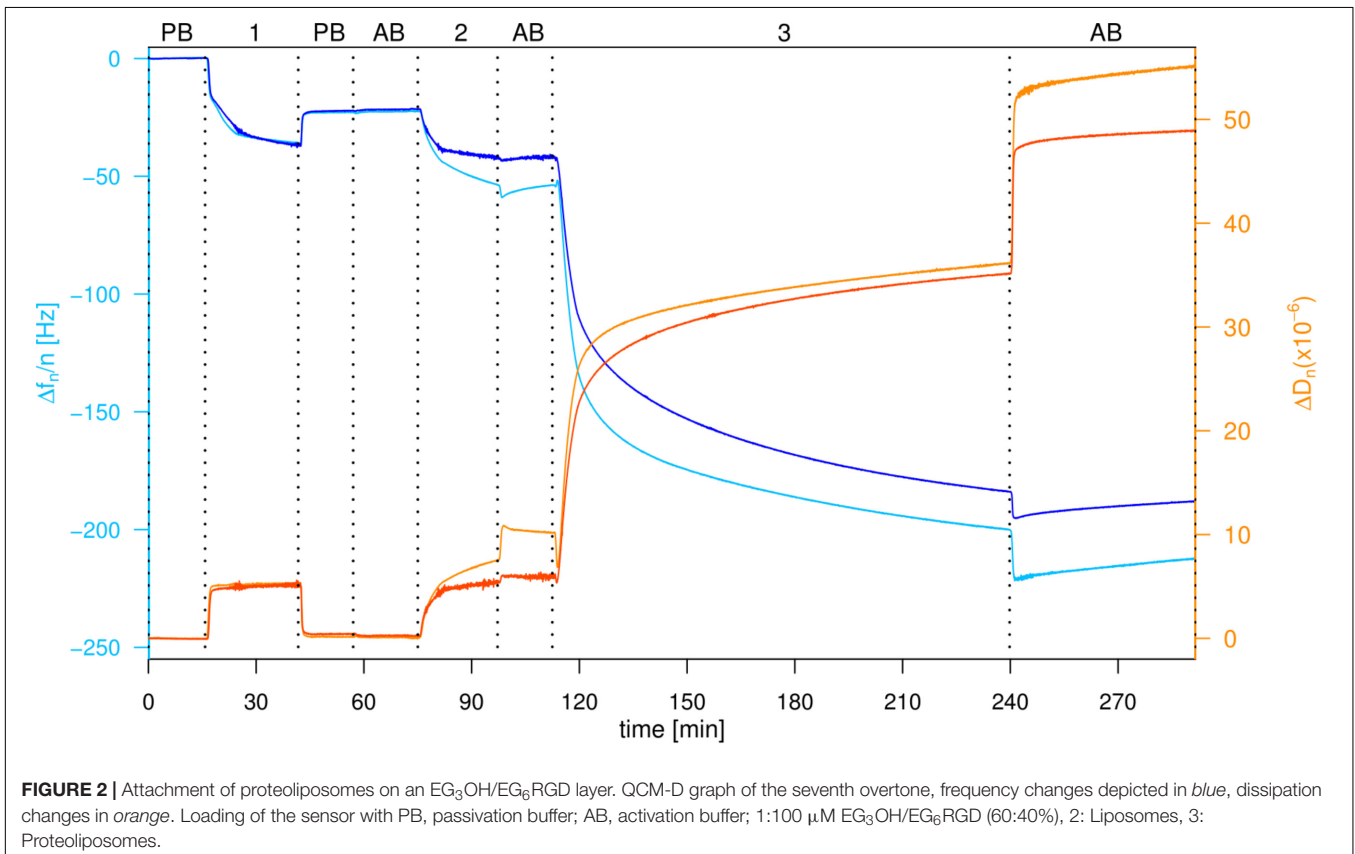


(EG<sub>3</sub>OH), OEG-alkanethiols functionalized with RGD motif (EG<sub>6</sub>RGD), and OEG-alkanethiols with a terminal azide group (EG<sub>6</sub>N<sub>3</sub>), were immobilized on the gold surface. Subsequently, end-alkylated HA was conjugated to the OEG-azide group in the immobilized OEG layer directly on the surface via an

*in situ* azide/alkyne cycloaddition reaction. This extended surface preparation approach facilitates the variation of the HA density and RGD density independently of each other, while a passivating background is maintained. **Figure 1** illustrates the working principle. Following the surface preparation, the attachment of liposomes and proteoliposomes on these well-defined surfaces was monitored using QCM-D. QCM-D is a label-free, real-time measurement technique for monitoring molecular adsorption and/or interactions on various surfaces covering a quartz crystal. As a direct impact of mass adsorption, changes in frequency of the oscillating quartz crystal are detected (Dixon, 2008). An observed shift in the dissipation provides insights regarding the viscoelastic properties and rearrangements of the adlayer (Dixon, 2008).

### Critical RGD Motif Density for Binding Proteoliposomes

The high-density presentation of RGD was achieved with a straightforward and fast method by first conjugating RGD to EG<sub>6</sub>N<sub>3</sub> via copper(I)-catalyzed azide-alkyne cycloaddition (CuAAC) and subsequently immobilizing on gold surfaces in the presence of EG<sub>3</sub>OH to adjust the density. As seen in the QCM-D profile, after approximately 30 min the decrease in frequency and increase in dissipation are stable, originating from adsorption of both OEG alkanethiols. After a subsequent washing step the frequency slightly increases and the dissipation decreases reaching a stable value indicating successful immobilization of



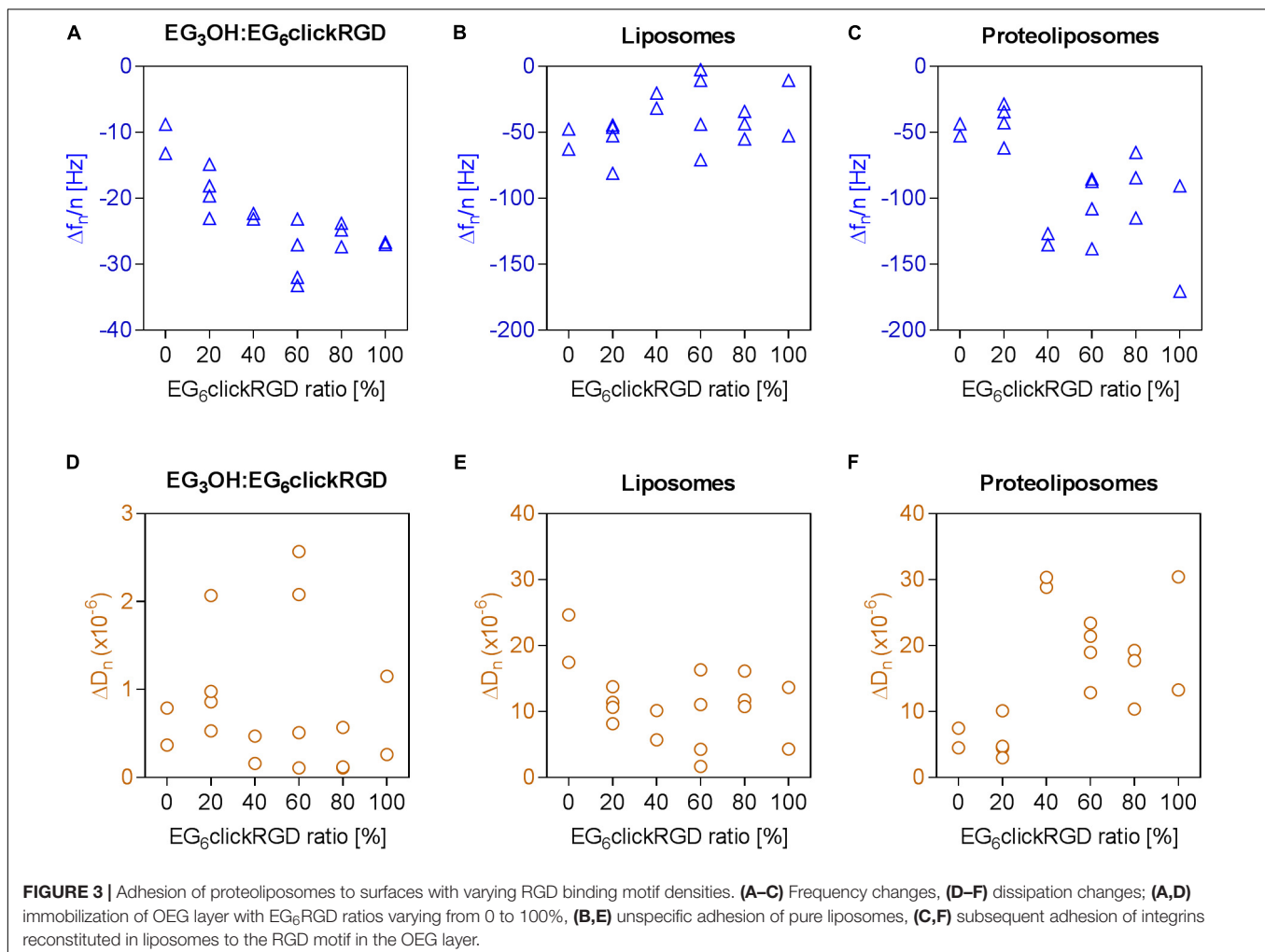
a dense OEG layer on the gold surface (**Figure 2**). When the buffer was changed from passivation buffer to the same buffer containing 2 mM divalent ions (1 mM  $Mn^{2+}$  and 1 mM  $Mg^{2+}$ , referred to as activation buffer) no change in frequency or dissipation was monitored. All further steps were performed in activation buffer since the affinity and specificity of integrins binding to the RGD motif is affected by the concentration of divalent ions (Zhang and Chen, 2012). As a control for unspecific attachment to the OEG and OEG-RGD layer, pure liposomes were washed over the modified surfaces. The frequency decreases again and the dissipation increases, indicating that liposomes adhere non-specifically and remain attached when washed with buffer. When proteoliposomes are washed over the modified surface, a frequency change as well as dissipation change is observed, which are even reinforced after a subsequent washing step. This observation indicates that the proteoliposomes stay intact and the integrins bind firmly to the RGD motif as they could not be removed by washing (**Figure 2**).

Based on this general experimental setup, the influence of the RGD motif density on the attachment of proteoliposomes was quantified. Modified surfaces were prepared with six different

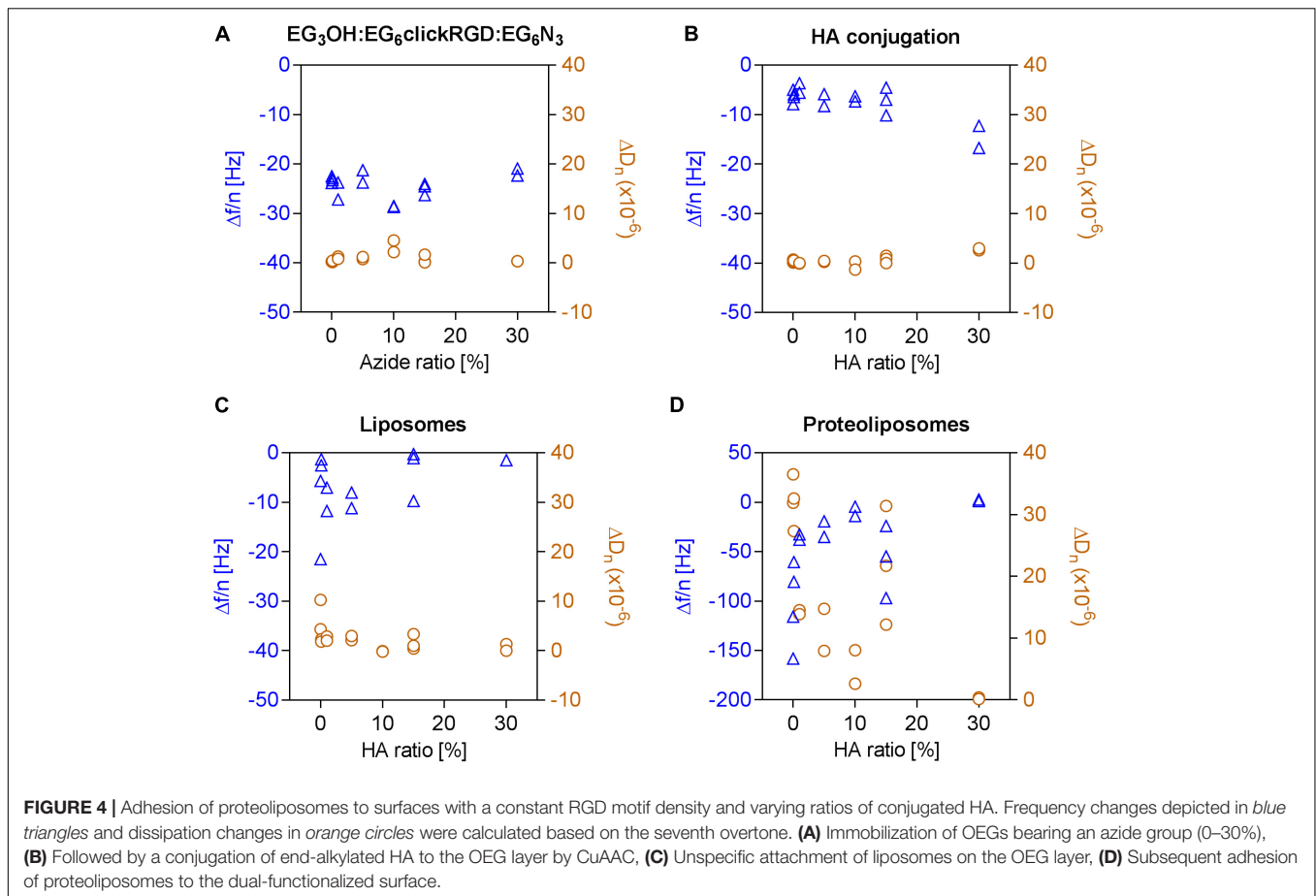
RGD motif densities ranging from 0 to 100% according to the adjustable well-defined system outlined above.

In the initial SAM formation of the OEG layer, an increasing frequency change is observed at higher RGD motif densities. This correlation is effected by the amount of  $EG_6$ RGD, which has a molecular weight of 1,120 g/mol and is consequently heavier than the  $EG_3$ OH molecules (molecular weight = 671 g/mol). Dissipation changes, mainly between  $0 \times 10^{-6}$  and  $1 \times 10^{-6}$ , indicate a rigid and well coupled OEG layer at all measured RGD densities (**Figures 3A,D**). Evaluation of the surface's unspecific binding activity demonstrates that bare liposomes attach unspecifically to some extent to the surface, independently of the RGD ratio. Thereby, the frequency and dissipation changes for all RGD concentrations fluctuate around  $-41.82 \pm 20.88$  Hz and  $11.28 \times 10^{-6} \pm 5.48 \times 10^{-6}$ , respectively (**Figures 3B,E**).

The subsequent attachment of proteoliposomes on the RGD motif functionalized surfaces was assessed in the next step. In general, decreasing frequency and dissipation values demonstrate a mass adsorption and formation of a viscoelastic adlayer, respectively. This indicates proteoliposome binding to the RGD motif on the surface via integrins. For







an increased ratio of EG<sub>6</sub>RGD the graph shows biphasic curve characteristics (**Figures 3C,F**). In the first part, when the ratio of EG<sub>6</sub>RGD to EG<sub>3</sub>OH is 0 or 20% a frequency change of  $43.98 \pm 11.02$  Hz and dissipation shift of  $5.72 \times 10^{-6} \pm 2.37 \times 10^{-6}$  occurs. Whereas in the second part, when the EG<sub>6</sub>RGD ratio exceeds or is equal to 40%, a higher frequency shift of  $-109.89 \pm 30.94$  Hz and simultaneously higher dissipation change of  $20.79 \times 10^{-6} \pm 7.04 \times 10^{-6}$  is detected. Based on these results an RGD motif density of 40% was employed for further experiments.

## Hyaluronan as Part of a Dual-Functionalized Surface Prevents Proteoliposome Binding

In order to examine the adhesion of integrins in the presence of HA, dual-functionalized surfaces were prepared following the previously described procedure. This was achieved by conjugation of end-alkylated HA to an OEG layer, containing varying amounts of EG<sub>6</sub>N<sub>3</sub> and EG<sub>3</sub>OH and a constant ratio of 40% EG<sub>6</sub>RGD. The immobilization of the OEG layers caused a constant frequency change, fluctuating around  $-24.25 \pm 2.33$  Hz, independently of the ratio of EG<sub>6</sub>N<sub>3</sub> with general low dissipation values ( $0.96 \times 10^{-6} \pm 1.12 \times 10^{-6}$ ). Directly after immobilization of the OEG layer, end-alkylated

HA was conjugated to the EG<sub>6</sub>N<sub>3</sub> in this OEG layer as indicated by the slight decrease in frequency and increase in dissipation, respectively (**Figures 4A,B**). Observation of the unspecific attachment of bare liposomes to these surfaces shows a constantly low level with a frequency change of  $-5.06 \pm 6.36$  Hz and dissipation change of  $2.31 \times 10^{-6} \pm 2.49 \times 10^{-6}$ . These signal changes indicate that conjugated HA reduces the unspecific attachment of pure liposomes, which has been detected on the surfaces presenting the RGD motif alone (**Figure 4C**).

Finally, the effect of the dual-functionalized surface on the adhesion of integrins was investigated. It was observed that the frequency and dissipation changes caused by the binding of proteoliposomes declines with a higher EG<sub>6</sub>N<sub>3</sub> content and consequently higher HA conjugation degree. At an initial EG<sub>6</sub>N<sub>3</sub> ratio of 30%, only slight shifts in frequency and dissipation are detected indicating that the adhesion of proteoliposomes fails.

Even at lower ratios of HA between 0.01 and 30%, fewer proteoliposomes attach to the surface (**Figure 4D**). Thus, it can be concluded that minimal amounts of conjugated HA are sufficient to prevent the attachment of proteoliposomes to a surface with a constant RGD motif density. In this experiment, sHA molecules with a radius of gyration of around 5.3 nm were immobilized. Therefore, each conjugated HA molecule covers several molecules in the OEG layer including RGD binding motifs.

## CONCLUSION

Within this study a biomimetic model was established to address the challenge of co-presenting HA and the RGD motif to study integrin binding. The adhesion of  $\alpha_{11b}\beta_3$  integrin, which was reconstituted in sphere-shaped lipid vesicles devoid of HA binding proteins, was quantified on HA and the RGD motif functionalized on an otherwise inert background. It is demonstrated that an RGD density of 40% has to be exceeded to achieve a prominent binding of proteoliposomes. Moreover, it is also concluded that even marginal amounts of HA are sufficient to significantly impact integrin attachment. The dissipation changes indicate that the proteoliposomes maintain an intact vesicle shape. Frohnmayer et al. (2015a,b) demonstrated that the adhesion of similarly prepared proteoliposomes on fibrinogen-coated surfaces, a protein which contains the RGD motif, results in decreased frequency and increased dissipation values within the same order of magnitude monitored in this study.

It would be especially beneficial to use these well-defined dual-functionalized surfaces to investigate the behavior of various cell lines in future studies. Especially, cancer cell lines are highly interesting since it is known that HA is highly enriched in their ECM. These cell-ECM interactions additionally involve binding of HA with receptors such as CD44 and RHAMM which are

associated with tumor progression and metastasis (Liang et al., 2016; Morath et al., 2016; Rankin and Frankel, 2016).

## DATA AVAILABILITY

The raw data supporting the conclusions of this manuscript will be made available by the authors, without undue reservation, to any qualified researcher.

## AUTHOR CONTRIBUTIONS

HB, BM, and CZ designed and conceived the experiments. BM performed preliminary experiments. CZ performed the experiments and analyzed the data. CZ and HB wrote the paper.

## ACKNOWLEDGMENTS

We thank Christine Mollenhauer for the extraction of integrins, Dorothea Brüggemann for fruitful discussions and Prof. Tanaka for providing the NanoZS for DLS measurements. Generous support by Prof. Joachim Spatz and the Max Planck Society is gratefully acknowledged.

## REFERENCES

- Akbarzadeh, A., Rezaei-Sadabady, R., Davaran, S., Joo, S. W., Zarghami, N., Hanifehpour, Y., et al. (2013). Liposome: classification, preparation, and applications. *Nanoscale Res. Lett.* 8:102. doi: 10.1186/1556-276X-8-102
- Almeida, B., and Shukla, A. (2017). Degradation of alkanethiol self-assembled monolayers in mesenchymal stem cell culture. *J. Biomed. Mater. Res. A* 105, 464–474. doi: 10.1002/jbm.a.35922
- Arima, Y., and Iwata, H. (2015). Preferential adsorption of cell adhesive proteins from complex media on self-assembled monolayers and its effect on subsequent cell adhesion. *Acta Biomater.* 26, 72–81. doi: 10.1016/j.actbio.2015.08.033
- Barczyk, M., Carracedo, S., and Gullberg, D. (2010). Integrins. *Cell Tissue Res.* 339, 269–280. doi: 10.1007/s00441-009-0834-6
- Benner, S. A., and Sismour, A. M. (2005). Synthetic biology. *Nat. Rev. Genet.* 6, 533–543. doi: 10.1038/nrg1637
- Berrier, A. L., and Yamada, K. M. (2007). Cell-matrix adhesion. *J. Cell. Physiol.* 213, 565–573. doi: 10.1002/jcp.21237
- Buhler, E., and Boué, F. (2004). Chain persistence length and structure in hyaluronan solutions: ionic strength dependence for a model semirigid polyelectrolyte. *Macromolecules* 37, 1600–1610. doi: 10.1021/ma0215520
- Cao, X., Pettit, M. E., Conlan, S. L., Wagner, W., Ho, A. D., Clare, A. S., et al. (2009). Resistance of polysaccharide coatings to proteins, hematopoietic cells, and marine organisms. *Biomacromolecules* 10, 907–915. doi: 10.1021/bm8014208
- Dicker, K. T., Gurski, L. A., Pradhan-Bhatt, S., Witt, R. L., Farach-Carson, M. C., and Jia, X. (2014). Hyaluronan: a simple polysaccharide with diverse biological functions. *Acta Biomater.* 10, 1558–1570. doi: 10.1016/j.actbio.2013.12.019
- Dixon, M. C. (2008). Quartz crystal microbalance with dissipation monitoring: enabling real-time characterization of biological materials and their interactions. *J. Biomol. Tech.* 19, 151–158.
- Erb, E. M., Tangemann, K., Bohrmann, B., Muller, B., and Engel, J. (1997). Integrin  $\alpha_{11b}\beta_3$  reconstituted into lipid bilayers is nonclustered in its activated state but clusters after fibrinogen binding. *Biochemistry* 36, 7395–7402. doi: 10.1021/bi9702187
- Evanko, S. P., Tammi, M. I., Tammi, R. H., and Wight, T. N. (2007). Hyaluronan-dependent pericellular matrix. *Adv. Drug Deliv. Rev.* 59, 1351–1365. doi: 10.1016/j.addr.2007.08.008
- Frohnmayer, J. P., Brüggemann, D., Eberhard, C., Neubauer, S., Mollenhauer, C., Boehm, H., et al. (2015a). Minimal synthetic cells to study integrin-mediated adhesion. *Angew. Chem.* 54, 12472–12478. doi: 10.1002/anie.201503184
- Frohnmayer, J. P., Brüggemann, D., Eberhard, C., Neubauer, S., Mollenhauer, C., Boehm, H., et al. (2015b). Synthetische Adhäsion von Integrin-Liposomen als minimales Zellmodell. *Angew. Chem.* 127, 12649–12655. doi: 10.1002/ange.201503184
- Gauthier, N. C., and Roca-Cusachs, P. (2018). Mechanosensing at integrin-mediated cell-matrix adhesions: from molecular to integrated mechanisms. *Curr. Opin. Cell Biol.* 50, 20–26. doi: 10.1016/j.cceb.2017.12.014
- Geiger, B., and Yamada, K. M. (2011). Molecular architecture and function of matrix adhesions. *Cold Spring Harb. Perspect. Biol.* 3:a005033. doi: 10.1101/cshperspect.a005033
- Hanke, M., Hoffmann, I., Christophis, C., Schubert, M., Hoang, V. T., Zepeda-Moreno, A., et al. (2014). Differences between healthy hematopoietic progenitors and leukemia cells with respect to CD44 mediated rolling versus adherence behavior on hyaluronan acid coated surfaces. *Biomaterials* 35, 1411–1419. doi: 10.1016/j.biomaterials.2013.11.011
- Hao, L., Fu, X., Li, T., Zhao, N., Shi, X., Cui, F., et al. (2016). Surface chemistry from wettability and charge for the control of mesenchymal stem cell fate through self-assembled monolayers. *Colloids Surf. B Biointerfaces* 148, 549–556. doi: 10.1016/j.colsurfb.2016.09.027
- Hu, B., Finsinger, D., Peter, K., Guttenberg, Z., Bärmann, M., Kessler, H., et al. (2000). Intervesicle cross-linking with integrin  $\alpha_{11b}\beta_3$  and cyclic-RGD-lipopeptide. *Biochemistry* 39, 12284–12294. doi: 10.1021/bi000144q
- Hynes, R. O. (2002). Integrins: bidirectional, allosteric signaling machines. *Cell* 110, 673–687. doi: 10.1016/S0092-8674(02)00971-6
- Jansen, K. A., Atherton, P., and Ballestrem, C. (2017). Mechanotransduction at the cell-matrix interface. *Semin. Cell Dev. Biol.* 71, 75–83. doi: 10.1016/j.semcdb.2017.07.027
- Jeon, H., Simon, C. G., and Kim, G. (2014). A mini-review: cell response to microscale, nanoscale, and hierarchical patterning of surface structure. *J. Biomed. Mater. Res. B Appl. Biomater.* 102, 1580–1594. doi: 10.1002/jbm.b.33158
- Lee, H., Lee, K., Kim, I. K., and Park, T. G. (2008). Synthesis, characterization, and in vivo diagnostic applications of hyaluronic acid immobilized gold

- nanoprobes. *Biomaterials* 29, 4709–4718. doi: 10.1016/j.biomaterials.2008.08.038
- Liang, J., Jiang, D., and Noble, P. W. (2016). Hyaluronan as a therapeutic target in human diseases. *Adv. Drug Deliv. Rev.* 97, 186–203. doi: 10.1016/j.addr.2015.10.017
- Love, J. C., Estroff, L. A., Kriebel, J. K., Nuzzo, R. G., and Whitesides, G. M. (2005). Self-assembled monolayers of thiolates on metals as a form of nanotechnology. *Chem. Rev.* 105, 1103–1170. doi: 10.1021/cr0300789
- Mecham, R. (2011). *The Extracellular Matrix: an Overview*. Berlin: Springer. doi: 10.1007/978-3-642-16555-9
- Minsky, B. B., Antoni, C. H., and Boehm, H. (2016). Controlled immobilization strategies to probe short hyaluronan-protein interactions. *Sci. Rep.* 6:21608. doi: 10.1038/srep21608
- Morath, I., Hartmann, T. N., and Orian-Rousseau, V. (2016). CD44: more than a mere stem cell marker. *Int. J. Biochem. Cell Biol.* 81, 166–173. doi: 10.1016/j.biocel.2016.09.009
- Müller, B., Zerwes, H., Tangemann, K., Peter, J., and Engel, J. (1993). Two-step binding mechanism of fibrinogen to alpha IIb beta 3 integrin reconstituted into planar lipid bilayers. *J. Biol. Chem.* 268, 6800–6808.
- Purnick, P. E. M., and Weiss, R. (2009). The second wave of synthetic biology: from modules to systems. *Nat. Rev. Mol. Cell Biol.* 10, 410–422. doi: 10.1038/nrm2698
- Rankin, K. S., and Frankel, D. (2016). Hyaluronan in cancer - from the naked mole rat to nanoparticle therapy. *Soft Matter* 12, 3841–3848. doi: 10.1039/c6sm00513f
- Streuli, C. H. (2016). Integrins as architects of cell behavior. *Mol. Biol. Cell* 27, 2885–2888. doi: 10.1091/mbc.E15-06-0369
- Takahashi, R., Kubota, K., Kawada, M., and Okamoto, A. (1999). Effect of molecular weight distribution on the solution properties of sodium hyaluronate in 0.2M NaCl solution. *Biopolymers* 50, 87–98. doi: 10.1002/(SICI)1097-0282(199907)50:1<87::AID-BIP8>3.0.CO;2-K
- Tidwell, C. D., Ertel, S. I., Ratner, B. D., Tarasevich, B. J., Atre, S., and Allara, D. L. (1997). Endothelial cell growth and protein adsorption on terminally functionalized. *Langmuir* 13, 3404–3413. doi: 10.1021/la9604341
- Tu, R. S., and Tirrell, M. (2004). Bottom-up design of biomimetic assemblies. *Adv. Drug Deliv. Rev.* 56, 1537–1563. doi: 10.1016/j.addr.2003.10.047
- Ventre, M., and Netti, P. A. (2016). Engineering cell instructive materials to control cell fate and functions through material cues and surface patterning. *ACS Appl. Mater. Interfaces* 8, 14896–14908. doi: 10.1021/acsami.5b08658
- Yao, X., Peng, R., and Ding, J. (2013). Cell-material interactions revealed via material techniques of surface patterning. *Adv. Mater.* 25, 5257–5286. doi: 10.1002/adma.201301762
- Zaidel-Bar, R., Cohen, M., Addadi, L., and Geiger, B. (2004). Hierarchical assembly of cell-matrix adhesion complexes. *Biochem. Soc. Trans.* 32(Pt 3), 416–420. doi: 10.1042/BST0320416
- Zhang, K., and Chen, J. (2012). The regulation of integrin function by divalent cations. *Cell Adh. Migr.* 6, 20–29. doi: 10.4161/cam.18702
- Zimmerman, E., Geiger, B., and Addadi, L. (2002). Initial stages of cell-matrix adhesion can be mediated and modulated by cell-surface hyaluronan. *Biophys. J.* 82, 1848–1857. doi: 10.1016/S0006-3495(02)75535-5

**Conflict of Interest Statement:** The authors declare that the research was conducted in the absence of any commercial or financial relationships that could be construed as a potential conflict of interest.

Copyright © 2018 Zapp, Minsky and Boehm. This is an open-access article distributed under the terms of the Creative Commons Attribution License (CC BY). The use, distribution or reproduction in other forums is permitted, provided the original author(s) and the copyright owner(s) are credited and that the original publication in this journal is cited, in accordance with accepted academic practice. No use, distribution or reproduction is permitted which does not comply with these terms.



# Generation and Neuronal Differentiation of hiPSCs From Patients With Myotonic Dystrophy Type 2

Paola Spitalieri<sup>1\*</sup>, Rosa V. Talarico<sup>1</sup>, Michela Murdocca<sup>1</sup>, Luana Fontana<sup>1</sup>, Marzia Marcaurelio<sup>1</sup>, Elena Campione<sup>2</sup>, Roberto Massa<sup>3</sup>, Giovanni Meola<sup>4</sup>, Annalucia Serafino<sup>5</sup>, Giuseppe Novelli<sup>1,6</sup>, Federica Sangiuolo<sup>1†</sup> and Annalisa Botta<sup>1\*†</sup>

<sup>1</sup> Medical Genetics Section, Department of Biomedicine and Prevention, University of Rome Tor Vergata, Rome, Italy, <sup>2</sup> Division of Dermatology, Department of Systems Medicine, University of Rome Tor Vergata, Rome, Italy, <sup>3</sup> Division of Neurology, Department of Systems Medicine, University of Rome Tor Vergata, Rome, Italy, <sup>4</sup> Department of Biomedical Science for Health, Policlinico San Donato (IRCCS), University of Milan, Milan, Italy, <sup>5</sup> Institute of Translational Pharmacology, Italian National Research Council, Rome, Italy, <sup>6</sup> Istituto Neurologico Mediterraneo (IRCCS), Pozzilli, Italy

## OPEN ACCESS

### Edited by:

Cesare Gargioli,  
Università degli Studi di Roma Tor  
Vergata, Italy

### Reviewed by:

Emanuele Berardi,  
Ku Leuven University, Belgium  
Chiara Mozzetta,  
Sapienza Università di Roma, Italy

### \*Correspondence:

Paola Spitalieri  
paola.spitalieri@uniroma2.it  
Annalisa Botta  
botta@med.uniroma2.it

<sup>†</sup>These authors have contributed  
equally to this work.

### Specialty section:

This article was submitted to  
Integrative Physiology,  
a section of the journal  
Frontiers in Physiology

Received: 29 March 2018

Accepted: 02 July 2018

Published: 27 July 2018

### Citation:

Spitalieri P, Talarico RV, Murdocca M,  
Fontana L, Marcaurelio M,  
Campione E, Massa R, Meola G,  
Serafino A, Novelli G, Sangiuolo F and  
Botta A (2018) Generation  
and Neuronal Differentiation  
of hiPSCs From Patients With  
Myotonic Dystrophy Type 2.  
*Front. Physiol.* 9:967.  
doi: 10.3389/fphys.2018.00967

Human induced pluripotent stem cells (hiPSCs)-patient specific are an innovative tool to reproduce a model of disease *in vitro* and summarize the pathological phenotype and the disease etiopathology. Myotonic dystrophy type 2 (DM2) is caused by an unstable (CCTG)<sub>n</sub> expansion in intron 1 of the *CNBP* gene, leading to a progressive multisystemic disease with muscle, heart and central nervous dysfunctions. The pathogenesis of CNS involvement in DM2 is poorly understood since no cellular or animal models fully recapitulate the molecular and clinical neurodegenerative phenotype of patients. In this study, we generated for the first time, two DM2 and two wild type hiPSC lines from dermal fibroblasts by polycistronic lentiviral vector (hSTEMCCA-loxP) expressing *OCT4*, *SOX2*, *KLF4*, and *cMYC* genes and containing loxP-sites, excisable by Cre recombinase. Specific morphological, molecular and immunocytochemical markers have confirmed the stemness of DM2 and wild type-derived hiPSCs. These cells are able to differentiate into neuronal population (NP) expressing tissue specific markers. hiPSCs-derived NP cells maintain (CCTG)<sub>n</sub> repeat expansion and intranuclear RNA foci exhibiting sequestration of MBNL1 protein, which are pathognomonic of the disease. DM2 hiPSCs represent an important tool for the study of CNS pathogenesis in patients, opening new perspectives for the development of cell-based therapies in the field of personalized medicine and drug screening.

**Keywords:** myotonic dystrophy type 2 (DM2), human induced pluripotent stem cells (hiPSCs), intranuclear foci, neuronal population (NP), muscleblind-like 1 and 2 (MBNL1 and 2)

## INTRODUCTION

Myotonic dystrophies (DMs) represent a group of autosomal dominant multisystemic diseases (Harper, 2001), including DM type 1 and type 2 and manifesting highly variability in term of age at onset, severity of the symptoms, and clinical pictures. Myotonic dystrophy type 1 (DM1, OMIM 160900) is one of the most common forms of muscular dystrophy in adults with a prevalence of

1/8000 worldwide (Harper et al., 2002). It is caused by expansion of a CTG trinucleotide repeat in the non-coding region of *myotonic dystrophy protein kinase* gene (*DMPK*; OMIM 605377), a gene located on chromosome 19q13.3 encoding a protein kinase (Brook et al., 1992; Fu et al., 1992; Mahadevan et al., 1992). Myotonic dystrophy type 2 (DM2, OMIM 602688) results from an unstable tetranucleotide CCTG repeat expansion in intron 1 of the *nucleic acid-binding protein* (*CNBP*) gene (previously known as *zinc finger 9* gene, *ZNF9*; OMIM 116955) on chromosome 3q21 (Liquori et al., 2001). The true prevalence of DM2 is still uncertain since DM2 is likely under diagnosed, not only due to the unfamiliarity with the disorder by most clinicians but also to the heterogeneous phenotype and the rather aspecific onset.

The disease mechanism proposed for the pathogenesis of DMs is complex and involves a common RNA gain-of-function mechanism in which the CUG and CCUG repeats cause the accumulation of the expanded transcripts into nuclear RNA foci (Wojciechowska and Krzyzosiak, 2011) which, in turn, sequester and deregulate RNA-binding proteins, such as *MBNL1* and *MBNL2*. These events lead to the impaired alternative splicing (AS) and expression of aberrant embryonic protein isoforms in adult tissues and thus, the spliceopathy observed in DMs is indicated as the main cause of the multisystemic features of the diseases (Ranum and Day, 2004). In addition to spliceopathy, RNA toxicity may trigger further pathogenic mechanisms including dysregulation of miRNAs and RNAi metabolism, RAN translation, defects in protein translation/turnover, activation of cellular stress and apoptotic pathways (Loro et al., 2010; Botta et al., 2013a,b; Meola and Cardani, 2015). To date, defects in the AS of several genes have been reported in DM1 brain, including the glutamate *NMDA* receptor1, *APP*, and *MAPT* genes (Caillet-Boudin et al., 2014). Although, *MBNL2* appears to be a crucial factor in the aberrant splicing of the nervous tissues (Charizanis et al., 2012; Goodwin et al., 2015), little is known about links between the molecular defects and the various CNS symptoms in DM1 patients.

Despite caused by similar mutations, DM1 and DM2 are clinically distinct diseases: they differ for the age at onset, pattern of muscle weakness and absence of congenital and childhood-onset of DM2. Different studies confirm central nervous system (CNS) involvement in DM1 and to a lesser extent in DM2, indicating that DMs can be considered, beyond muscle, true brain disorders (Meola and Sansone, 2007). The cerebral involvement of DM1 patients has been associated with difficulties in executive functions, visuospatial/constructive abilities, memory, facial emotion recognition, and psychomotor delay. In the most severe cases of DM1 (congenital/juvenile form), mental retardation has also been described (Machuca-Tzili et al., 2005; Schara and Schoser, 2006). Furthermore, approximately half of these young patients also have autism spectrum disorders, the frequency of which is related to the number of CTG repeat (Ekstrom et al., 2008). Brain involvement in DM2 is more controversial. There are only few studies regarding the neuropsychological involvement in DM2 pathology and each includes small number of patients

(Minnerop et al., 2011). Cognitive manifestations in DM2 include problems with organization, concentration, and word finding which are considerably milder than in DM1 (Romeo et al., 2010). A specific type of “avoidant” personality trait and a significant impairment in executive functions have been observed in both DMs (Meola et al., 2003). Recently, a significant dysexecutive syndrome and impairment of episodic verbal memory have been reported on a large cohort of DM2 patients (Peric et al., 2015), reflecting of frontostriatal and temporal lobe dysfunctions. In contrast to DM1, DM2 has not been associated with developmental abnormalities and thus does not cause severe childhood symptoms. This difference likely explains why no mental retardation similar to that reported in congenital and juvenile forms of DM1 has been described in DM2 patients. The characterization of CNS involvement in DM2 is an evolving field of research, however, no cellular or animal models fully recapitulate the molecular and clinical phenotype of DM2 patients, particularly their brain involvement. The lack of accessibility of neural tissue (both living and post-mortem), combined with difficulties in culturing of these cell types *in vitro*, emphasizes the need for a DM2 cellular system capable to reproduce the mechanisms underlying the CNS impairment in patients.

Human induced pluripotent stem cells (hiPSCs) offer a nearly limitless potential for disease modeling, thanks to their great self-renewal and wide differentiation capacity, coupled with the relative ease of producing patient-specific cells. hiPSCs, carrying mutations implicated in disease, make possible the generation of a wide range of cell types in culture (Yanovsky-Dagan et al., 2015; Spitalieri et al., 2016). Neuronal stem cells (NSCs) derived from Embryonic Stem cells (ESCs) or from hiPSCs have been already generated for DM1, demonstrating their ability to recapitulate important features of the disease, including RNA foci, MBNL sequestration and transcriptional/splicing defects (Marteyn et al., 2011; Denis et al., 2013; Xia and Ashizawa, 2015; Xia et al., 2015; Gourdon and Meola, 2017; Spitalieri et al., 2018).

In this study, we established, for the first time two DM2 and two healthy hiPSC lines as control from human dermal fibroblasts (HDFs), using lentiviral polycistronic vector containing Yamanaka's four factors (*OCT4*, *SOX2*, *KLF4*, and *c-MYC*). These cells are able to self-renew indefinitely and also to differentiate into neuronal population (NP) maintaining the major specific DM2 hallmarks, such CCTG repeat expansion and CCUG-containing intranuclear RNA foci, which are pathognomonic the disease. The development of a hiPSCs-based platform represents an important tool to study the neurodegenerative and neuromuscular nature of the DM2 mutation and to identify molecular targets for drug design in repeat expansion disorders.

## MATERIALS AND METHODS

### Skin Biopsy and Culture of Human Dermal Fibroblasts (HDFs)

Two DM2 patients, one male and one female, with a molecular diagnosis of DM2, and two age and sex-matched

healthy donors (wild type, WT) have been recruited for dermal biopsy (Table 1). Before participation, informed written consent was obtained. The project was approved by The Committees on Health Research Ethics of Tor Vergata Hospital (2932/2017) and in accordance with the Declaration of Helsinki. Skin biopsies (6 mm in diameter) have been digested with 2 mg/mL DISPASE (Sigma-Aldrich, St. Louis, MO, United States) clean off any adipose and epidermal tissue for overnight at +4°C. Tissues have been processed into 0.5 mm cubes, treated with 1 mg/mL COLLAGENASE type I (Sigma-Aldrich, St. Louis, MO, United States) for 4 h at 37°C and successively placed onto 0.1% gelatin-coated (from porcine skin Type A; Sigma-Aldrich, St. Louis, MO, United States) 35-mm culture plates and cultured in primary culture medium DMEM (Sigma-Aldrich, St. Louis, MO, United States) with 15% fetal bovine serum (FBS) (Gibco, Waltham, MA, United States), 1 mM L-Glutamine (Gibco, Waltham, MA, United States), 1% penicillin/streptomycin (Thermo Fisher Scientific, Waltham, MA, United States), 1% non-essential amino acid solution (Gibco, Waltham, MA, United States), 0.1 mM  $\beta$ -mercaptoethanol (Gibco, Waltham, MA, United States). Fibroblasts growing out from the dermal tissue have been expanded in conventional serum-containing culture media until passage 2.

### hiPS Cells Reprogramming

A single lentiviral “stem cell cassette” has been used, flanked by loxP-sites (hSTEMCCA-loxP), and encoding for all four reprogramming factors (*OCT4*, *SOX2*, *KLF4*, and *c-MYC*) in a single polycistronic vector (Spitalieri et al., 2015, 2018). Approximately  $1.5 \times 10^5$  HDFs have been seeded on plastic in 35 mm culture plates and infected in DMEM, containing 15% FBS. The medium has been replaced after 16 h with hiPSCs medium: Dulbecco’s Modified Eagle’s medium-F12 (DMEM/HAM’s F12) (Gibco, Waltham, MA, United States) with 20% knock out serum replacement (KSR) (Gibco, Waltham, MA, United States), 1 mM L-glutamine, 1% penicillin/streptomycin, 1% non-essential amino acid solution, 0.1 mM  $\beta$ -mercaptoethanol and 10 ng/ml of basic Fibroblast Growth Factor (bFGF) (PeproTech, London, United Kingdom) and changed every 2–3 days. hiPSCs colonies have been picked 20–25 days post-infection on the basis of morphology and expanded by plating on mitomycin C-treated MEFs in hiPSCs medium (Sigma-Aldrich, St. Louis, MO, United States). Successively, hiPSCs have been manually picked, passaged on human embryonic stem cell-qualified Matrigel-coated plates (0.05 mg/mL) (Corning, NY, United States) and cultured under feeder-free condition in mTeSR1 medium with Y-27632 ROCK inhibitor (StemCell, Canada), maintaining the stability over 20 and more passages.

### Neural Differentiation of hiPSCs

For neural induction, a modified method previously described was used (Chambers et al., 2009). hiPSCs were cultured in neural induction medium combining dual ALK inhibition

(SB + LDN:10  $\mu$ m SB431542 (Tocris Bioscience, Bristol, United Kingdom) and 0.2  $\mu$ m LDN193189 (Stemgent, United Kingdom) in KSR media. For differentiating neuronal cells into neurons, increasing amounts of N2 (Gibco, Waltham, MA, United States) (25, 50, and 75%) was added to the KSR media maintaining LDN193189. On day 5–9 sonic hedgehog (SHH; Curis, Lexington, MA United States) was added in N2 media followed by the addition on day 9 of BDNF (PeproTech, London, United Kingdom), ascorbic acid (Sigma-Aldrich, St. Louis, MO, United States) and FGF8 (PeproTech, London, United Kingdom) and matured on days 12–30 with BDNF, ascorbic acid, GDNF (PeproTech, London, United Kingdom), TGF $\beta$ 3 (Sigma-Aldrich, St. Louis, MO, United States), cAMP (Sigma-Aldrich, St. Louis, MO, United States) for dopaminergic subtype and retinoic acid (Sigma-Aldrich, St. Louis, MO, United States) for motor neuron cells.

### Alkaline Phosphatase (AP) and Immunofluorescence (IF) Analyses

Alkaline phosphatase staining was performed with the Vector Red Substrate Kit (Vector Laboratories, Burlingame, CA, United States<sup>1</sup>) according to the manufacturer’s protocol. For IF analysis, cells were fixed in 4% paraformaldehyde and incubated with the appropriate primary antibodies against OCT4 (Stemgent, United Kingdom), SSEA-4 (Stemgent, United Kingdom), TRA1-60 (Stemgent, United Kingdom), TRA1-81 (Stemgent, United Kingdom), NESTIN (Millipore, Burlington, NJ, United States), PAX6 (Abcam, Cambridge, United Kingdom), OLIG2 (Millipore, Burlington, NJ, United States), CHAT (Millipore, Burlington, NJ, United States), TH (Abcam, Cambridge, United Kingdom), TUJ1 (Covance, Princeton, NJ, United States), MAP2 (Sigma-Aldrich, St. Louis, MO, United States), GFAP (Millipore, Burlington, NJ, United States). Appropriate AlexaFluor 488 or 568 secondary antibodies were incubated for 1 h. Nuclei have been counterstained with 4,6-diamidino-2-phenylindole (DAPI; Sigma-Aldrich, St. Louis, MO, United States). Samples have been observed and acquired by fluorescence microscope (Zeiss Axioplan 2 microscope, Thornwood, NY, United States).

### RNA Fluorescence *in Situ* Hybridization (RNA-FISH) and IF Staining

Intranuclear foci containing (CCUG)<sub>exp</sub> RNA were detected in hiPSCs and NPs from DM2 patients using via RNA fluorescence *in situ* hybridization (FISH) using Cy3-labeled (CAGG)<sub>10</sub> DNA probe (Bonifazi et al., 2006). The cells have been fixed with 4% paraformaldehyde (PFA), permeabilized using 0.3% Triton 100-X, then blocked with 3% BSA and incubated with primary antibodies OCT4, TUJ1, MAP2, GFAP, ISLET1 (Abcam, Cambridge, United Kingdom), LIM3 (Millipore, Burlington, NJ, United States), and MBNL1 (3A4, Santa Cruz Biotechnology,

<sup>1</sup>www.vectorlabs.com

**TABLE 1** | Description of samples used in this study.

Samples used in the study						
Donor	Diagnosis	Genotype	Age of biopsy (range)	No of hiPS clonal lines generated	No of hiPS clonal lines used	Passage
C3	Healthy	WT/WT	40–46	21	5	23
C4	Healthy	WT/WT	40–46	17	5	21
D1	DM2	CCTGexp	40–46	13	5	22
D2	DM2	CCTGexp	40–46	7	5	21

**TABLE 2** | List of primers and TaqMan probes used in this study.

Primers	Forward (5'–3')	Reverse (5'–3')
5S	TCGTCTGATCTCGGAAGCTAAGCA	AAAGCCTACAGCACCCGGTATT
OCT-4	AACCTGGAGTTTGTGCCAGGGTTT	TGAACCTCACCTTCCCTCCAACCA
SOX-2	AGAAGAGGAGAGAGAAAGAAAGGAGAGA	GAGAGAGGCAAACCTGGAATCAGGATCAAA
NANOG	CCTGAAGACGTGTGAAGATGAG	GCTGATTAGGCTCCAACCATAC
KLF-4	ACGATCGTGGCCCCGGAAAAGGACC	TGATTGTAGTGTCTTCTGGCTGGGCTCC
C-MYC	CGAGAGGACCCGTGGATGCAGAG	TTGAGGGGCATCGTCGCGGGAGGCTG
REX-1	CAGATCCTAAACAGCTCGCAGAAT	GCGTACGCAAATTAAGTCCAGA
MAP2	CCATTTGCAACAGGAAGACAC	CAGCTCAAATGCTTTGCAACTAT
Olig2	CCTGAGGCTTTTCGGAGC	CTGGCGTCCGAGTCCAT
Peripherin	AGACCATTGAGACCCGGAAT	GGCCTAGGGCAGAGTCAAG
Nestin	CCTGACCTGTCAGAGAAT	CCCACCTTCTCCTCATCTG
GFAP	CCGACAGCAGGTCCATGTG	GTTGCTGGACGCCATTGC
HB9	CACCGAGACCCAGGTGAAGATTT	CCCTTCTGTTTCTCCGCTTCTCT
FNIP	GCAGCAGTATTTGTGGGAGTC	TCCAGGCATGTCCATTGG
MARK2	ACCAGCACAAATCGAAGCAG	AGGCAACAGGGACACGCT
PPIP5K1	CGAATCTTCAGGACTACGC	GGGCATTATGCAGTGTTCCT
KIF13A	TGCCACTTATGTTGAAGCCA	TGCATCTGACCACCTCTCCCTT
FMNL3	GCGGGAATTTCTGAATGATG	CACTAGGCGGGAGTTCTTCA
CD47	AAGCTGTAGAGGAACCCCTTAATG	GGTCTCATAGGTGACAACCAAGT
PALM	ACAAGCGAGTCTCCAACACG	GTCCGCTTTGTGGATGAGTT
ITGA6	ATCATCCTAGTGGCTATTCTCGC	ACTGTCATCGTACCTAGAGCGT
GAPDH	TTGCCCTCAACGACCCTTTG	CACCCTGTTGCTGTAGCCAAATTC
$\beta$ -actin	ATTGCCGACAGGATGCAGAA	GCTGATCCACATCTGCTGGAA
CL3N58D	GGCCTTATAACCATGCAAATG	GCCTAGGGGACAAAGTGAGA
OCT4-BSP	ATTTGTATTGAGTTTTGGAGGG	CATCACCTCCACCACCTAAA
$\beta$ -actin	4326315E	
<i>MBNL1</i>	Hs00253287_m1	
<i>MBNL2</i>	Hs01058996	
CNBP	Hs00231535_m1	

Dallas, TX, United States) labeled with AlexaFluor 488 or 568 secondary antibody. Nuclei have been counterstained with 4,6-diamidino-2-phenylindole. Samples have been observed by confocal microscopy (LEICA TCS SP5). Up to 50 serial sections (each section about 1  $\mu$ m in thickness), taken from the top to the bottom along the Z axis, have been used to obtain a 3D reconstruction of each analyzed field.

## Gene Expression and Splicing Analysis

RNA from HDFs, hiPSCs and NP was extracted by TRIzol (ThermoFisher Scientific, Waltham, MA, United States)

following manufacturer's instructions and reverse-transcribed with the High-Capacity cDNA Reverse Transcription Kit (Applied Biosystems, Foster City, CA, United States) for cDNA synthesis. Both SYBR Green and TaqMan chemistry with reference genes have been used to quantify mRNA expression. Oligonucleotide sequences and TaqMan probes used are listed in **Table 2**. RT-PCR for *MBNL1* selected target (*FNIP1*, *MARK2*, *PPIP5K1*, *KIF13A*, *FMNL3*, *CD47*, *PALM*, *ITGA6* genes) was carried out as reported in Venables et al. (2013). Electrophoresis of the PCR products for splicing analysis was carried out on a 2.5% agarose gel.

## Methylation Sensitive High Resolution Melting (MS-HRM) Analysis of the *OCT4* Gene Promoter

Bisulphite treatment of DNA converts all unmethylated cytosines to uracil, leaving methylated cytosines unaltered. Genomic DNA (2  $\mu$ g in 20  $\mu$ l) extracted from HDFs and hiPSCs cell lines was treated with EZ DNA Methylation-Gold Kit (Zymo Research, Irvine, CA, United States) according to the manufacturer's instructions. After bisulfite conversion, the genomic DNA was quantified by the Qubit<sup>®</sup> 2.0 Fluorometer (Invitrogen, Carlsbad, CA, United States) according to the manufacturer's instructions. The bisulphite converted DNA was then used for PCR amplification of *OCT4* gene promoter regions with primers designed using Methyl Primer Express Software v1.0 (Applied Biosystem). Primers (OCT4-BSP) were designed to amplify the promoter and exon 1 from -234 to +46 base pairs (NR\_034180) (Shi et al., 2013; **Table 2**). PCR amplification and HRM analysis of bisulphite-converted DNA was carried out on 7500 Fast Real-Time PCR System (Applied Biosystems, Foster City, CA, United States), as previously described (Spitalieri et al., 2015).

## Genotyping at the DM2 Locus

Genomic DNA was extracted from DM2 hiPSCs and NPs using Wizard Genomic DNA Purification Kit (Promega, Madison, WI, United States). Molecular characterization of the (CCTG)<sub>n</sub> expansion in the *CNBP* gene was obtained by a Long-Range PCR based protocol followed by oligospecific hybridization with a (CCTG)<sub>5</sub> radioactively labeled probe (Botta et al., 2006).

## Statistical Analysis

All values provided for RT-qPCR experiments and for foci analysis are from independent experiments and are reported as mean  $\pm$  SEM. Each cell line (10 from 2 WT donors and 10 for 2 DM2 donors) has been tested in triplicate and elaborated as mean  $\pm$  SEM, then for each donor a mean of these value has been further elaborated. Data have been compared using the two-tailed Student's *t*-test, for independent samples.

## RESULTS

### Generation and Characterization of DM2 and WT hiPSCs

HDFs from two DM2 patients and two healthy controls (WT) were reprogrammed using a single lentiviral "stem cell cassette" (hSTEMCCA-loxP), containing all defined genes necessary to obtain hiPSCs (Spitalieri et al., 2015, 2018). Thirty-eight hiPSC clonal lines from two healthy donors (WT) and 20 hiPSC clonal lines from two DM2 patients have been generated and 5 lines/each donor have been used (**Table 1**), molecular and IF analyses have been performed between passages p20 and p23 in culture. All hiPSCs exhibited an undifferentiated morphology with compact refractile, defined borders and high rate of proliferation. As shown in **Figure 1**, cells expressed alkaline

phosphatase activity (AP), the transcription factor OCT4 and surface stemness markers such as TRA 1-60, SSEA-4, TRA 1-81. The success of reprogramming has been also confirmed by RT-qPCR analysis, carried out using primers designed to specifically detect endogenous reprogramming transcription factors (*OCT4*, *NANOG*, *SOX2*, *KLF4*, *c-MYC*, *REX-1*) and to elude any possible contamination of exogenous transcripts expressed by the hSTEMCCA-loxP lentiviral vector. The results revealed a clear expression of embryonic marker genes in both DM2 and WT hiPSCs, compared to those detected in human embryonic stem cells (HUES-3) (**Figure 2**). No chromosomal aberrations in DM2 and WT hiPSCs have been observed by karyotype analysis (data not shown). Moreover, RNA-FISH, combined with IF analysis, revealed the presence of intranuclear CCUG-containing foci in OCT4-positive hiPSCs derived from DM2 patients, thus confirming the retention of expanded sequences accumulated within nuclei of pluripotent cells. No foci were detected in the healthy controls-derived hiPSCs (**Figure 3**).

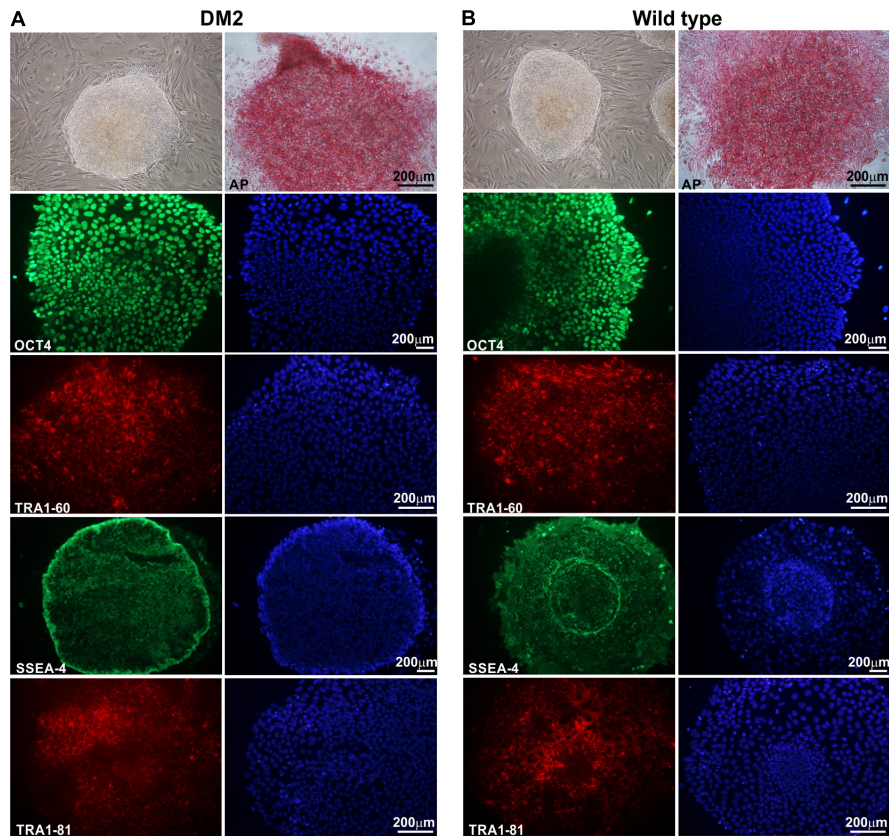
### Methylation Analysis of the *OCT-4* Promoter

Methylation Sensitive High Resolution Melting (MS-HRM) analysis has been used to examine if the *OCT4* expression observed in hiPSCs lines was correlated with the hypomethylation of minimal promoter and exon 1 of the gene. Eleven CpG dinucleotides have been analyzed within this region. The aligned melt curve profiles of standard with different ratios of methylated-to-unmethylated templates (0, 10, 25, 50, 80, and 100%), HDFs and hiPSCs lines are displayed in **Figure 4**. The methylation pattern of the *OCT4* region analyzed differs significantly between HDFs and hiPSCs lines. The percentage of *OCT4* methylation in both WT and DM2 HDFs (values ranging from 70 to 90%) resulted to be significantly higher respect to WT and DM2 hiPSCs (values ranging from 20 to 40%;  $p < 0.005$ ) (**Figure 4**). These data are in agreement with the activation of the *OCT4* gene that occurs along the HDFs to hiPSCs reprogramming process.

### *MBNL1* and *MBNL2* Are Involved in Pluripotent Stem Cell Reprogramming of WT and DM2 Lines

Previous studies have shown that both *MBNL1* and *MBNL2* have a lowest relative mRNA level in ESCs/hiPSCs compared to other cells and tissues (Han et al., 2013; Venables et al., 2013), confirming a conserved and prominent role for both genes in ESC-differential AS. In fact, MBNL proteins are shown to negatively regulate an ESC-differential AS network that controls pluripotency and reprogramming (Han et al., 2013). We therefore performed a gene expression analysis by RT-qPCR in order to quantify mRNA levels of *MBNL1* and *MBNL2* genes in our WT and DM2 HDF and hiPSC lines. Results clearly showed a variation in the expression of these genes among the four analyzed cell lines, independently from their genotypes.





**FIGURE 1 |** Morphological and immunocytochemical analysis of human hiPSC clones. A representative image, obtained by phase-contrast microscopy, of hiPSCs derived from a DM2 patient (**A**) and from a wild type (WT) (**B**). Cells have been analyzed at p22 (DM2) and p23 (WT) passages. hiPSCs are cultured under feeder-free condition in mTeSR1 medium, showing undifferentiated morphology, similar to hES cells, with compact refractile and defined borders. hiPSCs express alkaline phosphatase (AP) and are positive for stem cell markers OCT4 (green), TRA1-60 (red), SSEA-4 (green), and TRA1-81 (red). 4,6-Diamidino-2-phenylindole (DAPI) nuclear staining in blue (right column in **A,B**). Scale bars = 200  $\mu\text{m}$ .

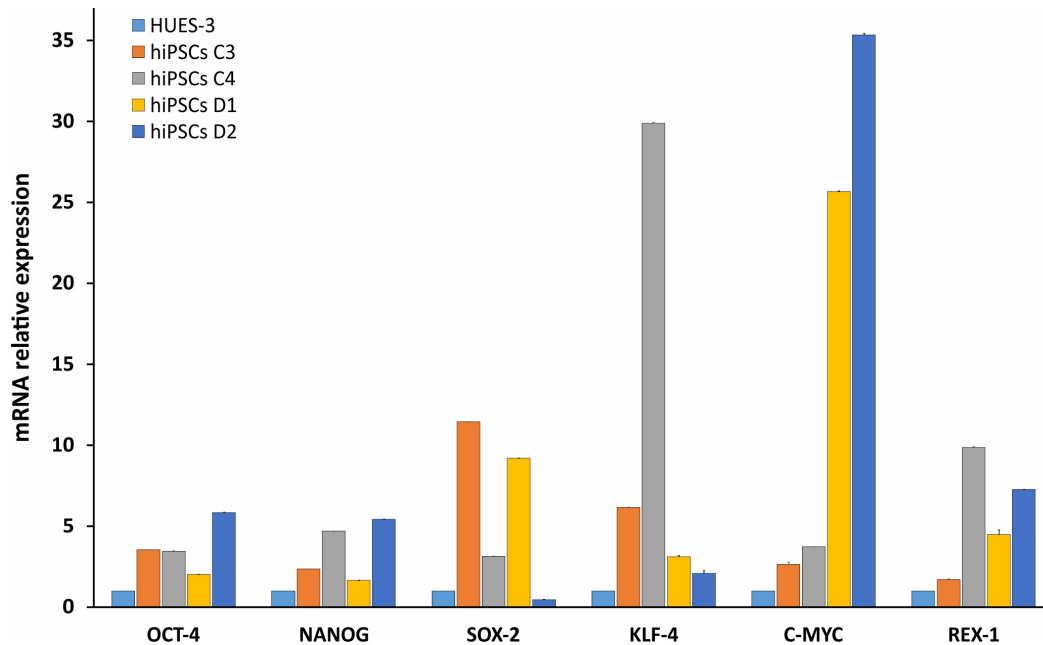
In particular, RT-qPCR assay revealed that HDFs express the higher levels of *MBNL1* and *MBNL2* transcripts (average values of DM2 and WT cell lines:  $0.648 \pm 0.07$  and  $0.603 \pm 0.03$ , respectively) compared to hiPSCs (average values of DM2 and WT cell lines:  $0.115 \pm 0.04$  and  $0.206 \pm 0.07$ , respectively) (**Figure 5A**). These data confirm that *MBNL2*, as well as *MBNL1*, is differently regulated during hiPSCs reprogramming and plays a central and negative regulatory role in pluripotency. However, comparison of the *MBNL1* and *MBNL2* expression pattern in WT (C3 and C4) and DM2 (D1 and D2) HDFs and hiPSCs did not revealed any significant differences.

We then focused our attention on a set of genes (*FNIP1*, *MARK2*, *PPP5K1*, *KIF13A*, *FMNL3*, *CD46*, *PALM*, and *ITGA6*), whose AS is controlled by the MBNL proteins during the HDFs to hiPSCs transition (Venables et al., 2013). As expected, a classical HDFs to hiPSCs switch-like splicing pattern has been observed for all the gene analyzed in both DM2 and WT cell lines (**Figure 5B**). Again, no significant differences have been observed among DM2 and WT cells, thus implying that the MBNLs sequestration into CCUG-containing ribonuclear foci does not perturb splicing changes

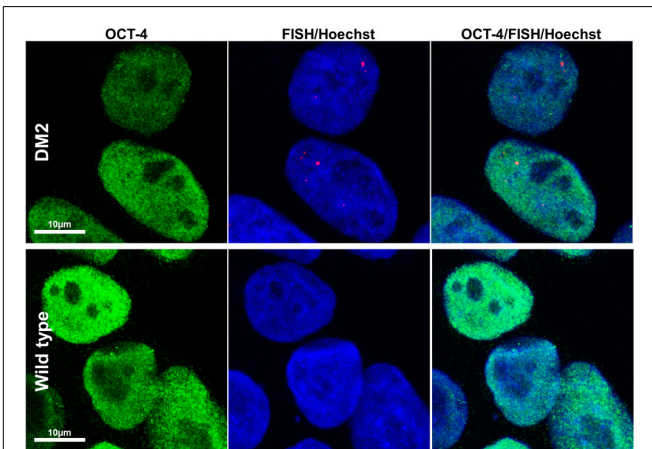
upon the induction of the original HDFs into the pluripotent state.

## Differentiation and Characterization of hiPSCs-Derived Neural Population (NPs)

Neuronal differentiation was performed using EB-based approach by DUAL inhibition of SMAD signaling, obtained with the addition of SB431542/LDN to achieve full neural conversion from WT and DM2 hiPSCs into NPs. The expression of neural stem cell marker, NESTIN, and dorsal forebrain marker, PAX6, showed a profile of neural induction after the first 12 days of the differentiation process, as revealed by immunofluorescence analysis (**Figure 6A**). Following the addition of several factors such as BDNF, ascorbic acid, TGF $\beta$ 3, GDFN, retinoic acid, and cAMP to neural precursors, at day 25 of differentiation, we observed a mixed population of cells expressing different neuronal markers specific for neurons, astrocytes, oligodendrocytes, early dopaminergic cells and early motor neuron precursors. After day 25, we obtained neuronal networks formed by precursors of oligodendrocytes and dopaminergic cells, as demonstrated by



**FIGURE 2 |** Molecular characterization of stemness markers in hiPSCs. RT-qPCR analysis of *OCT4*, *NANOG*, *SOX-2*, *KLF-4*, *c-MYC*, and *REX-1* transcripts evaluated in WT (C3 and C4) and DM2 (D1 and D2) hiPSCs. The values have been normalized respect to those obtained in a human embryonic stem cell line (HUES-3). 5S ribosomal gene is used as reference. Data are from independent experiments ( $n = 5$  clones for each donor indicated) and represented as mean  $\pm$  SEM.

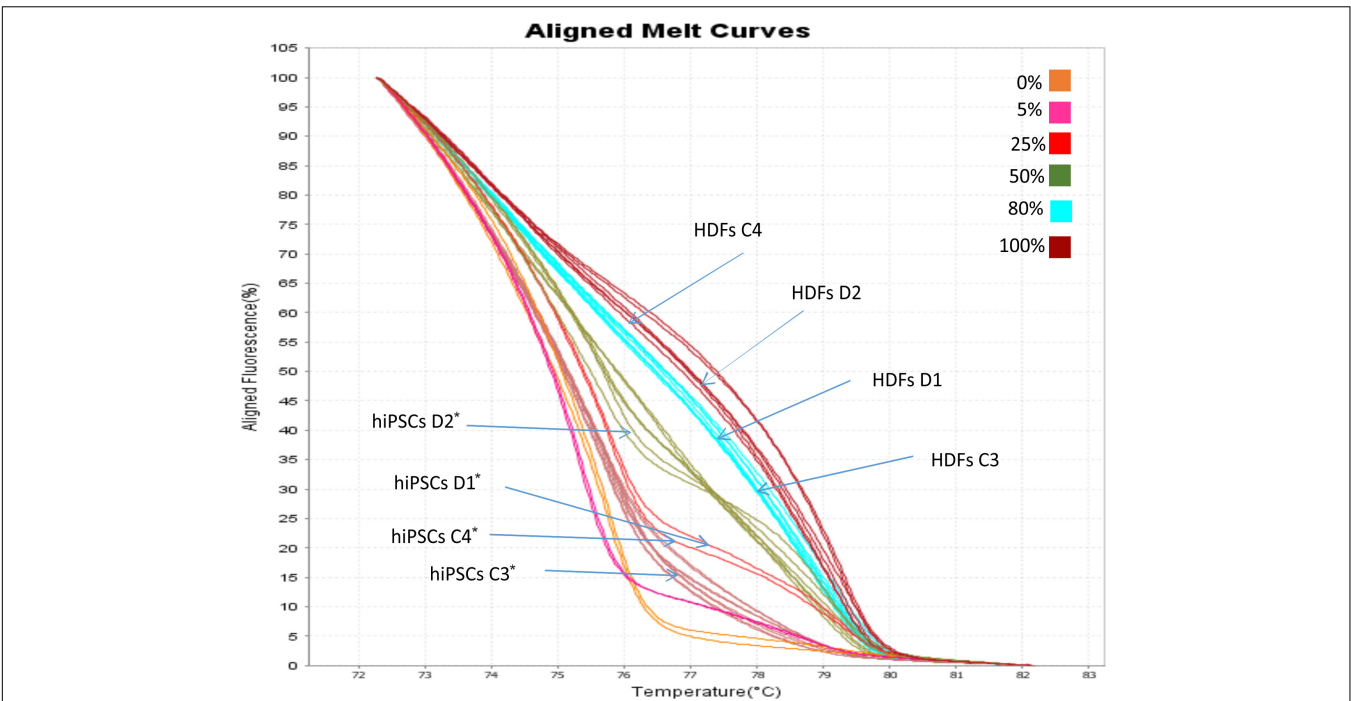


**FIGURE 3 |** RNA-FISH in hiPSCs. Representative confocal microscopic images showing the presence of CCUG-containing RNA foci (red) in DM2 nuclei, positive for stemness marker OCT-4 (green). Cells have been analyzed at p22 (DM2) and p21 (wild type) passages. Foci have been detected in 100% of DM2 hiPSCs, whereas no foci have been detected in WT hiPSCs. 4,6-Diamidino-2-phenylindole (DAPI) nuclear staining (blue). Scale bars = 10  $\mu$ m.

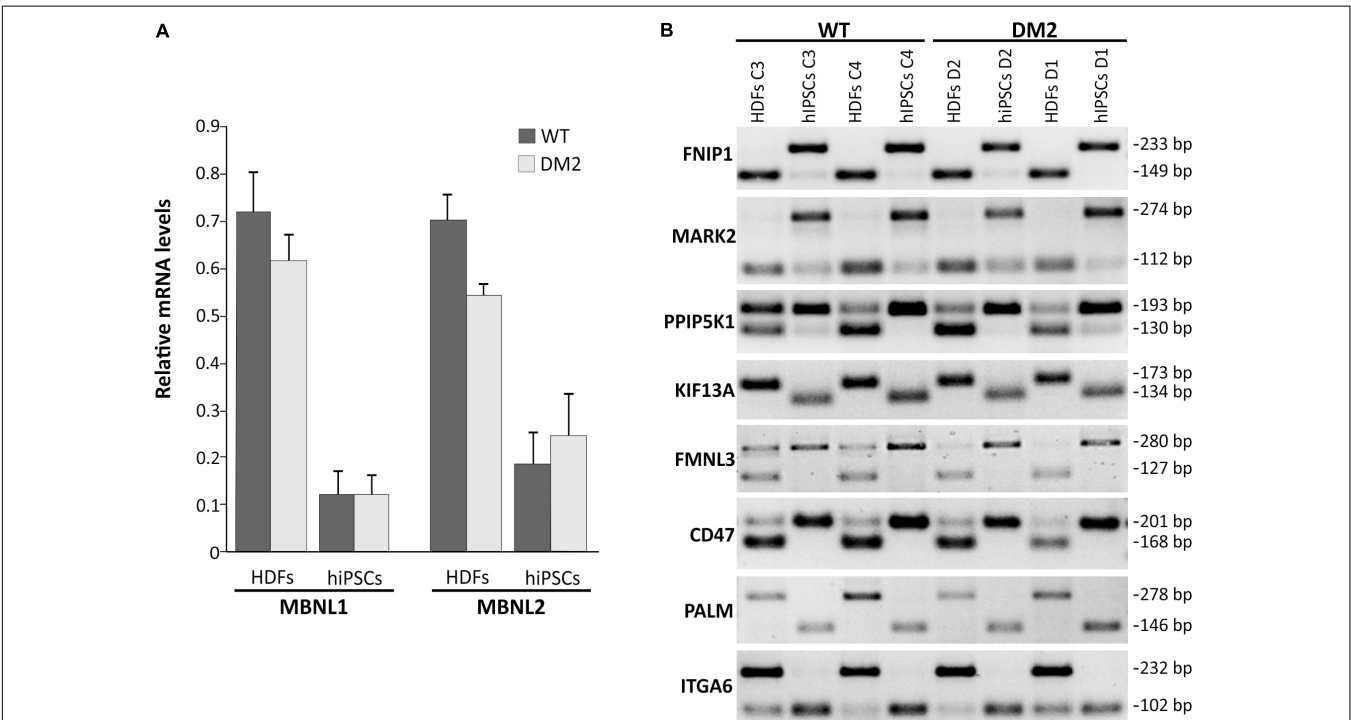
positive staining of OLIG2 and Tyrosine Hydroxylase (TH) antigen, respectively (**Figure 6A**). Cells also showed positivity for choline acetyltransferase marker (CHAT), one of the enzymes involved in the synthesis of the neurotransmitter acetylcholine (**Figure 6A**). The differentiation process has verified according to the protocol described in **Figure 6B**.

In order to test if NPs from DM2 patients retain the main molecular hallmark of the disease after the differentiation process, we evaluate the presence of intranuclear CCUG-containing RNA foci in cells expressing known neuronal markers. RNA-FISH, combined with IF analysis in DM2 and WT NPs, showed ribonuclear foci only in DM2 cells, positive to neuron-specific marker TUJ1, dendritic marker MAP2 and astrocytic marker GFAP (**Figure 7**). A further differentiation was obtained by adding retinoic acid until the appearance of motor neuron cells, in which ISLET1 and LIM3 markers together with RNA-foci have been detected by RNA-FISH. No foci were present in WT motor neurons (**Figure 8**). The quantification of ribonuclear foci in DM2 hiPSCs and NPs showed that the number of foci appears to be directly related with the neuronal differentiation. As shown in **Figure 9A**, the percentage of cells containing a number of foci/nucleus  $> 5$  was significantly higher in DM2 NPs respect to DM2 hiPSCs (82 and 20% of hiPSCs, respectively). We then wanted to verify if the observed increase in the number of CCUG-containing RNA foci could be related to the DM2 mutation size and/or *CNBP* expression. LR-PCR analysis on DNA extracted from DM2 hiPSCs and NPs revealed that in neural cells the number of CCTG repetition increases compared to hiPSCs in both lines (**Figure 9B**). Conversely, RT-qPCR showed variable expression levels of *CNBP* transcript with no significant differences between hiPSCs (median value normalized to  $\beta$ -actin gene:  $0.203 \pm 0.01$ ) and NP DM2 cell lines (median value normalized to  $\beta$ -actin gene:  $0.166 \pm 0.04$ ) (**Figure 9C**).

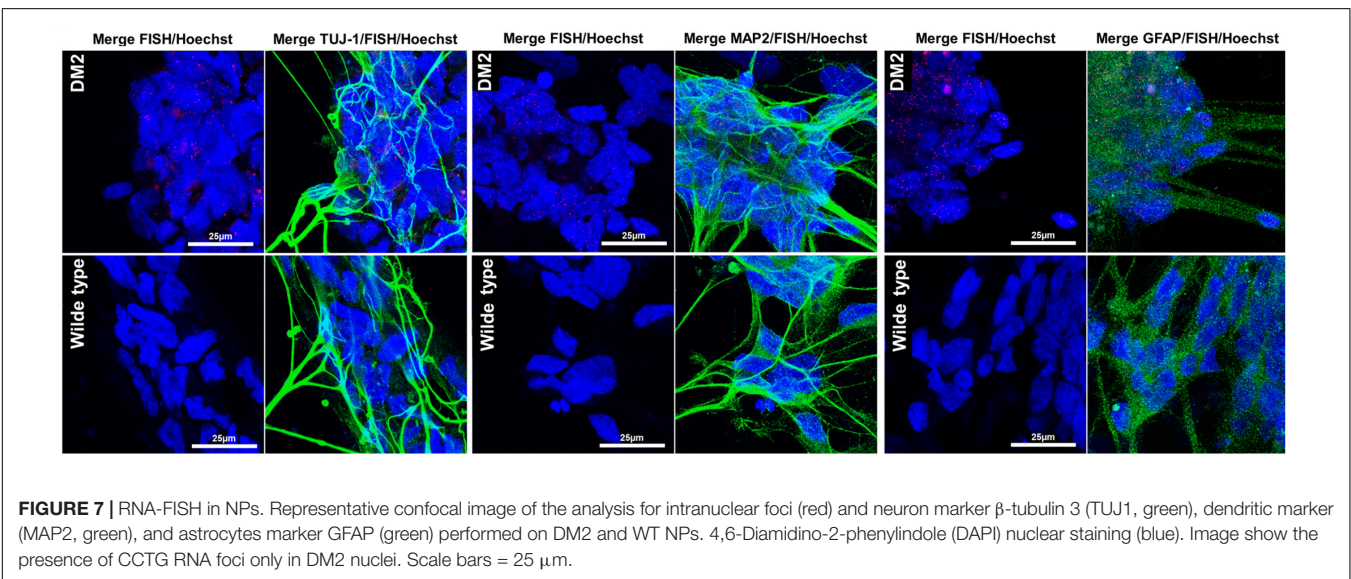
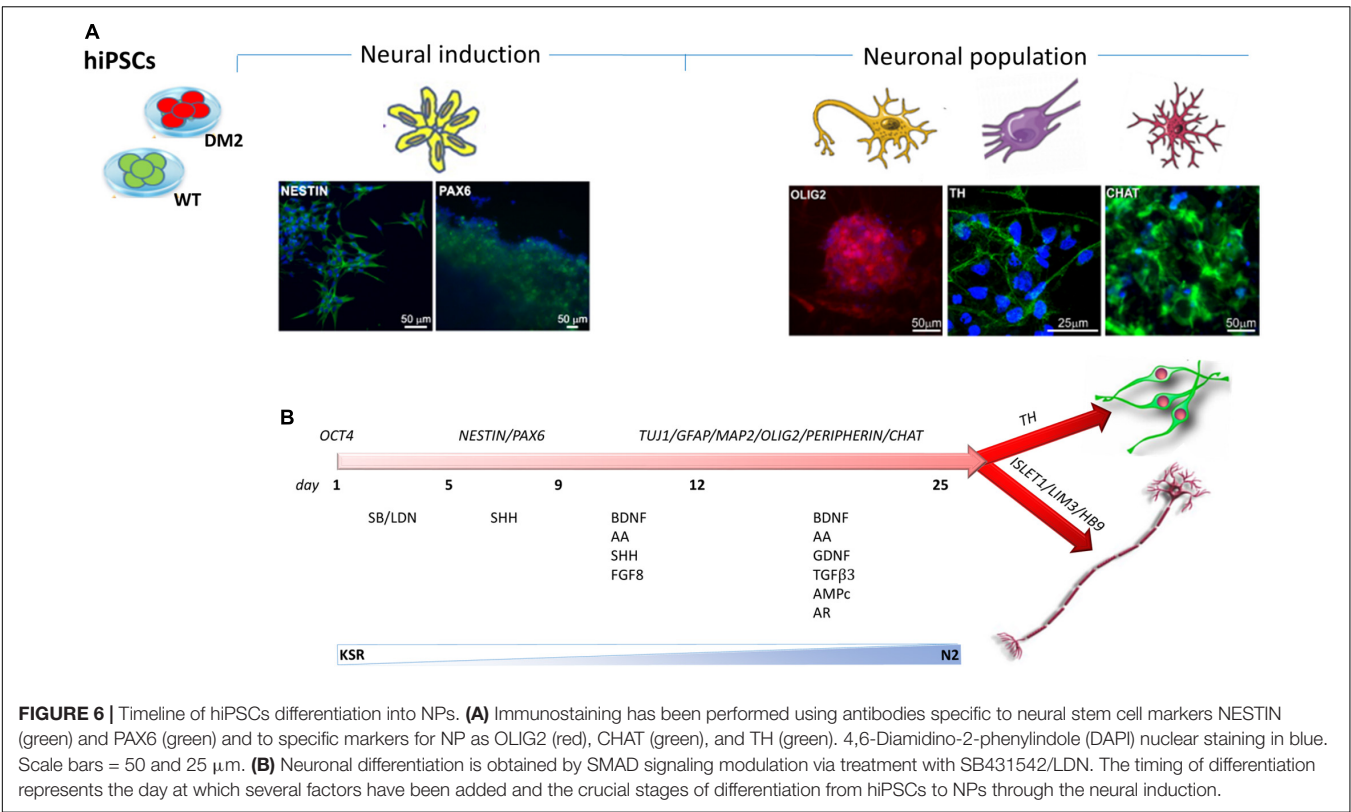
To further validate the differentiation capacity of DM2 and WT hiPSCs into NPs, we measured the expression



**FIGURE 4 |** MS-HRM analysis of the *OCT4* promoter region. Standard aligned melting curve corresponding to 0, 5, 25, 50, 80, and 100% of methylation. Aligned melting curves of hiPSCs and HDFs derived from DM2 patients (D1 and D2) and healthy control (C3 and C4). Student's *t*-test was used for statistical analysis. \**P* < 0.005.

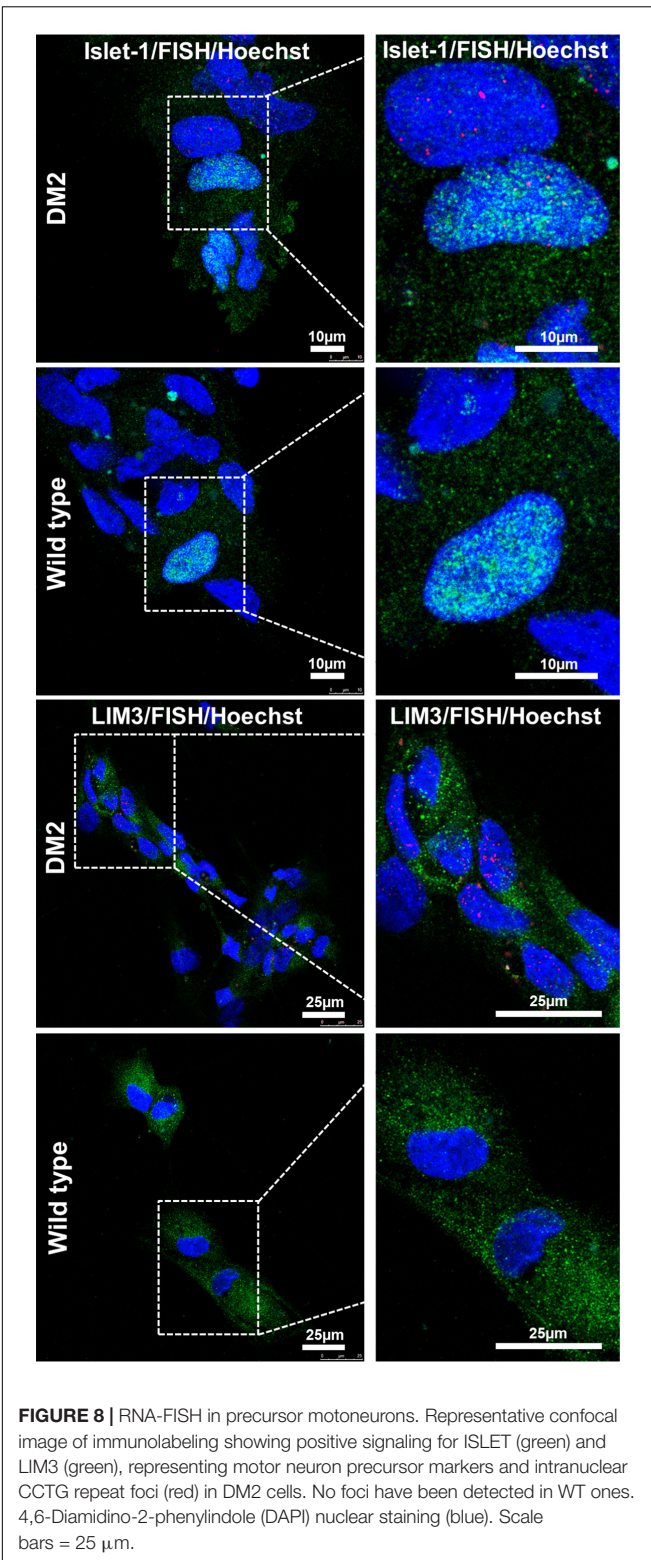


**FIGURE 5 |** RT-qPCR analysis of *MBNL1* and *MBNL2* gene and alternative splicing assay. **(A)** RT-qPCR assay for *MBNL1* and *MBNL2* genes expression in the HDFs to hiPSCs transition of WT and DM2 lines. Gene expression levels reported are an average of the WT and DM2 cell lines normalized to  $\beta$ -actin used as reference gene. **(B)** Eight-switch-like splicing changes of genes regulated by MBNL1 protein have been assessed by conventional RT-PCR analysis during the HDFs to hiPSCs transitions in WT and DM2 lines. The upper and lower bands on each gel represent the long (exon-included) and short (exon-omitted) isoforms, respectively.



levels of specific neural markers by RT-qPCR. This analysis revealed that NESTIN, an early marker of neural stem cell, resulted to be less expressed respect to markers of mature neurons, such as astrocytes and oligodendrocytes in both DM2 and WT cells. Specifically, after day 25th induction of neuronal and astrocytic differentiation resulted in transcriptional boost of lineage specific markers (i.e., MAP2, GFAP, peripherin). At the same time point of the *in vitro* differentiation, we also observed an evident expression level

of both oligodendrocyte transcription factor OLIG2, playing a crucial role in the neurogenesis, and of HB9, an early motor neuron marker ( $p < 0.01$ ) (Figure 10). These data demonstrated a robust patterning response in SB431542/LDN-treated neural progeny and derivation of relevant neuron subtypes after short differentiation periods (~25–30 days) compared to 40–50 days necessary for inducing rapid and complete neural conversion, as already reported (Perrier et al., 2004; Lee et al., 2007). Finally, the co-localization of ribonuclear



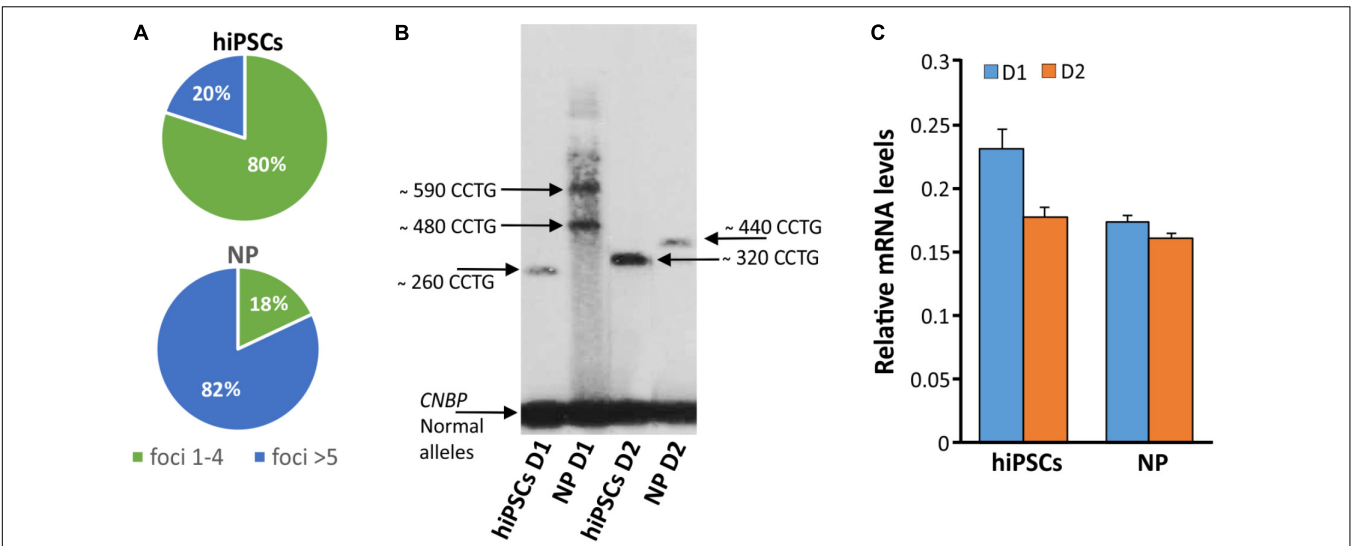
inclusion with MBNL1 protein typical of DM2 muscle cells (Cardani et al., 2014) is also present in DM2 NPs (Figure 11), showing that our neuronal cells are a functional DM2 modeling tool.

## DISCUSSION

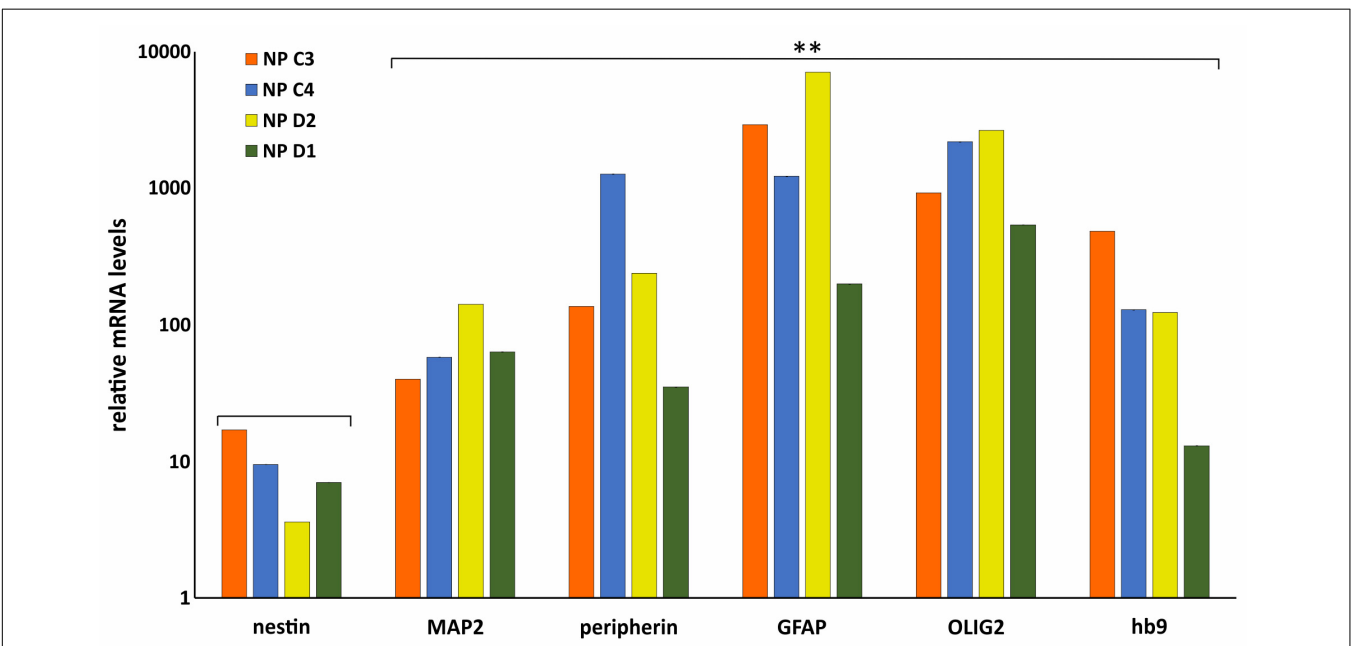
The majority of study in DM2 have been focused on the muscle pathology, but less is known about the impact of the CCTG expansion on the rest of the body. CNS symptoms, such as intellectual disability, behavioral issues and day time sleepness also have a large impact on patient's quality of life. However, the CNS is especially difficult to study as most material can only be obtained post-mortem. In this study we report, for the first time, that neural cells can be obtained by DM2 patient-specific hiPSCs, opening new avenues for modeling this complex multisystemic disease.

We obtained two hiPSCs from a male and a female affected by DM2. The analyses have been performed by comparing them to WT hiPSCs age- and sex-matched (Table 1). No isogenic lines were produced, but in order to improve the statistical significance, 5 cell lines from each patient, for a total of 10 lines DM2 and 10 lines WT, were always compared, considering cell-to-cell variability. In this way, even if partially, we have circumvented the limitation due to the lack of isogenic cells, in which a gene targeting approach has reversed the pathological phenotype (Spitalieri et al., 2018). The differentiation protocol used in the present study has considered the treatment with small molecules, SB and LDN that, effectively enhanced the differentiation of hiPSCs and changed their state toward a transitional EB state, inducing *in vitro* neural maturation. As previously described, the inhibition of BMP and TGF- $\beta$  signaling by the small molecules early during hiPSCs differentiation selectively blocks endodermal and mesodermal cell fates. This induces default neural specification, termed dual-SMAD inhibition, dramatically enriches neural ectodermal directly from pluripotent cells (Chambers et al., 2009; Sances et al., 2016). The following steps correspond to the neutralization through dual-SMAD inhibition, caudalization and ventralization through SHH activation by SHH protein and the consequent neural determination by neurotrophic factors such as BDNF, GDNF, TGF $\beta$ 3, and others for promoting neural maturation and survival. The robustness and modularity of the above strategy beyond hiPSCs differentiation offered an efficient defined and valid platform for the rapid generation of neural cell types including somatic motor neurons and dopamine neurons, as demonstrated by expression analyses of neural markers. Moreover, after differentiation no difference in term of differentiation efficiency has been observed among DM2 and WT cells. NPs obtained in this study typically contain heterogeneous cell progeny containing original neural stem cells (NSCs), including NSCs themselves and their progeny (Hawes and Pera, 2006), showing a similar response to induction factors during time-course.

The main pathognomonic molecular hallmark of DM2, represented by the presence intranuclear accumulation of CCUG-containing foci which sequester MBNL1 protein, are also conserved after neuronal differentiation. This suggests that RNA toxicity underlay CNS dysfunction in DM2 patients and allowed us to consider our hiPSCs-derived NP cells



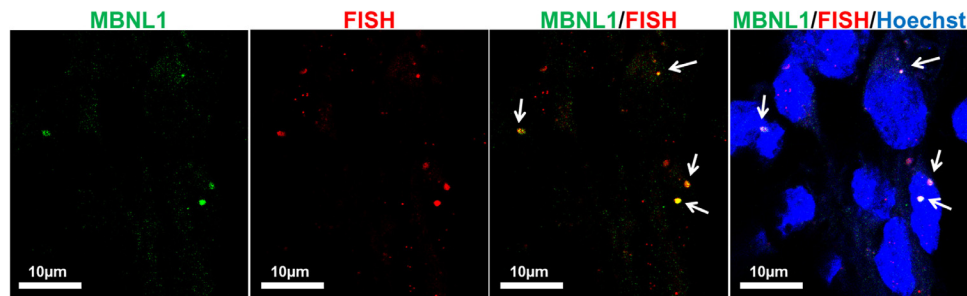
**FIGURE 9 |** Detection of DM2 mutation at DNA, expression of *CNBP* gene and RNA level during differentiation. **(A)** Percentages of nuclear foci (1–4 or >5) in hiPSCs and NP showing the increase of foci number along their differentiation process. **(B)** LR-PCR followed by hybridization with a (CTG)<sub>5</sub>-radioactively labeled probe on DNA extracted from DM2 hiPSCs and NPs, arrows indicated *CNBP* normal and expanded alleles. **(C)** RT-qPCR assay for *CNBP* expression in DM2 hiPSCs and NPs.  $\beta$ -actin is used as reference gene.



**FIGURE 10 |** Molecular characterization of NP. RT-qPCR analysis of *Nestin*, *MAP2*, *peripherin*, *GFAP*, *OLIG2*, and *HB9* in WT (C3 and C4) and DM2 (D1 and D2) NPs. Data are from independent experiments ( $n = 5$  clones for each donor indicated) and represented as mean  $\pm$  SEM; (\*\* $p < 0.01$ ). *GAPDH* is used as reference gene. Statistical analysis refers to *Nestin* gene expression.

as a good disease model. Interestingly, in DM patients the most severely affected tissues are those mainly formed by non-cycling cell populations (i.e., myotubes, neurons, and cardiomyocytes), on the contrary, self-renewing tissues are much less affected (Giagnacovo et al., 2012). This observation indicates that in these cells foci formation and the sequestration factors essential for RNA splicing and processing would be

a continuous and progressive phenomenon, eventually leading to the onset of disease symptoms. The quantification of ribonuclear foci during the neural differentiation of our DM2 hiPSCs showed that the number of foci increased after the neuronal differentiation and is not related to the number of passages in culture which is maintained after hiPSCs to NP transition. This observation is in accordance with previous



**FIGURE 11** | Co-localization of CCUG-containing ribonuclear foci with MBNL1 protein. Representative confocal microscopic images showing the presence of RNA-FISH of foci (red) co-stained with the splicing factor MBNL1 (green) in DM2-derived neuron (D2). 4,6-Diamidino-2-phenylindole (DAPI) nuclear staining (blue). Scale bars = 10  $\mu\text{m}$ .

data indicating that the number and density of ribonuclear foci progressively increase in cells that stop dividing and undergo differentiation (Cardani et al., 2009). Nevertheless, the expression level of the *CNBP* transcript does not differ significantly between hiPSCs and NP from DM2 patients. It is therefore possible that in non-cycling NP cells ribonuclear foci do not undergo relocation and degradation occurring during mitosis and progressively increase in number and size, due to a continuous accumulation of both expanded RNAs and protein factors.

Another important aspect still unknown in DM2 is the dynamic of the (CCTG) $n$  expansion in different cell types and the mechanism causing the (CCTG) $n$  expansion and/or contraction. The CCTG repeats expansion is highly unstable and tends to increase with age, while, differently from DM1, it usually decreases on transmission to the next generation being shorter in the children (Meola and Cardani, 2015). The cause for the instability is probably related to an *Alu*-mediated mechanism developed into the large CCTG expanded tract or to unequal crossing over (Dere et al., 2004; Kurosaki et al., 2012). This instability leads to the somatic mosaicism that gives rise to intra-tissue, inter-tissue, and cell-type variability over a patient's lifetime. Differently from DM1, the CCTG repetition number is not associated with phenotype severity, age, onset of disease. All together, these observations could explain some distinct features of DM2 such as the lack of a congenital form and anticipation and the later onset of symptoms (Udd et al., 2003). Interestingly the determination of the CCTG repetition number in our DM2 cells lines showed an increased in the expansion size during the neural differentiation. Of course, we are aware of all the limitations in determining the DM2 mutation size by LR-PCR, however, this analysis indicates a trend toward the expansion in our neuronal cell model which could be further investigated at molecular level.

Consistent with previous studies, we found that the *MBNL1* and *MBNL2* genes are expressed at minimal levels in hiPSCs compared to fibroblasts, confirming that both MBNL proteins negatively regulate pluripotency and reprogramming (Han et al., 2013). The direct consequences of MBNL downregulation in hiPSCs is the switch-like splicing pattern of a set of genes

whose AS is controlled by the MBNL proteins during the HDFs to hiPSCs transition (Venables et al., 2013). Interestingly, no differences have been observed in the splicing profile these MBNL-dependent genes in WT and DM2 cell lines. Consistently, once established, either DM2 and WT hiPSCs grew in a similar pattern with a high nuclear to cytoplasm ratio, expressed stem cells markers and had stem cells features of self-renewal and pluripotency. Taken together, our results indicate that sequestration of the MBNL proteins into the ribonuclear foci of DM2 cells does not exert a toxic effect on the reprogramming and differentiation capacity into NPs of hiPSCs.

Multiple RNA-based approaches have been investigated to induce the downregulation of the *DMPK* expanded transcripts (Thornton et al., 2017) and recently CRISPR/CAS9 genome editing technology has been successfully applied as a gene therapy approach for DM1 (Provenzano et al., 2017). The DM2-hiPSCs generated in our work could represent a powerful tool to study the potential role of genome editing and RNA-based therapeutic approaches also for DM2 pathology. Moreover, the detection of specific markers expressed in DM2 NPs could allow to follow the time-course of neurogenesis gaining further insights into the development of brain impairment in patients. The understanding/elucidation of the functional alteration affecting DM2 neural cells would help the finding of the more suitable pharmacological intervention to correct such abnormalities and would thus lay the bases for a future patient-tailored therapy.

## AUTHOR CONTRIBUTIONS

AB, FS, PS, and GN conceived the experiments. PS, RT, MiM and MaM conducted the experiments. EC, GM, and RM selected patients, LF and AS analyzed the data. AB, FS, and PS wrote the manuscript. All authors discussed and reviewed the manuscript.

## ACKNOWLEDGMENTS

Authors thank Graziano Bonelli for expert technical help.

## REFERENCES

- Bonifazi, E., Gullotta, F., Vallo, L., Iraci, R., Nardone, A. M., Brunetti, E., et al. (2006). Use of RNA fluorescence in situ hybridization in the prenatal molecular diagnosis of myotonic dystrophy type 1. *Clin. Chem.* 52, 319–322. doi: 10.1373/clinchem.2005.056283
- Botta, A., Bonifazi, E., Vallo, L., Gennarelli, M., Garrè, C., Salehi, L., et al. (2006). Italian guidelines for molecular analysis in myotonic dystrophies. *Acta Myol.* 25, 23–33.
- Botta, A., Malena, A., Loro, E., Del Moro, G., Suman, M., Pantic, B., et al. (2013a). Altered Ca<sup>2+</sup> homeostasis and endoplasmic reticulum stress in myotonic dystrophy type 1 muscle cells. *Genes* 4, 275–292. doi: 10.3390/genes4020275
- Botta, A., Malena, A., Tibaldi, E., Rocchi, L., Loro, E., Pena, E., et al. (2013b). MBNL142 and MBNL143 gene isoforms, overexpressed in DM1-patient muscle, encode for nuclear proteins interacting with Src family kinases. *Cell Death Dis.* 4:e770. doi: 10.1038/cddis.2013.291
- Brook, J. D., McCurrach, M., Harley, H. G., Buckler, A. J., Church, D., Aburatani, H., et al. (1992). Molecular basis of myotonic dystrophy: expansion of a trinucleotide (CTG) repeat at the 3' end of a transcript encoding a protein kinase family member. *Cell* 68, 799–808. doi: 10.1016/0092-8674(92)90154-5
- Caillet-Boudin, M. L., Fernandez-Gomez, F. J., Tran, H., Dhaenens, C. M., Buee, L., and Sergeant, N. (2014). Brain pathology in myotonic dystrophy: when tauopathy meets spliceopathy and RNAopathy. *Front. Mol. Neurosci.* 6:57. doi: 10.3389/fnmol.2013.00057
- Cardani, R., Giagnacovo, M., Rossi, G., Renna, L. V., Bugiardini, E., Pizzamiglio, C., et al. (2014). Progression of muscle histopathology but not of spliceopathy in myotonic dystrophy type 2. *Neuromuscul. Disord.* 24, 1042–1053. doi: 10.1016/j.nmd.2014.06.435
- Cardani, R., Mancinelli, E., Giagnacovo, M., Sansone, V., and Meola, G. (2009). Ribonuclear inclusion as biomarker of myotonic dystrophy type 2, even in important frozen or defrozen skeletal muscle biopsies. *Eur. J. Histochem.* 53, 107–111. doi: 10.4081/ejh.2009.e13
- Chambers, S. M., Fasano, C. A., Papapetrou, E. P., Tomishima, M., Sadelain, M., and Studer, L. (2009). Highly efficient neural conversion of human ES and iPS cells by dual inhibition of SMAD signaling. *Nat. Biotechnol.* 27, 275–280. doi: 10.1038/nbt.1529
- Charizanis, K., Lee, K. Y., Batra, R., Goodwin, M., Zhang, C., Yuan, Y., et al. (2012). Muscleblind-like 2-mediated alternative splicing in the developing brain and dysregulation in myotonic dystrophy. *Neuron* 75, 437–450. doi: 10.1016/j.neuron.2012.05.029
- Denis, J. A., Gauthier, M., Rachdi, L., Aubert, S., Giraud-Triboulet, K., and et al. (2013). mTOR-dependent proliferation defect in human ES-derived neural stem cells affected by myotonic dystrophy type 1. *J. Cell. Sci.* 126, 1763–1772. doi: 10.1242/jcs.116285
- Dere, R., Napierala, M., Ranum, L. P., and Wells, R. D. (2004). Hairpin structure-forming propensity of the (CCTG.CAGG) tetranucleotide repeats contributes to the genetic instability associated with myotonic dystrophy type 2. *J. Biol. Chem.* 279, 41715–41726. doi: 10.1074/jbc.M406415200
- Ekstrom, R. A., Osborn, R. W., and Hauer, P. L. (2008). Surface electromyographic analysis of the low back muscles during rehabilitation exercises. *J. Orthop. Sports. Ther.* 38, 736–745. doi: 10.2519/jospt.2008.2865
- Fu, Y. H., Pizzuti, A., Fenwick, R. G. Jr., King, J., Rajnarayan, S., Dunne, P. W., et al. (1992). An unstable triplet repeat in a gene related to myotonic muscular dystrophy. *Scienze* 255, 1256–1258. doi: 10.1126/science.1546326
- Giagnacovo, M., Malatesta, M., Cardani, R., Meola, G., and Pellicciari, C. (2012). Nuclear ribonucleoprotein-containing foci increase in size in non-dividing cells from patients with myotonic dystrophy type 2. *Histochem. Cell. Biol.* 138, 699–707. doi: 10.1007/s00418-012-0984-986
- Goodwin, M., Mohan, A., Batra, R., Lee, K. Y., Charizanis, K., Fernández Gómez, F. J., et al. (2015). MBNL Sequestration by toxic RNAs and RNA misprocessing in the myotonic dystrophy brain. *Cell. Rep.* 12, 1159–1168. doi: 10.1016/j.celrep.2015.07.029
- Gourdon, G., and Meola, G. (2017). Myotonic dystrophies: state of the art of new therapeutic developments for the CNS. *Front. Cell. Neurosci.* 11:101. doi: 10.3389/fncel.2017.00101
- Han, H., Irimia, M., Ross, P. J., Sung, H. K., Alipanahi, B., David, L., et al. (2013). MBNL proteins repress ES-cell-specific alternative splicing and reprogramming. *Nature* 498, 241–245. doi: 10.1038/nature12270
- Harper, P. S. (2001). *Myotonic Dystrophy*, 3rd Edn, London: WB Saunders.
- Harper, P. S., van Engelen, B. G., Eymard, B., Rogers, M., and Wilcox, D. (2002). 99th ENMC international workshop: myotonic dystrophy: present management, future therapy. 9–11 November 2001, Naarden, The Netherlands. *Neuromuscul. Disord.* 12, 596–599. doi: 10.1016/S0960-8966(02)00020-2
- Hawes, S., and Pera, M. F. (2006). “Identification and maintenance of cell lineage progenitors derived from human ES cells,” in *Essentials of Stem Cell Biology*, eds R. Lanza and A. Atala (Amsterdam: Elsevier), 355–362.
- Kurosaki, T., Ueda, S., Jshida, T., Abe, K., Ohno, K., and Matakaue, T. (2012). The unstable CCTG repeat responsible for myotonic dystrophy type 2 originates from an AluSx element insertion into an early primate genome. *PLoS One* 7:e38379. doi: 10.1371/journal.pone.0038379
- Lee, H., Shamy, G. A., Elkabetz, Y., Schofield, C. M., Harrision, N. L., Panagiotakos, G., et al. (2007). Directed differentiation and transplantation of human embryonic stem cell-derived motoneurons. *Stem Cells* 25, 1931–1939. doi: 10.1634/stemcells.2007-0097
- Liquori, C. L., Ricker, K., Moseley, M. L., Jacobsen, J. F., Kress, W., Naylor, S. L., et al. (2001). Myotonic dystrophy type 2 caused by CCTG expansion in intron 1 of ZNF9. *Science* 293, 864–867. doi: 10.1126/science.1062125
- Loro, E., Rinaldi, F., Malena, A., Masiero, E., Novelli, G., Angelini, C., et al. (2010). Normal myogenesis and increased apoptosis in myotonic dystrophy type-1 muscle cells. *Cell Death Differ.* 17, 1315–1314. doi: 10.1038/cdd.2010.33
- Machuca-Tzili, L., Brook, D., and Hilton-Jones, D. (2005). Clinical and molecular aspects of the myotonic dystrophies: a review. *Muscle Nerve* 32, 1–18. doi: 10.1002/mus.20301
- Mahadevan, M., Tsilfidis, C., Sabourin, L., Shuttler, G., Amemiya, C., Jansen, G., et al. (1992). Myotonic dystrophy mutation: an unstable CTG repeat in the 3' untranslated region of the gene. *Science* 255, 1253–1255. doi: 10.1126/science.1546325
- Marteyn, A., Maury, Y., Gauthier, M. M., Lecuyer, C., Vernet, R., Denis, J. A., et al. (2011). Mutant human embryonic stem cells reveal neurite and synapse formation defects in type 1 myotonic dystrophy. *Cell Stem Cell* 8, 434–444. doi: 10.1016/j.stem.2011.02.004
- Meola, G., and Cardani, R. (2015). Myotonic dystrophies: an update on clinical aspects, genetic, pathology, and molecular pathomechanisms. *Biochim. Biophys. Acta* 1852, 894–906. doi: 10.1016/j.bbadis.2014.05.019
- Meola, G., and Sansone, V. (2007). Cerebral involvement in myotonic dystrophies. *Muscle Nerve* 36, 294–306. doi: 10.1002/mus.20800
- Meola, G., Sansone, V., Perani, D., Scarone, S., Cappa, S., Dragoni, C., et al. (2003). Executive dysfunction and avoidant personality trait in myotonic dystrophy type 1 (DM-1) and in proximal myotonic myopathy (PROMM/DM-2). *Neuromuscul. Disord.* 13, 813–821. doi: 10.1016/S0960-8966(03)00137-8
- Minnerop, M., Weber, B., Schoene-Bake, J. C., Roeske, S., Mirbach, S., Anspach, C., et al. (2011). The brain in myotonic dystrophy 1 and 2: evidence for a predominant white matter disease. *Brain* 134, 3527–3543. doi: 10.1093/brain/awr299
- Peric, S., Mandic-Stojmenovic, G., Stefanova, E., Savic-Pavicevic, D., Pesovic, J., Ilic, V., et al. (2015). Frontostriatal dysexecutive syndrome: a core cognitive feature of myotonic dystrophy type 2. *J. Neurol.* 262, 142–148. doi: 10.1007/s00415-014-7545-y
- Perrier, A. L., Tabar, V., Barberi, T., Rubio, M. E., Bruses, J., Topf, N., et al. (2004). Derivation of midbrain dopamine neurons from human embryonic stem cells. *Proc. Natl. Acad. Sci. U.S.A.* 101, 12543–12548. doi: 10.1073/pnas.0404700101
- Provenzano, C., Cappella, M., Valaperta, R., Cardani, R., Meola, G., Martelli, F., et al. (2017). CRISPR/Cas9-mediated deletion of CTG expansion recovers normal phenotype in myogenic cells derived from myotonic dystrophy 1 patients. *Mol. Ther. Nucleic Acids* 15, 337–348. doi: 10.1016/j.omtn.2017.10.006
- Ranum, L. P., and Day, J. W. (2004). Pathogenic RNA repeats: an expanding role in genetic disease. *Trends Genet.* 20, 506–512. doi: 10.1016/j.tig.2004.08.004
- Romeo, V., Pegoraro, E., Ferrati, C., Squarzanti, F., Sorarù, G., Palmieri, A., et al. (2010). Brain involvement in myotonic dystrophies: neuroimaging and neuropsychological comparative study in DM1 and DM2. *J. Neurol.* 257, 1246–1255. doi: 10.1007/s00415-010-5498-3
- Sances, S., Brujijn, L. I., Chandran, S., Egan, K., Ho, R., Klim, J. R., et al. (2016). Modeling ALS with motor neurons derived from human induced pluripotent stem cells. *Nat. Neurosci.* 19, 542–553. doi: 10.1038/nn.4273



- Schara, U., and Schoser, B. G. (2006). Myotonic dystrophies type 1 and 2: a summary on current aspects. *Semin. Pediatr. Neurol.* 13, 71–79. doi: 10.1016/j.spn.2006.06.002
- Shi, J., Shi, W., Ni, L., Xu, X., Su, X., and Zia, L., et al. (2013). OCT4 is epigenetically regulated by DNA hypomethylation of promoter and exon in primary gliomas. *Oncol. Rep.* 30, 201–206. doi: 10.3892/or.2013.2456
- Spitalieri, P., Talarico, R. V., Botta, A., Murdocca, M., D'Apice, M. R., Orlandi, A., et al. (2015). Generation of Human induced pluripotent stem cells from extraembryonic tissues of fetuses affected by monogenic diseases. *Cell. Reprogram.* 14, 275–287. doi: 10.1089/cell.2015.0003
- Spitalieri, P., Talarico, R. V., Caioli, S., Murdocca, M., Serafino, A., Girasole, M., et al. (2018). Modelling the pathogenesis of Myotonic dystrophy type 1 cardiac phenotype through human iPSC-derived cardiomyocytes. *JMCC* 118, 95–109. doi: 10.1016/j.jmcc.2018.03.012
- Spitalieri, P., Talarico, R. V., Murdocca, M., Novelli, G., and Sangiuolo, F. (2016). Human induced pluripotent stem cells for monogenic disease modelling and therapy. *World Stem Cells* 8, 118–135. doi: 10.4252/wjsc.v8.i4.118
- Thornton, C. A., Wang, E., and Carrell, E. M. (2017). Myotonic dystrophy: approach to therapy. *Curr. Opin. Genet. Dev.* 44, 135–140. doi: 10.1016/j.gde.2017.03.007
- Udd, B., Meola, G., Krahe, R., Thornton, C., Ranum, L., Bassez, G., et al. (2003). Report of the 115th ENMC workshop: DM2/PROMM and other myotonic dystrophies. 3rd Workshop, 14–16 February 2003, Naarden, The Netherlands. *Neuromuscul. Disord.* 13, 589–596. doi: 10.1016/S0960-8966(03)00092-0
- Venables, J. P., Lapasset, L., Gadea, G., Fort, P., Klinck, R., Irimia, M., et al. (2013). MBNL1 and RBFOX2 cooperate to establish a splicing programme involved in pluripotent stem cell differentiation. *Nat. Commun.* 4:2480. doi: 10.1038/ncomms3480
- Wojciechowska, M., and Krzyzosiak, W. J. (2011). Cellular toxicity of expanded RNA repeats: focus on RNA foci. *Hum. Mol. Genet.* 20, 3811–3821. doi: 10.1093/hmg/ddr299
- Xia, G., and Ashizawa, T. (2015). Dynamic changes of nuclear RNA foci in proliferating DM1 cells. *Histochem. Cell Biol.* 143, 557–564. doi: 10.1007/s00418-015-1315-5
- Xia, G., Gao, Y., Jin, S., Subramony, S. H., Terada, N., Ranum, L. P., et al. (2015). Genome modification leads to phenotype reversal in human myotonic dystrophy type 1 induced pluripotent stem cell-derived neural stem cells. *Stem Cells* 33, 1829–1838. doi: 10.1002/stem.1970
- Yanovsky-Dagan, S., Mor-Shaked, H., and Eiges, R. (2015). Modeling diseases of noncoding unstable repeat expansions using mutant pluripotent stem cells. *World J. Stem Cells* 7, 823–838. doi: 10.4252/wjsc.v7.i5.823

**Conflict of Interest Statement:** The authors declare that the research was conducted in the absence of any commercial or financial relationships that could be construed as a potential conflict of interest.

The handling editor declared a shared affiliation, though no other collaboration, with several of the authors at time of review.

Copyright © 2018 Spitalieri, Talarico, Murdocca, Fontana, Marcaurelio, Campione, Massa, Meola, Serafino, Novelli, Sangiuolo and Botta. This is an open-access article distributed under the terms of the Creative Commons Attribution License (CC BY). The use, distribution or reproduction in other forums is permitted, provided the original author(s) and the copyright owner(s) are credited and that the original publication in this journal is cited, in accordance with accepted academic practice. No use, distribution or reproduction is permitted which does not comply with these terms.



# Dysfunction of Sister Chromatids Separation Promotes Progression of Hepatocellular Carcinoma According to Analysis of Gene Expression Profiling

Baozhen Sun<sup>1</sup>, Guibo Lin<sup>2</sup>, Degang Ji<sup>1</sup>, Shuo Li<sup>1</sup>, Guonan Chi<sup>2</sup> and Xingyi Jin<sup>2\*</sup>

<sup>1</sup> Department of Hepatopancreatobiliary, China-Japan Union Hospital of Jilin University, Changchun, China, <sup>2</sup> First Department of Neurosurgery, China-Japan Union Hospital of Jilin University, Changchun, China

## OPEN ACCESS

### Edited by:

Cesare Gargioli,  
Università degli Studi di Roma Tor  
Vergata, Italy

### Reviewed by:

Gabriele Grassi,  
University of Trieste, Italy  
Fabiola Moretti,  
National Council of Italy, Italy

### \*Correspondence:

Xingyi Jin  
jin5756@163.com

### Specialty section:

This article was submitted to  
Integrative Physiology,  
a section of the journal  
Frontiers in Physiology

**Received:** 23 February 2018

**Accepted:** 10 July 2018

**Published:** 27 July 2018

### Citation:

Sun B, Lin G, Ji D, Li S, Chi G and  
Jin X (2018) Dysfunction of Sister  
Chromatids Separation Promotes  
Progression of Hepatocellular  
Carcinoma According to Analysis  
of Gene Expression Profiling.  
*Front. Physiol.* 9:1019.  
doi: 10.3389/fphys.2018.01019

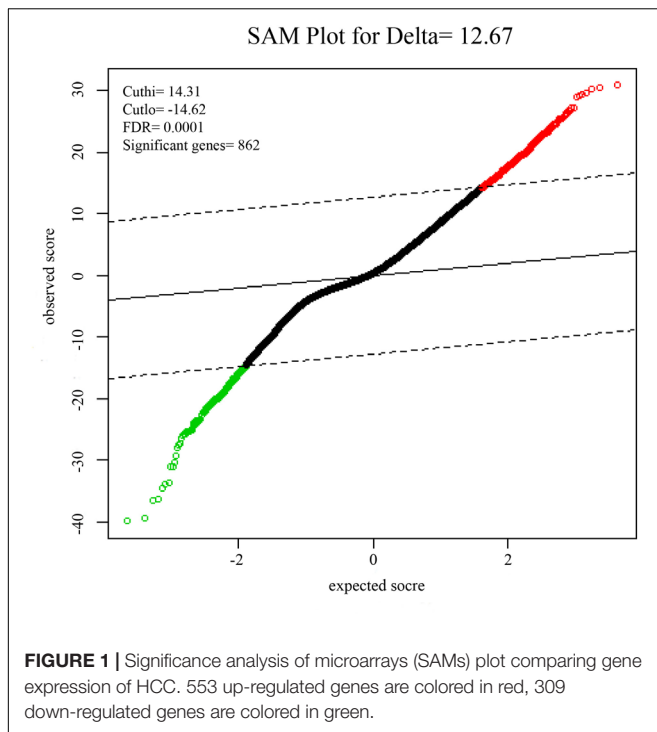
Despite studying the various molecular mechanisms of hepatocellular carcinoma (HCC), effective drugs and biomarkers in HCC therapy are still scarce. The present study was designed to investigate dysregulated pathways, novel biomarkers and therapeutic targets for HCC. The gene expression dataset of GSE14520, which included 362 tumor and their paired non-tumor tissues of HCC, was extracted for processing by the Robust multi-array average (RMA) algorithm in the R environment. SAM methods were leveraged to identify differentially expressed genes (DEGs). Functional analysis of DEGs was performed using DAVID. The GeneMania and Cytohubba were used to construct the PPI network. To avoid individual bias, GSEA and survival analysis were employed to verify the results. The results of these analyses indicated that separation of sister chromatids was the most aberrant phase in the progression of HCC, and the most frequently involved genes, EZH2, GINS1, TPX2, CENPF, and BUB1B, require further study to be used as drug targets or biomarkers in diagnosis and treatment of HCC.

**Keywords:** separation of sister chromatids, HCC, biomarker, SAM, GSEA

## INTRODUCTION

Hepatocellular carcinoma (HCC) is the third-leading cause of cancer-related deaths worldwide and its incidence continues to rise (Mittal and El-Serag, 2013). It mainly arise from hepatitis B virus (HBV) or hepatitis C virus (HCV) infections, and patients with cirrhosis have more opportunities to get HCC (El-Serag, 2002; Umemura et al., 2009). The limited knowledge on the molecular mechanisms of HCC contribute to poor prognosis and ineffective therapy, which leaves liver transplantation as the best choice of management (Ho et al., 2015; Turato et al., 2017). However, recurrence following transplantation is also associated with an unfavorable prognosis (Spinzi and Paggi, 2008; Sposito et al., 2013). Moreover, surgical intervention is ineffective in patients diagnosed at advanced stages of HCC (Rich et al., 2017). Therefore, new therapies for HCC are direly needed.

Although some molecular events that facilitate the progression to HCC have been investigated, the effective drug targets and potential biomarkers for early treatment and diagnosis of HCC are still unclear (Blum, 2005; Cha and Dematteo, 2005). Therefore, identifying the



dysregulated pathways and hub genes involved in this process would allow us to identify patients with HCC as early as possible. Findings from previous studies that have focused on this area are limited due to small sample sizes, resulting in an incomplete understanding of HCC (Jia et al., 2007; Lin et al., 2014; Yin et al., 2017).

In this study, we extracted the gene expression profiles from the GEO database of 362 HBV-related HCC tumors and their paired non-tumor tissues which are mostly accompany with liver cirrhosis. The significance analysis of microarrays (SAMs) algorithm was used to screen the differential expressed genes (DEG), which was performed for pathway enrichment and generation of PPI network. After that, hub genes were identified by GeneMANIA and CytoHubba in Cytoscape. Furthermore, we performed a gene set enrichment analysis (GSEA), which evaluates microarray data at the level of gene sets, to overcome the limitation of individual gene analysis. In the meantime, survival analysis was leveraged, using the TCGA database, to assess the risks of hub gene expression. Finally, five most significantly hub genes were verified by qPCR and IHC in human HCC to confirm the results.

## RESULTS

### Microarray Data Collection and Processing

The BioConductor package, Simpleaffy, was used for quality control and normalization of the microarray raw files (Supplementary Figure S1).

### Identification of DEGs

To identify DEGs from the tumor and non-tumor tissue of HCC patients, we used the SAM method at the delta 14.31, with the FDR < 0.1%. A total of 862 genes were identified as DEGs, including 553 up-regulated and 309 down-regulated genes (Figure 1).

### Functional Analysis of DEGs

Gene Ontology (GO) enrichment analysis revealed that GO terms were most significantly enriched in cell division ( $p = 1.09E-20$ ), sister chromatid cohesion ( $p = 2.79E-13$ ), mitotic nuclear division ( $p = 1.62E-11$ ) and DNA replication ( $p = 1.34E-09$ ; Figure 2). Reactome Pathway enrichment analysis showed that the separation of sister chromatids was the most significantly affected phase in HCC (Figure 3), which was in accordance with the results of the GO enrichment analysis.

### PPI Network Analysis of DEGs

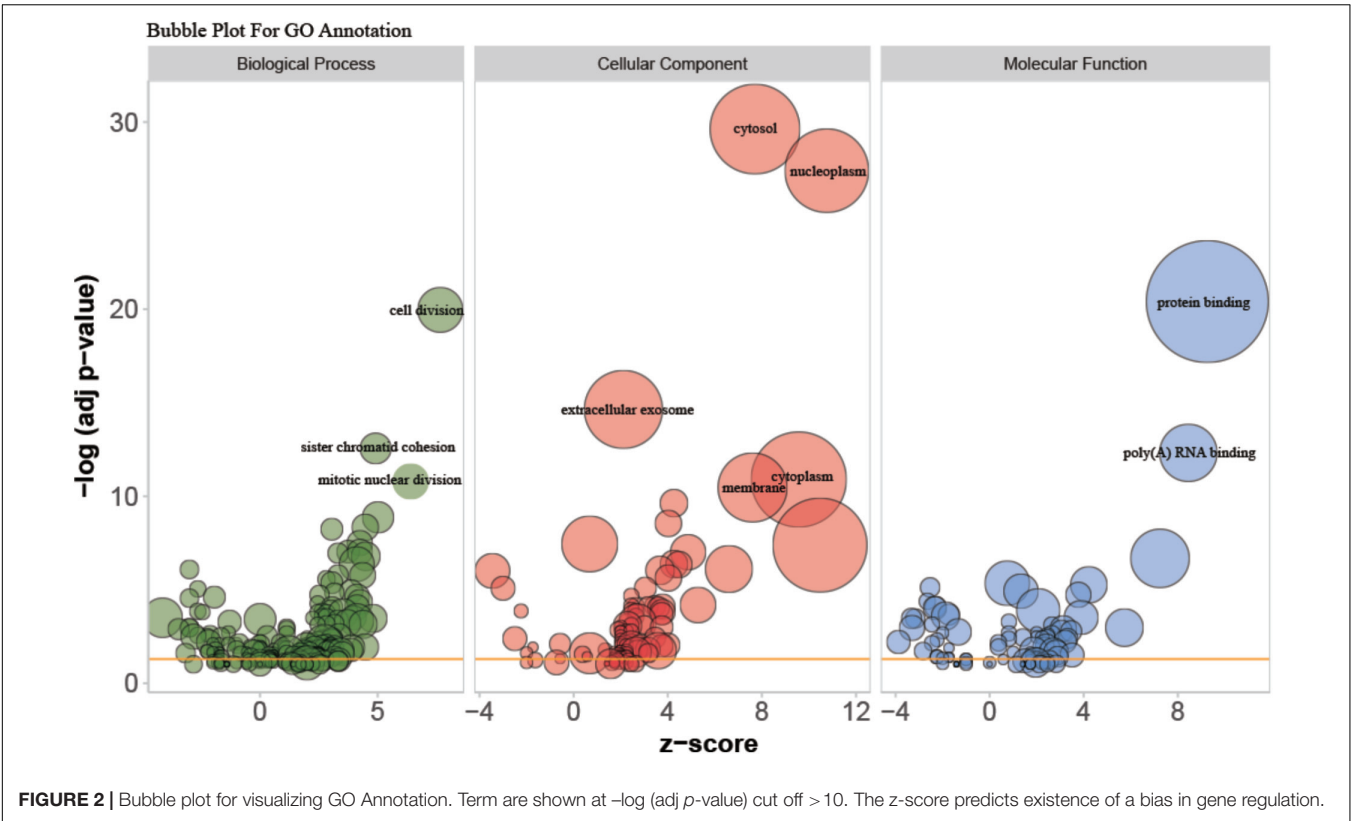
A PPI network with 873 nodes and 84,272 edges was generated via the GeneMANIA plugin, around the DEGs. A global metric was utilized in the determination of hub proteins, through the Cytohubba plugin. Following this, the relationship between the 20 top-ranked proteins was mapped, based on the MCC as shown in Figure 4. The majority of these were cell division-related genes, such as TOP2A, GINS1, BUB1B, TPX2, and CENPF. The 20 top-ranked proteins were all up-regulated DEGs.

### GSEA and Leading-Edge Analysis

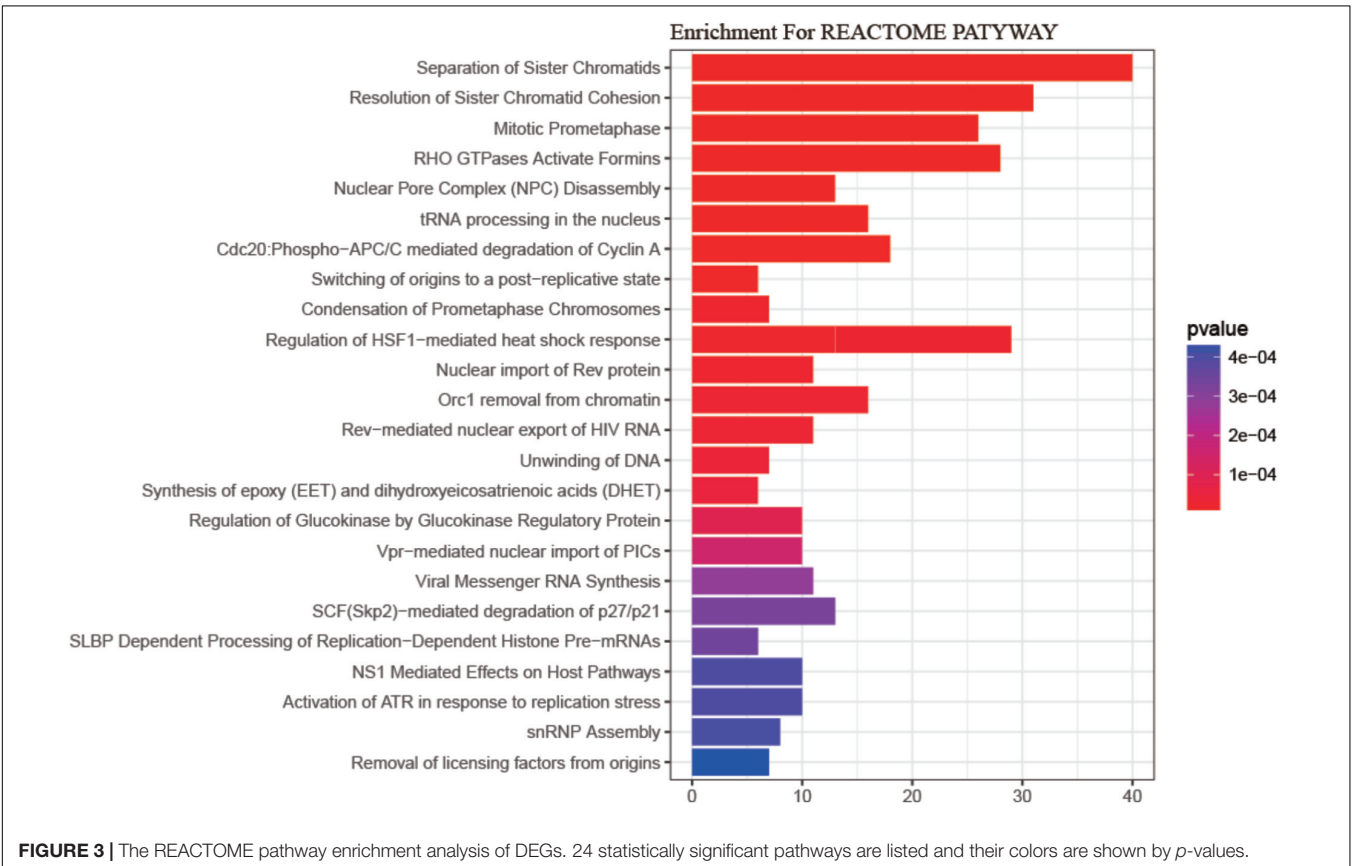
In order to further confirm the molecular mechanisms of HCC in the whole transcriptome, GSEA of the gene expression profile data from 362 tumor and paired non-tumor tissue of HCC patients was performed, based on the GO biological process. The results revealed that the most significant biological processes that were enriched were cell division-related processes, including GO\_REGULATION\_OF\_CELL\_DIVISION (FDR = 0.052), GO\_REGULATION\_OF\_MEIOTIC\_CELL\_CYCLE (FDR = 0.050), GO\_REGULATION\_OF\_NUCLEAR\_DIVISION (FDR = 0.051), GO\_SISTER\_CHROMATID\_COHESION (FDR = 0.051), GO\_REGULATION\_OF\_CHROMOSOME\_ORGANIZATION (FDR = 0.043), and GO\_SISTER\_CHROMATID\_SEGREGATION (FDR = 0.033), which are shown in Figure 5A. Leading-edge analysis was used to find the hub genes which appeared frequently in related gene sets, and the results showed that AURKB appeared in five gene sets, while BUB1B, CDC20, FBXO5, DLGAP5, ESPL1, BIRC5, BUB3, BUB1, CENPE, CENPF, and MAD2L1 appeared in four gene sets (Figures 5B,C).

### Kaplan–Meier Survival Analysis

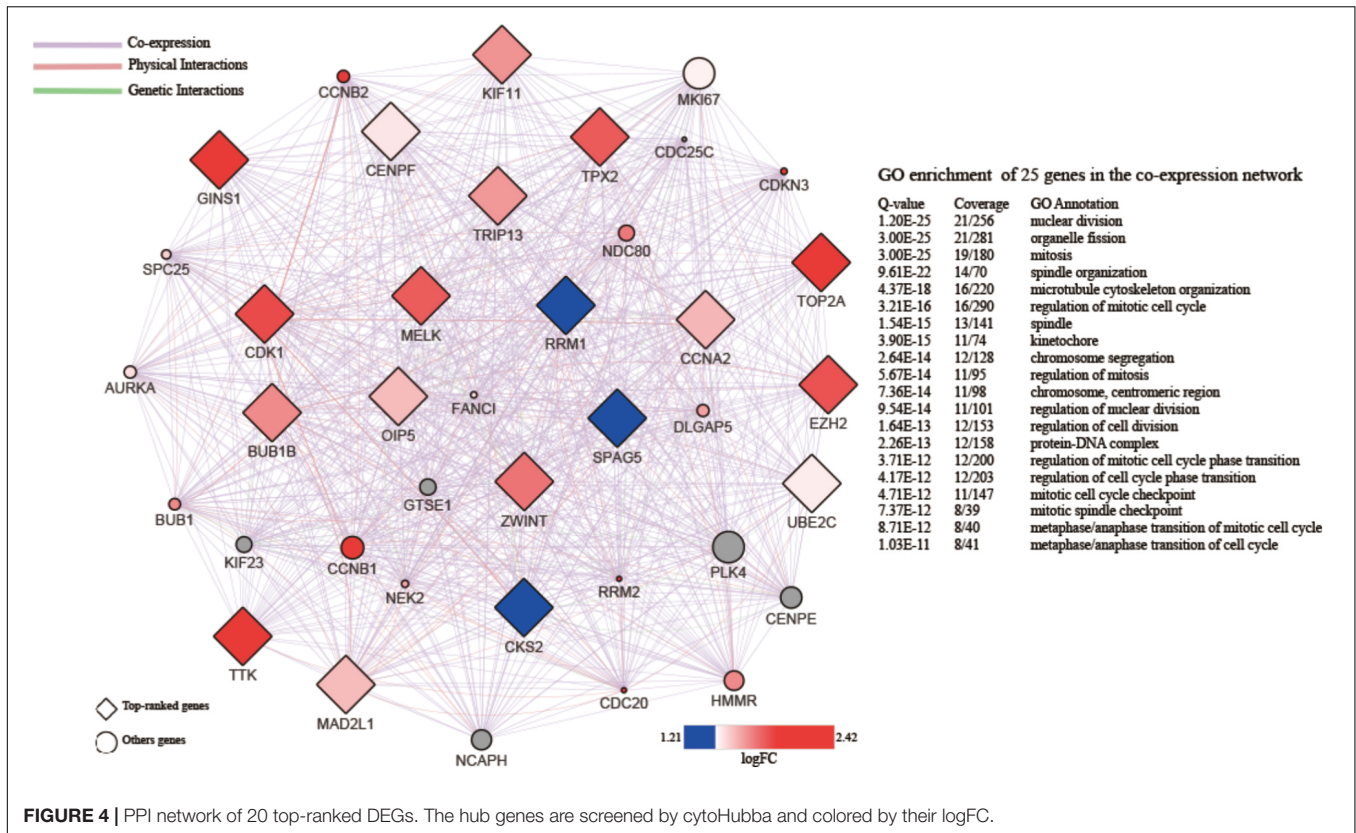
SurvExpress was engaged to explore the relationship between the hub genes and the survival of HCC patients in silico. Finally, survival analysis, based on clinical information from the TCGA-liver cancer datasets, revealed that the high expression of EZH2, GINS1, and TPX2 correlated positively with higher risk, CENPF and BUB1B were quite the contrary (Figure 6).



**FIGURE 2 |** Bubble plot for visualizing GO Annotation. Term are shown at  $-\log(\text{adj } p\text{-value})$  cut off  $> 10$ . The z-score predicts existence of a bias in gene regulation.



**FIGURE 3 |** The REACTOME pathway enrichment analysis of DEGs. 24 statistically significant pathways are listed and their colors are shown by p-values.



**FIGURE 4 |** PPI network of 20 top-ranked DEGs. The hub genes are screened by cytoHubba and colored by their logFC.

## Validation of Hub Genes by qPCR in Human HCC

Five most significantly hub genes, EZH2, GINS1, TPX2, CENPF, and BUB1B, were successfully validated by qPCR in 30 paired human HCC tissues which have no difference with the analysis results of gene expression profiling (Figure 7).

## Immunohistochemistry

IHC was employed to validate the results from bioinformatics analysis, which revealed the strong expression of five hub genes in HCC vs. the control group. However, CENPF and BUB1B were not outstandingly in our result, the individual difference may affect the outcome to some extent (Figure 8).

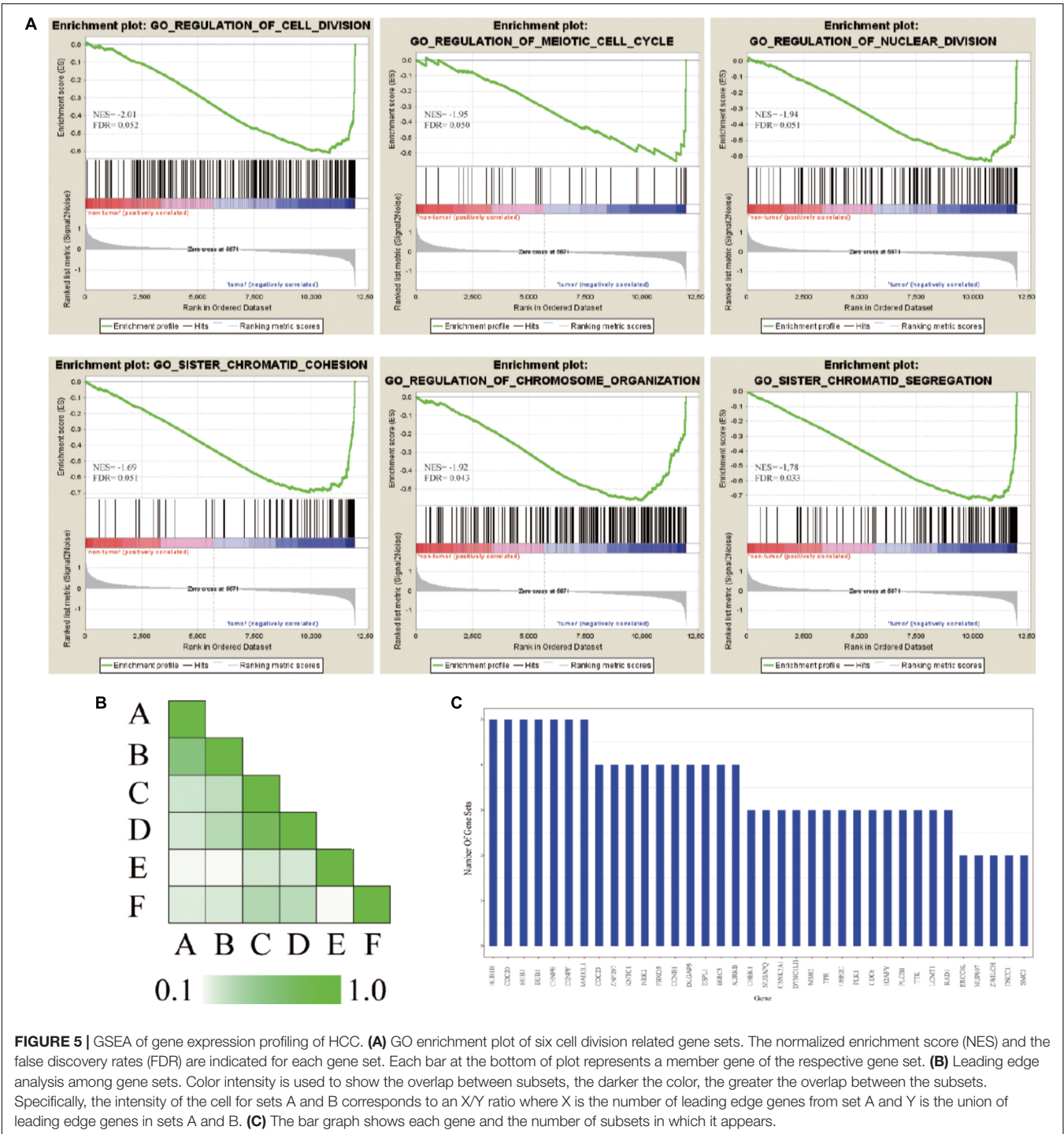
## DISCUSSION

In the present study, we explored the molecular mechanisms of HCC between tumor and non-tumor tissues, using bioinformatics analysis. Our results indicated that the separation of sister chromatids was the most significantly dysregulated pathway during the transition from cirrhosis to HCC, with the up-regulation of 12 hub genes.

One of the most miraculous events in the human cell cycle is the concurrent separation of 46 pairs of sister chromatids. Since this irreversible separation is highly monitored and regulated, neither damage to the genome, nor errors in chromosome alignment, can be easily rectified after separation (Nasmyth,

1999). The initiation of chromosomal segregation was supervised by the spindle assembly checkpoint (SAC), which ensures the genomic stability during mitosis (Dai, 2009). Defects in sister chromatid segregation could lead to aneuploidy (Panigrahi and Pati, 2009) and promote chromosome instability (CIN) during mitosis (Schvartzman et al., 2010). In addition, CIN may contribute to tumor initiation and/or progression, which has been demonstrated in cell lines (Zhang et al., 2004; Vader and Lens, 2008), mice models (Bernal et al., 2002; Dawlaty et al., 2008), and human tumors (Kronenwett et al., 2004; Carter et al., 2006). In the Sgo1<sup>±</sup> mouse model, mitotic error-induced CIN was shown to be an important early event in HCC development (Kronenwett et al., 2004). Furthermore, 120 HCC with 195 markers (Nagai et al., 1997), and 48 HCC with 275 chromosomal markers (Boige et al., 1997), indicated that CIN appears widely in HCC. Aneuploidy is a major manifestation of CIN and is seen in over 75% of cancers, and is also considered essential for tumorigenesis, by some biologists (Duesberg and Li, 2003). Therefore, dysregulation of sister chromatids separation might contribute to the initiation and progression of human HCC.

Based on the results of the PPI analysis by GeneMania and Cytohubba, 20 top-ranked proteins from 862 DEGs are thought to participate in the core pathway of HCC, such as TOP2, GINS1, EZH2, TTK2, CDK1, BUB1B, TPX2, CENPF, and MAD2L1. Furthermore, the high expression of GINS1, EZH2, and TPX2, correlates with high-risk in HCC, as confirmed by the survival analysis. BUB1B, TPX2, and CENPF appeared most often in related gene sets, which were demonstrated by GSEA at the level

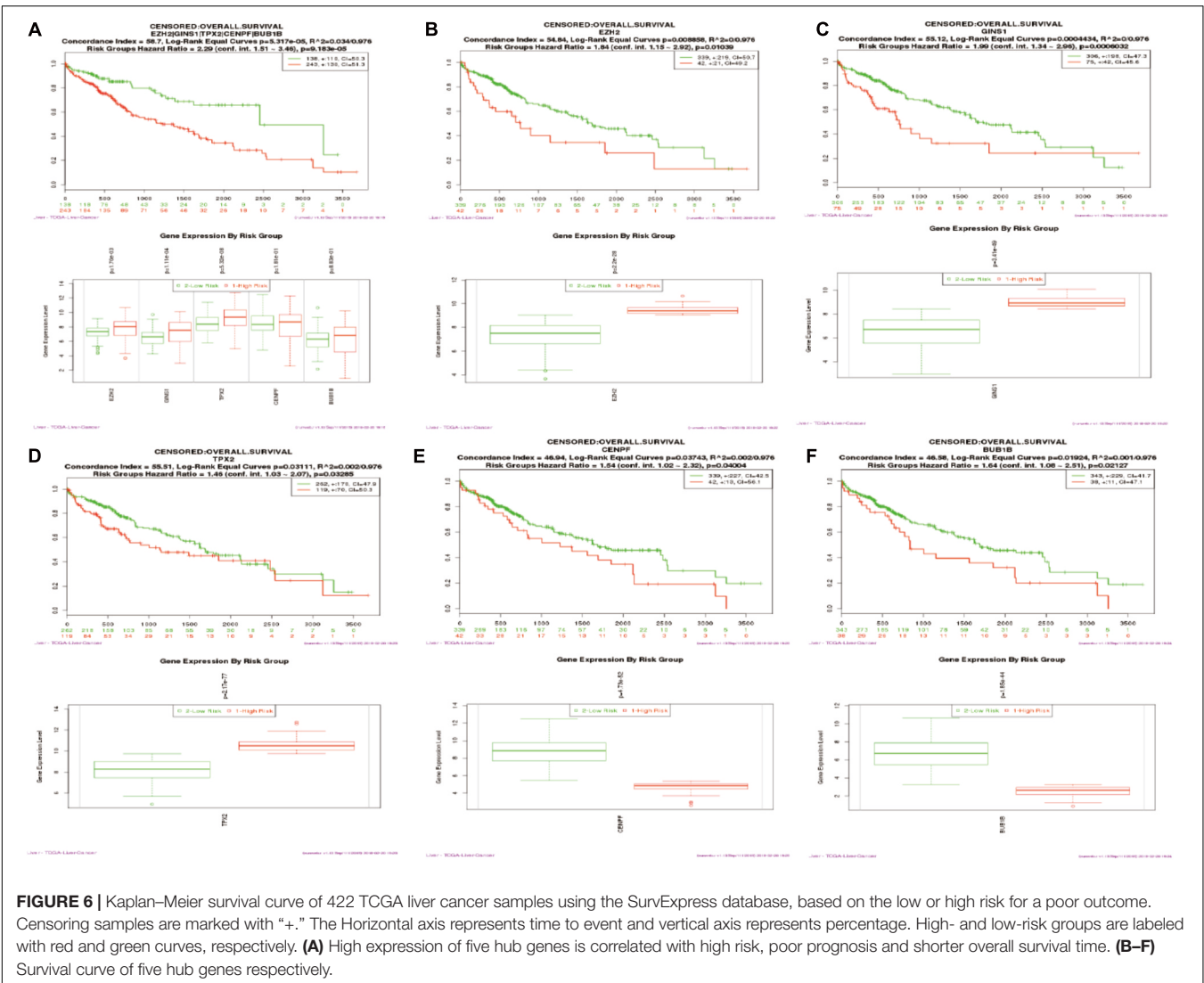


**FIGURE 5 |** GSEA of gene expression profiling of HCC. **(A)** GO enrichment plot of six cell division related gene sets. The normalized enrichment score (NES) and the false discovery rates (FDR) are indicated for each gene set. Each bar at the bottom of plot represents a member gene of the respective gene set. **(B)** Leading edge analysis among gene sets. Color intensity is used to show the overlap between subsets, the darker the color, the greater the overlap between the subsets. Specifically, the intensity of the cell for sets A and B corresponds to an X/Y ratio where X is the number of leading edge genes from set A and Y is the union of leading edge genes in sets A and B. **(C)** The bar graph shows each gene and the number of subsets in which it appears.

of gene sets. Therefore, EZH2, GINS1, TPX2, CENPF, and BUB1B are thought to be hub genes in HCC and are discussed below.

Epigenetic regulation of gene expression, particularly hypermethylation, plays an important role in tumorigenesis (Jones and Baylin, 2002). EZH2 is the enzymatic subunit of Polycomb repressive complex 2 (PRC2), which methylates H3K27, resulting in silence of the associated tumor suppressor genes (Margueron and Reinberg, 2011; Momparler et al., 2012).

EZH2 was up-regulated and expressed in many solid cancers, and YY1 can recruit EZH2 and suppress NFkB function in hepatitis B virus-dependent HCC (Chase and Cross, 2011). Additionally, EZH2 is clinically associated with tumor progression and multiple metastatic features, and epigenetically restrained a subset of miRNA in human HCC (Au et al., 2012). Thus, EZH2 may be regarded as a potential therapeutic target, and a few of compounds have been already investigated as inhibitors of

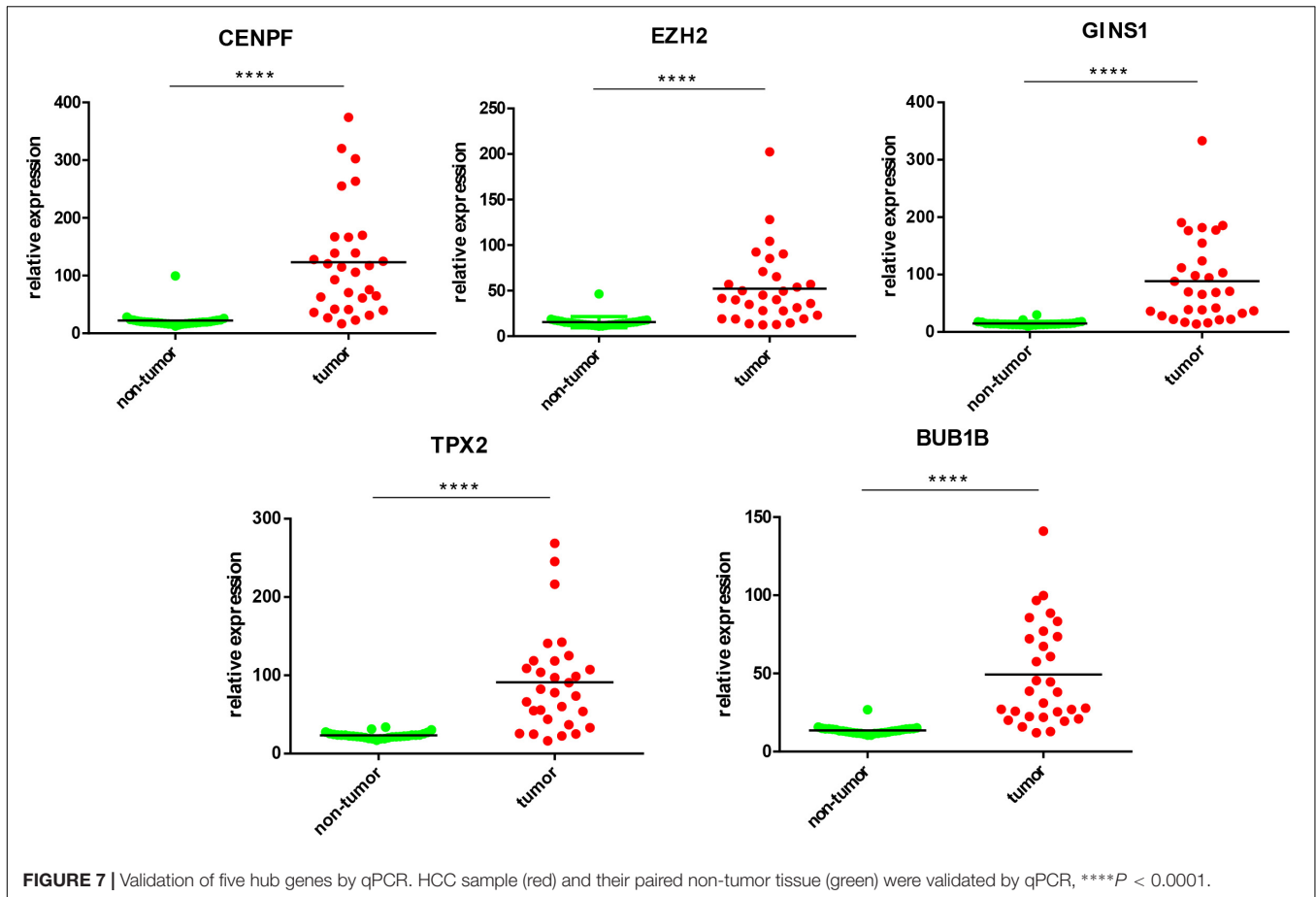


**FIGURE 6 |** Kaplan–Meier survival curve of 422 TCGA liver cancer samples using the SurvExpress database, based on the low or high risk for a poor outcome. Censoring samples are marked with “+.” The Horizontal axis represents time to event and vertical axis represents percentage. High- and low-risk groups are labeled with red and green curves, respectively. **(A)** High expression of five hub genes is correlated with high risk, poor prognosis and shorter overall survival time. **(B–F)** Survival curve of five hub genes respectively.

EZH2, in pre-clinical studies (Knutson et al., 2012, 2013; McCabe et al., 2012; Qi et al., 2012; Kim et al., 2013).

GINS1/PSF1 is a subunit of the GINS complex, which is involved in the DNA replication fork and the initiation of chromosome replication (Labib and Gambus, 2007). Research suggests that GINS1 and/or other GINS complex subunits are upregulated in some types of cancers and possess some tumorigenic characteristics (Hokka et al., 2013; Zhang et al., 2015; Zhou et al., 2015). GINS1 is expressed at high levels in HCC tissues, which is associated with more aggressive tumors and worse prognosis. Moreover, in a mouse xenograft model, high levels of GINS1 expression correspond to high proliferative activity, transplantation potential, and metastatic capability (Nagahama et al., 2010). In contrast, knockdown of GINS1 expression led to inhibited tumor growth by disrupting DNA replication and chromosomal segregation, and promoted apoptosis, particularly early apoptosis (Nagahama et al., 2010; Zhou et al., 2015). These findings may make GINS1 a potential therapeutic target in the future.

For many years, the function of TPX2 has been studied in mitosis and spindle assembly because of the chromatin-mediated TPX2/Importin $\alpha$ - $\beta$ /Ran signal and its control of Aurora A kinase (Asteriti et al., 2010). The location of TPX2 is at the long arm of chromosome 20, at position 20q11, which is often amplified in HCC and other tumors (Knuutila et al., 1998; Hodgson et al., 2003; Scotto et al., 2008; Beroukhim et al., 2010). The elevated TPX2 expression results in dysregulation of spindle formation and balanced chromosome segregation, by over activation of Aurora-A, which could lead to unscheduled phosphorylation of downstream targets. TPX2 knockdown inhibits cell proliferation and AKT signaling, and decreases the MMP2 and MMP9 expression in HCC cell lines (Liu et al., 2014). Clinical sample analysis also indicates that TPX2 expression is associated with the tumor–node–metastasis stage, tumor numbers, and tumor differentiation in the HCC tissues (Liu et al., 2015). Moreover, TPX2 inactivation experiments indicated anti-proliferative effects in cancer cells, suggesting the potential value of TPX2 as an anti-cancer



target (Fenner et al., 2005; Warner et al., 2009; Li et al., 2010).

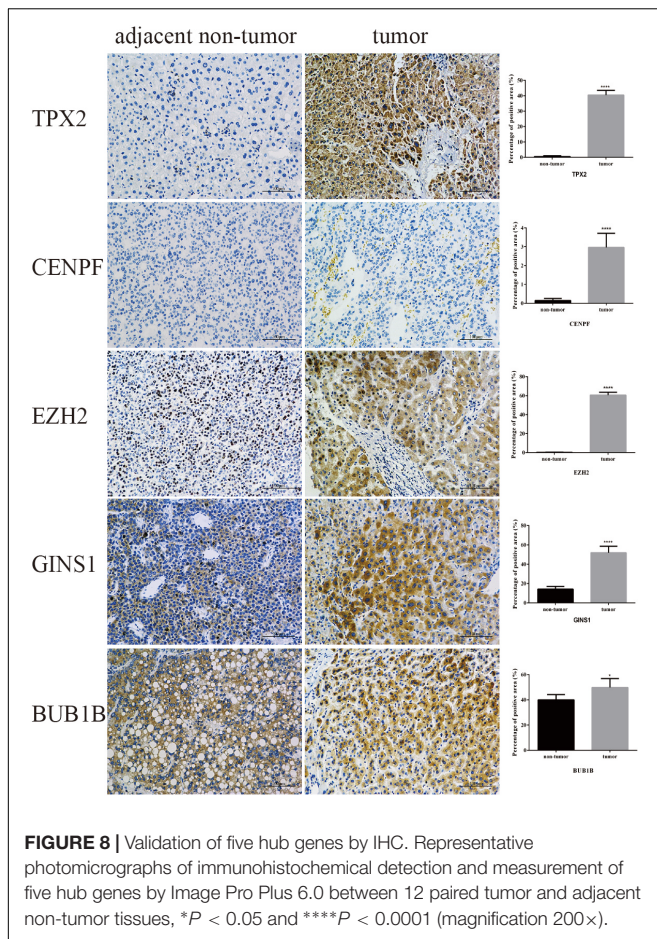
CENPF is a large coiled-coil protein whose expression and subcellular localization was cell cycle-dependent, and undergoes rapid degradation at the end of cell division. It is reported that CENPF plays a major role in kinetochore assembly, regulation of chromosome segregation, and control of SAC activity. CENPF may be a potential proliferation marker in the clinical diagnosis of HCC (Ma et al., 2006). CENPF is overexpressed in HCC (Kim et al., 2012) and other tumors (Varis et al., 2006). Additionally, the up-regulated CENPF expression has been shown to contribute to the proliferation of HCC rather than acting as a trigger for malignant cell growth. Consequently, CENPF could be an indicator of tumorigenesis, especially at early stages of HCC (Zhang et al., 2001).

BUB1B is a key component in the SAC protein family, which has been proven to be involved and upregulated in multiple human cancers (Seike et al., 2002; Shichiri et al., 2002; Gupta et al., 2003; Yamamoto et al., 2007; Fu et al., 2016). In mitosis, BUB1B accumulates cyclin B in G2 phase, by binding to CDC20 to inhibit APC/C activity and prolonging the checkpoint signaling by kinase activity at kinetochores (Malureanu et al., 2009). A human study reported that the role of BUB1B was to facilitate accurate chromosome

segregation and maintain chromosomal stability, to suppress cancer (Hanks et al., 2004). However, the phosphorylated BUB1B, which is tightly regulated through its own activation and subcellular localization (Bin et al., 1998; Li et al., 1999), was elevated in the SV40 Tag-derived prostate cancer models (Guo et al., 2006). The contradiction of BUB1B, between its role in suppressing cancer and upregulating cancers, is demonstrated in varying reports of cancer-associated missense and nonsense mutations in BUB1B, in several cancers (Cahill et al., 1998, 1999; Myrie et al., 2000; Saeki et al., 2002). However, the true mechanism of BUB1B in cancers remains to be elucidated.

In conclusion, we collectively analyzed the molecular mechanisms of human HCC through interpretation of the functions and PPI network of DEGs, which were confirmed by GSEA and survival analysis. In doing so, we ascertained the molecular genetic differences between tumor and non-tumor tissues of HCC, which suggest that separation of sister chromatids may have the most important influence on initiation and progression of human HCC. Errors in this process contribute to CIN and aneuploidy which were thought to be responsible for tumorigenic progression in human cells. The hub genes we found may be useful as biomarkers for diagnosis and prognosis or in tailoring treatment in human HCC. Finally, additional studies are needed to confirm the findings of these experiments.





## MATERIALS AND METHODS

### Microarray Data Collection and Processing

The gene expression dataset of GSE14520 was obtained from NCBI GEO database<sup>1</sup> which is based on the Affymetrix Human Genome U133A 2.0 Array. 362 tumor and paired non-tumor tissues of HCC patients were collected for analysis of genome microarrays. The detail of every HCC patient was shown in **Supplementary Table S1**. The Simpleaffy package was used to read the raw data and perform quality control and normalization by Robust multi-array average (RMA) algorithm in the R environment (Wilson and Miller, 2005). The mean gene expression was considered in multiple probe sets with one name.

### Identification of Differentially Expressed Genes (DEGs)

The DEGs in tumor and non-tumor tissues of HCC patients were determined using SAM (Grace and Nacheva, 2012). We used two class unpaired comparison analysis with  $t$ -statistics, and permutations of  $10^3$ . SAM uses permutations of repeated

measurements to estimate the percentage of genes identified by chance, and the false discovery rate (FDR).

### Functional Analysis of DEGs

Gene Ontology (GO) and Reactome Pathway enrichment analyses were performed using DAVID to explore the biological processes and signaling pathways in which the DEGs were involved (Ashburner et al., 2000; Huang et al., 2009; Fabregat et al., 2018). The enrichment results were visualized in a new R visualization package called GOplot (Walter et al., 2015).

### PPI Network Analysis of DEGs and the Screening of Hub Proteins

A PPI network analysis was performed to evaluate physical relationships between the proteins encoded by the DEGs. The GeneMania (Montejo et al., 2010) and Cytohubba (Chin et al., 2014) were used to construct the PPI network based on co-expression, physical interactions, and genetic interactions.

### Gene Set Enrichment Analysis (GSEA) and Leading-Edge Analysis

To further investigate the biological characteristics of HCC, we performed GSEA assay in non-tumor and tumor groups with permutations of  $10^4$  in the GO biological process, from the Molecular Signature Database (MSigDB). A leading-edge analysis was performed to elucidate hub genes of HCC according to the results of Reactome Pathway enrichment (Subramanian et al., 2005).

### Kaplan–Meier Survival Analysis

Kaplan–Meier analysis was performed with the online multi-cancer biomarker validation tool, SurvExpress, in the TCGA-liver cancer datasets containing 422 samples, using the hub genes as an input (Aguirre-Gamboa et al., 2013).

### Sample Collection

Thirty HBV-related HCC and their paired non-tumor tissues were collected from August 2014 to December 2017 at China-Japan Union Hospital of Jilin University. All the specimens were dealing with liquid nitrogen after surgical resection and stored at  $-80^{\circ}\text{C}$ . Three independent pathologists made the decision about the diagnosis of HCC and assessed the samples with HE staining.

### Quantitative RT-PCR

Total RNA of 30 HCC samples was extracted using Trizol (Invitrogen) as described everywhere, qRT-PCR was performed by One-Step qPCR Kit (Invitrogen) and CFX Connect<sup>TM</sup> Real-Time System (BIO-RAD) following manufacturer's instructions. The data of qPCR were processed by  $\Delta\Delta\text{Ct}$  method with normalizing to GAPDH as the reference gene. The sequence of primers was shown in **Supplementary Table S2**.

### Immunohistochemistry

The 4  $\mu\text{m}$  thick sections cut from formalin-fixed, paraffin-embedded HCC tissue were used for IHC of hub genes as described before (Ho et al., 2012). The primary antibodies against

<sup>1</sup><http://www.ncbi.nlm.nih.gov/geo/>

EZH2 (No. 191080, Abcam), BUB1B (No. 183496, Abcam), CENPF (No. 223847, Abcam), TPX2 (11741-1-AP, Proteintech) and GINS1 (No. D161403, Sangon Biotech) were employed for IHC. Image Pro Plus 6.0 (Media Cybernetics, Bethesda, MD, United States) was employed to measure the positive area of hub genes for quantitative analysis.

## Statistical Analysis

All data are shown as mean  $\pm$  SDs except for otherwise indicated. Significance was determined with two-tailed *t*-test when comparing the variance from HCC to the adjacent non-tumor tissue. GraphPad Prism 6 software (GraphPad Software, La Jolla, CA, United States) was used for analysis. A *P* < 0.05 is considered significant.

## ETHICS STATEMENT

This study was carried out in accordance with the recommendations of CIOMS. The protocol was approved by the institutional review boards of the China-Japan Union Hospital

of Jilin University. All subjects gave written informed consent in accordance with the Declaration of Helsinki.

## AUTHOR CONTRIBUTIONS

XJ conceived and designed the study. BS collected, analyzed the data, and wrote the manuscript. GL, DJ, SL, and GC revised the manuscript. All authors read and approved the manuscript.

## SUPPLEMENTARY MATERIAL

The Supplementary Material for this article can be found online at: <https://www.frontiersin.org/articles/10.3389/fphys.2018.01019/full#supplementary-material>

**FIGURE S1 |** (A) Data before normalization. (B) Data after normalization.

**TABLE S1 |** Samples detail.

**TABLE S2 |** qPCR primers used for tissues specific expression analysis.

## REFERENCES

- Aguirre-Gamboa, R., Gomez-Rueda, H., Martinez-Ledesma, E., Martinez-Torteya, A., Chacolla-Huaringa, R., Rodriguez-Barrientos, A., et al. (2013). SurvExpress: an online biomarker validation tool and database for cancer gene expression data using survival analysis. *PLoS One* 8:e74250. doi: 10.1371/journal.pone.0074250
- Ashburner, M., Ball, C. A., Blake, J. A., Botstein, D., Butler, H., Cherry, J. M., et al. (2000). Gene ontology: tool for the unification of biology. the gene ontology consortium. *Nat. Genet.* 25, 25–29. doi: 10.1038/75556
- Asteriti, I. A., Rensen, W. M., Lindon, C., Lavia, P., and Guarguaglini, G. (2010). The Aurora-A/TPX2 complex: a novel oncogenic holoenzyme? *Biochim. Biophys. Acta Rev. Cancer* 1806, 230–239. doi: 10.1016/j.bbcan.2010.08.001
- Au, S. L., Wong, C. C., Lee, J. M., Fan, D. N., Tsang, F. H., Ng, I. O., et al. (2012). Enhancer of zeste homolog 2 epigenetically silences multiple tumor suppressor microRNAs to promote liver cancer metastasis. *Hepatology* 56, 622–631. doi: 10.1002/hep.25679
- Bernal, J. A., Luna, R., Espina, A., Lazaro, I., Ramos-Morales, F., Romero, F., et al. (2002). Human securin interacts with p53 and modulates p53-mediated transcriptional activity and apoptosis. *Nat. Genet.* 32, 306–311. doi: 10.1038/ng997
- Beroukhi, R., Mermel, C. H., Porter, D., Wei, G., Raychaudhuri, S., Donovan, J., et al. (2010). The landscape of somatic copy-number alteration across human cancers. *Nature* 463, 899–905. doi: 10.1038/nature08822
- Bin, O. Y., Lan, Z. D., Meadows, J., Pan, H. Q., Fukasawa, K., Li, W. Q., et al. (1998). Human Bub1: a putative spindle checkpoint kinase closely linked to cell proliferation. *Cell Growth Diff.* 9, 877–885.
- Blum, H. E. (2005). Treatment of hepatocellular carcinoma. *Best Pract. Res. Clin. Gastroenterol.* 19, 129–145. doi: 10.1016/j.bpg.2004.11.008
- Boige, V., Laurentpuig, P., Fouchet, P., Flejou, J. F., Monges, G., Bedossa, P., et al. (1997). Concerted nonsyntenic allelic losses in hyperploid hepatocellular carcinoma as determined by a high-resolution allelotyping. *Cancer Res.* 57, 1986–1990.
- Cahill, D. P., Da Costa, L. T., Carson-Walter, E. B., Kinzler, K. W., Vogelstein, B., and Lengauer, C. (1999). Characterization of MAD2B and other mitotic spindle checkpoint genes. *Genomics* 58, 181–187. doi: 10.1006/geno.1999.5831
- Cahill, D. P., Lengauer, C., Yu, J., Riggins, G. J., Willson, J. K. V., Markowitz, S. D., et al. (1998). Mutations of mitotic checkpoint genes in human cancers. *Nature* 392, 300–303. doi: 10.1038/32688
- Carter, S. L., Eklund, A. C., Kohane, I. S., Harris, L. N., and Szallasi, Z. (2006). A signature of chromosomal instability inferred from gene expression profiles predicts clinical outcome in multiple human cancers. *Nat. Genet.* 38, 1043–1048. doi: 10.1038/ng1861
- Cha, C., and Dematteo, R. R. (2005). Molecular mechanisms in hepatocellular carcinoma development. *Best Pract. Res. Clin. Gastroenterol.* 19, 25–37. doi: 10.1016/j.bpg.2004.11.005
- Chase, A., and Cross, N. C. P. (2011). Aberrations of EZH2 in Cancer. *Clin. Cancer Res.* 17, 2613–2618. doi: 10.1158/1078-0432.Ccr-10-2156
- Chin, C. H., Chen, S. H., Wu, H. H., Ho, C. W., Ko, M. T., and Lin, C. Y. (2014). cytoHubba: identifying hub objects and sub-networks from complex interactome. *BMC Syst. Biol.* 8(Suppl. 4):S11. doi: 10.1186/1752-0509-8-S4-S11
- Dai, W. (2009). Suppression of genomic instabilities caused by chromosome Mis-segregation: a perspective from studying BubR1 and Sgo1. *J. Formos. Med. Assoc.* 108, 904–911. doi: 10.1016/s0929-6646(10)60002-2
- Dawlaty, M. M., Malureanu, L., Jeganathan, K. B., Kao, E., Sustmann, C., Tahk, S., et al. (2008). Resolution of sister centromeres requires RanBP2-mediated SUMOylation of topoisomerase II alpha. *Cell* 133, 103–115. doi: 10.1016/j.cell.2008.01.045
- Duesberg, P., and Li, R. (2003). Multistep carcinogenesis A chain reaction of aneuploidizations. *Cell Cycle* 2, 202–210. doi: 10.4161/cc.2.3.382
- El-Serag, H. B. (2002). Hepatocellular carcinoma: an epidemiologic view. *J. Clin. Gastroenterol.* 35, S72–S78. doi: 10.1097/00004836-200211002-00002
- Fabregat, A., Jupe, S., Matthews, L., Sidiropoulos, K., Gillespie, M., Garapati, P., et al. (2018). The reactome pathway knowledgebase. *Nucleic Acids Res.* 46, D649–D655. doi: 10.1093/nar/gkx1132
- Fenner, M., Wehrhan, F., Jehle, M., Amann, K., Radespiel-Troger, M., Grabenbauer, G., et al. (2005). Restricted-expressed proliferation-associated protein (repp86) expression in squamous cell carcinoma of the oral cavity. *Strahlentherapie Und Onkologie* 181, 755–761. doi: 10.1007/s00066-005-1430-7
- Fu, X., Chen, G., Cai, Z.-D., Wang, C., Liu, Z.-Z., Lin, Z.-Y., et al. (2016). Overexpression of BUB1B contributes to progression of prostate cancer and predicts poor outcome in patients with prostate cancer. *Oncotargets Ther.* 9, 2211–2220. doi: 10.2147/ott.S101994
- Grace, C., and Nacheva, E. P. (2012). Significance analysis of microarrays (SAM) offers clues to differences between the genomes of adult philadelphia positive all and the lymphoid blast transformation of CML. *Cancer Inform.* 11, 173–183. doi: 10.4137/CIN.S9258
- Guo, C., Wu, G., Chin, J. L., Bauman, G., Moussa, M., Wang, F., et al. (2006). Bub1 up-regulation and hyperphosphorylation promote malignant transformation in SV40 tag-induced transgenic mouse models. *Mol. Cancer Res.* 4, 957–969. doi: 10.1158/1541-7786.MCR-06-0168

- Gupta, A., Inaba, S., Wong, O. K., Fang, G. W., and Liu, J. W. (2003). Breast cancer-specific gene 1 interacts with the mitotic checkpoint kinase BubR1. *Oncogene* 22, 7593–7599. doi: 10.1038/sj.onc.1206880
- Hanks, S., Coleman, K., Reid, S., Plaja, A., Firth, H., Fitzpatrick, D., et al. (2004). Constitutional aneuploidy and cancer predisposition caused by biallelic mutations in BUB1B. *Nat. Genet.* 36, 1159–1161. doi: 10.1038/ng1449
- Ho, D. W. H., Kai, A. K. L., and Ng, I. O. L. (2015). TCGA whole-transcriptome sequencing data reveals significantly dysregulated genes and signaling pathways in hepatocellular carcinoma. *Front. Med.* 9, 322–330. doi: 10.1007/s11684-015-0408-9
- Ho, D. W. Y., Yang, Z. F., Yi, K., Lam, C. T., Ng, M. N. P., Yu, W. C., et al. (2012). Gene expression profiling of liver cancer stem cells by RNA-sequencing. *PLoS One* 7:e37159. doi: 10.1371/journal.pone.0037159
- Hodgson, J. G., Chin, K., Collins, C., and Gray, J. W. (2003). Genome amplification of chromosome 20 in breast cancer. *Breast Cancer Res. Treat.* 78, 337–345. doi: 10.1023/A:1023085825042
- Hokka, D., Maniwa, Y., Tane, S., Nishio, W., Yoshimura, M., Okita, Y., et al. (2013). Psf3 is a prognostic biomarker in lung adenocarcinoma. *Lung Cancer* 79, 77–82. doi: 10.1016/j.lungcan.2012.10.001
- Huang, D. W., Sherman, B. T., and Lempicki, R. A. (2009). Systematic and integrative analysis of large gene lists using DAVID bioinformatics resources. *Nat. Protoc.* 4, 44–57. doi: 10.1038/nprot.2008.211
- Jia, H. L., Ye, Q. H., Qin, L. X., Budhu, A., Forgues, M., Chen, Y., et al. (2007). Gene expression profiling reveals potential biomarkers of human hepatocellular carcinoma. *Clin. Cancer Res.* 13, 1133–1139. doi: 10.1158/1078-0432.CCR-06-1025
- Jones, P. A., and Baylín, S. B. (2002). The fundamental role of epigenetic events in cancer. *Nat. Rev. Genet.* 3, 415–428. doi: 10.1038/nrg816
- Kim, H.-E., Kim, D.-G., Lee, K. J., Son, J. G., Song, M.-Y., Park, Y.-M., et al. (2012). Frequent amplification of CENPE, GMNN and CDK13 genes in hepatocellular carcinomas. *PLoS One* 7:e43223. doi: 10.1371/journal.pone.0043223
- Kim, W., Bird, G. H., Neff, T., Guo, G. J., Kerenyi, M. A., Walensky, L. D., et al. (2013). Targeted disruption of the EZH2-EED complex inhibits EZH2-dependent cancer. *Nat. Chem. Biol.* 9, 643–650. doi: 10.1038/Nchembio.1331
- Knutson, S. K., Warholik, N. M., Wigle, T. J., Klaus, C. R., Allain, C. J., Raimondi, A., et al. (2013). Durable tumor regression in genetically altered malignant rhabdoid tumors by inhibition of methyltransferase EZH2. *Proc. Natl. Acad. Sci. U.S.A.* 110, 7922–7927. doi: 10.1073/pnas.1303800110
- Knutson, S. K., Wigle, T. J., Warholik, N. M., Sneeringer, C. J., Allain, C. J., Klaus, C. R., et al. (2012). A selective inhibitor of EZH2 blocks H3K27 methylation and kills mutant lymphoma cells. *Nat. Chem. Biol.* 8, 890–896. doi: 10.1038/Nchembio.1084
- Knuutila, S., Bjorkqvist, A. M., Autio, K., Tarkkanen, M., Wolf, M., Monni, O., et al. (1998). DNA copy number amplifications in human neoplasms - Review of comparative genomic hybridization studies. *Am. J. Pathol.* 152, 1107–1123.
- Kronenwett, U., Huwendiek, S., Ostring, C., Portwood, N., Roblick, U. J., Pawitan, Y., et al. (2004). Improved grading of breast adenocarcinomas based on genomic instability. *Cancer Res.* 64, 904–909. doi: 10.1158/0008-5472.can-03-2451
- Labib, K., and Gambus, A. (2007). A key role for the GINS complex at DNA replication forks. *Trends Cell Biol.* 17, 271–278. doi: 10.1016/j.tcb.2007.04.002
- Li, B., Qi, X. Q., Chen, X., Huang, X., Liu, G. Y., Chen, H. R., et al. (2010). Expression of targeting protein for *Xenopus* kinesin-like protein 2 is associated with progression of human malignant astrocytoma. *Brain Res.* 1352, 200–207. doi: 10.1016/j.brainres.2010.06.060
- Li, W. Q., Lan, Z. D., Wu, H. Y., Wu, S. C., Meadows, J., Chen, J., et al. (1999). BUBR1 phosphorylation is regulated during mitotic checkpoint activation. *Cell Growth Diff.* 10, 769–775.
- Lin, K. T., Shann, Y. J., Chau, G. Y., Hsu, C. N., and Huang, C. Y. F. (2014). Identification of latent biomarkers in hepatocellular carcinoma by ultra-deep whole-transcriptome sequencing. *Oncogene* 33, 4786–4794. doi: 10.1038/nc.2013.424
- Liu, Q., Tu, K., Zhang, H., Zheng, X., Yao, Y., and Liu, Q. (2015). TPX2 as a novel prognostic biomarker for hepatocellular carcinoma. *Hepatol. Res.* 45, 906–918. doi: 10.1111/hepr.12428
- Liu, Q., Yang, P., Tu, K., Zhang, H., Zheng, X., Yao, Y., et al. (2014). TPX2 knockdown suppressed hepatocellular carcinoma cell invasion via inactivating AKT signaling and inhibiting MMP2 and MMP9 expression. *Chin. J. Cancer Res.* 26, 410–417. doi: 10.3978/j.issn.1000-9604.2014.08.01
- Ma, L., Zhao, X. S., and Zhu, X. L. (2006). Mitosin/CENP-F in mitosis, transcriptional control, and differentiation. *J. Biomed. Sci.* 13, 205–213. doi: 10.1007/s11373-005-9057-3
- Malureanu, L. A., Jeganathan, K. B., Hamada, M., Wasilewski, L., Davenport, J., and Van Deursen, J. M. (2009). BubR1 N terminus acts as a soluble inhibitor of cyclin B Degradation by APC/C-Cdc20 in interphase. *Dev. Cell* 16, 118–131. doi: 10.1016/j.devcel.2008.11.004
- Margueron, R., and Reinberg, D. (2011). The Polycomb complex PRC2 and its mark in life. *Nature* 469, 343–349. doi: 10.1038/nature09784
- McCabe, M. T., Ott, H. M., Ganji, G., Korenchuk, S., Thompson, C., Van Aller, G. S., et al. (2012). EZH2 inhibition as a therapeutic strategy for lymphoma with EZH2-activating mutations. *Nature* 492, 108–112. doi: 10.1038/nature11606
- Mittal, S., and El-Serag, H. B. (2013). Epidemiology of hepatocellular carcinoma: consider the population. *J. Clin. Gastroenterol.* 47(Suppl.), S2–S6. doi: 10.1097/MCG.0b013e3182872f29
- Momparler, R. L., Idaghdour, Y., Marquez, V. E., and Momparler, L. F. (2012). Synergistic antileukemic action of a combination of inhibitors of DNA methylation and histone methylation. *Leuk. Res.* 36, 1049–1054. doi: 10.1016/j.leukres.2012.03.001
- Montejo, J., Zuberi, K., Rodriguez, H., Kazi, F., Wright, G., Donaldson, S. L., et al. (2010). GeneMANIA Cytoscape plugin: fast gene function predictions on the desktop. *Bioinformatics* 26, 2927–2928. doi: 10.1093/bioinformatics/btq562
- Myrie, K. A., Percy, M. J., Azim, J. N., Neeley, C. K., and Petty, E. M. (2000). Mutation and expression analysis of human BUB1 and BUB1B in aneuploid breast cancer cell lines. *Cancer Lett.* 152, 193–199. doi: 10.1016/S0304-3835(00)00340-2
- Nagahama, Y., Ueno, M., Miyamoto, S., Morii, E., Minami, T., Mochizuki, N., et al. (2010). PSF1, a DNA replication factor expressed widely in stem and progenitor cells, drives tumorigenic and metastatic properties. *Cancer Res.* 70, 1215–1224. doi: 10.1158/0008-5472.Can-09-3662
- Nagai, H., Pineau, P., Tiollais, P., Buendia, M. A., and Dejean, A. (1997). Comprehensive allelotyping of human hepatocellular carcinoma. *Oncogene* 14, 2927–2933. doi: 10.1038/sj.onc.1201136
- Nasmyth, K. (1999). Separating sister chromatids. *Trends Biochem. Sci.* 24, 98–104. doi: 10.1016/s0968-0004(99)01358-4
- Panigrahi, A. K., and Pati, D. (2009). Road to the crossroads of life and death: linking sister chromatid cohesion and separation to aneuploidy, apoptosis and cancer. *Crit. Rev. Oncol. Hematol.* 72, 181–193. doi: 10.1016/j.critrevonc.2008.12.002
- Qi, W., Chan, H. M., Teng, L., Li, L., Chuai, S. N., Zhang, R. P., et al. (2012). Selective inhibition of Ezh2 by a small molecule inhibitor blocks tumor cells proliferation. *Proc. Natl. Acad. Sci. U.S.A.* 109, 21360–21365. doi: 10.1073/pnas.1210371110
- Rich, N. E., Parikh, N. D., and Singal, A. G. (2017). Overdiagnosis: an understudied issue in hepatocellular carcinoma surveillance. *Semin. Liver Dis.* 37, 296–304. doi: 10.1055/s-0037-1608775
- Saeki, A., Tamura, S., Ito, N., Kiso, S., Matsuda, Y., Yabuuchi, I., et al. (2002). Frequent impairment of the spindle assembly checkpoint in hepatocellular carcinoma. *Cancer* 94, 2047–2054. doi: 10.1002/ncr.10448
- Schvartzman, J.-M., Sotillo, R., and Benzeira, R. (2010). Mitotic chromosomal instability and cancer: mouse modelling of the human disease. *Nat. Rev. Cancer* 10, 102–115. doi: 10.1038/nrc2781
- Scotto, L., Narayan, G., Nandula, S., Arias-Pulido, H., Subramaniam, S., Schneider, A., et al. (2008). Identification of copy number gain and overexpressed genes on chromosome arm 20q by an integrative genomic approach in cervical cancer: potential role in progression. *Genes Chromosomes Cancer* 47, 755–765. doi: 10.1002/gcc.20577
- Seike, M., Gemma, A., Hosoya, Y., Hosomi, Y., Okano, T., Kurimoto, F., et al. (2002). The promoter region of the human BUBR1 gene and its expression analysis in lung cancer. *Lung Cancer* 38, 229–234. doi: 10.1016/S0169-5002(02)00218-0
- Shichiri, M., Yoshinaga, K., Hisatomi, H., Sugihara, K., and Hirata, Y. (2002). Genetic and epigenetic inactivation of mitotic checkpoint genes hBUB1 and hBUBR1 and their relationship to survival. *Cancer Res.* 62, 13–17.
- Spinzi, G., and Paggi, S. (2008). Sorafenib in advanced hepatocellular carcinoma. *N. Engl. J. Med.* 359, 2497–2498. doi: 10.1056/NEJMc081780

- Sposito, C., Mariani, L., Germini, A., Flores Reyes, M., Bongini, M., Grossi, G., et al. (2013). Comparative efficacy of sorafenib versus best supportive care in recurrent hepatocellular carcinoma after liver transplantation: a case-control study. *J. Hepatol.* 59, 59–66. doi: 10.1016/j.jhep.2013.02.026
- Subramanian, A., Tamayo, P., Mootha, V. K., Mukherjee, S., Ebert, B. L., Gillette, M. A., et al. (2005). Gene set enrichment analysis: a knowledge-based approach for interpreting genome-wide expression profiles. *Proc. Natl. Acad. Sci. U.S.A.* 102, 15545–15550. doi: 10.1073/pnas.0506580102
- Turato, C., Balasso, A., Carloni, V., Tiribelli, C., Mastrotto, F., Mazzocca, A., et al. (2017). New molecular targets for functionalized nanosized drug delivery systems in personalized therapy for hepatocellular carcinoma. *J. Control. Release* 268, 184–197. doi: 10.1016/j.jconrel.2017.10.027
- Umamura, T., Ichijo, T., Yoshizawa, K., Tanaka, E., and Kiyosawa, K. (2009). Epidemiology of hepatocellular carcinoma in Japan. *J. Gastroenterol.* 44(Suppl. 19), 102–107. doi: 10.1007/s00535-008-2251-0
- Vader, G., and Lens, S. M. A. (2008). The Aurora kinase family in cell division and cancer. *Biochim. Biophys. Acta Rev. Cancer* 1786, 60–72. doi: 10.1016/j.bbcan.2008.07.003
- Varis, A., Salmela, A.-L., and Kallio, M. J. (2006). Cenp-F (mitosin) is more than a mitotic marker. *Chromosoma* 115, 288–295. doi: 10.1007/s00412-005-0046-0
- Walter, W., Sanchez-Cabo, F., and Ricote, M. (2015). GOrplot: an R package for visually combining expression data with functional analysis. *Bioinformatics* 31, 2912–2914. doi: 10.1093/bioinformatics/btv300
- Warner, S. L., Stephens, B. J., Nwokenkwo, S., Hostetter, G., Sugeng, A., Hidalgo, M., et al. (2009). Validation of TPX2 as a potential therapeutic target in pancreatic cancer cells. *Clin. Cancer Res.* 15, 6519–6528. doi: 10.1158/1078-0432.Ccr-09-0077
- Wilson, C., and Miller, C. (2005). Simpleaffy: a BioConductor package for affymetrix quality control and data analysis. *Bioinformatics* 21, 3683–3685. doi: 10.1093/bioinformatics/bti605
- Yamamoto, Y., Matsuyama, H., Chochi, Y., Okuda, M., Kawauchi, S., Inoue, R., et al. (2007). Overexpression of BUBR1 is associated with chromosomal instability in bladder cancer. *Cancer Genet. Cytogenet.* 174, 42–47. doi: 10.1016/j.cancergencyto.2006.11.012
- Yin, L., Chang, C., and Xu, C. (2017). G2/M checkpoint plays a vital role at the early stage of HCC by analysis of key pathways and genes. *Oncotarget* 8, 76305–76317. doi: 10.18632/oncotarget.19351
- Zhang, D. W., Hirota, T., Marumoto, T., Shimizu, M., Kunitoku, N., Sasayama, T., et al. (2004). Cre-loxP-controlled periodic Aurora-A overexpression induces mitotic abnormalities and hyperplasia in mammary glands of mouse models. *Oncogene* 23, 8720–8730. doi: 10.1038/sj.onc.1208153
- Zhang, J., Wu, Q., Wang, Z., Zhang, Y., Zhang, G., Fu, J., et al. (2015). Knockdown of PSF1 expression inhibits cell proliferation in lung cancer cells in vitro. *Tumor Biol.* 36, 2163–2168. doi: 10.1007/s13277-014-2826-8
- Zhang, J. Y., Zhu, W., Imai, H., Kiyosawa, K., Chan, E. K. L., and Tan, E. M. (2001). De-novo humoral immune responses to cancer-associated autoantigens during transition from chronic liver disease to hepatocellular carcinoma. *Clin. Exp. Immunol.* 125, 3–9. doi: 10.1046/j.1365-2249.2001.01585.x
- Zhou, L., Sun, X.-J., Liu, C., Wu, Q.-F., Tai, M.-H., Wei, J.-C., et al. (2015). Overexpression of PSF1 is correlated with poor prognosis in hepatocellular carcinoma patients. *Int. J. Biol. Mark.* 30, E56–E64. doi: 10.5301/ijbm.5000105

**Conflict of Interest Statement:** The authors declare that the research was conducted in the absence of any commercial or financial relationships that could be construed as a potential conflict of interest.

Copyright © 2018 Sun, Lin, Ji, Li, Chi and Jin. This is an open-access article distributed under the terms of the Creative Commons Attribution License (CC BY). The use, distribution or reproduction in other forums is permitted, provided the original author(s) and the copyright owner(s) are credited and that the original publication in this journal is cited, in accordance with accepted academic practice. No use, distribution or reproduction is permitted which does not comply with these terms.



# Toward Morphologically Relevant Extracellular Matrix *in Vitro* Models: 3D Fiber Reinforced Hydrogels

Ashok Williams<sup>1,2†</sup>, James F. Nowak<sup>1†</sup>, Rachel Dass<sup>1,2</sup>, Johnson Samuel<sup>1</sup> and K. L. Mills<sup>1,2\*</sup>

<sup>1</sup> Department of Mechanical, Aerospace, Nuclear Engineering, Rensselaer Polytechnic Institute, Troy, NY, United States,

<sup>2</sup> Center for Biotechnology and Interdisciplinary Studies, Rensselaer Polytechnic Institute, Troy, NY, United States

## OPEN ACCESS

### Edited by:

Giancarlo Forte,  
International Clinical Research Center  
(FNUSA-ICRC), Czechia

### Reviewed by:

Antonio Rinaldi,  
Energy and Sustainable Economic  
Development, Italy  
Pamela Mozetic,  
International Clinical Research Center  
(FNUSA-ICRC), Czechia

### \*Correspondence:

K. L. Mills  
millsk2@rpi.edu

<sup>†</sup>These authors have contributed  
equally to this work.

### Specialty section:

This article was submitted to  
Integrative Physiology,  
a section of the journal  
Frontiers in Physiology

**Received:** 06 April 2018

**Accepted:** 02 July 2018

**Published:** 24 July 2018

### Citation:

Williams A, Nowak JF, Dass R,  
Samuel J and Mills KL (2018) Toward  
Morphologically Relevant Extracellular  
Matrix *in Vitro* Models: 3D Fiber  
Reinforced Hydrogels.  
*Front. Physiol.* 9:966.  
doi: 10.3389/fphys.2018.00966

The extracellular matrix (ECM) is known to play an important role in the health of cells and tissues. Not only are chemical signals transmitted via bonds and tightly controlled diffusion, but the structure of the ECM also provides important physical signaling for the cells attached to it. The structure is composed of a mesh of fibrous proteins, such as collagen, embedded in a hydrated gel matrix of glycosaminoglycans. To study cell behavior with respect to the combined morphology and mechanics of such matrices is not currently possible with the types of 3D cell culture matrices available. Most of the cell culture matrices are single-phase bio- or polymeric hydrogels. Therefore, here we developed a continuous hybrid manufacturing process to make fiber-reinforced composite hydrogels. A far field electrospinning process was used to deposit the fibrous component with the aid of guiding electrodes; and a gravity-assisted, droplet-based system controlled the rate of addition of the cell-laden hydrogel component. The addition of the fibrous component slightly increased the elastic modulus of the pure hydrogel. The cells that were embedded into the fiber-reinforced hydrogels were viable for 8 days. The cells were randomly placed in the matrix such that some had no contact to the fibers and others were initially in proximity to fibers. The cells with no contact to fibers grew into spheroidal clusters within the hydrogel, and those in proximity to the fibers spread out and grew along the fibers showing that the fiber-reinforced hydrogels are able to control cell behavior with morphological cues.

**Keywords:** extracellular matrix, electrospinning, hydrogel, mechanobiology, cell-ECM interaction

## INTRODUCTION

The extracellular matrix (ECM) of connective tissues is composed of two distinctly different morphological components. One of these is a mesh of proteinaceous fibers, such as collagen, fibronectin, and elastin. The other is a highly hydrated gel composed of glycosaminoglycans. Together, they provide structural, biophysical, and biologically active support to the cells within this microenvironment (Theocharis et al., 2016). During the progression of solid tumors, the ECM is altered through increased fibrous protein deposition, reorganization, and cross-linking (Lu et al., 2012). The result is a stiffening, or desmoplasia, of the surrounding tissue (Croft et al., 2004). Pathologically desmoplastic tissues are a major contributor to the biomechanical properties of the tumor microenvironment (Berger et al., 2017). Although this phenomenon is frequently observed, the influence of these mechanical changes on cellular behavior toward the progression of the disease is not fully understood.

Although the mechanobiology of tumor cells is well researched (Makale, 2007), it is often done so in 2D Petri dishes where interactions of the tumor cells with the 3D fiber and gel composite structure of the ECM are ignored. This has led to a lack of fundamental understanding of the combined effects of matrix stiffening and ECM fiber density on tumor growth. Currently, many investigations utilize reconstituted ECM proteins to mimic the physiology *in vivo* (Narayanan et al., 2009). Although these systems provide 3D microenvironments with native bioactivity, they lack mechanical relevance, as these biomaterials cannot produce scaffolds stiff enough to match relevant physiological or pathophysiological mechanics. Chemical modifications have been used to increase stiffness, but they introduce confounding variables that make it difficult to correctly isolate only the effects of fibers (Erikson et al., 2008). Furthermore, these techniques are unable to control the density of fibrous proteins to correctly isolate their influence on cellular behaviors. Thus, it has been a non-trivial pursuit to produce a system that can capture both morphology and mechanical properties of the evolving tumor microenvironment.

Our main goal, therefore, was to create a 3D *in vitro* ECM model comprised of both fiber and hydrogel components into which cells may be embedded. Furthermore, the fiber density in this model must be readily tunable to capture tissue morphologies from healthy to cancerous. A common method for producing polymeric nano- to micro-scale fibers, often used in cell–material interaction studies, is electrospinning. Typical electrospinning setups produce aligned or random mats of densely packed fibers up to generally a few hundred microns in thickness. Whereas such 2D mats may be used to explore, for example, the contact guidance behavior of cells (Nisbet et al., 2008), they do not capture the 3D nature of the *in vivo* environment. It has proven to be challenging to extend the electrospinning process from easily producing 2D mats to producing 3D fiber networks. Researchers have sought to expand upon the electrospun mats to create hybrid fiber-gel 3D matrices. One method has been to build layered electrospun fiber mat-hydrogel structures (McCullen et al., 2010; Jang et al., 2013; Xu et al., 2013). Briefly, an electrospun mat is covered in a coating of hydrogel and then a second electrospun mat is layered on top and covered in a coating of hydrogel, and so on. This structured approach, however, leads to an imposed layered morphology, which will *a priori* influence the way the cells behave. To our knowledge, only one other research group has attempted to randomly mix electrospun polymeric fibers with a hydrogel matrix. Coburn et al. (2011) report manually collecting fibers that were spun into an organic solvent and mixing them with a poly(ethylene glycol)-diacrylate (PEG-DA) solution before UV exposure to cure the PEG-DA gel.

Here, we report a proof-of-principle study in which we developed a continuous hybrid manufacturing process capable of creating a uniformly random fiber-reinforced hydrogel composite matrix. Without the need for layering or post-electrospinning mixing, we demonstrate the ability to tune the fiber density between samples over a wide range. The process has been designed to incorporate cells into the hydrogel component

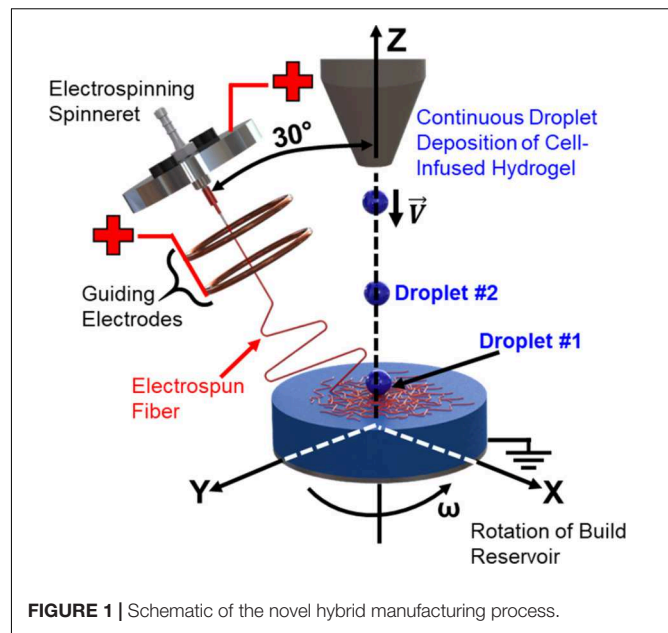


FIGURE 1 | Schematic of the novel hybrid manufacturing process.

during production, therefore, fully embedding the cells in the 3D matrix.

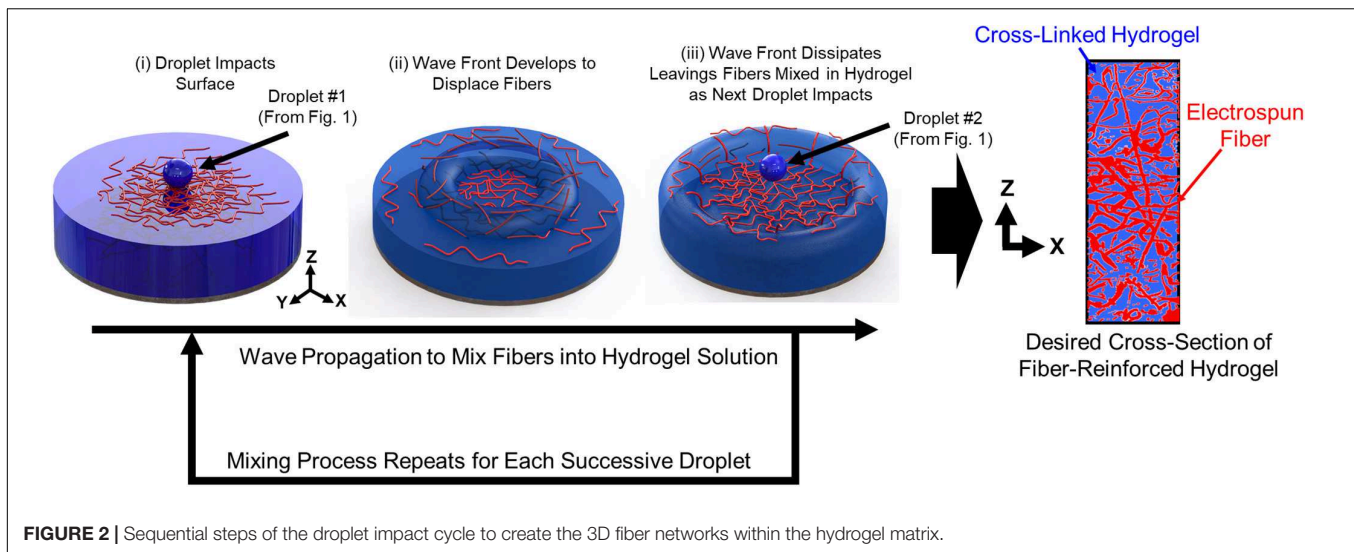
## MATERIALS AND METHODS

### Manufacturing System

In order to create three-dimensional fiber-reinforced hydrogels, as opposed to mats of hydrogel-soaked electrospun fibers, we developed a continuous hybrid manufacturing process (Figure 1). The process involves the combination of far-field electrospinning of polymer fiber reinforcement with droplet deposition of the cell-infused hydrogel solution. In order to allow for the combined deposition of both the fiber reinforcement and cell-infused hydrogel droplets, the far-field electrospinning printhead was angled at 30° off of the z-axis, while the path of the cell-infused hydrogel droplets was collinear to the z-axis. In addition, the build reservoir was also rotated about the z-axis. The major premise behind our hybrid manufacturing process is that the wavefront created by the hydrogel droplet impact (Worthington, 1882; Rein, 1993; Manzello and Yang, 2002; Yarin, 2006; Kavehpour, 2015), when combined with rotation of the reservoir, will result in the effective three dimensional distribution of the fibers.

The sequential steps of the droplet impact cycle to create the 3D fiber networks within the hydrogel matrix are as follows (Figure 2):

- Step 1: The hydrogel droplet lands on the surface of the build reservoir with its impact velocity.
- Step 2: A wave front is created as the kinetic energy from the droplet is dissipated into the surrounding fluid. The wave front displaces and mixes the electrospun fibers within the three dimensional build volume.



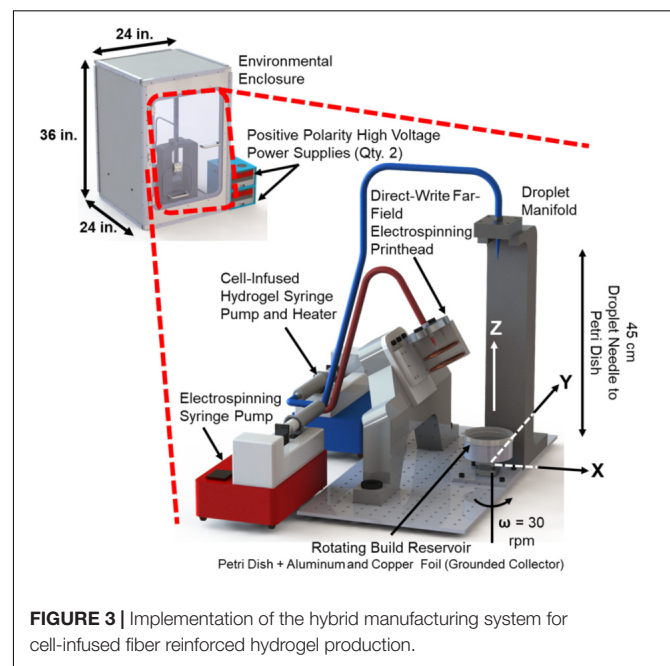
- Step 3: The wave front dissipates, and the next droplet in the sequence proceeds to impact the fluid surface.
- Step 4: Steps 1–3 are repeated until the desired thickness of the sample is achieved.
- Step 5: Upon gelation, the cross-section of the fiber network is characterized.

It should be noted the rotational motion of the build reservoir augments the mechanisms at play in Steps 2 and 3. This additional energy not only mixes the electrospun fibers in the fluid (Step 2) but it also introduces a new deposition zone for the electrospun fibers and hydrogel solution (Step 3).

The components of the manufacturing system include the far-field electrospinning print head, the electrospinning solution syringe pump (R99, Razel, St. Albans, VT, United States), two positive-polarity, high-voltage power supplies (ES-50P, Gamma High Voltage, Ormond Beach, FL, United States), the hydrogel dispensing printhead, the hydrogel solution syringe pump (R99, Razel, St. Albans, VT, United States) with syringe heating pad and controller (New Era Pump Systems, Farmingdale, NY, United States), and build reservoir on a rotary stepper motor stage (maximum rotational speed of 30 revolutions per minute). The manufacturing system was placed inside of an environmental enclosure (**Figure 3**) constructed from polypropylene, due to its high electrical resistivity and chemical resistance. The following section describes the components and process methodology of the system in detail.

### Electrospinning Process

The electrospinning process utilized a far-field setup, with guiding electrodes located underneath the spinneret needle. The spinneret design consists of a round, aluminum-6061-T6 alloy manifold (where the polymer solution was fed from a syringe pump). The spinneret voltage was applied to the manifold via a positive-polarity, high-voltage power supply in order to charge the polymer solution and blunt-ended needle (21-gauge by 12 mm long, stainless steel).



**TABLE 1** | Electrospinning process parameters.

Spinneret voltage	+16–19 kV
Guiding electrode voltage	+9–10 kV
Stainless steel needle size	820 $\mu\text{m}$ (21 G)
Solution feed rate	0.1 mL/min
Spinneret distance	25–30 cm

The round shape of the manifold was selected so that it would better transmit the electric field to the collection substrate.

The use of guiding electrodes has been used in previous electrospinning experiments to reduce the spread of the fiber deposition (Deitzel et al., 2001; Lee et al., 2012; Martinez-Prieto

et al., 2015). With the addition of these guiding electrodes (i.e., copper rings), a second positive-polarity, high-voltage power supply was required to allow for the independent control of both the spinneret voltage (applied to the needle), and the focusing electrode voltage (applied to the rings). Here, the guiding electrodes were two solid copper rings (rolled diameter 75 mm, tube diameter of 4 mm), mounted concentric to the manifold and needle assembly. The rings were rolled to a ring diameter of 75 mm. The two copper rings were located 40 and 60 mm, respectively, below the bottom surface of the manifold.

The electrospinning process parameters used in this setup are listed in **Table 1**. The ground electrode, required for electrospinning, was a round sheet of aluminum foil affixed to the bottom of the build reservoir (a 100 mm diameter polystyrene Petri dish).

### Hydrogel Dispensing

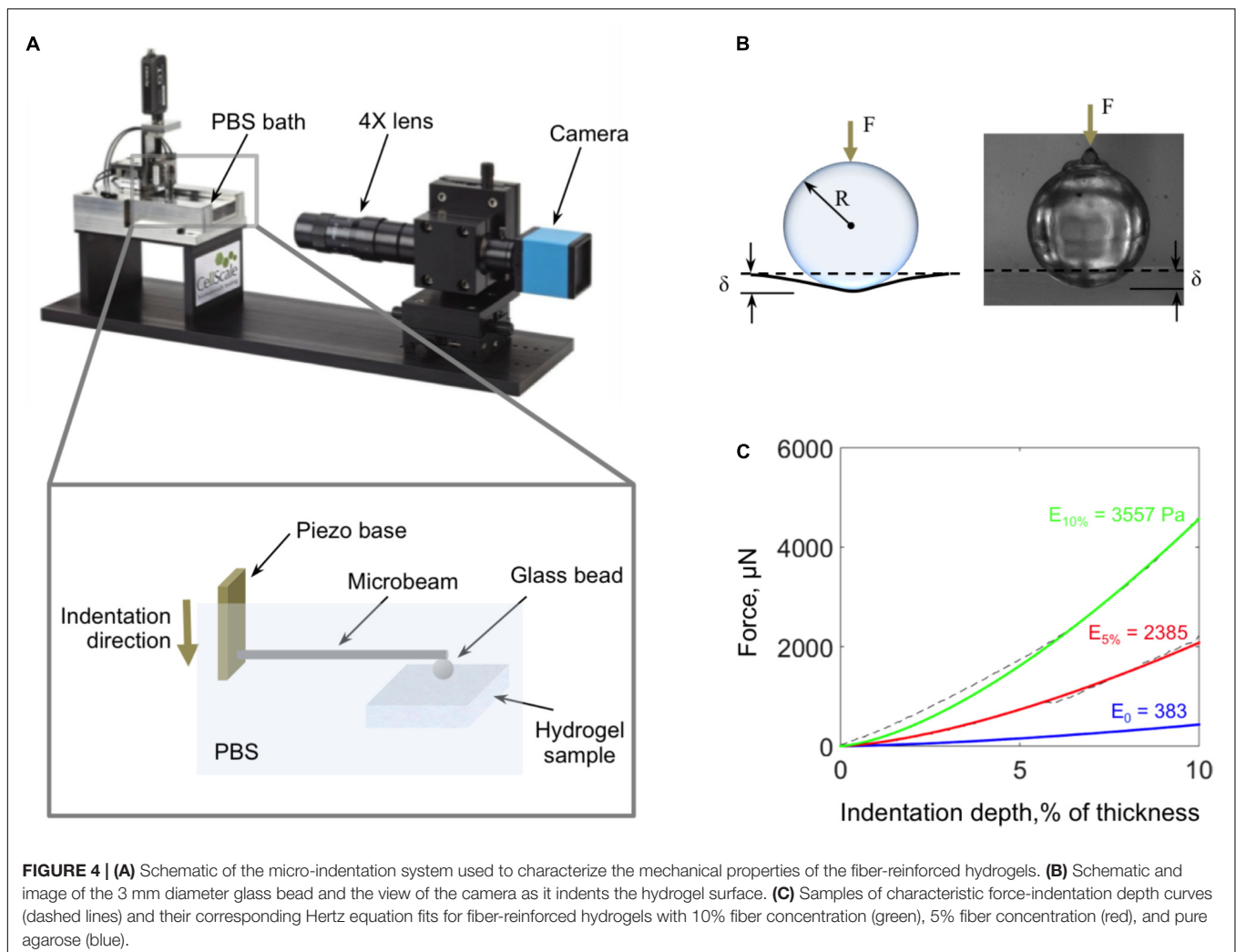
The hydrogel dispensing system was a gravity-assisted, droplet-based deposition system. The hydrogel solution was supplied to a dispensing head located directly above the build reservoir

through the use of a syringe pump. The syringe pump supplied pressure to force a droplet to grow at the tip of a tapered polypropylene dispensing needle (14-gauge, 1.6 mm inside diameter). The height at which the hydrogel dispensing head was located above the build reservoir dictated the velocity (and energy) of the impacting droplet. This was set constant at a height of 45 cm above the build reservoir, which resulted in a droplet velocity of approximately 3 m/s. When embedding cells, they were suspended in the hydrogel at 40°C (see section “Hydrogel” below) and aspirated into the syringe just before the manufacturing process began. The cell-infused hydrogel solution was maintained at a temperature of 40°C in the syringe using the syringe heater. The entire manufacturing process for one sample lasts approximately 3 min.

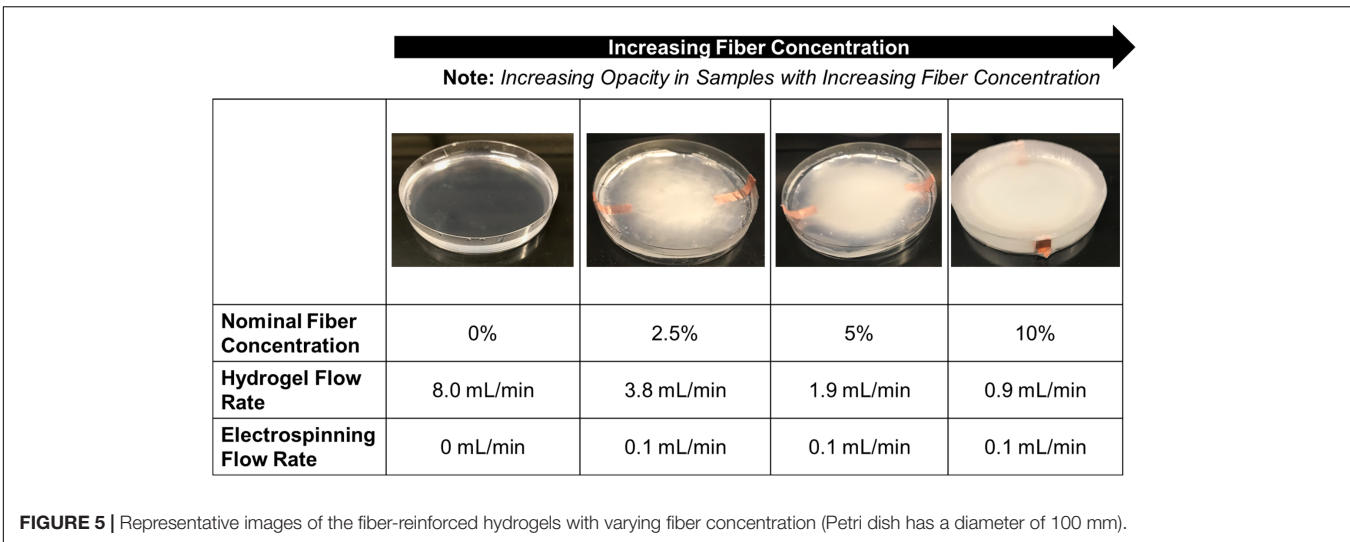
## Electrospinning and Hydrogel Materials

### Electrospinning Solution

Polycaprolactone (PCL) ( $M_n = 80,000$ , Sigma-Aldrich, St. Louis, MO, United States) was used as the material for the electrospun fiber-reinforcement. A concentration of 17 wt.%







was dissolved in glacial acetic acid (Sigma-Aldrich, St. Louis, MO, United States). While being biocompatible, PCL suffers from exhibiting hydrophobic properties, which can inhibit cell adhesion (Liverani and Boccaccini, 2016; Mirhosseini et al., 2016). In order to improve these wetting properties, pluronic acid F-127 (concentration 1.0 wt.%) was added to the electrospinning solution. The solution was mixed for 12–18 h at 60°C.

## Hydrogel

Low gelling temperature agarose (Sigma-Aldrich, St. Louis, MO, United States) was dissolved in incomplete McCoys 5A (Gibco) cell culture medium. For these experiments, the concentration of agarose used was 0.3% w/v to simulate the native ECM stiffness of the cells being used (Mills et al., 2011, 2014; Yu et al., 2011). When creating cell-laden matrices, cells were mixed into the agarose solution at a density of 80,000 cells/mL immediately prior to deposition. After the agarose was deposited, the sample was placed in the refrigerator (4°C) for 30 min to hasten gelation. After gelling, the sample was washed in incomplete medium three times for 5 min. The incomplete medium was then replaced with supplemented medium and the sample placed in the incubator. The washing steps removed traces of the solvent needed to create the fibers and brought the sample to physiological pH.

## Cell Culture and Staining

Human colon cancer cells (HCT 116) were embedded in the fiber-reinforced hydrogels. Once cells were embedded, the samples were hydrated with McCoys 5A cell culture medium supplemented with 10% fetal bovine serum, and 1% penicillin, streptomycin, and amphotericin. Samples were incubated at 37°C and 5% CO<sub>2</sub>. The cell-culture medium was changed every 48 h.

After 8 days of incubation and observation, cell-laden fiber-reinforced hydrogel samples were fixed and stained for fluorescence imaging with the confocal microscope. First, the samples were washed three times for 5 min each in phosphate

buffered saline (PBS). They were then fixed overnight at 4°C in 4% paraformaldehyde. After three more 5 min washes in PBS, the samples were permeabilized in 0.2% Triton X-100 detergent for 30 min followed by three further 5 min washes in PBS. The samples were blocked in 1% bovine serum albumin solution for 30 min before incubating in rhodamine phalloidin (1:75 dilution in PBS) to stain F-actin. The nuclei were then stained with Hoechst (0.2 µg/mL, Hoechst 33342, Thermo Fisher) at room temperature in dark for 4 h.

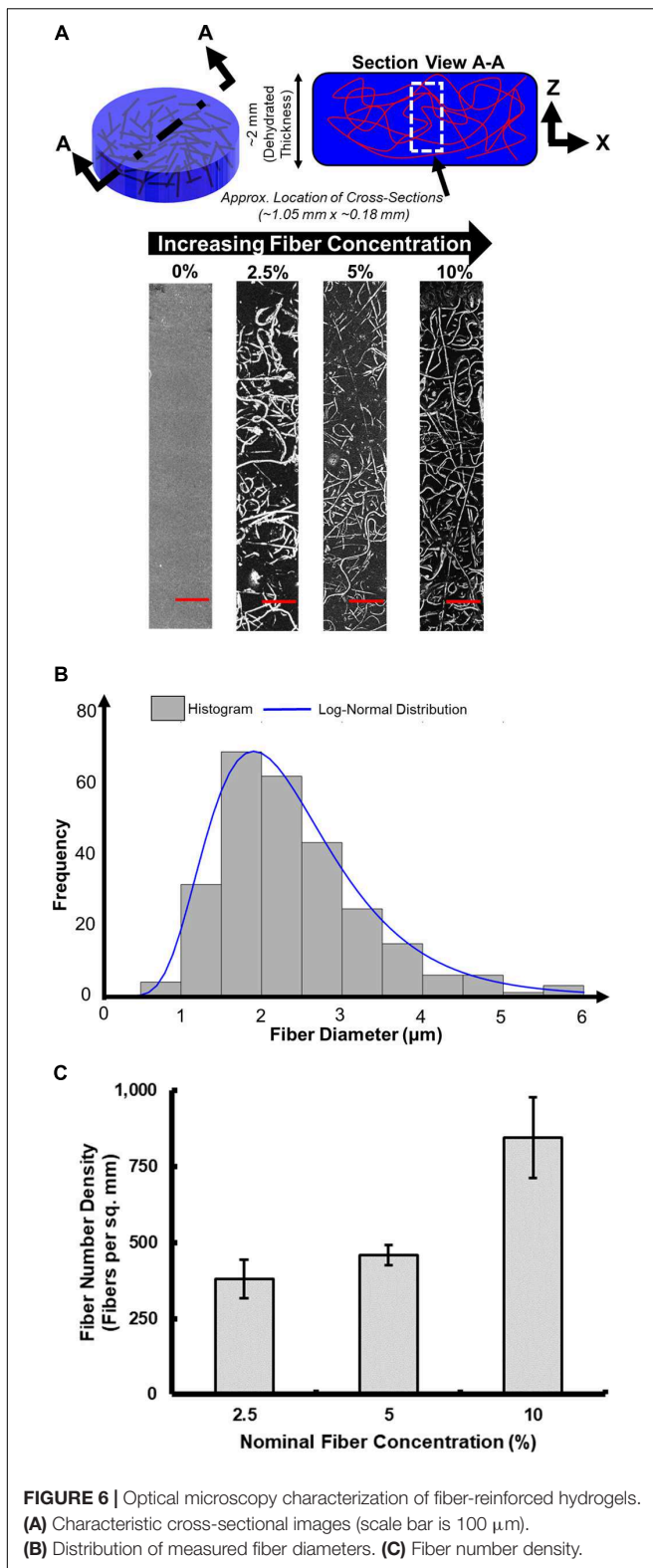
## Microscopy

### For Fiber Characterization

To obtain clean cross-sections for imaging, the fiber-reinforced hydrogel samples were dehydrated and cooled prior to sectioning. The samples were dehydrated in a series baths, of increasing ethanol concentration, over a period of 24 h. The sample was first placed in a 33% ethanol bath for 8 h, a 66% ethanol bath for 8 h, and finally in a 100% ethanol bath for 8 h. Then, the samples were cooled in a refrigerator (2–4°C) for 12 h. Finally, the samples were mechanically sectioned using a tungsten-carbide cutter. The cross-sections of these samples were imaged using an optical microscope (Zeta 20, Zeta Instruments, San Jose, CA, United States), at a magnification of 50×. Cross-sectional images were then analyzed in ImageJ image analysis software to measure the fiber diameter distribution, and fiber number density of the produced samples.

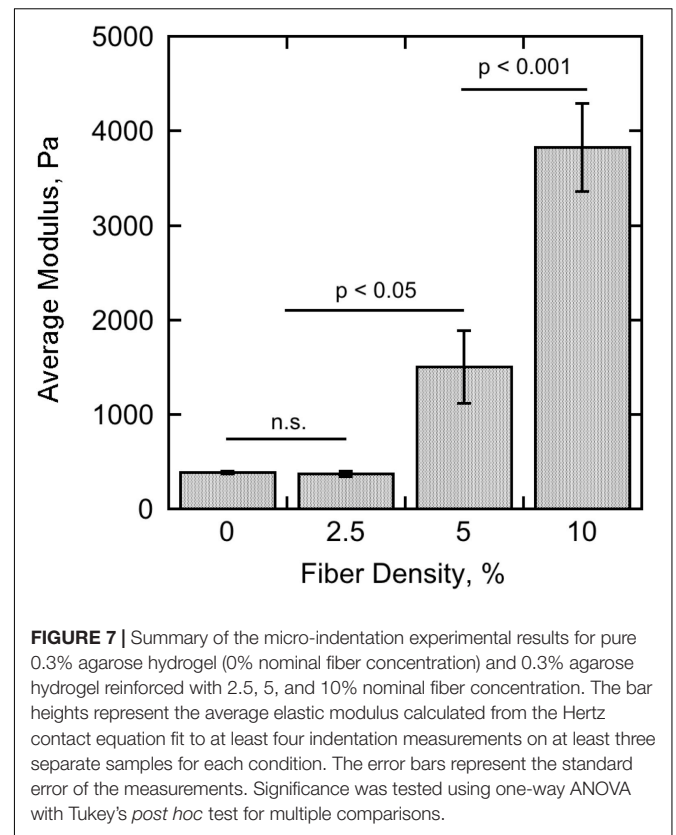
### For Cell Morphological Characterization

For the cell-incorporated fiber-reinforced hydrogels, an inverted optical microscope (Axio Vert.A1, Zeiss, Jena, Germany) was used to take images daily. Ten images were captured per sample in random regions, while making sure to document cell behavior near or on fibers and away from fibers. Fluorescence images of cells and fibers were acquired with a laser scanning confocal microscope (LSM 510 Meta, Zeiss, Jena, Germany).



## Mechanical Characterization

Micro-indentation tests were performed using a high-precision piezo-electric actuator controlled microcompression system

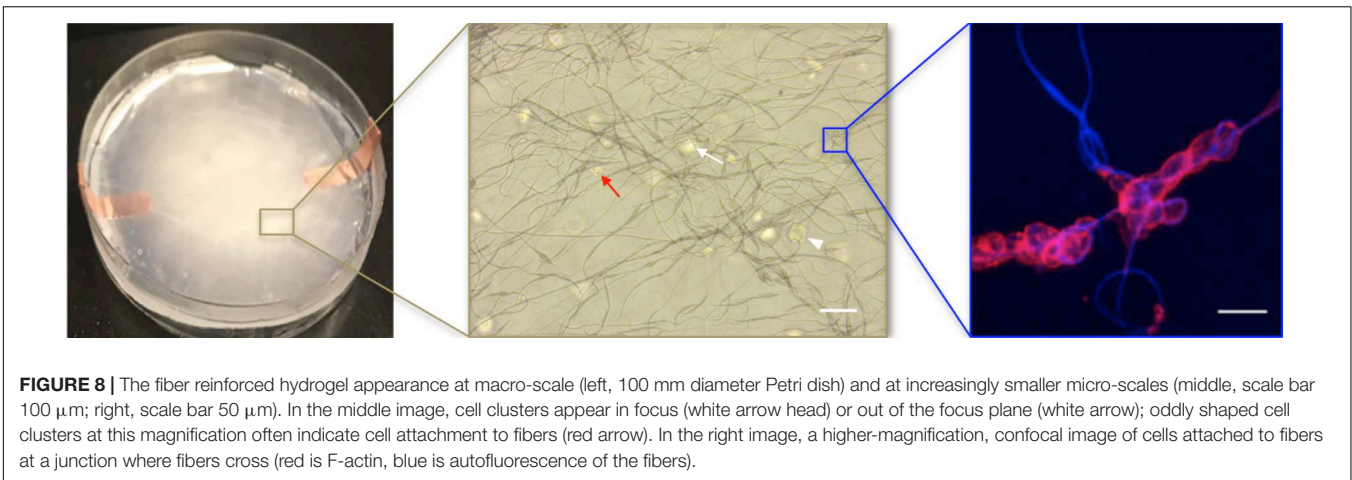


(CellScale Biomaterials Testing, Waterloo, ON, Canada; **Figure 4A**). The hydrogels were indented with a 3 mm glass bead, which was glued to the end of cantilevered steel microbeams of 0.2032 or 0.4064 mm diameter (**Figure 4B**). Indentation force,  $F$ , and depth,  $\delta$ , were continuously calculated during the experiment based on the deflection of the indenter end of the cantilevered beam (measured optically) and the piezo-controlled  $z$ -displacement of the cantilevered beam's fixed end. Experimental force-indentation depth curves were fit to determine the sample's elastic modulus,  $E$ , using the Hertz contact model for a spherical indenter (Yang et al., 2007):

$$F = \frac{4}{3} \frac{ER^{1/2}}{(1-\nu^2)} \delta^{3/2}$$

where  $R$  is the radius of the indenter and  $\nu$  is the Poisson's ratio, which was assumed to be 0.49 for the hydrogels (**Figure 4C**).

When testing, fiber-reinforced hydrogel samples were kept in 60 mm Petri dishes with the walls carefully removed, and the entire sample and microbeam were submerged in PBS. The indentation and retraction rates were the same and kept constant between tests at 4  $\mu\text{m/s}$ . The maximum indentation depth was 10% of the height of the sample.



## RESULTS

### Fiber-Reinforced Hydrogels Microscale Morphology

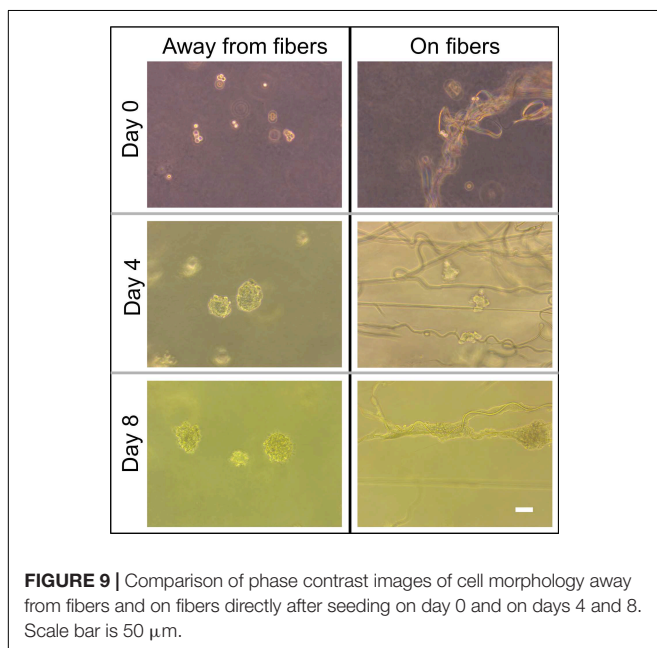
The use of a syringe pump allows for the volumetric flow rate of the hydrogel solution to be tailored to allow for varying fiber densities in the final fiber-reinforced hydrogel samples. Varying the volumetric flow rate of the hydrogel solution between 3.8 and 0.9 mL/min, with the electrospinning rate held constant at 0.1 mL/min, we observed nominal fiber densities between 2.5 and 10%, respectively (**Figure 5**).

Representative samples at the different fiber densities were selected for cross-sectioning and imaging (**Figure 6A**). From these images we observed the morphology of the fibrous network and whether it was deposited uniformly through the thickness of the sample, we also measured the fiber diameter (**Figure 6B**)

and fiber number density (**Figure 6C**). Visually we observe (**Figure 6A**) that the fibrous network uniformly penetrates the full imaged depth of the samples. The network appears to be comprised of randomly oriented fibers, both in-plane (observed as bright lines) and out-of-plane (observed as bright dots).

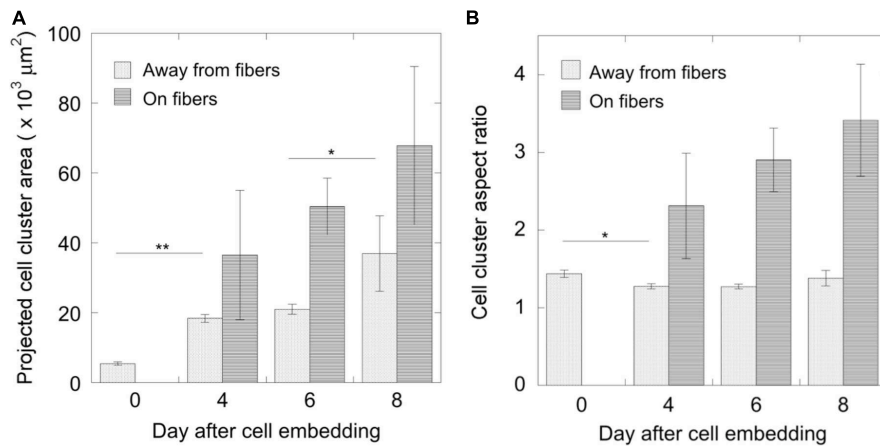
**Figure 6B** displays a histogram of the measured fiber diameters pooled across all the samples, consisting of varying fiber concentrations produced ( $n = 9$  samples). The distribution of fiber diameter followed a lognormal distribution, with a mean and standard deviation of 2.40 and 0.98  $\mu\text{m}$ , respectively. No significant changes in fiber diameter were seen across samples with different fiber concentrations, as the electrospinning parameters (listed in **Table 1**), and electrospinning solution (detailed in section Electrospinning Solution) remained constant throughout the production of all samples.

The fiber number density was also computed for the samples produced at different fiber concentrations. **Figure 6C** presents value of the fiber number density (i.e., number of fibers per unit area), seen in the optical microscopy images. A total of three optical microscopy images were analyzed for each fiber concentration on the plot. As the fiber concentration increases, the fiber number density also increases. Using this process, the fiber number density increase up to  $\sim 850$  fibers per sq. mm at the highest fiber concentration (10%) that was created.

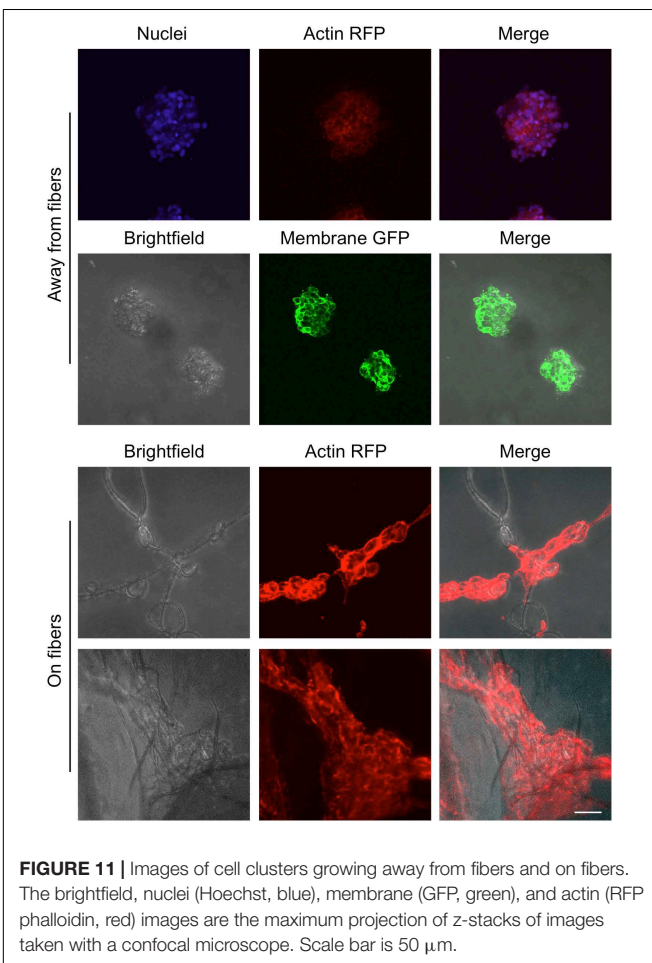


### Mechanical Characterization of the Fiber-Reinforced Hydrogels

At least three samples were produced of pure 0.3% agarose hydrogel and fiber-reinforced hydrogels with fiber densities of 2.5, 5, and 10% for mechanical testing by micro-indentation. The elastic moduli for pure 0.3% agarose and 2.5% fiber-reinforced hydrogel were found to be  $385 \pm 13$  Pa and  $368 \pm 28$  Pa, respectively, and not significantly different from one another. Upon the incorporation of higher concentrations of fibers, however, the elastic modulus rose to  $1,500 \pm 387$  Pa with 5% fiber concentration and  $3,830 \pm 466$  Pa with 10% fiber concentration (**Figure 7**). At least four indentation



**FIGURE 10** | Measurements of cell cluster development over 8 days. **(A)** The growth of cell clusters was quantified as their projected area and **(B)** their morphology as their aspect ratio (mean  $\pm$  standard error). For cell clusters growing away from fibers,  $N_0 = 35$ ,  $N_4 = 43$ ,  $N_6 = 27$ , and  $N_8 = 12$ ; for cell clusters growing on fibers,  $N_4 = 3$ ,  $N_6 = 4$ ,  $N_8 = 7$ . Significance was tested using one-way ANOVA with Tukey's *post hoc* test for multiple comparisons (\* $p < 0.05$ , \*\* $p < 0.001$ ).



**FIGURE 11** | Images of cell clusters growing away from fibers and on fibers. The brightfield, nuclei (Hoechst, blue), membrane (GFP, green), and actin (RFP phalloidin, red) images are the maximum projection of z-stacks of images taken with a confocal microscope. Scale bar is 50  $\mu\text{m}$ .

## Cell Growth and Morphological Characterization

For this proof of principle study we chose an approximately 4% fiber concentration as we found this was an optimal density that maximized the probability of cell-fiber interaction while maintaining optical transparency of the matrix to obtain microscope images of the cells (Figure 8 and Supplementary Figure 1). In order to initiate cell-fiber contact, a cluster of cells must be embedded in proximity to a fiber or bundle of fibers. Growth and morphology of the embedded HCT-116 cell clusters were monitored over an 8 days period in the fiber-reinforced hydrogels (Figures 9, 10). Characteristic images of cell clusters growing away from and on the fibers within the hydrogels show the obvious effects of the fibers on growth morphology (Figures 9, 11). We quantified the growth rates of the cell clusters as their projected area in the micrographs and their morphology as their projected aspect ratio over 8 days of growth (Figure 10). Initially (day 0), the embedded cell clusters are not apparently attached to fibers; therefore, no data is recorded for that day and condition. Cell clusters that are away from fibers and on fibers both exhibit steady growth (Figure 10, left). The most significant effect of the presence of the fibers on cell growth, however, is the morphology. Whereas cell clusters away from the fibers maintain an approximately spherical morphology (Figure 10, right; Figure 11, top rows), the clusters on fibers extend out along the fibers and project a more elongated shape over time (Figure 10, right; Figure 11, bottom rows). Since the probability of a cell cluster being embedded in contact with a fiber is relatively low, there are significantly fewer measurements for “on fiber” clusters as compared to “away from fibers” clusters. After the 8 days growth period, the samples were fixed and stained with either Hoechst (to visualize the nuclei) or RFP phalloidin (to visualize the F-actin network). Although the characterization of cell growth and morphology has been presented here for the HCT-116 colon cancer cell line, the applicability of the method

measurements per sample (12 total per condition) were collected for the averages and standard errors presented here.

to a second cell line (MDA-MB-231 breast adenocarcinoma) is presented in the Supplementary Materials (Supplementary Figure 2).

## DISCUSSION

Morphological guidance cues play an important role in determining cell behavior, from spreading and proliferation to apoptosis. It has been recognized for some time the need to culture cells in environments that more closely resemble their native 3D, soft, and structured ECM than 2D, stiff Petri dish plastic. However, the commonly used bio- and synthetic polymeric hydrogels lack the important protein fiber structures that are present in the body. Furthermore, the protein fiber structure is known to become significantly denser and stiffer due to increased deposition and cross-linking in diseases like fibrosis and cancer. Since no *in vitro* cell culture matrix is available that combines both the fibrous and gel components of the ECM, nor the ability to tune the fiber density and mechanical properties of the matrix, our major goal here was to produce such a matrix and demonstrate cell viability and morphological differences in it.

Here, we developed a continuous hybrid manufacturing process to make fiber-reinforced composite hydrogels. A far field electrospinning process was used to deposit the fibrous component with the aid of guiding electrodes; and a gravity-assisted, droplet-based system controlled the rate of addition of the cell-laden hydrogel component. An environmental enclosure was designed in which to carry out the manufacturing of the samples to avoid contamination. For these proof of principle experiments, we used PCL for the electrospun fibers and 0.3% agarose for the gel matrix due to their ease of use and cost effectiveness, but other commonly electrospun materials and hydrogels may also be implemented with little effort.

Cells were introduced into the fiber-reinforced hydrogels by suspending them in the hydrogel solution prior to its droplet deposition. The cells were therefore randomly placed in the matrices, sometimes lying near to or on fibers and sometimes away from fibers. We tracked how the cells grew and responded with respect to their position in the gels. Obvious differences could be seen between cells that were growing away from fibers, and cells growing along fibers. Such distinctive phenotypic differences were expected. Agarose is a bioinert, non-cell-adhesive hydrogel that only provides tissue-mechanics-mimicking structural support for cell growth. Therefore, it was not surprising that cell clusters that were only in contact with this gel maintained a compacted spheroidal shape. The use of other, bioactive hydrogels would add another layer of complexity to this system. With little to no modification of the manufacturing

system, other thermo-sensitive gelling materials may be used (e.g., gelatin; Supplementary Figure 3). Cells that were embedded near to or in contact with the PCL fibers, however, displayed a completely different phenotype. They attached to the PCL fibers, spreading out along them in long thin bundles. This demonstrated the ability to control cell behavior with a randomly embedded, 3D polymeric fiber mesh embedded in a hydrogel matrix. This will be a useful tool to study how cells interact with fibrotic and desmoplastic tissues, which are known to be part of the pathophysiology of tumor growth and metastasis. Excessive fibrous structures in and surrounding the tumor are known, for example, to provide highways upon which tumor cells migrate (Condeelis and Segall, 2003).

Continuous improvement of this manufacturing process will allow greater control over fiber density, and possibly fiber orientations, within the hydrogel matrix. Such fully tunable matrices will provide mechanobiologists a useful tool with which to study the interactions of cells with the ECM and determine their influence in health and disease.

## AUTHOR CONTRIBUTIONS

AW performed cell experiments, analyzed data, and wrote sections of the manuscript. JN designed and built the hybrid manufacturing process, characterized the fiber morphology of the samples, and wrote sections of the manuscript. RD developed the microindentation system and mechanically characterized the samples. JS guided the efforts related to the development of the hybrid manufacturing process and the subsequent fiber characterization. KM conceived and contributed to the design of the study, interpreted the results, and wrote sections of the manuscript. All authors contributed to manuscript revision, read, and approved the submitted version.

## FUNDING

JN acknowledges support from the U.S. National Science Foundation Graduate Research Fellowship Program (NSF GRFP) under Grant No. #DGE-1247271. JS acknowledges support from the U.S. National Science Foundation Grant No. #CMMI-1462648.

## SUPPLEMENTARY MATERIAL

The Supplementary Material for this article can be found online at: <https://www.frontiersin.org/articles/10.3389/fphys.2018.00966/full#supplementary-material>

## REFERENCES

- Berger, A. J., Linsmeier, K. M., Kreeger, P. K., and Masters, K. S. (2017). Decoupling the effects of stiffness and fiber density on cellular behaviors via an interpenetrating network of gelatin-methacrylate and collagen. *Biomaterials* 141, 125–135. doi: 10.1016/j.biomaterials.2017.06.039
- Coburn, J., Gibson, M., Bandalini, P. A., Laird, C., Mao, H. -Q., Moroni, L., et al. (2011). Biomimetics of the Extracellular matrix: an integrated three-dimensional fiber-hydrogel composite for cartilage tissue engineering. *Smart Struct. Syst.* 7, 213–222. doi: 10.12989/sss.2011.7.3.213
- Condeelis, J., and Segall, J. E. (2003). Intravital imaging of cell movement in tumours. *Nat. Rev. Cancer* 3, 921–930. doi: 10.1038/nrc1231

- Croft, D. R., Sahai, E., Mavria, G., Li, S., Tsai, J., Lee, W. M. F., et al. (2004). Conditional ROCK activation in vivo induces tumor cell dissemination and angiogenesis. *Cancer Res.* 64, 8994–9001. doi: 10.1158/0008-5472.CAN-04-2052
- Deitzel, J. M., Hirvonen, J. K., Beck Tan, N. C., and Kleinmeyer, J. D. (2001). Controlled deposition and collection of electro-spun poly (ethylene oxide) fibers. *Polymer* 42, 8163–8170. doi: 10.1016/S0032-3861(01)00336-6
- Erikson, A., Andersen, H. N., Naess, S. N., Sikorski, P., and de Lange Davies, C. (2008). Physical and chemical modifications of collagen gels: impact on diffusion. *Biopolymers* 89, 135–143. doi: 10.1002/bip.20874
- Jang, J., Lee, J., Seol, Y. J., Jeong, Y. H., and Cho, D. W. (2013). Improving mechanical properties of alginate hydrogel by reinforcement with ethanol treated polycaprolactone nanofibers. *Compos. B Eng.* 45, 1216–1221. doi: 10.1016/j.compositesb.2012.09.059
- Kavehpour, H. P. (2015). Coalescence of drops. *Annu. Rev. Fluid Mech.* 47, 245–268. doi: 10.1146/annurev-fluid-010814-014720
- Lee, J., Lee, S. Y., Jang, J., Jeong, Y. H., and Cho, D. W. (2012). Fabrication of patterned nanofibrous mats using direct-write electrospinning. *Langmuir* 28, 7267–7275. doi: 10.1021/la3009249
- Liverani, L., and Boccaccini, A. R. (2016). Versatile production of poly(Epsilon-Caprolactone) fiber by electrospinning using benign solvents. *Nanomaterials* 6, 15. doi: 10.3390/nano6040075
- Lu, P., Weaver, V. M., and Werb, Z. (2012). The extracellular matrix: a dynamic niche in cancer progression. *J. Cell Biol.* 196, 395–406. doi: 10.1083/jcb.201102147
- Makale, M. (2007). Cellular mechanobiology and cancer metastasis. *Birth Defects Res. C Embryo Today Rev.* 81, 329–343. doi: 10.1002/bdrc.20110
- Manzello, S. L. and Yang, J. C. (2002). An experimental study of a water droplet impinging on a liquid surface. *Exp. Fluids* 32, 580–589. doi: 10.1007/s00348-001-0401-8
- Martinez-Prieto, N., Abecasis, M., Xu, J., Guo, P., Cao, J., and Ehmman, K. F. (2015). Feasibility of fiber-deposition control by secondary electric fields in near-field electrospinning. *J. Micro Nanomanuf.* 3:6. doi: 10.1115/1.4031491
- McCullen, S. D., Miller, P. R., Gittard, S. D., Gorga, R. E., Pourdeyhimi, B., Narayan, R. J., et al. (2010). In Situ collagen polymerization of layered cell-seeded electrospun scaffolds for bone tissue engineering applications. *Tissue Eng. C Methods* 16, 1095–1105. doi: 10.1089/ten.tec.2009.0753
- Mills, K. L., Garikipati, K., and Kemkemer, R. (2011). Experimental characterization of tumor spheroids for studies of the energetics of tumor growth. *Int. J. Mater. Res.* 102, 889–895. doi: 10.3139/146.110532
- Mills, K. L., Kemkemer, R., Rudraraju, S., and Garikipati, K. (2014). Elastic Free energy drives the shape of prevascular solid tumors. *PLoS One* 9:e103245. doi: 10.1371/journal.pone.0103245
- Mirhosseini, M. M., Haddadi-Asl, V., and Zargarian, S. S. (2016). Fabrication and characterization of hydrophilic poly( $\epsilon$ -caprolactone)/pluronic P123 electrospun fibers. *J. Appl. Polym. Sci.* 133:11. doi: 10.1002/app.43345
- Narayanan, K., Leck, K. J., Gao, S., and Wan, A. W. (2009). Three-dimensional reconstituted extracellular matrix scaffolds for tissue engineering. *Biomaterials* 30, 4309–4317. doi: 10.1016/j.biomaterials.2009.04.049
- Nisbet, D. R., Forsythe, J. S., Shen, W., Finkelstein, D. I., and Horne, M. K. (2008). Review paper: a review of the cellular response on electrospun nanofibers for tissue engineering. *J. Biomater. Appl.* 24, 7–29. doi: 10.1177/088532820809086
- Rein, M. (1993). Phenomena of liquid drop impact on solid and liquid surfaces. *Fluid Dyn. Res.* 12, 61–93. doi: 10.1016/0169-5983(93)90106-K
- Theocharis, A. D., Skandalis, S. S., Gialeli, C., and Karamanos, N. K. (2016). Extracellular matrix structure *Adv. Drug Deliv. Rev.* 97, 4–27. doi: 10.1016/j.addr.2015.11.001
- Worthington, A. M. (1882). On impact with a liquid surface. *Proc. R. Soc. Lond.* 34, 217–230. doi: 10.1098/rspl.1882.0035
- Xu, T., Binder, K. W., Albanna, M. Z., Dice, D., Zhao, W., Yoo, J. J., et al. (2013). Hybrid printing of mechanically and biologically improved constructs for cartilage tissue engineering applications. *Biofabrication* 5:015001. doi: 10.1088/1758-5082/5/1/015001
- Yang, Y., Bagnaninchi, P. O., Ahearne, M., Wang, R. K., and Liu, K.-K. (2007). A novel optical coherence tomography-based micro-indentation technique for mechanical characterization of hydrogels. *J. R. Soc. Interface* 4, 1169–1173. doi: 10.1098/rsif.2007.1044
- Yarin, A. L. (2006). Drop impact dynamics: splashing, spreading, receding, bouncing. *Annu. Rev. Fluid Mech.* 38, 159–192. doi: 10.1146/annurev.fluid.38.050304.092144
- Yu, H., Mouw, J. K., and Weaver, V. M. (2011). Forcing form and function: biomechanical regulation of tumor evolution. *Trends Cell Biol.* 21, 47–56. doi: 10.1016/j.tcb.2010.08.015

**Conflict of Interest Statement:** The authors declare that the research was conducted in the absence of any commercial or financial relationships that could be construed as a potential conflict of interest.

The reviewer PM and handling Editor declared their shared affiliation.

Copyright © 2018 Williams, Nowak, Dass, Samuel and Mills. This is an open-access article distributed under the terms of the Creative Commons Attribution License (CC BY). The use, distribution or reproduction in other forums is permitted, provided the original author(s) and the copyright owner(s) are credited and that the original publication in this journal is cited, in accordance with accepted academic practice. No use, distribution or reproduction is permitted which does not comply with these terms.



# Metabolic Changes Associated With Muscle Expression of SOD1<sup>G93A</sup>

Gabriella Dobrowolny<sup>1,2\*†</sup>, Elisa Lepore<sup>1,2†</sup>, Martina Martini<sup>1</sup>, Laura Barberi<sup>1</sup>, Abigail Nunn<sup>2</sup>, Bianca Maria Scicchitano<sup>3</sup> and Antonio Musarò<sup>1,2\*</sup>

<sup>1</sup> Laboratory affiliated to Istituto Pasteur – Fondazione Cenci Bolognetti, DAHFMO – Unit of Histology and Medical Embryology, Sapienza University of Rome, Rome, Italy, <sup>2</sup> Center for Life Nano Science, Istituto Italiano di Tecnologia, Rome, Italy, <sup>3</sup> Istituto di Istologia ed Embriologia, Università Cattolica del Sacro Cuore, Fondazione Policlinico Universitario Agostino Gemelli, Rome, Italy

## OPEN ACCESS

### Edited by:

Cesare Gargioli,  
Università degli Studi di Roma  
"Tor Vergata", Italy

### Reviewed by:

Chiara Donati,  
Università degli Studi di Firenze, Italy  
Renée Morris,  
University of New South Wales,  
Australia

### \*Correspondence:

Gabriella Dobrowolny  
gabriella.dobrowolny@uniroma1.it  
Antonio Musarò  
antonio.musaro@uniroma1.it

<sup>†</sup> These authors have contributed  
equally to this work.

### Specialty section:

This article was submitted to  
Integrative Physiology,  
a section of the journal  
Frontiers in Physiology

**Received:** 30 March 2018

**Accepted:** 13 June 2018

**Published:** 10 July 2018

### Citation:

Dobrowolny G, Lepore E, Martini M,  
Barberi L, Nunn A, Scicchitano BM  
and Musarò A (2018) Metabolic  
Changes Associated With Muscle  
Expression of SOD1<sup>G93A</sup>.  
Front. Physiol. 9:831.  
doi: 10.3389/fphys.2018.00831

Amyotrophic lateral sclerosis (ALS) is a severe neurodegenerative disorder, classified into sporadic or familial forms and characterized by motor neurons death, muscle atrophy, weakness, and paralysis. Among the familial cases of ALS, approximately 20% are caused by dominant mutations in the gene coding for superoxide dismutase (SOD1) protein. Of note, mutant SOD1 toxicity is not necessarily limited to the central nervous system. ALS is indeed a multi-systemic and multifactorial disease that affects whole body physiology and induces severe metabolic changes in several tissues, including skeletal muscle. Nevertheless, whether alterations in the plasticity, heterogeneity, and metabolism of muscle fibers are the result of motor neuron degeneration or alternatively occur independently of it remain to be elucidated. To address this issue, we made use of a mouse model (MLC/SOD1<sup>G93A</sup>) that overexpresses the SOD1 mutant gene selectively in skeletal muscle. We found an alteration in the metabolic properties of skeletal muscle characterized by alteration in fiber type composition and metabolism. Indeed, we observed an alteration of muscle glucose metabolism associated with the induction of Phosphofructokinases and Pyruvate dehydrogenase kinase 4 expression. The upregulation of Pyruvate dehydrogenase kinase 4 led to the inhibition of Pyruvate conversion into Acetyl-CoA. Moreover, we demonstrated that the MLC/SOD1<sup>G93A</sup> transgene was associated with an increase of lipid catabolism and with the inhibition of fat deposition inside muscle fibers. All together these data demonstrate that muscle expression of the SOD1<sup>G93A</sup> gene induces metabolic changes, along with a preferential use of lipid energy fuel by muscle fibers. We provided evidences that muscle metabolic alterations occurred before disease symptoms and independently of motor neuron degeneration, indicating that skeletal muscle is likely an important therapeutic target in ALS.

**Keywords:** skeletal muscle, SOD1<sup>G93A</sup>, muscle fiber types, metabolic alterations, ALS, oxidative stress

## INTRODUCTION

Amyotrophic Lateral Sclerosis (ALS) is a multi-factorial and multi-systemic disease due to severe alterations in several tissues and cell compartments, such as motor neurons, glia, and muscle (Wijesekera and Leigh, 2009). In addition, energy balance is severely compromised in ALS patients, owing to higher consumption than intake with increased resting energy use, along with abnormal

lipid metabolism (Kasarskis et al., 1996; Desport et al., 2005; Dupuis et al., 2008; Bouteloup et al., 2009; Funalot et al., 2009).

Interestingly, while lower body fat represents an ALS premorbidity factor (Gallo et al., 2013), overweight or obese people have a lower risk to develop ALS (O'Reilly et al., 2013). A recent study has pointed out that ALS patients lose weight about 10 years before motor symptoms (Peter et al., 2017) and have higher daily energy intake to compensate the higher energy consumption that has been documented before clinical onset of the disease (Huisman et al., 2015).

Similar energetic alterations were found in transgenic animal models of ALS that ubiquitously express the mutant isoform of the gene coding for superoxide dismutase 1 (SOD1<sup>G93A</sup>) (Gurney et al., 1994). Indeed, the SOD1<sup>G93A</sup> mice are characterized by increased energy expenditure and by a concomitant skeletal muscle hypermetabolism (Dupuis et al., 2004). It has been demonstrated that a diet rich in lipids can delay disease onset and motor neuron degeneration and can extend life expectancy of mutant SOD1 mice (Dupuis et al., 2004).

During disease progression and muscle denervation, the SOD1<sup>G93A</sup> mice exhibit a loss of fast-twitch glycolytic fibers and show a transition of skeletal myosin from fast glycolytic type toward slower oxidative one (Peggion et al., 2017). The loss of fast glycolytic fibers is considered a consequence of the degeneration of fast fatigable motor neuron synapses that leads to a shift in muscle fiber type. In addition, skeletal muscle of ALS patients and transgenic ALS mouse models show mitochondrial functional impairment (Carri and Cozzolino, 2011); this mitochondria alteration together with increased energy expenditure might represent one of the first targets of ALS pathology, retrogradely affecting the nerve in a sort of dying back phenomenon (Shi et al., 2010).

It has been recently demonstrated, in the muscles of SOD1<sup>G93A</sup> mouse model, that the metabolic switch toward lipid use represents an early pathological event, suggesting that the metabolic defect is distinct from denervation (Palamiuc et al., 2015). However, the animal model chosen to conduct the study did not help to definitely disclose whether muscle metabolic changes and neuromuscular junction alterations, two pathogenic events associated with ALS, are a consequence of changes in synapse functionality or are independent of it.

In previous works we have demonstrated that muscle-selective expression of SOD1 mutation (MLC/SOD1<sup>G93A</sup>), induces alterations in the contractile apparatus, and causes mitochondrial dysfunction without affecting motor neuron survival (Dobrowolny et al., 2008). Recently, we found a significant reduced stability of muscles mitochondrial membrane potential, and we observed a reduced integrity of mitochondrial network in the region of the Neuromuscular Junctions (NMJ) of MLC/SOD1<sup>G93A</sup> transgenic mice, suggesting that mitochondrial alterations and accumulation of oxidative stress negatively impact on NMJ stability (Dobrowolny et al., 2018).

Here, taking advantage of MLC/SOD1<sup>G93A</sup> mice, we investigated whether muscle specific accumulation of SOD1<sup>G93A</sup> can induce metabolic changes that occur independently from motor neuron degeneration and precede muscle denervation.

## MATERIALS AND METHODS

### Mice

Four-month-old MLC/SOD1<sup>G93A</sup> mice overexpressing the mutant SOD1 gene (SOD1<sup>G93A</sup>) under the control of the Myosin Light Chain (MLC) muscle specific promoter (Dobrowolny et al., 2008) and 4-month-old Friend leukemia virus B (FVB) (Jackson Laboratories) have been used. Male and female mice were used indiscriminately. The animals were housed in a temperature controlled (22°C) room with a 12:12 h light–dark cycle and housed in a number of three to five per cage. All animal experiments were approved by the ethics committee of Sapienza University of Rome-Unit of Histology and Medical Embryology and were performed in accordance with the current version of the Italian Law on the Protection of Animals.

### Histological Analysis

Segments of tibialis anterior (TA) muscles isolated from both wild type (Wt) and MLC/SOD1<sup>G93A</sup> transgenic mice were embedded in tissue freezing medium and snap frozen in nitrogen-cooled isopentane. Ten  $\mu\text{m}$  sections were prepared for either NADH-transferase or PAS staining. Images were collected using a Zeiss AX10-Imager A2 connected to the Axiocam 503 color.

### RNA Preparation and Real-Time Analysis

Total RNA from Wt and MLC/SOD1<sup>G93A</sup> transgenic muscles was isolated from tibialis anterior muscles (TA) by TRIzolTM reagent (Thermo Fisher Scientific). The yield, quality, and integrity of RNA were determined using NanoDrop ND-2000 (Thermo Fisher Scientific).

Total RNA (1  $\mu\text{g}$ ) reverse-transcription was performed using Qiagen Reverse Transcription Kit (Qiagen) whereas 10 ng of RNA was reverse transcribed using the TaqMan micro-RNA Reverse Transcription Kit (Thermo Fisher Scientific). Quantitative PCR was performed using the ABI PRISM 7500 SDS (Thermo Fisher Scientific), TaqMan universal MMIX II (Thermo Fisher Scientific), and TaqMan probe (Thermo Fisher Scientific). Quantitative RT-PCR sample value was normalized for the expression of  $\beta$ -actin and U6 snRNA for mRNA and microRNA, respectively. The relative expression was calculated using the  $2^{-\Delta\Delta C_t}$  method (Livak and Schmittgen, 2001) and reported as fold change.

### Protein Extraction and Western Blot Analysis

Protein extraction from both Wt and MLC/SOD1<sup>G93A</sup> transgenic tibialis anterior muscles was performed in Sodium Chloride, 1 mM Phenylmethylsulfonyl fluoride, 1  $\mu\text{g}/\text{ml}$  Aprotinin, 1  $\mu\text{g}/\text{ml}$  Leupeptin, 1  $\mu\text{g}/\text{ml}$  Pepstatin, 1 mM Sodium orthovanadate, 1 mM Sodium fluoride. Equal amounts of protein from each muscle lysate were separated in SDS polyacrylamide gel and transferred onto a nitrocellulose membrane. Filters were saturated with 5% milk and then blotted



with antibodies against Slow myosin (1:3000) (Sigma Aldrich, United States), Glut4 (1:250) (Cell Signaling Technology, United States), PDH-E1 $\alpha$  (pSer300) (1:400) (Calbiochem, United States and Canada), Pyruvate Dehydrogenase complex (PDH; 1:600) (Cell Signaling, United States), Phospho-GSk3 $\beta$  (pSer9) and total GSk-3 $\beta$  (1:1000) (Cell Signaling, United States), ATGL (1:100) (Cell Signaling, United States), pACC(1:600) (Cell Signaling, United States), ACC(1:250) (Cell Signaling, United States), Plin2 (2 $\mu$ g/ml) (Life Span Biosciences, United States), and  $\alpha$ -tubulin (1:2000) (Sigma Aldrich, United States).

Then, filter was incubated with secondary antibodies Goat anti-mouse IgG HRP-conjugated (1:7000) (Bethyl, Montgomery, TX, United States) or Goat anti-rabbit IgG HRP-conjugated (1:7000) (Bethyl, Montgomery, TX, United States) in 1% milk for 1 h. All the antibodies were chosen as validated for western blot by manufactures.

### Glucose Tolerance Test

Four-month-old Wt and MLC/SOD1<sup>G93A</sup> transgenic mice were fasted for 18 h and blood was drawn from a small incision at the tip of the tail. Blood glucose levels were evaluated using a commercial Glucose multicare (BSI) kit. Glucose tolerance test (GTT) was performed measuring glucose before and after IP injection of 2 g/kg body mass of glucose. Changes in blood glucose were followed for 120 min with measurements taken every 30 min.

### CARS Microscopy

A multi modal non-linear microscope was used to record 3D stacks of images in cryosections of muscle tissue, using the strong CH vibration at 2840 cm<sup>-1</sup> of lipids as image contrast. In brief, a picosecond laser source (Levante Emerald OPO, APE Angewandte Physik & Elektronik GmbH, Germany, pumped by an Nd:Vanadate laser at 532 nm, High Q Laser GmbH, Austria) generated two pulses at 76 MHz repetition rate, with powers of 50 mW and 120 mW for the pump (817 nm) and Stokes (1064 nm) beams, respectively, that were spatially and temporally overlapped and then coupled to a modified inverted laser scanning confocal microscope (Nunn et al., 2016).

### Statistical Analysis

All details related to statistical tests, statistical parameters, including sample sizes ( $n$  = number of animal subjects per group), and significance are reported in Figure Legends.

For real-time PCR we considered sample size adequate when the two groups were significantly different ( $P < 0.05$ ). Unless otherwise indicated,  $P$ -values for simple pair-wise comparisons were performed using a two-tailed unpaired and non-parametric Mann-Whitney test and graph values are reported as mean  $\pm$  SEM. (error bars).

Data is considered statistically significant when  $p < 0.05$ . Asterisks in figures, indicate statistical significance \* $p < 0.05$ , \*\* $p < 0.05$ . All statistical analysis was performed using GraphPad PRISM 6 software.

## RESULTS

### MLC/SOD1<sup>G93A</sup> Mice Exhibit a Fast-to-Slow Shift in the Fiber Type Composition

In a previous work we have demonstrated that localized expression of SOD1<sup>G93A</sup> promoted the fiber-type switching from glycolytic toward more oxidative fibers in EDL muscle of MLC/SOD1<sup>G93A</sup> mice (St. Pierre et al., 2006). To further support this evidence, we analyzed NADH levels in the tibialis anterior (TA) muscle, which contains high proportion of the fastest glycolytic fibers. **Figure 1A** shows higher content of NADH in the TA muscle of MLC/SOD1<sup>G93A</sup> mice compared to that observed in the TA of Wt littermates.

To further investigate the metabolic profile of the MLC/SOD1<sup>G93A</sup> muscles we assayed the expression of Myosin Slow type I levels, and we observed a slight increase of Myosin Slow type I in the transgenic muscles compared to the Wt ones (**Figure 1B** and Supplementary Figure S1).

Recent evidences have demonstrated that the nuclear receptors PPAR $\beta/\delta$  and PPAR $\alpha$  play opposing roles upon the type I fiber specification program, regulating the expression of two non-coding RNA, MiR-208b, and MiR-499, both activating a signaling cascade for the expression of muscle slow twitch contractile proteins (van Rooij et al., 2009). In particular, it has been demonstrated that genetic ablation of PPAR $\alpha$  or the up-regulation of PPAR $\beta/\delta$  mediated by PGC-1 $\alpha$ , lead to significant accumulation of MiR-208b and MiR-499 and specify for a slow muscle fiber program (Gan et al., 2013).

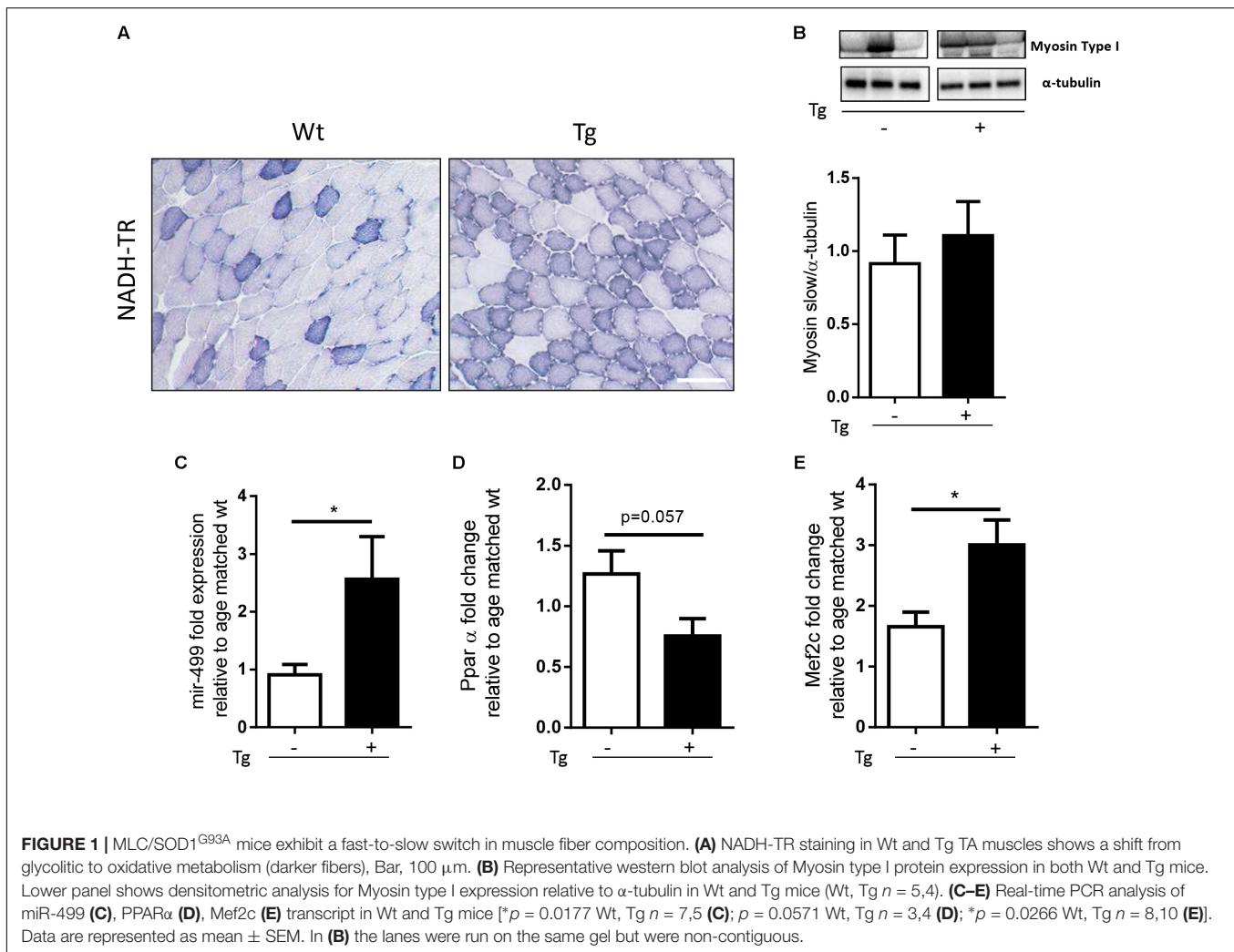
We analyzed the expression level of PPAR $\alpha$  and MiR-499 in both Wt and MLC/SOD1<sup>G93A</sup> (Tg) TA muscles and we observed a significant down-modulation of PPAR $\alpha$  expression levels and a concomitant up-regulation of MiR-499 (**Figures 1C,D**) in MLC/SOD1<sup>G93A</sup> mice compared to Wt littermates, suggesting that muscle specific expression of SOD1 mutant gene triggers a slow-oxidative program mediated by a PGC1 $\alpha$ /PPAR dependent regulatory circuit.

A key regulator of PGC-1 $\alpha$  expression is Mef2c, a transcriptional factor that is responsible for fast-to-slow switch of muscle fibers (Czubryt et al., 2003). We revealed a significant increased expression of Mef2C transcript in the muscle of MLC/SOD1<sup>G93A</sup> mice compared to that of the Wt littermates (**Figure 1E**), confirming the evidences of a metabolic transition of muscle fibers from glycolytic toward more oxidative type.

Overall these data indicate that perturbation in redox signaling cascades, induced by muscle specific expression of SOD1<sup>G93A</sup>, promoted a muscle metabolic adaptation in line with what observed in the skeletal muscle of SOD1<sup>G93A</sup> mice that ubiquitously express the mutant SOD1 gene (Palamiuc et al., 2015).

### Muscle Glucose Metabolism Is Altered in the MLC/SOD1<sup>G93A</sup> Mice

Glycolysis is a metabolic pathway that converts glucose into pyruvate, providing high energy substrate. Glycolysis is



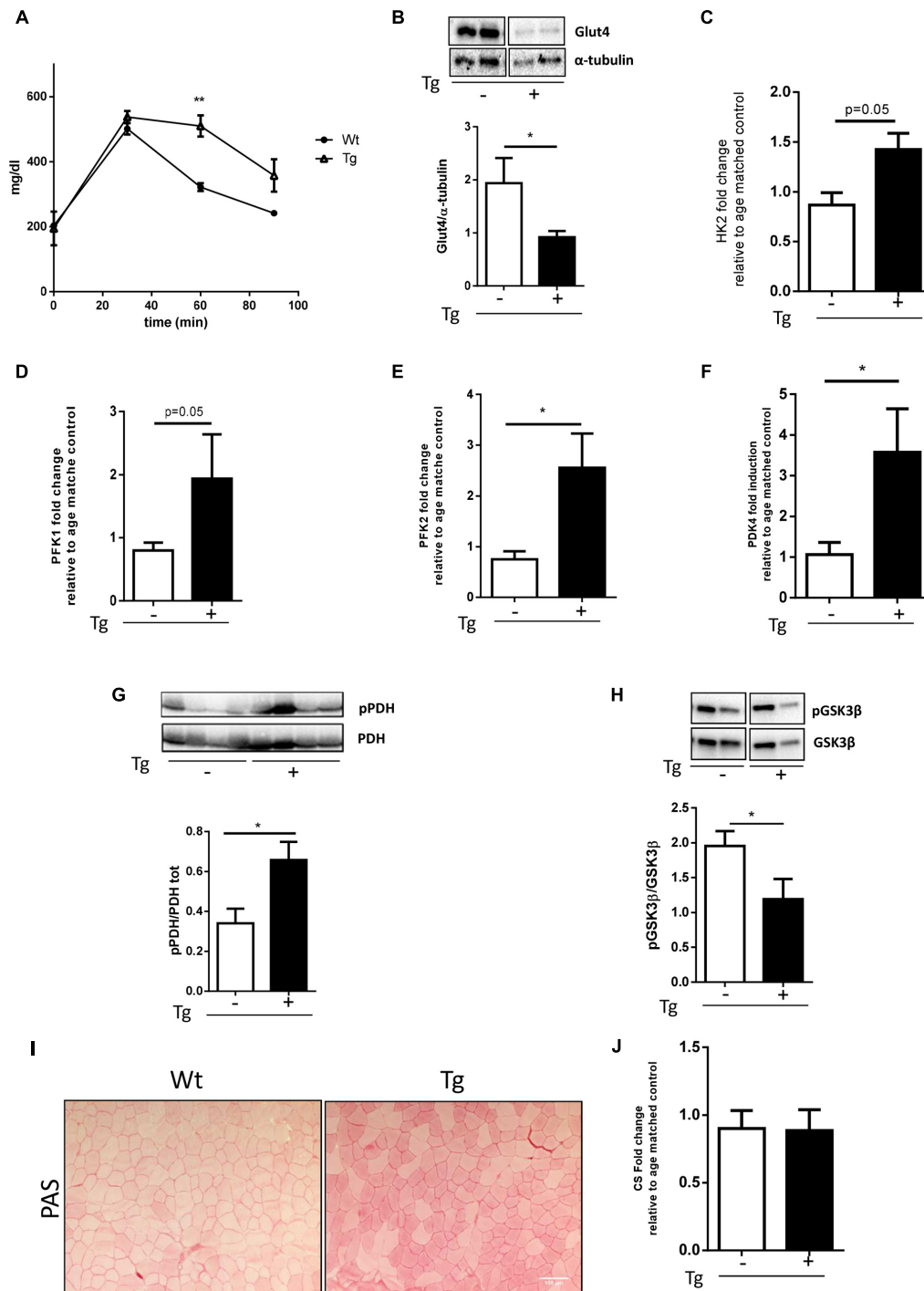
dysregulated in the animal model of ALS, the SOD1<sup>G93A</sup> mice that ubiquitously overexpress the mutant form of the SOD1 gene (Palamiuc et al., 2015). To verify whether glucose metabolism was also altered in the MLC/SOD1<sup>G93A</sup> mice, we performed the glucose tolerance test, demonstrating that transgenic mice, compared with Wt littermates, presented higher blood glucose 60 min after glucose supplementation (**Figure 2A**). This suggests that muscle specific expression of SOD1<sup>G93A</sup> determines a delay in glucose clearance. To substantiate this hypothesis, we analyzed the expression levels of Glut-4, a glucose receptor in muscle fibers, responsible for muscle glucose uptake. As shown in **Figure 2** protein levels of Glut4 was significantly down-modulated in the MLC/SOD1<sup>G93A</sup> muscles (**Figure 2B** and Supplementary Figure S2), suggesting that the clearance delay of glucose could mainly be due to a decreased capacity of transgenic muscle to uptake glucose from circulation.

Glycolysis is regulated by several enzymes such as the Hexokinase 2 (HK2) and Phosphofruktokinase 1/2, (PFK1, PFK2) that catalyze, respectively, the first and the second steps of glycolysis. In the asymptomatic animal model of ALS, the PFK

activity is significantly down-modulated and muscle glucose metabolism is inhibited (Palamiuc et al., 2015).

To verify whether glycolysis was also altered in the MLC/SOD1<sup>G93A</sup> mice, we analyzed the transcription levels of the Hexokinase 2 (HK2) and Phosphofruktokinase 1/2, (PFK1, PFK2) in TA muscles of transgenic mice. As shown in **Figure 2**, differently from that observed in ALS mouse model (Shi et al., 2010), the glycolytic enzyme was significantly up-regulated in the muscle of MLC/SOD1<sup>G93A</sup> mice compared to the Wt littermates (**Figures 2C–E**).

Pyruvate is the end product of Glycolysis and its levels are governed by the PDH that transforms Pyruvate into Acetyl-CoA. Acetyl-CoA enters the Krebs cycle and produces ATP and energy fuel for cells through oxidative phosphorylation. The Pyruvate kinase 4 (PDK4) is a negative regulator of PDH complex and inhibits PDH activity by phosphorylation (Denton et al., 1975). To investigate whether Pyruvate is efficiently converted into Acetyl-CoA we assessed the level of total and the phosphorylated isoform of PDH and the levels of PDK4. Interestingly we observed a significant accumulation of the phosphorylated isoform of PDH and a



**FIGURE 2** | Muscle glucose metabolism is altered in MLC/SOD1<sup>G93A</sup> mice. **(A)** Analysis of blood glucose levels in Wt and Tg mice for 120 min (\*\* $p < 0.01$  Wt, Tg  $n = 3,3$ ; Two-way ANOVA test Time  $p < 0.0001$ , Interaction  $p = 0.0003$ ). **(B)** Representative western blot analysis of Glut4 protein expression in both Wt and Tg mice. Lower panel shows densitometric analysis for Glut4 expression relative to  $\alpha$ -tubulin in Wt and Tg mice ( $t$ -test \* $p = 0.0285$  Wt, Tg  $n = 9,12$ ); **(C–F)** Real-time PCR analysis of HK2 **(C)**, PFK1 **(D)**, PFK2 **(E)**, PDK4 **(F)** transcripts in Wt and Tg mice [ $t$ -test  $p = 0.0532$  Wt, Tg  $n = 3,3$  **(C)**;  $p = 0.0571$  Wt, Tg  $n = 4,3$  **(D)**; \* $p = 0.0244$  Wt, Tg  $n = 9,9$  **(E)**; \* $p = 0.0482$  Wt, Tg  $n = 9,11$  **(F)**]; **(G)** Representative western blot analysis of pPDH/PDH protein expression in both Wt and Tg mice. Lower panel shows densitometric analysis for pPDH expression relative to PDH in Wt and Tg mice ( $t$ -test \* $p = 0.0261$  Wt, Tg  $n = 5,5$ ); **(H)** Representative western blot analysis of pGSK3 $\beta$  and GSK3 $\beta$  protein expression in both Wt and Tg mice. Lower panel shows densitometric analysis for pGSK3 $\beta$  expression relative to total GSK3 $\beta$  content normalized for protein loading in Wt and Tg mice ( $t$ -test \* $p = 0.0476$  Wt, Tg  $n = 10,10$ ); **(I)** representative microphotographs of PAS staining from Wt and Tg TA muscles. Bar, 100  $\mu$ m. **(J)** Real-time PCR analysis of CS (Wt, Tg  $n = 4,4$ ). Data are represented as mean  $\pm$  SEM. In **(B,G,H)** the lanes were run on the same gel but were noncontiguous.

concomitant up-regulation of PDK4, indicating the inhibition of Acetyl-CoA synthesis (Figures 2E,G and Supplementary Figure S3). Moreover, as pyruvate accumulation stimulates the conversion of glucose to glycogen, we assessed the glycogen synthesis in the MLC/SOD1<sup>G93A</sup> muscles. We observed a significant down-modulation of the inhibitory phosphorylated isoform of the Glycogen Synthase Kinase 3 $\beta$  (GSK3 $\beta$ ) and a concomitant increase in intramuscular glycogen deposition, assayed by Periodic acid-Schiff (PAS) staining, in the TA muscle of MLC/SOD1<sup>G93A</sup> mice compared to that of Wt littermates (Figures 2H,I and Supplementary Figure S4). Conversely, the mRNA level of Citrate Synthase (CS), the first enzyme of Krebs cycle, was comparable between Wt and MLC/SOD1<sup>G93A</sup> muscles (Figure 2J), suggesting that alternative catabolic pathway, such as proteolysis or lipolysis, can guarantee sufficient Acetyl-CoA synthesis.

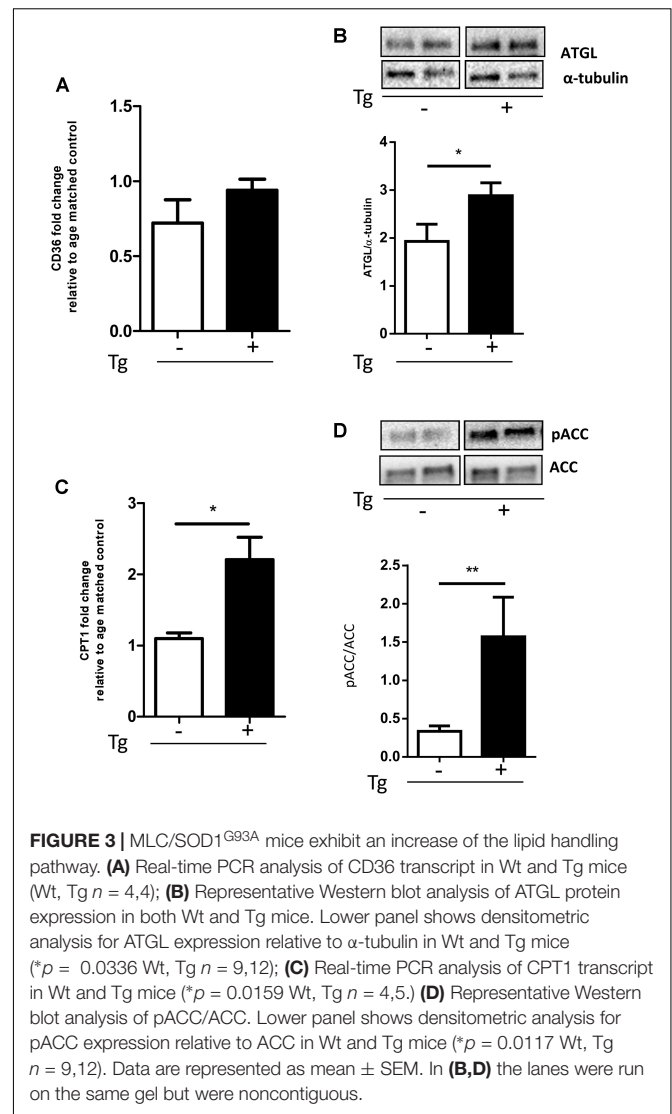
Overall these data suggest that muscle restricted expression of SOD1 mutant gene triggers the activation of the glycolysis process, which cannot efficiently contribute to oxidative phosphorylation and energy production.

### MLC/SOD1<sup>G93A</sup> Transgene Is Associated With the Increase of the Lipid Handling Pathway

Various factors, including increased fatty acid (FA) use by  $\beta$ -oxidation, stimulate PDK4 expression (Jeong et al., 2012). The  $\beta$ -oxidation process is strictly regulated by the levels of its inhibitor MalonylCoA that is in turn induced by the Acetyl-CoA carboxylase (ACC). Acetyl-CoA carboxylase strongly controls lipid synthesis/degradation flux, and its activity is inhibited by phosphorylation.

To investigate muscle fibers oxidative metabolism, we studied the expression levels of key proteins of the FA regulation: CD36, a membrane translocase that promotes FA entry into the cells, ATGL, a lipase involved in lipid droplet degradation, and CPT-1B, responsible for the FA transfer into mitochondria. When compared to Wt littermates, the MLC/SOD1<sup>G93A</sup> mice had a significant increase in the expression of all genes studied (Figures 3A–C and Supplementary Figure S5), including the pACC/ACC ratio (Figure 3D and Supplementary Figure S6), suggesting that lipid catabolism is stimulated and lipid synthesis is inhibited.

Qualitative analysis on lipid droplet accumulation inside muscle fibers confirmed a preferential use of lipid of the transgenic muscle. As described in Figure 4 no droplets were found inside muscle fibers; we observed a significant accumulation of fat residues just outside muscle fibers (Figure 4A). Quantitative analysis revealed a significant up-regulation of lipid droplet volume in the MLC/SOD1<sup>G93A</sup> muscle compared to Wt littermates (Figure 4B). This data was further supported by western blot analysis for Perilipin 2 (PLIN2) expression, a coat protein of lipid droplet. As shown in Figure 4C we observed a significant up-regulation of Perilipin-2 in MLC/SOD1<sup>G93A</sup> muscles compared to Wt ones (Figure 4C and Supplementary Figure S7).



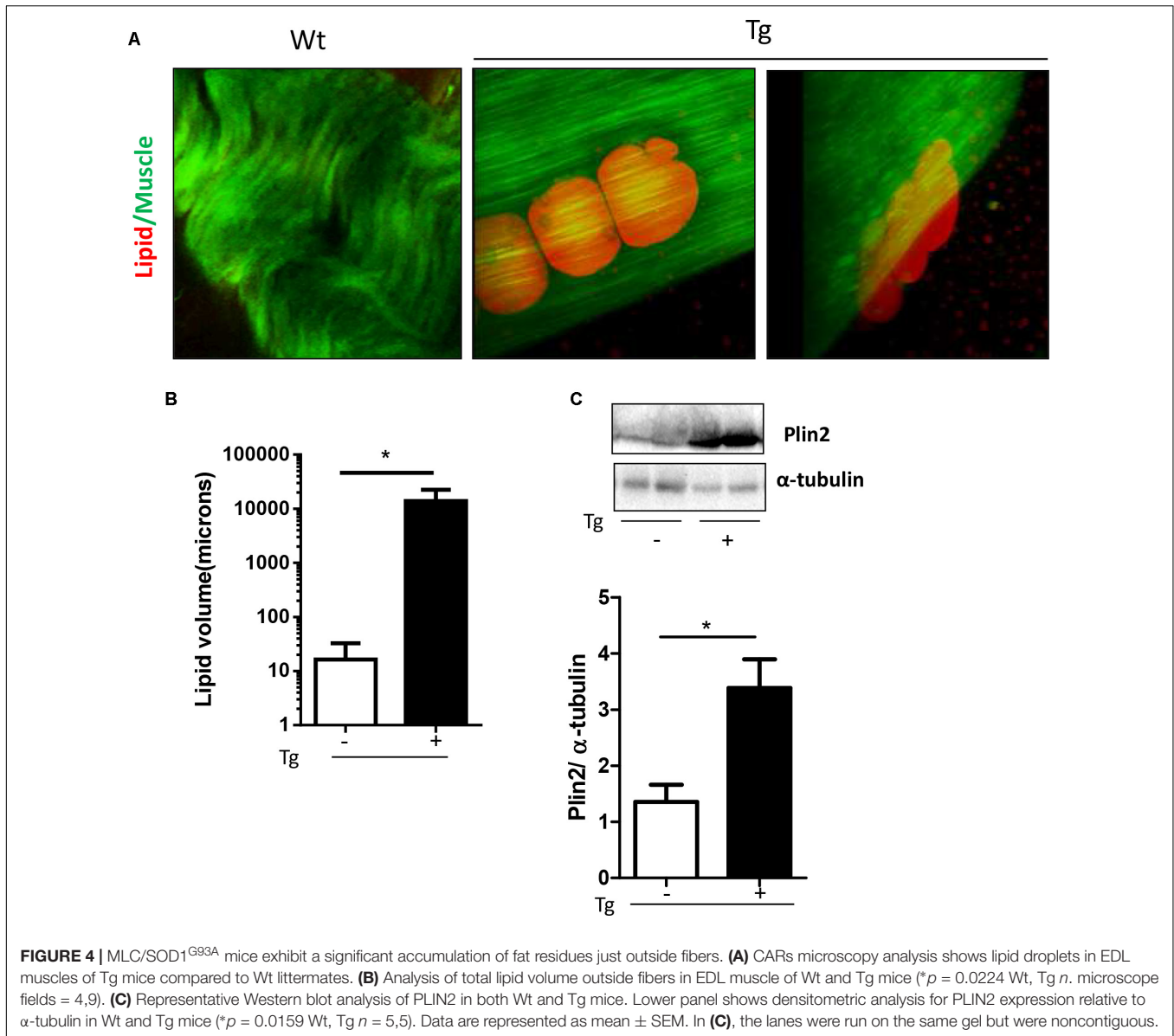
**FIGURE 3 |** MLC/SOD1<sup>G93A</sup> mice exhibit an increase of the lipid handling pathway. (A) Real-time PCR analysis of CD36 transcript in Wt and Tg mice (Wt, Tg  $n = 4,4$ ); (B) Representative Western blot analysis of ATGL protein expression in both Wt and Tg mice. Lower panel shows densitometric analysis for ATGL expression relative to  $\alpha$ -tubulin in Wt and Tg mice ( $*p = 0.0336$  Wt, Tg  $n = 9,12$ ); (C) Real-time PCR analysis of CPT1 transcript in Wt and Tg mice ( $*p = 0.0159$  Wt, Tg  $n = 4,5$ ). (D) Representative Western blot analysis of pACC/ACC. Lower panel shows densitometric analysis for pACC expression relative to ACC in Wt and Tg mice ( $*p = 0.0117$  Wt, Tg  $n = 9,12$ ). Data are represented as mean  $\pm$  SEM. In (B,D) the lanes were run on the same gel but were noncontiguous.

These data suggest that muscle specific expression of mutant SOD1 induces a preferential recruitment of FAs to skeletal muscle tissue to sustain lipid flux into the skeletal muscle fibers and to guarantee FAs muscle availability and  $\beta$ -oxidation (Morales et al., 2017).

## DISCUSSION

Our study demonstrates that perturbation in redox signaling cascades, induced by muscle specific expression of SOD1<sup>G93A</sup>, determines a muscle metabolic adaptation towards a more oxidative metabolism, demonstrating the activation of the slow-oxidative muscle fiber program and the preferential use of lipid fuel by the transgenic mice MLC/SOD1<sup>G93A</sup>.

Interestingly, we observed that muscle metabolic adaptation to oxidative stress does not involve significant changes in MyHC expression, in line with previous published works that have suggested a dissociation between metabolic and contractile



adaptive response to different stimuli (Schiaffino and Reggiani, 2011). Indeed, it has been demonstrated that moderate endurance training can induce metabolic changes without concomitant changes in MyHC composition. Moreover, slow-type electrical stimulation in rat fast muscles can early abrupt MyHC-2B to MyHC-2X transcript switch (Kirschbaum et al., 1990), in response to external stimuli of muscle activity or inactivity (Ausoni et al., 1990).

Our data support the evidences that metabolic and contractile properties are controlled by distinct signaling pathways and provide insight into the mechanism controlling the regulation of fast-glycolytic and slow-oxidative gene program, induced by muscle specific expression of SOD1<sup>G93A</sup>. In particular, among the possible mechanisms that account for the modulation of different fast and slow muscle genes, our data support the involvement of miRNAs hosted in *β/slow* and *slow-tonic* Myosin locus.

Recent works have demonstrated that some muscle-specific microRNAs are located within Myosin genes and thus are co-expressed with these genes (van Rooij et al., 2009). Among these microRNAs, miR-499 is located in an intron of Myh7b and targets a transcriptional repressor of *β/slow* Myosin, namely Sox6, during muscle development (van Rooij et al., 2008). Nevertheless, it remains to elucidate whether muscle-specific miRNAs and Sox6, controls of fiber type diversification in developing muscle, is also involved in the maintenance of fiber type properties in adult skeletal muscle (van Rooij et al., 2009; Gan et al., 2013). Here we provide evidences that the oxidative insult induced by SOD1 mutant gene expression can determine the modulation of miR-499 regulative circuit toward a slow muscle fiber program, in muscle tissue of adult mice.

The shift of muscle fibers, observed in MLC/SOD1<sup>G93A</sup> mice, toward the oxidative metabolism might represent a

compensatory mechanism activated to cope the toxic effects of mutant SOD1 protein.

In the SOD1<sup>G93A</sup> mice, which ubiquitously express the mutant gene (Gurney et al., 1994), the switch toward lipid use is considered an early sign of disease and occur early before symptomatic denervation (Palamiuc et al., 2015). It has been suggested that the early switch of glycolytic fibers toward oxidative phenotype is due to loss of connections of muscle fibers to large motoneurons, and to their subsequent reinnervation by slow motoneurons. Thus, these studies suggest that the oxidative switch of muscle fibers is a consequence of motor unit alteration, rather than an intrinsic property of muscle fibers plasticity that can change the metabolic properties independently from neuron physiology.

Here, we demonstrate that in the MLC/SOD1<sup>G93A</sup> fibers, the metabolic oxidative switch occurs independently from motor neuron degeneration (Dobrowolny et al., 2018) and along with neuromuscular instability and deficiency in mitochondrial chain function (Dobrowolny et al., 2018). Considering the mitochondria defects and the oxidative damage induced by muscle specific SOD1 mutant gene expression (Dobrowolny et al., 2008, 2018), we can speculate that the oxidative change in energy fuel of MLC/SOD1<sup>G93A</sup> fibers might reflect an adaptation to preserve muscle functionality (Blaauw et al., 2013). In addition, fiber type diversification may also reflect an adaptation to whole body metabolism and different pattern of activity. These observations are also in line of recent evidences that demonstrated how the up-regulation of Mir-499 and Mir-208b is associated with a reduced atrophy of type I fibers in muscle biopsies of ALS patients with slow progressive disease (Di Pietro et al., 2017).

The metabolic shift towards lipid use in the TA muscles in the ALS mouse model that ubiquitously express the SOD1 mutant gene (Gurney et al., 1994) is accompanied by lower levels of PFK activity in both presymptomatic and symptomatic stages of the disease (Palamiuc et al., 2015). These data are in apparent contrast with the up-regulation of both PFK1 and PFK2 observed in the MLC/SOD1<sup>G93A</sup> mice. In the ALS mouse model at the presymptomatic stage of the disease, higher levels of Pyruvates correlate with a decrease of PFK activity; conversely at the end stage of the disease low levels of Pyruvate correlates with low levels of PFK activity, due to the inhibitory feed-back of Pyruvate. Therefore, although the glycolysis is enhanced in the MLC/SOD1<sup>G93A</sup> mice, Pyruvate levels could

be still not sufficient to induce a Pyruvate dependent inhibitory signal of glucose catabolism. Moreover, Pyruvate can be used in other compensative pathways that do not involve mitochondria machinery, such as glycogen synthesis or anaerobic glycolysis.

In conclusion, our data reveal that localized expression of SOD1<sup>G93A</sup> induces metabolic changes in skeletal muscle independently of motor neuron degeneration and further indicate that skeletal muscle is likely an important target for therapeutic intervention in ALS.

## ETHICS STATEMENT

The experimental protocol was approved by the Ethical Committee (OPBA) of the Sapienza University of Rome and by the Italian Ministry of Health, Italy (26/2014, authorization number 609/2015-PR).

## AUTHOR CONTRIBUTIONS

AM conceptualized the study, contributed the resources, supervised the project, and did the project administration. GD, EL, MM, LB, AN, and BMS contributed to the methodology. GD, EL, MM, BMS, and AM contributed to the validation. GD, EL, MM, LB, BMS, and AM carried out the formal analysis and curated the data. GD, EL, LB, MM, and BMS contributed to the investigation. AM and GD wrote the original draft, the review, and edited the manuscript. GD, EL, LB, MM, BMS, and AM contributed to the observation. AM and BMS acquired the funding.

## FUNDING

This study was supported by Fondazione Roma, Telethon (GGP14066), ASI, progetti ateneo to AM; and Progetto di ricerca d'interesse di Ateneo-Università Cattolica (D3.2-2015) to BMS.

## SUPPLEMENTARY MATERIAL

The Supplementary Material for this article can be found online at: <https://www.frontiersin.org/articles/10.3389/fphys.2018.00831/full#supplementary-material>

## REFERENCES

- Ausoni, S., Gorza, L., Schiaffino, S., Gundersen, K., Lomo, T. (1990). Expression of myosin heavy chain isoforms in stimulated fast and slow rat muscles. *J. Neurosci.* 10, 153–160. doi: 10.1523/JNEUROSCI.10-01-00153.1990
- Blaauw, B., Schiaffino, S., Reggiani, C. (2013). Mechanisms modulating skeletal muscle phenotype. *Compr. Physiol.* 3, 1645–1687. doi: 10.1002/cphy.c130009
- Bouteloup, C., Desport, J. C., Clavelou, P., Guy, N., Derumeaux-Burel, H., Ferrier, A., et al. (2009). Hypermetabolism in ALS patients: an early and persistent phenomenon. *J. Neurol.* 256, 1236–1242. doi: 10.1007/s00415-009-5100-z
- Carri, M. T., and Cozzolino, M. (2011). SOD1 and mitochondria in ALS: a dangerous liaison. *J. Bioenerg. Biomembr.* 43, 593–599. doi: 10.1007/s10863-011-9394-z
- Czubryt, M. P., McAnally, J., Fishman, G. I., and Olson, E. N. (2003). Regulation of peroxisome proliferator-activated receptor gamma coactivator 1 alpha (PGC-1 alpha) and mitochondrial function by MEF2 and HDAC5. *Proc. Natl. Acad. Sci. U.S.A.* 100, 1711–1716. doi: 10.1073/pnas.0337639100
- Denton, R. M., Randle, P. J., Bridges, B. J., Cooper, R. H., Kerbey, A. L., Pask, H. T., et al. (1975). Regulation of mammalian pyruvate dehydrogenase. *Mol. Cell. Biochem.* 9, 27–53. doi: 10.1007/BF01731731
- Desport, J. C., Tornoy, F., Lacoste, M., Preux, P. M., and Couratier, P. (2005). Hypermetabolism in ALS: correlations with clinical and paraclinical parameters. *Neurodegener. Dis.* 2, 202–207. doi: 10.1159/000089626
- Di Pietro, L., Baranzini, M., Berardinelli, M. G., Lattanzi, W., Monforte, M., Tasca, G., et al. (2017). Potential therapeutic targets for ALS: MIR206, MIR208b and MIR499 are modulated during disease progression in the skeletal muscle of patients. *Sci. Rep.* 7:9538. doi: 10.1038/s41598-017-10161-z

- Dobrowolny, G., Aucello, M., Rizzuto, E., Beccafico, S., Mammucari, C., Boncompagni, S., et al. (2008). Skeletal muscle is a primary target of SOD1G93A-mediated toxicity. *Cell Metab.* 8, 425–436. doi: 10.1016/j.cmet.2008.09.002
- Dobrowolny, G., Martini, M., Scicchitano, B. M., Romanello, V., Boncompagni, S., Nicoletti, C., et al. (2018). Muscle expression of SOD1(G93A) triggers the dismantlement of neuromuscular junction via PKC-theta. *Antioxid. Redox Signal.* 28, 1105–1119. doi: 10.1089/ars.2017.705
- Dupuis, L., Corcia, P., Fergani, A., Gonzalez De Aguilar, J. L., Bonnefont-Rousselot, D., Bittar, R., et al. (2008). Dyslipidemia is a protective factor in amyotrophic lateral sclerosis. *Neurology* 70, 1004–1009. doi: 10.1212/01.wnl.0000285080.70324.27
- Dupuis, L., Oudart, H., Rene, F., Gonzalez De Aguilar, J. L., Loeffler, J. P. (2004). Evidence for defective energy homeostasis in amyotrophic lateral sclerosis: benefit of a high-energy diet in a transgenic mouse model. *Proc. Natl. Acad. Sci. U.S.A.* 101, 11159–11164. doi: 10.1073/pnas.0402026101
- Funalot, B., Desport, J. C., Sturtz, F., Camu, W., and Couratier, P. (2009). High metabolic level in patients with familial amyotrophic lateral sclerosis. *Amyotroph. Lateral Scler.* 10, 113–117. doi: 10.1080/17482960802295192
- Gallo, V., Wark, P. A., Jenab, M., Pearce, N., Brayne, C., Vermeulen, R., et al. (2013). Prediagnostic body fat and risk of death from amyotrophic lateral sclerosis: the EPIC cohort. *Neurology* 80, 829–838. doi: 10.1212/WNL.0b013e3182840689
- Gan, Z., Rumsey, J., Hazen, B. C., Lai, L., Leone, T. C., Vega, R. B. et al. (2013). Nuclear receptor/microRNA circuitry links muscle fiber type to energy metabolism. *J. Clin. Invest.* 123, 2564–2575. doi: 10.1172/JCI67652
- Gurney, M. E., Pu, H., Chiu, A. Y., Dal Canto, M. C., Polchow, C. Y., Alexander, D. D., et al. (1994). Motor neuron degeneration in mice that express a human Cu,Zn superoxide dismutase mutation. *Science* 264, 1772–1775. doi: 10.1056/NEJM19941223312516
- Huisman, M. H., Seelen, M., van Doormaal, P. T, de Jong, S. W., de Vries, J. H., van der Kooij, A. J., et al. (2015). Effect of presymptomatic body mass index and consumption of fat and alcohol on amyotrophic lateral sclerosis. *JAMA Neurol.* 72, 1155–1162. doi: 10.1001/jamaneurol.2015.1584
- Jeong, J. Y., Jeoung, N. H., Park, K. G., Lee, I. K. (2012). Transcriptional regulation of pyruvate dehydrogenase kinase. *Diabetes Metab. J.* 36, 328–335. doi: 10.4093/dmj.2012.36.5.328
- Kasarskis, E. J., Berryman, S., Vanderleest, J. G., Schneider, A. R., and McClain, C. J. (1996). Nutritional status of patients with amyotrophic lateral sclerosis: relation to the proximity of death. *Am. J. Clin. Nutr.* 63, 130–137. doi: 10.1093/ajcn/63.1.130
- Kirschbaum, B. J., Schneider, S., Izumo, S., Mahdavi, V., Nadal-Ginard, B., Pette, D. (1990). Rapid and reversible changes in myosin heavy chain expression in response to increased neuromuscular activity of rat fast-twitch muscle. *FEBS Lett.* 268, 75–78. doi: 10.1016/0014-5793(90)80976-P
- Livak, K. J., and Schmittgen, T. D. (2001). Analysis of relative gene expression data using real-time quantitative PCR and the  $2^{-\Delta\Delta C_T}$  method. *Methods* 25, 402–408. doi: 10.1006/meth.2001.1262
- Morales, P. E., Bucarey, J. L., and Espinosa, A. (2017). Muscle lipid metabolism: role of lipid droplets and perilipins. *J. Diabetes Res.* 2017:1789395. doi: 10.1155/2017/1789395
- Nunn, A. D., Scopigno, T., Pediconi, N., Levrero, M., Hagman, H., Kiskis, J., et al. (2016). The histone deacetylase inhibiting drug Entinostat induces lipid accumulation in differentiated HepaRG cells. *Sci. Rep.* 6:28025. doi: 10.1038/srep28025
- O'Reilly, E. J., Wang, H., Weisskopf, M. G., Fitzgerald, K. C., Falcone, G., McCullough, M. L., et al. (2013). Premorbid body mass index and risk of amyotrophic lateral sclerosis. *Amyotroph. Lateral Scler. Frontotemporal Degener.* 14, 205–211. doi: 10.3109/21678421.2012.735240
- Palamiuc, L., Schlagowski, A., Ngo, S. T., Vernay, A., Dirrig-Grosch, S., Henriques, A., et al. (2015). A metabolic switch toward lipid use in glycolytic muscle is an early pathologic event in a mouse model of amyotrophic lateral sclerosis. *EMBO Mol. Med.* 7, 526–546. doi: 10.15252/emmm.201404433
- Peggon, C., Massimino, M. L., Biancotto, G., Angeletti, R., Reggiani, C., Sorgato, M. C., et al. (2017). Absolute quantification of myosin heavy chain isoforms by selected reaction monitoring can underscore skeletal muscle changes in a mouse model of amyotrophic lateral sclerosis. *Anal. Bioanal. Chem.* 409, 2143–2153. doi: 10.1007/s00216-016-0160-2
- Peter, R. S., Rosenbohm, A., Dupuis, L., Brehme, T., Kassubek, J., Rothenbacher, D., et al. (2017). Life course body mass index and risk and prognosis of amyotrophic lateral sclerosis: results from the ALS registry Swabia. *Eur. J. Epidemiol.* 32, 901–908. doi: 10.1007/s10654-017-0318-z
- Schiaffino, S., and Reggiani, C. (2011). Fiber types in mammalian skeletal muscles. *Physiol. Rev.* 91, 1447–1531. doi: 10.1152/physrev.00031.2010
- Shi, P., Gal, J., Kwinter, D. M., Liu, X., and Zhu, H. (2010). Mitochondrial dysfunction in amyotrophic lateral sclerosis. *Biochim. Biophys. Acta* 1802, 45–51. doi: 10.1016/j.bbadis.2009.08.012
- St. Pierre, J., Drori, S., Uldry, M., Silvaggi, J. M., Rhee, J., Jager, S., et al. (2006). Suppression of reactive oxygen species and neurodegeneration by the PGC-1 transcriptional coactivators. *Cell* 127, 397–408. doi: 10.1016/j.cell.2006.09.024
- van Rooij, E., Liu, N., Olson, E. N. (2008). MicroRNAs flex their muscles. *Trends Genet.* 24, 159–166. doi: 10.1016/j.tig.2008.01.007
- van Rooij, E., Quiat, D., Johnson, B. A., Sutherland, L. B., Qi, X., Richardson, J. A., et al. (2009). A family of microRNAs encoded by myosin genes governs myosin expression and muscle performance. *Dev. Cell* 17, 662–673. doi: 10.1016/j.devcel.2009.10.013
- Wijesekera, L. C., and Leigh, P. N. (2009). Amyotrophic lateral sclerosis. *Orphanet J. Rare Dis.* 4:3. doi: 10.1186/1750-1172-4-3

**Conflict of Interest Statement:** The authors declare that the research was conducted in the absence of any commercial or financial relationships that could be construed as a potential conflict of interest.

Copyright © 2018 Dobrowolny, Lepore, Martini, Barberi, Nunn, Scicchitano and Musarò. This is an open-access article distributed under the terms of the Creative Commons Attribution License (CC BY). The use, distribution or reproduction in other forums is permitted, provided the original author(s) and the copyright owner(s) are credited and that the original publication in this journal is cited, in accordance with accepted academic practice. No use, distribution or reproduction is permitted which does not comply with these terms.



# Cellular Mechanotransduction: From Tension to Function

Fabiana Martino<sup>1,2,3</sup>, Ana R. Perestrelo<sup>1</sup>, Vladimír Vinarský<sup>1,3</sup>, Stefania Pagliari<sup>1</sup> and Giancarlo Forte<sup>1,3,4\*</sup>

<sup>1</sup> Center for Translational Medicine, International Clinical Research Center, St. Anne's University Hospital, Brno, Czechia, <sup>2</sup> Department of Biology, Faculty of Medicine, Masaryk University, Brno, Czechia, <sup>3</sup> Competence Center for Mechanobiology in Regenerative Medicine, INTERREG ATCZ133, Brno, Czechia, <sup>4</sup> Department of Biomaterials Science, Institute of Dentistry, University of Turku, Turku, Finland

## OPEN ACCESS

### Edited by:

Leonardo Alexandre Peyré-Tartaruga,  
Universidade Federal do Rio Grande  
do Sul (UFRGS), Brazil

### Reviewed by:

Tetsuya S. Tanaka,  
Elixirgen, LLC, United States  
Luis A. Martinez-Lemus,  
University of Missouri, United States  
Maurizio Ventre,  
Università degli Studi di Napoli  
Federico II, Italy

### \*Correspondence:

Giancarlo Forte  
giancarlo.forte@fnusa.cz

### Specialty section:

This article was submitted to  
Integrative Physiology,  
a section of the journal  
Frontiers in Physiology

**Received:** 25 March 2018

**Accepted:** 12 June 2018

**Published:** 05 July 2018

### Citation:

Martino F, Perestrelo AR, Vinarský V, Pagliari S and Forte G (2018) Cellular Mechanotransduction: From Tension to Function. *Front. Physiol.* 9:824. doi: 10.3389/fphys.2018.00824

Living cells are constantly exposed to mechanical stimuli arising from the surrounding extracellular matrix (ECM) or from neighboring cells. The intracellular molecular processes through which such physical cues are transformed into a biological response are collectively dubbed as mechanotransduction and are of fundamental importance to help the cell timely adapt to the continuous dynamic modifications of the microenvironment. Local changes in ECM composition and mechanics are driven by a feed forward interplay between the cell and the matrix itself, with the first depositing ECM proteins that in turn will impact on the surrounding cells. As such, these changes occur regularly during tissue development and are a hallmark of the pathologies of aging. Only lately, though, the importance of mechanical cues in controlling cell function (e.g., proliferation, differentiation, migration) has been acknowledged. Here we provide a critical review of the recent insights into the molecular basis of cellular mechanotransduction, by analyzing how mechanical stimuli get transformed into a given biological response through the activation of a peculiar genetic program. Specifically, by recapitulating the processes involved in the interpretation of ECM remodeling by Focal Adhesions at cell-matrix interphase, we revise the role of cytoskeleton tension as the second messenger of the mechanotransduction process and the action of mechano-responsive shuttling proteins converging on stage and cell-specific transcription factors. Finally, we give few paradigmatic examples highlighting the emerging role of malfunctions in cell mechanosensing apparatus in the onset and progression of pathologies.

**Keywords:** mechanotransduction, nucleoskeleton, focal adhesion, mechanobiology, mechanosensor

## INTRODUCTION

The correct regulation of cell function *in vivo* requires the integration of numerous biological and mechanical signals arising from the surrounding cells and the extracellular matrix (ECM).

The nanostructure and the composition of the ECM is strictly controlled in a tissue-specific fashion during development and in adulthood in order to favor cell and organ function (Smith et al., 2017). Changes in ECM composition and mechanics are encountered during the progression of all degenerative diseases as the result of aging or as a compensatory attempt of the tissue to preserve its function (Kim et al., 2000; Parker et al., 2014; Klaas et al., 2016). Changes in ECM compliance are now considered of prognostic value for solid tumors (Calvo et al., 2013; Hayashi and Iwata, 2015; Reid et al., 2017).



## Glossary

Extracellular Matrix (ECM)	Network and reservoir of extracellular and signaling molecules which are secreted locally to ensure cell and tissue cohesion
Focal adhesions (FAs)	Integrin-based cell-matrix physical contacts that transduce and integrate mechanical and biochemical cues from the environment through the recruitment of intracellular multiprotein assemblies connected to actin cytoskeleton
Mechanosensing	The ability of a cell to sense mechanical cues of its micro-environment, including not only all components of force, stress and strain but also substrate rigidity, topography and adhesiveness.
Mechanotransduction	Molecular process transforming a physical stimulus in a biological response
Mechanotransducers	Individual or protein complexes that produce or enable a chemical signal in response to a mechanical stimulus
Mechanical instability	Is the result of substrate mechanical oscillations at cell-ECM interface, that induces internal cellular and molecular rearrangements, in order to recover to an equilibrium state
Tension	Pulling force transmitted axially by means of an object
Tensional homeostasis	A basal equilibrium stress state in which cells counteract external force application by moving toward a previous force setpoint that had been established before external force application
Stiffness	Resistance of an elastic body to deflection or deformation by an applied force
Stress fibers (SFs)	Bundles of F-actin and myosin II held together by cross-linking proteins ensuring the cytoskeletal contractility

The best example of how pathology-driven changes in ECM mechanics and architecture impact on tissue and organ function is cardiac remodeling. Following a cardiovascular event (ischemic insult, long term exposure to pressure or volume overload), cardiac matrix is degraded and substituted by a scar, having a different nanostructure and compliance (Spinale, 2007). The structural changes occurring within the myocardial ECM affect cardiomyocyte function (Engler et al., 2008), thus compromising the overall structure and function of the whole myocardium.

Similar effects of altered ECM mechanics on the function of different cell types have been recently demonstrated (Engler et al., 2006; Natarajan et al., 2015; Zarkoob et al., 2015).

The concept that cells can interpret and respond to mechanical cues is not exactly new to the scientific community. Nonetheless, only lately, the elucidation of the molecular mechanisms by which the cell perceives and transforms the mechanics of the ECM has become the subject of intense investigation and a number of intracellular molecules has been identified that can react to mechanical stimulation and - in turn - modify cell function.

So far, the definition of cellular mechanosensor has been applied to a number of molecules - mainly proteins - displaying a status change in response to mechanical stimulation. The nature and the degree of the change imposed by mechanical cues can vary significantly and post-translational modifications (Sawada et al., 2006; Dong et al., 2009; Hayakawa et al., 2011; Swift et al., 2013; Guilluy et al., 2014; Qin et al., 2015; Sathe et al., 2016; Lachowski et al., 2018), intracellular shuttling (Gumbiner, 1995; Gottardi et al., 1996; Huber et al., 1996; Lewis et al., 1996; Orsulic and Peifer, 1996; Nix and Beckerle, 1997; Dupont et al., 2011), protein unfolding (del Rio et al., 2009), the creation of novel interactions (Humphries et al., 2007) are considered as positive signatures of mechanical responsiveness. All these responses can be found during the transmission of mechanical signals from the ECM to the nucleus, a molecular process collectively known as mechanotransduction.

Cells perceive mechanical stimuli through diverse mechanosensitive molecules at the cell membrane including integrins, stretch-activated ion channels, G protein coupled-receptors, growth factor receptors, activating different

mechanotransduction pathways (Martinac, 2014; Luis Alonso and Goldmann, 2016).

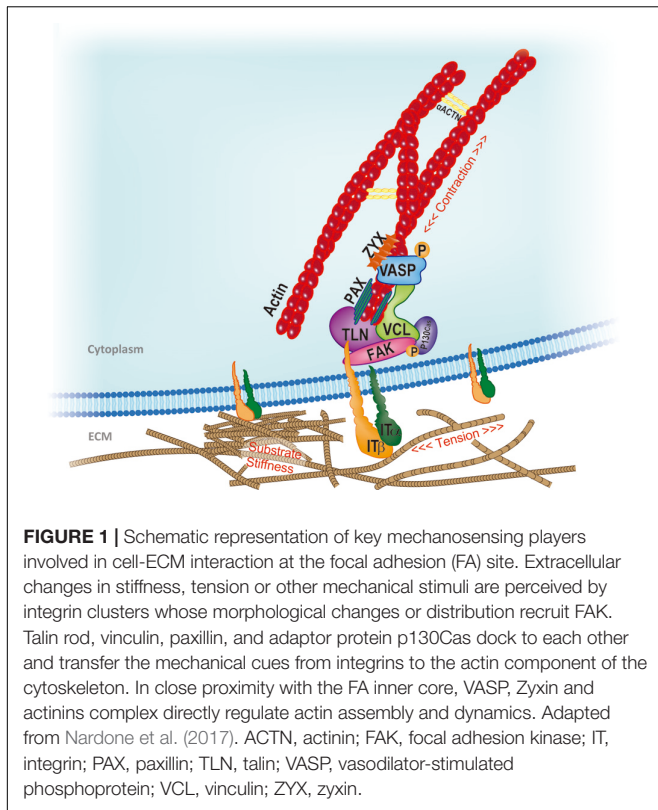
In the present review, we focus on the cellular mechanical response through ECM-integrin-cytoskeleton-nucleus axis and critically discuss the molecular basis of focal adhesion cell mechanosensing. We highlight how different intracellular molecules respond to mechanical loading and transfer the information from the very site of cell-ECM interaction - the membrane - to the nucleus, where the mechanosensitive genes are eventually activated.

## FOCAL ADHESIONS: THE MAIN HUB FOR CELL-MATRIX INTERACTION

The primary site of force transmission to the cell is the cellular membrane, where the direct contact with the extracellular matrix (ECM) occurs.

Cells in contact with a stiff surface typically develop discrete multiprotein complexes under the membrane named focal adhesions (FAs), which are the main hub of cell-ECM interaction.

Focal adhesions mechanosensing activity consists in perceiving and transferring the mechanical cues arising from the extracellular milieu to the cellular cytoskeleton. To do so, they are built as complex structures, that can be divided in a transmembrane and in an intracellular layer. The intracellular layer of FAs is composed by scaffolding, docking, and signaling proteins that collectively serve as interface between the transmembrane components directly contacting the ECM (integrins) and the actin cytoskeleton. The molecular composition of FA core is extremely variable and sensitive to ECM composition and mechanics, as perceived by integrin binding. In fact, different degrees of integrin clustering, as determined by the spacing and availability of ECM adhesion sites, affect the recruitment of FA proteins to the binding site (Cavalcanti-Adam et al., 2007; Schiller and Fässler, 2013). Among the proteins composing the intracellular FA layer, some have been shown to be mechano-responsive, while others are mostly known to participate in outside-in signal transduction.



Given the complexity of FA structure and the number and nature of the proteins involved, the modalities by which the FAs act as primary mechanosensor cannot be described collectively; thus, the response of few key FA components to mechanical loading will be herewith described. A representation of the mechanosensing machinery of the FAs is depicted in **Figure 1**.

### Integrin Assembly at Cell-Ecm Interface

The amount of tension generated by a given FA is thought to directly correlate with its size and with the amount of structural, docking and functional proteins recruited to the site (Goffin et al., 2006).

Focal adhesions are dynamically built following the assembly of transmembrane proteins deputed to physically interact with components of ECM, namely fibronectin, vitronectin, collagens, laminins, and named integrins. Integrins are heterodimers composed of  $\alpha$ - and  $\beta$ -subunits, whose assembly is guided by ECM composition and whose specificity is given in mammals by the combination of 24  $\alpha$ - and 9  $\beta$ -subunits and by alternative splicing events. The combination of  $\alpha$ - and  $\beta$ -subunits defines the affinity of the receptor for different ECM components and its cell type specificity.

Integrin affinity for its ECM ligand can be regulated within the cell in a process called “inside-out signaling” or prompted by extracellular mechanical stimuli, inducing a high-affinity conformation change (Chen W. et al., 2012). Following such events, integrins are activated, cluster and reinforce molecular links at the cell-matrix interface (Oría et al., 2017; Strohmeyer

et al., 2018). Their extracellular domain contacts the ECM, while the cytoplasmic tail interacts with cytoskeletal actin through a number of docking proteins, forming the inner core of the FAs.

Extracellular matrix composition drives precise integrin subsets expression which, being coupled with different signaling cascades, induces specific cellular responses (Seetharaman and Etienne-Manneville, 2018).

Apart from being responsive to changes in ECM biochemical composition and mechanics, cells also adjust their own mechanical state by altering cytoskeletal architecture, modulating cellular elasticity, or generating a concomitant contractile response to applied forces (Webster et al., 2014). The interplay between the external and internal mechanical state of cells is defined by tensional homeostasis, a basal equilibrium stress state in which cells maintain defined levels of tension with their surroundings, despite mechanical perturbations (Brown et al., 1998). In this regard, specific combinations of  $\alpha$ - $\beta$  integrins are known to play different roles in mechanosensing and force generation (Seetharaman and Etienne-Manneville, 2018). Although the mechanical responsiveness of the integrins appears to be diverse, single cell tensional homeostasis is finely tuned mainly by an equilibrium between  $\beta$ 3 and  $\beta$ 1 integrins (Milloud et al., 2017). In fact, deletion of  $\beta$ 3 causes traction forces to increase, whereas the deletion of  $\beta$ 1 integrin results in a strong decrease of contractile forces. Interestingly, the distribution of these subunits within the cell membrane is inhomogeneous in static cells, with  $\beta$ 1 subunit being more expressed at the perinuclear ring and  $\beta$ 3 integrin being restricted to the cell edge (Shiu et al., 2018). Moreover,  $\beta$ 3 and  $\beta$ 1 integrins have a differential distribution at the leading edge as compared to the rear part of migrating cells (Galbraith et al., 2007) where they trigger distinct signaling pathways (Schiller et al., 2013). Given the incredible number of possible combinations between the subunits and their discrete distribution within the cell membrane, integrins set the pitch of cell mechanosensing at the nanometric scale.

### Focal Adhesion Kinase (FAK)

Focal adhesion kinase is one of the first molecules recruited to developing FA in response to external mechanical stimuli. Its activation by autophosphorylation is considered the trigger to intracellular mechanotransduction, by activating downstream mechanotransducers within the cytoplasm (Lachowski et al., 2018). Downstream signals like cytoskeletal contraction and cell spreading reinforce FAK activation in a positive loop; so FAK phosphorylation can be increased by exogenous force application (such as stretching or resistance by a rigid substrate) (Michael et al., 2009). The interplay between FAK and the contractile cytoskeletal network is tightly controlled in the cell as to maintain tension at critical sites of the cell and to regulate force transfer to the nucleus (Zhou et al., 2015). For example, during processes requiring cell polarization and nucleus deformation, like directional migration, FAK activation occurs at specific sites to favor cytoskeleton local reorganization and nucleus squeezing (Jung et al., 2012). Due to its complexity, the physical mechanism of FAK mechanosensing has been the target of several molecular dynamics and mechano-biochemical network simulations that

suggest FAK sensor is homeostatic, spontaneously self-adjusting to reach a state where its range of maximum sensitivity matches the substrate stiffness (Bell and Terentjev, 2017).

## Talin

Talin is a 270 kDa protein composed of an N-terminal globular head, a flexible rod domain and C-terminal helices. While the helices are involved in protein dimerization (Golji and Mofrad, 2014), the head interacts with both  $\beta$ -integrin cytoplasmic domain and F-actin through its FERM domain, recruiting protein 4.1, ezrin, radixin and moesin docking proteins (Ciobanasu et al., 2018). Talin rod features an additional binding site for integrin, and two sites for actin (Gingras et al., 2009). It also contains several binding sites for vinculin, its main partner at the FA site (Gingras et al., 2005). The nanomechanical properties of the protein have been recently characterized and its complexity partly described: talin displays stepwise unfolding dynamics due to the characteristic transition kinetics of its 13 C-terminal mechanosensitive rod subdomains and thus behaves as a force buffer. By stochastic rounds of unfolding/refolding, talin rod domains ensure that force-transmission can be maintained at a low state even across very different talin end-to-end fluctuations (Yao et al., 2016). Altogether, these events set the physiological force range defining the mechanical stability of cell–matrix adhesions (Neumann and Gottschalk, 2016; Yao et al., 2016).

The most recognized effect of force loading to talin consists in its unfolding to expose cryptic hydrophobic binding sites to host vinculin head (del Rio et al., 2009; Hirata et al., 2014; Maki et al., 2017; Rahikainen et al., 2017). In the absence of force, talin rod remains fully structured, and no vinculin binding sites (VBS) are available; under low-force regimes, only the weakest bundle unfolds revealing its VBS. This activates one vinculin molecule, releasing it from its autoinhibited state. As the force applied to talin increases, more bundles are unfolded, revealing more VBSs and thus activating an increasing number of vinculin molecules (Haining et al., 2016). This process is called talin–vinculin mechanosensitivity. In fact, the successful binding of vinculin to talin is considered essential to stabilize talin–F-actin interaction and thus transfer the mechanical signal inward (Humphries et al., 2007).

## Vinculin

Vinculin is one of the main components of FA inner core and its recruitment to the site requires talin activation by mechanical forces (Giannone, 2015): vinculin presence at the FAs correlates directly with the force applied on the same FA (Dumbauld et al., 2013). According to the most recognized model of action, when recruited to the FA, vinculin binds to VBS of talin via its head domain. Once bound to talin at the FA site, vinculin encounters fast conformational changes in its tertiary structure, by switching between an inactive and a low-affinity state (del Rio et al., 2009; Carisey et al., 2013; Hirata et al., 2014). An early model of vinculin mechanosensitivity proposed that the mechanical pertinence of the proteins was conferred by its tail domain. Indeed, cells lacking vinculin show a reduced contractility and this effect can be rescued by transfecting the vinculin tail domain but not the head domain (Mierke et al., 2008). The protein undergoes perpetual

cycles of association and dissociation from the FA complex being mediated by its tail domain. Mutants of such domain reinforce FA stability as if the cell was growing on a stiff surface (Rahikainen et al., 2017).

Another model describes a more complex activity: when recruited to FAs, vinculin couples cell area and traction force with differential contribution coming from the head and tail domains. In fact, vinculin transmits force inside-out by increasing ECM-bound integrin–talin complexes via the head domain, while the tail domain is needed to propagate force to the actin cytoskeleton (Dumbauld et al., 2013).

## Paxillin

Paxillin is a 70 kDa phosphotyrosine-containing docking protein being mainly localized at the FA intracellular layer. Here the protein is traditionally believed to integrate mechanical cues arising from the ECM and biological signals propagated via the growth factor receptors. The protein contains different interacting domains (LIM, SH2, SH3 and LD) which confer paxillin high-affinity binding properties to bring together structural and signaling partners (Kadmas and Beckerle, 2004). The mechanosensing properties of paxillin lie in its ability to bind activated vinculin and paxillin LD motif–binding protein (actopaxin) through the LD domain, thus stabilizing FA–cytoskeleton interaction. To do so, paxillin needs to be phosphorylated by FAK, or by Proto-oncogene tyrosine-protein kinase (Src) on tyrosines 31 and 118. Phosphorylated paxillin exposes additional binding sites for the adaptor molecule Crk, which, in turn, activates the MAPK signaling cascade. The phosphorylation of tyrosine and serine residues in LIM domain has been detected on rigid substrates. Nevertheless, it is still unclear whether these rounds of phosphorylation account for paxillin mechanosensing activity (Bae et al., 2014; Qin et al., 2015).

When extracellular tension is reduced, FA sites lose the ability to recruit paxillin and detach from the relaxed substrate. This event abrogates actin polymerization, resulting in slow actin recovery and increased incidence of stress fiber breaks (Smith et al., 2013). Paxillin has also a shuttling activity which will be described below.

## Zyxin, Ena/VASP, p130<sup>Cas</sup> and Actinins

Zyxin is a 61 kDa phosphoprotein containing three C-terminal LIM domains and nuclear exclusion sequence (NES). The presence of such domains accounts for its localization to the FAs and for the interaction with a number of FA partners. Zyxin mechanosensing activity consists in its dynamic diffusion through different cell compartments: zyxin is released from FAs when cells are grown on a soft substrate or when the mechanical load is reduced by inhibiting the actomyosin interaction (Uemura et al., 2011). Stretching restores zyxin accumulation in the FAs even in the absence of actomyosin tension, thus demonstrating the mechanosensitive behavior of the protein (Colombelli et al., 2009; Hoffman et al., 2012). Recently, the protein was found to directly regulate F-actin polymerization by interacting with Ena/VASP at the filament barbed end. Zyxin ability to promote actin filament assembly is consistent with its mechanosensitive

role in the cytoskeletal reinforcement in response to cyclic stretching (Yoshigi et al., 2005). Zyxin was also found to shuttle to the nucleus. Such activity will be discussed below.

Another zyxin direct interactor is the stretch-sensitive adaptor protein p130<sup>Cas</sup>, recently proposed as a novel mechanosensor (Sawada et al., 2006). P130<sup>Cas</sup> contains SH3 domains by which it interacts with vinculin and FAK at the FA site. Following integrin clustering and activation, the protein is recruited to the FAs, it unfolds and exposes tyrosine residues that can be phosphorylated. In fact, p130<sup>Cas</sup> phosphorylation only occurs when cells are stretched (Sawada et al., 2006). The ability of phosphorylated p130<sup>Cas</sup> to prompt different signaling cascades upon mechanical stimuli, proposes the protein as a hub for the force transmission apparatus with growth factor-stimulated signaling. Additionally, p130<sup>Cas</sup>-vinculin interaction has been proposed to freeze vinculin in the opened conformation, thus promoting talin binding and FA stability (Janoštiak et al., 2014).

The main role of actinins is in crosslinking F-actin fibers and organizing actin filament cytoskeletal network. The knockdown of  $\alpha$ -actinin causes aberrant ECM rigidity sensing, loss of contractility, and enables the cells to proliferate on soft matrices (Meacci et al., 2016). Interestingly, in a compendium of studies, Roca-Cusachs et al. (2013) showed that  $\alpha$ -actinin transmits force to nascent FAs, and favor tension-dependent FA maturation. The establishment of this multistep mechanotransduction phenomenon that enables cells to adjust forces on matrices unveil a role of  $\alpha$ -actinin that is different from its well-studied function as actin cross-linker (Roca-Cusachs et al., 2013). Furthermore, Lee and Kumar (2016) have determined the mechanical stability and kinetics of human  $\alpha$ -actinin-1 highlighting a novel action as molecular shock absorber.

## CYTOSKELETAL TENSION AS SECOND MESSENGER FOR MECHANICAL SIGNALS

The propagation of extracellular and cell-generated forces is ensured by the regulation of cytoskeleton tension (Discher, 2005).

The cytoskeleton is a dynamic structure composed by filamentous and crosslinking proteins. It provides mechanical support to the cells and controls their motility, shape and tension homeostasis (Fletcher and Mullins, 2010). The disruption of cytoskeleton organization can lead to changes in gene expression and the consequent alteration of cell biological response (Tamada et al., 2004; Jaalouk and Lammerding, 2009; Dupont et al., 2011; Iyer et al., 2012).

The mechanical properties of the cytoskeleton depend on the dynamics, geometry and polarity of its components: *actin fibers* (F-actin), *microtubules* (MTs) and *intermediate filaments* (IFs). Each of the components displays a highly organized structure contributing to intracellular organelle integrity and maintenance (Fabry et al., 2001; Chen et al., 2010).

Cytoskeleton contractility is ensured by F-actin sliding on the motor protein myosin II. F-actin and myosin II are held together by crosslinking proteins (e.g.,  $\alpha$ -actinin, fascin, filamin.) in complex structures called *stress fibers* (SFs).

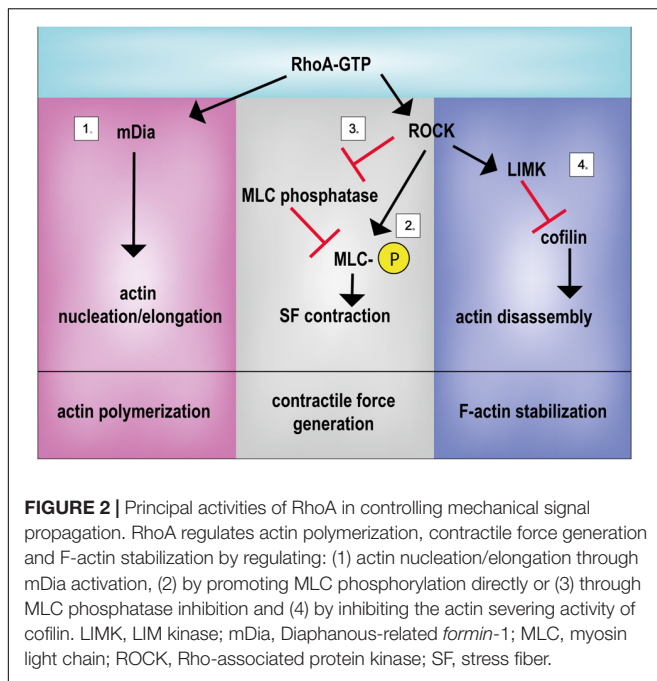
By pulling on FAs, SFs propagate force from the ECM to the cell and *vice versa* (Cramer et al., 1997; Pellegrin and Mellor, 2007; Naumanen et al., 2008). Based on their structural organization, assembly and FA connectivity, SFs have been grouped in different specialized subtypes (Small et al., 1998; Hotulainen and Lappalainen, 2006). Anchored to FAs only at one end, the dorsal SFs do not contain myosin II, therefore only act as stabilizers that cannot contract (Tojkander et al., 2012). Transverse arcs are, instead, curved contractile SFs characterized by a periodic pattern of  $\alpha$ -actinin and myosin II and are only indirectly connected to FAs through dorsal SFs. Dorsal SFs and transverse arcs, generated by *de novo* polymerization, directly interact among them by creating a dynamical network from which ventral SFs can be formed (Hotulainen and Lappalainen, 2006). Ventral SFs are contractile acto-myosin bundles rich of myosin II motors, anchored to FAs at both ends and positioned at the cell base. A recently identified subtype of actin fiber with peculiar function is the perinuclear actin cap, composed of actomyosin bundles wrapped around the nucleus and connecting the nuclear envelope to FAs (Khatau et al., 2009). Through this direct connection, mechanical forces propagate directly from cell periphery to the nucleus (Kim et al., 2012; Li et al., 2014; Shiu et al., 2018).

During the mechanotransduction process, SFs and FAs cooperate and stabilize each other. For example, the relocation of FA protein zyxin and other crosslinkers upon mechanical loading fosters SFs reinforcement and increases cytoskeletal tension (Yoshigi et al., 2005; Colombelli et al., 2009; Fabry et al., 2011). On the other hand, SFs contractility prompts vinculin recruitment to the FAs (Yamashita et al., 2014), where the protein participates in FA composition and organization (Pasapera et al., 2010; Carisey et al., 2013).

Many actin-binding proteins dynamically regulate actin cytoskeleton dynamics in response to intra or extracellular stimuli. Nucleation-promoting factors (Arp2/3, profilin), capping proteins, depolymerizing factors (ADF/cofilin), stabilizing proteins and crosslinkers contribute to control the architecture and the mechanical properties of the network (Pollard and Cooper, 2009; Bugyi and Carlier, 2010; Wiggan et al., 2012).

The main process by which actin cytoskeleton is stabilized by tensile force application consists in the inhibition of the actin severing activity of cofilin (McGough et al., 1997; Hayakawa et al., 2011). When active in the dephosphorylated form, cofilin severs F-actin fibers and exposes the barbed end, at which the protein can be depolymerized (G-actin). This event reduces cell tension. On the contrary, upon mechanical stimulation, cofilin is constantly phosphorylated by LIMK, a kinase activated by Rho/ROCK pathway (Fukata et al., 2001; Hayakawa et al., 2011).

ROCK activation by RhoA also induces myosin II activation by direct phosphorylation of myosin regulatory light chain (MLC) mainly at the Ser-19 residue or by inhibition of MLC phosphatase (MLCP) (Amano et al., 1996; Burrige and Chrzanowska-Wodnicka, 1996). MLC phosphorylation induces actin-myosin interaction and the activation of myosin II ATPase generating contractile force.



Besides, ROCK directly participates in cytoskeletal stabilization: Rho/ROCK pathway activates the formin Diaphanous (mDia), which directly or through the Arp2/3 complex promotes F-actin polymerization (Palazzo et al., 2001; Zigmond, 2004; Lessey et al., 2012) (**Figure 2**).

As expected, alterations in the function of Rho or its downstream effectors can affect cell responsiveness to extracellular environment. Indeed, myosin II depletion leads to contractile defects, reduction of FAs, alteration of SFs organization and inhibition of nascent FA maturation (Burrige and Chrzanowska-Wodnicka, 1996; Even-Ram et al., 2007; Cai et al., 2010).

Three isoforms of the motor protein Myosin II (MyoIIA, MyoIIB, MyoIIC) were described in mammals that display different localization, tissue expression and enzymatic properties. As described before, MyoIIA is responsible for generating traction force in order to stabilize FAs in a Rho/ROCK-dependent mechanism. Due to its fast turnover, MyoIIA allows rapid cytoskeleton remodeling. MyoIIB is, instead, an actin fiber stabilizer with no motor function; it is localized at the perinuclear actin cap and involved in maintenance of cell polarity (Kovács et al., 2003).

SFs are physically connected to the MT network (Jiu et al., 2015). MTs, the stiffest cytoskeletal components, are involved in crucial biological processes, such as intracellular trafficking, mitotic spindle formation and cell polarity (Fletcher and Mullins, 2010; Zhang et al., 2014). MTs respond to mechanical stress, as demonstrated by mitotic cells exposed to stretching: following mechanical loading, dividing cells display an alignment of the mitotic spindle parallel to the applied force (Fink et al., 2011). MTs can also affect Rho GTPase signaling via Guanine exchange factor GEF-H1. MTs disruption leads to a higher level of GEF-H1 available for RhoA activation, thus causing SF formation

and increased contractility (Krendel et al., 2002). Like MTs, also keratins and vimentin IFs interact with RhoA-GEFs (Solo and GEF-H1, respectively) and control RhoA mediated-SF assembly (Fujiwara et al., 2016; Jiu et al., 2017).

IFs are highly flexible and more stable as compared to F-actin and MTs. Their dynamics and interaction with numerous signaling pathways are regulated by post-translational modifications (Snider and Omary, 2014).

Taking advantage of cytoskeleton-targeting natural compounds or pharmacological drugs (**Table 1**) several groups have identified kinases and transcription factors (Miralles et al., 2003; Olson and Nordheim, 2010; Dupont et al., 2011) modulated by cytoskeletal dynamics.

Actin-targeting compounds are widely used in research to investigate the effect of cytoskeletal integrity and several drugs interfering with cytoskeleton contractility have been recently synthesized. The need for specific inhibitors is a global concern in this field of research: besides perturbing Rho/ROCK pathway and altering cytoskeletal tension, contractility and mechanical properties (Darenfed et al., 2007), the existing drugs may also affect other downstream signaling pathways.

## MECHANO-ACTUATED SHUTTLING PROTEINS: DELIVERING THE MESSAGE TO THE NUCLEUS

The mechanical information arising from modifications of the ECM, perceived by the FAs and propagated at the cytoskeleton level, impacts on proteins residing at the membrane or in the cytoplasm and induces their structural modification and their subsequent shuttling to the nucleus.

Among the first proteins to be identified to shuttle across the nuclear envelope following mechanical signals are the tight junction protein, ZO-1, which accumulates in cell nuclei in a cell density-dependent fashion (Gottardi et al., 1996), tyrosine kinase c-Abl, shuttling from the FAs to the nucleus in response to cell cycle cues (Lewis et al., 1996), and  $\beta$ -catenin, a protein mostly localized at the cell-cell adherens junctions and moving inside the nucleus in response to cytoskeleton remodeling (Gumbiner, 1995; Huber et al., 1996; Orsulic and Peifer, 1996).  $\beta$ -catenin is a component of the cadherin adhesion system at the plasma membrane and has a double function as structural docking protein and as a transcriptional co-activator.

The molecular basis of  $\beta$ -catenin mechanosensitivity have been compellingly demonstrated by single-molecule force spectroscopy (SMFS), showing that the Armadillo Repeat Region (ARM) is mechanically unstable and displays multiple alternative unfolding rounds (Valbuena et al., 2012).

After the discovery of  $\beta$ -catenin shuttling ability, a number of other proteins have been shown to relocate to the nucleus following modifications in ECM composition and mechanics.

Among the proteins sitting at the FAs in static conditions, and shown to detach from the membrane site and move to the nucleus following dynamic stretching, is zyxin (Nix and Beckerle, 1997). As described above, the protein contains a Nuclear Exclusion Signal (NES) that regulates its intracellular localization,

and zinc-binding LIM domains, responsible for protein–protein interactions. LIM domains have crucial role in regulating zyxin activity by binding actin at the FA site or transcription factors in the nucleus (Kadmas and Beckerle, 2004). Although no systematic analysis of its activity as gene expression regulator has been so far provided, a role for zyxin in activating few mechanosensitive genes, like endothelin B receptor (ETB-R), matrix protein tenascin-C and plasminogen activator inhibitor-1 (PAI-1) in smooth muscle cells has been suggested (Cattaruzza et al., 2004).

Paxillin is also credited of having a structural function at the adhesion sites while shuttling to cell nucleus in response

to mechanical stress. This protein is predominantly localized to the FAs and its localization can be modified following different rounds of phosphorylation on tyrosine and serine residues by FAK in response to modifications in cell spreading and polarity (Dong et al., 2009; Sathe et al., 2016). Its detachment from the FA complex and its translocation to the nucleus have been shown to be independent of ECM chemical composition, but guided exclusively by mechanical cues (Zhou et al., 2017).

A new class of shuttling proteins acting as mechanotransducers, by moving back and forth from the nucleus without being physically associated to FAs, has been

**TABLE 1** | Synthetic and natural cytoskeleton targeting compounds.

Category	Target	Compound	Origin	Mechanism	Reference	
Actin-targeting compounds	Actin stabilizers	Phallotoxin (Phalloidin)	Natural compound ( <i>Amanita phalloides</i> )	F-actin binding, ATP hydrolysis and depolymerization inhibition	Estes et al., 1981	
		Jasplakinolide	Natural compound ( <i>Jaspis johnstoni</i> )	F-actin nucleation and polymerization enhancement	Bubb et al., 1994, 2000; Holzinger, 2009	
		Cucurbitacin E	Natural compound ( <i>Cucurbitaceae</i> )	F-actin covalent bound and depolymerization inhibition	Sørensen et al., 2012	
	Actin destabilizers	Latrunculins	Natural compound ( <i>Latrunculia magnifica</i> )	G-actin bound, monomers polymerization prevention	Morton et al., 2000	
		Cytochalasins	Natural compound ( <i>Helminthosporium</i> )	Capping F-actin barbed-ends preventing actin elongation	Brown and Spudich, 1981	
		Swinholide A	Natural compound ( <i>Theonella swinhoel</i> )	Actin polymerization inhibition by G-actin sequestering	Klenchin et al., 2005	
		Misakinolide A	Natural compound ( <i>Theonella</i> )	Inhibition of F actin elongation by sequestering G-actin and capping F-actin barbed ends	Terry et al., 1997	
Rho/ROCK/Myosin pathway	Rho activators	CN03	Natural compound (Bacterial cytotoxic necrotizing factor)	Deamidation of Gln-63 in RhoGTPase	Flatau et al., 1997	
		Rho inhibitor	C. Botulinum C3 exoenzyme	Natural compound ( <i>Clostridium botulinum</i> )	ADP-ribosylation on Asp41 in the GTPase binding domain	Tautzenberger et al., 2013
	ROCK inhibitors	Y27632	Synthetic compound	Catalytic site competitive binding	Ishizaki et al., 2000	
		Fasudil (HA1077)	Synthetic compounds	Catalytic site competitive binding	Yamaguchi et al., 2006	
		GSK269962A and SB772077B	Synthetic compounds	Catalytic site competitive binding	Doe et al., 2007	
	Myosin II activator	Calyculin A	Natural compound ( <i>Theonellidae</i> )	Inactivation of phosphatase and promotion of MLC phosphorylation	Peterson et al., 2004	
	Myosin II inhibitors	Blebbistatin	Synthetic compound	Block of myosin in an actin-detached state by binding to the myosin-ADP-P <sub>i</sub> complex	Kovács et al., 2003; Straight et al., 2003	
		ML7- ML9	Synthetic compound	Interaction with ATP-binding site of MLCK	Saitoh et al., 1987; Shi et al., 2007	
	Microtubules	MTs stabilizers	Paclitaxel	Natural compound ( <i>Taxus brevifolia</i> )	Prevention of MTs disassembly targeting tubulin	Rao et al., 1994; Arnal and Wade, 1995
			Taccalonolides (AF and AJ)	Natural compound ( <i>Tacca chantrieri</i> )	Regulation of tubulin nucleotide state and GTP hydrolysis inhibition	Wang et al., 2017
MTs destabilizers		Nocodazole	Synthetic compound	Inhibition of MTs polymerization sequestering free tubulin dimers	Head et al., 1985	
		Colchicine	Natural compound ( <i>Colchicum autumnale</i> )	Prevention of MTs polymerization complexing with tubulin	Skoufias and Wilson, 1992	

recently described, which will be discussed in detail in the following section.

Yes-associated protein (YAP) and WW Domain-Containing Transcription Regulator Protein 1 (WWTR1/TAZ) are transcriptional co-activators being the downstream effectors of Hippo pathway (Oka and Sudol, 2009). In response to a number of stimuli coming from the ECM, they shuttle inside the nucleus where they interact with stage- and cell-specific transcription factors to activate a given genetic program. Although being recently credited of exerting rather distinct roles in cell function, the paralog proteins share common structural features (WW, PDZ domains) and are both considered as molecular relays for ECM mechanics given their sensitivity to substrate stiffness (Dupont et al., 2011), cell–cell interaction (Kim et al., 2011) and cell spreading (Nardone et al., 2017) (**Figure 3**).

The definitive demonstration of YAP acting as a mechanosensitive protein was recently given through an elegant experiment performed by the group of Rocha-Cusachs: besides being translocated upon nuclear pore opening following the application of force on the cell, YAP shuttling to the nucleus was shown to depend on the intrinsic protein mechanical instability (Elosegui-Artola et al., 2017).

YAP/TAZ paradigmatic ON/OFF switch-like behavior has been reported in a number of cell types and, if coupled to their acknowledged role in controlling organ shape and size during organogenesis, is the perfect example of how ECM composition and mechanics can impact organ function. YAP/TAZ persistence in the nucleus is regulated by the phosphorylation on specific Serine residues (S127 for YAP, S89 for TAZ) operated by Hippo pathway upstream regulator LATS1/2 and can be released by dynamic modifications in substrate compliance or nanostructure (Mosqueira et al., 2014). Distinct reports have indicated that YAP/TAZ can be sequestered to the adherens junctions by the cadherin-catenin system and by ZO-1 protein (Kim et al., 2011), while a role for Fibronectin/FAK/Src signaling pathway has also been described (Kim and Wirtz, 2015). Evidence that Rho/ROCK-mediated cytoskeleton stability is needed for YAP/TAZ relocation to the nucleus has also been given (Mo et al., 2012), while their sensitivity to mitogens including Epidermal Growth Factor (EGF), Insulin, Thrombin and Lipopolysaccharides (LPA) has been proven (Fan et al., 2013; Haskins et al., 2014). Due to the absence of a nuclear localization sequence in Hippo effectors, the mechanisms involved in their translocation to the nucleus remain elusive for long time. Only recently, the direct association of YAP with the intracellular C-terminal fragment of ErbB-4 has been shown to promote its nuclear localization (Komuro et al., 2003). Moreover, the formation of a shuttling complex YAP/TAZ/SMAD has been shown to be regulated by cell density, with the complex consistently localizing in the nucleus of sparse cells not sensing cell-cell interaction (Grannas et al., 2015).

Since the main annotation for YAP/TAZ transcription targets lies within the proliferation category, the activity of Hippo effectors in the nucleus has been historically associated with cell growth and tumor spreading (Zanconato et al., 2015), while our group and others lately proved that the mechanotransduction role of YAP is to be ascribed to its ability to directly promote the

transcription of genes involved in cell-matrix interaction, ECM composition (Nardone et al., 2017) and cytoskeleton integrity (Morikawa et al., 2015). This mechanism has been described as a feed-forward control system by which YAP is controlled by ECM and in turn alters its composition (Calvo et al., 2013).

## NUCLEAR MECHANOTRANSDUCTION AND MECHANICALLY ACTIVATED TRANSCRIPTION FACTORS

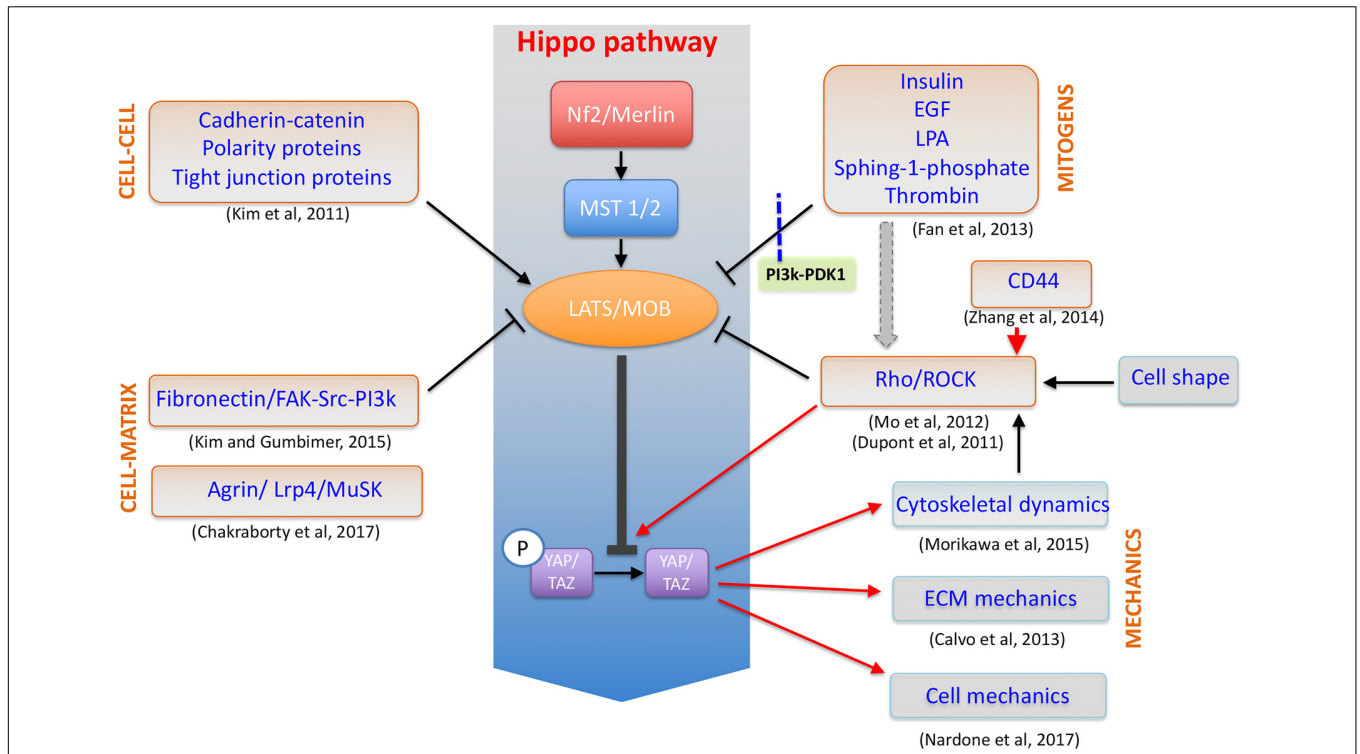
Although recent reports suggested mechanical signals influence the expression of mechanosensitive genes, the molecular processes by which mechanical forces are transmitted from the periphery to the nucleus of the cell, the largest and stiffest organelle in eukaryotic cells, are still largely unknown (Dahl et al., 2008). In fact, only lately, few studies suggested the possibility that the nucleus possesses its own mechanosensitive apparatus (Wang et al., 2009; Cho et al., 2017).

The existence of a connection between nucleus and cell membrane has been proven by experiments showing that the application of mechanical forces on integrin receptors at the cell membrane is followed shortly by nuclear structural reorganization and deformation in the direction of the pulling force (Guilak, 1995; Guilak et al., 2000; Jaalouk and Lammerding, 2009; Neelam et al., 2015) and by chromatin reorganization (Booth-Gauthier et al., 2012).

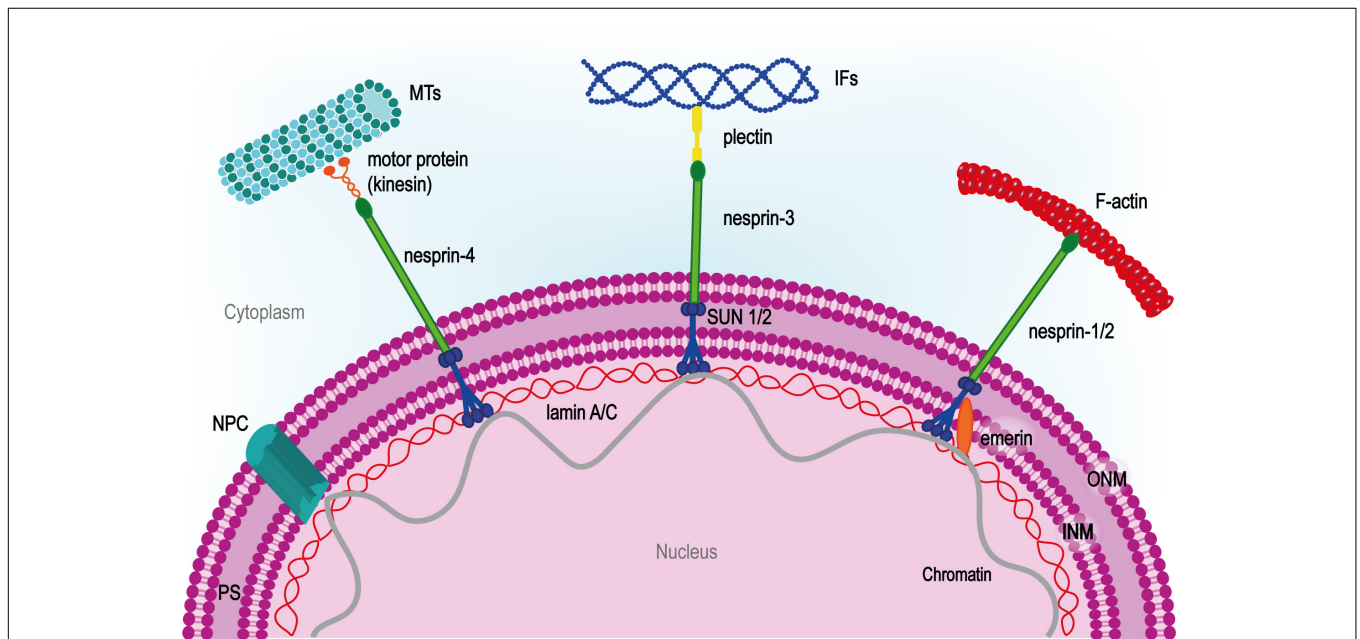
The nuclear-cytoskeletal coupling is crucial for force transmission to the nucleus and, consequently, for the biological response. Many studies have pointed at the nuclear envelope as a regulator of biochemical and physical connection between nucleus and cytoskeleton (Crisp et al., 2006; Fedorchak et al., 2014; Uzer et al., 2016). Indeed, the inner (INM) and the outer nuclear membrane (ONM) of the nuclear envelope host the complex responsible for tying together nucleoskeleton, nuclear envelope and cytoskeleton: the Linker of Nucleoskeleton and Cytoskeleton (LINC).

The main components of LINC system so far identified are SUN and nesprin proteins. Although different isoforms for each class have been identified, SUN-1/2 and nesprin-1/2 are the most widespread. SUN proteins contain an N-terminal nucleoplasmic region followed by a transmembrane helix at the INM, and the SUN domain at the C-terminal tail. Thanks to this peculiar structure, SUN proteins organize in trimers that span through the INM and bind the C-terminal KASH domain on nesprins in the perinuclear space (Sosa et al., 2012). Nesprins project through the ONM to establish a strong connection between the two nuclear membranes (Crisp et al., 2006). On the cytoplasmic side of the nucleus, multiple nesprin isoforms either bind the cytoskeleton directly or through molecular linkers such as kinesin-1, plectin or dynein (Méjat and Misteli, 2010; Taranum et al., 2012) (**Figure 4**). SUN proteins also interact with nuclear pore complexes (NPC) controlling their organization and distribution on the nuclear envelope (Liu Q. et al., 2007).

LINC components gather at nuclear apical region to form the so-called transmembrane actin-associated nuclear line (TAN) (Luxton et al., 2010). Similar to FAs, TANs appear as discrete



**FIGURE 3 |** YAP/TAZ at the crossroad of cellular mechanotransduction. Schematic representation of YAP/TAZ factors as the downstream effectors of a number of distinct mechanosensing and biological pathways in the cell and acting to control cytoskeleton dynamics, cell mechanics and in a feed-forward loop to stabilize ECM structure.



**FIGURE 4 |** LINC complex at the center of nuclear-cytoskeletal coupling. On the cytoplasmic side, different nesprin isoforms connect the nucleus to the cytoskeleton. Nesprin-1/2 directly bind actin, nesprin-3 is connected to intermediate filaments (IFs) by plectin and nesprin-4 binds microtubules (MTs) through kinesin-1 or other microtubule motor proteins. In the perinuclear space (PS), nesprins bind SUN proteins which span the inner nuclear membrane (INM) and interact with the nuclear lamina through lamin A. The inner nuclear membrane protein emerin anchors SUN protein to lamin A and interacts directly with chromatin. NPC, nuclear pore complex.



spots where LINC proteins get in contact with cytoskeleton and nucleoskeleton, and that accumulate upon mechanical stimulation (Lombardi and Lammerding, 2011; Chambliss et al., 2013).

LINC perturbation has been associated with actin cytoskeleton derangement (Folker et al., 2011; Ho and Lammerding, 2012), nuclear movements and distortion, changes in signal transduction, centrosome positioning and chromatin dynamics (Burke and Roux, 2009; Fridolfsson and Starr, 2010; Gimpel et al., 2017).

On the internal side of the nucleus, SUN proteins link intimately to the nuclear lamina through the main stabilizer of the INM, the intermediate filament lamin A (Haque et al., 2006; Ho and Lammerding, 2012; Gruenbaum and Medalia, 2015). This interaction is credited of propagating the mechanical stimuli from the cytoskeleton to the nucleoskeleton.

Indeed, changes in lamin A protein levels have been detected when tissue rigidity is modified, with soft substrates inducing its phosphorylation and consequent dissociation from the nucleoskeleton (Swift et al., 2013; Buxboim et al., 2014). Lamin A detachment from the nucleoskeleton or its depletion has been associated with the fragility of the nucleus itself and defective nuclear mechanics (Lammerding et al., 2004).

SUN nucleoplasmic domain and lamin A are connected to nuclear chromatin, thus possibly affecting directly gene regulation (Haque et al., 2006; Camozzi et al., 2014). Lamin A-chromatin interaction can be direct or through regulatory proteins like emerin, an integral membrane actin-capping protein promoting nuclear F-actin polymerization (Plessner et al., 2015).

Emerin has been recently described as a sensor of tension upon mechanical stimulation: in isolated nuclei exposed to mechanical stimulation, emerin undergoes phosphorylation by Src kinase, thus leading to lamin A accumulation at the nuclear envelope and nuclear stiffening (Guilluy et al., 2014; Osmanagic-Myers et al., 2015). Cells lacking lamin A, emerin or other LINC components show reduced expression of genes typically targeted downstream of the activation of mechanosensing pathways. For example, nesprin-1 knockdown prevents YAP nuclear shuttling upon mechanical stimulation, proving LINC complex involvement in YAP/TAZ mechanotransduction pathway (Driscoll et al., 2015). Consistent with this hypothesis, mutation in lamin A/C gene (LMNA) causes YAP signaling pathway deregulation (Bertrand et al., 2014).

In a similar fashion, LINC complex and nucleoskeleton components are involved in Wnt pathway regulation; emerin overexpression prevents  $\beta$ -catenin nuclear shuttling and its activity, whereas emerin-depleted cells show substantial accumulation of  $\beta$ -catenin in the nucleus (Markiewicz et al., 2006).

These results appear more interesting when corroborated by the evidence that lamin A and emerin associate with multiple factors involved in transcription regulation, chromatin organization and mRNA processing, thus implying that mechanical cues can impact on mRNA translation through LINC complex (Wilkinson et al., 2003; Dorner et al., 2007).

The association of transcription regulators, LINC complex and nucleoskeleton components at the nuclear periphery has been

linked to both the activation and the repression of transcription. Transcriptional activity has been correlated with chromatin rearrangement at the nuclear periphery, in particular to the interaction between euchromatin and NPCs. NPCs are indeed recognized as active transcription sites connected with both cytoskeleton and DNA (Akhtar and Gasser, 2007; Krull et al., 2010; Ibarra and Hetzer, 2015).

Another way by which INM proteins can modulate gene expression in a mechanosensitive fashion is represented by reducing the accessibility of chromatin to transcription regulators. Lamin A binds sites of transcriptionally silent heterochromatin at the INM, while transcriptionally active euchromatin is distributed at the center of the nucleus. According to this model, the nuclear periphery can serve as a resting site for transcription factors, sequestering them and preventing their interaction with target genes (Heessen and Fornerod, 2007).

C-Fos represents a well-described example of transcription factor being sequestered by lamin A/C at the periphery of the nucleus (Ivorra et al., 2006; Scaffidi and Misteli, 2008).

The interaction of nucleoskeleton with transcription factors known to be directly activated by mechanical signals deserves more attention: Mega-karyoblastic leukemia 1 (MKL1, also known as MRTF-A and MAL), member of myocardin family, is a mechanosensitive transcription factor which dissociates from G-actin in the cytoplasm upon mechanical stimulation and activates SRF in the nucleus. Alterations in nucleoskeleton organization affects MKL1 pathway as demonstrated by impaired MKL1 nuclear translocation in lamin A/C depleted cells (Ho et al., 2013).

Also, NF- $\kappa$ B, which is mechanically induced to translocate in the nucleus, suffers defects in the nuclear-cytoskeletal coupling (Lammerding et al., 2004).

## BIOLOGICAL RESPONSES TO CELLULAR MECHANOSENSING

The interpretation of mechanical cues by the cell is completed by the activation of a given genetic program which induces the cell to adapt to the new conditions.

An example of how cells can respond to mechanical conditioning is given by experiments in which mesenchymal stem cells (MSCs) are grown onto surfaces displaying stiffness gradients. Consistent with the acknowledged ability of the cells to perceive different substrate stiffness, MSCs were shown to migrate toward the stiff area, in a mechanism dubbed durotaxis, which is dependent on cytoskeleton dynamics (Vincent et al., 2013). Since stiffness gradients have been identified in a number of pathological conditions, durotaxis appears to be a general attraction strategy for MSCs to fibrotic areas. An interesting compendium to this study provides evidence that vascular smooth muscle cells undergo durotaxis only in the presence of fibronectin *in vitro*, while laminin seems to restrict their response (Hartman et al., 2016), thus highlighting the substrate-specific nature of the phenomenon.

A number of reports described specific effects of substrate stiffness on cell proliferation, like in endothelial cells (Yeh et al., 2012), airway smooth muscle cells (Shkumatov et al., 2015), and dermal fibroblasts (Razinia et al., 2017). Since all these results were obtained by comparing different stiffness values within the physiological range, it is reasonable to assume that stiffer substrates favor cell cycle. However, contrasting statements can be found in literature (Tan et al., 2014). The variability of conditions and models used in *in vitro* studies can lead to discrepancies and different interpretations of results. In order to have a clear overview, the experimental design must consider the stiffness range specific for each organ/tissue. Depending on the function in the body, softer tissues such as brain (1 kPa) and harder tissues such as bone (1 GPa) can be identified (Handorf et al., 2015).

Increased tissue stiffness has been generally associated with diseased conditions and start to be considered as prognostic factor in cancer progression (Wei and Yang, 2016; Reid et al., 2017). A fibrotic tissue can be 10–100 times stiffer than its healthy counterpart: for example, glaucomatous trabecular meshwork stiffness is 80,8 kPa, while the healthy tissue ranges around 4,0 kPa (Last et al., 2011). A general *consensus* exists that tissue-specific progenitors can be induced to maturation when cultured on substrates resembling the physiological and characteristic stiffness of the tissue they belong to. Indeed, neural stem cells (Saha et al., 2008), pre-osteoblasts (Tse and Engler, 2011), myoblasts (Engler et al., 2004) and adult cardiac progenitors (Forte et al., 2008; Mosqueira et al., 2014) acquire the given phenotype when in contact with matrix displaying a compliance similar to the one they experience *in vivo*. An effect of substrate compliance on the terminal differentiation of embryonic (Bhana et al., 2010) and neonatal (Forte et al., 2012) cardiomyocytes has also been demonstrated. Finally, MSCs have also been shown to be sensitive to substrate mechanics while switching between the osteogenic and the adipogenic lineages. It now appears improbable that MSCs could be induced to become neurogenic, when cultured on substrates mimicking neural stiffness environments (Engler et al., 2006). Neural differentiation is clearly beyond the plasticity of progenitors of the mesodermal lineage.

In living organisms, cells reside in physically confined niches where the surrounding cells and scaffolding ECM present spatially heterogeneous and dynamic mechanical cues (Paul et al., 2017). As such, topography is perceived by cells as a tissue-specific feature. Therefore, engineered materials able to mimic the physiological environment are considered a powerful tool to control cell behavior (Nguyen et al., 2016). The surface topography of a substrate can be defined by parameters like roughness, lateral spacing, height and periodicity (Nguyen et al., 2016).

Cells can distinguish between micro- and nano-scale features as demonstrated by MSCs cultured on gratings of different width. MSCs align and elongate to the grating axis and show smaller and more elongated FAs on nanogratings (250 nm width) as compared to microgratings (10  $\mu$ m width) or unpatterned surfaces (Yim et al., 2007). The spatial distribution and the

alignment of the FAs depends on the periodicity of the grid (Teixeira et al., 2006; Teo et al., 2013).

By controlling nanostructured materials periodicity and spacing, as to match integrin size and spacing through nanodots of 8 nm, it was indeed possible to tune integrin clustering and cell adhesion. By increasing the spacing between the nanodots, integrin clustering was abolished and cell adhesion compromised (Comisar et al., 2012). Similar results were obtained by culturing MSCs on vertically oriented nanotubes, where the reduction of lateral spacing enhanced cell survival, migration and differentiation capacity (Park et al., 2007). The reduction of micropattern height was also shown to affect FA maturation and positioning (Seo et al., 2011).

Finally, a broad spectrum of *in vitro* cell confinement models have been proposed with the aim to reproduce cell constraints by controlling cell shape, area and spreading (Pouidel et al., 2012). Cell body confinement on micropatterned surfaces has been shown to control the commitment of stem cells to a specific lineage. As a paradigm, single MSCs constrained on micropatterned surfaces undergo adipogenic lineage specification, while osteoblastic lineage is favored on islands allowing cell spreading (McBeath et al., 2004). Lateral or vertical confinement has been instead used to study directional cell migration, thus showing that MSCs switch from the mesenchymal to the amoeboid migration mode when vertically confined (Liu et al., 2015).

## EVIDENCES FOR CLINICAL RELEVANCE OF MECHANOSENSING SYSTEM

Following the concentric scheme used in the previous sections, we can find evidences of the clinical relevance of the different layers of the mechanotransduction apparatus. Mutations or the aberrant activation of the mechanosensing apparatus as well as pathological responses to mechanical stimuli are, in fact, involved in myopathies, fibrosis, atherosclerosis, and cancer (Jaalouk and Lammerding, 2009). Mutations in mechanosensing, structural, and contractile apparatus have been found to be a source of inherited diseases in tissues exposed to continuous mechanical stress, like striated muscle. Integrins have been described to modulate key effectors of cardiac fibrosis, like angiotensinogen, following sustained pressure overload or mechanical stretch (Graf et al., 2000). In a positive loop, angiotensin II activates integrin  $\alpha$ v $\beta$ 3 in the cardiomyocytes (Kawano et al., 2000).

In cardiac muscle, integrins interplay with the dystrophin-sarcoglycan system to mediate the interaction of the contractile apparatus (sarcomere) with ECM at specialized Z-band sites named costameres. The discrete distribution of the costameres in correspondence of the intercalated disks and Z-bands appears as the most efficient way to ensure the transmission of the forces to the sarcomere; indeed, the derangement of the costameres is a common feature of dilated (DCM) and hypertrophic cardiomyopathy (HCM) (Peter et al., 2011).

Due to its involvement in the stretching activity of the cardiomyocytes *in vivo* (Yutao et al., 2006), in beta-adrenergic stimulation, and in hypertrophic response after hemodynamic

load (Li et al., 2012), integrin- $\beta$ 1 inhibition results in heart dilation (Stewart et al., 2014).

Interestingly, inherited mutations in integrins are not common cause of myopathies, but mutations and increased expression of integrin- $\beta$ 1 have been associated with poor prognosis in breast cancer (dos Santos et al., 2012).

The next layer of mechanical signaling within the cell is the link between cellular membrane and cytoskeleton represented by mechanosensors talin, vinculin and its muscle isoform metavinculin (Chorev et al., 2018). Increased expression of talin has been associated with tumor invasiveness and metastatic properties (Sakamoto et al., 2010). The molecular mechanism proposed suggests talin-mediated activation of a pro-survival signaling through integrin, which prevents anoikis and favors cancer growth (Sakamoto and Kyprianou, 2010; Jin et al., 2015).

Given its prominent role as a docking protein at the cell-ECM interaction site, vinculin has been historically suspected of being the main FA switch in cancer progression and invasion. Indeed, vinculin is thought to be crucial in controlling cell anchorage to the ECM. Thus its loss or aberrant expression results in cell migration and, potentially, metastasis spreading (Liu M. et al., 2007).

Its activation by substrate stiffening, such as ECM produced by cancer cells, promotes tumor progression through PI3-kinase activation and basal membrane invasion (Rubashkin et al., 2014; Chang et al., 2017).

Interestingly, the shuttling mechanotransducer YAP has been lately described as one of the key determinants in the positive feedback loop fueling cancer spreading: after being activated in cancer-associated fibroblasts, YAP causes the remodeling of the surrounding ECM and possibly favors tumor spreading (Calvo et al., 2013). The derangement of YAP control has been associated with the growth of a number of tumors, including melanoma, liver, prostate, pancreatic cancer and other neoplastic conditions (Zanconato et al., 2016).

Among YAP upstream control switches, Rho/ROCK pathway has been shown to play a role in leukocytes polarization and migration following their adhesion to the endothelium (Filippi, 2016). The increased activity of Rho/ROCK signaling axis in immune cells has been shown to contribute to early atherosclerotic lesion formation (Mallat et al., 2003), vascular remodeling (Kataoka et al., 2002), and is an independent prognostic marker for survival in cardiovascular outcomes (Kajikawa et al., 2014). The balance between beneficial and deleterious effects in cardiac muscle is more nuanced (Surma et al., 2011). Pharmacological studies indicate that Rho/ROCK axis signaling promotes cardiac hypertrophy, whilst cardiomyocyte-specific conditional expression of low levels of activated RhoA protects from ischemic injury (Xiang et al., 2011). On the other hand, mice suffering from the cardiomyocyte-specific ablation of RhoA have normal hearts and develop compensated hypertrophy before becoming more dilated and less fibrotic in chronic phase (Lauriol et al., 2014). Cardiac fibrosis in response to pressure overload can be inhibited by ROCK inhibition (Phrommintikul et al., 2008), while sustained ROCK-1 activation is responsible for cardiomyocyte apoptosis (Chang et al., 2006).

The following layer of mechanotransduction is the nuclear envelope where the signal sensed from the cytoskeleton is transferred into the nucleus. Mutations in proteins contributing to the nuclear-cytoskeletal coupling lead to altered mechanotransduction signaling and cause a broad range of diseases collectively defined as laminopathies (Capell and Collins, 2006; Worman and Bonne, 2007; Prokocimer et al., 2009).

So far more than 600 mutations in LMNA gene, encoding for lamin A and lamin C via alternative splicing, have been described in humans<sup>1</sup>, the majority of which are missense mutations. LMNA mutations can result in defective lamin A processing, alteration in protein stability, assembly and folding (Wiesel et al., 2008; Bollati et al., 2012).

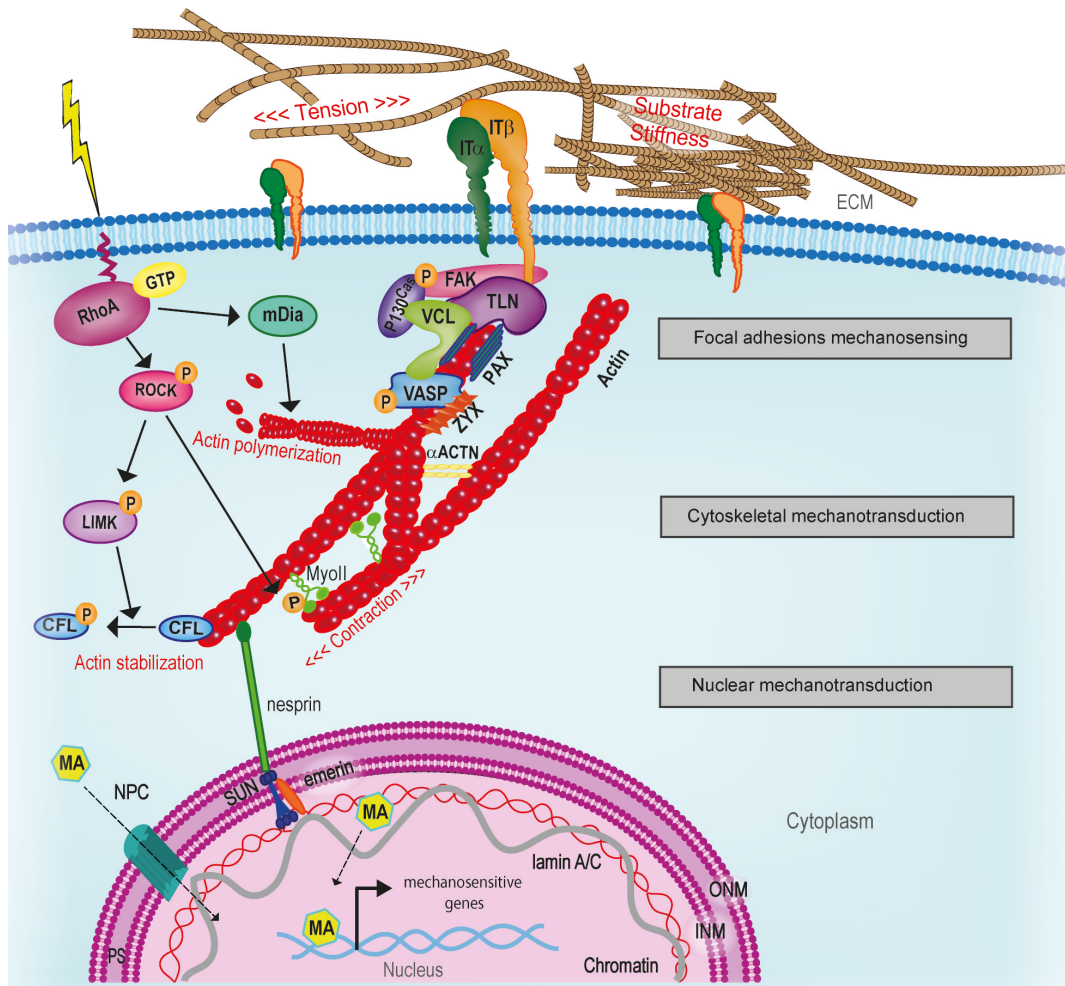
Lamins are expressed in all tissues but laminopathies have specific targets: tissues exposed to mechanical stress as skeletal or cardiac muscle and bone are the most affected by LMNA mutations. Laminopathies present a wide range of phenotypes and can be grouped according to the affected tissue: neuromuscular disorders [Emery-Dreifuss muscular dystrophy (EDMD), limb-girdle muscular dystrophy], cardiopathies (dilated cardiomyopathy), metabolic diseases (familial partial lipodystrophy) and premature aging disorders (Hutchinson-Gilford progeria syndrome, HGPS) (De Sandre-Giovannoli et al., 2002; Worman and Bonne, 2007; Schreiber and Kennedy, 2013; Brayson and Shanahan, 2017).

Skeletal and cardiac muscular dystrophies are the laminopathies identified most frequently and include limb-girdle muscular dystrophy, autosomal dominant EDMD, and congenital muscular dystrophy (Maggi et al., 2016).

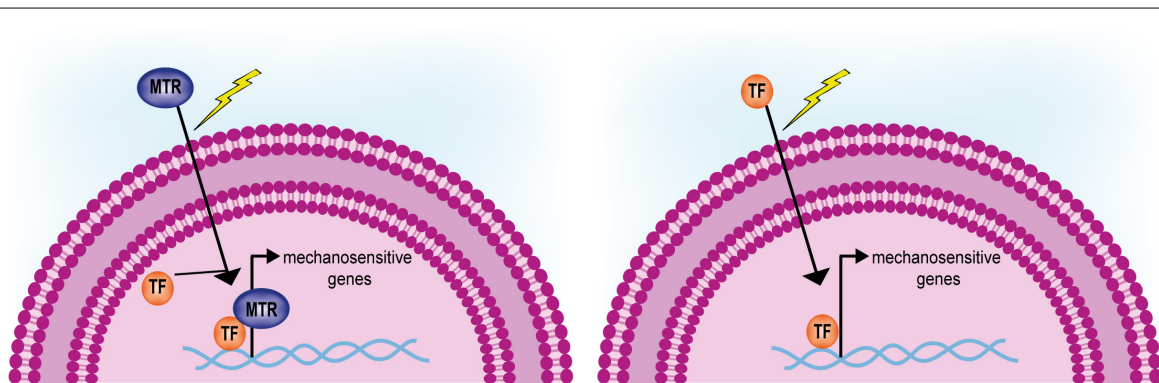
Animal experiments show that lamin A/C knock-out mice develop cardiac and skeletal muscular dystrophy and cells isolated from these mice show defects in the nuclear shape, the distribution of nuclear pore complexes and the mislocalization of nuclear envelope components, such as the inner nuclear membrane protein emerin (Sullivan et al., 1999). Interestingly, mutations in the EDMD gene, encoding emerin, or SYNE1 and SYNE2 genes, encoding nesprins, can also result in skeletal or cardiac dystrophies (X-linked EDMD) (Emery and Dreifuss, 1966; Schreiber and Kennedy, 2013; Meinke et al., 2014).

The molecular basis of the laminopathies are still debated. Due to the role of lamin A as a scaffolding protein of the nucleus, LMNA mutations can result in LINC organization impairment and, consequently, in defects in anchoring the nucleus to the cytoskeleton. Indeed, LMNA-mutated or knock-out cells show defective nuclear-cytoskeletal coupling, deranged nesprin-1 positioning and altered TAN line anchoring. They are thus more susceptible to mechanical stress (Lammerding et al., 2004; Folker et al., 2011; Chen C.Y. et al., 2012; Chen et al., 2014; Zwerger et al., 2013). As expected, these defects in mechanotransduction signaling are more severe in contractile cells (Nikolova-Krstevski et al., 2011; Bertrand et al., 2014), in which nucleoskeleton derangement is usually paralleled by the mislocalization of desmin and connexins (Nikolova et al., 2004).

<sup>1</sup><http://www.umd.be/LMNA/>



**FIGURE 5 |** Schematic representation of cellular mechanotransduction layers. Extracellular physical stimuli are perceived by FAs at the cell-ECM interface; the signals are propagate by the cytoskeleton and transferred to the nucleus where mechanosensitive genes are activated by mechanoactuators (MA). MA can be shuttling mechanotransducers or mechanosensitive transcription factors. Adapted from Nardone et al. (2017). ACTN, actinin; CFL, cofilin; FAK, focal adhesion kinase; INM, inner nuclear membrane; IT, integrin; LIMK, LIM kinase; mDia, Diaphanous-related formin-1; MyoII, myosin II; NPC, nuclear pore complex; ONM, outer nuclear membrane; PAX, paxillin; PS, perinuclear space; ROCK, Rho-associated protein kinase; TLN, talin; VASP, vasodilator-stimulated phosphoprotein; ZYX, zyxin.



**FIGURE 6 |** Activation of mechanosensitive genes driven by shuttling mechanotransducers or mechanoresponsive transcription factors. Mechanotransducers (MTR) shuttling from the cytoplasm in response to mechanical stimuli interact and activate given transcription factors (TF, **left**). Only few mechanosensitive transcription factors have been so far identified that are induced to shuttle from the cytoplasm and activate a given genetic program (**right**).

Together with its role as nuclear scaffolding protein, lamin A also functions as an anchor site for chromatin to the nuclear periphery. As such, it interacts with components of the transcription machinery. Therefore LMNA alterations can prompt chromatin derangement and changes in gene expression. Nuclear envelope defects, heterochromatin displacement from nuclear periphery and nuclear membrane fragility are common features in cells obtained from EDMD patients (Fidziańska and Hausmanowa-Petrusewicz, 2003).

Besides, laminopathies can result from defective lamin A processing (Navarro et al., 2006; Worman et al., 2009). Lamin A protein maturation goes through the production of a lamin A precursor, which is eventually processed via post-translational modifications; LMNA mutations can alter lamin A maturation and can cause its precursor accumulation, like seen in patients affected by HGPS, featuring nuclear morphology alteration and chromatin disorganization (Goldman et al., 2004; Scaffidi and Misteli, 2006).

## DISCUSSION

The consensus over the importance of mechanical signals in shaping cell and tissue function started building with the evidence that cell fate (Engler et al., 2006) and function (Bhana et al., 2010; Yeh et al., 2012; Vincent et al., 2013) can possibly be directed by substrate mechanics.

Modifications in the compliance of ECM are typically associated with the onset and the progression of degenerative diseases (Spinale, 2007) and are now recognized as prognostic tools for the progression of solid tumors (Reid et al., 2017).

Indeed, a simple Pubmed search for “*mechanotransduction*”, a term which applies to all the molecular processes contributing to transform physical cues into a biological response (Jaalouk and Lammerding, 2009), returns a steady increase in results in the last few years.

In the present review, we critically analyzed the recent scientific literature to give a comprehensive compendium of the most important pathways being associated with the complex network of cellular mechanotransduction. Within such pathways, we focused on the integrin-activated axis and highlight the proteins which stand out for their ability to encounter modifications in their structure or function in response to changes in ECM mechanics.

It is worth noting that the definition of cellular mechanosensor chosen in the preparation of the present review applies to all intracellular molecules able to perceive and respond to mechanical loading. Although a consensus is still to be found among the research community on the minimal characteristics a mechanosensor should have in order to be defined as such, the one proposed here appears broad enough as to include different molecular species credited of changing their state or function in response to physical stimuli.

It comprises proteins that unfold to expose cryptic binding sites (del Rio et al., 2009), those that encounter post-translational modifications (Sawada et al., 2006; Dong et al., 2009; Hayakawa et al., 2011; Swift et al., 2013; Guilly et al., 2014; Qin et al., 2015;

Sathe et al., 2016; Lachowski et al., 2018), proteins induced to shuttle (Gumbiner, 1995; Gottardi et al., 1996; Huber et al., 1996; Lewis et al., 1996; Orsulic and Peifer, 1996; Nix and Beckerle, 1997; Dupont et al., 2011), or the ones building novel interactions (Humphries et al., 2007) when subjected to mechanical load.

The argument that the mechanosensor definition should be used only to define molecules, mostly proteins, that change their conformation when exposed to mechanical stress comes from a reductionist approach which cannot be extrapolated to this growing field. Instead, a clearer distinction among proteins perceiving the mechanical signal (mechano-sensor), those transducing the information toward the nucleus (mechano-transducer) and those activating target mechanosensitive genes (mechano-actuator) would be beneficial in drawing the borders of this rather new discipline.

By adopting these definitions, the intracellular processes favoring the interpretation of mechanical cues can be described in discrete and concentric groups acting to deliver the message coming from ECM dynamic remodeling to the nucleus (Figure 5). In this context, the first step is universally recognized as the activation of integrins, which are bound to set the mechanosensing pitch at the nanoscale level (Goffin et al., 2006).

This hypothesis is supported by the evidence that different integrin subsets displaying distinct mechanosensing properties can be expressed in scattered areas of the cell and organized in domains (Shiu et al., 2018). This arrangement suggests that during events like migration, in which the polarization of the cell is required, the cell integrates nanometer-scale mechanosensing response in a timely manner. For this reason FAs rapidly form and break allowing the continuous adjustment and the timely execution of the cellular response (Berginski et al., 2011).

Mechanical signal transduction from the cytoplasm to the nucleus relies on the dynamic regulation of cell cytoskeleton organization and on the tight interplay between specialized contractile structures dispersed in the cytosol and on the nuclear envelope, the latter bridging cytoskeleton and nucleoskeleton (Dahl and Kalinowski, 2011). While the complex regulation of cytoskeleton dynamics is known at least at a certain extent (Discher, 2005), the understanding of the mechanisms by which the tension, propagated through cytoskeleton, regulates the shuttling of mechanotransducers to the nucleus is still elusive. Besides, although recent evidence was provided that force applied on the nucleus can regulate nuclear pores opening and the passive diffusion of mechanotransducers through nuclear envelope (Elosegui-Artola et al., 2017), the processes involved in mechanotransduction at the nucleoskeleton requires further investigation.

Additionally, very few studies addressed the modalities of activation of the mechanosensitive genes so far. Two hypotheses can be drawn, which are depicted in Figure 6: (1) following the interpretation of the mechanical signals, shuttling mechanotransducers enter the nucleus and function as adaptors for cell- and stage-specific transcription factors; (2) mechanoresponsive transcription factors exist that are only activated or made available for transcription following alterations of ECM mechanics. Although the former appears more realistic in the light of the example of YAP/TAZ co-transcription

activators (Dupont et al., 2011), a systematic approach will be needed to rule out the latter.

An important task for future research will be to elaborate integrated strategies aimed at unraveling the interactions among different mechanobiology pathways, which at the moment appear to be intertwined in a complex web (Hansen et al., 2015).

Finally, a further challenge for the future will be represented by the need to scale up mechanobiology studies as to fit a 3D setting, in order to make them more predictive of the *in vivo* situation. This approach would eventually help building more reliable models of mechanosensing failure and identify pathological conditions due to the derangement of the mechanotransduction apparatus.

## REFERENCES

- Akhtar, A., and Gasser, S. M. (2007). The nuclear envelope and transcriptional control. *Nat. Rev. Genet.* 8, 507–517. doi: 10.1038/nrg2122
- Amano, M., Ito, M., Fukata, Y., Chihara, K., Nakano, T., Matsuura, Y., et al. (1996). Phosphorylation and activation of Myosin by Rho-associated kinase (Rho-kinase). *J. Biol. Chem.* 271, 20246–20249. doi: 10.1074/jbc.271.34.20246
- Arnal, I., and Wade, R. H. (1995). How does taxol stabilize microtubules? *Curr. Biol.* 5, 900–908. doi: 10.1016/S0960-9822(95)00180-1
- Bae, Y. H., Mui, K. L., Hsu, B. Y., Liu, S. L., Cretu, A., Razinia, Z., et al. (2014). A FAK-Cas-Rac-lamellipodin signaling module transduces extracellular matrix stiffness into mechanosensitive cell cycling. *Sci. Signal.* 7:ra57. doi: 10.1126/scisignal.2004838
- Bell, S., and Terentjev, E. M. (2017). Focal adhesion kinase: the reversible molecular mechanosensor. *Biophys. J.* 112, 2439–2450. doi: 10.1016/j.bpj.2017.04.048
- Berginski, M. E., Vitriol, E. A., Hahn, K. M., and Gomez, S. M. (2011). High-resolution quantification of focal adhesion spatiotemporal dynamics in living cells. *PLoS One* 6:e22025. doi: 10.1371/journal.pone.0022025
- Bertrand, A. T., Ziaei, S., Ehret, C., Duchemin, H., Mamchaoui, K., Bigot, A., et al. (2014). Cellular microenvironments reveal defective mechanosensing responses and elevated YAP signaling in LMNA-mutated muscle precursors. *J. Cell Sci.* 127(Pt 13), 2873–2884. doi: 10.1242/jcs.144907
- Bhana, B., Iyer, R. K., Chen, W. L. K., Zhao, R., Sider, K. L., Likhitpanichkul, M., et al. (2010). Influence of substrate stiffness on the phenotype of heart cells. *Biotechnol. Bioeng.* 105, 1148–1160. doi: 10.1002/bit.22647
- Bollati, M., Barbiroli, A., Favalli, V., Arbustini, E., Charron, P., and Bolognesi, M. (2012). Structures of the lamin A/C R335W and E347K mutants: implications for dilated cardiomyopathies. *Biochem. Biophys. Res. Commun.* 418, 217–221. doi: 10.1016/j.bbrc.2011.12.136
- Booth-Gauthier, E. A., Alcoser, T. A., Yang, G., and Dahl, K. N. (2012). Force-induced changes in subnuclear movement and rheology. *Biophys. J.* 103, 2423–2431. doi: 10.1016/j.bpj.2012.10.039
- Brayson, D., and Shanahan, C. M. (2017). Current insights into LMNA cardiomyopathies: Existing models and missing LINC. *Nucleus* 8, 17–33. doi: 10.1080/19491034.2016.1260798
- Brown, R. A., Prajapati, R., McGrouther, D. A., Yannas, I. V., and Eastwood, M. (1998). Tensional homeostasis in dermal fibroblasts: mechanical responses to mechanical loading in three-dimensional substrates. *J. Cell. Physiol.* 175, 323–332. doi: 10.1002/(SICI)1097-4652(199806)175:3<323::AID-JCP10>3.0.CO;2-6
- Brown, S. S., and Spudich, J. A. (1981). Mechanism of action of cytochalasin: evidence that it binds to actin filament ends. *J. Cell Biol.* 88, 487–491. doi: 10.1083/jcb.88.3.487
- Bubb, M. R., Senderowicz, A. M. J., Sausville, E. A., Duncan, K. L. K., and Korn, E. D. (1994). Jasplakinolide, a cytotoxic natural product, induces actin polymerization and competitively inhibits the binding of phalloidin to F-actin. *J. Biol. Chem.* 269, 14869–14871.
- Bubb, M. R., Spector, I., Beyer, B. B., and Fosen, K. M. (2000). Effects of Jasplakinolide on the kinetics of actin polymerization: an explanation for certain *in vivo* observations. *J. Biol. Chem.* 275, 5163–5170. doi: 10.1074/jbc.275.7.5163

## AUTHOR CONTRIBUTIONS

FM proposed the subject and conceived the general structure of the review. FM, AP, VV, and SP revised the existing literature and contributed to all the sections. GF revised the text and contributed the discussion and conclusion.

## ACKNOWLEDGMENTS

This work was funded by the European Social Fund and European Regional Development Fund—Project MAGNET (No. CZ.02.1.01/0.0/0.0/15\_003/0000492).

- Bugyi, B., and Carlier, M.-F. (2010). Control of actin filament treadmilling in cell motility. *Annu. Rev. Biophys.* 39, 449–470. doi: 10.1146/annurev-biophys-051309-103849
- Burke, B., and Roux, K. J. (2009). Nuclei take a position: managing nuclear location. *Dev. Cell* 17, 587–597. doi: 10.1016/j.devcel.2009.10.018
- Burridge, K., and Chrzanowska-Wodnicka, M. (1996). Focal adhesions, contractility, and signaling. *Annu. Rev. Cell Dev. Biol.* 12, 463–519. doi: 10.1146/annurev.cellbio.12.1.463
- Buxboim, A., Swift, J., Irianto, J., Spinler, K. R., Dingal, P. C. D. P., Athirasala, A., et al. (2014). Matrix elasticity regulates lamin-A,C phosphorylation and turnover with feedback to actomyosin. *Curr. Biol.* 24, 1909–1917. doi: 10.1016/j.cub.2014.07.001
- Cai, Y., Rossier, O., Gauthier, N. C., Biais, N., Fardin, M.-A., Zhang, X., et al. (2010). Cytoskeletal coherence requires myosin-IIA contractility. *J. Cell Sci.* 123, 413–423. doi: 10.1242/jcs.058297
- Calvo, F., Ege, N., Grande-Garcia, A., Hooper, S., Jenkins, R. P., Chaudhry, S. I., et al. (2013). Mechanotransduction and YAP-dependent matrix remodelling is required for the generation and maintenance of cancer-associated fibroblasts. *Nat. Cell Biol.* 15, 637–646. doi: 10.1038/ncb2756
- Camozzi, D., Capanni, C., Cenni, V., Mattioli, E., Columbaro, M., Squarzon, S., et al. (2014). Diverse lamin-dependent mechanisms interact to control chromatin dynamics, focus on laminopathies. *Nucleus* 5, 427–440. doi: 10.4161/nucl.36289
- Capell, B. C., and Collins, F. S. (2006). Human laminopathies: nuclei gone genetically awry. *Nat. Rev. Genet.* 7, 940–952. doi: 10.1038/nrg1906
- Carisey, A., Tsang, R., Greiner, A. M., Nijenhuis, N., Heath, N., Nazgiewicz, A., et al. (2013). Vinculin regulates the recruitment and release of core focal adhesion proteins in a force-dependent manner. *Curr. Biol.* 23, 271–281. doi: 10.1016/j.cub.2013.01.009
- Cattaruzza, M., Lattrich, C., and Hecker, M. (2004). Focal adhesion protein zyxin is a mechanosensitive modulator of gene expression in vascular smooth muscle cells. *Hypertension* 43, 726–730. doi: 10.1161/01.HYP.0000119189.82659.52
- Cavalcanti-Adam, E. A., Volberg, T., Micoulet, A., Kessler, H., Geiger, B., and Spatz, J. P. (2007). Cell spreading and focal adhesion dynamics are regulated by spacing of integrin ligands. *Biophys. J.* 92, 2964–2974. doi: 10.1529/biophysj.106.089730
- Chambless, A. B., Khatau, S. B., Erdenberger, N., Robinson, D. K., Hodzic, D., Longmore, G. D., et al. (2013). The LINC-anchored actin cap connects the extracellular milieu to the nucleus for ultrafast mechanotransduction. *Sci. Rep.* 3:1087. doi: 10.1038/srep01087
- Chang, J., Xie, M., Shah, V. R., Schneider, M. D., Entman, M. L., Wei, L., et al. (2006). Activation of Rho-associated coiled-coil protein kinase 1 (ROCK-1) by caspase-3 cleavage plays an essential role in cardiac myocyte apoptosis. *Proc. Natl. Acad. Sci. U.S.A.* 103, 14495–14500. doi: 10.1073/pnas.0601911103
- Chang, T. T., Thakar, D., and Weaver, V. M. (2017). Force-dependent breaching of the basement membrane. *Matrix Biol.* 5, 178–189. doi: 10.1016/j.matbio.2016.12.005
- Chen, C. Y., Chi, Y. H., Mutalif, R. A., Starost, M. F., Myers, T. G., Anderson, S. A., et al. (2012). Accumulation of the inner nuclear envelope protein Sun1

- is pathogenic in progeric and dystrophic laminopathies. *Cell* 149, 565–577. doi: 10.1016/j.cell.2012.01.059
- Chen, T. J., Wu, C. C., Tang, M. J., Huang, J. S., and Su, F. C. (2010). Complexity of the tensegrity structure for dynamic energy and force distribution of cytoskeleton during cell spreading. *PLoS One* 5:e14392. doi: 10.1371/journal.pone.0014392
- Chen, W., Lou, J., Evans, E. A., and Zhu, C. (2012). Observing force-regulated conformational changes and ligand dissociation from a single integrin on cells. *J. Cell Biol.* 199, 497–512. doi: 10.1083/jcb.201201091
- Chen, Z.-J., Wang, W.-P., Chen, Y.-C., Wang, J.-Y., Lin, W.-H., Tai, L.-A., et al. (2014). Dysregulated interactions between lamin A and SUN1 induce abnormalities in the nuclear envelope and endoplasmic reticulum in progeric laminopathies. *J. Cell Sci.* 127, 1792–1804. doi: 10.1242/jcs.139683
- Cho, S., Irianto, J., and Discher, D. E. (2017). Mechanosensing by the nucleus: from pathways to scaling relationships. *J. Cell Biol.* 216, 305–315. doi: 10.1083/jcb.201610042
- Chorev, D. S., Volberg, T., Livne, A., Eisenstein, M., Martins, B., Kam, Z., et al. (2018). Conformational states during vinculin unlocking differentially regulate focal adhesion properties. *Sci. Rep.* 8:2693. doi: 10.1038/s41598-018-21006-8
- Ciobanaru, C., Wang, H., Henriot, V., Mathieu, C., Fente, A., Csillag, S., et al. (2018). Integrin-bound talin head inhibits actin filament barbed-end elongation. *J. Biol. Chem.* 293, 2586–2596. doi: 10.1074/jbc.M117.808204
- Colombelli, J., Besser, A., Kress, H., Reynaud, E. G., Girard, P., Caussinus, E., et al. (2009). Mechanosensing in actin stress fibers revealed by a close correlation between force and protein localization. *J. Cell Sci.* 122, 1928–1928. doi: 10.1242/jcs.054577
- Comisar, W., Mooney, D., and Linderman, J. (2012). Integrin organization?: linking adhesion ligand nanapatterns with altered cell responses. *J. Theor. Biol.* 274, 120–130. doi: 10.1016/j.jtbi.2011.01.007
- Cramer, L. P., Siebert, M., and Mitchison, T. J. (1997). Identification of novel graded polarity actin filament bundles in locomoting heart fibroblasts: Implications for the generation of motile force. *J. Cell Biol.* 136, 1287–1305. doi: 10.1083/jcb.136.6.1287
- Crisp, M., Liu, Q., Roux, K., Rattner, J. B., Shanahan, C., Burke, B., et al. (2006). Coupling of the nucleus and cytoplasm: role of the LINC complex. *J. Cell Biol.* 172, 41–53. doi: 10.1083/jcb.200509124
- Dahl, K. N., and Kalinowski, A. (2011). Nucleoskeleton mechanics at a glance. *J. Cell Sci.* 124, 675–678. doi: 10.1242/jcs.069096
- Dahl, K. N., Ribeiro, A. J. S., and Lammerding, J. (2008). Nuclear shape, mechanics, and mechanotransduction. *Circ. Res.* 102, 1307–1318. doi: 10.1161/CIRCRESAHA.108.173989
- Darenfed, H., Dayanandan, B., Zhang, T., Hsieh, S. H.-K., Fournier, A. E., and Mandato, C. A. (2007). Molecular characterization of the effects of Y-27632. *Cell Motil. Cytoskeleton* 64, 97–109. doi: 10.1002/cm.20168
- De Sandre-Giovannoli, A., Chaouch, M., Kozlov, S., Vallat, J.-M., Tazir, M., Kassouri, N., et al. (2002). Homozygous defects in LMNA, encoding lamin A/C nuclear-envelope proteins, cause autosomal recessive axonal neuropathy in human (charcot-marie-tooth disorder type 2) and mouse. *Am. J. Hum. Genet.* 70, 726–736. doi: 10.1086/339274
- del Rio, A., Perez-Jimenez, R., Liu, R., Roca-Cusachs, P., Fernandez, J. M., and Sheetz, M. P. (2009). Stretching single talin rod molecules activates vinculin binding. *Science* 323, 638–641. doi: 10.1126/science.1162912
- Discher, D. E. (2005). Tissue cells feel and respond to the stiffness of their substrate. *Science* 310, 1139–1143. doi: 10.1126/science.1116995
- Doe, C., Bentley, R., Behm, D. J., Lafferty, R., Stavenger, R., Jung, D., et al. (2007). Novel Rho kinase inhibitors with anti-inflammatory and vasodilatory activities. *J. Pharmacol. Exp. Ther.* 320, 89–98. doi: 10.1124/jpet.106.110635
- Dong, J.-M., Lau, L.-S., Ng, Y.-W., Lim, L., and Manser, E. (2009). Paxillin nuclear-cytoplasmic localization is regulated by phosphorylation of the LD 4 motif: evidence that nuclear paxillin promotes cell proliferation. *Biochem. J.* 418, 173–184. doi: 10.1042/BJ20080170
- Dorner, D., Gotzmann, J., and Foisner, R. (2007). Nucleoplasmic lamins and their interaction partners, LAP2 $\alpha$ , Rb, and BAF, in transcriptional regulation. *FEBS J.* 274, 1362–1373. doi: 10.1111/j.1742-4658.2007.05695.x
- dos Santos, P. B., Zanetti, J. S., Ribeiro-Silva, A., and Beltrão, E. I. C. (2012). Beta 1 integrin predicts survival in breast cancer: a clinicopathological and immunohistochemical study. *Diagn. Pathol.* 7:104. doi: 10.1186/1746-1596-7-104
- Driscoll, T. P., Cosgrove, B. D., Heo, S. J., Shurden, Z. E., and Mauck, R. L. (2015). Cytoskeletal to nuclear strain transfer regulates YAP signaling in mesenchymal stem cells. *Biophys. J.* 108, 2783–2793. doi: 10.1016/j.bpj.2015.05.010
- Dumbauld, D. W., Lee, T. T., Singh, A., Scrimgeour, J., Gersbach, C. A., Zamir, E. A., et al. (2013). How vinculin regulates force transmission. *Proc. Natl. Acad. Sci. U.S.A.* 110, 9788–9793. doi: 10.1073/pnas.1216209110
- Dupont, S., Morsut, L., Aragona, M., Enzo, E., Giulitti, S., Cordenonsi, M., et al. (2011). Role of YAP/TAZ in mechanotransduction. *Nature* 474, 179–184. doi: 10.1038/nature10137
- Elosegui-Artola, A., Andreu, I., Beedle, A. E. M., Lezamiz, A., Uroz, M., Kosmalka, A. J., et al. (2017). Force triggers YAP nuclear entry by regulating transport across nuclear pores. *Cell* 171, 1397.e14–1410.e14. doi: 10.1016/j.cell.2017.10.008
- Emery, A. E., and Dreifuss, F. E. (1966). Unusual type of benign x-linked muscular dystrophy. *J. Neurol. Neurosurg. Psychiatry* 29, 338–342. doi: 10.1136/jnnp.29.4.338
- Engler, A. J., Carag-Krieger, C., Johnson, C. P., Raab, M., Tang, H.-Y., Speicher, D. W., et al. (2008). Embryonic cardiomyocytes beat best on a matrix with heart-like elasticity: scar-like rigidity inhibits beating. *J. Cell Sci.* 121, 3794–3802. doi: 10.1242/jcs.029678
- Engler, A. J., Griffin, M. A., Sen, S., Bönnemann, C. G., Sweeney, H. L., and Discher, D. E. (2004). Myotubes differentiate optimally on substrates with tissue-like stiffness: pathological implications for soft or stiff microenvironments. *J. Cell Biol.* 166, 877–887. doi: 10.1083/jcb.200405004
- Engler, A. J., Sen, S., Sweeney, H. L., and Discher, D. E. (2006). Matrix elasticity directs stem cell lineage specification. *Cell* 126, 677–689. doi: 10.1016/j.cell.2006.06.044
- Estes, J. E., Selden, L. A., and Gershman, L. C. (1981). Mechanism of action of phalloidin on the polymerization of muscle actin. *Biochemistry* 20, 708–712. doi: 10.1021/bi00507a006
- Even-Ram, S., Doyle, A. D., Conti, M. A., Matsumoto, K., Adelstein, R. S., and Yamada, K. M. (2007). Myosin IIA regulates cell motility and actomyosin-microtubule crosstalk. *Nat. Cell Biol.* 9, 299–309. doi: 10.1038/ncb1540
- Fabry, B., Klemm, A. H., Kienle, S., Schäffer, T. E., and Goldmann, W. H. (2011). Focal adhesion kinase stabilizes the cytoskeleton. *Biophys. J.* 101, 2131–2138. doi: 10.1016/j.bpj.2011.09.043
- Fabry, B., Maksym, G. N., Butler, J. P., Glogauer, M., Navajas, D., and Fredberg, J. J. (2001). Scaling the microrheology of living cells. *Phys. Rev. Lett.* 87:148102. doi: 10.1103/PhysRevLett.87.148102
- Fan, R., Kim, N.-G., and Gumbiner, B. M. (2013). Regulation of Hippo pathway by mitogenic growth factors via phosphoinositide 3-kinase and phosphoinositide-dependent kinase-1. *Proc. Natl. Acad. Sci. U.S.A.* 110, 2569–2574. doi: 10.1073/pnas.1216462110
- Fedorchak, G. R., Kaminski, A., and Lammerding, J. (2014). Cellular mechanosensing: Getting to the nucleus of it all. *Prog. Biophys. Mol. Biol.* 115, 76–92. doi: 10.1016/j.pbiomolbio.2014.06.009
- Fidziańska, A., and Hausmanowa-Petrusewicz, I. (2003). Architectural abnormalities in muscle nuclei. Ultrastructural differences between X-linked and autosomal dominant forms of EDMD. *J. Neurol. Sci.* 210, 47–51. doi: 10.1016/S0022-510X(03)00012-1
- Filippi, M.-D. (2016). Chapter two - mechanism of diapedesis: importance of the transcellular route. *Adv. Immunol.* 129, 25–53. doi: 10.1016/bs.ai.2015.09.001
- Fink, J., Carpi, N., Betz, T., Bétard, A., Chebah, M., Azioune, A., et al. (2011). External forces control mitotic spindle positioning. *Nat. Cell Biol.* 13, 771–778. doi: 10.1038/ncb2269
- Flatau, G., Lemichez, E., Gauthier, M., Chardin, P., Paris, S., Florentini, C., et al. (1997). Toxin-induced activation of the G protein p21 Rho by deamidation of glutamine. *Nature* 387, 729–733. doi: 10.1038/42743
- Fletcher, D. A., and Mullins, R. D. (2010). Cell mechanics and the cytoskeleton. *Nature* 463, 485–492. doi: 10.1038/nature08908
- Folker, E. S., Ostlund, C., Luxton, G. W. G., Worman, H. J., and Gundersen, G. G. (2011). Lamin A variants that cause striated muscle disease are defective in anchoring transmembrane actin-associated nuclear lines for nuclear movement. *Proc. Natl. Acad. Sci. U.S.A.* 108, 131–136. doi: 10.1073/pnas.1000824108

- Forste, G., Carotenuto, F., Pagliari, F., Pagliari, S., Cossa, P., Fiaccavento, R., et al. (2008). Criticality of the biological and physical stimuli array inducing resident cardiac stem cell determination. *Stem Cells* 26, 2093–2103. doi: 10.1634/stemcells.2008-0061
- Forste, G., Pagliari, S., Ebara, M., Uto, K., Tam, J. K., Romanazzo, S., et al. (2012). Substrate stiffness modulates gene expression and phenotype in neonatal cardiomyocytes in vitro. *Tissue Eng. Part A* 18, 1837–1848. doi: 10.1089/ten.tea.2011.0707
- Fridolfsson, H. N., and Starr, D. A. (2010). Kinesin-1 and dynein at the nuclear envelope mediate the bidirectional migrations of nuclei. *J. Cell Biol.* 191, 115–128. doi: 10.1083/jcb.201004118
- Fujiwara, S., Ohashi, K., Mashiko, T., Kondo, H., and Mizuno, K. (2016). Interplay between Solo and keratin filaments is crucial for mechanical force-induced stress fiber reinforcement. *Mol. Biol. Cell* 27, 954–966. doi: 10.1091/mbc.E15-06-0417
- Fukata, Y., Kaibuchi, K., Amano, M., and Kaibuchi, K. (2001). Rho-Rho-kinase pathway in smooth muscle contraction and cytoskeletal reorganization of non-muscle cells. *Trends Pharmacol. Sci.* 22, 32–39. doi: 10.1016/S0165-6147(00)01596-0
- Galbraith, C. G., Yamada, K. M., and Galbraith, J. A. (2007). Polymerizing actin fibers position integrins primed to probe for adhesion sites. *Science* 315, 992–995. doi: 10.1126/science.1137904
- Giannone, G. (2015). Super-resolution links vinculin localization to function in focal adhesions. *Nat. Cell Biol.* 17, 845–847. doi: 10.1038/ncb3196
- Gimpel, P., Lee, Y. L., Sobota, R. M., Calvi, A., Koullourou, V., Patel, R., et al. (2017). Nesprin-1 $\alpha$ -dependent microtubule nucleation from the nuclear envelope via Akap450 is necessary for nuclear positioning in muscle cells. *Curr. Biol.* 27, 2999.e9–3009.e9. doi: 10.1016/j.cub.2017.08.031
- Gingras, A. R., Ziegler, W. H., Bobkov, A. A., Joyce, M. G., Fasci, D., Himmel, M., et al. (2009). Structural determinants of integrin binding to the talin rod. *J. Biol. Chem.* 284, 8866–8876. doi: 10.1074/jbc.M805937200
- Gingras, A. R., Ziegler, W. H., Frank, R., Barsukov, I. L., Roberts, G. C. K., Critchley, D. R., et al. (2005). Mapping and consensus sequence identification for multiple vinculin binding sites within the talin rod. *J. Biol. Chem.* 280, 37217–37224. doi: 10.1074/jbc.M508060200
- Goffin, J. M., Pittet, P., Csucs, G., Lussi, J. W., Meister, J. J., and Hinz, B. (2006). Focal adhesion size controls tension-dependent recruitment of  $\alpha$ -smooth muscle actin to stress fibers. *J. Cell Biol.* 172, 259–268. doi: 10.1083/jcb.200506179
- Goldman, R. D., Shumaker, D. K., Erdos, M. R., Eriksson, M., Goldman, A. E., Gordon, L. B., et al. (2004). Accumulation of mutant lamin A causes progressive changes in nuclear architecture in Hutchinson-Gilford progeria syndrome. *Proc. Natl. Acad. Sci. U.S.A.* 101, 8963–8968. doi: 10.1073/pnas.0402943101
- Golji, J., and Mofrad, M. R. K. (2014). The talin dimer structure orientation is mechanically regulated. *Biophys. J.* 107, 1802–1809. doi: 10.1016/j.bpj.2014.08.038
- Gottardi, C. J., Arpin, M., Fanning, A. S., and Louvard, D. (1996). The junction-associated protein, zonula occludens-1, localizes to the nucleus before the maturation and during the remodeling of cell-cell contacts. *Proc. Natl. Acad. Sci. U.S.A.* 93, 10779–10784. doi: 10.1073/pnas.93.20.10779
- Graf, K., Neuss, M., Stawowy, P., Hsueh, W. A., Fleck, E., and Law, R. E. (2000). Angiotensin II and v3 integrin expression in rat neonatal cardiac fibroblasts. *Hypertension* 35, 978–984. doi: 10.1161/01.HYP.35.4.978
- Grannas, K., Arngården, L., Lönn, P., Mazurkiewicz, M., Blokzijl, A., Zieba, A., et al. (2015). Crosstalk between hippo and TGF $\beta$ : subcellular localization of YAP/TAZ/Smad Complexes. *J. Mol. Biol.* 427, 3407–3415. doi: 10.1016/j.jmb.2015.04.015
- Gruenbaum, Y., and Medalia, O. (2015). Lamins: the structure and protein complexes. *Curr. Opin. Cell Biol.* 32, 7–12. doi: 10.1016/j.ceb.2014.09.009
- Guilak, F. (1995). Compression-induced changes in the shape and volume of the chondrocyte nucleus. *J. Biomech.* 28, 1529–1541. doi: 10.1016/0021-9290(95)00100-x
- Guilak, F., Tedrow, J. R., and Burgkart, R. (2000). Viscoelastic properties of the cell nucleus. *Biochem. Biophys. Res. Commun.* 269, 781–786. doi: 10.1006/bbrc.2000.2360
- Guilluy, C., Osborne, L. D., Van Landeghem, L., Sharek, L., Superfine, R., Garcia-Mata, R., et al. (2014). Isolated nuclei adapt to force and reveal a mechanotransduction pathway in the nucleus. *Nat. Cell Biol.* 16, 376–381. doi: 10.1038/ncb2927
- Gumbiner, B. (1995). Signal transduction by B-catenin. *Curr. Opin. Cell Biol.* 7, 634–640. doi: 10.1016/0955-0674(95)80104-9
- Haining, A. W. M., Von Essen, M., Attwood, S. J., Hytönen, V. P., and Del Río Hernández, A. (2016). All subdomains of the talin rod are mechanically vulnerable and may contribute to cellular mechanosensing. *ACS Nano* 10, 6648–6658. doi: 10.1021/acsnano.6b01658
- Handorf, A. M., Zhou, Y., Halanski, M. A., and Li, W. J. (2015). Tissue stiffness dictates development, homeostasis, and disease progression. *Organogenesis* 11, 1–15. doi: 10.1080/15476278.2015.1019687
- Hansen, C. G., Moroiishi, T., and Guan, K. L. (2015). YAP and TAZ: a nexus for Hippo signaling and beyond. *Trends Cell Biol.* 25, 499–513. doi: 10.1016/j.tcb.2015.05.002
- Haque, F., Lloyd, D. J., Smallwood, D. T., Dent, C. L., Shanahan, C. M., Fry, A. M., et al. (2006). SUN1 interacts with nuclear lamin A and cytoplasmic nesprins to provide a physical connection between the nuclear lamina and the cytoskeleton. *Mol. Cell Biol.* 26, 3738–3751. doi: 10.1128/MCB.26.10.3738-3751.2006
- Hartman, C. D., Isenberg, B. C., Chua, S. G., and Wong, J. Y. (2016). Vascular smooth muscle cell durotaxis depends on extracellular matrix composition. *Proc. Natl. Acad. Sci. U.S.A.* 113, 11190–11195. doi: 10.1073/pnas.1611324113
- Haskins, J. W., Nguyen, D. X., and Stern, D. F. (2014). Neuregulin 1-activated ERBB4 interacts with YAP to induce Hippo pathway target genes and promote cell migration. *Sci. Signal.* 7:ra116. doi: 10.1126/scisignal.2005770
- Hayakawa, K., Tatsumi, H., and Sokabe, M. (2011). Actin filaments function as a tension sensor by tension-dependent binding of cofilin to the filament. *J. Cell Biol.* 195, 721–727. doi: 10.1083/jcb.201102039
- Hayashi, K., and Iwata, M. (2015). Stiffness of cancer cells measured with an AFM indentation method. *J. Mech. Behav. Biomed. Mater.* 49, 105–111. doi: 10.1016/j.jmbm.2015.04.030
- Head, J., Lee, L. L., Field, D. J., and Lee, J. C. (1985). Equilibrium and rapid kinetic studies on interaction. *J. Biol. Chem.* 260, 11060–11066.
- Heessen, S., and Fornerod, M. (2007). The inner nuclear envelope as a transcription factor resting place. *EMBO Rep.* 8, 914–919. doi: 10.1038/sj.embor.7401075
- Hirata, H., Tatsumi, H., Lim, C. T., and Sokabe, M. (2014). Force-dependent vinculin binding to talin in live cells: a crucial step in anchoring the actin cytoskeleton to focal adhesions. *AJP Cell Physiol.* 306, C607–C620. doi: 10.1152/ajpcell.00122.2013
- Ho, C. Y., Jaalouk, D. E., Vartiainen, M. K., and Lammerding, J. (2013). Lamin A/C and emerin regulate MKL1-SRF activity by modulating actin dynamics. *Nature* 497, 507–511. doi: 10.1038/nature12105
- Ho, C. Y., and Lammerding, J. (2012). Lamins at a glance. *J. Cell Sci.* 125, 2087–2093. doi: 10.1242/jcs.087288
- Hoffman, L. M., Jensen, C. C., Chaturvedi, A., Yoshigi, M., and Beckerle, M. C. (2012). Stretch-induced actin remodeling requires targeting of zyxin to stress fibers and recruitment of actin regulators. *Mol. Biol. Cell* 23, 1846–1859. doi: 10.1091/mbc.E11-12-1057
- Holzinger, A. (2009). Jasplakinolide: an actin-specific reagent that promotes actin polymerization. *Methods Mol. Biol.* 586, 71–87. doi: 10.1007/978-1-60761-376-3\_4
- Hotulainen, P., and Lappalainen, P. (2006). Stress fibers are generated by two distinct actin assembly mechanisms in motile cells. *J. Cell Biol.* 173, 383–394. doi: 10.1083/jcb.200511093
- Huber, O., Korn, R., McLaughlin, J., Ohsugi, M., Herrmann, B. G., and Kemler, R. (1996). Nuclear localization of  $\beta$ -catenin by interaction with transcription factor LEF-1. *Mech. Dev.* 59, 3–10. doi: 10.1016/0925-4773(96)00597-7
- Humphries, J. D., Wang, P., Streuli, C., Geiger, B., Humphries, M. J., and Ballestrem, C. (2007). Vinculin controls focal adhesion formation by direct interactions with talin and actin. *J. Cell Biol.* 179, 1043–1057. doi: 10.1083/jcb.200703036
- Ibarra, A., and Hetzer, M. W. (2015). Nuclear pore proteins and the control of genome functions. *Genes Dev.* 29, 337–349. doi: 10.1101/gad.256495.114
- Ishizaki, T., Uehata, M., Tamechika, I., Keel, J., Nonomura, K., Maekawa, M., et al. (2000). Pharmacological properties of Y-27632, a specific inhibitor of rho-associated kinases. *Mol. Pharmacol.* 57, 976–983.
- Ivorra, C., Kubicek, M., González, J. M., Sanz-González, S. M., Álvarez-Barrientos, A., O'Connor, J. E., et al. (2006). A mechanism of AP-1 suppression



- through interaction of c-Fos with lamin A/C. *Genes Dev.* 20, 307–320. doi: 10.1101/gad.349506
- Iyer, K. V., Pulford, S., Mogilner, A., and Shivashankar, G. V. (2012). Mechanical activation of cells induces chromatin remodeling preceding MKL nuclear transport. *Biophys. J.* 103, 1416–1428. doi: 10.1016/j.bpj.2012.08.041
- Jaalouk, D. E., and Lammerding, J. (2009). Mechanotransduction gone awry. *Nat. Rev. Mol. Cell Biol.* 10, 63–73. doi: 10.1038/nrm2597
- Janošiak, R., Pataki, A. C., Brábek, J., and Rösel, D. (2014). Mechanosensors in integrin signaling: the emerging role of p130Cas. *Eur. J. Cell Biol.* 93, 445–454. doi: 10.1016/j.ejcb.2014.07.002
- Jin, J. K., Tien, P. C., Cheng, C. J., Song, J. H., Huang, C., Lin, S. H., et al. (2015). Talin1 phosphorylation activates  $\beta$ 1 integrins: a novel mechanism to promote prostate cancer bone metastasis. *Oncogene* 34, 1811–1821. doi: 10.1038/onc.2014.116
- Jiu, Y., Lehtimäki, J., Tojkander, S., Cheng, F., Jääliñoja, H., Liu, X., et al. (2015). Bidirectional interplay between vimentin intermediate filaments and contractile actin stress fibers. *Cell Rep.* 11, 1511–1518. doi: 10.1016/j.celrep.2015.05.008
- Jiu, Y., Peränen, J., Schaible, N., Cheng, F., Eriksson, J. E., Krishnan, R., et al. (2017). Vimentin intermediate filaments control actin stress fiber assembly through GEF-H1 and RhoA. *J. Cell Sci.* 130, 892–902. doi: 10.1242/jcs.196881
- Jung, O., Choi, S., Jang, S.-B., Lee, S.-A., Lim, S.-T., Choi, Y.-J., et al. (2012). Tetraspan TM4SF5-dependent direct activation of FAK and metastatic potential of hepatocarcinoma cells. *J. Cell Sci.* 125, 5960–5973. doi: 10.1242/jcs.100586
- Kadmas, J. L., and Beckerle, M. C. (2004). The LIM domain: from the cytoskeleton to the nucleus. *Nat. Rev. Mol. Cell Biol.* 5, 920–931. doi: 10.1038/nrm1499
- Kajikawa, M., Noma, K., Tatsuya, M., Mikami, S., Iwamoto, Y., Iwamoto, A., et al. (2014). Rho-associated kinase activity is a predictor of cardiovascular outcomes. *Hypertension* 63, 856–864. doi: 10.1161/HYPERTENSIONAHA.113.02296
- Kataoka, C., Egashira, K., Inoue, S., Takemoto, M., and Ni, W. (2002). Important role of rho-kinase in the pathogenesis of cardiovascular inflammation and remodeling induced by long-term blockade of nitric oxide synthesis in rats. *Sci. Technol.* 39, 245–250. doi: 10.1161/hy0202.103271
- Kawano, H., Cody, R. J., Graf, K., Goetze, S., Kawano, Y., Schnee, J., et al. (2000). Angiotensin II enhances integrin and alpha-actinin expression in adult rat cardiac fibroblasts. *Hypertension* 35, 273–279. doi: 10.1161/01.HYP.35.1.273
- Khatau, S. B., Hale, C. M., Stewart-Hutchinson, P. J., Patel, M. S., Stewart, C. L., Searson, P. C., et al. (2009). A perinuclear actin cap regulates nuclear shape. *Proc. Natl. Acad. Sci. U.S.A.* 106, 19017–19022. doi: 10.1073/pnas.0908686106
- Kim, D. H., Khatau, S. B., Feng, Y., Walcott, S., Sun, S. X., Longmore, G. D., et al. (2012). Actin cap associated focal adhesions and their distinct role in cellular mechanosensing. *Sci. Rep.* 2:555. doi: 10.1038/srep00555
- Kim, D. H., and Wirtz, D. (2015). Cytoskeletal tension induces the polarized architecture of the nucleus. *Biomaterials* 48, 161–172. doi: 10.1016/j.biomaterials.2015.01.023
- Kim, H. E., Dalal, S. S., Young, E., Legato, M. J., Weisfeldt, M. L., and D'Armiento, J. (2000). Disruption of the myocardial extracellular matrix leads to cardiac dysfunction. *J. Clin. Invest.* 106, 857–866. doi: 10.1172/JCI8040
- Kim, N.-G., Koh, E., Chen, X., and Gumbiner, B. M. (2011). E-cadherin mediates contact inhibition of proliferation through Hippo signaling-pathway components. *Proc. Natl. Acad. Sci. U.S.A.* 108, 11930–11935. doi: 10.1073/pnas.1103345108
- Klaas, M., Kangur, T., Viil, J., Mäemets-Allas, K., Minajeva, A., Vadi, K., et al. (2016). The alterations in the extracellular matrix composition guide the repair of damaged liver tissue. *Sci. Rep.* 6:27398. doi: 10.1038/srep27398
- Klenchin, V. A., King, R., Tanaka, J., Marriott, G., and Rayment, I. (2005). Structural basis of swinholide a binding to actin. *Chem. Biol.* 12, 287–291. doi: 10.1016/j.chembiol.2005.02.011
- Komuro, A., Nagai, M., Navin, N. E., and Sudol, M. (2003). WW domain-containing protein YAP associates with ErbB-4 and acts as a co-transcriptional activator for the carboxyl-terminal fragment of ErbB-4 that translocates to the nucleus. *J. Biol. Chem.* 278, 33334–33341. doi: 10.1074/jbc.M305597200
- Kovács, M., Wang, F., Hu, A., Zhang, Y., and Sellers, J. R. (2003). Functional divergence of human cytoplasmic myosin II. Kinetic characterization of the non-muscle IIA isoform. *J. Biol. Chem.* 278, 38132–38140. doi: 10.1074/jbc.M305453200
- Krendel, M., Zenke, F. T., and Bokoch, G. M. (2002). Nucleotide exchange factor GEF-H1 mediates cross-talk between microtubules and the actin cytoskeleton. *Nat. Cell Biol.* 4, 294–301. doi: 10.1038/ncb773
- Krull, S., Dörries, J., Boysen, B., Reidenbach, S., Magnius, L., Norder, H., et al. (2010). Protein Tpr is required for establishing nuclear pore-associated zones of heterochromatin exclusion. *EMBO J.* 29, 1659–1673. doi: 10.1038/emboj.2010.54
- Lachowski, D., Cortes, E., Robinson, B., Rice, A., Rombouts, K., and Del Río Hernández, A. E. (2018). FAK controls the mechanical activation of YAP, a transcriptional regulator required for durotaxis. *FASEB J.* 32, 1099–1107. doi: 10.1096/fj.201700721R
- Lammerding, J., Schulze, P. C., Takahashi, T., Kozlov, S., Sullivan, T., Kamm, R. D., et al. (2004). Lamin A/C deficiency causes defective nuclear mechanics and mechanotransduction. *J. Clin. Invest.* 113, 370–378. doi: 10.1172/JCI200419670
- Last, J. A., Pan, T., Ding, Y., Reilly, C. M., Keller, K., Acott, T. S., et al. (2011). Elastic modulus determination of normal and glaucomatous human trabecular meshwork. *Investig. Ophthalmol. Vis. Sci.* 52, 2147–2152. doi: 10.1167/iovs.10-6342
- Lauriol, J., Keith, K., Jaffré, F., Couvillon, A., Saci, A., Goonasekera, S. A., et al. (2014). RhoA signaling in cardiomyocytes protects against stress-induced heart failure but facilitates cardiac fibrosis. *Sci. Signal.* 7:ra100. doi: 10.1126/scisignal.2005262
- Lee, S., and Kumar, S. (2016). Actomyosin stress fiber mechanosensing in 2D and 3D. *F1000Res.* 5:2261. doi: 10.12688/f1000research.8800.1
- Lessey, E. C., Guilluy, C., and Burridge, K. (2012). From mechanical force to RhoA activation. *Biochemistry* 51, 7420–7432. doi: 10.1021/bi300758e
- Lewis, J. M., Baskaran, R., Taagepera, S., Schwartz, M. A., and Wang, J. Y. (1996). Integrin regulation of c-Abl tyrosine kinase activity and cytoplasmic-nuclear transport. *Proc. Natl. Acad. Sci. U.S.A.* 93, 15174–15179. doi: 10.1073/pnas.93.26.15174
- Li, Q., Kumar, A., Makhija, E., and Shivashankar, G. V. (2014). The regulation of dynamic mechanical coupling between actin cytoskeleton and nucleus by matrix geometry. *Biomaterials* 35, 961–969. doi: 10.1016/j.biomaterials.2013.10.037
- Li, R., Wu, Y., Manso, A. M., Gu, Y., Liao, P., Israeli, S., et al. (2012).  $\beta$ 1 integrin gene excision in the adult murine cardiac myocyte causes defective mechanical and signaling responses. *Am. J. Pathol.* 180, 952–962. doi: 10.1016/j.ajpath.2011.12.007
- Liu, M., Öberg, K., and Zhou, Y. (2007). Expression and function of vinculin in neuroendocrine tumors. *Tumor Biol.* 28, 196–204. doi: 10.1159/000107415
- Liu, Q., Pante, N., Misteli, T., Elsagga, M., Crisp, M., Hodzic, D., et al. (2007). Functional association of Sun1 with nuclear pore complexes. *J. Cell Biol.* 178, 785–798. doi: 10.1083/jcb.200704108
- Liu, Y. J., Le Berre, M., Lautenschlaeger, F., Maiuri, P., Callan-Jones, A., Heuzé, M., et al. (2015). Confinement and low adhesion induce fast amoeboid migration of slow mesenchymal cells. *Cell* 160, 659–672. doi: 10.1016/j.cell.2015.01.007
- Lombardi, M. L., and Lammerding, J. (2011). Keeping the LINC: the importance of nucleocytoskeletal coupling in intracellular force transmission and cellular function. *Biochem. Soc. Trans.* 39, 1729–1734. doi: 10.1042/BST20110686
- Luis Alonso, J., and Goldmann, W. H. (2016). Cellular mechanotransduction. *AIMS Biophys.* 3, 50–62. doi: 10.3934/biophy.2016.1.50
- Luxton, G. W. G., Gomes, E. R., Folker, E. S., Vintinner, E., and Gundersen, G. G. (2010). Linear arrays of nuclear envelope proteins harness retrograde actin flow for nuclear movement. *Science* 329, 956–959. doi: 10.1126/science.1189072
- Maggi, L., Carboni, N., and Bernasconi, P. (2016). Skeletal muscle laminopathies: a review of clinical and molecular features. *Cells* 5:E33. doi: 10.3390/cells5030033
- Maki, K., Nakao, N., and Adachi, T. (2017). Nano-mechanical characterization of tension-sensitive helix bundles in talin rod. *Biochem. Biophys. Res. Commun.* 484, 372–377. doi: 10.1016/j.bbrc.2017.01.127
- Mallat, Z., Gojova, A., Sauzeau, V., Brun, V., Silvestre, J. S., Esposito, B., et al. (2003). Rho-associated protein kinase contributes to early atherosclerotic lesion formation in mice. *Circ. Res.* 93, 884–888. doi: 10.1161/01.RES.0000099062.55042.9A
- Markiewicz, E., Tilgner, K., Barker, N., Van De Wetering, M., Clevers, H., Dorobek, M., et al. (2006). The inner nuclear membrane protein Emerin regulates  $\beta$ -catenin activity by restricting its accumulation in the nucleus. *EMBO J.* 25, 3275–3285. doi: 10.1038/sj.emboj.7601230

- Martinac, B. (2014). The ion channels to cytoskeleton connection as potential mechanism of mechanosensitivity. *Biochim. Biophys. Acta* 1838, 682–691. doi: 10.1016/j.bbame.2013.07.015
- McBeath, R., Pirone, D. M., Nelson, C. M., Bhadriraju, K., and Chen, C. S. (2004). Cell shape, cytoskeletal tension, and RhoA regulate stem cell lineage commitment. *Dev. Cell* 6, 483–495. doi: 10.1016/S1534-5807(04)00075-9
- McGough, A., Pope, B., Chiu, W., and Weeds, A. (1997). Cofilin changes the twist of F-actin: implications for actin filament dynamics and cellular function. *J. Cell Biol.* 138, 771–781. doi: 10.1083/jcb.138.4.771
- Meacci, G., Wolfenson, H., Liu, S., Stachowiak, M. R., Iskratsch, T., Mathur, A., et al. (2016).  $\alpha$ -Actinin links extracellular matrix rigidity-sensing contractile units with periodic cell-edge retractions. *Mol. Biol. Cell* 27, 3471–3479. doi: 10.1091/mbc.E16-02-0107
- Meinke, P., Mattioli, E., Haque, F., Antoku, S., Columbaro, M., Straatman, K. R., et al. (2014). Muscular dystrophy-associated SUN1 and SUN2 variants disrupt nuclear-cytoskeletal connections and myonuclear organization. *PLoS Genet.* 10:e1004605. doi: 10.1371/journal.pgen.1004605
- Méjat, A., and Misteli, T. (2010). LINC complexes in health and disease. *Nucleus* 1, 40–52. doi: 10.4161/nucl.1.1.10530
- Michael, K. E., Dumbauld, D. W., Burns, K. L., Hanks, S. K., and Garcia, A. J. (2009). Focal adhesion kinase modulates cell adhesion strengthening via integrin activation. *Mol. Biol. Cell* 20, 2508–2519. doi: 10.1091/mbc.E08-01-0076
- Mierke, C. T., Kollmannsberger, P., Zitterbart, D. P., Smith, J., Fabry, B., and Goldmann, W. H. (2008). Mechano-coupling and regulation of contractility by the vinculin tail domain. *Biophys. J.* 94, 661–670. doi: 10.1529/biophysj.107.108472
- Milloud, R., Destaing, O., de Mets, R., Bourrin-Reynard, I., Oddou, C., Delon, A., et al. (2017).  $\alpha$ v $\beta$ 3 integrins negatively regulate cellular forces by phosphorylation of its distal NPXY site. *Biol. Cell* 109, 127–137. doi: 10.1111/boc.201600041
- Miralles, F., Posern, G., Zaromytidou, A. I., and Treisman, R. (2003). Actin dynamics control SRF activity by regulation of its coactivator MAL. *Cell* 113, 329–342. doi: 10.1016/S0092-8674(03)00278-2
- Mo, J. S., Yu, F. X., Gong, R., Brown, J. H., and Guan, K. L. (2012). Regulation of the Hippo-YAP pathway by protease-activated receptors (PARs). *Genes Dev.* 26, 2138–2143. doi: 10.1101/gad.197582.112
- Morikawa, Y., Zhang, M., Heallen, T., Leach, J., Tao, G., Xiao, Y., et al. (2015). Actin cytoskeletal remodeling with protrusion formation is essential for heart regeneration in Hippo-deficient mice. *Sci. Signal.* 8:ra41. doi: 10.1126/scisignal.2005781
- Morton, W. M., Ayscough, K. R., and McLaughlin, P. J. (2000). Latrunculin alters the actin-monomer subunit interface to prevent polymerization. *Nat. Cell Biol.* 2, 376–378. doi: 10.1038/35014075
- Mosqueira, D., Pagliari, S., Uto, K., Ebara, M., Romanazzo, S., Escobedo-Lucea, C., et al. (2014). Hippo pathway effectors control cardiac progenitor cell fate by acting as dynamic sensors of substrate mechanics and nanostructure. *ACS Nano* 8, 2033–2047. doi: 10.1021/nn4058984
- Nardone, G., Oliver-De La Cruz, J., Vrbsky, J., Martini, C., Pribyl, J., Skládal, P., et al. (2017). YAP regulates cell mechanics by controlling focal adhesion assembly. *Nat. Commun.* 8:15321. doi: 10.1038/ncomms15321
- Natarajan, V., Berglund, E. J., Chen, D. X., and Kidambi, S. (2015). Substrate elasticity regulates primary hepatocyte functions. *RSC Adv.* 5:80956. doi: 10.1039/C5RA15208A
- Naumanen, P., Lappalainen, P., and Hotulainen, P. (2008). Mechanisms of actin stress fibre assembly. *J. Microsc.* 231, 446–454. doi: 10.1111/j.1365-2818.2008.02057.x
- Navarro, C. L., Cau, P., and Lévy, N. (2006). Molecular bases of progeroid syndromes. *Hum. Mol. Genet.* 15Spec No 2:R151–R161. doi: 10.1093/hmg/ddl214
- Neelam, S., Chancellor, T. J., Li, Y., Nickerson, J. A., Roux, K. J., Dickinson, R. B., et al. (2015). Direct force probe reveals the mechanics of nuclear homeostasis in the mammalian cell. *Proc. Natl. Acad. Sci. U.S.A.* 112, 5720–5725. doi: 10.1073/pnas.1502111112
- Neumann, J., and Gottschalk, K. E. (2016). The integrin-talin complex under force. *Protein Eng. Des. Sel.* 29, 503–512. doi: 10.1093/protein/gzw031
- Nguyen, A. T., Sathe, S. R., and Yim, E. K. F. (2016). From nano to micro: topographical scale and its impact on cell adhesion, morphology and contact guidance. *J. Phys. Condens. Matter.* 28:183001. doi: 10.1088/0953-8984/28/18/183001
- Nikolova, V., Leimena, C., McMahon, A. C., Tan, J. C., Chandar, S., Jogle, D., et al. (2004). Defects in nuclear structure and function promote dilated cardiomyopathy in lamin A/C-deficient mice. *J. Clin. Invest.* 113, 357–369. doi: 10.1172/JCI200419448
- Nikolova-Krstevski, V., Leimena, C., Xiao, X. H., Kesteven, S., Tan, J. C., Yeo, L. S., et al. (2011). Nesprin-1 and actin contribute to nuclear and cytoskeletal defects in lamin A/C-deficient cardiomyopathy. *J. Mol. Cell. Cardiol.* 50, 479–486. doi: 10.1016/j.yjmcc.2010.12.001
- Nix, D. A., and Beckerle, M. C. (1997). Nuclear-cytoplasmic shuttling of the focal contact protein, zyxin: a potential mechanism for communication between sites of cell adhesion and the nucleus. *J. Cell Biol.* 138, 1139–1147. doi: 10.1083/jcb.138.5.1139
- Oka, T., and Sudol, M. (2009). Nuclear localization and pro-apoptotic signaling of YAP2 require intact PDZ-binding motif. *Genes Cells* 14, 607–615. doi: 10.1111/j.1365-2443.2009.01292.x
- Olson, E. N., and Nordheim, A. (2010). Linking actin dynamics and gene transcription to drive cellular motile functions. *Nat. Rev. Mol. Cell Biol.* 11, 353–365. doi: 10.1038/nrm2890
- Oria, R., Wiegand, T., Escibano, J., Elosegui-Artola, A., Uriarte, J. J., Moreno-Pulido, C., et al. (2017). Force loading explains spatial sensing of ligands by cells. *Nature* 552, 219–224. doi: 10.1038/nature24662
- Orsulic, S., and Peifer, M. (1996). An in vivo structure-function study of Armadillo, the  $\beta$ -catenin homologue, reveals both separate and overlapping regions of the protein required for cell adhesion and for wingless signaling. *J. Cell Biol.* 134, 1283–1300. doi: 10.1083/jcb.134.5.1283
- Osmanagic-Myers, S., Dechat, T., and Foisner, R. (2015). Lamins at the crossroads of mechanosignaling. *Genes Dev.* 29, 225–237. doi: 10.1101/gad.25596.8.114
- Palazzo, A. F., Cook, T. A., Alberts, A. S., and Gunderson, G. G. (2001). mDia mediates Rho-regulated formation and orientation of stable microtubules. *Nat. Cell Biol.* 3, 723–729. doi: 10.1038/35087035
- Park, J., Bauer, S., Von Der Mark, K., and Schmuki, P. (2007). Nanosize and vitality: TiO<sub>2</sub> nanotube diameter directs cell fate. *Nano Lett.* 7, 1686–1691. doi: 10.1021/nl070678d
- Parker, M. W., Rossi, D., Peterson, M., Smith, K., Sikstroff, K., White, E. S., et al. (2014). Fibrotic extracellular matrix activates a profibrotic positive feedback loop. *J. Clin. Invest.* 124, 1622–1635. doi: 10.1172/JCI71386
- Pasapera, A. M., Schneider, I. C., Rericha, E., Schlaepfer, D. D., and Waterman, C. M. (2010). Myosin II activity regulates vinculin recruitment to focal adhesions through FAK-mediated paxillin phosphorylation. *J. Cell Biol.* 188, 877–890. doi: 10.1083/jcb.200906012
- Paul, C. D., Hung, W., and Wirtz, D. (2017). Engineered models of confined cell migration. *Annu. Rev. Biomed. Eng.* 18, 159–180. doi: 10.1146/annurev-bioeng-071114-040654.Engineered
- Pellegrin, S., and Mellor, H. (2007). Actin stress fibres. *J. Cell Sci.* 120, 3491–3499. doi: 10.1242/jcs.018473
- Peter, A. K., Cheng, H., Ross, R. S., Knowlton, K. U., and Chen, J. (2011). The costamere bridges sarcomeres to the sarcolemma in striated muscle. *Prog. Pediatr. Cardiol.* 31, 83–88. doi: 10.1016/j.ppedcard.2011.02.003
- Peterson, L. J., Rajfur, Z., Maddox, A. S., Freel, C. D., Chen, Y., Edlund, M., et al. (2004). Simultaneous stretching and contraction of stress fibers in vivo. *Mol. Biol. Cell* 15, 3497–3508. doi: 10.1091/mbc.E03
- Phrommintikul, A., Tran, L., Kompa, A., Wang, B., Adrahtas, A., Cantwell, D., et al. (2008). Effects of a Rho kinase inhibitor on pressure overload induced cardiac hypertrophy and associated diastolic dysfunction. *Am. J. Physiol. Heart Circ. Physiol.* 294, H1804–H1814. doi: 10.1152/ajpheart.01078.2007
- Plessner, M., Melak, M., Chinchilla, P., Baarlink, C., and Grosse, R. (2015). Nuclear F-actin phalloidin nuclear F-actin formation and reorganization upon cell spreading. *J. Biol. Chem.* 290, 11209–11216. doi: 10.1074/jbc.M114.627166
- Pollard, T. D., and Cooper, J. A. (2009). Actin, a central player in cell shape and movement. *Science* 326, 1208–1212. doi: 10.1126/science.1175862
- Poudel, I., Menter, D. E., and Lim, J. Y. (2012). Directing cell function and fate via micropatterning: role of cell patterning size, shape, and interconnectivity. *Biomed. Eng. Lett.* 2, 38–45. doi: 10.1007/s13534-012-0045-z

- Prokocimer, M., Davidovich, M., Nissim-Rafinia, M., Wiesel-Motiuk, N., Bar, D. Z., Barkan, R., et al. (2009). Nuclear lamins: key regulators of nuclear structure and activities. *J. Cell. Mol. Med.* 13, 1059–1085. doi: 10.1111/j.1582-4934.2008.00676.x
- Qin, R., Schmid, H., Münzberg, C., Maass, U., Krndija, D., Adler, G., et al. (2015). Phosphorylation and turnover of paxillin in focal contacts is controlled by force and defines the dynamic state of the adhesion site. *Cytoskeleton* 72, 101–112. doi: 10.1002/cm.21209
- Rahikainen, R., Von Essen, M., Schaefer, M., Qi, L., Azizi, L., Kelly, C., et al. (2017). Mechanical stability of talin rod controls cell migration and substrate sensing. *Sci. Rep.* 7:3571. doi: 10.1038/s41598-017-03335-2
- Rao, S., Krauss, N. E., Heerding, J. M., Swindell, C. S., Ringel, I., Orr, G. A., et al. (1994). 3'-(p-Azidobenzamido)taxol photolabels the N-terminal 31 amino acids of  $\beta$ -tubulin. *J. Biol. Chem.* 269, 3132–3134.
- Razinia, Z., Castagnino, P., Xu, T., Vázquez-Salgado, A., Puré, E., and Assoian, R. K. (2017). Stiffness-dependent motility and proliferation uncoupled by deletion of CD44. *Sci. Rep.* 7:16499. doi: 10.1038/s41598-017-16486-z
- Reid, S. E., Kay, E. J., Neilson, L. J., Henze, A.-T., Serneels, J., McGhee, E. J., et al. (2017). Tumor matrix stiffness promotes metastatic cancer cell interaction with endothelium. *EMBO J.* 36, 2373–2389. doi: 10.15252/embj.201694912
- Roca-Cusachs, P., del Rio, A., Puklin-Faucher, E., Gauthier, N. C., Biais, N., and Sheetz, M. P. (2013). Integrin-dependent force transmission to the extracellular matrix by  $\alpha$ -actinin triggers adhesion maturation. *Proc. Natl. Acad. Sci. U.S.A.* 110, E1361–E1370. doi: 10.1073/pnas.1220723110
- Rubashkin, M. G., Cassereau, L., Bainer, R., DuFort, C. C., Yui, Y., Ou, G., et al. (2014). Force engages vinculin and promotes tumor progression by enhancing PI3K activation of phosphatidylinositol (3,4,5)-triphosphate. *Cancer Res.* 74, 4597–4611. doi: 10.1158/0008-5472.CAN-13-3698
- Saha, K., Keung, A. J., Irwin, E. F., Li, Y., Little, L., Schaffer, D. V., et al. (2008). Substrate modulus directs neural stem cell behavior. *Biophys. J.* 95, 4426–4438. doi: 10.1529/biophysj.108.132217
- Saito, S. Y., Watabe, S., Ozaki, H., Fusetani, N., and Karaki, H. (1994). Mycalolide B, a novel actin depolymerizing agent. *J. Biol. Chem.* 269, 29710–29714.
- Saitoh, M., Ishikawa, T., Matsushima, S., Naka, M., and Hidaka, H. (1987). Selective inhibition of catalytic activity of smooth muscle myosin light chain kinase. *J. Biol. Chem.* 262, 7796–7801.
- Sakamoto, S., and Kyprianou, N. (2010). Targeting anoikis resistance in prostate cancer metastasis. *Mol. Aspects Med.* 31, 205–214. doi: 10.1016/j.mam.2010.02.001
- Sakamoto, S., McCann, R. O., Dhir, R., and Kyprianou, N. (2010). Talin1 promotes tumor invasion and metastasis via focal adhesion signaling and anoikis resistance. *Cancer Res.* 70, 1885–1895. doi: 10.1158/0008-5472.CAN-09-2833
- Sathe, A. R., Shivashankar, G. V., and Sheetz, M. P. (2016). Nuclear transport of paxillin depends on focal adhesion dynamics and FAT domains. *J. Cell Sci.* 129, 1981–1988. doi: 10.1242/jcs.172643
- Sawada, Y., Tamada, M., Dubin-Thaler, B. J., Cherniavskaya, O., Sakai, R., Tanaka, S., et al. (2006). Force sensing by mechanical extension of the Src family kinase substrate p130Cas. *Cell* 127, 1015–1026. doi: 10.1016/j.cell.2006.09.044
- Scaffidi, P., and Misteli, T. (2006). Lamin A – dependent nuclear defects in human aging. *Environ. Heal.* 312, 1059–1063. doi: 10.1126/science.1127168
- Scaffidi, P., and Misteli, T. (2008). Lamin A-dependent misregulation of adult stem cells associated with accelerated ageing. *Nat. Cell Biol.* 10, 452–459. doi: 10.1038/ncb1708
- Schiller, H. B., and Fässler, R. (2013). Mechanosensitivity and compositional dynamics of cell-matrix adhesions. *EMBO Rep.* 14, 509–519. doi: 10.1038/embor.2013.49
- Schiller, H. B., Hermann, M. R., Polleux, J., Vignaud, T., Zanivan, S., Friedel, C. C., et al. (2013).  $\beta$  1 - And  $\alpha$  v -class integrins cooperate to regulate myosin II during rigidity sensing of fibronectin-based microenvironments. *Nat. Cell Biol.* 15, 625–636. doi: 10.1038/ncb2747
- Schreiber, K. H., and Kennedy, B. K. (2013). When lamins go bad: Nuclear structure and disease. *Cell* 152, 1365–1375. doi: 10.1016/j.cell.2013.02.015
- Seetharaman, S., and Etienne-Manneville, S. (2018). Integrin diversity brings specificity in mechanotransduction. *Biol. Cell* 110, 49–64. doi: 10.1111/boc.201700060
- Seo, C. H., Furukawa, K., Montagne, K., Jeong, H., and Ushida, T. (2011). The effect of substrate microtopography on focal adhesion maturation and actin organization via the RhoA/ROCK pathway. *Biomaterials* 32, 9568–9575. doi: 10.1016/j.biomaterials.2011.08.077
- Shi, J., Takahashi, S., Jin, X. H., Li, Y. Q., Ito, Y., Mori, Y., et al. (2007). Myosin light chain kinase-independent inhibition by ML-9 of murine TRPC6 channels expressed in HEK293 cells. *Br. J. Pharmacol.* 152, 122–131. doi: 10.1038/sj.bj.0707368
- Shiu, J. Y., Aires, L., Lin, Z., and Vogel, V. (2018). Nanopillar force measurements reveal actin-cap-mediated YAP mechanotransduction. *Nat. Cell Biol.* 20, 262–271. doi: 10.1038/s41556-017-0030-y
- Shkumatov, A., Thompson, M., Choi, K. M., Sicard, D., Baek, K., Kim, D. H., et al. (2015). Matrix stiffness-modulated proliferation and secretory function of the airway smooth muscle cells. *Am. J. Physiol. Lung Cell. Mol. Physiol.* 308, L1125–L1135. doi: 10.1152/ajplung.00154.2014
- Skoufias, D. A., and Wilson, L. (1992). Mechanism of inhibition of microtubule polymerization by colchicine: inhibitory potencies of unliganded colchicine and tubulin-colchicine complexes. *Biochemistry* 31, 738–746. doi: 10.1021/bi00118a015
- Small, J. V., Rottner, K., Kaverina, I., and Anderson, K. I. (1998). Assembling an actin cytoskeleton for cell attachment and movement. *Biochim. Biophys. Acta* 1404, 271–281. doi: 10.1016/S0167-4889(98)00080-9
- Smith, L., Cho, S., and Discher, D. E. (2017). Title: Mechanosensing of matrix by stem cells: from contractility and matrix heterogeneity to cardiogenesis and muscle stem cells. *Semin. Cell Dev. Biol.* 71, 84–98. doi: 10.1016/j.semcdb.2017.05.025
- Smith, M. A., Blankman, E., Deakin, N. O., Hoffman, L. M., Jensen, C. C., Turner, C. E., et al. (2013). LIM domains target actin regulators paxillin and zyxin to sites of stress fiber strain. *PLoS One* 8:e69378. doi: 10.1371/journal.pone.0069378
- Snider, N. T., and Omary, M. B. (2014). Post-translational modifications of intermediate filament proteins: Mechanisms and functions. *Nat. Rev. Mol. Cell Biol.* 15, 163–177. doi: 10.1038/nrm3753
- Sörensen, P. M., Jacob, R. E., Fritzsche, M., Engen, J. R., Briehner, W. M., Charras, G., et al. (2012). The natural product cucurbitacin e inhibits depolymerization of actin filaments. *ACS Chem. Biol.* 7, 1502–1508. doi: 10.1021/cb300254s
- Sosa, B. A., Rothballer, A., Kutay, U., and Schwartz, T. U. (2012). LINC complexes form by binding of three KASH peptides to domain interfaces of trimeric SUN proteins. *Cell* 149, 1035–1047. doi: 10.1016/j.cell.2012.03.046
- Spinale, F. G. (2007). Myocardial matrix remodeling and the matrix metalloproteinases: influence on cardiac form and function. *Physiol. Rev.* 87, 1285–1342. doi: 10.1152/physrev.00012.2007
- Stewart, J. A., Gardner, J. D., Brower, G. L., and Janicki, J. S. (2014). Temporal changes in integrin-mediated cardiomyocyte adhesion secondary to chronic cardiac volume overload in rats. *Am. J. Physiol. Heart Circ. Physiol.* 306, H101–H108. doi: 10.1152/ajpheart.00541.2013
- Straight, A. F., Cheung, A., Limouze, J., Chen, I., Westwood, N. J., Sellers, J. R., et al. (2003). Dissecting temporal and spatial control of cytokinesis with a myosin II inhibitor. *Science* 299, 1743–1747. doi: 10.1126/science.1081412
- Strohmeier, N., Bharadwaj, M., Costell, M., Fässler, R., and Müller, D. J. (2018). Fibronectin-bound  $\alpha$ 5 $\beta$ 1 integrins sense load and signal to reinforce adhesion in less than a second. *Nat. Mater.* 16, 1262–1270. doi: 10.1038/NMAT5023
- Sullivan, T., Escalante-Alcalde, D., Bhatt, H., Anver, M., Bhat, N., Nagashima, K., et al. (1999). Loss of A-type lamin expression compromises nuclear envelope integrity leading to muscular dystrophy. *J. Cell Biol.* 147, 913–919. doi: 10.1083/jcb.147.5.913
- Surma, M., Wei, L., and Shi, J. (2011). Rho kinase as a therapeutic target in cardiovascular disease. *Future Cardiol.* 7, 657–671. doi: 10.2217/fca.11.51
- Swift, J., Ivanovska, I. L., Buxboim, A., Harada, T., Dingal, P. C. D. P., Pinter, J., et al. (2013). Nuclear lamin-A scales with tissue stiffness and enhances matrix-directed differentiation. *Science* 341:1240104. doi: 10.1126/science.1240104
- Tamada, M., Sheetz, M. P., and Sawada, Y. (2004). Activation of a signaling cascade by cytoskeleton stretch. *Dev. Cell* 7, 709–718. doi: 10.1016/j.devcel.2004.08.021
- Tan, Y., Tajik, A., Chen, J., Jia, Q., Chowdhury, F., Wang, L., et al. (2014). Matrix softness regulates plasticity of tumour-repopulating cells via H3K9 demethylation and Sox2 expression. *Nat. Commun.* 5:4619. doi: 10.1038/ncomms5619
- Taranum, S., Sur, I., Müller, R., Lu, W., Rashmi, R. N., Munck, M., et al. (2012). Cytoskeletal interactions at the nuclear envelope mediated by Nesprins. *Int. J. Cell Biol.* 2012:736524. doi: 10.1155/2012/736524

- Tautzenberger, A., Förtsch, C., Zwerger, C., Dmochewitz, L., Kreja, L., Ignatius, A., et al. (2013). C3 Rho-inhibitor for targeted pharmacological manipulation of osteoclast-like cells. *PLoS One* 8:e85695. doi: 10.1371/journal.pone.0085695
- Teixeira, A., McKie, G., Foley, J., Bertics, P., Nealey, P., and Murphy, C. (2006). The effect of environmental factors on the response of human corneal epithelial cells to nanoscale substrate topography. *Biomaterials* 27, 3945–3954. doi: 10.1038/ja.2013.113.Ventriculidin
- Teo, B. K. K., Wong, S. T., Lim, C. K., Kung, T. Y. S., Yap, C. H., Ramagopal, Y., et al. (2013). Nanotopography modulates mechanotransduction of stem cells and induces differentiation through focal adhesion kinase. *ACS Nano* 7, 4785–4798. doi: 10.1021/nn304966z
- Terry, D. R., Spector, I., Higa, T., and Bubba, M. R. (1997). Misakinolide A is a marine macrolide that caps but does not sever filamentous actin. *J. Biol. Chem.* 272, 7841–7845. doi: 10.1074/jbc.272.12.7841
- Tojkander, S., Gateva, G., and Lappalainen, P. (2012). Actin stress fibers - assembly, dynamics and biological roles. *J. Cell Sci.* 125, 1855–1864. doi: 10.1242/jcs.098087
- Tse, J. R., and Engler, A. J. (2011). Stiffness gradients mimicking in vivo tissue variation regulate mesenchymal stem cell fate. *PLoS One* 6:e15978. doi: 10.1371/journal.pone.0015978
- Uemura, A., Nguyen, T. N., Steele, A. N., and Yamada, S. (2011). The LIM domain of zyxin is sufficient for force-induced accumulation of zyxin during cell migration. *Biophys. J.* 101, 1069–1075. doi: 10.1016/j.bpj.2011.08.001
- Uzer, G., Rubin, C. T., and Rubin, J. (2016). Cell mechanosensitivity is enabled by the LINC nuclear complex. *Curr. Mol. Biol. Rep.* 2, 36–47. doi: 10.1007/s40610-016-0032-8
- Valbuena, A., Vera, A. M., Oroz, J., Menéndez, M., and Carrión-Vázquez, M. (2012). Mechanical properties of  $\beta$ -catenin revealed by single-molecule experiments. *Biophys. J.* 103, 1744–1752. doi: 10.1016/j.bpj.2012.07.051
- Vincent, L. G., Choi, Y. S., Alonso-Latorre, B., Del Álamo, J. C., and Engler, A. J. (2013). Mesenchymal stem cell durotaxis depends on substrate stiffness gradient strength. *Biotechnol. J.* 8, 472–484. doi: 10.1002/biot.201200205
- Wang, N., Tytell, J. D., and Ingber, D. E. (2009). Mechanotransduction at a distance: Mechanically coupling the extracellular matrix with the nucleus. *Nat. Rev. Mol. Cell Biol.* 10, 75–82. doi: 10.1038/nrm2594
- Wang, Y., Yu, Y., Li, G. B., Li, S. A., Wu, C., Gigant, B., et al. (2017). Mechanism of microtubule stabilization by taccalonolide AJ. *Nat. Commun.* 8:15787. doi: 10.1038/ncomms15787
- Webster, K. D., Ng, W. P., and Fletcher, D. A. (2014). Tensional homeostasis in single fibroblasts. *Biophys. J.* 107, 146–155. doi: 10.1016/j.bpj.2014.04.051
- Wei, S. C., and Yang, J. (2016). Forcing through tumor metastasis: the interplay between tissue rigidity and epithelial-mesenchymal transition. *Trends Cell Biol.* 26, 111–120. doi: 10.1016/j.tcb.2015.09.009
- Wiesel, N., Mattout, A., Melcer, S., Melamed-Book, N., Herrmann, H., Medalia, O., et al. (2008). Laminopathic mutations interfere with the assembly, localization, and dynamics of nuclear lamins. *Proc. Natl. Acad. Sci. U.S.A.* 105, 180–185. doi: 10.1073/pnas.0708974105
- Wiggin, O., Shaw, A. E., DeLuca, J. G., and Bamburg, J. R. (2012). ADF/cofilin regulates actomyosin assembly through competitive inhibition of myosin II binding to F-actin. *Dev. Cell* 22, 530–543. doi: 10.1016/j.devcel.2011.12.026
- Wilkinson, F. L., Holaska, J. M., Zhang, Z., Sharma, A., Manilal, S., Holt, I., et al. (2003). Emerin interacts in vitro with the splicing-associated factor, YT521-B. *Eur. J. Biochem.* 270, 2459–2466. doi: 10.1046/j.1432-1033.2003.03617.x
- Worman, H. J., and Bonne, G. (2007). “Laminopathies”: a wide spectrum of human diseases. *Exp. Cell Res.* 313, 2121–2133. doi: 10.1016/j.yexcr.2007.03.028
- Worman, H. J., Fong, L. G., Muchir, A., and Young, S. G. (2009). Laminopathies and the long strange trip from basic cell biology to therapy. *J. Clin. Invest.* 119, 1825–1836. doi: 10.1172/JCI37679
- Xiang, S. Y., Vanhoutte, D., Del Re, D. P., Purcell, N. H., Ling, H., Banerjee, I., et al. (2011). RhoA protects the mouse heart against ischemia/reperfusion injury. *J. Clin. Invest.* 121, 3269–3276. doi: 10.1172/JCI44371
- Yamaguchi, H., Kasa, M., Amano, M., Kaibuchi, K., and Hakoshima, T. (2006). Molecular mechanism for the regulation of rho-kinase by dimerization and its inhibition by fasudil. *Structure* 14, 589–560. doi: 10.1016/j.str.2005.11.024
- Yamashita, H., Ichikawa, T., Matsuyama, D., Kimura, Y., Ueda, K., Craig, S. W., et al. (2014). The role of the interaction of the vinculin proline-rich linker region with vinexin in sensing the stiffness of the extracellular matrix. *J. Cell Sci.* 127, 1875–1886. doi: 10.1242/jcs.133645
- Yao, M., Goult, B. T., Klapholz, B., Hu, X., Toseland, C. P., Guo, Y., et al. (2016). The mechanical response of talin. *Nat. Commun.* 7:11966. doi: 10.1038/ncomms11966
- Yeh, Y. T., Hur, S. S., Chang, J., Wang, K. C., Chiu, J. J., Li, Y. S., et al. (2012). Matrix stiffness regulates endothelial cell proliferation through septin 9. *PLoS One* 7:e46889. doi: 10.1371/journal.pone.0046889
- Yim, E. K. F., Pang, S. W., and Leong, K. W. (2007). Synthetic nanostructures inducing differentiation of human mesenchymal stem cells into neuronal lineage. *Exp. Cell Res.* 313, 1820–1829. doi: 10.1016/j.yexcr.2007.02.031
- Yoshigi, M., Hoffman, L. M., Jensen, C. C., Yost, H. J., and Beckerle, M. C. (2005). Mechanical force mobilizes zyxin from focal adhesions to actin filaments and regulates cytoskeletal reinforcement. *J. Cell Biol.* 171, 209–215. doi: 10.1083/jcb.200505018
- Yutao, X., Geru, W., Xiaojun, B., Tao, G., and Aiqun, M. (2006). Mechanical stretch-induced hypertrophy of neonatal rat ventricular myocytes is mediated by  $\beta$ 1-integrin-microtubule signaling pathways. *Eur. J. Heart Fail.* 8, 16–22. doi: 10.1016/j.ejheart.2005.05.014
- Zanconato, F., Cordenonsi, M., and Piccolo, S. (2016). YAP/TAZ at the roots of cancer. *Cancer Cell* 29, 783–803. doi: 10.1016/j.ccell.2016.05.005
- Zanconato, F., Forcato, M., Battilana, G., Azzolin, L., Quaranta, E., Bodega, B., et al. (2015). Genome-wide association between YAP/TAZ/TEAD and AP-1 at enhancers drives oncogenic growth. *Nat. Cell Biol.* 17, 1218–1227. doi: 10.1038/ncb3216
- Zarkoob, H., Bodduluri, S., Ponnaluri, S. V., Selby, J. C., and Sander, E. A. (2015). Substrate stiffness affects human keratinocyte colony formation. *Cell. Mol. Bioeng.* 8, 32–50. doi: 10.1007/s12195-015-0377-8
- Zhang, J., Guo, W.-H., and Wang, Y.-L. (2014). Microtubules stabilize cell polarity by localizing rear signals. *Proc. Natl. Acad. Sci. U.S.A.* 111, 16383–16388. doi: 10.1073/pnas.1410533111
- Zhou, D. W., Lee, T. T., Weng, S., Fu, J., and García, A. J. (2017). Effects of substrate stiffness and actomyosin contractility on coupling between force transmission and vinculin-paxillin recruitment at single focal adhesions. *Mol. Biol. Cell* 28, 1901–1911. doi: 10.1091/mbc.E17-02-0116
- Zhou, J., Aponte-Santamaría, C., Sturm, S., Bullerjahn, J. T., Bronowska, A., and Gräter, F. (2015). Mechanism of focal adhesion kinase mechanosensing. *PLoS Comput. Biol.* 11:e1004593. doi: 10.1371/journal.pcbi.1004593
- Zigmond, S. H. (2004). Formin-induced nucleation of actin filaments. *Curr. Opin. Cell Biol.* 16, 99–105. doi: 10.1016/j.ceb.2003.10.019
- Zwerger, M., Jaalouk, D. E., Lombardi, M. L., Isermann, P., Mauermann, M., Dialynas, G., et al. (2013). Myopathic lamin mutations impair nuclear stability in cells and tissue and disrupt nucleo-cytoskeletal coupling. *Hum. Mol. Genet.* 22, 2335–2349. doi: 10.1093/hmg/ddt079

**Conflict of Interest Statement:** The authors declare that the research was conducted in the absence of any commercial or financial relationships that could be construed as a potential conflict of interest.

Copyright © 2018 Martino, Perestrelo, Vinarský, Pagliari and Forte. This is an open-access article distributed under the terms of the Creative Commons Attribution License (CC BY). The use, distribution or reproduction in other forums is permitted, provided the original author(s) and the copyright owner(s) are credited and that the original publication in this journal is cited, in accordance with accepted academic practice. No use, distribution or reproduction is permitted which does not comply with these terms.



# Every Breath You Take: Non-invasive Real-Time Oxygen Biosensing in Two- and Three-Dimensional Microfluidic Cell Models

Helene Zirath<sup>1,2\*†</sup>, Mario Rothbauer<sup>1,2\*†</sup>, Sarah Spitz<sup>1,2†</sup>, Barbara Bachmann<sup>1,2,3†</sup>, Christian Jordan<sup>1</sup>, Bernhard Müller<sup>4</sup>, Josef Ehgartner<sup>4</sup>, Eleni Priglinger<sup>2,3</sup>, Severin Mühleder<sup>2,3</sup>, Heinz Redl<sup>2,3</sup>, Wolfgang Holthoner<sup>2,3</sup>, Michael Harasek<sup>1</sup>, Torsten Mayr<sup>4</sup> and Peter Ertl<sup>1,2</sup>

<sup>1</sup> Institute of Applied Synthetic Chemistry, Institute of Chemical Technologies and Analytics, Institute of Chemical, Environmental and Bioscience Engineering, Vienna University of Technology, Vienna, Austria, <sup>2</sup> Austrian Cluster for Tissue Regeneration, Vienna, Austria, <sup>3</sup> Ludwig Boltzmann Institute for Experimental and Clinical Traumatology, Allgemeine Unfallversicherungsanstalt (AUVA) Research Centre, Vienna, Austria, <sup>4</sup> Institute of Analytical Chemistry and Food Chemistry, Graz University of Technology, NAWI Graz, Graz, Austria

## OPEN ACCESS

### Edited by:

Alberto Rainer,  
Università Campus Bio-Medico, Italy

### Reviewed by:

Christoffer Laustsen,  
Aarhus University, Denmark  
Giovann Vozzi,  
Università degli Studi di Pisa, Italy

### \*Correspondence:

Helene Zirath  
helene.zirath@tuwien.ac.at  
Mario Rothbauer  
mario.rothbauer@tuwien.ac.at

<sup>†</sup> These authors have contributed  
equally to this work.

### Specialty section:

This article was submitted to  
Integrative Physiology,  
a section of the journal  
Frontiers in Physiology

**Received:** 12 April 2018

**Accepted:** 11 June 2018

**Published:** 03 July 2018

### Citation:

Zirath H, Rothbauer M, Spitz S,  
Bachmann B, Jordan C, Müller B,  
Ehgartner J, Priglinger E, Mühleder S,  
Redl H, Holthoner W, Harasek M,  
Mayr T and Ertl P (2018) Every Breath  
You Take: Non-invasive Real-Time  
Oxygen Biosensing in Two-  
and Three-Dimensional Microfluidic  
Cell Models. *Front. Physiol.* 9:815.  
doi: 10.3389/fphys.2018.00815

Knowledge on the availability of dissolved oxygen inside microfluidic cell culture systems is vital for recreating physiological-relevant microenvironments and for providing reliable and reproducible measurement conditions. It is important to highlight that *in vivo* cells experience a diverse range of oxygen tensions depending on the resident tissue type, which can also be recreated *in vitro* using specialized cell culture instruments that regulate external oxygen concentrations. While cell-culture conditions can be readily adjusted using state-of-the-art incubators, the control of physiological-relevant microenvironments within the microfluidic chip, however, requires the integration of oxygen sensors. Although several sensing approaches have been reported to monitor oxygen levels in the presence of cell monolayers, oxygen demands of microfluidic three-dimensional (3D)-cell cultures and spatio-temporal variations of oxygen concentrations inside two-dimensional (2D) and 3D cell culture systems are still largely unknown. To gain a better understanding on available oxygen levels inside organ-on-a-chip systems, we have therefore developed two different microfluidic devices containing embedded sensor arrays to monitor local oxygen levels to investigate (i) oxygen consumption rates of 2D and 3D hydrogel-based cell cultures, (ii) the establishment of oxygen gradients within cell culture chambers, and (iii) influence of microfluidic material (e.g., gas tight vs. gas permeable), surface coatings, cell densities, and medium flow rate on the respiratory activities of four different cell types. We demonstrate how dynamic control of cyclic normoxic-hypoxic cell microenvironments can be readily accomplished using programmable flow profiles employing both gas-impermeable and gas-permeable microfluidic biochips.

**Keywords:** microfluidics, 3D culture, biosensor, oxygen, oxygen gradient, organ-on-a-chip, lab-on-a-chip, hydrogel

## INTRODUCTION

With the emergence of advanced cell-based *in vitro* models, which resemble the architecture and physiology of actual native tissue, the ability to control and manipulate cellular microenvironment has become an important aspect in microfluidic cell culture systems. Spatio-temporal control over the cellular microenvironment includes (i) physical forces such as shear stress, (ii) biological cues such as direct and indirect cell–cell interactions, and (iii) chemical signals such as pH, oxygenation, and nutrient supply. Among biochemical signals, oxygen plays a key role in regulating mammalian cell functions in human health and disease. It is also important to note that oxygen concentration varies tremendously throughout the human body ranging from 14% in lungs and vasculature down to 0.5% in less irrigated organs such as cartilage and bone marrow (Jagannathan et al., 2016). Despite the different demand of oxygen in different tissues, routine cell culture is predominantly conducted under atmospheric oxygen tension of 21%. This elevated levels of oxygen exposure of cells is referred to as hyperoxia and can lead to altered cell behavior (Gille and Joenje, 1992). For instance, studies have shown that physiologic oxygen tension modulates stem cell differentiation (Mohyeldin et al., 2010), neurogenesis (Zhang et al., 2011), and is involved in a number of cellular mechanisms needed to maintain tissue function (Pugh and Ratcliffe, 2003; Volkmer et al., 2008). In turn, prolonged oxygen deprivation in a hypoxic oxygen milieu can result in a variety of human pathologies including cancer (Pouysségur et al., 2006), tumor development (Harris, 2002), necrosis (Harrison et al., 2007), infection (Zinkernagel et al., 2007), and stroke (Hossmann, 2006). The importance of monitoring and control of oxygen levels in mammalian cell cultures has therefore led to the implementation of a wide variety of sensing strategies ranging from standard electrochemical electrodes (Nichols and Foster, 1994) and enzymatic sensors (Weltin et al., 2014) to fluorescent and luminescent optical biosensors (Wolfbeis Otto, 2015; Ehgartner et al., 2016b). Of these methods, optical detection based on oxygen-sensitive dyes that are embedded in a polymer matrix are ideally suited for the integration in lab-on-a-chip systems due to the facile integration of sensor spots in microfluidic channels, their long-term stability, reliability, and cost-effectiveness of the sensing probes (Wang and Wolfbeis, 2014; Lasave et al., 2015; Sun et al., 2015). Luminescent intensity as well as decay time of the phosphorescent indicator dye is affected by the amount of the surrounding molecular oxygen, thus providing information on the local oxygen concentration (Gruber et al., 2017). Especially porphyrin-based sensor dyes are well suited for oxygen monitoring in cell-based microfluidic devices due to their high sensitivity, biocompatibility, and reversible quenching behavior (Ungerbock et al., 2013; Ehgartner et al., 2014). Typically, time-resolved optical oxygen monitoring of microfluidic cell culture systems is performed using a measurement set-up consisting of the biochip, optical fibers, a read-out system, and a data acquisition device (Oomen et al., 2016; Gruber et al., 2017). As an example, a polydimethylsiloxane (PDMS) microfluidic chip with oxygen flow-through sensors at the inlet and outlet and an optical oxygen sensor in the cell

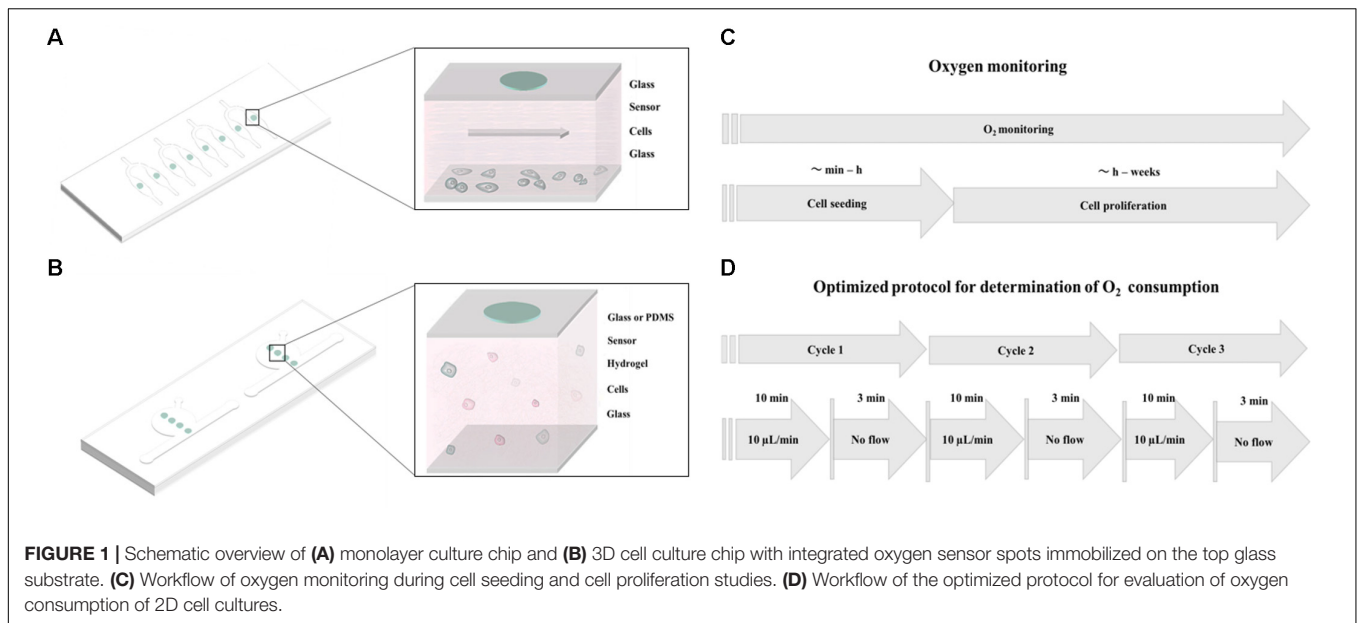
culture chamber has been realized for a real-time monitoring of respiratory rates of mouse embryonic stem cell cultures and for Chinese hamster ovary cells in monolayers for several days of culture (Super et al., 2016). Oxygen sensor spots were also integrated into microfluidic reaction chambers made of glass and silicon for monitoring of biocatalytic transformations (Ehgartner et al., 2016b). To create a more accessible read-out strategy for a broader research audience, a color CCD-camera mounted to a fluorescent microscope was used for 2D sensing of oxygen distribution inside microfluidic microchannels (Ungerbock et al., 2013). An additional multi-parametric analysis setup was established for simultaneous detection of oxygen and pH using core-shell nanoparticles incorporating oxygen- and pH-sensitive dyes (Ehgartner et al., 2016a). Despite these recent advances, little is still known on spatio-temporal variations of oxygen concentrations inside microfluidic 2D and 3D cell culture systems.

In this method paper, we investigate the influence of cell numbers, extra-cellular matrix (ECM) surface coatings, different cell types, as well as oxygen permeability of chip materials to determine the key microfluidic parameters needed to reliably monitor and precisely control oxygen levels during 2D and 3D cell cultivation. To gain deeper insight into oxygen supply to and demand of 2D and 3D cell cultures, we have developed two different microfluidic devices containing embedded sensor arrays as shown in **Figures 1A,B**. Material selection in particular influences gas exchange through the bulk chip material, which therefore directly influences the ability to control oxygen within the microfluidic environment. Initially, we have established two protocols for oxygen monitoring; **Figure 1C** shows the general methodology that can be used for oxygen monitoring of cell cultures during seeding, adhesion, and long-term cultivation. Additionally, another protocol, referred to hereafter as “optimized protocol,” is established for precise determination of oxygen consumption rates in 2D microfluidic cultures as shown in **Figure 1D**. Further, we have compared oxygen consumption of cells from epithelial, endothelial, and mesenchymal origin including cancer cells (A549 lung epithelial cells) and primary cells [e.g., normal human dermal fibroblasts (NHDF), adipose-derived stem cells (ASC), and human umbilical vein endothelial cells (HUVEC)]. The effect of a controlled oxygen gradient throughout fibrin hydrogels during vascular network formation over a 7-day culture period is demonstrated using a 3D vascular co-culture model based on HUVEC endothelial cells and ASC stem cells. A final practical application of the oxygen monitoring method involves the early identification of cell necrosis within hydrogel constructs, thus providing quality control information on 3D-cell-laden hydrogel and microtissue cultures.

## RESULTS AND DISCUSSION

### Non-invasive Oxygen Monitoring in 2D Microfluidic Cell Cultures

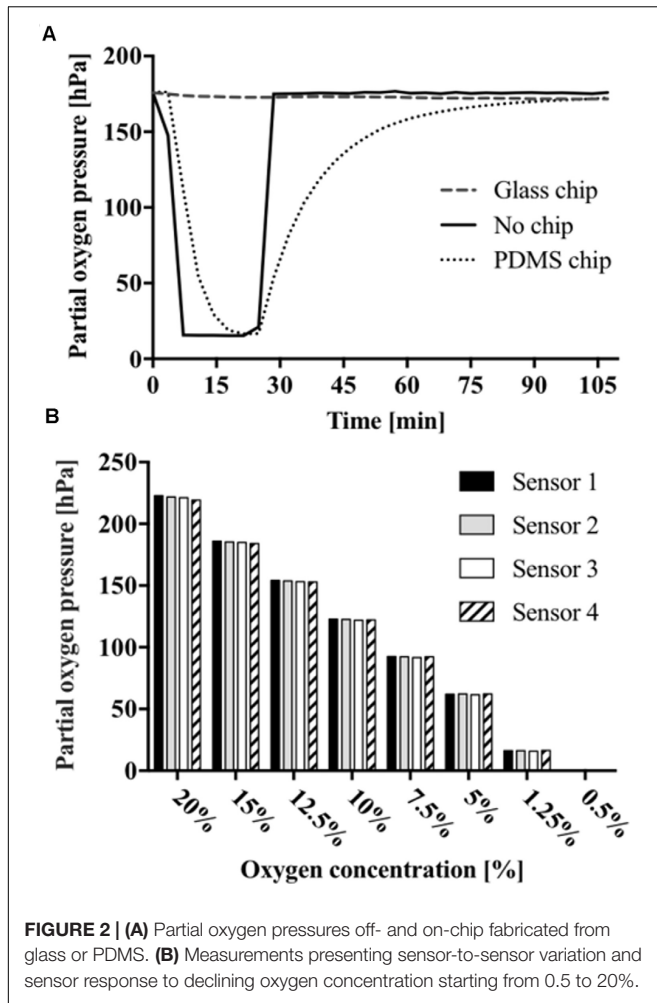
Prior to oxygen monitoring of 2D cell cultures, the influence of chip material permeability was evaluated based on the response



of the oxygen-sensitive microparticle-based sensors. Therefore, gaseous oxygen content within sealed microchannels was monitored for microfluidic chips fabricated either from oxygen-permeable PDMS or impermeable glass (see **Supplementary Figure S1**). Both devices were simultaneously exposed to an oxygen environment of 2.5% for 20 min before re-oxygenation. As shown in **Figure 2A**, no sensor response was observable for gas-impermeable glass chips with no detectable decrease in partial oxygen pressure. Microfluidic chips made of gas-permeable PDMS showed a decrease in partial oxygen pressure from 176.4 to 15.4 hPa with a  $t_{90}$ -value of 15 min and a delay in full recovery to atmospheric oxygen after 87 min. These results demonstrate the importance of material selection during microfluidic chip fabrication. Differences in de- and re-oxygenation linked to material permeability offer the opportunity to either inhibit or allow external oxygen supply to the cell cultures. In turn, sensor-to-sensor variation was evaluated using oxygen concentrations ranging from 20 to 0.5% via small gas feeding by a CO<sub>2</sub>/O<sub>2</sub> controller equipped with zirconium-based oxygen sensor, which was connected to the inlet ports of the microfluidic chips. As shown in **Figure 2B**, sensor-to-sensor variation among the individual sensor spots was  $221.2 \pm 1.3$  hPa for 20%,  $122.4 \pm 0.3$  for 10%,  $61.9 \pm 0.2$  hPa for 5%, and  $0.2 \pm 0.1$  hPa for 0.5% oxygen, respectively. These results show excellent reproducibility despite the manual dispensing of the sensor spots into the microfluidic devices.

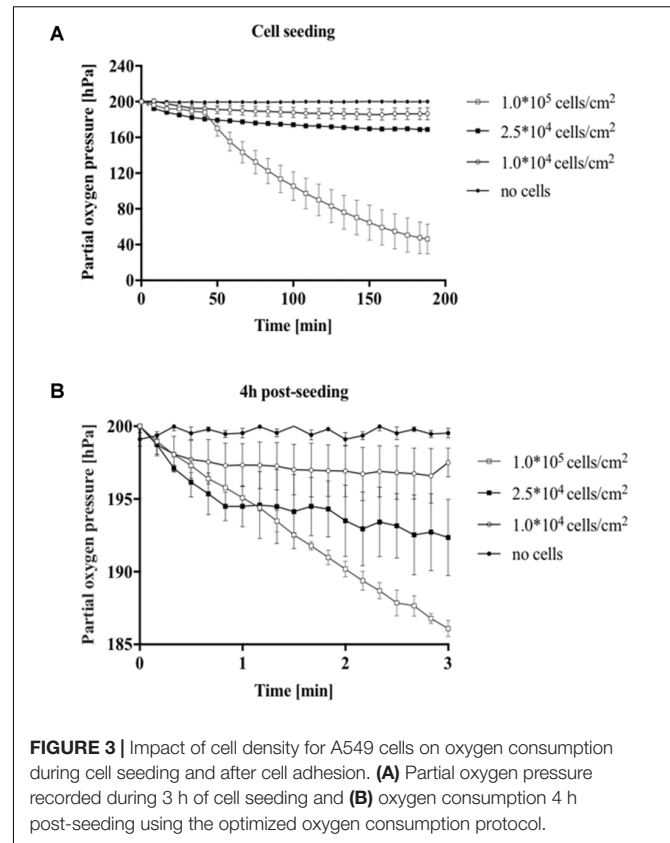
In the next set of experiments, the impact of cell density on oxygen consumption was evaluated during cell seeding and for fully attached cell cultures. A549 lung epithelial cells were seeded in gas-impermeable microfluidic chips at initial cell seeding densities ranging from  $1 \times 10^4$  to  $1 \times 10^5$  cells/cm<sup>2</sup>. **Figure 3A** shows a partial oxygen pressure around 200 hPa right after seeding, which accurately represents ambient oxygen levels in cell culture media at 37°C. Difference in partial oxygen pressure for increasing cell numbers was observable already

10 min after cell seeding, thus pointing at higher oxygen demand in the presence of larger cell numbers. Interestingly, while similar oxygen depletion values were observed in the first 40 min, rapid increase in oxygen consumption was found already after 50 min for  $1.0 \times 10^5$  cells/cm<sup>2</sup> (see **Supplementary Figure S2**), which can be linked to completed cell adhesion and start of exponential cell growth (Rehberg et al., 2013). Cell densities of  $1 \times 10^4$  and  $2.5 \times 10^4$  cells/cm<sup>2</sup> resulted in moderate total oxygen depletion values of  $13.4 \pm 6.7$  hPa and  $31.1 \pm 1.5$  hPa, respectively. A more pronounced oxygen depletion was found for the highest cell density of  $1 \times 10^5$  cells/cm<sup>2</sup> of  $153.8 \pm 16.7$  hPa. Results of this study show that in the presence of high cell densities oxygen depletion occurs 3 h after cell seeding when using gas-impermeable glass microfluidic chips. Next, an optimized protocol was established for precise measurements of oxygen consumption rates (see **Figure 1D** for details). To ensure oxygen consumption measurements, a flow rate of 10 µL/min over period of 10 min prior to the measurements was introduced to maintain oxygenated conditions of around 200 hPa. Flow rates below this threshold did not show full oxygenation (data not shown). For the actual determination of oxygen consumption rates, flow was halted and the decrease in oxygen partial pressure was immediately recorded for 3 min in all chambers. **Figure 3B** shows decreasing oxygen levels over a period of 3 min ( $n = 3$ ) in the presence of increasing numbers of fully attached A549 lung cells after 4 h of post-seeding, indicating that sufficient re-oxygenation prior to measurement markedly improves data quality. Calculated total oxygen consumption rates of 0.8 hPa/min for  $1 \times 10^4$  cells/cm<sup>2</sup>, 2.6 hPa/min for  $2.5 \times 10^4$  cells/cm<sup>2</sup>, and 4.6 hPa/min for  $1 \times 10^5$  cells/cm<sup>2</sup>. Overall, integration of sensor spots above the cell monolayer culture are sensitive enough to estimate oxygen availability and cell population oxygen demands in microfluidic cell cultivation chambers.



## Impact of Cell Type on Oxygen Consumption Rates

Differences in oxygen consumption rates between well-established primary cell types (Manning et al., 2015; Haase and Kamm, 2017; Zhang et al., 2017) and cancer cell lines (Cooper et al., 2016) were investigated to further evaluate the presented non-invasive microfluidic oxygen monitoring method. Partial oxygen pressure was monitored during cell seeding for cells from epithelial (A549), endothelial (HUVEC), and mesenchymal origin (NHDF and ASC) at the same initial seeding density of  $2.5 \times 10^4$  cells/cm<sup>2</sup> corresponding to  $5.5 \times 10^3$  cells per microchannel. As shown in **Figure 4A** the different cell types can be readily distinguished by cell type-specific variations in oxygen depletion during adhesion to the surface of the microfluidic channels. NHDF fibroblast cells showed highest oxygen depletion values leveling off at a partial oxygen pressure of 17 hPa, which corresponds to a total oxygen consumption of  $183 \pm 0.4$  hPa oxygen in 3 h during cell adhesion. The oxygen consumption for the other cell types were lower with 104.2 hPa ( $n = 1$ ) for A549 lung cells,  $28.4 \pm 0.4$  hPa for HUVEC endothelial cells, and  $59.4 \pm 15.4$  hPa for ASC stem cells, respectively. Next, oxygen consumption rates were determined using the optimized

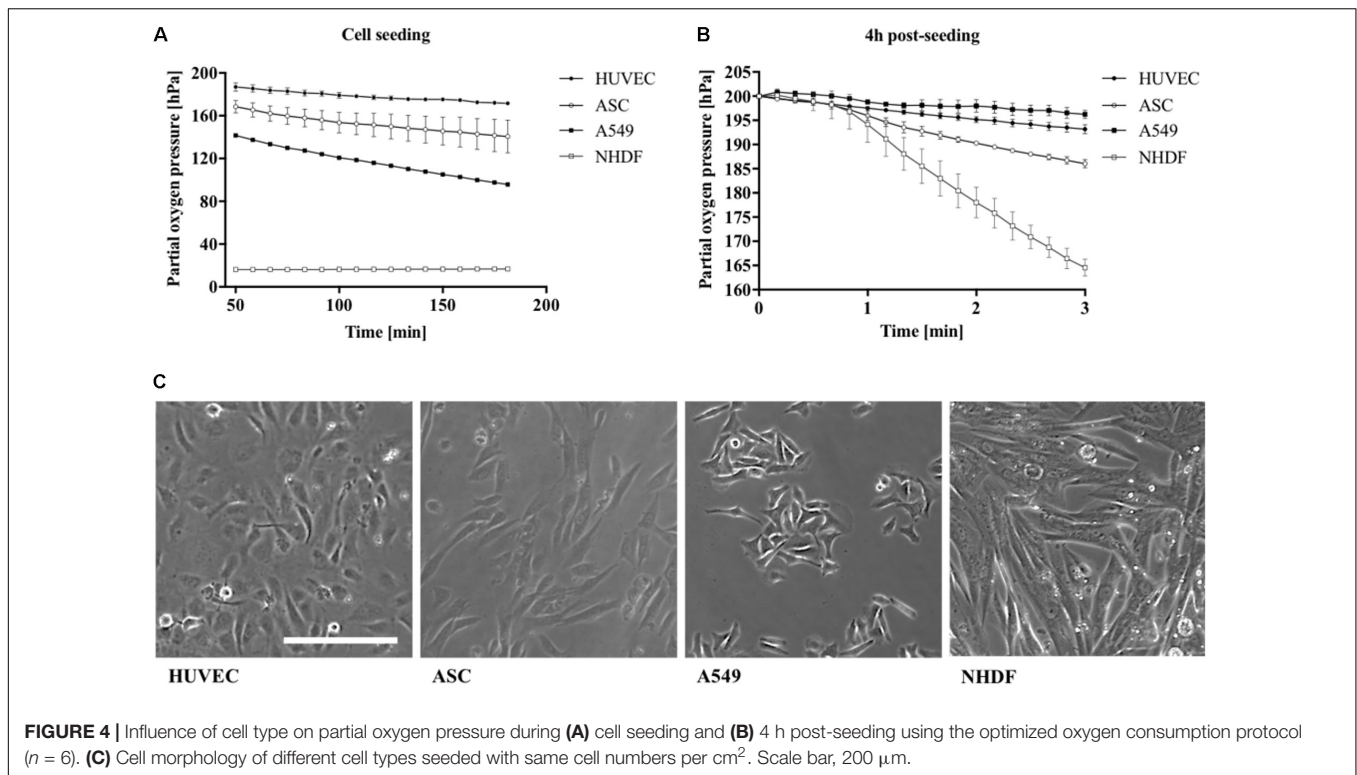


protocol as shown in **Figure 4B**. Oxygen consumption varied heavily between the different cell types exhibiting low cellular respiratory activity of  $3.7 \pm 1.2$  hPa ( $1.2 \pm 0.4$  hPa/min) for A549 lung cells and  $6.8 \pm 2.1$  hPa ( $2.3 \pm 0.7$  hPa/min) for HUVEC,  $13.9 \pm 1.6$  hPa ( $4.7 \pm 0.5$  hPa/min) for ASC, and highest rates observable of  $35.4 \pm 2.5$  hPa ( $11.8 \pm 0.8$  hPa/min) for fibroblast cells. Overall, these results correspond well with literature values the specific cell types demonstrating the good performance of the presented microfluidic oxygen sensing method (Heidemann et al., 1998; Powers et al., 2008; Abaci et al., 2010; Zhang et al., 2014). In addition, **Figure 4C** shows differences in both cell morphology and cell size with a cell size of  $72.4 \mu\text{m}^2$  for HUVEC endothelial cells,  $71.6 \mu\text{m}^2$  for A549,  $232.9 \mu\text{m}^2$  for NHDF fibroblast cells, and  $125.3 \mu\text{m}^2$  for ASC stem cells. Cell size directly correlates with oxygen consumption, (Wagner et al., 2011) which explains the high respiratory activity of fibroblast cells displaying the biggest cell size.

## Impact of Cell Adhesion Promoters on Oxygen Consumption Rates

Since mammalian cells strongly interact and respond to surface properties such as the biocompatibility and functionalization of the interface, the influence of ECM surface promoters including 1% gelatin and collagen I was investigated on the respiratory activity of HUVEC endothelial cells during cell seeding and 3 h after attachment. As shown in **Figure 5A** already 3 min following the introduction of endothelial cells





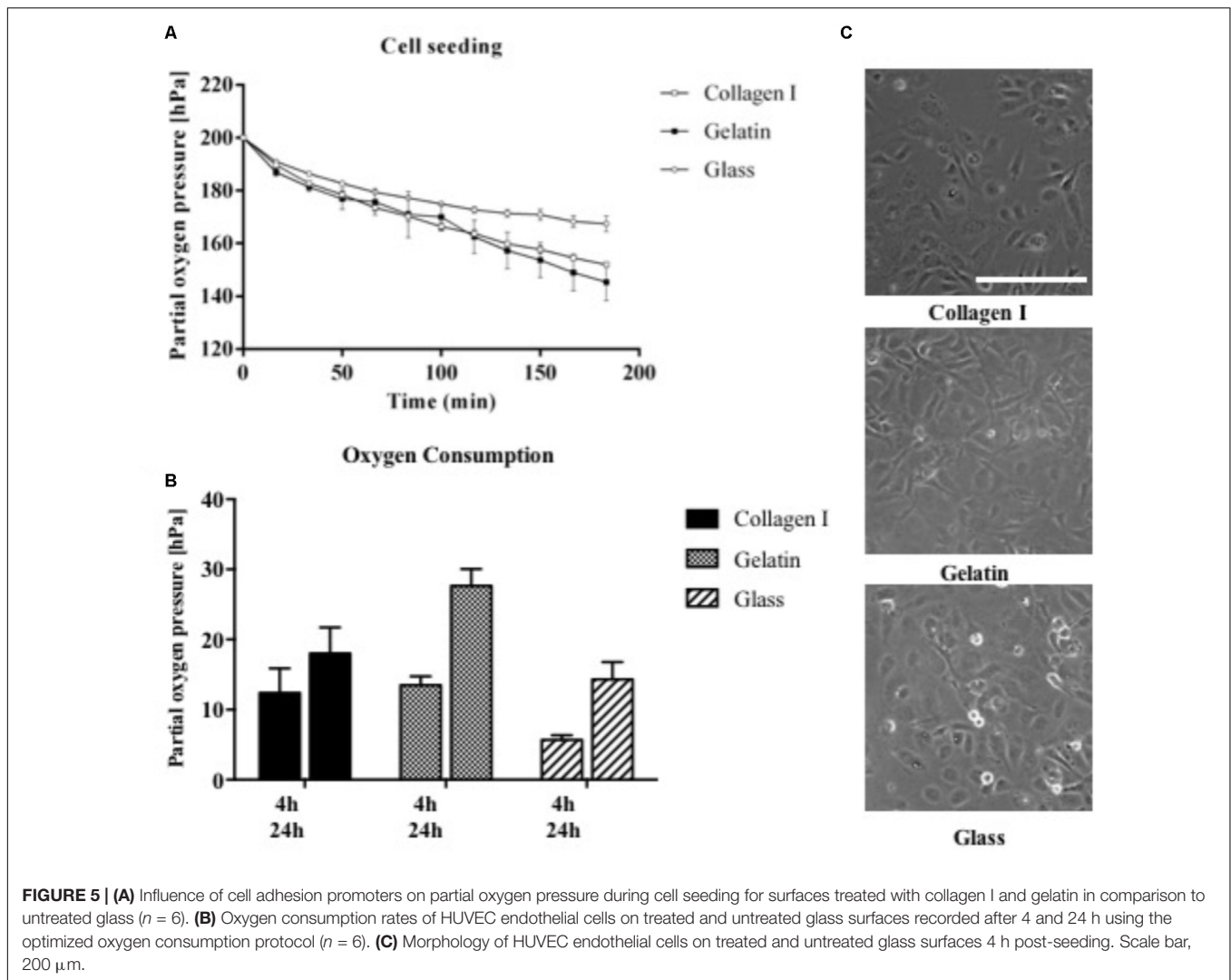
**FIGURE 4 |** Influence of cell type on partial oxygen pressure during **(A)** cell seeding and **(B)** 4 h post-seeding using the optimized oxygen consumption protocol ( $n = 6$ ). **(C)** Cell morphology of different cell types seeded with same cell numbers per  $\text{cm}^2$ . Scale bar, 200  $\mu\text{m}$ .

seeded on gelatin and collagen I-coated microchannels, a drop in partial oxygen pressure by 1 hPa was recorded. In contrast, partial oxygen pressure of 200 hPa remained in the absence of cells. In turn, after completion of cell attachment and establishment of endothelial cell monolayers, both adhesion promoters initiated elevated respiratory activities in the range of 130–150 hPa compared to untreated glass with partial oxygen pressure around  $165.7 \pm 5$  hPa. **Figure 5B** shows that respiration of HUVEC endothelial cells further increased from 4 to 24 h post-seeding by 140% for collagen I coating and 170% for gelatin-coated microchannels. Even though respiratory activity of HUVEC endothelial cells cultured on untreated glass displayed highest relative increase of 250% after 24 h, however, absolute respiration rates were 20–40% lower than cells cultivated on ECM-like adhesion promoters. These findings can be explained by incomplete adhesion of cells on untreated surfaces, where 10% of the cells were only partially attached as shown in **Figure 5C**. In other words, our results demonstrate that our non-invasive on-chip oxygen detection method can also be applied for adhesion and biocompatibility studies, where metabolic assays as well as microscopic inspection of cell phenotype alone can result in overestimation of cellular activity.

## Non-invasive Oxygen Monitoring in Three-Dimensional Microfluidic Cell Cultures

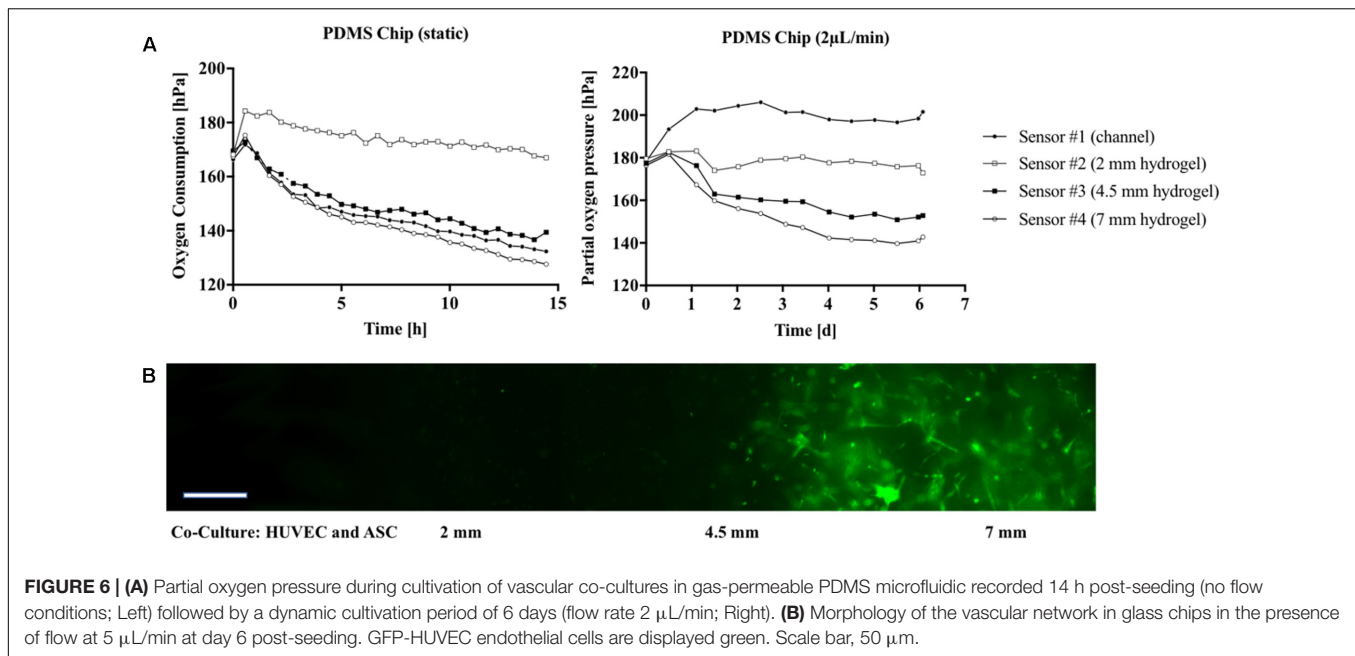
Since state-of-the-art *in vitro* models frequently employ 3D-hydrogel-based cell cultures, the integrated oxygen sensor array

was evaluated using a well-established co-culture model of ASC stem cells with HUVEC endothelial cells (Muhleder et al., 2018). Here, an oxygen-permeable PDMS-based microfluidic biochip containing four spatially resolved sensor spots (see also **Figure 1B**) was seeded with a HUVEC/ASC cell co-culture. Oxygen monitoring was performed for medium supply channels (sensor #1) as well as at 2 to 7 mm within the fibrin hydrogel (sensors #2–4). On the first day of culture, cell co-cultures settled and established direct cell-cell contacts and reciprocal exchange of pro-angiogenic factors using a static stop-flow cultivation period over 24 h. **Figure 6A** (left panel) shows that after 45 min of hydrogel polymerization, partial oxygen pressure of the feeding channel stayed constant around  $169.0 \pm 1.1$  hPa for the first day of culture. In contrast, within the hydrogel construct oxygen levels slowly decreased over time to around  $132.4 \pm 5.4$  hPa independent of diffusion distance through the hydrogel with an average oxygen decrease of 2.5 hPa/h. After the first day of culture, continuous medium supply was initiated at a flow rate of 2  $\mu\text{L}/\text{min}$  for the next 5 days of culture. **Figure 6A** (right panel) shows that at day 6 of vascular network formation, an oxygen gradient was established starting at steady atmospheric partial oxygen pressure of around 198.4 hPa for sensor #1 at the medium feeding channel, and linear decreasing values of 176.3 hPa for sensor #2 at 2 mm, 152.1 hPa for sensor #3 at 4.5 mm, and 140.9 hPa for sensor #4 at 7 mm distance from the feeding channel. Overall, average decrease of partial oxygen pressure of 10 hPa per day was observed for the deepest regions of the hydrogel construct. **Figure 6B** shows that even though a linear oxygen gradient was established, vascular network formation with interconnecting endothelial tubes started at a



distance of 4.5 mm from the feeding channel. This means that a reduction of partial oxygen pressure by 70 hPa does not affect vascular network formation. In turn, similar vascularization experiments were performed for oxygen-impermeable glass-based microfluidics to generate stronger oxygen gradients. Due to limited oxygen supply from the humidified incubator atmosphere through the bulk chip material, oxygen can exclusively be controlled by adjustment of medium flow rate, thus amount of dissolved oxygen fed to the HUVEC/ASC cell co-culture. To elucidate this mechanism, *in silico* experiments performed using finite volume CFD simulations (Ansys FLUENT® 6.3.26) of oxygen distribution in fibrin hydrogel in the absence of cellular respiratory load were conducted to determine the oxygen saturation within the fibrin hydrogel by medium supply exclusively. **Supplementary Figure S3** shows that already during the first 60 min of medium perfusion, 50% of the supplied oxygen diffuses 2 mm into the hydrogel chamber. Rapid oxygen diffusion then results in a supply of 75% of dissolved oxygen into the depth of the chamber after 6 h and complete oxygen saturation of the chamber within 12 h after initiation of perfusion with

the theoretical assumption of oxygen-free conditions at time point zero. **Figure 7A** (left panel) shows that during perfused hydrogel culture within oxygen-impermeable microfluidics right after 45 min of hydrogel polymerization, at a flow rate of 2  $\mu$ L/min oxygen saturation at a partial oxygen pressure of  $197.1 \pm 3.2$  hPa was observable for the medium feeding channel as well as up to 2 mm into the hydrogel construct. At distances between 4.5 and 7 mm, partial oxygen pressures decreased to  $161.2 \pm 9.5$  hPa with a mean oxygen depletion rate of 5 hPa/h, which is twofold higher compared to the rate found with oxygen-permeable microfluidic chips. In turn, **Figure 7A** (right panel) shows that the combination of impermeable microfluidic biochips with optical in-line oxygen monitoring can be used to control oxygen within microfluidic cultures. By exploiting the respiratory activity of cells within the 3D hydrogel construct, this method can be used to control oxygen levels during long-term cultivation of 3D cells cultures without the need for external oxygen controllers such as CO<sub>2</sub>/O<sub>2</sub> incubators, gas controls units for gas mixing, as well as nitrogen gas- or oxygen-scavenging chemicals for oxygen depletion. A pre-programmed flow profile



in the range of 0–2  $\mu\text{L}/\text{min}$  was used to expose cells to alternating cycles of normoxic and hypoxic culture conditions with peak-to-peak values for partial oxygen pressure of max. 200 hPa down to min. 17 hPa and an average cycle time around 2.5 h over several days for 3D cell culture. **Figure 7A** (bottom panel) shows that due to the cycling of normoxic and hypoxic conditions, formation of a vascular network with decreased length and thickness of vascular sprouts was observable; however, more even distribution of the network was observable starting already at 2 mm distance from the medium feeding channel. In a final set of experiments, we demonstrated how the presented non-invasive microfluidic oxygen monitoring method can be applied not only for oxygen control, but also for evaluation of cell health status during oxygen- and nutrient-dependent limitation of three-dimensional cultures in the absence of medium perfusion. As shown in **Figure 7B** (top panel) an oxygen gradient was established in the absence of medium perfusion due to the respiratory activity of intact cell co-cultures until day 3 post-seeding corresponding to vascular network formation (see **Figure 7B** bottom left image). Over the course of 36 h of nutrient and oxygen limitation, partial oxygen pressure gradually recovered to fully oxygenated conditions around 200 hPa, which is the result of cell death by nutrient and oxygen depletion over 6 days. **Figure 7B** shows a residual pattern of GFP-containing cell remnants (visible in the bottom center image) that resembles the vascular network morphology from day 3. These patterns were not observable for cell co-cultures closest to the medium feeding channel, which did not form vascular networks (bottom right image).

## CONCLUSION

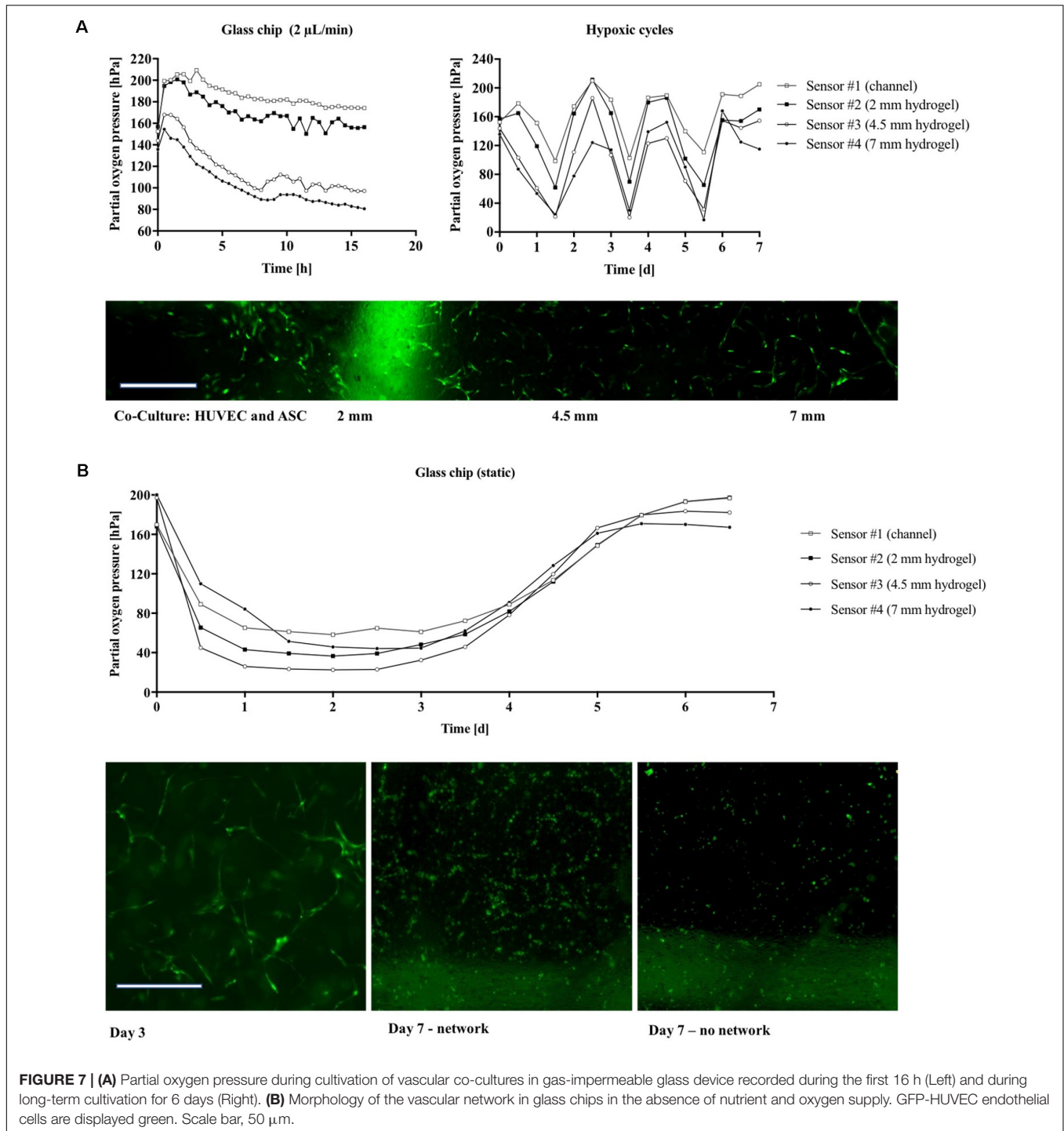
In this method paper, we demonstrate the ability to reliably and reproducibly detect dissolved oxygen levels and cellular oxygen

demands in 2D and 3D microfluidic cell culture systems. The integration of oxygen-sensitive microparticle-based sensor spots enables time-resolved monitoring of partial oxygen pressures, thus allowing the estimation of cellular oxygen consumption rates of cell monolayers in the presence of increasing flow rates, varying cell numbers, cell types, and ECM-coatings. The total oxygen consumption observed for the different cell densities increased linearly. This means that the presented measurement method has the potential to be used for indirect monitoring of cell viability in toxicological screening studies. Additionally, we show that metabolic evaluation of complex 3D tissue-engineered constructs can be accomplished using biologically relevant co-cultures. The ability to monitor complex 3D physiological cellular microenvironments further highlights the benefits of sensor integration in microfluidic systems to control, mitigate, and accurately predict cell behavior (Charwat et al., 2013, 2014; Ertl et al., 2014; Mahto et al., 2015; Rothbauer et al., 2015a,b). The presented on-chip-integrated oxygen-sensing method is well suited for applications in advanced organ-on-a-chip systems, because it enables non-invasive, real-time, label-free, *in situ* monitoring of oxygen demands, metabolic activity, oxygen uptake rates, and cell viability. We believe that the integration of cost-efficient and reliable sensor technology in microfluidic devices holds great promise for the reliable establishment of physiologic or pathologic tissue conditions, thus opening new avenues in biomedical research and pharmaceutical development.

## MATERIALS AND METHODS

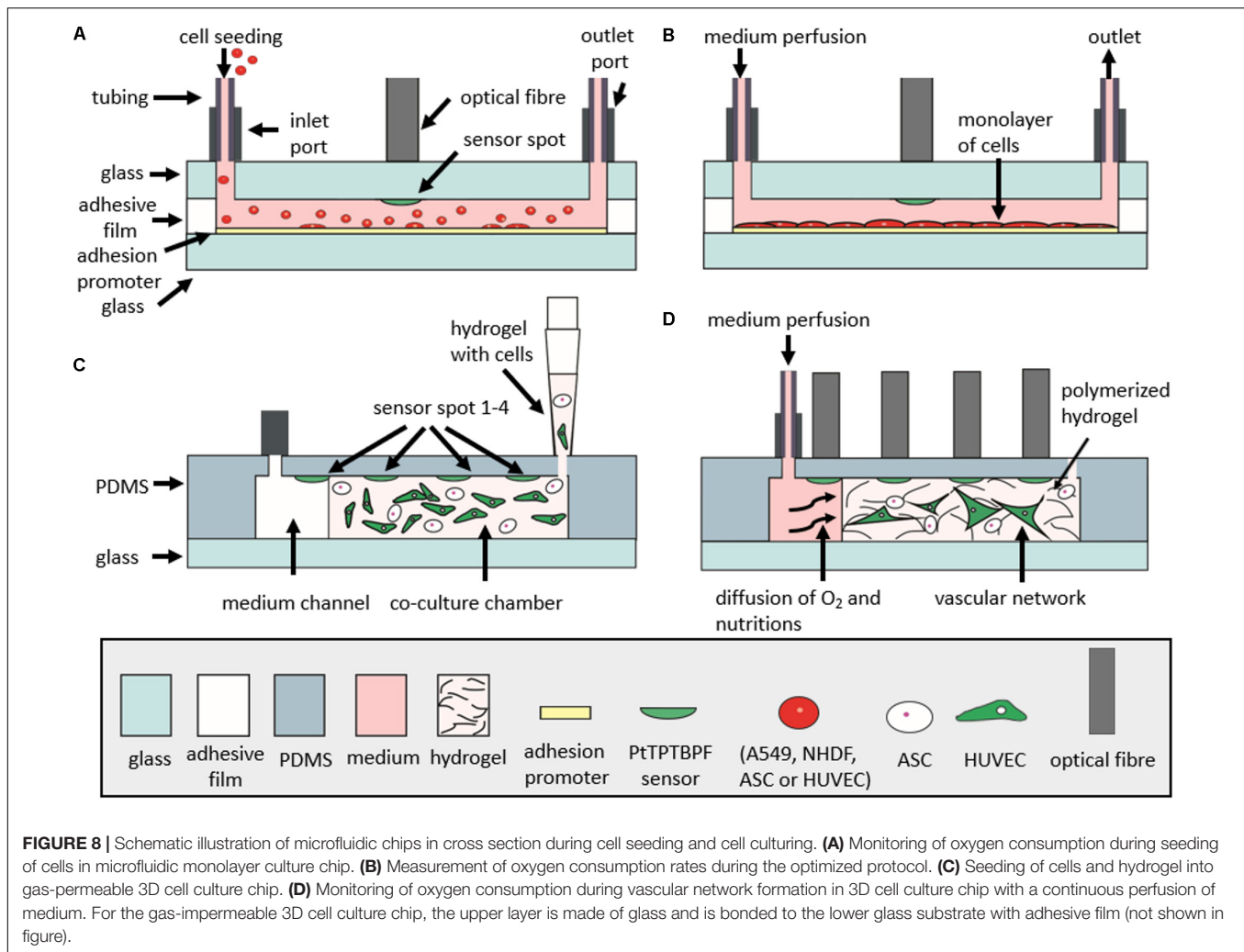
### Preparation of the Oxygen Sensor

Amine-functionalized polystyrene beads (500  $\mu\text{L}$  of a 50 mg/mL stock solution, micromer<sup>®</sup> product code 01-01-303, micromod,



Germany) were diluted with water (2 mL) and THF (200  $\mu$ L). This dispersion was stirred for 30 min at room temperature. Afterward, an oxygen indicator solution [188  $\mu$ L of a THF solution containing 2 mg/mL platinum (II) meso-tetra (4-fluorophenyl) tetrabenzoporphyrin (PtTPTBPF)] was added dropwise, the dispersion was sonicated for 30 min, centrifuged at a relative centrifugation force of 6200, and the supernatant was decanted. The particles were purified using multiple

washing, centrifugation, and decantation steps. The purification process was repeated with water (1–2 times) at the beginning, followed by ethanol (3–5 times) and finished with water (1–2 times). After the final decantation step the particles were diluted with water to a particle concentration of approx. 50 mg/mL. Characterization and calibration of oxygen sensor was performed as described previously (Ehgartner et al., 2016b).



**FIGURE 8 |** Schematic illustration of microfluidic chips in cross section during cell seeding and cell culturing. **(A)** Monitoring of oxygen consumption during seeding of cells in microfluidic monolayer culture chip. **(B)** Measurement of oxygen consumption rates during the optimized protocol. **(C)** Seeding of cells and hydrogel into gas-permeable 3D cell culture chip. **(D)** Monitoring of oxygen consumption during vascular network formation in 3D cell culture chip with a continuous perfusion of medium. For the gas-impermeable 3D cell culture chip, the upper layer is made of glass and is bonded to the lower glass substrate with adhesive film (not shown in figure).

## Microfluidic Chips and Sensor Integration

The microdevices for monolayer cultures were comprised of two glass substrates (VWR) bonded together with adhesive film containing the fluidic structure. Microfluidic chambers and channels were designed with CAD (AutoCAD 2017) and cut into the adhesive film (ARcare 8259 and ARseal 90880, Adhesive Research, Ireland) with a desktop vinyl cutter (GS-24 Desktop Cutter, Roland DGA Corporation, Germany). Three layers of adhesive film were used to obtain a chamber height of 460  $\mu\text{m}$ . The chip contained 8 cell-culture chambers of 0.22  $\text{cm}^2$  (10  $\mu\text{L}$  volume) with one inlet connected to two chambers with a 400  $\mu\text{m}$  wide channel (**Figure 1A**). Holes for inlets and outlets were drilled into the upper glass substrate before integration of sensor particles. Oxygen sensor microparticles were applied by pipetting directly to the glass substrate. After drying for 2 h at room temperature, the microparticles were immobilized to the glass substrate and the fluidic structures were sealed with adhesive film via pressure activation. Devices for three-dimensional (3D) hydrogel cultures had a circular hydrogel chamber (65  $\mu\text{L}$  volume) adjacent to a medium channel (see **Figure 1B**).

Microstructures were either fabricated by soft lithography using PDMS (Sylgard<sup>®</sup> 184 Silicone Elastomer Kit, Dow Corning, Germany) from 3D-printed molds (immaterialize, Denmark) or sandblasted into glass slides. Oxygen-sensitive conjugated microparticles were again applied via pipetting directly to the glass substrate and immobilized after 2 h of drying. PDMS devices were sealed by plasma bonding to glass slides using air plasma (Harrick Plasma, High Power, 2 min) and glass devices were sealed using adhesive film (ARseal 90880, Adhesive Research, Ireland).

## Cell Culture

A549 human lung carcinoma epithelial-like cell line (ATCC) were cultured in RPMI 1640 Medium (Gibco) supplemented with 10% fetal bovine serum, L-glutamine, and 1% antibiotic/antimycotic solution. NHDF (Lonza) were cultured in high glucose Dulbecco's modified Eagle's medium (DMEM, Sigma Aldrich) supplemented with 10% fetal bovine serum, 2 mM glutamine, and 1% antibiotic-antimycotic solution. Primary human ASC and HUVEC were isolated as previously described (Petzelbauer et al., 1993; Wolbank et al., 2007; Priglinger et al., 2017)

and maintained in fully supplemented endothelial cell growth medium 2 (EGM-2, PromoCell) with 5% fetal calf serum until passage 5–9. GFP-labeled endothelial cells were prepared as previously described (Knezevic et al., 2017; Muhleder et al., 2018) All cell cultures were maintained in a humidified atmosphere at 37°C and 5% CO<sub>2</sub>. Cell culture media used during perfusion of the microfluidic monolayer chambers was supplemented with 0.5% HEPES (Sigma Aldrich). Prior to cell seeding, microfluidic tubing and valves were sterilized with 70% ethanol and rinsed thoroughly with PBS (Sigma Aldrich) and cell culture medium. The assembled microfluidic biochips were disinfected using 70% ethanol and rinsed with sterile PBS prior to coating with 5% collagen I solution (Sigma Aldrich, Austria).

## On-Chip Oxygen Monitoring

Oxygen monitoring was carried out at a sampling frequency of 1 Hz using a FireStingO2 optical oxygen meter (Pyroscience, Germany<sup>1</sup>) connected to optical fibers (length 1 m, outer diameter 2.2 mm, fiber diameter 1 mm). Integrated sensors were calibrated using a CO<sub>2</sub>/O<sub>2</sub> oxygen controller (CO<sub>2</sub>-O<sub>2</sub>-Controller 2000, Pecon GmbH, Germany) equipped with integrated zirconium oxide oxygen sensors. Oxygen measurements were initiated directly after injection of cell solutions and partial oxygen pressure was monitored up to a maximum duration of 7 days. To evaluate the influence of cell number on oxygen consumption, A549 lung cells were seeded at concentrations of  $1 \times 10^4$  cells/cm<sup>2</sup> ( $2.2 \times 10^3$  cells/chamber),  $2.5 \times 10^4$  cells/cm<sup>2</sup> ( $5.5 \times 10^3$  cells/chamber), and  $1.0 \times 10^5$  cells/cm<sup>2</sup> ( $22 \times 10^3$  cells/chamber). For oxygen monitoring of different cell types, A549 lung epithelial cells, NHDF fibroblast cells, HUVEC endothelial cells, and ASC stem cells were seeded at a concentration of  $2.5 \times 10^4$  cells/cm<sup>2</sup> ( $5.5 \times 10^3$  cells/chamber) To investigate the influence of adhesion promoters on oxygen consumption, HUVEC endothelial cells were seeded at a concentration of  $2.5 \times 10^4$  HUVEC/cm<sup>2</sup> ( $5.5 \times 10^3$  cells/chamber) on different surfaces including untreated glass 5% collagen I and 1% gelatin. For oxygen monitoring of 3D fibrin hydrogels, ASC stem cells and HUVEC endothelial cells were mixed at a cell density of  $5 \times 10^5$  cells/mL ( $32.5 \times 10^3$  cells/chamber, 65  $\mu$ L chamber volume) per cell type in fibrinogen and thrombin (TISSEEL®, Baxter, Austria) to obtain a final concentration of 2.5 mg/mL fibrinogen and 1 U/mL thrombin. The hydrogel was loaded into the hydrogel chambers of the microfluidic chip and allowed to polymerize for 45 min before the addition of fully supplemented EGM-2 culture medium. Thereafter, vascular 3D cell cultures were maintained at a flow rate of 2  $\mu$ L/min. In **Figures 8A–D**, schematic illustrations depict the cell seeding and measurement setup of monolayer culture chips (A–B) and 3D culture chips (C–D).

## Optimized Protocol for On-Chip Oxygen Consumption Measurements

For determination of oxygen consumption, an optimized protocol was established recording three consecutive measuring

<sup>1</sup>www.pyro-science.com

cycles. Each cycle comprised of an oxygen saturation phase of 10  $\mu$ L/min for 10 min followed by a recording phase under stop-flow conditions for 3 min.

## CFD Simulation of Oxygen

Oxygen saturation was simulated using a multipurpose finite volume CFD simulation (Ansys FLUENT®, v6.3.26). The hydrogel region was approximated as a porous zone with a porosity of  $\epsilon = 0.99$  and isotropic viscous resistances of  $R = 6.67 \times 10^{-12}$  1/m<sup>2</sup>. Simulations were performed using an oxygen diffusion coefficient of  $2 \times 10^{-9}$  m<sup>2</sup>/s.

## AUTHOR CONTRIBUTIONS

HZ, MR, SS, BB, and PE conceived the project and designed the experimental outline. HZ, MR, SS, and BB performed the microfluidic experiments and analyzed the data. CJ and MH conceived and performed finite volume CFD simulations. BM, JE, and TM prepared the optical sensors for oxygen biosensing. EP, SM, WH, and HR isolated and transfected the primary endothelial and adipose-derived stem cell cultures and shared their expertise in vascular tissue engineering. HZ, MR, SS, and BB drafted the manuscript. All authors contributed to and revised the final manuscript.

## FUNDING

This work was funded by the European Union's Horizon 2020 research and innovation programme (685817) and the Austrian Research Promotion Agency (FFG; 849791). The authors acknowledge the TU Wien University Library for financial support through its Open Access Funding Program.

## ACKNOWLEDGMENTS

The authors acknowledge the band “The Police” for their fundamental contribution to the title and Christoph Eilenberger for image analysis and fruitful discussions.

## SUPPLEMENTARY MATERIAL

The Supplementary Material for this article can be found online at: <https://www.frontiersin.org/articles/10.3389/fphys.2018.00815/full#supplementary-material>

**FIGURE S1** | Images of microfluidic devices. **(A)** Microfluidic glass chip (76 mm × 26 mm × 2.3 mm) for monolayer culture containing eight chambers with a sensor spot centralized in each chamber. **(B)** Microfluidic glass chip (76 mm × 26 mm × 4.4 mm) for three-dimensional (3D) hydrogel cultures with four sensor spots in each chamber. Scale bar represent 10 mm.

**FIGURE S2** | Partial oxygen pressure recorded during 3 h of cell seeding zoomed in to the first 50 min of oxygen monitoring.

**FIGURE S3** | Finite volume simulation of oxygen distribution in 3D hydrogel after **(A)** 1 h, **(B)** 6 h, and **(C)** 12 h of medium perfusion without cells showing complete saturation of hydrogel with oxygen within 12 h.

## REFERENCES

- Abaci, H. E., Truitt, R., Luong, E., Drazer, G., and Gerecht, S. (2010). Adaptation to oxygen deprivation in cultures of human pluripotent stem cells, endothelial progenitor cells, and umbilical vein endothelial cells. *Am. J. Physiol. Cell Physiol.* 298, C1527–C1537. doi: 10.1152/ajpcell.00484.2009
- Charwat, V., Joksich, M., Sticker, D., Purtscher, M., Rothbauer, M., and Ertl, P. (2014). Monitoring cellular stress responses using integrated high-frequency impedance spectroscopy and time-resolved ELISA. *Analyst* 139, 5271–5282. doi: 10.1039/c4an00824c
- Charwat, V., Rothbauer, M., Tedde, S. F., Hayden, O., Bosch, J. J., Muellner, P., et al. (2013). Monitoring dynamic interactions of tumor cells with tissue and immune cells in a lab-on-a-chip. *Anal. Chem.* 85, 11471–11478. doi: 10.1021/ac4033406
- Cooper, J. R., Abdullatif, M. B., Burnett, E. C., Kempell, K. E., Conforti, F., Tolley, H., et al. (2016). Long term culture of the A549 cancer cell line promotes multilamellar body formation and differentiation towards an alveolar type II pneumocyte phenotype. *PLoS One* 11:e0164438. doi: 10.1371/journal.pone.0164438
- Ehgartner, J., Strobl, M., Bolivar, J. M., Rabl, D., Rothbauer, M., Ertl, P., et al. (2016a). Simultaneous determination of oxygen and pH inside microfluidic devices using core-shell nanosensors. *Anal. Chem.* 88, 9796–9804.
- Ehgartner, J., Sulzer, P., Burger, T., Kasjanow, A., Bouwes, D., Krühne, U., et al. (2016b). Online analysis of oxygen inside silicon-glass microreactors with integrated optical sensors. *Sens. Actuators B Chem.* 228, 748–757. doi: 10.1016/j.snb.2016.01.050
- Ehgartner, J., Wiltsche, H., Borisov, S. M., and Mayr, T. (2014). Low cost referenced luminescent imaging of oxygen and pH with a 2-CCD colour near infrared camera. *Analyst* 139, 4924–4933. doi: 10.1039/c4an00783b
- Ertl, P., Sticker, D., Charwat, V., Kasper, C., and Lepperdinger, G. (2014). Lab-on-a-chip technologies for stem cell analysis. *Trends Biotechnol.* 32, 245–253. doi: 10.1016/j.tibtech.2014.03.004
- Gille, J. J., and Joenje, H. (1992). Cell culture models for oxidative stress: superoxide and hydrogen peroxide versus normobaric hyperoxia. *Mutat. Res.* 275, 405–414. doi: 10.1016/0921-8734(92)90043-O
- Gruber, P., Marques, M. P. C., Szita, N., and Mayr, T. (2017). Integration and application of optical chemical sensors in microreactors. *Lab Chip* 17, 2693–2712. doi: 10.1039/c7lc00538e
- Haase, K., and Kamm, R. D. (2017). Advances in on-chip vascularization. *Regen. Med.* 12, 285–302. doi: 10.2217/rme-2016-0152
- Harris, A. L. (2002). Hypoxia — a key regulatory factor in tumour growth. *Nat. Rev. Cancer* 2, 38–47. doi: 10.1038/nrc704
- Harrison, B. S., Eberli, D., Lee, S. J., Atala, A., and Yoo, J. J. (2007). Oxygen producing biomaterials for tissue regeneration. *Biomaterials* 28, 4628–4634. doi: 10.1016/j.biomaterials.2007.07.003
- Heidemann, R., Lütkemeyer, D., Büntemeyer, H., and Lehmann, J. (1998). Effects of dissolved oxygen levels and the role of extra- and intracellular amino acid concentrations upon the metabolism of mammalian cell lines during batch and continuous cultures. *Cytotechnology* 26, 185–197. doi: 10.1023/A:1007917409455
- Hossmann, K.-A. (2006). Pathophysiology and therapy of experimental stroke. *Cell. Mol. Neurobiol.* 26, 1055–1081. doi: 10.1007/s10571-006-9008-1
- Jagannathan, L., Cuddapah, S., and Costa, M. (2016). Oxidative stress under ambient and physiological oxygen tension in tissue culture. *Curr. Pharmacol. Rep.* 2, 64–72. doi: 10.1007/s40495-016-0050-5
- Knezevic, L., Schapper, M., Muhleder, S., Schimek, K., Hasenberg, T., Marx, U., et al. (2017). Engineering blood and lymphatic microvascular networks in fibrin matrices. *Front. Bioeng. Biotechnol.* 5:25. doi: 10.3389/fbioe.2017.00025
- Lasave, L. C., Borisov, S. M., Ehgartner, J., and Mayr, T. (2015). Quick and simple integration of optical oxygen sensors into glass-based microfluidic devices. *RSC Adv.* 5, 70808–70816. doi: 10.1039/C5RA15591F
- Mahto, S. K., Charwat, V., Ertl, P., Rothen-Rutishauser, B., Rhee, S. W., and Sznitman, J. (2015). Microfluidic platforms for advanced risk assessments of nanomaterials. *Nanotoxicology* 9, 381–395. doi: 10.3109/17435390.2014.940402
- Manning, C. N., Martel, C., Sakiyama-Elbert, S. E., Silva, M. J., Shah, S., Gelberman, R. H., et al. (2015). Adipose-derived mesenchymal stromal cells modulate tendon fibroblast responses to macrophage-induced inflammation in vitro. *Stem Cell Res. Ther.* 6:74. doi: 10.1186/s13287-015-0059-4
- Mohyeldin, A., Garzón-Muvidi, T., and Quiñones-Hinojosa, A. (2010). Oxygen in stem cell biology: a critical component of the stem cell niche. *Cell Stem Cell* 7, 150–161. doi: 10.1016/j.stem.2010.07.007
- Muhleder, S., Pill, K., Schapper, M., Labuda, K., Priglinger, E., Hofbauer, P., et al. (2018). The role of fibrinolysis inhibition in engineered vascular networks derived from endothelial cells and adipose-derived stem cells. *Stem Cell Res. Ther.* 9:35. doi: 10.1186/s13287-017-0764-2
- Nichols, M. G., and Foster, T. H. (1994). Oxygen diffusion and reaction kinetics in the photodynamic therapy of multicell tumour spheroids. *Phys. Med. Biol.* 39, 2161–2181. doi: 10.1088/0031-9155/39/12/003
- Oomen, P. E., Skolimowski, M. D., and Verpoorte, E. (2016). Implementing oxygen control in chip-based cell and tissue culture systems. *Lab Chip* 16, 3394–3414. doi: 10.1039/c6lc00772d
- Petzelbauer, P., Bender, J. R., Wilson, J., and Pober, J. S. (1993). Heterogeneity of dermal microvascular endothelial cell antigen expression and cytokine responsiveness in situ and in cell culture. *J. Immunol.* 151, 5062–5072.
- Pouyssegur, J., Dayan, F., and Mazure, N. M. (2006). Hypoxia signalling in cancer and approaches to enforce tumour regression. *Nature* 441, 437–443. doi: 10.1038/nature04871
- Powers, D. E., Millman, J. R., Huang, R. B., and Colton, C. K. (2008). Effects of oxygen on mouse embryonic stem cell growth, phenotype retention, and cellular energetics. *Biotechnol. Bioeng.* 101, 241–254. doi: 10.1002/bit.21986
- Priglinger, E., Schuh, C., Steffenhagen, C., Wurzer, C., Maier, J., Nuernberger, S., et al. (2017). Improvement of adipose tissue-derived cells by low-energy extracorporeal shock wave therapy. *Cytotherapy* 19, 1079–1095. doi: 10.1016/j.jcyt.2017.05.010
- Pugh, C. W., and Ratcliffe, P. J. (2003). Regulation of angiogenesis by hypoxia: role of the HIF system. *Nat. Med.* 9, 677–684. doi: 10.1038/nm0603-677
- Rehberg, M., Ritter, J. B., Genzel, Y., Flockerzi, D., and Reichl, U. (2013). The relation between growth phases, cell volume changes and metabolism of adherent cells during cultivation. *J. Biotechnol.* 164, 489–499. doi: 10.1016/j.jbiotec.2013.01.018
- Rothbauer, M., Praisler, I., Docter, D., Stauber, R. H., and Ertl, P. (2015a). Microfluidic impedimetric cell regeneration assay to monitor the enhanced cytotoxic effect of nanomaterial perfusion. *Biosensors* 5, 736–749. doi: 10.3390/bios5040736
- Rothbauer, M., Wartmann, D., Charwat, V., and Ertl, P. (2015b). Recent advances and future applications of microfluidic live-cell microarrays. *Biotechnol. Adv.* 33, 948–961. doi: 10.1016/j.biotechadv.2015.06.006
- Sun, S., Ungerbock, B., and Mayr, T. (2015). Imaging of oxygen in microreactors and microfluidic systems. *Methods Appl. Fluoresc.* 3:034002. doi: 10.1088/2050-6120/3/3/034002
- Super, A., Jaccard, N., Cardoso Marques, M. P., Macown, R. J., Griffin, L. D., Veraitch, F. S., et al. (2016). Real-time monitoring of specific oxygen uptake rates of embryonic stem cells in a microfluidic cell culture device. *Biotechnol. J.* 11, 1179–1189. doi: 10.1002/biot.201500479
- Ungerbock, B., Charwat, V., Ertl, P., and Mayr, T. (2013). Microfluidic oxygen imaging using integrated optical sensor layers and a color camera. *Lab Chip* 13, 1593–1601. doi: 10.1039/c3lc41315b
- Volkmer, E., Drosse, I., Otto, S., Stangelmayer, A., Stengele, M., Kallukalam, B. C., et al. (2008). Hypoxia in static and dynamic 3D culture systems for tissue engineering of bone. *Tissue Eng. Part A* 14, 1331–1340. doi: 10.1089/ten.tea.2007.0231
- Wagner, B. A., Venkataraman, S., and Buettner, G. R. (2011). The rate of oxygen utilization by cells. *Free Radic. Biol. Med.* 51, 700–712. doi: 10.1016/j.freeradbiomed.2011.05.024
- Wang, X. D., and Wolfbeis, O. S. (2014). Optical methods for sensing and imaging oxygen: materials, spectroscopies and applications. *Chem. Soc. Rev.* 43, 3666–3761. doi: 10.1039/c4cs00039k
- Weltin, A., Slotwinski, K., Kieninger, J., Moser, I., Jobst, G., Wego, M., et al. (2014). Cell culture monitoring for drug screening and cancer research: a transparent, microfluidic, multi-sensor microsystem. *Lab Chip* 14, 138–146. doi: 10.1039/c3lc50759a
- Wolbank, S., Peterbauer, A., Fahrner, M., Hennerbichler, S., van Griensven, M., Stadler, G., et al. (2007). Dose-dependent immunomodulatory effect of human

- stem cells from amniotic membrane: a comparison with human mesenchymal stem cells from adipose tissue. *Tissue Eng.* 13, 1173–1183. doi: 10.1089/ten.2006.0313
- Wolfbeis Otto, S. (2015). Luminescent sensing and imaging of oxygen: fierce competition to the Clark electrode. *Bioessays* 37, 921–928. doi: 10.1002/bies.201500002
- Zhang, J., Wei, X., Zeng, R., Xu, F., and Li, X. (2017). Stem cell culture and differentiation in microfluidic devices toward organ-on-a-chip. *Future Sci. OA* 3:F50187. doi: 10.4155/fsoa-2016-0091
- Zhang, K., Zhu, L., and Fan, M. (2011). Oxygen, a key factor regulating cell behavior during neurogenesis and cerebral diseases. *Front. Mol. Neurosci.* 4:5. doi: 10.3389/fnmol.2011.00005
- Zhang, L., Marsboom, G., Glick, D., Zhang, Y., Toth, P. T., Jones, N., et al. (2014). Bioenergetic Shifts during transitions between stem cell states (2013 Grover Conference series). *Pulm. Circ.* 4, 387–394. doi: 10.1086/677353
- Zinkernagel, A. S., Johnson, R. S., and Nizet, V. (2007). Hypoxia inducible factor (HIF) function in innate immunity and infection. *J. Mol. Med.* 85, 1339–1346. doi: 10.1007/s00109-007-0282-2

**Conflict of Interest Statement:** The authors declare that the research was conducted in the absence of any commercial or financial relationships that could be construed as a potential conflict of interest.

Copyright © 2018 Zirath, Rothbauer, Spitz, Bachmann, Jordan, Müller, Ehgartner, Priglinger, Mühleder, Redl, Holnthoner, Harasek, Mayr and Ertl. This is an open-access article distributed under the terms of the Creative Commons Attribution License (CC BY). The use, distribution or reproduction in other forums is permitted, provided the original author(s) and the copyright owner(s) are credited and that the original publication in this journal is cited, in accordance with accepted academic practice. No use, distribution or reproduction is permitted which does not comply with these terms.





# AFM Monitoring the Influence of Selected Cryoprotectants on Regeneration of Cryopreserved Cells Mechanical Properties

Martin Golan<sup>1†</sup>, Sarka Jelinkova<sup>2,3†</sup>, Irena Kratochvílová<sup>1</sup>, Petr Skládal<sup>4</sup>, Martin Pešíl<sup>2,3,5</sup>, Vladimír Rotrekl<sup>2,3</sup> and Jan Pribyl<sup>4\*</sup>

<sup>1</sup> Department of Analysis of Functional Materials, Institute of Physics, Academy of Sciences Czech Republic, Prague, Czechia, <sup>2</sup> Department of Biology, Faculty of Medicine, Masaryk University, Brno, Czechia, <sup>3</sup> International Clinical Research Center, St. Anne's University Hospital, Brno, Czechia, <sup>4</sup> Central European Institute of Technology, Masaryk University, Brno, Czechia, <sup>5</sup> First Department of Internal Medicine/Cardioangiology, Masaryk University, Brno, Czechia

## OPEN ACCESS

### Edited by:

Cesare Gargioli,  
Università degli Studi di Roma Tor  
Vergata, Italy

### Reviewed by:

Simone Dinarelli,  
Istituto di Struttura della Materia (ISM),  
Italy

Francisco Javier Rodríguez-Lozano,  
Universidad de Murcia, Spain

### \*Correspondence:

Jan Pribyl  
pribyl@nanobio.cz

†These authors have contributed  
equally to this work.

### Specialty section:

This article was submitted to  
Integrative Physiology,  
a section of the journal  
Frontiers in Physiology

Received: 01 April 2018

Accepted: 08 June 2018

Published: 29 June 2018

### Citation:

Golan M, Jelinkova S, Kratochvílová I,  
Skládal P, Pešíl M, Rotrekl V and  
Pribyl J (2018) AFM Monitoring the  
Influence of Selected Cryoprotectants  
on Regeneration of Cryopreserved  
Cells Mechanical Properties.  
Front. Physiol. 9:804.  
doi: 10.3389/fphys.2018.00804

Cryopreservation of cells (mouse embryonic fibroblasts) is a fundamental task for wide range of applications. In practice, cells are protected against damage during freezing by applications of specific cryoprotectants and freezing/melting protocols. In this study by using AFM and fluorescence microscopy we showed how selected cryoprotectants (dimethyl sulfoxide and polyethylene glycol) affected the cryopreserved cells mechanical properties (stiffness) and how these parameters are correlated with cytoskeleton damage and reconstruction. We showed how cryopreserved (frozen and thawed) cells' stiffness change according to type of applied cryoprotectant and its functionality in extracellular or intracellular space. We showed that AFM can be used as technique for investigation of cryopreserved cells surfaces state and development *ex vivo*. Our results offer a new perspective on the monitoring and characterization of frozen cells recovery by measuring changes in elastic properties by nanoindentation technique. This may lead to a new and detailed way of investigating the post-thaw development of cryopreserved cells which allows to distinguish between different cell parts.

**Keywords: cryopreservation, cell stiffness, AFM, fluorescence microscopy, DMSO, PEG**

## INTRODUCTION

The aim of cryopreservation is to reanimate frozen cells to physiological life with negligible loss of viability and functionality. Effective cryopreservation is an important problem in medicine (Woods et al., 2016), pharmaceutical, food industries, and agriculture. A major drawback of cryopreservation is that ice crystallization appearing during the freezing process can significantly damage the cells which then lose viability after melting (Chen et al., 2013; Rajan et al., 2016; Ding et al., 2017). The fact that big part of cells from a multitude of prokaryotic and eukaryotic organisms can be recovered from temperatures down to almost  $-200^{\circ}\text{C}$  below the freezing point is thus achieved due to a trick—the presence of cryoprotectants. A multitude of factors affect the effectiveness of cryopreservation in microorganisms, for example, species, strain, cell size and form, growth phase and rate, incubation temperature, growth medium composition, pH, osmolarity, cell water content, lipid content and composition of the cells, density at freezing, composition of the freezing medium, cooling rate, storage temperature and duration of storage, warming rate, and recovery medium (Hubalek, 2003; Kratochvílová et al., 2017).

Based on the extent to which the cryoprotectant is able to enter into the cell, three categories of additives can be distinguished: (1) cryoprotectants penetrating both cell and nuclear membrane [dimethylsulfoxide (DMSO), glycerol]; (2) cryoprotectants penetrating cell membrane but not nuclear membrane (mono- and disaccharides, amino acids); (3) cryoprotectants not penetrating even cell membrane (proteins, polysaccharides, PEG-1500 where 1500 denotes molecular mass).

The type of cryoprotectant is usually defined according to its cell penetration depth and speed. Quickly penetrating cryoprotectants [e.g., ethylene glycol, propylene glycol, dimethylsulfoxide (DMSO)] usually permeate the whole cell volume within 30 min. The permeation rate of glycerol is comparatively slower. Non-permeating cryoprotectants [polyvinyl pyrrolidone, PEG-1500, or polyvinyl alcohol (PVA)] cannot enter the cell due to their high molecular mass (Hubalek, 2003).

The studies of changes in surface characteristics of cell membranes caused by freeze-thawing can be important for assessment of structural and functional integrity of cells and understanding the mechanisms responsible for their damage under extreme conditions (Mandumpal et al., 2011). Deleterious changes in cytoskeletal component such as disruption of the actin filaments were observed in thawed cells. This damage was caused mainly by the freezing process itself (Ragoonanan et al., 2010; Xu et al., 2012). This disruption of actin filaments was identified to be caused by defective F-actin polymerization after freezing process (Chinnadurai et al., 2014).

It has been demonstrated that cell mechanical stiffness is mainly determined by the cytoskeleton, especially the networks of actin and intermediate filaments and other proteins associated with them. And thus disruption and other remodeling processes could contribute to cell stiffness changes. Among the many devices for microindentation (Levental et al., 2010), the Atomic Force Microscope (AFM) is commercially available and has been widely applied to characterize mechanical properties of living cells and tissues (Wang et al., 2009). AFM (Alessandrini and Facci, 2005; Masek et al., 2011a,b; Fekete et al., 2012; Cartagena-Rivera et al., 2015; Pesl et al., 2016) allows to scan living cell topography under ambient conditions (liquid medium), and also offers a force spectroscopy mode. In this mode, cell is indented at many sites and its complete elastic response is recorded which enables to reconstruct its stiffness map (Ogden, 1972).

Using AFM we studied changes of mechanical properties of cells resulting from their exposure to cryogenic temperatures after application of cryoprotectants either penetrating both cell membrane and nuclear membrane (DMSO) or penetrating neither of these membranes (PEG 1500) (Dokukin et al., 2013; Guz et al., 2014; Gavara, 2016; Dokukin and Sokolov, 2017). These factors have an impact on cellular structure, which in turn influences cell elasticity (Ofek et al., 2009; Masek et al., 2011a).

By combination of AFM and fluorescence microscopy we showed how selected cryoprotectants (DMSO, PEG) affected mechanical properties and cytoskeleton remodeling of

cryopreserved cells (mouse embryonic fibroblasts). Significant differences of the investigated properties of the thawed cells were found as a response to the cryoprotectant used in the freezing process.

## MATERIALS AND METHODS

### Cell Culture, Freezing, and Sample Preparation

Mouse embryonic fibroblasts (MEFs) (CF-1 mouse strain; Eiselleova et al., 2008) were propagated on 100 mm Petri dish in MEF medium [MEF medium consists of Knockout Dulbecco's modified Eagle's medium (KO-DMEM; Gibco), 10% heat-inactivated fetal bovine serum (FBS; Invitrogen), 1% L-glutamine (Gibco), 1% non-essential amino acids (PAA), 1% penicillin-streptomycin (PAA), and 0.1 mM  $\beta$ -mercaptoethanol (Sigma)] until passage 2 (P2). A confluent grown cell culture was incubated with SIR F-Actin (Spirochrome, distributed by tebu-bio, Offenbach, Germany) in concentration of 1  $\mu$ M, and verapamil in concentration 1  $\mu$ M for 90 min. The cells were washed with PBS and trypsinized (Trypsin EDTA, Invitrogen, Ca USA) for 2 min and collected into centrifuge tube. The cell suspension was spinned by 200 g/4 min and resuspended to concentration 1,000,000 cells/ml. 200,000 cells (in 0.2 ml of MEF medium) were placed into 2 ml cryo tube (TPP, Trasadingen, Switzerland). Freezing was done by addition of 0.2 ml of ice-cold freezing medium drop by drop into the tube.

Variable freezing media were used in final concentrations as follows: DMSO freezing medium consisting of 80% KO-DMEM, 10% FBS, and 10% DMSO (Hybri-Max<sup>TM</sup>, Sigma); PEG1500 freezing medium consisting of 82.5% KO-DMEM, 10% FBS, and 7.5% polyethylene glycol (Mw 1500; PEG1500; kind gift from Dr. Karel Pomeisl, Institute of Physics, Academy of Sciences Czech Republic). The tubes were placed in Nalgene dish for 24 h in  $-80^{\circ}\text{C}$ , then transferred to liquid nitrogen (at least for 24 h) until measurement.

Cryo tube with MEFs P2 was taken out from liquid nitrogen (Dewar flask) and cell suspension was quickly thawed in stream of hot water until the point, where a few remaining crystals were visible in the tube. The whole volume was immediately transferred into the 15 ml centrifuge tube and 12 ml of cold ( $4^{\circ}\text{C}$ ) MEF medium was added dropwise from Pasteur pipette. The tube was centrifuged (200 g,  $4^{\circ}\text{C}$ ) for 4 min, the excess of MEF medium above the cell pellet was removed by pipette, cells were resuspended in 1 ml of MEF medium ( $37^{\circ}\text{C}$ ) and 0.5 ml distributed onto 35 mm low ibidi dish (ibidi GmbH, Martinsried, DE) for AFM measurements and 0.5 ml into 35 mm Glass Bottom Culture Dish (MaETek corporation, Ashland, MA, USA) for Life Imaging procedures. The dishes were placed into standard  $\text{CO}_2$  incubator for 20 min for the cells to attach. For AFM measurements, all unattached cells from ibidi dish were removed by PBS wash and fresh MEF medium was added into the dish with 100 nmol/l of SIR F-Actin, installed in the AFM dish holder pre-heated during the calibration process and after the AFM instrument adjustment, the force mapping measurement was immediately started.

## Young's Modulus Mapping by Atomic Force Microscope

Standard bio AFM microscope JPK NanoWizard 3 (JPK, Berlin, Germany) was used to perform force mapping procedure. The scanning-by-probe head (maximal visualization range 100–100–15  $\mu\text{m}$  in X-Y-Z axis) of the AFM system was placed on inverted optical microscope Olympus IX-81 (Olympus, Tokyo, Japan), 10x objective was used to find proper area covered with cells and to place cantilever in the proper position for the force mapping procedure. Plastic Petri dish with either the distilled water for instrument calibration or with the fibroblast culture was placed inside the Petri dish heater (JPK) pre-heated to 37°C.

We compared set points, indentation depths and the Young's modulus (YM) of cultivated cells for measurements performed by the spherical and pyramidal AFM tips, respectively. For spherical tip and small set points (e.g., lower than 0.5 nN) the contact parts of force curves were not sufficient for reliable fits. On the other hand, force curves obtained with pyramidal tip and higher set point values (1.5 nN and above) were often not smooth. The notches observed on the curves likely corresponded to structural damage of the measured cells.

When using a spherical probe at high (1 nN) set point, cells were indented down to similar depth as when using the pyramidal probe at low set point (lower than 0.5 nN) with close values (deviation less than 8%) of obtained Young's modulus. Based on these considerations, we chose to use the spherical probe with set point 1 nN. Thus, the elastic properties of the cells could be probed down to significant indentation depths ( $\sim 0.5$ – $1 \mu\text{m}$ ) while avoiding structural damage to the measured cells. Furthermore, the obtained YM values were less susceptible to variations caused by small-scale membrane and submembrane features thanks to the large contact surface of the colloidal probe (as opposed to the pyramidal tip). Non-coated silicon nitride cantilevers with colloidal sphere probe made of hydrophilic silicon dioxide (diameter, 6.62  $\mu\text{m}$ ) sCUBE CP-sq-SCONT-SiO-C (sQUBE, Bickenbach, Germany) were used for experiments with spherical indenter. Non-coated silicon nitride AFM cantilever Hydra 2R-100N (AppNano, Mountain View, CA, USA) equipped with silicon pyramidal probe (side angle 18°) were used in the optimization study, i.e., to compare pyramidal and spherical probe indentation. The probe was calibrated prior to every experiment as described below.

The calibration procedure was done in double distilled water, when the whole setup was pre-heated (Petri dish heater) to 37°C for 30 min. Then the laser reflection sum was maximized, followed by centering of the laser detector. The AFM probe was introduced in contact with the surface during a standard process of landing. The sensitivity of the AFM setup was determined as a slope of the force-distance curve measured by lifting the cantilever with Z-height of 450 nm, time per curve was 3 s. The sensitivity was found in the range 15.07–15.37 nm/V, cantilever stiffness was calibrated by measurement of its thermal noise and lay between 17.34 and 19.19 mN/m for different days of experiments.

The bio AFM setting was identical for all the force mapping procedure. Set Point value was 1.0 nN (relative to baseline value), time per curve 0.45 s, Z-length 15.0  $\mu\text{m}$ , speed of curve

recording 33.3  $\mu\text{m/s}$ , the force-distance curves were recorded with data sample rate of 2 kHz. The force mapping procedure was performed as step-by-step recording of force-distance curves in the network of 64  $\times$  64 points on 75  $\times$  75 to 100  $\times$  100  $\mu\text{m}^2$  covering area of either single or more fibroblast cells.

Reproducibility of the nanomechanical measurement was performed by 5-times repeated force mapping process on identical place (scanning over the identical cell). Neither medium exchange nor AFM instrument adjustment was involved during the repeated mapping procedure.

Place-to-place reproducibility was studied, when the identical force mapping experiments were subsequently performed on two different places found randomly on the Petri dish surface covered with fibroblasts.

Before the measured AFM data were further processed and interpreted, all parts of each sample corresponding to the plastic dish were algorithmically removed using Wolfram Mathematica (Wolfram, 2017).

The fluorescence stack images were recorded periodically between the capturing of the force maps, when the AFM detection laser was switched off and the AFM indenter was not in the contact with the surface, however the AFM measuring head was kept in the position to be able to start another indentation process immediately. The fluorescence images of the SiR-actin stained cells were recorded using the Olympus IX-81S1F-3 inverted microscope equipped with U-MF2 ET-CY5 filtration cube (Olympus) and mercury lamp Olympus U-RFL-T. The stack images were recorded using the Andor Zyla 5.5 sCMOS camera (Andor, Belfast, UK). Both, inverted microscope and sCMOS camera, were driven by Olympus CellSens Dimension software. This software was used to record and post-process the stack images—i.e., a series of images taken in different focal length, typically 15–25 images were recorded with step of 0.23  $\mu\text{m}$ ). The stack images were afterwards combined to produce final image showing the structure of cytoskeleton.

## Combined Monitoring of the Post-thawing Properties of the Cryopreserved Cells

Surface stiffness of the fibroblasts cultured on a Petri dish 30 min after thawing process was monitored till 4.5 h after thawing by nanomechanical mapping of the fibroblast cell. The scanned area was not changed during the whole monitoring. The AFM measurements were combined with fluorescence imaging.

In detail, Petri dish containing freshly thawed suspension of cells was pre-incubated in a standard CO<sub>2</sub> incubator. When first cells started to adhere (30 min after thawing), culturing medium in the dish was completely exchanged and fluorescence stack imaging (see previous chapter for details) periodically followed by force mapping process was started immediately.

Culturing medium inside the dish was changed for the new one after each force-mapping procedure, when the tip was not in contact with the sample surface. Following parameters were used for the FM procedure: Setpoint value was either 0.75 nN for pyramidal tip or 1.0 nN when the spherical indenter was used. Time per curve was 0.5 s, Z-length 15.0  $\mu\text{m}$ , speed of curve recording 30.0  $\mu\text{m/s}$ , the force distance curves were recorded with data sample rate of 2 kHz. The force mapping procedure was

performed as step by step recording of force distance curves in the network of  $64 \times 64$  points on  $75 \times 75$  to  $100 \times 100 \mu\text{m}^2$  covering area of either single or more fibroblast cells.

Force mapping process provides a network of force-distance curves (FDC, dependency of tip-sample interaction force on tip height above the surface), so called force maps (FM) (Dimitriadis et al., 2002; Touhami et al., 2003). The absolute value of Young's modulus can be determined by fitting the FDC by equation 1 (spherical probe, Hertz-Sneddon model; Sneddon, 1965; Gavara and Chadwick, 2012).

$$P = \frac{E}{(1-\nu^2)} \left( \frac{R^2 + a^2}{2} \text{Log} \left( \frac{R+a}{R-a} \right) - aR \right),$$

$$\delta = \frac{a}{2} \text{Log} \left( \frac{R+a}{R-a} \right) \quad (1)$$

Where  $P$  is load,  $E$ —Young's modulus,  $\nu$ —Poisson ration (0.5 for incompressible materials),  $\delta$ —depth of indentation;  $a$ —contact radius,  $R$ —radius of the spherical probe.

The fitting of FDC by Equation (1) was performed in the AtomicJ software (Hermanowicz et al., 2014), with the contact point position estimated by an incorporated Robust Exhaustive algorithm and best fit found by the Robust HLTA algorithm. Poisson ratio was set to 0.5. In all cases, the fitting was performed on the approach curve. Resulting Young's modulus maps were exported in order to be post-processed in Wolfram Mathematica (Wolfram, 2017).

After the fitting, some points were removed from the YM maps based on the values of various parameters of the corresponding fit. First, a threshold of 10 kPa was introduced for the YM value in order to exclude all curves measured over the dish surface or over very thin cell regions.

Furthermore, all fits yielding indentation greater than  $2 \mu\text{m}$  were filtered out as such a large indentation always meant a faulty contact point estimation. Here, indentation was defined as the indentation depth difference between the shallowest (i.e., contact) point and the deepest point of the fitted part of the FDC.

Also, if the indentation force at the deepest point of the fitted region was less than 80% of the total set point, the corresponding curve was removed. Thus, FDCs whose fitted region was too small were not taken into consideration.

Among other benefits, these constraints helped us to exclude force curves which couldn't be well-described by the Hertz-Sneddon model with single  $E$  value (i.e., they typically contained a significantly stiffened region at larger depths). Such curves were typically located in the border regions of the measured cells. In the remaining curves, it was therefore not necessary to employ modified indentation models incorporating e.g., the bottom effect cone correction (Gavara and Chadwick, 2012).

Finally, the adequacy of the Hertz-Sneddon model was checked. The curves kept for final statistical analysis had root-mean-square deviation of the model from the actual data points smaller than 5% of the maximum set point, and at each point the maximum deviation of the model values from the measured data was always smaller than 7% of the maximum set point.

After applying all filters, 90% of curves measured on cells and corresponding YM values were left for statistical analysis.

## Live Imaging

The thawed cells were left to attach to the culture dish for 30 min, after the complete exchange of medium, the dish was left for additional 10 min in the incubator then transferred onto inverted confocal Zeiss LSM700 microscope with  $37^\circ\text{C}$  and 5%  $\text{CO}_2$ . Time Series video was taken with 3 min interval for 120 cycles (6 h) on 40x Oil immersion objective, with laser intensity 1.8%, pinhole 228.6 ( $6.2 \mu\text{m}$ ) and samples were excited with 639 nm laser and fluorescence detected in far red spectrum (for actin labeling) and in phase contrast (for cell morphology) (acquisition speed 25–30 s per image). Videos were managed and exported using ZEN Black or ZEN Blue system.

## Viability of Cells

Flow cytometry was used to quantify survival and apoptosis in cells that were frozen with or without cryoprotectants. The Muse<sup>®</sup> Cell Analyser (Merck Millipore) and Muse<sup>®</sup> Annexin V and Dead Cell Assay Kit (MCH100105, Millipore), which can discriminate between live, early apoptotic, late apoptotic/necrotic and dead cells, were used according to Hofer et al. (2016).

The viability of the fibroblast cells was tested by standard TrypanBlue test. Time points of the test were selected to be identical with the force mapping procedure, i.e., viability was checked every 30 min, from 0.5 h till 4.5 h after thawing. The wells of standard microtitration plate were washed to exclude floating cells, trypsinized and collected into tubes. Cell suspension was then incubated in 0.5% TrypanBlue solution (1:1) for 2 min and viable cell ratio was counted on hemacytometer. For the testing of cell viability after freezing/thawing, 10 experiments were performed for each cryoprotectant.

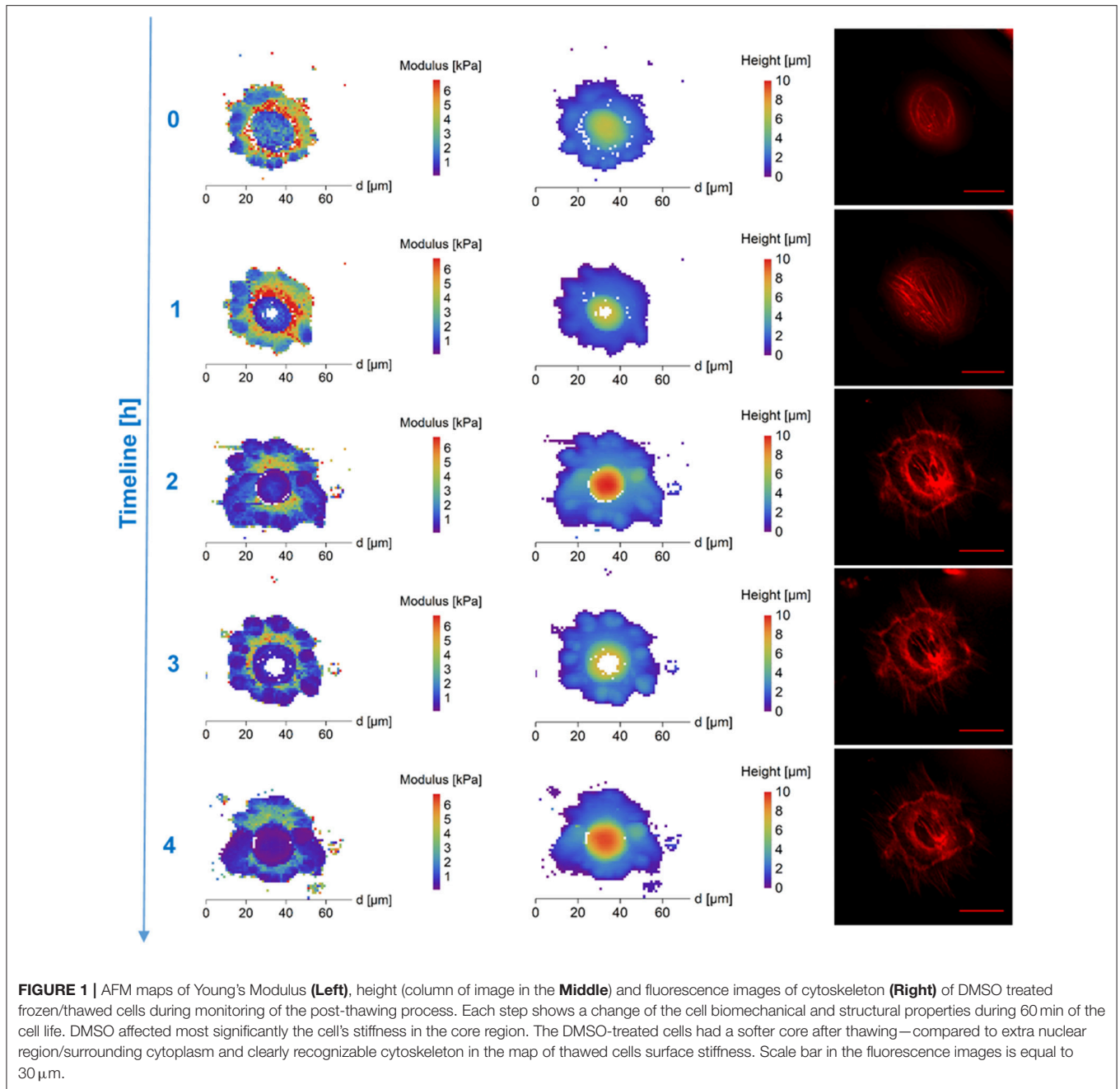
## Statistical Evaluation of Data

For each cryoprotectant, 3 experiments were performed. Total number of mapped DMSO treated frozen/thawed cells was 9 because in some maps, multiple cells were present. Mapping of cells frozen/thawed in PEG-1500 was done on 8 cells. The normality of the distribution of  $E$  values obtained from different cells at a certain time point was evaluated by Shapiro Wilk method thus proving the data normality at 0.05 level. Standard error of the mean values for each time point was less than 7%.

After measuring the force curves across the whole area, each force curve was fitted with the Hertz-Sneddon model, which yielded the YM value. Then, we removed the YM values that resulted from a faulty (aforementioned) fit (or rather a fit of faulty curves which occasionally occurred in the set). In the remaining set of curves, we analyzed the distribution of YM values in different surface parts (upper and lower half) and also calculated mean and median of the whole cell YM.

## RESULTS AND DISCUSSION

Using flow cytometry, we first checked how the application of cryoprotectants (DMSO, PEG) affected cell viability. Both



DMSO- and PEG-treated non-frozen cells had viability over 90% (Supplementary Table 1). Next, we measured cell viability of cells after freezing/thawing. Without cryoprotectants, almost all frozen cells died after being thawed; only <5% survived thawing. The highest cryoprotective effect was provided by DMSO (>80% thawing survival). The improvement of cell viability by PEG was also relatively large: close to 50% of cells survived thawing. Thanks to its small size and physical-chemical properties, DMSO is able to penetrate both into the cell cytoplasm and the nucleus where it protects cells against freezing damage very effectively (Dong et al., 2010). On the

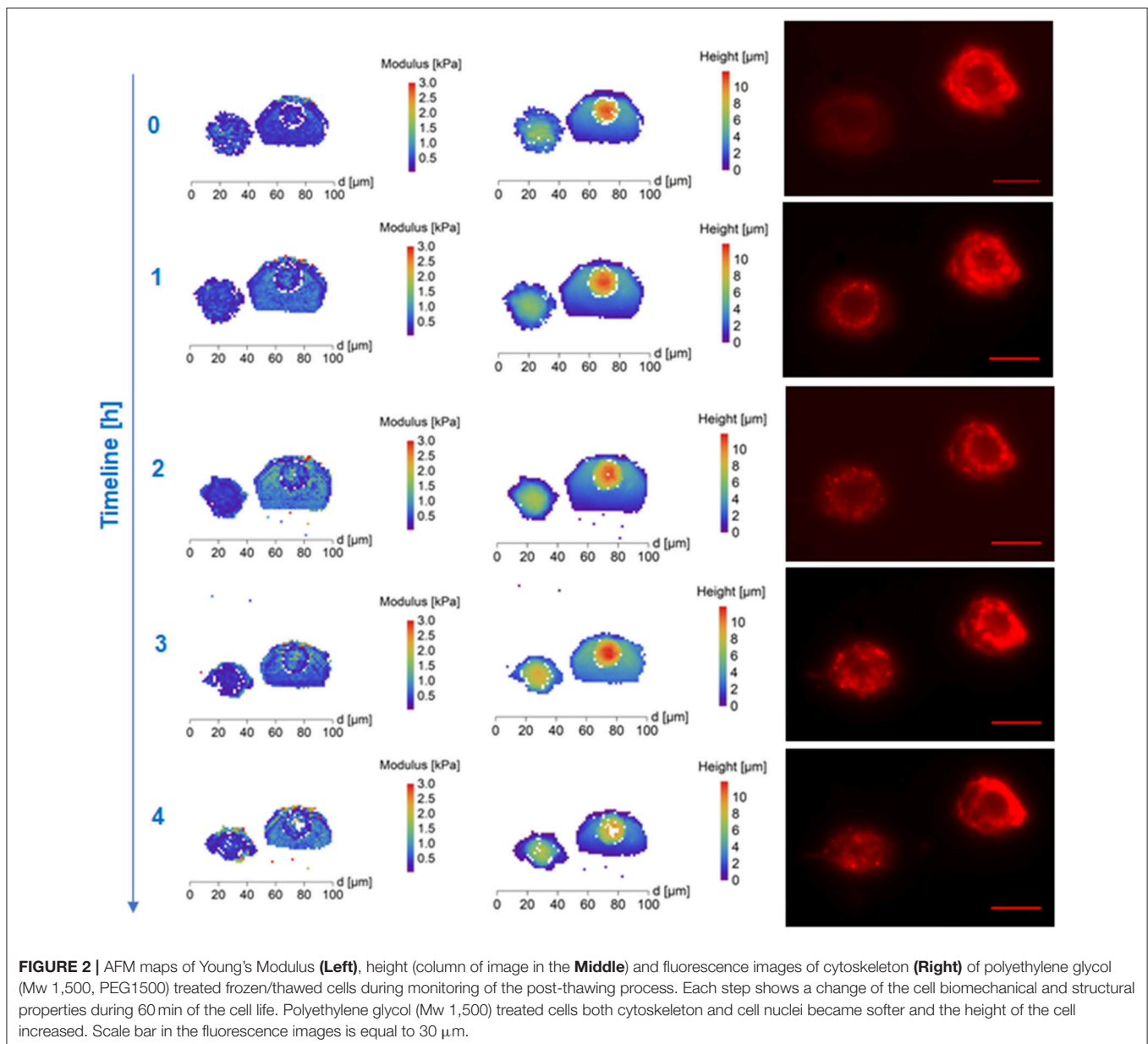
contrary, PEG 1500 due to its high molecular mass is not able to penetrate even cell membrane and protects the cell only from the extracellular space, which limits its cryoprotective efficiency.

The viability of the cells tested by AFM was measured at the time points from 30 min to 4.5 h after thawing (Supplementary Table 2) in order to correspond to force mapping procedures. During this whole time, the survival rate of DMSO-cryopreserved cells remained twice as high as the population of PEG-cryopreserved cells. For either treatment, the cell viability didn't significantly decrease during the AFM monitoring.

In order to determine the cryopreservation properties of the selected cryoprotectants on the cytoskeleton remodeling upon thawing we measured the surface stiffness of cells treated with DMSO or PEG. By repetitive measurements we further observed the dynamics of the development of the cell surface stiffness in detail (**Figure 1**). In order to see the differential effect of cryoprotectants on different parts of the cryopreserved cells we correlated the surface stiffness maps and cell surface height (**Figure 1**). We distinguished two major regions, the core/nuclear region forming 50–100% of the total cell height and cell edges located outside the nuclear region which formed 0–50% of the total height of the cell. In order to project the changes in cell surface stiffness into the remodeling cytoskeleton we combined the AFM with standard fluorescence-based method for live cytoskeleton visualization which demonstrated that cell surface

stiffness closely resembles the cell cytoskeleton regeneration occurring after freezing/thawing.

DMSO affected most significantly the cell's stiffness in the core region. Approximately 30 min after thawing, the DMSO-treated cells had a softer nucleus (mean values)—compared to surrounding cytoplasm in the map of thawed cells surface stiffness with clearly recognizable cytoskeleton in fluorescent microscopy (**Figure 1**, Supplementary Figure 2). The stiff perinuclear area presents itself with a dense ring of structured actin that seems to correlate with observed higher stiffness. After forming of linear actin stress fibers (observed 70 min after thawing), the area with the highest density of these structures remains also the stiffest (**Figure 1**) as was also shown in fibrous cartilage samples where presence of fiber increases the local stiffness (e.g., Loparic et al., 2010; Kasas et al., 2013). That



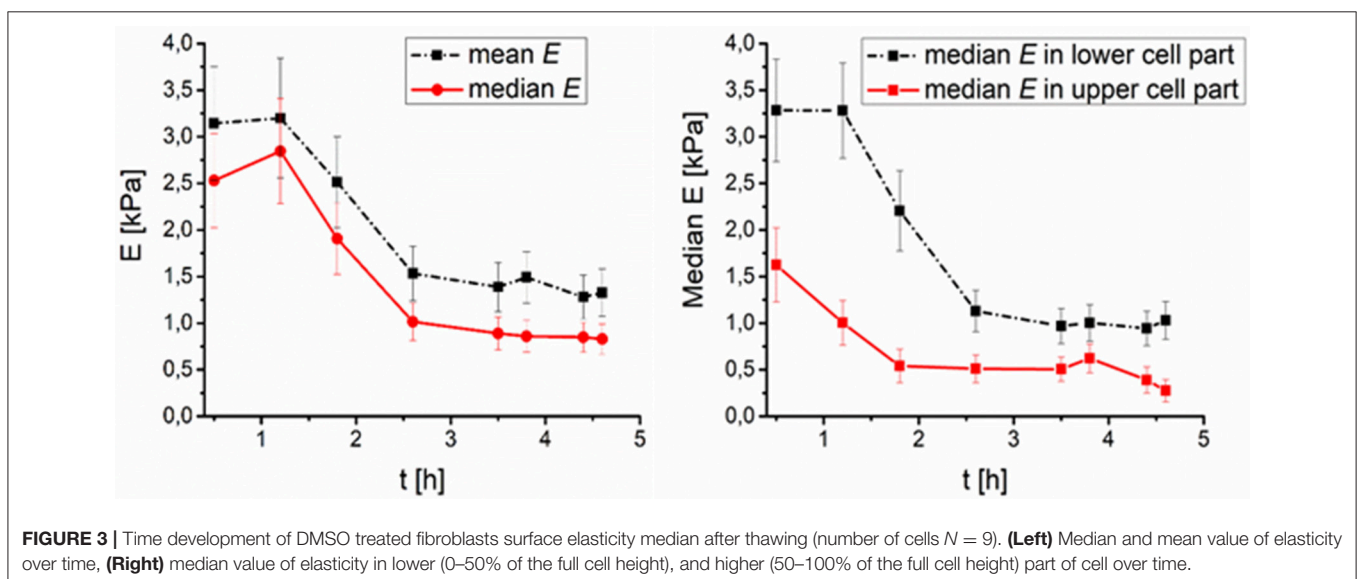
could be explained by the property of DMSO to bundle actin filaments into thick fibers (Lampugnani et al., 1987), which could be better protected against the very low temperatures. Gradual development of the round shaped structures at the border of the cells can be seen in case of DMSO cryoprotected fibroblasts (Figure 1, time points 0.5–4.5 h post-thaw). This may correspond to the development of lamellipodia, which are a part of the cell adhesion apparatus (Parsons et al., 2010). This is supported by the fluorescence images in Figure 1 which show an increasing amount of actin fibers. On the contrary, PEG-cryopreserved cells present more spheroidal shape after thawing and initial attaching, with rather homogeneous spatial distribution of stiffness (mean values). The stiffness of PEG-treated frozen/thawed cells nuclei are close to stiffness of the surrounding cytoplasm (mean values) (Figure 2, Supplementary Figure 3). That suggests decreased actin remodeling potential, since the actin cytoskeleton pattern is unstructured or broken, showed by homogeneous low stiffness of the whole cell area. The actin disruption could be caused by absent protection of cytoskeleton proteins inside the cells, since PEG is a non-penetrating chemical. Due to low temperatures, the actin structures are damaged (Ragoonanan et al., 2010; Pogoda et al., 2012; Xu et al., 2012) and expression of new actin proteins is affected too (Lin and Tsai, 2012) causing decline in regeneration of actin structures responsible for support to the cell membrane.

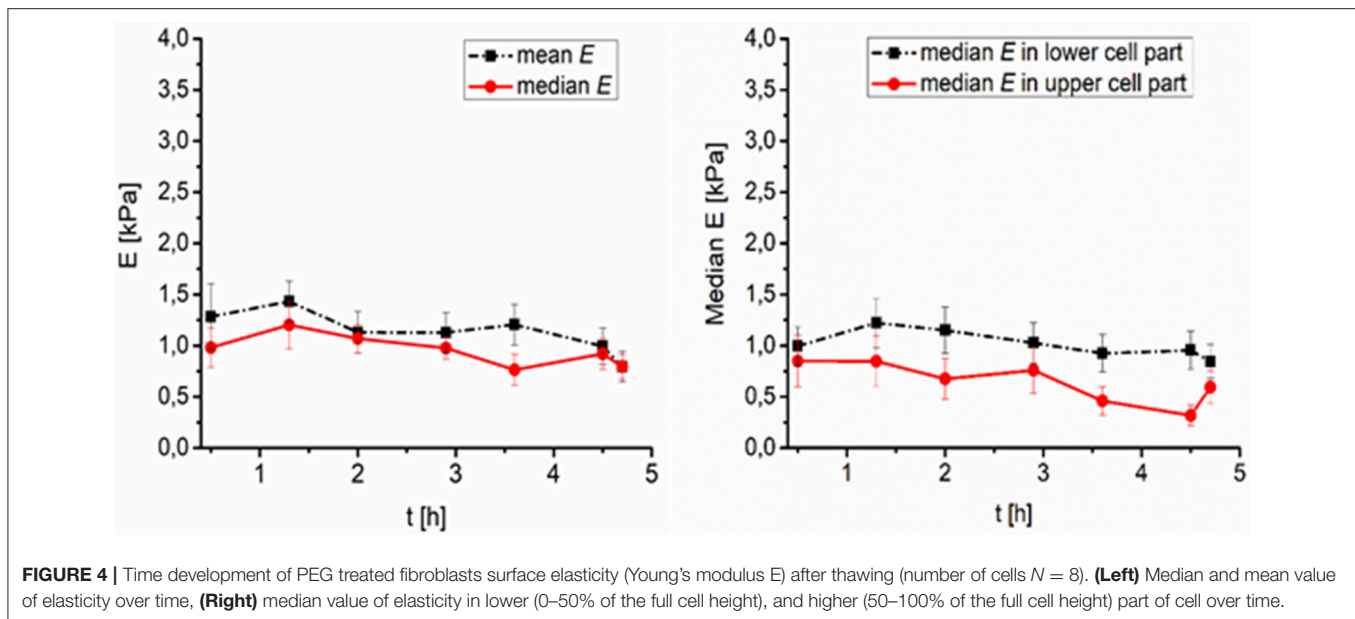
Time development of stiffness of cryopreserved cells reflects the cryoprotectant interaction with the cell and cryoprotective functionality of the material. The stiffness of PEG treated frozen and thawed cells was low (compared to DMSO treated cells) and homogeneous over the whole cells. The stiffness of PEG treated cells change in time is relatively (compared to DMSO treated cells) mild (mean values changes) after thawing. The time required for proper attachment and forming of linear stress fibers significantly differ between DMSO and PEG medium. The time required for flattening of the cell, which was accompanied by change of dense ring structure around the nucleus remodeled into first linear fibers of actin was  $27 \pm 15$  min in DMSO (10

cells) and  $53 \pm 24$  min in PEG1500 (5 cells) freezing medium. This corresponds to the measured greater height of the PEG frozen cells and constant lower elasticity as the cytoskeleton is remodeling slowly into fibers. While DMSO frozen cells create a dense actin ring around the nucleus after plating, which increases stiffness in the perinuclear area in correspondence to actin fiber presence, the non-structured filaments in PEG frozen cells have no effect on stiffness elevation of the cell and thus the whole cell is softer. These data correspond to the possible DMSO protection function of actin fibers (Lampugnani et al., 1987) which start to remodel soon after thawing. Conversely, these data suggest a lack of protection by PEG, leading to actin fiber disruption and a slowdown of initiation of new actin protein expression caused by the freezing process (Lin and Tsai, 2012). Development of the cytoskeleton in a real time was monitored by confocal microscopy for period of 5 h and can be seen as videos in the Supplementary Material section (video captions are shown as Supplementary Figure 1).

As far as cell stiffness time development after thawing is concerned, the stiffness of DMSO-cryopreserved cells significantly decreases during first 2 h (up to 60%), while the stiffness change of the PEG1500-cryopreserved cell remains low (maximum decrease of 20%) even till 4.5 h after thawing (Figures 3, 4). For DMSO or PEG treated frozen and thawed cells the values of  $E$  from the core part of the cell had the smallest spatial deviation from median  $E$ —less than 10%. Such deviation corresponds to relatively sharp distributions of  $E$  values (within core regions) measured with a spherical tip. Spatial deviation of  $E$  from the whole area median of  $E$  was for extra-nuclear cells regions smaller than 20%.

Small DMSO molecules enter even the nuclei of the cells and affect the freezing process of the cells so that the median of the stiffness is higher (compared to PEG treated frozen/thawed cells), cell nuclei is softest part of the cell immediately after thawing. The difference in stiffness between the core and the edge of DMSO treated/thawed cells was reduced within 2.5 h after thawing.





## CONCLUSIONS

Using AFM we studied stiffness of DMSO or PEG treated cryopreserved cells. Cryoprotectants used were of two types: penetrating both cell membrane and nuclear membrane (DMSO) or not penetrating even cell membrane (PEG 1500). The median stiffness of PEG treated frozen and thawed cells was lower compared to DMSO treated cells stiffness. PEG-cryopreserved cells viability was lower than DMSO treated cryopreserved cells. PEG treated cells were more round and taller immediately after thawing, with homogeneous spatial distribution of stiffness.

On the contrary, DMSO treated cells had considerably higher viability after thawing than PEG treated cells and cryopreserved stiffness maps of thawed DMSO treated cells were not homogeneous. Immediately after thawing DMSO treated cell nuclei are typically the softest part of the cells. The cytoskeleton is also clearly distinguishable in the modulus maps due to its comparatively higher stiffness. From 0.5 till 4.5 h after thawing, the spatial variation of stiffness of the DMSO-treated cells' surface gradually decreased. The median of the DMSO treated cryopreserved cells stiffness is higher than PEG treated cryopreserved cells. The selection of proper freezing medium has effect on cytoskeleton remodeling after freeze/thaw cycle, as DMSO seems to have protecting abilities toward actin filaments, while non-penetrating PEG protection of these molecules is insufficient and connected with longer remodeling time and higher elasticity of the cell.

We showed that AFM can be used as technique for investigation of cryopreserved cells surfaces state and development *ex vivo*. Our results offer a new perspective on the monitoring and characterization of frozen cells' recovery by measuring their elastic response to external mechanical stimuli. This may lead to a new and detailed way of investigating the post-thaw development of cryopreserved cells which allows to distinguish between different cell parts.

## DATA AVAILABILITY STATEMENT

The datasets of the raw data (raw force map files recorded by the AFM microscope, force map files processed by AtomicJ software, fluorescence stack images and live cell imaging video recorded by confocal microscope) for this study can be found in the Zenodo file repository under following link: <https://doi.org/10.5281/zenodo.1209827>. Amount of the data files stored here exceeds 40 GB.

## AUTHOR CONTRIBUTIONS

MG AFM data processing and interpretation, writing parts of the manuscript. IK project initiation, writing parts of the manuscript. PS, MP, and VR writing parts of the manuscript. SJ cell culture and freezing/thawing manipulation, Life imaging, actin data interpretation, and manuscript writing. JP AFM force nanoindentation process, fluorescence stack imaging, data processing and interpretation, manuscript writing.

## ACKNOWLEDGMENTS

This work was supported by the Ministry of Education, Youth, and Sports of the Czech Republic (FUNBIO CZ.2.16/3.1.00/21568, SAFMAT LM 2015088, LTC17083 in frame of the COST CA15107), National Program of Sustainability II CEITEC 2020 (LQ1601, LO1409) and Grant Agency of the Czech Republic (GACR) grant no: P302/12/G157.

## SUPPLEMENTARY MATERIAL

The Supplementary Material for this article can be found online at: <https://www.frontiersin.org/articles/10.3389/fphys.2018.00804/full#supplementary-material>



## REFERENCES

- Alessandrini, A., and Facci, P. (2005). AFM: a versatile tool in biophysics. *Meas. Sci. Technol.* 16, R65–R92. doi: 10.1088/0957-0233/16/6/R01
- Cartagena-Rivera, A. X., Wang, W. H., Geahlen, R. L., and Raman, A. (2015). Fast, multi-frequency, and quantitative nanomechanical mapping of live cells using the atomic force microscope. *Sci. Rep.* 5:11692. doi: 10.1038/srep11692
- Chen, S. W., Odorico, M., Meillan, M., Vellutini, L., Teulon, J.-M., Parot, P., et al. (2013). Nanoscale structural features determined by AFM for single virus particles. *Nanoscale* 5, 10877–10886. doi: 10.1039/c3nr02706f
- Chinnadurai, R., Garcia, M. A., Sakurai, Y., Lam, W. A., Kirk, A. D., Galipeau, J., et al. (2014). Actin cytoskeletal disruption following cryopreservation alters the biodistribution of human mesenchymal stromal cells *in vivo*. *Stem Cell Rep.* 3, 60–72. doi: 10.1016/j.stemcr.2014.05.003
- Dimitriadis, E. K., Horkay, F., Maresca, J., Kachar, B., and Chadwick, R. S. (2002). Determination of elastic moduli of thin layers of soft material using the atomic force microscope. *Biophys. J.* 82, 2798–2810. doi: 10.1016/S0006-3495(02)75620-8
- Ding, Y., Xu, G. K., and Wang, G. F. (2017). On the determination of elastic moduli of cells by AFM based indentation. *Sci. Rep.* 7:45575. doi: 10.1038/srep45575
- Dokukin, M. E., Guz, N. V., and Sokolov, I. (2013). Quantitative study of the elastic modulus of loosely attached cells in AFM indentation experiments. *Biophys. J.* 104, 2123–2131. doi: 10.1016/j.bpj.2013.04.019
- Dokukin, M. E., and Sokolov, I. (2017). Nanoscale compositional mapping of cells, tissues, and polymers with ringing mode of atomic force microscopy. *Sci. Rep.* 7:11. doi: 10.1038/s41598-017-12032-z
- Dong, J., Malsam, J., Bischof, J. C., Hubel, A., and Aksan, A. (2010). Spatial distribution of the state of water in frozen mammalian cells. *Biophys. J.* 99, 2453–2459. doi: 10.1016/j.bpj.2010.08.035
- Eiseloeva, L., Peterkova, I., Neradil, J., Slaninova, I., Hampl, A., and Dvorak, P. (2008). Comparative study of mouse and human feeder cells for human embryonic stem cells. *Int. J. Dev. Biol.* 52, 353–363. doi: 10.1387/ijdb.082590le
- Fekete, L., Kusova, K., Petrak, V., and Kratochvilova, I. (2012). AFM topographies of densely packed nanoparticles: a quick way to determine the lateral size distribution by autocorrelation function analysis. *J. Nanoparticle Res.* 14:10. doi: 10.1007/s11051-012-1062-7
- Gavara, N. (2016). A beginner's guide to atomic force microscopy probing for cell mechanics. *Microsc. Res. Tech.* 1, 1–10. doi: 10.1002/jemt.22776
- Gavara, N., and Chadwick, R. S. (2012). Determination of the elastic moduli of thin samples and adherent cells using conical atomic force microscope tips. *Nat. Nanotechnol.* 7, 733–736. doi: 10.1038/nnano.2012.163
- Guz, N., Dokukin, M., Kalaparthy, V., and Sokolov, I. (2014). If cell mechanics can be described by elastic modulus: study of different models and probes used in indentation experiments. *Biophys. J.* 107, 564–575. doi: 10.1016/j.bpj.2014.06.033
- Hermanowicz, P., Sarna, M., Burda, K., and Gabrys, H. (2014). AtomicJ: an open source software for analysis of force curves. *Rev. Sci. Instr.* 85:063703. doi: 10.1063/1.4881683
- Hofer, M., Falk, M., Komurkova, D., Falkova, I., Bacikova, A., Klejdus, B., et al. (2016). Two new faces of Amifostine: protector from DNA damage in normal cells and inhibitor of DNA repair in cancer cells. *J. Med. Chem.* 59, 3003–3017. doi: 10.1021/acs.jmedchem.5b01628
- Hubálek, Z. (2003). Protectants used in the cryopreservation of microorganisms. *Cryobiology* 46, 205–229. doi: 10.1016/S0011-2240(03)00046-4
- Kasas, S., Longo, G., and Dietler, G. (2013). Mechanical properties of biological specimens explored by atomic force microscopy. *J. Phys. D Appl. Phys.* 46:133001. doi: 10.1088/0022-3727/46/13/133001
- Kratochvilová, I., Golan, M., Pomeisl, K., Richter, J., Sedlakova, S., Sebera, J., et al. (2017). Theoretical and experimental study of the antifreeze protein AFP752, trehalose and dimethyl sulfoxide cryoprotection mechanism: correlation with cryopreserved cell viability. *RSC Adv.* 7, 352–360. doi: 10.1039/C6RA25095E
- Lampugnani, M. G., Pedenovi, M., Niewiarowski, A., Casali, B., Donati, M. B., Corbascio, G. C., et al. (1987). Effects of dimethyl sulfoxide (DMSO) on microfilament organization, cellular adhesion, and growth of cultured mouse B16 melanoma cells. *Exp. Cell Res.* 172, 385–396. doi: 10.1016/0014-4827(87)90396-X
- Levental, I., Levental, K. R., Klein, E. A., Assoian, R., Miller, R. T., Wells, R. G., et al. (2010). A simple indentation device for measuring micrometer-scale tissue stiffness. *J. Phys. Condens. Matter* 22:194120. doi: 10.1088/0953-8984/22/19/194120
- Lin, C., and Tsai, S. (2012). The effect of cryopreservation on DNA damage, gene expression and protein abundance in vertebrate. *Ital. J. Anim. Sci.* 11:e21. doi: 10.4081/ijas.2012.e21
- Loparic, M., Wirz, D., Daniels, A. U., Raiteri, R., Vanlandingham, M. R., Guex, G., et al. (2010). Micro- and nanomechanical analysis of articular cartilage by indentation-type atomic force microscopy: validation with a gel-microfiber composite. *Biophys. J.* 98, 2731–2740. doi: 10.1016/j.bpj.2010.02.013
- Mandumpal, J. B., Kreck, C. A., and Mancera, R. L. (2011). A molecular mechanism of solvent cryoprotection in aqueous DMSO solutions. *Phys. Chem. Chem. Phys.* 13, 3839–3842. doi: 10.1039/c0cp02326d
- Mašek, J., Bartheldyova, E., Korvasova, Z., Skrabalova, M., Koudelka, S., Kulich, P., et al. (2011a). Immobilization of histidine-tagged proteins on monodisperse metalchelation liposomes: preparation and study of their structure. *Anal. Biochem.* 408, 95–104. doi: 10.1016/j.ab.2010.08.023
- Masek, J., Bartheldyova, E., Turanek-Knotigova, P., Skrabalova, M., Korvasova, Z., Plockova, J., et al. (2011b). Metallochelating liposomes with associated lipophilised norAbuMDP as biocompatible platform for construction of vaccines with recombinant His-tagged antigens: preparation, structural study and immune response towards rHsp90. *J. Control. Release* 151, 193–201. doi: 10.1016/j.jconrel.2011.01.016
- Ofek, G., Wiltz, D. C., and Athanasiou, K. A. (2009). Contribution of the cytoskeleton to the compressive properties and recovery behavior of single cells. *Biophys. J.* 97, 1873–1882. doi: 10.1016/j.bpj.2009.07.050
- Ogden, R. W. (1972). Large deformation isotropic elasticity - correlation of theory and experiment for compressible rubberlike solids. *Proc. R. Soc. Lond. Ser. A* 328, 567–583. doi: 10.1098/rspa.1972.0096
- Parsons, J. T., Horwitz, A. R., and Schwartz, M. A. (2010). Cell adhesion: integrating cytoskeletal dynamics and cellular tension. *Nat. Rev. Mol. Cell Biol.* 11, 633–643. doi: 10.1038/nrm2957
- Pesl, M., Pribyl, J., Acimovic, I., Vilotic, A., Jelinkova, S., Salykin, A., et al. (2016). Atomic force microscopy combined with human pluripotent stem cell derived cardiomyocytes for biomechanical sensing. *Biosens. Bioelectron.* 85, 751–757. doi: 10.1016/j.bios.2016.05.073
- Pogoda, K., Jaczewska, J., Wiltowska-Zuber, J., Klymenko, O., Zuber, K., Fornal, M., et al. (2012). Depth-sensing analysis of cytoskeleton organization based on AFM data. *Eur. Biophys. J.* 41, 79–87. doi: 10.1007/s00249-011-0761-9
- Ragoonanan, V., Hubel, A., and Aksan, A. (2010). Response of the cell membrane-cytoskeleton complex to osmotic and freeze/thaw stresses. *Cryobiology* 61, 335–344. doi: 10.1016/j.cryobiol.2010.10.160
- Rajan, R., Hayashi, F., Nagashima, T., and Matsumura, K. (2016). Toward a molecular understanding of the mechanism of cryopreservation by polyampholytes: cell membrane interactions and hydrophobicity. *Biomacromolecules* 17, 1882–1893. doi: 10.1021/acs.biomac.6b00343
- Sneddon, I. N. (1965). The relation between load and penetration in the axisymmetric boussinesq problem for a punch of arbitrary profile. *Int. J. Eng. Sci.* 3, 47–57. doi: 10.1016/0020-7225(65)90019-4
- Touhami, A., Nysten, B., and Dufrene, Y. F. (2003). Nanoscale mapping of the elasticity of microbial cells by atomic force microscopy. *Langmuir* 19, 4539–4543. doi: 10.1021/la034136x

- Wang, J., Wan, Z. F., Liu, W. M., Li, L., Ren, L., Wang, X. Q., et al. (2009). Atomic force microscope study of tumor cell membranes following treatment with anti-cancer drugs. *Biosens. Bioelectron.* 25, 721–727. doi: 10.1016/j.bios.2009.08.011
- Wolfram, I. (2017). “*Mathematica*,” Wolfram Research.
- Woods, E. J., Thirumala, S., Badhe-Buchanan, S. S., Clarke, D., and Mathew, A. J. (2016). Off the shelf cellular therapeutics: factors to consider during cryopreservation and storage of human cells for clinical use. *Cytotherapy* 18, 697–711. doi: 10.1016/j.jcyt.2016.03.295
- Xu, X., Liu, Y., Cui, Z., Wei, Y., and Zhang, L. (2012). Effects of osmotic and cold shock on adherent human mesenchymal stem cells during cryopreservation. *J. Biotechnol.* 162, 224–231. doi: 10.1016/j.jbiotec.2012.09.004

**Conflict of Interest Statement:** The authors declare that the research was conducted in the absence of any commercial or financial relationships that could be construed as a potential conflict of interest.

Copyright © 2018 Golan, Jelinkova, Kratochvílová, Skládal, Pešl, Rotrekl and Pribyl. This is an open-access article distributed under the terms of the Creative Commons Attribution License (CC BY). The use, distribution or reproduction in other forums is permitted, provided the original author(s) and the copyright owner(s) are credited and that the original publication in this journal is cited, in accordance with accepted academic practice. No use, distribution or reproduction is permitted which does not comply with these terms.



# Vesicle-Mediated Control of Cell Function: The Role of Extracellular Matrix and Microenvironment

Gorjana Rackov<sup>1\*†</sup>, Noemi Garcia-Romero<sup>2†</sup>, Susana Esteban-Rubio<sup>2,3†</sup>, Josefa Carrión-Navarro<sup>2</sup>, Cristobal Belda-Iniesta<sup>2</sup> and Angel Ayuso-Sacido<sup>1,2,3\*</sup>

<sup>1</sup> IMDEA Nanoscience Institute, Madrid, Spain, <sup>2</sup> Fundación de Investigación HM Hospitales, Madrid, Spain, <sup>3</sup> Facultad de Medicina (IMMA), Universidad CEU San Pablo, Madrid, Spain

## OPEN ACCESS

### Edited by:

Giancarlo Forte,  
International Clinical Research Center  
(FNUSA-ICRC), Czechia

### Reviewed by:

Wolfgang Holthoner,  
Ludwig Boltzmann Gesellschaft  
(LBG), Austria  
Rosemary Wangenstein,  
Universidad de Jaén, Spain

### \*Correspondence:

Gorjana Rackov  
gorjanarackov@gmail.com  
Angel Ayuso-Sacido  
ayusosacido@gmail.com

<sup>†</sup> These authors have contributed  
equally to this work.

### Specialty section:

This article was submitted to  
Integrative Physiology,  
a section of the journal  
Frontiers in Physiology

**Received:** 31 March 2018

**Accepted:** 14 May 2018

**Published:** 05 June 2018

### Citation:

Rackov G, Garcia-Romero N,  
Esteban-Rubio S, Carrión-Navarro J,  
Belda-Iniesta C and Ayuso-Sacido A  
(2018) Vesicle-Mediated Control  
of Cell Function: The Role  
of Extracellular Matrix  
and Microenvironment.  
*Front. Physiol.* 9:651.  
doi: 10.3389/fphys.2018.00651

Extracellular vesicles (EVs) — including exosomes, microvesicles and apoptotic bodies — have received much scientific attention last decade as mediators of a newly discovered cell-to-cell communication system, acting at short and long distances. EVs carry biologically active molecules, thus providing signals that influence a spectrum of functions in recipient cells during various physiological and pathological processes. Recent findings point to EVs as very attractive immunomodulatory therapeutic agents, vehicles for drug delivery and diagnostic and prognostic biomarkers in liquid biopsies. In addition, EVs interact with and regulate the synthesis of extracellular matrix (ECM) components, which is crucial for organ development and wound healing, as well as bone and cardiovascular calcification. EVs carrying matrix metalloproteinases (MMPs) are involved in ECM remodeling, thus modifying tumor microenvironment and contributing to premetastatic niche formation and angiogenesis. Here we review the role of EVs in control of cell function, with emphasis on their interaction with ECM and microenvironment in health and disease.

**Keywords:** extracellular vesicles, exosomes, extracellular matrix, microenvironment, cell function

## INTRODUCTION

Most cell types secrete different types of EVs that can be found in all body fluids, as well as in cell culture supernatant. These vesicles are composed of a lipid bilayer that encloses molecules — lipids, proteins, DNA, mRNA and miRNA — derived from the donor cell. These molecules retain their biological function (Valadi et al., 2007) and may affect the function of recipient cells at a long distance, since they can travel in circulation encapsulated by the lipid bilayer. This concept sheds new light on fundamental process of intercellular communication, beyond the need for direct cell-to-cell contact or secretion of soluble factors that act only on neighboring cells. In addition, this feature puts EVs in focus of biomarker research, since mutation-bearing EVs originating from rare or inaccessible tumor cells can be detected in a liquid biopsy in a non-invasive manner (García-Romero et al., 2017).

There are various types of EVs that can form either at the plasma membrane or at the lumen of intracellular compartment. Large membrane vesicles (1000–5000 nm) are released during the late

**Abbreviations:** ECM, extracellular matrix; EGF, epidermal growth factor; EGFR, epidermal growth factor receptor; EVs, extracellular vesicles; FGF, fibroblast growth factor; MMPs, matrix metalloproteinases; MVs, matrix vesicles; PD-L1, programmed death ligand 1; TGF- $\beta$ , transforming growth factor beta; TNF $\alpha$ , tumor necrosis factor alpha; VEGF, vascular endothelial growth factor.

stages of cell death in the form of apoptotic bodies. Microvesicles, also referred to as microparticles, range between 100 and 1000 nm and arise by outward budding and shedding directly from the plasma membrane. Exosomes, between 30 and 100 nm in diameter, form by inward budding of the endosomal membrane, giving rise to multivesicular bodies, which are subsequently released to extracellular space by fusion of late endosome with the plasma membrane. As a consequence of this mechanism, exosome transmembrane proteins retain the same orientation as that of the donor cell plasma membrane (Chaput et al., 2005), which allows their interaction with recipient cell receptors. These surface proteins include tetraspanins (CD9, CD63, and CD81), integrins, ICAM1 (intercellular adhesion molecule 1) and phosphatidylserine, which is also found on the surface of microvesicles and apoptotic bodies (Théry et al., 2009). Following their recognition by cellular receptors, exosomes can directly fuse with the recipient cell membrane, thus incorporating their membrane proteins to the plasma membrane and delivering their cargo to the cytoplasm of the recipient cell. In addition, exosomes derived from infected macrophages, tumor cells, or antigen-presenting cells, contain antigen-bearing MHC classes I and II molecules, as well as co-stimulatory molecules, that can activate T cells and trigger the immune response (Wolfers et al., 2001; Thery et al., 2002; Giri and Schorey, 2008). EVs thus emerged as important mediators of intercellular communication and became subject of increasing scientific interest in the past decade.

Different EV populations can be separated based on their density, centrifugation speed, or markers expressed on their surface; however, the isolation of pure EV subtypes remains a major challenge (Momen-Heravi et al., 2013; Witwer et al., 2013). In addition, their quantification and characterization mostly rely on markers that can be found in different types of EVs, or may not be expressed by all EVs of the particular type (Théry et al., 2006). It is thus difficult to compare between the results of different laboratories and future studies need to be undertaken to improve and standardize EV isolation and characterization techniques.

The ECM functions as a reservoir of growth factors, which can be released during ECM remodeling and can regulate cell proliferation, migration and organ morphogenesis. Dysregulation of ECM components or aberrant ECM remodeling can lead to various pathologies, including cancer. Recent reports have found growth factors and other soluble mediators, such as TNF- $\alpha$ , EGF, FGF, as well as their receptors, associated with the exosome membrane, suggesting their physiological role in disseminating these soluble factors (Zhang et al., 2006; Sanderson et al., 2008; Seelenmeyer et al., 2008). In addition, EVs carry MMPs with proteolytic activity, which can alter EV content, contribute to ECM degradation and actively participate in tumor progression.

Here, we review the recent advances in our understanding of how EVs mediate cell-to-cell communication and their interaction with ECM components. We also discuss the role of EVs in RNA and protein transfer between cells, influencing the invasion of tumor cells, immune evasion, dissemination of developmental signals during organogenesis and tissue repair, and calcification during bone development and

pathological conditions, such as arterial plaque and kidney stone formation.

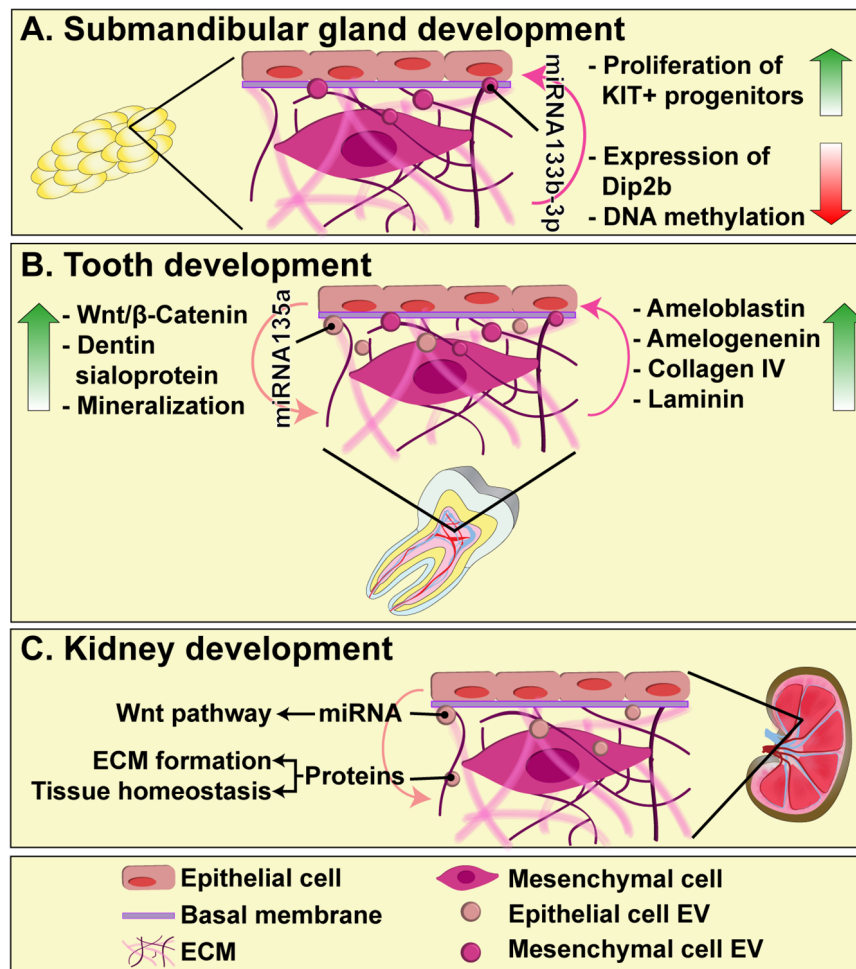
## THE ROLE OF EVs IN DEVELOPMENT AND ORGANOGENESIS

During development and organogenesis, great coordination needs to be achieved between the cells, ECM and the signaling mechanisms. Developmental signals, including Wnt, Hedgehog, bone morphogenetic proteins, and Notch ligands can be soluble, bound to the ECM or associated to the membrane. Some of these signaling proteins are modified by the addition of a lipid during their biogenesis, hence their solubility and long-range diffusion might be compromised. It has been suggested that EVs could act as vehicles for these signals, allowing cell-to-cell communication and coordinated growth during development. Indeed, recent advances in our understanding of EV biogenesis and function reveal that they are essential mediators of intercellular communication, and thus their role in developmental programming, embryonic induction and organogenesis needs to be highlighted (Valadi et al., 2007; McGough and Vincent, 2016).

The formation of organs, such as salivary glands, teeth, lung, kidney, and mammary glands, is marked by branching morphogenesis processes, in which the interaction between epithelium and mesenchyme needs to be tightly coordinated. The epithelial-mesenchymal interactions occur in both directions, and are primarily regulated by ECM and soluble growth factors, as well as EVs (Puthiyaveetil et al., 2016).

The formation of submandibular glands is a good model to study the communication between mesenchymal and epithelial cells, as well as their interaction with the basal membrane, since it reflects the importance of ECM as a dynamic medium necessary for cell proliferation, apoptosis, differentiation, and migration (Patel et al., 2006; Tucker, 2007). Exosomes derived from mesenchymal cells can pass through the basement membrane and deliver mature forms of miR-133b-3p to epithelial cells, which do not express the primary miRNA. In this manner, miRNA-containing exosomes induce the reduction of Dip2b (Disk-interacting protein 2 homolog B) and DNA methylation in KIT<sup>+</sup> progenitors, leading to their proliferation (**Figure 1A**) (Hayashi et al., 2017).

During the formation of teeth, exosomes have an indispensable role, since their reciprocal endocytic uptake by epithelial and mesenchymal cells, directly mediates the regulation of cell differentiation and matrix synthesis. Exosomes derived from epithelial cells are able to induce mesenchymal cells to produce dentin sialoprotein and trigger the mineralization processes (Jiang et al., 2017). This occurs through exosomal miR-135a, which leads to activation of Wnt/ $\beta$ -catenin in mesenchymal cells, a critical signaling pathway for matrix synthesis and dentinogenesis (O'Connell et al., 2012). On the other hand, exosomes derived from mesenchymal cells induce epithelial cells to produce collagen type IV and laminin, components of the basement membrane, and scaffolding proteins, such as ameloblastin and amelogenin (Jiang et al., 2017). Therefore,



**FIGURE 1 |** The role of EVs in epithelial-mesenchyme interaction during submandibular gland (A), tooth (B), and kidney (C) development. EVs diffuse through the basal membrane and participate in intercellular communication between epithelial and mesenchymal cells, carrying proteins and miRNAs that regulate key events for organogenesis, such as cell proliferation, differentiation and ECM synthesis.

exosomes are essential mediators of the epithelial–mesenchyme interaction that occurs through the basement membrane, and their regulation, including their release and cargo incorporation, are not yet completely understood (Figure 1B).

Kidney organogenesis is mediated by the sequential and reciprocal interactions between the epithelial-derived ureteric bud (UB) and metanephric mesenchyme (MM). One of the key players in these interactions is Wnt pathway, by which epithelial UB induces MM transformation and the development of nephrons (Kispert et al., 1998; Pietilä and Vainio, 2014). Very recently, it has been shown that UB-derived exosomes can be taken up by MM cells and transfer their cargo, including miRNAs that play a role in Wnt pathway, as well as proteins involved in ECM organization and tissue homeostasis (Krause et al., 2018). Exosomes thus emerge as an important mechanism of embryonic signaling during kidney development and organogenesis in general, although their content and the mechanism by which they selectively influence different cellular populations, remains to be investigated (Figure 1C).

## THE ROLE OF EVs IN TISSUE REPAIR

Wound repair is a process of re-establishing tissue homeostasis after injury, and it relies on signaling pathways that also act during development. In general, wound repair involves different cell types — including epithelial, immune and endothelial cells — as well as the components of ECM, mostly resulting in scar formation. EVs facilitate coordinating this process, as carriers of pro-resolving mediators. During chronic inflammation, as seen in inflammatory bowel disease, tissue integrity is compromised and epithelial barrier function needs to be re-established. In response to injury, epithelial cells of the intestine secrete EVs that contain a pro-resolving mediator Annexin A1, and thus control wound repair (Leoni et al., 2015).

Cellular therapies, together with the development of biomaterials for the generation of scaffolds, represent the main strategies used in regenerative medicine. Many ongoing studies are directed to elucidate the possible reparative function of

EVs and, therefore, evaluate their potential as mediators of cell regeneration.

Diabetes patients commonly present renal disease, characterized by podocyte loss, hypertrophy of mesangial cells (MCs), increase in the ECM protein production and tubulointerstitial fibrosis (Forbes and Cooper, 2013). Key molecules implicated in this processes are TGF- $\beta$  and miR-21, which induce collagen and fibronectin production, as well as the up-regulation of matrix protein expression activators, like mTOR (Dey et al., 2012). EVs derived from bone-marrow and human liver stem cells, were shown to transfer miR-222 to MCs and downregulate TGF- $\beta$  and miR21 in an *in vitro* model of MCs hyperglycaemia, thus serving as potential therapeutic agents to protect MCs from hyperglycaemia-induced damage and collagen production (Gallo et al., 2016).

Osteoporosis treatment is currently limited to approaches stimulating bone formation and anti-resorptive agents (Cheng et al., 2013), thus new studies focused on local transplantation therapies need to be developed. Currently, regenerative strategies for osteoporosis treatment are based on three fundamental lines: mesenchymal stem cells (MSCs), the use of biomaterials for the generation of scaffolds, or the combination of both approaches to achieve a greater regenerative effect (Weinand et al., 2006). However, there are numerous disadvantages when using MSCs as therapy, including the high invasiveness of the procedures needed for harvesting them from donors, possible alteration during cell culture and the presence of MHC proteins that can induce rejection (Izadpanah et al., 2008; Robey, 2011). Advances in the study of cell reprogramming allow the generation of MSCs from induced pluripotent stem cells (iPSCs), which facilitates their management and their use in osteogenesis, although it may also increase the risk of tumorigenesis (Villa-Diaz et al., 2012; Zou et al., 2013). Recently, the osteogenic potential of exosomes derived from hiPSC-MSC (hiPSC-MSC-Exos) has been evaluated in order to overcome the drawbacks related to cell therapy. It was shown that hiPSC-MSC-Exos induce angiogenesis and osteogenesis in ovariectomized rat model, and promote bone regeneration when incorporated on a classical porous  $\beta$ -TCP scaffold (Qi et al., 2016).

Neovascularization is crucial for restoring tissue function after ischemia, although this process is not completely understood. Tissue repair requires the recruitment of proangiogenic mediators and microvesicles, as well as stem and progenitor cells. Many studies focus on endothelial progenitor cell (EPC)-based therapy, since these cells are involved in revascularization processes (Rafii and Lyden, 2003) and may drastically improve regeneration and patients' outcome (Lara-Hernandez et al., 2010). These cells, nonetheless, require *ex vivo* expansion (Kalka et al., 2000) and may generate HLA incompatibility (Basak et al., 2009). For this reason, the use of EPC-derived EVs emerged as an alternative possibility. During EPC-mediated revascularization, the released EVs induce reprogramming of mature quiescent endothelial cells through horizontal transfer of mRNA, which activates major pathways involved in angiogenesis and leads to endothelial cell proliferation and tissue repair (Deregibus et al., 2007). In addition, EPCs release microvesicles containing angiogenic miRNA-126 and miRNA-296 and thus

trigger neoangiogenesis in a murine model of hindlimb ischemia, suggesting the use of EPC-derived microvesicles for treatment of peripheral arterial disease (Ranghino et al., 2012).

Cardiac repair requires endothelial activation, which may be achieved through a proangiogenic factor-inducing therapy. Exosomes contain proteins, such as EMMPRIN (Vrijssen et al., 2010), highlighting the possibility of using EVs as carriers of angiogenesis-stimulating factors for treatment of cardiac ischemia. Indeed, exosomes derived from cardiomyocyte progenitor cells (CMPC) and MSC were shown to carry high levels of EMMPRIN, and may thus regulate VEGF signaling, endothelial cell migration and capillary formation (Vrijssen et al., 2016).

Liver regeneration involves several complex mechanisms, including the mature liver cell reprogramming and proliferation, directed by stem cell populations (Alison et al., 2000; Michalopoulos, 2007). Therefore, obtaining therapies to reduce the recovery time of liver function became a major challenge in this field. In this sense, Dr. Herrera's group used microvesicles isolated from human liver stem cells (HLSC) as a new approach to improve the degree of regeneration (Herrera et al., 2006). Indeed, in a classical model of 70% hepatectomy in rats, treatment with microvesicles led to increased liver cell proliferation and decreased apoptosis, overall significantly decreasing the liver regeneration time (Herrera et al., 2010).

Extracellular vesicles, as vehicles for proteins and nucleic acids, are thus key mediators of intercellular communication during organogenesis and tissue repair, and their use in regenerative medicine drastically improves current cellular therapies. In addition, the specificity of the uptake by the recipient cells needs to be considered since it increases the potential of EVs as therapeutic vectors.

## THE ROLE OF EVs IN BONE CALCIFICATION

Matrix vesicles (MVs) are particles secreted by a mineralizing tissue to the ECM, and their main function is to promote mineralization. Their *in vitro* and *in vivo* reported size ranges between 0.1 and 2  $\mu$ m. Furthermore, such MVs may be generated by shedding from plasma membrane or by the endosomal pathway. In this sense, MVs share typical exosomal protein markers, such as the GTPase-Ras family, tetraspanins CD9 and CD63, annexins, integrin receptors and Hsp70 (Shapiro et al., 2015).

Although it is still not clear whether the initial process of mineral formation occurs inside the cell or later in the ECM, several studies point that MVs carry the pre-nucleation complex of calcium phosphate, and that their binding to the ECM attracts other MVs, thus initiating the nucleation phase followed by the apatite formation (Gebauer et al., 2014). Apart from that, MVs also contribute to pathological calcification as found in calcific valvular stenosis, dental plaque, atherosclerosis and calculus renal formation (Anderson et al., 2010).

Bones are formed by collagen fibrils type I, platelets of carbonated hydroxyapatite and calcium phosphate

(Mahamid et al., 2011). During osteogenic differentiation most cells die, releasing calcium, MVs, and apoptotic bodies, which become nucleation sites of the hydroxyapatite crystals. Afterwards, the osteoblasts attach to the ECM and differentiate to osteocytes (Grzesiak et al., 2017).

The formation of hydroxyapatite crystals may occur following two main steps. Firstly, when mineral concentrations are imbalanced, calcium and phosphate accumulate and enter the MVs. Secondly, the mineral propagation step occurs when hydroxyapatite crystals are exposed in MV membrane, acting as loci to promote the generation of new crystals (New and Aikawa, 2013). Moreover, it has been reported that the enzyme alkaline phosphatase present in the MVs could help the calcification process (Ali and Griffiths, 1983).

The released MVs could play three different roles in matrix mineralization. The MVs derived by osteoblasts could regulate the ion concentrations, causing the mineralization of the fibrillar collagen ECM (Golub and Boesze-Battaglia, 2007). Another proposed mechanism involves the accumulation of phosphate and calcium within MVs, whose release allow the interaction between MVs and collagen fibrils (Golub, 2009). Finally, the formation of apatite crystals may take place within MVs, which are deposited into collagen fibrils (Harmey et al., 2004).

The degeneration of articular cartilage, also known as osteoarthritis, is characterized by the abnormal calcification in the cartilage matrix. Unfortunately, there is no cure for this disease, and current treatment is only palliative. For that reason, new therapies are being investigated. The injection of MSCs seems like a promising tool, since it shows chondroprotective effect *in vitro* and in mice models. Additionally, it has been suggested that these effects are due to MSC-derived exosomes and microvesicles, which inhibit macrophage activation and chondrocyte apoptosis (Cosenza et al., 2017). Similarly, in a rat model with osteochondral defects, exosome injection promoted cartilage repair, suggesting their possible use as cell-free MSC therapy (Zhang et al., 2016).

Several studies revealed higher amount of MVs in patients compared with healthy controls, suggesting that the presence of these MVs increases extracellular calcium levels and induces hypermineralization (Anderson et al., 2010).

Altogether, we are still far from understanding the precise process of matrix mineralization; therefore, further studies are required to address the function of MVs in those mechanisms.

## THE ROLE OF EVs IN CARDIOVASCULAR CALCIFICATION

Cardiovascular diseases are the main cause of death in the world, and vascular calcification is one of the most common complications. In this sense, the lipid accumulation and inflammation of the medium and large arteries precede atherosclerosis, the principal condition leading to heart attacks (Falk, 2006).

The calcification process mediated by the release of MVs appears as an adaptive response to the inflammation process (Anderson et al., 2010). An important variety of MVs, derived

from arterial endothelial cells, vascular smooth muscle cells (VSMCs) and macrophages are being associated with the calcification process (Badimon et al., 2017).

In this sense, it is known that in chronic kidney disease macrophage-derived MVs trigger the calcification of atherosclerotic plaques through high concentration of the calcium binding protein S100A9 and annexin V. In addition, after adding  $\text{Ca}^{2+}/\text{P}$  to macrophage cell culture, phosphatidylserine translocates to MV external membrane and binds to S100A9-Annexin V complex, promoting hydroxyapatite nucleation. Typical exosomal markers, such as CD9, CD63, and TSG101, are also expressed in this MV population (New et al., 2013).

In these patients, VSMCs increase the secretion of calcifying EVs, decreasing the concentration of extracellular mineralization inhibitors, such as matrix Gla protein or fetuin-A. In addition, elevated levels of TNAP and annexins are found in VSMC-derived EVs, which form microcalcifications when they are delivered into the ECM. This annexin might increase the influx of  $\text{Ca}^{2+}$  inside MVs and could mediate the interaction of collagen with the ECM (Chen et al., 2008). Afterwards, the calcification propagation is mediated by the collagen fibrils (Bakhshian Nik et al., 2017). Other studies suggest that VSMCs secrete  $\text{Ca}^{2+}$  and P crystals in the intimal layer of arteries (Kapustin et al., 2017). The mechanism of protein package seems to be highly selective, as cargo of non-calcifying EVs significantly differs from the one seen in calcifying EVs (Shanahan et al., 2012). In addition, under non-calcifying conditions EVs carry miRNAs and inhibitor factors that prevent the calcification pathway (Krohn et al., 2016).

Atherosclerotic plaques display regions with apoptotic cell death, which may be an early event preceding the plaque calcification. In this sense, it has been reported that MVs derived from apoptotic VSMCs contain proapoptotic protein BAX and may initiate the calcification process (Kockx et al., 1998). Furthermore, apoptotic bodies derived from VSMCs undergoing cell death are similar to MVs and could also act as nucleation sites for vascular calcification (Proudfoot et al., 2000).

Other vesicles secreted by devitalized connective tissue cells were also found in calcific valvular stenosis and in the calcification of artificial heart valves (Anderson et al., 2010). Similarly, in the calcific aortic valve disease, valvular interstitial cells secrete pro-calcific EVs that remodel the ECM through the interaction with endothelial cells (Bakhshian Nik et al., 2017).

## THE ROLE OF EVs IN RENAL CALCIFICATION

Kidney stones or renal calculi, also referred to as nephrolithiasis, are formed by the nucleation and growth of calcium oxalate (CaOx), calcium phosphate (CaP) or urate crystals (Aggarwal et al., 2013). The incidence of kidney stones is twice as greater in men than in women, and stones submitted by men are more likely to have calcium oxalate crystals, while the stones submitted by women are more likely to have hydroxyapatite (Lieske et al., 2014; Jayachandran et al., 2015). Interestingly, EVs isolated from urine reveal different distribution and protein profile in men and

women, which could be related with the above-mentioned gender differences (Jayachandran et al., 2015).

Renal, vascular and bone calcification follow similar pathways, although little is known about the precise mechanism of calcification and matrix synthesis. Similarly to the observations in vascular and bone calcification, renal calcification begins with the release of renal tubular epithelial cell-derived MVs, which serve as nucleation sites in the tubular basement membrane (Anderson et al., 2010). In addition, recent high-resolution microscopy studies have revealed important phenotypic differences between calcifying EVs and MVs in the bone (Bakhshian Nik et al., 2017), reflecting their different cellular origin, biogenesis mechanism and type of mineral they form. Further studies are thus needed to focus on the specific MV subpopulations, as well as the technical methodology to separate and enrich them, for which the different density between calcifying and non-calcifying EVs may play an important role (Hutcheson et al., 2014).

## THE ROLE OF EVs IN CANCER AND IMMUNITY

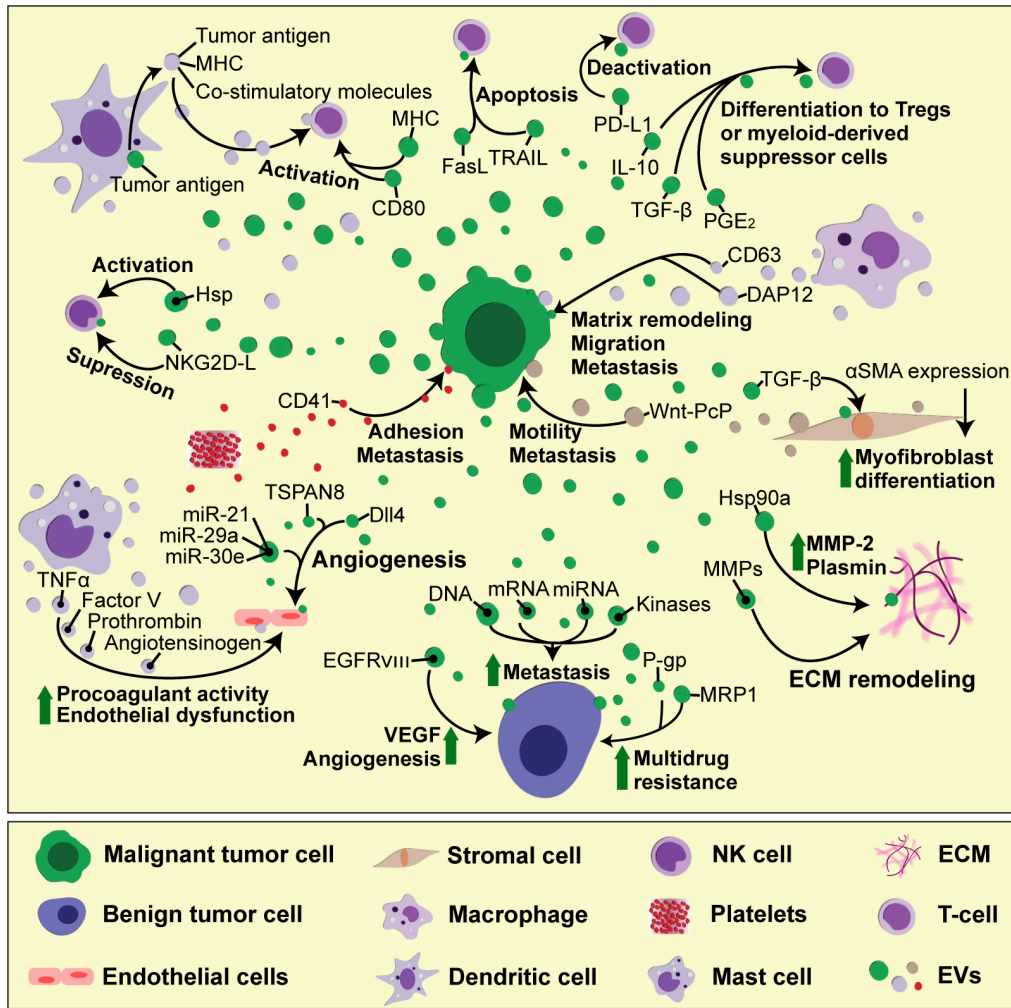
The EVs play an important role in supporting tumor development (Figure 2). Most cancer cells release increased amounts of EVs compared to their non-malignant counterparts (Martins et al., 2013). These EVs carry tumor-specific proteins or DNA mutations that can be used as biomarkers in a liquid biopsy (Garcia-Romero et al., 2017). In addition, tumor-derived EVs carry bioactive molecules, such as functional mRNA, which can get transferred to other cells, altering their behavior and contributing to tumor heterogeneity. In this manner, highly malignant cells can change the phenotype of benign tumor cells, increasing their migratory behavior and metastatic capacity (Zomer et al., 2015). In brain tumor, the oncogenic form of epidermal growth factor receptor (EGFRvIII) can be included as EV cargo and transferred between tumor cells, leading to propagation of transforming activity in cells which lack the primary genetic mutation (Al-Nedawi et al., 2008). This non-genetic horizontal transfer mediated by EVs is particularly important for acquiring resistance to chemotherapy. Functional plasma membrane multidrug efflux transporters, such as P-glycoprotein (P-gp) or Multidrug Resistance-Associated Protein 1 (MRP-1), can be shed from resistant cancer cells as cargo of membrane microvesicles and transferred to drug-sensitive recipient cells (Bebawy et al., 2009; Lu et al., 2013). Apart from directly transferring the effector molecules, EVs can also carry intermediary regulators, such as miRNAs or kinases, which then control gene expression and downstream signaling pathways in recipients cells (Gong et al., 2014).

Tumor microenvironment plays a major role in tumor development. It consists of cells, ECM scaffold, tumor-associated vasculature and soluble factors such as growth factors (Joyce and Pollard, 2009). During wound healing and scar formation, TGF- $\beta$ -activated fibroblasts upregulate the expression of alpha-smooth muscle actin ( $\alpha$ -SMA) and differentiate into myofibroblasts, which are responsible for altering tissue architecture. In TGF- $\beta$ -rich tumor microenvironment, the

exaggerated myofibroblast activity leads to fibrosis, ultimately supporting tumor growth, vascularization and metastasis (Tomasek et al., 2002). Prostate cancer-derived exosomes are loaded with functional TGF- $\beta$  tethered by betaglycan on exosome surface, and can thus induce  $\alpha$ -SMA overexpression and persistent fibroblast-to-myofibroblast differentiation (Webber et al., 2010). Highly invasive breast cancer cells secrete exosomes containing molecular chaperone heat shock protein 90a (hsp 90a), which activates extracellular proteases such as MMP-2 and plasmin, thus promoting tumor cell motility and invasion (McCready et al., 2010). Non-tumor cells in tumor microenvironment — such as fibroblasts or activated immune cells — also secrete EVs, which can promote angiogenesis, tumor cell migration and metastasis. EVs derived from tumor-associated fibroblasts cause increased motility and metastatic potential of breast cancer cells (Luga et al., 2012), by stimulating the non-canonical Wnt planar cell polarity (PCP) signaling — a pathway related with rearranging tissue during development (Gray et al., 2011). Platelet-derived exosomes carry integrins, such as CD41 which can increase the adhesion properties in lung and breast cancer cells, thus increasing their metastatic potential (Janowska-Wieczorek et al., 2005). Exosome-mediated transfer of macrophage-derived antigens such as CD163 and DAP12 increases matrix remodeling and migration potential in breast and rectal cancer cells and associates with advanced tumor grade and high rates of metastases (Shabo and Svanvik, 2011). Mast cells are major players in IgE-mediated allergic responses, but they also accumulate in tumor microenvironment and secrete MMPs, pro-angiogenic and growth factors, as well as pro- and anti-inflammatory signals, that modify tumor cell proliferation and invasiveness (Stockmann et al., 2014; Maciel et al., 2015). Mast cell-derived exosomes contain TNF- $\alpha$ , angiotensinogen, factor V and prothrombin, which all induce the expression of plasminogen activator inhibitor type 1 (PAI-1) in endothelial cells, causing procoagulant activity and endothelial dysfunction (Al-Nedawi et al., 2005). Acidic pH and hypoxia, hallmarks of tumor microenvironment, have also been reported to modify tumor-derived exosome release and uptake. In acidic conditions, the fluidity and lipid composition of exosomal membrane are changed due to increased sphingomyelin/ganglioside GM3 content, which leads to increased exosome fusion capacity of melanoma exosomes, particularly in metastatic cells (Parolini et al., 2009). Under hypoxia, tumor cells exhibit reduced adhesive properties and increased production of MMPs and invasiveness, accompanied by increased secretion of proteins involved in angiogenesis and immune cell recruitment, all of which found to be enriched in tumor-derived exosomes (Park et al., 2010).

Tumor-derived EVs carry MHC molecules loaded with tumor antigens, as well as co-stimulatory molecules that stimulate antigen-specific T cell responses. In addition, exosomal heat shock proteins (HSP) function as endogenous danger signals that can stimulate NK cell responses (Khalil et al., 2011). Tumor-derived EVs thus have the potential to boost immune responses, providing a promising strategy for anticancer immunotherapy. Indeed, tumor-derived exosomes can serve as antigen source for dendritic cells (DCs), resulting in production of DC-derived





**FIGURE 2 |** The complexity of cell-to-cell interactions in tumor microenvironment mediated by EVs. During tumor progression, different cell types found in tumor microenvironment — including tumor, stromal, immune and vascular cells — interact reciprocally with each other, as well as with the ECM components, through EVs. These interactions result in immune cell activation or deactivation, which can either hamper or promote tumor growth, depending on the availability of soluble factors, which modulate the microenvironment status. In addition, tumor cell-derived EVs can spread drug resistance and invasive characteristics to other tumor cells, thus boosting tumor growth and the ability to form pre-metastatic niche.

exosomes that are able to present antigens and activate T cell-mediated antitumor responses (Pitt et al., 2014; Gu et al., 2015).

However, the cargo of tumor-derived EVs and their immunomodulatory effects seems to depend on tumor microenvironment and the functional status of the immune cells. In most cases, tumors develop different strategies to evade the immune system, and these are reflected in their EV content. Tumor-derived EVs directly participate in immune evasion, for example by generation of suppressive myeloid cells (Valenti et al., 2006), by expressing FasL and inducing T cell death (Andreola et al., 2002; Kim et al., 2005), as well as other suppressive molecules, such as PD-L1, TRAIL, IL-10, and TGF-β, which induce regulatory T cells (Tregs). Tumor-derived exosomes carry NKG2D ligands, which lead to suppression of NK cell function and correlate with poor clinical outcome in patients (Ashiru et al., 2010). The uptake of tumor-derived

exosomes blocks DC maturation (Yu et al., 2007), and induces myeloid-derived suppressor cell (MDSC) differentiation through PGE2 (prostaglandin E2) and TGF-β (Xiang et al., 2009).

A number of studies have demonstrated a role for tumor-derived EVs in promoting angiogenesis *in vitro* and *in vivo* (Kim et al., 2002). As mentioned earlier, glioma cells shed EVs containing an oncogenic form of EGF receptor, which increases VEGF expression and contributes to angiogenic signaling in recipient tumor cells (Al-Nedawi et al., 2008). In response to VEGF stimulation, endothelial cells increase motility and proliferation, while simultaneously increasing the expression of Notch ligand Delta-like 4 (Dll4), to inhibit the proliferation of adjacent cells (Phng and Gerhardt, 2009). While this is a well-known mechanism of juxtacrine cell-to-cell inhibition during developmental angiogenesis, VEGF-dependent Dll4 expression in tumor cells promotes tumor growth by enhancing blood

vessel diameter and perfusion, which renders these tumors responsive to anti-VEGF therapy with bevacizumab (Li et al., 2007). Interestingly, it has recently been discovered that tumor-derived exosomes contain Dll4 and can thus modulate vessel development in distant recipient cells, providing a new aspect to Notch signaling that does not require direct cell-to-cell contact (Sheldon et al., 2010). The response of endothelial cells to Dll4-containing exosomes seems to differ in a 2D cell culture from a chemically controlled 3D microenvironment with a VEGF concentration gradient (Sharghi-Namini et al., 2014), suggesting that, *in vitro*, just as *in vivo*, tissue microenvironment represents an important factor in the exosome-mediated control of cell function. In another 3D culture model, it was shown that melanoma exosomes can move between endothelial cells by tunneling nanotube networks that contain actin cytoskeleton, similarly as HIV particles or endosomal organelles travel from one cell to another (Rustom et al., 2004; Sowinski et al., 2008; Hood et al., 2009). These exosomes are able to induce tubule branching and the production of endothelial spheroids and sprouts in dose-dependent manner, thus influencing angiogenesis (Hood et al., 2009). Tumor-derived exosomes can also induce endothelial cell activation, proliferation and branching through tetraspanin 8 (formerly known as D6.1A/CO-029), which is associated with poor prognosis in patients with gastrointestinal cancer (Gesierich et al., 2006; Nazarenko et al., 2010). In glioblastoma, one of the most angiogenic solid tumors, several microRNAs (miR-21, miR-29a, and miR-30e) that promote tube formation and angiogenesis are increased within cancer stem cell-derived exosomes, while miR-1, which has a suppressive role, is downregulated (Bronisz et al., 2014; Sun et al., 2017).

Tumor vesicles contain proteinases that are able to degrade ECM and promote tumor invasiveness *in vitro* (Ginestra et al., 1998). Increased tissue factor activity in tumor EVs causes blood coagulation (Zhou et al., 2014), which facilitates tumor cells to adhere to blood vessels and promotes tissue invasion (Dvorak et al., 1981). In addition to endothelial cell proliferation, the tumor induces a distinct blood vessel phenotype characterized by increased permeability that allows tumor cells to enter the circulation and colonize and proliferate at a distant site (Jain, 2005). This vascular leakiness can be induced by melanoma-derived exosomes and represents an early event in pre-metastatic niche formation (Peinado et al., 2012). Bone marrow-derived cells are crucial for this process, and their pro-metastatic phenotype is induced by horizontal transfer of tumor-derived exosomes containing MET oncoprotein (Peinado et al., 2012). Melanoma-derived exosomes are also involved in lymphangiogenesis and lymphatic dissemination, since they carry the metastatic factors that lead to the induction of ECM factors necessary for trapping the metastatic cells in the lymph nodes (Hood et al., 2011). Tumor infiltration and invasion relies mainly on activation of signaling pathways that promote cell migration, ECM remodeling and the expression of MMPs. In addition, this process is accompanied by the production of inflammatory triggers, such as cytokines, chemokines, and

reactive oxygen species, which attract bone marrow-derived cells. Alveolar epithelial cells, forming part of the lung stroma microenvironment, express toll-like receptor 3, which recognizes the endogenous small nuclear RNAs carried by tumor-derived exosomes (Liu et al., 2016). As a consequence, alveolar epithelial cells start secreting chemokines, which attracts neutrophils and initiates pro-metastatic inflammatory responses in the lung (Liu et al., 2016).

## CONCLUDING REMARKS

Here we reviewed recent research on the role of EVs in intercellular communication and control of cell function, with special emphasis on their interaction with ECM and cell microenvironment. It is becoming evident that EVs can substitute the classical communication through cell-cell contact or protein-receptor interaction, since they carry a greater spectrum of bioactive molecules. In 3D cell culture systems or biological scaffold materials used in regenerative medicine, ECM-bound EVs can influence cell behavior, including cell growth, proliferation, survival, migration and differentiation. These EV properties can be used for tissue repair and regeneration; however, further studies are needed to finely define their cargo signature and functional roles. In addition, current cell therapies impose several disadvantages, such as immunogenicity and tumorigenicity, which may be overcome with the use of EVs for clinical applications. In cancer, therapeutic strategy to inhibit EV secretion might decrease metastatic potential, drug resistance, immune suppression and cancer-associated coagulation disorder. EV-related research is currently flourishing and there is a great interest in deciphering the mechanisms of EV cargo selective packaging and targeting of recipient cells, as well as profiling EV content for biomarker research. However, EV isolation and quantification techniques must be completely standardized before reaching their full potential for clinical applications.

## AUTHOR CONTRIBUTIONS

AA-S contributed to the design, writing, financial support, and final approval of the manuscript. GR contributed to the design and writing and final approval of the manuscript. NG-R and SE-R contributed to the design and writing of the manuscript. JC-N made the figures. CB-I reviewed the manuscript.

## ACKNOWLEDGMENTS

We are grateful for the financial support from the 'Fondo de Investigaciones Sanitarias (FIS) (PI14\_00077), the Miguel Servet Program (CP11/00147) del Instituto de Salud Carlos III (AAS), and the Ministerio de Economía y Competitividad-FEDERER (RTC-2016-4990-1, RTC-2015-3846-1)'. SE-R was supported by FPI-CEU predoctoral fellowship.

## REFERENCES

- Aggarwal, K. P., Narula, S., Kakkar, M., and Tandon, C. (2013). Nephrolithiasis: molecular mechanism of renal stone formation and the critical role played by modulators. *Biomed Res. Int.* 2013:292953. doi: 10.1155/2013/292953
- Ali, S. Y., and Griffiths, S. (1983). Formation of calcium-phosphate crystals in normal and osteoarthritic cartilage. *Ann. Rheum. Dis.* 42, 45–48. doi: 10.1136/Arth.42.Suppl\_1.45
- Alison, M. R., Poulosom, R., Jeffery, R., Dhillon, A. P., Quaglia, A., Jacob, J., et al. (2000). Hepatocytes from non-hepatic adult stem cells. *Nature* 406:257. doi: 10.1038/35018642
- Al-Nedawi, K., Meehan, B., Micallef, J., Lhotak, V., May, L., Guha, A., et al. (2008). Intercellular transfer of the oncogenic receptor EGFRvIII by microvesicles derived from tumour cells. *Nat. Cell Biol.* 10, 619–624. doi: 10.1038/ncb1725
- Al-Nedawi, K., Szymraj, J., and Cierniewski, C. S. (2005). Mast cell-derived exosomes activate endothelial cells to secrete plasminogen activator inhibitor type 1. *Arterioscler. Thromb. Vasc. Biol.* 25, 1744–1749. doi: 10.1161/01.ATV.0000172007.86541.76
- Anderson, H. C., Mulhall, D., and Garimella, R. (2010). Role of extracellular membrane vesicles in the pathogenesis of various diseases, including cancer, renal diseases, atherosclerosis, and arthritis. *Lab. Invest.* 90, 1549–1557. doi: 10.1038/labinvest.2010.152
- Andreola, G., Rivoltini, L., Castelli, C., Huber, V., Perego, P., Deho, P., et al. (2002). Induction of lymphocyte apoptosis by tumor cell secretion of FasL-bearing microvesicles. *J. Exp. Med.* 195, 1303–1316. doi: 10.1084/jem.20011624
- Ashiru, O., Boutet, P., Fernández-Messina, L., Agüera-González, S., Skepper, J. N., Valés-Gómez, M., et al. (2010). Natural killer cell cytotoxicity is suppressed by exposure to the human NKG2D ligand MICA\*008 that is shed by tumor cells in exosomes. *Cancer Res.* 70, 481–489. doi: 10.1158/0008-5472.CAN-09-1688
- Badimon, L., Suades, R., Arderiu, G., Peña, E., Chiva-Blanch, G., and Padró, T. (2017). Microvesicles in Atherosclerosis and Angiogenesis: From Bench to Bedside and Reverse. *Front. Cardiovasc. Med.* 4:77. doi: 10.3389/fcvm.2017.00077
- Bakhshian Nik, A., Hutcheson, J. D., and Aikawa, E. (2017). Extracellular vesicles as mediators of cardiovascular calcification. *Front. Cardiovasc. Med.* 4:78. doi: 10.3389/fcvm.2017.00078
- Basak, G. W., Yasukawa, S., Alfaro, A., Halligan, S., Srivastava, A. S., Min, W.-P., et al. (2009). Human embryonic stem cells hemangioblast express HLA-antigens. *J. Transl. Med.* 7:27. doi: 10.1186/1479-5876-7-27
- Bebawy, M., Combes, V., Lee, E., Jaiswal, R., Gong, J., Bonheure, A., et al. (2009). Membrane microparticles mediate transfer of P-glycoprotein to drug sensitive cancer cells. *Leukemia* 23, 1643–1649. doi: 10.1038/leu.2009.76
- Bronisz, A., Wang, Y., Nowicki, M. O., Peruzzi, P., Ansari, K., Ogawa, D., et al. (2014). Extracellular vesicles modulate the glioblastoma microenvironment via a tumor suppression signaling network directed by miR-1. *Cancer Res.* 74, 738–750. doi: 10.1158/0008-5472.CAN-13-2650
- Chaput, N., Täieb, J., Scharzt, N., Flament, C., Novault, S., André, F., et al. (2005). The potential of exosomes in immunotherapy of cancer. *Blood Cells Mol. Dis.* 35, 111–115. doi: 10.1016/j.bcmd.2005.05.009
- Chen, N. X., O'Neill, K. D., Chen, X., and Moe, S. M. (2008). Annexin-mediated matrix vesicle calcification in vascular smooth muscle cells. *J. Bone Miner. Res.* 23, 1798–1805. doi: 10.1359/jbmr.080604
- Cheng, N., Dai, J., Cheng, X., Li, S., Miron, R. J., Wu, T., et al. (2013). Porous CaP/silk composite scaffolds to repair femur defects in an osteoporotic model. *J. Mater. Sci. Mater. Med.* 24, 1963–1975. doi: 10.1007/s10856-013-4945-y
- Cosenza, S., Ruiz, M., Toupet, K., Jorgensen, C., and Noël, D. (2017). Mesenchymal stem cells derived exosomes and microparticles protect cartilage and bone from degradation in osteoarthritis. *Sci. Rep.* 7:16214. doi: 10.1038/s41598-017-15376-8
- Deregibus, M. C., Cantaluppi, V., Calogero, R., Lo Iacono, M., Tetta, C., Biancone, L., et al. (2007). Endothelial progenitor cell derived microvesicles activate an angiogenic program in endothelial cells by a horizontal transfer of mRNA. *Blood* 110, 2440–2448. doi: 10.1182/blood-2007-03-078709
- Dey, N., Ghosh-Choudhury, N., Kasinath, B. S., and Choudhury, G. G. (2012). TGFβ-stimulated microRNA-21 utilizes PTEN to orchestrate AKT/mTORC1 signaling for mesangial cell hypertrophy and matrix expansion. *PLoS One* 7:e42316. doi: 10.1371/journal.pone.0042316
- Dvorak, H. F., Quay, S. C., Orenstein, N. S., Dvorak, A. M., Hahn, P., Bitzer, A. M., et al. (1981). Tumor shedding and coagulation. *Science* 212, 923–924. doi: 10.1126/science.7195067
- Falk, E. (2006). Pathogenesis of atherosclerosis. *J. Am. Coll. Cardiol.* 47, C7–C12. doi: 10.1016/j.jacc.2005.09.068
- Forbes, J. M., and Cooper, M. E. (2013). Mechanisms of diabetic complications. *Physiol. Rev.* 93, 137–188. doi: 10.1152/physrev.00045.2011
- Gallo, S., Gili, M., Lombardo, G., Rossetti, A., Rosso, A., Dentelli, P., et al. (2016). Stem cell-derived, microRNA-Carrying extracellular vesicles: a novel approach to interfering with mesangial cell collagen production in a hyperglycaemic setting. *PLoS One* 11:e0162417. doi: 10.1371/journal.pone.0162417
- García-Romero, N., Esteban-Rubio, S., Rackov, G., Carrión-Navarro, J., Beldaniesta, C., and Ayuso-Sacido, A. (2017). Extracellular vesicles compartment in liquid biopsies: clinical application. *Mol. Aspects Med.* 60, 27–37. doi: 10.1016/j.mam.2017.11.009
- Gebauer, D., Kellermeyer, M., Gale, J. D., Bergström, L., and Cölfen, H. (2014). Pre-nucleation clusters as solute precursors in crystallisation. *Chem. Soc. Rev.* 43, 2348–2371. doi: 10.1039/C3CS60451A
- Gesierich, S., Berezovskiy, I., Ryschich, E., and Zoller, M. (2006). Systemic induction of the angiogenesis switch by the tetraspanin D6.1A/CO-029. *Cancer Res.* 66, 7083–7094. doi: 10.1158/0008-5472.CAN-06-0391
- Ginestra, A., La Placa, M. D., Saladino, F., Cassara, D., Nagase, H., and Vittorelli, M. L. (1998). The amount and proteolytic content of vesicles shed by human cancer cell lines correlates with their in vitro invasiveness. *Anticancer. Res.* 18, 3433–3437.
- Giri, P. K., and Schorey, J. S. (2008). Exosomes derived from *M. bovis* BCG infected macrophages activate antigen-specific CD4<sup>+</sup> and CD8<sup>+</sup> T cells *in vitro* and *in vivo*. *PLoS One* 3:e2461. doi: 10.1371/journal.pone.0002461
- Golub, E. E. (2009). Role of matrix vesicles in biomineralization. *Biochim. Biophys. Acta* 1790, 1592–1598. doi: 10.1016/j.bbagen.2009.09.006
- Golub, E. E., and Boesze-Battaglia, K. (2007). The role of alkaline phosphatase in mineralization. *Curr. Opin. Orthop.* 18, 444–448. doi: 10.1084/jem.93.5.415
- Gong, J., Luk, F., Jaiswal, R., and Bebawy, M. (2014). Microparticles mediate the intercellular regulation of microRNA-503 and proline-rich tyrosine kinase 2 to alter the migration and invasion capacity of breast cancer cells. *Front. Oncol.* 4:220. doi: 10.3389/fonc.2014.00220
- Gray, R. S., Roszko, I., and Solnica-Krezel, L. (2011). Planar cell polarity: coordinating morphogenetic cell behaviors with embryonic polarity. *Dev. Cell* 21, 120–133. doi: 10.1016/j.devcel.2011.06.011
- Grzesiak, J., Śmieszek, A., and Marycz, K. (2017). Ultrastructural changes during osteogenic differentiation in mesenchymal stromal cells cultured in alginate hydrogel. *Cell Biosci.* 7:2. doi: 10.1186/s13578-016-0128-0
- Gu, X., Erb, U., Büchler, M. W., and Zöller, M. (2015). Improved vaccine efficacy of tumor exosome compared to tumor lysate loaded dendritic cells in mice. *Int. J. Cancer* 136, E74–E84. doi: 10.1002/ijc.29100
- Harmey, D., Hesse, L., Narisawa, S., Johnson, K. A., Terkeltaub, R., and Millán, J. L. (2004). Concerted regulation of inorganic pyrophosphate and osteopontin by Akp2, Enpp1, and Ank. *Am. J. Pathol.* 164, 1199–1209. doi: 10.1016/S0002-9440(10)63208-7
- Hayashi, T., Lombaert, I. M., Hauser, B. R., Patel, V. N., and Hoffman, M. P. (2017). Exosomal microRNA transport from salivary mesenchyme regulates epithelial progenitor expansion during organogenesis. *Dev. Cell* 40, 95–103. doi: 10.1016/j.devcel.2016.12.001
- Herrera, M. B., Bruno, S., Buttiglieri, S., Tetta, C., Gatti, S., Deregibus, M. C., et al. (2006). Isolation and characterization of a stem cell population from adult human liver. *Stem Cells* 24, 2840–2850. doi: 10.1634/stemcells.2006-0114
- Herrera, M. B., Fonsato, V., Gatti, S., Deregibus, M. C., Sordi, A., Cantarella, D., et al. (2010). Human liver stem cell-derived microvesicles accelerate hepatic regeneration in hepatectomized rats. *J. Cell. Mol. Med.* 14, 1605–1618. doi: 10.1111/j.1582-4934.2009.00860.x
- Hood, J. L., Pan, H., Lanza, G. M., and Wickline, S. A. (2009). Paracrine induction of endothelium by tumor exosomes. *Lab. Invest.* 89, 1317–1328. doi: 10.1016/j.fertnstert.2010.09.017.Development

- Hood, J. L., Roman, R. S., and Wickline, S. A. (2011). Exosomes released by melanoma cells prepare sentinel lymph nodes for tumor metastasis. *Cancer Res.* 71, 3792–3801. doi: 10.1158/0008-5472.CAN-10-4455
- Hutcheson, J. D., Goettsch, C., Pham, T., Iwashita, M., Aikawa, M., Singh, S. A., et al. (2014). Enrichment of calcifying extracellular vesicles using density-based ultracentrifugation protocol. *J. Extracell. Vesicles* 3:25129. doi: 10.3402/jev.v3.25129
- Izadpanah, R., Kaushal, D., Kriedt, C., Tsien, F., Patel, B., Dufour, J., et al. (2008). Long-term in vitro expansion alters the biology of adult mesenchymal stem cells. *Cancer Res.* 68, 4229–4238. doi: 10.1158/0008-5472.CAN-07-5272
- Jain, R. K. (2005). Normalization of tumor vasculature: an emerging concept in antiangiogenic therapy. *Science* 307, 58–62. doi: 10.1126/science.1104819
- Janowska-Wieczorek, A., Wycoczynski, M., Kijowski, J., Marquez-Curtis, L., Machalinski, B., Ratajczak, J., et al. (2005). Microvesicles derived from activated platelets induce metastasis and angiogenesis in lung cancer. *Int. J. Cancer* 113, 752–760. doi: 10.1002/ijc.20657
- Jayachandran, M., Lugo, G., Heiling, H., Miller, V. M., Rule, A. D., and Lieske, J. C. (2015). Extracellular vesicles in urine of women with but not without kidney stones manifest patterns similar to men: a case control study. *Biol. Sex Differ.* 6, 1–11. doi: 10.1186/s13293-015-0021-2
- Jiang, N., Xiang, L., He, L., Yang, G., Zheng, J., Wang, C., et al. (2017). Exosomes mediate epithelium-mesenchyme crosstalk in organ development. *ACS Nano* 11, 7736–7746. doi: 10.1021/acsnano.7b01087
- Joyce, J. A., and Pollard, J. W. (2009). Microenvironmental regulation of metastasis. *Nat. Rev. Cancer* 9, 239–252. doi: 10.1038/nrc2618
- Kalka, C., Masuda, H., Takahashi, T., Kalka-Moll, W. M., Silver, M., Kearney, M., et al. (2000). Transplantation of ex vivo expanded endothelial progenitor cells for therapeutic neovascularization. *Proc. Natl. Acad. Sci. U.S.A.* 97, 3422–3427. doi: 10.1073/pnas.070046397
- Kapustin, A. N., Schoppet, M., Schurgers, L. J., Reynolds, J. L., McNair, R., Heiss, A., et al. (2017). Prothrombin loading of vascular smooth muscle cell-derived exosomes regulates coagulation and calcification. *Arterioscler. Thromb. Vasc. Biol.* 37, e22–e32. doi: 10.1161/ATVBAHA.116.308886
- Khalil, A. A., Kabapy, N. F., Deraz, S. F., and Smith, C. (2011). Heat shock proteins in oncology: diagnostic biomarkers or therapeutic targets? *Biochim. Biophys. Acta* 1816, 89–104. doi: 10.1016/j.bbcan.2011.05.001
- Kim, C. W., Lee, H. M., Lee, T. H., Kang, C., Kleinman, H. K., and Gho, Y. S. (2002). Extracellular membrane vesicles from tumor cells promote angiogenesis via sphingomyelin. *Cancer Res.* 62, 6312–6317.
- Kim, J. W., Wieckowski, E., Taylor, D. D., Reichert, T. E., Watkins, S., and Whiteside, T. L. (2005). Fas Ligand - positive membranous vesicles isolated from sera of patients with oral cancer induce apoptosis of activated T lymphocytes Fas ligand - positive membranous vesicles isolated from sera of patients with oral cancer induce apoptosis of activated T. *Clin. Cancer Res.* 11, 1010–1020.
- Kispert, A., Vainio, S., and McMahon, A. (1998). Wnt-4 is a mesenchymal signal for epithelial transformation of metanephric mesenchyme in the developing kidney. *Development* 125, 4225–4234.
- Kockx, M. M., De Meyer, G. R., Muhring, J., Jacob, W., Bult, H., and Herman, A. G. (1998). Apoptosis and Related Proteins in Different Stages of Human Atherosclerotic Plaques Mark. *Circulation* 97, 2307–2315. doi: 10.1161/01.CIR.97.23.2307
- Krause, M., Rak-Raszewska, A., Naillat, F., Saarela, U., Schmidt, C., Ronkainen, V.-P., et al. (2018). Exosomes as secondary inductive signals involved in kidney organogenesis. *J. Extracell. Vesicles* 7:1422675. doi: 10.1080/20013078.2017.1422675
- Krohn, J. B., Hutcheson, J. D., and Mart, E. (2016). Extracellular vesicles in cardiovascular calcification: expanding current paradigms. *J. Physiol.* 11, 2895–2903. doi: 10.1113/JP271338
- Lara-Hernandez, R., Lozano-Villardell, P., Blanes, P., Torreguitart-Mirada, N., Galmes, A., and Besalduch, J. (2010). Safety and efficacy of therapeutic angiogenesis as a novel treatment in patients with critical limb ischemia. *Ann. Vasc. Surg.* 24, 287–294. doi: 10.1016/j.avsg.2009.10.012
- Leoni, G., Neumann, P., Kamaly, N., Quiros, M., Nishio, H., Jones, H. R., et al. (2015). Annexin A1 - containing extracellular vesicles and polymeric nanoparticles promote epithelial wound repair. *J. Clin. Invest.* 125, 1215–1227. doi: 10.1172/JCI76693
- Li, J.-L., Sainson, R. C., Shi, W., Leek, R., Harrington, L. S., Preusser, M., et al. (2007). Delta-like 4 Notch ligand regulates tumor angiogenesis, improves tumor vascular function, and promotes tumor growth in vivo. *Cancer Res.* 67, 11244–11253. doi: 10.1158/0008-5472.CAN-07-0969
- Lieske, J. C., Rule, A. D., Krambeck, A. E., Williams, J. C., Bergstralh, E. J., Mehta, R. A., et al. (2014). Stone composition as a function of age and sex. *Clin. J. Am. Soc. Nephrol.* 9, 2141–2146. doi: 10.2215/CJN.05660614
- Liu, Y., Gu, Y., Han, Y., Zhang, Q., Jiang, Z., Zhang, X., et al. (2016). Tumor exosomal RNAs promote lung pre-metastatic niche formation by activating alveolar epithelial TLR3 to recruit neutrophils. *Cancer Cell* 30, 243–256. doi: 10.1016/j.ccell.2016.06.021
- Lu, J. F., Luk, F., Gong, J., Jaiswal, R., Grau, G. E. R., and Bebawy, M. (2013). Microparticles mediate MRP1 intercellular transfer and the re-templating of intrinsic resistance pathways. *Pharmacol. Res.* 76, 77–83. doi: 10.1016/j.phrs.2013.07.009
- Luga, V., Zhang, L., Vitoria-Petit, A. M., Ogunjimi, A. A., Inanlou, M. R., Chiu, E., et al. (2012). Exosomes mediate stromal mobilization of autocrine Wnt-PCP signaling in breast cancer cell migration. *Cell* 151, 1542–1556. doi: 10.1016/j.cell.2012.11.024
- Maciel, T. T., Moura, I. C., and Hermine, O. (2015). The role of mast cells in cancers. *Fl000Prime Rep.* 7:9. doi: 10.12703/P7-09
- Mahamid, J., Sharir, A., Gur, D., Zelzer, E., Addadi, L., and Weiner, S. (2011). Bone mineralization proceeds through intracellular calcium phosphate loaded vesicles: a cryo-electron microscopy study. *J. Struct. Biol.* 174, 527–535. doi: 10.1016/j.jsb.2011.03.014
- Martins, V. R., Dias, M. S., and Hainaut, P. (2013). Tumor-cell-derived microvesicles as carriers of molecular information in cancer. *Curr. Opin. Oncol.* 25, 66–75. doi: 10.1097/CCO.0b013e32835b7c81
- McCready, J., Sims, J. D., Chan, D., and Jay, D. G. (2010). Secretion of extracellular hsp90a via exosomes increases cancer cell motility: a role for plasminogen activation. *BMC Cancer* 10:294. doi: 10.1186/1471-2407-10-294
- McGough, I. J., and Vincent, J.-P. (2016). Exosomes in developmental signalling. *Development* 143, 2482–2493. doi: 10.1242/dev.126516
- Michalopoulos, G. K. (2007). Liver regeneration. *J. Cell. Physiol.* 213, 286–300. doi: 10.1002/jcp.21172
- Momen-Heravi, F., Balaj, L., Alian, S., Mantel, P. Y., Halleck, A. E., Trachtenberg, A. J., et al. (2013). Current methods for the isolation of extracellular vesicles. *Biol. Chem.* 394, 1253–1262. doi: 10.1515/hsz-2013-0141
- Nazarenko, I., Rana, S., Baumann, A., McAlear, J., Hellwig, A., Trendelenburg, M., et al. (2010). Cell surface tetraspanin Tspan8 contributes to molecular pathways of exosome-induced endothelial cell activation. *Cancer Res.* 70, 1668–1678. doi: 10.1158/0008-5472.CAN-09-2470
- New, S. E., and Aikawa, E. (2013). Role of extracellular vesicles in de novo mineralization: AN additional novel mechanism of cardiovascular calcification. *Arterioscler. Thromb. Vasc. Biol.* 33, 1753–1758. doi: 10.1161/ATVBAHA.112.300128
- New, S. E., Goettsch, C., Aikawa, M., Marchini, J. F., Shibasaki, M., Yabusaki, K., et al. (2013). Macrophage-derived matrix vesicles: an alternative novel mechanism for microcalcification in atherosclerotic plaques. *Circ. Res.* 113, 72–77. doi: 10.1161/CIRCRESAHA.113.301036
- O'Connell, D. J., Ho, J. W., Mammoto, T., Turbe-Doan, A., O'Connell, J. T., Haseley, P. S., et al. (2012). A Wnt-bmp feedback circuit controls intertissue signaling dynamics in tooth organogenesis. *Sci. Signal.* 5:ra4. doi: 10.1126/scisignal.2002414
- Park, J. E., Tan, H. S., Datta, A., Lai, R. C., Zhang, H., Meng, W., et al. (2010). Hypoxic tumor cell modulates its microenvironment to enhance angiogenic and metastatic potential by secretion of proteins and exosomes. *Mol. Cell. Proteomics* 9, 1085–1099. doi: 10.1074/mcp.M900381-MCP200
- Parolini, I., Federici, C., Raggi, C., Lugini, L., Palleschi, S., De Milito, A., et al. (2009). Microenvironmental pH is a key factor for exosome traffic in tumor cells. *J. Biol. Chem.* 284, 34211–34222. doi: 10.1074/jbc.M109.041152
- Patel, V. N., Rebutini, I. T., and Hoffman, M. P. (2006). Salivary gland branching morphogenesis. *Differentiation* 74, 349–364. doi: 10.1111/j.1432-0436.2006.00088.x
- Peinado, H., Alečković, M., Lavotshkin, S., Matei, I., Costa-Silva, B., Moreno-Bueno, G., et al. (2012). Melanoma exosomes educate bone marrow progenitor

- cells toward a pro-metastatic phenotype through MET. *Nat. Med.* 18, 883–891. doi: 10.1038/nm.2753
- Phng, L. K., and Gerhardt, H. (2009). Angiogenesis: a team effort coordinated by Notch. *Dev. Cell* 16, 196–208. doi: 10.1016/j.devcel.2009.01.015
- Pietilä, I., and Vainio, S. J. (2014). Kidney development: an overview. *Nephron Exp. Nephrol.* 126, 40–44. doi: 10.1159/000360659
- Pitt, J. M., Charrier, M., Viaud, S., Andre, F., Besse, B., Chaput, N., et al. (2014). Dendritic cell-derived exosomes as immunotherapies in the fight against cancer. *J. Immunol.* 193, 1006–1011. doi: 10.4049/jimmunol.140703
- Proudfoot, D., Skepper, J. N., Hegyi, L., Bennett, M. R., Shanahan, C. M., and Weissberg, P. L. (2000). Apoptosis regulates human vascular calcification in vitro: evidence for initiation of vascular calcification by apoptotic bodies. *Circ. Res.* 87, 1055–1062. doi: 10.1161/01.RES.87.11.1055
- Puthiyaveetil, J. S. V., Kota, K., Chakkarayan, R., Chakkarayan, J., and Thodiyil, A. K. P. (2016). Epithelial – Mesenchymal interactions in tooth development and the significant role of growth factors and genes with emphasis on mesenchyme – A review. *J. Clin. Diagnostic Res.* 10, ZE05–ZE09. doi: 10.7860/JCDR/2016/21719.8502
- Qi, X., Zhang, J., Yuan, H., Xu, Z., Li, Q., Niu, X., et al. (2016). Exosomes secreted by human-induced pluripotent stem cell-derived mesenchymal stem cells repair critical-sized bone defects through enhanced angiogenesis and osteogenesis in osteoporotic rats. *Int. J. Biol. Sci.* 12, 836–849. doi: 10.7150/ijbs.14809
- Rafii, S., and Lyden, D. (2003). Therapeutic stem and progenitor cell transplantation for organ vascularization and regeneration. *Nat. Med.* 9, 702–712. doi: 10.1038/nm0603-702
- Ranghino, A., Cantaluppi, V., Grange, C., Vitillo, L., Fop, F., Biancone, L., et al. (2012). Endothelial progenitor cell-derived microvesicles improve neovascularization in a murine model of hindlimb ischemia. *Int. J. Immunopathol. Pharmacol.* 25, 75–85. doi: 10.1177/039463201202500110
- Robey, P. G. (2011). Cell sources for bone regeneration: the good, the bad, and the ugly (But Promising). *Tissue Eng. Part B Rev.* 17, 423–430. doi: 10.1089/ten.teb.2011.0199
- Rustom, A., Saffrich, R., Markovic, I., Walther, P., and Gerdes, H.-H. (2004). Nanotubular highways for intercellular organelle transport. *Science* 303, 1007–1010. doi: 10.1126/science.1093133
- Sanderson, M. P., Keller, S., Alonso, A., Riedle, S., Dempsey, P. J., and Altevogt, P. (2008). Generation of novel, secreted epidermal growth factor receptor (EGFR/ErbB1) isoforms via metalloprotease-dependent ectodomain shedding and exosome secretion. *J. Cell. Biochem.* 103, 1783–1797. doi: 10.1002/jcb.21569
- Seelenmeyer, C., Stegmayer, C., and Nickel, W. (2008). Unconventional secretion of fibroblast growth factor 2 and galectin-1 does not require shedding of plasma membrane-derived vesicles. *FEBS Lett.* 582, 1362–1368. doi: 10.1016/j.febslet.2008.03.024
- Shabo, I., and Svanvik, J. (2011). Expression of macrophage antigens by tumor cells. *Adv. Exp. Med. Biol.* 714, 141–150. doi: 10.1007/978-94-007-0782-5\_7
- Shanahan, C. M., Crouthamel, M. H., Kapustin, A., and Giachelli, C. M. (2012). Arterial calcification in chronic kidney disease: key roles for calcium and phosphate. *Circ. Res.* 109, 697–711. doi: 10.1161/CIRCRESAHA.110.234914
- Shapiro, I. M., Landis, W. J., and Risbud, M. V. (2015). Matrix vesicles: Are they anchored exosomes? *Bone* 79, 29–36. doi: 10.1016/j.bone.2015.05.013
- Sharghi-Namini, S., Tan, E., Ong, L. L. S., Ge, R., and Asada, H. H. (2014). Dll4-containing exosomes induce capillary sprout retraction in a 3D microenvironment. *Sci. Rep.* 4:4031. doi: 10.1038/srep04031
- Sheldon, H., Heikamp, E., Turley, H., Dragovic, R., Thomas, P., Oon, C. E., et al. (2010). New mechanism for Notch signaling to endothelium at a distance by delta-like 4 incorporation into exosomes. *Blood* 116, 2385–2394. doi: 10.1182/blood-2009-08-239228
- Sowinski, S., Jolly, C., Berninghausen, O., Purbhoo, M. A., Chauveau, A., Kohler, K., et al. (2008). Membrane nanotubes physically connect T cells over long distances presenting a novel route for HIV-1 transmission. *Nat. Cell Biol.* 10, 211–219. doi: 10.1038/ncb1682
- Stockmann, C., Schadendorf, D., Klose, R., and Helfrich, I. (2014). The impact of the immune system on tumor: angiogenesis and vascular remodeling. *Front. Oncol.* 4:69. doi: 10.3389/fonc.2014.00069
- Sun, X., Ma, X., Wang, J., Zhao, Y., Wang, Y., Bihl, J. C., et al. (2017). Glioma stem cells-derived exosomes promote the angiogenic ability of endothelial cells through miR-21/VEGF signal. *Oncotarget* 8, 36137–36148. doi: 10.18632/oncotarget.16661
- Théry, C., Amigorena, S., Raposo, G., and Clayton, A. (2006). Isolation and characterization of exosomes from cell culture supernatants. *Curr. Protoc. Cell Biol.* Chapter 3, Unit3.22.
- Thery, C., Duban, L., Segura, E., Veron, P., Lantz, O., and Amigorena, S. (2002). Indirect activation of naive CD4+ T cells by dendritic cell-derived exosomes. *Nat. Immunol.* 3, 1156–1162. doi: 10.1038/ni854
- Théry, C., Ostrowski, M., and Segura, E. (2009). Membrane vesicles as conveyors of immune responses. *Nat. Rev. Immunol.* 9, 581–593. doi: 10.1038/nri2567
- Tomasek, J. J., Gabbiani, G., Hinz, B., Chaponnier, C., and Brown, R. A. (2002). Myofibroblasts and mechano-regulation of connective tissue remodelling. *Nat. Rev. Mol. Cell Biol.* 3, 349–363. doi: 10.1038/nrm809
- Tucker, A. S. (2007). Salivary gland development. *Semin. Cell Dev. Biol.* 18, 237–244. doi: 10.1016/j.semcdb.2007.01.006
- Valadi, H., Ekstrom, K., Bossios, A., Sjostrand, M., Lee, J. J., and Lotvall, J. O. (2007). Exosome-mediated transfer of mRNAs and microRNAs is a novel mechanism of genetic exchange between cells. *Nat. Cell Biol.* 9, 654–659. doi: 10.1038/ncb1596
- Valenti, R., Huber, V., Filipazzi, P., Pilla, L., Sovena, G., Villa, A., et al. (2006). Human tumor-released microvesicles promote the differentiation of myeloid cells with transforming growth factor- $\beta$ -mediated suppressive activity on T lymphocytes. *Cancer Res.* 66, 9290–9298. doi: 10.1158/0008-5472.CAN-06-1819
- Villa-Diaz, L. G., Brown, S. E., Liu, Y., Ross, A. M., Lahann, J., Parent, J. M., et al. (2012). Derivation of mesenchymal stem cells from human induced pluripotent stem cells cultured on synthetic substrates. *Stem Cells* 30, 1174–1181. doi: 10.1002/stem.1084
- Vrijen, K. R., Maring, J. A., Chamuleau, S. A., Verhage, V., Mol, E. A., Deddens, J. C., et al. (2016). Exosomes from cardiomyocyte progenitor cells and mesenchymal stem cells stimulate angiogenesis via EMMPRIN. *Adv. Healthc. Mater.* 5, 2555–2565. doi: 10.1002/adhm.201600308
- Vrijen, K. R., Sluiter, J. P., Schuchardt, M. W., van Balkom, B. W., Noort, W. A., Chamuleau, S. A., et al. (2010). Cardiomyocyte progenitor cell-derived exosomes stimulate migration of endothelial cells. *J. Cell. Mol. Med.* 14, 1064–1070. doi: 10.1111/j.1582-4934.2010.01081.x
- Webber, J., Steadman, R., Mason, M. D., Tabi, Z., and Clayton, A. (2010). Cancer exosomes trigger fibroblast to myofibroblast differentiation. *Cancer Res.* 70, 9621–9630. doi: 10.1158/0008-5472.CAN-10-1722
- Weinand, C., Pomerantseva, I., Neville, C. M., Gupta, R., Weinberg, E., Madisch, I., et al. (2006). Hydrogel- $\beta$ -TCP scaffolds and stem cells for tissue engineering bone. *Bone* 38, 555–563. doi: 10.1016/j.bone.2005.10.016
- Witwer, K. W., Buzás, E. I., Bemis, L. T., Bora, A., Lässer, C., Lötvall, J., et al. (2013). Standardization of sample collection, isolation and analysis methods in extracellular vesicle research. *J. Extracell. Vesicles* 2, 1–25. doi: 10.3402/jev.v2i0.20360
- Wolfers, J., Lozier, A., Raposo, G., Regnault, A., Théry, C., Masurier, C., et al. (2001). Tumor-derived exosomes are a source of shared tumor rejection antigens for CTL cross-priming. *Nat. Med.* 7, 297–303. doi: 10.1038/85438
- Xiang, X., Poliakov, A., Liu, C., Liu, Y., Deng, Z., Wang, J., et al. (2009). Induction of myeloid-derived suppressor cells by tumor exosomes. *Int. J. Cancer* 124, 2621–2633. doi: 10.1002/ijc.24249
- Yu, S., Liu, C., Su, K., Wang, J., Liu, Y., Zhang, L., et al. (2007). Tumor exosomes inhibit differentiation of bone marrow dendritic cells. *J. Immunol.* 178, 6867–6875. doi: 10.4049/jimmunol.178.11.6867
- Zhang, H.-G., Liu, C., Su, K., Yu, S., Zhang, L., Zhang, S., et al. (2006). A membrane form of TNF- presented by exosomes delays T cell activation-induced cell death. *J. Immunol.* 176, 7385–7393. doi: 10.4049/jimmunol.176.12.7385
- Zhang, S., Chu, W. C., Lai, R. C., Lim, S. K., Hui, J. H., and Toh, W. S. (2016). Exosomes derived from human embryonic mesenchymal stem cells promote osteochondral regeneration. *Osteoarthritis Cartilage* 24, 2135–2140. doi: 10.1016/j.joca.2016.06.022

- Zhou, L., Qi, X., Xu, M., Mao, Y., Liu, M., and Song, H. (2014). Microparticles: new light shed on the understanding of venous thromboembolism. *Acta Pharmacol. Sin.* 35, 1103–1110. doi: 10.1038/aps.2014.73
- Zomer, A., Maynard, C., Verweij, F. J., Kamermans, A., Schäfer, R., Beerling, E., et al. (2015). In vivo imaging reveals extracellular vesicle-mediated phenocopying of metastatic behavior. *Cell* 161, 1046–1057. doi: 10.1016/j.cell.2015.04.042
- Zou, L., Luo, Y., Chen, M., Wang, G., Ding, M., Petersen, C. C., et al. (2013). A simple method for deriving functional MSCs and applied for osteogenesis in 3D scaffolds. *Sci. Rep.* 3:2243. doi: 10.1038/srep02243

**Conflict of Interest Statement:** The authors declare that the research was conducted in the absence of any commercial or financial relationships that could be construed as a potential conflict of interest.

Copyright © 2018 Rackov, Garcia-Romero, Esteban-Rubio, Carrión-Navarro, Belda-Iniesta and Ayuso-Sacido. This is an open-access article distributed under the terms of the Creative Commons Attribution License (CC BY). The use, distribution or reproduction in other forums is permitted, provided the original author(s) and the copyright owner are credited and that the original publication in this journal is cited, in accordance with accepted academic practice. No use, distribution or reproduction is permitted which does not comply with these terms.



# Vascular Morphogenesis in the Context of Inflammation: Self-Organization in a Fibrin-Based 3D Culture System

Beate M. Rüger<sup>1\*</sup>, Tanja Buchacher<sup>2</sup>, Alexander Giurea<sup>3</sup>, Bernd Kubista<sup>3</sup>, Michael B. Fischer<sup>1,4</sup> and Johannes M. Breuss<sup>5</sup>

<sup>1</sup> Department of Blood Group Serology and Transfusion Medicine, Medical University of Vienna, Vienna, Austria, <sup>2</sup> Turku Centre for Biotechnology, University of Turku and Åbo Akademi University, Turku, Finland, <sup>3</sup> Department of Orthopedics, Medical University of Vienna, Vienna, Austria, <sup>4</sup> Department of Health Sciences and Biomedicine, Danube University Krems, Krems an der Donau, Austria, <sup>5</sup> Department of Vascular Biology and Thrombosis Research, Center of Physiology and Pharmacology, Medical University of Vienna, Vienna, Austria

**Introduction:** New vessel formation requires a continuous and tightly regulated interplay between endothelial cells with cells of the perivascular microenvironment supported by mechanic-physical and chemical cues from the extracellular matrix.

**Aim:** Here we investigated the potential of small fragments of synovial tissue to form *de novo* vascular structures in the context of inflammation within three dimensional (3D) fibrin-based matrices *in vitro*, and assessed the contribution of mesenchymal stromal cell (MSC)-immune cell cross-talk to neovascularization considering paracrine signals in a fibrin-based co-culture model.

**Material and Methods:** Synovial tissue fragments from patients with rheumatoid arthritis (RA) and inflammatory osteoarthritis (OA) were cultivated within 3D fibrin matrices for up to 4 weeks. Cellular and structural re-arrangement of the initially acellular matrix were documented by phase contrast microscopy and characterized by confocal laser-scanning microscopy of topographically intact 3D cultures and by immunohistochemistry. MSC-peripheral blood mononuclear cell (PBMC) co-cultures in the 3D fibrin system specifically addressed the influence of perivascular cell interactions to neo-vessel formation in a pro-inflammatory microenvironment. Cytokine levels in the supernatants of cultured explant tissues and co-cultures were evaluated by the Bio-Plex cytokine assay and ELISA.

**Results:** Vascular outgrowth from the embedded tissue into the fibrin matrix was preceded by leukocyte egress from the tissue fragments. Neo-vessels originating from both the embedded sample and from clusters locally formed by emigrated mononuclear cells were consistently associated with CD45<sup>+</sup> leukocytes. MSC and PBMC in co-culture formed vasculogenic clusters. Clusters and cells with endothelial phenotype emerging from them, were surrounded by a collagen IV scaffold. No vascular structures were observed in control 3D monocultures of PBMC or MSC. Paracrine signals released by cultured OA tissue fragments corresponded with elevated levels of granulocyte-colony stimulating factor, vascular endothelial growth factor and interleukin-6 secreted by MSC-PBMC co-cultures.

## OPEN ACCESS

### Edited by:

Cesare Gargioli,  
Università degli Studi di Roma Tor  
Vergata, Italy

### Reviewed by:

Stefano Maria Cannata,  
Università degli Studi di Roma Tor  
Vergata, Italy  
Peggy Lafuste,  
Université Paris-Est Créteil Val de  
Marne, France

### \*Correspondence:

Beate M. Rüger  
beate.rueger@meduniwien.ac.at

### Specialty section:

This article was submitted to  
Integrative Physiology,  
a section of the journal  
Frontiers in Physiology

**Received:** 28 February 2018

**Accepted:** 15 May 2018

**Published:** 05 June 2018

### Citation:

Rüger BM, Buchacher T, Giurea A, Kubista B, Fischer MB and Breuss JM (2018) Vascular Morphogenesis in the Context of Inflammation: Self-Organization in a Fibrin-Based 3D Culture System. *Front. Physiol.* 9:679. doi: 10.3389/fphys.2018.00679

**Conclusion:** Our results show that synovial tissue fragments with immune cell infiltrates have the potential to form new vessels in initially avascular 3D fibrin-based matrices. Cross-talk and cluster formation of MSC with immune cells within the 3D fibrin environment through self-organization and secretion of pro-angiogenic paracrine factors can support neo-vessel growth.

**Keywords:** neovascularization, inflammation, 3D fibrin matrix, synovial tissue, mesenchymal stromal cells, self-organization

## INTRODUCTION

Neovascularization plays an important role throughout postnatal life during regenerative processes after tissue and organ damage by ischemia or injury, in the course of acute or chronic inflammation and during auto-immune diseases. Neo-vessel formation is mainly accomplished by angiogenesis—the expansion of a pre-existing vascular network by endothelial cell sprouting—and is assisted by a process called postnatal vasculogenesis where precursor cells from the bone marrow are mobilized into the circulation, home to sites of active angiogenesis and differentiate into mature endothelial cells (Masuda and Asahara, 2003). Key cellular players of the neovascularization process in an inflammatory setting are immune cells, including neutrophils, macrophages and lymphocytes recruited to perivascular sites (i.e., perivascular niches) together with endothelial progenitor cells (EPC), as well as resident endothelial- and stromal cells. The leakage of fibrinogen into the perivascular space during inflammatory processes creates a microenvironment suitable for these cell types to interact with each other directly or indirectly through the secretion of paracrine factors (Davalos and Akassoglou, 2012). Cytokines act in concert within complex networks, where pro-angiogenic factors amplify the process of inflammation (Aplin et al., 2006) and continuous pro-inflammatory signals promote the process of neovascularization providing evidence for a regulatory intercommunication between inflammation and neovascularization in pathological situations (Costa et al., 2007). Further complexity is added by the pleiotropic effects and redundancy of most cytokines involved in neovascularization and inflammation. Interleukin (IL)-6 has both pro- and anti-inflammatory properties (Scheller et al., 2011) and can indirectly cause an increase in vascular permeability and neovascularization by inducing the expression of vascular endothelial growth factor (VEGF) (Cohen et al., 1996; Tzeng et al., 2013), a cytokine playing a well-known key role in both physiological and pathological angiogenesis (Ferrara et al., 2003). Both VEGF and granulocyte-colony stimulating factor (G-CSF) can contribute to postnatal neovascularization by mobilizing bone marrow-derived EPC (Asahara et al., 1999; Powell et al., 2005), and G-CSF has been shown to modulate the expression of leukocyte adhesion molecules (Sugimori et al., 1999; Suzuki et al., 2002), activate endothelial cells (Bussolino et al., 1989) and enhance angiogenesis (Natori et al., 2002). G-CSF is induced by inflammatory stimuli, and depending on context plays either beneficial or detrimental roles. In mice

endogenous G-CSF is a critical mediator of acute and chronic inflammatory arthritis (Lawlor et al., 2004). Beneficial effects of systemic G-CSF administration, however, have been reported in human inflammatory bowel disease associated with changes in memory cell cytokine production (Mannon et al., 2009).

A large range of *in vitro* models of both angiogenesis and vasculogenesis have used fibrin matrices as scaffold to study the mechanisms of endothelial cell assembly into microvascular networks (reviewed in Morin and Tranquillo, 2013). Amongst various endothelial cell (EC) types, human umbilical vein EC (HUVEC) and human dermal microvascular EC have been studied either as monoculture or in co-culture with support cells, such as fibroblasts, smooth muscle cells, mesenchymal stromal cells (MSC), and pericytes (Morin and Tranquillo, 2013). Both stromal cells from the bone marrow and adipose tissue can, when co-cultured *in vitro*, support HUVEC organization into vascular-like structures, which, however, lack a lumen (Verseijden et al., 2010), and adipose-derived stem cells form vascular-like structures when co-cultured with late outgrowth endothelial cells derived from peripheral blood (Holnthoner et al., 2015). These studies provide important information primarily about blood vessel assembly, but they do not take into account the well-recognized connection between neo-vessel formation and inflammation in pathological situations, as *in vivo* blood vessels are surrounded by connective tissue, which contains stromal cells, immune cells and extracellular matrix (ECM)-bound signaling molecules.

Excessive neo-vessel formation is a common feature of many chronic inflammatory disorders including rheumatoid arthritis (RA), and both neovascularization and inflammation also contribute to the pathogenesis of osteoarthritis (OA) (Scanzello et al., 2008; Sokolove and Lepus, 2013). Fibrin deposition is one of the most consistent features of RA in humans and experimental animal models of arthritic disease (Flick et al., 2007), and invasive granulation tissue is present in RA and advanced OA joints (Furuzawa-Carballeda et al., 2008). We have previously shown that synovial tissue of patients with RA and OA harbor EPC and MSC demonstrating the *in vivo* presence of crucial building blocks for postnatal vasculogenesis in an inflammatory microenvironment (Rüger et al., 2004; Giurea et al., 2006). In this study we aimed to provide a platform to investigate the interplay between neovascularization and inflammation. We hypothesized that small pieces of tissues infiltrated with inflammatory cells might be capable to generate neo-vessels when cultured in a biologically relevant 3D environment, even in the absence of exogenously



added pro-angiogenic growth factors. We argued that the explant culture would provide a model that integrates complex cellular interactions and paracrine signals involved in pathological neovascularization. Therefore we established a 3D fibrin matrix system for the culture of inflamed synovial tissue fragments of RA and OA patients as exploratory *in vitro* tool reflecting the complexity of remodeling *in vivo*, including both vascular compartment and perivascular inflammatory environment and their cell-cell interactions and paracrine signaling. In order to specifically address the contribution of perivascular cells to neo-vessel formation, the interaction of MSC with peripheral blood mononuclear cells (PBMC) was studied in 3D fibrin matrices. Outgrowth cells/structures, cellular re-arrangement and architectural re-structuring within the first 2 weeks of culture were characterized within topographically intact whole 3D fibrin matrices by a specially adapted 3D-culture immunofluorescence method and confocal laser-scanning microscopy (CLSM), and the release of relevant cytokines, e.g., G-CSF, VEGF, IL-6, and interleukin (IL)-10, during explant- and co-cultures was analyzed.

## MATERIALS AND METHODS

### Ethics Statement

The local ethics committee at the Medical University of Vienna approved the use of human synovial tissue (EK 791/2008 and EK1192/2015), human bone marrow MSC (EK1193/2015) and human PBMC (EK1168/2015) in order to perform this study. All donors provided written informed consent.

### Synovial Tissue, PBMC, and MSC

Synovial tissues of RA and OA patients were obtained at the time of surgery for arthroplasty or synovectomy. Fresh tissue samples were used for 3D cultures and an adjacent piece was fixed in 4.5% buffered formalin and embedded in paraffin for immunohistochemistry and immunohistochemical double labeling. PBMC were isolated from leukocyte-reduction chambers, a waste product obtained during platelet apheresis, from healthy donors by density gradient centrifugation. MSC were isolated from bone marrow and bone fragments obtained during hip-replacement surgery and expanded in complete  $\alpha$ MEM medium (Invitrogen, Carlsbad, CA) containing 10% fetal bovine serum (GE Healthcare Life Sciences, Marlborough, MA), 100 U/ml penicillin, 100  $\mu$ g/ml streptomycin and 250 ng/ml amphotericin B (Sigma, St. Louis, MO) at 37°C (20% O<sub>2</sub> and 5% CO<sub>2</sub> humidified atmosphere). MSC were characterized by flow cytometry analyses using CD90FITC (Stem Cell Technologies, Cologne, Germany), CD73PE (BD, Heidelberg, Germany), CD105FITC (BD), CD31PE (Biolegend, San Diego, CA), CD34PE (BD), CD45FITC (BD), and CD14PE (BD) antibodies and a FACS Canto II<sup>TM</sup> instrument (BD, San Jose, CA). Cells expressed typical MSC markers, CD90, CD73, CD105, lacked expression of CD31, CD34, CD45, and CD14, and could be differentiated into adipocytes, chondrocytes and osteoblasts. For 3D culture experiments passage two to four MSC were used.

### 3D Synovial Tissue Explant Culture System

Freshly excised synovial tissue samples (2–4 mm diameter fragments) from 10 OA patients and 8 RA patients were embedded in fibrin scaffolds in individual wells of 24-well culture plates (Corning, Corning, NY). Fibrin matrices were prepared as described previously with minor modifications (Rüger et al., 2008). In brief, human fibrinogen (2 mg/ml; Calbiochem, Darmstadt, Germany) was dissolved in PBS supplemented with 200 U/ml aprotinin (Gerot Pharmaceutica, Vienna, Austria) to prevent fibrinolysis. Human plasma thrombin (0.6 U/ml, Sigma) was added to the fibrinogen solution and gel formation occurred by incubation at 37°C for 30 min. The tissue fragments were cultured using complete M199 medium (Invitrogen) containing 10% fetal bovine serum (GE Healthcare Life Sciences), 100 U/ml penicillin, 100  $\mu$ g/ml streptomycin and 250 ng/ml amphotericin B (Sigma) without additional growth factors for up to 4 weeks. The culture medium was changed every 3–4 days. The egress of cells into the fibrin matrix, cell growth and structural re-organization including vascular tube formation were monitored using a phase contrast microscope (Olympus IMT-2, Tokyo, Japan) and documented using a digital camera (Olympus DP50). The length of vascular sprouts was assessed in tissue fragments of four OA and RA patients, respectively, after 3 weeks of culture using the cell\* Imaging Software (Olympus).

### Co-culture of PBMC With Stromal Cells in 3D Fibrin Matrices

3D co-cultures of PBMC with MSC ( $n = 6$ ) were performed in 12-well plates (Corning). Cells were embedded in fibrin matrices in a ratio 1:100 (MSC:PBMC) using  $2.5 \times 10^6$  PBMC/cm<sup>2</sup> and cultured for up to 2 weeks in complete  $\alpha$ MEM medium (Invitrogen) containing 10% fetal bovine serum (GE Healthcare Life Sciences). Fibrin matrices were prepared as described above, but without addition of aprotinin. Control experiments were performed culturing PBMC separated from MSC by a 0.4  $\mu$ m transwell insert (Corning), PBMC without support of stromal cells and MSC alone. To investigate the effect of paracrine inflammatory signals on stromal cells in the absence of immune cells, MSC ( $n = 4$ ) were embedded in fibrin matrices in 24-well plates (Corning) at  $2.5 \times 10^4$  cells/cm<sup>2</sup> and cultured for 6 days in complete  $\alpha$ MEM medium (Invitrogen) containing 10% fetal bovine serum (GE Healthcare Life Sciences) supplemented with 5 ng/ml tumor necrosis factor (TNF) $\alpha$  (PeproTech, Rocky Hill, NJ) and 10 ng/ml interferon (IFN) $\gamma$  (PeproTech). Control experiments were performed in complete  $\alpha$ MEM medium without cytokine supplementation. Cultures were maintained at 37°C (20% O<sub>2</sub> and 5% CO<sub>2</sub> humidified atmosphere), and medium was changed every 3 days. Cellular re-arrangement was monitored using a phase contrast microscope (Olympus) and documented using a digital camera (Olympus).

### Cell Tracking

In order to investigate the physical interaction of MSC with PBMC in the 3D matrix, MSC were labeled with Cell Tracker Orange fluorescent probe (Molecular Probes, Thermo Fisher Scientific, MS, USA) and PBMC with Cell Tracker Green fluorescent probe (Molecular Probes) according to the

manufacturers protocol. Cells were mixed in a ratio of 1:100 (MSC:PBMC), embedded in fibrin gels and cultured for up to 7 days in high resolution chamber slides (ibidi) using complete  $\alpha$ MEM medium. For CLSM, cells were fixed with 4% paraformaldehyde and nuclei stained with DAPI.

## Immunohistochemistry and Double Labeling

Fibrin gels containing the synovial tissue were fixed in formalin and processed for paraffin embedding. Immunohistochemistry was performed on 5  $\mu$ m sections using the following mouse monoclonal antibodies, CD45 (1.4  $\mu$ g/ml, Dako, Glostrup, Denmark), CD34 (2  $\mu$ g/ml, Immunotech, Marseille, France) and podocalyxin (2  $\mu$ g/ml, kindly supplied by Prof. Dentscho Kerjaschki, Department of Pathology, Medical University Vienna, Austria), two markers for both endothelial and stem/progenitor cells, endothelial markers CD31 (4.5  $\mu$ g/ml, Dako) and von Willebrand factor (vWF) (5.8  $\mu$ g/ml, Dako), CD68 (0.5  $\mu$ g/ml, clone KP-1, Dako), Collagen type-IV (Col-IV) (3.2  $\mu$ g/ml, Dako), bcl-2 (3.2  $\mu$ g/ml, Dako), cleaved caspase-3 (4  $\mu$ g/ml, Cell Signaling Technology, Danvers, MA) and c-kit (CD117) (1.3  $\mu$ g/ml, rabbit pAb, Dako) together with the Vectastain ABC kit (Vector, Burlingame, CA). Control experiments were included by omission of primary antibodies. Visualization of antibody binding was achieved by 3-amino-9-ethyl-carbazole (Sigma), followed by counterstaining with Mayer's hemalum. Double labeling of cleaved caspase-3 and bcl-2 was performed using a peroxidase/alkaline phosphatase technique as reported previously (Rüger et al., 2004).

## Confocal Laser Scanning Microscopy of Intact 3D Cultures

In order to perform CLSM of whole 3D cultures, synovial tissue samples (eight, 12 and 13 tissue fragments from three individual OA patients, respectively) were embedded in fibrin matrices using special imaging chambers for high resolution microscopy (ibidi GmbH, Martinsried, Germany). Neo-vessels and the surrounding cellular and extracellular microenvironment present in the fibrin scaffolds were characterized by immunofluorescence analyses using a modified protocol of a previously published method (Lee et al., 2007). Immunofluorescence analyses of intact 3D PBMC-MSC co-cultures were performed in 12-well plates and stained fibrin gels transferred to ibidi chambers for CLSM. Briefly, fibrin matrices were fixed with 4% paraformaldehyde and incubated with a buffer solution containing 0.1% BSA, 0.2% Triton X-100, 0.05% Tween 20 in PBS followed by a blocking step with 20% normal donkey serum (Jackson Immuno Research, West Grove, PA). Fibrin gels were incubated with anti-human CD31 (mouse IgG<sub>1</sub>, 8  $\mu$ g/ml, Dako) or anti-human CD34 (mouse IgG<sub>1</sub>, 4  $\mu$ g/ml, Cell Marque, Rocklin, CA) together with rabbit anti-Col-IV (7.5  $\mu$ g/ml, Novus Biologicals, Cambridge, UK) for 6 h at room temperature. The cultures were washed with buffer solution and incubated simultaneously with donkey anti-mouse IgG<sub>1</sub> Alexa Fluor (AF)488 and donkey anti-rabbit AF555 (2.6  $\mu$ g/ml, Molecular Probes, Life Technologies, Carlsbad, CA) and cell nuclei stained with DAPI. CD34/ $\alpha$ -smooth muscle actin ( $\alpha$ -SMA) double-labeling was performed using monoclonal  $\alpha$ -SMA antibody (mouse IgG<sub>1</sub>, clone HHF35, 1  $\mu$ g/ml, Sigma)

and donkey anti-mouse IgG<sub>1</sub> AF555 followed by a blocking step using 20% mouse serum (Jackson Immuno Research), and incubation with biotinylated CD34 (mouse IgG<sub>1</sub>, 10  $\mu$ g/ml, Stem Cell Technologies, Cologne, Germany) followed by Streptavidin AF488 (2.6  $\mu$ g/ml, Molecular Probes, Life Technologies). For triple labeling, the gels were incubated simultaneously with antibody cocktails CD31/Col-IV, CD31/STRO-1/Col-IV (STRO-1, mouse IgM, 10  $\mu$ g/ml, R&D Systems, Minneapolis, MN), CD34/STRO-1/Col-IV and CD34/STRO-1/c-kit (c-kit, rabbit pAb, Dako), followed by isotype- and species-specific AF-labeled secondary antibody cocktails (Molecular Probes, Life Technologies). Omission of primary antibodies and the use of isotype-matched non-immune antibodies served as controls. After blocking with 20% mouse serum, the 3D constructs stained with CD31 and Col-IV antibodies were incubated with AF647-mouse anti-CD45 (2.5  $\mu$ g/ml, Biolegend). The cultures were washed with buffer solution, cell nuclei stained with DAPI, and 3D gels kept in PBS at +4°C until CLSM analyses. All 3D cultures were evaluated using a LSM 700 or LSM 780 confocal laser scanning microscope (Carl Zeiss, Jena, Germany) and the acquired images analyzed with the ZEN image processing and analysis software program (Zeiss).

## Cytokine Determination

The levels of G-CSF, VEGF, IL-6, and IL-10 were determined by the Bio-Plex 200 system (Bio-Rad, Vienna, Austria) in cell-free explant culture supernatants derived from three OA patients. In all three cases, samples were taken at times of medium exchange at days 4, 8, 15, and 19. We chose tissues from OA patients whose therapy is usually limited to pain control to avoid possible effects of the potent disease-modifying anti-rheumatic drugs commonly taken by RA patients. To account for intra-tissue variations three separate tissue fragments from each individual patient cultured in separate wells were used. Experiments were performed with each sample in duplicate, and data are expressed as mean values  $\pm$  SD. The supernatants of 3D MSC-PBMC co-cultures were taken after 24 h, on days 3 and 6; supernatants of the corresponding 3D PBMC- and MSC-monocultures were taken on day 6. G-CSF, VEGF, and IL-6 levels were determined using commercially available ELISA Duoset systems (R&D). In 3D co-cultures where MSC and PBMC were physically separated by a transwell insert, G-CSF and VEGF levels in the supernatants were measured by ELISA (R&D) on day 6. Supernatants of MSC cultured in fibrin gels with and without inflammatory stimulation were taken on days 3 and 6, and VEGF and G-CSF levels analyzed by ELISA (R&D). The assays were performed according to the reference manual, and the samples were measured in technical duplicates. Optical density values were measured at 450 nm on an ELISA plate reader (Victor3 Multilabel plate reader, PerkinElmer).

## Statistics

Statistical analyses were performed using the software package SPSS Statistics for Windows, version 22.0 (SPSS Inc., Chicago, IL). When comparing two groups, data were analyzed by the non-parametric Wilcoxon rank sum test. Data are expressed as means  $\pm$  SD. Significance was accepted at  $p \leq 0.05$  (\*),  $p \leq 0.01$  (\*\*), and  $p \leq 0.001$  (\*\*\*)

## RESULTS

### Vascular Outgrowth From Synovial Tissue Explants Is Preceded by Leukocyte Egress

With the aim to explore the mechanisms of new vessel formation in the context of inflammation under conditions that closely mimic the *in vivo* situation, a 3D explant model preserving the complexity of tissue architecture and environment was established. Intact synovial tissue fragments from patients with RA and OA containing high numbers of CD45<sup>+</sup> inflammatory cells (Supplemental Figure 1E) were cultured for up to 4 weeks in fibrin matrices in the absence of additional pro-angiogenic growth factors. Dependent on the size of the synovial tissue samples obtained, five to ten tissue fragments from each patient were sandwiched between two fibrin gels in individual wells of the culture plate. We chose fibrin as matrix as it occurs at virtually any site of overt tissue damage and forms a three-dimensional scaffold that provides cell-attachment sites and mechanical support for infiltrating leukocytes as well as invading endothelial and stromal cells. Phase contrast microscopy was a suitable tool to observe the spatial organization of the cellular outgrowth in the initially avascular and translucent fibrin matrix. Noticeable in all samples with considerable inflammation was that in the first days of culture, tissue-derived mononuclear cells migrated into the fibrin matrix (Figure 1A) occasionally forming cell clusters (Figure 1A, insert). Spindle-shaped cells appeared within the first week of cultivation emanating from the explant and radially growing into the 3D fibrin gels infiltrated with the previously invaded mononuclear cells (Figure 1B). Peripheral spindle-shaped cells formed cellular strands that continued to grow outward building cord like structures (Figure 1C). The sprouts developed in different planes within the fibrin gel and were closely associated with mononuclear cell clusters (Figure 1D). After 3 weeks of culture complex vascular structures measuring up to one and two mm of length were detected (Figures 1E,F). There were no apparent differences in vascular outgrowth between RA and inflammatory OA samples. One to three tissue fragments from four RA and three OA patients did not show mononuclear cell egress and the outgrowth was predominantly fibroblastic (Supplemental Figure 2A). In accordance, histological analysis of such cultured tissue fragments revealed only negligible inflammation (data not shown).

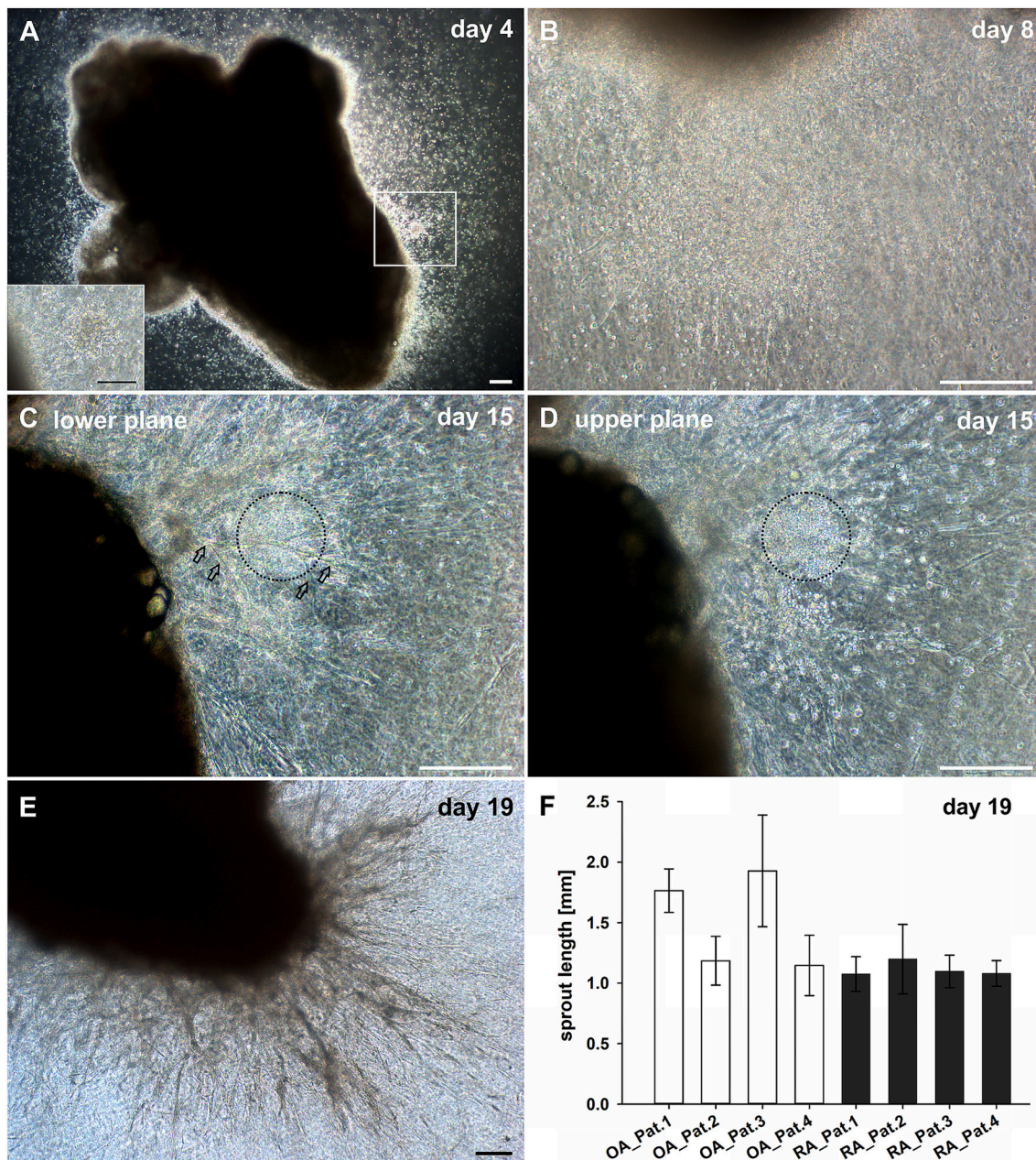
### Neo-Vessels Develop in Close Physical Contact With Inflammatory Cells

The phenotypic characterization of vascular structures in fibrin gels was performed by immunohistochemistry and double labeling on paraffin sections, and immunofluorescence staining and CLSM of intact 3D cultures. Neo-vessels present in fibrin gels originating from the embedded tissues consisted of CD31<sup>+</sup> endothelial cells surrounded by cells expressing Col-IV and a Col-IV positive basement membrane with some CD31<sup>+</sup> cells co-expressing this ECM protein (Figures 2A–C). The newly formed vascular structures showed positive staining for several other endothelial cell markers including CD34, podocalyxin and vWF (Supplemental Figures 1A–C), and were

surrounded by  $\alpha$ -SMA<sup>+</sup> mural cells (Supplemental Figure 3). Among the outgrowth cells were also cells expressing CD68, most of them not showing the typical appearance of monocytes/macrophages indicating a possible non-myeloid origin (Gottfried et al., 2008). Interestingly, the architecture of the embedded synovial tissue samples appeared intact even after 4 weeks of culture in the 3D fibrin matrix (Figures 2D–F and Supplemental Figure 1F). Immunohistochemistry on sections of cultured tissue fragments could be performed successfully and showed that vessel growth—as assessed by CD31 staining—was exclusively directed toward the fibrin matrix (Figure 2D). The spatial organization of CD45<sup>+</sup> inflammatory cells still present in the cultured tissue demonstrated a similar orientation where leukocytes were aligned and closely associated with the intra-synovial vascular sprouts (Figure 2F). Neo-vessels were surrounded by cells/clusters strongly expressing Col-IV (Figure 2E). There was a noticeable decrease of CD45<sup>+</sup> cells in the cultured tissues (Supplemental Figure 1F) when compared to pre-culture control sections of an adjacent tissue fragment (Supplemental Figure 1E). This was not entirely surprising due to the considerable egress of mononuclear cells from the tissues into the fibrin gel during culture which obviously led to a reduction of inflammatory cells within the explant fragments. The close physical association of immune cells with developing neo-vessels was also found in vascular sprouts newly formed *within* the fibrin matrix as demonstrated by triple-immunofluorescence staining of intact 3D cultures for CD45, CD31, and Col-IV. Here, CD45<sup>+</sup> cells were found intimately lodged alongside immature proliferating CD31<sup>+</sup> endothelial cells that co-expressed Col-IV (Figures 2G–J).

### Cell Clusters Formed by Emigrated Mononuclear Cells Are an Origin of Neo-Vessels

Mononuclear cells found in the fibrin gels after egress from synovial explant fragments formed cell clusters external from the tissue within the 3D matrix (Figure 1A, insert). From these clusters vascular sprouts emanated (Figure 3A) resembling developmental vasculogenesis. Considering the phenotypic similarities to previously described vasculogenic clusters in 3D fibrin cultures of unselected bone marrow mononuclear cells (Rüger et al., 2008), we investigated the progenitor marker profile of these clusters using the stem cell markers CD34, c-kit and STRO-1. While clusters and neo-vessels expressed CD34 (Figures 3B,F) and c-kit (Figures 3C,F), the mesenchymal stem cell marker STRO-1 was detected alongside newly forming vessel sprouts in a predominantly dotted staining pattern (Figures 3D,F), consistent with the perivascular STRO-1 deposition found previously in RA and OA synovial tissue (Rüger et al., 2004; Giurea et al., 2006). Similar clusters with apparent vascular outgrowth were also found *within* the embedded tissue samples after 9 days of culture, i.e., shortly before or around the time of the first appearance of vascular tubes in the fibrin matrix. Here, the neo-vessels emanating from Col-IV positive intra-tissue cell clusters expressed CD34,

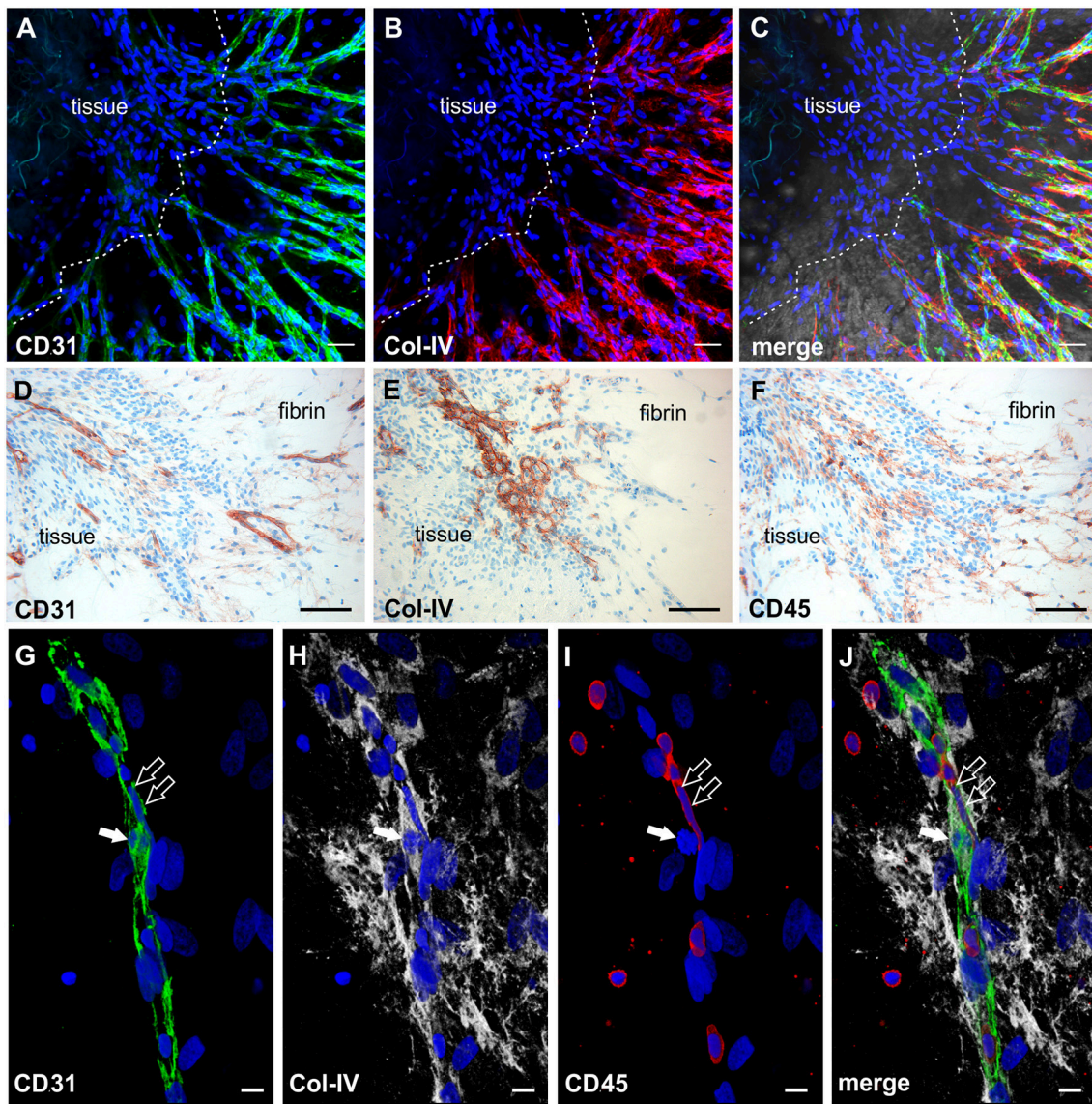


**FIGURE 1** | Culture of synovial tissue in fibrin gels leads to the development of vascular structures preceded by egress of inflammatory cells into the 3D matrix. **(A)** Mononuclear cells present at day four around the embedded explant tissue forming a cluster (insert, represents magnified area of white box). **(B)** Dense infiltration of mononuclear cells invading the fibrin gel accompanied by spindle-shaped cells after 1 week of culture. **(C)** Neo-vessels emanating from the synovial tissue after 2 weeks of culture (open arrows). **(D)** Vascular sprouts develop in close proximity to inflammatory cells (black dashed circles). Images **(C,D)** represent two different planes of the same area within the gel **(C, lower plane; D, upper plane)**. **(E)** A complex vascular network is present within the fibrin gel after 19 days of explant tissue culture. **(A–E)** Sequential phase contrast microscopy images of representative inflammatory OA explant tissue in 3D fibrin gel taken on indicated days. **(F)** Maximum length of vascular sprouts measured in representative explant cultures of four OA and RA patients, respectively. Scale bars, 200  $\mu$ m.

CD31, vWF, c-kit and bcl-2 surrounding caspase 3 expressing apoptotic cells (Supplemental Figure 4). Numerous cells with condensed nuclei were also present in the immature sprouts originating from clusters formed externally from the synovial tissue (Figure 3E).

### Lumen Formation Is Associated With Apoptosis of Central Vascular Cord Cells

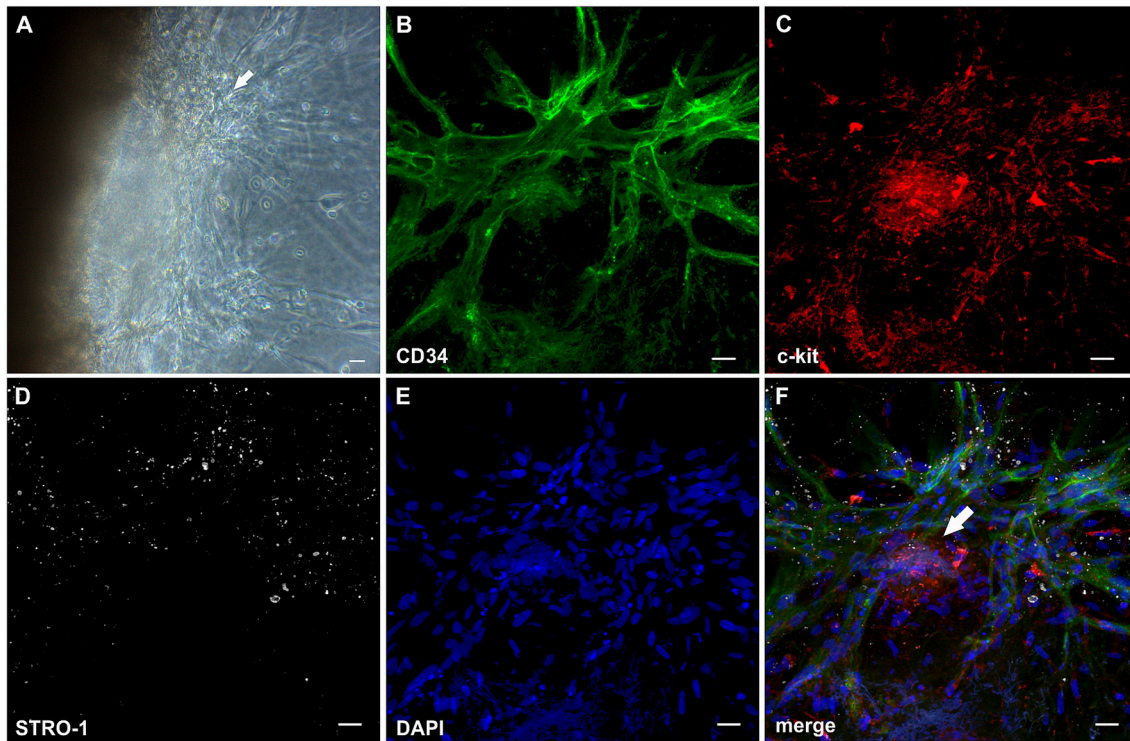
The establishment of a vascular lumen is an important developmental step concerning the functionality of newly formed blood vessels. In our model—a static system in the absence



**FIGURE 2 |** Neo-vessel growth from synovial explants occurs in association with inflammatory cells. Complex vascular network within the fibrin matrix originating from the embedded tissue fragment expressing (A) CD31 (green) and showing (B) Col-IV positive basement membrane and mural cells (red). (C) Merged image of (A,B) demonstrating partial co-expression of CD31 and Col-IV. The tissue itself is unstained due to poor penetration of antibodies. (A–C) CLSM images of an intact fibrin gel on day 19, collapsed 13  $\mu\text{m}$ -z-stack consisting of 9 consecutive images. Scale bars, 50  $\mu\text{m}$ . (D) Cultured tissue fragment showing CD31<sup>+</sup> vessels that grow in direction of the surrounding fibrin matrix and CD31<sup>+</sup> vascular structures within the fibrin gel. (E) Cultured synovial tissue containing numerous round Col-IV positive clusters. (F) Intra-synovial neo-vessels aligned and closely associated with CD45<sup>+</sup> inflammatory cells. (D–F) Immunohistochemistry on consecutive paraffin sections of a day 28 explant culture sample. Scale bars 100  $\mu\text{m}$ . (G–J) Immature vascular sprout developing within the fibrin matrix consisting of (G) CD31<sup>+</sup> endothelial cells that are surrounded by (H) Col-IV<sup>+</sup> stromal cells. (I) Numerous CD45<sup>+</sup> leukocytes are integrated in the growing cell cord and surround the vascular sprout. Note the CD45<sup>–</sup> dividing cell that co-expresses CD31 and Col-IV (arrow) and the elongated nucleus of the CD45<sup>+</sup> cell (open arrows) with (J) partial co-expression of CD31. CLSM images of an intact fibrin gel on day 20, collapsed 15  $\mu\text{m}$ -z-stack consisting of 16 consecutive images. All images are shown with DAPI counterstain in blue. Scale bars, 10  $\mu\text{m}$ .

of a blood circulation—lumens appeared to be formed in association with cell apoptosis. Apoptotic cells were present in the core of vascular cords developing in the fibrin matrix (external from the embedded tissue) (Figures 4A–D) showing expression of CD31 (Supplemental Figure 5 and Supplemental Video 1), and also within the cultured synovial tissue where they

were localized exclusively to the intraluminal space of vessels (Figure 4E). The intraluminal cells with typical condensed nuclei expressed caspase 3 and were surrounded by bcl-2<sup>+</sup> endothelial cells reflecting the interdependent mechanisms of co-ordinated construction and deconstruction during a morphogenetic process (Figure 4F).



**FIGURE 3** | Cell clusters within fibrin gels are an origin of neo-vessels formed by vasculogenesis. **(A)** Phase contrast microscopy image of a representative inflamed synovial tissue sample in 3D fibrin matrix on day 10 of culture, showing a cell cluster (arrow) external from the embedded tissue fragment in the fibrin gel with outgrowing elongated structures. The image was taken before IF staining. **(B–F)** CLSM images (collapsed 32  $\mu\text{m}$ -z-stack consisting of 20 consecutive images) showing the same cluster (arrow in **F**) depicted in **(A)**. Both cluster and neo-vessels co-express **(B)** CD34 and **(C)** c-kit. **(D)** MSC marker STRO-1. **(E)** DAPI stain. **(F)** Merge. Scale bars, 20  $\mu\text{m}$ .

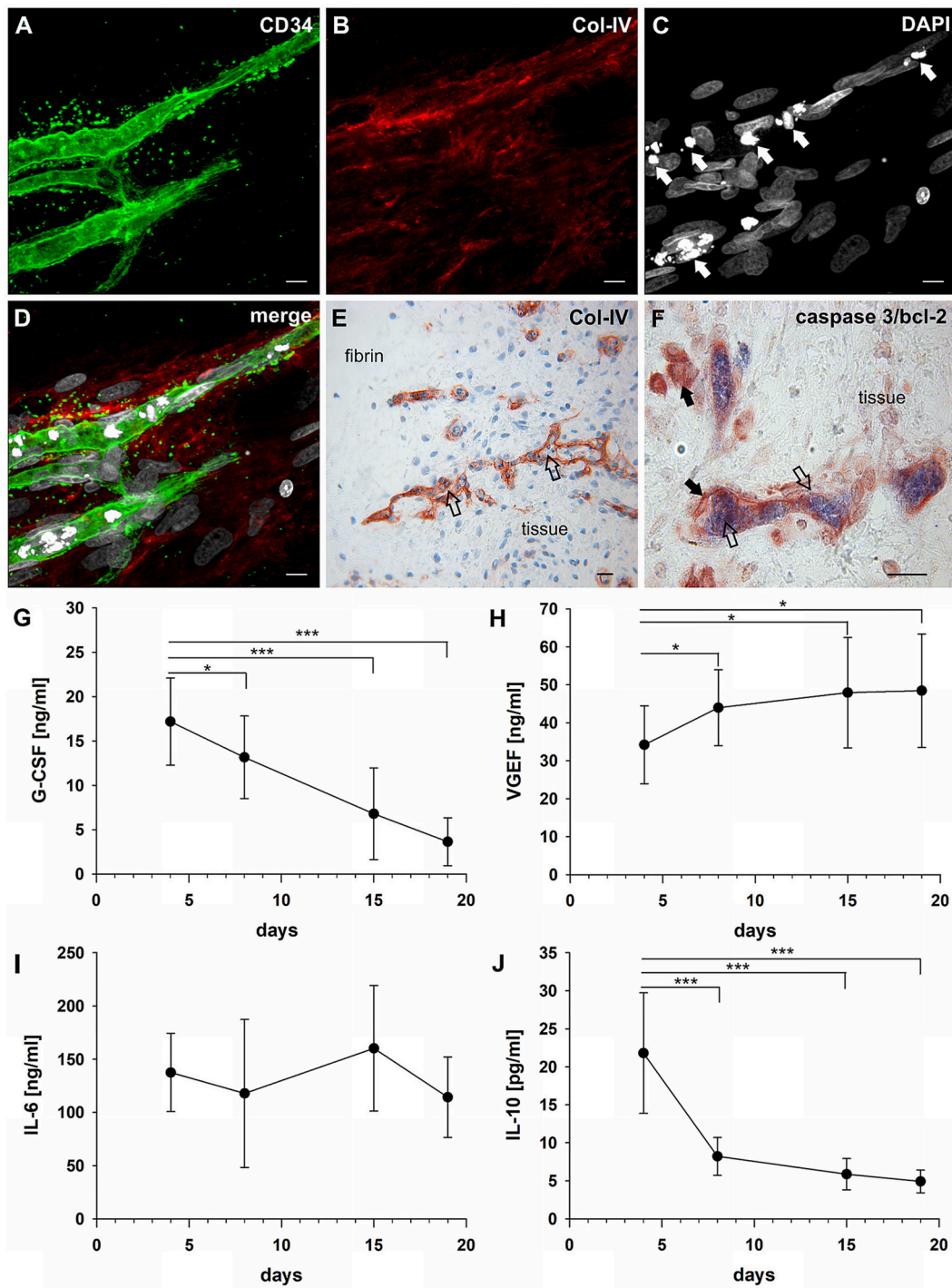
## G-CSF, VEGF, and IL-6 Are Secreted During Inflammatory Neo-Vessel Development

In order to investigate the paracrine signature during neo-vessel formation by synovial explant tissues we analyzed the time-dependent release of relevant cytokines/growth factors typically involved in inflammation and neovascularization. The secretion of G-CSF, VEGF, IL-6, and IL-10 were determined in cell-free supernatants of 3D-cultured synovial explants from three individual osteoarthritis patients (**Figures 4G–J**). G-CSF levels were extremely high on day four of culture (17 ng/ml  $\pm$  5) and gradually declined over time, but were still significantly above normal serum levels on day 19 (4 ng/ml  $\pm$  3) (**Figure 4G**). The time-dependent secretion of VEGF showed an inverse correlation with the corresponding G-CSF release. High VEGF values on day four (34 ng/ml  $\pm$  10) gradually increased even further during culture (day 19: 48 ng/ml  $\pm$  15) (**Figure 4H**). The increase of VEGF coincided with the progressive neo-vessel growth in the 3D gels. IL-6 secretion of inflamed synovial explant tissues was high during the whole culture period with levels above 100 ng/ml, but without statistically significant change over time (**Figure 4I**). IL-10 levels were low on day four (22 pg/ml  $\pm$  8), sharply declined further during the first week of culture and remained low (**Figure 4J**). When we analyzed the cytokine secretion in one of the tissue fragments showing fibroblastic outgrowth,

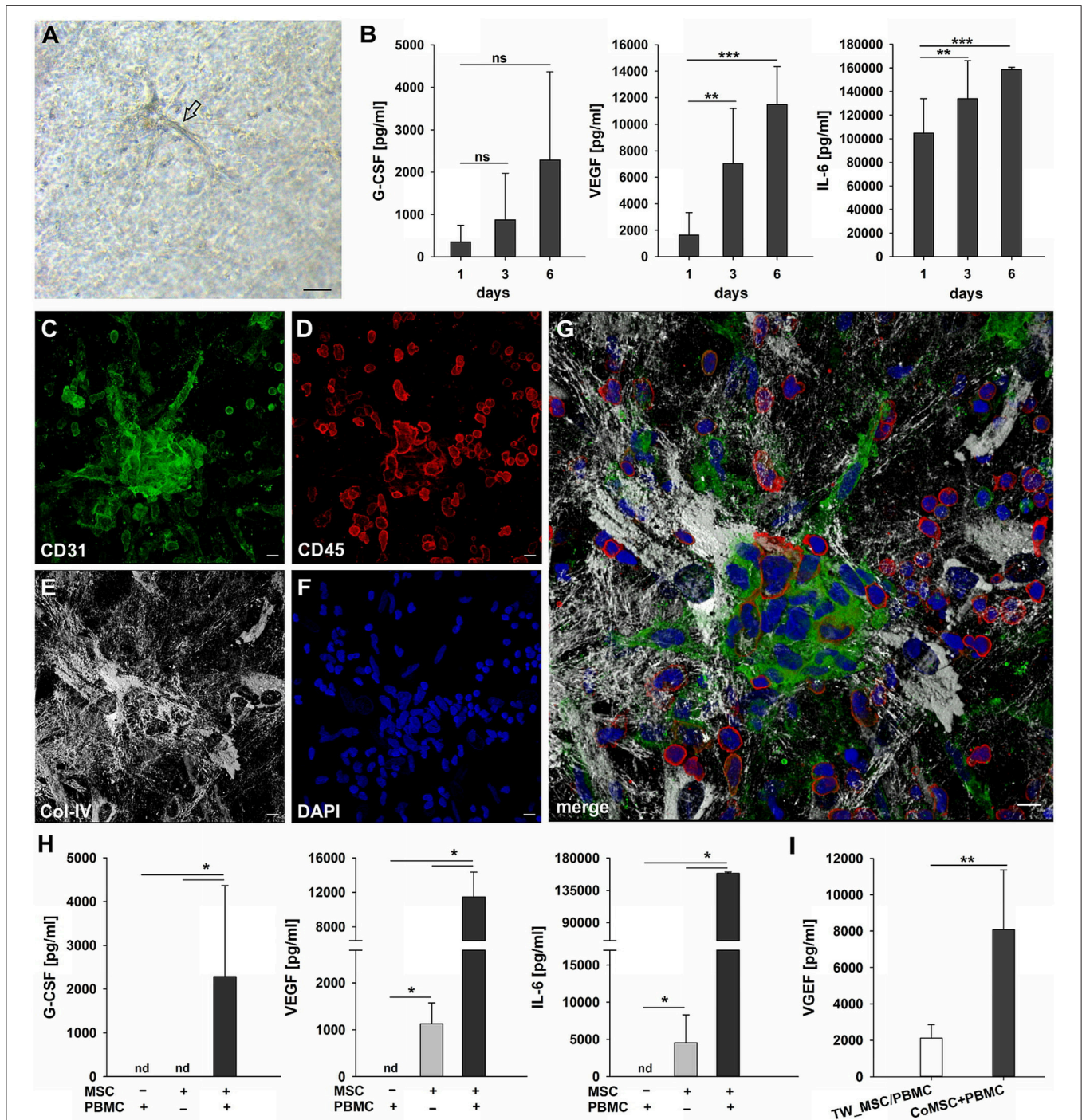
considerably lower G-CSF, VEGF and IL-6 levels were measured compared to inflammatory OA samples (Supplemental Figures 2B–D).

## Co-cultures of MSC and PBMC Form Cell Clusters and Secrete VEGF, G-CSF, and IL-6

MSC as progenitor cells of the connective tissue are found in almost all organs throughout the body residing mostly close to blood vessels (Crisan et al., 2008), where they play an essential role in regenerative processes through co-operation with inflammatory cells. To simulate the cross-talk between MSC and immune cells in the perivascular space and its contribution to vascular remodeling in a pro-inflammatory environment we co-cultured bone marrow- and bone-derived MSC and PBMC in fibrin matrices for up to 14 days. Co-cultures were performed using  $\alpha$ -MEM medium containing 10% FBS, but without additional growth factors. In a self-organization process, MSC co-cultured with PBMC formed clusters in the fibrin matrix from which cellular strands emanated (**Figure 5A**). The formation of cell clusters and their sprouting was detected from day four onwards and could be observed throughout the culture

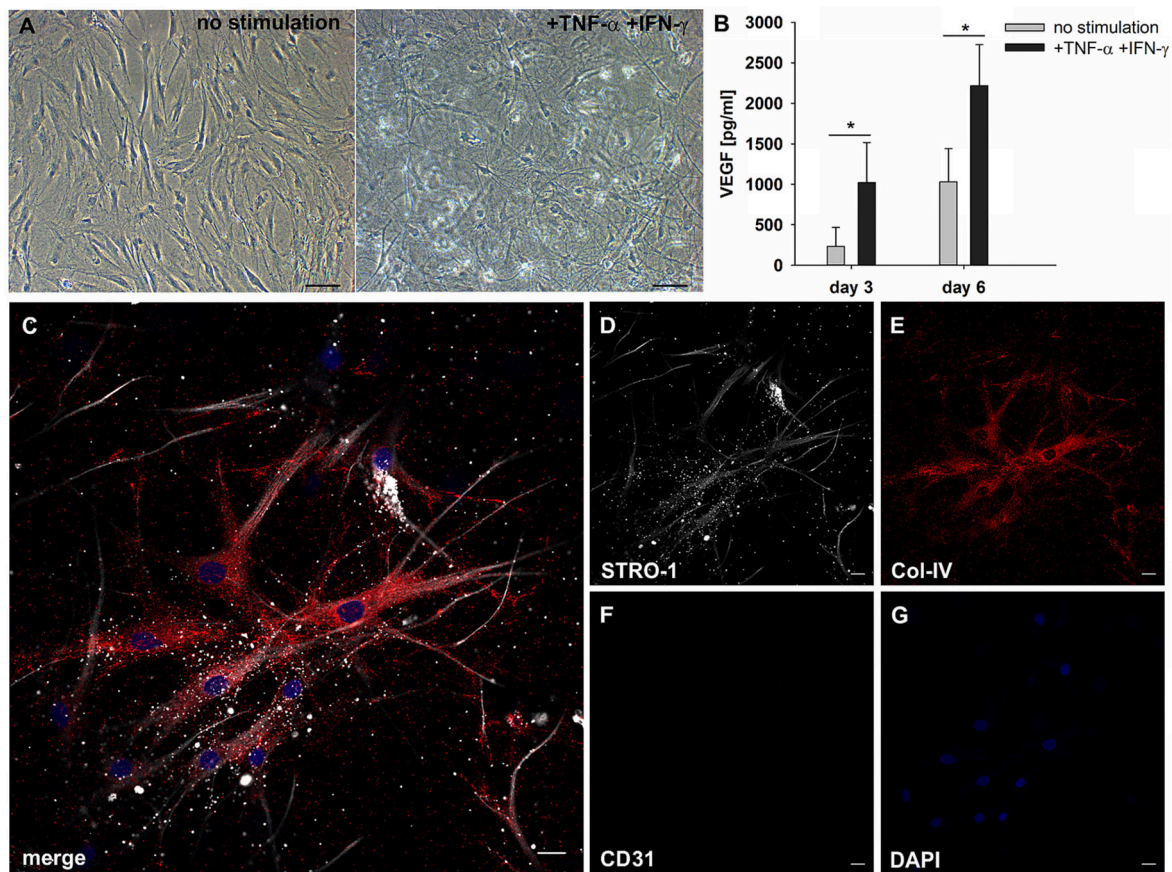


**FIGURE 4 |** Vascular lumen formation is associated with apoptosis. Immature vascular sprout within the fibrin matrix expressing (A) CD34 and surrounded by (B) Col-IV<sup>+</sup> stromal/mural cells. (C) DAPI stain showing that the core of the developing vascular sprout contains several cells with condensed nuclei (arrows). (D) Merge. (A–D) CLSM images of intact fibrin gel culture of OA synovial tissue on day 21, collapsed 13 μm-z-stack consisting of 17 consecutive images. Scale bars, 10 μm. (E) Neo-vessels of cultured synovial tissue surrounded by Col-IV positive basement membrane and mural cells showing intraluminal cells with condensed nuclei (apoptotic cells) *within* and *outside* of the embedded tissue fragment (open arrows). Note the regular nuclear morphology of the extravascular cells within the tissue after extended explant culture. (F) Caspase-3<sup>+</sup> intraluminal apoptotic cells (blue, open arrows) *within* the synovial tissue surrounded by bcl-2<sup>+</sup> endothelial cells (arrows). (E) Immunohistochemistry and (F) peroxidase/alkaline phosphatase double-labeling on paraffin sections of RA explant tissue cultured for 28 days. Scale bars, 20 μm. Kinetics of cytokine secretion during inflammatory neo-vessel development. Determination of (G) G-CSF, (H) VEGF, (I) IL-6, and (J) IL-10 using Bio-Plex 200 system in cell-free explant culture supernatants from three patients with inflammatory OA (n = 9) taken at days 4, 8, 15, and 19, respectively. Experiments were performed with each sample in duplicate, and data are expressed as mean values ± SD. \*p ≤ 0.05, \*\*\*p ≤ 0.001.



**FIGURE 5 |** Cluster formation, paracrine signaling and emergence of endothelial cells in 3D MSC-PBMC co-culture. **(A)** Phase contrast microscopy image of representative 3D fibrin co-culture of MSC with PBMC on day 6, demonstrating vascular sprouts (arrow). Scale bar, 50  $\mu$ m. **(B)** Determination of G-CSF, VEGF and IL-6 by ELISA in cell-free supernatants of 3D MSC-PBMC co-cultures ( $n = 6$ ) after 24 h, on day 3 and on day 6, respectively. The data are expressed as mean values  $\pm$  SD.  $^{**}p \leq 0.01$ .  $^{***}p \leq 0.001$ . ns not significant. **(C–G)** Representative CLSM images of MSC-PBMC co-culture in 3D fibrin matrix on day 6 showing organized structures consisting of **(C)** CD31<sup>+</sup> cell clusters with **(D)** partial co-expression of CD45. Note the numerous CD45<sup>+</sup> round leukocytes surrounding the cell cluster. CD31<sup>+</sup>/CD45<sup>-</sup> outgrowth cells with EC morphology emerge from the cluster. The cluster is embedded in a meshwork of **(E)** Col-IV positive stromal cells and matrix. **(G)** Merge. **(F)** DAPI stain. Collapsed 16  $\mu$ m z-stack consisting of 33 consecutive images. Scale bars, 10  $\mu$ m. **(H)** Determination of G-CSF, VEGF and IL-6 by ELISA in cell-free supernatants of 3D PBMC mono-cultures ( $n = 4$ ), MSC mono-cultures ( $n = 4$ ) and corresponding MSC-PBMC co-cultures on day 6. **(I)** VEGF levels in cell-free supernatants of 3D co-cultures where MSC were physically separated from PBMC by a transwell insert with 0.4  $\mu$ m pore size and corresponding 3D MSC-PBMC co-cultures on day 6 ( $n = 6$ ). The data are expressed as mean values  $\pm$  SD. nd = not detected.  $^{*}p \leq 0.05$ .  $^{**}p \leq 0.01$ .





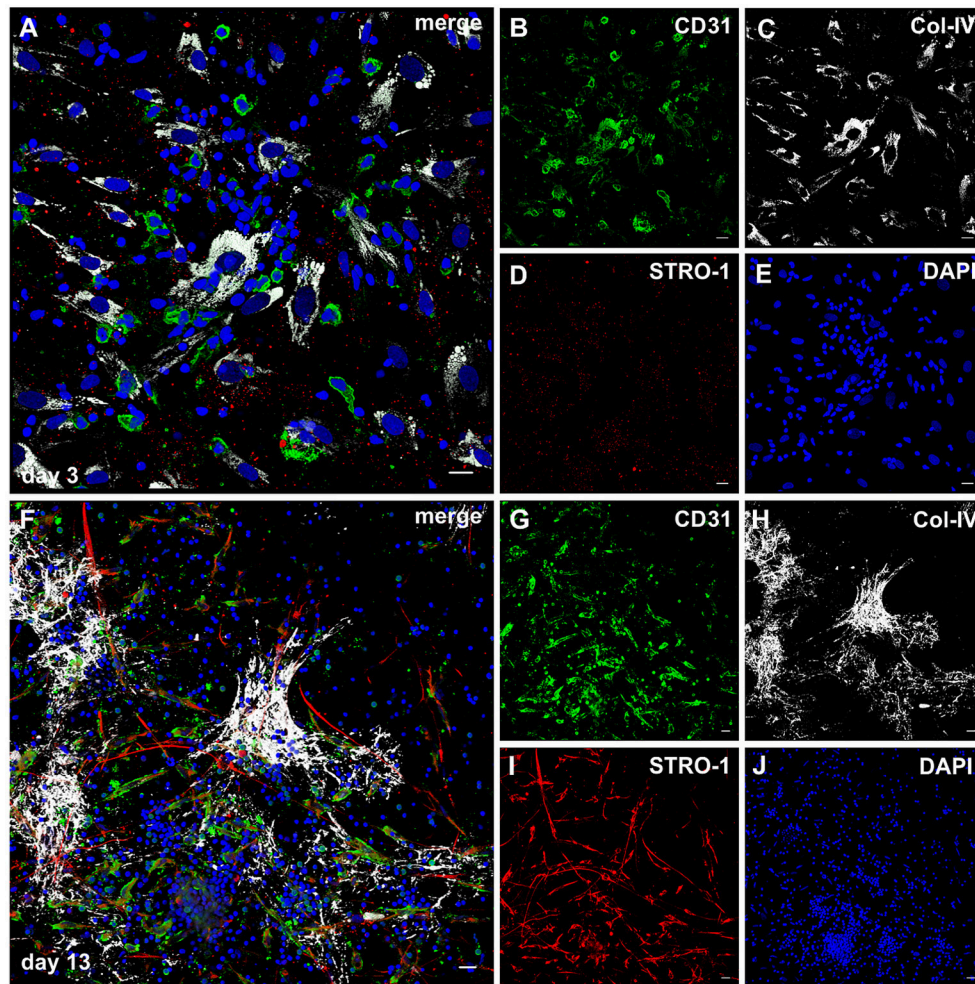
**FIGURE 6** | MSC respond to inflammatory signals and develop filopodia. **(A)** Representative phase contrast images of bone marrow-derived MSC cultured in 3D fibrin matrices for 6 days. Unstimulated MSC with mainly spindle-shaped morphology, and TNF $\alpha$ /IFN $\gamma$ -stimulated MSC showing multiple long cell protrusions resembling filopodia. Scale bars, 100  $\mu$ m. **(B)** VEGF secretion by unstimulated and stimulated MSC on day 3 and day 6 \* $p \leq 0.05$ . **(C–G)** Representative CLSM images of MSC in 3D fibrin matrix with the addition of TNF $\alpha$  and IFN $\gamma$  showing **(D)** STRO-1 expression in filopodia. **(E)** MSC produce Col-IV and **(F)** do not express CD31. **(C)** Merge. **(G)** DAPI stain. Scale bars, 20  $\mu$ m.

period (Figure 5, Supplemental Figure 6). The elongated cells originating from the clusters displayed an endothelial phenotype expressing CD31 (Figure 5C) and lacking CD45 staining (Figure 5D), and were surrounded by Col-IV<sup>+</sup> cells (Figure 5E). No fibrinolysis was evident in co-cultures. Cluster cells expressed CD31, showed close contact with CD45<sup>+</sup> leukocytes partly co-expressing CD31 (Figure 5G) and were wrapped in a network of stromal cells producing a collagen IV<sup>+</sup> vault-like scaffold (Figures 5E,G, Supplemental Figures 6C,E, Supplemental Videos 2, 3). MSC did not form clusters in fibrin gels in the absence of PBMC, and no vascular-like structures were detected (data not shown). Based on the first appearance of cell clusters and sprouting on day four, we investigated the production of VEGF, G-CSF and IL-6 by co-cultures within the first week, i.e., after 24 h, on day 3 and on day 6. Secretion of these three cytokines progressively increased over the culture period (Figure 5B), and large amounts of these cytokines were found in the supernatants of co-cultured cells on day 6 (G-CSF, 2285 pg/ml  $\pm$  2084; VEGF, 11485 pg/ml  $\pm$  2865; IL-6, 158713 pg/ml  $\pm$  1921). No cytokine secretion was detected in PBMC cultures without stromal support (Figure 5H), and the gels demonstrated extensive

fibrinolysis (data not shown). In the absence of PBMC, MSC did not release G-CSF, whereas detectable levels of VEGF and IL-6 were measured in the supernatants of MSC mono-cultures, albeit significantly lower compared to MSC co-cultured with PBMC (MSC only: VEGF, 1130 pg/ml  $\pm$  443; IL-6, 4528 pg/ml  $\pm$  3769). VEGF secretion was significantly lower in co-cultures where MSC-PBMC contact was prevented by a transwell insert (0.4  $\mu$ m pore size) (TW-MSC/PBMC: 2118 pg/ml  $\pm$  741; coMSC/PBMC: 8075 pg/ml  $\pm$  3290) (Figure 5I). Contact-inhibition also decreased G-CSF secretion in co-cultures, however, the difference did not reach significance level (Supplemental Figure 7).

### MSC Respond to Paracrine Inflammatory Signals in 3D Fibrin Matrices by Development of Filopodia-Like Cell Protrusions and Increased VEGF Production

MSC are responsive to pro-inflammatory cytokines, and cytokines produced during an immune response, e.g., TNF $\alpha$



**FIGURE 7 |** STRO-1 expression during MSC-PBMC co-culture in 3D fibrin gels. **(A)** MSC-PBMC co-culture on day 3 showing close physical contact of mononuclear cells with Col-IV<sup>+</sup> STRO-1<sup>+</sup> MSC. Some mononuclear cells are CD31<sup>+</sup>. **(C)** MSC express Col-IV. **(D)** STRO-1 in MSC shows a granular staining pattern. **(E)** DAPI stain. **(F)** 3D MSC-PBMC co-culture on day 13 demonstrating elongated cells that co-express **(G)** CD31 and **(I)** STRO-1. CD31<sup>+</sup>STRO-1<sup>+</sup> cells are associated with **(H)** Col-IV positive cell clusters. Note that round CD31<sup>+</sup> cells are STRO-1<sup>-</sup>. STRO-1<sup>+</sup>CD31<sup>-</sup> MSC show long cell protrusions. **(J)** DAPI stain. **(A–J)** Representative CLSM images of MSC-PBMC co-cultures within 3D fibrin matrices. Scale bars, 20  $\mu$ m.

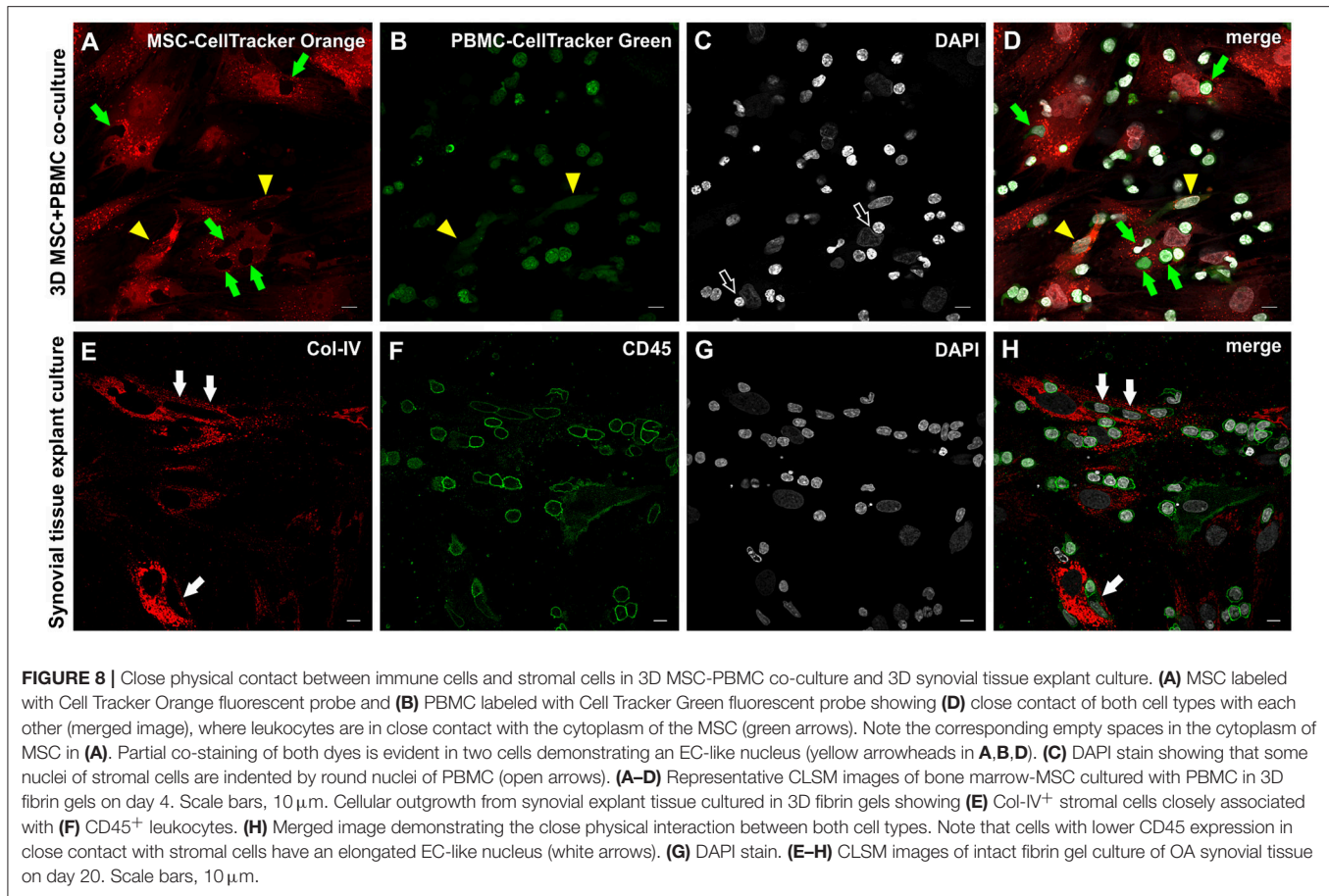
and IFN $\gamma$ , affect the secretion of pro-angiogenic mediators by MSC. MSC were embedded in 3D fibrin matrices, stimulated with TNF $\alpha$  and IFN $\gamma$  and the release of VEGF and G-CSF was measured in cell-free supernatants by ELISA. Without stimulation MSC released 231 pg/ml  $\pm$  234 VEGF on day 3, and the levels increased to 1,021 pg/ml  $\pm$  496 after 6 days of culture. VEGF secretion was significantly upregulated by cytokine stimulation (day 3: 1,029 pg/ml  $\pm$  413; day 6: 2,216 pg/ml  $\pm$  510) (**Figure 6B**). No G-CSF was detected in the supernatants of either unstimulated or cytokine-stimulated MSC cultures (data not shown). Stimulated MSC did not generate cell clusters, however, the pro-inflammatory microenvironment led to dramatic morphological changes of MSC characterized by the formation of numerous long cell protrusions resembling filopodia (**Figures 6A,C**). STRO-1 was localized to filopodia showing

a predominantly granular staining pattern (**Figure 6D**). MSC produced collagen IV (**Figure 6E**), and did not express CD31 (**Figure 6F**).

### Cellular Sprouts Emerging From Co-culture-Derived Clusters Display a Mixed Endothelial/Mesenchymal Phenotype

The notion that MSC can differentiate into endothelial cells is still under debate (Oswald et al., 2004; Corotchi et al., 2013). STRO-1 is an accepted and widely used mesenchymal stem cells marker, and has been described more recently as endothelial antigen (Ning et al., 2011).

Considering the fact that the pro-angiogenic milieu in co-cultures is dependent on MSC-PBMC contact, and given the plasticity of MSC in response to cues from the



microenvironment, we investigated the expression of STRO-1 in the fibrin based 3D co-cultures of MSC and PBMC. When structurally organized cell clusters surrounded by a Col-IV scaffold had formed (**Figures 7F–J**), elongated cells with EC morphology and mixed endothelial/mesenchymal phenotype expressing CD31 and STRO-1 emanated from these clusters (**Figures 7G, I**, Supplemental Video 4). These hybrid-type cells were absent at day three (**Figures 7A–E**). CD31<sup>+</sup> cells with round morphology did not express STRO-1. In control 3D mono-cultures, a minority of MSC expressed STRO-1; in PBMC mono-cultures, STRO-1 was not detected at all (data not shown).

## MSC and Leukocytes Establish Close Cell-Cell Contacts in 3D Fibrin Matrices

In order to examine the MSC interaction/communication with immune cells in this pro-angiogenic environment, we performed cell tracking experiments. PBMC were labeled with CellTracker Green dye, and co-cultured in 3D fibrin gels for 4–7 days together with CellTracker Orange dye-labeled MSC. PBMC (green, **Figure 8B**) were detected in intimate contact with MSC (red, **Figure 8D**) clearly demonstrated by the empty spaces in labeled MSC (**Figure 8A**) and the partly deformed nuclei of the MSC (**Figure 8C**) due to the close contact with immune cells. In few cells with elongated nuclei both dyes appeared to be present

(**Figure 8D**, yellow arrowheads). In both, the explant and the co-culture model, MSC-PBMC contact coincided with weak CD45 expression (**Figures 8E–H** and Supplemental Figures 8A–E). Triple immunofluorescence staining (CD31/CD45/Col-IV) and CLSM of 3D co-cultures revealed the close spatial relationship between cells of the stromal and hematopoietic lineages (Supplemental Figures 8F–J). Cells co-expressing CD31/CD45 showed variations in the expression level of either marker with some cells exclusively expressing CD31. CD31 expression in the absence of CD45 was associated with nuclear elongation possibly indicating differentiation toward the endothelial lineage.

## DISCUSSION

The regeneration of damaged tissues is usually initiated by an inflammatory response that eventually is down-regulated and associated with physiological neovascularization in order to re-establish normal tissue function. If this process is not properly organized, however, it results in a persistent cycle of inflammation and repetitive tissue damage with concomitant excessive neo-vessel formation as it is found in various chronic inflammatory diseases. The cross-talk between both processes—inflammation and neovascularization—occurs in a specific perivascular microenvironment, where key molecular

players of the coagulation cascade like fibrinogen/fibrin combined with a complex network of chemical signals and cell interactions initiate and sustain the process (Davalos and Akassoglou, 2012). In this study we have established a contextual *in vitro* model for neovascularization in an inflammatory environment by embedding freshly excised inflamed synovial tissue fragments in 3D fibrin matrices using human fibrinogen at physiological concentrations for the fabrication of malleable translucent scaffolds. This enabled the observation of vascular morphogenesis and cellular interactions, and involved paracrine signaling in a complex inflammatory microenvironment close to the *in vivo* setting (albeit lacking perfusion of the preexisting vessels). The contribution of perivascular niche cell interactions to neo-vessel formation during an inflammatory process was simulated in a complexity-reduced system by co-culturing MSC with freshly isolated PBMC in 3D fibrin matrices. This initially EC-free co-culture set-up provided evidence that *de novo* vessel development can be promoted by the formation of mixed cell clusters with vasculogenic potential and concomitant secretion of pro-angiogenic cytokines.

The 3D explant culture model represents a straightforward method for closely recapitulating complex *in vivo* regenerative processes. The embedded tissue samples remained viable even after extended culture in fibrin scaffolds demonstrating that the diffusion of nutrients was sufficient, not only to support their survival, but also to promote intra-tissue remodeling in this 3D microenvironment. Originating from the embedded synovial tissue, inflammatory mononuclear cells and spindle-shaped cells migrated into the initially acellular 3D fibrin matrices to form a radially emanating network of increasing density leading to the development of complex organized neo-vessels within 3–4 weeks. The core of the newly formed vascular structures consisted of endothelial cells as indicated by expression of the common endothelial markers CD31, CD34, vWF, and podocalyxin, and was surrounded by a Col-IV<sup>+</sup> basement membrane and by cells also expressing Col-IV. Neo-vessels emerged directly from the tissue fragments developing from intra-synovial cell clusters expressing Col-IV and growing outward into the fibrin gels, and in addition, were created via cell clusters formed by emigrated mononuclear cells found in the fibrin matrix surrounding the explant tissue. CD45<sup>+</sup> cells were consistently seen integrated within and around developing vascular sprouts. Similar clusters with vasculogenic potential were formed when PBMC were cultured in fibrin gels together with MSC. Cells with endothelial morphology and phenotype (CD31<sup>+</sup>CD45<sup>-</sup>) emerged from CD31<sup>+</sup> cell clusters showing close physical contact with CD45<sup>+</sup> leukocytes and a surrounding Col-IV<sup>+</sup> scaffold demonstrating that the co-operation of cells of the hematopoietic and mesenchymal lineages initiated a self-organization process that included cellular differentiation. Interestingly, CD31<sup>+</sup>CD45<sup>-</sup> cells showed elongated nuclei even in the absence of fluid shear stress. Nuclear elongation might have been the result of culturing cells in “mechanically stressed” fibrin gels that resemble granulation tissue. PBMC cultures without stromal cell support did not produce clusters with vasculogenic potential indicating that the presence and interactions of both MSC and PBMC were required for this response. Evidence for

vascular development through mesenchymal cell-hematopoietic cell co-operation was provided by us in a previous study where we have shown that bone marrow-derived mononuclear cells embedded in fibrin matrices can form vascular structures through a dynamic self-organization process originating from cell clusters expressing CD34 and c-kit (Rüger et al., 2008). In the current study, a similar progenitor marker profile was found in intra-synovial cell clusters as well as in synovial tissue-derived mononuclear cell clusters external from the cultured tissue fragments, where CD34<sup>+</sup> vascular sprouts emanated in close association with c-kit<sup>+</sup> cells. C-kit is expressed by a subpopulation of MSC in the highly vascularized adipose tissue showing increased proliferative activity and self-renewal capacity (Blazquez-Martinez et al., 2014), and *in vivo* vascular niches of synovial tissues from patients with RA and OA contain STRO-1 positive MSC found in clusters together with EPC as demonstrated by our group previously (Rüger et al., 2004). It is possible that EPC located in areas of new vessel formation within the synovial tissue migrated into the fibrin matrix or alternatively were generated *in situ* and either assisted in new capillary sprouting by angiogenesis, or in co-operation with MSC initiated *de novo* formation of vessel structures by vasculogenesis. Supporting this possibility are recent studies showing that EPC can form vessel-like structures in fibrin matrices when co-cultured with adipose-derived MSC (Holnthoner et al., 2015), and that fibrin is a suitable matrix for the growth, differentiation and angiogenesis capability of EPC enhancing cell retention and paracrine cytokine release relevant for neovascularization (Barsotti et al., 2011).

A fundamental step in vascular morphogenesis is the stabilization of newly formed vascular structures through pericyte recruitment and basement membrane matrix deposition including collagen IV production (Stratman et al., 2009). In our study, neo-vessels formed during explant culture produced a Col-IV<sup>+</sup> basement membrane and were surrounded by cells expressing Col-IV. Similarly, in co-cultures of MSC with PBMC, CD31<sup>+</sup> endothelial cells originating from cell clusters were closely associated with Col-IV<sup>+</sup> stromal cells and a Col-IV<sup>+</sup> extracellular matrix scaffold. Our finding that MSC produce large amounts of Col-IV was particularly interesting as vascular basement membrane assembly (including the deposition of Col-IV) coincides with pericyte recruitment (Stratman et al., 2009), and confirms the association of MSC with a subset of pericytes (Crisan et al., 2008). The development of a vascular lumen is essential for the formation of a functional vasculature. In the presented model of inflammatory neovascularization, caspase-3<sup>+</sup> apoptotic cells were exclusively found in the core of neo-vessels that developed within and outside of the embedded synovial explant tissues suggesting that in this static setting, lacking blood circulation, lumen formation occurred through cavitation. At present it is generally thought that cord- or cell-hollowing—the formation of a lumen by creation of fluid-filled spaces between cells or within single cells (Sigurbjörnsdóttir et al., 2014)—are the major mechanisms of vascular lumen formation. However, it has also been shown that during rat glomerular development capillary lumen formation relies on apoptosis (Fierlbeck et al., 2003) and recent data indicate that apoptosis is also involved in

lumen formation during placental vasculogenesis (Tertemiz et al., 2005). It is possible that both mechanisms contribute to lumen formation in a context-dependent fashion.

MSC actively interact and co-operate with immune cells and have the ability to adopt different phenotypes in response to sensing an inflammatory environment thereby regulating tissue homeostasis (Bernardo and Fibbe, 2013). Here we show that MSC in a 3D fibrin environment respond to paracrine inflammatory signals such as TNF $\alpha$  and IFN $\gamma$  with increased development of STRO-1<sup>+</sup> filopodial protrusions, structures reported to act as antennae for cells to probe their environment (Galbraith et al., 2007), and involved in numerous cellular processes, including wound healing, adhesion to the extracellular matrix and guidance toward chemoattractants (Mattila and Lappalainen, 2008). MSC filopodia may have promoted physical contact and direct cell-cell communication between stromal cells and immune cells in MSC-PBMC co-cultures thereby also influencing the cell fate of emerging cellular entities. STRO-1 has been classically defined as mesenchymal stem cells marker, but more recently has also been found in endothelial cells (Ning et al., 2011). In our co-culture model STRO-1 positivity was associated with both stromal- and endothelial cells. While MSC-PBMC co-cultures generated cells of endothelial phenotype co-expressing CD31 and STRO-1, MSC under paracrine inflammatory stimulation but without immune cell contact exclusively expressed the mesenchymal marker STRO-1 and were CD31 negative. These results suggest that MSC-PBMC contact was necessary for the generation of cells of this mixed phenotype indicating that STRO-1 expression might be associated with vascular development in the presence of immune cells, e.g., during inflammatory processes.

The paracrine signature of the inflammatory niche environment is dependent on and influenced by the interaction and co-operation of niche cells and in turn affects cell fate decisions and structural remodeling. The results of the co-culture experiments in fibrin-based scaffolds indicate that the communication of inflammatory cells with MSC induce a dynamic increase of pro-angiogenic factors concurrent with the generation of cells participating in neovascularization. Cluster formation and cellular re-structuring toward neo-vessel growth was associated with increased release of VEGF, IL-6 and G-CSF when MSC were co-cultured with PBMC in the 3D environment. Direct and indirect MSC-PBMC interactions seemed to be essential for their secretion, as none of the cytokines were produced at detectable levels by PBMC cultured without stromal support. MSC secreted considerable (but lower) levels of VEGF in the absence of PBMC, and VEGF production in fibrin gels was augmented by pro-inflammatory cytokines supporting previous reports (Kagiyada et al., 2008; Yang et al., 2017). When MSC were co-cultured with PBMC, VEGF secretion increased 11-fold compared to control MSC mono-cultures, and this increase was cell-contact dependent, as VEGF release was significantly decreased in transwell co-cultures dropping to levels comparable to those produced by MSC stimulated by TNF $\alpha$  and IFN $\gamma$ . The dramatic increase of VEGF coincided with the formation of vasculogenic cell clusters with emerging EC-like cells in the fibrin matrices suggesting that both paracrine and physical stromal cell-immune cell co-operation mechanisms were responsible for cells

of endothelial phenotype to arise. The cell-tracking experiments of this study provide evidence for such close physical contact. Paracrine signals from MSC, e.g., VEGF, might have promoted the *in situ* growth of EPC in MSC-PBMC co-cultures leading to further increase of VEGF levels and subsequent development of endothelial cells. Interestingly, *early EPC*—a hematopoietic subset of EPC secreting angiogenic cytokines including VEGF and showing *in vivo* vasculogenic capacity—can be obtained by short-term culture of PBMC on fibronectin-coated plates in endothelial cell culture medium containing VEGF (Hur et al., 2004). These findings corroborate our line of thought that paracrine signals from MSC (i.e., VEGF) may have promoted *in situ* EPC differentiation in the fibrin matrix, an environment that provides optimal support for the growth and differentiation of peripheral blood EPC (Barsotti et al., 2011). While VEGF and IL-6 were secreted by MSC even in the absence of PBMC, albeit at levels much lower than in co-culture, G-CSF was detected only in the presence of both MSC and PBMC, and the G-CSF release was largely dependent on direct cell-cell communication, as contact-prevention between MSC and PBMC led to greatly reduced secretion levels. Growth factor secretion by explant cultures demonstrated striking similarities to the cytokine pattern released by MSC-PBMC co-cultures (i.e., increased secretion of G-CSF, VEGF, and IL-6) suggesting related cellular interactions in both culture settings. Our data on the cytokine profile of cultured synovial explant tissues are in line with published clinical data showing that IL-6 is elevated in the synovial fluid and serum of patients with RA and OA (Houssiau et al., 1988; Pearson et al., 2017), and are consistent with previous reports demonstrating that both IL-6 and G-CSF can stimulate new vessel growth by promoting the production of VEGF (Cohen et al., 1996; Ohki et al., 2005). Furthermore, the paracrine signals produced by cultured synovial tissues correspond to prior work where high G-CSF concentrations were found in the serum and synovial fluid of patients with RA and OA (Nakamura et al., 2000; Mabey et al., 2014), and where raised VEGF levels in RA and OA patients correlated with disease severity (Ballara et al., 2001; Mabey et al., 2014), demonstrating that the synovial tissue fragments can long-term retain their *in vivo* paracrine signature in the 3D culture setting. Recent data suggest that the cross-talk between MSC and immune cells could be the basis of a vicious circle driving RA chronicity and progression (De Bari, 2015). High G-CSF levels in RA could be a result from such a cross-talk, and this possibility is supported by our co-culture data showing that MSC interaction with PBMC in fibrin matrices leads to enhanced G-CSF secretion with concomitant generation cells participating in neo-vessel formation. We therefore believe that the co-culture model approximates important aspects of the *in vivo* co-operative mechanisms between stromal cells and immune cells in the context of a pro-inflammatory environment. However, due to ethical reasons we were not able to perform control experiments using healthy synovial tissue posing an obvious limitation in this study. Even so, vascular outgrowth was dependent on the presence of inflammatory cells. Tissue pieces lacking inflammatory cells and thus leukocyte egress did not generate vascular outgrowth. Thus, such tissue pieces might be considered a surrogate control supporting our findings.

Therefore, despite this limitation, we believe that the *in vitro* 3D culture system and the two presented models add important aspects to complex *in vivo* regenerative processes at the tissue level and may contribute to better understanding of complex cell-cell interactions underlying chronic inflammatory diseases.

## CONCLUDING REMARKS

In conclusion, our study has shown that the 3D fibrin matrix system represents a highly suitable biologically relevant environment for the long-term culture of tissue fragments and provides a useful model to investigate context-dependent new vessel formation during pathological inflammatory processes. The *in vitro* explant tissue culture model offers a disease-related platform to integrate complex cell-cell and cell-matrix interactions with associated paracrine signaling patterns in a setting that mimics the *in vivo* situation. Therefore, it might provide a suitable tool to decode microenvironmental cues that promote chronic inflammation and disease in order to find new treatment options. The 3D co-culture model is equally useful for unveiling novel mechanisms of cellular co-operation during regenerative processes and chronic inflammatory diseases emphasizing the relevance of stromal cell-immune cell interactions thereby adding new aspects to the principles underlying self-organization. It can help to

elucidate distinct cellular behavior patterns in a physiological 3D environment that—dependent on the specific combination of environmental cues—physically and chemically influences cell migration, differentiation and survival.

## AUTHOR CONTRIBUTIONS

BMR designed the work, generated, analyzed and interpreted data and wrote the paper. TB generated, analyzed and interpreted data and revised the work for intellectual content. AG and BK supported the study by providing synovial tissue; MBF and JMB revised the work for intellectual content.

## ACKNOWLEDGMENTS

We thank Marion Gröger and Sabine Rauscher from the Imaging Facility of the Medical University Vienna for their help with CLSM.

## SUPPLEMENTARY MATERIAL

The Supplementary Material for this article can be found online at: <https://www.frontiersin.org/articles/10.3389/fphys.2018.00679/full#supplementary-material>

## REFERENCES

- Aplin, A. C., Gelati, M., Fogel, E., Carnevale, E., and Nicosia, R. F. (2006). Angiopoietin-1 and vascular endothelial growth factor induce expression of inflammatory cytokines before angiogenesis. *Physiol. Genomics* 27, 20–28. doi: 10.1152/physiolgenomics.00048.2006
- Asahara, T., Takahashi, T., Masuda, H., Kalka, C., Chen, D., Iwaguro, H., et al. (1999). VEGF contributes to postnatal neovascularization by mobilizing bone marrow-derived endothelial progenitor cells. *EMBO J.* 18, 3964–3972. doi: 10.1093/emboj/18.14.3964
- Ballara, S., Taylor, P. C., Reusch, P., Marme, D., Feldmann, M., Maini, R. N., et al. (2001). Raised serum vascular endothelial growth factor levels are associated with destructive change in inflammatory arthritis. *Arthritis Rheum.* 44, 2055–2064. doi: 10.1002/1529-0131(200109)44
- Barsotti, M. C., Magera, A., Armani, C., Chiellini, F., Felice, F., Dinucci, D., et al. (2011). Fibrin acts as biomimetic niche inducing both differentiation and stem cell marker expression of early human endothelial progenitor cells. *Cell Prolif.* 44, 33–48. doi: 10.1111/j.1365-2184.2010.00715.x
- Bernardo, M. E., and Fibbe, W. E. (2013). Mesenchymal stromal cells: sensors and switchers of inflammation. *Cell Stem Cell* 13, 392–402. doi: 10.1016/j.stem.2013.09.006
- Blazquez-Martinez, A., Chiesa, M., Arnalich, F., Fernandez-Delgado, J., Nistal, M., and De Miguel, M. P. (2014). c-Kit identifies a subpopulation of mesenchymal stem cells in adipose tissue with higher telomerase expression and differentiation potential. *Differentiation* 87, 147–160. doi: 10.1016/j.diff.2014.02.007
- Bussolino, F., Wang, J. M., Defilippi, P., Turrini, F., Sanavio, F., Edgell, C. J., et al. (1989). Granulocyte- and granulocyte-macrophage-colony stimulating factors induce human endothelial cells to migrate and proliferate. *Nature* 337, 471–473. doi: 10.1038/337471a0
- Cohen, T., Nahari, D., Cerem, L. W., Neufeld, G., and Levi, B. Z. (1996). Interleukin 6 induces the expression of vascular endothelial growth factor. *J. Biol. Chem.* 271, 736–741. doi: 10.1074/jbc.271.2.736
- Corotchi, M. C., Popa, M. A., Remes, A., Sima, L. E., Gussi, I., and Lupu Plesu, M. (2013). Isolation method and xeno-free culture conditions influence multipotent differentiation capacity of human Wharton's jelly-derived mesenchymal stem cells. *Stem Cell Res. Ther.* 4:81. doi: 10.1186/scrt232
- Costa, C., Incio, J., and Soares, R. (2007). Angiogenesis and chronic inflammation: cause or consequence? *Angiogenesis* 10, 149–166. doi: 10.1007/s10456-007-9074-0
- Crisan, M., Yap, S., Castella, L., Chen, C. W., Corselli, M., Park, T. S., et al. (2008). A perivascular origin for mesenchymal stem cells in multiple human organs. *Cell Stem Cell* 3, 301–313. doi: 10.1016/j.stem.2008.07.003
- Davalos, D., and Akassoglou, K. (2012). Fibrinogen as a key regulator of inflammation in disease. *Semin. Immunopathol.* 34, 43–62. doi: 10.1007/s00281-011-0290-8
- De Bari, C. (2015). Are mesenchymal stem cells in rheumatoid arthritis the good or bad guys? *Arthritis Res. Ther.* 17:113. doi: 10.1186/s13075-015-0634-1
- Ferrara, N., Gerber, H.-P., and Lecouter, J. (2003). The biology of VEGF and its receptors. *Nat. Med.* 9, 669–676. doi: 10.1038/nm0603-669
- Fierlbeck, W., Liu, A., Coyle, R., and Ballermann, B. J. (2003). Endothelial cell apoptosis during glomerular capillary lumen formation *in vivo*. *J. Am. Soc. Nephrol.* 14, 1349–1354. doi: 10.1097/01.ASN.0000061779.70530.06
- Flick, M. J., Lajeunesse, C. M., Talmage, K. E., Witte, D. P., Palumbo, J. S., Pinkerton, M. D., et al. (2007). Fibrin(ogen) exacerbates inflammatory joint disease through a mechanism linked to the integrin alphaMbeta2 binding motif. *J. Clin. Invest.* 117, 3224–3235. doi: 10.1172/JCI30134
- Furuzawa-Carballeda, J., Macip-Rodriguez, P. M., and Cabral, A. R. (2008). Osteoarthritis and rheumatoid arthritis pannus have similar qualitative metabolic characteristics and pro-inflammatory cytokine response. *Clin. Exp. Rheumatol.* 26, 554–560.
- Galbraith, C. G., Yamada, K. M., and Galbraith, J. A. (2007). Polymerizing actin fibers position integrins primed to probe for adhesion sites. *Science* 315, 992–995. doi: 10.1126/science.1137904
- Giurea, A., Rüger, B. M., Hollemann, D., Yanagida, G., Kotz, R., and Fischer, M. B. (2006). STRO-1+ mesenchymal precursor cells located in synovial surface projections of patients with osteoarthritis. *Osteoarthr. Cartil.* 14, 938–943. doi: 10.1016/j.joca.2006.02.014

- Gottfried, E., Kunz-Schughart, L. A., Weber, A., Rehli, M., Peucker, A., Müller, A., et al. (2008). Expression of CD68 in non-myeloid cell types. *Scand. J. Immunol.* 67, 453–463. doi: 10.1111/j.1365-3083.2008.02091.x
- Holthoner, W., Hohenegger, K., Husa, A. M., Muehleder, S., Meinl, A., Peterbauer-Scherb, A., et al. (2015). Adipose-derived stem cells induce vascular tube formation of outgrowth endothelial cells in a fibrin matrix. *J. Tissue Eng. Regen. Med.* 9, 127–136. doi: 10.1002/term.1620
- Houssiau, F. A., Devogelaer, J. P., Van Damme, J., De Deuxchaisnes, C. N., and Van Snick, J. (1988). Interleukin-6 in synovial fluid and serum of patients with rheumatoid arthritis and other inflammatory arthritides. *Arthritis Rheum.* 31, 784–788. doi: 10.1002/art.1780310614
- Hur, J., Yoon, C. H., Kim, H. S., Choi, J. H., Kang, H. J., Hwang, K. K., et al. (2004). Characterization of two types of endothelial progenitor cells and their different contributions to neovascularogenesis. *Arterioscler. Thromb. Vasc. Biol.* 24, 288–293. doi: 10.1161/01.ATV.0000114236.77009.06
- Kagiyama, H., Yashiki, T., Ohshima, A., Tadokoro, M., Nagaya, N., and Ohgushi, H. (2008). Human mesenchymal stem cells as a stable source of VEGF-producing cells. *J. Tissue Eng. Regen. Med.* 2, 184–189. doi: 10.1002/term.79
- Lawlor, K. E., Campbell, I. K., Metcalf, D., O'donnell, K., Van Nieuwenhuijze, A., Roberts, A. W., et al. (2004). Critical role for granulocyte colony-stimulating factor in inflammatory arthritis. *Proc. Natl. Acad. Sci. U.S.A.* 101, 11398–11403. doi: 10.1073/pnas.0404328101
- Lee, G. Y., Kenny, P. A., Lee, E. H., and Bissell, M. J. (2007). Three-dimensional culture models of normal and malignant breast epithelial cells. *Nat. Methods* 4, 359–365. doi: 10.1038/nmeth1015
- Mabey, T., Honsawek, S., Saetan, N., Poovorawan, Y., Tanavalee, A., and Yuktanandana, P. (2014). Angiogenic cytokine expression profiles in plasma and synovial fluid of primary knee osteoarthritis. *Int. Orthop.* 38, 1885–1892. doi: 10.1007/s00264-014-2406-y
- Mannon, P. J., Leon, F., Fuss, I. J., Walter, B. A., Begnami, M., Quezado, M., et al. (2009). Successful granulocyte-colony stimulating factor treatment of Crohn's disease is associated with the appearance of circulating interleukin-10-producing T cells and increased lamina propria plasmacytoid dendritic cells. *Clin. Exp. Immunol.* 155, 447–456. doi: 10.1111/j.1365-2249.2008.03799.x
- Masuda, H., and Asahara, T. (2003). Post-natal endothelial progenitor cells for neovascularization in tissue regeneration. *Cardiovasc. Res.* 58, 390–398. doi: 10.1016/S0008-6363(02)00785-X
- Mattila, P. K., and Lappalainen, P. (2008). Filopodia: molecular architecture and cellular functions. *Nat. Rev. Mol. Cell Biol.* 9, 446–454. doi: 10.1038/nrm2406
- Morin, K. T., and Tranquillo, R. T. (2013). *In vitro* models of angiogenesis and vasculogenesis in fibrin gel. *Exp. Cell Res.* 319, 2409–2417. doi: 10.1016/j.yexcr.2013.06.006
- Nakamura, H., Ueki, Y., Sakito, S., Matsumoto, K., Yano, M., Miyake, S., et al. (2000). High serum and synovial fluid granulocyte colony stimulating factor (G-CSF) concentrations in patients with rheumatoid arthritis. *Clin. Exp. Rheumatol.* 18, 713–718.
- Natori, T., Sata, M., Washida, M., Hirata, Y., Nagai, R., and Makuuchi, M. (2002). G-CSF stimulates angiogenesis and promotes tumor growth: potential contribution of bone marrow-derived endothelial progenitor cells. *Biochem. Biophys. Res. Commun.* 297, 1058–1061. doi: 10.1016/S0006-291X(02)02335-5
- Ning, H., Lin, G., Lue, T. F., and Lin, C.-S. (2011). Mesenchymal stem cell marker Stro-1 is a 75 kd endothelial antigen. *Biochem. Biophys. Res. Commun.* 413, 353–357. doi: 10.1016/j.bbrc.2011.08.104
- Ohki, Y., Heissig, B., Sato, Y., Akiyama, H., Zhu, Z., Hicklin, D. J., et al. (2005). Granulocyte colony-stimulating factor promotes neovascularization by releasing vascular endothelial growth factor from neutrophils. *FASEB J.* 19, 2005–2007. doi: 10.1096/fj.04-3496fj
- Oswald, J., Boxberger, S., Jørgensen, B., Feldmann, S., Ehninger, G., Bornhäuser, M., et al. (2004). Mesenchymal stem cells can be differentiated into endothelial cells *in vitro*. *Stem Cells* 22, 377–384. doi: 10.1634/stemcells.22-3-377
- Pearson, M. J., Herndler-Brandstetter, D., Tariq, M. A., Nicholson, T. A., Philp, A. M., Smith, H. L., et al. (2017). IL-6 secretion in osteoarthritis patients is mediated by chondrocyte-synovial fibroblast cross-talk and is enhanced by obesity. *Sci. Rep.* 7:3451. doi: 10.1038/s41598-017-03759-w
- Powell, T. M., Paul, J. D., Hill, J. M., Thompson, M., Benjamin, M., Rodrigo, M., et al. (2005). Granulocyte colony-stimulating factor mobilizes functional endothelial progenitor cells in patients with coronary artery disease. *Arterioscler. Thromb. Vasc. Biol.* 25, 296–301. doi: 10.1161/01.ATV.0000151690.43777.e4
- Rüger, B., Giurea, A., Wanivenhaus, A. H., Zehetgruber, H., Hollemann, D., Yanagida, G., et al. (2004). Endothelial precursor cells in the synovial tissue of patients with rheumatoid arthritis and osteoarthritis. *Arthritis Rheum.* 50, 2157–2166. doi: 10.1002/art.20506
- Rüger, B. M., Breuss, J., Hollemann, D., Yanagida, G., Fischer, M. B., Mosberger, I., et al. (2008). Vascular morphogenesis by adult bone marrow progenitor cells in three-dimensional fibrin matrices. *Differentiation* 76, 772–783. doi: 10.1111/j.1432-0436.2007.00259.x
- Scanzello, C. R., Plaas, A., and Crow, M. K. (2008). Innate immune system activation in osteoarthritis: is osteoarthritis a chronic wound? *Curr. Opin. Rheumatol.* 20, 565–572. doi: 10.1097/BOR.0b013e32830aba34
- Scheller, J., Chalaris, A., Schmidt-Arras, D., and Rose-John, S. (2011). The pro- and anti-inflammatory properties of the cytokine interleukin-6. *Biochim. Biophys. Acta* 1813, 878–888. doi: 10.1016/j.bbamcr.2011.01.034
- Sigurbjörnsdóttir, S., Mathew, R., and Leptin, M. (2014). Molecular mechanisms of de novo lumen formation. *Nat. Rev. Mol. Cell Biol.* 15, 665–676. doi: 10.1038/nrm3871
- Sokolove, J., and Lepus, C. M. (2013). Role of inflammation in the pathogenesis of osteoarthritis: latest findings and interpretations. *Ther. Adv. Musculoskelet. Dis.* 5, 77–94. doi: 10.1177/1759720X12467868
- Stratman, A. N., Malotte, K. M., Mahan, R. D., Davis, M. J., and Davis, G. E. (2009). Pericyte recruitment during vasculogenic tube assembly stimulates endothelial basement membrane matrix formation. *Blood* 114, 5091–5101. doi: 10.1182/blood-2009-05-222364
- Sugimori, N., Nakao, S., Yachie, A., Niki, T., Takami, A., Yamazaki, H., et al. (1999). Administration of G-CSF to normal individuals diminishes L-selectin+ T cells in the peripheral blood that respond better to alloantigen stimulation than L-selectin- T cells. *Bone Marrow Transplant.* 23, 119–124. doi: 10.1038/sj.bmt.1701552
- Suzuki, S., Kobayashi, M., Chiba, K., Horiuchi, I., Wang, J., Kondoh, T., et al. (2002). Autocrine production of epithelial cell-derived neutrophil attractant-78 induced by granulocyte colony-stimulating factor in neutrophils. *Blood* 99, 1863–1865. doi: 10.1182/blood.V99.5.1863
- Tertemiz, F., Kayisli, U. A., Arici, A., and Demir, R. (2005). Apoptosis contributes to vascular lumen formation and vascular branching in human placental vasculogenesis. *Biol. Reprod.* 72, 727–735. doi: 10.1095/biolreprod.104.034975
- Tzeng, H.-E., Tsai, C.-H., Chang, Z.-L., Su, C.-M., Wang, S.-W., Hwang, W.-L., et al. (2013). Interleukin-6 induces vascular endothelial growth factor expression and promotes angiogenesis through apoptosis signal-regulating kinase 1 in human osteosarcoma. *Biochem. Pharmacol.* 85, 531–540. doi: 10.1016/j.bcp.2012.11.021
- Verseijden, F., Posthumus-Van Sluijs, S. J., Pavljasevic, P., Hofer, S. O. P., Van Osch, G. J. V. M., and Farrell, E. (2010). Adult human bone marrow- and adipose tissue-derived stromal cells support the formation of prevascular-like structures from endothelial cells *in vitro*. *Tissue Eng. Part A* 16, 101–114. doi: 10.1089/ten.tea.2009.0106
- Yang, K.-Q., Liu, Y., Huang, Q.-H., Mo, N., Zhang, Q.-Y., Meng, Q.-G., et al. (2017). Bone marrow-derived mesenchymal stem cells induced by inflammatory cytokines produce angiogenic factors and promote prostate cancer growth. *BMC Cancer* 17:878. doi: 10.1186/s12885-017-3879-z

**Conflict of Interest Statement:** The authors declare that the research was conducted in the absence of any commercial or financial relationships that could be construed as a potential conflict of interest.

The reviewer SC and handling Editor declared their shared affiliation.

Copyright © 2018 Rüger, Buchacher, Giurea, Kubista, Fischer and Breuss. This is an open-access article distributed under the terms of the Creative Commons Attribution License (CC BY). The use, distribution or reproduction in other forums is permitted, provided the original author(s) and the copyright owner are credited and that the original publication in this journal is cited, in accordance with accepted academic practice. No use, distribution or reproduction is permitted which does not comply with these terms.

# Advantages of publishing in Frontiers



## OPEN ACCESS

Articles are free to read for greatest visibility and readership



## FAST PUBLICATION

Around 90 days from submission to decision



## HIGH QUALITY PEER-REVIEW

Rigorous, collaborative, and constructive peer-review



## TRANSPARENT PEER-REVIEW

Editors and reviewers acknowledged by name on published articles

## Frontiers

Avenue du Tribunal-Fédéral 34  
1005 Lausanne | Switzerland

Visit us: [www.frontiersin.org](http://www.frontiersin.org)

Contact us: [info@frontiersin.org](mailto:info@frontiersin.org) | +41 21 510 17 00



## REPRODUCIBILITY OF RESEARCH

Support open data and methods to enhance research reproducibility



## DIGITAL PUBLISHING

Articles designed for optimal readership across devices



## FOLLOW US

[@frontiersin](https://twitter.com/frontiersin)



## IMPACT METRICS

Advanced article metrics track visibility across digital media



## EXTENSIVE PROMOTION

Marketing and promotion of impactful research



## LOOP RESEARCH NETWORK

Our network increases your article's readership